

Tom Proulx *Editor*

Experimental and Applied Mechanics, Volume 6

Proceedings of the 2010 Annual Conference on
Experimental and Applied Mechanics



 Springer

The Springer logo, which consists of a stylized chess knight piece inside a white circle, followed by the word 'Springer' in a serif font.

Conference Proceedings of the Society for Experimental Mechanics Series

For other titles published in this series, go to
www.springer.com/series/8922

Tom Proulx
Editor

Experimental and Applied Mechanics, Volume 6

Proceedings of the 2010 Annual Conference on Experimental
and Applied Mechanics

Editor

Tom Proulx
Society for Experimental Mechanics, Inc.
7 School Street
Bethel, CT 06801-1405
USA
tom@sem1.com

ISSN 2191-5644 e-ISSN 2191-5652
ISBN 978-1-4419-9497-4 e-ISBN 978-1-4419-9792-0
DOI 10.1007/978-1-4419-9792-0
Springer New York Dordrecht Heidelberg London

Library of Congress Control Number: 2011928691

© The Society for Experimental Mechanics, Inc. 2011

All rights reserved. This work may not be translated or copied in whole or in part without the written permission of the publisher (Springer Science+Business Media, LLC, 233 Spring Street, New York, NY 10013, USA), except for brief excerpts in connection with reviews or scholarly analysis. Use in connection with any form of information storage and retrieval, electronic adaptation, computer software, or by similar or dissimilar methodology now known or hereafter developed is forbidden.

The use in this publication of trade names, trademarks, service marks, and similar terms, even if they are not identified as such, is not to be taken as an expression of opinion as to whether or not they are subject to proprietary rights.

Printed on acid-free paper

Springer is part of Springer Science+Business Media (www.springer.com)

Preface

Experimental and Applied Mechanics represents the largest of six tracks of technical papers presented at the Society for Experimental Mechanics Annual Conference & Exposition on Experimental and Applied Mechanics, held at Indianapolis, Indiana, June 7-10, 2010. The full proceedings also include volumes on Dynamic Behavior of Materials, Role of Experimental Mechanics on Emerging Energy Systems and Materials, Application of Imaging Techniques to Mechanics of Materials and Structures, along with the 11th International Symposium on MEMS and Nanotechnology, and the Symposium on Time Dependent Constitutive Behavior and Failure/Fracture Processes.

Each collection presents early findings from experimental and computational investigations on an important area within Experimental Mechanics. The current volume on the *Experimental and Applied Mechanics* includes studies on Nano-Engineering, Micro-Nano Mechanics, Measurements and Modeling, Applied Photoelasticity Residual Stress Measurement Techniques, Thermal Methods, Bio-Composites Cell Mechanics, Interfacial Fracture Phenomena, Mechanics and Mechanobiology of Soft Tissues and Hydrogels, Fatigue, Fracture, Structural Dynamics/Acoustics Residual Stress and Fatigue in Fracture, Recent Progress in DIC Methodology Design and Processing of Composites, Inverse Problems, and Characterization of Materials

Experimental and Applied Mechanics covers the wide variety of subjects that are related to the broad field of experimental or applied mechanics. It is SEM's mission to disseminate information on a good selection of subjects. To this end, research and application papers relate to the broad field of experimental mechanics.

The organizers would like to thank the authors, presenters, session organizers and session chairs for their participation in this track

The Society would like to thank the organizers of the track, Ryszard J. Pryputniewicz, *Worcester Polytechnic Institute*; John Lambros, *University of Illinois at Urbana-Champaign*; Hugh A. Bruck, *University of Maryland, College Park* for their efforts.

Bethel, Connecticut

Dr. Thomas Proulx
Society for Experimental Mechanics, Inc

Contents

1 High Accuracy Optical Measurements of Surface Topography	1
C.A. Sciammarella, L. Lamberti, F.M. Sciammarella	
2 Industrial Finishes of Ceramic Surfaces at the Micro-level and its Influence on Strength	9
F.M. Sciammarella, C.A. Sciammarella, L. Lamberti, B. Burra	
3 Elastic Properties of Living Cells	17
M.C. Frassanito, L. Lamberti, P. Pappalettere	
4 Standards for Validating Stress Analyses by Integrating Simulation and Experimentation	23
E. Hack, G. Lampeas, J. Mottershead, E.A. Patterson, T. Siebert, M. Whelan	
5 Avalanche Behavior of Minute Deformation Around Yield Point of Polycrystalline Pure Ti	31
G. Murasawa, T. Morimoto, S. Yoneyama, A. Nishioka, K. Miyata, T. Koda	
6 The Effect of Noise on Capacitive Measurements of MEMS Geometries	43
J.L. Chee, J.V. Clark	
7 Effects of Clearance on Thick, Single-Lap Bolted Joints Using Through-the-thickness Measuring Techniques	53
J. Woodruff, G. Marannano, G. Restivo	
8 Deformation and Performance Measurements of MAV Flapping Wings	63
P. Wu	
9 Dynamic Constitutive Behavior of Aluminum Alloys: Experimental & Numerical Studies	65
S. Abotula	
10 Estimating Surface Coverage of Gold Nanoparticles Deposited on MEMS	67
N. Ansari, K.M. Hurst, W.R. Ashurst	

11 Functionally Graded Metallic Structure for Bone Replacement S. Bender	69
12 Dissipative Energy as an Indicator of Material Microstructural Evolution N. Connesson, F. Maquin, F. Pierron	71
13 Temporal Phase Stepping Photoelasticity by Load or Wavelength M.J. Huang, H.L. An	73
14 Determination of the Isoclinic Map for Complex Photoelastic Fringe Patterns P. Siegmann, C. Colombo, F. Díaz-Garrido, E. Patterson	79
15 A Study on the Behaviors and Stresses of O-ring Under Uniform Squeeze Rates and Internal Pressure by Transparent Type Photoelastic Experiment J.-S. Hawong, D.-C. Shin, J.H. Nam	87
16 Strength Physics at Nano-scale and Application of Optical Interferometry S. Yoshida	95
17 Light Generation at the Nano Scale, Key to Interferometry at the Nano Scale C.A. Sciammarella, L. Lamberti, F.M. Sciammarella	103
18 Mechanical Characterization of Nanowires Using a Customized Atomic Force Microscope E. Celik, I. Guven, E. Madenci	117
19 Blast Performance of Sandwich Composites With Functionally Graded Core N. Gardne, A. Shukla	127
20 Thermal Softening of an UFG Aluminum Alloy at High Rates E.L. Huskins, K.T. Ramesh	129
21 Blast Loading Response of Glass Panels P. Kumar, A. Shukla	131
22 Novel Approach to 3D Imaging Based on Fringe Projection Technique D.A. Nguyen	133
23 Measuring Shear Stress in Microfluidics Using Traction Force Microscopy B. Mueller	135
24 Efficiency Enhancement of Dye-sensitized Solar Cell C.-H. Chien, M.-L. Tsai, T.-H. Su, C.-C. Hsieh, Y.-H. Li, L.-C. Chen, H.-D. Gau	137
25 Integration of Solar Cell With TN-LC Cell for Enhancing Power Characteristics C.-Y. Chen, Y.-L. Lo	145

26 Full-field Measuring System for the Surface of Solar Cell	151
S.-A. Tsai, Y.-L. Lo	
27 Photographic Diagnosis of Crystalline Silicon Solar Cells by Electroluminescence	159
T. Fuyuki, A. Tani	
28 Novel Interfacial Adhesion Experiments With Individual Carbon Nanofibers	163
T. Ozkan, I. Chasiotis	
29 Dynamic Constitutive Behavior of Reinforced Hydrogels Inside Liquid Environment	165
S. Padamati	
30 Osteon Size Effect on the Dynamic Fracture Toughness of Bone	167
M. Raetz	
31 Radial Inertia in Non-cylindrical Specimens in a Kolsky Bar	169
O. Sen	
32 Core Deformation of Sandwich Composites Under Blast Loading	171
E. Wang, A. Shukla	
33 Influence of Friction-stir-welding Parameters on Texture and Mechanical Behavior	173
Z. Yu, H. Choo, W. Zhang, Z. Feng, S. Vogel	
34 Measurement of Stresses in Pipelines Using Hole Drilling Rosettes	175
G.R. Delgadillo, F. Fiorentini, L.D. Rodrigues, J.L.F. Freire, R.D. Vieira	
35 Incremental Computation Technique for Residual Stress Calculations Using the Integral Method	185
G.S. Schajer, T.J. Rickert	
36 Experimental Investigation of Residual Stresses in Water and Air Quenched Aluminum Alloy Castings	193
B. Xiao, Y. Rong, K. Li	
37 Residual Stress on AISI 300 Sintered Materials	201
C. Casavola, C. Pappalettere, F. Tursi	
38 Practical Experiences in Hole Drilling Measurements of Residual Stresses	209
P.S. Whitehead	
39 Destructive Methods for Measuring Residual Stresses: Techniques and Opportunities	221
G.S. Schajer	
40 The Contour Method Cutting Assumption: Error Minimization and Correction	233
M.B. Prime, A.L. Kastengren	

41 Measurements of Residual Stress in Fracture Mechanics Coupons	251
M.R. Hill, J.E. VanDalen, M.B. Prime	
42 Analysis of Large Scale Composite Components Using TSA at Low Cyclic Frequencies	259
J.M. Dulieu-Barton, D.A. Crump	
43 Determining Stresses Thermoelastically Around Neighboring Holes Whose Associated Stresses Interact	267
A.A. Khaja, R.E. Rowlands	
44 Crack Tip Stress Fields Under Biaxial Loads Using TSA	275
R.A. Tomlinson	
45 Extending TSA With a Polar Stress Function to Non-circular Cutouts	279
A.A. Khaja, R.E. Rowlands	
46 Novel Synthetic Material Mimicking Mechanisms From Natural Nacre	289
A. Juster, F. Latourte, H.D. Espinosa	
47 Mechanical Characterization of Synthetic Vascular Materials	291
A.R. Hamilton, C. Fourastie, A.C. Karony, S.C. Olugebefola, S.R. White, N.R. Sottos	
48 MgO Nanoparticles Affect on the Osteoblast Cell Function and Adhesion Strength of Engineered Tissue Constructs	295
M. Khandaker, K. Duggan, M. Perram	
49 Mechanical Interactions of Mouse Mammary Gland Cells With a Three-dimensional Matrix Construct	301
M.d.C. Lopez-Garcia, D.J. Beebe, W.C. Crone	
50 Tracking Nanoparticles Optically to Study Their Interaction With Cells	307
J.-M. Gineste, P. Macko, E. Patterson, M. Whelan	
51 Coherent Gradient Sensing Microscopy: Microinterferometric Technique for Quantitative Cell Detection	311
M. Budyansky, C. Madormo, G. Lykotrafitis	
52 Rate Effects in the Failure Strength of Extraterrestrial Materials	317
J. Kimberley, K.T. Ramesh, O.S. Barnouin	
53 Determination of Dynamic Tensile Properties for Low Strength Brittle Solids	321
R. Chen, F. Dai, L. Lu, F. Lu, K. Xia	
54 The Mechanical Response of Aluminum Nitride at Very High Strain Rates	327
G. Hu, K.T. Ramesh, J.W. McCauley	

55 Dynamic and Quasi-static Measurements of C-4 and Primasheet P1000 Explosives	329
G.W. Brown, D.G. Thompson, R. DeLuca, P.J. Rae, C.M. Cady, S.N. Todd	
56 Dynamic Characterization of Mock Explosive Material Using Reverse Taylor Impact Experiments	337
L. Ferranti, Jr., F.J. Gagliardi, B.J. Cunningham, K.S. Vandersall	
57 Mechanical Behavior of Hierarchically-structured Polymer Composites	347
A.L. Gershon, H.A. Bruck	
58 Composite Design Through Biomimetic Inspirations	355
S.A. Tekalur, M. Raetz, A. Dutta	
59 Nano-composite Sensors for Wide Range Measurement of Ligament Strain	359
T. Hyatt, D. Fullwood, R. Bradshaw, A. Bowden, O. Johnson	
60 Advanced Biologically-inspired Flapping Wing Structure Development	365
L. Xie, P. Wu, P. Ifju	
61 Characterization of Electrode-electrolyte Interface Strengths in SOFCs	373
S. Akanda, M.E. Walter	
62 Die Separation Strength for Deep Reactive Ion Etched Wafers	383
D.A. Porter, T.A. Berfield	
63 Temperature Moisture and Mode Mixity Dependent EMC- Copper (Oxide) Interfacial Toughness	393
A. Xiao, G. Schlottig, H. Pape, B. Wunderle, K.M.B Jansen, L.J. Ernst	
64 An Integrated Experimental and Numerical Analysis on Notch and Interface Interaction in Same-materials	405
A. Krishnan, L.R. Xu	
65 Differentiation of Human Embryonic Stem Cells Encapsulated in Hydrogel Matrix Materials	415
M. Salick, R.A. Boyer, C.H. Koonce, T.J. Kamp, S.P. Palecek, K.S. Masters, W.C. Crone	
66 Nonlinear Viscoelasticity of Native and Engineered Ligament and Tendon	423
J. Ma, E.M. Arruda	
67 Spinal Ligaments: Anisotropic Characterization Using Very Small Samples	429
R.J. Bradshaw, A.C. Russell, A.E. Bowden	
68 In-Flight Wing-membrane Strain Measurements on Bats	437
R. Albertani, T. Hubel, S.M. Swartz, K.S. Breuer, J. Evers	

69 The Mechanical Properties of Musa Textilis Petiole	447
N.-S. Liou, S.-F. Chen, G.-W. Ruan	
70 Analysis of Strain Energy Behavior Throughout a Fatigue Process	451
O. Scott-Emuakpor, T. George, C. Cross, M.-H.H. Shen	
71 Relating Fatigue Strain Accumulation to Microstructure Using Digital Image Correlation	459
J. Carroll, W. Abuzaid, M. Casperson, J. Lambros, H. Sehitoglu, M. Spottswood, R. Chona	
72 High Cycle Fatigue of Structural Components Using Critical Distance Methods	463
S. Chattopadhyay	
73 Crack Propagation Analysis of New Galata Bridge	471
K. Ozakgul, O. Caglayan, O. Tezer, E. Uzgider	
74 Stress-dependent Elastic Behaviour of a Titanium Alloy at Elevated Temperatures	479
T.K. Heckel, A.G. Tovar, H.-J. Christ	
75 Numerical and Experimental Modal Analysis Applied to the Membrane of Micro Air Vehicles Pliant Wings	487
U.K. Chakravarty, R. Albertani	
76 Objective Determination of Acoustic Quality in a Multipurpose Auditorium	501
B. Hayes, C. Braden, R. Averbach, V. Ranatunga	
77 Identification and Enhancement of On-stage Acoustics in a Multipurpose Auditorium	517
C. Braden, B. Hayes, R. Averbach, V. Ranatunga	
78 Fractional Calculus of Hydraulic Drag in the Free Falling Process	529
Y. Wan, R.M. French	
79 Fatigue Cracks In Fibre Metal Laminates in the Presence of Rivets and Cold Expanded Holes	541
D. Backman, E.A. Patterson	
80 Effect of Nonlinear Parametric Model Accuracy in Crack Prediction and Detection	549
T.A. Doughty, N.S. Higgins	
81 Optical Based Residual Strain Measurements	557
J. Burnside, W. Ranson, D. Snelling	
82 Correlating Fatigue Life With Elastic and Plastic Strain Data	561
S.M. Grendahl, D.J. Snoha, B.S. Matlock	

83 Monitoring Crack Tip Plastic Zone Size During Fatigue Loading	569
Y. Du, A. Patki, E. Patterson	
84 Studying Thermomechanical Fatigue of Hastelloy X Using Digital Image Correlation	575
M. Casperson, J. Carroll, W. Abuzaid, J. Lambros, H. Sehitoglu, M. Spottswood, R. Chona	
85 Understanding Mechanisms of Cyclic Plastic Strain Accumulation Under High Temperature Loading Conditions	579
W. Abuzaid, H. Sehitoglu, J. Lambros, J. Carroll, M. Casperson, R. Chona	
86 Simulated Corrosion-fatigue via Ocean Waves on 2024-aluminum	583
E. Okoro, M.N. Cavalli	
87 The Effect of Processing Conditions on the Properties of Thermoplastic Composites	591
F.P. Cook, S.W. Case	
88 Calculation of Shells and Plates Constructed From Composite Materials	599
R. Tskvedadze, G. Kipiani, D. Tabatadze	
89 Reducing Build Variation in Arched Guitar Plates	607
E. Efendy, M. French	
90 Rotation Angle Measurement Using an Electro-optic Heterodyne Interferometer	621
J.-F. Lin, C.-J. Weng, K.-L. Lee, Y.-L. Lo	
91 Digital Shadow Moiré Measurement of Out-of-Plane Hygrothermal Displacement of TFT-LCD Backlight Modules	627
W.-C. Wang, Y.-H. Chang	
92 Theory and Applications of Universal Phase-shifting Algorithm	641
T. Hoang, Z. Wang, D. Nguyen	
93 Evaluation of Crash Energy Absorption Capacity of a Tearing Tube	647
Y. Ko, K. Ahn, H. Huh, W. Choi, H. Jung, T. Kwon	
94 Fracture Studies Combining Photoelasticity and Coherent Gradient Sensing for Stress Determination	655
S. Kramer	
95 Strength and Fracture Behavior of Diffusion Bonded Joints	677
A.H.M.E. Rahman, M.N. Cavalli	
96 Fabrication and Characterization of Novel Graded Bone Implant Material	683
S. Bender, S.D. El Wakil, V.B. Chalivendra, N. Rahbar, S. Bhowmick	

97	A Dynamic Design Model for Teaching T.K. Kundra	689
98	Video Demonstrations to Enhance Learning of Mechanics of Materials Inside and Outside the Classroom M. Dietzler, W.C. Crone	697
99	Experimentation and Product-making Workshop Simplified for Easy Execution in Classroom T. Nakazawa, M. Matsubara, S. Mita, K. Saitou	703
100	Illustrating Essentials of Experimental Stress Analysis Using a U-Shaped Beam M.E. Tuttle	711
101	Demonstration of Rod-wave Velocity in a Lecture Class D. Goldar	721
102	Influence of Friction-stir-welding Parameters on Texture and Tensile Behavior Z. Yu, H. Choo, W. Zhang, Z. Feng, S. Vogel	725
103	Comparing Two Different Approaches to the Identification of the Plastic Parameters of Metals in Post-necking Regime A. Baldi, A. Medda, F. Bertolino	727
104	Determination of Hardening Behaviour and Contact Friction of Sheet Metal in a Multi-layered Upsetting Test S. Coppieters, P. Lava, H. Sol, P. Van Houtte, D. Debruyne	733
105	Measuring the Elastic Modulus of Soft Thin Films on Substrates M.J. Wald, J.M. Considine, K.T. Turner	741
106	Characterization in Birefringence/Diattenuation of an Optical Fiber in a Fiber-type Polarimetry T.-T.-H. Pham, P.-C. Chen, Y.-L. Lo	749
107	Predictive Fault Detection for Missile Defense Mission Equipment and Structures J.S. Yalowitz, R.K. Youree, A. Corder, T.K. Ooi	757
108	Portable Maintenance Support Tool Enhancing Battle Readiness of MDA Structures and Vehicles T. Niblock, J. O'Day, D. Darr, B.C. Laskowski, H. Baid, A. Mal, T.K. Ooi, A. Corder	765
109	A Compact System for Measurement of Absorbance of Light A.J. Masi, M. Sesselmann, D.L. Rodrigues	773
110	Fracture Mechanics Analysis in Frost Breakage of Reservoir Revetment on Cold Regions X. Liu, L. Peng	781

111 Combined Experimental/Numerical Assessment of Compression After Impact of Sandwich Composite Structures	793
M.W. Czabaj, A.T. Zehnder, B.D. Davidson, A.K. Singh, D.P. Eisenberg	
112 Mechanical Behavior of Co-continuous Polymer Composites	801
L. Wang, J. Lau, N.V. Soane, M.J. Rosario, M.C. Boyce	
113 Laboratory Evaluation of a Silicone Foam Sealant for Field Application on Bridge Expansion Joints	805
R.B. Malla, B.J. Swanson, M.T. Shaw	
114 Effect of Prior Cold Work on the Mechanical Properties of Weldments	817
M. Acar, S. Gungor, P.J. Bouchard, M.E. Fitzpatrick	
115 Use of Viscoplastic Models for Prediction of Deformation of Polymer Parts	827
N.G. Ohlson	
116 Mechanical Characterization of SLM Specimens With Speckle Interferometry and Numerical Optimization	837
C. Barile, C. Casavola, G. Pappalettera, C. Pappalettere	
117 Torsion/compression Testing of Grey Cast Iron for a Plasticity Model	845
T.A. Doughty, M. LeBlanc, L. Glascoe, J. Bernier	
118 Nucleation and Propagation of Portevin-Le Châtelier Bands in Austenitic Steel With Twinning Induced Plasticity	855
L.G. Hector, Jr., P.D. Zavattieri	
119 Identification and Enhancement of On-stage Acoustics in a Multipurpose Auditorium	865
C. Braden, B. Hayes, R. Averbach, V. Ranatunga	
120 Determination of Objective Architectural Acoustic Quality of a Multi-purpose Auditorium	867
B. Hayes, C. Braden, R. Averbach, V. Ranatunga	
121 Notch-interface Experiments to Determine the Crack Initiation Loads	869
A. Krishnan	
122 Mechanical Characterization of Alternating Magnetic Field Responsive Hydrogels at Micro-scale	871
S. Meyer, L. Nickelson, R. Shelby, J. McGuirt, J. Peng, S. Ghosh	
123 Investigation of a Force Hardening Spring System	873
E. Jones, D. Prisco	
124 Resonance Behavior of Magnetostrictive Sensor in Biological Agent Detection	875
M. Ramasamy, B.C. Prorok	

125 Detection of Damage Initiation and Growth of Carbon Nanotube Reinforced Epoxy Composites V.K. Vadlamani	877
126 Nano-mechanical Characterization of Polypropylene Fibers Exposed to Ultraviolet and Thermal Degradation N.D. Wanasekara	879
127 Detachment Dynamics of Cancer Cells C.C. Wong, J. Reboud, J. Soon, P. Neuzil, K. Liao	881
128 Compression Testing of Biomimetic Bones With 3D Deformation Measurements H. Yao, W. Tong	883

HIGH ACCURACY OPTICAL MEASUREMENTS OF SURFACE TOPOGRAPHY

C.A. Sciammarella*, L. Lamberti**, F.M. Sciammarella*

*Northern Illinois University, Department of Mechanical Engineering, 590 Garden Road, DeKalb, IL 60115, USA

**Politecnico di Bari, Dipartimento di Ingegneria Meccanica e Gestionale, Viale Japigia 182, Bari, 70126, ITALY

E-mail: sciammarella@niu.edu, sciammarella@iit.edu, lamberti@poliba.it

Abstract

Surface characterization is a very important aspect of industrial manufacturing. All engineering parts are strongly affected in their performance by properties depending on surface topography. For this reason methodologies able to provide a functional representation of surface topography are of paramount importance. Among the many techniques available to get surface topography optical techniques play a fundamental role. A digital moiré contouring technique recently proposed by the authors provides a new approach to the study of surface topography. This paper presents further developments in surface topography analysis particularly with respect to the resolution that can be currently obtained. The validity of the proposed approach is checked by analyzing existing standards for surface roughness determination. Optical results are compared with NIST certified standard specimen.

1. INTRODUCTION

Surface characterization is a very important aspect of industrial manufacturing because structural behavior of all engineering parts is strictly related with surface topography. For example, fatigue strength decreases dramatically as surface roughness increases. Another example of the deep relationships between mechanical behavior and surface properties occurs in contact problems where distribution of strains and stresses can be determined at different scales each of which corresponds to a specified level of roughness.

Surface topography can be reconstructed by means of mechanical probes or non contact optical techniques. The latter approach is certainly preferable as optical methods provide full-field information at high vertical and lateral resolution. Ref. [1] illustrated the successful application of a new measurement technique based on the use of non conventional illumination to the analysis of the contact between rough surfaces. The methodology proposed in [1] is based on the emission of coherent light from the same surface that is under analysis through the phenomenon of the generation of plasmons.

This paper presents further developments in surface topography analysis particularly with respect to the resolution that can be currently obtained. The validity of the proposed approach is checked by analyzing existing standards for surface roughness determination. Optical results are compared with NIST certified standard specimen. The paper is structured as follows. After the introduction section, Section 2 describes the methodology prescribed by standards for roughness determination. Section 3 outlines the theoretical basis of the measurement technique. The experimental setup is described in Section 4. Results are presented and discussed in Section 5. Finally, the main findings of the study are summarized in Section 6.

2. MEASUREMENTS OF SURFACE ROUGHNESS ACCORDING TO ANSI B46.1 STANDARDS

Figure 1a shows the HQC226 precision standard (Holts, Dambury, CT) analyzed in this paper. The specimen geometry is sketched in Figure 1b: the standard is shaped as a saw tooth pattern. The specimen is realized by molding. The nominal distance from peak to peak is 100 μm . The nominal height of the peak is 6 μm .

Accordingly to the ANSI B46.1 standard [2], the value of roughness R_a is defined as the area of a triangle divided by width (also mean of height, area in blue in Figure 1b). In the NIST procedure, the profile of the standard is measured by a stylus with radius of curvature of 2 μm . A region of 4 mm is assessed. The stylus follows the precision standard surface and records the waviness of the surface. The point coordinates describing the profile are filtered. Since the nominal wavelength of asperities is 100 μm , anything larger than that is removed by the filter. The wavelength corresponding to the lowest frequency filter to be used in the analysis of experimental data is defined as the sampling length. Most standards recommend the measurement length be at least 7 times longer than the sampling length. The Nyquist-Shannon's sampling theorem states that the measurement length should be at least ten times longer than the wavelength of

interesting features. The assessment length or evaluation length is the length containing the data used for the analysis. One sampling length is usually discarded from each end of measurement length.

Figure 1c shows the five locations on the standard where traces were run. The measured values for Ra are also indicated in the figure: the mean value of Ra is 3.03276 microns (i.e. 119.4 microinches).

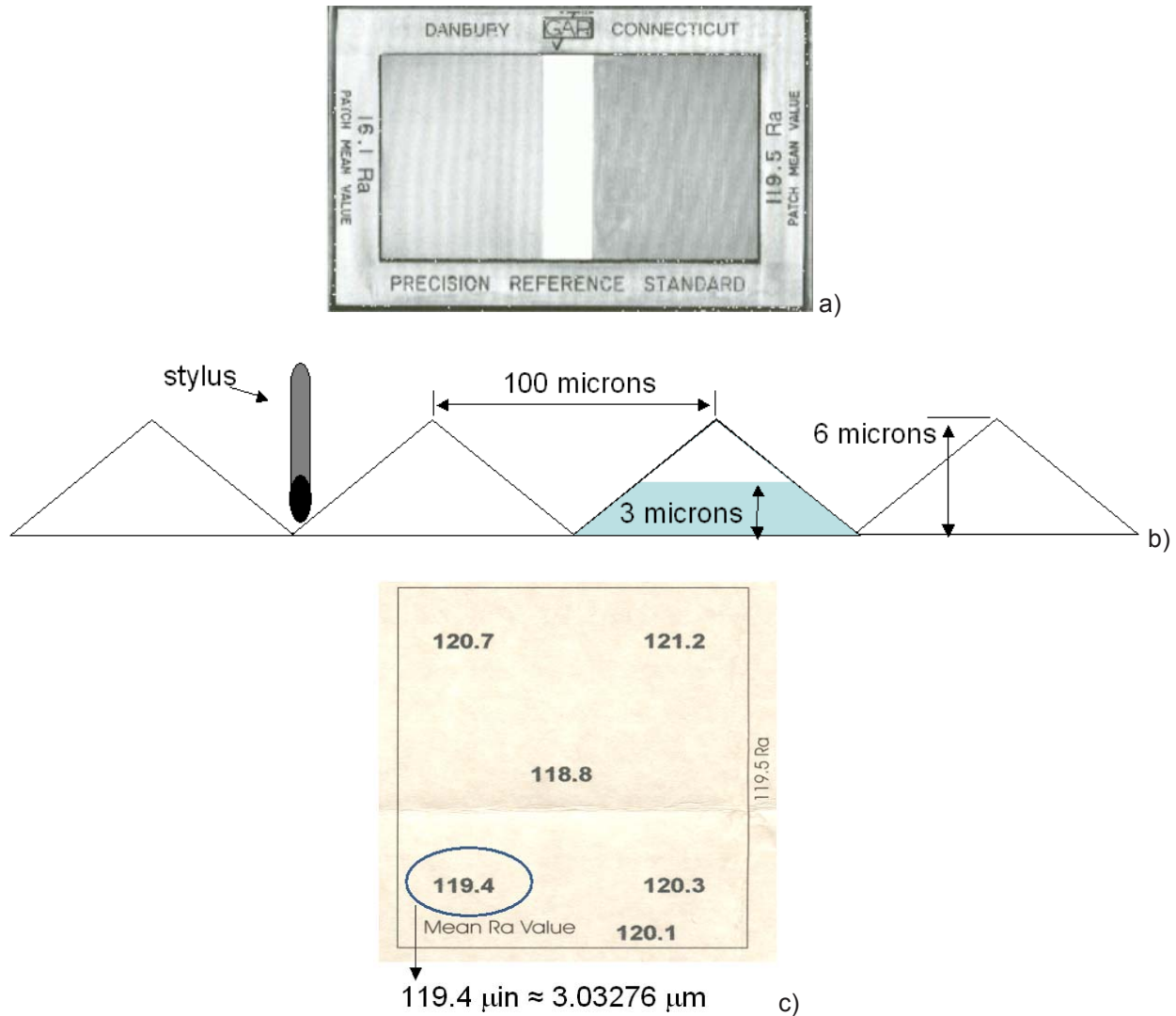


Figure 1. a) HQC226 standard; b) Schematic of the standard; c) Roughness values measured by NIST in the target area

3. DESCRIPTION OF THE CONTOURING MODEL

The theoretical foundation of the measurement method was explained in [1]. The experimental set up includes a double interface creating a cavity. This cavity then acts as a passive optical resonator so that resonances can be observed from the emitted light. In order to utilize this information three aspects should be considered: (i) direction of the emerging wave vectors; (ii) changes of the gap depth; (iii) polarization of the light. [1]

In the experimental setup of [1] the cavity was represented as a Fabry-Perot resonator. The illumination system consisted of a beam going through a glass plate and impinging in the surface of the glass plate at an angle with respect to the normal to the plate larger than the limit angle. The system of fringes thus generated is equivalent to the first diffraction order of a sinusoidal grating of pitch [1]:

$$p = \frac{\lambda}{2 \sin \theta_i} \quad (1)$$

where θ_i is the angle that the beam forms with the surface.

The illumination process of the surface was modified in this research by introducing an actual grating on top of the surface to be measured. The actual process of fringe formation is very complex because the illumination of the surface is obtained through evanescent fields. In the limited context of this article it is not possible to present all the derivations but results can be summarized as follows. For single illumination, it holds:

$$h = \frac{p}{2 \cdot n \sin \theta_o} \quad (2)$$

where p is the pitch of the utilized grating, n is the diffraction order observed and θ_o is the angle of illumination with respect to the normal to the surface of the grating. The value of θ_o is computed with the following equation:

$$\theta_o = \frac{\pi}{2} - \arcsin \left(\frac{1}{2} \cdot \frac{\lambda}{p} \right) \quad (3)$$

That is, the inclination of the beam with respect to the normal to the surface is larger than that of the limit angle of total reflection. Consequently, the illumination of the surface is done through the evanescent field. In the applications presented in this paper the utilized values are: $p=2.5 \mu\text{m}$; $\lambda=0.635 \mu\text{m}$. With the above values, for $n=1$, it follows:

$$\theta_o = 90^\circ - \arcsin \left(\frac{1}{2} \cdot \frac{0.635}{2.5} \right) = 82.704^\circ \quad (4)$$

The resulting sensitivity is:

$$S = \frac{2.5}{\sin(82.704^\circ)} = 2.520 \mu\text{m} \quad (5)$$

In the case of double illumination, the corresponding equation is:

$$h = \frac{p}{2 \cdot 2n \sin \theta_o} \quad (6)$$

while sensitivity is:

$$S = \frac{2.5}{2 \cdot 2 \sin(82.704^\circ)} = 1.260 \mu\text{m} \quad (7)$$

From Eq. (2), we obtain:

$$h(x, y) = S \frac{\phi(x, y)}{2\pi} \quad (8)$$

where h is the height of the surface with respect to the reference plane that must be defined: in this case, the glass surface is utilized as the reference plane; S is the sensitivity computed using Eq. (7) with $n=1$; the factor $\frac{\phi(x, y)}{2\pi}$ is the order n . $\phi(x, y)$ is obtained by the usual procedure applied in the moiré method when the carrier is recorded.

4. EXPERIMENTAL SET UP

The experimental setup is very similar to that described in [1] when a NIST traceable standard was used to successfully validate the method. [Figure 2](#) shows the experimental setup. Details on the laser source and the

viewing system are presented in Table 1. By using double illumination it is possible to increase the sensitivity of the measurements, which was calculated in Section 3 as $1.27 \mu\text{m}$.

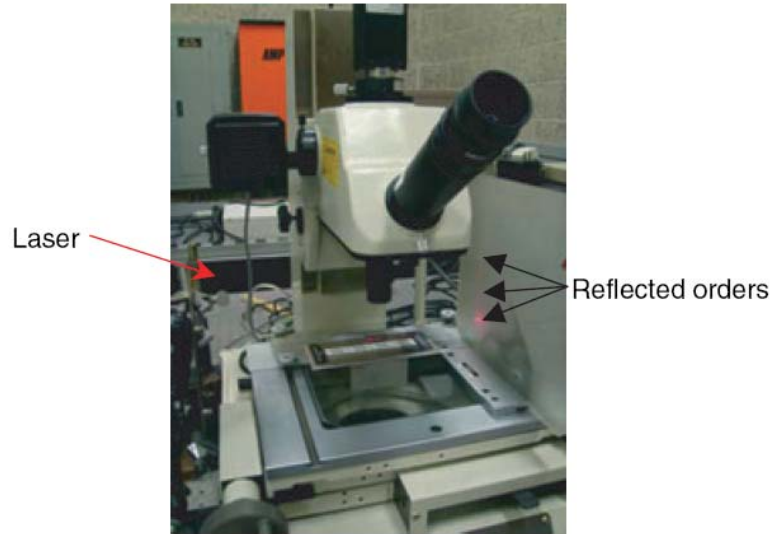


Figure 2. View of experimental setup

Table 1. Details of the experimental setup used in profile measurements

Illumination	
Microscope	Mitutoyo – Measuring Microscope – 176-847A
Objective	Mitutoyo; Magnification: 10X, NA: 0.3; WD: 16 mm; Depth-of-field: $8.5 \mu\text{m}$
Laser	Stocker Yale Lasiris; He-Ne ($\lambda=660 \text{ nm}$), 50 mW
Imaging	
CCD camera	Bassler A640f; 1624×1236 pixels

Figure 3a shows the view of $119.5 \mu\text{m}$ rough side of the HQC226 sample illuminated with white light. The bright lines correspond to the top of each tooth. Figure 3b shows the same specimen with the $2.5 \mu\text{m}$ pitch grating superimposed on it. The field of view represented in the image covered 16 peaks/valleys for a nominal length of 1.5 mm.

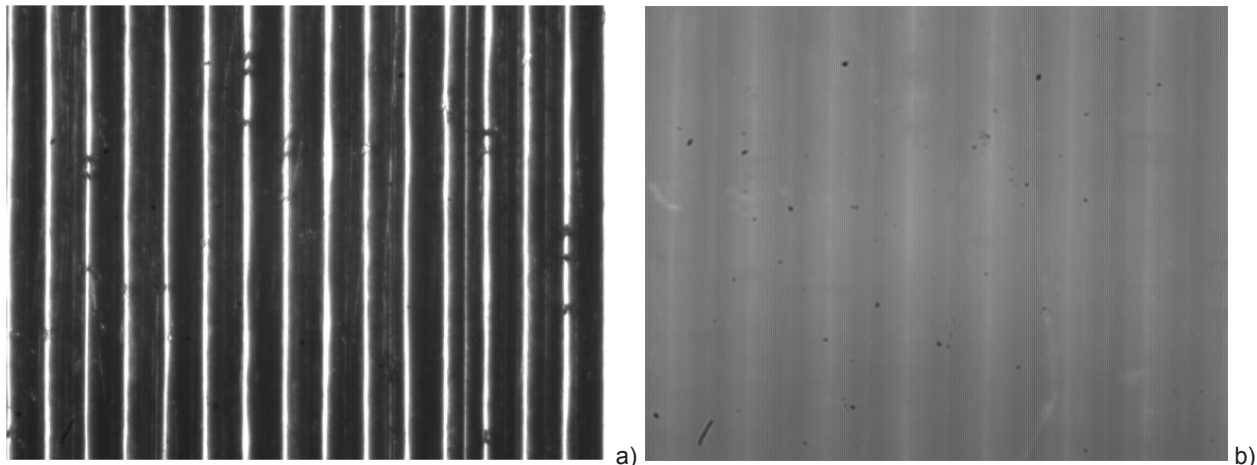


Figure 3. (a) View of the HQC226 standard illuminated with white light; (b) View of the standard with superimposed grating

Figure 4 shows the image of the standard specimen with the superimposed grating obtained by illuminating the specimen itself with coherent light. Besides the grating lines there is a system of fringes resulting from the complex interaction between the diffraction pattern coming from the grating and the wavefront coming from the standard surface. These orders become modulated by the depth of the surface. From the region limited by the rectangular mask marked in red on the image, a square area was extracted and then re-pixelated to 2048×2048 in order to precisely reconstruct the profile of one tooth.

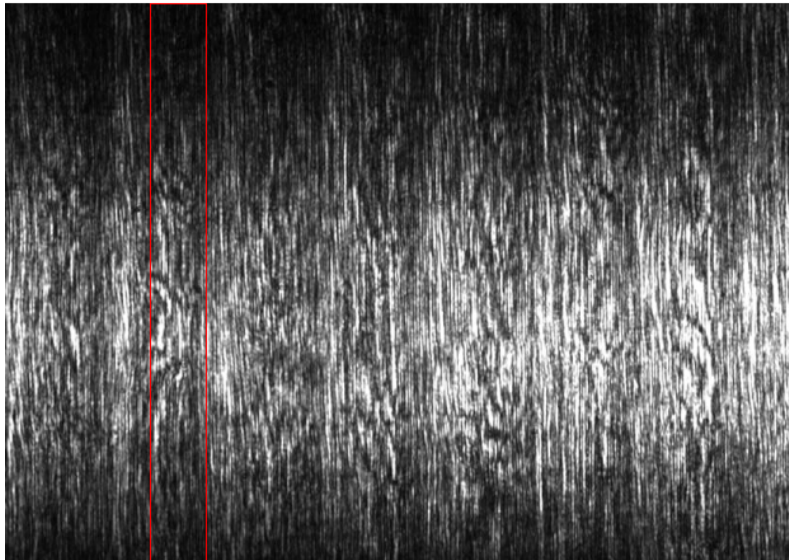


Figure 4. View of the standard with the superimposed grating when coherent illumination is used

All image patterns recorded were processed with the Holo-Moiré Strain Analyzer™ (HMSA) Version 2.0 [3] fringe analysis software package developed by Sciammarella and his collaborators and supplied by General Stress Optics Inc. (Chicago, IL USA). The HMSA package includes a very detailed library of state-of-the-art fringe processing tools based on Fourier analysis (Fast Fourier Transform, filtering, carrier modulation, fringe extension, edge detection and masking operations, removal of discontinuities, etc.). The software has been continuously developed over the years and can deal practically with any kind of interferometric pattern. All experimental results are presented and discussed in the next section.

5. RESULTS AND DISCUSSION

By simply counting moiré fringes it is possible to reconstruct the profile of the specimen surface. The moiré pattern results from subtracting the frequency of the reference grating from the modulated frequency. The roughness can then be measured by multiplying the total depth thus obtained by one half of the tooth width. Although very simple, this approach allowed surface roughness to be estimated at a good level of accuracy. For example, the computed value for Ra was 2.99 μm vs. 3.03276 μm measured by NIST (see Figure 1c).

A more detailed analysis of the specimen profile is shown in Figure 5a. The size of the region of interest shown in the figure is 700 μm . The average measured pitch is 101.24 μm with a standard deviation of ± 0.322 μm . The average measured depth is 6.078 μm . Consequently, the average value of Ra is 3.039 μm which is within the range of NIST's measurements.

Figure 5b shows the detailed view of the tooth included in the 2048×2048 re-pixelated region. It can be seen that the local height of the tooth profile is 6.0645 μm , practically the same as the nominal height of 6 μm , while the local length of the tooth is 101.3 μm that is very close to the nominal length of 100 μm .

The 3D map of the reconstructed surface is shown in Figure 6. The average Ra of the standard is 3.05054 μm and oscillates between 3.0175 μm and 3.07848 μm . By extracting different profiles it was possible to make an estimate of the average surface finish of the standard. The average depth thus determined is 6.035 \pm 0.1367 μm . Therefore, the finish of surface standard can be estimated as 0.1367/0.635, that is about $\lambda/5$.

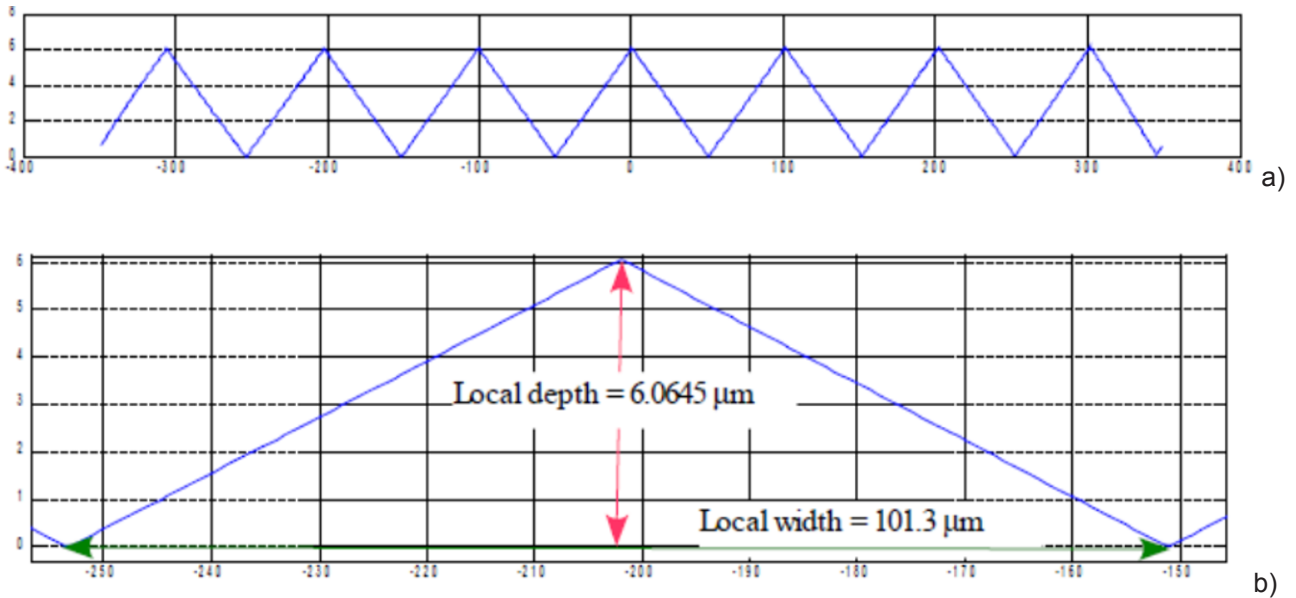


Figure 5. a) Profile of the HQC226 standard reconstructed with the contouring technique; b) Detail of one tooth

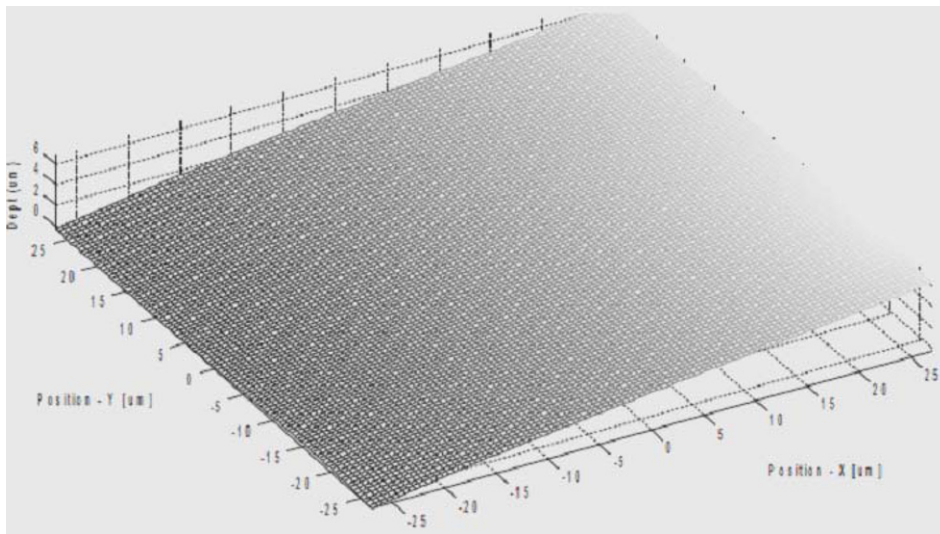


Figure 6. 3D MATLAB representation of the reconstructed surface of half of one tooth

6. CONCLUSION

This paper presented an advanced optical method for digital moiré contouring. The method was tested on HQC226 precision standards. Experimental results were within the range of measurement of the standard. It appears that the optical method presented here is a very powerful tool that can be used for the determination of surface roughness values for any kind of material and to analyze relationships between surface properties and mechanical behavior (see for example the study on flexural strength of ceramic materials presented in [4]) The fact that this technique can be extended to a traditional far field microscope opens the possibilities to many other kinds of analysis.

7. REFERENCES

- [1] Sciammarella C.A., Lamberti L., Sciammarella F.M., Demelio G.P., Dicuonzo A. and Boccaccio A. "Application of plasmons to the determination of surface profile and contact strain distribution". *Strain*, 2010. *In Press*.
- [2] ASME Standard B46.1 (2002) *Surface Texture, Surface Roughness, Waviness and Lay*, American Society of Mechanical Engineers, New York, NY.

- [3] General Stress Optics Inc. (2008) *Holo-Moiré Strain Analyzer Software HoloStrain*, Version 2.0. General Stress Optics Inc., Chicago, IL (USA), <http://www.stressoptics.com>
- [4] Sciammarella F.M., Sciammarella C.A., Lamberti L. and Burra V. "Industrial finishes of ceramic surfaces at the micro-level and its influence on strength". SEM Annual Conference & Exposition on Experimental & Applied Mechanics, June 7–10, 2010, Indianapolis, Indiana.

INDUSTRIAL FINISHES OF CERAMIC SURFACES AT THE MICRO-LEVEL AND ITS INFLUENCE ON STRENGTH

F.M. Sciammarella*, C.A. Sciammarella*, L. Lamberti**, V. Burra*

*Northern Illinois University, Department of Mechanical Engineering, 590 Garden Road, DeKalb, IL 60115, USA

**Politecnico di Bari, Dipartimento di Ingegneria Meccanica e Gestionale, Viale Japigia 182, Bari, 70126, ITALY

E-mail: sciammarella@niu.edu, sciammarella@iit.edu, lamberti@poliba.it

Abstract

The mechanical properties of ceramic materials are influenced by surface finishing procedures. This paper presents a brief introduction to an advanced methodology of digital moiré contouring utilized to get surface information in the micro-range that is a generalization of a method developed for metallic surfaces [1]. Five types of surface treatments are considered. Two of the finishes utilize diamond grinding with a rough grit (100) and a smoother grit (800). The third type is laser assisted machining of the ceramic. The fourth type is simply applying the laser without machining. The final type is the as received ceramic resulting from the process of fabrication. A total of 63 specimens, nine of each kind were tested in four-point-bending. The strength of the specimens was statistically analyzed using the Gaussian and the Weibull distributions. The statistical strength values are correlated with the statistical distributions of surface properties obtained using this advanced digital moiré contouring method. The paper illustrates the practical application of this method that was developed to analyze surfaces at micro level and beyond.

1. INTRODUCTION

Ceramics more specifically Si_3Ni_4 are known to have very high coefficient of friction, excellent compression strength and resistance to corrosion especially at elevated temperatures. These qualities make them great candidates for a variety of engine components as well as for bearings [2,3]. There are two major factors however that currently limits the use of ceramics for these types of applications. The first has to do with control of surface defects, due to their brittle nature a reduction or elimination of flaws that can prove critical in the failure of ceramics is required. The second factor has to do with cost. The manufacturing costs to diamond grind can be as much as 70% to 90% of the total component cost for complex components [4]. The wide application of advanced ceramics has been restrained largely because of the difficulty and high cost associated with shaping these hard and brittle materials into products. Laser assisted machining (LAM) of ceramics is proving to be a viable alternative to conventional manufacturing methods in terms of cost. Machining time can be cut down drastically and with proper arrangement other more complex machining operations may be possible. Information on the development of a commercially viable system for LAM of ceramics is presented in [5]. One of the main issues now is ensuring that the surface finish of these ceramics be good enough or better than the conventional diamond grind process. Therefore, in order to carry out measurements in the micro range and beyond one must have a very robust yet accurate non contact method. This paper describes the experimental procedures and measurements made on the ceramic samples that were utilized for the bending tests. With this advanced digital moiré contouring method a spatial resolution on the order of a micron was achieved. This level of accuracy enables the micro/nano contouring of the surfaces which can then be represented by a variety of surface roughness measurements such as Ra. These values are then compared to the four-point-bending tests where it does show an experimental relationship between the surface roughness and its bending strength.

2. ADVANCED DIGITAL MOIRÉ CONTOURING METHOD

Most of the information on how this method was developed and why it works were explained in [1]. While this work was described for metallic surfaces we can only assume at this point that there must be similar conditions with the ceramic material that enabled us to obtain the experimental results presented in this paper. In other words we must assume that there is some photonic absorption by the ceramic that enables a similar effect to take place. That is why the focus in this section lies on extracting the necessary information from the experimental measurements of the ceramic test pieces.

It is important to remember that the experimental set up should have a double interface creating a cavity. This cavity then acts as a passive optical resonator so that resonances can be observed from the emitted light. For

this information to be used successfully there are three factors that must be defined. The first relates to the direction of the emerging wave vectors, second is the effect of the changes of the gap depth and the third deals with polarization of the light. Again we can refer to [1] to see the detailed solutions and equations.

This approach will provide the necessary equations to reproduce the topography of the ceramic surface at the micron and sub-micron level. The derivation of these equations given in [1] assimilates the cavity that was represented to a Fabry-Perot resonator. For this contouring method the illumination system consisted of a beam going through a glass plate and impinging to the surface of the glass plate at an angle with respect to the normal to the plate larger than the limit angle. In this way a system of fringes was generated. This system of fringes was equivalent to the first diffraction order of a sinusoidal grating of pitch [1]:

$$p = \frac{\lambda}{2 \sin \theta_i} \quad (1)$$

where θ_i is the angle that the beam forms with the surface. In the present case, the illumination process of the surface was modified by introducing an actual grating on top of the surface to be measured. The actual process of fringe formation is very complex because the illumination of the surface is obtained through evanescent fields. In the limited context of this paper it is not possible to present all the derivations but the result is the following for single illumination:

$$h = \frac{p}{2 \cdot n \sin \theta_o} \quad (2)$$

where p is the pitch of the utilized grating, n is the diffraction order observed and θ_o is the angle of illumination with respect to the normal to the surface of the grating. The value of θ_o is computed with the following equation:

$$\theta_o = \frac{\pi}{2} - \arcsin \left(\frac{1}{2} \cdot \frac{\lambda}{p} \right) \quad (3)$$

That is, the inclination of the beam with respect to the normal to the surface is larger than that of the limit angle of total reflection. Consequently, the illumination of the surface is done through the evanescent field. In the applications presented in this paper the utilized values are: $p = 2.5 \mu\text{m}$, $\lambda = .635 \mu\text{m}$. With the above values, for $n=1$, it follows:

$$\theta_o = 90^\circ - \arcsin \left(\frac{1}{2} \cdot \frac{0.635}{2.5} \right) = 82.704^\circ \quad (4)$$

The resulting sensitivity is:

$$S = \frac{2.5}{\sin(82.704^\circ)} = 2.520 \mu\text{m} \quad (5)$$

In the case of double illumination, the corresponding equation is:

$$h = \frac{p}{2 \cdot 2 n \sin \theta_o} \quad (6)$$

while sensitivity is:

$$S = \frac{2.5}{2 \cdot 2 \sin(82.704^\circ)} = 1.260 \mu\text{m} \quad (7)$$

From Eq. (2), we obtain:

$$h(x, y) = S \frac{\phi(x, y)}{2\pi} \quad (8)$$

where h is the height of the surface with respect to the reference plane that must be defined: in this case, the glass surface is utilized as the reference plane; S is the sensitivity computed using Eq. (7) with $n=1$; the factor $\frac{\phi(x, y)}{2\pi}$ is the order n . $\phi(x, y)$ is obtained by the usual procedure applied in the moiré method when the carrier is recorded.

3. EXPERIMENTAL SET UP

There were two different providers of ceramic rods (length=6", diameter=1") with a total of five different surface conditions. For ceramic rod K the treatments were: *As Received*, *Diamond Grind* (100 grit), and *LAMC*. For ceramic rod B the treatments were: *As Received*, *Diamond Grind* (800 grit), *Laser Glazed*, and *LAMC*. Once the samples were made each rod was sectioned into three arc segments with a smaller size (19 mm thick, 19 mm wide, and 50 mm long (Figure 1a). These arc segment specimens were tested under flexure (Figure 1b) with the machined surface in tension at loads less than 4000 N (880 pounds); this geometry gave three test bars from each 25-mm diameter silicon nitride rod. This arc segment specimen geometry was used for other ceramics [6]. The complete testing procedure (specimens, fixturing, calculations) is described in detail by Quinn [7].

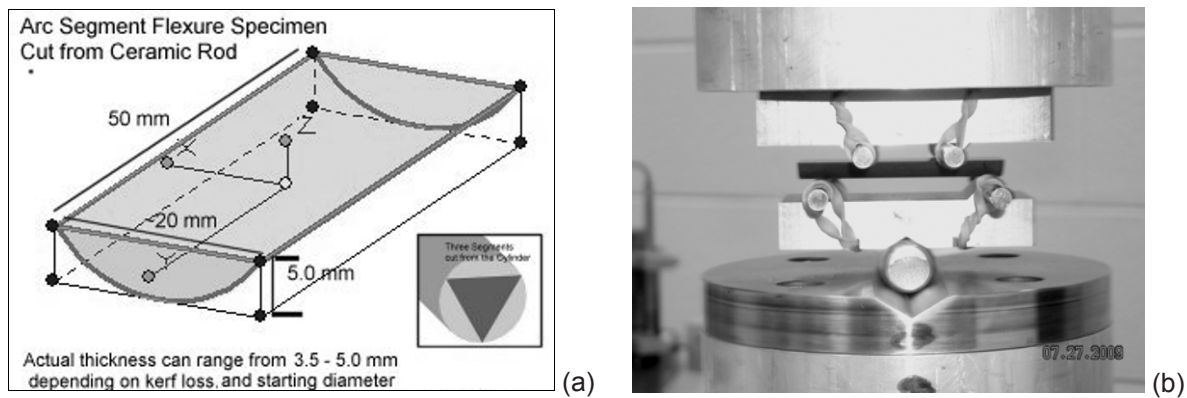


Figure 1. (a) Schematic of arc samples used for 4-point-bending tests; (b) view of experimental setup.

Prior to having samples subject to the four-point-bending test, samples were analyzed using the advanced digital moiré contouring method with the set up shown in Figure 2a. This set up is very similar to that described in [1] when a NIST traceable standard was used to successfully validate the method. For these measurements a special fixture (Figure 2b) was designed to hold these sliced specimens along with the grating, ensuring proper contact. It was important to maintain the total internal reflection at the interface of the grating and the ceramic; for this purpose an angle of illumination computed with equation (4) was utilized. By using double illumination it is possible to increase the sensitivity of the measurements, which was calculated in Section 2 as 1.27 microns.

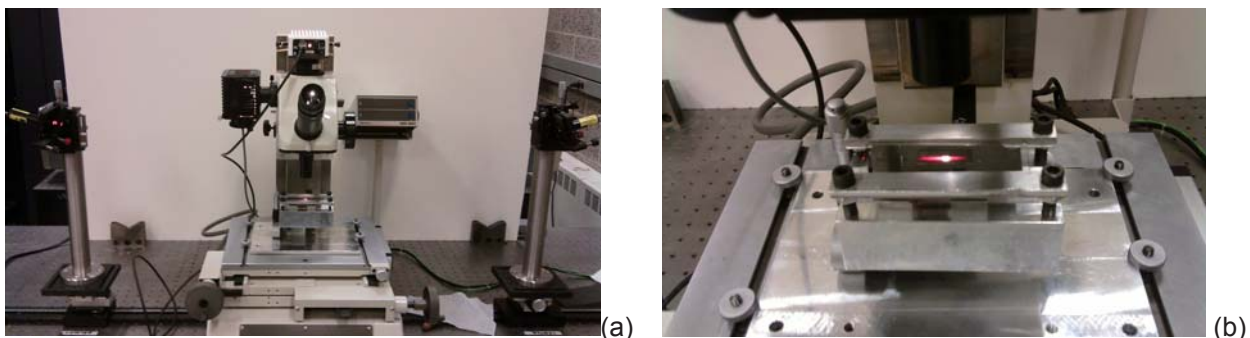


Figure 2. (a) View of entire set up for advanced digital moiré contouring method; (b) close up view of fixture.

For the first set of data taken from the K samples the field of view was 450×450 microns. There was one image that was recorded per sample with a total of 9 samples per condition: there were provided 27 separate images to be analyzed. For the second set of data taken from the B samples the field of view was 325×325

microns. This time three images were recorded per sample giving a total of 27 images to analyze per condition.

Two procedures were utilized depending on the actual roughness of the surface. If the roughness of the surface is larger than the sensitivity of the set up the standard processing with fringe unwrapping is applied. If the roughness is less than the grating pitch the two images taken (left and right) are subtracted from each other. Since there is less than a fringe between the two patterns, we are dealing with fractional orders. Consequently, there is no need to perform any fringe unwrapping and the results obtained from the subtraction give us the surface profile of the ceramic directly.

All image patterns recorded were processed with the Holo-Moiré Strain Analyzer™ (HMSA) Version 2.0 [8] fringe analysis software package developed by Sciammarella and his collaborators and supplied by General Stress Optics Inc. (Chicago, IL USA). The HMSA package includes a very detailed library of state-of-the-art fringe processing tools based on Fourier analysis (Fast Fourier Transform, filtering, carrier modulation, fringe extension, edge detection and masking operations, removal of discontinuities, etc.). The software has been continuously developed over the years and can deal practically with any kind of interferometric pattern. [Figure 3a](#) shows the ceramic surface for the diamond grind condition (800 grit). [Figure 3b](#) shows the final result obtained after subtraction and processing using HMSA™ software. All the results are provided in the next section.

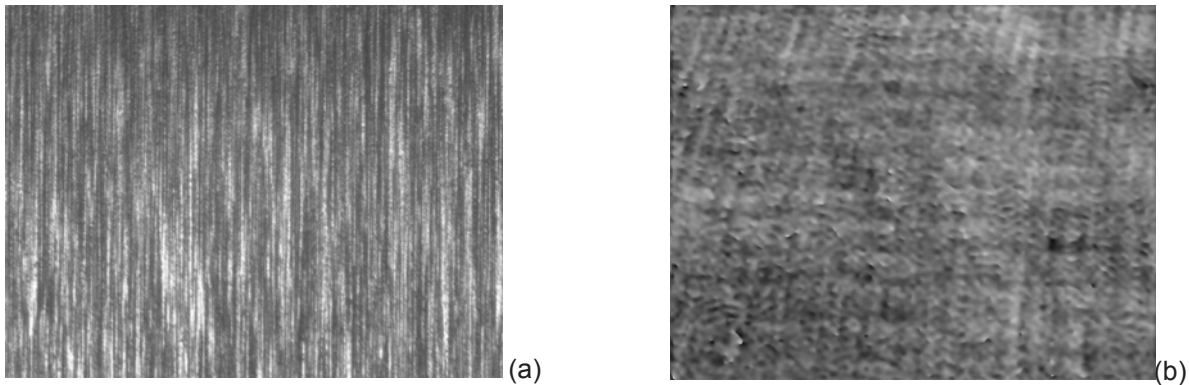


Figure 3. (a) View of diamond grind surface from microscope; (b) view of final result after processing.

4. EXPERIMENTAL RESULTS

There were two types of measurements performed on the ceramic samples: 1) Mechanical and 2) Optical. Prior to the mechanical testing, the samples were placed into the advanced digital moiré contouring system to obtain full field images of the ceramic surface so that surface roughness (Ra) measurement could be made. After the images were taken, the samples were put into a four-point-bending test to determine the bend strength. This section provides the results obtained from testing.

4.1 Mechanical Testing

[Tables I & II](#) show the results obtained from the four-point-bending test. Specimens were tested at room temperature in an Instron testing machine, using an articulated fixture (40 mm-20 mm spans) with rolling tool steel bearings ([Figure 1b](#)). The cross head rate was 0.125 mm/min. Each specimen was tested with the curved face in tension (down).

Table I. Experimental results from four-point-bending tests for ceramic K

Diamond Grind		Laser-Assisted Machine		As-Received	
Bar ID	Strength (MPa)	Bar ID	Strength (MPa)	Bar ID	Strength (MPa)
1A	433.2	4A	447.2	7A	475.7
1B	419.8	4B	300.2	7B	604.0
1C	464.2	4C	422.6	7C	544.2
2A	408.3	5A	622.6	8A	588.3
2B	452.6	5B	606.6	8B	552.9
2C	496.2	5C	615.6	8C	540.8
3A	530.9	6A	600.3	9A	528.1
3B	505.3	6B	609.1	9B	468.6
3C	510.9	6C	540.9	9C	414.8

Table II. Experimental results from four-point-bending tests for ceramic B

As-Received		800 Grit Dia. Grind		Laser Glaze		LAM Turned	
Bar #	Stress (MPa)	Bar	Stress (MPa)	Bar #	Stress(MPa)	Bar #	Stress (MPa)
1B1	410	1A1	456	15B1	524	18A1	624
1B2	401	1A2	434	15B2	541	18A2	618
1B3	388	1A3	625	15B3	494	18A3	523
2B1	476	2A1	559	15A1	570	16B1	543
2B2	445	2A2	502	15A2	511	16B2	469
2B3	499	2A3	457	15A3	488	16B3	571
3B1	429	3A1	474	16A1	580	18B1	605
3B2	441	3A2	544	16A2	459	18B2	561
3B3	437	3A3	430	16A3	588	18B3	531

Because ceramics fail in a brittle fashion statistical analysis for determining bend strength must be implemented. In this particular case, a two parameter Weibull Analysis was performed on bend stress results. Despite the low number of measurements this was done to give some statistical meaning to the experimental data. The scale parameter determines the most probable location where (in this case) the bend strength would be and the shape parameter (m) indicates the distribution. A high m value means that there is almost no spread in the data and that most values should fall within the most probable range (95%), a low m value means there is a lot of spread in the data. In addition to obtaining the 95% confidence value, the upper and lower bounds are also determined.

All data were obtained directly through MATLAB which include canned functions to perform these calculations. [Tables III & IV](#) provide the results obtained using the Weibull Analysis from MATLAB.

Table III. Results from Weibull Analysis of Bend Strength for ceramic K

	Flexural Strength (MPa)			m values		
	Lower Bound	95%	Upper Bound	Lower Bound	95%	Upper Bound
LAM 4	360.69	416.35	480.60	3.01	8.24	22.55
Diamond (100)	462.91	487.99	514.42	7.78	13.09	22.02
As Received	516.50	549.00	583.54	6.66	11.27	19.08
LAM 5&6	596.79	609.77	623.04	18.81	38.37	78.26

Table IV. Results from Weibull Analysis of Bend Strength for ceramic B

	Flexural Strength (MPa)			m values		
	Lower Bound	95%	Upper Bound	Lower Bound	95%	Upper Bound
As Received	429.27	452.10	476.14	4.94	7.97	12.85
Diamond (800)	482.55	526.53	574.51	8.26	13.39	21.72
LASER Only	522.05	547.88	574.99	8.52	14.31	24.01
LAM	554.10	581.97	611.25	8.33	14.05	23.67

4.2 Image Analysis

The images recorded using the HMSA™ software provided the full field view of the ceramic surface. [Figure 4a](#) shows the 3-D view of the diamond grind surface (100 grit). [Figure 4b](#) shows the 3-D view of the LAM surface.

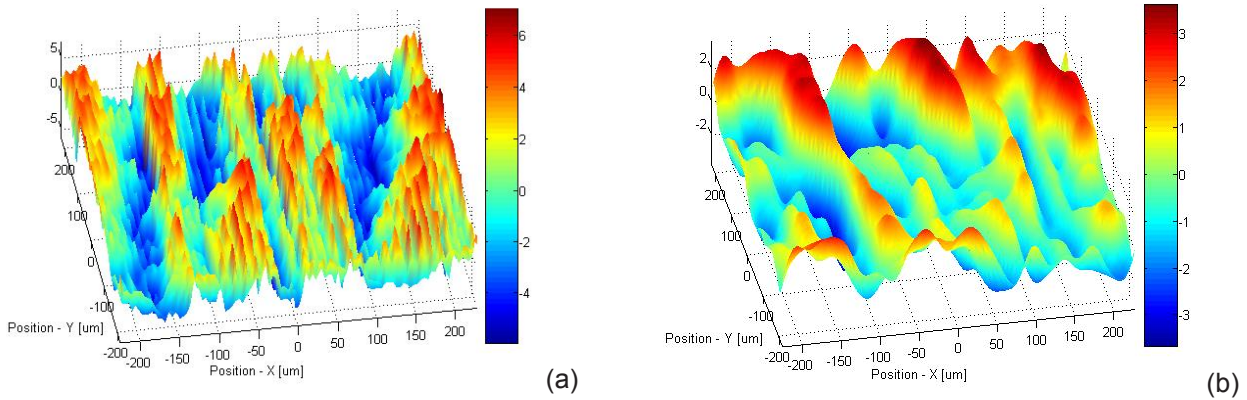


Figure 4. (a) 3-D view of diamond grind (100 grit) surface (b) 3-D view of LAM surface.

A dedicated MATLAB program was created to take the output file from the HMSA™ software which contains (1024 × 1024) the actual surface information to calculate the Ra value. Then for each sample this value was stored and then placed into the Weibull Analysis program that was used for the bend strength. Table V & VI shows the data in terms of Ra (microns) and its corresponding m value.

Table V. Results from Weibull Analysis of Ra for ceramic K

	Ra (microns)			m values		
	Lower Bound	95%	Upper Bound	Lower Bound	95%	Upper Bound
LAM 4	0.951	1.376	1.991	1.11	1.63	2.40
Diamond (100)	1.156	1.336	1.544	1.93	2.44	3.08
As Received	0.981	1.260	1.619	1.15	1.47	1.88
LAM 5&6	0.856	0.956	1.067	2.88	4.00	5.57

Table VI. Results from Weibull Analysis of Ra for ceramic B

	Ra (microns)			m values		
	Lower Bound	95%	Upper Bound	Lower Bound	95%	Upper Bound
As Received	0.968	1.088	1.223	5.61	7.55	10.15
Diamond (800)	1.170	1.332	1.517	4.29	5.37	6.71
LASER Only	0.966	1.063	1.171	5.22	6.53	8.16
LAM	0.846	0.912	0.983	6.35	8.23	10.65

5. DISCUSSION AND CONCLUSIONS

Looking through Tables III-VI it is clear that the LAM process provides the best results in terms of bending strength and surface roughness. For each table the LAM holds among the highest m value meaning that it creates a high confidence in terms of repeatability. One other interesting outcome from the first round was that sample #4 from the LAM trial experienced much lower bend strength values than #s 5 and 6. At first it was not clear why but after analyzing the Ra we can see that #4 values are much higher than those of #s 5 and 6. In this first run the LAM parameters were not controlled and therefore it is possible that some other factor may have influenced the higher Ra value (i.e. cutting tool, force of tool, etc.). During the second trials all possible factors were controlled and observed. This is evidenced by the data from Table II being more consistent.

Figure 5 is a plot of all the data obtained from the Weibull Analysis that shows Bend Strength (MPa) vs. Ra (microns). We can clearly see that in fact there is a correlation between the values measured for bend strength and those measured for surface roughness. Further investigation will be carried out to see if a determination can be made into why this relationship exists.

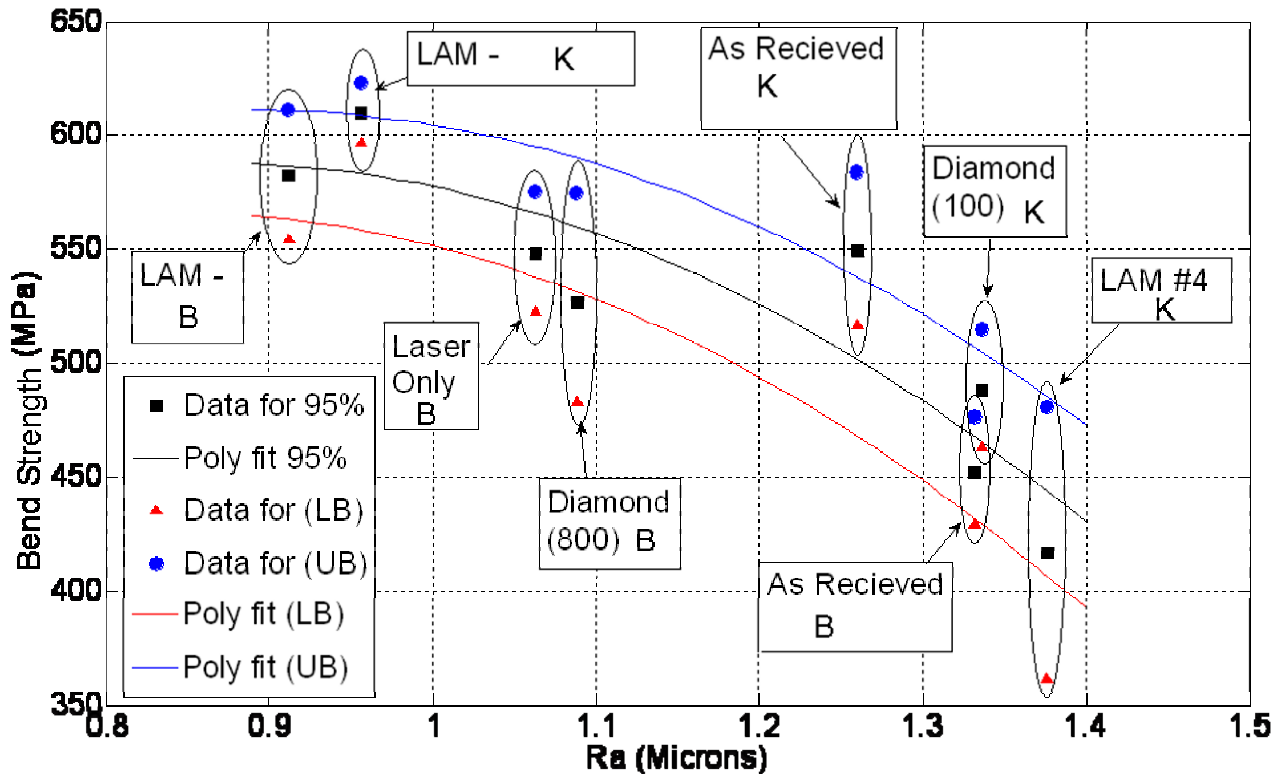


Figure 5. Relationship between roughness and bend strength for different specimens

The correlation is an experimental fact that needs to be explained. The correlation indicates that as the Ra values increase the strength decreases. It can also be seen that variations of Ra of few hundreds nanometers have a sizable effect on the strength. Figure 5 shows that from Ra=900 nm to Ra=1400 a considerable change of the strength occurs. Further investigations will be carried out to see the factors that can explain the reason for the observed correlation. It appears that the optical method presented here is a very powerful tool that can be used for the determination of surface roughness values for any kind of material. The fact that this technique can be extended to a traditional far field microscope opens the possibilities to many other kinds of analysis.

6. ACKNOWLEDGEMENTS

This work would not have been possible without the financial support of NIU's College of Engineering and Engineering Technology R&D outreach program – Rapid Optimization for Commercial Knowledge (ROCK) Director Dr. Richard Johnson, Assistant Director Alan Swiglo, Senior Project Manager Dr. Joe Santner. The authors would also like to the folks at Reliance Tool & Manufacturing, Dick Roberts, Jeff Staes, and Ricardo Deleon for all of their expertise in Manufacturing. Recognition must also go to Dr. Stephen Goczy of Gateway Materials Technology Inc. for his support and expertise in ceramics. Finally thanks to Mike Matusky current graduate student in the ME Dept. at NIU for all of his work in the LAM project.

7. REFERENCES

- [1] Sciammarella C.A., Lamberti L., Sciammarella F.M., Demelio G.P., Dicuonzo A. and Boccaccio A. "Application of plasmons to the determination of surface profile and contact strain distribution". *Strain*, 2010. *In Press*.
- [2] Takebayashi H., Johns T.M, Rukkaku K., and Tanimoto K., "Performance of Ceramic Bearings in High-Speed Turbine Application" *Society of Automotive Engineers*, Paper No. 901629, Milwaukee, WI (1990).
- [3] Chudecki J.F., "Ceramic Bearings - Applications and Performance Advantages in Industrial Applications," SAE Technical Paper Series 891904 (1989)
- [4] Marinescu I.D., *Handbook of Advanced Ceramic Machining*, CRC Press, (2007).
- [5] Sciammarella F.M., Santner J., Staes J., Roberts R., Pfefferkorn F. and Goczy S., "Production Focused

Laser Assisted Machining of Silicon Nitride”, *Proceedings of the 34th International Conference on Advanced Ceramics & Composites (ICACC)*, January 2010.

[6] Swab J.J., Wereszczak A.A., Tice J., Caspe R., Kraft R.H. and Adams J.W., “Mechanical and Thermal Properties of Advanced Ceramics for Gun Barrel Applications”. Army Research Laboratory Report ARL-TR-3417, February (2005).

[7] Quinn G.D., “The Segmented Cylinder Flexure Strength Test”, *Ceramic Eng. and Sci. Proc.*, 27 [3], 295–305 (2006).

[8] General Stress Optics Inc. (2008) *Holo-Moiré Strain Analyzer Software HoloStrain*, Version 2.0. General Stress Optics Inc., Chicago, IL (USA), <http://www.stressoptics.com>

ELASTIC PROPERTIES OF LIVING CELLS

M.C. Frassanito, L. Lamberti and C. Pappalettere

*Politecnico di Bari, Dipartimento di Ingegneria Meccanica e Gestionale
Viale Japigia 182, Bari, 70126, ITALY*

E-mail: mcfiras@poliba.it, lamberti@poliba.it, carpa@poliba.it

Abstract

Constitutive behavior of living cells is in deep relationship with their biological properties. For that reason gathering the most detailed information on cell mechanical behavior as it is feasible becomes extremely useful in assessing therapeutic protocols. However, investigation of elastic properties of living cells is a fairly complicated process that requires the use of advanced sensing devices. For example, Atomic Force Microscopy (AFM) is a research tool largely used by biomedical engineers and biophysicists for studying cell mechanics. Experimental data can be given in input to finite element models to predict cell behavior and to simulate the tissue response to biophysical, chemical or pharmacological stimuli of different nature. The paper analyzes different aspects involved in the numerical simulation of AFM measurements on living cells focusing in particular on the effect of constitutive behavior.

1. INTRODUCTION

Nanoindentation is a widely used technique to measure the mechanical properties of films with thickness ranging from nanometers to micrometers. In case of biological samples, a convenient tool to probe living cells at the nanometer scale is the Atomic Force Microscope (AFM) because it enables measurements of samples in a physiologic aqueous cell culture environment [1-5].

The AFM was designed primarily to provide high resolution images of non-conductive samples and, among the plethora of application subsequently developed, the instrument can also be operated as a nanoindenter to gather information about the mechanical properties of the sample. AFM is based on the following principle: a nanometer sized sharp tip placed at the free end of a cantilever is put into contact with the surface of the sample [6]. The building block of the instrument is shown in Figure 1.

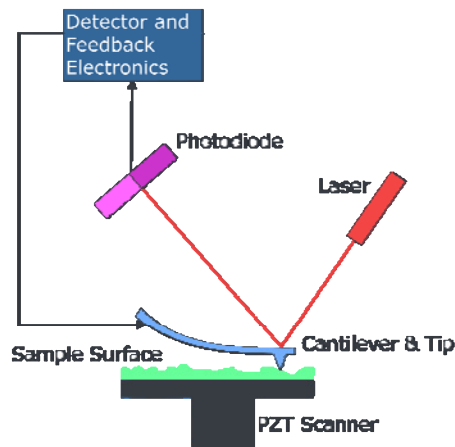


Figure 1. Schematic diagram of Atomic Force Microscopy (AFM). Deflection of the AFM cantilever probe is sensed from the reflection of a laser onto a four-quadrant photodetector, and the position of the probe is controlled by a piezoelectric ceramic actuator (PZT).

When the tip scans, indents or otherwise interacts with the sample, it determines a deflection of the microscopic sized cantilever probe which is tracked by a laser based optical method. The cantilever is rectangular or "V"-shaped, 100 to 300 micron long and about half a micron thick, microfabricated of silicon or silicon-nitride. The tip actually comes in contact with the sample while the cantilever act as a soft spring to measure the contact force. The spring constant K of the cantilever is determined by its physical and geometric properties and the value of k typically ranges from 0.01N/m to 1N/m for biomechanics application. Then, deflection h of the cantilever is converted into a contact force with the standard equation of the spring:

$F=Kh$. The tip dimension determines the spatial resolution of the instrument: sharpened pyramids, etched silicon cones, carbon nanotubes and other high aspect ratio tip have been developed for scanning samples with ultra high resolution. [6]

When AFM is used as a nanoindenter, elasticity measurements are performed by pushing a tip onto the sample of interest and monitoring force versus distance curves. This results in a deformation which is the sum of the deformation of the tip and the deformation of the investigated sample (indentation) under the tip. The relationship between force and indentation depends upon the tip geometry and the mechanical properties of the specimen. In indentation experiments, usage of ultra-sharp tip is avoided because such tips have been shown to penetrate the cell membrane and cause damage to living cells. In this case pyramid shaped or conical tip are preferred.

In order to determine reliably the mechanical properties of the samples with AFM technology, it is important to identify accurately the influence on the indentation problem of the methodological issues related with the shape and the size of the probe tip. In particular, when indenting a soft material, the contact area of the probe increases with indentation. It follows that the resulting force depth relationship is non linear and it is difficult to distinguish the contribution of the intrinsic properties of the sample and of the tip geometry.

In literature, classical infinitesimal strain theory is mostly applied to extract a Young's modulus for the material as non-linearity of the indentation response is usually attributed solely to the tip geometry. This approach is appealing due to the rather simple form of the theoretical equation. However, when studying AFM indentation of biological samples, the application of the Hertz theory [7,8] is questionable [4]. In fact, the key assumptions of the Hertz theory are that the sample is a homogeneous, isotropic, linear elastic half space subject to infinitesimally small strains while most biological materials are heterogeneous, anisotropic and exhibit non linear constitutive behavior. Besides this, AFM indentation of soft material is typically 20-500nm which cannot be considered infinitesimal compared to the thickness of the sample (often $< 10\mu\text{m}$) or to the size of the indenter tip ($\sim 10\text{-}50\text{nm}$ radius of curvature).

Analyses of AFM indentation based on infinitesimal strain theory may be inappropriate and a much better understanding of contact mechanics between the AFM tip and the soft biological material is obtained by finite element modeling. The aim of this study is to analyze AFM indentation data in case of soft specimens. Results of finite element analyses carried out on a $5\mu\text{m}$ thick membrane indented by a silicon nitride sharp tip are presented in the paper. The indentation process is simulated for two different constitutive behaviors of the membrane: linear elasticity and hyper-elasticity.

2. FINITE ELEMENT ANALYSIS

Finite element modelling and analysis were carried out with the ANSYS® Version 11.0 general purpose FEM software developed by ANSYS Inc., Canonsburg (PA), USA. The FE model of the biological membrane is shown in Figure 2. The mesh of the conical tip included 3040 PLANE42 4-node elements and 3300 nodes. The membrane was modelled as a linearly elastic material or a two-parameter Mooney Rivlin hyperelastic material: in the former case the mesh included 7500 PLANE42 4-node elements and 7500 nodes while in the latter case the mesh included 7500 PLANE182 4-node elements (the PLANE182 element supports hyperelasticity) and the same number of nodes. The surface of the membrane is covered by a layer including 1001 target elements TARGE169 while the indenter tip is covered by a layer including 509 contact elements CONTACT175.

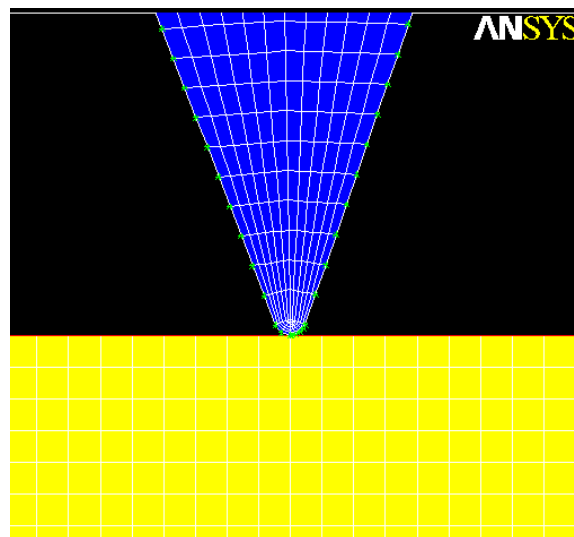


Figure 2. Finite element model of the nanoindentation experiment

The tip considered in the study was shaped as a blunt cone. This geometry is commonly used in AFM experiments on biological samples. Figure 3 summarizes the main geometric parameters of the tip.

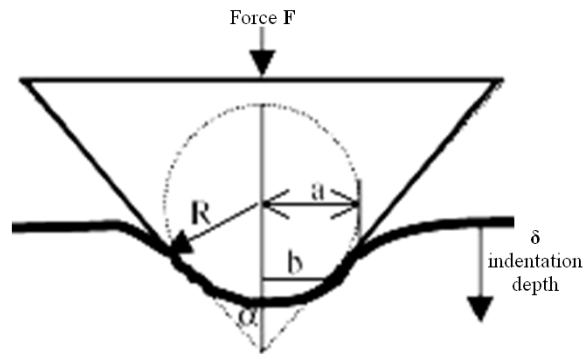


Figure 3. Schematic of the geometry of the blunt conical tip

Two different constitutive models were hypothesized for the biological membrane: (i) linearly elastic; (ii) hyperelastic, following the two-parameter Mooney-Rivlin (MR) law [9-11]. The former model is described by the Hooke's law $\sigma = E\varepsilon$. The strain energy density function for the Mooney-Rivlin model is:

$$W = a_{10}(\bar{I}_1 - 3) + a_{01}(\bar{I}_2 - 3) \quad (1)$$

where a_{10} and a_{01} are the Mooney-Rivlin constants given in input to ANSYS as material properties. Strain invariants are defined, respectively, as $\bar{I}_1 = \text{tr}[C]$ and $\bar{I}_2 = \frac{1}{2}(\text{tr}^2[C] - \text{tr}[C]^2)$ where $[C]$ is the Cauchy-Green strain tensor.

In most of the AFM studies presented in literature, the indentation problem is analyzed on the basis of infinitesimal strain theory. In order to assess the accuracy in the estimation of the material properties when applying the so called "Hertz model" [7,8] to extract the Young's modulus of the material, finite element results were compared with the theoretical predictions provided by the Hertzian model. When a rigid axisymmetric probe indents an homogeneous, semi-infinite elastic material, infinitesimal theory predicts the following relationship between force F and indentation depth δ :

$$F = 2\pi \hat{E} f(\delta) \quad (2)$$

The generalized elastic modulus \hat{E} is equivalent to:

- ❖ $\frac{E}{2(1-\nu^2)}$ for linear elastic material;
- ❖ $4(a_{10} + a_{01})$ for an hyperelastic material;

and $f(\delta)$ is a function depending on the indenter geometry which determines the relationship between the depth and the indentation response. For a blunt cone indenter with tip angle α , contact radius a and transition radius b into spherical tip of radius R (see nomenclature in Figure 3), the $f(\delta)$ function can be expressed as [12]:

$$f(\delta) = \frac{2}{\pi} \left\{ \left[a\delta - \frac{a^2}{2\text{tg}(\alpha)} \left(\frac{\pi}{2} - \arcsin\left(\frac{b}{a}\right) \right) - \frac{a^2}{3R} + (a^2 - b^2)^{1/2} \left(\frac{b}{2\text{tg}(\alpha)} + \frac{(a^2 - b^2)}{3R} \right) \right] \right\} \quad (3)$$

In the finite element model developed in this paper the nanoindentation process was simulated by increasing progressively the force F applied to the indenter. This is actually the axial component of the reaction force exercised on the indenter tip. The axial displacement of the indenter computed by ANSYS as the tip surface elements come into contact with the membrane target layer is the indentation depth δ . We were interested in the relationship between F and δ as those are the output parameters measured by AFM.

In order to reproduce experimental conditions usually encountered in AFM measurements on biological samples, membrane displacements were not constrained in the direction orthogonal to the tip movement. The augmented Lagrangian model available as default in ANSYS was utilized in the computation. Finite element analyses accounted for the large deformations experienced by the hyper-elastic membrane: the geometric non-linearity option was activated by switching on the NLGEOM command in ANSYS. Convergence analysis was carried out in order to obtain mesh independent solutions. All finite element analyses were run on a standard personal computer.

4. RESULTS AND DISCUSSION

The following parameters were given in input to the FE program:

- tip angle α equal to 20° ;
- blunt cone tip radius of curvature equal to 10nm;
- membrane thickness equal to $5\mu\text{m}$;
- Young's modulus of the tip (silicon nitride) equal to 150 GPa;
- Young's modulus of the membrane modeled as linearly elastic equal to 50 kPa;
- Mooney-Rivlin constants a_{10} and a_{01} of the membrane modeled as hyperelastic equal to 10 kPa and 2.5 kPa, respectively: these value yield the same equivalent Young's modulus of 50 KPa.

Figure 4 shows the F - δ curve predicted by ANSYS for the indentation of a blunt conical tip onto a linearly elastic membrane. As expected in view of the Hertzian model depicted by Eq. (4), numerical values were fitted very precisely by a linear regression.

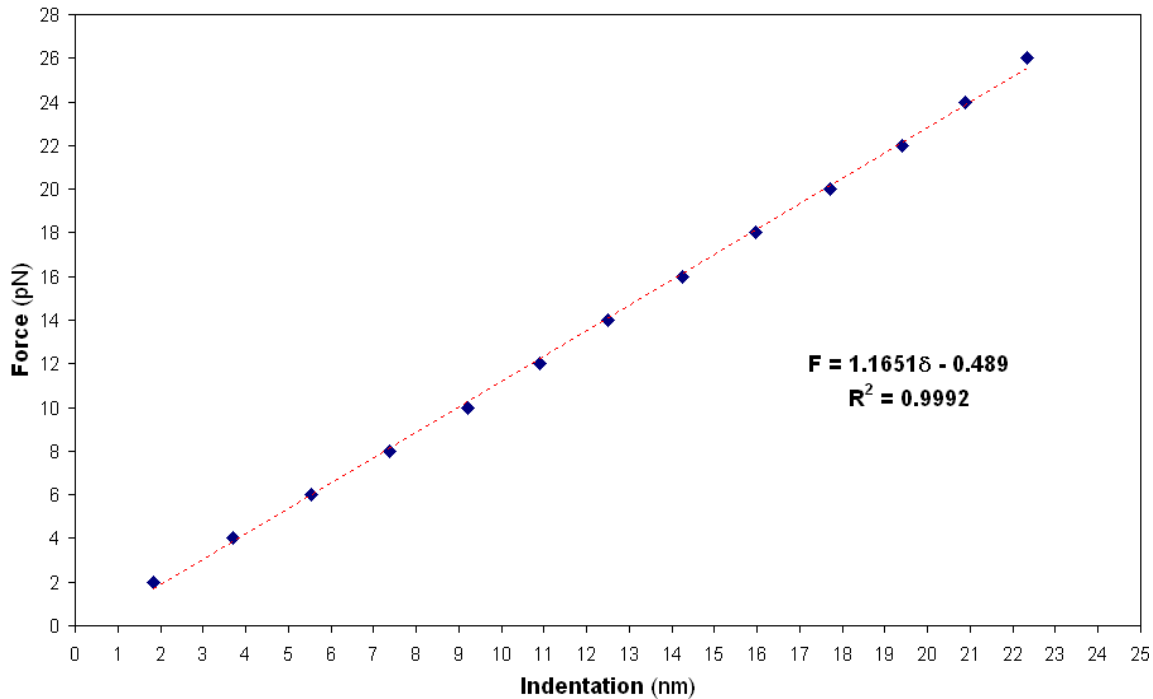


Figure 4. Force-indentation curve (blue dots) computed by ANSYS for a blunt cone tip and linearly elastic membrane compared with the Hertzian theoretical model (dashed red line)

From the slope of the linear fitting, the value of the equivalent Young's modulus can be determined by combining equations (2) and (4). One can obtain the value 69.9 kPa which is fairly close to the value of 50 kPa given in input to the model. The obtained results confirm that in the case of linear elasticity and in presence of very small indentations the Hertzian model describes well the contact problem.

In the case of hyperelastic membrane the F - δ curve was again well fitted by a linear regression but the slope resulted much smaller than in the previous case of linear elasticity. The Young's modulus derived from data fitting is 0.835 kPa, about 85 times lower than the value included in the FE model. This indicates that the Hertzian model should not be applied to hyperelastic membranes to derive reliably the value of equivalent Young's modulus and confirms that the indentation response results from the combination of geometric and material nonlinearities.

5. CONCLUDING REMARKS

This paper analyzed the suitability of Hertzian model in nano-indentation of soft materials. It was found that the classical theory does not work well. However, a deeper analysis should be carried out in order to understand better this complicated phenomenon. The main limitation of this study is the fact that the stiffness value was derived from a closed form relationship. The best approach to material characterization is to formulate the identification problem in fashion of an optimization problem where the unknown material properties are included as design variables. The cost function to be minimized is the error functional Ω defined by summing over the differences between displacements measured experimentally and those predicted numerically by a finite element model. Each time the optimizer perturbs material properties, the finite element model is updated and a new analysis is executed until the process converges. The identification problem for a material with NMP unknown properties can be stated as follows:

$$\left\{ \begin{array}{l} \text{Min} \left[\Omega(X_1, X_2, \dots, X_{\text{NMP}}) = \sqrt{\frac{1}{N_{\text{CNT}}} \sum_{j=1}^{\text{NCNT}} \left(\frac{\delta_{\text{FEM}}^j - \bar{\delta}^j}{u_{\text{FEM}}^j} \right)^2} \right] \\ G_p(X_1, X_2, \dots, X_{\text{NMP}}) \geq 0 \\ X_1^L \leq X_1 \leq X_1^U \\ X_2^L \leq X_2 \leq X_2^U \\ \dots \\ X_{\text{NMP}-1}^L \leq X_{\text{NMP}-1} \leq X_{\text{NMP}-1}^U \\ X_{\text{NMP}}^L \leq X_{\text{NMP}} \leq X_{\text{NMP}}^U \end{array} \right. \quad (4)$$

where the design vector $\mathbf{X}(X_1, X_2, \dots, X_{\text{NMP}})$ includes the NMP unknown material parameters to be determined in the identification process. The constraint functions $G_p(\mathbf{X})$ may be introduced in the optimization in order to ensure that the hypothesized constitutive behavior is physically reliable and may satisfy constraints on numerical stability especially in case of high non-linearity.

In the above equation, δ^j and $\bar{\delta}^j$ denote, respectively, the values of indentation at the j^{th} loading step predicted by the finite element model and their counterpart measured experimentally. Experimental values are taken as target in the identification process since AFM measurements do not require values of material properties to be known a priori. Conversely, correct values for material properties must be given in input to the finite element program in order to calculate the value of indentation at a given load.

The above mentioned approach is currently being utilized in order to reproduce experimental tests involving AFM measurements carried out on biological specimens having the same material properties considered in this study.

REFERENCES

- [1] Costa K.D. "Single cell elastography: probing for disease with the atomic force microscope" *Disease Markers*, **19**, 139–154, 2004.
- [2] Suresh S. "Biomechanics and biophysics of cancer cells", *Acta Biomaterialia*, **3**, 413–438, 2007.
- [3] Vinckier A., Semenza G. "Measuring elasticity of biological materials by atomic force microscopy", *FEBS Letters*, **430**, 12–16, 2008.

- [4] Costa K.D., Sim A. J.F., Yin C.P. "Non-Hertzian approach to analyzing mechanical properties of endothelial cells probed by atomic force microscopy", *Journal of Biomechanical Engineering*, **128**, 176–184, 2006.
- [5] Charles R., Sekatski S., Dietler G., Catsicas S., Lafont F., Kasas S. "Stiffness tomography by atomic force microscopy", *Biophysical Journal*, **97**, 674–677, 2009.
- [6] Bhushan B. "*Handbook of Nanotechnology*", Springer, 2007.
- [7] Hertz H. "On the contact of elastic solids", *J. Reine Angew. Mathematik*, **92**, 156–171, 1881.
- [8] Johnson K.L. "*Contact Mechanics*", Cambridge University Press, New York, 1985.
- [9] Mooney M. A theory of large elastic deformation. *Journal of Applied Physics*, **11**, 582–592, 1940.
- [10] Rivlin R.S. "Large elastic deformations of isotropic materials I. Fundamental concepts". *Philosophical Transactions of the Royal Society of London*, **A240**, 459–490, 1948.
- [11] Rivlin R.S., "Large elastic deformations of isotropic materials IV. Further developments of the general theory". *Philosophical Transactions of the Royal Society of London*, **A241**, 379–397, 1948.
- [12] Briscoe B.J., Sebastian K.S., Adams M.J., "The effect of indenter geometry on the elastic response to indentation". *Journal of Physics D: Applied Physics*, **27**, 1156–1162, 1994.

Standards for Validating Stress Analyses by Integrating Simulation and Experimentation

Erwin Hack¹, George Lampeas², John Mottershead³, Eann Patterson⁴, Thorsten Siebert⁵ and Maurice Whelan⁶

¹ Laboratory of Electronics/Metrology/Reliability, EMPA, Duebendorf, Switzerland

² Department of Mechanical Engineering and Aeronautics, University of Patras, Greece

³ Department of Mechanical Engineering, University of Liverpool, UK

⁴ Composite Vehicle Research Center, Michigan State University, East Lansing, MI 48824, USA. eann@egr.msu.edu

⁵ Dantec Dynamics GmbH, Ulm, Germany

⁶ Institute for Health and Consumer Protection, European Commission DG Joint Research Centre, Italy.

ABSTRACT

A reference material and a series of standardized tests have already been developed for respectively calibrating and evaluating optical systems employed for measuring in-plane static strain (for draft standard see: www.twa26.org). New work has commenced on the design of a reference material (RM) for use with instruments or systems capable of measuring three-dimensional displacements and strains during dynamic events. The rational decision-making process is being utilized and the initial stages have been completed, i.e. the identification and weighting of attributes for the design, brain-storming candidate designs and evaluation of candidate designs against the attributes. Twenty-five attributes have been identified and seven selected as being essential in any successful design, namely: the boundary conditions must be reproducible; a range of in-plane and out-of-plane displacement values must be present inside the field of view; the RM must be robust and portable; there is a means of verifying the performance in situ; and for cyclic loading it must be possible to extract data throughout the cycle. More than thirty candidate designs were generated and have been reduced to nine viable designs for further evaluation. In parallel with this effort to design a reference material, work is also in progress to optimize methodologies for conducting analyses via both simulations and experiments. Image decomposition methods are being explored as a means to making quantitative comparisons full-field data maps from simulations and experiments in order to provide a comprehensive validation procedure.

1. INTRODUCTION

1.1 Engineering context

The Olympic motto is "Citius, Altius, Fortius" which translates as "Faster, Higher, Stronger"; for the modern design engineer this could be modified only slightly to "Faster, Lighter, Stronger". In an era where global competition dominates industry, everyone wants everything to be faster so that you can gain edge on your competitors and generally speaking it is easier to achieve swiftness with lighter designs while the dangers inherent in great speed imply the need for greater strength. Lighter and stronger also provide advantages in terms of environmental footprint since lighter usually implies more energy efficient both in terms of service and manufacturing resources, and stronger offers the potential for a longer life cycle. In the quest for "Faster, Lighter, Stronger" structural analysis plays a crucial part in optimizing the performance of devices, machines and vehicles of all types and ensuring that safety requirements are achieved. In most design processes, computational modeling is the dominant form of structural analysis and so the reliability of the model becomes a critical issue for engineers involved in making design decisions. Schwer [1] has described in outline a 'Guide for verification and validation in

computational solid mechanics' [2]. In this context verification is defined as being two processes: first, identifying and eliminating errors of logic and programming from the code used for modeling; and second, quantifying the errors arising from the code as a consequence of discretizations required for the modeling. So verification can be largely performed without reference to the real-world whereas validation is concerned with establishing how well the model represents the real-world, at least in the context of the anticipated use of the model for solid mechanics or more particularly, design. It is recommended that validation should be achieved by reference to experiments conducted specifically for this purpose but the guide provides no insight or guidelines for the conduct of such experiments. This is not surprising since the computational mechanics community was responsible for the guide's preparation; however, the experimental mechanics community has not been idle in this regard and made a first step with a draft proposed standard for the calibration and evaluation of optical system for in-plane, static strain measurement in 2007 [3]. An outline description of this proposed standard is provided below and then work in progress to extend it to include three-dimensional measurements in dynamic loading cases is reported.

1.2 Calibration and evaluation of measurement systems for in-plane, static strain

Technical Working Area 26: Full-field Optical Stress and Strain Measurement [4] of VAMAS [5] was formed in 1999 with the aim of bringing together those concerned with the use of optical techniques for full field measurements of stress and strain in order to develop internationally accepted standards. In 2002 a consortium of European organisations embracing universities, research laboratories, instrument manufacturers, end users and national laboratories was formed to pursue SPOTS (Standardisation Project for Optical Techniques for Strain measurement) [6]. SPOTS was an EC shared cost RTD contract (no. G6RD-CT-2002-00856 (SPOTS)) which lasted for three years and in 2006 issued a proposed standard for calibration and assessment of optical strain measurement systems [4, 6]. This document has been endorsed by VAMAS TWA26 following independent international review and is currently awaiting recommendation by VAMAS to ISO.

The SPOTS standard relates to optical systems designed for making measurements of static strain over a field of view which can be approximated to a plane. A reference material, shown in [figure 1](#), and accompanying experimental protocol are provided for the calibration of such instruments at any scale. Indeed the standard recommends that the calibration should be conducted at the same scale as the planned experiment and for the same range of strain values.

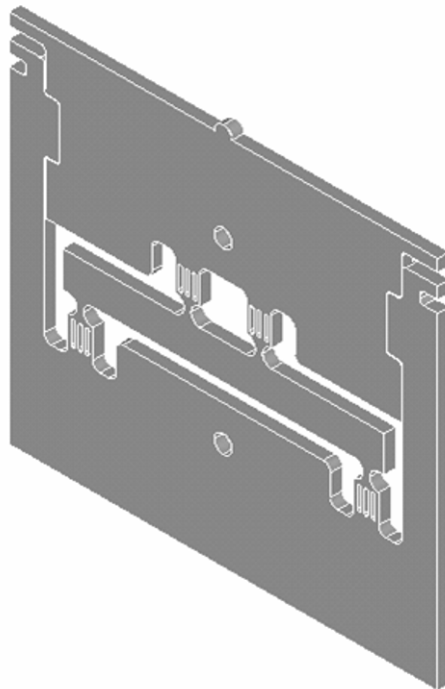


Figure 1: Three-dimensional view of the physical reference material (*EU Community Design Registration 000213467*) which is scalable to any size and can be manufactured in any material. (©SPOTS consortium)

Briefly, the reference material consists of a monolithic frame surrounding a beam subject to four-point bending. The gauge section of the reference material is the central portion of the beam. The beam is connected to the frame by a series of whiffle-trees which are designed to minimize the constraints applied to the beam. The frame ensures that the boundary and loading conditions are easily reproducible which earlier round-robin had demonstrated were a limiting issue in making comparisons between datasets [7]. The load can be applied in compression by placing the reference material on a platen and loading the nipple on the top surface, or in tension using the two circular holes along its center-line. The load is monitored as a relative displacement of the upper and lower portions of the frame which can be measured via a calibrated displacement transducer at the top left and top right corners. The use of calibrated displacement transducers provides the first link in the chain of traceability to the length standard. The importance of traceability in this context has been discussed by Hack et al [8]. The flowchart in figure 2 illustrates the experimental protocol for the use of the reference material and an exemplar of its use is provided by Whelan et al [9]. The values to be reported from the calibration process are highlighted in a box on the right of the flow chart and include the uncertainties in the calibration which are the minimum uncertainties that would be obtained in any subsequent experiment using the calibrated instrument. These uncertainties allow confidence limits to be defined for measured strain data which significantly improves the quality of data provided for the validation process.

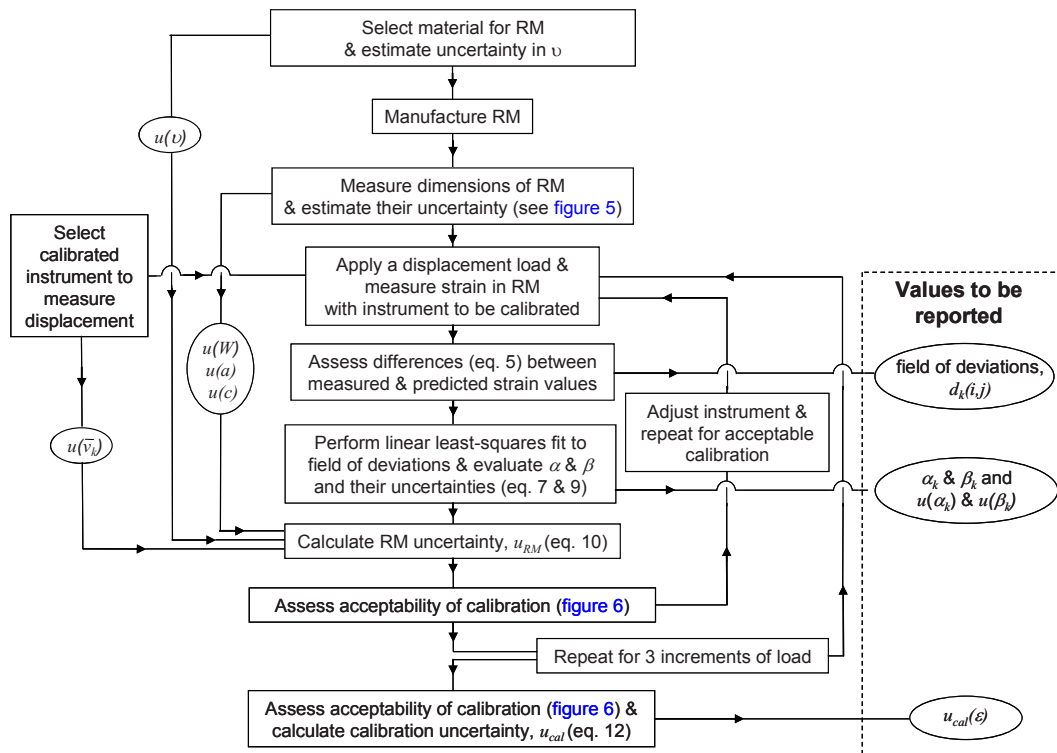


Figure 2: Flow-chart for performing a calibration of an optical system for full-field strain measurement using the SPOTS reference material where u is uncertainty, W , a and c are characteristic dimensions, ν is Poisson ratio and α and β are fit parameters relating to the correlation of the experimental and analytical strain distribution for the gauge section of the beam. References to figures and equations relate to the SPOTS standard found in [6] (© SPOTS consortium)

The SPOTS consortium also provided the design and protocol for a standardised test material [6, 10] for use in evaluating an optical system against its design specification or other instruments. The strain distribution in the gauge section of the standardised test material is significantly more complicated than the simple linear distribution in the reference material and is designed to be a challenge to the capabilities of the most sophisticated instrument. As shown in figure 3, the gauge section consists of a disc in contact with a semi-infinite half-plane and is surrounded by a monolithic frame as in the reference material. The standardised test material can only be loaded in compression and contains the same feature for protecting the gauge section from overload and for monitoring the displacement load although in this case traceability to the length standard is not required. The rigid motion implicit in the contact loading presents difficulties for many strain measurement techniques and can be reduced substantially by loading the test material upside down as shown in figure 3. However, it should be noted that many real-world scenarios will involve significant rigid body motion.

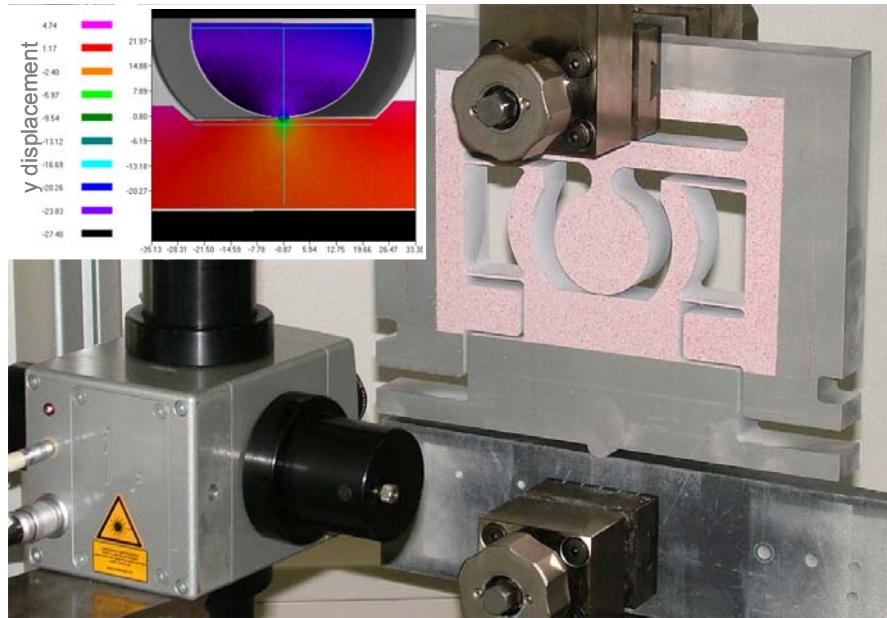


Figure 3: A physical standardised test material (*EU Community Design Registration 000299094*) manufactured from aluminium having a disc diameter of 50mm being tested using an ESPI system (Dantec Dynamics Q300) with typical results shown inset. (© SPOTS consortium)

2. VALIDATION OF DYNAMIC ANALYSES

2.1 The ADVISE Project

The SPOTS project was completed in early 2006 and a new consortium was formed during 2008 under the title of ADVISE (Advanced Dynamic Validations using Integrated Simulation and Experimentation) [11] with the purpose of extending the work into three dimensions and dynamic loading. ADVISE is a three-year program partly funded by the EU 7th Framework Programme. The members were selected to provide continuity from the SPOTS project, to create an international collaboration and to span the innovation process from concept through product development and manufacture to end-use. The partners in ADVISE are: Airbus (UK), Centro Ricerche Fiat (Italy), Dantec Dynamics GmbH (Germany), EC Joint Research Centre, EMPA Swiss Federal Laboratories for Materials Testing and Research (Switzerland), High Performance Space Structure Systems GmbH (Germany), Michigan State University (USA), University of Liverpool (UK) and the University of Patras (Greece).

The goals of the ADVISE project are: to develop a reference material and associated protocol for the calibration of optical systems capable of measuring displacements in a wide range of dynamic applications so that a system can be certified and the measurement uncertainties quantified; and to develop a methodology for making quantitative comparisons between full-field data sets from such systems and computational models. Composite structures used in the transport industry are being used as a vehicle for testing these capabilities.

2.2 Design of a reference material

The rational decision making model [12] is being employed to guide the design of the new reference material following its successful use in the SPOTS project and because it has the considerable advantage of providing clear opportunities for input by the wider experimental mechanics community. In outline, this model involves the definition and subsequent weighting, in terms of importance, of attributes that the design either must (essential attributes) or should (desirable attributes) possess. Candidate designs are then developed, often through brainstorming, and then evaluated on the extent to which they possess the attributes. Designs that do not or could not be modified to possess all of the essential attributes are discarded and the remainder are ranked based on the weighted sum of the degree of possession of each attribute. The top ranked designs are taken forward for detailed embodiment and further evaluation.

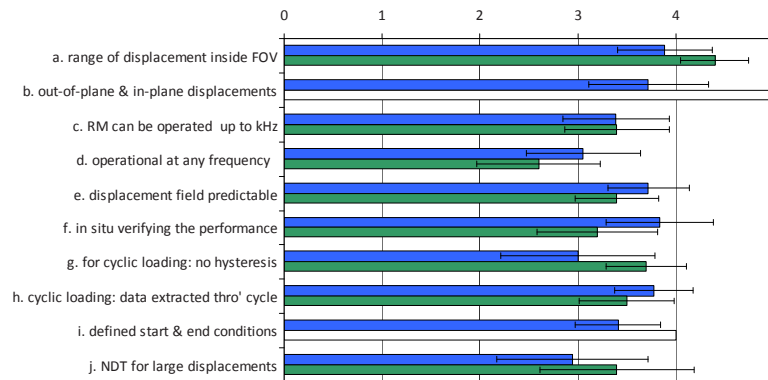


Figure 4: Attributes and their weightings for the displacement field in the dynamic reference material. The weightings (1 - unimportant, 2 - preferred, 3 - important, 4 - highly desirable, or 5 – essential) assigned by individual partners in the project were averaged (*green*) and the same exercise repeated for the wider community (*blue*). Some attributes were suggested by the community during the weighting process (*white*) and so were not weighted by a significant number of participants. (© ADVISE consortium)

The ADVISE consortium developed a set of attributes in early 2009 which were presented to the community at a VAMAS TWA26 workshop held at the Society for Experimental Mechanics Conference in Albuquerque, NM in June 2009. Participants at the workshop and members of the Society were invited by email to suggest additional attributes and to weight them. The results are presented in figures 4 and 5 together with the weightings based on input from the ADVISE partners. The essential attributes were chosen as those for which the sum of the mean and a standard deviation was greater than 4.0 when the data from the ADVISE consortium was merged with that from the community. The essential attributes are listed below:

- there is a range of displacement values inside the field of view
- in-plane and out-of-plane displacements available
- there is a means of verifying the performance in situ
- for cyclic loading: data can be extracted throughout the cycle
- the boundary conditions are reproducible
- it is portable
- it is robust

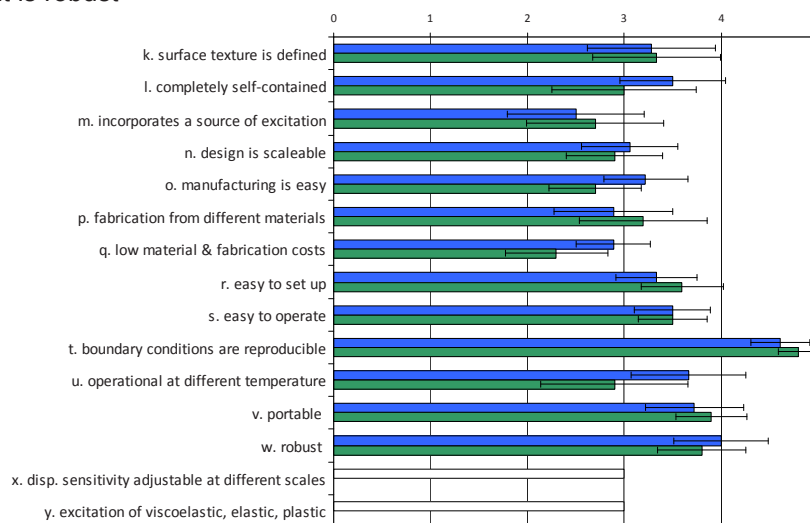


Figure 5: Attributes and their weightings for the physical embodiment of the dynamic reference material. The weightings (1 - unimportant, 2 - preferred, 3 - important, 4 - highly desirable, or 5 – essential) assigned by individual partners in the project were averaged (*green*) and the same exercise repeated for the wider community (*blue*). Some attributes were suggested by the community during the weighting process (*white*) and so were not weighted by a significant number of participants. (© ADVISE consortium)

The ADVISE consortium met in Fall 2009 to brainstorm candidate designs for the reference material that would be appropriate for cyclic loading, single high-speed loading events that result in deformations that vary linearly with load and single high-speed loading events that result in deformations that vary non-linearly with load. More than thirty candidate designs were generated but after assessment for the possession of the essential attributes only nine designs have been retained for further evaluation. At the time of writing these designs are undergoing evaluation involving both experimentation and computational modeling in order to gain a full understanding of their potential, prior to selecting a final design for detailed development and preparation of an accompanying protocol for its use.

3. DISCUSSION AND CONCLUSIONS

A guide for the verification and validation of computational solid mechanics was published in 2006 [1, 2] and has been complemented by a proposed standard for the calibration and evaluation of optical systems for full-field strain measurement [3, 4, 6]. The latter is applicable only to in-plane, static strain distributions but nevertheless represented a substantial effort that included one of the first attempts to quantify the uncertainties involved in measuring strain over a wide field of view.

A new project was launched in late 2008 to extend the proposed standard to include three-dimensional strain analysis in dynamic cases. A single reference material is being sought that would allow calibration of optical systems capable of measuring displacement and, or strain in three dimensional components subject to dynamic loading which might or might not be cyclical and that may or may not induce non-linear responses. This is wide and challenging design brief which is being tackled with the aid of the rational decision making model and with input from the community. The consortium undertaking the development has an international membership with representation from across the innovation process and appears to be broadly representative of the wider experimental mechanics community as indicated by the excellent correlation of the weighting of design attributes shown in [figure 6](#).

The new design of reference material is due for completion in late 2011 and following a period of testing within the ADVISE consortium will be available via a round-robin for more comprehensive tests within the wider community. A protocol for its use and the reporting of results will also be produced. In parallel, research is underway to establish viable methods for making quantitative comparisons of large data fields generated from computational and experimental approaches to structural analysis. Ultimately it is expected that this new work will be incorporated into a revised draft standard by VAMAS TWA26.

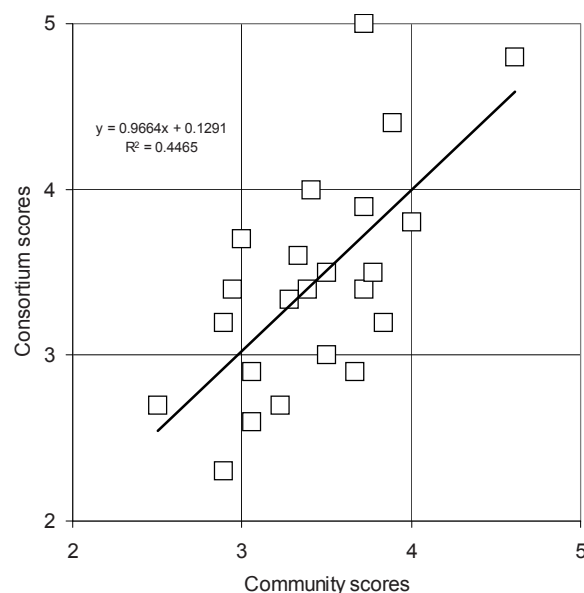


Figure 6: Correlation of the weightings by the ADVISE consortium partners and the members of the scientific community of the attributes required or desired in the dynamic reference material. (© ADVISE consortium)

ACKNOWLEDGEMENTS

The authors cheerfully acknowledge the inputs of the following persons in the ADVISE project: Richard Burguete, Mara Feligiotti, Alexander Ihle, George Lampeas, John Mottershead, Andrea Pipino, Hans Reinhard Schubach, Thorsten Siebert, and Victor Wang. The ADVISE project is a Seventh Framework Programme Collaborative Project within Theme 7: Transportation including Aeronautics (Grant no. 218595) funding of which is gratefully acknowledged.

REFERENCES

1. L.E. Schwer, 'An overview of the PTC 60/V&V 10: guide for verification and validation in computation solid mechanics', *Engineering with Computers*, **23**:245-252 (2007)
2. ASME V&V 10-2006, Guide for verification and validation in computational solid mechanics, American Society of Mechanical Engineers, New York, 2006.
3. E.A. Patterson, E. Hack, P. Brailly, R.L. Burguete, Q. Saleem, T. Siebert, R.A. Tomlinson, M.P. Whelan, 'Calibration and evaluation of optical systems for full-field strain measurement', *Optics and Lasers in Engineering*, 45(5):550-564, 2007.
4. www.twa26.org
5. www.vamas.org
6. www.opticalstrain.org
7. D. -A. Mendels, E. Hack, P. Siegmann, E.A. Patterson, L. Salbut, M. Kujawinska, H.R. Schubach, M. Dugand, L. Kehoe, C. Stochmil, P. Brailly, M.P. Whelan, 'Round robin exercise for optical strain measurement', Proc. 12th Int. Conf. Exptl. Mechanics, Advances in Experimental Mechanics edited by C. Pappalettere, McGraw-Hill, Milano, pp.695-6, 2004.
8. E. Hack, R.L. Burguete, E.A. Patterson, 'Traceability of optical techniques for strain measurement', Proc. BSSM Int. Conf. on Advanced Experimental Mechanics, Southampton, UK, published as Applied Mechanics & Materials, vols.3-4, pp.391-396, 2005.
9. M.P. Whelan, D. Albrecht, E. Hack, E.A. Patterson, 'Calibration of a speckle interferometry full-field strain measurement system', *Strain*, 44(2):180-190, 2008.
10. E.A. Patterson, P. Brailly, R.L. Burguete, E. Hack, T. Siebert, M.P. Whelan, 'A challenge for high performance full-field strain measurement systems', *Strain*, 43(3):167-180, 2007.
11. www.dynamicvalidation.org
12. N. Cross, *Engineering Design Methods* (John Wiley & Sons, London, 1989)

Avalanche Behavior of Minute Deformation Around Yield Point of Polycrystalline Pure Ti

G. Murasawa*, T. Morimoto*, S. Yoneyama**, A. Nishioka*, K. Miyata* and T. Koda*

*Department of Mechanical Engineering, Yamagata University, 4-3-16, Jonan, Yonezawa, Yamagata 992-8510, Japan, Japan. murasawa@yz.yamagata-u.ac.jp

**Department of Mechanical Engineering, Aoyama Gakuin University, 5-10-1 Fuchinobe, Sagami-hara, Kanagawa 229-8558, Japan.

ABSTRACT

The aim of present study is to investigate the avalanche behavior of minute deformation around yield point of polycrystalline pure Ti. Firstly, we prepare commercial polycrystalline pure Ti (99.5%) thin plate, and investigate the pole figures and inverse pole figure distribution for rolling direction on the surface of specimen, which is obtained from Electron Backscatter Diffraction Patterns (EBSD). Secondly, tensile specimens are cut out from 0°, 30°, 45° and 90° relative to rolling direction of thin plate. Then, we attempt to measure macroscopic stress-strain curve, local strain distribution and minute deformation arising in specimens under tensile loading. In this time, the in-house measurement system integrated with tensile machine control system, local strain distribution measurement system and minute deformation measurement system is constructed suited on a LabVIEW platform. Local strain distribution is measured by in-house system on the basis of Digital Image Correlation (DIC). Also, minute deformation behavior is measured by in-house other one on the basis of acoustic emission (AE). Finally, we discuss about the mechanism of avalanche behavior of minute deformation around yield point of polycrystalline pure Ti on the basis of results in present study.

1. INTRODUCTION

Macroscopic deformation behavior, such as stress-strain curve, is subject to the minute deformation behavior like the motion of slip or twinning deformation. Such minute deformation behavior reveals the phenomena of "Intermittent deformation behavior", "Spatial clustering and avalanche behavior" and "Self-similar or scale free". These phenomena are not continuous deformation, but discontinuous deformation. Although continuum approaches are selectively useful for describing deformation, they completely fail to account for well-known discontinuous deformation phenomena.

Steel and Aluminum alloys usually show local deformation behavior such as the propagation of Luders band, Portevin Le Chatelier effect and necking. Recently, some researchers began to study about the nucleation and propagation of shear band for some metal materials (Kuroda et al., 2007; Tong et al., 2005; Zhang et al., 2004; Cheong et al., 2006; Tang et al., 2005; Hoc et al., 2001; Louche et al., 2001). These studies are that predicting macroscopic deformation is tried by continuum approaches, but it is difficult to describe the detailed behavior based on the mechanism of deformation for solid materials.

In recent years, Weiss and Uchic are aggressively studying about the minute deformation behavior for solid materials. Weiss measured the motion of slip under creep deformation for single- and poly- crystalline ice by using Acoustic Emission (AE) technique. They reported that minute deformation shows avalanche behavior and its behavior is different between single- and poly- crystalline. Also, Uchic fabricated the micro-order specimen of pure Ni by focused ion beam process. Then, they conducted uniaxial compression test for the micro-order specimen. They reported that minute deformation shows the phenomenon of scale free.

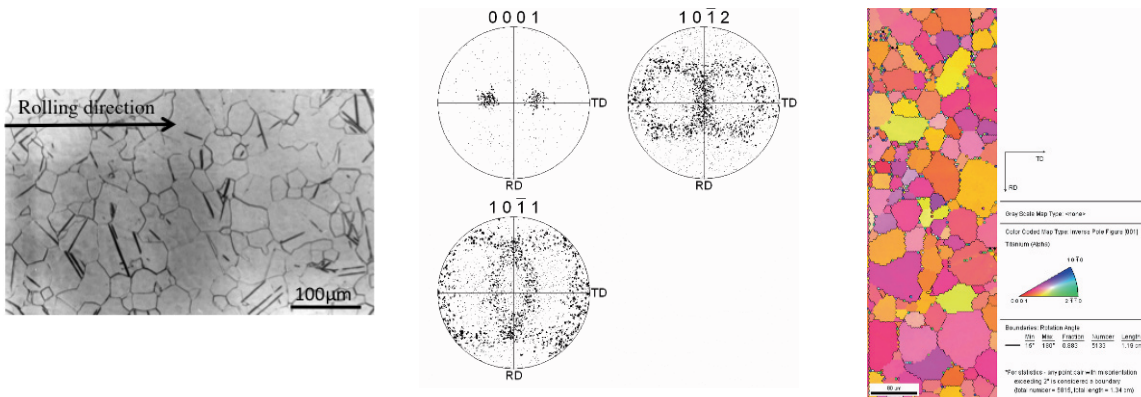
The aim of present study is to investigate the avalanche behavior of minute deformation around yield point of polycrystalline pure Ti. Firstly, we prepare commercial polycrystalline pure Ti (99.5%) thin plate, and investigate

the pole figures and inverse pole figure distribution for rolling direction on the surface of specimen, which is obtained from Electron Backscatter Diffraction Patterns (EBSD). Secondly, tensile specimens are cut out from 0°, 30°, 45° and 90° relative to rolling direction of thin plate. Then, we attempt to measure macroscopic stress-strain curve, local strain distribution and minute deformation arising in specimens under tensile loading. In this time, the in-house measurement system integrated with tensile machine control system, local strain distribution measurement system and minute deformation measurement system is constructed suited on a LabVIEW platform. Local strain distribution is measured by in-house system on the basis of Digital Image Correlation (DIC). Also, minute deformation behavior is measured by in-house other one on the basis of acoustic emission (AE). Finally, we discuss about the mechanism of avalanche behavior of minute deformation around yield point of polycrystalline pure Ti on the basis of results in present study.

2. MATERIAL AND METHODS

2.1 Materials

Material is commercial polycrystalline pure Ti (99.5%) thin plate (Nilaco co.). Pure Ti shows hexagonal close-packed structure. The deformation mode is mainly twinning deformation. Figure 1(a) shows an optical image of microstructure for present Ti. Also, Fig. 1(b) shows pole figures, (0001), (1012) and (1011) planes, of present Ti plate. Figure 1(c) demonstrates the inverse pole figure distribution for rolling direction on the surface of specimen, which is obtained from Electron Backscatter Diffraction Patterns (EBSD). Tensile specimens are cut out from 0°, 30°, 45° and 90° relative to rolling direction of thin plate as shown in Fig. 2(a). Figure 2(b) shows specimen configuration. The stainless steel tabs are attached to the specimen by epoxy resin. Also, random pattern is created on the surface of specimen by spraying black and white paint for measuring strain distribution by Digital Image Correlation (DIC) method.

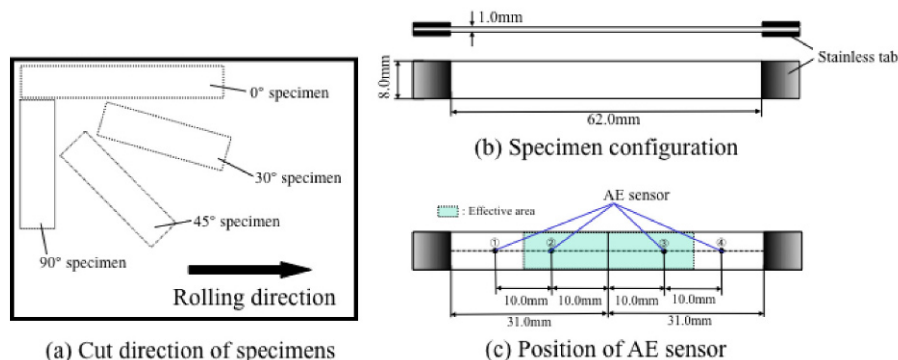


(a) Microstructure

(b) pole figures

(c) inverse pole figure distribution

Figure 1. Microstructure, pole figures and inverse pole figure distribution for polycrystalline pure Ti



(a) Cut direction of specimens

(b) Specimen configuration

(c) Position of AE sensor

Figure 2. Specimen configuration

2.2 Measurement Method of Local Deformation Behavior (LDB)

Digital Image Correlation (DIC) software is in-house software, and the details of DIC are presented in the references. In these references, Yoneyama et al. proposed the principal method and its algorithm of DIC to calculate displacement field from two pictures (i.e., undeformed image and deformed image). Also, they have applied this method to the measurement of stress intensity factor around crack tip and bridge deflection.

A test system, local deformation behavior (LDB) measurement system, is also constructed on the basis of DIC as an in-house software suited on a LabVIEW platform. We can semi-automatically measure strain distribution by using the test system. The test system consists of three parts as follows: (A) Image acquisition, (B) Digital image correlation, (C) Calculation of local strain distribution. Firstly, the images used in DIC are taken at an interval during the deformation of specimen. Secondly, two images (i.e., undeformed image and deformed image) are selected from whole images, and the displacement all over the surface of specimen can be calculated by comparing these two images in DIC. Thirdly, the local strain all over the surface of specimen is calculated from the distribution of displacement. Its details of test system, especially in the calculation method of strain field obtained from displacement field, are presented in the references.

2.3 Measurement Method of Minute Deformation Behavior and Data Analysis Method

Acoustic emission (AE) is a powerful technique for studies about minute deformation behavior that arise from the motion of dislocation and twinning deformation. Acoustic waves are generated by dislocation and twinning glide, and many information of deformation can be obtained from detected acoustic waves.

2.3.1 Measurement of AE

In present study, the AE signals generated from twinning deformation are monitored by four small AE sensors, which are mounted on the surface of the specimen. Four small AE sensors are aligned on a center straight line of the surface of the specimen as shown in Fig. 2(c). In present experiment, we use No.1 and No.4 sensors as guard sensor, and No.2 and No.3 sensors as effective sensor in order to get AE signals only from effective area. A method to distinguish the AE signals from effective area with that from other area, is as follows; (1) Four AE signals are monitored for a event during deformation, (2) Arrival times (No.1 sensor: t_1 , No.2 sensor: t_2 , No.3 sensor: t_3 , No.4 sensor: t_4) are recorded from the AE signals, (3) If $t_1 < t_2$ or $t_4 < t_3$, then AE signals are regarded as a signal out of effective area. In other case, AE signals are regarded as a signal from effective area. These processes are automatically conducted during deformation of materials by in-house software suited on a LabVIEW platform.

2.3.2 Analysis of AE-count data

Also, we can obtain the relationship between cumulative AE counts and time from detected AE signals. Furthermore, we can calculate the AE-count speed-time relation from the cumulative AE counts-time curves. AE-count speed is the slope of cumulative AE counts-time curves at each time. Avalanche behavior can be seen from these curves. Calculation method of AE-count speed is shown in Fig. 3. Firstly, an arbitrary point on the cumulative AE counts-time curve is selected, and its before and after points, 50 points, are pointed as shown in Fig. 3(a). Secondly, these 51 points are approximated by quadratic least squares method. Thirdly, the slope of approximated quadratic curve is obtained at the point x_0 as shown in Fig. 3(b). The value of slope is AE-count speed at the point x_0 . This calculation is conducted at all points on cumulative AE counts-time curve. Obtained AE-count speed-time relation is shown in Fig. 3(c). Calculation is automatically conducted for all data by in-house data analysis software suited on a LabVIEW platform.

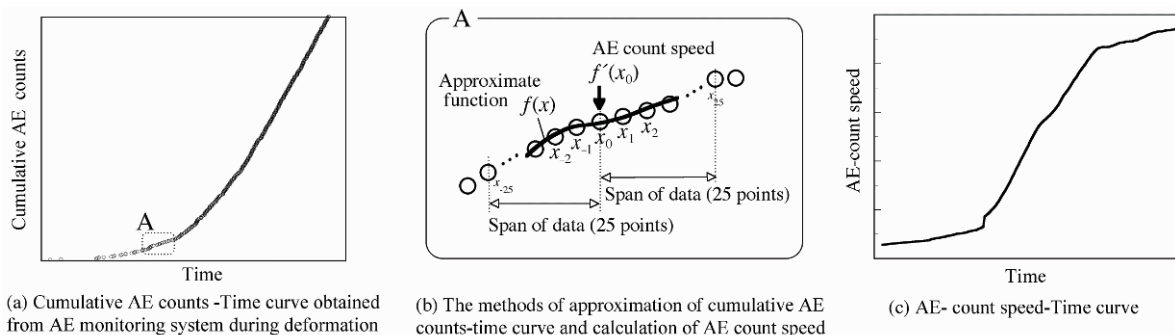


Figure 3. Method for calculating the AE-count speed

2.3.3 Wave analysis of AE

Figure 4 shows a typical AE signal monitored from No.2 and No.3 sensors. For each event, wave analysis allows us to record two parameters, the arrival time t_0 (the time at which the signal reaches threshold value A_{min}) and the maximum amplitude A_0 . Recording is automatically conducted for all data by in-house wave analysis software suited on a LabVIEW platform.

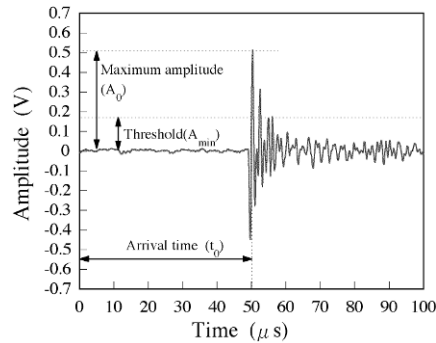


Figure 4. Detected AE wave

2.4 Experimental Setup of System Integrated with LDB and AE Measurement

The integrated experimental setup is shown in Fig. 5(a). Uniaxial tensile loading is performed for specimens at room temperature (21°C). Autograph (AGS- 5KNG, Shimadzu) is used in present tensile loading test, and it is controlled by in-house software suited on a LabVIEW platform. Tests are performed at strain rate, 0.08%/min. A CCD camera (HC-HR70, Sony) is set in front of the specimen as shown in Fig. 5(b). A 50mm lens (VCL-50Y-M, Sony) is attached to the CCD camera. The images of specimen are taken into computer every 120 second during tensile loading. Four small AE sensors with frequency bandwidth of 300kHz-2MHz (AE-900M, NF corporation) are mounted on another surface of the specimen like Fig. 5(c). The output signals are amplified 40 dB by the pre-amplifier (9916, NF corporation) and then 20 dB by the discriminator (AE9922, NF corporation), and fed to oscilloscope and computer. We set the proper threshold value (about 1mV) of AE signal. Data are sampled at an interval of 100 ns. We use the computer with a GPIB interface (NI GPIB-USB-HS, National Instrument) to control tensile machine, a monochrome PCI frame grabber (mVTITAN-G1, Matrix Vision) to acquire 1024×768 8-bit grayscale digital image from the CCD camera and two 12-bit AD converters (PCI-3163, Interface) to acquire AE signals from the AE sensors. Then, the in-house software integrated with tensile machine control system, LDB measurement system and AE measurement system is constructed suited on a LabVIEW platform as shown in Fig. 5(d).

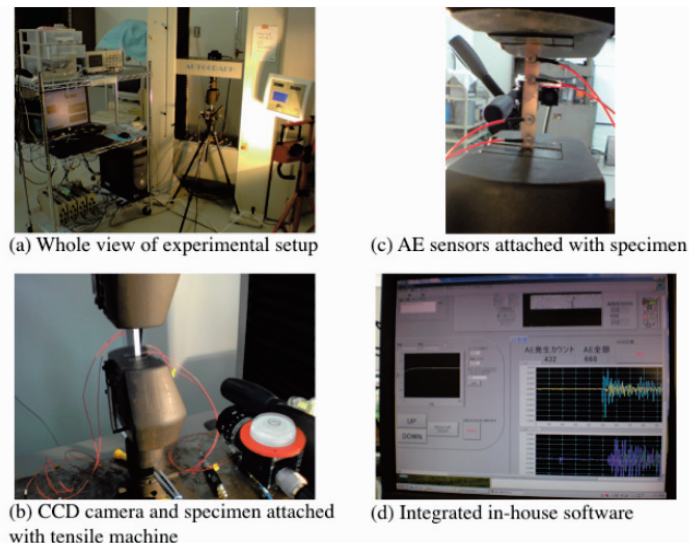


Figure 5. Experimental setup

3. RESULTS

3.1 Macroscopic Stress-strain Curves of Polycrystalline Pure Ti

Figure 6 shows macroscopic stress-strain (and stress-time) curves at room temperature (21°C) for different specimens which are cut out from 0°, 30°, 45° and 90° relative to rolling direction of pure Ti thin plate. From these results, it is seen that the results of 0° and 30° specimens show the same behavior. On the other hand, 45° specimen shows a little larger stress-strain curve than that of 0° and 30° specimens, and 90° specimen shows more larger one than others, around yield point.

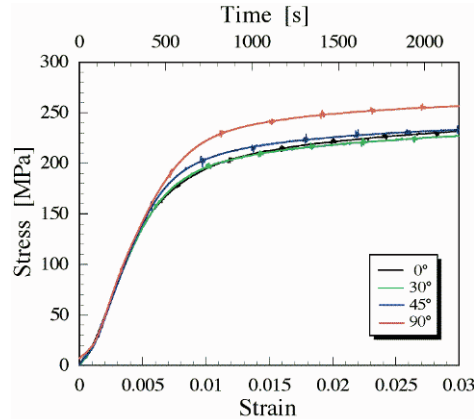
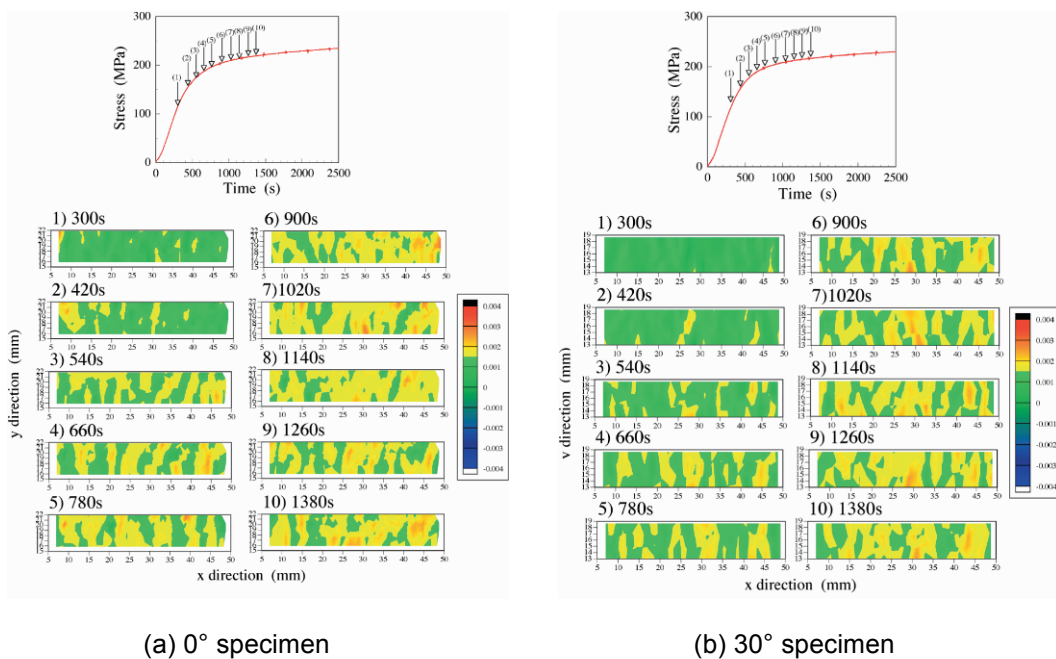


Figure 6. Macroscopic stress-strain (-time) curves for polycrystalline pure Ti

3.2 Local Deformation Behavior Around Yield Point of Polycrystalline Pure Ti

Figures 7(a)~(d) demonstrate stress-time curve and longitudinal local strain distribution for 0°, 30°, 45° and 90° specimens of polycrystalline pure Ti under uniaxial tensile loading at room temperature (21°C). Local strain distribution is measured at the points indicated as (1)~(10) or (12) in Figs. 7(a)~(d). Also, local strain distributions are acquired every 120s, which is corresponding to the nominal strain of 0.16%. The value of strain is shown in right hand scale level in Fig. 7. The longitudinal and transversal axes of the results for local strain distribution in Figs. 7(a)~(d) show the position on picture used in DIC, which are along to x (horizontal axis) direction and y (vertical axis) direction in picture. From even a cursory examination of Fig. 7(a)~(d), it is seen that all specimens reveal



(a) 0° specimen

(b) 30° specimen

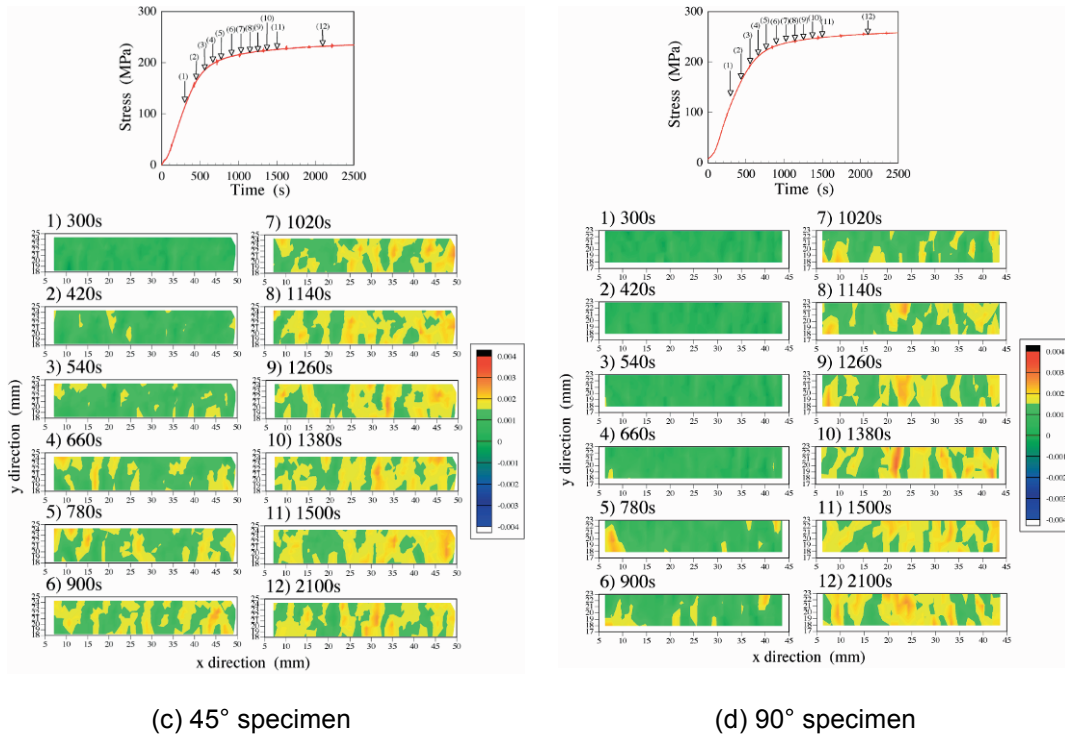


Figure 7. Longitudinal strain distribution under uniaxial tensile loading for polycrystalline pure Ti

inhomogeneous deformation behavior, and the cluster of local strain gradually increase around yield point of stress-strain curve. Also, the initiation for the cluster of local strain depends on the cut direction of specimen, and it becomes late from 0° to 90°.

3.3 Minute Deformation Behavior Around Yield Point of Polycrystalline Pure Ti

Figure 8 gives stress-time curve, cumulative AE counts-time curve and AE-count speed-time curve around yield point for all specimens during tensile loading. As shown in these figures, it can be seen that these curves depend on the cut direction of specimen. Also, from the results of AE-count speed-time curves, 0° and 30° specimens

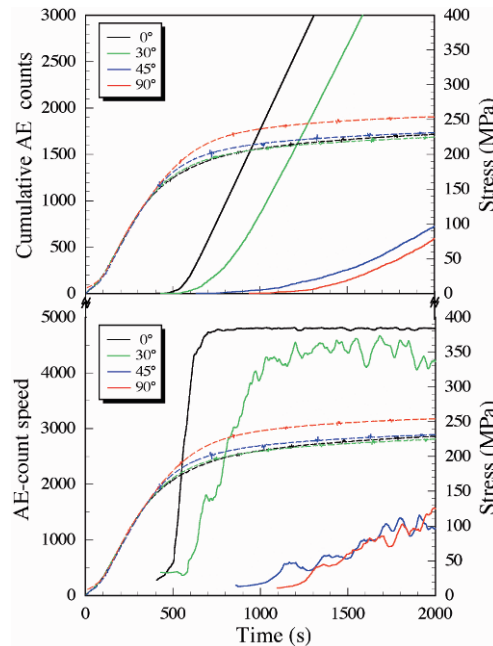


Figure 8. Cumulative AE count – time curves and AE count speed – time curves under uniaxial tensile loading for polycrystalline pure Ti

suddenly show the phenomenon such as avalanche of minute deformation around the early stage of yield point, and especially 0° specimen demonstrates large avalanche behavior. AE-count speed becomes equilibrium state after showing avalanche behavior during tensile loading. On the other hand, minute deformation does not appear around the early stage of yield point for 45° and 90° specimens. Then, their specimens show slow avalanche behavior at the latter stage of yield point or the beginning stage of plastic flow, as compared with former ones.

4. DISCUSSION

4.1 Multi-scale Deformation Structure

We could measure the macroscopic inhomogeneity of local strain and the avalanche behavior of minute deformation for polycrystalline pure Ti under uniaxial loading by using digital image correlation and acoustic emission techniques. From these results, following deformation structure can be supposed. Figure 9 shows the schematic illustration of macroscopic inhomogeneity arising in polycrystalline pure Ti under uniaxial loading. Firstly, the clusters of local strain appear during the elastic deformation for macroscopic stress – strain curve. Secondly, the regions of cluster drastically increase around yield point. Thirdly, the increase of clusters becomes constant under plastic deformation. Figure 10 illustrates the mechanism of deformation for polycrystalline pure Ti under uniaxial loading. As shown in this figure, a cluster consists of a lot of twinning deformation regions. A twinning deformation region consists of some grains at which are appeared twinning bands (Fig.10(b)). Also, some researchers reported that the amplitudes of the acoustic signals are related to the area swept by the fast-moving dislocations and hence to the energy dissipated during deformation events. In present study, AE count is measured as the number of twinning deformation region. The amplitudes of the acoustic signals are related to the size of twinning deformation region. Also, a twinning band in a grain is illustrated as zigzag shape of crystal structures (Fig.10(c)).

It is well known that polycrystalline pure Ti shows anisotropic characteristics in macroscopic stress – strain curve. Then, the key points of mechanism of deformation are “initiation behavior” and “avalanche behavior” of minute deformation.

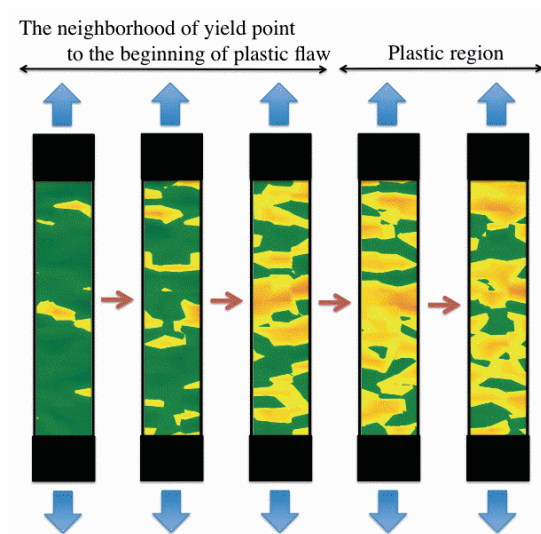


Figure 9. Increase of macroscopic inhomogeneity local strain

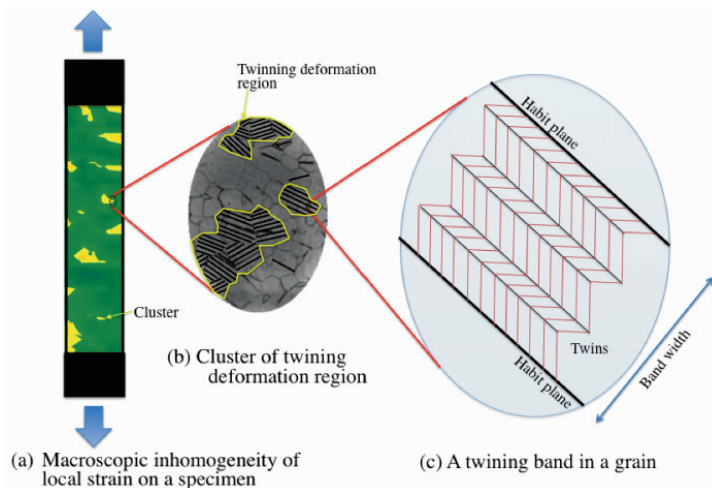


Figure 10. Schematic illustration of multi-scale deformation for structure for polycrystalline pure Ti

4.2 Mechanism of Initiation for Minute Deformation

Initiation of minute deformation is governed by the direction of grains in polycrystalline. Texture data is much important information to obtain the direction of grains for polycrystalline. In present study, texture data of polycrystalline pure Ti is obtained by EBSD equipment. Figure 1(b) shows pole figures, (0001), (1012) and (1011) planes, of present Ti plate. Figure 1(c) demonstrates the inverse pole figure distribution for rolling direction on the surface of specimen

In general, it is well known that (1012) or (1011) twin boundary in deformed polycrystalline pure Ti can be observed by high-resolution electron microscopy. It has been also reported that its structure has essentially a pure mirror symmetry. The structure is characterized by a mirror plane which corresponds to the coalescence of two separate atomic planes (0001) into a single plane (1012) or (1011). The angle of misorientation is close to 87° . From the results of Fig.1, it is seen that (1012) and (1011) planes randomly exist for the in-plane direction. On the other hand, the result of (0001) plane strongly shows anisotropy and its direction is parallel to rolling direction of specimen. Macroscopic experimental results show the anisotropic characteristics in macroscopic stress – strain curve and in initiation of the cluster of local strain, and in minute deformation behavior. That is to say, (0001) plane is something to do with the mechanism for the initiation of minute deformation. Twinning deformation occurs in a grain in polycrystalline under shear deformation for metal materials with hexagonal close-packed structure. Figure 11 shows the schematic illustration of the mechanism for the initiation of twinning band. In this time, it is assumed that the twinning plane is parallel to habit plane under applied load. Also, lattice transformation due to applied load occurs around habit plane (Fig.11(a)). Then, twinning deformation instantaneously develops as shown in Fig.11(b). In this time, we can see that the degree of initiation of twinning is strongly caused by the direction of plane which is firstly transformed lattice in a grain region by applied load. In other words, (0001) plane is initiation-related direction of plane. The closer (0001) plane before deformation is to plane which is firstly transformed lattice around habit plane, the easier occurrence of twinning is. In present study, (0001) plane is parallel to the rolling direction. The twinning deformation becomes hard to occur if the longitudinal direction of tensile specimen leaves from the rolling direction.

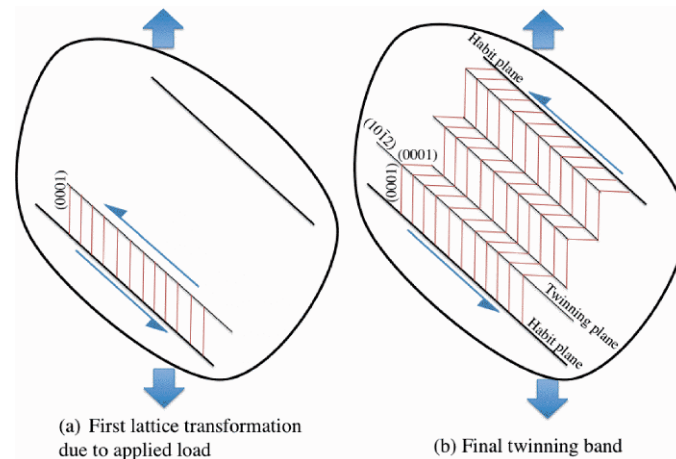


Figure 11. Schematic illustration of the mechanism for initiation of twinning deformation due to applied load

4.3 Mechanism of Avalanche Behavior for Minute Deformation

In present study, avalanche behavior can be investigated by evaluating AE counts. Furthermore, it is assumed that the amplitudes of the acoustic signals are related to the size of twinning deformation region, and the avalanche behavior can be connected with the size of twinning deformation region. Also, from the results of local strain distribution measurement and such an AE measurement, we can lead the mechanism of avalanche behaviors, such as the avalanche behavior of minute deformation causes the macroscopic inhomogeneity of local strain and so on. From the results of Fig.8, 0° and 30° specimens show strong avalanche behavior around yield point. On the other hand, 45° and 90° specimens show slow avalanche behavior at the latter stage of yield point or the beginning stage of plastic flow, as compared with former ones. This can imply that twinning deformation regions actively increase at the timing between the neighborhood of yielding point and the beginning stage of plastic flow.

Next, we take the size of twinning deformation region around yield point under uniaxial tensile loading into consideration for polycrystalline pure Ti. Figure 12 displays the cumulative number of event – amplitude relation obtained from AE signals for different specimens which are cut out from 0° , 30° , 45° and 90° relative to rolling direction of pure Ti thin plate. The cumulative number of event – amplitude relation is obtained by following ways. Firstly, 2000 AE signals during measurement are prepared, and maximum voltage is detected for each AE signal.

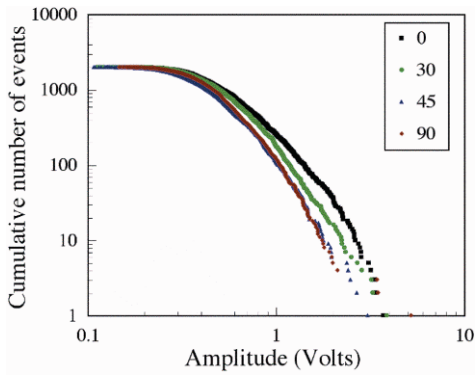


Figure 12. The cumulative number of event – amplitude relation obtained from all AE signals of present measurement

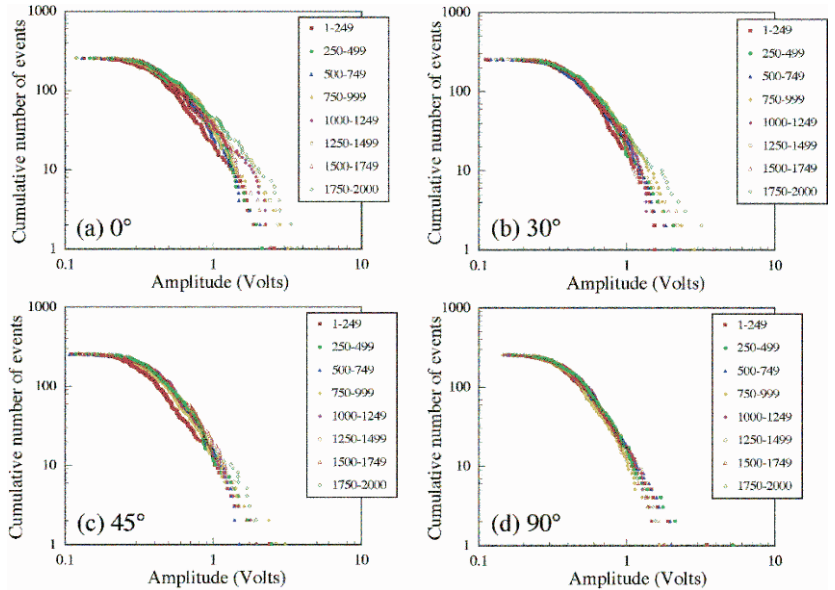


Figure 13. The cumulative number of events – amplitude relations for each 250 events during measurement

This maximum voltage is corresponding to the size of twinning deformation region for each event. Secondly, these maximum voltages are listed in order of amplitude. Thirdly, listed voltages are numbered from highest one to lowest one. The number and voltage are the cumulative number of event and amplitude in Fig. 12. As shown in Fig. 12, the cumulative number of events – amplitude relation for 90° specimen is the same as 45° specimen. On the other hand, it seems that the relation tends to shift to high amplitude with decreasing of the cut orientation. This implies that larger size of twinning deformation regions exist with decreasing of the cut orientation during measurement. Therefore, we try arranging the size of twinning deformation regions with the number of counts. Figure 13 demonstrates the cumulative number of events – amplitude relations for each 250 events during measurement, for 0°, 30°, 45° and 90° specimens. From these figures, we can see the dependency of the specimen orientation on the cumulative number of events – amplitude relations. In other words, as considered with results of Figs. 7 and 8 during measurement, twinning deformation regions of smaller size nucleate for 90° specimens. On the other hand, those of larger size nucleate for 0° specimens during measurement.

Figure 14 shows the schematic illustration of the mechanism for the initiation of twinning deformation region and its

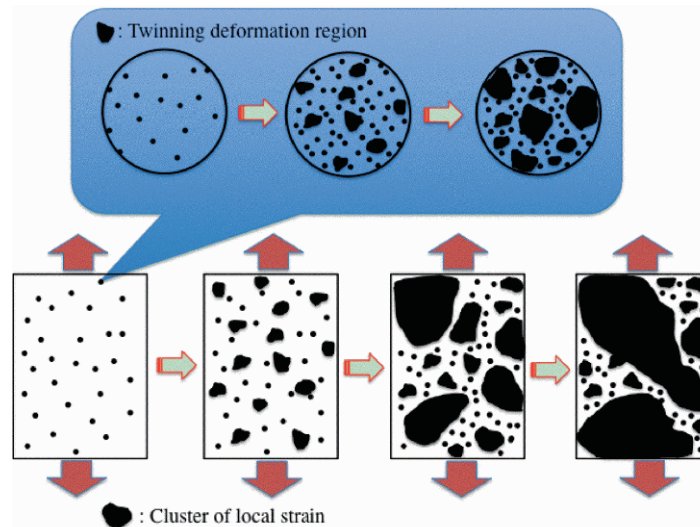


Figure 14. Schematic illustration of the mechanism for avalanche of minute deformation

cluster arising in polycrystalline pure Ti. As illustrated in this figure, firstly, twinning deformation regions nucleate with a certain space under mechanical deformation. Then, larger twinning deformation regions increase at the space between initiated smaller twinning deformation regions. The size of twinning deformation regions grow up under mechanical deformation, and it becomes the cluster of local strain which we can confirm from the results of local strain behavior measurements. While the size of twinning deformation regions is growing up under mechanical deformation, AE counts show the avalanche behavior. Then, it is much important for us to study “how do the twinning deformation regions behave in polycrystalline pure Ti during mechanical loading”. The study about the information for the initiated location of twinning deformation region, is future work.

5. CONCLUSIONS

Firstly, we prepare commercial polycrystalline pure Ti thin plate, and investigate the pole figures and inverse pole figure distribution for rolling direction on the surface of specimen. Secondly, tensile specimens are cut out from 0°, 30°, 45° and 90° relative to rolling direction of thin plate. Then, we measure macroscopic stress-strain curve, local strain distribution and minute deformation arising in specimens under tensile loading. Local deformation behavior measurement system is constructed on the basis of DIC and minute deformation behavior measurement system is constructed on the basis of AE. Then, we developed both of their in-house software suited on a LabVIEW platform. Obtained results are as followings.

- (1) From the results of macroscopic stress-strain curves, the results of 0° and 30° specimens show the same behavior. On the other hand, 45° specimen shows a little larger stress-strain curve than that of 0° and 30° specimens, and 90° specimen shows more larger one than others, around yield point.
- (2) From the results of local strain distribution, all specimens reveal inhomogeneous deformation behavior, and the cluster of local strain gradually increase around yield point of stress-strain curve. Also, the initiation for the cluster of local strain depends on the cut direction of specimen, and it becomes late from 0° to 90°.
- (3) From the results of minute deformation behavior, 0° and 30° specimens suddenly show the phenomenon such as avalanche of minute deformation around the early stage of yield point, and especially 0° specimen demonstrates large avalanche behavior. AE-count speed becomes equilibrium state after showing avalanche behavior during tensile loading. On the other hand, minute deformation does not appear around the early stage of yield point for 45° and 90° specimens. Then, their specimens show slow avalanche behavior at the latter stage of yield point or the beginning stage of plastic flow, as compared with former ones.

ACKNOWLEDGEMENTS

The author would like to express my deep gratitude to Prof. Mitsutoshi Kuroda (Yamagata University, Japan) and Associate Prof. Takuya Uehara (Yamagata University, Japan) for fruitfully discussing about present study. Also, The author would like to express my deep gratitude to Dr. Tadaaki Satake (Yamagata University, Japan) for the help of using EBSD.

REFERENCES

- Agnew and Duygulu. Plastic anisotropy and the role of non-basal slip in magnesium alloy AZ31B. *Int J Plasticity* (2005) vol. 21 (6) pp. 1161-1193
- Agnew et al. Application of texture simulation to understanding mechanical behavior of Mg and solid solution alloys containing Li or Y. *Acta Materialia* (2001) vol. 49 (20) pp. 4277-4289
- AKHTAR. Basal Slip and Twinning in a-Titanium Single Crystals. *METALLURGICAL TRANSACTIONS A* (1975) vol. 6A pp. 1105-1113
- BAK et al. SELF-ORGANIZED CRITICALITY - AN EXPLANATION OF 1/F NOISE. *Phys Rev Lett* (1987) vol. 59 (4) pp. 381-384
- BAK et al. SELF-ORGANIZED CRITICALITY. *Phys Rev A* (1988) vol. 38 (1) pp. 364-374
- Battaini et al. Orientation effect on mechanical properties of commercially pure titanium at room temperature. *Metall Mater Trans A* (2007) vol. 38A (2) pp. 276-285
- Braisaz et al. High-resolution electron microscopy study of the $\{10\bar{1}2\}$ twin and defects analysis in de-

- formed polycrystalline alpha-titanium. *Phil Mag Lett* (1996) vol. 74 (5) pp. 331-338
- Cai et al. Evolution equations of deformation twins in metals - Evolution of deformation twins in pure titanium. *Physica B* (2008) vol. 403 (10-11) pp. 1660-1665
- Capolungo et al. Slip-assisted twin growth in hexagonal close-packed metals. *Scripta Materialia* (2009) vol. 60 (1) pp. 32-35
- Carpinteri et al. Morphological Fractal Dimension Versus Power-law Exponent in the Scaling of Damaged Media. *International Journal of Damage Mechanics* (2008) vol. 18 (3) pp. 259-282
- Carpinteri et al. Critical defect size distributions in concrete structures detected by the acoustic emission technique. *Meccanica* (2008) vol. 43 (3) pp. 349-363
- Cheong and Busso. Effects of lattice misorientations on strain heterogeneities in FCC polycrystals. *J Mech Phys Solids* (2006) vol. 54 (4) pp. 671-689
- CHRISTIAN and MAHAJAN. DEFORMATION TWINNING. *Prog Mater Sci* (1995) vol. 39 (1-2) pp. 1-157
- Chun et al. Effect of deformation twinning on microstructure and texture evolution during cold rolling of CP-titanium. *Mat Sci Eng A-Struct* (2005) vol. 398 (1-2) pp. 209-219
- Dimiduk et al. Scale-free intermittent flow in crystal plasticity. *Science* (2006) vol. 312 (5777) pp. 1188-1190
- Dimiduk et al. Size-affected single-slip behavior of pure nickel microcrystals. *Acta Materialia* (2005) vol. 53 (15) pp. 4065-4077
- Ghoniem et al. On dislocation interaction with radiation-induced defect clusters and plastic flow localization in fcc metals. *Philos Mag A* (2001) vol. 81 (11) pp. 2743-2764
- Guelorget et al. Strain rate measurement by Electronic Speckle Pattern Interferometry: A new look at the strain localization onset. *Mat Sci Eng A-Struct* (2006) vol. 415 (1-2) pp. 234-241
- Hasnaoui et al. Interaction between dislocations and grain boundaries under an indenter - a molecular dynamics simulation. *Acta Materialia* (2004) vol. 52 (8) pp. 2251-2258
- Jakobsen et al. Formation and subdivision of deformation structures during plastic deformation. *Science* (2006) vol. 312 (5775) pp. 889-892
- Kuroda and Kuwabara. Shear-band development in polycrystalline metal with strength-differential effect and plastic volume expansion. *P Roy Soc Lond A Mat* (2002) vol. 458 (2025) pp. 2243-2259
- Lebyodkin et al. Spatio-temporal dynamics of the Portevin-Le Chatelier effect: Experiment and modelling. *Acta Materialia* (2000) vol. 48 (10) pp. 2529-2541
- Mayama et al. Influence of twinning deformation and lattice rotation on strength differential effect in polycrystalline pure magnesium with rolling texture. *COMPUTATIONAL MATERIALS SCIENCE* (2009) pp. 1-8
- Miguel et al. Intermittent dislocation flow in viscoplastic deformation. *Nature* (2001) vol. 410 (6829) pp. 667-671
- Murasawa et al. Macroscopic stress-strain curve, local strain band behavior and the texture of NiTi thin sheets. *Smart Mater Struct* (2009) vol. 18 (5) pp. 055003
- Nemat-Nasser et al. Mechanical properties and deformation mechanisms of a commercially pure titanium. *Acta Materialia* (1999) vol. 47 (13) pp. 3705-3720
- Pollock. Acoustic emission-2 Acoustic emission amplitudes. *Non-destructive testing* (1973) vol. 6 (5) pp. 264-269
- Proust et al. Modeling the effect of twinning and detwinning during strain-path changes of magnesium alloy AZ31. *Int J Plasticity* (2009) vol. 25 (5) pp. 861-880
- Rechenmacher. Grain-scale processes governing shear band initiation and evolution in sands. *J Mech Phys Solids* (2006) vol. 54 (1) pp. 22-45
- Richeton et al. Breakdown of avalanche critical behaviour in polycrystalline plasticity. *Nat Mater* (2005) vol. 4 (6) pp. 465-469
- Richeton et al. Dislocation avalanches: Role of temperature, grain size and strain hardening. *Acta Materialia* (2005) vol. 53 (16) pp. 4463-4471
- Sethna et al. Crackling noise. *Nature* (2001) vol. 410 (6825) pp. 242-250
- Staroselsky and Anand. A constitutive model for hcp materials deforming by slip and twinning: application to magnesium alloy AZ31B. *Int J Plasticity* (2003) vol. 19 (10) pp. 1843-1864
- Sun and Gu. Tensile and low-cycle fatigue behavior of commercially pure titanium and Ti-5Al-2.5Sn alloy at 293 and 77 K. *Mat Sci Eng A-Struct* (2001) vol. 316 (1-2) pp. 80-86

- Tong et al. Time-resolved strain mapping measurements of individual Portevin-Le Chatelier deformation bands. *Scripta Materialia* (2005) vol. 53 (1) pp. 87-92
- Uchic and Dimiduk. A methodology to investigate size scale effects in crystalline plasticity using uniaxial compression testing. *Mat Sci Eng A-Struct* (2005) vol. 400 pp. 268-278
- Wang et al. A high-resolution transmission electron microscopy study of long-period grain-boundary structure in alpha-Ti. *Phil Mag Lett* (1997) vol. 75 (2) pp. 91-95
- Weiss and Marsan. Three-dimensional mapping of dislocation avalanches: Clustering and space/time coupling. *Science* (2003) vol. 299 (5603) pp. 89-92
- Weiss and Grasso. Acoustic Emission in Single Crystals of Ice. *J. Phys. Chem. B* (1997) vol. 101 (32) pp. 6113-6117
- Yoneyama and Morimoto. Accurate displacement measurement by correlation of colored random patterns. *Jsm Int J A-Solid M* (2003) vol. 46 (2) pp. 178-184
- Yoneyama et al. Automatic evaluation of mixed-mode stress intensity factors utilizing digital image correlation. *Strain* (2006) vol. 42 (1) pp. 21-29

The Effect of Noise on Capacitive Measurements of MEMS Geometries

Joo Lien Chee¹ and Jason V. Clark^{1,2}

¹School of Electrical and Computer Engineering

²School of Mechanical Engineering

Purdue University

Birck Nanotechnology Center, 1205 W. State Street, West Lafayette, IN 47907

joolien@purdue.edu, jvclark@purdue.edu

ABSTRACT

Small variations in the geometry of Micro Electro Mechanical Systems (MEMS) can yield very large variations in performance. Variations in geometry are a consequence of the MEMS fabrication process, and are unavoidable with current fabrication technology. To achieve quick, accurate, and precise measurements of MEMS geometry, we have previously reported on our pioneering use of capacitance to measure MEMS geometry. The ability to capacitively probe MEMS geometries has the potential to more precisely obtain geometric uncertainties, and to realize autonomous on-chip measurements in-the-field. The precision of measurement method depends on the precision of the capacitance meter, which is subject to various sources of noise. In this paper, we examine the effect of this noise using our off-chip capacitive measurement method. In our present approach, we consider four sources of noise and analyze how they individually contribute to the uncertainty in the extraction of MEMS geometry. The four sources of noise are: noise from the voltage source, internal noise of the capacitance meter, noise from external electromagnetic fields, and thermal noise. We verify our analytical results with simulation and validate our results with experiment. With off-chip capacitive probing, we find that the uncertainty in geometric extraction is most strongly affected by external electromagnetic fields, moderately affected by noise from the measurement equipment and thermal noise, and least affect by the applied voltage. We measure the uncertainty in geometry due to shielded and unshielded conditions, and we predict the uncertainty in geometry due to the voltage source and thermal noises.

1 INTRODUCTION

Although Micro Electro Mechanical Systems (MEMS) have been used in a wide variety of application areas, intrinsic variations in the structural dimensions of each fabricated device impedes technological advancement. These structural variations are primarily caused by the totality of natural variations within a fabrication process [1-3]. It is because of these variations that the predicted geometry from layout does not match fabrication. In addition to variations in geometry, there are variations in material properties for each MEMS device on a chip. The change in geometry overcut in going from layout to fabricated device is often small, on the order of a tenth of a micron. However, small changes in geometry can translate to large changes in performance. For instance, Clark [4] showed that a 0.25 micron (10%) variation in overcut of the width of a commonly-used folded flexure results in a change in spring stiffness of 100%. And the change in stiffness is exacerbated if the uncertainty of Young's modulus (typically 10%) is taken into account.

An overview of several conventional tools used to characterize MEMS geometry is provided by Novak [5]. The tools include: optical microscopy, contact stylus profilometry, electron microscopy, interferometry microscopy, scanning confocal microscopy, atomic force microscopy, atomic force microscopy, laser Doppler vibrometers, and digital holography. Although these tools are adequately suited for individualized laboratory investigations, they are not well-suited for batch-fabricated industrial scale measurements, or for post-packaged measurements in the in-the-field. Such abilities may be achieved with electronically-probed measurements of MEMS geometries. Work in this area has been pioneered by Gupta [11] and Clark [4]. In Gupta's method, electrical measurements of static deflections and resonance frequencies are fed into a 3D computer modeling and simulation tool to determine geometry. In Gupta's method, it is assumed that material properties of the process are known. In Clark's method,

electrical measurements of static deflections are fed into analytical equations to determine geometry, independent of material properties. In one version Clark's method, MEMS fabricated within close proximity of each other are assumed to share the same unknown variations. The latter metrology method is called electro micro metrology (EMM). We chose to use EMM in this work to avoid having to measure material properties, which would create additional uncertainties in our analyses.

We developed an EMM test bed to capacitively measure the planar geometry of our MEMS structure in [6]. Our test bed has a geometric resolution of ~ 60 nanometers (nm) which corresponds to our measured capacitance uncertainty of ~ 1 femtofarads (fF). We expect that this resolution can be improved by lowering the magnitude of the uncertainty in capacitance to the zeptofarad (zF) regime [7,12] or by improving the sensitivity through design optimization [4]. In this paper, we use our test bed to study how noise affects the extracted uncertainty in geometry due to the uncertainty in measured capacitance. We consider four sources of noises: Noise from our voltage source, from our capacitance meter, from external electromagnetic fields, and from thermal noise. We measure how each source of noise affects geometric uncertainty using an EMM model.

Following the introduction, the rest of this paper is organized as follows. In Section 2 we describe how EMM theory is used to extract geometric uncertainty in terms of noise. In Section 3 we describe our EMM test bed which we use to obtain measurement parameters for the theoretical equations discussed in the previous section. In Section 4, we describe our noise models and determine the effect of such noise on our EMM measurement of geometry. Last, in Section 5 we summarize what we learn from this work.

2 THEORY

2.1 ELECTRO MICRO METROLOGY (EMM)

EMM exploits the strong and sensitive electrical to mechanical coupling at the microscale to express mechanical properties as functions of electrical measurands. We express planar geometry as a function of changes in capacitance as follows. Consider two test structures a and b . One of our structures is shown in Figure 1. The difference between structures a and b is that the layout widths w_{layout} of the flexures of b are slightly larger than those of a due to a layout parameter n chosen by the MEMS designer; that is, $w_{b,layout} = n w_{a,layout}$. We assume that structures a and b are fabricated within close proximity to each other such they share the same unknown material properties and geometrical errors. The fabricated widths (w_a and w_b) are related to layout widths ($w_{a,layout}$ and $w_{b,layout}$) by

$$w_a = w_{a,layout} + \Delta w \quad (1)$$

and

$$w_b = n w_{a,layout} + \Delta w, \quad (2)$$

where Δw is the geometrical difference in going from layout to fabrication, which is to be determined. It is important to understand that although the true width of a MEMS fabricated flexure varies along the length of its flexure due to

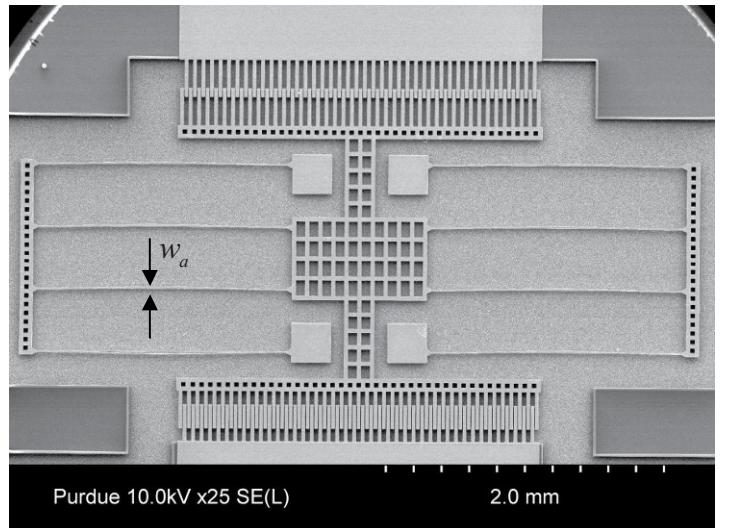


Figure 1: Folded flexure comb drive resonator. The four large square anchors are each attached to a flexure. There are 4 flexures of equal length and width. The 2 inner-most beams of both folded flexures attach to a backbone with comb drives. The device is composed of nickel for our related RF investigations. The flexure lengths are $2000\mu\text{m}$, flexure widths of a are $7\mu\text{m}$ and of b are $8\mu\text{m}$, thickness is $20\mu\text{m}$, distance between flexures are $500\mu\text{m}$, comb drive gaps are $8\mu\text{m}$, there are 42 fingers on each drive, and the layout parameter (see Equation 2) is $n = 8 / 7$.

the coarse sidewalls, the expressions in (1) and (2) correspond to the effective width that a smooth sidewalled flexure (i.e. that of an analytical model) needs to be such that its performance matches that of a true flexure with coarse sidewalls.

In the electrical domain, the electrostatic force that is generated on a comb drive is $F = \frac{1}{2}V^2 \partial C/\partial y$. Applying a voltage V across a comb drive produces an electrostatic force F and corresponding deflection y , which results in a change in capacitance ΔC . So for each of our structures a and b , we have

$$F_a = \frac{1}{2}V^2 \frac{\Delta C_a}{\Delta y_a} \quad (3)$$

and

$$F_b = \frac{1}{2}V^2 \frac{\Delta C_b}{\Delta y_b}, \quad (4)$$

where partial derivative symbols have been replaced with difference symbols due to the linearity of comb drives; that is $\partial C/\partial y \rightarrow \Delta C/\Delta y$. Equations (3) and (4) account for fringing field effects, asymmetry in comb fingers, and planar residual strain gradients as long as the deflection is only in the y direction. Since the comb drives in a and b are assumed to share the same geometric errors, then a voltage V applied across the comb drives generates the same electrostatic forces. That is,

$$F_a(V) = F_b(V). \quad (5)$$

Hence, equating (3) and (4) yields a ratio between unknown displacements and measured capacitances,

$$\frac{\Delta y_a}{\Delta y_b} = \frac{\Delta C_a}{\Delta C_b}. \quad (6)$$

And from the mechanical domain, using Hooke's law for small deflections, we have

$$F_a = k_a \Delta y_a \quad (7)$$

and

$$F_b = k_b \Delta y_b, \quad (8)$$

Due to (5) we are able to equate (7) and (8), which yields a ratio between unknown displacements and unknown stiffnesses,

$$\frac{\Delta y_a}{\Delta y_b} = \frac{k_b}{k_a}. \quad (9)$$

Since (6) and (9) correspond to the same displacement ratios $\Delta y_a/\Delta y_b$, equating (6) and (9) yields a ratio in stiffnesses in terms of capacitance,

$$\frac{k_b}{k_a} = \frac{\Delta C_a}{\Delta C_b}. \quad (10)$$

Now the stiffnesses k_a and k_b are proportional to unknown flexure widths cubed (w_a^3 and w_b^3), Young's modulus E , layer thickness h , and inversely proportional to beam length cubed L^3 . Since we are assuming that the two structures share the same unknown geometric and material properties, then the unknown quantities E , h , L cancel each other out in the ratio. And (10) reduces to

$$\begin{aligned} \frac{\Delta C_a}{\Delta C_b} &= \frac{w_b^3}{w_a^3} \\ &= \frac{(n w_{a,layout} + \Delta w)^3}{(w_{a,layout} + \Delta w)^3}, \end{aligned} \quad (11)$$

where we have substituted (1) and (2) for the fabricated widths on the second line. Equation (11) has one unknown, Δw , which is the difference between layout and fabrication. Solving (11) for Δw we find

$$\Delta w = w_{a,layout} \frac{n (\Delta C_b / \Delta C_a)^{1/3} - 1}{(\Delta C_b / \Delta C_a)^{1/3} - 1}. \quad (12)$$

In essence, by using EMM we are able to express in (12) the change in geometry in going from layout to fabrication (Δw) in terms of precisely measured changes in capacitance (ΔC_a and ΔC_b), and exactly known layout parameters ($w_{a,layout}$ and n).

2.2 GEOMETRIC UNCERTAINTY IN TERMS OF CAPACITIVE UNCERTAINTY

In Section 2.1 we determined the change in geometry as a function of change in capacitance, Equation (12). According to our EMM modeling assumptions, uncertainty in geometry is attributed to uncertainty in capacitance. A measurement of capacitance is has the form

$$C \pm \delta C \quad (13)$$

where various sources of noise is lumped into capacitance uncertainty δC . Depending on analysis, δC may be taken as the last flickering digit on a capacitance meter of a single measurement, or δC may be taken as the standard deviation resulting from a multitude of repeated measurements. Substituting (13) for the capacitance quantities in (12) we have

$$\Delta w \pm \delta w = w_{a,layout} \frac{n \left(\frac{\Delta C_b \pm \delta C}{\Delta C_a \pm \delta C} \right)^{1/3} - 1}{\left(\frac{\Delta C_b \pm \delta C}{\Delta C_a \pm \delta C} \right)^{1/3} - 1}, \quad (14)$$

where we have assumed that each measurement of capacitance contains the same order of uncertainty. Expanding (14) in a Taylor series about δC yields to first order

$$\Delta w \pm \delta w = w_{a,layout} \frac{n \left(\frac{\Delta C_b}{\Delta C_a} \right)^{1/3} - 1}{\left(\frac{\Delta C_b}{\Delta C_a} \right)^{1/3} - 1} \pm \delta C \left[\frac{\sqrt{2}}{3} \frac{w_{a,layout} (n-1) (\Delta C_a - \Delta C_b) \left(\frac{\Delta C_b}{\Delta C_a} \right)^{1/3}}{\Delta C_a \Delta C_b \left(\left(\frac{\Delta C_b}{\Delta C_a} \right)^{1/3} - 1 \right)^2} \right], \quad (15)$$

where the second term on the right hand side is the uncertainty in geometry δw , and the square-bracketed quantity in this term is the sensitivity in geometry Δw as a function of change in capacitance δC . That is

$$\delta w = \delta C \left[\frac{\partial \Delta w}{\partial \delta C} \right] = \delta C \left[\frac{\sqrt{2}}{3} \frac{w_{a,layout} (n-1) (\Delta C_a - \Delta C_b) \left(\frac{\Delta C_b}{\Delta C_a} \right)^{1/3}}{\Delta C_a \Delta C_b \left(\left(\frac{\Delta C_b}{\Delta C_a} \right)^{1/3} - 1 \right)^2} \right]. \quad (16)$$

In practice, the order of the square-bracketed expression (the sensitivity) can be quite large, say, $O(10^8)$. It is therefore necessary that the uncertainty in capacitance δC be much smaller than the sensitivity, such that the product $\delta C [\partial \Delta w / \partial \delta C]$ achieves the desired uncertainty in geometry. Techniques to reduce the uncertainty in geometry include: reducing the uncertainty in capacitance δC by using a capacitance meter with better precision; reducing δC by reducing the magnitude of noise contributions from various sources (see below); or reducing the sensitivity $[\partial \Delta w / \partial \delta C]$ by modifying the geometric configuration a priori. That is, geometry affects stiffness and or capacitance, which affects the change in capacitance due to a given applied voltage. For instance, in Figure 2 we show the dependence of sensitivity of our test structure (shown in Figure 1) as a function the number of comb drive fingers and comb drive gap. We use such analysis to improve EMM measurement for a given capacitance meter's uncertainty.

3 EMM TEST BED

A salient attribute of EMM is its ease of use for MEMS metrology by electrical probing of capacitance. In our present test bed we use an off-the-shelf capacitance meter for \$15. Typically, capacitance meters are available in most laboratories. This attribute of EMM is in stark contrast to most other metrology methods that required expensive equipment not readily available in most labs, and that require specialized training due to the intricacy in using such equipment.

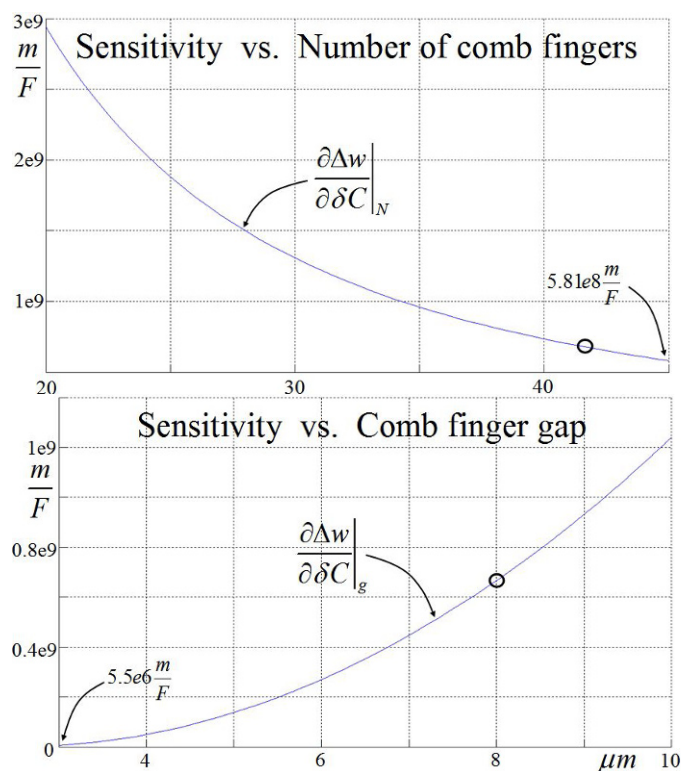


Figure 2: Sensitivity as a function of geometry. (Top): Sensitivity $\partial \Delta w / \partial \delta C$ as a function of the number of comb fingers N . The sensitivity at $N = 45$ is $5.81E8 \text{ m/F}$. **(Bottom):** Sensitivity $\partial \Delta w / \partial \delta C$ as a function of comb finger gap g . The sensitivity at $g = 3 \mu m$ is $5.5E6 \text{ m/F}$. The circle on the curve indicates the sensitivity with respect to Figure 1.

We have developed a test bed especially designed to characterize EMM. Our test bed is shown in [Figure 3](#). The test bed comprises the following low-noise features: a Faraday cage to reduce noise interference from external electro-magnetic fields; an air-damped table to reduce the noise due to building vibrations; low-reflective interior cage walls to reduce the noise due to light; and low-parasitic shielded capacitance probes. Other components of the test bed include a MEMS wafer is held in place by a vacuum chuck; micromanipulators for positioning the electrical probes; a small 200x digital microscope camera mounted onto a boom stand; shielded probe leads; and an inexpensive capacitance meter chip with 4 attofarad resolution, by Analog Devices AD7746 [8]. However, our current test bed configuration shown in [Figure 3](#) yields a capacitance noise floor of 1.2 femtofarads, leaving much room for further improvement. Measurement using our present test bed yields a difference between layout to fabrication of $2.5 \mu\text{m}$ with an uncertainty of $\pm 0.062 \mu\text{m}$. We validated our measurement against scanning electron microscope in [6]. Analysis for various sources of noise contributions to the uncertainty in our measurement follows.

4 NOISE MODELS

In our noise model we assume to have four source of noise: noise from the power supply voltage source; noise from internal electronics; noise from external electromagnetic radiation; and thermal noise. In Equation (13) we lump the totality of noise into the uncertainty in capacitance δC . In [Figure 4](#) we provide our computational noise model, which we used to better understand our experimental results. Our computational model comprises an experimentally-fitted finite element model of our device modeled in COMSOL [10], coupled to a various sources of noise inputs to the model by using SIMULINK [9]. Our computer model is displayed graphically in [Figure 5](#).

4.1 NOISE DUE TO VOLTAGE SUPPLY

As discussed in Section 1, we obtain a change in capacitance by applying a voltage across the comb drive. The voltage produces an electrostatic force which deflects the comb drive to yield a change in capacitance. However, if the applied voltage is perturbed, then so too is the corresponding comb drive force. This disturbance in force changes the comb drive deflection, which affects the magnitude of measured capacitance.

The voltage supply used in our present

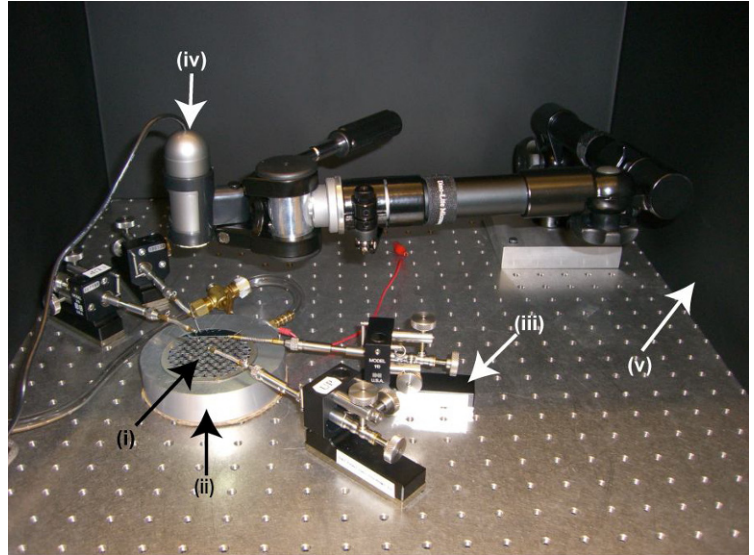


Figure 3: EMM test bed. The MEMS structure under test and the testing apparatus are enclosed within a Faraday cage to reduce the noise due to external electromagnetic interference. Major components of the test bed are: (i) a 7.6 cm wafer comprising a several folded flexure comb drive structures; (ii) a vacuum chuck to hold the wafer in place; (iii) micromanipulators to position electronic probes; (iv) a digital microscope camera mounted on a boom stand; and (v) the Faraday cage.

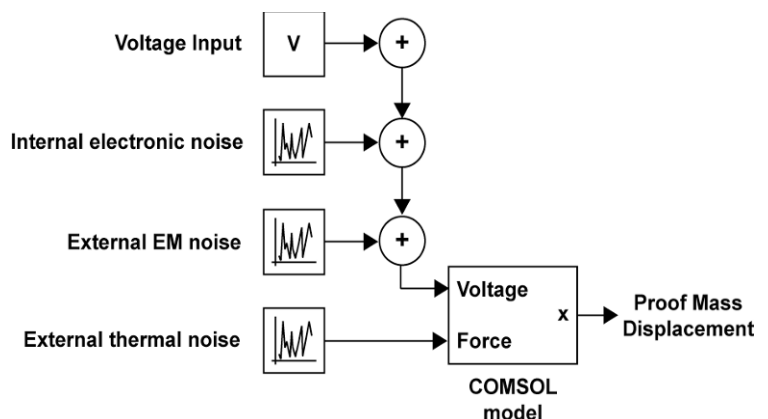


Figure 4: SIMULINK schematic our noise model. Using SIMULINK, we explore various types and combinations of noise sources to our finite element model of our MEMS (see [Figure 1](#)). Sources of noise contributions include the power supply, system electronics, external electromagnetic fields, and thermal noise. Although the output of our model is displacement, we show in Section 5 that deflection is directly related to EMM geometry. See [Figure 5](#) for COMSOL model.

analysis is the Agilent 6645A High Voltage Power Supply. We selected this voltage source due to its wide voltage range, which is necessary for our related RF investigations. The 170V range is able to actuate our MEMS structure $200\mu\text{m}$. At the nominal 25°C operating condition, the power supply has a DC noise voltage of 0.06% of programmed voltage plus an additional 51mV, and an AC noise voltage of 7mV peak-to-peak. With the voltage supply acting alone in our computational model, we apply the maximal voltage plus and then minus the uncertainty in voltage. The model yields an uncertainty in deflection that corresponds to an uncertainty in geometry of 4nm. That is, the change in geometry (Δw) from layout to fabrication that is due to error in the applied voltage supply alone is $\Delta w \pm 4\text{nm}$.

4.2 NOISE FROM INTERNAL ELECTRONICS AND FROM EXTERNAL ELECTROMAGNETIC RADIATION

Our present test bed yields an uncertainty in capacitance of 1.2fF. We obtain this value by enclosing our MEMS in a Faraday cage, connecting it to our capacitance meter, and determining the standard deviation of our measured capacitance distribution curve. For each measurement, we disconnected the electrical probes from the electrode pads, which create a slightly different contact parasitic capacitance upon each trial. After 90 trials, we compute the uncertainty as the standard deviation of our distribution curve. We apply this 1.2fF uncertainty in capacitance alone to our computational model (Figure 4) as a change in capacitance to determine the equivalent deflection. In doing so, we compute an 800nm displacement, which corresponds to an equivalent geometric uncertainty of 62nm.

By opening the Faraday cage to expose our MEMS to radio, light, and other forms of electromagnetic radiation, we measure an uncertainty in capacitance of 5.1fF. Similarly, this value of uncertainty was obtained by taking a multitude of measurements of capacitance and calculating the standard deviation of the distribution data. Upon applying the 5.1fF uncertainty due to external

electromagnetic (EM) radiation to our computational model (Figure 4) we compute a deflection of $4.9\mu\text{m}$, which corresponds to an uncertainty in geometry of 263.5nm. Figure 6 shows the two states of our test bed: shielded external EM radiation versus exposed to external EM radiation.

4.3 THERMAL NOISE

MEMS are susceptible to thermally-induced vibration due to small stiffness values. Since stiffness scales by a factor of length-scale L , then as the size of the device decreases, then

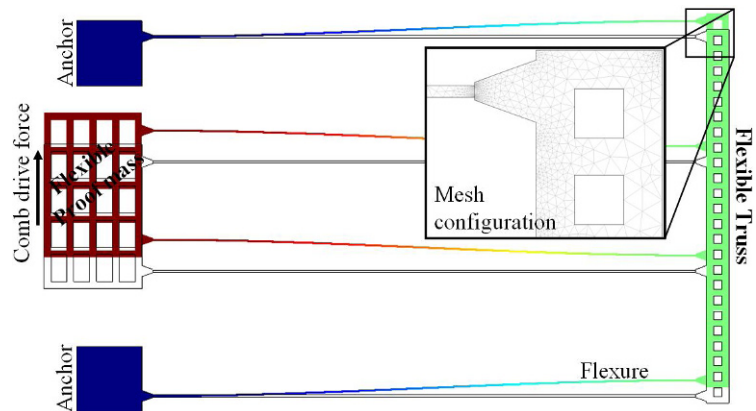


Figure 5: Finite element model. For computational efficiency, we model half of the symmetric folded flexure of our microdevice and do not show the comb drives. To produce the correct performance, we double its stiffness and we apply a resultant electrostatic comb drive force instead of including electrostatic physics about a multitude of comb drive fingers. Not including the field calculations saves a lot of computational time. We configure the geometry of the models to match the true geometries. The color map corresponds to total deflection. I.e., blue for zero deflection to red for maximum deflection. The length and width of the flexures are $2497.5\mu\text{m}$ and $9.5\mu\text{m}$. The layer thickness and Young's modulus are $20\mu\text{m}$, and $215\text{GPa}+14.59\%$, where the 14.59% adjustment is used to match simulation to the measured deflection.

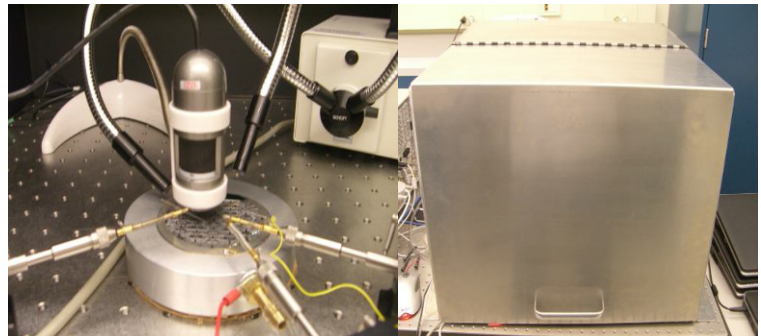


Figure 5: Test bed states for external radiation. With the Faraday cage open to EM exposure (left), the uncertainty in capacitance is 5.1fF. And with experiment shielded from EM radiation (right) the uncertainty in capacitance is 1.2 fF.

so to dose the stiffness. As given in [13] by Hutter and Bechhoefer, the relationship between the expected amplitude of deflection and temperature is

$$\frac{1}{2}k\langle y^2 \rangle = \frac{1}{2}k_B T, \quad (17)$$

where k_B is Boltzmann constant and T is the absolute temperature. Solving (17) for the expected amplitude due to thermally-induced vibrations, we have

$$y = \sqrt{\frac{k_B T}{k}}. \quad (18)$$

The stiffness k of our computational model is 0.267N/m. From (18), a temperature of 300K is expected to yield an amplitude of motion of 0.12nm. This corresponds to an uncertainty contribution in geometry of 0.014nm. We plot the expected relationship between deflection and temperature for our device [Figure 7](#). Measuring thermal noise is beyond the resolution of our present device and capacitance meter. Improvements to our experiment are underway.

5. CONCLUSION

Since small variations in geometry can yield very large variations in performance in many MEMS, measurement of geometry of each device may be required. Electro Micro Metrology (EMM) offers a quick and practical way to measure geometry by using off-the-shelf equipment that is readily available in most laboratories. Depending on the analyst's desired precision in measurement, an understanding the effect of various sources of noise on EMM can be used to reduce the uncertainty in EMM measurements of geometry. In this paper we examined the effect of four sources of noise on geometric measurement: noise from the voltage source, internal noise of the capacitance meter, noise from external electromagnetic fields, and thermal noise. By applying our experimental measurements of noise to our EMM analytical model and computer model, we determined the effect of noise on capacitive measurements of geometry. With our test bed equipment and MEMS sample, we found the following. By not shielding our experiment from external electromagnetic fields from the environment, we found that this condition resulted in the largest uncertainty in measurement of geometry, $\delta w = 263\text{nm}$. By shielding our experiment, the effect on geometric uncertainty due to noise within the capacitance meter (i.e. meter precision) was found to be $\delta w = 62\text{nm}$. And predicted geometric uncertainties due to variation in voltage from the voltage source and due to thermally-induced vibrations had the smallest effect, $\delta w = 4\text{nm}$ and $\delta w = 0.12\text{nm}$ respectively. The next step in this effort is to use the results found in this work to further reduce the uncertainty in EMM measurement of geometry for both unshielded and shielded measurements. We expect this can be done by modifying our MEMS design to improve its sensitivity to such measurement, and by improving the resolution of capacitance measurement. We are also examining the case of variation mismatch by relaxing our assumption that both structures share the same variations in geometry.

REFERENCES

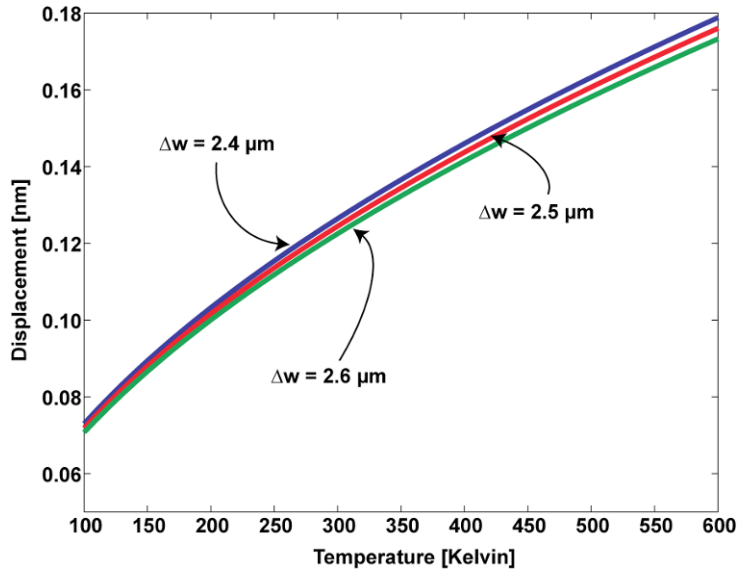


Figure 4: Displacement amplitude versus temperature. The stiffness used for this plot is extracted from our MEMS shown in (Figure 5). Using three flexure changes in widths of 2.4 μm , 2.5 μm , and 2.6 μm , the corresponding stiffnesses are 0.276N/m, 0.267N/m, and 0.259N/m. For temperatures ranging from 100K to 600K, the thermally-induced displacement amplitude ranges from $\sim 7\text{nm}$ to $\sim 18\text{nm}$.

- [1] H. I. Smith, "Review of submicron lithography," *Superlattices and Microstructures*, v. 2, n. 2, pp. 129-142, 1985.
- [2] B. Wu and A. Kumar, "Extreme ultraviolet lithography: A review," *Journal of Vacuum Science and Technology B: Microelectronics and Nanometer Structures*, v. 25, n. 6, pp. 1743-1761, 2007.
- [3] M. J. Madou, "Fundamentals of Microfabrication (2nd ed.)," *CRC Press*, 2002.
- [4] J. V. Clark, "Electro Micro Metrology," *Ph.D. Dissertation*, University of California Berkeley, Berkeley, California, 2005.
- [5] E. Novak, "MEMS metrology techniques," *Progress in Biomedical Optics and Imaging – Proceedings of SPIE*, v. 5716, pp. 173-181, 2005.
- [6] J. Chee, J. V. Clark, and D. Peroulis, "Measuring the Planar Geometry of MEMS by Measuring Comb Drive Capacitance" (*In review*).
- [7] T. Tran, D. R. Oliver, D. J. Thomson, and G. E. Bridges, "Sub-zeptofarad sensitivity scanning capacitance microscopy," *Canadian Conference on Electrical and Computer Engineering*, v. 1, pp. 455-459, 2002.
- [8] Analog Devices AD7746, *Analog Devices, Inc.*, 3 Technology Way, Norwood, MA 02062, United States.
- [9] Matlab Simulink, *The Mathworks*, 3 Apple Hill Drive, Natick, MA 01760.
- [10] COMSOL Multiphysics, *COMSOL*, 1 New England Executive Park, Suite 350, Burlington, MA 01803.
- [11] R. K. Gupta, "Electronically Probed Measurements of MEMS Geometries," *Journal of Microelectromechanical Systems*, vol. 9, no.3, pp. 380-389, (2000).
- [12] J. Green, et. al., "New iMEMS Angular Rate-Sensing Gyroscope," *Analog Devices, Dialogue*, pp. 37-03, (2003).
- [13] Hutter and Bechhoefer, "Calibration of Atomic-Force Microscope Tips," *Review of Scientific Instruments*, No. 64 (7) pp. 1868-1873, (1993).

Effects of Clearance on Thick, Single-Lap Bolted Joints Using Through-the-Thickness Measuring Techniques

John Woodruff, Giuseppe Marannano, Gaetano Restivo
Composite Vehicle Research Center, Michigan State University
2727 Alliance Drive, Lansing, MI 48910

Abstract

Composite materials have increasingly become more common in ground transportation. As this occurred thicker panels, as compared to composite panels used in aviation, become necessary in order to withstand high impact loads and day to day degradation. The effectiveness of these panels was often limited by the strength of the joint in which the panel was attached to the frame of the vehicle. Investigating methods of reducing strain concentrations within these joints would increase the effectiveness in using composite materials in ground transportation applications by increasing the load necessary for joint failure to occur.

In this study, fiber optic strain gages were embedded in a composite panel along the bearing plane of a thick, single-lap, bolted joint. The gages allow for the strain profile above the hole to be determined experimentally. Several clearance values were then implemented in the bolt to determine their effect on the strain concentrations. Strain increased at every gage, by nearly the same proportion, when clearance was increased from zero to three percent. When clearance was further increased to five percent strain only continued to increase at gages three and four, with one and two remaining similar in value to what was seen at three percent clearance. Ultimately, like in thin composite panels, the zero percent clearance condition was the stiffest.

Introduction

Large advancements have occurred in the field of composite materials for use in automotive and aerospace application. Advancements have been generated by demands for “greener”, more fuel efficient vehicles that also maintained or increased in overall safety capabilities. In order to maintain the safety aspects of a ground transportation vehicle, thicker panels were developed. Panels were made thicker in order to provide a safe ride in a more hazardous environment. Such an environment would include heavy day to day wear and tear, as well as the prospect of collisions with other objects or vehicles. Other hazards, such as projectiles, have been included in this environment when composite panels were used in military vehicles. Failure of the composite panel by impact with these objects has been a real possibility.

The location where the composite panel is fastened to the metallic frame is of great importance. At this location stress concentrations develop upon impact with objects in the course of the vehicle’s journey. And stress concentrations may cause the panel to fail. If a composite panel is to be utilized to its full potential, then the load transfer between the composite panel and the aluminum frame of the vehicle has to be further developed. A single-lap, bolted joint has typically been used to represent the fastening of the composite panel to the aluminum frame vehicle for experimental purposes. The test setup typically consists of a single composite plate bolted to an aluminum plate of equal dimensions. Bolting is chosen as the means of fastening since it provides the fastest method of securing or removing a panel from a vehicle frame, while still providing a strong connection. The single-lap bolted joint is a standard test setup for composite fastening.

Clearance between the bolt and the hole of the composite panel has been an important factor in the strength of the joint. When the lap joint is pulled in tension, the bolt tilts, which provides a variation in the contact surface area between the bolt and the hole surface. The larger the contact surface area that is maintained during testing the better the load distribution between the bolt and the hole surface. Initial clearance between the bolt and the

hole has a significant effect on the ability to maintain the maximum surface area contact and the strength of the joint.

In order to properly develop the single-lap, bolted joint, a literature review was conducted. Papers were compiled and reviewed in order to determine what was currently known about clearance in thick composite panels. Studies reviewed included many numerical and experimental techniques.

A study was performed with a thin single-lap joint with an 8 mm diameter hole, which was tested for small clearance values [1]. It was seen that as clearance increased, the contact surface area decreased, from 160 – 170 degrees around the hole for a zero percent clearance condition, to 105 – 110 degrees at the largest clearance value of three percent. The same author performed another study which had shown the effects of clearance on stiffness and how bearing strength was affected [2]. In this study, increased clearance showed a decrease in joint stiffness. However ultimate bearing strength was not affected by clearance. Other numerical studies have found similar results when clearance is tested to determine its effects [3]. One such study concluded that clearance decreased the load capacity of the joint and was overall a negative design characteristic. This was a very general statement, but in line with other research groups findings.

Interest in further analyzing clearance effects on the lap joint has led to developments in measuring techniques. Fiber optic strain gages of various types have been considered for use in taking through-the-thickness measurements within the composite panel. These gages have the advantage of being very small in size, are immune to electromagnetic interference and they can be embedded non-invasively into a composite panel [5]. The material properties in the region of the gage do not change and point measurements of strain are available. Measurements can then be used to experimentally validate finite element models.

One study exists as an attempt at developing an understanding of the strain profile at low loads [6]. In this study, fiber optic strain gages were embedded within a thick 12.7mm (0.5”) composite panel of the single-lap joint at regular intervals through-the-thickness above the hole. Numerical analyses were performed using ANSYS as pre-processor and LS-DYNA as solver. The overall goal was to evaluate the magnitude of contact strains around the hole and through the thickness of the composite. The values were analyzed and compared with the FEM results: the finite element analysis correlated reasonably well with the experiments. An investigation of error causes was also carried out, in particular to evaluate the influence of incorrect gage positioning and the effect of friction coefficients.

The next logical step in the development of the lap-joint was then to use embedded fiber optic strain gage technology to understand the effects of clearance. Creating a specimen similar to [6] provided a more thorough understanding of the actual strain profile when tested through a higher loading range. Also, changes in the strain profile above the hole when clearance is present were experimentally determined.

Composite Manufacturing

A composite specimen for testing was constructed using a hand layup process with vacuum bagging. The process included attaching the Bragg grating fiber optic strain gages to the plies prior to creating the specimen. Then, once the gages are secured and their location marked, the layup process began. The plies were inserted with the attached gages in the proper order to know their location in the thickness direction of the final specimen. Finally a vacuum bag was used to pull out any unnecessary resin and obtain a higher fiber volume fraction in the specimen.

The specimen tested was constructed from a plain weave S-Glass material and an epoxy resin. The S-Glass was chosen due to having superior tensile strength than the E-glass. The epoxy resin is 635 Epoxy and uses a 3:1 ratio of Epoxy to hardener. The epoxy, hardener and fiber are supplied by US Composites.

The actual dimensions of the panel are chosen as ratios of the hole diameter. The hole diameter was known to be 12.7mm (0.5 inches) for this panel. A thickness to hole diameter ratio of 1:1 was used. Also, the ratio of edge distance to hole diameter was 4:1 moving laterally from the hole, and 3:1 from the top of the plate to the center of the hole. The locations of the gages within the composite plate are shown in [Figure \(1\)](#).

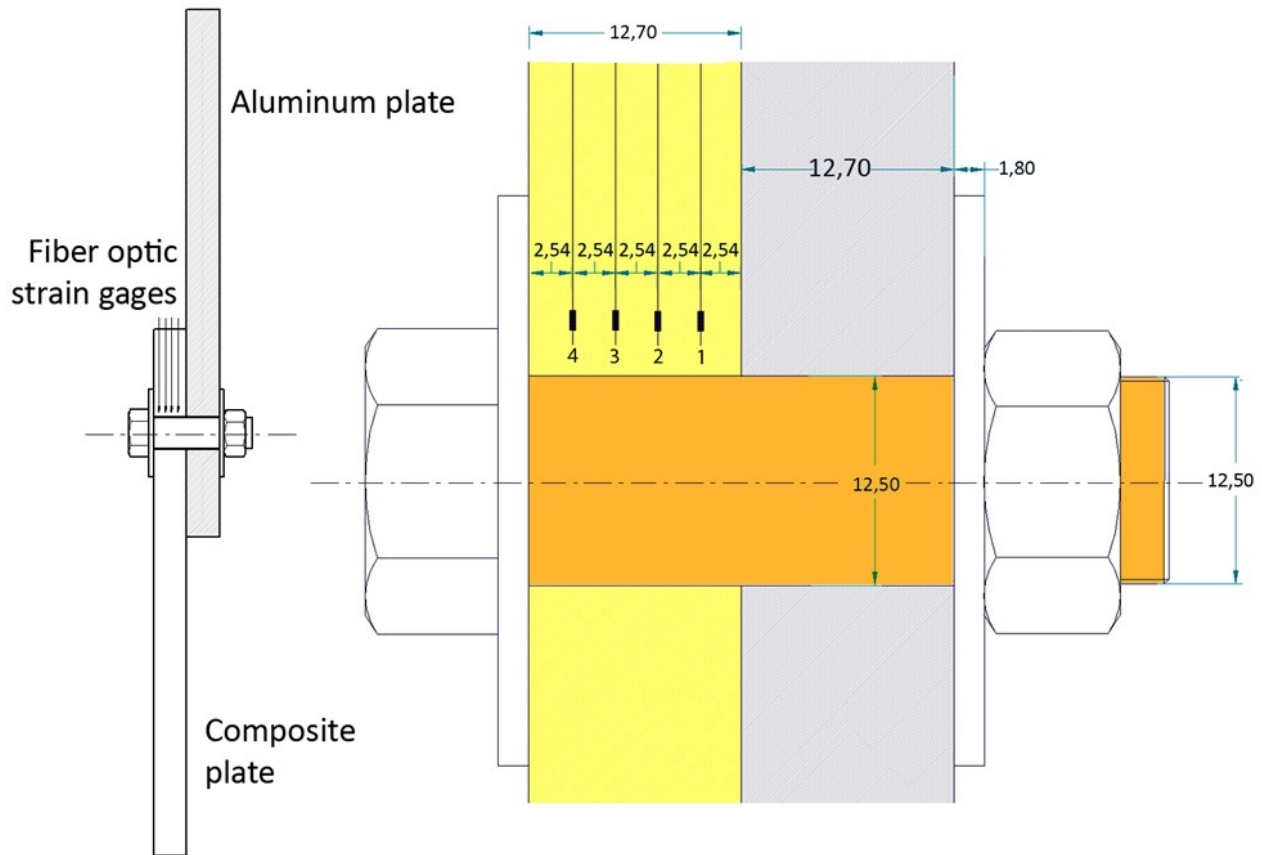


Figure 1: Dimensions of the FOS gage locations within the composite panel

The two fiber optic strain gages to be used in this experiment are provided by Technica SA and are located at the places designated as 3 and 4 on the above diagram. In order to obtain data for the 1 and 2 locations the specimen was simply reversed. The gages are Bragg grating fiber optic strain gages and have a gage length of 2mm with a maximum strain output of approximately 12,000 microstrain. The 2mm gage length was chosen since it is small, and works accurately for taking strain readings at specified points in the presence of a large strain gradient. Also, a 3mm protective armor cable was used to protect the internal fiber optic cable from shearing off at the ingress/egress point after construction. Further protection was provided at the adapter, where the cable connects to the interrogator.

The gages were applied to a ply prior to the hand layup process. This was done by first marking the edges of the specimen and the location of the center of the gage with a thin black cotton string as shown in [Figure \(2\)](#).

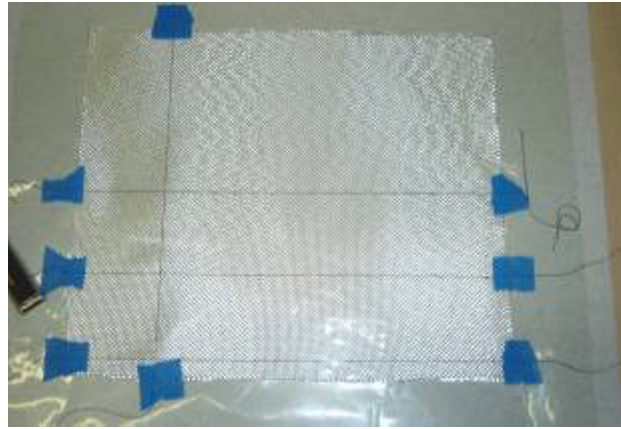


Figure 2: Location of the gage and edges of specimen

String was used so that during the layup process the plies with gages can be aligned via the string. Lastly, the gage was glued in place using the same epoxy and hardener that will be used during the hand layup process and is shown in [Figure \(3\)](#).

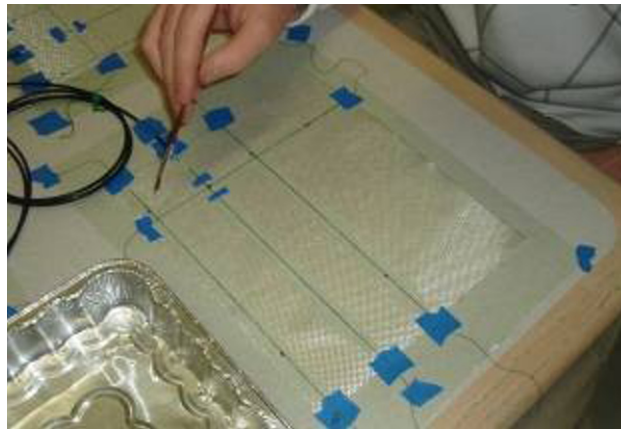


Figure 3: Gages are glued in place with epoxy resin

The composite panel was created large enough so that specimens for tensile tests could be cut from the same panel that the test specimen would be made from. Tensile tests were used to determine the material properties of the composite panel for use in a finite element model. By cutting tensile test specimens from the same panel the lap joint specimen was made from there is a high degree of accuracy in determining the material properties of the lap joint test specimen itself.

The hand layup process was performed by inserting the plies with the gages at the desired interval. Overall, 60 plies were used including the two with gages attached. Since the gages were inserted at locations 0.1 inches and 0.2 inches in from the front surface, this meant they were located as plies 12 and 24. A vacuum bag system was used to pull extra resin out of the specimen after the layup process was completed. The setup for the panel construction can be viewed in [Figure \(4\)](#).

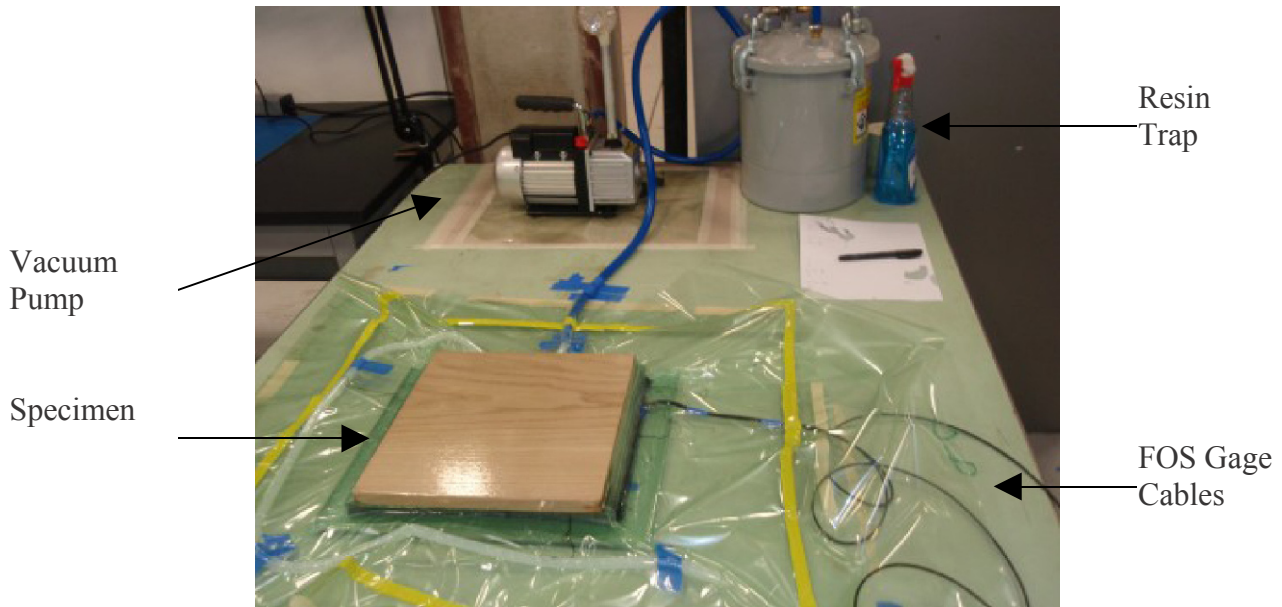


Figure 4: Vacuum bag setup for hand layup process.

Experimental Setup

The specimen was tested using a tensile testing machine. Wedge grips were used to hold in place a mounting device created to hold the specimen. A mounting device was used since the lap joint specimen was too thick to fit into the wedge grips of the MTS machine. The device mentioned is pictured in [Figure \(5\)](#).

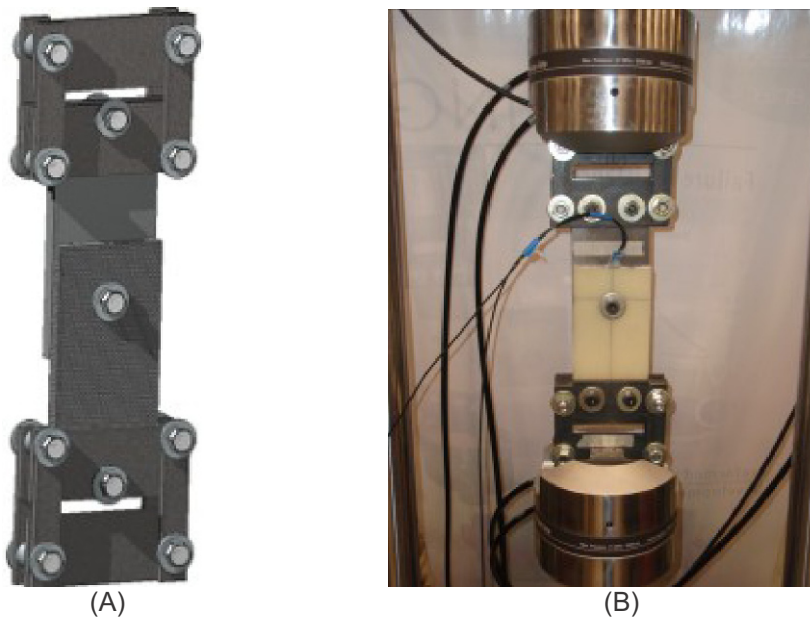


Figure 5: (A) Mechanical mounting device, (B) Specimen loaded into MTS

Displacement was set to 1.0 mm per minute and the specimen was loaded from 0 – 10,500 N. This loading range was sufficient to develop a linear trend for stiffness data. Fiber optic strain gage data was compiled by Labview software. Testing was performed to determine the optimum bolt to hole clearance condition. For these tests the hole size would remain constant while the bolt would be varied in diameter to reflect clearance values of 0,1,2,3,4

and five percent. As a precaution, testing was first performed on gage locations three and four since lower strains were expected at the gages. After these tests were successfully concluded, tests were carried out for gage locations one and two.

Experimental Results

As mentioned, tensile tests were first performed to determine material properties for use in FEA. Young's modulus for the through the thickness direction was specified as that of the matrix material. [Table \(1\)](#) shows the material properties. A completed FEA analysis was not available at the time of submission of the paper but will be shown during the presentation.

Embedded Specimen	
Ex (GPa)	19.56
ν_{12}	-0.12133

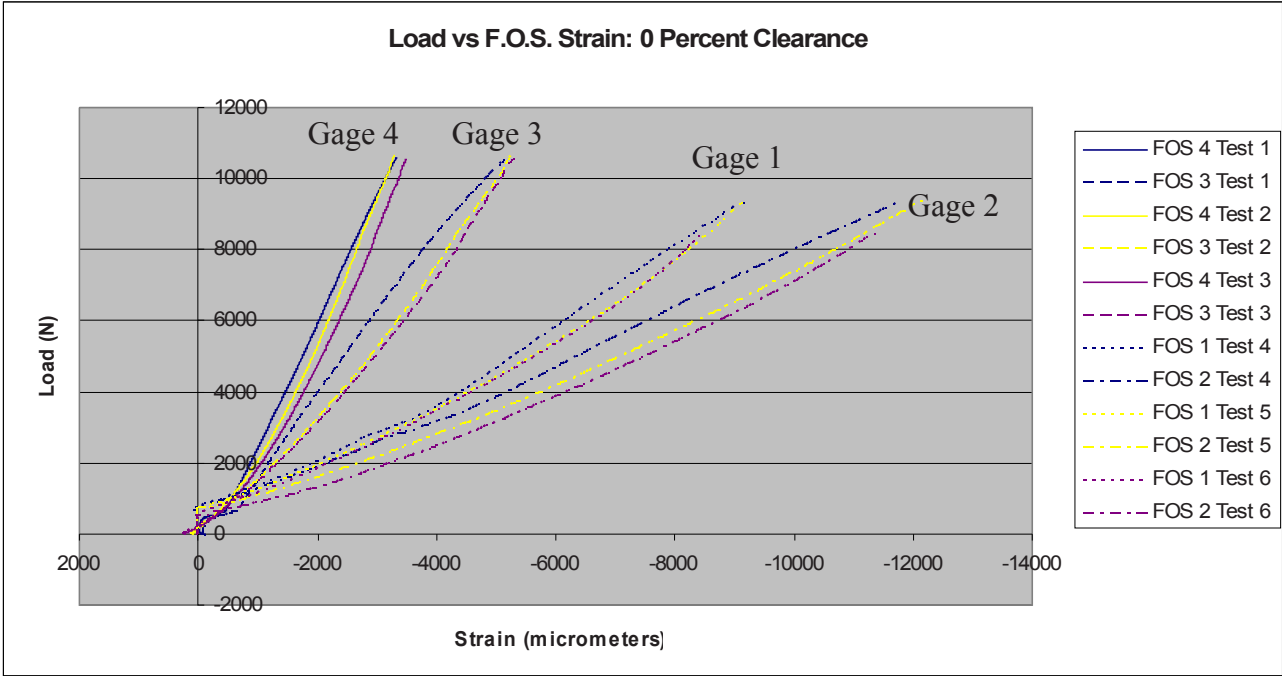
Table 1: Material properties of the composite specimen

Stiffness testing on the specimen provided results that are similar to what was seen in tests on much thinner panels. The stiffest condition was seen when there was no clearance between the bolt and the bolt hole. All clearance results can be seen in [Table \(2\)](#). The zero clearance condition was seen to be the optimal configuration of the joint, with the five percent clearance the poorest performing configuration.

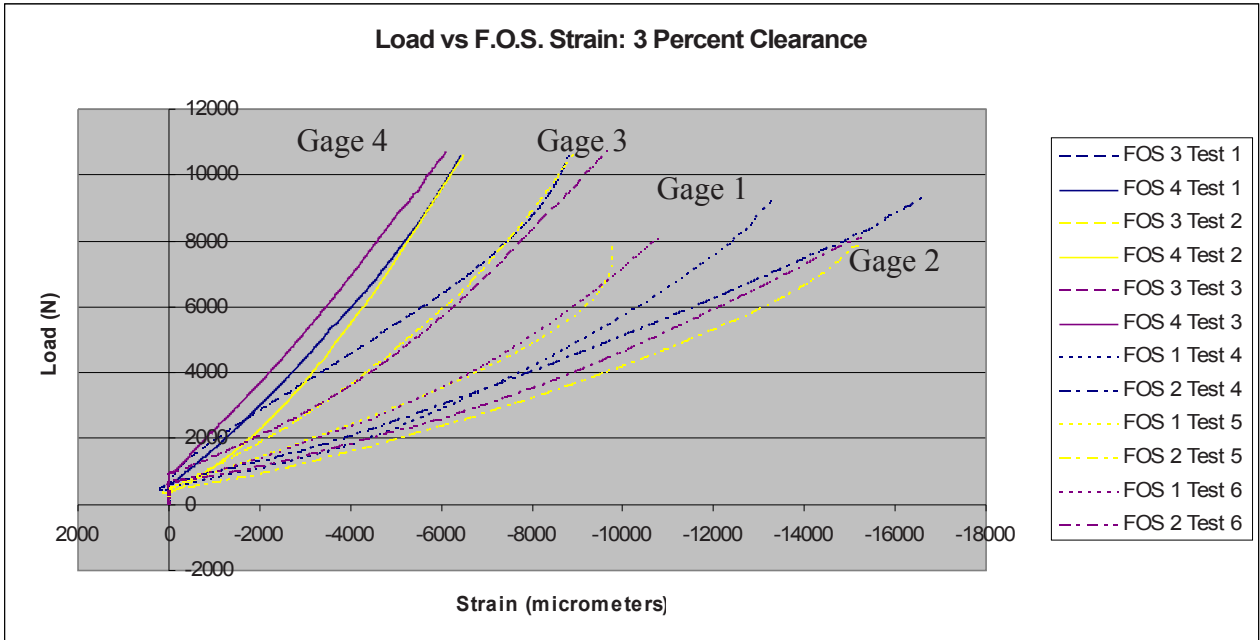
Embedded Specimen Stiffness Results (N/mm)						
Test #	0%	1%	2%	3%	4%	5%
1	8296	7610	8182	7438	9517	8317
2	10564	7628	7602	8945	8252	9213
3	10858	8438	7859	9133	8977	8273
4	9970	9806	10003	10209	9014	8638
5	10359	10334	10160	9376	9179	8772
6	10387	9947	9973	8963	9621	9040
Average	10072	8961	8963	9011	9093	8709
Δ from 0 (%)	N/A	-11.04	-11.01	-10.54	-9.72	-13.54

Table 2: Stiffness characteristics of each test configuration.

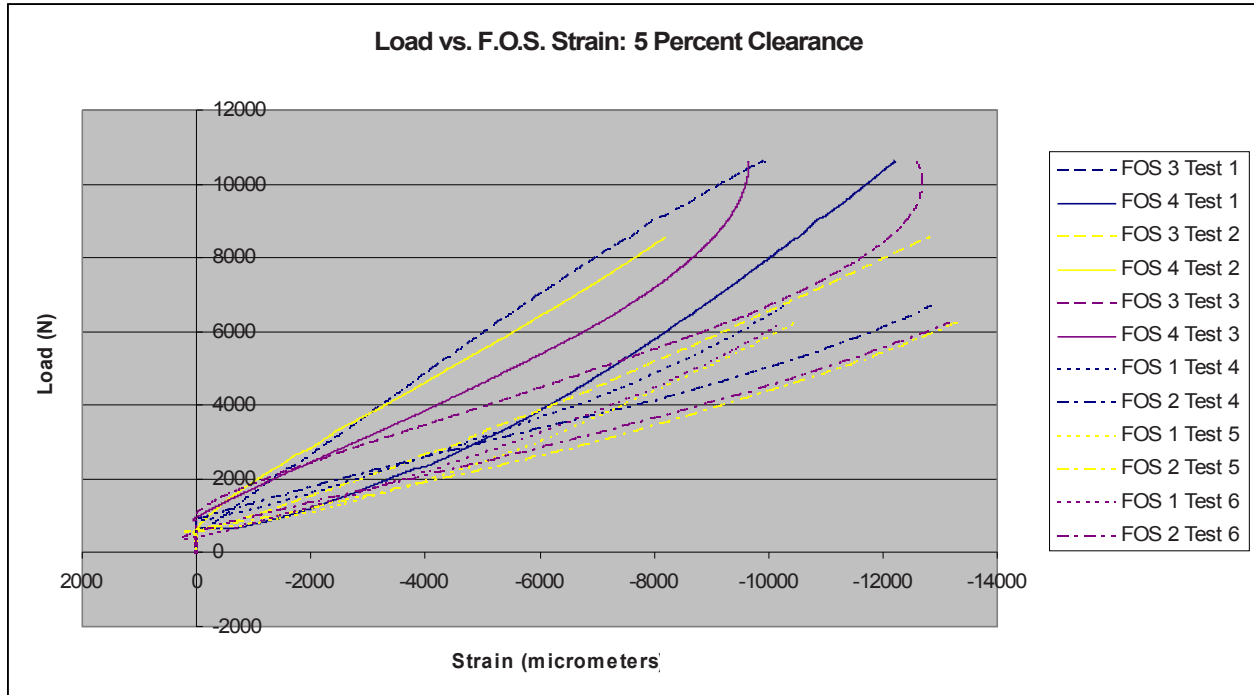
Fiber optic strain gages have provided very interesting data of the strain profile through the thickness of the specimen as shown in [Figure \(7\)](#). Gage two had higher strains than gage one for all tests. Increased clearance from zero to three percent increased the strain seen at all gage by similar proportions to the values at zero percent. However, once clearance was further increased to five percent only the strains at the gages furthest from the interface between the aluminum plate and the composite panel continued to see increased strain.



(A)



(B)



(C)

Figure 7: (A) 0 percent clearance, (B) 3 percent clearance, (C) 5 percent clearance

Discussion

During the fabrication of the specimen there was a slight misalignment of the Bragg grating fiber optic strain gages. Although less than a millimeter of horizontal misalignment was determined from visual inspection after construction, there was still error in strain readings associated with the misalignment. The cause of the misalignment was the hand-rolling process of applying the resin.

Experimentation has shown the optimal value of clearance as well as interesting data on the strain profile during loading for the thick, single, lap-bolted joint. There is much alignment between the stiffness data created in these tests and what has been seen for similar research projects on joints that were constructed of mainly thinner panels. In the embedded specimen, stiffness was seen to be optimized when clearance does not exist at all. There was an 11 percent decrease in stiffness from the zero percent to the one percent conditions. Such a large decrease in stiffness has shown the importance of maintaining a tight tolerance on the bolt-hole clearance for use of such a composite plate when used in field applications.

The strain profile through the thickness at the two gage locations was very revealing. Past numerical studies have all shown that the highest strain values are at the interface of the composite plate and the aluminum plate and decrease substantially away from the interface of the two plates. Experimental evidence provided by the embedded Bragg grating fiber optic strain gages has revealed that the highest strain values are located a little further in from this interface at the location of gage two. However, gages one and two did both read substantially higher than gages three and four. The difference in what was seen in experimentation and other numerical studies was largely due to the sliding of the gages during the embedding process.

Conclusions

The focal point of this study was to determine the effects of clearance on the strain profile through the thickness of the specimen and the optimal stiffness value for a thick composite panel. The composite specimen contained 60 layers of S-glass in an Epoxy resin resulting in a 12.7mm (0.5 inch) thick composite panel. Point measurements

for strain in the bearing plane of the composite specimen were determined experimentally using Bragg grating fiber optic strain gages embedded into the specimen.

Analysis of the data provided conclusions regarding the effects of clearance on strain concentrations and on the stiffness of the joint. The concentration was highest at gage two, which was toward the front of the specimen, but further into the thickness than gage 1. Also, strain seen under three percent of clearance was increased from the zero percent clearance conditions at all gages by approximately the same proportion. A further increase in strain to five percent only resulted in an increase in strain at gages three and four, the gages furthest from the interface between the two plates.

Stiffness was seen to follow similar trends to thin composite panels. Any increase in clearance beyond the zero clearance condition lead to a decrease in stiffness. Zero clearance was then the optimum condition at 10.02 KN / mm and five percent was the least stiff at 8.7 KN / mm.

REFERENCES

- [1] McCarthy, M.A., McCarthy, C.T. (2004). "Three-dimensional finite element analysis of single-bolt, single-lap composite bolted joints: part II-effects of bolt-hole clearance" Composite Structures **71**: 159-175
- [2] McCarthy, M.A., Lawlor, V.P., et al. (2002) "Bolt-hole clearance effects and strength criteria in single-bolt, single-lap, composite bolted joints." Composites Science and Technology **62**: 1415-1431.
- [3] Chen, Wen-Hwa, Lee, Shyh-Shiaw, et al. (1995) "Three-dimensional contact stress analysis of a composite laminate with bolted joint." Composite Structures **30**: 287-297
- [4] Baldwin, C., Mendex, Alexis. (2005) "Introduction to Fiber Optic sensing with Emphasis on Bragg Grating Sensor Technologies; short course 102" SEM Annual Conference and Exposition on Experimental and Applied Mechanics
- [5] Lopez-Anido, R., Fifield, S. (2003). "Experimental Methodology for Embedding Fiber Optic Strain Sensors in Fiber Reinforced Composites Fabricated by the VARTM/SCRIMP Process". Structural Health Monitoring **247** – 254.
- [6] Restivo, G., Marannano G., Isaicu, G.A. (2010). "Three-Dimensional Strain Analysis of Single-Lap Bolted Joints in Thick Composites using Fiber-Optic Strain gages and Finite Element Method", Journal of Strain Analysis for Engineering Design, Accepted for publication.

Deformation and Performance Measurements of MAV Flapping Wings

Wu, Pin. University of Florida, MAE-A #231, Gainesville, FL, 32611

INTRODUCTION

If bumblebees and hummingbirds could speak to us, could they tell us how they fly? Probably not. "How they fly" has been a fascinating question to biologists and aerodynamicists. Recently, attention is directed to micro air vehicle (MAV) research, which is aimed to develop sub 150 mm wingspan aircraft for reconnaissance and surveillance. The hummingbird poses as a perfect emulation target: they can dash like a jet fighter, hover like a helicopter, and they are on the MAV length scale. Warrick et al.¹ examined the aerodynamics of hummingbird hovering with digital particle image correlation to capture the airflow structure. The authors found that the hummingbird's upstroke and downstroke are not symmetrical in producing lift (thrust): the downstroke responsible for about 75% of the body weight and the upstroke about 25%. This is very different from insects, which have a more symmetrical load distribution. The differences are results of wing kinematics and structure. If a robotic hummingbird or insect is to be developed, understanding the causal relationship between kinematics, deformation and aerodynamics is essential. On the other hand, Tobalske et al.² documented the kinematics of hummingbirds in forward flight at different speeds. The authors used a few parameters to describe wing trajectories and angles. However such description may be considered insufficient for reconstructing the same kinematics. Therefore, in order to facilitate the research of flapping wing MAVs, an experimental method that can describe the complete wing kinematics and deformation, and correlate with aerodynamic loads, is called for. This paper presents an experimental technique for studying hummingbird-size flapping wings in MAV research. A sophisticated experimental setup featuring a customized digital image correlation system is described; several anisotropic flexible membranous wings are tested and post processed results are presented.

EXPERIMENTAL SETUP

The experimental setup consists of a flapping mechanism, a force and torque sensor, a digital image correlation (DIC) system, a vacuum chamber, composite wings and computer user interface, shown in [Figure 1](#). The flapping mechanism actuates the wings in a frequency range of 0~40 Hz at $\pm 35^\circ$. It can be adjusted for different amplitudes. A force and torque sensor (load cell) Nano 17 is mounted underneath the mechanism.

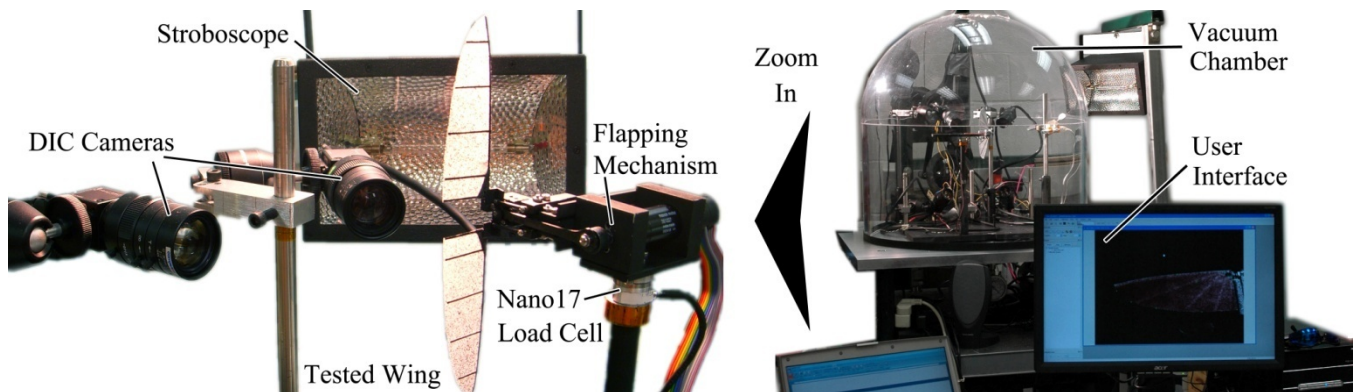


Figure 1. The experimental setup for flapping wing kinematics and deformation measurements.

The Nano17 (0.3 gram sensitivity) is used to measure the aerodynamic loads produced by the flapping wings. For measuring wing kinematics and deformation, a four-camera DIC system with stroboscope is used. The use of two pairs of cameras allows capturing wing surface at large flapping and rotation angles. A vacuum chamber is used to isolate inertial deformation from aerodynamic effects. The user interface allows the computer to control all

instruments simultaneously. The measurement procedure is shown in Figure 2, including input, operation, data acquisition and analysis. On the right, data correlation results between average thrust and deformation is plotted.

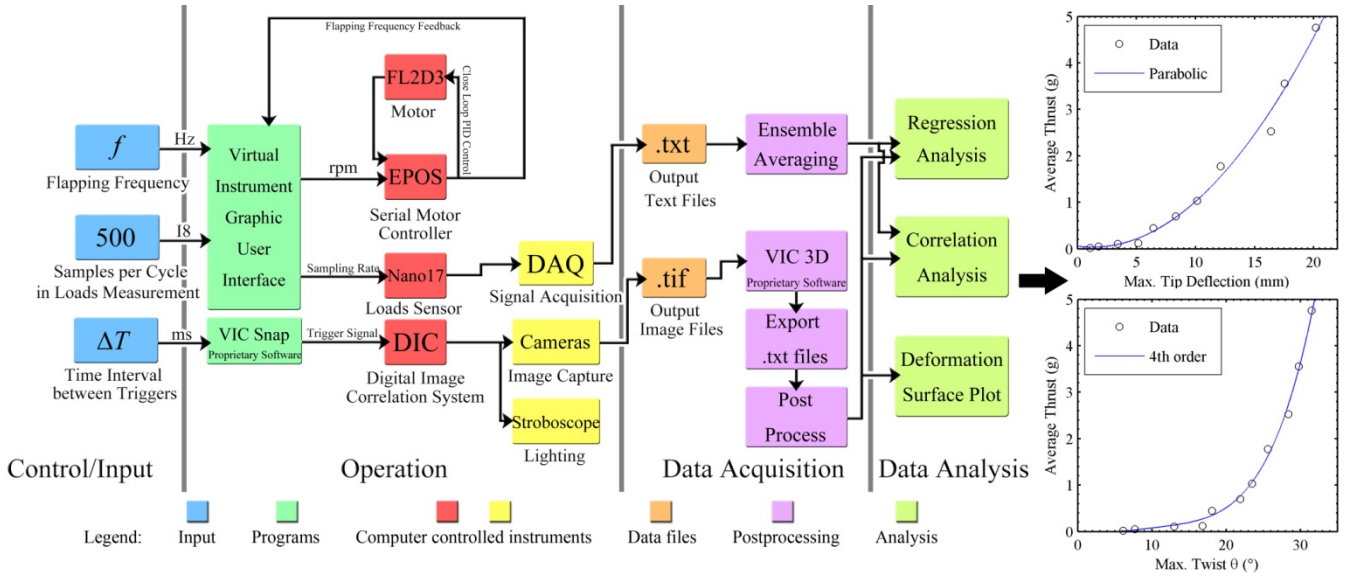


Figure 2. Measurement procedure on the left, correlation results on the right.

RESULTS AND CONCLUSIONS

Results are shown in Figure 2 and Figure 3. In Figure 2, the average thrust data correlates well with maximal wing tip deflection and twist. In Figure 3, upstroke and downstroke kinematics are shown with color contour describing the out of surface deformation (w/c , normalized to the chord length 25 mm). The grey line indicates the rigid body kinematics without any deformation. Comparison between the results in air and vacuum identifies the deformation caused by aerodynamic effects. In conclusion, an experimental technique is developed to measure the kinematics, deformation and performance of flapping wings for micro air vehicle research.

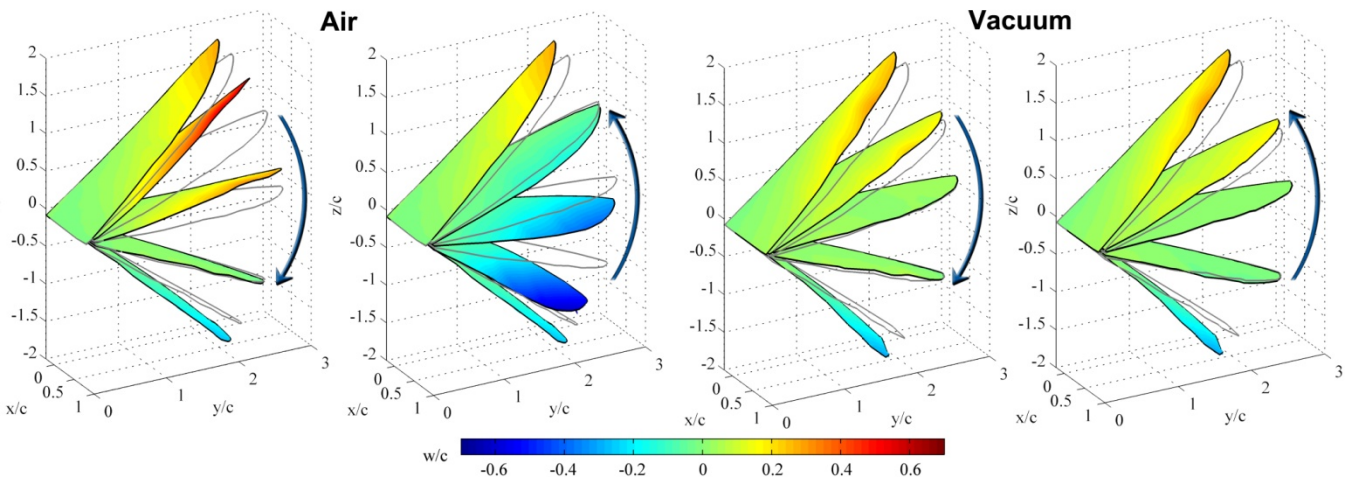


Figure 3. Wing kinematics and deformation measurement at 25 Hz in both air and vacuum.

REFERENCES

1. Warrick, D.R., Tobalske, B.W., and Powers, D.R., "Aerodynamics of the Hovering Hummingbird," *Nature*, Vol. 435 No. 23, June, 2005, pp. 1094-1097. DOI: 10.1038
2. Tobalske, B.W., Warrick, D.R., Clark, C.J., Powers, D.R., Hedrick, T.L., Hyder, G.A., and Biewener, A., "Three-dimensional Kinematics of Hummingbird Flight," *J. of Exp. Bio.*, Vol. 210, 2007, pp. 2368-2382.

Dynamic Constitutive Behavior of Aluminum Alloys: Experimental & Numerical Studies

Sandeep Abotula
Department of Mechanical, Industrial and Systems Engineering
University of Rhode Island, Kingston, RI 02881, USA

ABSTRACT

Split Hopkinson pressure bar (SHPB) setup was used to investigate dynamic constitutive behavior of aerospace Aluminum alloys both experimentally and numerically. The study was conducted in the strain rate regime of 500/s -10000/s. Both regular solid and modified hollow transmission bars were employed in realizing this strain rate regime. Four different Aluminum alloys namely 7075-T4, 2024-T3, 6061-T6 and 5182-O were considered for investigation. Copper-110 alloy pulse shaper was used to obtain better force equilibrium conditions at the bar-specimen interfaces. Plastic kinematic model was used to model rate dependent behavior of Aluminum alloys using commercially available LS-DYNA software. It was identified from the final results that experimentally determined dynamic constitutive behavior matches very well with that of numerical in the strain rate regime of 2000/s- 5000/s.

INTRODUCTION

The growing requirement for fuel efficient vehicles has made a renewed interest in aluminum alloys as a replacement for other metals in aerospace and automobile bodies due to their high strength-to-weight ratio. When studying the crashworthiness of these vehicles, dynamic behavior of these alloys must be well understood in developing numerical models. For the first time, Campbell [1] reported dynamic constitutive behavior of Aluminum alloy by subjecting long rods to compression impact and showed significant difference in the flow stress when it was compared with quasi-static case. Maiden and Green [2] conducted experiments using Hopkinson pressure bar setup to and found out that Aluminum 6061-T651 and 7075-T6 alloys showed no strain rate sensitivity in that strain range. Based on above literature search, it was identified that there exists no consistency in the results of high-strain rate constitutive behavior of aluminum alloys. Hence, for the first time, this paper discuss about both experimental and numerical investigation of high-strain rate behavior of four different aerospace aluminum alloys 7075-T4, 2024-T3, 6061-T6 and 5182-O under above said range.

EXPERIMENTAL DETAILS

Quasi-static Characterization

The quasi-static compression tests were performed using Instron materials testing system-5585 as per ASTM standard E9. Experiments were performed at 10mm/min extension rate and the tests were continued until crosshead extension reaches a value of 2.5mm. Since AA 5182-O was received as a sheet material, a dog bone specimen configuration as per ASTM standard E8M was tested using Instron materials testing system 5582.

Dynamic Characterization

Traditional Split Hopkinson Pressure Bar (SHPB) was used to study the dynamic behavior of aluminum alloys. Incident and transmission bars (Maraging steel) have the diameter of 12.5mm and length up to 1220mm. Copper 110 alloy was used as a pulse shaper to generate force equilibrium conditions. Since the AA5182-O has thickness of 1.70mm, a diameter of 3.22mm hollow transmission bar was used. Due to brevity of space, the description and theory of SHPB is not explained here and it can be referred in Kolsky[3] paper.

NUMERICAL MODELING DETAILS

To study the dynamic behavior of these aluminum alloys, three dimensional axi-symmetric split Hopkinson pressure bar setup was modeled using the commercially available LS-DYNA software package for strain rates ranging from 1700/s to 7000/s. All components were modeled using 3D Solid 164 element type. Cowper-Symonds model based on plastic kinematic material model available in LS-DYNA was used to model strain rate constitutive material behavior of all four aluminum alloys.

RESULTS AND DISCUSSION

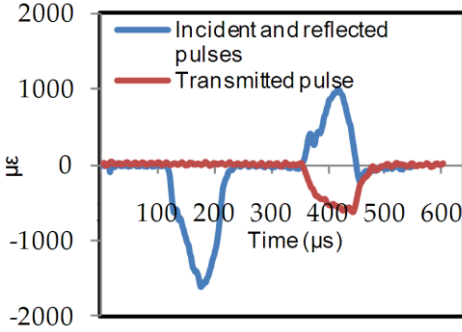


Fig. 1. Typical real time strain pulses obtained from SHPB

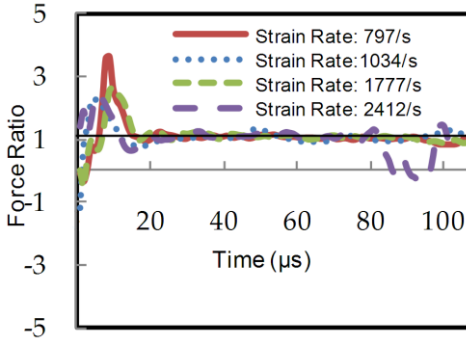


Fig. 3. Force equilibrium conditions for Al 7075-T4

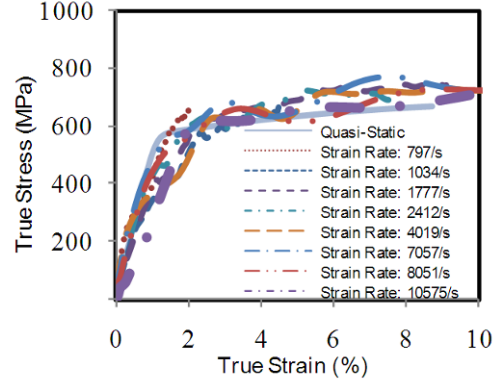


Fig. 2. True stress strain curve for Al 7075-T4

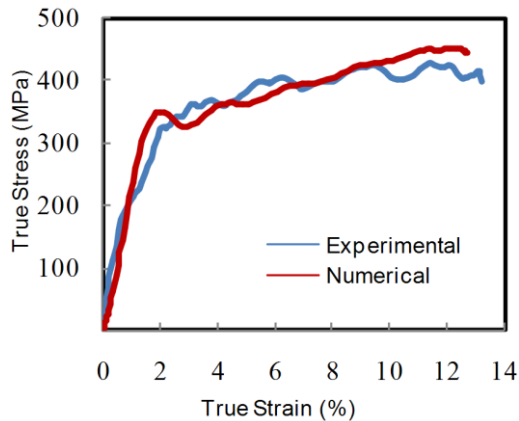


Fig. 4. Comparison of numerical dynamic true stress-strain behavior with those of experiments for Al 7075-T4

Dynamic Constitutive Response

The typical real-time strain pulses obtained for Al 6061-T6 alloy for an average strain rate of 3025/s is shown in Fig. 1. The dynamic true stress-strain curves for different strain rates are plotted against the quasi-static true stress-strain curves for Al 7075-T4 in Fig. 2. It can be noticed from the figure that Al 7075-T4 shows no significant rate sensitivity and there is no change in the yield strength as the strain rate increases. Force equilibrium conditions of Al 7075-T4 is shown in Fig. 3, and it can be seen that good equilibrium can be achieved by using C110 alloy as a pulse shaper. Comparison of experimental and numerical true stress strain behavior is plotted in Fig. 4. Figure shows that the experimental results match very well with the numerical results.

ACKNOWLEDGEMENTS

I would like to thank Dr. Vijaya Chalivendra for guiding me throughout the project. Also I would like to thank Dr. Arun Shukla for his valuable suggestions on this paper.

REFERENCES

1. Campbell, J. D.: An Investigation of the Plastic Behavior of Metal Rods Subjected to Longitudinal Impact. *Journal of mechanical Physics Solids*, **1**, 113-123, 1953.
2. Maiden, C. J., Green, S. J.: Compressive Strain-Rate Tests on Six Selected Materials at Strainrates from 10^{-3} to 10^6 in./in./sec. *Journal of Applied Mechanics*, **33**, 496-504 1966.
3. Kolsky, H.: An investigation of mechanical properties of materials at very high strain rates of loadings, *Proceedings of the Physical Society of London*, **B62**, 676-700, 1949.

Estimating surface coverage of gold nanoparticles deposited on MEMS

N. Ansari^{a,*}, K. M. Hurst^a and W. R. Ashurst^a

^aDepartment of Chemical Engineering, Auburn University, Auburn, AL-36849, USA

*Corresponding author: ansarna@auburn.edu [N. Ansari]

Introduction

Commercialization of a whole spectrum of useful MEMS is still hindered by surface phenomena that dominate at the micron scale. Altering the roughness and surface chemistry of MEMS surfaces by depositing nanoparticles on them is being considered by the MEMS community as a useful strategy to address tribological issues. Although, gold nanoparticle monolayer is reported to reduce adhesion in MEMS, determining its surface coverage still remains a challenge [1]. A technique to determine the surface coverage of deposited gold nanoparticles is needed, so that its effect on the tribology of MEMS surfaces can be studied.

Design, Fabrication and Testing Procedure of the Test Structure

The design of our test structure (referred to as Resonator) is based on a single mask scheme, thereby making its fabrication facile and inexpensive. The Resonator is fabricated using the standard surface micromachining technology on a SOI wafer. The resonating structure is fabricated in a 1.84 μm thin film of Si(100) and is suspended 2 μm above the substrate, which is 500 μm thick. Fig. 1 is an optical image of a fabricated and released Resonator

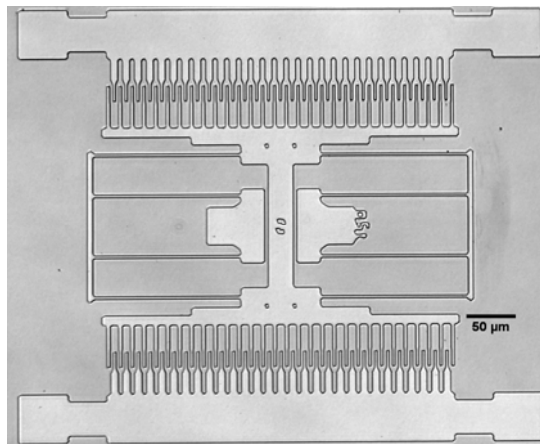


Figure 1: Optical image of a released Resonator.

The Resonator is actuated electrostatically. Electrical contacts are made by touching the structure with sharp tungsten probe tips. The resonating structure, ground plane and one set of comb electrodes are grounded and an AC voltage with a DC offset is applied to the other set of comb electrodes. The resonator is observed under high magnification as the frequency of the driving signal is gradually increased. Resonance is determined optically using the pattern etched on the resonating structure.

Estimation of Surface Coverage

The resonance frequency (f_R) of the resonator is given by eq.1, where k_x is the stiffness of the folded beams supporting the suspended structure and M_{eff} is the effective mass of the resonating structure. The stiffness of the folded beams as given by eq.2 depends on the Young's modulus (E) and the thickness (t) of the structural film as

$$f_R = \frac{1}{2\pi} \sqrt{\frac{k_x}{M_{\text{eff}}}} \quad [1]$$

well as the width (w) and length (L) of the folded beams. The deposition of gold nanoparticles on the resonating structure increases the mass of the resonating structure, which in turn decreases its resonance frequency according to eq.1. By comparing the resonance frequency of gold nanoparticle coated and uncoated resonators, the increase in the mass of the coated resonator, which is the mass of deposited gold nanoparticles can be determined using eq.3. This increase in the mass of the coated resonator is then used to determine the coverage of gold nanoparticle monolayer deposited on the resonator.

$$k_x = 2Et \left(\frac{w}{L} \right)^3 \quad [2]$$

$$\Delta M_{\text{eff}} = \frac{-4\pi M_{\text{eff}}^{3/2} \Delta f_R}{\sqrt{k_x}} \quad [3]$$

Deposition of Gold Nanoparticles

After fabrication, the Resonator is released by etching it in conc. (49 wt.%) HF. The etchant is completely displaced by deionized (DI) water, after which the Resonator is placed in hot H₂O₂ (Temp. = 75°C) for 10 mins. H₂O₂ is further displaced by DI water, which in turn is displaced by isopropanol (IPA). After completely rinsing away the IPA with anhydrous hexane, gold nanoparticles are deposited on the Resonator using the CO₂ gas-expanded liquid technique reported by Hurst et. al. [1].

Results and Discussion

Length (μm)	Resonance Frequency, f_R +/- std.dev. (KHz)		$\Delta M_{\text{eff}} \times 10^{12}$ (Kg)	Coverage of Au nanoparticles (%)
	Uncoated	Coated		
300	8.34 +/- 0.01	8.28 +/- 0.01	4.0 +/- 0.31	61 +/- 4.7
350	6.14 +/- 0.01	6.09 +/- 0.01	3.7 +/- 0.36	59 +/- 5.6
400	4.72 +/- 0.01	4.68 +/- 0.01	4.1 +/- 0.45	63 +/- 6.9
450	3.92 +/- 0.01	3.88 +/- 0.01	4.5 +/- 0.55	68 +/- 8.3
500	3.64 +/- 0.01	3.61 +/- 0.01	4.2 +/- 0.71	61 +/- 10.1

Table 1: Surface coverage of gold nanoparticles deposited using the CO₂ gas-expanded liquid technique on a MEMS chip.

Resonators from different regions of the chip coated with gold nanoparticles are tested to determine the uniformity of coating. Table 1 above lists the resonance frequencies of both uncoated and gold nanoparticle coated resonators along with the lengths of their folded suspension beams. The results reported in table 1 indicate that the coating is uniform throughout the chip and it has a coverage of 64 +/- 4 %.

Conclusions

We have demonstrated a simple technique based on optically determined resonance to determine the coverage and uniformity of a gold nanoparticle monolayer deposited on a MEMS chip using the CO₂ gas-expanded liquid technique. This technique can also be used to compare the number densities of gold nanoparticle solutions, since the coverage of gold nanoparticle monolayer depends strongly on the number density of the starting gold nanoparticle solution.

References

1. Hurst, K. M., Roberts, C. B., Ashurst, W. R., "A gas-expanded liquid nanoparticle deposition technique for reducing the adhesion of silicon microstructures", Nanotechnology, 20(18), 185303(9pp), 2009.

Functionally Graded Metallic Structure for Bone Replacement

S. Bender

University of Massachusetts Dartmouth, 285 Old Westport Rd. North Dartmouth MA, 02747

ABSTRACT

Processes for the creation and characterization of functionally graded metallic structures for use as artificial bone tissue were investigated. The metallic structure consists of a solid surface layer, a graded porosity layer and a homogeneous porous core. Porous compacts with varied densities were created using traditional powder metallurgy techniques. The surfaces of the compacts were subjected to a densification process with the use of a specially designed indentation tool. Investigations on the effect of the initial density of the compact and the depth of indentation during the densification process on the densified layer and graded porosity region were studied. Compacts with an initial density of 86 % of the true density were indented to depths of approximately 1.8, 1.25, 1, and 0.65 mm. Compacts with initial densities of 67, 70, and 73% were indented to a depth of 1 mm. Optical microscopy and scanning electron microscopy (SEM) were implemented to characterize the morphology of the porous structure. Results show that deeper indentation during the densification process yielded a larger densified layer. The variation of Young's modulus along the porosity gradation is investigated using micro-indentation. The graded structures are also investigated for fracture parameters and crack growth behavior using digital image correlation techniques.

INTRODUCTION

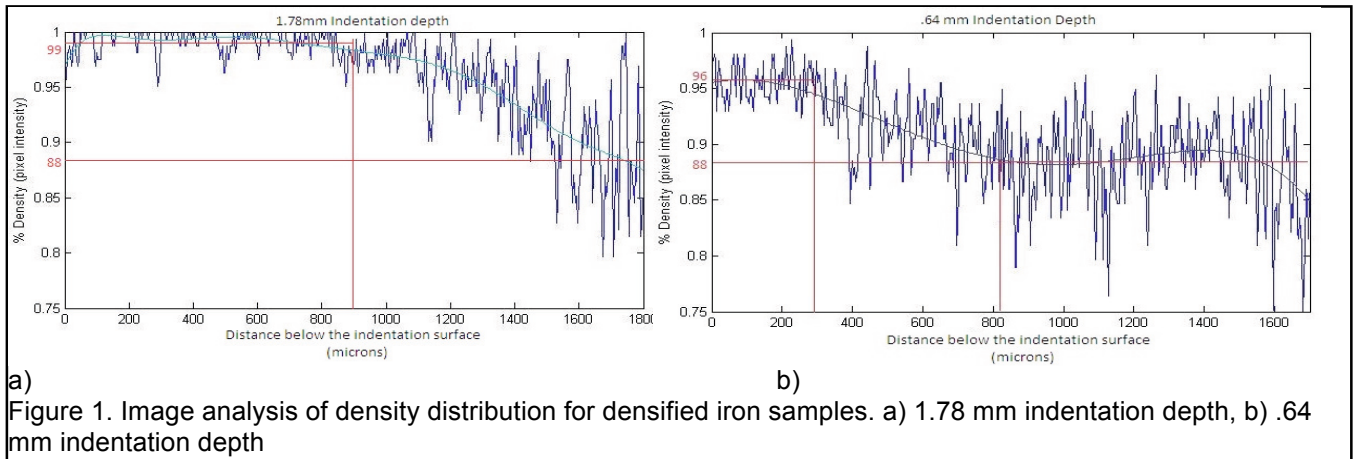
Bone tissue replication is a rapidly evolving field of study. Many methods and materials are used to create artificial bone structures with porosity distributions. Pelletier et al. [1] tested poly(methyl methacrylate) cured at different temperatures and found at higher temperatures they could obtain a solid structure with a porous core. Tape casting of alumina ceramics has also been used to create a porous region in a solid structure and was shown to have enhanced toughness values by Zeming et al [2]. Most of the research involving metallic structures has been focused on purely porous structures, such as the work by Gradzka-Dahlke et al. [3]. This paper suggests a method for creating a metallic structure with a porous core, a graded porosity layer, and a solid surface layer.

EXPERIMENTAL METHODS

Iron compacts were created using traditional powder metallurgy techniques. The powder was compacted in a die and later sintered in an argon atmosphere. An initial density of the sintered compact of 86% of the true density of iron was obtained. Since stainless steel powder does not possess the favorable compactability similar to iron, loose sintering techniques, similar to those described by El Wakil [4], were used to produce the porous stainless steel substrates. To achieve a variety of substrate densities the sintering temperature was varied. Sintering temperatures of 1300, 1350, and 1400°C produced initial densities of 67, 70, and 73% respectively. The surface densification of the porous substrate was achieved through the use of a specially designed indentation tool. The tool consists of a ball-point which is used to penetrate into surface of the substrate. Iron substrates with an initial density of 86% were densified to depths of 1.78, 1.27, 1, and 0.64 mm. The stainless steel substrates of initial densities of 67, 70, and 73 % were all densified to a depth of 1 mm.

RESULTS

Cut and polished cross sections of the densified surface were imaged using optical microscopy. Image analysis using MATLAB tools, was performed to determine the morphology of the porous structure from the solid surface to the porous core. Figure 1 shows the image analysis for the maximum and minimum densification depths (1.78 and .64 mm). The length of the solid region is observed to increase as the depth of indentation increases. The corresponding solid region lengths are 0.3, 0.65, 0.75 and 0.85 mm for densification depths of 0.64, 1, 1.27, and 1.78 mm respectively. The density of the solid region also appeared to increase about 1% for each of the densification depths. Figure 2 shows the results of the stainless steel substrates of varied initial densities that were densified to a depth of 1 mm. It was observed that the difference in the initial density had a negligible effect on the length of the solid surface. An increase in initial density did show a decrease in slope of the change in



a) Figure 1. Image analysis of density distribution for densified iron samples. a) 1.78 mm indentation depth, b) .64 mm indentation depth

porosity in the graded porous region. SEM images of the 1.78 mm densification depth on an iron substrate were taken at increasing depth below the surface of densification. In the region of the solid surface it was observed that the pores were mostly collapsed. While images toward the core region revealed a decreased ratio of collapsed pores to rounded pores. The SEM images at 0.5 mm intervals below the densified surface are shown in figure 3.

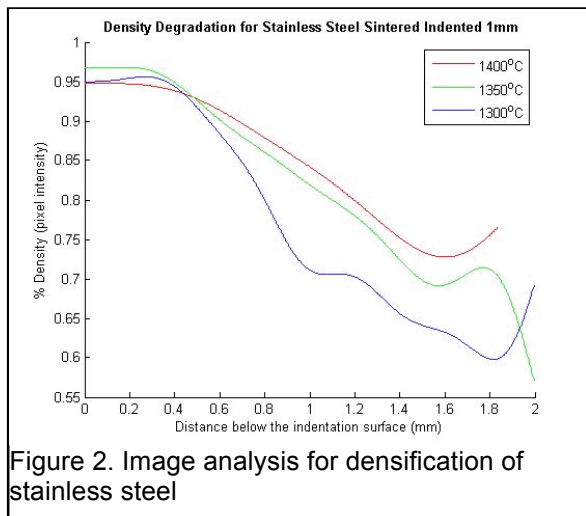


Figure 2. Image analysis for densification of stainless steel

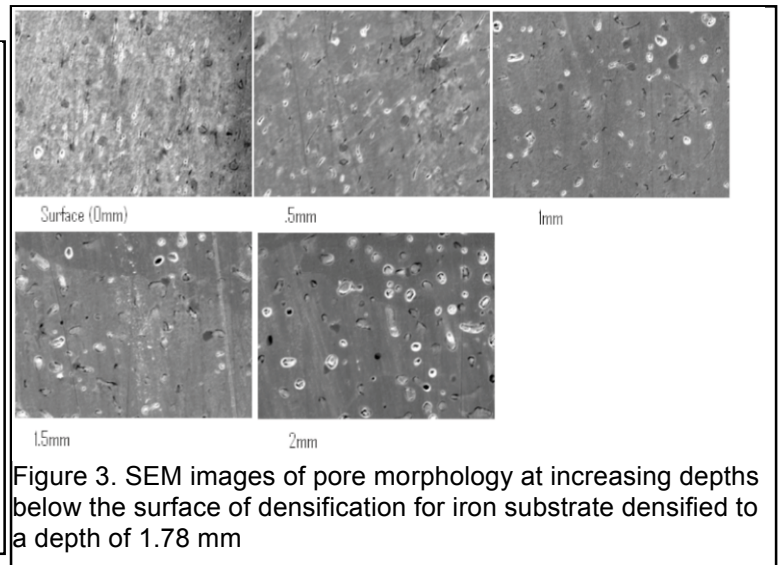


Figure 3. SEM images of pore morphology at increasing depths below the surface of densification for iron substrate densified to a depth of 1.78 mm

EXPERIMENTS IN PROGRESS

Micro indentation experiments using a Vickers indentation tip are in progress to determine the mechanical properties of the solid surface and the graded porous region. Quasi-static fracture and flexure tests are also in progress. Both homogeneously porous and densified samples are used to determine the porosity gradient's effect on fracture toughness and flexure strength. The results of these experiments will be presented at the conference.

REFERENCES

- [1] Pelletier M. H. et al., Pore Distribution and Mechanical Properties of Bone Cement Cured at Different Temperatures, *Acta Biomaterialia*, Actbio 995, 2009
- [2] Zeming He et al, Dynamic Fracture Behavior of Layer Alumina Ceramics..., *Materials Letters*, 59, 901-904, 2005
- [3] Gradzka-Dahlke M. et al., Modification of Mechanical Properties of Sintered Implant Materials..., *Journal of Materials Processing Technologies*, 204, 199-205, 2008
- [4] El Wakil S.D., Khalifa H., Cold Formability of Billets by Loose Powder Sintering, *The International Journal of Powder Metallurgy and Powder Technologies*, 19, 1, 21-27, 1983

Dissipative energy as an indicator of material microstructural evolution

N. Connesson^{1,a} F. Maquin^{2,a} F. Pierron^{3,a}

¹nathanael.connesson@gmail.com, ²francois.maquin@chalons.ensam.fr, ³fabrice.pierron@chalons.ensam.fr

^aLaboratoire de mécanique et procédés de fabrication (LMPF), Arts et Métiers ParisTech, rue St Dominique, BP 508, 51006 Châlons-en-Champagne cedex, France

1. Introduction

Rapid fatigue limit estimation methods are of strong interest to industry. Some authors proposed rapid experimental methods to estimate the fatigue limit based on the material temperature increase under cyclic loading [1,2]. Yet, heat dissipation phenomena need to be more thoroughly studied in order to give better physical grounds to such methods.

Usually, the dissipative energy is explained by internal friction phenomena and is mainly attributed to dislocation movements [3]. The dissipative energy should thus depend on the material dislocation characteristics. Yet, these characteristics are usually modified during the loading history [4-6].

In this work, it was thus chosen to experimentally study the correlation between the dissipative energy and the cold work of a dual phase steel (DP600, Yield limit at 0.02% of 220 MPa), both phenomena being related to the microstructural dislocation structure.

2. Experimental procedure and results

A specimen has been machined from a 2 mm thick DP600 steel plate and has been uniaxially loaded. The applied harmonic load has been defined by $R_\sigma = \sigma_{\min}/\sigma_{\max} = 0.1$ where σ_{\min} and σ_{\max} are respectively the minimal and maximal stresses. For each loading sequence, as the plastic strain is monotonic with these loading characteristics, the solicitation has been maintained during a high enough number of cycles so that the material reached a steady state (stabilized mean strain). The material cold work has then been characterized after each test: the residual plastic strain ε^p has been measured while no loading was applied to the specimen by using a strain gauge.

During each loading sequence, the specimen temperature variation has also been measured with an infrared camera. The dissipative energy per cycle E_d^m has then been estimated by solving the heat balance equation [7] and by using the experimental method described in [8]. As this measurement has been performed in steady state condition and with a positive loading ratio, no alternate plastic strain occurred during the thermal acquisition: here, the dissipated energy is only due to internal friction phenomena and has not been influenced by the yield limit variation due to cold work (if the loading ratio R_σ were negative, the alternate plastic strain could have been modified with the cold work).

Therefore, this experimental setup provides the plastic strain ε^p measurement while the specimen is not loaded and the dissipative energy E_d^m measurement under cyclic loading and in steady state behaviour.

Four measurements sequences (Phase I to IV) have been developed in this study to monitor the correlation between dissipative energy and plastic strain. These test sequences have been sketched in the upper graph of [Figure 1\(a\)](#). In this representation, each point represents three successive tests:

- a cyclic loading at the maximal stress σ_{\max} (represented by the point ordinate) applied until a steady behaviour is reached,
- then a dissipative energy measurement in the same loading conditions,
- and eventually a residual plastic strain measurement ε^p after unloading.

The cumulated plastic strain ε^p at the end of each test is presented in the bottom graph of [Figure 1\(a\)](#).

The four measurement sequences have been designed to reach different goals: the material initial behaviour is analyzed during Phase I where small plastic stains occurred. The material is then plastically strained during Phase II and its dissipative energy evolution is analyzed. Phase III and IV are then performed to monitor the changes in the material dissipative energy due to the previous two phases.

The dissipative energy per cycle is presented for each phase versus the alternate stress σ_a and the maximal stress σ_{max} in Figure 1(b). The dissipative energy per cycle increases with the alternate stress, which can be explained with a simple Kelvin-Voigt model. The dissipative energies during Phase I and the first steps of Phase II (Tests up to D₀) are identical. Thus, the plastic strain occurring during Phase I does not change the dissipative energy behaviour; the dissipative energy measurement is reproducible if the material is not plastically strained (ie, no change in the dislocation density).

The dissipative energies of the tests D₀ to D₁₀, which have all been performed at the same maximal stress $\sigma_{max}=240$ MPa and in steady state behaviour, increase gradually along with the material cumulated plastic strain (sub graph in Figure 1(b)). The material microstructural changes occurring during Phase II have thus progressively increased the dissipated energy. Moreover, the dissipative energy during Phase III is always greater than the dissipative energy during Phase II. These results confirm that the dissipated energy is an indicator of the material microstructural state.

Eventually, the measurements achieved during Phase IV point out a good reproducibility of the dissipative energy measurements on the same specimen. Phase III and IV are thus the characterization of the material dissipative energy stabilized behaviour and this curve could be seen as the "signature" of this material dislocation structure.

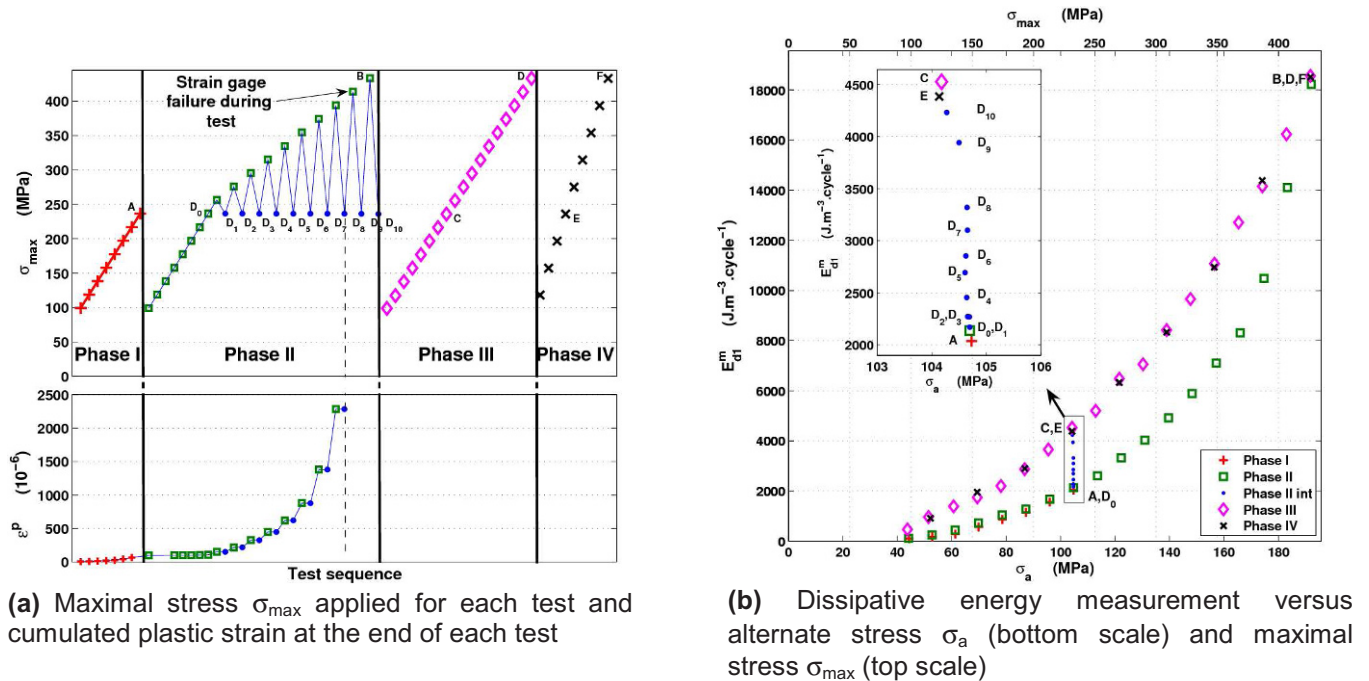


Fig 1. Experimental sequence and results

3. Conclusion

The dissipative energy of a dual phase steel has been proved to increase with the material cold work. The dissipative energy is thus an indicator of the material state. As this measurement has been achieved during a few hundreds of cycles at $R_\sigma=0.1$, correlation between the material dissipative energy and its microstructure evolution during fatigue tests still need to be studied and will be addressed in future work.

References

- [1] H.F. Moore, J.B. Koppers, *Chemical and Metallurgical Engineering* 25, (1921) 1141-1144
- [2] G. Fargione, A. Geraci, G. La Rosa, A. Risitano, *International Journal of Fatigue* 24, (2002) 11-19
- [3] D. Caillard, J.L. Martin, *Thermally activated mechanisms in crystal plasticity* (Pergamon, Amsterdam London 2003) 85-123
- [4] A. Granato, K. Lücke, *Journal of Applied Physics*, 27:6, (1956) 583-593
- [5] T. Tanaka, S. Hattori, *Bulletin of the JSME*, (21:161) (1978) 1557-1564
- [6] H. Mughrabi, F. Ackermann, K. Herz, *ASTM Special Technical Publication*, 675, (1979) 69-105
- [7] A. Chrysochoos, H. Louche, *International Journal of Engineering Science* 16, (2000) 1759-1788
- [8] F. Maquin, F. Pierron, *Mechanics of Materials* 41, (2009) 928-942

Temporal Phase Stepping Photoelasticity by Load or Wavelength

M.J. Huang and H.L. An

Mechanical Engineering, National Chung Hsing University,
250, Kuo-Kuang Road, Taichung, Taiwan 40227, R.O.C.

ABSTRACT

Phase-stepping techniques in photoelasticity own the isoclinic-isochromatic interaction problem, which causes phase ambiguity zone on the photoelastic phase map and bothers engineers of this field very much. Temporal phase unwrapping is an effective method for circumventing the above problem. In this work, the load stepping and wavelength stepping approaches are applied both but individually on photoelastic samples to compare the different characteristics of them including in accuracy of results, ease of applied technologies, and automation of stepping etc. Load stepping approach is not applicable for stress frozen sample while wavelength stepping is. The constant increment of loading percentage is not easy to be controlled under complex loading conditions. The control of wavelength stepping if integrated with electro-optic components is very flexible and versatile. However, the birefringence error of optical wave plate for different wavelength should be carefully calibrated to minimize the errors. Experimental works are studied to practically verify the differences and limitation of these two approaches.

Keywords: Photoelasticity, temporal phase unwrapping, load stepping, Isoclinic, Isochromatic.

1. Introduction

Phase unwrapping (PU) consists of retrieval of the true phase field from wrapped format data, which is restricted in a $[-\pi, \pi]$ for 2π modulo. This problem is encountered in the phase stepping digital photoelasticity [1-4]. However, the interaction between the isoclinic parameter and relative retardation makes the phase retrieval work very difficult. Many papers [5-19] had been published to solve the related problems. Wang and Patterson [5] used signal analysis and fuzzy sets theory to investigate these difficulties. The ambiguity existing problem can be also overcome with the development of load stepping. Ramesh and Tamrakar [6] proposed a new methodology for data reduction in load stepping to remove the noise points in the model domain. However, the methodology requires three times the number of images required for normal phase stepping method. Ramesh et. al. [7, 8] proposed a new interactive methodology to remove the ambiguity.

Temporal phase unwrapping is an effective way to circumvent this problem. It is usually implemented by the load stepping method [9, 10] but however, this technique can not be applicable for stress frozen sample. An alternative is to change the wavelength of the light source to generate phase stepping. Chen [11] successfully utilized this technique by two different wavelengths and checked the phase changes between them that had successfully solved the isoclinic-isochromatic interaction problem. In this work, some comparisons are further investigated.

2. PHASE STEPPING PHOTOELASTICITY

A general optical arrangement of a plane polariscope and a circular polariscope are shown in Fig. 1 and Fig. 2, respectively. White light is used as the light source and a general digital camera with RGB filters is used as the fringes recorder. Table 1 summarizes the used phase stepping parameters and their corresponding intensity results. The isoclinic φ_w and isochromatic δ_w parameters can be obtained as follows.

$$\begin{aligned}\phi_w &= \frac{1}{4} \tan^{-1} \left\{ \frac{n \langle I_4^s - I_0 \rangle - n \langle I_2^s - I_0 \rangle}{n \langle I_3^s - I_0 \rangle - n \langle I_1^s - I_0 \rangle} \right\} \\ &= \frac{1}{4} \tan^{-1} \left\{ \frac{\sin \phi}{\cos \phi} \right\},\end{aligned}\quad (1)$$

$$\phi = W^{-1} \{ \phi_w \}, \quad (2)$$

$$\begin{aligned}\delta_w &= \tan^{-1} \left\{ \frac{(I_9 - I_7) \sin 2\phi + (I_8 - I_{10}) \cos 2\phi}{I_5 - I_6} \right\} \\ &= \tan^{-1} \left\{ \frac{I_a \sin \delta}{I_a \cos \delta} \right\},\end{aligned}\quad (3)$$

where

$$I_0 = \frac{1}{4} (I_1^s + I_2^s + I_3^s + I_4^s), \quad (4)$$

$$I_j^s = \frac{1}{3} (I_{j,R} + I_{j,G} + I_{j,B}) \quad \text{for } j = 1, \dots, 4, \quad (5)$$

$W^{-1} \{ \}$ represents the unwrapping operator, and $n \langle \rangle$ means normalization operator to eliminate any effect caused by isochromatic parameter. $\tan^{-1} \{ \}$ of Eq. (1) and Eq. (3) is arctan2 function with their results ranging between $-\pi/4 \sim \pi/4$ and $-\pi \sim \pi$, respectively. Since the isochromatic data is dependent on the isoclinic data, the isoclinic data should be correctly unwrapped and ranged in the range of $-\pi/2 \sim \pi/2$ before substituting into Eq. (3). Provided the substituted isoclinic data are correct, the isochromatic calculation is ambiguity free and that makes the following retrieval work of the isochromatic data extremely easy.

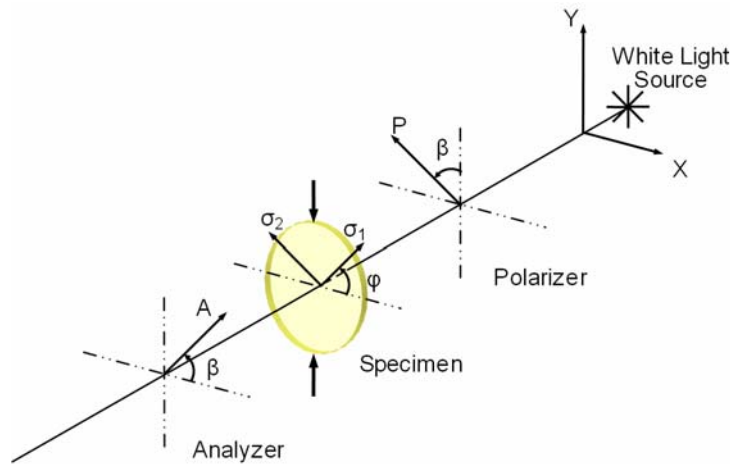


Fig. 1. The optical arrangement of plane polariscope

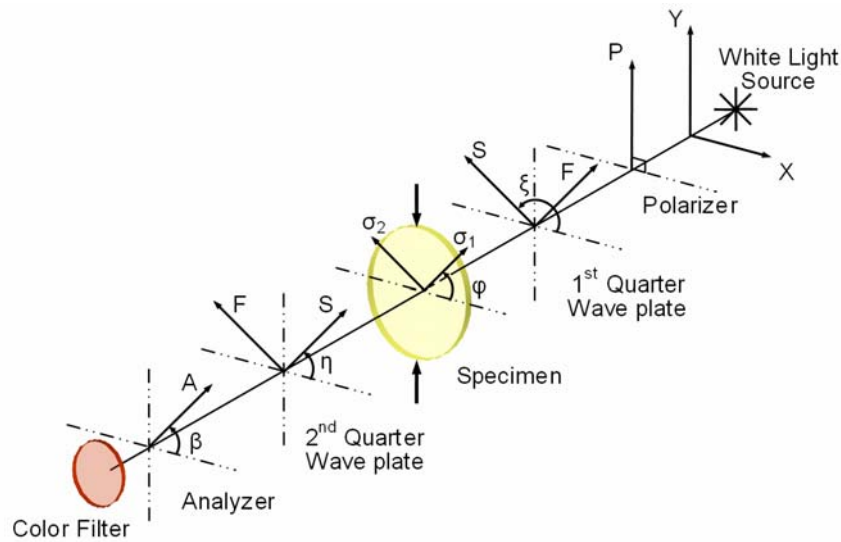


Fig. 2. The optical arrangement of circular polariscope

Table 1 Polariscope arrangement and the intensity results for phase stepping algorithm

ξ	η	β	Intensity equation
-	-	0	$I_{1,i} = I_{B,i} + \frac{1}{2}I_{A,i} \sin^2 \frac{1}{2} \delta_i (1 - \cos 4\alpha)$
-	-	$\pi/8$	$I_{2,i} = I_{B,i} + \frac{1}{2}I_{A,i} \sin^2 \frac{1}{2} \delta_i (1 - \sin 4\alpha)$
-	-	$\pi/4$	$I_{3,i} = I_{B,i} + \frac{1}{2}I_{A,i} \sin^2 \frac{1}{2} \delta_i (1 + \cos 4\alpha)$
-	-	$3\pi/8$	$I_{4,i} = I_{B,i} + \frac{1}{2}I_{A,i} \sin^2 \frac{1}{2} \delta_i (1 + \sin 4\alpha)$
$3\pi/4$	$\pi/4$	$\pi/2$	$I_5 = I_b + \frac{1}{2}I_a (1 + \cos \delta)$
$3\pi/4$	$\pi/4$	0	$I_6 = I_b + \frac{1}{2}I_a (1 - \cos \delta)$
$3\pi/4$	0	0	$I_7 = I_b + \frac{1}{2}I_a (1 - \sin 2\phi \sin \delta)$
$3\pi/4$	$\pi/4$	$\pi/4$	$I_8 = I_b + \frac{1}{2}I_a (1 + \cos 2\phi \sin \delta)$
$\pi/4$	0	0	$I_9 = I_b + \frac{1}{2}I_a (1 + \sin 2\phi \sin \delta)$
$\pi/4$	$3\pi/4$	$\pi/4$	$I_{10} = I_b + \frac{1}{2}I_a (1 - \cos 2\phi \sin \delta)$

3. LOAD STEPPING AND WAVELENGTH STEPPING

In this work, the load stepping work of Ref. 9 is used. Two isochromatic fringes of loading stages with and without load increment are checked. Compare the isochromatic phases of the sample with load increment with that of same sample without load increment. Whenever its isochromatic phases of the load increment one is less than that of the one without load increment, that means its corresponding isoclinic data should be added or subtracted by $\pi/2$ depending on its isoclinic data is negative or positive, respectively. This restored isoclinic data is then further substituted into the isochromatic formulation to eliminate the original (wrapped) isoclinic induced phase ambiguities of the isochromatic fringes. Since the load increment percentage is known, which should be accurately controlled by the photoelastic engineer to ensure the percentage of the load increment, and the isochromatic data differences of the tested sample before and after load increment implementation are also collected experimentally, their division yields the correct isochromatic phase of the tested sample. It is simple and effective. However, this technique is not applicable for the stress frozen sample because the loading condition has been frozen into the sample which can not be loaded any further.

It is known that the isochromatic data is proportional to the applying loading but inversely proportional to the wavelength of the light source. Therefore, similarly as load stepping, an alternative way to shift the isochromatic

phase is to keep loading fixed but to change the wavelength of the photoelastic experiment. And because it is implemented by different color filtering which is not done mechanically, sometimes it is much easier to be implemented digitally like using color camera filtering technique. The fast growing digital camera market makes the color filtering technique remarkable progress.

4. EXPERIMENT RESULTS

A curve beam under tension is tested here. Fig. 3(a) shows the wrapped isoclinic. Fig. 3(b) is the isochromatic fringes under the substitution of Fig. 3(a) into isochromatic formulation. Using load stepping technique, the wrapped isoclinic can be restored into Fig. 3(c) and its corrected isochromatic result is shown as Fig. 3(d). It is clearly shown that the results are with certain degree of noise, which very probably is due to the point detection between two different loading isochromatics. The result is not as good as that from spatial photoelastic unwrapping.

The sample is also unwrapped using wavelength stepping technique and the results are shown as Fig. 4(a) and Fig. 4(b). It is also shown that since the temporal (wavelength) unwrapping is done by checking individual isochromatic data in correspondence. Therefore, isoclinic and isochromatic results are very easily influenced by any local noise and thus lead to the results of Fig. 4(a) and Fig. 4(b). It is very clear that these results are not as good as those unwrapped by the newly-developed regional phase unwrapping algorithm [12] for photoelastic data.

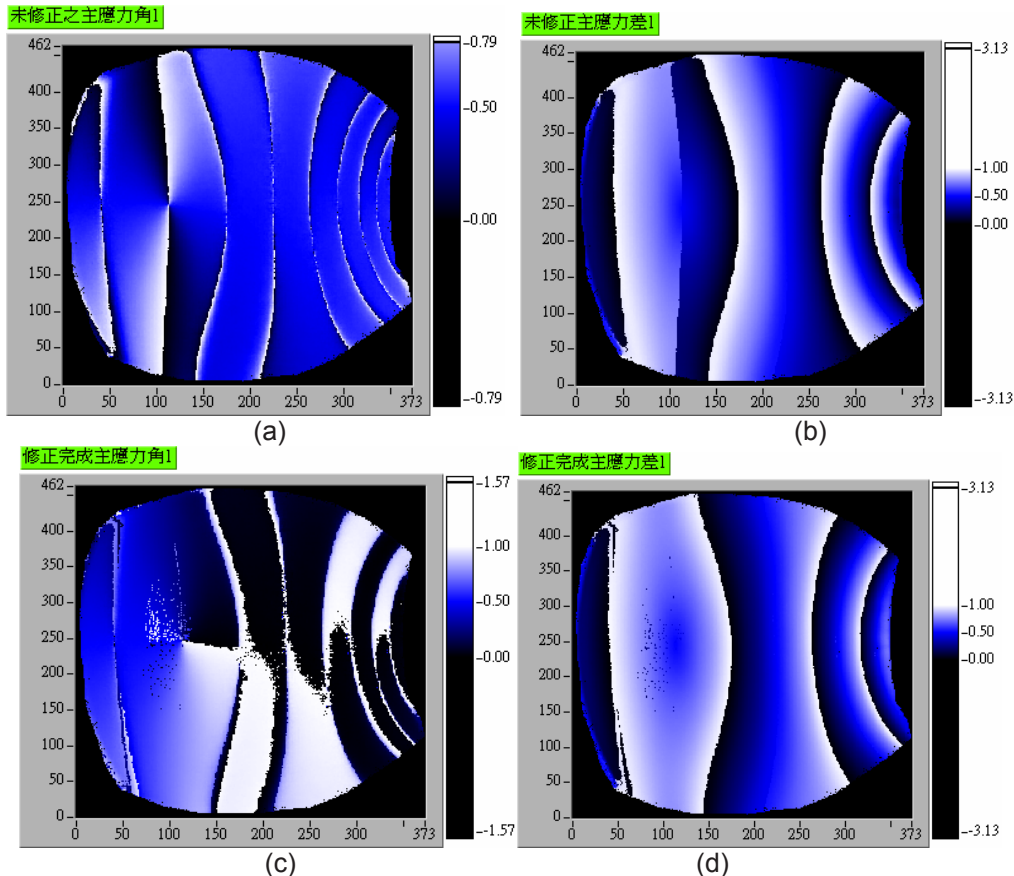


Fig. 3. The isoclinic and isochromatic of curve beam under tension (a) wrapped isoclinic (b) isochromatic derived from wrapped isoclinic (c) unwrapped isoclinic (d) isochromatic data derived from unwrapped isoclinic

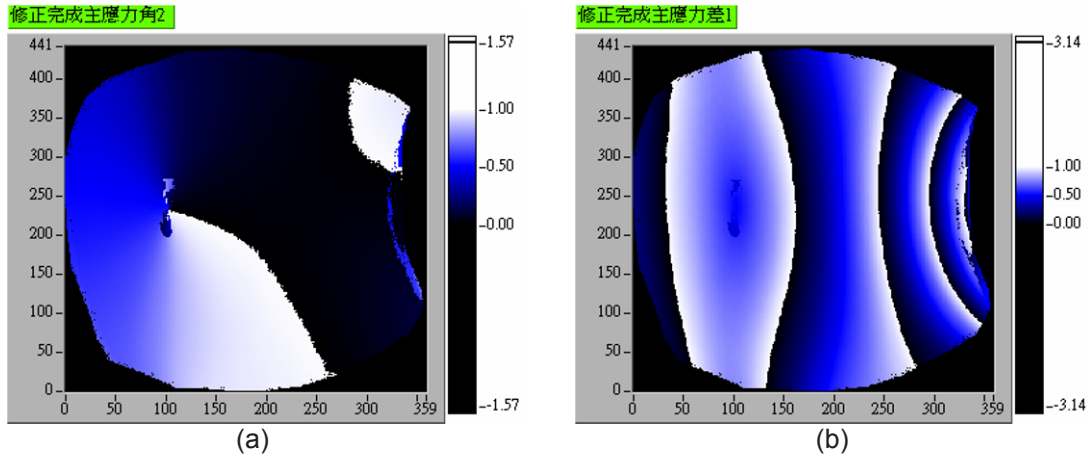


Fig. 4. Wavelength stepping result (a) isoclinic (b) isochromatic.

5. DISCUSSION AND CONCLUSION

Two approaches, load stepping and wavelength stepping, of temporal photoelastic phase unwrapping are discussed in this study. It is found that temporal phase unwrapping is very easy to unwrap its isoclinic and isochromatic data by the comparison of data of any point between the two different temporal conditions. It is also because this kind of data comparison way that unwrapped results are full of noise than those from spatial unwrapping algorithm.

In addition, data obtain from wavelength stepping are much better than those from loading stepping technique. It can be give reasons from the difficulty of accurate control of the loading condition and is a difficult task which should be carefully done by the photoelastic engineers.

Acknowledgments

The authors would like to thank the National Science Council of the Republic of China for financially supporting this research under contract Number NSC98-2221-E-005-009.

References

- [1] A.V. Sarma, S.A. Pillai, G. Subramanian and T.K. Varadan, "Computerized image processing for whole-field determination of isoclinics and isochromatics," *Experimental Mechanics*, pp. 24-29, 1992.
- [2] K. Ramesh and V. Ganapathy, "Phase-shifting methodologies in photoelastic analysis – the application of Jones calculus," *Journal of Strain Analysis*, vol. 31, pp. 423-432.
- [3] K. Ramesh and S.K. Mangal, "Automation of data acquisition in reflection photoelasticity by phaseshifting methodology" *Strain*, pp. 95-100, 1997.
- [4] S. Yoneyama, Y. Morimoto and R. Matsui, "Photoelastic fringe pattern analysis by real-time phase-shifting method," *Optics and Lasers in Engineering*, vol. 39, pp. 1-13, 2003.
- [5] Z.F. Wang and E.A. Patterson, "Use of phase-stepping with demodulation and fuzzy sets for birefringence measurement," *Optics and Lasers in Engineering*, vol. 22, pp. 91-104, 1995.
- [6] K. Ramesh and D.K. Temrakar, "Improved determination of retardation in digital photoelasticity by load stepping," *Optics and Lasers in Engineering*, vol. 33, pp. 387-400, 2000.
- [7] V.S. Prasad, K.R. Madhu and K. Ramesh, "Towards effective phase unwrapping in digital photoelasticity," *Optics and Lasers in Engineering*, vol. 42, pp. 421-436, 2004.
- [8] K. Ashokan and K. Ramesh, "A novel approach for ambiguity removal in isochromatic phasemap in digital elasticity," *Measurement Science and Technology*, vol. 17, pp. 2891-2896, 2006.
- [9] A. Baldi, F. Bertolino, and F. Ginesu, "A temporal phase unwrapping algorithm for photoelastic stress analysis," *Optics and Lasers in Engineering*, vol. 45, pp. 612-617, 2007
- [10] T.Y. Chen, "A simple method for the determination of photoelastic fringe order," *Experimental Mechanics*, vol. 40, pp. 256-260, 2000.
- [11] T.Y. Chen, "Digital determination of photoelastic birefringence using two wavelengths," *Experimental Mechanics*, vol. 37, pp. 232-236, 1997.
- [12] M.J. Huang and Po-Chi Sung, "Regional phase unwrapping algorithm for photoelastic phase map," *Optics Express*, vol. 18, pp. 1419-1429, 2010.

Determination of the isoclinic map for complex photoelastic fringe patterns

Philip Siegmann¹, Chiara Colombo², Francisco Díaz-Garrido³ and
Eann Patterson⁴

¹ Departamento de Teoría de la Señal y Comunicaciones, Universidad de Alcalá, 28805 Madrid, SPAIN.

² Department of Mechanics, Politecnico di Milano, 20156 Milano, ITALY

³ Departamento de Ingeniería Mecánica y Minera, Universidad de Jaén, Campus las Lagunillas, Edif. A3, 23071, Jaén, SPAIN.

⁴ Composite Vehicle Research Center, Michigan State University, East Lansing, MI 48824, USA.

ABSTRACT

Most of the existing algorithms used for processing phase-shifted photoelastic data attempt to compute the unambiguous or demodulated isoclinic map in order to obtain the unambiguous or continuous isochromatic map. However, in some cases experiments on engineering components yield isoclinic maps that are severely corrupted due to the interaction between isoclinics and isochromatic. The result is that some of these algorithms fail in the direct demodulation of isoclinic maps from phase-shifted photoelastic data. An indirect way to obtain the isoclinic map by computing first the unambiguous isochromatic map is presented. The employed approach is based on a regularisation process that, by minimising a cost function, selects the appropriate value of the relative retardation angle at each pixel. In this way, an unambiguous map can be straightforwardly unwrapped and calibrated to generate an isochromatic map. The unambiguous isoclinic angle map is then calculated using the regularized isochromatic map. The process has been demonstrated to be robust and reasonably quick for crack tip fringe patterns.

Keywords: Photoelasticity, isoclinics, isochromatics, cost function.

1. INTRODUCTION

Photoelastic stress analysis is based on the temporary birefringence exhibited by all transparent materials when subjected to stress [1]. In a few incidences, such as in the glass industry, this property is used directly to evaluate stresses however in most cases either a photoelastic model is made or a transparent coating is bonded to an opaque part using a reflective adhesive. Two-dimensional models can be viewed directly while subject to load whereas stress must be 'frozen' into three-dimensional models that can be subsequently sliced physically or optically. Coatings act as strain witnesses and reproduce the surface strains in the component, and are considered to be locally planar. In all cases, a planar section or slice is viewed in polarised light using a polariscope, revealing fringes of constant color known as isochromatics, which are contours of constant principal stress difference, and black fringes known as isoclinics which are loci of points where the directions of the principal stresses are aligned to the polarising axes of the polariscope.

Traditionally, photoelastic analysis has involved the tedious manual analysis (counting) of fringes however, in the last twenty years a wide range of digital methods have been developed for photoelasticity and have been reviewed in detail elsewhere [2]. Among these methods phase-stepping or phase-shifting has gained in popularity since it was first applied to photoelasticity by amongst others, Hecker and Morche [3]. Phase-stepping is usually

conducted in monochromatic light conditions and involves the stepped or incremental rotations of a polariser and quarter waveplate of the polariscope, usually the output pair of optical elements are employed. Digital images are captured at each increment or step as illustrated in Figure 1; and then the set of images are combined to generate maps of the relative retardation or phase difference, which is related to the isochromatic fringe order, and of the isoclinic angle (shown in Figure 2). The relative retardation is directly proportional to the principal stress difference but when generated with these techniques its sign is ambiguous or undetermined, i.e. it is unclear whether the value relates to the maximum minus the minimum principal stress or the minimum minus the maximum principal stress. In most phase-stepping techniques, the calculation of the relative retardation requires the use of the evaluated isoclinic angle which is related to the direction of either the maximum or minimum principal stress but which, i.e. maximum or minimum, is unknown. Indeed, left uncorrected most phase-stepping methods will generate a map of interlocking areas in which the relative retardation alternates between the two possible definitions, i.e. proportional to maximum minus minimum principal stress and minimum minus maximum.

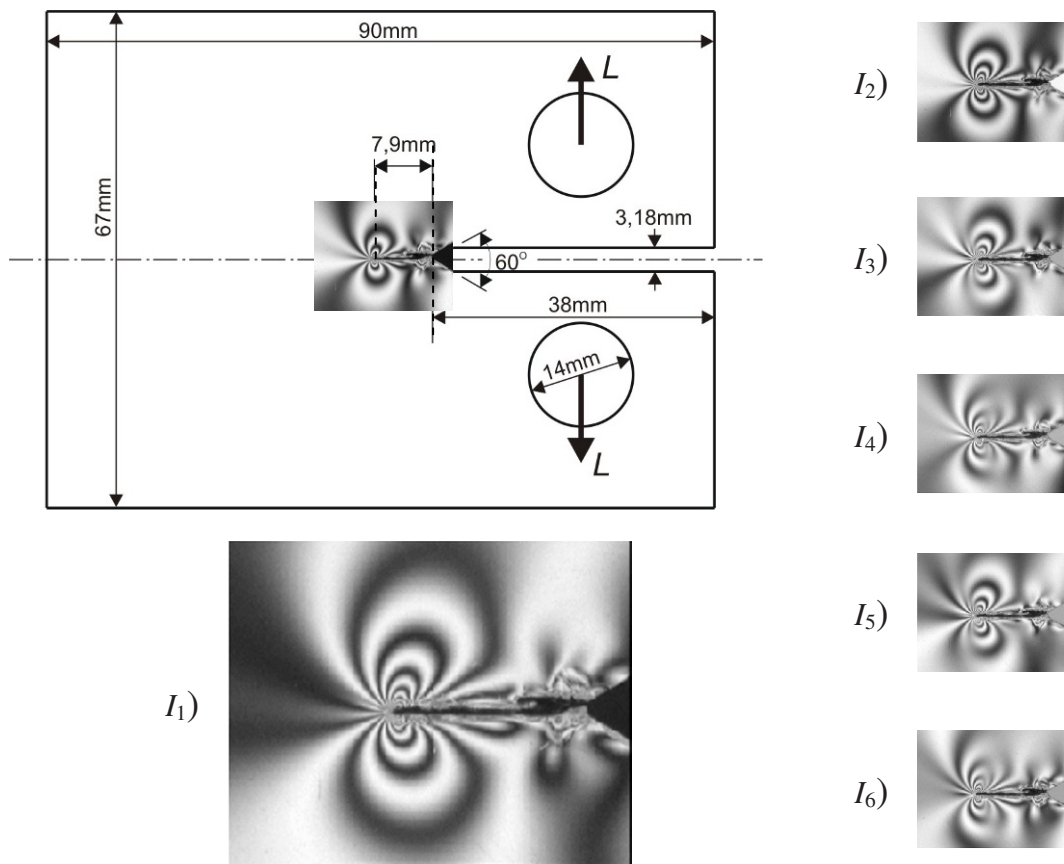


Fig.1 Geometry and dimensions of the 2 mm thick polycarbonate CT specimen with a 7.9 mm long fatigue crack [13] (*top left*) and the corresponding six phase-shifted fringe patterns [14] (*bottom left and right*) from obtained with an applied load of 90N. Note that I_1 corresponds to a dark-field circular polariscope.

Much effort has been expended on developing robust methods of processing phase-stepped photoelastic data that eliminate the ambiguity described above. One possible option is to collect images at several wavelengths; however, this significantly increases the required number of images and makes real-time data capture almost impossible. In ambient conditions, using monochromatic light a theoretical minimum of four images are required to solve for the relative retardation and isoclinic angle and can be collected simultaneously [5]. Hence, it is desirable to restrict the number of images required to as close to four as possible. In 1993 Wang and Patterson [4] developed a method of resolving the ambiguity based on six phase-stepped images combined with fuzzy set classification. This technique and its derivatives [6, 7] are fast and almost completely automatic in that very little

user interaction is required however, they fail when the fringe density is high or the shape of the fringes becomes very complex. Two approaches to creating more robust, automatic techniques for resolving the ambiguity have been taken recently. Ramji and Ramesh [8] have used ten images combined with a pixel by pixel application of the quality map proposed by Siegmann et al [7] which yields a more robust approach at the expense of complexity and time required for data collection and processing. The second approach proposed by Quiroga and González-Cano [9] utilises regularised phase-tracking (RPT) using five phase-shifted images [10] to obtain the relative retardation and the isoclinic angle [11]. Recently, this second approach has been combined with methods derived from the earlier work of Wang and Patterson [4] to generate a fast, robust and essentially automatic algorithm [12]. The motivation for the study reported here is the solution of problems associated with processing the stress field around a fatigue crack propagating in polycarbonate compact tension specimens (Figure 1). The corrupted isoclinic map (Figure 2) does not allow the use of most of the up-to-date existing techniques [4, 6 - 8] and only those based on regularised phase-tracking [9, 12] have been found to be successful with that due to Siegmann et al [12] being much faster.

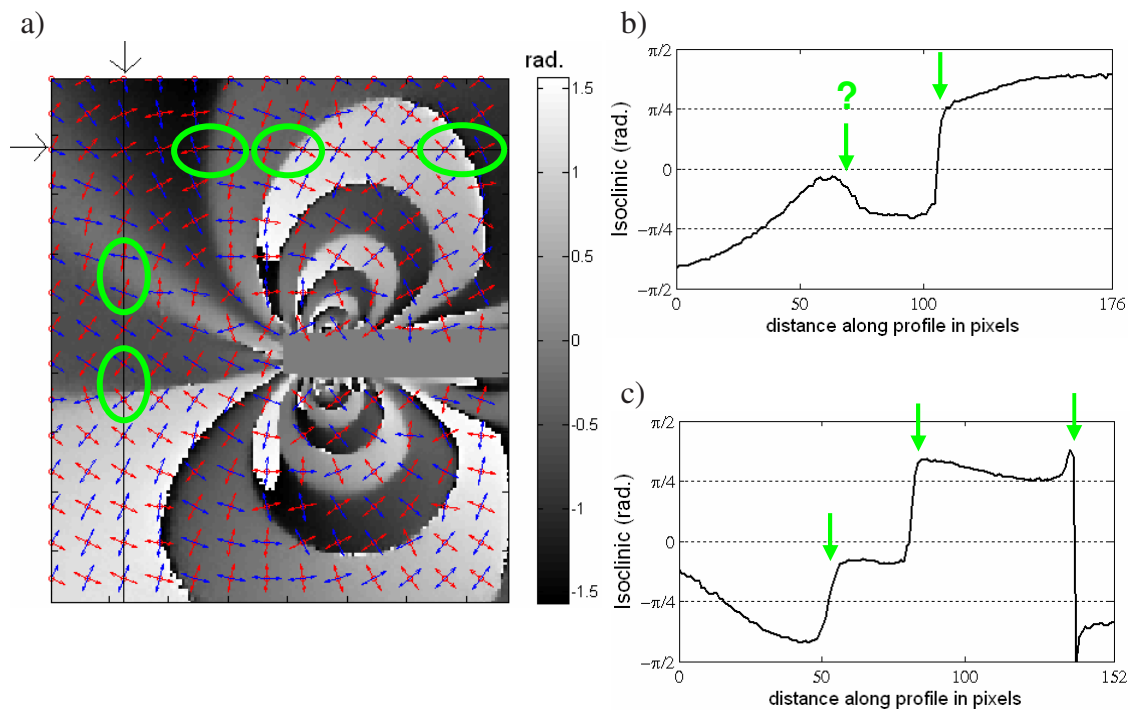


Fig. 2. a) The ambiguous (without demodulation) isoclinic phase map obtained from the data in figure 1 using equation (2) and b) the vertical and c) the horizontal profiles along the lines shown in (a) with changes in the principal stress directions indicated by green arrows and ellipses.

2. PHASE-STEPPING ALGORITHM

The six-step photoelastic phase-stepping approach is selected here because it is employed in industrial and research laboratories although other phase-stepping methods can be used. The six steps are chosen such that the combination of the intensity levels are related to the isoclinic angle, θ and the relative retardation δ as follows:

$$\begin{aligned}
 I_5 - I_3 &= 2I_v \sin \delta \sin 2\theta, \\
 I_4 - I_6 &= 2I_v \sin \delta \cos 2\theta, \\
 I_2 - I_1 &= 2I_v \cos \delta,
 \end{aligned} \tag{1}$$

where I_v accounts for stray light. A number of combinations of the optical elements of the polariscope will generate appropriate images however in this work those proposed by Patterson and Wang [14] were employed and are illustrated for a fatigue crack in Figure 1. From these intensity patterns, the ambiguous isoclinic angle and the wrapped and ambiguous relative retardation can be obtained using:

$$\theta_a = \frac{1}{2} \arctan \left(\frac{I_5 - I_3}{I_4 - I_6} \right), \quad (2)$$

$$\delta_{w,a} = \arctan \left[\frac{(I_5 - I_3) \sin 2\theta_a + (I_4 - I_6) \cos 2\theta_a}{I_1 - I_2} \right], \quad (3)$$

Grey scale images for θ_a and $\delta_{w,a}$ in the CT specimen are shown in Figures 2(a) and 3(a) and, as can be seen, their values are ambiguous and the modulo of retardation is between 0 and 2π . It should be pointed out that in equation (3), the four quadrant arctan function [15] is used to obtain Figure 3(a) and, as has been highlighted before the form of equation (3) guarantees a high modulation over the field [16] thereby reducing the isoclinic-isochromatic interaction [12]. An unambiguous isoclinic angle would allow an unambiguous relative retardation map to be obtained since both are related through equation (3). However, it is not always possible to retrieve an unambiguous or demodulated isoclinic angle. This is the case in the CT specimen, where strong variations of both the isoclinic angle and relative retardation or isochromatic fringe order create large areas with isoclinic-isochromatic interactions.

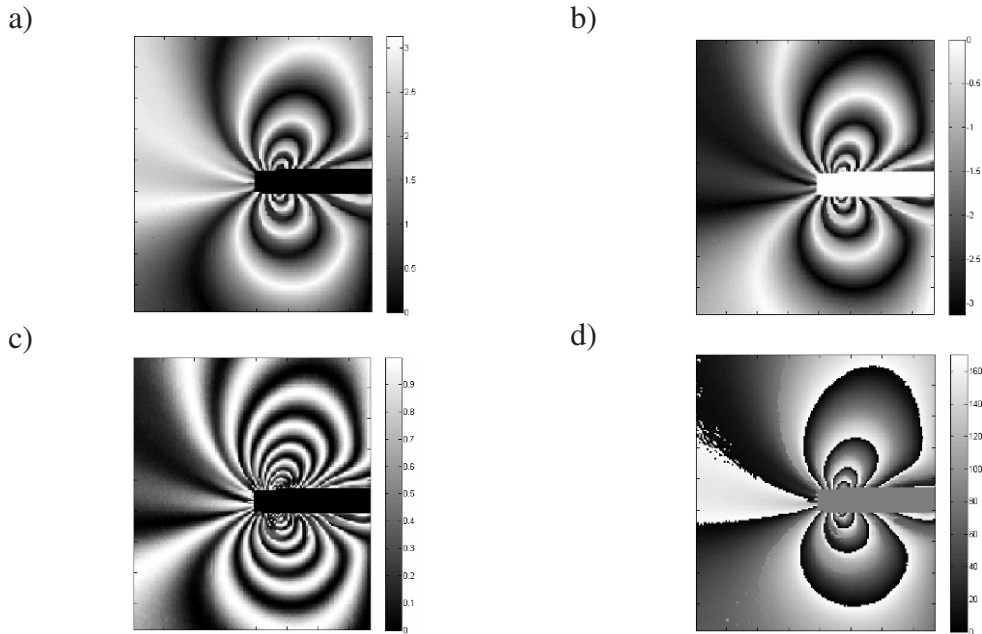


Fig. 3. a) Ambiguous and wrapped isochromatic phase map (in radians) obtained using the data in Fig.2a.; b) Inverse of (a); c) Quality map ; d) Regularized and wrapped isochromatic phase map (in degrees)

3. REGULARIZATION ALGORITHM

3.1 Regularization process

The method chosen to process the photoelastic fringe patterns associated with the fatigue crack in the CT specimen is based on the one proposed by Siegmann et al [12]. The ambiguity problem is solved by processing

the information directly from $\delta_{w,a}$ provided by equation (3). From the experimental data there are for each pixel in the image of the sample two possible values of the wrapped relative retardation, namely $\delta_{w,a}^+ = \delta_{w,a}$ and $\delta_{w,a}^- = -\delta_{w,a}$, depending on the sign given to the isoclinic angle. The two maps $\delta_{w,a}^+$ and $\delta_{w,a}^-$ are shown in [Figure 3\(a\)](#) and [\(b\)](#), and were obtained using the four quadrant arctangent function (arctan2) in equation (3) [15] as mentioned previously. In order to select at each pixel the correct value of $\delta_{w,a}$, a path guided algorithm is followed through all of the pixels of the image and at each new pixel, the selection of the correct value of the relative retardation (δ_w) is performed by taking the one that minimizes a cost function (U_Γ):

$$U_\Gamma(\delta_w) = \min[U_\Gamma(\delta_{w,a}^+), U_\Gamma(\delta_{w,a}^-)], \quad (4)$$

This cost function ensures the continuity of either the value of the relative retardation or the gradient of the value of the relative retardation with respect to the already processed pixels, and is defined as:

$$U_\Gamma(\mathbf{i}; \lambda) = Q(\mathbf{i})A_\Gamma(\mathbf{i}) + \frac{10^\lambda}{Q(\mathbf{i})}B_\Gamma(\mathbf{i}), \quad (5)$$

where $\mathbf{i}=(x,y)$ is the pixel position, Γ is a window around \mathbf{i} used to consider the spatial dependence, λ is a regularization parameter, Q is a quality map, and the two terms A_Γ and B_Γ account for the continuity in the value and the gradient of the selected relative retardation respectively, and are defined as:

$$A_\Gamma(\mathbf{i}) = \sum_{\mathbf{j} \in \Gamma} \frac{1}{2\pi} |\delta_w(\mathbf{j}) - \delta_{w,a}^\pm(\mathbf{i})| s(\mathbf{j}),$$

$$B_\Gamma(\mathbf{i}) = \sum_{\mathbf{j} \in \Gamma} \sqrt{\left(\frac{\partial_h \delta_w(\mathbf{j})}{\partial x} - \frac{\partial_h \delta_{a,w}^\pm(\mathbf{i})}{\partial x} \right)^2 + \left(\frac{\partial_h \delta_w(\mathbf{j})}{\partial y} - \frac{\partial_h \delta_{a,w}^\pm(\mathbf{i})}{\partial y} \right)^2} s(\mathbf{j}), \quad (6)$$

where s is equal to 1 if the pixel has already been processed and 0 otherwise. The partial derivatives are computed over a distance h in the x -direction as follows:

$$\frac{\partial_h \delta(x,y)}{\partial x} = \frac{\delta(x+h,y) - \delta(x-h,y)}{2h+1}, \quad (7)$$

and in a corresponding manner for the y -direction. A quality map is employed to perform two fundamental functions: to select the path followed by the process; and to act as the weighting factor between A_Γ and B_Γ . Thus, the quality map is defined as:

$$Q(\mathbf{i}) = \sin^2(\delta_{w,a}(\mathbf{i})). \quad (8)$$

[Figure 3\(c\)](#) shows the quality map for the data in [Figure 1](#), and [Figure 3\(d\)](#) shows the computed unambiguous relative retardation obtained by following this quality map and using expression (5) as the cost function in the regularization process. The parameters used to process these data were $\lambda=1$, $\Gamma=7 \times 7$, and $h=3$.

The regularization process described above requires a relative long processing time, which is strongly dependent on the size of the images. For the data in [Figure 1](#), 150 s were required to regularize 177×154 pixels using a Pentium 4 with CPU speed of 3.20 GHz and with the algorithm programmed in Matlab. However, it is much faster than the one proposed in [9], because it eliminates the need to perform a minimization process at each pixel; instead the new cost function has only to be evaluated for the two values of the relative retardation.

3.2 Determination of the isoclinic angle

The demodulation of the isoclinic angle can be performed at the same time as the regularization process is applied to the relative retardation using the same cost function. As for the retardation, there are two possible values of the isoclinic angle at each pixel: $\theta^+ = \theta_a$ and $\theta^- = \theta_a + \pi/2$. The selection of the unambiguous isoclinic angle at each pixel is performed in a similar manner: if $\delta_w = \delta_{w,a}^+$ then $\theta = \theta^+$, else if $\delta_w = \delta_{w,a}^-$ then $\theta = \theta^-$. Figure 5 shows the resultant demodulated isoclinic map superimposed with a mesh of arrows at equidistant points, aligned with the directions of the corresponding principal stresses.

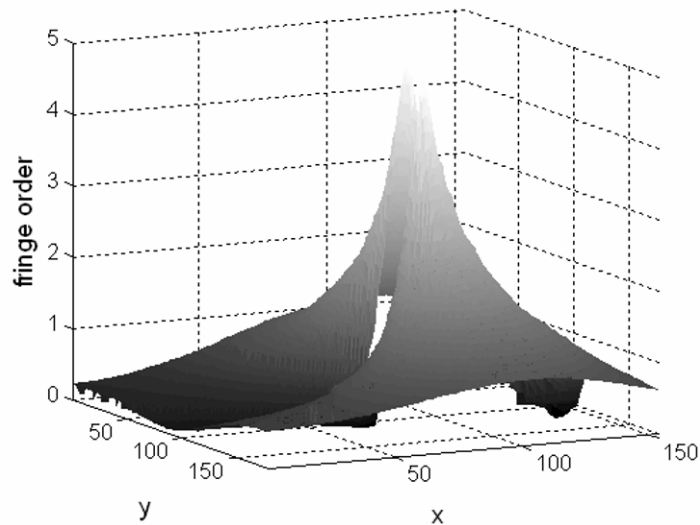


Fig. 4. Unwrapped and regularized isochromatic phase map (units: calibrated fringe order).

4. DISCUSSION AND CONCLUSIONS

A robust and fast algorithm for processing phase-stepped photoelastic data has been demonstrated for a specimen geometry that has proven troublesome in the past as consequence of the large amount of interaction between the isoclinic and isochromatic parameters, and the density and complexity of the fringes in the vicinity of the crack tip. Most existing algorithms employing a small number of phase-stepped images failed to produce satisfactory results or required an excessively long time for processing. In the past, such issues tended to be avoided by masking out a large area around the crack tip because it was not relevant to the analysis of fatigue cracks based on linear elastic fracture mechanics; however, in this case, the strains associated with the plastic enclave and wake generated around the crack during fatigue were of primary interest, and hence it was necessary to process the photoelastic fringe patterns as close to the crack as possible. The problem could have been resolved by using a much larger number of phase-steps and corresponding number of images captured at a single monochromatic wavelength or a number of wavelengths; however since a propagating fatigue crack was the subject of interest increasing the complexity and time required for data capture was not an appropriate option. Similarly long processing times were unattractive so combining the robustness of earlier work by Quiroga and González-Cano [9] with the speed of algorithms produced by Patterson and his co-workers [4, 7] was a good proposition. The resultant algorithm works with almost no user intervention after defining the area of interest and the selection of the three parameters λ , Γ and h . The algorithm appears to be more robust when there is a large variation of relative retardation and tends to introduce noise when the relative retardation is near constant in magnitude. The algorithm is straightforward to implement and the elimination from the algorithm of the need to perform a minimization of a cost function at each pixel, as in the method of Quiroga and González-Cano [9], renders it significantly faster.

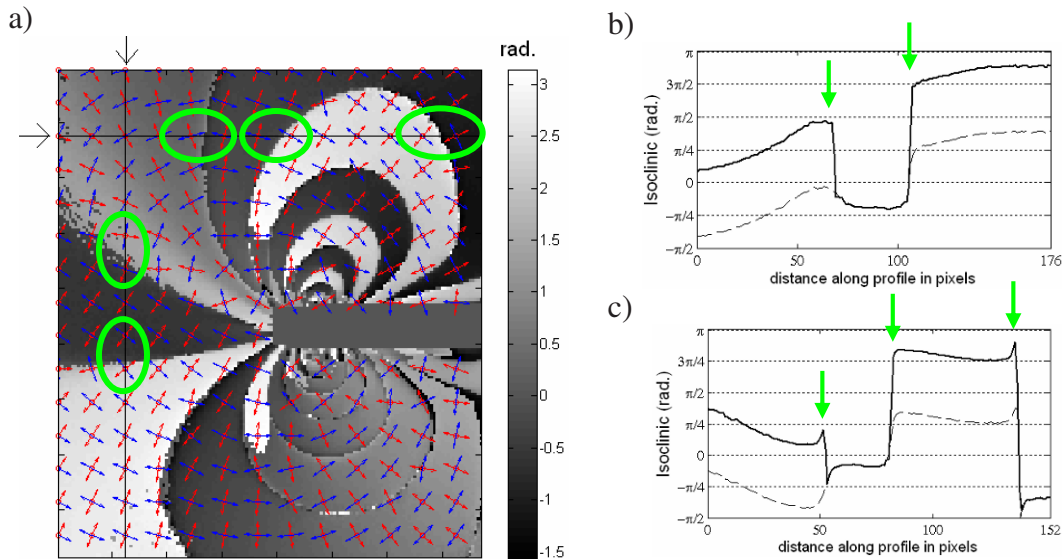


Fig. 5. a) Demodulated isoclinic phase map; b) and c) shows respectively the vertical and horizontal profiles of the demodulated (solid line) and not demodulated (dashed line) isoclinic angle along the same lines as shown in Fig. 2a

5. REFERENCES

- [1] J.W. Dally and W.F. Riley. *Experimental Stress Analysis*, 3rd Ed., New York. (McGraw-Hill Inc, 1991).
- [2] K. Ramesh. *Digital Photoelasticity*. Berlin. (Springer, 2000).
- [3] F. W. Hecker and B. Morche, Computer-aided measurement of relative retardations in plane photoelasticity. In *Experimental Stress Analysis*, ed. H. Weiringa. Martinus Nijhoff Publishers, Dordrecht, The Netherlands, 1986, pp. 532-42.
- [4] Z.F. Wang and E.A. Patterson, "Use of Phase-stepping with Demodulation and Fuzzy Sets for Birefringence Measurement," *Opt. Laser. Eng.* **22**, 91–104 (1995).
- [5] J.R. Lesniak, S.J. Zhang and E.A. Patterson, 'The design and evaluation of the poleidoscope: a novel digital polariscope,' *Experimental Mechanics*, 44(2):128-135 (2004).
- [6] N. Plouzenec, J.C. Depuré and A. Lagarde, "Whole field determination of isoclinic and isochromatic parameters," *Exp. Tech.* **23**, 30-33 (1999).
- [7] P. Siegmann, D. Backman and E.A. Patterson, "A robust approach to demodulating and unwrapping phase-stepped photoelastic data," *Exp. Mech.* **45**(3), 278-289 (2005).
- [8] M. Ramji and K. Ramesh "Whole field evaluation of stress components in digital photoelasticity – Issues", implementation and application, *Opt. Laser. Eng.* **46**(3), 257-271, (2008)
- [9] J.A. Quiroga and A. González-Cano, "Separation of isoclinics and isochromatics from photoelastic data with a regularized phase-tracking technique," *Appl. Opt.* **39**, 2931-2940 (2000).
- [10] M. Servin, J.L. Marroquin and F.J. Cuevas, "Demodulation of a single interferogram by use of a two-dimensional regularized phase-tracking technique," *Appl. Opt.* **36**(19), 4540-4548 (1997).
- [11] J. Villa, J.A. Quiroga and E. Pascual. "Determination of isoclinics in photoelasticity with a fast regularized estimator," *Opt. Laser Eng.* **46**, 236-242 (2008).
- [12] P. Siegmann, F. Díaz-Garrido and E. Patterson, "Robust approach to regularize an isochromatic fringe map", *Appl. Opt.* **48**(22), E24-E34 (2009).
- [13] M.N. Pacey, M.N. James and E.A. Patterson, 'A new photoelastic model for studying fatigue crack closure', *Experimental Mechanics*, 45(1):42-52 (2005).
- [14] E.A. Patterson and Z.F. Wang. "Towards Full-field Automated Photoelastic Analysis of Complex Components," *Strain*, **27**, 49–56 (1991).
- [15] MATLAB Function Reference at:
www.mathworks.com/access/helpdesk/help/techdoc/ref/atan2.html
- [16] J.A. Quiroga and A. González-Cano. "Phase measuring algorithm for extraction of isochromatics of photoelastic fringe pattern," *Appl. Opt.* **36**(32), 8397-8402 (1997).

A Study on the Behaviors and Stresses of O-ring under Uniform Squeeze Rates and Internal Pressure by Transparent Type Photoelastic Experiment

Jai-Sug Hawong¹, Dong-Chul Shin² and Jeong Hwan Nam¹

¹School of Mechanical Engineering, Yeungnam University, 214-1, Dae-dong, Gyeongsan, Gyeongbuk 712-749, Korea

²School of Mechanical Engineering, Pusan National University, 30, Jangjeon, Geumjeong, Busan 609-735, Korea

ABSTRACT

Rubber O-rings have been used as packing elements for high pressure vessels, oil pressure parts, air-plane parts and nuclear generator parts. The design criterion of an O-ring can be determined through analysis of stresses and deformation behavior of O-ring for various loading conditions, which are dependant on the internal pressure and the fitting conditions of the O-ring. The shape of the O-ring under uniform squeeze rates and internal pressures is changed with squeeze rates, internal pressures and time. Therefore the stresses of O-rings under the uniform squeeze rates and internal pressures should be studied with real time. To achieve this, a loading device for transparent type photoelastic experiment through which various squeeze rates and internal pressures are applied was developed in this research. The validity of the loading device was verified. It was established through this research that the lower corner space of O-ring was filled with the changes of O-ring after the forcing out of O-ring was produced. The stresses of O-ring under uniform squeeze rates and internal pressures were analyzed with the forcing out procedures of O-ring.

Key words: Behaviour of O-ring, Internal Pressures, Forcing Out, Loading Device, Photoelastic Experiment

INTRODUCTION

The O-ring is applied to protect against leakage of oil or air from vessels and structures under high or low pressure. Therefore the O-ring plays a significant role in pressurized vessels and structures and many researchers have analyzed the stress condition of the O-ring [1-6]. It is known that leaking conditions of O-rings are dependant on the contact lengths of O-rings, contact pressures of O-rings and the O-ring behavior of under various loading conditions [7-8].

Contact lengths of the O-ring as well as the behavior of the O-ring under various loading conditions are very important for protection of pressure vessels against leakage. In order to estimate their performance, O-rings should be analyzed to determine the contact lengths and their behaviors under various loading conditions. The main purpose of this research is to analyze the behavior of the O-ring under uniform squeeze rates and internal pressures. A loading device with which the stress distributions and behavior of the O-ring under uniform squeeze

rates and internal pressures can be studied was developed in this study. Results from application of this device together with the photoelastic experimental hybrid method are reported in this paper

2. BASIC THEORY

2.1 Hertz Contact Theory

Equation (1) is the stress components of plane stresses using potential function ϕ and ψ of Muskhelishvili [9].

$$\begin{aligned}\sigma_x &= \mathbf{Re}[2\phi(z) - \bar{z}\phi'(z) - \psi(z)] \\ \sigma_y &= \mathbf{Re}[2\phi(z) + \bar{z}\phi'(z) + \psi(z)] \\ \tau_{xy} &= \mathbf{Im}[\bar{z}\phi'(z) + \psi(z)]\end{aligned}\quad (1)$$

As shown in equation (1), stress components are composed of two complex functions $\phi(z)$ and $\psi(z)$. Therefore if the two complex functions are known, stress components are determined.

In general, the contact problems are half plane problems. If the upper portion of a body ($z > 0$) is half plane, complex functions $\phi(z)$ and $\psi(z)$ are involved in the region. Therefore in the half plane of lower portion of the body ($z < 0$), the analytic complex function is defined as equation (2) [10].

$$\psi(z) = -\phi(z) - \overline{\phi(\bar{z})} - z\phi'(z) \quad (2)$$

As stress functions are analytic functions, they can be represented as power series.

$$\phi(z) = \sum_{n=0}^N C_n z^{\frac{n}{2}}, \quad \Psi(z) = \sum_{n=0}^N D_n z^{\frac{n}{2}} \quad (3)$$

Substituting equation (3) in equation (2), the relative equation between the complex coefficients of complex function is determined as shown in equation (4).

$$D_n = -\frac{n}{2}C_n - \bar{C}_n \quad (4)$$

Substituting $\phi'(z)$, $\psi'(z)$ and $\phi''(z)$ in equation (1), equation (5) is determined

$$\begin{aligned}\sigma_x(z) &= \sum_{n=1}^N \mathbf{Re}\{C_n[2F(n,z) - G(n,z)] + \bar{C}_n F(n,z)\} \\ \sigma_y(z) &= \sum_{n=1}^N \mathbf{Re}\{C_n[2F(n,z) + G(n,z)] - \bar{C}_n F(n,z)\} \\ \tau_{xy}(z) &= \sum_{n=1}^N \mathbf{Im}\{C_n G(n,z) - \bar{C}_n F(n,z)\}\end{aligned}\quad (5)$$

Where $F(n,z) = \frac{n}{2} z^{\frac{n-1}{2}}$, $G(n,z) = \frac{n}{2} \left[\left(\frac{n-1}{2} \right) \bar{z} - \frac{n}{2} z \right] z^{\frac{n-2}{2}}$

2.2 Photoelastic Experimental Hybrid Method

Equation (6.a) is a stress optic law for isotropic material [11].

$$\left(\frac{f_{\sigma} \cdot N_f}{t}\right)^2 = (\sigma_x - \sigma_y)^2 + (2\tau_{xy})^2 \quad (6a)$$

$$\left(\frac{f_{\sigma} \cdot N_f}{t}\right)^2 - (\sigma_x - \sigma_y)^2 - (2\tau_{xy})^2 = D(\varepsilon) \quad (6.b)$$

Substituting stress fringe value (f_{σ}), fringe order (N_f), thickness of specimen (t), position coordinates of fringe orders in equation (6.a), then equation (6.a) becomes a function of a_n and b_n only. Substituting the precise experimental data for equation (6.a), errors are produced as shown in (6.b). Therefore $D(\varepsilon)$ cannot be zero. In order to minimize the errors, Hook-Jeeves numerical method is used in this research [12] with the limiting condition being $D(\varepsilon) \leq 10^{-5}$. Substituting equation (5) in equation (6.b), equation (7) is obtained.

$$D(\varepsilon) = \left(\frac{f_{\sigma} \cdot N_f}{t}\right)^2 - \left\{ \sum_{n=1}^N a_n \operatorname{Re}[2F(n,z) - 2G(n,z)] + \sum_{n=1}^N b_n \operatorname{Im}[2F(n,z) + 2G(n,z)] \right\}^2 - \left\{ \sum_{n=1}^N a_n \operatorname{Im}[2G(n,z) - 2F(n,z)] + \sum_{n=1}^N b_n \operatorname{Re}[2F(n,z) + 2G(n,z)] \right\}^2 \quad (7)$$

When values of measured fringe orders (N_f), position coordinates of fringe orders ($z = x + iy$), specimen thickness (t) and stress fringe value (f_{σ}) are substituted in equation (7), it becomes a function of a_n and b_n only. Applying the Hook-Jeeves numerical method to equation (7) with experimental data, a_n and b_n are determined when the limit of errors is satisfied. Substituting a_n and b_n in the corresponding equation, the stress functions $\Phi(z)$ and $\psi(z)$ are determined. Substituting $\phi(z)$ and $\psi(z)$ in eq. (1), stress components σ_x , σ_y and τ_{xy} produced in the structure under the arbitrary load are determined. These procedures are called photoelastic experimental hybrid method.

3 EXPERIMENT AND EXPERIMENTAL METHOD

Fig. 1-(a) shows the schematic of transmission photoelastic experimental device used in this research while Fig. 1-(b) shows the developed loading device. Both the squeeze rates and internal pressures can be controlled using this device. This made it possible to study the deformation behaviors of the O-ring under uniform squeeze rate and internal pressures using the transmission photoelastic device. The material used in this research was epoxy resin XN 1019 whose mechanical properties are: $f_{\sigma} = 0.2352$ kN/m, $E = 2.94$ MPa and $\nu = 0.42$.

The cross-sectional diameter of O-ring used in this study was 6.98 ± 0.15 mm with a thickness of 6.0 ± 0.02 mm. When the O-ring was assembled, gap widths equal to 0.2mm, 0.3mm and 0.5mm could be obtained. The gap widths were made by electronic spark machining. Glass sheets of 10mm were affixed to the front and back side of the frame with the O-ring. Using the loading device in Fig. 1(b), uniform squeeze rate of 20% and internal

pressures were applied to the specimen. Oil pressures were controlled by hand pump from 0 (zero) MPa to the forcing out pressure of O-ring at which point the same pressure was maintained by the check valve. The model specimen was an infinitesimal part of the O-ring hereafter referred to as disk with a height of 6 ± 0.02 mm made from XN 1019 epoxy resin. When the disk was subjected to a uniform squeeze rate of 20% and various internal pressures, its behavior could be monitored and the isochromatic fringes continuously recorded at intervals of 0.125 sec.

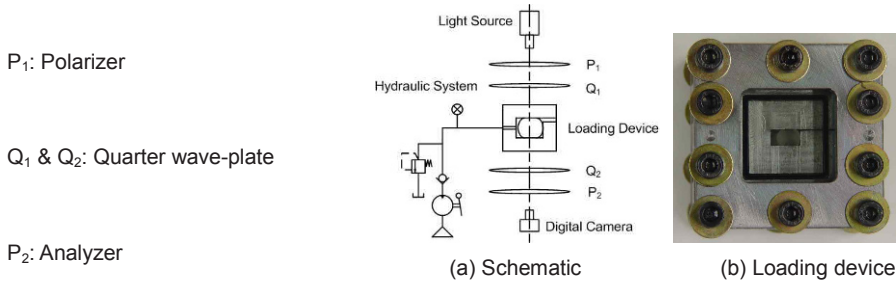


Fig. 1. Transparent photoelastic experimental device

4 EXPERIMENTAL RESULTS AND DISCUSSIONS

Fig. 2 shows the actual isochromatic fringe patterns of the O-ring obtained from high temperature epoxy resin when the squeeze rate is 20% and assembly gap 0.1mm. These isochromatic fringe patterns were obtained from sliced specimens of the O-ring to which stress freezing was done. When the internal pressure (P_i) was 7.84 MPa, forcing out occurred on the O-ring as shown in Fig. 2(a). Forcing out of the O-ring may be defined as the situation when the portion of the O-ring is forced out of the continued boundary of the front side. After forcing out of the O-ring was done, it was observed that the corner space between the contact portion of lower side and the contact portion of the front side was not filled up. Studies from X-ray tomography and finite element method have indicated that the corner space between the contact portion of the lower side and the contact portion of the front side was filled up before forcing out of the O-ring made of rubber was done.

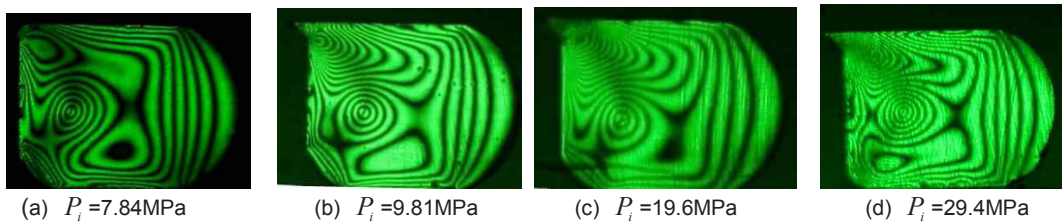


Fig. 2. Isochromatic fringe patterns from stress freezing method for O-ring made from high temperature epoxy resin (squeeze rate = 20%, gap = 0.1mm)

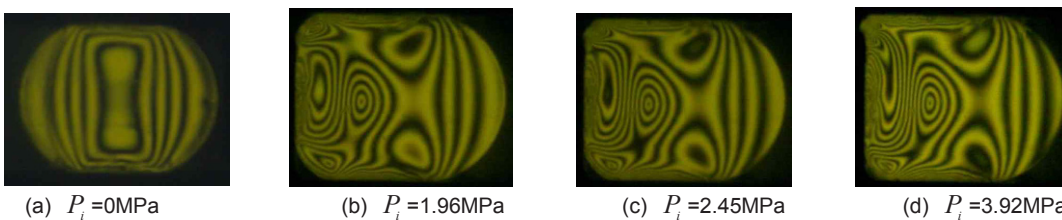


Fig. 3. Isochromatic fringe patterns from the transparent type photoelastic experiment for O-ring made from XN1019 (squeeze rate = 20%, gap = 0.3mm)

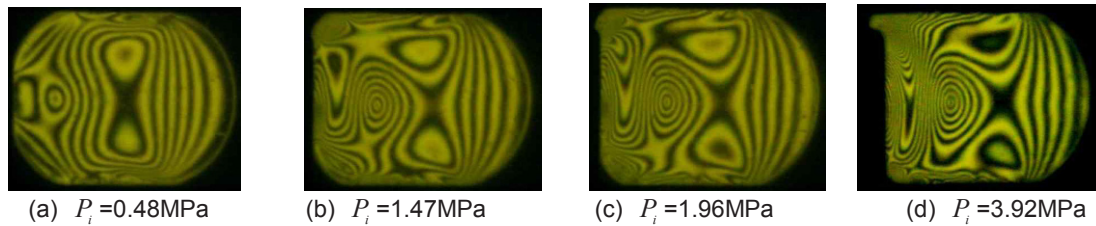


Fig. 4. Isochromatic fringe patterns from the transparent type photoelastic experiment for O-ring made from XN1019 (squeeze rate = 20%, gap = 0.5mm)

Fig. 3 and Fig. 4 are isochromatic fringe patterns of the O-ring made from XN 1019 when assembly gaps are 0.3mm and 0.5 mm respectively with squeeze rate of 20%. The isochromatic fringe patterns were continuously obtained when disk was subjected to uniform squeeze rates and various pressures. It is observed that the forcing out of the O-ring occurred when the internal pressures were 2.45MPa and 1.47MPa and the assembly gaps of the O-ring were 0.3mm and 0.5mm respectively. It should be noted that the smaller the gap of the O-ring, the later the forcing out occurred. It was also found that the corner space between the contact portion of the lower side and the contact portion of the front side was not filled up before and after the forcing out of O-ring was done. Fig. 4(d) however shows that the corner space between the contact portion of the lower side and contact portion of front side was filled up after the forcing out of O-ring was done for a while. Fig. 3(c) and Fig. 4(b) showed that the closing patterns of isochromatics near the front wall were transformed to the opening patterns when forcing out occurred. Therefore, it can be known whether the forcing out is done or not through the transformation of isochromatic patterns. The isochromatic fringe patterns with various assembly gaps of O-ring and internal pressures are almost similar to each other except for the regions to which stress concentrations occurred.

It is demonstrated from Fig. 2, Fig. 3 and Fig. 4 that the fringe patterns obtained from the stress freezing method are similar to those from the transparent type photoelastic technique. However, the isochromatics obtained from the stress freezing method are tilted towards the assembly gap of the O-ring. Moreover, the corner space between the contact portion of the lower side of the O-ring and the contact portion of the front side of the O-ring is not filled up (not realistic) after forcing out of the O-ring occurred and continued for a while. Comparing Fig. 2(d) and Fig. 4(d) it is observed that the isochromatic fringe patterns of Fig. 2(d) are almost identical to those of Fig. 4(d) even though the O-ring of Fig. 2(d) was taken away from the assembly gap. On the basis of these results, it can be deduced that the actual behaviors of the O-ring can be analyzed using the loading device developed in this research instead of the 3-dimensional stress analysis of the O-ring.

Fig. 5 shows the actual and graphic isochromatics of obtained from photoelastic hybrid method of the upper and front side regions of the O-ring at a squeeze rate of 20% and assembly gap of 0.5mm when internal pressures were 1.47MPa (starting of forcing out) and 2.94MPa (end of forcing out). The graphic isochromatic patterns were obtained from photoelastic hybrid method with the x and y axes being normalized by the contact length ($=a$). The

rectangular box (\square) in the actual isochromatic fringe pattern refers to the region from which the graphic isochromatic fringe patterns were obtained. Cross marks “+” on the graphic isochromatic fringe patterns indicate positions from which experimental data was measured. The actual experimental data were measured along the center lines of the black and white bands. The results that cross marks “+” are almost located along the center lines indicate that the photoelastic experimental hybrid method and loading device developed in this research are effective. It is also observed from Fig. 5-(a) that the isochromatic fringe patterns of the upper side are different from those of the lower side. This difference can be explained on the basis that the upper side is connected to the outside while the lower side is not and compressed air exists in the space between the O-ring and the cylinder. Fig. 5-(b) shows the isochromatic fringe patterns of O-ring under uniform squeeze and internal pressures when the forcing out of the O-ring has already occurred. From Fig. 5-(b), it is known that the shape of the isochromatics of the upper side of the cylinder front wall had been transformed into opening type.

Fig. 6 and Fig. 7 show the contact stresses distributions along the contact line of the upper and front sides of the O-ring respectively. Since contact stresses are uniformly distributed, the effectiveness of the sealing function of the O-ring is ensured. In the Figures, “P” refers to the internal pressure (kg/cm^2) while “G” refers to the assembly gap in mm. It is observed from Figs. 6 and 7 that the contact stresses on the contact portion between the O-ring and cylinder increased when forcing out of O-ring started. The contact stresses were then recovered into the general stress distribution after forcing out. Fig. 6 shows that the maximums of σ_x and σ_y occurred at the center of contact line in accordance to the contact theory of Hertz. Fig. 7 on the other hand shows that the maximums of σ_x and σ_y occurred a little distance to the left side from the center of the contact line. These results seem to disagree with the result where the O-ring made from rubber fractured around assembly fillet.

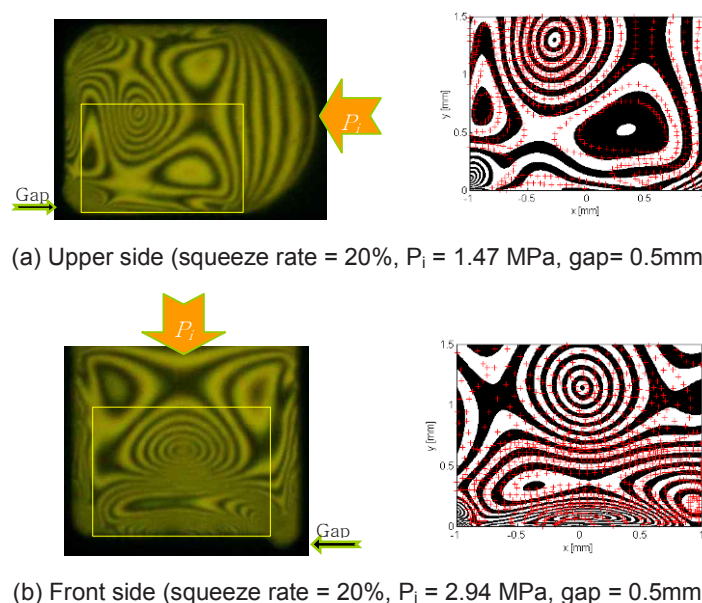


Fig. 5. Actual and graphic isochromatics of O-ring from photoelastic experimental hybrid method

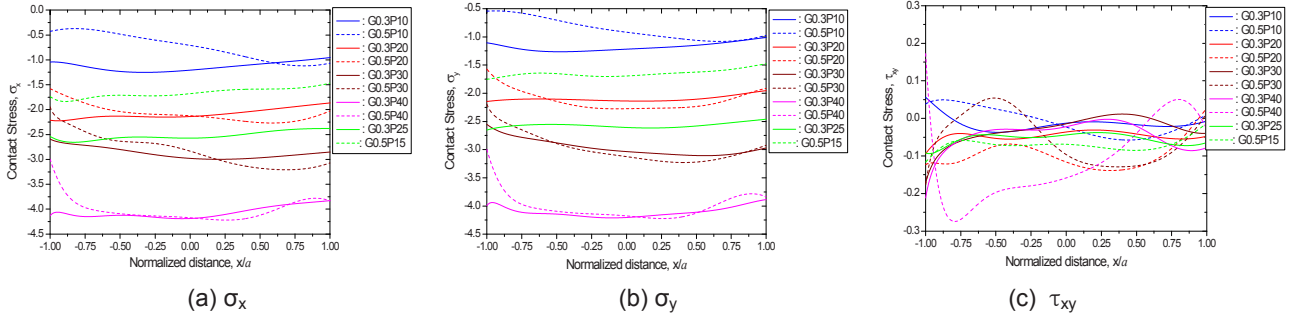


Fig. 6. Distributions of contact stresses along the contact line of the upper side of O-ring

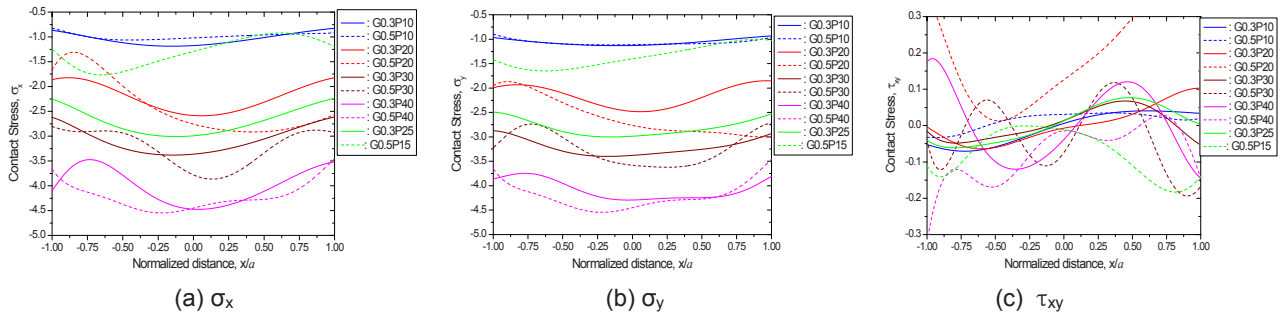


Fig. 7. Distributions of contact stresses along the contact line of the front side of O-ring

Fig. 8 shows maximum shear stress distributions along the contact line of front side of the O-ring under a uniform squeeze rate of 20% and internal pressure. It is observed from Fig. 8 that the maximums of the maximum shear stresses occurred at the groove fillet. These results are identical to those in which the O-ring made from rubber fractured around assembly fillet. It is therefore demonstrated that the material is generally weak in shear (rubber is a mild material).

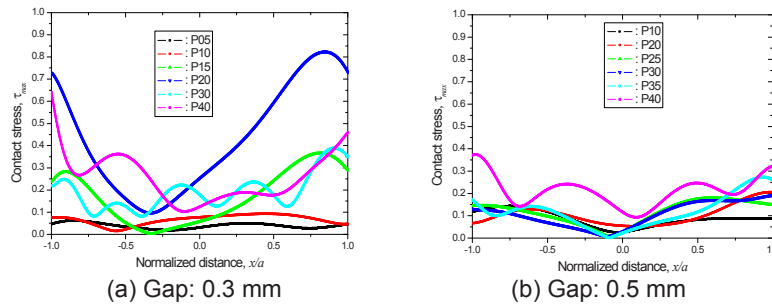


Fig. 8. Maximum shear stress distributions along the contact line of front side

5 CONCLUSIONS

Based on the study on actual deformation behaviors and the contact stress distributions of O-ring under uniform squeeze rates and internal pressure by transparent type photoelastic experiment, the following conclusions were made.

1. The space at the corner between the lower side and front side of O-ring is filled up after forcing out of the O-ring occurred under uniform squeeze rate of 20% and internal pressure.

2. The maximums of contact stresses in the O-ring under uniform squeeze rate and internal pressure occurred a little distance to the left side from the center of the contact line.
3. The maximums of the maximum shear stresses occurred at the groove fillet. These results are identical to the results in which the O-ring made from rubber fractured around assembly fillet.
4. When forcing out of the O-ring begins, the magnitudes of stress components (σ_x , σ_y , τ_{xy}) in the upper side region are greater than those in the front side region.
5. After forcing out of the O-ring occurred, magnitudes of stress components (σ_x , σ_y) in the front side region are greater than those in the upper side region. Magnitudes of shear stress in the front side are very similar to those in the upper side region.

REFERENCES

- [1] Golerik, B. M., Bukhina, M. F. and Ratner, A. V., "Variation of the contact Area in the Deformation of Rubber Cylinders and Rings," Soviet Rubber Technology, Vol. 20, No. 1, pp. 10-14, 1961
- [2] Antonio Strozzi, "Static Stresses in an Unpressurized, Rounded, Rectangular, Elastometric Seal", Asle Transactions, Vol.29, No. 4, pp.558-564, 1986.
- [3] E. Dragoni and A. Strozzi, "Theoretical Analysis of an Unpressurized Elastomeric O-Ring Seal into a rectangular Groove", Elsevier Sequoia, Wear, 130, pp. 41-51, 1989.
- [4] E. Dragoni and A. Strozzi, "Analysis of an Unpressurized, Laterally Restrained, Elastomeric O-Ring Seal", Journal of Tribology, Vol. 110, pp. 193-200, 1988
- [5] A. Karaszkievicz, "Geometry and Contact Pressure of an O-Ring Mounted in a Seal Groove", Ind. Eng. Chem. Res. 29, pp. 2134-2137, 1990.
- [6] Yokoyama, K., Okazaki, M., Komito, T., "Effect of Contact Pressure and Thermal Degradation on the Sealability of O-ring," JSAE Review, Vol. 19, 1998, pp. 123-128.
- [7] Nam, J. H., Hawong, J. S., Han, S. L. and Park, S. H., "Contact stress of O-ring under uniform squeeze rate by Photoelastic experimental hybrid method," Journal of Mechanical Science and Technology, Vol. 22, No. 11, pp. 2337-2349, 2008.
- [8] Hawong, J. S., Nam, J. H., Han, S. L., Kwon, O. S, and Park, S. H., "A Study on the Analysis of O-ring under Uniform Squeeze Rate and Internal Pressure by Photoelastic Experimental Hybrid Method," Journal of Mechanical Science and Technology, Vol. 23 No. 8, pp. 2330-2340, 2009.
- [9] N. I. Muskhelishvili, "Some Basic Problems of Mathematical Theory of Elasticity," 4th Edition, P. Noordhoff Ltd., Groningen Netherlands, (1963).
- [10] D. A. Hills, D. Nowell and A. Sackfield, "Mechanics of Elastic Contacts," Butterworth-Heinemann, U.S.A. (1993).
- [11] R. C. Sampson, "A Stress-optic law for Photoelastic Analysis of Orthotropic Composites, " Experimental Mechanics, Vol. 10, pp. 210-215, (1970).
- [12] M. S. Bazaraa and C. M. Shetty, "Nonlinear Programming Theory and Algorithms," John Wiley & Sons Inc. U.S.A. (1979).

Strength Physics at Nano-scale and Application of Optical Interferometry

Sanichiro Yoshida

Southeastern Louisiana University, Department of Chemistry and Physics
SLU 10878, Hammond, LA 70402, USA, syoshida@selu.edu

ABSTRACT The theoretical basis of the physical mesomechanical approach of strength physics is described. Based on a fundamental principle of physics known as local symmetry, this approach is capable of describing deformation and fracture comprehensively, and applicable to any scale level. It is thus useful to describe strength physics at the nano/microscopic without relying on phenomenology. An optical interferometric technique capable of resolving displacement at sub-nanometer level is introduced. Being capable of quantitative measurement, this technique is useful for characterization of material strength at the nano/microscopic level.

1. Introduction

Much remains unexplained in physics behind the transition from deformation to fracture of solid state materials. Most prevailing theories of plasticity and fracture are empirical and phenomenological. They can describe phenomena observed before and after the appearance of a crack respectively, but not comprehensively. In particular, strength physics of nano/microscopic systems has not yet been systematically formulated. These systems are too small to apply continuum mechanics, and at the same time, too large to apply quantum mechanics. It is widely known that constitutive parameters of nano/microscopic systems can be substantially different from macroscopic systems of the same material. This situation leads to difficulty in designing nano/microscopic systems for required strength. A breakthrough theoretical development is essential.

In this regard, a field theoretical approach developed by a recent theoretical system called physical mesomechanics [1, 2] is advantageous. Based on a fundamental physical principle known as local symmetry [3], this approach has intrinsic mechanism to describe different stages of deformation including the fracturing stage, and different scale levels comprehensively. This fills the gap between continuum mechanics and quantum mechanics with respect to discontinuity of materials. Continuum mechanics handles materials as collections of point masses and therefore does not have a built-in mechanism to formulate defects. Quantum mechanics, on the other hand, handles materials as groups of molecules connected by electronic orbits or other intermolecular interactions. Discontinuity could be considered via potentials, but for a large number of molecules there are too many interactions to be taken into account and it is not practical. From this viewpoint, the concept of mesoscopic structural level introduced by physical mesomechanics is important. Essentially, the mesoscopic level is the smallest volume element with finite volume that has rotational degrees of freedom. At one scale level above, different rotations of these mesoscopic elements represent rotational mode of deformation. This is contrastive to the formalism of elastic theory where the rotational part of the strain tensor represents rigid body rotation. In the mesomechanical approach, discontinuities in a bulk material such as defects can be naturally introduced as the space between neighboring mesoscopic volume elements experiencing different rotations. While allowing these volume elements to rotate differently, physical mesomechanical approach requests that the underlying physics is invariant before and after the rotational deformation. This is where the concept of local symmetry is used in the theory. Moreover, this approach characterizes the progress of deformation as development from a smaller scale level to a larger scale level where the deformation at the lower scale level serves as a source of deformation at

the larger scale level. Therefore, advancement in strength physics at nano/microscopic scale level is important for macroscopic mechanics as well.

Quantitative measurement of displacement and other parameters characterizing strength physics is another important issue in nano/microscopic level. Recent advancement in microscopy enables us to view extremely small objects. However, quantitative measurement is not as easy as qualitative observations. Often, the size of the object is beyond the diffraction limit determined by the wavelength of the light. From this standpoint, optical interferometry is quite powerful. It uses the phase of light to quantify the size of object without being limited by the diffraction limit of the light source.

The aim of this paper is to describe the theoretical basis of the physical mesomechanical approach of strength physics, and introduce an optical interferometric technique useful for measurement of small displacement. After discussing the deformation theory focusing on the dynamics of defects, the resulting dynamics of deformation at larger scale level, and the irreversibility of plastic deformation, we will consider an optical interferometric configuration suitable for out-of-plane displacement at the scale level beyond the diffraction limit of typical light sources. Note that the same interferometric principle is applicable to other types of measurement such as in-plane displacement and strain with moderate modification of the optical configuration.

2. Formulation

2.1 Deformation transformation and local symmetry

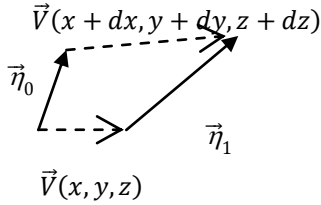


Fig. 1 Line element $\vec{\eta}_0$ transforms to $\vec{\eta}_1$ via coordinate dependent displacement \vec{V} .

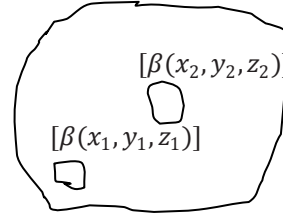


Fig. 2 Different parts of the object transform coordinate dependent transformation matrix β

Consider a line element vector transforms from $\vec{\eta}_0$ to $\vec{\eta}_1$ in Fig. 1. By defining displacement vector $\vec{V}(x, y, z)$, we can describe this deformation as differential displacement between the tip and tail of the line element vector; $\vec{V}(x + dx, y + dy, z + dz) - \vec{V}(x, y, z)$. The corresponding distortion matrix $[\beta]$ can be put as below.

$$[\beta] = \begin{bmatrix} \frac{\partial u}{\partial x} & \frac{\partial u}{\partial y} & \frac{\partial u}{\partial z} \\ \frac{\partial v}{\partial x} & \frac{\partial v}{\partial y} & \frac{\partial v}{\partial z} \\ \frac{\partial w}{\partial x} & \frac{\partial w}{\partial y} & \frac{\partial w}{\partial z} \end{bmatrix} \quad (1)$$

Now consider that the transformation varies from location to location, i.e., $[\beta]$ depends on the coordinates. Since components of $[\beta]$ contain derivatives, the coordinates dependence of this matrix indicates that the derivative depends on the coordinates, and that therefore it is necessary to replace the usual derivatives with covariant derivatives. In other words, it is necessary to introduce a gauge so that the underlying physics is invariant [1, 4].

$$D_\mu = \partial / \partial x_\mu - \Gamma_\mu \quad (2)$$

Here is the covariant derivative and is the gauge. In the present context, the gauge represents the inter-relationship among different parts of the material experiencing different elastic deformation. Dynamics of plastic deformation can be described as the characteristics of this gauge.

2.2 Defect dynamics

Replacing the usual derivatives in the conventional Lagrangian of elastic deformation with covariant derivatives and deriving an equation of motion from the resultant Lagrangian, Egorushkin [5] obtained the following set of equations.

$$\frac{\partial}{\partial x_\alpha} J_\mu^\alpha = -\frac{\partial}{\partial t} (\ln u_\mu) \quad (3.1)$$

$$\epsilon_{\mu\chi\delta} \frac{\partial J_\delta^\alpha}{\partial x_\chi} = -\frac{\partial \alpha_\mu^\alpha}{\partial t} \quad (3.2)$$

$$\frac{\partial \alpha_\mu^\alpha}{\partial x_\alpha} = 0 \quad (3.3)$$

$$\epsilon_{\mu\chi\delta} \frac{\partial \alpha_\delta^\alpha}{\partial x_\chi} = \frac{1}{\tilde{c}^2} \frac{\partial J_\mu^\alpha}{\partial t} + \sigma_\mu^\alpha - P_\mu^\beta \frac{C_{\alpha\beta}^{\mu\nu}}{E} \quad (3.4)$$

$$\frac{1}{c^2} \frac{\partial v_\mu}{\partial t} = \frac{\partial \sigma_\mu^\alpha}{\partial x_\alpha} - \frac{\partial P_\nu^\beta}{\partial x_\alpha} \frac{C_{\alpha\beta}^{\mu\nu}}{E} \quad (3.5)$$

Here J and α are the dimensionless flux density and density of line defects (discontinuities in displacement u). Egorushkin [6] interprets these equations as follows. The right-hand side of eq. (3.1) is the rate of elastic deformation, $\epsilon_{\mu\chi\delta}$ is the Levi-Civita density, \tilde{c}^2 is the velocity of the plastic deformation front, σ_μ^α is the elastic stress, P_μ^β is the plastic part of distortion, and c is the sound velocity in the material, Eq. (3.1) is the continuity equation of a medium with defects. Eq. (3.2) represents the consistency of plastic deformation. Note that it indicates that the defect density changes over time in proportion to the rotation of the defect flow, not divergence. Eq. (3.3) represents the continuity of line defects; there is no charge (source) for the rotational component of plastic deformation field. Eq. (3.4) indicates that either a change in the defect flow rate (the first term on the right-hand side) or elastic stress (the second term on the right-hand side) produces change in the rotation of defect density (the left-hand side). The second and third terms on the right-hand side represent the source of plastic deformation whereas the second term represents the effect that elastic stress yields plasticity and the third term represents the initial plasticity. Eq. (3.5) indicates that the elastic velocity changes over time due to the elastic stress minus plastic stress. Also note that in this case the source is elastic stress's spatial variation, not the stress itself as is the case of eq. (3.4) (plastic case).

2.3 Continuum mechanics local and global

Requesting local symmetry under transformation $[\beta]$ and using a different Lagrangian, we can derive another set of field equations [1, 4]. From the physical point of view, this set of field equations represents the conservation of translational momentum [7].

$$\nabla \cdot \vec{v} = j^0 \quad (4.1)$$

$$\nabla \times \vec{v} = \frac{\partial \vec{\omega}}{\partial t} \quad (4.2)$$

$$\nabla \times \vec{\omega} = -\frac{1}{c^2} \frac{\partial \vec{v}}{\partial t} - \vec{j} \quad (4.3)$$

$$\nabla \cdot \vec{\omega} = 0 \quad (4.4)$$

where $j^0 = g^{ij} \eta_i^\alpha \eta_{j\alpha} / l^2$ and $\vec{j}^\mu = g^{ij} \eta_i^\alpha (D_\nu \eta_j^\beta) C_{\alpha\beta}^{\mu\nu} / l^2$ are the time and space components of the symmetry charges associated with the transformation. g^{ij} is the metric tensor, $C_{\alpha\beta}^{\mu\nu}$ is the dimensionless elastic constant and l is the characteristic length of the local area where distortion matrix $[\beta]$ can be considered to be constant.

By putting $c^2 = \gamma/\rho$ where γ and ρ are the shear modulus and density of the material, we can interpret eq. (4.3) to be the equation of motion representing the dynamics of a unit volume [7]. With this interpretation, j^0 appearing on the right-hand side of eq. (4.1) represents strain concentration. The first term on the right-hand side of eq. (4.3) represents the recovery force in plasticity whereas the second term \vec{j} represents longitudinal force on the unit volume exerted by the \vec{v} field. In the plastic regime, the longitudinal force is dissipative [4, 7]. Eq. (4.4) indicates there is no source for rotational mode of deformation.

From eqs. (4.2) and (4.3), we can derive a wave equation, which represents the decaying wave characteristic of the displacement field in the plastic regime [8]. Experiments indicate that when a deformation develops at a certain level, the \vec{v} field shows strain concentration represented by j^0 [8]. When this happens, the field loses oscillatory character, or the wave decays [7]. Another experiment shows that acoustic emission accompanies the appearance of this type of strain concentration [9]. This observation can be interpreted as the strain concentration is generated by the above defect dynamics as an irreversible process as discussed in the next section.

2.4 Irreversibility in plasticity

Irreversibility of plastic deformation must be described in accordance with thermodynamics. According to the second law of thermodynamics, the entropy change dS of a system undergoing any infinitesimal reversible process is given by dQ/T , where dq is the heat supplied to the system and T is the absolute temperature of the system. In a deforming material, part of the material exerts force on the neighboring part causing stress. As an example, consider a part of a material being stretched by neighboring parts in Fig. 3. The increase in volume of this part causes the entropy change of this part dS to be positive, because the degree to which the probability of the system is spread out over different possible microstates increases. Here a microstate specifies all molecular details about the system including the position and velocity of every molecule. If this deformation process is to be reversible, this positive change in entropy must be compensated by a negative change in entropy by some other part of the material so that the total entropy of the whole material is zero and that the entropy must flow from the other part to this part in the form of heat dQ . Consequently, the temperature of the other part of the material must decrease. This phenomenon is known as thermo-elastic effect.

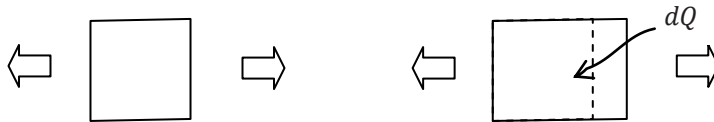


Fig. 3 Part of material being stretched by neighboring parts (left). As a consequence, the volume of this part increases and so does the entropy. The positive change in the entropy can be compensated by a heat flow in from other parts (right).

If the deformation is irreversible, the entropy of this part must be increased without exchange of heat or the entropy increase is greater than the heat flow, $dS > dQ/T$. Egorushkin [6] expresses this situation by the following expression.

$$\rho \frac{dS}{dt} = -\nabla \cdot I_s + \sigma_s \quad (5)$$

where ρ is the density of the material, I_s is the entropy flow and σ_s is the entropy production. In ref. 6, Egorushkin derives an expression for the entropy product from eqs. (3.2) and (3.4) as

$$\sigma_s = \frac{\chi(\nabla T)^2}{T^2} - \frac{\rho}{T^2} ([\alpha v], \nabla T) + \rho \frac{v_h \sigma}{T}. \quad (6)$$

Here χ is the thermal conductivity, T is the temperature, ρ is the density of the material, α is the linear defect density, σ is the elastic stress, $v_h = -\tilde{c}j$ where \tilde{c} being the plastic deformation front velocity and j the flux of linear defect (the plastic front flows, as the defects flows, in the opposite direction under very high stress associated with the work needed to push the defects to go through the material [10]), and $v_h \sigma$ represents the work associated with the defect flow due to hydrostatic tension. Note that the right-hand side of entropy production expression (6) contains elastic stress σ , showing the mechanism of transition from elastic to plastic deformation. When the temperature gradient is zero, the condition of irreversibility becomes

$$\rho \frac{v\sigma}{T} > 0 \quad (7)$$

The entropy of metals is associated with lattice vibration [11]. An increase in entropy thus is associated with some sort of acoustic phenomenon. This is consistent with the above-mentioned observation that when the material shows irreversible deformation causing energy dissipation, acoustic emission is recorded.

3. Supporting experimental results

Experimental verification of the above theory at the nano/microscopic level is a future subject. However, there is experimental evidence observed at the macroscopic scale level that supports the gist of the above theory. Fig. 4 shows a plastic deformation wave, a transverse wave solution to the above-mentioned wave equation derived from eqs. (4.2) and (4.3), observed in a tensile experiment on an aluminum alloy thin plate at a constant pulling rate [8]. The displacement was monitored at three reference points along the tensile axis. It is seen that the oscillatory characteristic of the displacement at the lowest reference point is advanced indicating that the wave travels from the lowest part toward the highest part of the specimen. Also shown is the stress variation recorded simultaneously. The displacement wave rises when the stress level is about to reach the yield stress, indicating that the wave characteristics are associated with plastic deformation.

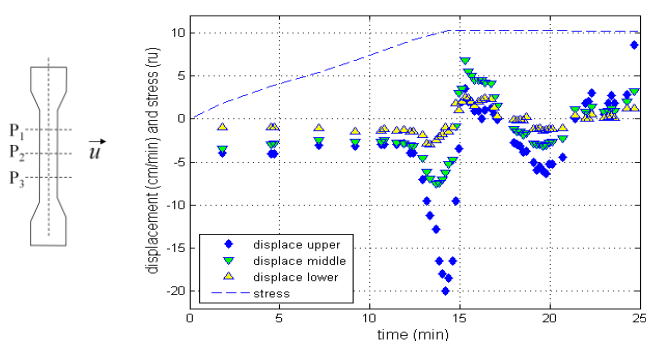


Fig. 4 Plastic deformation wave observed in an aluminum alloy specimen under a tensile load. Displacement perpendicular to the tensile load is recorded at three reference points $P_1 - P_3$.

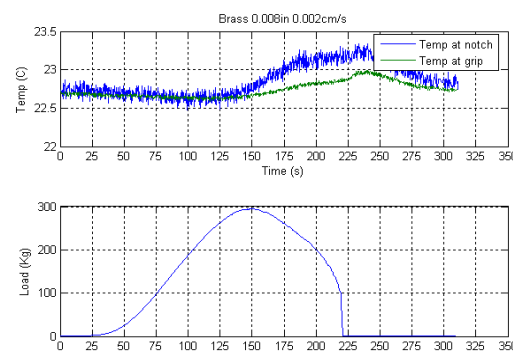


Fig. 5 Temperature rise observed in a similar experiment as Fig 4 with a notch at the vertical center of the specimen.

Fig. 5 shows the temperature rise measured in a similar experiment to Fig. 4, where we applied a tensile load to a brass thin plate with a notch on one side near the vertical center. The upper plots are the temperatures recorded near the notch and at an end of the specimen near the grip of the tensile machine, and the lower plot is the loading curve. Clearly seen is that the temperature constantly decreases from the beginning of the experiment until the applied load reaches the yield point. This effect, known as the thermo-elastic effect, indicates that even with the notch, the initial deformation experienced by this specimen is accompanied by heat flow and therefore at least to some extent reversible. However, when the deformation passes the yield point, the temperature rises. This indicates that the stretch causes totally irreversible deformation at this point and on.

4. Optical interferometric techniques for measurement of small displacement

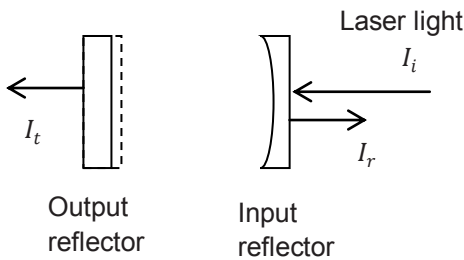


Fig. 6 Optical resonator consisting of a flat output reflector and curved input reflector

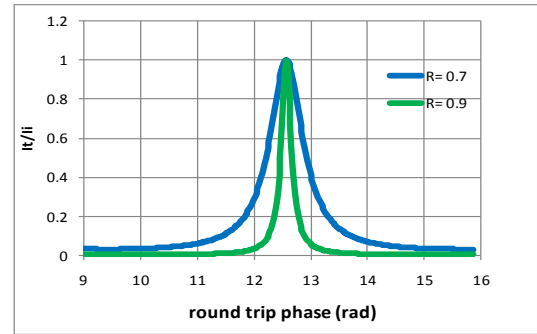


Fig. 7 Transmission of optical power as a function of round trip optical phase

Consider an optical resonator consisting of a pair of mirrors in Fig. 6. A laser light is incident to this resonator from the right. The amount of the optical power coupled into the resonator depends on the resonator's reflectance R and the optical phase corresponding to one round trip in the resonator $\delta = 4\pi L/\lambda$, where L is the resonator length and λ is the laser wavelength. The ratio of the transmitted/reflected power to the incident power can be given by the following equations.

$$\frac{I_t}{I_i} = \frac{(1-R)^2}{(1-R)^2 + 4R \sin^2(\delta/2)}, \quad \frac{I_r}{I_i} = \frac{4R \sin^2(\delta/2)}{(1-R)^2 + 4R \sin^2(\delta/2)} \quad (8)$$

Here I_i , I_t and I_r are the incident, transmitted and reflected optical intensity. Fig. 7 shows the dependence of I_t/I_i on δ for $R = 0.7$ and $R = 0.9$. The phase at which the curve shows the peak corresponds to the resonant resonator length. Thus by monitoring transmitted power, or alternatively the reflected power, we can measure the mirrors position relative to the resonance.

With a servo control, it is possible to increase the sensitivity drastically. Fig. 8 shows the principle schematically. This method is known as the Pound-Drever-Hall scheme [12] and used in ground based gravitational wave detectors of LIGO (Laser Interferometer for Gravitational wave Observatory) project [13]. With the use of a frequency stabilized laser, the designed sensitivity of initial LIGO detector corresponding to the length change on the order of 10^{-18} m has been achieved [14]. In this scheme, the incident laser is phase modulated to generate a pair of side bands. The carrier frequency is tuned to resonate when the resonator length is at the nominal value, whereas the side band frequency is off-tuned and therefore reflected under the resonance condition. The photo detector picks up the reflected light. When the resonator length is at the resonance, the photo detector signal contains only the side band; when the resonator is off resonance, it contains both the carrier and side band, and therefore, the output voltage contains the beat signal as eq. (9) indicates.

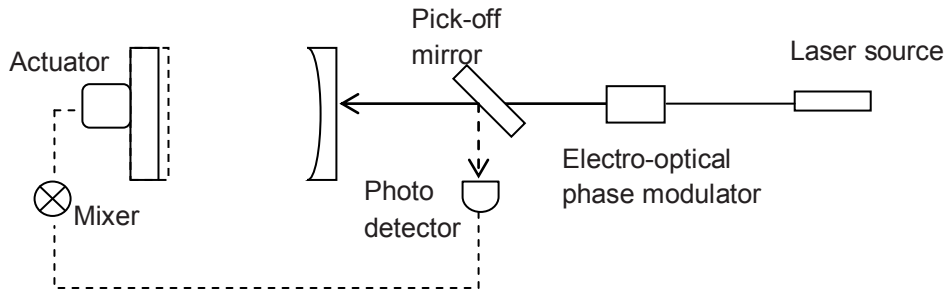


Fig. 8 Optical resonator with servo control .Photo detector picks off reflected power to create error signal and actuator correct the total reflector position to zero the error signal.

$$P(t) = \cos(\omega t + \Omega t) \cos(\omega t + \phi + \delta_l) \cong \delta_l \cos(\Omega t) \pm \sin(\Omega t) \quad (9)$$

Here $\phi = \pi/2$ is an artificially introduced phase, and Ω is the modulation frequency. The electric mixer demodulates this photo detector output signal at the modulation frequency. The in-phase term of the resultant voltage (the first term on the right-hand side of the below equation) becomes proportional to δ_l [15, 16].

$$\int P(t) dt = \int \{\delta_l \cos(\Omega t) \pm \sin(\Omega t)\} dt \propto \delta_l \quad (10)$$

The actuator corrects the reflector's position by zeroing the error signal represented by eq. (10). By monitoring the error signal, we can know the mirror's location with reference to the resonant location precisely.

5. Summary

We have quickly reviewed physical mesomechanical formulation of strength physics. Based on the physical principle known as local symmetry, this formalism is capable of describing deformation and fracture comprehensively, regardless of the scale level. The irreversibility of plasticity is explained as the increase in entropy as a consequence of linear defects' motion due to local elastic stress exerted by surrounding materials. On the larger scale level, plastic deformation is characterized as a transverse, decaying wave nature of the displacement field. The irreversible motion of the defects at the lower scale level is the source of energy dissipation in the wave dynamics, causing the displacement wave to decay.

These formulations are yet to be experimentally verified at the nano/microscopic level. There are a number of experimental observations that support the formulations at the macroscopic level. To conduct experiments at the nano/microscopic level, quantitative measurement of displacement is essential. We have discussed an optical interferometric technique suitable for extremely small displacement. It is expected that with various optical configurations, this or similar interferometric techniques are used in the future for advancement of strength physics at the nano/microscopic scale level.

Acknowledgement

The financial support by the Southeastern Louisiana University Alumni Association is highly appreciated.

References

1. V. E. Panin, Yu. V. Grinyaev, V. E. Egoruskin, I.L. Buchbinder and S. N. Kul'kov, "Spectrum of excited states and the rotational mechanical field in a deformed crystal", Sov. Phys. J. 30, 24-38 (1987)

2. V. E. Panin (ed.), *Physical Mesomechanics of Heterogeneous Media and Computer-Aided Design of Materials*, vol. 1, Cambridge International Science, Cambridge (1998)
3. J. P. Elliott and P. G. Dawber, *Symmetry in physics*, Macmillan, London (1979)
4. S. Yoshida, "Field theoretical approach to dynamics of plastic deformation and fracture", AIP Conference Proceedings, Vol. 1186, pp. 108-119 (2009)
5. V.E. Egorushkin, "Dynamics of plastic deformation: waves of localized plastic deformation in solids", Sov. Phys. J. 33, 2 135-149 (1990)
6. V.E. Egorushkin, "Dynamics of plastic deformation: waves of localized plastic deformation in solids", Rus. Phys. J. 35, 4 316-334 (1992)
7. S. Yoshida, "Dynamics of plastic deformation based on restoring and energy dissipative mechanisms in plasticity", *Physical Mesomechanics*, 11, 3-1, 140-146 (2008)
8. S. Yoshida et al. "Observation of plastic deformation wave in a tensile-loaded aluminum-alloy" *Phys. Lett. A*, 251, 54-60 (1999)
9. S. Yoshida, "Optical interferometric study on deformation and fracture based on physical mesomechanics", *J. Phys. Meso. Mech.*, 2, 4, 5 – 12 (1999)
10. V. E. Egorushkin, private communication (2008)
11. C. Kittel, *Introduction to solid state physics*, 2nd edition, John Wiley and sons, Inc New York 118-156 (1956)
12. R.Drever, J. Hall, F. Kowalski, J. Hough, G. Ford, A. Munley and H. Ward, "Laser phase and frequency stabilization using an optical resonator," *Appl. Phys. B*, 31, 97-105 (1983)
13. B. C. Barish and R. Weiss, "LIGO and detection of Gravitational waves," *Physics Today*, 52, 10, 44-50 (1999)
14. LIGO Scientific Collaboration, "LIGO: The Laser Interferometer Gravitational-Wave Observatory", *Rep. Prog. Phys.* 72, 076901 (pp 25) (2009)
15. P. R. Saulson, *Fundamentals of Interferometric Gravitational-wave Detectors* (World Science, 1994)
16. S. Yoshida, "Detection of 10-21 strain of space-time with an optical interferometer", Proc 2005 SEM Annual conference, June 7–9, 2005 Portland, Oregon, paper No. 303, 7 pages (2005)

LIGHT GENERATION AT THE NANO SCALE, KEY TO INTERFEROMETRY AT THE NANO SCALE

C.A. Sciammarella^{1,2}, L. Lamberti² and F.M. Sciammarella¹

¹*Northern Illinois University, Department of Mechanical Engineering, 590 Garden Road, DeKalb, IL 60115, USA*

²*Politecnico di Bari, Dipartimento di Ingegneria Meccanica e Gestionale, Viale Japigia 182, Bari, 70126, ITALY*

E-mail: sciammarella@iit.edu, lamberti@poliba.it, sciammarella@niu.edu

Abstract

The feasibility of recording optical information at the nanometric level was considered for a long time restricted by the wavelength of light. The concept of wavelength of light in classical optics is a direct consequence of the standard solution of the Maxwell equations for purely harmonic functions. Propagating harmonic light waves in vacuum or air satisfy the required mathematical conditions imposed by the Maxwell equations. Hence, in classical optics, the concept of wavelength of light was associated with that type of waves. Mathematically speaking, one can derive solutions of the Maxwell equations utilizing Fourier integrals and show that light generated in a volume with dimensions much smaller than the wavelength of light will have periods in the sub-wavelength region. Every oscillator, whether a mass on a spring, a violin string, or a Fabry–Perot cavity, share common properties deriving from the mathematics of vibrating systems and the solutions of the differential equations that govern vibratory motions. In this paper, some common properties of vibrating systems are utilized to analyze the process of light generation in nano-domains. Although simple, the present model illustrates the process of light generation without getting into the very complex subject of the solution of quantum resonators.

1. INTRODUCTION

The optical observation of nano-size objects is at the frontier of current optical technology. Many important advances have been achieved in this field and today it is possible to get results that less than one decade ago were thought not possible. For a long time, a classical solution of the Maxwell equations corresponding to a harmonic oscillator yield the basic concept of wavelength leading to the well known limits of optical resolution. However, one can derive solutions of Maxwell equations utilizing Fourier integrals and show that light generated in a volume with dimensions much smaller than the wavelength of light will have periods falling in the sub-wavelength region. In [1,2], there are presented experimental investigations resulting in the reconstruction of simple geometry objects (prisms and spheres) with accuracies within few nanometers. In more recent work [3, 4], a similar methodology was applied to complex geometries of microscopic surfaces reaching nanometer accuracy. The paper returns to some of the original work presented in [1,2] to illustrate some of the mechanisms through which information in the nano-range can be obtained. These mechanisms are based on the phenomena related with the evanescent optical fields and the properties of optical resonators. Complex optical processes and intricate systems are briefly described and then analyzed in view of resonator models. The goal is to provide an overview of complex optical phenomena that would require quantum optics to be correctly and completely explained. However, a heuristic overview can be given in terms of classical oscillator systems.

2. OPTICAL SYSTEM TO VIEW IMAGES

Figure 1 shows the optical system utilized to observe objects at the nanometric range. An optical microscope is used to view the interface between the microscope slide and the saline solution. The observed objects are located on the microscope slide. Following the classical arrangement of

TIR, a He-Ne laser beam with nominal wavelength 632.8 nm impinges normally to the face of a prism designed to produce limit angle illumination on the interface between a microscope slide (supported by the prism itself) and a saline solution of sodium chloride contained in a small cell supported by this slide. Consequently, evanescent light is generated inside the saline solution. The resulting effect of this particular optical system is complex. The prism has residual stresses that provide one of the important tools in the process of observation. Figure 2 presents an approximate model of the glass prism boundary.

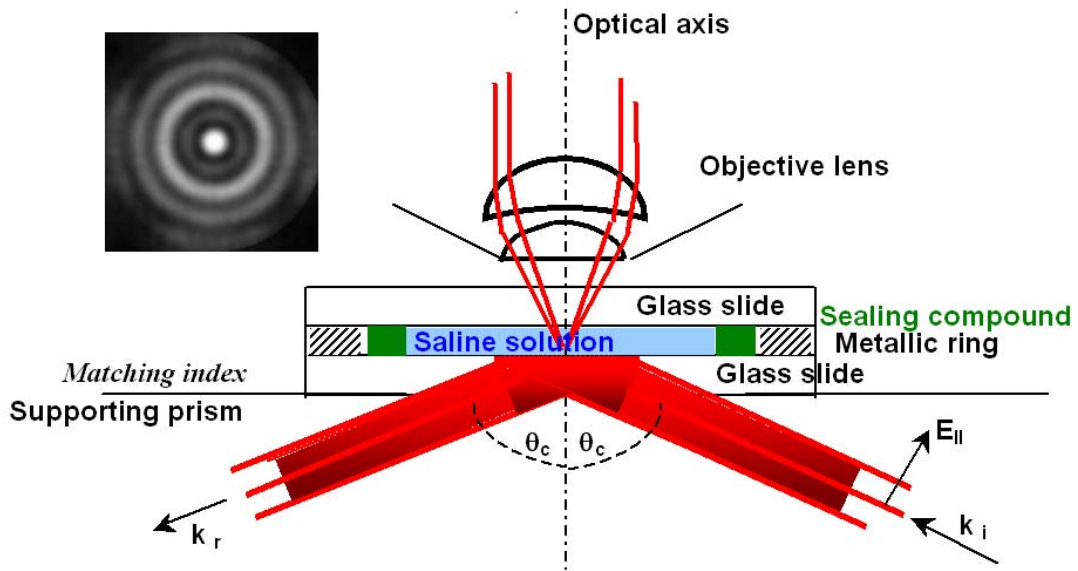


Figure 1. Optical system utilized to make observations in the nanometric range

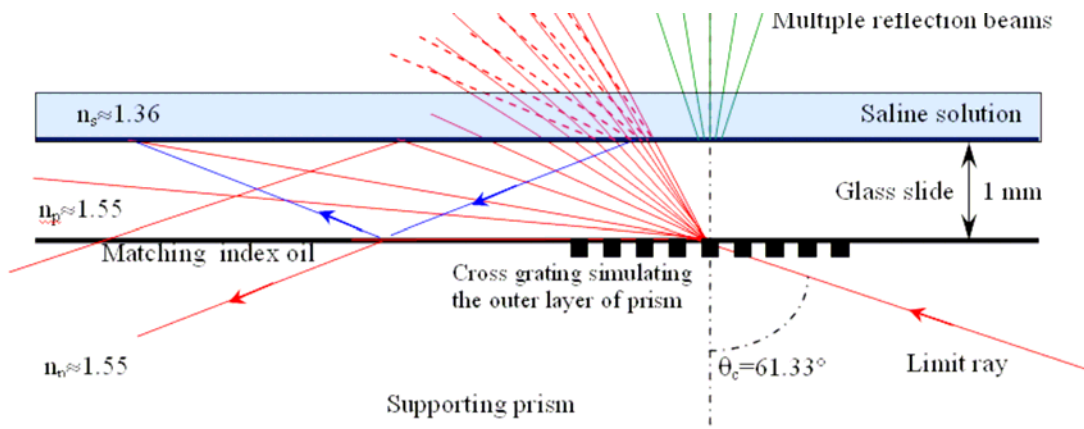


Figure 2. Schematic representation of interfaces: 1) prism-microscopic slide, 2) microscopic slide-saline solution

The presence of residual stresses can be approximately modeled by the presence of a grating that produces different diffraction orders. However, these diffraction orders correspond to evanescent optical waves and not to ordinary waves. The effect of the evanescent diffraction

orders is to excite electromagnetic oscillations in the inner space of the microscope slide that acts as a Fabry-Pérot interferometer. The electromagnetic oscillations of the Fabry-Pérot result in the generation of interference fringes that are actually photoelastic fringes that play an important role in the sub-wavelength observations.

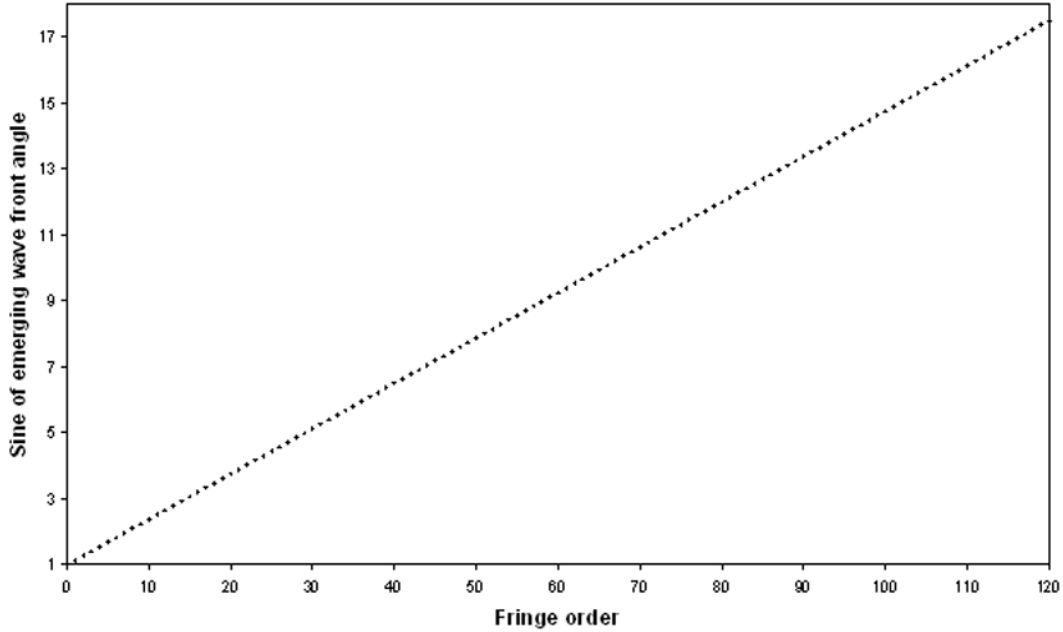


Figure 3. Plot of $\sin\theta_r$ vs. fringe order for the p-polarization plane wavefronts generated by the evanescent waves. The order 0 corresponds to the direction of the impinging laser beam.

In Figure 3, the sine of the emerging wavefronts is plotted with respect to fringe orders recorded from the FT of the analyzed image. It can be seen that all the emerging orders except the first one are in the range of complex sine. Since values of $\sin\theta_r$ are greater than 1, then angles θ_r are complex numbers, with a real part and an imaginary part. This implies a generalization of the trigonometric function to complex values of the argument. Utilizing the plane wave complex solutions of the Maxwell equations, one arrives to a system of fringes whose variable intensity which will be recorded by the sensor can be expressed as follows:

$$I(x) = I_0 + I_1 \cos\left[\frac{2\pi}{p_0} N_0 \frac{n_{sol}}{n_g}\right] x \quad (1)$$

where: p_0 is the pitch of the fringes, N_0 is the fringe order, n_{sol} is the index of refraction of the saline solution, n_g is the index of refraction of the microscope slide. The relationship between p_0 and the wavelength of light is given by the equation:

$$\sin \phi = \frac{\lambda_c}{n_{sol} \frac{2p_0}{N_0}} \quad (2)$$

where ϕ is the angle of the diffraction order with respect to the zero order. The effective wavelength λ_e given by the ratio:

$$\lambda_e = \frac{\lambda}{N} \quad (3)$$

In the above equation, λ_e is the actual wavelength of the light generating the evanescent wave and the integers $N=1,2,3$ represent the fraction of the wavelength generating interference fringes.

In Figure 4, the theoretical results provided by Eq. (1) are plotted in abscissas vs. the experimental values represented in ordinates. The cross correlation indicates an excellent matching between the experimental and the theoretical values (“System 1” and “System 2” refer to p-polarization and s-polarization beams, respectively). In the present case, the effective wavelength was obtained by setting $N=2$: that is, interference fringes correspond to an effective wavelength which is half of the actual wavelength of light. It appears from the figure that the experimental values are in excellent agreement with theoretical computations done with Eq. (1).

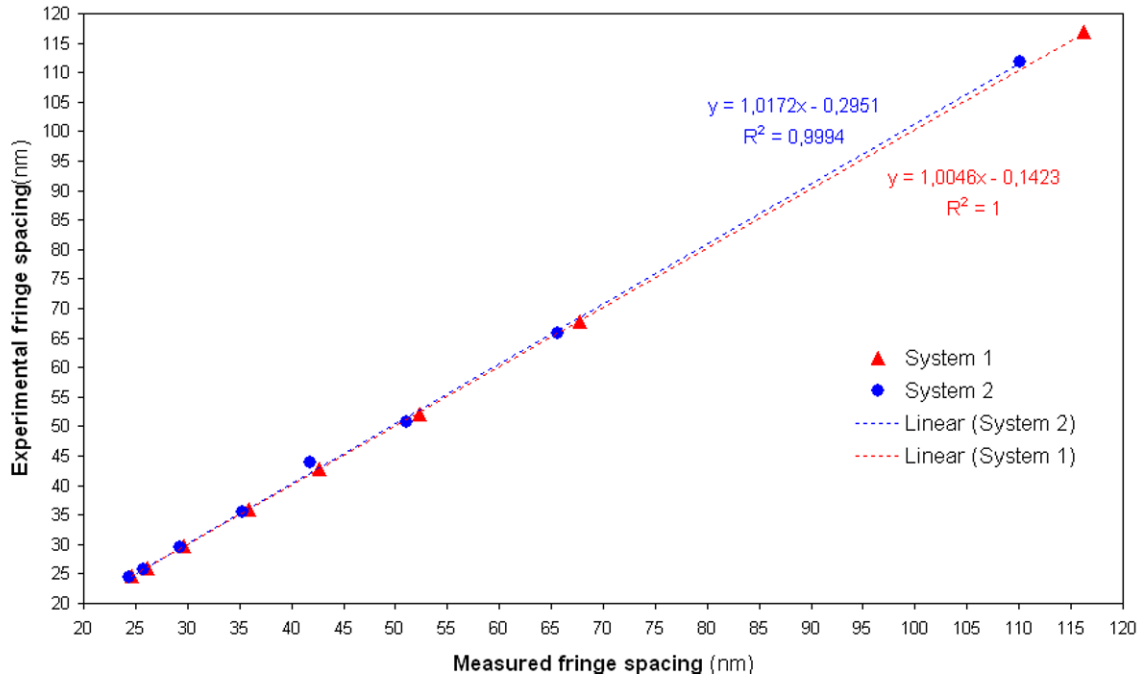


Figure 4. Measured fringe spacing vs. theoretical values of pitch computed via Eq. (1)

Figure 5 shows the values of the measured pitches as a function of the fringe order. This relationship can be put in the following analytical form:

$$p_n = \frac{p_0}{N_0} \quad (4)$$

The values of the resulting hyperbolic law written above provide, for each order N_0 , the pitch p_n of fringes as a function of the fundamental pitch p_0 of each of the two families of interference fringes generated by the p-polarized and the s-polarized waves, respectively. Point and triangle dots in

the figure correspond to values measured experimentally. The continuous curves portray the correlation equations shown in Figure 5.

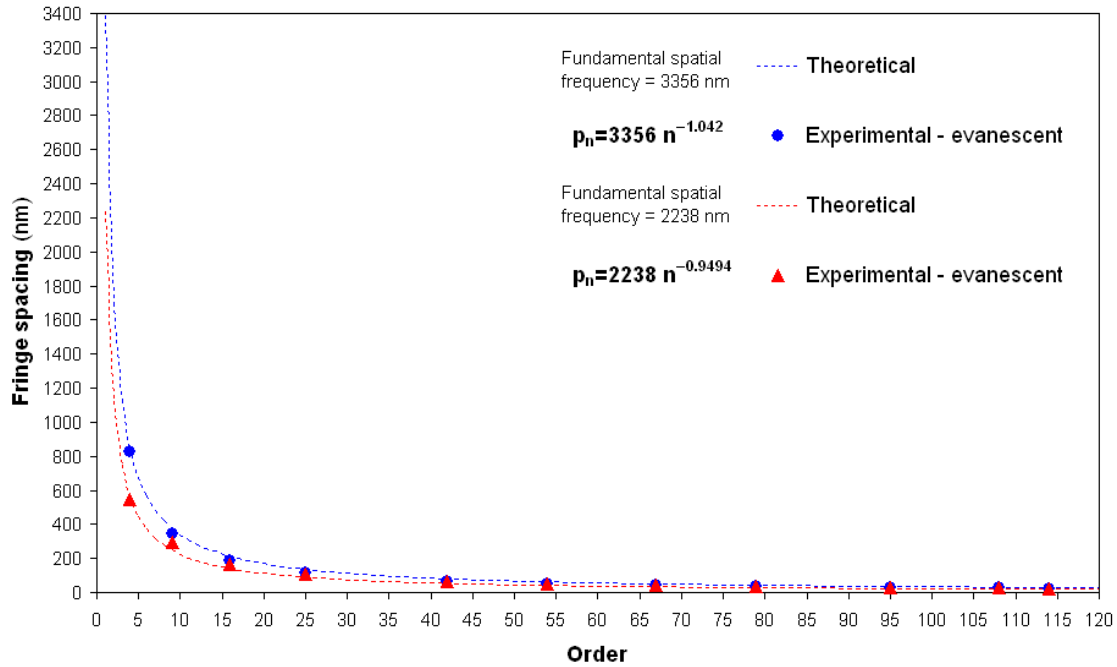


Figure 5. Orders plotted vs. measured fringes pitches

The process of formation of fringes that are multiple interference fringes produced by the interaction between the outer layers of the prism and the microscope glass slide is now analyzed. In Ref. [5], there is thorough discussion on the multiple interference fringes arising from light incident at the limit angle at an interface where there are high gradients of the index of refraction caused by residual stresses in the glass. The region of high gradient behaves as a diffraction grating that generates a number of wavefronts that emerge at different angles (Figure 2) and then enter the microscope.

3. ANALYSIS OF THE BIREFRINGENCE THAT PRODUCES THE OBSERVED FRINGES

Figure 6 shows the laser light incident at the interface between the saline solution and the microscope slide. Two beams are entering the saline solution at angles ϕ_p and ϕ_s , for the p and s-polarized waves, respectively. These two beams have originated in the prism due to the birefringence generated by residual stresses at the boundary between glass slide and prism. It will be shown that these two beams experience a $\pi/2$ rotation inside the glass slide and continue their trajectory to the interface between the glass slide and the saline solution as they were originated at the interface between the glass slide and the prism. Since there is not a significant difference between the index of refraction of the prism and the glass slide, the beams will continue approximately with the same direction impinging in the boundary region between the microscope slide and the saline solution.

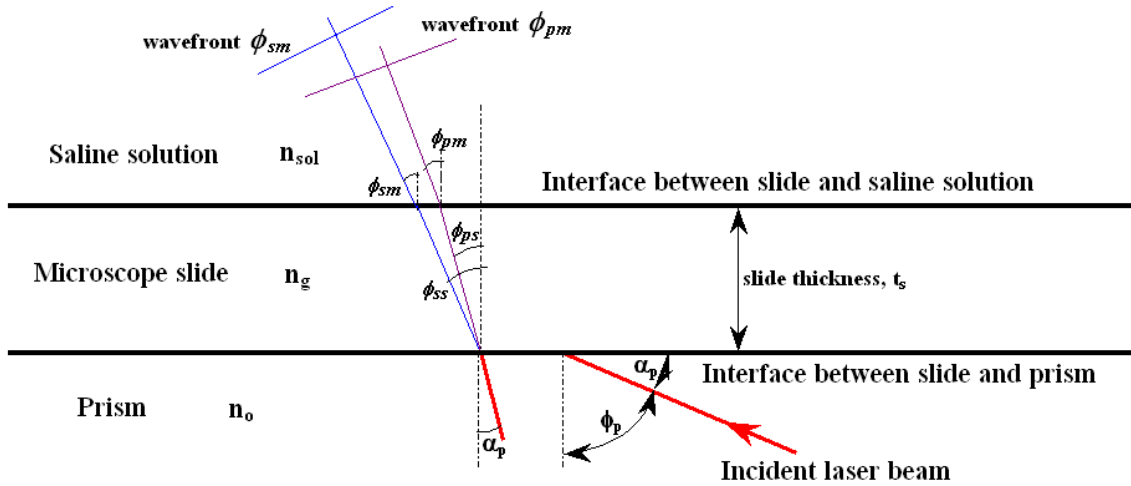


Figure 6. Beam illuminating the microscope observations

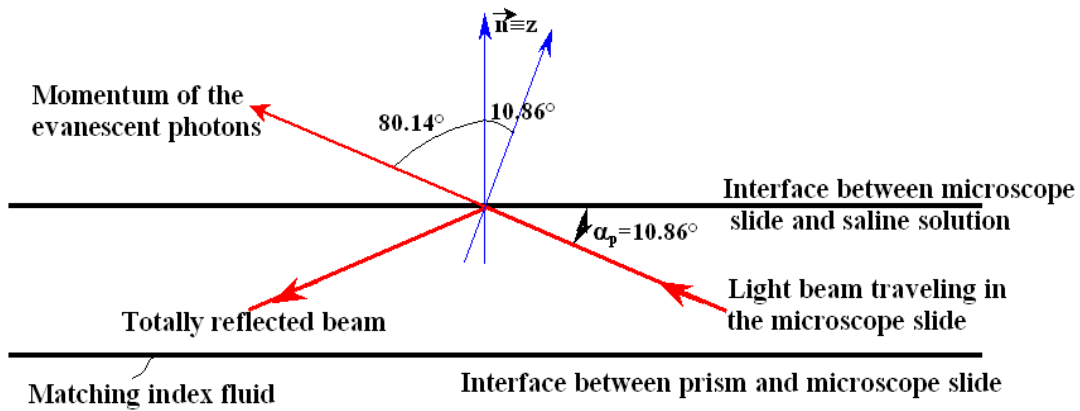


Figure 7. Angle of incidence of the illuminating beam and actually observed beam.

Figure 7 shows again the wavefronts involved in the formation of the observed images. The illuminating beam is totally reflected at the interface microscope slide – saline solution. The illuminating beam generates the evanescent waves that, according to the preservation of the momentum, will produce in the medium in contact with the interface (i.e. the saline solution) propagating wavefronts. As stated earlier, two beams were observed: the ordinary and the extraordinary beams entering the saline solution (Figure 6). The angles of inclination of these beams are respectively ϕ_{pp} and ϕ_{sp} where the first subscripts “p” and “s” indicate the type of polarization while the second subscript indicates that these wavefronts come from the prism. The two wavefronts are originated by the p-polarized beam and the s-polarized beam produced by the birefringence of the prism outer layers. The p-wave front order emerges at the angle ϕ_{pm} in the saline solution while the s-wave front emerges at the angle ϕ_{sm} in the saline solution. Those angles can be determined experimentally by utilizing the following relationships:

$$\begin{cases} \sin \phi_{pm}^{sper} = \frac{\lambda}{p_{pm}} \\ \sin \phi_{sm}^{sper} = \frac{\lambda}{p_{sm}} \end{cases} \quad (5)$$

where p_{pm} and p_{sm} , respectively, correspond to the spatial frequencies of the two families of fringes formed by the p and s-waves travelling through the thickness of the glass slide. The pitches p_{pm} and p_{sm} were measured experimentally by retrieving the sequence of orders produced by the two beams from the FT of the formed images as shown in [Figure 5](#).

The experimental values hence are:

$$\begin{cases} \sin \phi_{pm}^{sper} = \frac{0.6328}{3.356} \\ \sin \phi_{sm}^{sper} = \frac{0.6328}{2.238} \end{cases} \Rightarrow \begin{cases} \phi_{pm}^{sper} = a \sin(0.1886) = 10.860^\circ \\ \phi_{sm}^{sper} = a \sin(0.2828) = 16.425^\circ \end{cases} \quad (6)$$

4. ROLE OF THE MICROSCOPE SLIDE AS A FABRY-PEROT INTERFEROMETER

An optical cavity or optical resonator is a system of mirrors that produces standing waves. The electrical field confined in the cavity is reflected multiple times inside the cavity producing standing waves for certain resonance frequencies that depend on the geometry of the cavity and properties of the mirrors. The standing wave patterns thus generated are called modes: each mode is characterized by a frequency f_n , where the subscript n is an integer. Optical cavities are characterized by the quality factor, or Q factor. The Q factor is a dimensionless parameter that characterizes the resonator's bandwidth relatively to its center frequency. Low Q's indicate high losses of energy in the cavity and a wide bandwidth. High values of Q indicate a low rate of energy loss in the cavity with respect to the stored energy of the oscillator and a narrow bandwidth. In general, Q is defined in terms of the ratio of the energy stored in the resonator to the energy being lost in one cycle:

$$Q = 2\pi \frac{\text{Energy Stored}}{\text{Energy loss per cycle}} \quad (7)$$

For a simple type of resonator with two flat surfaces, the Q factor is given by [6]:

$$Q = \frac{2\pi f_0 \ell}{cT} \quad (8)$$

where f_0 is the resonance frequency, ℓ is the length of the cavity, c is the speed of light in the vacuum, and T is the transmittance of the faces of the cavity. The behavior of the resonator is described by the eigen-values that characterize the system. If separation of variables is possible, the eigen-function can be defined in terms of a geometrical factor $G(r)$, with r indicating the spatial coordinates, and a temporal factor $\varphi(t)$:

$$\Psi(t,r) = \varphi(t)G(r) \quad (9)$$

The $\varphi(t)$ function is the solution of the harmonic oscillator:

$$\frac{d^2\varphi}{dt^2} + Q_{\text{leak}}^{-1} \frac{d\varphi}{dt} + \omega_o\varphi = 0 \quad (10)$$

where ω_o is the resonant angular frequency and Q_{leak}^{-1} is the energy leaked, in the present case, to the saline solution. In the case analyzed in the paper there will be many wave solutions because the actual phenomena depend on the solution of the forced equation:

$$\frac{d^2\varphi}{dt^2} + Q_{\text{leak}}^{-1} \frac{d\varphi}{dt} + \omega_o\varphi = F(t) \quad (11)$$

where $F(t)$ represents the different harmonics that enter the oscillator and create resonances at different frequencies.

It can be proven that the maximum energy will concentrate in the direction of the normal to the face of the slide. Say α the inclination of the rays with respect to the normal, ℓ the thickness of the interferometer. The transmission reaches unity if $\ell = m\lambda/2\cos\alpha$ and $\alpha=0$ [6]. Hence there will be a 0, or fundamental resonance mode, with maximum energy. As a consequence of the resonator oscillations, the beams generating the interference fringes emerge as they have experienced a change in direction of $\pi/2$, as it was concluded by analysis of the experimental results.

5. FORMATION OF THE INTERFERENCE FRINGES

The mechanism of formation of interference fringes can be explained as follows. At the interface between the prism and the glass slide the p and s-waves arrive at angles larger than the critical angle, [Figure 2](#). If we neglect birefringence in the glass slide, the following relationships can be written at the boundary between the glass slide and the prism taking into consideration the $\pi/2$ rotation of the wavefronts:

$$\begin{cases} n_{pp} \sin \alpha_s = n_g \sin \phi_{ps} \\ n_{sp} \sin \alpha_p = n_g \sin \phi_{ss} \end{cases} \quad (12)$$

where: n_{pp} and n_{sp} are respectively the indices of refraction for the p and s-waves travelling in the prism; n_g is the refraction index in the glass slide; α_p and α_s indicate the equivalent angles of incidence of the p and s-waves, respectively, due to the $\pi/2$ rotation. It can be written:

$$\begin{cases} \sin \alpha_p = \cos \phi_{pp} \\ \sin \alpha_s = \cos \phi_{sp} \end{cases} \quad (13)$$

where ϕ_{pp} is the inclination angle of the ray of p-polarization in the prism and ϕ_{sp} is the corresponding inclination angle of the ray of s-polarization.

Equations (13) can be rewritten as:

$$\begin{cases} \sin \alpha_p = \cos \phi_{pp} = \sqrt{1 - \sin^2 \phi_{pp}} \\ \sin \alpha_s = \cos \phi_{sp} = \sqrt{1 - \sin^2 \phi_{sp}} \end{cases} \quad (14)$$

By substituting equations (12) in (14), we obtain:

$$\begin{cases} \sin \alpha_p = \sqrt{1 - \left(\frac{n_g}{n_{pp}}\right)^2} = \frac{1}{n_{pp}} \sqrt{n_{pp}^2 - n_g^2} \\ \sin \alpha_s = \sqrt{1 - \left(\frac{n_g}{n_{sp}}\right)^2} = \frac{1}{n_{sp}} \sqrt{n_{sp}^2 - n_g^2} \end{cases} \quad (15)$$

The above equations can be rewritten as:

$$\begin{cases} n_{pp} \sin \alpha_p = \sqrt{n_{pp}^2 - n_g^2} \\ n_{sp} \sin \alpha_s = \sqrt{n_{sp}^2 - n_g^2} \end{cases} \quad (16)$$

At the interface between the prism and the glass slide, the law of refraction for the two propagating p and s-waves yields:

$$\begin{cases} n_{pp} \sin \alpha_p = n_g \sin \phi_{ps} \\ n_{sp} \sin \alpha_s = n_g \sin \phi_{ss} \end{cases} \quad (17)$$

At the interface between glass and the saline solution, the law of refraction for the two waves can be written as:

$$\begin{cases} n_g \sin \phi_{ps} = n_{sol} \sin \phi_{pm} \\ n_g \sin \phi_{ss} = n_{sol} \sin \phi_{sm} \end{cases} \quad (18)$$

By combining equations (17) and (18), it follows:

$$\begin{cases} n_{pp} \sin \alpha_p = n_{sol} \sin \phi_{pm} \\ n_{sp} \sin \alpha_s = n_{sol} \sin \phi_{sm} \end{cases} \quad (19)$$

By combining equations (16) and (19), we obtain:

$$\begin{cases} \sqrt{n_{pp}^2 - n_g^2} = n_{sol} \sin \phi_{pm} \\ \sqrt{n_{sp}^2 - n_g^2} = n_{sol} \sin \phi_{sm} \end{cases} \quad (20)$$

Finally, from Eq. (20), the angles of the p and s-wave fronts emerging in the saline solution can be expressed as:

$$\begin{cases} \sin \phi_{pm} = \frac{\sqrt{n_{pp}^2 - n_g^2}}{n_{sol}} \\ \sin \phi_{sm} = \frac{\sqrt{n_{sp}^2 - n_g^2}}{n_{sol}} \end{cases} \quad (21)$$

The theoretical values of the angles of inclination of the p and s-wavefronts can be compared with the corresponding values measured experimentally. There are two unknowns in Eqs. (21): the indices of refraction n_{pp} and n_{sp} . The index of refraction of the glass slide n_g was provided by the manufacturer: 1.5234. The index of refraction of the saline solution was determined from the solution concentration: 1.36.

The Maxwell-Neumann equations can be written for the p and s-wave fronts travelling through the stressed region of the prism,

$$n_{pp} - n_o = A\sigma_1 + B\sigma_2 \quad (22)$$

$$n_{sp} - n_o = B\sigma_1 + A\sigma_2 \quad (23)$$

where n_o is the index of refraction corresponding to the prism in the unstressed state while n_{pp} and n_{sp} correspond to the indices of refraction of the extraordinary wavefronts in the stressed prism. Equations (22) and (23) contain also the constants A and B and the residual compressive stresses σ_1 and σ_2 generated in prism by the manufacturing process.

By comparing the expressions of the index of refraction n_o of the ordinary beam it follows:

$$n_o = n_{pp} - (A\sigma_1 + B\sigma_2) \Leftrightarrow n_o = n_{sp} - (B\sigma_1 + A\sigma_2) \quad (24)$$

where the two members of equation (24) must coincide.

The optimization problem can be stated in fashion of Eq. (25). The objective function Ψ represents the average difference between the theoretical angles at which the p and s-wave fronts emerge in the saline solution and their counterpart measured experimentally. The Maxwell-Neumann equations are included as constraints in the optimization process: the equality constraint on the ordinary wave, equation (24), must be satisfied within 2% tolerance. There are 6 optimization variables: the two indices of refraction n_{pp} and n_{sp} in the error function; the two constants A and B and the residual stresses σ_1 and σ_2 in the constraint equation. The last unknown of the optimization problem, the refraction index n_o corresponding to the unstressed prism, was instead removed from the vector of design variables by combing the Maxwell-Neumann relationships into the constraint equation (24).

Optimization runs were started from three different initial points: (i) lower bounds of design variables (Run A); (ii) mean values of design variables (Run B); (iii) upper bounds of design variables (Run C).

The optimization problem (25) was solved by combining response surface approximation and line search [7]. Sequential Quadratic Programming performed poorly as design variables range over very different scales. Results of different optimization runs are reported in [Table 1](#). Besides the residual error on the optimized value of Ψ and the value of constraint margin (24), the table shows also the resulting value of the index of refraction of the ordinary beam n_o , the photoelastic constant $C=A-B$ and the shear stress τ in the prism determined as $|(\sigma_1 - \sigma_2)/2|$.

It can be seen that the residual error on the emerging wave angles is always smaller than 0.4%. The error on the refraction index of the ordinary beam is less than 1.8%.

The convergence curves corresponding to the three optimization runs are shown in [Figure 8](#). The optimization process was completed within an average number of 20 iterations. Some

oscillations in the error function were seen only in the first iterations but were progressively reduced as the search algorithm approached the optimum design.

$$\left\{ \begin{array}{l} \text{Min } \Psi(n_{pp}, n_{sp}, A, B, \sigma_1, \sigma_2) = \frac{1}{2} \left[\left(\frac{\sqrt{n_{pp}^2 - n_g^2} - \sin \phi_{pm}^{sper}}{n_{sol} \sin \phi_{pm}^{sper}} \right)^2 + \left(\frac{\sqrt{n_{sp}^2 - n_g^2} - \sin \phi_{sm}^{sper}}{n_{sol} \sin \phi_{sm}^{sper}} \right)^2 \right] \\ 0.98 \leq \left| \frac{n_{pp} - (A\sigma_1 + B\sigma_2)}{n_{sp} - (B\sigma_1 + A\sigma_2)} \right| \leq 1.02 \\ 1.5235 \leq n_{pp} \leq 1.575 \\ 1.5235 \leq n_{sp} \leq 1.575 \\ -0.8 \cdot 10^{-11} \leq A \leq -0.3 \cdot 10^{-11} \\ -3.5 \cdot 10^{-11} \leq B \leq -2.5 \cdot 10^{-11} \\ -180 \cdot 10^6 \leq \sigma_1 \leq -120 \cdot 10^6 \\ -180 \cdot 10^6 \leq \sigma_2 \leq -120 \cdot 10^6 \end{array} \right.$$

Table 1. Results of optimization runs

Design parameter	Run A	Run B	Run C
n_{pp}	1.5447	1.5447	1.5468
n_{sp}	1.5716	1.5709	1.5699
n_o	1.5399	1.5399	1.5405
A (m ² /N)	$-0.5167 \cdot 10^{11}$	$-0.3017 \cdot 10^{11}$	$-0.6994 \cdot 10^{11}$
B (m ² /N)	$-2.8096 \cdot 10^{11}$	$-2.9645 \cdot 10^{11}$	$-3.1390 \cdot 10^{11}$
$C=AB$ (m ² /N)	$2.2929 \cdot 10^{11}$	$2.6628 \cdot 10^{11}$	$2.4396 \cdot 10^{11}$
σ_1 (MPa)	-135.30	-142.50	-161.85
σ_2 (MPa)	-145.01	-145.83	-164.90
τ (MPa)	4.8549	1.6657	1.5279
Error Ψ (%)	0.3872	0.2732	0.3394
Error on n_o (%)	1.730	1.673	1.485

6. CONCLUSIONS

As stated in the introduction of the paper, light generation at the nano-level is one key in the process of making optical measurements at the nano-range. In the case analyzed in this paper, the light generation occurs by a complex process involving several fundamental aspects.

- 1) Creation of excitation or forcing function $F(t)$ by generating diffraction orders via evanescent light fields.
- 2) Presence of a resonator, in this case a Fabry-Perot interferometer, that provides the mechanism of linkage between two medias, glass slide and saline solution.
- 3) Introduction of a medium, in this case the saline solution, capable of generating propagating waves from the excitation generated by the evanescent fields.

The presence of a resonator is a fundamental step in the process of creating sub-wavelength light fields. The resonator produces eigen-modes that are localized in the space. The localization of modes in this example was implemented by a simple mirror-cavity-mirror structure. The resonator must be a leaking resonator because its role is to transmit energy from the evanescent fields to a medium capable to convert evanescent field electromagnetic waves to light propagating waves.

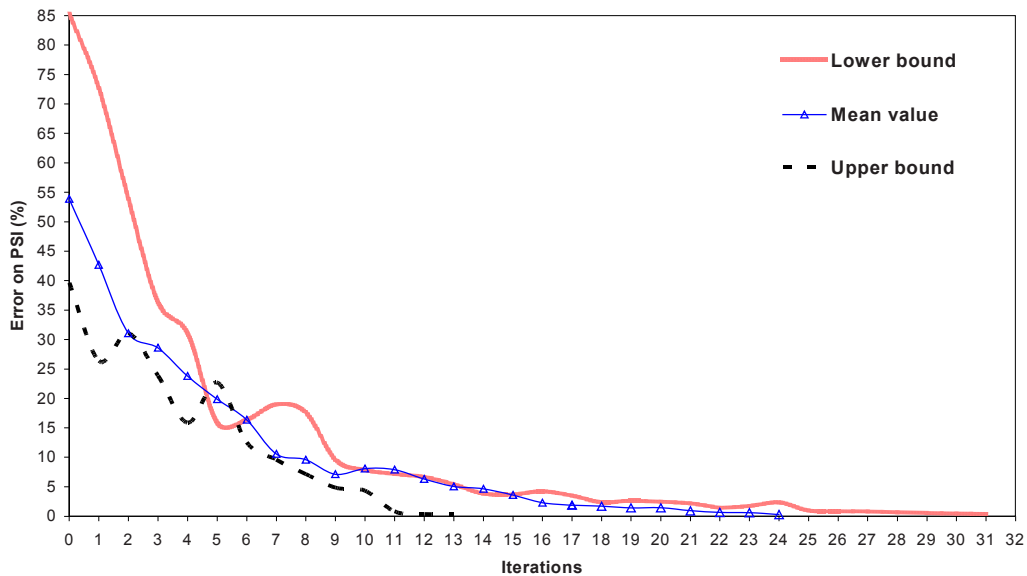


Figure 8. Convergence curves for different optimization runs

Through the above presented analysis we have successfully supported the model of conversion of evanescent field energy into propagating light energy. The analysis relates the pitch of the observed fringes and the residual stresses at the boundary between the glass prism and the glass microscope slide. The solution shows two principal stresses that are almost equal as it should be in the case of a rectangular block of glass cooled down from the molten state to room temperature. Away from edges the residual stresses are equal in magnitude and both compressive as was found by optimization. The numerical values of the residual stresses are low and well within acceptable limits. The photoelastic constants of the glass are also of the correct magnitude and very close to the values found in the literature for glass. The optimization process has been a fundamental and powerful tool to verify that the model can predict successfully the observed phenomena.

7. REFERENCES

- [1] Sciammarella C.A. "Experimental mechanics at the nanometric level", *Strain* **44**: 3–19, 2008.
- [2] Sciammarella C.A., Lamberti L., and Sciammarella F.M. "The equivalent of Fourier Holography at the nano-scale", *Experimental Mechanics* **49**: 747–773, 2009.

- [3] Sciammarella C.A., Lamberti L., Sciammarella F.M., Demelio G.P., Dicuonzo A. and Boccaccio A. "Application of plasmons to the determination of surface profile and contact strain distribution". *Strain*, 2010. *In Press*.
- [4] Sciammarella F.M., Sciammarella C.A., Lamberti L. and Burra V. "Industrial finishes of ceramic surfaces at the micro-level and its influence on strength". SEM Annual Conference & Exposition on Experimental & Applied Mechanics, June 7–10, 2010, Indianapolis, Indiana.
- [5] Guillemet C. *L'interférométrie à ondes multiples appliquée à détermination de la répartition de l'indice de réfraction dans un milieu stratifié*, PhD Dissertation, Faculté de Sciences, University of Paris, Imprimerie Jouve, Paris (France), 1970.
- [6] Davies C.C. *Laser and Electro-Optics: Fundamentals and Engineering*. Cambridge University Press, Cambridge (UK), 2002.
- [7] Vanderplaats GN. *Numerical Optimization Techniques for Engineering Design*. VR&D Inc., Colorado Springs (USA), 1998.

Mechanical Characterization of Nanowires Using a Customized Atomic Force Microscope

Emrah Celik, Ibrahim Guven and Erdogan Madenci*

Aerospace and Mechanical Engineering, The University of Arizona, Tucson, AZ, 85721, USA

* E-mail: madenci@email.arizona.edu, Phone: 1-520-621-6113, Fax: 1-520-621-8191

Abstract

A new experimental method is introduced in order to characterize the mechanical properties of metallic nanowires. An accurate mechanical characterization of nanowires requires the imaging with scanning electron microscope (SEM) and the bending of nanowires with an atomic force microscope (AFM). In this study, an AFM is located inside an SEM in order to establish the visibility of the nanowires. The tip of the AFM cantilever is utilized to bend and break the nanowires. Nanowire specimens are prepared by electroplating of metal ions into the nanoscale pores of the alumina membranes. The mechanical properties are extracted by using existing analytical formulation along with the experimental force versus bending displacement response. Preliminary results revealed that copper nanowires have unique mechanical properties such as high flexibility in addition to high strength compared to their bulk counterparts.

1. Introduction

Nanowires offer broad range of applications due to their unique properties especially in the fields of nano-electronics and computing technology. Mechanical characterization of nanowires is necessary in order to establish the feasibility of replacement of current electrical, mechanical and optical devices with nanowire integrated devices based on the reliability requirement. Although the characterization of electrical and optical properties of different types of nanowires has been studied extensively, mechanical characterization of nanowires still poses challenges to many existing testing and measurement techniques because of their small length scale. Manipulation and installation of individual nanowires in a test setup is rather challenging. Therefore, new mechanical characterization methods must be developed to quantify the mechanical properties of these nanostructures.

Existing nanowire mechanical characterization techniques in the literature can be grouped as: 1) resonation of nanowires in an electron microscope, 2) mechanical characterization via axial loading and 3) bending of nanowires using atomic force microscope. The first technique involves the oscillation of nanowires inside an electron microscope by applying alternating voltage and examining the corresponding natural frequencies of nanowires [1-4]. Frequencies are then related to elastic properties. Although this method is easy to perform, it is limited only to elastic properties of nanowires. Therefore, the yield and failure stresses, deformation and defect initiation mechanisms cannot be obtained. Mechanical characterization of nanowires has been performed by applying axial loading as well [5, 6]. In this method, nanowires or nanotubes are clamped in between two cantilevers and subjected to tension or compression loads in electron microscope. This technique requires significant amount of specimen preparation time and is not practical for testing of high number of nanowire specimens. The last group of mechanical characterization techniques involves bending of nanowires by using the tip of a commercially available AFM cantilever and this technique has been used successfully by several researchers [7-9]. However, commercial AFMs used in these studies are not capable of real time imaging of nanowires during testing. The correct alignment of nanowires according to AFM test probe poses a challenge due to the lack of nanowire visibility during testing. Also, deformation mechanism of nanowires cannot be investigated during testing. Therefore, there is a need for a new testing technique for mechanical characterization of nanowires that provides coexistence of two components of experimental analysis which are imaging and mechanical testing. A custom AFM placed in SEM for improved visibility can satisfy this requirement.

This study presents a new experimental test setup for bending test of nanowires involving a custom AFM and a SEM. The AFM is placed inside the chamber of the SEM; this high magnification imaging capability allows for correct alignment and placement of the specimens. Metallic nanowires with different sizes are fabricated using electroplating technique that employs membrane templates with nanoholes. Bending deformation measurements of nanowires concern different materials in different sizes.

2. Materials and Methods

2.1 Specimen Preparation

Metallic nanowire specimens are prepared by electro-deposition of metal ions into nanopores of commercially available Whatman alumina membranes. Up to date, only copper nanowires have been grown in porous membranes with 200 nm pore diameter with this technique. A thin layer of metal is deposited on one side of the alumina membrane as a contact layer into which the nanowires grow. During electroplating, copper ions existing in electrolyte solution (0.5 M CuSO_4) are deposited into the nanopores of the alumina membrane cathode. For the electroplating of copper, cathode voltage is set to -0.1 mV relative to the reference electrode and deposition duration is varied between 5 to 30 minutes which results in the deposition of nanowires in different lengths. After the nanowires are electroplated into the alumina membrane, the membrane is dissolved in 3M NaOH solution for 1 hour. Then, nanowires attached to the bottom metal layer are washed with distilled water and dissolved in

toluene in ultrasonic bath. The vibration in the bath breaks the bonds between the nanowires and the thin metal layer and a homogenous distribution of nanowires in toluene is obtained. Nanowires dissolved in toluene solution are then spread over a silicon substrate. The substrate involves pre-etched trenches with the thickness range of 5 μm to 10 μm and the depth of 5 μm . After evaporation of toluene, some of the nanowires are suspended on the trenches and used for mechanical testing. Nanowires suspending over trenches must possess the mechanical support or clamping conditions necessary for the bending tests. The clamping can be obtained by conformal deposition of a thin metal layer over all nanowires. The deposited thin metal film glues the nanowires to silicon substrate and provides them mechanical support for the mechanical testing. After the nanowire specimens are prepared and clamped over the trenches of silicon substrate, they are tested using a custom AFM located inside a SEM chamber.

2.2 Experimental Setup

The experimental setup combines the mechanical testing ability of AFM with imaging capability of SEM. The concept of locating a custom made AFM inside a SEM chamber is shown in Fig. 1.a. The detailed view of the custom AFM is given in Fig. 1.b. Main components of the setup are numbered in Fig. 1.b as follows:

- | | |
|----------------|-------------------------|
| 1. AFM head | 5. Piezoactuator |
| 2. Micromotor | 6. Mirrors |
| 3. Laser diode | 7. Manual control knobs |
| 4. Photodiode | |

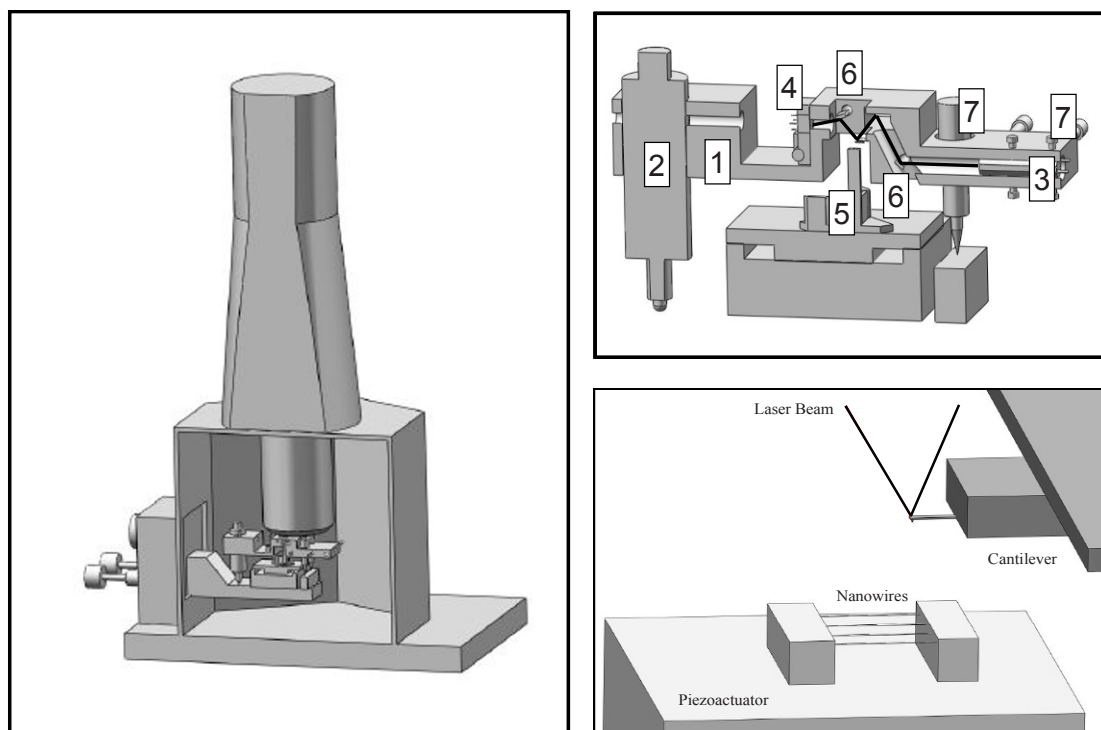


Figure 1. Experimental setup for mechanical testing of nanowires

a) Location of AFM inside SEM chamber, b) Custom AFM design, c) Details of AFM cantilever and nanowires

Electronic components (Micro motor, laser diode, piezoactuator and photodiode) are connected to a computer via National Instruments (NI) data acquisition boards. NI's Labview software is utilized in order to acquire photodiode signal and to control micromotor, laser diode and piezoactuator from outside the SEM chamber. The laser beam is used to monitor the deflection of the AFM cantilever during mechanical testing. In Fig. 1.b, the path of the laser beam from laser source to the photodetector is sketched. The laser beam is reflected by two mirrors before reaching the AFM cantilever. The third reflection of the laser occurs at the back of the cantilever and the reflected beam is directed to the final mirror before reaching to the quadrant photodiode.

After the laser beam is positioned at the intended position of the photodiode, the nanowires located on the piezoactuator are aligned with respect to the AFM cantilever. Then, the AFM cantilever is lowered by using the micromotor (Part No. 2 in Fig. 1.b) controlled by Labview software until the vertical position of the AFM tip is lower than the nanowire plane. At this stage of the test, AFM cantilever and the nanowires are brought side by side without touching each other. The positions of the AFM cantilever and the laser beam on photodiode at this instant are sketched in Fig. 2.a. After the vertical alignment is completed, the piezoactuator and the sample are moved towards the AFM tip, perpendicular to the nanowire axis establishing physical contact and causing the bending of the nanowires at the contact point by AFM tip. The lateral force acting between the nanowire and the AFM tip results in twisting of the cantilever and therefore changes the position of the laser beam on photodiode (Fig. 2.b). The continuation of piezoactuator movement and hence, the application of further load causes the nanowire to fracture and the laser beam goes back to original non-contact position on photodiode (Fig. 2.c).

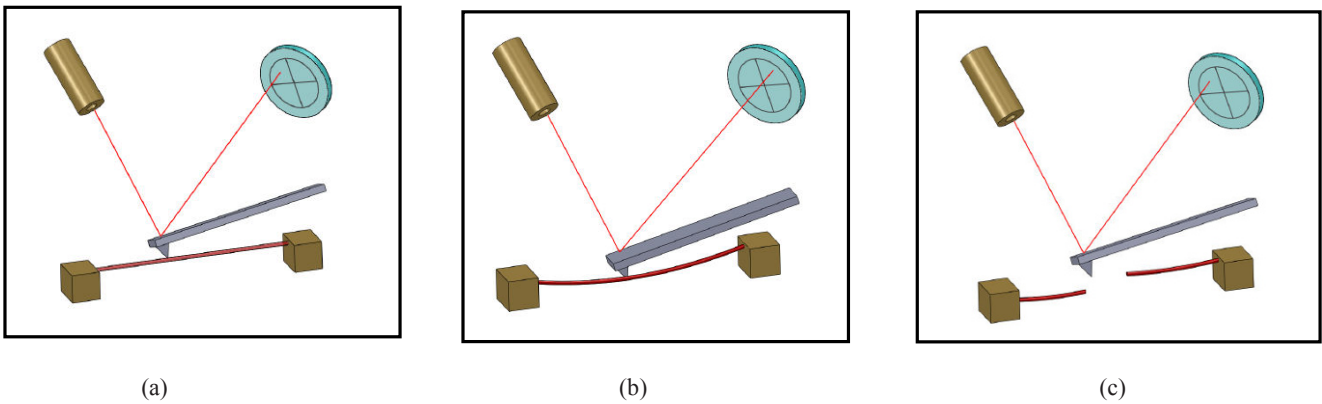


Figure 2. Nanobending experiment using AFM. a) Initial untouched state b) Contact state c) Nanowire failure

The change in the deflection of the AFM cantilever and the position of the laser beam on photodiode leads to change of the photodiode voltage. Therefore, the change in deflection of the AFM cantilever as a function of the total piezoactuator movement can readily be obtained. This data are converted into the data of force versus bending displacement of the nanowires in order to extract mechanical properties. The force exerted on nanowires can be obtained by multiplying the lateral deflection and the lateral stiffness of the AFM cantilever as given by Eq. (1).

$$F = k \times \delta_{cantilever} \quad (1)$$

where k is lateral stiffness and $\delta_{cantilever}$ denotes the lateral deflection of the AFM cantilever. The lateral stiffness of the cantilever is obtained by using the dimensions and the shear modulus of the AFM cantilever as given in Eq. (2) derived by [10].

$$k = \frac{Gwt^3}{4L_c^2l} \quad (2)$$

where G is the shear modulus of cantilever material and w , t , L_c , l are width, thickness and the length of the cantilever and l denotes the length of the AFM cantilever tip. The displacement of the piezoactuator during the experiment results in bending of the nanowire as well as deflection of the AFM cantilever. Therefore, in order to obtain bending displacement of the nanowire at the contact point, piezo displacement is subtracted from the deflection of the cantilever as follows

$$\delta_{bending} = \delta_{piezo} - \delta_{cantilever} \quad (3)$$

where $\delta_{bending}$, δ_{piezo} and $\delta_{cantilever}$ represent bending displacement, piezo displacement and cantilever deflection, respectively. By using Eqs. (1) and (3), deflection-piezo displacement data can be converted into force versus bending displacement data. After obtaining force versus bending displacement relationship experimentally, the analytical relations are utilized to extract mechanical properties of the nanowires.

2.3 Extracting Mechanical Properties Using Analytical Relations

In linear beam bending theory, the force acting on the mid-section of a double clamped beam is related to the bending displacement at the same location as follows

$$F = \frac{192EI}{L^3} \delta_{bending} \quad (4)$$

where E , I , L are Young's modulus, moment of inertia and length of the clamped portion of the beam. Therefore, the force is assumed to change linearly as a function of bending displacement. However, if the deformation of the nanowire beam is much larger than the diameter of the beam, the axial tensile force acting on the beam becomes significantly important which leads to the enhancement of nanowire rigidity [11] and nonlinearity in force versus displacement variation. For the case of large deformation of the nanowire beam, Eq. (4) takes the form below;

$$F = \frac{192EI}{L^3} \left(\frac{\alpha}{48 - \frac{192 \tanh(\sqrt{\alpha}/4)}{\sqrt{\alpha}}} \right) \delta_{bending} \quad (5)$$

The variable α is related to the bending displacement via the transcendental equation (6).

$$\frac{\alpha \cosh^2(\sqrt{\alpha}/4)}{2 + \cosh(\sqrt{\alpha}/2) - \frac{6 \sinh(\sqrt{\alpha}/2)}{\sqrt{\alpha}}} \left(1 - \frac{4 \tanh(\sqrt{\alpha}/4)}{\sqrt{\alpha}} \right)^2 = \delta_{bending}^2 \left(\frac{A}{I} \right) \quad (6)$$

An approximate solution for the Eq. (5) is given by [11] by superimposing the small and large deflection limits. The equation of approximate solution having maximum error of 18% is given in Eq. (8) as.

$$F = \frac{192EI}{L^3} \delta_{bending} \left(1 + \frac{A}{24I} \delta_{bending}^2 \right) \quad (7)$$

An approximate solution given in Eq. (7) is used in this study in order to analyze the mechanical properties of the nanowires. The elastic limit of the nanowires can be estimated by using the linear and nonlinear analytical equations described above. The plastic zone is achieved after which the force versus bending displacement curve starts deviating from the predicted responses defined by Eqs. (4) and (7). The force at the deviation location is defined as the yielding force and at this point the yield stress can be described as follows according to [12].

$$\sigma_y = \frac{F_y L}{4\pi r^2 \delta_y} \quad (8)$$

where r denotes the nanowire radius and F_y and σ_y are yielding force and yield stress respectively. δ_y is the bending displacement at the yield point. Similarly ultimate stress can be calculated by the equation described [12].

$$\sigma_u = \frac{F_u L}{4\pi r^2 \delta_u} \quad (9)$$

where F_u , δ_u and σ_u are force, bending displacement and the ultimate stress at the failure point, respectively.

3. Results

Bending displacement versus force relations obtained in four independent tests on copper nanowires are given in Fig. 3. According to these results, the force increases nonlinearly and decreases rapidly after the fracture of nanowires. The fracture points where the maximum force is achieved are marked by the arrows in the figure.

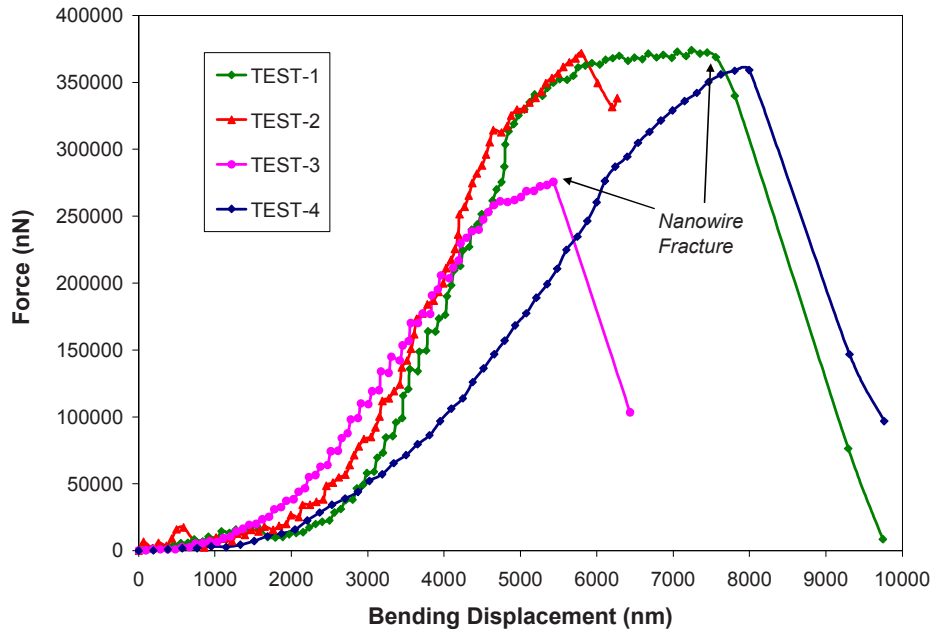


Figure 3. Force versus bending displacement variation of copper nanowires.

In order to extract elastic modulus, force-bending displacement response of the nanowires obtained experimentally was compared against the predicted response described by Eq. (7). The elastic modulus values were obtained by matching the experimental and the predicted values. An example of the comparison between two data is given in Fig. 4. Force versus bending displacement data shows a remarkable agreement with the analytical model until the nanowire starts yielding, and the two responses deviate from each other.

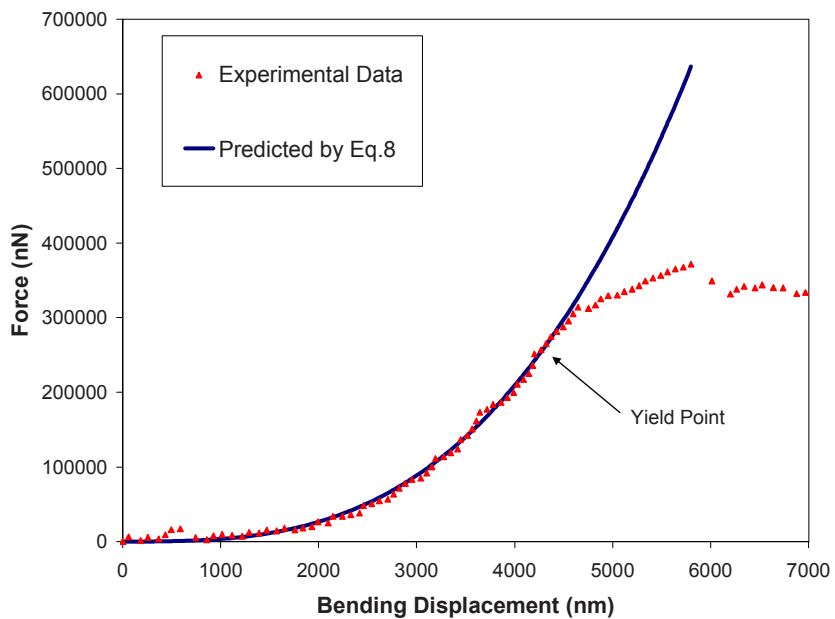


Figure 4. Comparison between experimental data and predictions.

The elastic modulus values for copper nanowires with 200 nm diameter were obtained between 2 to 3.5 GPa with an average of 2.7GPa. The elastic modulus of bulk copper is given as 110 GPa in the literature. The elastic moduli of the nanowires tested have been observed to be significantly lower than that of the bulk material. In other words, copper nanowires are much more flexible than their bulk counterparts.

The yield stress values were calculated by using the Eq. (8) in four different tests and the results are given in Fig. 5. As captured in this figure, the yield stress of copper nanowires with 200 nm diameter was obtained between 1.01 and 3.09 GPa with an average value of 2.3 GPa. The yield stress of bulk copper is given in the literature as 55-300 MPa which is represented by the horizontal rectangular area in Fig. 5. The average value of yield stress obtained in four tests is nearly an order of magnitude larger than the yield stress of the bulk copper.

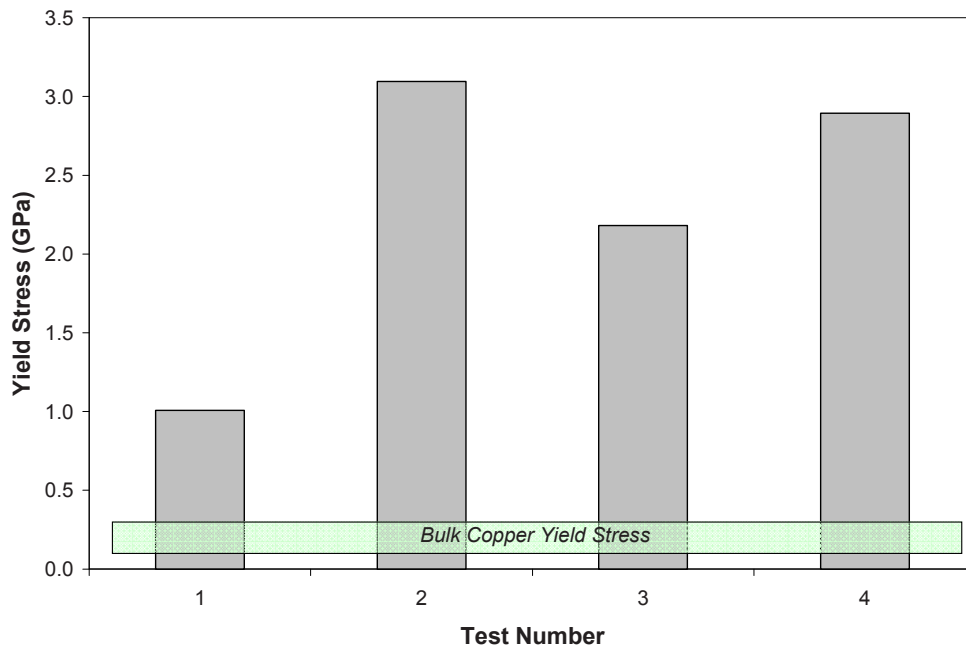


Figure 5. The yield stress of the nanowires calculated by Eq. (8).

The ultimate stress values of the nanowires were calculated by using Eq. (9) and the experimental data shown in Fig.3. The variation of ultimate stress values is given in Fig.6 for the four tests completed. According to this figure, the ultimate stress of copper nanowires were obtained between 2.32 and 3.31 GPa with an average value of 2.83 GPa. The ultimate stress of bulk copper is given in the literature as 230-380 MPa as shown in Fig. 6. The average value of ultimate stress obtained in this study is also an order of magnitude larger than the ultimate stress of bulk copper.

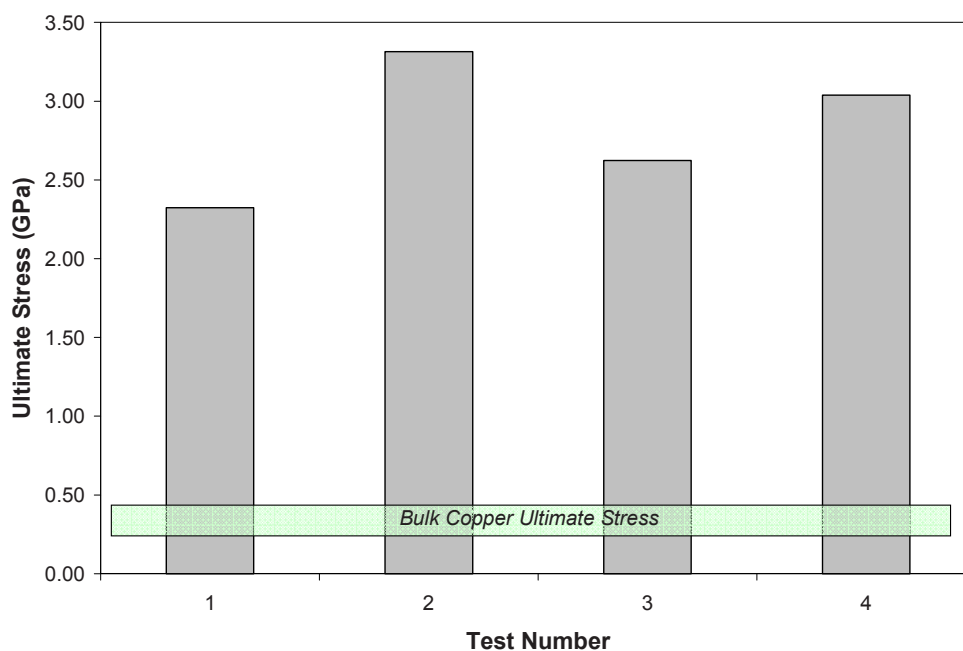


Figure 6. The Ultimate stress of the nanowires calculated by Eq. (9).

4. Conclusions

The preliminary results indicate that the elastic modulus (2.7 GPa) for copper nanowires with 200 nm diameter is significantly lower than that of the bulk material (110 GPa). Although, the copper nanowires are much more flexible than their bulk counterparts, the yield and ultimate strengths have been observed to be an order of magnitude higher than those of the bulk copper. Higher mechanical strength can be explained due to reduced defect density at nanoscale compared to the bulk scale [9]. These unique mechanical properties of copper nanowires make them excellent candidates for the future generation nanowire applications because material flexibility is desirable in addition to the high mechanical strength for many applications such as flexible electronics.

References

1. Wang, Z. L., Mechanical properties of nanowires and nanobelts, Dekker Encyclopedia of Nanoscience and Nanotechnology, pp.1773-85, 2004.
2. Liu. K. H., Wang W. L., Xu Z., Liao L., Bai X. D., and Wang E. G., In situ probing mechanical properties of individual tungsten oxide nanowires directly grown on tungsten tips inside transmission electron microscope, Applied Physics Letters, Vol. 86, 22908, 2006.
3. Huang Y., Bai X. and Zhang Y., In situ mechanical properties of individual ZnO nanowires and the mass measurement of nanoparticles, Journal of Physics: Condensed Matter, Vol. 18, pp. L179-84, 2006.

4. Chen C. Q., Shi Y., Zhang Y. S., Zhu J., and Yan Y. J., Size dependence of Young's modulus in ZnO nanowires, *Physical Review Letters*, Vol. 96, 075505, 2006.
5. Yu M. F., Lourie O., Dyer M. J., Moloni K., Kelly T. F., Ruoff R. S., Strength and Breaking Mechanism of Multiwalled Carbon Nanotubes Under Tensile Load, *Science*, Vol. 287, pp. 637-640, 2000.
6. Lin C.H., Chang M., Li X. and Deka J.R., Measurement of Mechanical Properties of Boron Nanowire Using Nanomanipulation System, *Proceedings of the 35th International MATADOR Conference*, pp.275-278, 2007.
7. Paulo S., Bokor J., Howe R. T., He R., Yang P., Gao D., Carraro C., and Maboudian R., Mechanical elasticity of single and double clamped silicon nanobeams fabricated by the vapor-liquid-solid method, *Applied Physics Letters*, Vol. 87, 053111, 2005.
8. Ni H., Li X., and Gao H., Elastic modulus of amorphous SiO₂ nanowires, *Applied Physics Letters*, Vol. 88, 043108, 2006.
9. Wu B., Heidelberg A. and Boland J. J., Mechanical properties of ultrahigh-strength gold nanowires, *Nature Materials*, Vol. 4, pp. 525-9, 2005.
10. Schwarz U. D., Ster P. K., and Wiesendanger R., Quantitative analysis of lateral force microscopy experiments, *Rev. Sci. Instrum.*, Vol. 67 (7), 1996.
11. Heidelberg A., Ngo L. T., Wu B., Phillips M. A., Sharma S.,[‡] Kamins T. I., Sader J. E., and Boland J. J., A Generalized Description of the Elastic Properties of Nanowires, *Nano Letters*, Vol. 6, No. 6, pp. 1101-6, 2006.
12. Ngo L. T., Almecija D., Sader J. E. Daly B., Petkov N., Holmes J. D., Erts D., and Boland J. J., Mechanical properties of individual electrospun polymer-nanotube composite nanofibers, *Carbon*, vol47, pp. 2253-8, 2008.

Blast Performance of Sandwich Composites with Functionally Graded Core

Nate Gardner and Arun Shukla

Dynamic Photomechanics Laboratory, Dept. of Mechanical Engineering & Applied Mechanics
 The University of Rhode Island, 92 Upper College Road, Kingston, RI, 02881, USA

INTRODUCTION

Sandwich structures have important applications in the naval and aerospace industry, especially when they are subjected to high-intensity impulse loadings such as air blasts. During this event, the core materials play a vital role in the dynamic behavior of the sandwich structure. Since the material properties of a functionally graded/layered core can be designed and controlled, they show great potential to be an effective core design for absorbing the blast energy and improving the overall blast response of the sandwich structure. In this paper, an experimental investigation focuses on the blast resistance of sandwich composites with a functionally graded foam core subjected to shock wave loading. Four types of sandwich composites with a foam core graded/layered based on monotonically increasing the core layer wave impedance, while varying the number of core layers, have been studied. The experimental results show that monotonically increasing the core layer wave impedance while increasing the number of core layers, greatly reduces the wave impedance mismatch between consecutive layers and improves the overall blast resistance of the structure.

MATERIAL AND SPECIMEN GEOMETRY

The skin materials were E-glass Vinyl-ester (EVE) composites, which consisted of woven roving E-glass fibers (18 oz/yd² areal density plain weave) placed in a quasi-isotropic layout [0/45/90/-45]_s. The core materials were Corecell™ A series styrene foams, which were manufactured by Gurit SP Technologies. The four types of Corecell™ A series foam that were used were A300, A400, A500, and A800 with a theoretical elastic wave impedance of 740 m/s, 770 m/s, 835 m/s, 885 m/s respectively. The sandwich panels had dimensions of 102 mm wide, 254 mm long with 5 mm front and back skins, with individual core layer thickness of 19mm (.75in), 19mm (.75in), 13mm (.5in) and 9.375mm (.375in) for one, two, three and four layer core gradation respectively. Due to the brevity of space available only one and four layer core gradation will be presented in this paper.

Fig. 1 shows the two core configurations and the shock wave loading direction.

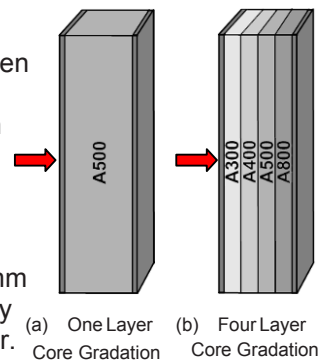


Fig. 1 Two of the four core configurations and shock wave loading direction

EXPERIMENTAL PROCEDURE

A shock tube apparatus was used to generate a controlled shock wave loading of approximately 1 MPa. The shock tube apparatus, along with detailed dimensions and locations of the muzzle, specimen, supports and pressure transducers are shown in **Fig. 2a** and **2b** respectively. Pressure transducers are mounted at the end of the muzzle section to measure the incident and reflected pressures during the experiment. The specimen was placed in the support fixture, which ensured simply supported boundary conditions and placed within 1.5 mm of the muzzle end. Three high-speed digital cameras were used, one to capture the real time side-view deformation and two for digital image correlation (DIC) on the back face of the sandwich structure. All three cameras were operating at 20,000 fps with an interframe time of 50 μs.

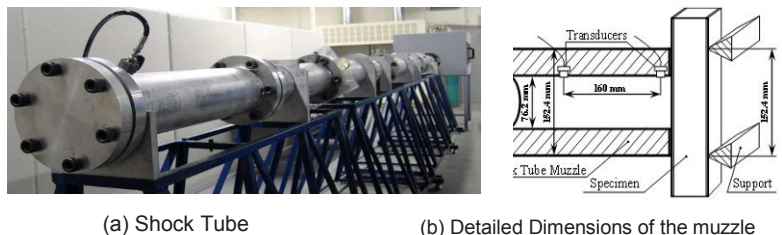


Fig. 2 Shock Tube apparatus

EXPERIMENTAL RESULTS AND DISCUSSION

The real time observation of the transient behavior and response of the core layer arrangements under shock wave loading are shown in Fig. 3. For the sandwich composites with one layer core gradation, the main deformation mechanism was bending. Core compression was evident in the first core layer followed by two large shear cracks propagating from the back face towards the front face. Finally, delamination between the homogeneous core layers, as well as between the front face sheet and core is evident.

For the sandwich composites with four layers of core gradation, the main failure mechanisms were core compression and bending. With the ability to compress in a stepwise manner, the core shear cracks took longer to initiate and were not as prominent. Delamination did occur in this composite as well, but again it was not as extensive as it was in the sandwich composites with a one layer core gradation.

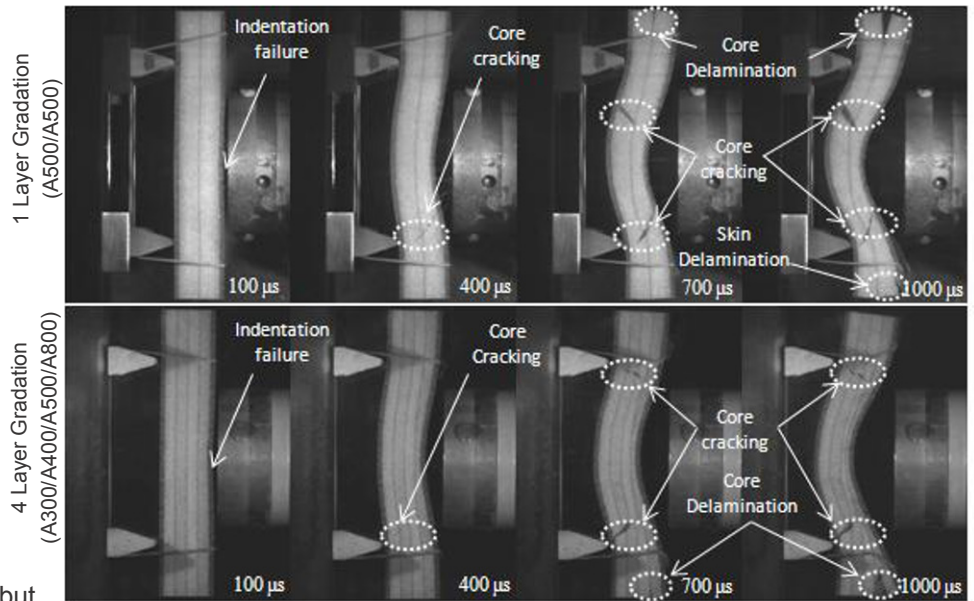


Fig. 3. Real Time Side View Deformation Under Shock Loading

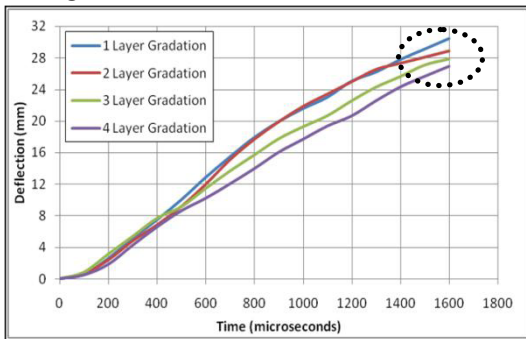
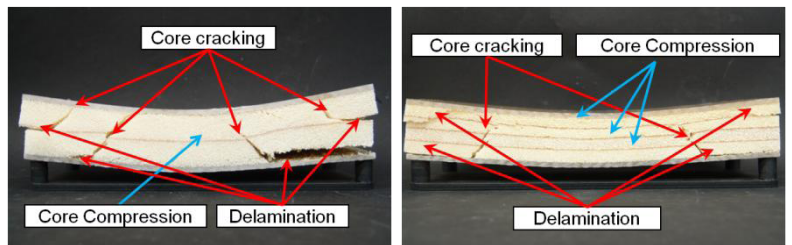


Fig. 4. Back Face Deflection for all Gradations



(a) One Layer Core Gradation (b) Four Layer Core Gradation

Fig. 5. Post Mortem Images of Sandwich Composites

Fig. 4 shows the back face deflections for all of the gradations. It can be observed that the back face of the sandwich composite with a one layer core gradation deflects 13% more than that of a sandwich composite with a four layer core gradation. The post mortem images of the damaged sandwich composites can be observed in Fig. 5. It can be seen that the one layer core gradation shows much heavier damage (delamination, core cracking, etc.). Overall, the sandwich composite with four layer core gradation experimentally outperformed the sandwich composite with one layer core gradation. Therefore it was concluded that monotonically increasing the core layer wave impedance while increasing the number of core layers, greatly reduces the wave impedance mismatch between consecutive layers and improves the overall blast resistance of the structure.

ACKNOWLEDGEMENT

The author kindly acknowledges the financial support of the Office of Naval Research (ONR) Grant No. N00014-04-1-0268 as well as the support provided by the Department of Homeland Security (DHS) under Cooperative Agreement No. 2008-ST-061-ED0002. The author also thanks Dr. Stephen Nolet and TPI Composites for providing the facility for creating the materials used in this study.

REFERENCES

[1] Wang, E., Gardner, N., and Shukla, A., 2009. The blast resistance of sandwich composites with stepwise graded core. International Journal of Solids and Structures 46 (18-19) 3492-3502.

Thermal Softening of an UFG Aluminum Alloy at High Rates

Emily L. Huskins*, K.T. Ramesh*

*Johns Hopkins University, 3400 North Charles St, Baltimore, MD 21218

ABSTRACT

In recent years there has been increased interest in ultra-fine grained (UFG) and nanocrystalline aluminum alloys due to their low density (1/3 that of steel). Failure of these materials often initiates at areas of localized deformation. It cannot be assumed that global temperature and strain rate conditions apply at these locations. In order to understand how reduced grain size and these localized conditions lead to failure we have tested UFG Al-5083 at both high strain rates (4000s^{-1}) and high temperatures (298K – 573K). Experiments were performed using a compression Kolsky bar modified for high temperature testing. It was found that while the microstructure of this UFG material is thermally stable, thermal softening has a significant effect on dislocation mobility.

INTRODUCTION

As the search continues for new lightweight, strong material many have looked towards development of aluminum alloys, specifically Al-5083 (Al-Mg-Mn). Current research on this alloy has focused on optimization of strength while maintaining ductility. Grain size refinement is the dominant strengthening mechanism and many works have looked at processing techniques to produce bulk material. Like their coarse grained counterparts, UFG aluminum alloys at high rates fail through adiabatic shear bands: during deformation large amounts of plastic work localizes and temperatures rise due to adiabatic conditions. The material in this region can no longer carry load; therefore, the ultimate failure of the bulk material is dependent on the local material response.

Room temperature testing of UFG aluminum alloys at high rates can be found throughout the literature; however these macro scale tests do not provide all the necessary information for modeling the deformation and failure. The goal of this work is to explore the mechanical response of UFG Al-5083 at both dynamic rates and high temperatures in order to resolve local thermal softening in UFG materials. More specifically, to determine for UFG materials what effects temperature has on strengthening mechanisms as well as strain hardening.

EXPERIMENTAL TECHNIQUE

One material was investigated in this work, Al-5083, which was cryomilled and Q1 forged at 250C. Dynamic compression tests were performed with a Kolsky bar to achieve strain rates of $4 \times 10^{+3} \text{ s}^{-1}$ over a temperature range of 289K-573K. The Kolsky bar consists of two metal bars, referred to as the input and output bars, which sandwich a cylindrical specimen with aspect ratio 0.5-1. A projectile strikes the input bar creating a compressive stress pulse that travels down the input bar and loads the specimen. Some of this incident pulse is reflected back while some is transmitted through the output bar where strain rate and stress information is determined respectively.

A modified Kolsky bar (Fig 1.) was used for high temperature testing. A K-type thermocouple is connected to the specimen and provides feedback to the power controller. The specimen is heated by an infra-red spot heater that can reach a final temperature in less than 60 seconds. The thermocouple wire also holds the specimen suspended 2mm from both the input and output bars. A bar actuator is triggered with a delay as the projectile is

fired. The actuator moves the input bar into contact with the specimen which therefore makes contact with the output bar. The time during which contact is made, but before the compressive stress pulse arrives, is called cold contact time and is maintained at 2-4 ms to reduce transfer of heat to the bars.

Three sets of experiments were performed on this material: A, B, and C. For A, samples were pre-heated to the desired temperature, held at temperature and tested at dynamic rates. For B, samples were pre-heated to the desired temperature, removed and let to cool back to room temperature, then tested at dynamic rates. For C, the same procedure as B is followed except samples are tested at QS strain rates (10^{-3} s^{-1}).

RESULTS AND DISCUSSION

In order to determine temperature effects on strengthening mechanisms and strain hardening it is best to view the problem from another angle. Thermal softening can occur two ways, by altering the microstructure during preheating (grain growth, annealing, etc) and through thermal activation of dislocations. Plastic deformation occurs as dislocation move through the crystal. Flow stress is determined by the strength of the obstacles which impede dislocation motion. Additional energy provided by increased temperature makes dislocations more mobile, therefore reducing the flow stress.

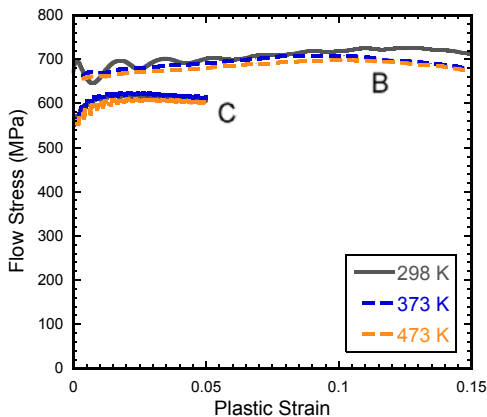


Fig. 2: Stress-strain curve of UFG Al-5083 preheated to different temperatures and tested at room temperature at QS and dynamic rates

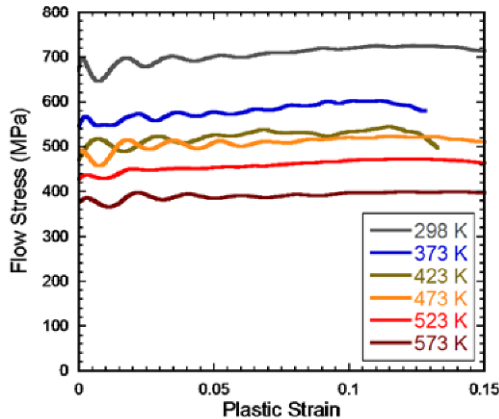


Fig. 3: Stress-strain curve of UFG Al-5083 tested at different temperatures at 4000 s^{-1}

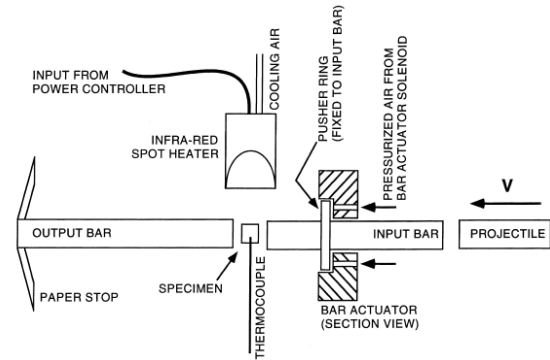


Fig. 1: Modified Kolsky bar setup to achieve high temperature dynamic compression tests

First, we examined thermal effects on the microstructure. Fig. 2 shows stress-strain plots for sets B and C. In both QS and dynamic testing there is no significant change in the stress-strain curves including little strain hardening. This has been verified by TEM of preheated, untested samples. The microstructure is therefore independent of preheating temperature. Fig. 3 show stress-strain plots for set A. The flow stress decreases with increasing temperature, while again the strain hardening remains nearly perfectly plastic. Sets B and C determined that the initial microstructures are the same; therefore variations in flow stress must be due to temperature effects during deformation.

Two conclusions can be made from these experiments regarding UFG Al-5083: The microstructure is thermally stable for preheating temperatures ranging from 373K-573K and thermal softening is due to thermal activation increasing dislocation mobility.

REFERENCES

1. Cao B *et al.*, Strengthening Mechanisms in Cryomilled Ultrafine Grained Aluminum Alloy at Quasi-static and Dynamic Rates of Loading, *Scripta Materialia*, vol. 60 iss. 8, pg:619-622, 2009.
2. Kim Y.G., *et al.*, Dynamic Deformation and Fracture Behavior of Ultrafine Grained Aluminum Alloy Fabricated by Equal Angular Pressing, *Met. and Mat. Trans. A*, vol. 36 iss. 11, pg: 2947-2955, 2005
3. Han B.Q., *et al.*, Processing and Behavior of Nanostructured Metallic Alloys and Composites by Cromilling, *Journal of Mats Sci.*, vol. 42 issue 5, pg: 1660-1672, 2007.

Blast Loading Response of Glass Panels

Puneet Kumar and Arun Shukla

Dept. of Mechanical, Industrial and Systems Engineering,
 The University of Rhode Island, 92 Upper College Road, Kingston, RI 02881, USA.

INTRODUCTION

Accidental explosions or bomb blast cause extreme loading on glass structures. This results in the shattering of glass panels. The shattered glass pieces have sharp edges and are moving at very high velocities. Most of the damage to humans is caused by these high velocity glass fragments. Apart from this, the blast pressure entering the building through the shattered window panels can also cause additional injuries to the occupants. Thus a controlled study has been performed to understand the physics behind the fracture and damage mechanisms in glass panels. This will enable us to reduce the shattering of the panels which in turn minimizes the injuries to the occupants.

EXPERIMENTAL SET-UP

The shock tube apparatus was utilized to obtain the controlled blast loading (fig. 1). It has an overall length of 8 m, consisting of a driver, driven and muzzle section. The high-pressure driver section and the low pressure driven section are separated by a diaphragm. By pressurizing the high-pressure section, a pressure difference across the diaphragm is created. When this difference reaches a critical value, the diaphragm ruptures. This rapid release of gas creates a shock wave, which travels down the tube to impart dynamic loading on the specimen.

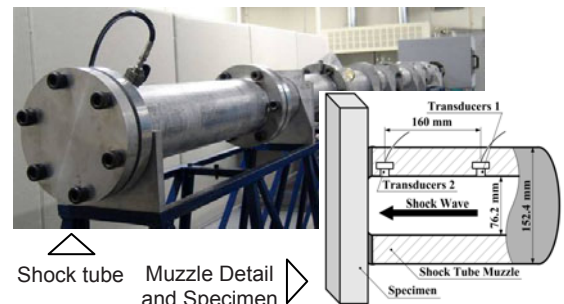


Fig. 1 Shock tube apparatus

Fig. 1 also shows detailed dimensions and locations of the muzzle, specimen, supports and the pressure sensors (PCB102A). The sensors are mounted at the end of the muzzle section to measure the incident pressure and the reflected pressure during the experiment. The final muzzle diameter is 0.0762 m (3 in). The distance between the two sensors is 0.16m and the distance between the second sensor and the end of the muzzle is 0.02m. The specimen was placed in the supports and positioned close to the end of the muzzle. These support fixtures ensure fully clamped boundary conditions as shown in fig. 2.

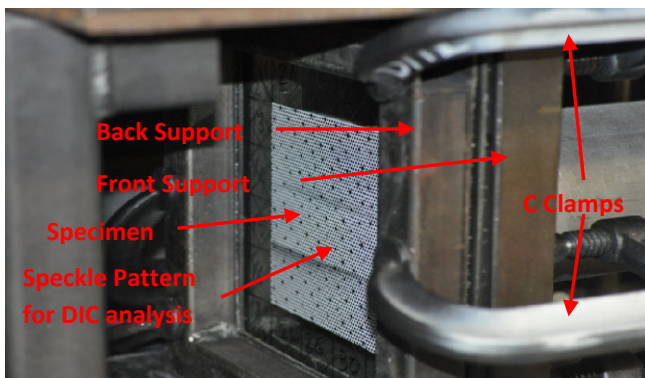


Fig. 2 Fixture and boundary conditions

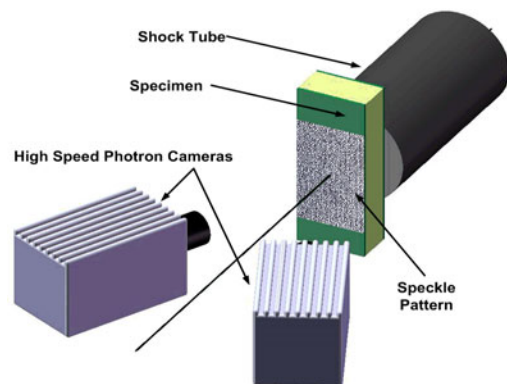


Fig. 3 Schematics of experimental set up

In the present study, a diaphragm of 2 plies of 0.005 mm thick mylar sheets was utilized to generate an impulse loading on the specimen with an incident peak pressure of approximately 0.5 Mpa and a wave velocity of approximately 820 m/s. Two high speed digital cameras, PHOTRON SA 1, were used to capture the real time back-view deformation of the specimen with an interframe time of 33 μ s. Fig. 3 shows the experimental setup. The high speed images captured from the cameras were utilized to perform Digital Image Correlation Analysis (DIC). For the purpose of the DIC analysis, the specimen was pre-speckled before the test as shown in fig. 2.

EXPERIMENTAL RESULTS AND DISCUSSION

Four different panels, namely plane glass, sandwiched glass, wired glass, and tempered glass were used in the experiments. The panels had a length of 304.8mm, width of 304.8mm and a thickness of 12.7mm. A fully clamped boundary condition was applied as shown in fig. 3. The typical experimental pressure profile is shown in fig. 4. Digital Image Correlation technique was used to obtain the deflection and strain in the four specimens. Due to brevity of space, the deflection plot over the surface for sandwich glass panel only, is shown in fig. 5. Other results will be presented during the meeting. The sandwich glass panel had a maximum deflection of 15 mm when the panel fractured, whereas it was 6 mm in the case of the tempered glass panel, 2 mm in the case of the wired glass panel and 1 mm in the case of the plane glass panel.

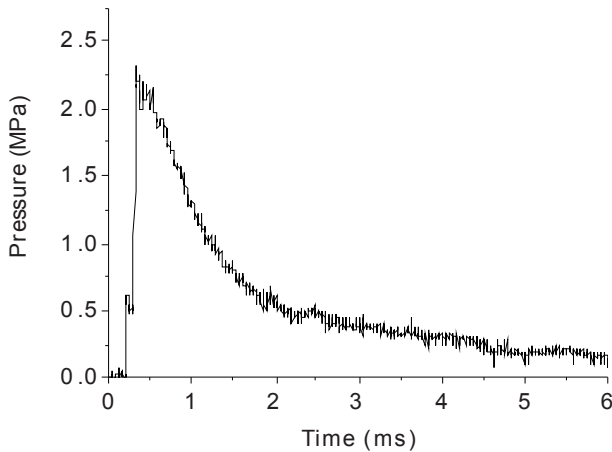


Fig. 4 Typical experimental pressure

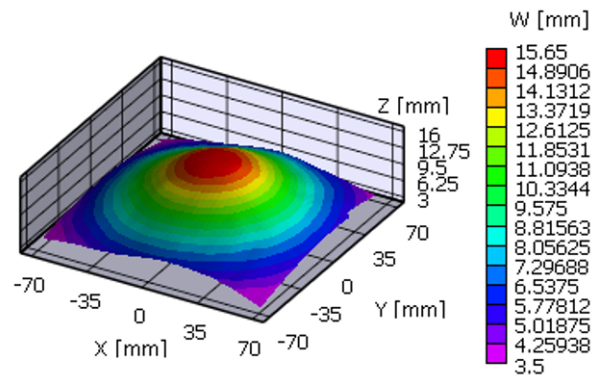


Fig. 5 Deflection profile in sandwich glass panel

The in-plane strain in sandwich glass panel is shown in fig. 6. The results for the other panels will be shown in the meeting. The sandwich glass panel had a strain of 5% before the fracture started, whereas in the case of tempered glass panel it was 2%, 1% for the wired glass panel and 0.01% for the plane glass panel. This shows that the sandwiched glass panel behaved in a more ductile manner as compared to the other glass panels. Also, the postmortem analysis of the four panels showed that the sandwiched glass panel had minimum shattering as compared to the other three glass panels. In the case of tempered and plane glass, the panel completely shattered into pieces. Thus the sandwiched glass panel had a better blast resistance as compared to the other three glass panels.

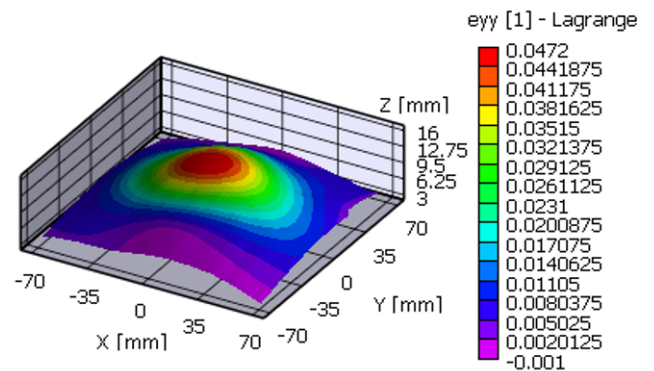


Fig. 6 In-plane strain in sandwich glass panels

ACKNOWLEDGEMENT

The support provided by the Department of Homeland Security (DHS) under Cooperative Agreement No. 2008-ST-061-ED0002 is acknowledged.

REFERENCES

[1] Wang E, Gardner N, and Shukla A. The blast resistance of sandwich composites with stepwise graded cores. International Journal of Solids and Structures, 46(18-19), 3492-3502, 2009.

Novel Approach to 3D Imaging Based on Fringe Projection Technique

Dung A. Nguyen
The Catholic University of America
620 Michigan Ave., Washington DC, 20064 USA

ABSTRACT

In recent years, three-dimensional (3D) imaging system based on Fringe Projection Profilometry (FPP) has been developed tremendously fast [1]. However, all current systems can provide either fast speed [2] or high accuracy measurement, but not both. In addition, very few of them can deal with multiple complex-shaped and separated 3D objects at real-time speed. This proposed paper presents a novel approach to a real-time FPP-based 3D imaging system that is able to handle multiple 3D objects at super high-speed, high-accuracy, and full-field measurement for practical applications, such as object detection, digital model generation, reverse engineering, rapid prototyping, product inspection, quality control, etc. The approach takes advantage of a special design for FPP-based 3D system that utilizes the color wheel mechanism of single chip projector to achieve real-time speed. Furthermore, multiple-frequency technique is fully developed to cope with multiple objects as well as to significantly increase the accuracy. The system with this approach is capable of imaging at 30 3D-views per second with an accuracy of 1/2,000 or 10 3D-views per second with a very high accuracy of 1/12,000.

System Design

Figure 1 shows a schematic design of the system. Every single-chip Digital Light Processing (DLP) has a color wheel between the lamp and the DLP chip. This color wheel is divided into four sectors, including three in primary colors of red (R), green(G), and blue(B), and a transparent colorless sector for enhancing the brightness of the projected image or video. When this color wheel is removed, gray scale images of R, G and B channels are projected instead of colorful composite images. So, by using a fast speed monochrome CMOS camera with suitable timing to capture all those gray scale images, in a single cycle, three different images can be captured if they are encoded respectively in R, G, and B channels and combined into a single source image. The synchronization is best done by an external circuit based on microcontroller. In this way, the speed of 3D measurement can be increased remarkably since there is no delay between projecting and capturing processes.

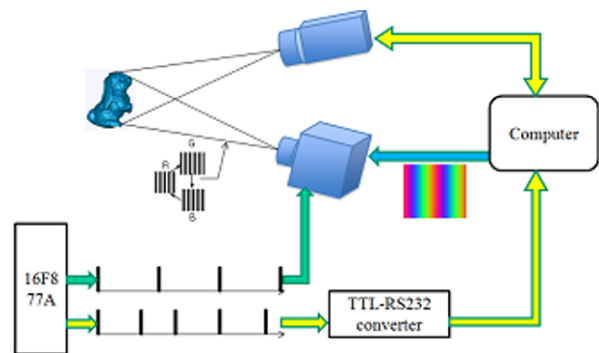


Figure 1. Schematic of the 3D imaging system

Multiple Frequency Approach

During the 3D measurement, a set of fringe patterns are projected onto the surfaces of the objects of interest. The surface height/depth information is naturally encoded into the distorted fringe patterns. FPP-based techniques generally employ phase shifting scheme to obtain the full-field wrapped phase distributions of the projection fringes. When the object or object system of interest involves complex shapes and/or multiple separated objects, the phases of the projection fringes on each object and among different objects are often discontinuous. This issue can be well addressed by using multi-frequency fringe projection approach, which uses fringes of various

frequencies (e.g., from one to tens of fringes in the field). The direct phase unwrapping approach based on multi-frequency fringe projection can obtain the full-field unwrapped phase distributions in an ultrafast manner and is suitable for measuring multiple objects with complex shapes without any additional processing. More details about multiple frequency approach and other advanced techniques involved can be found from our recent paper [3].

Experiments

Many experiments have been carried out to prove the validity and applicability of the approach. In those experiments, a DLP U4-Plus projector operating at 120 Hz and a 204 fps Epix SV643M camera are employed. Due to the limitation of the camera and computing performance at real-time speed, four projection cycles are needed to capture three phase-shifted images. The fastest speed that can be achieved is $120/4 = 30$ 3D views/s when single fringe frequency is used. At this speed, the relative accuracy of 3D shape measurement, which is defined as the ratio of depth-error to the width of the measured field, is $1/2,000$ or $0.5\text{mm}/1\text{m}$ for whole field measurement. For accuracy test, three different frequencies, 1, 9 and 27 fringes, are utilized to measure a 101.60 mm gage block. The measurement, which is operated at 10-3D views/s, indicates that the height of the is $101.65\text{mm} \pm 0.33\text{mm}$ with a standard deviation of 0.07mm over the block surface. So the relative accuracy is $(101.65\text{mm}-101.60\text{mm})/600\text{mm} = 1/12,000$. This high accuracy is very important for industrial applications.

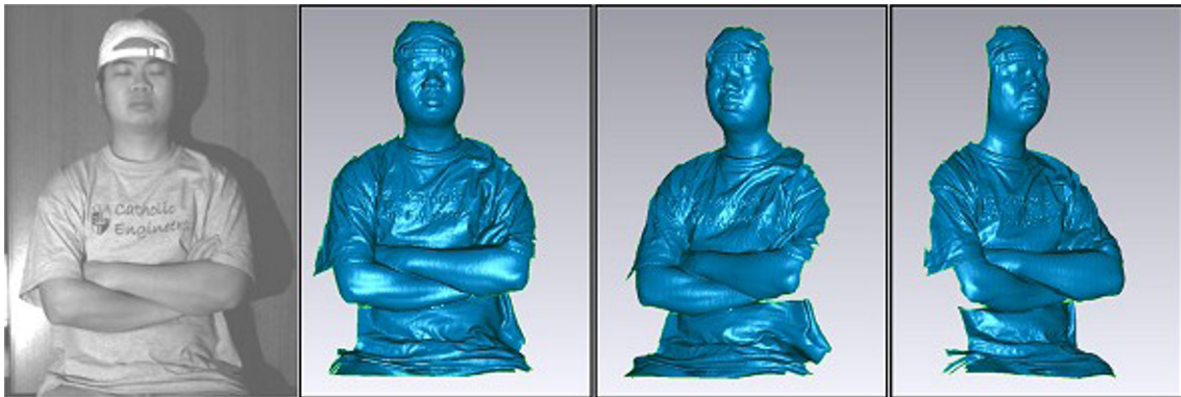


Figure 2. Demonstration of 3D shape measurement of a human body

To further prove the superior performance of the system, the 3D body measurement of a student is conducted. Figure 2 illustrates a representative result showing a single view at three different angles. This experiment shows the ability of measuring very complex object in a large area with relatively high accuracy and fast speed. In another attempt, eight different views of a Snoopy model have been captured; they are then easily combined to reconstruct a complete 360° 3D model, as shown in Figure 3.

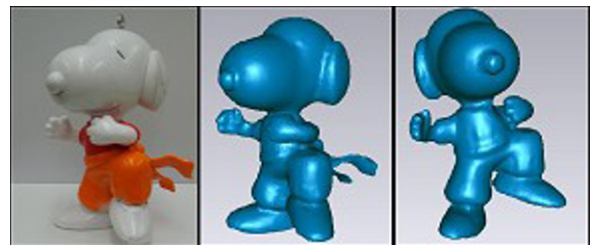


Figure 3. 360° reconstructed model of a Snoopy

Conclusion

This paper presents a novel approach to 3D imaging based on FPP. The proposed technique is capable of measuring 3D shape and deformation of complex objects at 30 3D-views/s with an accuracy of $1/2,000$ or 10 3D-views/s with an accuracy up to $1/12,000$.

Acknowledgments

This work was supported by National Science Foundation (under grant 0825806).

References

- [1] S. Gorthi and P. Rastogi, "Fringe projection techniques: Whither we are?," *Optics and Lasers in Engineering*, Vol. 48, 133–140, 2010.
- [2] S. Zhang and P. Huang, "High-resolution, real-time 3-D shape acquisition," *IEEE Computer Vision and Pattern Recognition Workshop*, Vol. 03, 28-35, 2004.
- [3] Z. Wang, D. Nguyen, J. Barnes, "Some practical considerations in fringe projection profilometry," *Optics and Lasers in Engineering*, Vol. 48, No. 2, 218-225, 2010.

Measuring Shear Stress in Microfluidics using Traction Force Microscopy

Bryant Mueller, University of Wisconsin–Madison, 1513 University Avenue, Madison WI 53706

INTRODUCTION

Traction force microscopy is a previously-developed method to measure shear forces exerted by biological cells on substrates to which they are adhered (Dembo, 1999). The technique determines the shear stress applied on the surface of a soft polymeric substrate with known mechanical properties by measuring the displacement of micron-scale beads or patterned markers embedded in the surface. Marker displacement is monitored by capturing images of the embedded beads in the substrate when a load is applied. The surface shear stresses can then be calculated from the measured displacement and known elastic properties of the substrate.

Measurements of shear stresses in microfluidic channels are essential for understanding and validating device designs. Traction force microscopy provides a new route to measure shear stresses in microfluidic channels and overcomes several limitations of existing shear stress measurement approaches. As the technique requires only a continuous polymeric layer on the channel wall, thermal sensors, pressure sensors, or other moving mechanical devices are not required to determine the shear stress. The relative simplicity of the technique translates to rapid, affordable device fabrication allowing customization to measure stresses with a range of magnitudes. A key advantage of traction force microscopy is that it allows both the magnitude *and* distribution of the shear stresses over an observed wall area to be quantified. Most other methods, in comparison, can only measure shear stress *magnitude* at a single location unless arrayed geometries are employed.

The objective of this work is to develop, implement, and evaluate a traction force microscopy method to characterize wall shear stress magnitude and distribution in polymer microfluidic channels.

METHODS

Figure 1 illustrates the overall microfluidic device design and the layer for measuring shear stresses. The microfluidic channel (**a**, see **Figure 1**) is bound by a glass cover slip at the base (**b**), coated with a thin layer of soft, controlled-stiffness PDMS (**c**), and closed at top and sides by a much stiffer PDMS channel (**d**). Shear stress applied by the fluid flow over the soft polymer layer on the channel bottom causes elastic deformation of the substrate and deformation of the surface resulting in displacement of the embedded fluorescent microbeads (**e**). The transparent substrate layer containing the beads is a cast, lightly cross-linked PDMS that has a low modulus (~500 kPa) and can be tailored to allow reasonable marker displacements for a range of applied shear stresses from 0 to 800 Pa. Fluorescent magnetic beads (1.6 μm in diameter) are embedded in the PDMS during casting and are pulled to the surface by a magnetic field during curing. Elastic modulus of the substrate is determined via tensile tests and AFM indentation measurements.

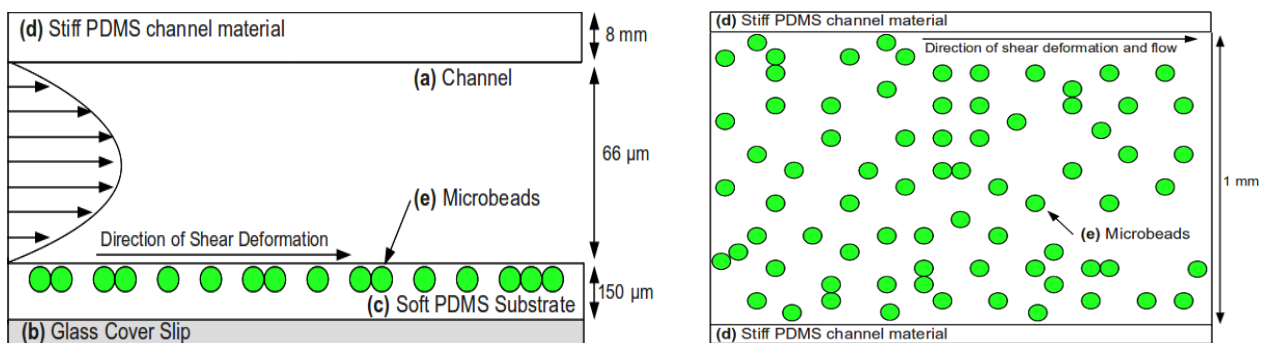


Figure 1: Side and top view of test device, relative dimensions not drawn to scale

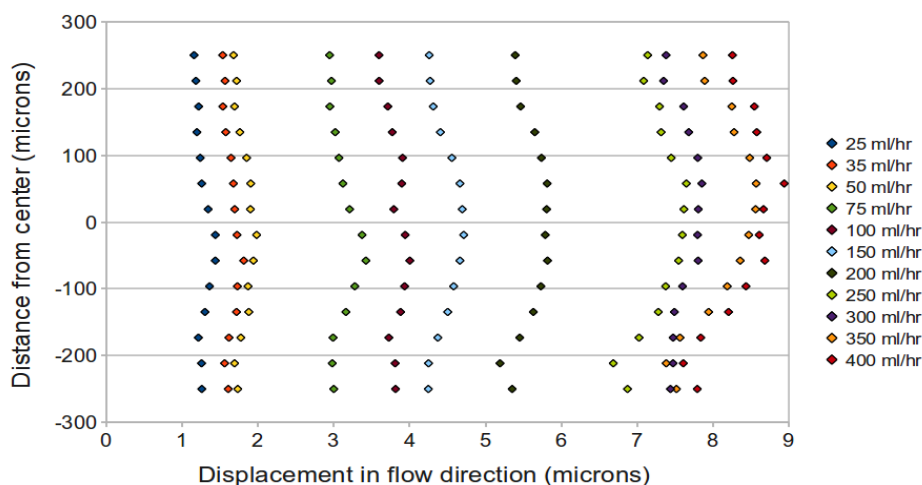


Figure 2: Marker displacement with flow rate in a channel with dimensions of Figure 1

In the experiments in this work, shear stresses are measured in the test device by supplying a defined flow rate and recording the marker displacement relative to the zero stress position. This is done for multiple flow rates. A syringe pump is used to achieve constant flow rates from 0 to 500 ml/hr. Images of the beads, captured by a digital camera fixed on an optical microscope with fluorescence capability and a 20x objective, are acquired at each flow rate as well as the relaxed starting condition. The acquired images capture the beads as shown in the top view of [Figure 1](#), allowing the in-plane displacements of a field of embedded beads to be tracked simultaneously. Following the image acquisition, the tracked bead displacements are calculated using a particle tracking algorithm in MATLAB. The program assigns a matrix of windows to the image, sectioning the image into multiple windows of controllable size. Displacements for each of these smaller windows are then individually calculated, outputting a displacement field over the entire image. The shear stress field for the simple test geometry is determined by comparing the calculated displacements to those from a finite element model of the device loaded with a range of appropriate stresses. In general, the shear stresses can be determined using linear elasticity theory with the substrate assumed to be an elastic isotropic halfspace (Schwarz, 2003).

RESULTS AND DISCUSSION

An example set of results from a test on a channel with dimensions listed in [Figure 1](#) illustrate a clear relationship between the applied flow rate and substrate displacement in the flow direction. [Figure 2](#) plots calculated marker displacement across the width of the channel for flow rates ranging from 25 to 400 mL/hr, with displacements ranging from about 1 to 9 μm in the flow direction. The observed 500 μm section of channel width is centered in the 1000 μm wide channel, 250 μm on each side of the channel center line.

CONCLUSIONS

In general, the marker displacement data from the example results of [Figure 2](#) agree with the expected behavior for the tested channel geometry, showing an increase in substrate displacement with increasing flow rates and shear stress. At high flow rates, the results show some non-linearity in the flow rate-to-displacement relationship, as well as an increase in displacement variation along the channel width. These trends, possibly attributable to compression of the substrate resulting from the high pressure required to drive the high flow rates, require further investigation.

REFERENCES

1. Dembo, M., and Wang, Y. "Stresses at the cell-to-substrate interface during locomotion of fibroblasts" *Biophysical Journal*. 76:2307-2316, 1999.
2. Schwarz, U.S., Balaban, N.Q, Rivelino, D., et al. "Measurement of cellular forces at focal adhesions using elastic micro-patterned substrates" *Materials Science and Engineering C*. 23:387-394, 2003.

Efficiency Enhancement of Dye-Sensitized Solar Cell

Chi-Hui Chien^{a,*}, Ming-Lang Tsai^a, Ting-Hsuan Su^a, Chi-Chang Hsieh^b, Yan-Huei Li^a,
Li-Chong Chen^a, Hua-De Gau^a

^aDepartment of Mechanical and Electro-Mechanical Engineering,
National Sun Yat-Sen University,
70, Lien-Hai Road, Kaohsiung 80424, Taiwan ROC

^bDepartment of the Mechanical and Automation Engineering,
National Kaohsiung First University of Science and Technology,

* Corresponding Author, chchien@faculty.nsysu.edu.tw

ABSTRACT

Thin nanoporous TiO₂ film with a metal-based light reflective layer was investigated in dye sensitized solar cell (DSSC). In cost-effective DSSC module, the thickness reduction of the nanoporous TiO₂ film was used to reduce the photoactive dye loading. However, the thin nanoporous TiO₂ film has poor light scattering ability so that the film is generally optical transparency, which means many transmitted light would be lost in the electrolyte solution. In order to improve the light scattering issue, we proposed a metal-based light reflective layer which was used on the thin nanoporous TiO₂ film to reflect the transmitted light readdressing in the film. The results show that the photovoltaic performance of DSSC was enhanced when using the metal-based light reflective layer.

Keywords: dye-sensitized solar cell; dye loading; nanoporous TiO₂ film; metal-based light reflective layer

1. Introduction

Photoactive dye in dye-sensitized solar cell (DSSC) [1,2] was the most key component since it controls the light-to-electricity operation and its price could be one of the decisive factors in determining the DSSC price. One solution in cost-effective DSSC module was the reduction of dye loading in working electrode. In reality, the dye loading is controlled by the thickness of nanoporous TiO₂ film because of decreasing the thickness of nanoporous TiO₂ film will decrease the surface area to absorb the dye [3]. Thus, a thin nanoporous TiO₂ film can be used to reduce the dye loading and meet the cost-effective DSSC, however, the thin nanoporous TiO₂ film has poor light scattering ability so that the film is generally optical transparency [4]. In order to improve the light scattering issue, a light scattering layer [4-8] has been used to scatter the transmitted light that allows a many part of transmitted light to be readdressed and rescattered in the thin nanoporous TiO₂ film. Nevertheless, the light scattering layer is generally formed by large size TiO₂ particles (d>100nm) or a mixture with different size particles, and the layer thickness must be controlled in several microns because the scattering layer thickness increases as the internal impedance increases [9-12] and the filling factor decreases [13,14] in DSSC thereby reducing the light-to-electricity

efficiency. In the thin light scattering layer, a part scattering light will still transmit the scattering layer [15,16] and loss in the electrolyte solution, said phenomenon could be strongly observed while the thickness of nanoporous TiO₂ film is more reduced as well as the film transmittance is larger than 50%.

In this work, we proposed a metal-based light reflective layer (MLRL) to replace the known light scattering layer in thin nanoporous TiO₂ film of DSSC, wherein the metal-based light reflective layer are composed of a plurality of Al@SiO₂ core shell microflakes. The optical behavior of the metal-based light reflective layer is similar to a light reflector not a light scatter, which mainly reflects the transmitted light readdressing in the thin nanoporous TiO₂ film, and then the readdressing light will be rescattered by the TiO₂ nanoparticles and absorbed by the photoactive dye. The use of the metal-based light reflective layer is able to minimize the light scattering loss thereby enhancing the light harvesting efficiency.

2. Experiment

2.1 TiO₂ Working electrode and preparation of metal-based light reflective layer (MLRL)

The TiO₂ working electrode was fabricated by the procedures described bellow. First, an acetic solution was prepared by mixing 2 g citric acid, 0.08 mL acetylacetone, 0.2 mL Triton X-100 and 0.2 mL tetrabutyl orthotitanate in 3 mL purified water. Then, a TiO₂ paste was prepared by mixing 1 g TiO₂ nanopowder (P25, Degussa) with the acetic solution and stirring for one hour. The nanoporous TiO₂ film was obtained by coating the TiO₂ paste on an FTO glass substrate (Hartford Glass Co., USA, fluorine-doped SnO₂ overlayer, sheet resistance: 7 Ω/sq) using a screen printing method and then sintered at 450 °C for 30 minutes. After sintering, the thickness of nanoporous TiO₂ film was 3 μm measured using an Alpha-Step profilometer and the active area was approximately 0.25 cm².

The metal-based light reflective layer (MLRL) was prepared by three procedures of the preparation of Al@SiO₂ core shell microflakes, the preparation of Al@SiO₂ core shell microflakes containing paste and the formation of MLRL. In order to prevent the low cost aluminum microflakes dissolving in the electrolyte solution, a SiO₂ shell layer as a protective layer will be coated onto the surface of aluminum microflakes. The Al@SiO₂ core shell microflakes were prepared by mixing 1 g aluminum microflakes (flake size between 2-14 μm) in 8 mL ethanol and stirring for 30 minutes to ensure complete dispersion. Then 0.5 mL tetraethyl orthosilicate (TEOS) and 0.3 mL NH₃ · H₂O were added to carry out the silica growth reaction at room temperature under continuous stirring for 6 hours; meanwhile silica directly coated onto the surface of aluminum microflakes to form Al@SiO₂ core shell microflakes. The Al@SiO₂ core shell microflakes were then filtered with ethanol washing, and dried in an oven at 150 °C for 3 hours.

The first step in Al@SiO₂ core shell microflakes containing paste preparation was preparation of an acetic solution by mixing 2 g citric acid, 0.6 mL Triton X-100 and 1 mL tetrabutyl orthotitanate in 3 mL purified water. Then, the paste was prepared by mixing the Al@SiO₂ core shell microflakes with the acetic solution using a weight ratio of

1:10 and stirring for 30 minutes. The MLRL was obtained by coating the paste on the nanoporous TiO_2 film using a screen printing method and then sintered at $400\text{ }^\circ\text{C}$ for 15 minutes, wherein the thickness of MLRL was $10\text{ }\mu\text{m}$ after sintering. Dye sensitization is carried out by immersing the TiO_2 working electrode with the MLRL into a dye solution of 0.3 mM N719 dye (Solaronix) in ethanol for 12 hours.

2.2 Counter electrode and cell fabrication

For the counter electrode, platinum (thickness 2 nm) was sputtered onto an FTO glass substrate. Then, dye-sensitized TiO_2 working electrode and Pt counter electrode were sandwiched with $60\text{ }\mu\text{m}$ thick (before melting) surlyn polymer foil (Solaronix) as a spacer. Sealing was done by keeping the structure in a hot-pressing at $100\text{ }^\circ\text{C}$ for few seconds. The liquid electrolyte consisting of 0.05 M iodine, 0.1 M lithium iodide, 0.5 M 4-tert-butylpyridine (TBP) and 0.3 M 1,2-dimethyl-3-propylimidazolium iodide (DMPPI) in 3-methoxy propionitrile (MPN) was introduced into the cell gap through edged injection hole, and then a sealing adhesive was used to seal the injection hole thereby preventing the electrolyte solution from leaking. In this study, two different DSSC modules were prepared: cell A was the nanoporous TiO_2 film with MLRL and cell B was the nanoporous TiO_2 film without MLRL were shown in [Figure 1](#).

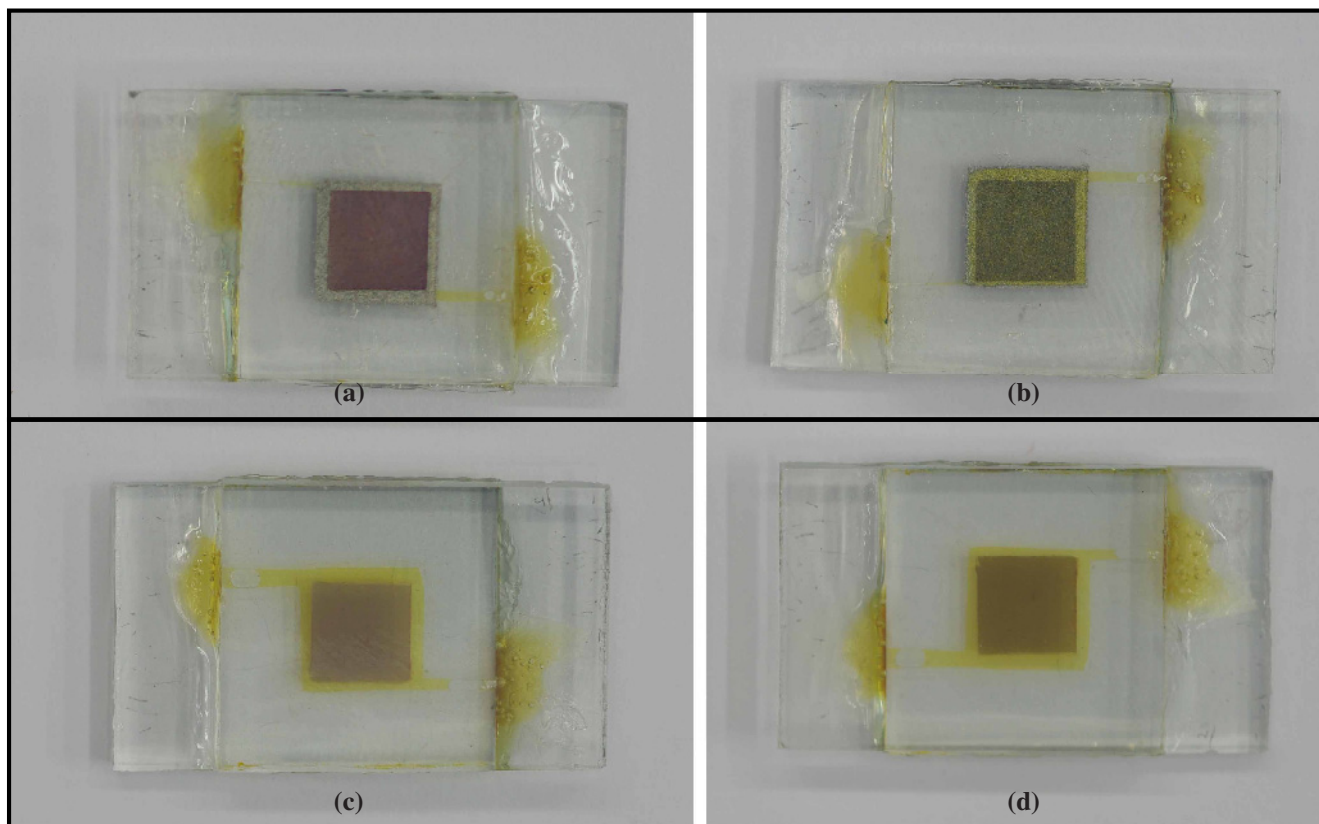


Figure 1: Photograph of two DSSC modules; (a) front view of cell A, (b) rear view of cell A, (c) front view of cell B, and (d) rear view of cell B.

2.3 Measurements

The microstructure of TiO_2 working electrode with the MLRL and the chemical composition of Al@SiO_2 core shell microflakes were observed with a field emission scanning electron microscope (FE-SEM) & energy dispersive spectrometer (EDS). The specular transmittance spectra of the nanoporous TiO_2 film and the MLRL coated on the nanoporous TiO_2 film were analyzed by a UV/VIS spectrophotometer respectively. The short-circuit current density (J_{sc}) and open-circuit voltage (V_{oc}) were measured using a computer-controlled digital source meter (Keithley, Model: 2400) under one sun illumination of 100 mW/cm^2 (AM 1.5 simulated light radiation).

3. Results and discussions

3.1 FE-SEM&EDS observation

The FE-SEM micrograph of TiO_2 working electrode with the MLRL was shown in [Figure 2](#). The nanoporous TiO_2 film is homogenous and well attached to the FTO glass substrate, and further no cracks have been identified. Besides, the well adhesion between MLRL and nanoporous TiO_2 film was achieved by using the tetrabutyl orthotitanate. The FE-SEM micrograph and the EDS analysis of Al@SiO_2 core shell microflakes were shown in [Figure 3](#). The Al@SiO_2 core shell microflakes were stacked piece by piece to form the metal-based light reflective layer and also formed many micro flow channels to ensure the electrolyte solution could pass easily. The EDS result confirmed the SiO_2 layer was coated on the surface of aluminum microflake. The thickness of SiO_2 layer was controlled by the usage volume of tetraethyl orthosilicate (TEOS) and the growth reaction time. In general, the aluminum microflakes were hydrophobic and very difficult to disperse in the solution. The aluminum microflakes with the SiO_2 shell layer would become hydrophilic and disperse easily.

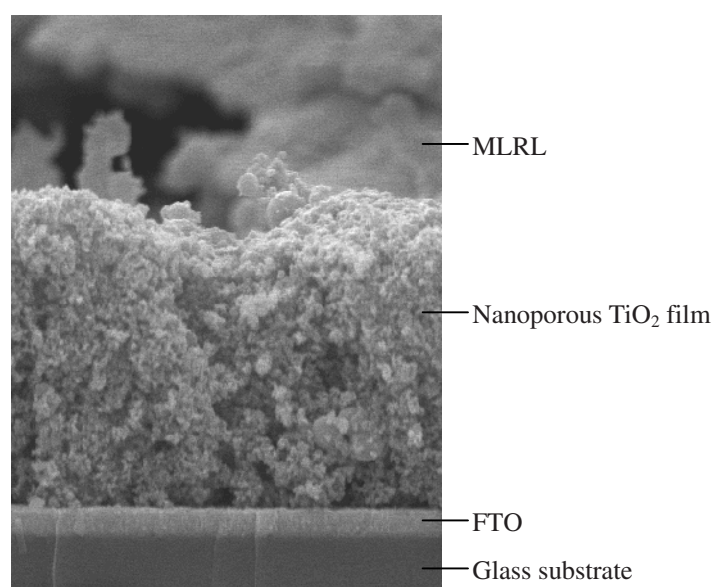


Figure 2: FE-SEM micrograph of TiO_2 working electrode with the MLRL.

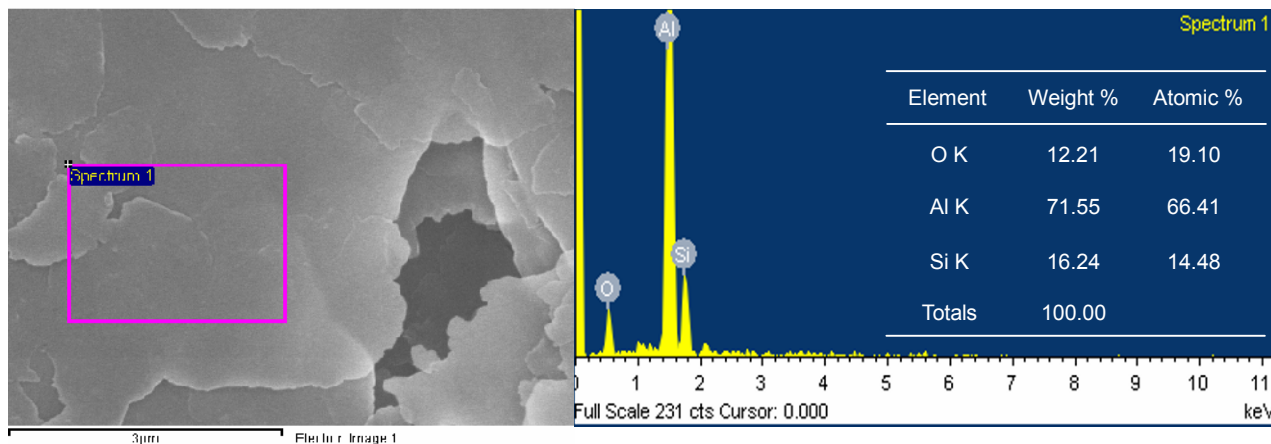


Figure 3: FE-SEM micrograph and EDS analysis of Al@SiO₂ core shell microflakes.

3.2 Specular transmittance spectra analysis

Figure 4 shows the nanoporous TiO₂ film (thickness 3 µm) was partial transparency in visible and near infrared regions, which means many transmitted light would be lost in the electrolyte solution. Figure 4 also shows the specular transmittance became ~zero in visible and near infrared regions while the metal-based light reflective layer (MLRL) was coated on the nanoporous TiO₂ film, which confirms the MLRL could effectively reflect the transmitted light readdressing in the thin nanoporous TiO₂ film thereby enhancing the light harvesting efficiency.

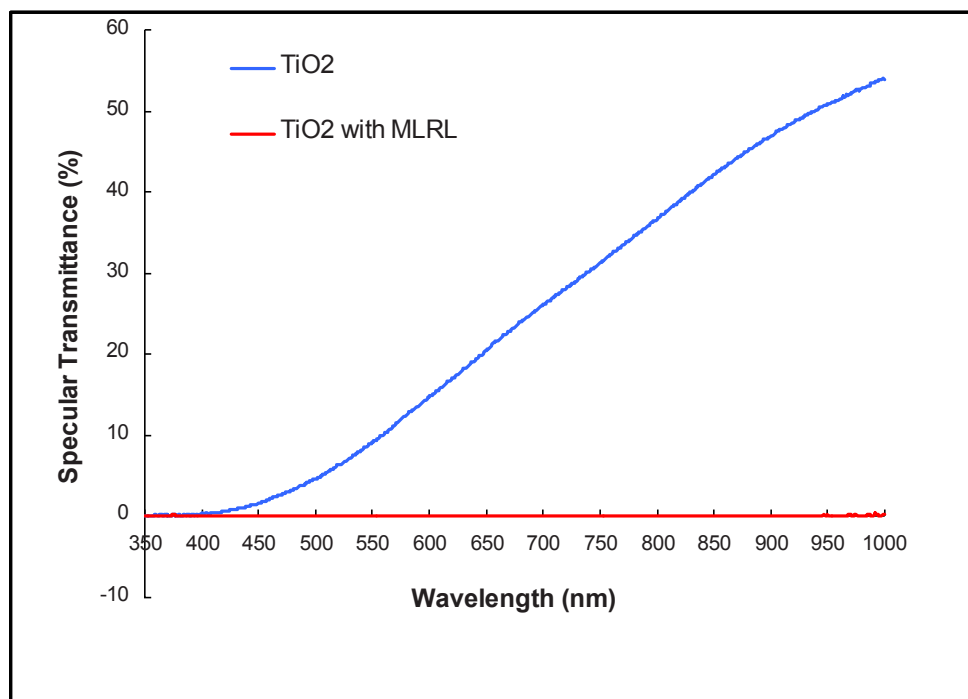


Figure 4: Specular transmittance spectra of (a) nanoporous TiO₂ film alone and (b) nanoporous TiO₂ film with MLRL.

3.3 Photovoltaic performances of DSSCs

Figure 5 and Table 1 present the photocurrent density-voltage (J-V) curves and photovoltaic performances of cell A and cell B. Under one sun illumination of 100 mW/cm^2 (AM 1.5), the short-circuit current density (J_{sc}) and the solar energy-to-electricity conversion efficiency (η) for the cell B based on the nanoporous TiO_2 film without the metal-based light reflective layer (MLRL) reached only 1.61 mA/cm^2 and 0.87% , respectively. After, the MLRL coated on the nanoporous TiO_2 film (cell B), the short-circuit current density and the solar energy-to-electricity conversion efficiency were improved to 4.16 mA/cm^2 and 2.07% , respectively. It should be noted that the photovoltaic performance was enhanced when using the MLRL.

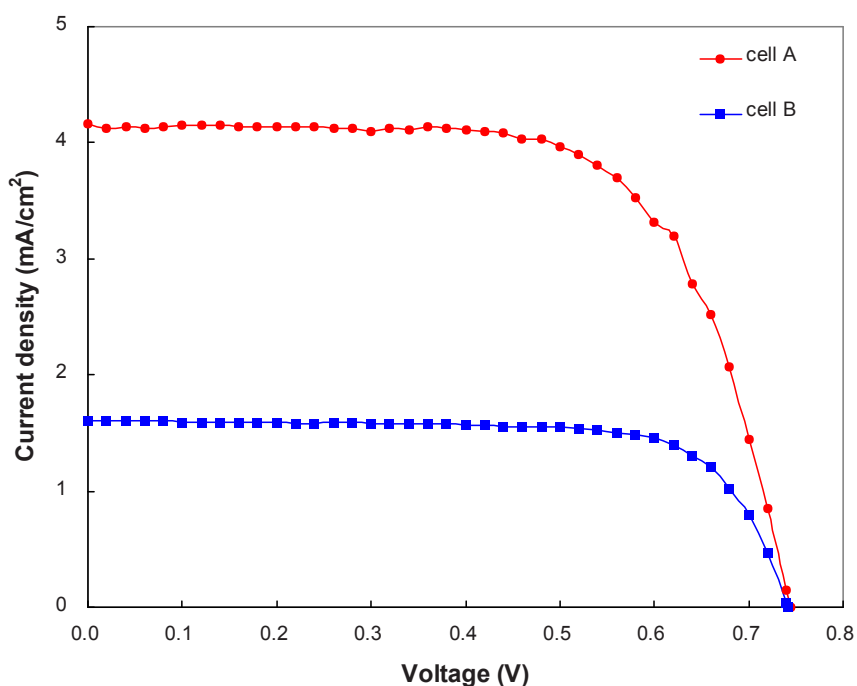


Figure 5: Photocurrent density-voltage curves of cell A (with MLRL) and cell B (without MLRL). Under one sun illumination of 100 mW/cm^2 (AM 1.5).

Table 1: Photovoltaic performances of cell A and cell B

DSSC module	J_{sc} (mA/cm^2)	V_{oc} (V)	FF (%)	η (%)
cell A	4.16	0.744	66.9	2.07
cell B	1.61	0.742	73.4	0.87

4. Conclusion

We have presented a comparison of photovoltaic performances of DSSCs based on the nanoporous TiO_2 film with and without the metal-based light reflective layer (MLRL). The results show that a metal-based light reflective layer on top of a very thin nanoporous TiO_2 film is sufficient to enhance the current density and the conversion efficiency.

The optical performance of metal-based light reflective layer also shows the low cost Al@SiO₂ core shell microflakes were high reflective and capable of effectively reflecting the transmitted light readdressing in the thin nanoporous TiO₂ film. In cost-effective DSSC module, the use of thin nanoporous TiO₂ film can reduce the dye loading in cell production; however, the metal-based light reflective layer used on the thin nanoporous TiO₂ film can improve the light scattering issue thereby enhancing the light harvesting efficiency and the photovoltaic performances.

5. Acknowledgements

This study is sponsored by the National Science Council (grants no. NSC97-2221-E-110-068 and NSC 98-2221-E-110 -030).

6. References

- [1] McConnell, R. D., Assessment of the dye-sensitized solar cell, *Renewable and Sustainable Energy Reviews*, Vol. 6, Iss. 3, pp. 273-295, 2002.
- [2] Marsh, G., Can dye sensitised cells deliver low-cost PV?, *Renewable Energy Focus*, Vol. 9, Iss. 5, pp. 58-62, 2008.
- [3] Yang, L., Lin, Y., Jia, J., Xiao, X., Li, X., and Zhou, X., Light harvesting enhancement for dye-sensitized solar cells by novel anode containing cauliflower-like TiO₂ spheres, *Journal of Power Sources*, Vol. 182, Iss. 1, pp. 370-376, 2008.
- [4] Rothenberger, G., Comte, P., and Grätzel, M., A contribution to the optical design of dye-sensitized nanocrystalline solar cells, *Solar Energy Materials and Solar Cells*, Vol. 58, Iss. 3, pp. 321-336, 1999.
- [5] Ferber, J. and Luther, J., Computer simulations of light scattering and absorption in dye-sensitized solar cells, *Solar Energy Materials and Solar Cells*, Vol. 54, Iss. 1-4, pp. 265-275, 1998.
- [6] Ito, S., Nazeeruddin, M. K., Zakeeruddin, S. M., Pechy, P., Comte, P., Grätzel, M., Mizuno, T., Tanaka, A., and Koyanagi, T., Study of dye-sensitized solar cells by scanning electron micrograph observation and thickness optimization of porous TiO₂ electrodes, *International Journal of Photoenergy*, Vol. 2009, Article ID 517609, 2009.
- [7] Kay, A. and Grätzel, M., Low cost photovoltaic modules based on dye sensitized nanocrystalline titanium dioxide and carbon powder, *Solar Energy Materials and Solar Cells*, Vol. 44, Iss. 1, pp. 99-117, 1996.
- [8] Usami, A., Theoretical study of application of multiple scattering of light to a dye-sensitized nanocrystalline photoelectrochemical cell, *Chemical Physics Letters*, Vol. 277, Iss. 1-3, pp. 105-108, 1997.
- [9] Bisquert, J., Theory of the impedance of electron diffusion and recombination in a thin layer, *Journal of Physical Chemistry B*, Vol. 106, Iss. 2, pp. 325-333, 2002.
- [10] Fabregat-Santiago, F., Bisquert, J., Garcia-Belmonte, G., Boschloo, G., and Hagfeldt, A., Influence of electrolyte in transport and recombination in dye-sensitized solar cells studied by impedance spectroscopy, *Solar Energy Materials & Solar Cells*, Vol. 87, Iss. 1-4, pp. 117-131, 2005.
- [11] Wang, Q., Moser, J., and Grtzel, M., Electrochemical impedance spectroscopic analysis of dye-sensitized solar

- cell, *Journal of Physical Chemistry B*, Vol. 109, Iss. 31, pp. 14945-14953, 2005.
- [12] Kern, R., Sastrawan, R., Ferber, J., Stangl, R., and Luther, J., Modeling and interpretation of electrical impedance spectra of dye solar cells operated under open-circuit conditions, *Electrochimica Acta*, Vol. 47, Iss. 26, pp. 4213-4225, 2002.
- [13] Koide, N., Islam, A., Chiba, Y., and Han, L., Improvement of efficiency of dye-sensitized solar cells based on analysis of equivalent circuit, *Journal of Photochemistry and Photobiology A: Chemistry*, Vol. 182, Iss. 3, pp. 296-305, 2006.
- [14] Han, L., Koide, N., Chiba, Y., Islam, A., and Mitate, T., Modeling of an equivalent circuit for dye-sensitized solar cells: improvement of efficiency of dye-sensitized solar cells by reducing internal resistance, *Comptes Rendus Chimie*, Vol. 9, Iss. 5-6, pp. 645-651, 2006.
- [15] Usami, A., Rigorous solutions of light scattering of neighboring TiO_2 particles in nanocrystalline films, *Solar Energy Materials and Solar Cells*, Vol. 59, Iss. 3, pp. 163-166, 1999.
- [16] Tachibana, Y., Akiyama, H. Y., and Kuwabata, S., Optical simulation of transmittance into a nanocrystalline anatase TiO_2 film for solar cell applications, *Solar Energy Materials & Solar Cells*, Vol. 91, Iss. 2-3, pp. 201-206, 2007.

Integration of Solar Cell with TN-LC Cell for Enhancing Power Characteristics

Chin-Yu Chen^{1,2}, Yu-Lung Lo^{1,*}

¹ Department of Mechanical Engineering, National Cheng Kung University, Taiwan, R.O.C.

² Southern Taiwan Science Park Administration (STSPA), Taiwan, R.O.C.

*Phone: +886-6-2757575 Ext. 62123, Fax: +886-6-2352973, E-Mail: loyl@mail.ncku.edu.tw

Address: No.1, University Road, Tainan City 701, Taiwan, R.O.C.

ABSTRACT

This study improves the output power and brightness characteristics of a translucent hydrogenated amorphous silicon (a-Si:H) solar cell by integrating the solar cell with a novel twist nematic (TN) liquid crystal (LC) cell incorporating a sub-wavelength metal grating (SWMG) polarization beam splitter (PBS). In this study, a SWMG-PBS is used to replace not only the sheet polarizers in the conventional TN-LC cell, but also the upper and lower alignment layers and transparent electrodes. Therefore, a translucent a-Si:H solar cell integrating with the novel TN-LC cell with the SWMG-PBS could improve power efficiency and durability in UV ray environment. The experimental results show that the transmittance gap between the “on” and “off” states of the enhanced translucent a-Si:H solar cell / novel TN-LC cell is of the order of 26.6% on 800 nm, 6.3% on 400 nm and 2.7% on 510 nm. Moreover, it is shown that the novel TN-LC cell increases the maximum electrical power developed by the translucent a-Si:H solar cell and improves its power conversion efficiency by 0.209% in the “off” state and 0.417% in the “on” state. In other words, the gain factors, the power efficiency of the novel TN-LC cell with translucent a-Si:H solar cell divided by the power efficiency of the standalone translucent solar cell, are determined to be 1.101 (or 110.1 %) in the “off” state and 1.201 (or 120.1 %) in the “on” state. As a result, the proposed device represents an ideal solution for building integrated photovoltaic (BIPV) systems, automobile industry applications, and many other adjustable brightness photovoltaic applications.

1. INTRODUCTION

Translucent solar cells are applied in many different photovoltaic applications to transmit light and generate electricity, and are particularly suitable for rapidly growing photovoltaic market segments [1]. However, the translucent solar cells have a relatively poor power efficiency and, moreover, do not provide the ability to adjust the brightness of the output light. Twist nematic (TN) LC cells are used for a wide variety of commercial adjustable-brightness display applications, such as monitors, televisions, and so forth. Despite the many advantages of TN-LC cells, they suffer a number of practical limitations. For example, the sheet polarizers gradually decay when exposed to UV light and have a poor light efficiency. Furthermore, the fiber residues and static charges introduced by the rubbed polymer layers can cause defects for LC cell devices. In addition, fabricating the ITO transparent electrodes used in the TN-LC cell inevitably incurs a relatively high cost. In an attempt to resolve these problems, various researchers have proposed replacing the PI alignment layers in the TN-LC cell with a micro-groove grating structure [2-3]. Many researchers have investigated the optical properties of SWMG-PBS (or so-called wire grid polarizers) [4-6]. These gratings perform a SWMG-PBS function, i.e. they transmit one polarized component of the incident light and reflect the other, and are suitable for a wide variety of polarization applications, including high-performance projection displays, for example. Moreover, the structure of wire-grid polarizers has an identical effect to that of micro-groove grating structures, and therefore facilitates their use for alignment purposes in TN-LC cells. In addition, SWMG-PBSs deposited on glass substrates are highly robust in UV ray environments [6]. Therefore, the potential exists to improve the robustness and light efficiency of conventional TN-LC cells by replacing not only the sheet polarizers, but also the upper and lower alignment layers and electrodes with a SWMG-PBS.

The results confirm that the proposed structure not only provides an enhanced brightness adjustment capability, but also increases both the electric power developed by the translucent a-Si:H solar cell and its power efficiency. This design is suitable for building integrated photovoltaic (BIPV) systems, automobile industry applications, and other adjustable brightness photovoltaic applications.

2. BASIC DESIGN OF TRANSLUCENT a-Si:H SOLAR CELL WITH INTEGRATED TN-LC CELL

Fig.1 illustrates the two solar cell / TN-LC cell structures considered in this study, namely a translucent a-Si:H solar cell integrated with a conventional TN-LC cell (see Fig. 1(a)) and a translucent a-Si:H solar cell integrated with a novel TN-LC cell incorporating a SWMG-PBS (see Fig. 1(b)). In both cases, the upper glass plate of the translucent a-Si:H solar cell has a thickness of 1.9 mm and is positioned on a SnO₂ transparent electrode with a thickness of 0.6 μm. The p-layers, i-layers and n-layers in the two devices have thicknesses of 0.1 μm, 0.45 μm and 0.1 μm, respectively, and are deposited on a lower ZnO:Al (AZO) transparent electrode with a thickness of 0.6 μm. The translucent a-Si:H solar cell submodule was formed by connecting 12 cells in series on a single substrate.

The novel TN-LC cell was fabricated using a commercial aluminum SWMG-PBS (Moxtek PPL03 grade; TA 90°). The grating was mounted on a glass substrate measuring 34.0 mm x 29.0 mm and was sandwiched at either end by a sputter-deposited aluminum bar with a width of 2.5 mm in order to ensure a full electrical connectivity of all the grating lines in the grating structure. According to the manufacturer, the period, line width and groove depth of the SWMG-PBS were 160 nm, 80 nm and 185 nm, respectively. According to Chiou et al. [2] and Lin et al. [3], a grating groove depth of more than 56 nm and a period of less than 4 μm ensure a strong anchoring strength with the alignment layers of the TN-LC cell. Therefore, the Moxtek PPL03 grade SWMG-PBS used in the present study ensures the robustness of the TN-LC structure. In the novel TN-LC cell structure shown in Fig. 1(b), the SWMG-PBS performs three major functions, namely a PBS, a micro-groove non-rubbing alignment layer, and a transparent electrode. The novel TN-LC cell was created by sandwiching 6 μm Mylar spacers between two orthogonally-arranged gratings (i.e. O-mode operation) to create an active area with dimensions of 29 mm x 29 mm x 6 μm. As in the conventional TN-LC cell, the active area was filled with Merck E7 nematic liquid crystal. The conventional TN-LC cell was fabricated following conventional manufacturing process and the same size of the glass substrate of the novel TN-LC cell.

3. EXPERIMENTAL SETUP AND RESULTS

3.1 Optical characteristics of translucent a-Si:H solar cells with and without TN-LC cell

Figure 2 illustrates the experimental setup used to measure the wavelength-dependent transmittance and reflectance characteristics. In the experiments, the LC cells were driven by a programmable linear power supply, with the “on” and “off” states obtained with voltages of 0 V and 6 V, respectively.

Figures 3(a) and 3(b) illustrate the variation of the transmittance and reflectance characteristics. It is also observed that in both states, the reflectance of the novel TN-LC cell is significantly higher than that of the conventional TN-LC cell over the full wavelength range of 400~800 nm.

Fig. 4 illustrates the transmittance characteristics. The results presented in Fig. 4 show that both solar cell / TN-LC devices provide a good range of brightness adjustment as the driving voltage supplied to the TN-LC cell is switched from 0 V to 6 V. From inspection, the maximum transmittance gap of the translucent a-Si:H solar cell integrated with the conventional TN-LC cell is found to be 6.4% (i.e. 1.0%~7.4%) on 400 nm, 2.7% (i.e. 0~2.7%) on 510 nm and 17.7% (i.e. 19.3%~36.9%) on 800 nm, respectively. Similarly, for the translucent a-Si:H solar cell integrated with the novel TN-LC cell, the maximum transmittance gap is determined to be 6.3% (i.e. 10.8%~17.1%) on 400 nm, 2.7% (i.e. 0~2.7%) on 510 nm and 26.6% (i.e. 4.3~30.9%) on 800 nm.

3.2 Electrical characteristics of translucent a-Si:H solar cell with and without TN-LC cell

The electrical characteristics were evaluated using a ScienceTech 150W fully reflective solar simulator and I-V measurement system (Teltec Semiconductor Pacific Limited) under standard illumination conditions of AM1.5 at 25°C. The output power of the lamp was set to 100 mW/cm² and was calibrated using a reference solar cell (PV Measurement, Inc., PVM 203).

Figure 5 and Table 1 present the I-V curves and output power characteristics, respectively. The I-V curves and output power characteristics of the translucent a-Si:H solar cell integrated with the conventional TN-LC cell are virtually identical to those of the standalone translucent a-Si:H solar cell in both the “on” and the “off” states since the conventional TN-LC cell provides virtually zero reflectance. Fig.5 shows that the addition of a conventional TN-LC cell to the a-Si:H solar cell improves the power conversion efficiency of the solar cell by 0.013% in the “off” state and 0.015% in the “on” state. By contrast, the power conversion efficiency of the a-Si:H solar cell integrated with the novel TN-LC cell is increased by 0.209% and 0.417%, respectively, in the “off” and “on” states. In other words, the gain factors, the power efficiency of the novel TN-LC cell with translucent a-Si:H solar cell divided by the power efficiency of the standalone translucent solar cell, are determined to be 1.101 (or 110.1 %) in the “off” state and 1.201 (or 120.1 %) in the “on” state. Thus, it is apparent that the novel TN-LC cell yields a greater improvement in the photovoltaic performance of the translucent a-Si:H cell than the conventional TN-LC cell.

4. CONCLUSIONS

This study has improved the brightness and output power characteristics of a conventional translucent a-Si:H solar cell / TN-LC cell device by replacing the sheet polarizers, upper and lower alignment layers, and upper and lower ITO electrodes in the TN-LC with two SWMG-PBS structures. The experimental results show that the transmittance gap between the “on” and “off” states of the enhanced translucent a-Si:H solar cell / novel TN-LC cell is of the order of 26.6% on 800 nm, 6.3% on 400 nm and 2.7% on 510 nm. Moreover, the proposed TN-LC structure improves the power conversion efficiency of a standalone a-Si:H solar cell by 0.209% in the “off” state and 0.417% in the “on” state. In other words, the gain factors, the power efficiency of the novel TN-LC cell with translucent a-Si:H solar cell divided by the power efficiency of the standalone translucent solar cell, are determined to be 1.101 (or 110.1 %) in the “off” state and 1.201 (or 120.1 %) in the “on” state. Compared to conventional a-Si:H solar cell / TN-LC cell devices, the novel structure proposed in this study not only has improved brightness and output power characteristics, but is also more robust to the effects of UV light. As a result, it provides an ideal solution for a variety of photovoltaic applications, including BIPV systems, automobile applications, and so forth.

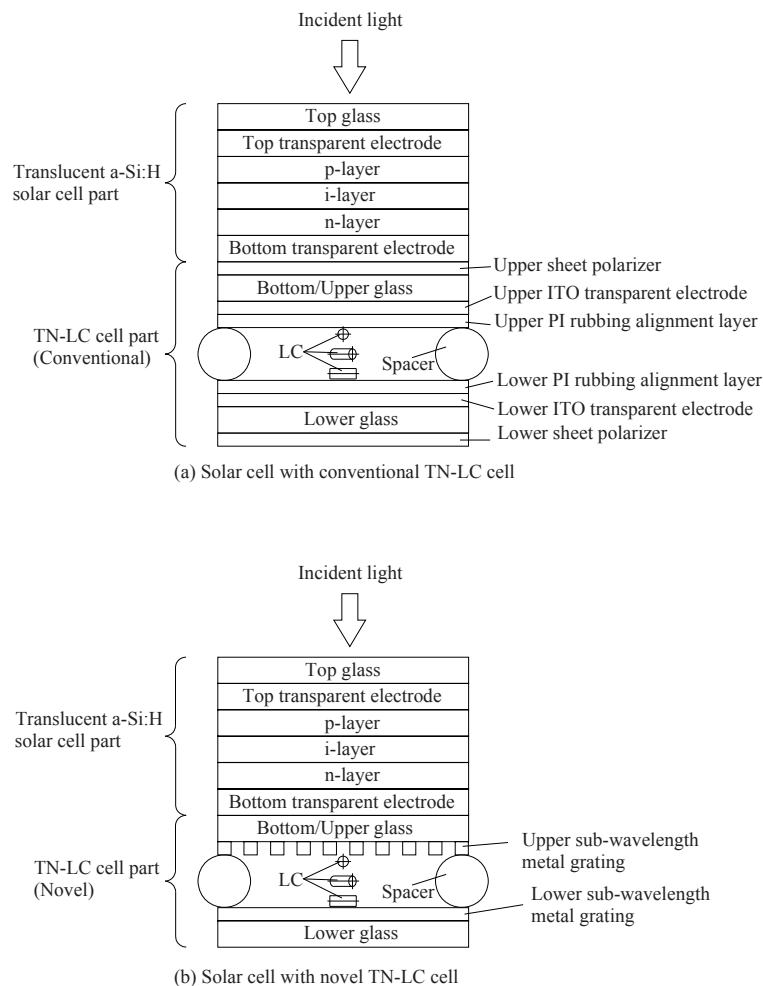


Fig. 1. Schematic illustration showing structure of translucent a-Si:H solar cell with integrated TN-LC cell: (a) solar cell with conventional TN-LC cell; and (b) solar cell with novel TN-LC cell.

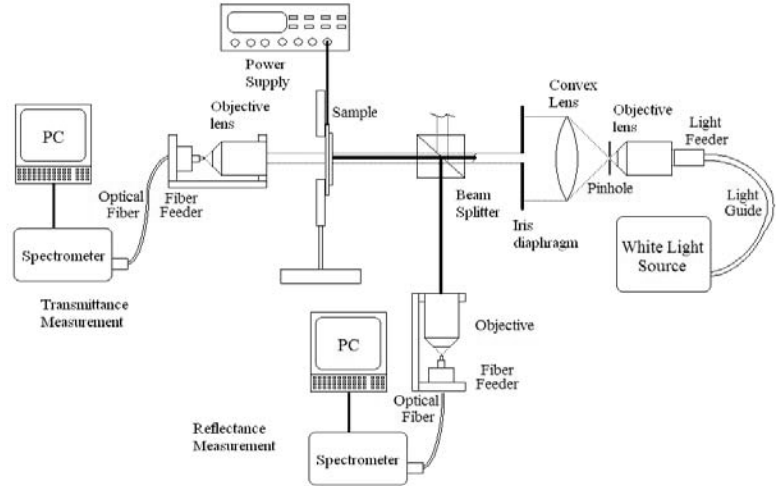
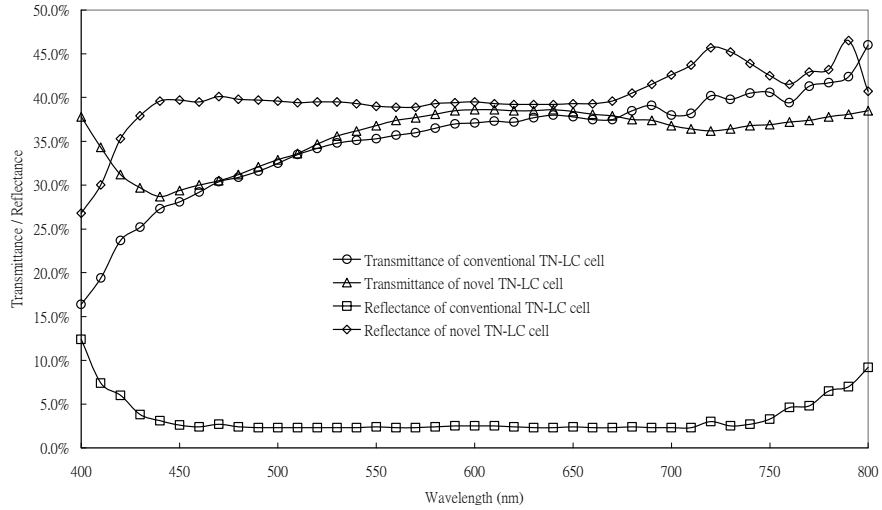
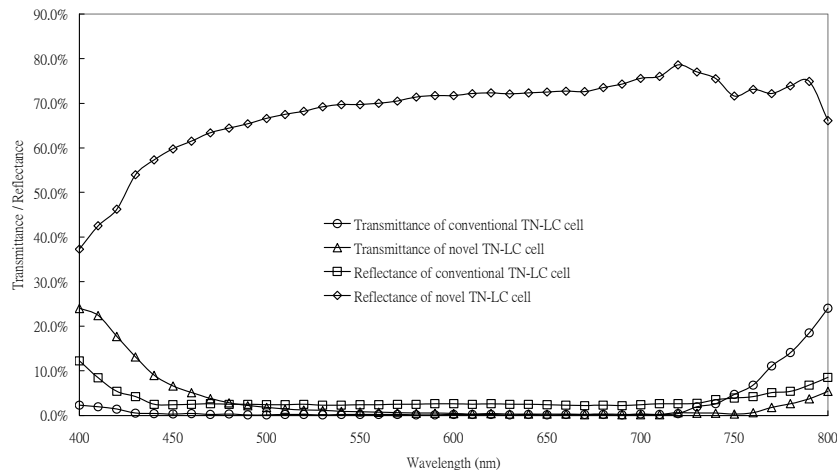


Fig. 2. Experimental setup for transmittance and reflectance measurements.



(a) Voltage "off" state



(b) Voltage "on" state

Fig. 3 Transmittance and reflectance characteristics of conventional TN-LC cell and novel TN-LC cell in: (a) voltage "off" state; and (b) voltage "on" state.

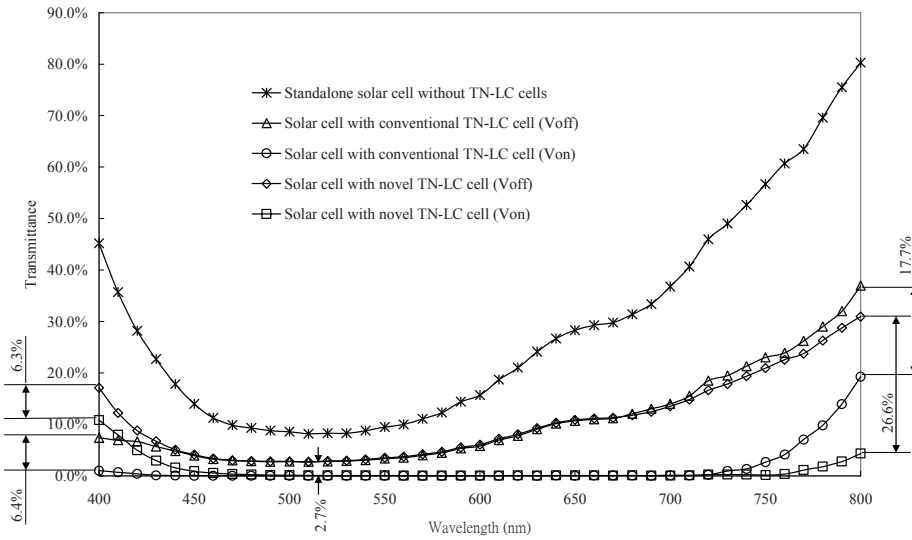


Fig. 4 Transmittance characteristics of translucent a-Si:H solar cell with and without TN-LC cells.

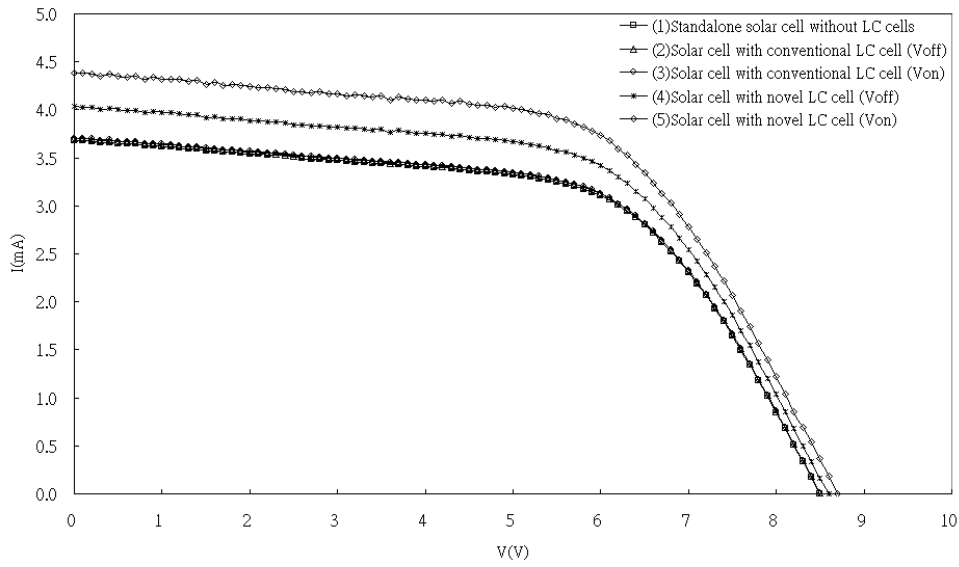


Fig. 5 I-V curves of translucent a-Si:H solar cell with and without TN-LC cells.

Table 1 Parameter values of translucent a-Si:H solar cell with and without TN-LC cells.

Sample	I_m (mA)	J_m (A/m ²)	V_m (V)	P_m (W/m ²)	I_{SC} (mA)	J_{SC} (A/m ²)	V_{OC} (V)	FF (%)	η (%)	Increase (%)	Gain (%)
(1)	3.061	3.401	6.1	20.74	3.682	4.091	8.5	59.659	2.074	-	-
(2)	3.079	3.421	6.1	20.87	3.703	4.114	8.5	59.677	2.087	0.013	100.6%
(3)	3.082	3.424	6.1	20.89	3.706	4.118	8.5	59.680	2.089	0.015	100.7%
(4)	3.368	3.742	6.1	22.83	4.033	4.481	8.6	59.231	2.283	0.209	110.1%
(5)	3.676	4.084	6.1	24.91	4.385	4.872	8.7	58.770	2.491	0.417	120.1%

REFERENCE

- [1] A. Takeoka, S. Kouzuma, H. Tanaka, H. Inoue, K. Murata, M. Morizane, N. Nakamura, H. Nishiwaki, M. Ohnishi, S. Nakano, and Y. Kuwano, *Sol. Energ. Mat. Sol. C.* 29 (1993) 243-252.
- [2] D. R. Chiou, K. Y. Yeh, and L. J. Chen, *Appl. Phys. Lett.* 88 (2006) 133123-133125.
- [3] Y. F. Lin, M. C. Tsou, and R. P. Pan, *Chinese Journal of Physics*, 43 (2005) 1066-1073.
- [4] H. Tamada, T. Doumuki, T. Yamaguchi, and S. Matsumoto, *Opt. Lett.* 22 (1997) 419-421.
- [5] B. Schnabel, E. B. Kley, F. Wyrowski, *Opt. Eng.* 38 (1999) 220–226.
- [6] C. Pentico, E. Gardner, D. Hansen, and R. Perkins, *SID Symposium Digest* 32 (2001) 1287-1289.

Full-field Measuring System for the Surface of Solar Cell

Shiou-An Tsai and *Yu-Lung Lo

Department of Mechanical Engineering, National Cheng Kung University,
No.1, Ta-Hsueh Road, Tainan 701, Taiwan

*Corresponding author: loyl@mail.ncku.edu.tw

ABSTRACT

In this paper, we propose a scheme to measure the difference of the surface of the solar cell during manufacturing and packaging. The measurement in the full-field of the solar cell based on the Imaging Ellipsometry has been developed in this study. By using a complex programmable logic device (CPLD) and a charge-coupled device (CCD), integrating buckets with multiple frames are achieved. The sequentially measuring scheme and the algorithm are designed to achieve full-field range measurement. Also, we can figure out the condition of the surface of the solar cell by using the 2-D distributions of (Ψ, Δ) . Based on the optical model, we can obtain the defect of the solar cell more precisely. Hence, the proposing system has the ability to tell the difference form the surface of the solar cell. In addition, the intensity noises induced by environmental disturbance can be reduced by the elimination of the DC component of the output light intensity in the algorithm.

1. Introduction

It's well known that the ellipsometry is noninvasive, surface-sensitive and well-developed optical method widely applied for characterizing the optical properties of the thin film. In general, the interpretation of measurement results is rather difficult from the absolute values of (Ψ, Δ) . Thus, construction of an optical model is required for data analysis. From this data analysis, physical properties including the optical constants and film thickness of the sample can be extracted.

The optical properties of thin film, including the thickness and refractive index which can be characterized the change in the polarization state of a monochromatic plane wave that is reflected by the surface of the test sample at oblique incidence. In 1887, ellipsometry was developed by Drude who also derived the equations of ellipsometry, which are used even today [1]. In 1971, Pail and Bockris [2] pointed out that the normal incidence reflectance, R , can also be used as a third experimental parameter for the analysis of ellipsometric data. The following three types of automated ellipsometers are most widely used nowadays as spectroscopic ellipsometers: (i) rotating analyzer ellipsometry (RAE) [3]; (ii) rotating compensator ellipsometry (RCE) [4]; and (iii) phase modulation ellipsometry (PME) [5]. The RAE was presented by Aspnes et al. in 1975 [3]. In the past, conventional ellipsometers which often were used based on single-point detection incorporated two polarizers and a quarter-wave plate, at least one of which is rotating, and therefore it took a long time to obtain the full-field information of a sample.

Recently, heterodyne detection has been extended from single-point detection to array detection and has been applied to various interference techniques, including heterodyne holography [6] and low-coherence heterodyne interferometer [7]. Aguanno et al. [8] presented a full-field heterodyne interferometer based on alternative demodulation approach by using CMOS-DSP CCD in 2004. Therefore, it had the capability of carrying out high-sensitive phase measurements, in terms of displacement in the order of nanometers and velocity in micron per second. Hariharan et al. [9] also presented the phase-shifting interferometer and provided the means of

measuring the optical phase with high accuracy. Several phase-shifting interferometers-based algorithms have now been proposed, including the three-step algorithm, the four-step algorithm. In our previous paper, Lo et al. [11] presented a full-field heterodyne interferometer with an image signal processing method for the sequential principal axis and phase retardation measurements. The success of the proposed method relied on achieving a high-speed sampling of the frequency modulation optical carrier.

In this paper, the method we proposed can determine ellipsometric parameters (Ψ, Δ) of the surface from the measurement. The intensity noises induced by environmental disturbance can be reduced by the elimination of the DC component of the output light intensity in the algorithm. And, the system has the advantages of reducing the perturbation of the environment and improving the signal-to-noise ratio (SNR) of the detected signal. Therefore, the slight difference of the surface of solar cell could be measured and investigated.

2. Principles of the Ellipsometry

The change in polarization state after reflection can be determined by measuring the ratio of the complex coefficients, namely $r_p = |r_p| \exp(i\delta_p)$, $r_s = |r_s| \exp(i\delta_s)$ of parallel (P) and perpendicular (S) polarized components of monochromatic plane wave with respect to the incident plane using the equation:

$$\rho = \frac{r_p}{r_s} = \frac{|r_p|}{|r_s|} \exp(i(\delta_p - \delta_s)) = \tan \psi e^{i\Delta} = \left(\frac{E_{rp}}{E_{ip}} \right) / \left(\frac{E_{rs}}{E_{is}} \right) \quad (1)$$

where $(|r_p|, |r_s|)$ and (δ_p, δ_s) are the absolute amplitude reflectance and phase shifts of r_p and r_s respectively.

The angles $\Psi = \arctan \theta(|r_p|/|r_s|)$ and $\Delta = \delta_p - \delta_s$ are defined as the ellipsometric parameters. However, the change of the polarization state can be deduced from the Fransnel equations via the complex amplitude reflectance r_p and r_s , which are fully interpreted by (Ψ, Δ) simultaneously. Therefore the thickness, refractive index and extinction coefficient of the thin film can be calculated precisely in terms of (Ψ, Δ) and the incident angle.

The schematic illustration of the experimental setup used in this study to measure the ellipsometric parameters of the sample is shown in Fig.1. The laser beam passes sequentially through a polarizer, and electro-optic (EO) modulator, a beam expander, the quarter-wave plate, reflected by the sample, and an analyzer before being incident on the CCD. In this optical configuration of ellipsometry instruments, the polarizer and quarter-wave plate are adjusted to 0° , and the analyzer is adjusted to -45° , respectively. It should be noticed that the origination in all optical components are aligned based on the slow axis of an EO modulator.

The Jones matrix of the sample can be written as follows:

$$[Sample] = \begin{bmatrix} \sin \psi \exp(i\Delta) & 0 \\ 0 & \cos \psi \end{bmatrix} \quad (2)$$

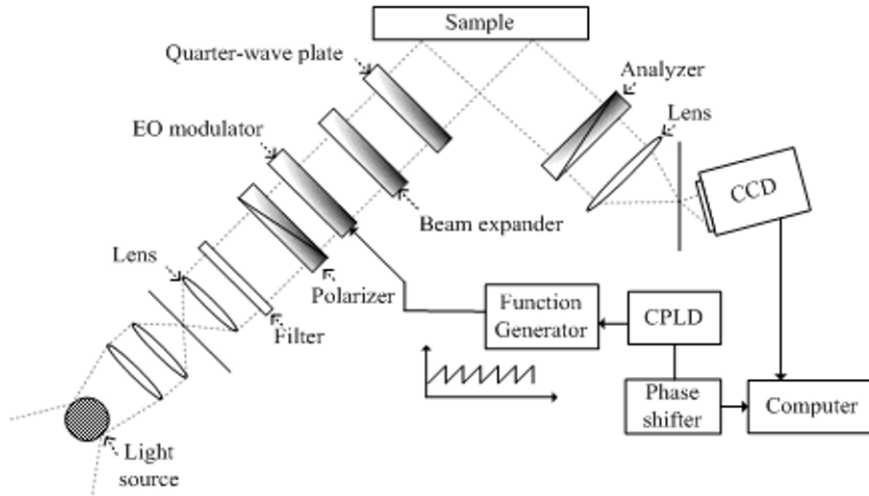


Figure 1 Full-field ellipsometry for sequential measurement

The light vector emerging from the configuration in Fig.1 is given by

$$\begin{aligned}
 E_1 &= A(-45^\circ) \cdot S(\Psi, \Delta) \cdot Q(0^\circ) \cdot EO(-45^\circ, \omega t) \cdot P(0^\circ) \cdot E_{in} \\
 &= \frac{1}{2} \begin{bmatrix} 1 & -1 \\ -1 & 1 \end{bmatrix} [Sample] \begin{bmatrix} 1 & 0 \\ 0 & -i \end{bmatrix} \begin{bmatrix} \cos \frac{\omega t}{2} & i \sin \frac{\omega t}{2} \\ i \sin \frac{\omega t}{2} & \cos \frac{\omega t}{2} \end{bmatrix} \begin{bmatrix} E_0 \\ 0 \end{bmatrix} e^{i\omega_0 t}
 \end{aligned} \quad (3)$$

where E_0 is the amplitude of the incident electric field, $P(0^\circ)$ represents the Jones matrix of the polarizer aligned with x-axis, $Q(0^\circ)$ represents the Jones matrix of the quarter-wave plate, whose slow axis is aligned with x-axis, $S(\Psi, \Delta)$ represents the Jones matrix of the sample. Furthermore, $EO(-45^\circ, \omega t)$ represents the Jones matrix of the EO modulator driven by a saw tooth voltage waveform with an angular frequency ω and its slow axis is oriented at -45° related to the x-axis, and $A(-45^\circ)$ represents the Jones matrix of the analyzer whose transmission axis forms an angle -45° with the x-axis.

As a result, the intensity of the detected signal is given by

$$I_1 = I_{dc} (1 + \sin 2\Psi \cos \Delta \sin \omega t - \cos 2\Psi \cos \omega t) = I_{dc} + R_1 \sin(\omega t + \Phi_1) \quad (4)$$

where $I_{dc} = E_0^2 / 4$ is the dc component of the output intensity, and E_0^2 is the intensity of the input light. R_1 represents the amplitude, and Φ_1 represents the phase. Therefore, as the polarizing elements are arranged as shown in Fig.1, the measured principal axis direction of the sample would be the slow axis. The signal as shown in Eq.(4) will be further proceeded in CCD and introduced in the next section.

The time varying signal I_1 in Eq.(4) can be integrated successively over the four quarters of modulation period T . This integration is performed in a parallel manner using a two-dimensional (2D) CCD. The three frames of the image obtained by integrating the time-varying signal over the individual quarters of the modulation period are given by [10].

$$\begin{aligned}
S_1(x, y) &= \int_0^{T/4} I_1(x, y, t) dt = \frac{T}{4} I_{dc} + \frac{I_{dc} \sin 2\Psi \cos \Delta}{\omega} + \frac{I_{dc} \cos 2\Psi}{\omega} \\
S_2(x, y) &= \int_{T/4}^{2T/4} I_1(x, y, t) dt = \frac{T}{4} I_{dc} + \frac{I_{dc} \sin 2\Psi \cos \Delta}{\omega} - \frac{I_{dc} \cos 2\Psi}{\omega} \\
S_3(x, y) &= \int_{2T/4}^{3T/4} I_1(x, y, t) dt = \frac{T}{4} I_{dc} - \frac{I_{dc} \sin 2\Psi \cos \Delta}{\omega} - \frac{I_{dc} \cos 2\Psi}{\omega}
\end{aligned} \tag{5}$$

From Eq.(5), the 2-D distributions of the ellipsometric parameters (Ψ, Δ) can be obtained as:

$$\Psi = 0.5 \cos^{-1}(4I_{dc} \cos 2\Psi) \tag{6}$$

$$\Delta = \cos^{-1}(4I_{dc} \cos \Delta)$$

where

$$S_1 - S_2 = -\frac{2I_{dc} \cos 2\Psi}{\omega} \quad \text{and} \quad S_2 - S_3 = \frac{2I_{dc} \sin 2\Psi \cos \Delta}{\omega}.$$

From Eq. (5), it is seen that the outcomes of $-(S_1-S_2)$ and $S_2 - S_3$ vary in accordance with $\sin \Psi$ and $\cos \Psi$. Therefore, the proposed image processing algorithm applies the following quadrant determination process to determine the correct value of Ψ . If $-(S_1-S_2) > 0$ and $S_2 - S_3 > 0$, the measured phase term is located in the I-quadrant. Conversely, if $-(S_1-S_2) > 0$ and $S_2 - S_3 < 0$, the measured phase term is located in the II-quadrant. Meanwhile, if $-(S_1-S_2) < 0$ and $S_2 - S_3 < 0$, the measured phase term is located in the III-quadrant. Finally, if $-(S_1-S_2) < 0$ and $S_2 - S_3 > 0$, the measured phase term is located in the IV-quadrant. Thus, a full scale (i.e. $0 \sim 360^\circ$) measurement of ellipsometric parameters (Ψ, Δ) are obtained, and hence a full range (i.e. $0^\circ \sim 180^\circ$) measurement of the optical properties is also achieved.

3. Experimental Setup and Results

In Fig.1, the measurement system was set up for demonstration. A He-Ne laser was used as a light source and we use two materials as the samples. One is the silicon substrate coating aluminum (100nm), and the other one is the solar cell which is coated the polycrystalline silicon ($500 \mu\text{m}$) on the Si substrate. The frequency of the saw tooth signal from a function generator that applied to the EO modulator was 1 kHz. The experimental setup includes two Glan-Thompson polarizers with extinction ratios of 5×10^{-6} , one quarter wave plates (CVI, Model QWPO-633-04-4-R10). A beam expander (Edmund Industrial Optics 20X) was used to expand the light beam for the 2-D measurement, and a 8-bit gray-level CCD (JAI CV-A11) was applied.

Fig. 2 illustrates the relationship between the CPLD and the CCD. The control clocks in the CPLD are processed using several frequency dividers in an embedded 2 MHz oscillator. As shown, the frequencies of the external trigger signals for the function generator and the CCD are 1 kHz and 10 Hz, respectively. The exposure time of CCD (JAI, CV-A11) is set for quarter period (0.25ms) for the acquisition of the frames S_1 , S_2 and S_3 . For the three-frame integrating-bucket method, the trigger signal is firstly set only for the acquisition of the frame S_1 which is derived by acquiring (i.e. integrating) the first quarter period of the interference signal. A bits delay controller is then used to sequentially shift the phase of the CCD trigger signal through $\pi/2$ and π for the acquisition of images S_2 and S_3 respectively. A computer is used to control the exposure time, trigger mode and other settings of CCD through IMAQ 1409 and RS 232.

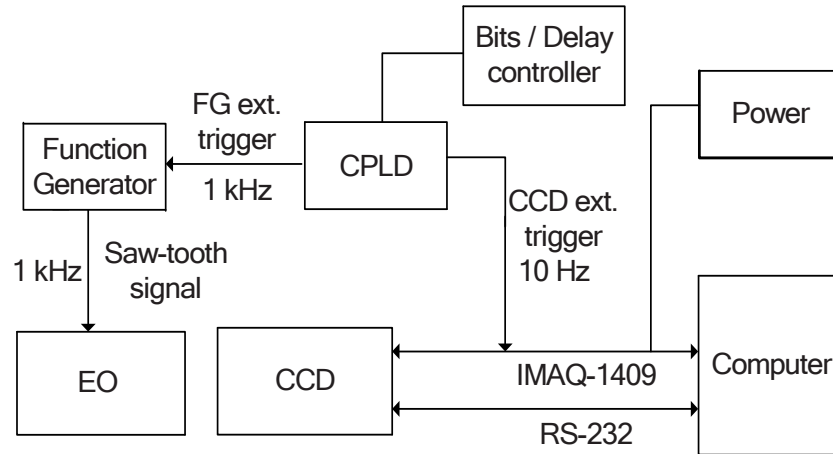


Figure 2 Electronic block diagram showing relationship between CCD and CPLD [10]

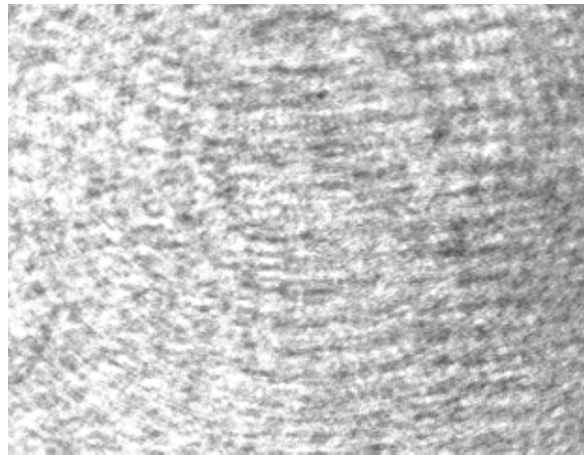


Figure 3 Typical image acquired by CCD camera during measurement process (Al / Si)

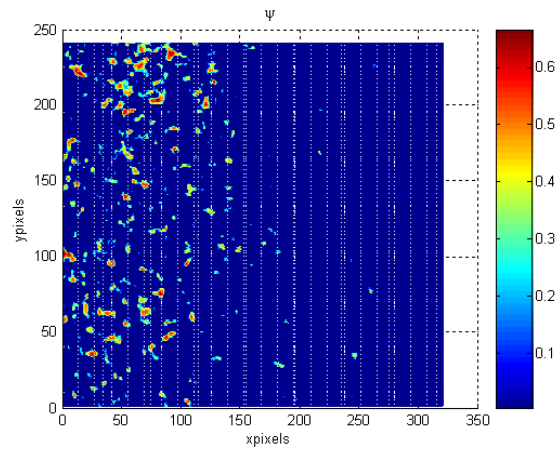


Figure 4 Measured 2-D distributions of Ψ (Al / Si)

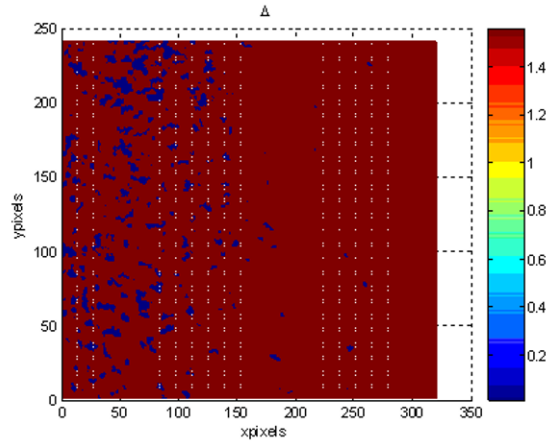


Figure 5 Measured 2-D distributions of Δ (Al / Si)

Figure 3 presents a typical image acquired by the CCD camera during the measurement process. The diffraction patterns visible in the image are the result of small particles on the surface of lens and interference fringes introduced by the optical components within the instrument setup. In order to investigate the feasibility of the proposed surface defect ellipsometry measurement process, it was verified using a silicon substrate coating aluminum (100nm) as a sample. Figures 4~5 present the 2-D distributions of the measured (Ψ, Δ) for the Al/Si sample whose thickness has been known.

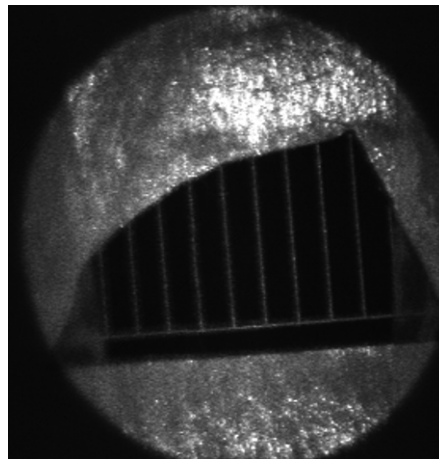


Figure 6 Typical image acquired by CCD camera during measurement process (the solar cell)

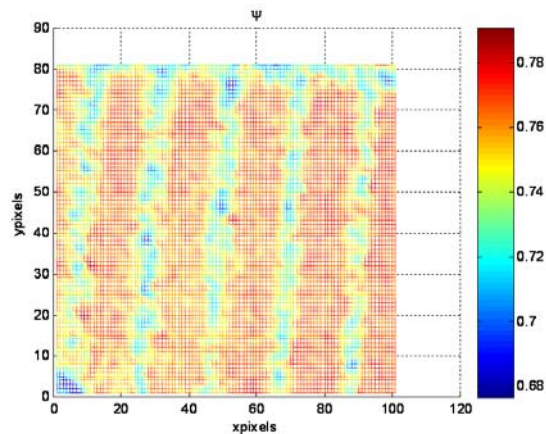


Figure 7 Measured 2-D distributions of Ψ (the solar cell)

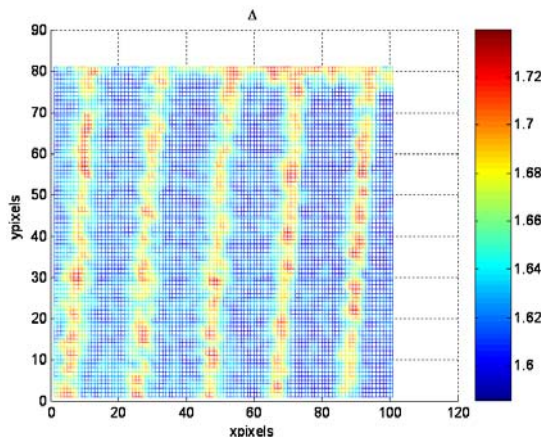


Figure 8 Measured 2-D distributions of Δ (the solar cell)

The experimental results confirm that the proposed sequential measurement method has the ability to obtain accurate values of the (Ψ, Δ) of solar cell material over the full range. In addition, the results show that the ellipsometric parameters (Ψ, Δ) have slight difference on the pattern Ψ of the solar cell. And the slight non-uniformity of the 2-D distributions of the (Ψ, Δ) may be the result of slight imperfections in the optical elements within the measurement system or may be caused by misalignment errors when constructing the measurement platform.

4. Conclusions

This study has presented a sequential method for obtaining full-field measurements of the surface of solar cell using the ellipsometry. It combined with a heterodyne interferometer and an image processing algorithm based on a three-integrating-bucket method. The experimental results have shown that the proposed method yields to tell the slight difference from the surface of solar cell by using the ellipsometric parameters (Ψ, Δ) . In addition, the presence of environmental disturbances via the use of a common-path configuration for the interferometer system cannot affect the measurement results by eliminating the DC component of the output light intensity signal in the image processing algorithm.

In the future study, we will apply the full-field imaging ellipsometry to measure anisotropic materials and characterize the optical parameters. Thus, the construction of a larger optical database and more complicated ellipsometry data analysis will be required in this field.

References

- [1] P. Drude, *Ann. Phys.*, 32 (1887) 584; *Ann. Phys.*, 34 (1888) 489.
- [2] W. Paik and J. O'M Bockris, "Exact ellipsometric measurement of thickness and optical properties of a thin light-absorbing film without auxiliary measurements", *Surf. Sci.*, 28 (1971) 61-68.
- [3] D. E. Aspnes and A. A. Studna, "High precision scanning ellipsometer", *Appl. Opt.*, 14 (1975) 220-228
- [4] P. S. Hauge and F. H. Dill, "A rotating-compensator Fourier ellipsometer", *Opt. Commun.*, 14 (1975) 431-437
- [5] S. N. Jasperson and S. E. Schnatterly, "An improved method for high reflectivity ellipsometry based on a new polarization modulation technique", *Rev. Sci. Instrum.*, 40 (1969) 761-767
- [6] Clerc, F. L., Collot, L., and Gross, M., "Numerical heterodyne holography with two-dimensional photodetector arrays," *Opt. Lett.* 25, 716–718 (2000).
- [7] Akiba, M., Chan, K. P., and Tanno, N., "Real-time, micrometer depth resolved imaging by low-coherence reflectometry and a two-dimensional heterodyne detection technique," *Jpn. J. Appl. Phys. Part 2* 39, L1194–L1196 (2000).
- [8] Hariharan, P., Orbel, B. F., and Eiju, T., "Digital phase-shifting interferometry: a simple error-compensating phase calculation algorithm," *Appl. Opt.* 26, 2504–2505 (1987).
- [9] Aguanno, M. V., Lakestani, F., Whelan, M. P., and Connelly, M. J., "Single pixel carrier based approach for full field laser interferometry using a CMOS-DSP camera", *Proc. SPIE* 5251, 304-312, (2004).

- [10] Lo, Y. L., Chih, H.W., Yeh, C. Y., and Yu, T. C., "Full-field heterodyne polariscope with an image signal processing method for principal axis and phase retardation measurements," *Appl. Opt.* 45, 8006-8012 (2006).

Photographic Diagnosis of Crystalline Silicon Solar Cells by Electroluminescence

Takashi Fuyuki and Ayumi Tani

Nara Institute of Science and Technology

8916-5 Takayama, Ikoma, Nara 630-0192 JAPAN fuyuki@ms.naist.jp

ABSTRACT

Crystalline Si solar cells emit infrared light under the forward bias as so called “Electroluminescence, EL”. The photographic imaging of EL intensity gives spatial information of solar cell performance with high resolution in less than one second. The EL intensity is proportional to the total number of minority carriers in Si substrates determined by the minority carrier lifetime. The quantitative analysis under various injection conditions can reveal cell performances such as the open circuit voltage. Photographic imaging represents the spatial distribution of minority carrier number at a glance. Intrinsic recombination centers such as crystal defects and grain boundaries which reduce the minority carrier density can be clearly detected as dark parts (spots, lines and areas) due to decreased EL intensity. Extrinsic deficiencies such as substrate breakage and hidden mechanical cracks can also be found easily since they are strong drains of minority carriers. In addition, electrode breakdown and inferior contacts also become visible due to less injection carriers. The EL technique is a versatile diagnosis tool to get the improved performance and high reliability of solar cells.

1. Introduction

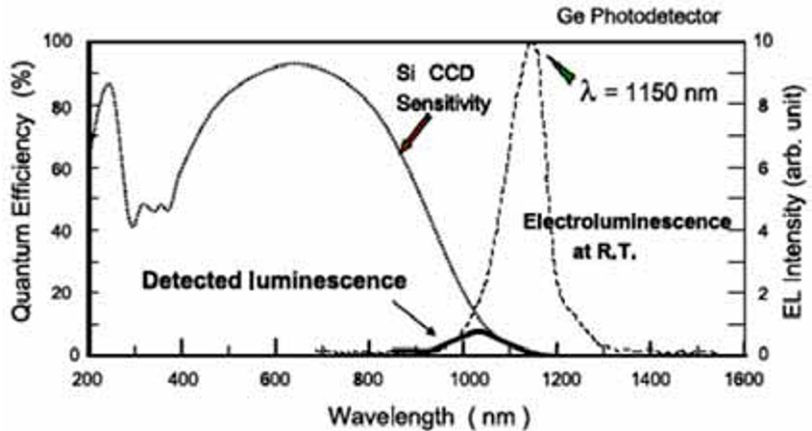
An electroluminescence (EL) imaging technique has caught much attention as a powerful photographic diagnosis tool to provide spatially resolved information about the electronic material properties of solar cells [1-4]. In addition mechanical deficiencies affecting the electrical performance of solar cells such as substrate breakage and/or electrode breakdown can be easily detected in a short time. A silicon Charge Coupled Device (Si-CCD) camera captures the EL signal emitted by current injection under forward bias. The intensity of EL is proportional to the total excess minority carrier density [3]. All the intrinsic defects and extrinsic deficiencies which reduce the minority carrier density will induce the spatial variation or inhomogeneities of EL intensity, and be displayed as dark parts (spots, lines or clouds) in EL images. In this report, the overview of EL imaging technique is introduced, and especially the distinction between the intrinsic crystallographic defects with the extrinsic mechanical deficiencies will be discussed using EL measurement at different temperatures.



Fig.1 Experimental Setup.

2. Experimental

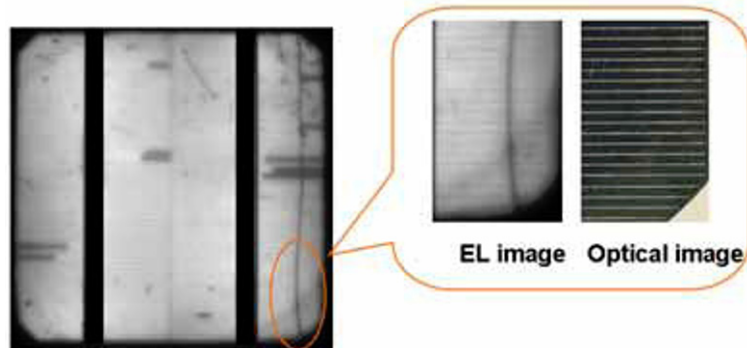
The experimental set up is shown in Fig.1 explained in elsewhere [1]. The system is simply composed a cooled Si CCD camera and a personal computer to capture EL images. The exposure time of the camera was 0.5 – 1 sec depending on the EL intensity. An IR filter matched with the detection wavelength (e.g., around 1150 nm in the case of crystalline Si cells [4]) was



attached in front of the camera lens. Forward bias voltage was applied to the sample to flow the current of around 30 - 40mA/cm². It should be noted that this forward current was almost the same as photo-generated current under 1 sun irradiation, and so the EL measurement was considered to reflect the working state of solar cells. Typical measurements were done at room temperature, but for the temperature dependent analysis discussed in the section4, the sample stage was elevated up to 100 C by Peltier heaters. All the experiments were conducted in a dark room. Spatial resolution was limited by the optical lens system and varied based on the magnification scale of the frame.

3. Typical electroluminescence images in crystalline Si cells

The emission spectrum of a crystalline Si cell taken by an infrared sensitive Ge detector was shown in Fig.2 by a dashed line. The dominant peak was at 1150nm, which was the band-to-band radiative recombination assisted by phonons. The sensitivity of Si-CCD was shown by a dotted line in Fig.2. The limited portion of the EL



could be detected. The absorption coefficient of Si at 1050nm was 16.3cm⁻¹, and so re-absorption was negligible in the case of typical Si cells with a thickness of 200 – 300μm.

The specific EL image in the case of defective single crystalline Si cell was shown in Fig.3. Generally speaking, uniform emission was expected due to the homogeneous material properties as seen in a major part of the cell surface. But, straight dark lines and scattered dark spots were observed, and they were caused by the breakdown of finger electrodes and process induced faults (dust, etc.). The long winding line was due to the wafer breakage which could not be detected by the conventional optical image as shown in the inset. These mechanical faults will reduce the production yield and affect the long term reliability of the cell. The EL method is an easy and quick way to detect these “extrinsic deficiencies”.

Typical EL images in the case of polycrystalline Si cells were shown in Fig.4. It shows a versatile aspect of EL technique, that is, we can detect the specific location of large module simply by zooming into the target position. In contrast to the single crystalline case, crystallographic defects such as grain boundaries, dislocations and aggregation of point defects were observed as

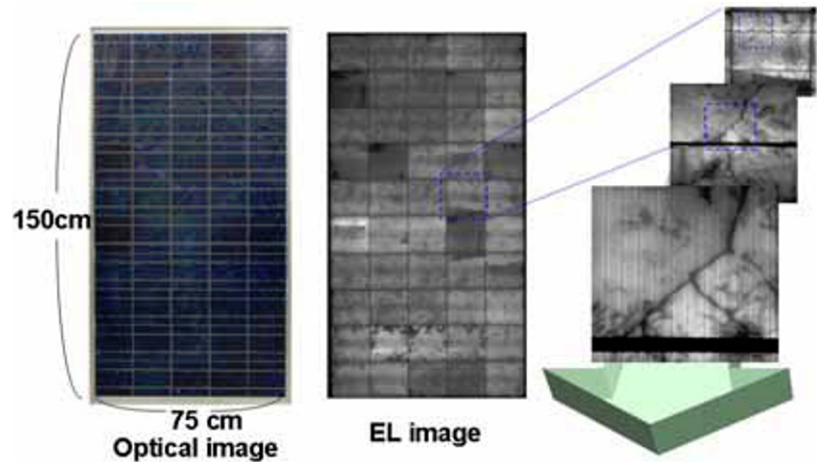


Fig.4 EL images in polycrystalline Si cells and module.

the cracks by substrate breakage or hidden cracks. The EL intensity is proportional to the total number of minority carriers in Si substrates. Not only the intrinsic defects but also extrinsic deficiencies induce the reduction of minority carrier number in polycrystalline Si cells. Especially, the extrinsic deficiencies cause serious problem in the reliability by the thermal heat cycles and mechanical distortions under actual installation conditions. So, the distinction of extrinsic deficiencies with intrinsic defects becomes very important in mass production of Si cells and modules. The devised method of EL measurement at different temperatures is proposed and discussed in the following section.

4. Distinction between intrinsic defects and extrinsic deficiencies

All the causes to reduce the minority carrier number can be detected as dark parts (dots, lines, and clouds, etc.) easily, but it is very difficult to distinct the actual origin of these “dark parts”. We have proposed a devised method to distinct the extrinsic deficiencies and intrinsic defects in polycrystalline Si cells by analyzing EL images taken at different temperatures [2]. Figures 5 show the evolution of EL images of polycrystalline Si cells with elevating

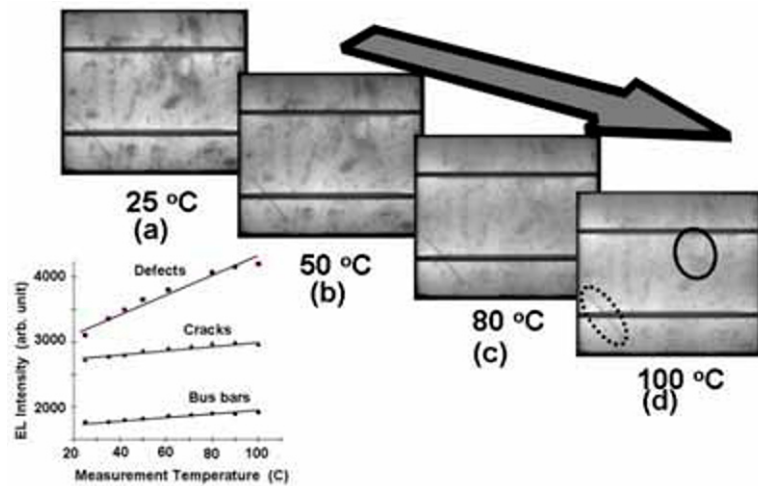


Fig.5 EL images measured at different temperatures.

the measurement temperature. The sample was heated by Peltier devices attached to the sample stage. If we compare the image taken at 100 C ((d)) with that at room temperature ((a)), we can recognize the following points. The dark parts enclosed by solid circle became unclear with elevating the temperature with less contrast. On the contrary, the dark lines in the dashed circle remained without losing the contrast. As shown in the inset, the EL intensity at the defects increased with elevating temperature since the capturing by traps is reduced with increasing sample temperature (the captured electrons are easily de-captured by the temperature). While, the intensity at the mechanical cracks remained dark since the electronic levels of traps become so deep not be de-captured by elevating temperature. By subtracting the images at high and low temperatures, we can distinct the extrinsic deficiencies and intrinsic defects by simple image processing method as shown in Fig.6.

5. Conclusions

Photographic diagnosis method of Si solar cells using electroluminescence was reviewed. The electroluminescence imaging technique was a versatile method to reveal the defective parts in solar cells visually in a short time. Extrinsic deficiencies such as substrate breakage and hidden cracks could be detected discriminating with the intrinsic defects by the temperature subtraction method, which is suitable for the quality control in the cell production process.

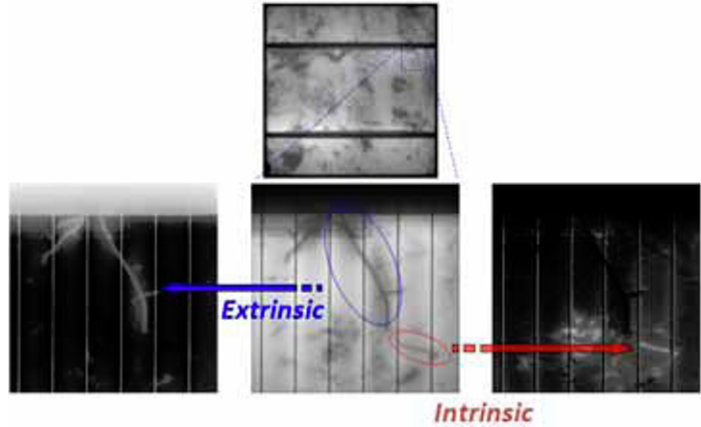


Fig.6 Distinction of extrinsic deficiencies and intrinsic defects by temperature subtraction method.

Acknowledgements

This work is supported in part by NEDO (New Energy and Industrial Technology Development Organization) as a part of the Innovative Solar Cells R&D Program.

References

- [1] A.Kitiyanan, A.Ogane, A.Tani, T.Hatayama, H.Yano, Y.Uraoka, and T.Fuyuki, "Comprehensive study of electroluminescence in multicrystalline silicon solar cells", *J. Appl. Phys.*, 106, 043717, (2009).
- [2] T.Fuyuki, and A.Kitiyanan, "Photographic diagnosis of crystalline silicon solar cells utilizing electroluminescence", *Appl. Phys. A*, DOI: 10.1007/s00339-008-4986-0, (2008).
- [3] T.Fuyuki, H.Kondoh, Y.Kazi, A.Ogane and Y.Takahashi, "Analytic findings in the electroluminescence characterization of the crystalline silicon solar cells", *J. Appl. Phys.*, 101, 023711, (2007).
- [4] T.Fuyuki, H.Kondo, T.Yamazaki, Y.Takahashi and Y.Uraoka, "Photographic Surveying of Minority Carrier Diffusion Length in Polycrystalline Silicon Solar Cells by Electroluminescence", *Appl. Phys. Lett.*, 86, 262108, (2005)

Novel Interfacial Adhesion Experiments with Individual Carbon Nanofibers

Tanil Ozkan¹, Ioannis Chasiotis¹

¹Aerospace Engineering, University of Illinois at Urbana-Champaign, Urbana, IL 61801, U.S.A.

ABSTRACT

A novel experimental method for the interfacial mechanics of nanofibers embedded in polymeric matrices was developed. The debond force was determined by MEMS devices whose motion was precisely measured from optical images by digital image correlation. This method is based on a novel approach to embed nanofiber and nanotubes in a thermoplastic or thermosetting polymer with submicron control of the embedded length and orientation of the nanofiber. The cross-head displacement resolution of this optical method is ~20 nm and the force resolution is of the order of nanonewtons. A traceable force calibration technique was integrated to calibrate the MEMS force sensors. Experiments were conducted for the first time with vapor grown carbon nanofibers embedded in EPON epoxy to reveal the role of nanofiber surface roughness and functionalization in the interfacial shear strength. It was established that the nanoscale surface roughness of nanofibers strongly promotes interfacial strength while surface functionalization can increase the interfacial adhesion strength by more than a factor of three. The present experiments are the first of their kind both in their fidelity and accuracy of the applied experimental method and the data scatter is dramatically reduced compared to prior experimental attempts.

INTRODUCTION

One of the fundamental axioms of emerging nanoscience and technology is the superior mechanical and functional properties of multiscale composites through the inclusion of nanoscale reinforcement and functionalization agents. In this regard, vapor grown carbon nanofibers (VGCNFs) have received significant interest due to their potential as structural reinforcement for various polymeric matrices. In mechanical terms, a strong and perfectly bonded interface is a prerequisite for effective stress transfer. The interfacial shear strength (IFSS) is a primary measure indicating the mechanical quality of the interface as it defines the capability of the matrix to transfer forces to the nanoscale reinforcement, in this case the carbon nanofibers. Until quite recently, experimental characterization of the mechanical behavior of interfaces in polymer matrix composites was limited to microscale reinforcements due to experimental limitations in force and strain metrology at the submicron scale. The first experimental inquiries of nanoscale interfacial phenomena became possible with the in-situ application of scanning probe microscopy cantilevers [1,2]. Although they represent significant experimental milestones, such cantilever deflection based drag-out and pull-out techniques have obvious deficiencies such as the applied loading being not uniaxial in nature as required for a pull-out test, hence causing mixed mode fracture at the interface. More recently, another study attempted to extend these cantilever based IFSS measurements to thermosetting matrices by embedding high-temperature-heat and surfactant treated VGCNFs within an epoxy [3]. The force metrology and thus the interfacial strength measurement was identical to its predecessor studies, which couldn't overcome experimental limitations of precise embedded length definition and mixed mode fracture, resulting in nonphysical IFSS values exceeding 400 MPa. This short paper presents a novel method that overcomes previous experimental limitations to obtain consistent and physically sound experimental measurements of the interfacial adhesion of carbon nanofibers in polymeric matrices.

NOVEL INTERFACIAL STRENGTH EXPERIMENTS

Three grades of individual VGCNFs with diameters varying from 150-300 nm were tested for their interfacial adhesion in Epon 828/Epikure 3140 epoxy matrix: As-grown nanofibers (PR-24-PS), high temperature heat-treated non-functionalized VGCNFs (PR-24-HHT-LD), and high temperature heat treated and surface functionalized VGCNFs (PR-24-HHT-OX). The single nanofiber pull-out experiments were conducted by a novel MEMS-based experimental method, which overcame the limitations and deficiencies of earlier techniques for nanofiber pull-out experiments. Key in this development was the combined use of on-chip actuated polysilicon loadcells with auxiliary polysilicon bridges acting as nanofiber mounts. For embedment purposes, 0.8 μm deep trenches were ion-milled by a focused ion beam (FIB) to facilitate the initial deposition of epoxy, which was cured at 90°C for 30 minutes. Shallower trenches of 0.3 μm depth were ion-milled in the middle of the initial larger

trenches filled with epoxy to guarantee sufficient polymer containment in the region surrounding the nanofiber. Subsequently, the FIB was used to define the nanofiber embedded length with submicron accuracy. Pull-out experiments were executed with double-column folded beam MEMS-scale loadcells, whose true stiffness was determined by the calibration process discussed in [4]. The actuation of the nanofiber pull-out apparatus and the data acquisition were performed similarly to the methodology described in [5]. The ultimate loadcell deflection required to determine the IFSS was measured by digital image correlation (DIC) with an accuracy of 20 nm which is translated to an accuracy of a few tens of nanonewton in force measurement. Post-mortem SEM images of the remaining pull-out channels and the debonded VGCNFs, as shown in Figures 1a and 1b, pointed out to purely interfacial failure for the PR-24-PS and PR-24-HHT-LD nanofiber grades, and rather mixed interfacial and matrix failure for the PR-24-HHT-OX grade. A uniform yielding criterion was used to quantify the IFSS given the measurement of the force in the nanofiber at the instant of debonding.

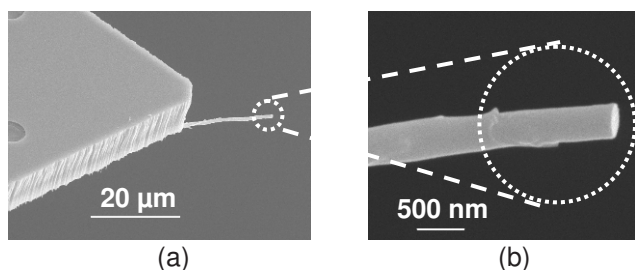


Figure 1. SEM images of a pulled-out VGCNF nanofiber: (a) at the MEMS loadcell grip and (b) detail of the nanofiber showing clear matrix debonding.

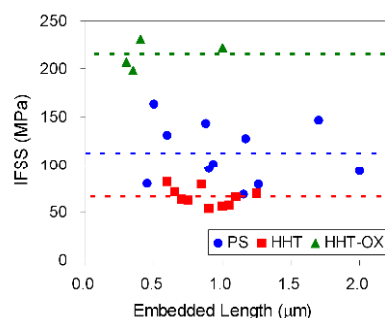


Figure 2. IFSS of as-fabricated (PS), high temperature heat treated (HHT), and oxidized HHT (HHT-OX) VGCNFs.

RESULTS AND CONCLUSION

Figure 2 shows the IFSS measured for the different nanofiber grades as a function of nanofiber embedded length. The IFSS of as-grown VGCNFs (PR-24-PS) to EPON epoxy was 112 ± 32 MPa, which was higher than that for non-functionalized PR-24-HHT-LD that averaged 66 ± 10 MPa. TEM imaging revealed that the adhesion of the heat-treated nanofibers was decreased because of a reduction in the nanofiber surface roughness from 5 nm to approximately 2 nm. This resulted in smaller area for interfacial adhesion and therefore smaller bonding strength. Much higher IFSS values of 215 ± 15 MPa were measured for oxidatively surface treated nanofibers (PR-24-HHT-OX), indicating that VGCNF functionalization can increase the IFSS dramatically by more than a factor of three compared to the PR-24-HHT-LD grade. The reported IFSS values correlate well with overall trends in composite level fracture toughness measurements, indicating the direct relationship between the local and the effective composite properties. The consistent results of this investigation provide a definitive step towards establishing a robust experimental method for the interfacial mechanics of nanoscale reinforcements in soft matrices.

REFERENCES

1. Cooper et al., "Detachment of nanotubes from a polymer matrix", *Applied Physics Letters*, 81(20), pp. 3873-3875, 2002.
2. Barber et al., "Interfacial fracture energy measurements for multi-walled carbon nanotubes pulled from a polymer matrix", *Composites Science and Technology*, 64(15), pp. 2283–2289, 2004.
3. Manoharan et al., "The interfacial strength of carbon nanofiber epoxy composite using single fiber pullout experiments", *Nanotechnology*, 20, 295701(5pp), 2009.
4. Naraghi M., Chasiotis I., "Optimization of Comb-Driven Devices for Mechanical Testing of Polymeric Nanofibers Subjected to Large Deformations", *Journal of Microelectromechanical Systems*, 18(5), pp. 1032-1046, 2009.
5. Naraghi et al., "Novel method for mechanical characterization of polymeric nanofibers", *Review of Scientific Instruments*, 78(8), 085108 (7pp), 2007.

Dynamic Constitutive Behavior of Reinforced Hydrogels inside Liquid Environment

Sashank Padamati

University of Massachusetts Dartmouth, 285 Old Westport Road, North Dartmouth, MA, 02747

ABSTRACT

Dynamic compressive behavior of three different types of hydrogels used for soft tissue applications are tested using a modified split Hopkinson pressure bar. Three kinds of hydrogels: (a) plain epoxy hydrogels, (b) epoxy hydrogels reinforced with three-dimensional polyurethane fibers and (c) fumed silica nano particles reinforced hydrogels with different cross linking densities are considered in this study. The three dimensional pattern of the fibers are generated by a rapid robo-casting technique. A pulse shaping technique is used to increase the rising time of the incident pulse to obtain dynamic stress equilibrium. A novel liquid environment technique was implemented to observe the dynamic behavior of hydrogels when immersed in water. Experiments are carried out for different strain rates with and without water environment. Preliminary results show that the yield strength of these hydrogels decreases when they are immersed in water.

INTRODUCTION

Mimicking human tissues with artificial materials which are bio-compatible and bio-degradable are of vast interest. Hydrogels are extensively used in biomedical applications [1] especially in tissue engineering. They are used as scaffolds to guide the growth of new tissues. Hydrogels are highly corrosion-resistant and their swelling nature provides an aqueous environment comparable to soft tissues. When hydrogels are completely saturated with water they tend to have poor mechanical properties. Attempts were made to increase the mechanical properties of hydrogels by adding glass fibers and were partially successful [2]. In this study three-dimensional polyurethane fibers and fumed silica nano particles are reinforced into different hydrogels to improve low mechanical properties. Hydrogels are placed in water environment and tested to observe the variations in mechanical properties. A novel liquid environment chamber built with acrylic glass is developed for testing hydrogels in water Fig. 1. Rubber washers were used to ensure a seal proof chamber. In this study, investigation of dynamic constitutive behavior of the hydrogels at different strain rates with and without the water environment is carried out.

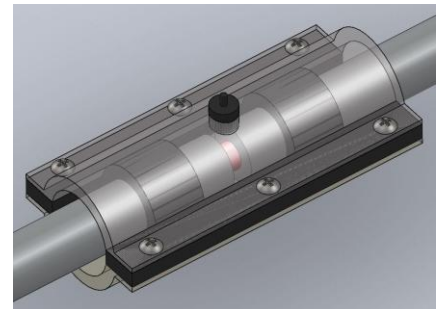


Fig. 1 liquid environment specimen fixture

EXPERIMENTAL DETAILS

Hydrogels are prepared by mixing an epoxy Polyethylene glycerol diglycidylether (PEGDGE) with Jeffamine (ED600) in aqueous solution. The cross linking density is controlled by varying the molar ratio's of epoxy and amine components. The mixture is cured for 24 hours to complete the reactions to form a gel. A three dimensional robo-casting technique is applied to generate a patterned polyurethane fiber structure. In this technique computer controlled dispensing needle moves in x-y-z direction generating well defined patterned structure. Needle has a diameter of 100microns. Fig. 2 shows the image of a three-dimensional fiber generated from the rapid robo-casting technique. These fiber's are reinforced into hydrogel using ultrasonication process. To prepare a nano particle gel oligomers are mixed with 0.5% weight fraction of camphorquinone, 0.5 % weight fraction of dimethyl-toluidine and 2% weight fraction of fumed silica particles. Photo polymerization is implied to cure the solution. Hydrogels are tested in the modified split Hopkinson Pressure Bar (SHPB) setup to determine the dynamic constitutive behavior under compression. The experimental setup consists of a striker bar, an incident bar, and a transmission bar made of Aluminum 7075-T651. All bars have an equal diameter of 25.4mm, while incident bar is approximately 1.8m long and transmission

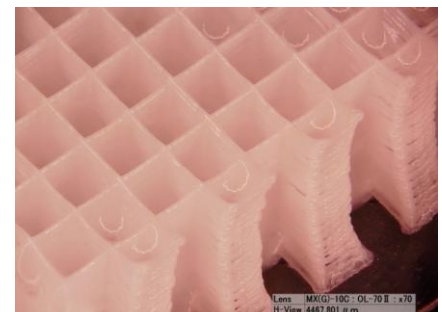


Fig. 2 Image of 3D fiber

bar is 1.2m long. The striker bar used in these experiments is 304.8mm. Due to brevity of space, theory for this setup are referred in [3]. All experiments were carried out at a constant pressure of 0.13MPa (20psi). Annealed copper C11000 is used as a pulse shaper to obtain better equilibrium conditions at bar-specimen interface. The dynamic constitutive behavior of hydrogels were investigated for both with and without water conditions using SHPB for a strain rate range of 2000/s - 4000/s. Typical pulses obtained from the SHPB set up for hydrogels are shown in Fig. 3.

RESULTS AND DISCUSSION

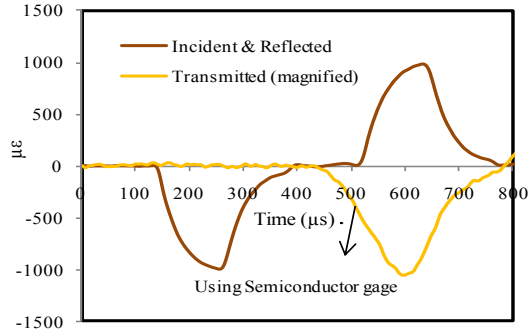


Fig. 3. Typical pulses obtained from SHPB set up

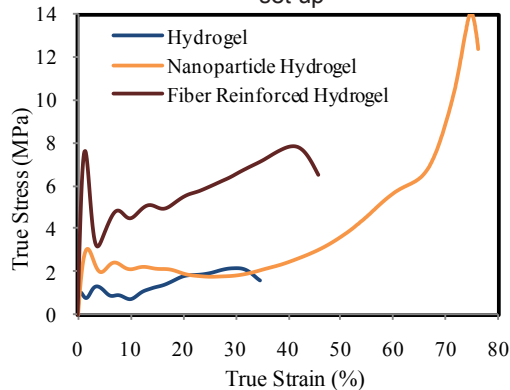


Fig. 5. True compressive stress-strain curve for hydrogels (with water environment)

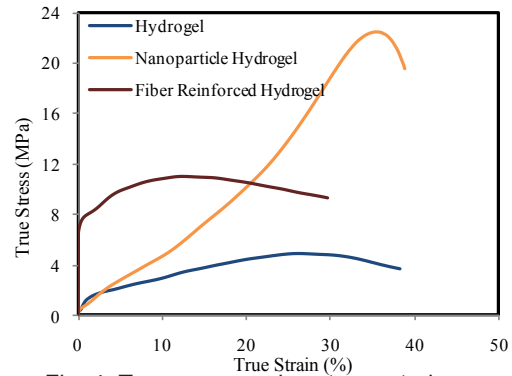


Fig. 4. True compressive stress-strain curve for hydrogels (without water environment)

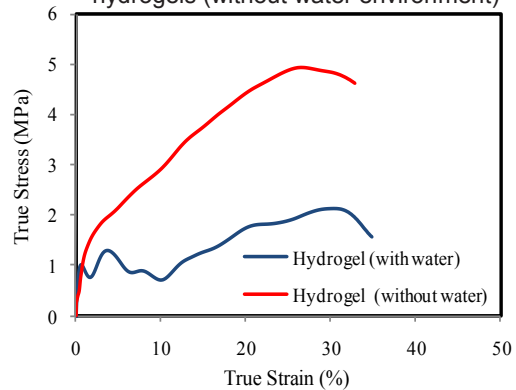


Fig. 6. True compressive stress-strain curve for plain hydrogels (with and without water environment)

The true stress-strain behavior of three different hydrogels when tested without any water environment is shown in Fig.4. It can be noticed from Fig.4 that the fiber reinforced hydrogel has the highest yield strength compared to other hydrogels and plain hydrogel has the lowest yield strength. Fig. 5. shows the true stress-strain behavior of these hydrogels when tested under water environment. These results also show that the fiber reinforced hydrogel has the highest yield strength and plain hydrogel has low yield strength. Same pattern is observed under both the conditions for all three kinds of hydrogels. From Fig. 6 it can be observed that the yield strength decreased when tested under water conditions.

ACKNOWLEDGEMENTS

I would like to thank Dr. Vijaya Chalivendra for guiding me throughout the project. Also I would like to thank Animesh Agarwal for helping me in preparation of hydrogels.

REFERENCES

1. Metters AT, and Lin CC, Biodegradable Hydro gels: Tailoring Properties and Function through Chemistry and Structure, Biomaterials, Wong JY, and Bronzino JD, Eds. NY: CRC Press, 5.1-5.44, 2007
2. Yang, Shukui L, Lili Y, Dongmei H and Fuchi W: Dynamic compressive properties and failure mechanism of glass fiber reinforced silica hydrogel, Material Science and Engineering., 824-827, 2010
3. Kolsky, H:, An investigation of mechanical properties of materials at very high strain rates of loadings, Proceedings of the Physical Society of London, B62, 676-700, 1949.

Osteon Size Effect on the Dynamic Fracture Toughness of Bone

Michelle Raetz, Mechanical Engineering Graduate Student
Michigan State University, East Lansing, Michigan 48824

INTRODUCTION

Bone is a highly studied material due to its complex microstructure and its ability to withstand fracture. It is a strong and lightweight material that has strengthening mechanisms that would be ideal if replicated in composite materials. At quasi-static loading it has been shown to have several strengthening mechanisms. One of the main

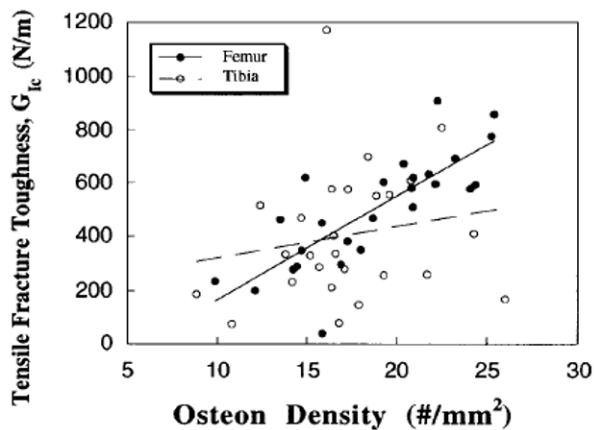


Figure 1. Correlation between osteon density and tensile fracture toughness at static loading^[2]

proponents against fracture in the transverse direction (perpendicular to the loading axis) is crack deflection^[1]. Cortical bone, which is comprised of tube-like structures called osteons, is able to deflect a propagating crack up to 90°^[4] which can reduce the driving force for crack advance up to 50% when compared to the undeflected crack^[3]. It does this by rerouting the crack along the weaker cement lines that are present along the outside of osteons. It has also been shown that the size and orientation of osteons have an influence on mechanical properties^[1]. Smaller osteons increase the tensile fracture toughness^[2] but due to bone's anisotropic nature, it is unclear if this relation holds true under dynamic loading. Bone loaded at strain rates greater than 1s⁻¹ will yield different results when compared to static loading^[5]. This study aims to determine which size and density of osteons will yield the greatest resistance to fracture at dynamic loading.

METHODS AND RESULTS

Bone specimens were extracted from the mid-diaphysis of bovine femurs and machined into beam shapes with dimensions 40x10x8mm (Figure 2). They were kept in PBS (phosphate buffered saline solution) until ready for testing. The specimens were impacted in 3-point bending at velocities ranging from 1 to 10 m/s using a drop weight impact tower and filmed using a high speed camera at up to 180,000 frames per second.

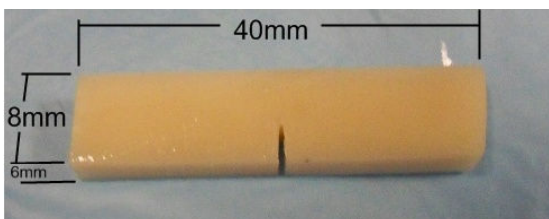


Figure 2. Image of bone specimen with dimensions

Using Digital Image Correlation (DIC), the fracture toughness was calculated from the high speed images captured (Figure 3). After impact, the bones were inspected with an optical microscope to measure osteon size and density. This information will be correlated with the velocity of impact and the fracture toughness calculated

to discover what importance the size and density of osteons has on bones ability to withstand impact. It is hypothesized that smaller, more densely packed osteons will yield higher fracture toughness values.

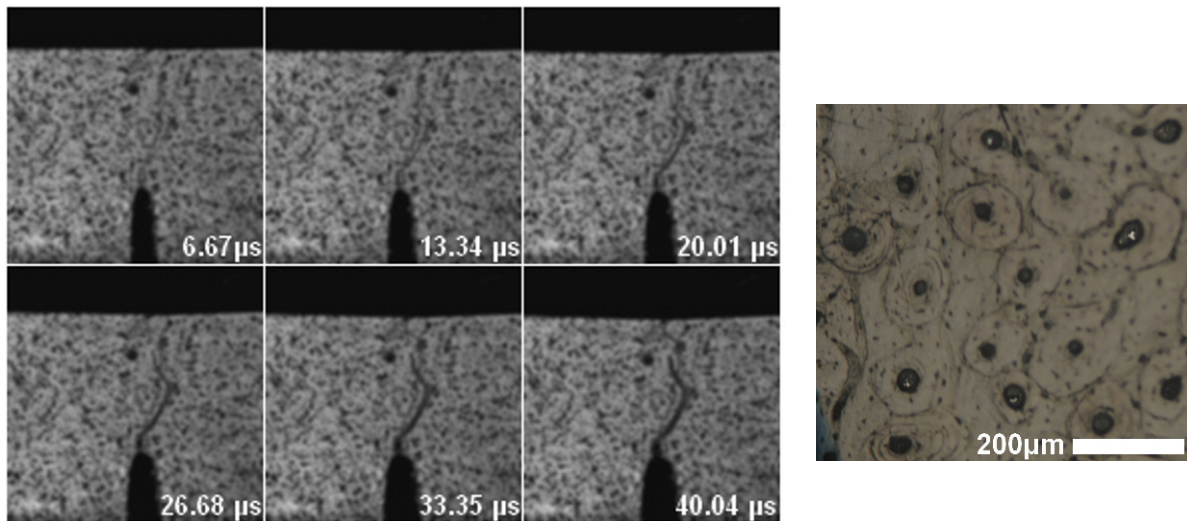


Figure 3. Sequential images of bone impacted at 10m/s and filmed at 150,000 frames per second(left), cross-section of osteons from impacted specimen

REFERENCES

1. Ritchie, R.O. et al: A fracture mechanics and mechanistic approach to the failure of cortical bone. *Fatigue and Fracture of Engineering Materials and Structures*. 28, 4. (2005)
2. Yeni, Y.N. et al: The influence of bone morphology on fracture toughness of the human femur and tibia. *American Society of Mechanical Engineers, Bioengineering Division BED*. v 35 (1997)
3. Nalla, R.K. et al: Mechanistic fracture criteria for the failure of human cortical bone. *Nat, Mater*. v 2, p164 (2003)
4. Bang, X.D. et al: Changes in the fracture toughness of bone may not be reflected in its mineral density, porosity, and tensile properties – Effects of sampling sites and crack orientation. *Bone* 23,67 (1998)
5. J.H. McElhaney: Dynamic response of bone and muscle tissue. *Journal of Applied Physiology*. 21, 4. (1966)

Radial Inertia in Non-cylindrical Specimens in a Kolsky Bar

Oishik Sen, Department of Mechanical Engineering,
Michigan State University, East Lansing, MI-48824

ABSTRACT

For high-strain rate testing of non-cylindrical specimens using a Split Hopkinson Pressure Bar (Kolsky Bar), a correction for radial inertia has been developed, based on a first order approximation of stress-variation in the specimen's cross-section. The motivation for such a work is the difficulty in machining fragile specimens to an exact cylindrical shape, as is typically required in a Split Hopkinson Pressure Bar Experiment. The correction term has been shown to be dependant on the geometry of the specimen's cross-section, the Poisson's Ratio and the length of the sample chosen, and has been compared to a similar correction factor, previously developed for a cylindrical specimen. The latter has been found to be a special case of the formula developed here.

INTRODUCTION

The Kolsky Bar or a Split Hopkinson Pressure Bar (SHPB) is an experimental set-up for characterizing the dynamic behavior of materials at impact rates of strain (10^2 /s– 10^4 /s) [1,2]. In a Kolsky Bar, a compressive wave is generated in a cylindrical specimen of the material to be tested, which is sandwiched between two long, symmetric pressure bars, called the incident bar and the transmission bar. A major assumption [3,4] in such an experiment is that there is uniform radial stress distribution in the specimen. However, as the specimen is loaded in compression, the specimen tries to expand radially, which is opposed by the radial inertia of the specimen. Based on a first order approximation for stress variation in the specimen, Davies and Hunter [5] developed the following relation, incorporating the correction for the radial inertia:

$$\sigma_s = \sigma_b + \rho_s \left(\frac{1}{6} h^2 - \frac{1}{2} \nu_s^2 a^2 \right) \ddot{\epsilon} \quad (1)$$

where ρ_s , ν_s are the density and Poisson's Ratio, a and h are the diameter and length of the sample, and σ_s and σ_b are the stress needed to deform the specimen one-dimensionally, and the stress measured at the transmitter face [6] respectively. Following this, several corrections for radial inertia for cylindrical specimens were developed [7-11] taking into consideration the convective component of the stress, effects of friction, brittleness and softness of the specimen etc.

RESULTS

The testing of fragile biological specimens [12], and the combination of Digital Image Correlation Techniques [13] with the SHPB techniques, necessitates the use of specimens that are not necessarily circular in cross-section. In



Figure 1: A Specimen Sandwiched between Incident and Transmission Bar

the present investigation, radial inertia of a non-cylindrical specimen has been accounted for, and a corrected expression for obtaining the one-dimensional stress in such a specimen in an SHPB experiment has been derived, based on a first order approximation of stress variation along the cross-section of the specimen. For specimens with rectangular and regular hexagonal cross-sections, the resulting expressions take the following forms respectively:

$$\sigma_s = \sigma_b + \rho_s \left\{ \frac{1}{6} h^2 - \frac{1}{12} v^2 (a^2 + b^2) \right\} \quad (2a)$$

$$\sigma_s = \sigma_b + \rho_s \left(\frac{1}{6} h^2 - \frac{5}{12} v^2 t^2 \right) \quad (2b)$$

where a and b are the width and depth of the cross-section of the rectangular prism and t is the edge-length of the cross-section of a regular hexagonal. To validate the expression developed for arbitrary cross-sections, experiments were performed using Aluminum 6061 specimens, with rectangular and hexagonal cross-sections. The length of the samples was such chosen that the inertia correction term would explicitly drop out in some of them. To obtain the one-dimensional stress in the specimen, a Finite Element algorithm had been used and the proposed expression for one-dimensional stresses, after correcting for radial inertia, was compared with the stresses obtained from Finite Element Analysis of the specimen. Further, the expression obtained by Davies and Hunter[6] (Eq. 1) for correction of radial inertia was derived as a special case of the same developed in the present investigation.

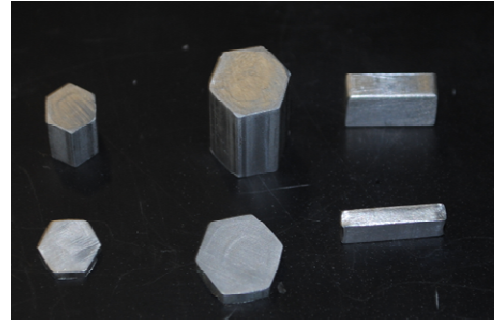


Figure 2: Specimens for Determination of Correction Factor for Radial Inertia

REFERENCES

1. Kolsky H, An investigation of the mechanical properties of materials at very high rates of loading, Proc R Soc London, B 62:679-700, 1949
2. Ravichandran G and Subash G, Critical appraisal of limiting strain rates for compression testing of ceramics in a split Hopkinson pressure bar, J. Am. Ceram. Soc 77 [1], 263-67, 1994
3. Gama A. Bazle, Lopatnikov Sergey L, Gillespie John W, Hopkinson bar experimental technique: A critical review. Appl Mech Rev, Vol 57, no 4,223-250, 2004
4. Al-Mousawi M. M., Reid S. R., Deans W.F., The use of the split Hopkinson bar techniques in high strain rate materials testing, Proc Instn Mech Engrs Vol 211 Part C, 273-292, 1997
5. Davies E., Hunter S. C., The dynamic compression testing of materials by the method of the split Hopkinson pressure bar, J Mech Phys Solids, 11:155-179, 1963
6. Bertholf L.D., Karnes C.H, Two-dimensional analysis of the split Hopkinson pressure bar system, J. Mech Phys Solids, 23:1-19, 1975
7. Samanta S.K., Dynamic deformation of aluminum and copper at elevated temperatures. J Mech Phys Solids, Vol 19, 117-135, 1971
8. Gorham DA, Specimen inertia in high strain-rate compression, J. Phys, D, Appl Phys 22:1888-1893, 1989
9. Gorham DA, The effect of specimen dimensions on high strain rate compression measurements of copper. J Phys D, Appl Phys 24:1489-1492, 1991
10. Song B , Ge Y, Chen W.W., Weerasoriya T.,Radial inertia effects in Kolsky bar testing of extra-soft specimens, Exp. Mech. 47: 659-670, 2007
11. Forrestal M.J., Wright T.W., Chen W., The effect of radial inertia on brittle samples during the split Hopkinson pressure bar test, International Journal of Impact Engineering, 34: 405-411, 2007
12. Mayer George, Sarikaya Mehmet, Rigid biological composite materials: Structural examples for biomimetic design, Experimental Mechanics, Vol 42, 4:395-403, 2001
13. Gilat A, Schmidt T.E., Walker A.L., Full field strain measurement in compression and tensile split Hopkinson bar experiments, Experimental Mechanics, 49:291-302, 2009.

Core Deformation of Sandwich Composites under Blast Loading

Erheng Wang and Arun Shukla

Dynamic Photomechanics Lab, Dept. of Mechanical, Industrial and Systems Engineering
The University of Rhode Island, 92 Upper College Road, Kingston, RI 02881, USA

INTRODUCTION

During blast loading, the core of a sandwich composite demonstrates complicated stress/strain behavior. The shear stress/strain in the core is the primary consideration. Though the shear strain profile is non-linear, the transverse strain in the core is generally modeled with a linear or constant profile in numerical simulation. However, recent numerical studies have found that the transverse strain in the core also has a highly non-linear profile through the thickness. This is important in understanding the mechanism of pulse mitigation in sandwich composites. To date, no experimental investigations have been done to visualize the strain profile in the core of sandwich composites subjected to blast loading. In this paper, the high-speed 3-D Digital Image Correlation (DIC) technique was utilized to characterize such strain profiles. The real-time deformation images of the core material in a sandwich panel were captured by a high-speed photography system. The strain profiles and histories were calculated from these real-time images using DIC technique. These results were carefully analyzed and discussed.

MATERIALS AND EXPERIMENTAL SETUP

The skin materials of the sandwich composites are E-Glass Vinyl Ester (EVE) composites. The woven roving E-glass fibers of the skin material were placed in a quasi-isotropic layout $[0/45/90/-45]_s$. The front skin and the back skin consisted of identical layup and materials. The core materials of the sandwich composites are Corecell™ P600 styrene foams, which are manufactured by Gurit SP Technologies. The overall dimensions for the specimen were 102 mm wide, 254 mm long and 45.7 mm thick. The foam core itself was 38.1 mm thick, while the skin thickness was 3.8 mm. The average areal density of the samples was 19.58 kg/m^2 .

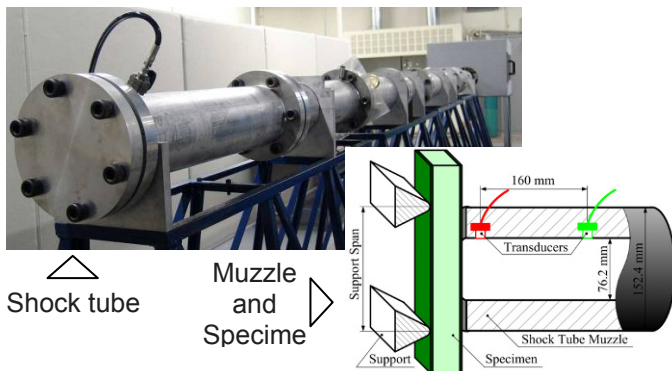


Fig. 1 Shock tube apparatus

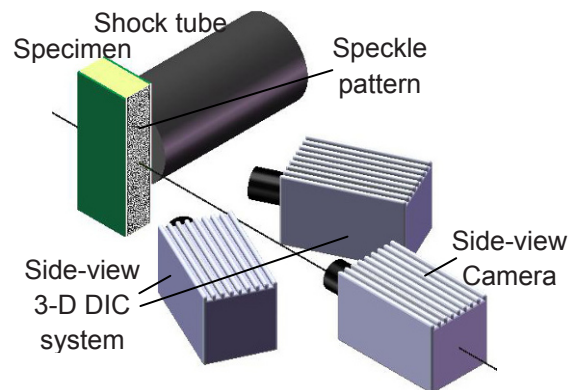
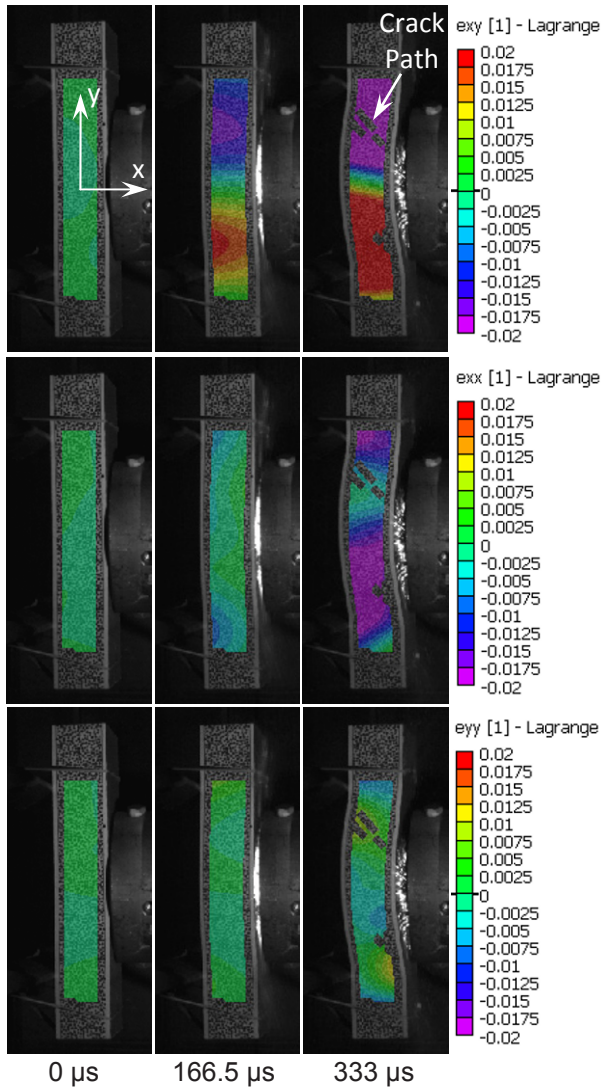


Fig. 2 Experimental setup

A shock tube apparatus as shown in [fig. 1](#) (with a detailed image of the muzzle) was utilized here to give a shock wave loading with initial overpressure of 1.25 MPa. A simply supported boundary condition is applied. [Fig. 2](#) shows a typical experimental pressure profile. A high-speed photography system with three cameras was utilized to capture real-time deformation images. It consists of a side-view 3-D DIC system with two cameras and an

additional side-view camera. Since the cameras in the 3-D DIC system need to capture images from different tilted angles, the lens axis of the additional camera is set to be perpendicular to the side surface of the specimen. To ensure good image quality, a speckle pattern with good contrast was put on the side of the core material.

EXPERIMENTAL RESULTS AND DISCUSSION



0 μs 166.5 μs 333 μs
 Fig. 3 contour histories of the strain

Fig. 3 shows the contour histories of the strains e_{xy} , e_{xx} and e_{yy} from 3-D DIC analysis. During the core crack formation, It is apparent that the strain e_{xy} is concentrated around the core crack path, indicating that the shear strain (or stress) cause the core cracks. The strains e_{xx} and e_{yy} have no concentration around the core crack path.

Fig.4 shows the history of the strain e_{xx} at the middle point located behind the front face sheet. The strain e_{xx} at this point was always negative (compression) when the sandwich panel was suffering large deflection (after cracks appeared), but could be positive when the deflection was very small. The e_{xx} behavior before 200 μs agrees with the numerical results in ref[2]. The detailed analysis of e_{xx} shows that in the first 200 μs, the normal strain through thickness has a linear profile. After that, when the sandwich panel was suffering large deflection, the normal strain shows a nonlinear profile.

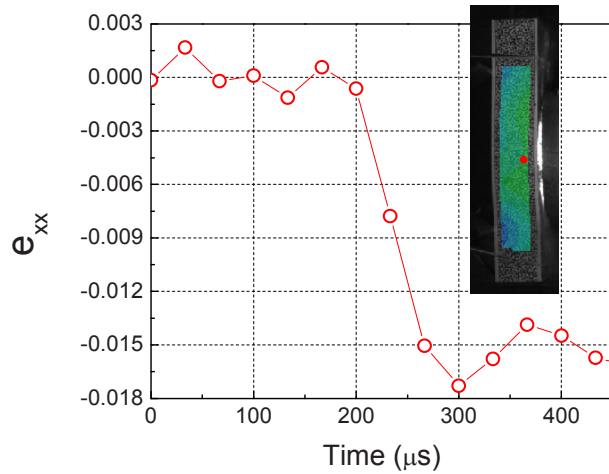


Fig. 4 history of the strain e_{xx} at the middle point located behind the front face sheet

ACKNOWLEDGEMENT

The support of Office of Naval Research (ONR) Grant No. N00014-04-1-0268 is gratefully acknowledged. The support provided by the Department of Homeland Security (DHS) under Cooperative Agreement No. 2008-ST-061-ED0002 is also acknowledged.

REFERENCES

[1] Vinson JR. The Behavior of Sandwich Structures of Isotropic and Composite Materials, Lancaster, Technomic Publishing Company, 1999.
 [2] Li R, Kardomateas GA and Simitse GJ. Point-wise impulse (blast) response of a composite sandwich plate including core compressibility effects. International Journal of Solids and Structures, 46, 2216–2223, 2009.

Influence of Friction-Stir-Welding Parameters on Texture and Mechanical Behavior

Zhenzhen Yu¹, Hahn Choo¹, Wei Zhang², Zhili Feng², and Sven Vogel³

1. Department of Materials Science and Engineering, University of Tennessee, Knoxville, TN 37996, USA
2. Materials Science and Technology Division, Oak Ridge National Laboratory, Oak Ridge, TN, 37831, USA
3. Los Alamos Neutron Science Center, Los Alamos National Laboratory, Los Alamos, NM, 87545, USA

1. INTRODUCTION

During friction stir welding (FSW), a cylindrical threaded tool pin rotates and plunges into the workpieces and produces a stirring action that joins the workpieces together, while the shoulder part of the tool forges down the workpiece providing frictional heating. The joining is accomplished by running the rotating tool along the weld line. Significant heat is generated mainly from the friction between the tool shoulder and workpiece, while a severe plastic deformation occurs in the softened material by the stirring pin. As a result, a severely-deformed 'stir zone' with fine grains is produced through dynamic recrystallization (DRX). To date, the challenge remains in the fundamental understanding of the governing mechanisms for the grain refinement, texture formation, and the resulting mechanical behavior after FSW of Mg alloys. It is noted that, for hcp crystalline structure, deformation condition dominates the active deformation modes (slip vs. twinning), and, hence, the development of texture [1]. In this study, the objective was to investigate the influence of thermo-mechanical input during FSW on texture development and the corresponding mechanical behavior after FSW of AZ31B Mg alloy. A series of FSW experiments were designed to cover a wide range of deformation conditions by varying the rotation and travel speeds of the tool. Subsequently, the changes in texture of the stir zone were investigated using neutron diffraction technique. The tensile behavior of the FSW plates was also examined. Finally, the relationship among the processing parameters, texture evolution, and the mechanical behavior of the FWP Mg alloy plate is discussed.

2. RELATIONSHIP BETWEEN PROCESSING PARAMETERS AND THERMO-MECHANICAL INPUT DURING FSW: THEORETICAL ANALYSIS

In order to design FSW processes covering a wide thermo-mechanical input range, two empirical equations are used to estimate the maximum temperature [2], T , (Eq. (1)) and average strain rate [3], $\dot{\epsilon}$, (Eq. (2)) in stir zone during FSW, respectively.

$$\frac{T}{T_m} = K \left(\frac{\omega}{2.362v \times 10^4} \right)^a \quad (1);$$

$$\dot{\epsilon} = \frac{R_m \cdot 2\pi r_e}{L_e} \quad (2),$$

where T_m is the melting temperature, ω is the tool rotation speed, and v is the travel speed. K and a are constants. r_e and L_e are the effective radius and depth of the stir zone. R_m is the average flow rate, which is about half of the pin rotational speed, ω . Then, the two primary deformation parameters, strain rate ($\dot{\epsilon}$) and temperature (T), are incorporated into Zener-Hollomon parameter, Z , which is defined as below [1, 3]:

$$Z = \dot{\epsilon} \exp(Q/RT) \quad (3)$$

where R is the gas constant, Q is the activation energy for diffusion, which is 135 kJ/mol [3]. When deformed at lower Z values, slip mode should be the dominant deformation mechanisms. On the other hand, when deformed at higher Z , twinning should play an important role during DRX, which would strongly influence the texture of the stir zone. Fig. 1 shows the relationship among ω , v , and Z used in this study based on the three equations above.

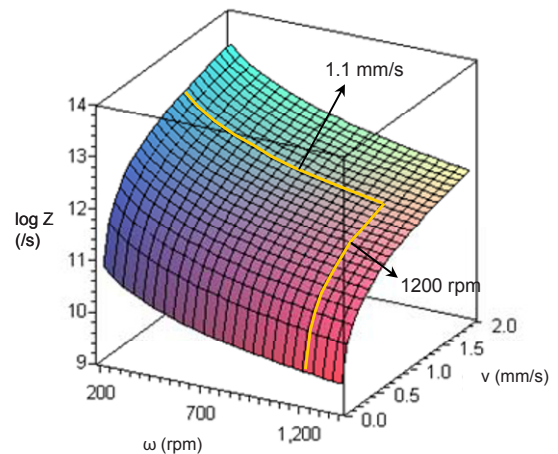


Fig. 1. The relationship among Zener Hollomon parameter (Z), rotation speed (ω), and travel rate (v) in Mg alloy AZ31 estimated from empirical equations.

3. EXPERIMENT DETAILS

Based on Fig. 1, six different cases were designed following the yellow lines. For cases 1 to 3, ω was set to be 1200rpm, as v varies from 0.25, 0.64, and 1.1 mm/s, Z increases from 6.37×10^{10} , 2.19×10^{11} to $4.52 \times 10^{11} \text{ s}^{-1}$. In cases 4 to 6, v was kept at 1.1 mm/s, while ω decreases from 600, 400, to 300 rpm, and therefore Z further increase from 1.50×10^{12} , 3.07×10^{12} to $5.15 \times 10^{12} \text{ s}^{-1}$. The crystallographic texture of the SZ was measured from all 6 cases using neutron diffraction at the HIPPO beamline at the Los Alamos Neutron Science Center. The results provide volume-averaged ($5 \times 5 \times 6.4 \text{ mm}^3$) texture analysis from the SZ. In order to study the tensile behavior of the stir zone, subsize tensile samples were prepared from the six FSW cases in longitudinal direction, with a gage section of 25mm in length, 6mm in width and 4.8mm in thickness. Tensile tests were conducted at an initial strain rate of $5 \times 10^{-4} \text{ s}^{-1}$ at room temperature.

4. RESULTS AND DISCUSSION

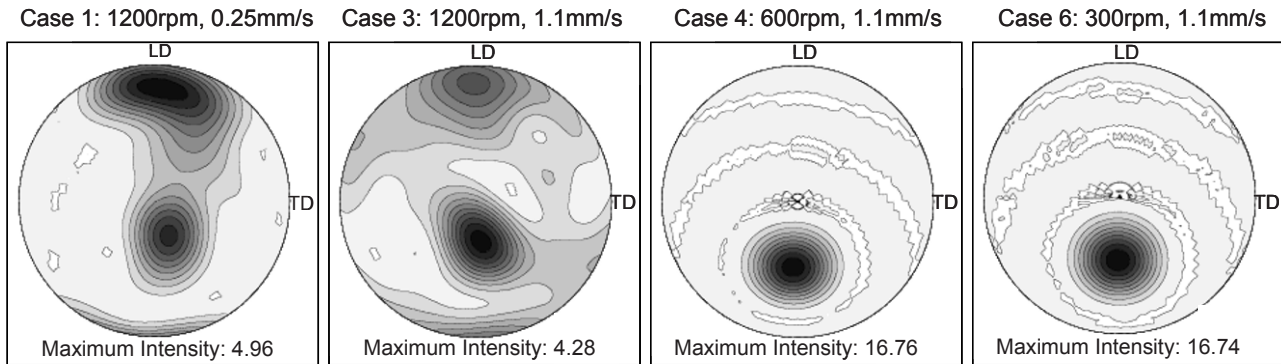


Fig.2. $\{0002\}$ pole figures for four different FSW cases are plotted using gray scale with the maximum intensity marked at the bottom of each figure. LD is longitudinal direction (parallel to travel direction of the tool during FSW as well as the rolling direction of the plate), and TD is transverse direction.

Fig. 2 shows the $\{0002\}$ texture measured from the SZ of FSW Mg plates. The as-received hot-rolled Mg plate shows a typical strong basal texture parallel to normal direction (ND) of the plate. After FSW, as shown in Fig.2, systematic changes in crystallographic texture in stir zone corresponding to different FSW parameters were observed. In cases 1-3, a two-component-texture was developed. The near- $\langle 0001 \rangle // \text{LD}$ texture component is a texture generated from shear deformation when material flows with the rotating tool by slip. The intensity of the other texture component, near- $\langle 0001 \rangle // \text{ND}$, tends to gradually increase comparing case 3 to 1. As in cases 4-6, the near- $\langle 0001 \rangle // \text{LD}$ component disappears. The possible reason is in high Z cases due to the less heat input but higher deformation rate, twinning mode should be more easily activated in the early stage of deformation, and dramatically influence the DRX process and corresponding texture development, which could lead to a $\sim 90^\circ$ shift of the near- $\langle 0001 \rangle // \text{LD}$ component towards ND. Fig. 3 shows the tensile behavior of SZ along longitudinal direction as a function of Z parameter. Clear changes in the strength and ductility are observed, which is consistent with the changes in the texture. Specimens with two-component-texture (Cases 1-3) shows high tensile strength with low ductility, while specimens with near-normal basal texture (Cases 4-6) exhibits a relatively low yield strength and better ductility when tested along the LD.

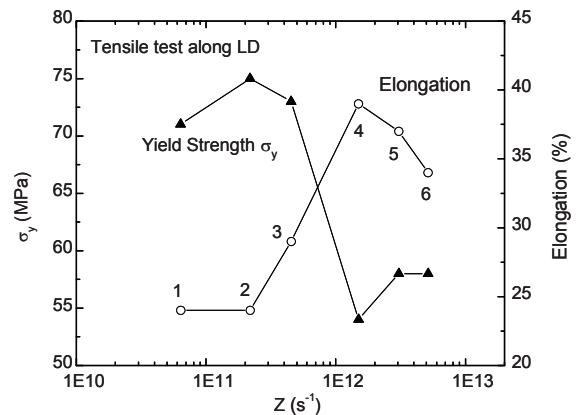


Fig.3. Yield strength and elongation from tensile test results for six FSW cases as a function of Z in LD.

In summary, this study shows a good correlation among the processing parameters, texture development, and deformation mechanisms for the FSWed Mg alloy AZ31B. The results could be useful for the design of desired final properties in FSWed Mg alloys.

Acknowledgements: This research is supported by NSF Major Research Instrumentation (MRI) program under contract DMR.0421219. The authors are grateful to staff in Materials Science and Technology Division in Oak Ridge National Laboratory, and Los Alamos Neutron Science Center for their great help in performing the experiments.

Reference: [1] Galiyev A., Kaibyshev R., Gottstein G., Correlation of Plastic Deformation and Dynamic Recrystallization in Magnesium Alloy ZK60. *Acta Mater.* 49, 1199-1207, 2001. [2] Arbegast W.J., Modeling Friction Stir Joining as a Metalworking Process. *Hot Deform. of Aluminum Alloys III*, Z. Jin, ed. TMS, 2003. [3] Chang C.I., Lee C.J., Huang J.C., Relationship between Grain Size and Zener-Holloman Parameter during Friction Stir Processing in AZ31 Mg Alloys. *Scripta Mater.* 51, 509-514, 2004.

Measurement of Stresses in Pipelines Using Hole Drilling Rosettes

G.R. Delgadillo, Pontifical Catholic University of Rio de Janeiro, PUC-Rio

F. Fiorentini, ENSAM, France

L.D. Rodrigues, Pontifical Catholic University of Rio de Janeiro, PUC-Rio

J.L. F. Freire, Pontifical Catholic University of Rio de Janeiro, PUC-Rio

R.D. Vieira, Pontifical Catholic University of Rio de Janeiro, PUC-Rio

ABSTRACT

On-shore buried pipelines are loaded by internal pressure, by longitudinal displacement restrictions caused by support or soil interaction, and by temperature differential. If a referential initial state of stress can be established by some means, conventional strain gage techniques can be used to determine the existing loads relative to the reference state. If a reference cannot be established, residual stress measurement techniques are strong candidates for use in the measurements because they measure the absolute state of stress present at the assessed point of the pipeline. This paper aims to provide laboratory test results to show how uncertain measurements using conventional strain gage or residual stress techniques can be when used in determining existing loads. The tests utilized a special device designed and built for applying combined states of stress. The device had a U-shaped format. The horizontal part of the U-shaped device consisted of the specimen to be tested: a segment of an API 5L X60 steel pipe with length, diameter and thickness equal to 910mm, 323.3mm and 9.7mm, respectively. The pipe segment was capped at both ends by welding two reinforced plates that formed the two vertical legs or arms of the U-shaped device. A pressurized water inlet was introduced into one of the caps to provide for the internal pressure loading of the test specimen. Besides capping the pipe, the vertical leg-plates were connected by two threaded spindles. The spindles and the long plate arms made it possible to apply axial forces and intrinsically coupled bending moments to the pipe segment. The spindles were instrumented with four electrical resistance strain gages in a full bridge arrangement to measure the applied forces. The resulting applied stress states in the pipe walls caused by normal force, bending moment and internal pressure were measured using several rosettes of electrical resistance strain gages that were appropriate for applying the blind-hole-drilling technique. Three sets of data points were collected during the tests. The first set consisted of measurements of strains caused by applying simple or complex load combinations. The second set consisted of strain measurements made after the blind holes were drilled in order to determine the residual stresses caused in the fabrication of the steel pipe. The third set of data consisted of measurements of strain variations caused by unloading the device. All the data of the experiment were analyzed and compared with strains calculated by means of analytic (Strength of Materials) and numeric (Finite Elements) methods. These comparisons helped to reach the conclusion that the use of a residual stress measurement technique such as the blind-hole drilling method to determine pressure induced and soil movement loading in operating pipeline will furnish inaccurate results even if a reasonable number of measurement points are used to describe the stress states of points along the analyzed cross sections. The reason for this is the possibility of a large variation in the residual fabrication stresses not only along the outer perimeter of one cross section of the pipe, but also the large variation in the distributions that occur along neighboring sections of a short pipe segment. For the case of predicting strains generated by the complex loading applied to the pipe test specimen, the comparison of experimentally and analytically determined strains allowed for the evaluation of an overall strain prediction uncertainty of $50\mu\epsilon$. Furthermore, an uncertainty value of $26\mu\epsilon$ for the hole drilling method was also determined by comparing the initially imposed combined strain states with those measured after drilling the blind holes and unloading the test specimen.

INTRODUCTION

Pipelines are loaded by operating conditions - basically, internal pressure and temperature - and by interaction with the surrounding soil, which includes soil movement. Integrity assessments of pipelines that are threatened by soil movement require knowledge of stress states at critical points. Initial stress states superpose those caused

by operation and soil movement. Initial stress states are caused by residual pipe stresses and by the pipe settling in place. Residual stresses are caused by the fabrication of the steel pipe and by overloads generated during operation or during pipeline construction.

Measuring the absolute stress states acting at certain points of a pipe section may give a good indication of how far the section is from failure. Residual stress measurement techniques are natural candidates to be utilized in determining absolute stress states. The integrity assessment analysis may be simplified in two possible ways. In the first way, sections with points showing stress values under the steel's yield strength are indicative of overall material elastic behavior. Consequently, this means it is possible to use stress analysis to determine live loads, and specifically, the loads caused by soil movement. In the second way, sections with points subjected to very high stresses near the yield strength, and which cover a high percentage of the section's perimeter, indicate possible failure by plastic collapse caused by the live loads.

This paper discusses the utilization of the blind-hole residual stress measurement technique to determine the live loads acting on the pipeline section, and more specifically, the measurement of strains and calculation of associated loads caused by soil movement, taking in to consideration the fact that the combination of these loads does not cause plasticity.

Use of the blind-hole technique requires drilling a hole that releases the elastic stress at the measurement point. Strains measured by an optical method or by a resistance strain gage rosette may be transformed into a total elastic stress state $[\sigma]$ resulting from the superposition of the pipe fabrication residual stress state $[\sigma]_R$, the stress state caused by the internal (operation) pressure $[\sigma]_p$ and by the stress states caused by construction and soil movement $[\sigma]_M$. Consequently, if $[\sigma]$ is measured, if $[\sigma]_p$ is accounted for by simple analytic calculation or by the unloading and loading of some of the internal pressure, and if $[\sigma]_R$ is estimated by some experimental procedure, the soil interaction stress state $[\sigma]_M$ can be determined. Measuring the stress states for at least three points allows for calculating the moment and axial loads acting on the pipe section. An overly deterministic approach may be used to determine the unknowns and to minimize the error associated with the measurement and calculation procedure.

This calculation procedure is conceptually simple and straightforward but it suffers from drawbacks due to serious uncertainties regarding the tube fabrication and pipeline construction induced residual stress distributions, and due to the uncertainties generated in the strain measurements [1-3]. A similar calculation scheme using the blind-hole technique combined with strain measurements made with a suitable, portable optical interferometer proved to be competitive when compared to measurements made with strain gage rosettes [4]. Unfortunately, the scheme's overall analysis technique suffered from a lack of representativeness once it measured the residual fabrication stresses using a short segment of pipe in the laboratory.

The present paper aims to provide laboratory test results that are helpful in considering how residual stresses are distributed along the perimeter of a section and how these distributions change along short longitudinal lengths of a pipe. It also aims to show how measurements made with conventional strain gages compare with strains predicted by simple analytic or numerical techniques, and to show what the uncertainty generated by these measurements and predictions is.

The tests carried out in the present investigation utilized a special U-shaped device designed and built for applying combined states of stress, which were generated by a normal force, by a bending moment and by internal pressure. The horizontal leg of the U-shaped device was the test specimen, which consisted of a segment of an American Petroleum Institute API 5L X60 steel pipe that could be loaded by internal pressure. The vertical legs of the U-shaped device were welded to the ends of the pipe in order to cap its ends and to apply the normal forces and bending moments. The resulting applied stress states in the pipe walls were measured using rosettes of electrical resistance strain gages that were suitable for applying the hole-drilling technique. Three sets of data points were collected during the tests. The first set consisted of measurements of strains caused by applying simple or complex load combinations. The second set consisted of strain measurements made after the blind-holes were drilled in order to determine the residual stresses caused during the fabrication of the steel pipe. The third set of data consisted of measurements of strain variations caused by unloading the device. All the data

from the experiment were analyzed and compared with strains calculated by means of analytic (Strength of Materials) and numeric (Finite Elements) methods.

EXPERIMENTAL METHODS

The special U-shaped device designed and built for applying combined states of stress is presented in [Figure 1](#). The device consisted of a segment of API 5L X60 steel pipe with length, diameter and thickness equal to 910mm, 323.3mm and 9.7mm, respectively. The pipe segment was capped at both ends by welding on two reinforced plates. These plates were long enough to cap the pipes at one end and to support two threaded spindles in the other end. The spindles and the long plate arms made it possible to apply axial forces and bending moments to the pipe segment. The spindles were instrumented with four electrical resistance uniaxial strain gages in a full bridge arrangement to measure the applied forces. The resulting applied stress states in the pipe walls caused by normal force, by bending moment and by internal pressure were measured using rosettes of electrical resistance strain gages (PA-06-062RE-120L from EXCEL Sensors Ind. Com. Exp. Ltda., SP, Brazil) that were suitable for applying the hole-drilling technique. All residual stress measurements and calculations followed the standard American Society of Testing Materials ASTM E837 [5]. Drilling the blind holes was done with special 1.56mm square-ended drills using low speed (4cps). Final hole diameters were measured to be $2R_0 = 1.59\text{mm}$. The median diameter of the center of the strain gages of the rosette was $2R = 5.2\text{mm}$. Measurements of stress variations were made for each 0.5mm depth step along the drilling process to a maximum hole depth of 2mm. Except for the residual stress measurements taken at the seam weld, all the data of the experiment proved to be very close to the uniform stress states along the 2mm range of measurement depth. The proper procedure recommended by the ASTM E837 standard [5] was used to verify this claim of uniformity.

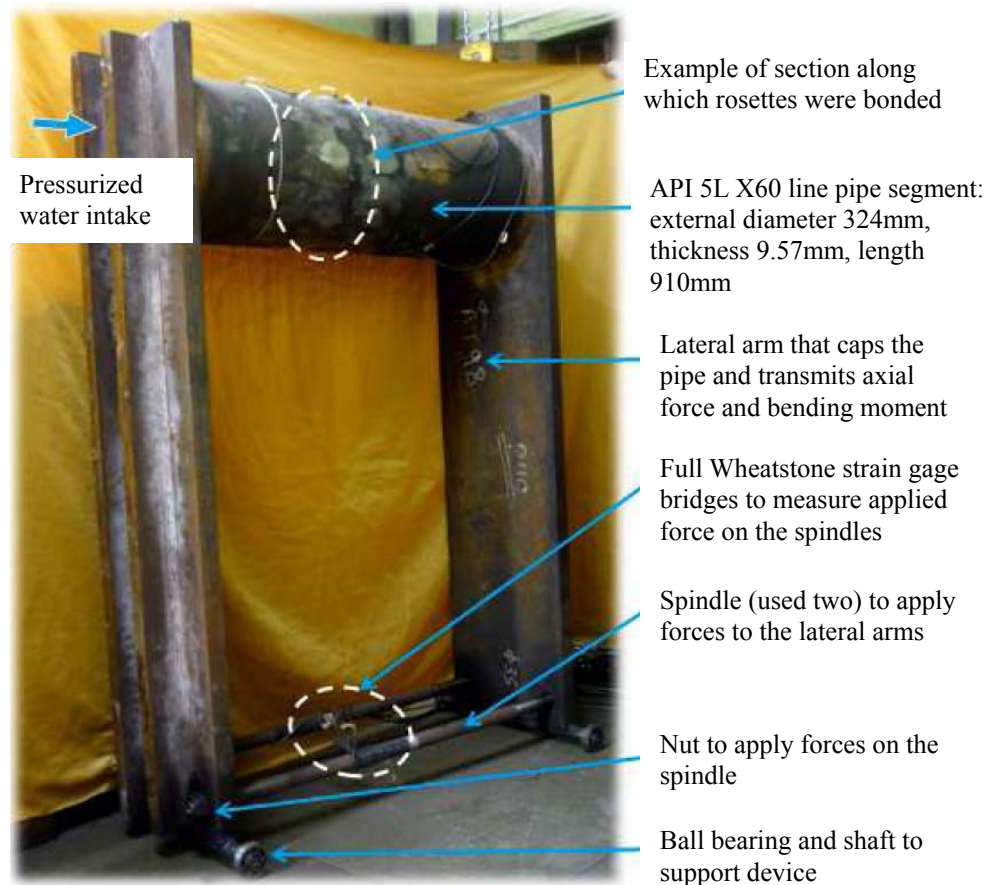


Figure 1: U-shaped device built to apply combined loading of internal pressure, axial force and bending moment to the API 5L X60 line pipe segment

[Figure 2](#) depicts the location of the data points used herein (sections 1 and 2) and in other previous investigation reports - sections 3 and 4 from [1,2] and section 5 from [6] - which used the same piece of pipe test specimen.

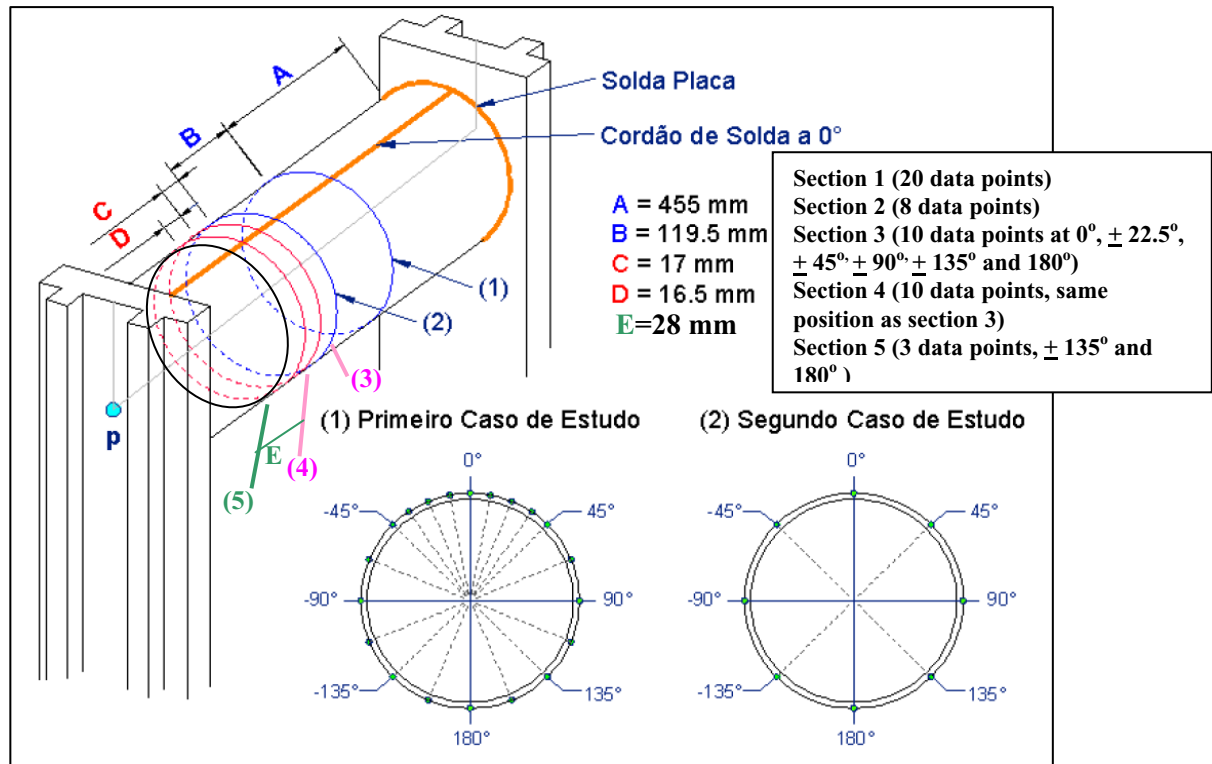


Figure 2: Data points used in the present and in previous investigations [1-3,6] using the same piece of pipe segment.

The following procedure was used in the tests to load the pipe, and to collect and analyze the strain data from sections 1, 2 and 5. Data from sections 3 and 4 have already been published [2] and will be used in the present article for comparison purposes.

- 1 – Surface preparation and rosette bonding and cabling to signal conditioner.
- 2 – Pressure loading (5MPa), strain data collection, and pressure unloading.
- 3 – Axial force and (coupled) bending moment application of 20kN and 24.7kNm, respectively; strain data collection and unloading.
- 4 – Combined pressure (5MPa) and axial force - bending moment loading of 20kN and 24.7kNm, respectively; strain data collection.
- 5 – Hole drilling and measurement of strain data variations caused by the release of residual strains. Calculation of the residual stresses at each analyzed point using ASTM E837.
- 6 – General unloading of the device and data collection of variations in the strain-gage readings caused by the unloading. Calculation of the nominal strains for each gage direction based on the strain data collected using Kirsch equations for an infinite plate with a through-thickness circular hole under a biaxial state of stress [7].

RESULTS AND DISCUSSION

Analytical and numerical solutions were developed using the conventional Strength of Materials and Finite Element methods to generate elastic stress and strain distributions so that they could be compared with the strain gage results determined for the external loading applied to the device. Although it is beyond the scope of this study to show the detailed solutions and results of both analyses, it should be mentioned that both agreed quite well except for the presence of some ovalization due to pressure loading, which appeared in the FE and which was not expected with the basic Strength of Materials solution. The FE analysis was developed using a well-tested commercial program. Two highly detailed grid solutions were developed that yielded similar results, except for points located at or very near the seam weld due to different options involving more detail or less in order to simulate the geometry of this area.

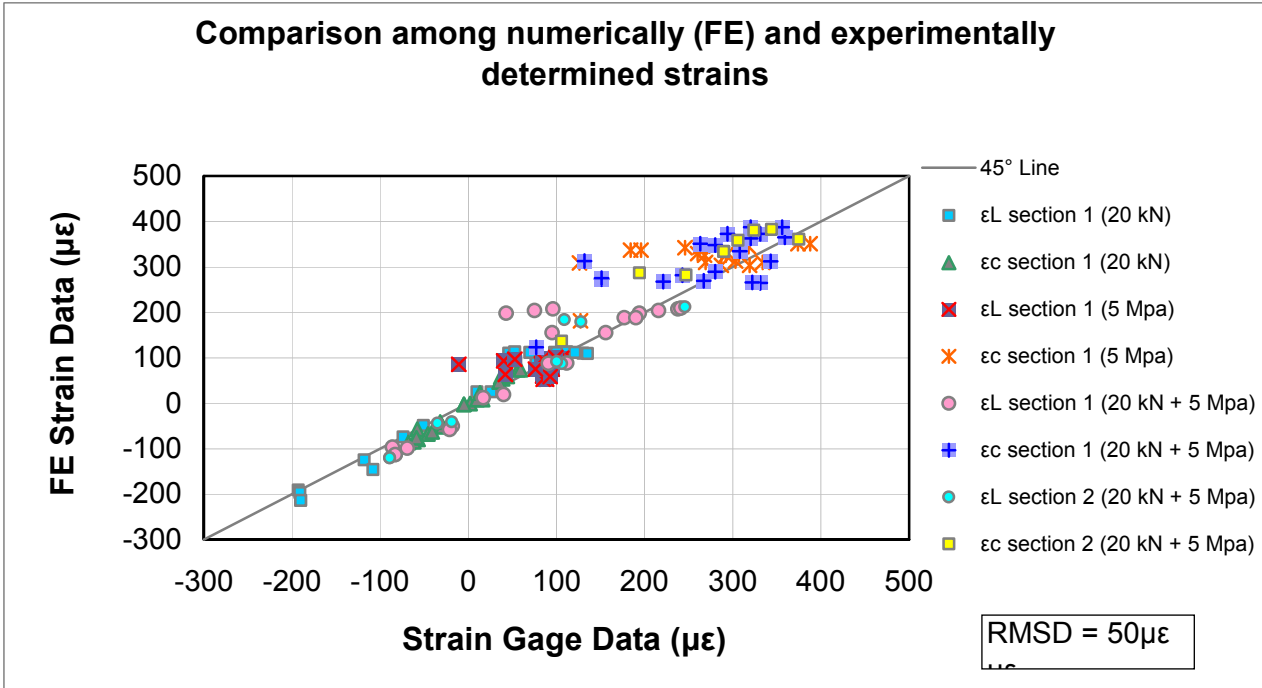


Figure 3: Circumferential and longitudinal strains measured by the hole-drilling rosettes (before drilling) compared with the finite element strain results determined for hydrostatic internal pressure loading of 5MPa, coupled axial force and bending moment loading of 20kN and 24.7kNm, and combined loading.

Figure 3 presents a plot that summarizes the comparison among experimental and numerical circumferential and longitudinal strains determined for simple (internal pressure or axial force and coupled bending moment) or combined loading cases. Each point coordinate is given by the calculated strain and the measured strain at the same location and direction for a given loading case. The data analyzed were taken from tests that measured strains for the instrumented points located in sections 1 and 2 shown in Figure 2. The root mean square deviation RMSD was calculated and was equal to $50\mu\epsilon$ in the case shown in the Figure, which corresponds to the more-refined FE grid, and $54\mu\epsilon$ in the case of the less-refined FE grid. Data points that contributed more to this deviation were those determined for rosettes at or near the seam weld (rosettes at positions between 0° and $\pm 22.5^\circ$ of sections 1 and 2 – see Figure 2).

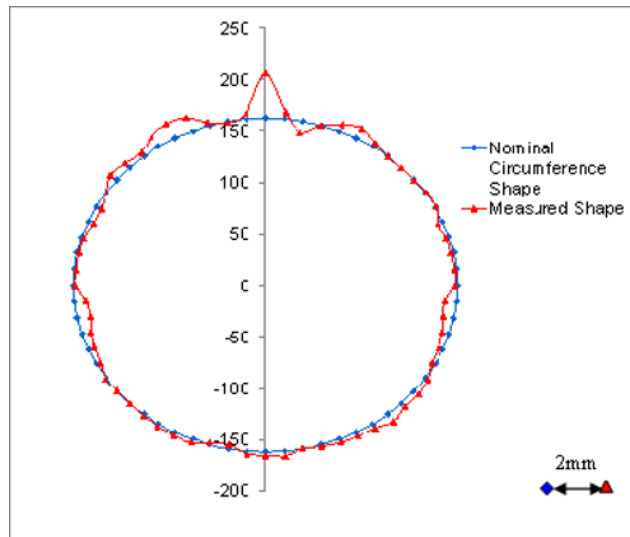


Figure 4: Comparison between the expected nominal circumferential shape and the actual measured shape. Existing deviations in both shapes are magnified. The deviations' approximate scale is given in the figure.

To better understand the causes of overall deviations in the experimental and numerical results, measurements of the actual profile of both sections and its possible deviation from circularity were taken. Figure 4 presents these deviations for section 1. In the seam weld region, the pipe displays dents and protuberances of about 0.5mm, except at the center weld position, where the deviation is 2mm, caused by the weld reinforcement. It is well known that localized bending stresses in smooth dents or protuberances acting on the outer surface layers of the walls of thin pipes loaded by internal pressure can be significantly higher than the calculated nominal hoop or longitudinal stresses. A simple analysis renders a stress concentration factor of $1 + 6 \times e/t$, where e is the circularity deviation (which can be positive if inward and negative if outward) and t is the thickness of the thin pipe. Considering that the pipe's thickness is 9.7mm, the stress concentration factor for $e = 0.5\text{mm}$ can be as high as 1.31. The overall shape of section 1 shows non-circularities that can be credited to the steps taken during the forming process, called UOE. These steps are shown in Figure 5 and include the formation of the U shape, the O-shaped completion of the rounding process, the seam process consisting of the submerged arc welding SAW to close the section gap, and finally, the E-expansion of the pipe. The "E" expansion is made by an internal tool that travels along the tube and contains shoes that expand in the radial direction. The expansion takes place by means of equal steps that develop along the length of the tube, starting at and running from one end of the tube to the other in order to improve and guarantee circularity.

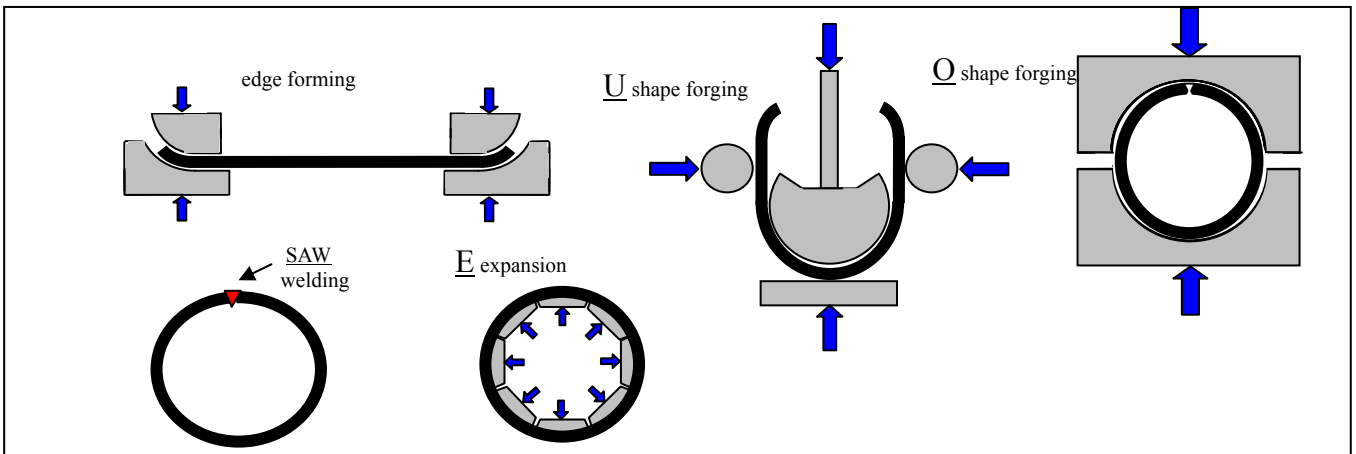


Figure 5: Illustration of the fabrication of the UOE-SAW line pipe

It is believed that the UOE fabrication process greatly influences the heterogeneous residual stress distributions that exist for pipes fabricated by this process. Residual stress measurements were measured at several points on the external surface of the present test specimen in order to investigate their variation along different sections of the short pipe segment. These results complement other data acquired using the same test specimen [1,2,6]

Figures 6 and 7 present residual stress measurement results for the longitudinal and circumferential directions determined by the hole drilling technique applied to all rosettes positioned in sections 1 to 5 of the segment of steel pipe tested. These results correspond to step 5 in the test and analysis procedure described in the previous section. The plots in Figures 6 and 7 present the residual stress distributions along the external perimeter of all five sections analyzed.

The longitudinal and circumferential stress plots presented in Figures 6 and 7 show steep variations in both stresses along the perimeter of each section and from section to section. The stress values range from zero value to positive or negative values that are of the order of the material yield strength. A word of caution is warranted: results where residual stresses are larger than 50% of the material yield strength may be seen as merely qualitative [7]. Another word of caution should be given regarding the fitting curves shown in Figures 6 and 7. These curves are included to connect the data point sequence and to make it easier to visualize. However, they are by no means proposed as shape distributions of the residual stress variations in the investigated cross sections.

Given the nature of uncertainties generated in the pipe fabrication process, and considering the fact that in the present case the blind-hole measurement technique generated measurements with low uncertainties - as will be discussed later using Figure 8 - it can be concluded that the resulting measurements for neighboring points on the cross sections that are as close together as 16.6mm (sections 3 and 4) replicate quite well. This conclusion does not apply when sections are located far from each other or when they are close to the ends of the tube. Data on residual stresses for the 48 measuring point locations displayed in the plots covering the perimeter of the five cross sections positioned along the 910mm long segment of the pipe show a large spread that has to be credited to the fabrication procedure. Although at some locations - particularly for the longitudinal stress distributions - similar trends may be observed, there are differences of more than 200MPa for the stresses in some angular locations. Thus, it can be concluded that there are variations in these distributions, and that such variations may be credited to heterogeneity distributions of residual fabrication stresses along the short length of the tested segment. These variations may be caused either by different “U” or “O” shapes generated during the forming of the tube or by different cold form straining along sections of the pipe segment caused by the progressive “E” cold expansion steps occurring along the length of the tube.

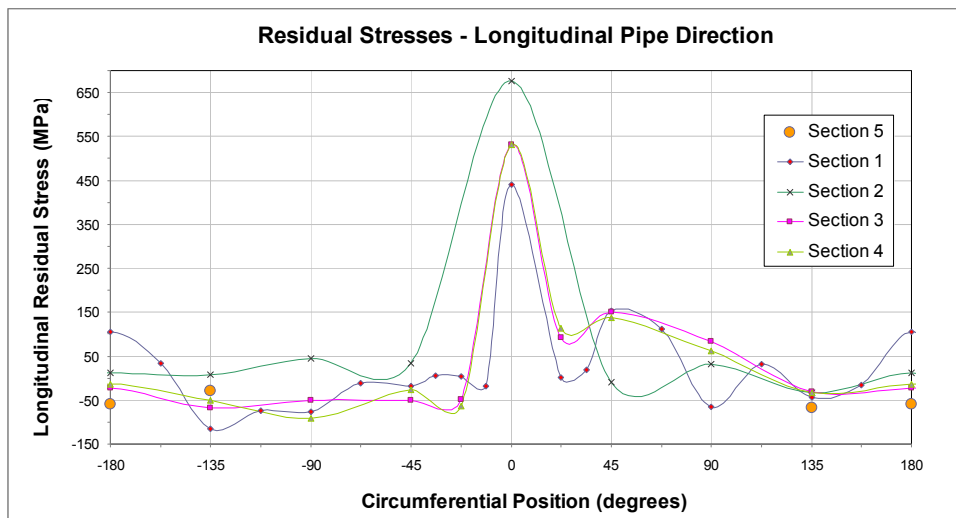


Figure 6: Longitudinal residual stress distributions along the circumferential position of five sections comprising a total length of 636mm (distance between sections 1 and 5)

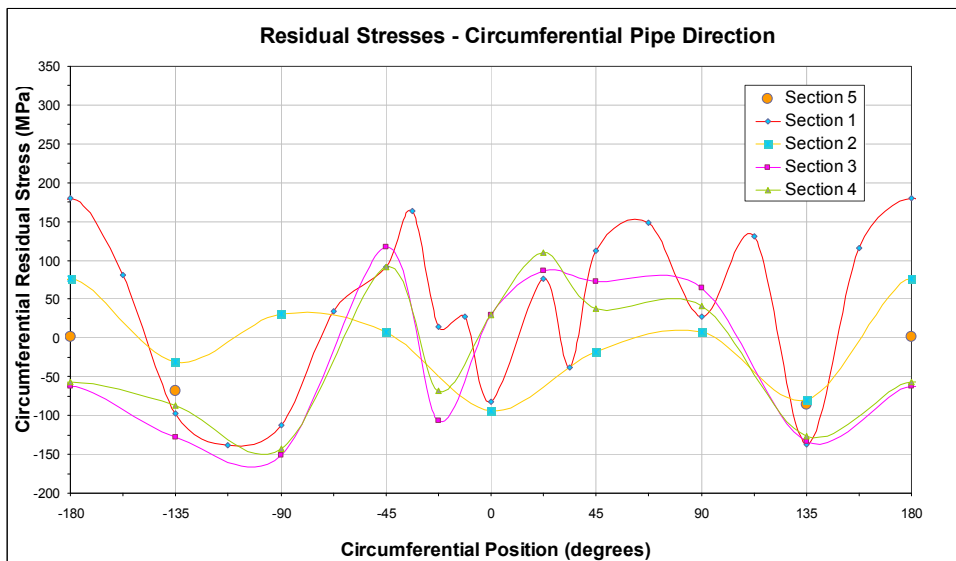


Figure 7: Circumferential residual stress distributions along the circumferential position of five sections comprising a total length of 636mm (distance between sections 1 and 5)

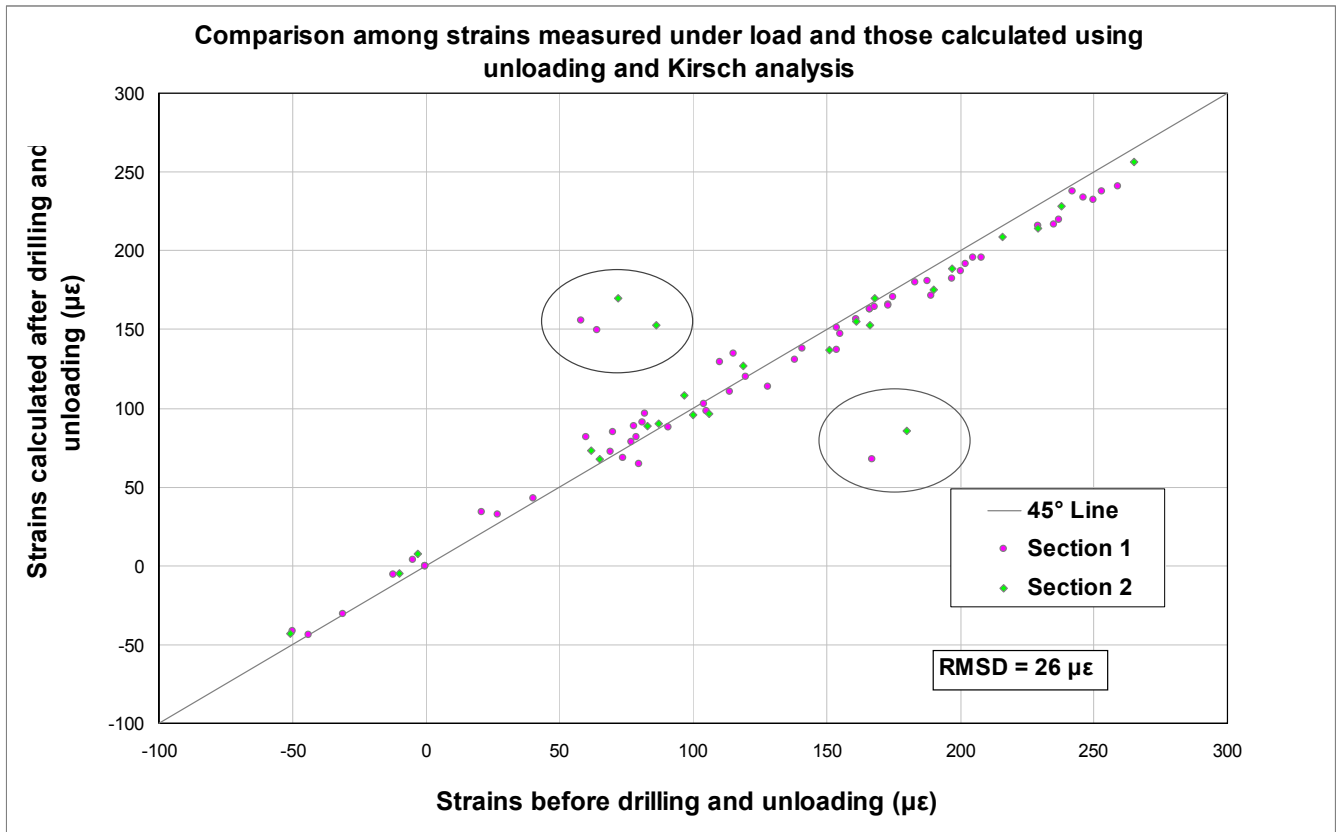


Figure 8: Comparison among radial strains measured along the gages belonging to the rectangular and 45° directions of the rosettes before unloading and drilling, with strains calculated along the same directions after drilling and unloading using the Kirsch equations applied to a through hole in an infinite plate under biaxial state of stress. Circle-highlighted data points belong to rosettes placed on the seam weld, where the hypothesis of uniformity of stresses along the measuring depth is not valid.

In order to determine the intrinsic accuracy of the hole drilling method using the triaxial strain gage rosettes, the linear strains generated by the unloading of the device were measured. These strain measurements are directly related to the unloading of the primary biaxial strain or stress states existing previously in the neighborhood of each hole. As the primary strains related to the combined loading process were measured before the holes were drilled and recorded on a data sheet, applying the Kirsch equations for a through hole in an infinite plate to the measured strains caused by the unloading process can help to analytically determine strains to be compared with the initial strains [7]. The analytical strains were calculated in the radial direction for the central position of each strain gage belonging to each rosette. The plotting of points on a graph whose coordinates are the primarily measured radial strain for each strain gage and the corresponding strain calculated from the unloading process and Kirsch equations should fall over a 45° line. Deviations in the plotted points were relatively small and an overall uncertainty was evaluated by calculating the root mean square deviation RMSD, which turned out to be 26 $\mu\epsilon$. Figure 8 shows a graph illustrating a comparison among the radial strains measured and among the gages belonging to the rectangular and 45° directions of the rosettes before unloading and drilling, after drilling and unloading, and after using the Kirsch equations. Agreement is shown to be good except for the circle highlighted data points. These points belong to rosettes placed on the seam weld, where the hypothesis of uniformity of stresses along the measuring depth is not valid. Moreover, the high strain values that some of them show may indicate plastic behavior around the hole, rendering the application of the elastic equations used in the problem invalid. The above method of calculating uncertainties was adapted from reference [7], which uses a similar method to calibrate material and geometric factors to be used in the blind-hole residual stress technique.

CONCLUSIONS

This article has presented residual stress distributions along five cross sections of one short segment of UOE-SAW thin walled line pipe classified as API 5L X60. It corroborates the following conclusions, which were also arrived at in a previous article [2]: a) the residual stress distributions are complex-shaped along a given cross section; b) these distributions are similar for cross sections very close to each other, but they differ significantly when the cross sections are reasonably spaced in a given segment of pipe; c) similar pipe segments from a given pipeline may have completely different residual stress distributions. A consequence of these conclusions is that the use of a residual stress measurement technique such as the blind-hole drilling method to determine general primary and soil movement loading in operating pipeline will furnish inaccurate results even if a reasonable number of measurement points are used to describe the stress states of points along the analyzed cross sections. Furthermore, the present investigation used a device that made it possible to apply combined loading: axial force, bending moment and internal pressure. Stress states at several points were measured using strain gage rosettes, and the results were compared with Strength of Material and Finite Element solutions. The overall uncertainty evaluated from the comparison of strains determined from the experimental and analytic and numerical methods turned out to be around $50\mu\epsilon$. The uncertainty of the hole drilling method was also evaluated by comparing the initially imposed combined strain state and the calculated strains from the measured unloading of the combined loads. Calculations in this case used the analytic Kirsch solution for an infinite plate with a through hole under a biaxial stress loading. Uncertainty evaluated in this way was only $26\mu\epsilon$.

ACKNOWLEDGMENTS

The authors wish to acknowledge Fluke Engenharia, Macaé, RJ, Brazil, for the construction of the U-shaped device used in the experiments.

REFERENCES

1. L.D. Rodrigues, "Measurement of residual stresses in pipes driving the determination of efforts in buried pipelines," MSc. Dissertation, Department of Mechanical Engineering, Pontifical Catholic University of Rio de Janeiro / PUC-Rio, Brazil, 2007 (in Portuguese).
2. L.D.Rodrigues, J.L.F.Freire, R.D.Viera, "Measurement of residual stresses in UOE-SAW line pipes," *Experimental Techniques*, 58-62, January / February, 2008.
3. G.W.R. Delgadillo, "Residual stress measurements in pipes subjected to combined loads," MSc. Dissertation, Department of Mechanical Engineering, Pontifical Catholic University of Rio de Janeiro / PUC-Rio, Brazil, 2009 (in Portuguese).
4. J.C. Freitas, A.A. Gonçalves Jr., M.R. Viotti, "A historical case in the Brazil-Bolivia natural gas pipeline: 5 years of stress monitoring at the Curriola river slope," Paper IBP1042-2009, Proceedings of the Rio Pipeline 2009 Conference and Exposition, Instituto Brasileiro de Petróleo, Gás e Biocombustíveis, Av. Almirante Barroso 52/26th floor, Rio de Janeiro, Brazil.
5. ASTM-E837-08, "Standard test method for determining residual stress by the hole drilling strain-gage method," American Society for Testing Materials, 100 Barr Harbor Drive, West Conshohocken, PA, USA, January, 2008.
6. F. Fiorentini, "Measurement of applied stresses in a pipe under combined loadings using the blind-hole residual stress technique," Mechanical Engineering Department, ENSAM Châlons-en-Champagne, France, 2008.
7. Tech-Note; TN-503-6, "Measurement of residual stresses by the hole-drilling strain gage method," Vishay Micro-Measurements Group, Raleigh, NC, USA, August, 2007.

Incremental Computation Technique for Residual Stress Calculations Using the Integral Method

Gary S. Schajer

Dept. Mechanical Engg, Univ. British Columbia,
Vancouver, Canada V6T 1Z4
schajer@mech.ubc.ca

Theo J. Rickert

American Stress Technologies
Cheswick, PA
theo.rickert@astresstech.com

Abstract

The Integral Method for determining residual stresses involves making surface deformation measurements after a sequence of small increments of material removal depth. Typically, the associated matrix equation for solving the residual stresses within each depth increment is ill-conditioned. The resulting error sensitivity of the residual stress evaluation makes it essential that data measurement errors are minimized and that the residual stress solution method be as stable as possible. These two issues are addressed in this paper. The proposed method involves using incremental deformation data instead of the total deformation data that are conventionally used. The technique is illustrated using an example ESPI hole-drilling measurement.

Introduction

Methods for measuring through-thickness profiles of residual stress in materials typically involve measuring surface deformations at a sequence of steps as stressed material is incrementally removed [1]. Examples of such techniques are hole-drilling [2,3], slitting [4,5] and layer removal [6,7]. Evaluation of the through-thickness stress profile from the measured deformations requires the solution of an inverse equation [8]. Such calculations are well known to be ill-conditioned, causing amplification of modest measurement errors into relatively much larger errors in the evaluated stresses. This error amplification places severe demands on the quality of the measurement technique to ensure that stress evaluation errors remain within an acceptable range. Care must also be taken with the mathematical method used to evaluate the residual stress profile from the measured data. Numerical techniques have been developed to reduce the effects of measurement errors through data averaging [9] and regularization [10].

This paper describes a technique that can improve the quality of the measured data and help stabilize the residual stress calculation method. In present practice, deformation data measured at each step during an incremental material removal process are referenced to the initial uncut condition. The proposed procedure is to alter the computational approach so that the stresses are instead evaluated in terms of the deformation change during each material removal step. When using optical methods such as ESPI [11,12,13], Moiré interferometry [14,15,16] or Digital Image Correlation [17,18], this change reduces the time interval between pairs of image sets, thereby reducing drift, improving optical correlation and enhancing image quality. Mathematically, the change to using incremental data leads to a better-conditioned set of equations to be solved because they become more diagonally dominant [19]. The proposed method is illustrated using an ESPI hole-drilling residual stress measurement as an example.

Theory

For compactness of discussion, the theoretical procedure will be presented using ESPI hole drilling as a specific example. However, the ideas presented apply equally to other incremental material removal methods for measuring residual stress, such as slitting and layer removal, and also to other deformation measurement methods such as Moiré interferometry.

Figure 1 shows the cross-section of a hole drilled in a material containing in-plane residual stresses. These stresses vary smoothly with depth from the specimen surface, as shown by the dashed line. When using the Integral method, the stresses are assumed to vary in the stepwise manner shown. The depth steps for the stresses correspond to the hole depth steps used for the incremental hole-drilling measurements. The ESPI measurement method involves taking a reference set of phase-stepped images of the specimen surface around the hole before the start of hole drilling, and then sets of images after each incremental increase in hole depth

[20]. In the conventional technique, the images measured after each increment in hole depth are correlated with the initial set, from which the total deformation of the specimen surface around the hole is determined. The relationship between the measured deformation \mathbf{f} measured after each step and the stresses $\boldsymbol{\sigma}$ within each step can be expressed as a matrix equation [21]

$$\mathbf{G}\boldsymbol{\sigma} = \mathbf{f} \quad (1)$$

where \mathbf{G} is a matrix and \mathbf{f} and $\boldsymbol{\sigma}$ are vectors. Matrix element G_{ij} represents the total surface deformation measured after hole depth increment i caused by a unit stress within increment j . Figure 2 illustrates this representation. Equation (1) shows how the total deformation measured after a given hole depth increment i is the sum of the effects of the stresses within all the increments $1 \leq j \leq i$ within the hole. There is no sensitivity to stresses below the hole, so matrix \mathbf{G} is lower triangular.

For strain gauge measurements, the elements of matrix \mathbf{G} are single numbers representing the relationship between the measured strain and the interior stresses [21]. For ESPI measurements, each element of the measured deformation vector \mathbf{f} represents the n measured pixels around the drilled hole, where n is a large number, typically many thousands or even millions of pixels. This excess of data causes equation (1) to be overdetermined. The lower triangular shape of \mathbf{G} is in blocks, each block comprising n rows. In this case, the equation can be solved in a least squares sense using [19,22].

$$\mathbf{G}^T \mathbf{G} \boldsymbol{\sigma} = \mathbf{G}^T \mathbf{f} \quad (2)$$

The residual stress evaluation involves computing the matrix \mathbf{G} , typically using finite element calculations [21], measuring the deformation quantities \mathbf{f} , and then solving equation (2) to determine the stresses $\boldsymbol{\sigma}$. Equation (3) illustrates the character of matrix \mathbf{G} using typical numerical values from strain gauge measurements [21]. Strain gauge measurements were chosen for compactness for this example because each strain gauge gives a single strain number in each matrix position, rather than n rows.

$$\mathbf{G} = \begin{bmatrix} -0.0490 & & & & & \\ -0.0671 & -0.0399 & & & & \\ -0.0754 & -0.0507 & -0.0242 & & & \\ -0.0792 & -0.0547 & -0.0305 & -0.0116 & & \\ -0.0810 & -0.0563 & -0.0325 & -0.0151 & -0.0037 & \end{bmatrix} \quad (3)$$

The negative signs of the matrix elements in Equation (3) occur because the strains are measured while the hole-drilling causes the residual stresses to be subtracted rather than added. The smallest elements of matrix \mathbf{G} occur along the diagonal, which is a mathematically undesirable feature because it gives a small determinant value, causing the matrix to be ill-conditioned [14]. The decreasing diagonal elements of \mathbf{G} as the matrix grows downward, mirrors the rapidly decreasing sensitivity of the surface deformations to stresses at greater distances from the specimen surface. Thus, the matrix ill-conditioning progressively gets worse as the hole gets deeper.

Equation (1) can be reformulated in terms of the differential deformation \mathbf{d} that occurs within each hole depth increment, where $d_i = f_i - f_{i-1}$, for $2 \leq i \leq j$.

$$\mathbf{D}\boldsymbol{\sigma} = \mathbf{d} \quad (4)$$

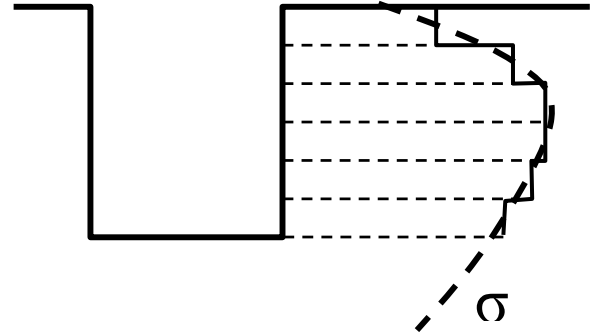


Figure 1. Cross-section of a hole drilled into a material with residual stresses varying with depth.

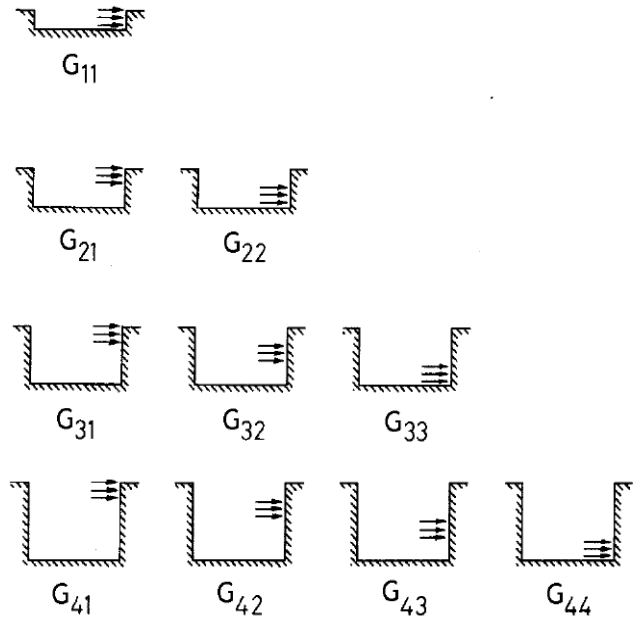


Figure 2. Physical interpretation of matrix coefficients G_{ij} for the hole-drilling method [21].

To accommodate the change on the right side, matrix \mathbf{G} needs to be expressed in differential form. Each row of the differential matrix \mathbf{D} equals the corresponding row of \mathbf{G} minus the preceding row. Exceptionally, the first rows are identical. For the example values of \mathbf{G} in Equation (3), the corresponding values in \mathbf{D} are:

$$\mathbf{D} = \begin{bmatrix} -0.0490 & & & & \\ -0.0181 & -0.0399 & & & \\ -0.0083 & -0.0108 & -0.0242 & & \\ -0.0038 & -0.0040 & -0.0063 & -0.0116 & \\ -0.0018 & -0.0016 & -0.0020 & -0.0035 & -0.0037 \end{bmatrix} \quad (5)$$

Matrix \mathbf{D} is diagonally dominant, and so is much better conditioned than matrix \mathbf{G} . Thus, it is expected to be much less prone to error amplification. For the strain gauge case where matrices \mathbf{G} and \mathbf{D} are square, equations (1) and (4) are just linear variants of the same equation, and thus they give identical solutions. However, for over-determined solutions using least-squares calculations such as equation (2), significantly different results are achieved. In this case, the data associated with the largest matrix elements tend to be weighted more heavily. A least-squares calculation using matrix \mathbf{D} in equation (6) gives a more stable result than with matrix \mathbf{G} in equation (2) because the largest matrix elements are along the diagonal.

$$\mathbf{D}^T \mathbf{D} \boldsymbol{\sigma} = \mathbf{D}^T \mathbf{d} \quad (6)$$

ESPI Measurements

Figure 3 schematically shows the apparatus used here for the example ESPI hole-drilling measurements (PRISM, American Stress Technologies, Cheswick, PA). Light from a coherent laser source is split into an illumination light and a reference light. The illumination light illuminates the specimen surface, which is imaged by a CCD camera. The reference light passes through a piezo phase stepper and goes via a fiber link directly to the CCD surface. The two light beams interfere on the CCD surface to form a speckle pattern. The local phase of this speckle pattern is determined at each pixel from a set of four phase-stepped speckle images [20]. Deformations of the measured surface are evaluated by making subsequent sets of phase-stepped speckle images, computing the local phase angles, and subtracting the initial phase angle measurements. For the optical arrangement shown in Figure 3, the phase changes indicate surface displacements in the direction of the bisector of the illumination and object beams, called the sensitivity vector.

The specimen used for this study was from a construction steel, StE355, with its surface shot-peened to an intensity of 0.20 - 0.25. This treatment created equi-biaxial compressive residual stresses near the material surface, with tensile stresses extending into the interior to maintain equilibrium. The shot-peened specimen was chosen because it has a steep stress gradient near the surface and thus gives a challenge to the stress evaluation method.

A high-speed (50,000rpm) electric drill mounted on a precision traverse (not shown in Figure 3) was used to drill a hole for the example hole-drilling residual stress measurements. An initial ESPI phase map was measured on the specimen surface before starting the hole drilling. Further ESPI phase maps were measured after 16 successive hole depth increments of 25 μm . Exceptionally, the first hole depth increment was 10 μm to provide greater surface detail. The hole diameter was 1.59mm ($1/16$ ").

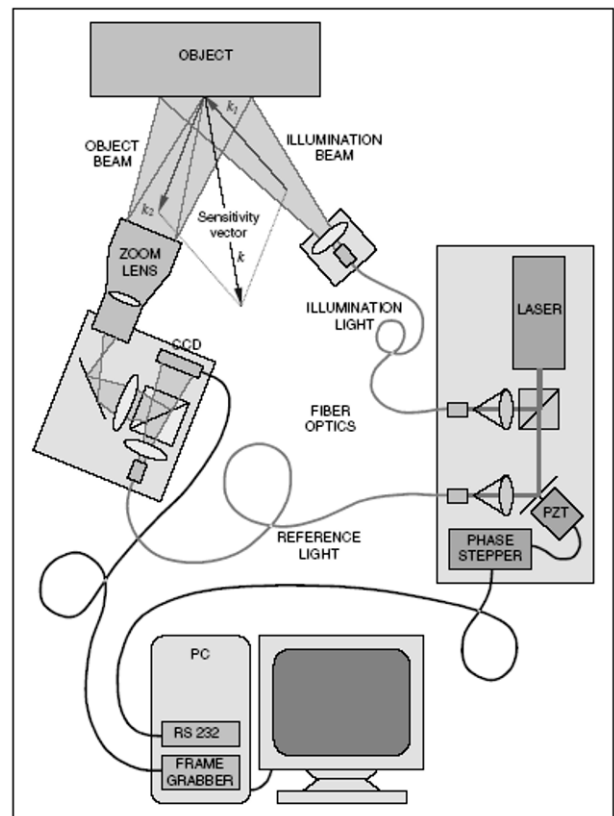


Figure 3. Schematic of equipment used for ESPI measurements (from Steinzig [14]).

Figure 4 shows the fringe pattern for the final (16th) ESPI measurement. This measurement was completed within one hour after the initial surface measurement taken before commencing the hole drilling. Figure 4(a) shows the fringe pattern for the 16th ESPI measurement referenced to the initial (0th) ESPI measurement. The central ellipse indicates the edge of the drilled hole. This elliptical shape appears because the circular hole was imaged non-perpendicularly. The camera was set at an angle of 27° to allow space for operation of the electric drill. The stress calculation takes this angle into account [22]. The two outer ellipses enclose the pixels used for the residual stress calculation. The positions of these ellipses were chosen to exclude the pixels immediately adjacent to the hole edge, which tend to get damaged by the passage of the chips from the hole cutting, and the pixels in the far field, which are too far away from the hole to contain much useful data.

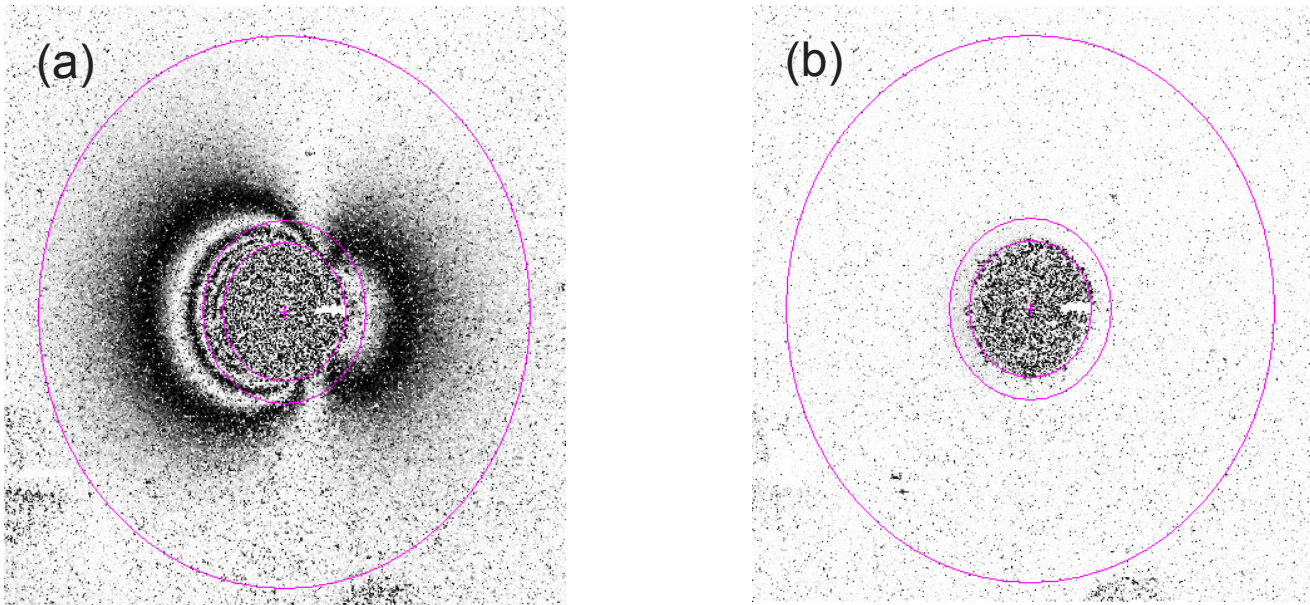


Figure 4. Fringe patterns for the 16th ESPI measurement:
 (a) referenced to the initial measurement, (b) referenced to the immediately prior measurement

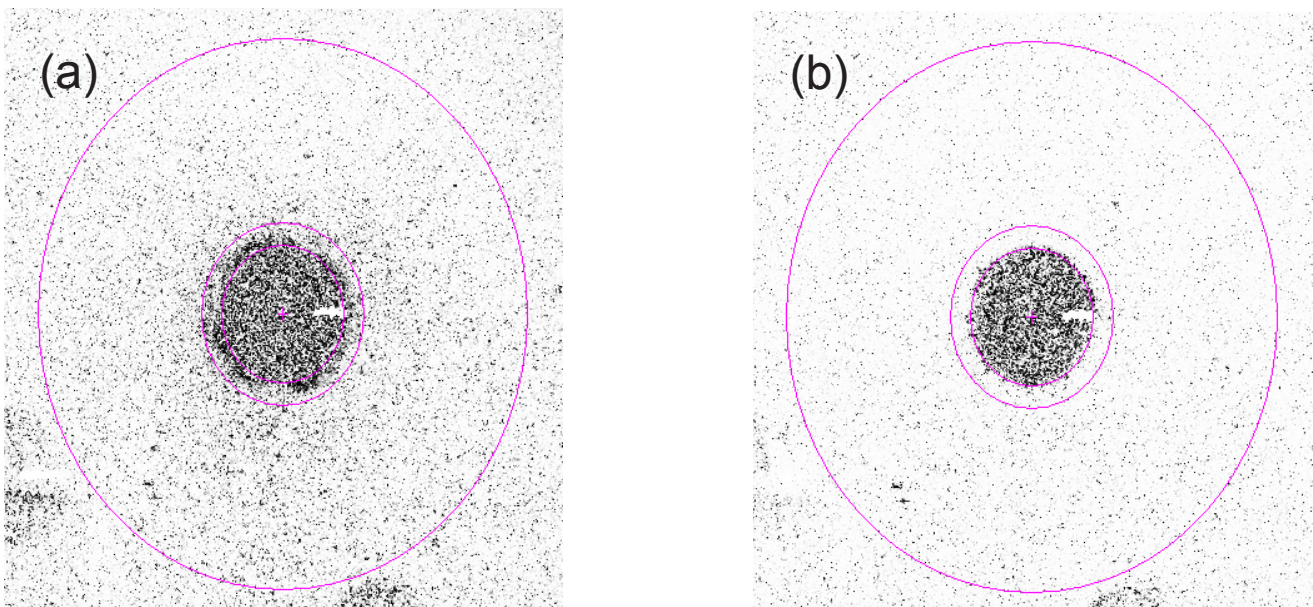


Figure 5. Residuals for the 16th ESPI measurement:
 (a) referenced to the initial measurement, (b) referenced to the immediately prior measurement.

Figure 4(a) shows a distinctive fringe pattern contained within a somewhat noisy background. This noisy background is typical of ESPI measurements. Figure 4(b) shows the fringe pattern for the same 16th ESPI measurement, but here referenced to the immediately prior (15th) ESPI measurement. Since there had been very little further surface deformation between the 15th and 16th depth increments, the fringe pattern in Figure 4(b) is barely visible. This small deformation presents no difficulty because the calculation method can successfully respond to the small deformations indicated. However, the much-reduced noise within the data is notable because it improves the quality of the ESPI data and significantly reduces noise in the residual stress evaluations.

A further indication of the lower noise contained in prior referenced data can be seen in the residual plots for the two types of data referencing. The "residual" is the quantity remaining after the theoretical data corresponding to the computed stresses (as described below) are subtracted from the measured data. Ideally, the measured and theoretical data should be identical, so a small residual is a desirable feature. Figure 5(a) shows the residual in the 16th initially referenced ESPI measurement. It shows a pattern of noise similar to that seen in Figure 4(a). Figure 5(b) shows the corresponding residual in the 16th prior referenced ESPI measurement. As expected, it shows a similar pattern of reduced noise to that seen in Figure 4(b).

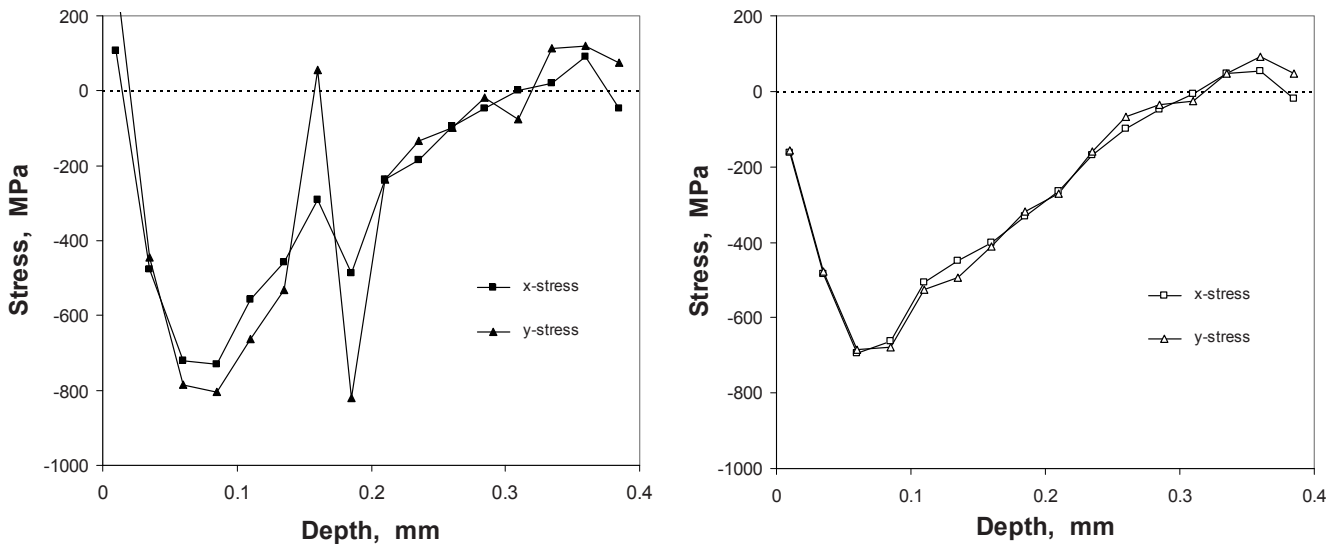


Figure 6. Residual stress vs. depth profiles: (a) computed using initially referenced ESPI measurements, (b) computed using prior referenced ESPI measurements

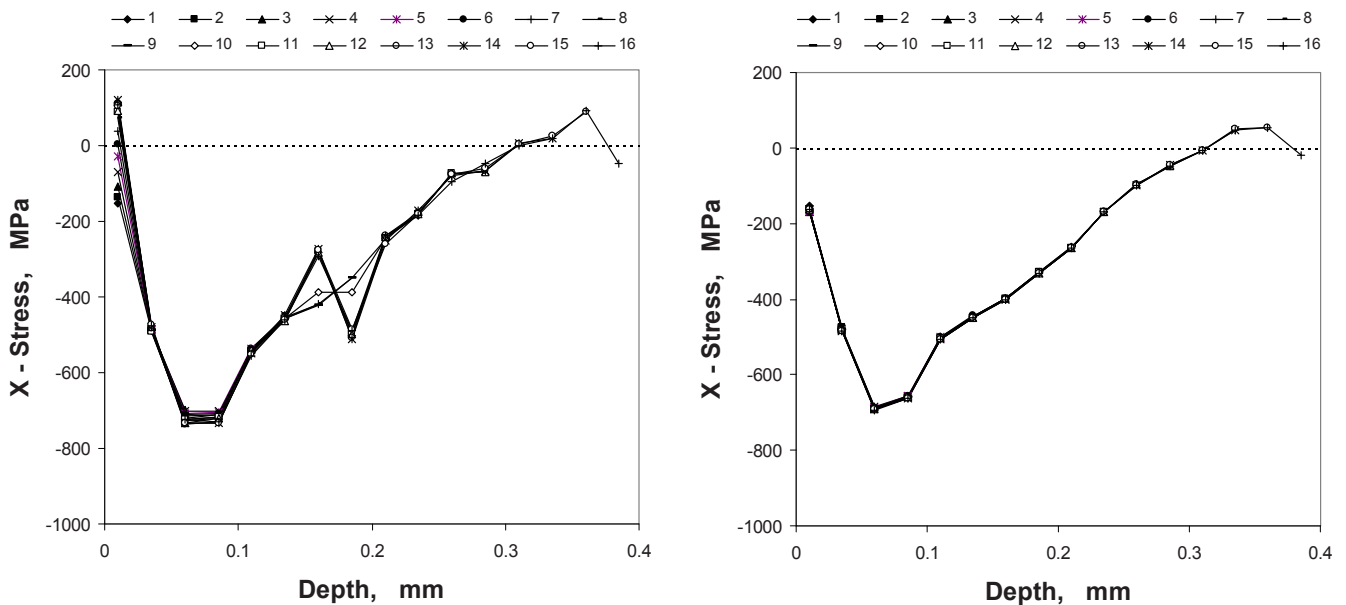


Figure 7. Residual x-stress vs. depth calculated using first 1, 2, 3, ... data: (a) computed using initially referenced ESPI measurements, (b) computed using prior referenced ESPI measurements

Figure 6(a) shows the stresses calculated using equation (2) with initially referenced ESPI measurements. The curves show the expected peak compression below the surface, with x- and y- stresses approximately equal, as also observed by Lord *et al.* [18]. However, measurement noise has caused substantial irregularities of the graphs. Also of concern are the indicated tensile stresses immediately adjacent to the surface and the differences between the x- and y-stresses. Figure 6(b) shows the stresses calculated using equation (6) with each ESPI measurement referenced to the prior measurement. The calculated stresses are much more realistic; they have a smoother trend, the indicated stresses at the surface are compressive, and the x- and y-stresses are closely similar.

The tensile stresses reported at the surface in Figure 6(a) are an artefact caused by the large off-diagonal elements in the lower left corner of matrix **G**, such as shown in equation (3). During the least-squares evaluation in equation (2), these large matrix elements have correspondingly large influence, causing the interior stresses to distort the evaluation of the near-surface stresses. Matrix **D** is diagonally dominant, and so does not display this effect when used in equation (6).

Figure 7 shows a further important feature of using prior-referenced data. Figure 7(a) shows the results of a progressively growing series of x-stress calculations using equation (2). The first calculation of the series computes only the first stress using the first ESPI measurement, the second computes the first two stresses using the first two ESPI measurements, and so on until the 16th measurement. This sequence illustrates the cumulative effects of the interior stresses on the surface stress calculation. Figure 7(a) shows that the surface stress is realistically calculated when only few subsurface stresses are included in the calculation, but that it becomes increasingly tensile as further subsurface stresses are involved. In addition, the effects of measurement noise are readily apparent in Figure 7(a). In contrast, the corresponding results using prior referenced ESPI data and equation (6) show consistently compressive stresses at the surface and much reduced noise elsewhere.

Discussion

Figures 4-7 clearly show the significant improvement achieved in calculations of residual stresses when using prior referenced ESPI data in place of initially referenced data. A practical question arises as to whether a similar advantage could be obtained when doing traditional hole-drilling residual stress measurements with strain gauges. While there is a great similarity between strain gauge and ESPI hole-drilling, there are also significant differences. An important difference is that strain gauge measurements provide a just-sufficient amount of data. There are no excess data, and thus the “least squares” solutions to equations (2) and (6) provide identical “exact” results. In addition, the lack of excess data provides no quality advantage in using prior referenced measurements. Any drift that may occur during the course of a set of strain gauge measurements similarly affects initial and prior referenced data. Thus, there is no particular advantage or disadvantage in using prior referenced data with traditional strain-gauge hole-drilling measurements. In contrast, prior referencing does significantly improve the average quality of the excess data available with optical techniques such as ESPI, and it provides a more balanced “best-fit” to those data.

Conclusions

In present practice, optical data measured at each step of an incremental material removal process for measuring residual stresses are referenced to the initial uncut condition. In the procedure proposed here, the measurement and computational approaches are altered so that the stresses are evaluated in terms of the deformation change during each material removal step. This change provides two important benefits, the first that the time between corresponding pairs of optical measurements is minimized, thereby greatly improving image and phase unwrapping quality, and the second that the associated mathematical relationship between measured deformations and residual stresses is much better conditioned and gives more stable results. An example ESPI hole-drilling measurement demonstrates the substantial measurement quality and calculation stability improvements. The proposed method is effective particularly when used with optical measurements, where there is a great excess of data available. For measurements using strain gauges, there typically are no excess data, in which case the method then gives neither advantage nor disadvantage.

Acknowledgments

Financial support for this work was provided by the Natural Sciences and Engineering Research Council of Canada (NSERC), and by American Stress Technologies, Cheswick, PA. Mr. Anthony An kindly assisted with the experimental work.

References

1. Schajer, G. S. and Prime, M. B. "Use of Inverse Solutions for Residual Stress Measurements." *Journal of Engineering Materials and Technology*. Vol.128, No.3, pp.375-382, 2006.
2. ASTM. "Determining Residual Stresses by the Hole-Drilling Strain-Gage Method." ASTM Standard Test Method E837-08. American Society for Testing and Materials, West Conshohocken, PA. 2008.
3. Lu, J. "Handbook of Measurement of Residual Stresses," Chapter 2: "Hole-Drilling and Ring Core Methods." Fairmont Press, Lilburn, GA, 1996.
4. Prime, M. B. "Residual Stress Measurement by Successive Extension of a Slot: The Crack Compliance Method." *Applied Mechanics Review*, Vol.52, No.2, pp.75-96. 1999.
5. Cheng, W., and Finnie, I. "Measurement of Residual Hoop Stress in Cylinders Using the Compliance Method." *Journal of Engineering Materials and Technology*, 108, pp.87-92, 1986.
6. Sachs, G. and Espey, G. "Measurement of Residual Stresses in Metal." *Iron Age*, 148, Sept. 18, pp. 63-71; Sept. 25, pp. 36-42, 1941.
7. Treuting, R. G. and Read, W. T. "A Mechanical Determination of Biaxial Residual Stress in Sheet Materials," *Journal of Applied Physics*, Vol.22, No.2, pp.130-134, 1951.
8. Parker, R. L. "Geophysical Inverse Theory." Princeton University Press, New Jersey, 1994.
9. Schajer, G. S. "Strain Data Averaging for the Hole-Drilling Method." *Experimental Techniques*, Vol.15, No.2, pp.25-28, 1991.
10. Schajer, G. S. "Hole-Drilling Residual Stress Profiling with Automated Smoothing." *Journal of Engineering Materials and Technology*, Vol.129, No.3, pp.440-445, 2007.
11. Nelson, D.V. and McCrickerd, J.T. "Residual-stress Determination Through Combined Use of Holographic Interferometry and Blind-Hole Drilling." *Experimental Mechanics*, Vol.26, No.4, pp.371-378, 1986.
12. Díaz, F. V., Kaufmann, G. H. and Möller, O. Residual Stress Determination Using Blind-hole Drilling and Digital Speckle Pattern Interferometry with Automated Data Processing." *Experimental Mechanics*, Vol.41, No. 4, pp.319-323, 2001.
13. Steinzig, M. and Ponslet, E. "Residual Stress Measurement Using the Hole Drilling Method and Laser Speckle Interferometry: Part I." *Experimental Techniques*, Vol.27, No.3, pp.43-46, 2003.
14. McDonach, A., McKelvie, J., MacKenzie, P. and Walker, C. A. "Improved Moiré Interferometry and Applications in Fracture Mechanics, Residual Stress and Damaged Composites." *Experimental Techniques*, Vol.7, No.6, pp.20-24, 1983.
15. Nicoletto, G. "Moiré Interferometry Determination of Residual Stresses in the Presence of Gradients," *Experimental Mechanics*, Vol.31, No.3, pp.252-256, 1991.
16. Wu, Z., Lu, J. and Han, B. "Study of Residual Stress Distribution by a Combined Method of Moiré Interferometry and Incremental Hole Drilling." *Journal of Applied Mechanics*, Vol.65, No.4 Part I: pp.837-843, Part II: pp.844-850, 1998.
17. McGinnis, M.J., Pessiki, S. and Turker, H. "Application of Three-dimensional Digital Image Correlation to the Core-drilling Method." *Experimental Mechanics*, Vol.45, No.4, pp.359-367, 2005.
18. Lord J.D., Penn D. and Whitehead, P. "The Application of Digital Image Correlation for Measuring Residual Stress by Incremental Hole Drilling." *Applied Mechanics and Materials*, Vols. 13-14, pp 65-73, 2008.
19. Dahlquist, G., Björck, Å., and Anderson, N., 1974, *Numerical Methods*, Prentice-Hall, Englewood Cliffs, NJ.
20. Sirohi, R. S. "Speckle Metrology." Marcel Dekker, New York, 1993.
21. Schajer, G. S. "Measurement of Non-Uniform Residual Stresses Using the Hole-Drilling Method." *Journal of Engineering Materials and Technology*, Vol.110, No.4, Part I: pp.338-343, Part II: pp.344-349, 1988.
22. Schajer, G. S. and Steinzig, M. "Full-Field Calculation of Hole-Drilling Residual Stresses from ESPI Data." *Experimental Mechanics*, Vol.45, No.6, pp.526-532, 2005.

Experimental Investigation of Residual Stresses in Water and Air Quenched Aluminum Alloy Castings

Bowang Xiao¹, Yiming Rong¹ and Keyu Li²

1. Manufacturing Engineering, Worcester Polytechnic Institute, 100 Institute Rd, Worcester, MA 01609, USA. bowangxiao@gmail.com

2. Mechanical Engineering Department, Oakland University, Rochester Hills, MI 48309, USA

ABSTRACT

Cast aluminum alloys are usually subject to heat treatment including quenching for improved mechanical properties. A significant amount of residual stresses can be developed in aluminum castings during heat treatment. This paper investigates experimentally residual stress differences between water quenched aluminum castings and air quenched ones. The residual stresses in aluminum castings were measured mainly using resistance strain rosettes hole-drilling method. Other measured methods such as Interferometric Strain/Slope Rosette (ISSR), X-ray diffraction method and neutron diffraction method were also applied in this investigation. In comparison with water quenching, air quenching significantly reduces the residual stresses.

KEYWORDS

Resistance Strain Gauge, Incremental Hole-drilling Method, Residual Stress, Quenching, Aluminum Alloy Casting

1. INTRODUCTION

With the increasing demand of reducing weight and improving fuel efficiency, cast aluminum components have been widely used in critical automotive components such as engine blocks, cylinder heads, and suspension parts. In order to increase mechanical properties, cast aluminum alloys are usually subject to a T6/T7 heat treatment which includes a solution treatment at a relatively high temperature, quenching in a cold medium such as water or forced air flow, and age hardening at an intermediate temperature. A significant amount of residual stresses can be developed in aluminum castings during the heat treatment process [1-4]. Residual stresses are those remaining in a component after manufacture or heat treating processing. The existence of residual stresses in a structural component can have a significant influence on its performance. Fatigue performance of cast aluminum components can be dramatically affected by the presence of residual stresses, in particular, the tension residual stresses in the surface layer. Therefore, it is of increasing interest to measure and control residual stresses in critical components.

Many methods have been developed to measure residual stresses in manufactured parts. Mechanical approaches such as hole drilling, curvature measurements, and crack compliance measure residual stress by changes in component distortion. Diffraction techniques such as X-ray diffraction and neutron diffraction measure elastic strains in the components due to residual stresses [5].

In this investigation, the residual stresses in aluminum castings after water quenching and air quenching were measured mainly using RSR (Resistance Strain Rosette) in conjunction with hole-drilling method. Other measured methods such as Interferometric Strain/Slope Rosette (ISSR), X-ray diffraction and neutron diffraction were also applied in this investigation. The purpose of this investigation is to see the differences of residual stresses in castings between after water quenching and after air quenching.

2. THEORETICAL BACKGROUND OF RESIDUAL STRESS MEASUREMENT METHODS

This section reviews the residual stress measurement methods applied in the measurement of residual stresses.

RESISTANCE STRAIN ROSETTES HOLE-DRILLING METHOD

The widely used RSR (hole-drilling) method is included in the ASTM standard E837 [6]. The detailed procedures are also documented in Measurement Group's technique note 503 [7]. In the measurement of residual stress using center hole-drilling method, a strain gauge rosette is mounted onto the surface of the sample and a small hole is drilled at the center of the three strain gauges and used to measure relieved strains during the hole-drilling. The general expression for the relieved radial strains due to a plane biaxial residual stress state is Equation 1 [7]. The measured strains are then used to back-calculate residual stresses, and the integral hole-drilling method was developed to calculate residual stresses in multiply layers drilling for non-uniform residual stress fields [8].

$$\begin{aligned}\varepsilon_1 &= A(\sigma_x + \sigma_y) + B(\sigma_x - \sigma_y)\cos 2\alpha \\ \varepsilon_2 &= A(\sigma_x + \sigma_y) + B(\sigma_x - \sigma_y)\cos 2\beta \\ \varepsilon_3 &= A(\sigma_x + \sigma_y) + B(\sigma_x - \sigma_y)\cos 2\gamma\end{aligned}\quad (1)$$

where $\varepsilon_{1,2,3}$ =measured strain relieved from strain gauge 1, 2 and3, respectively

σ_x, σ_y =stress in x and y direction, respectively

A, B =calibration coefficients

$\alpha \beta \gamma$ =angle measured counterclockwise from the x direction to the axis of the strain gauge 1, 2 and 3, respectively

Since the coefficients A and B for blind hole-drilling cannot be calculated directly from theoretical considerations, they are usually obtained by numerical procedures such as finite-element analysis [7, 8]. Some tables of the coefficients defined in Equation 3 were published [8, 9]. It is suggested that the coefficients A and B can be interpolated or extrapolated from the published nondimensionless coefficients [8, 9]. However, errors are always introduced in this procedure. More accurate residual stresses can be calculated if the interpolation can be avoided, e.g. determine the calibration coefficients directly using FEA for a specific measurement [10].

INTERFEROMETRIC STRAIN/SLOPE ROSETTE (ISSR)

The ISSR is a laser based technique that measures the strain changes based on diffraction and interference of laser light [11]. ISSR consists of three micro-indentations and has the configuration of delta or rectangular rosette [11]. A delta rosette, also called 60-deg ISSR, contains three six-faced indentations and the three indentations form an equilateral triangle. Under illumination by an incident laser beam, the six facets of each indentation in a delta rosette reflect and diffract the light in six directions. The motion of the fringes is related to the displacements between the indentations and hence to the strains and slopes. The strains and slopes are determined through tracing the shifts of fringe patterns.

The ISSR/Ring-core method is a combination of the ISSR method and ring-core cutting method [12, 13]. The ring-core cutting method is a stress-relief method. The ring-core cutting is to remove a ring of the material around the ISSR and the relieved strains and slopes are measured by the ISSR. The relative positions of the ring-core center and the ISSR are shown in [Figure 1](#). Similar to strain gauge hole-drilling method, the relieved strains and slopes are used to back-calculate residual stresses with calibration coefficients which are calibrated numerically [12, 13]. It is worthy to mention that the gage length of the ISSR on the core area is normally in the range of 50 μm and 250 μm while the resistance strain rosette (RSR used for the hole drilling method) has a 5mm gage length and the core size with the ISSR is less than 1 mm which is also much smaller than that used in the RSR. Thus, more localized residual stresses, especially in the small areas with the high stress gradients, can be measured by the ISSR/ring-core method.

X-RAY DIFFRACTION METHOD

Different from strain gauge and ISSR methods, X-ray diffraction method and neutron diffraction method are nondestructive methods. When a monochromatic X-ray beam irradiates a solid material, it is scattered by the atoms composing the material. Because of the regular distribution of atoms (for a perfect crystalline material), the scattered waves lead to interferences similar to visible light diffraction by an optical diffraction pattern. If the material is composed of many grains (crystallites) randomly oriented, there is always a group of them suitably oriented to produce a diffracted beam. If the specimen is stressed, due to elastic deformation, the lattice spacing

varies. Thus, the crystal lattice is used as a strain gauge which can be read by diffraction experiments. A diffraction peak is the result of X-rays scattering by many atoms in many grains, so a change in the lattice spacing will result in a peak shift only if it is homogeneous over all these atoms and grains. The strain determined from peak shift measurements is representative of a macroscopic elastic strain (residual or applied). Therefore, residual stresses can be calculated from the residual strains measured in several directions and the elasticity constants of the material [5].

Please note that any crystal defects (vacancies, dislocations, stacking faults, etc) lead to a local fluctuation of the lattice spacing which results in a peak broadening and this method can only measured residual stresses on surface [5].

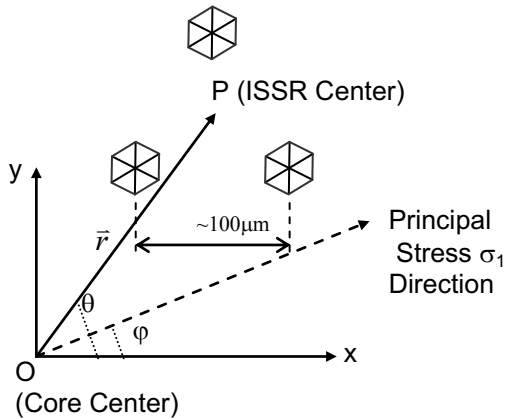


Figure 1. Rectangular and polar coordinates in the ISSR/ring-core method

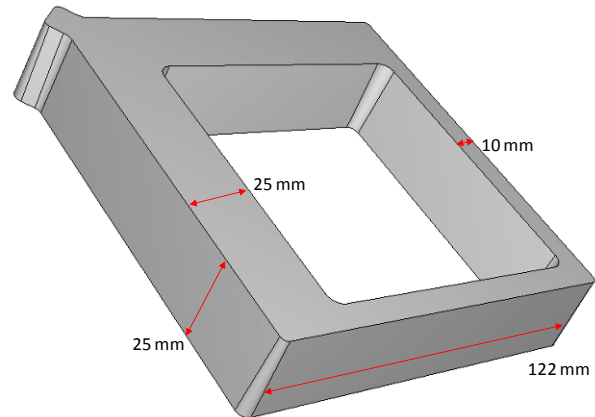
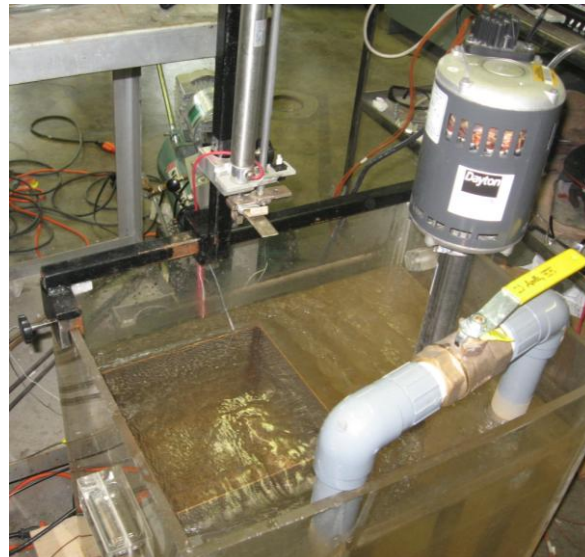
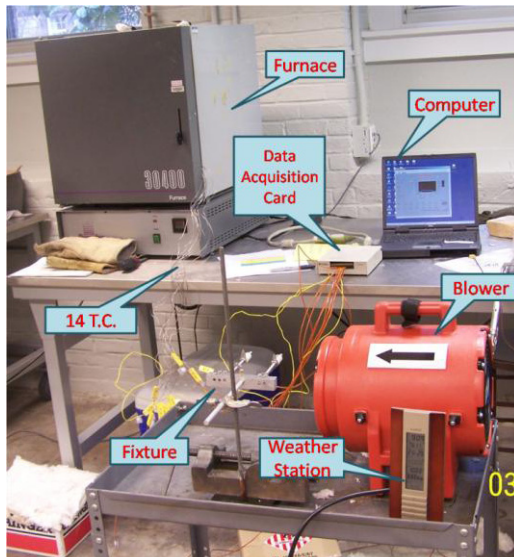


Figure 2. Sketch drawing of the aluminum alloy casting

NEUTRON DIFFRACTION METHOD

The physical principle of residual strain measurement by neutron is the same as X-ray diffraction. However, the deep penetration of thermal neutrons into engineering materials means that the strain information obtained nondestructively are at depth complements. In other words, the neutron diffraction can determine residual strains (stresses) throughout the thickness of a component, whereas X-rays provide a measurement of the strains average over a few microns near the surface [5].

3. AIR QUENCHING AND WATER QUENCHING OF ALUMINUM ALLOY CASTING



a) b) Figure 3. Experimental set-up for: a) air quenching; b) water quenching

In air quenching tests, the aluminum casting shown in [Figure 2](#) was first heated to a designated solution temperature in the furnace, and then quickly moved out of the furnace (within 10 seconds) and placed onto the fixture which was under the forced air generated by a blower as shown in [Figure 3a](#). The input voltage of the blower was adjusted by a variac so that different air velocities can be obtained. In this investigation, the forced air velocity was calibrated to 18m/s using an anemometer by setting a proper input voltage.

A quenching bed shown in [Figure 3b](#) was built. The aluminum alloy casting was heated in the furnace and moved out and fixed to the pneumatic lifting system after it had reached a uniform specified temperature. The pneumatic system then lowered to immerse the casting into water at a constant speed. In this experiment, the water was heated up to a high temperature to simulate real production condition for water quenching of cylinder head. For experiments with agitation, the water was pump and circulated. The water flow velocities at the location where the test casting was quenched were calibrated and found to be very uniform at 0.08m/s. After the test casting was cooled down to water temperature, the test casting was taken out by the pneumatic lifting system.

4. RESIDUAL STRESS MEASUREMENT AND COMPARISON

Residual stresses on the aluminum alloy castings were measured use different methods. For the casting quenched in water, resistance strain rosette (RSR) hole-drilling method, ISSR ring-core method, X-ray diffraction method and neutron diffraction method were used. For the casting quenched in air flow, only resistance strain rosette (RSR) hole-drilling method was applied. [Figure 4a](#) shows the measurement of residual stresses at the top of the thin legs using RSR and ISSR methods on one of castings, and [Figure 4b](#) shows the measurements of residual stresses on thin and thick legs using RSR methods.

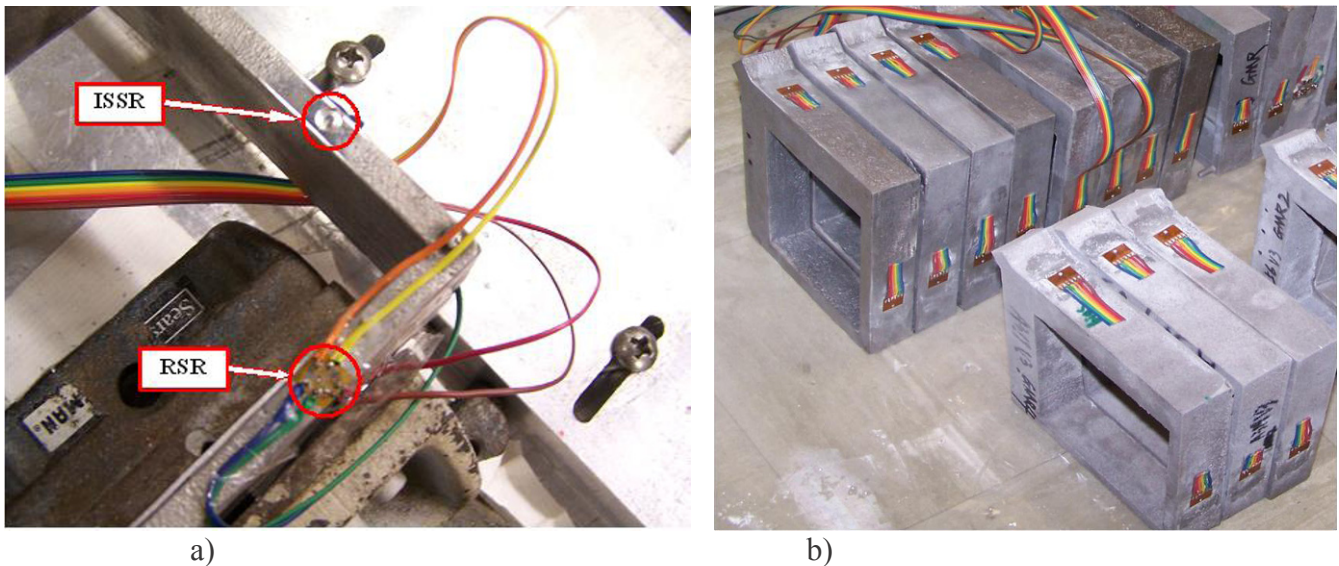


Figure 4. a) RSR hole-drilling and ISSR/ring-core on top of the water-quenched aluminum casting; b) RSR hole-drilling measurements on the side of air quenched and water quenched castings

[Figure 5](#) illustrates the locations of all the applied methods. Please note that [Figure 5](#) is for the purpose of illustrating relative locations of these methods and in reality different methods might be used on different castings. All measurements are at or near to surfaces, except the neutron diffraction method, which measures residual stresses inside of the castings.

[Figure 6](#) compares the residual stresses on the top surface of the thin legs of water-quenched casting. [Figure 6a](#) shows the measured residual stress distributions using ISSR technique. It is seen that the distribution of the residual stresses changes dramatically near the top surface. For the location measured, the residual stress varies from -200 MPa on the surface to about 10 MPa in the area about 0.7 mm below the surface. [Figure 6b](#) shows the residual stresses measured using RSR. Similar to the results shown in [Figure 6a](#), a substantial compressive residual stress was developed at the top surface of the thin leg during water quenching process. By comparing the data in both figures, it can be concluded that the results from two methods (RSR and ISSR) are comparable.

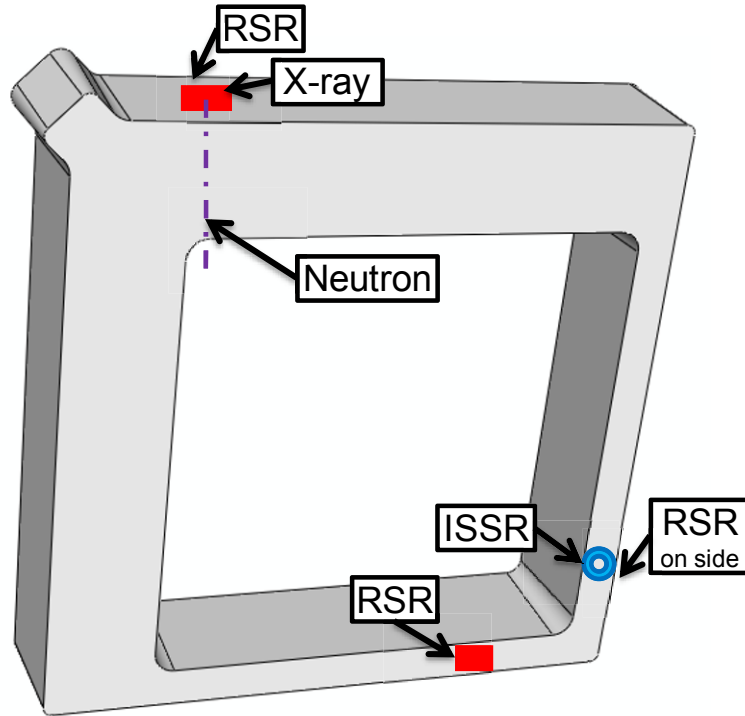


Figure 5. Locations of measurements using different methods

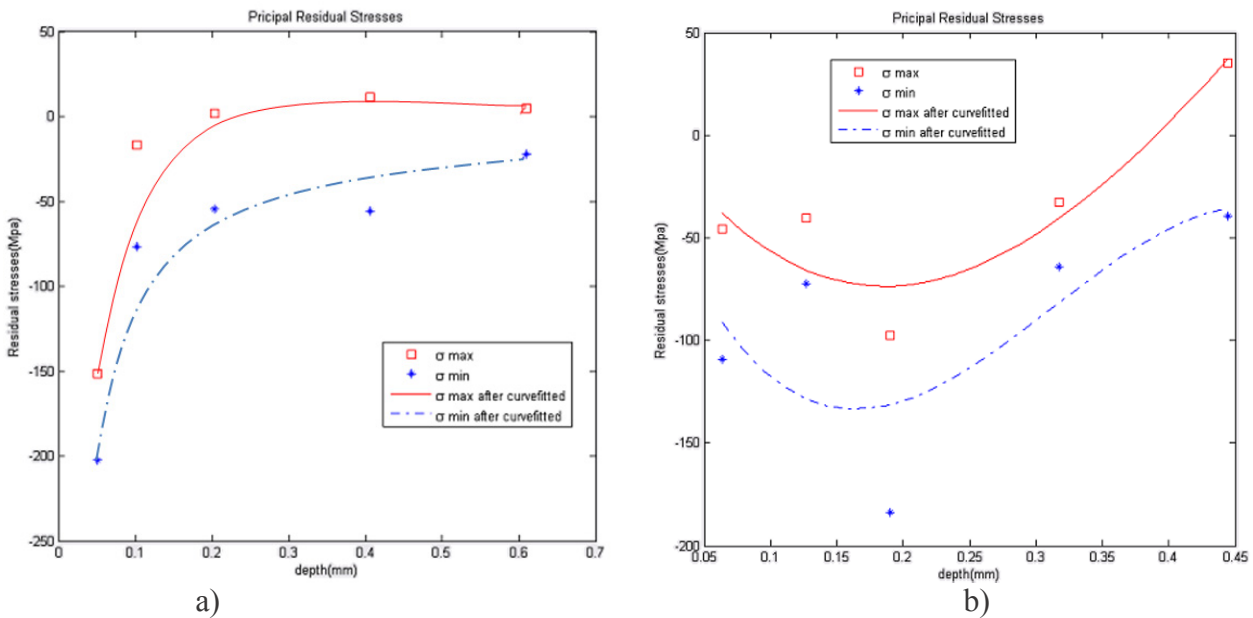


Figure 6. Residual stresses after water quenching: a) Residual stresses measured by ISSR method at the top surface of the thin leg; b) Residual stresses measured by RSR at the top surface of the thin leg

Figure 7 compares the residual stresses measured at thick leg by both RSR and neutron diffraction methods [14]. X-ray diffraction measurements [15] were also made at the location as shown in Figure 5. The RSR measured the residual stress distribution from the surface to 0.45 mm deep, the X-ray diffraction measured the residual stresses from the surface to 1 mm deep by etching and removing the surface material, and neutron diffraction method measured residual stresses across the whole thickness but started from 1.5 mm below the surface. By comparing the data in Figure 7, it is seen that the general trend of residual stress distribution measured at this

location by RSR and neutron techniques is similar. The residual stresses measured by neutron are negative (the outer side surface), which agree with those measured by RSR. The residual stresses measured by both methods indicate that the stresses increase from surface to inside. The minimum principle residual stress measured by RSR method increases from about -100 MPa to -80 MPa as the depth increases from 0.05 mm to 0.45 mm. It is expected that the minimum principle residual stresses increases to about -40 MPa when the depth increases to 1.5 mm, which is the measurement result by neutron method. The maximum residual stress measured by RSR increases from about -50 MPa to -40 MPa as the depth increases from 0.05 to 0.45mm. It is expected that the maximum residual stresses increases to about -20 MPa when the depth increases to 1.5 mm, which is the measurement result by neutron diffraction method. The minimum residual stress measured by X-ray increases from about -130 MPa to -90 MPa as the depth increases from 0.0127 to 0.5 mm, , which agrees with the measurement result by RSR method (Figure 7a). The maximum residual stress measured by X-ray increases from about -70 MPa to -40 MPa as the depth increases from 0.0127 to 0.5 mm, which is agreeable with the measurement result by RSR method (Figure 7a).

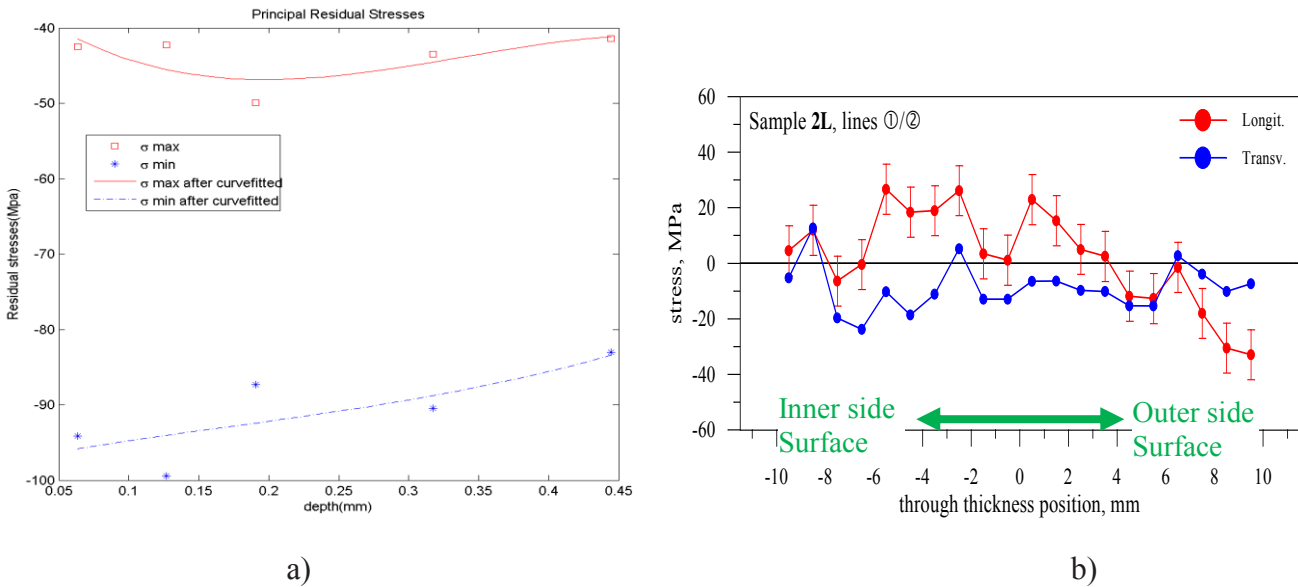


Figure 7. Residual stresses measured on thick leg using (a) RSR; and (b) Neutral diffraction method [3].

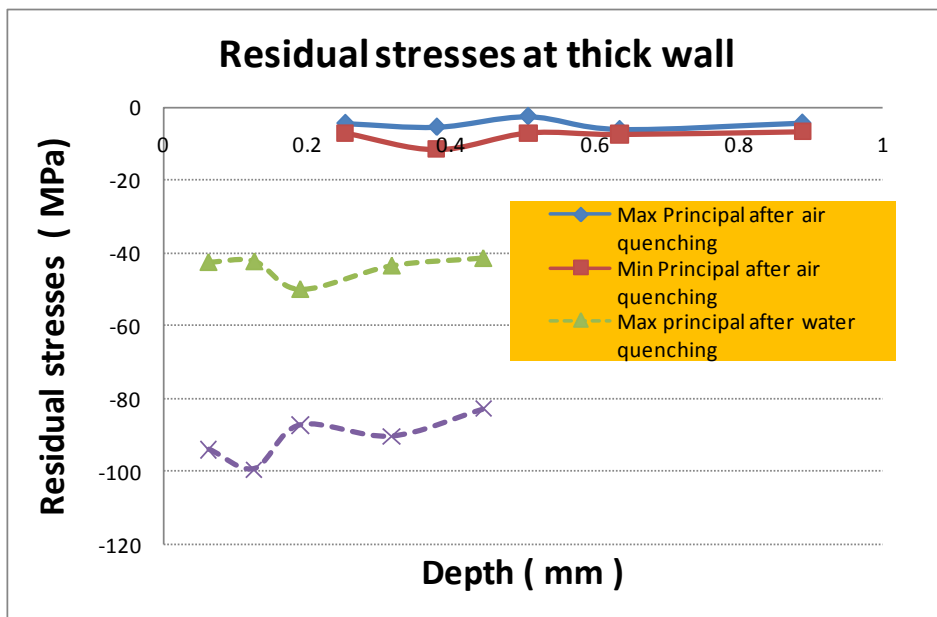


Figure 8. Comparison of the measured residual stresses at thick wall of the aluminum castings after air and water quenching

Figure 8 compares the residual stress distributions measured at the thick wall of the air-quenched aluminum casting to those of the water-quenched casting. It is seen that the residual stresses in the air-quenched aluminum casting are less than 10 MPa and pretty uniform, but in the water-quenched aluminum casting, the absolute values of residual stresses vary from 40 MPa to 100 MPa. Small and uniform residual stresses in air-quenched castings are good to the fatigue life and distortion control.

5. CONCLUSIONS

The residual stresses in aluminum castings generated in air quenching and water quenching were measured using resistance strain rosettes hole-drilling method, Interferometric Strain/Slope Rosette, X-ray diffraction method and neutron diffraction method in this investigation. A significant amount of residual stresses can be developed in cast aluminum alloys during water quench after solution treatment. In comparison with water quenching, air quenching significantly reduces the residual stresses.

6. ACKNOWLEDGEMENT

The authors would like to thank Dr. Qigui Wang from General Motors Company and Prof. Richard D. Sisson from CHTE (Center for Heat Treating Excellence) at WPI for their valuable help in the experimental work.

REFERENCES

- [1] Elkhatny, I., Morsi, Y., Blicblau, A. S., 2003, "Numerical Analysis and Experimental Validation of High Pressure Gas Quenching," *International Journal of Thermal Sciences*, 42(4) pp. 417-423.
- [2] Rose, A., Kessler, O., Hoffmann, F., 2006, "Quenching Distortion of Aluminum Castings-Improvement by Gas Cooling," *Materialwissenschaft Und Werkstofftechnik*, 37(1) pp. 116-121.
- [3] Li, K., Xiao, B., and Wang, Q., 2009, "Residual Stresses in as-Quenched Aluminum Castings," *SAE International Journal of Materials & Manufacturing*, 1(1) pp. 725-731.
- [4] Li, M., and Allison, J. E., 2007, "Determination of Thermal Boundary Conditions for the Casting and Quenching Process with the Optimization Tool OptCast," *Metallurgical and Materials Transactions B*, 38B(4) pp. 567-574.
- [5] Lu, J., and James, M., 1996, "Handbook of measurement of residual stresses," Fairmont Press, Inc, Lilburn, GA, USA, pp. 237.
- [6] ASTM designation: E837-01, 2002, ASTM international, Philadelphia, PA, pp. 703-712.
- [7] Vishaymicro-Measurements, 2007, "Tech Note TN-503: Measurement of Residual Stresses by the Hole-Drilling Strain Gage Method," 2009pp. 33.
- [8] Schajer, G. S., 1988, "Measurement of Non-Uniform Residual Stresses using the Hole-Drilling Method. Part I- Stress Calculation Procedures," *J.Eng.Mater.Technol.(Trans.ASME)*, 110pp. 338-343.
- [9] Schajer, G. S., 1988, "Measurement of Non-Uniform Residual Stresses using the Hole-Drilling Method. Part II- Practical Application of the Integral Method," *J.Eng.Mater.Technol.(Trans.ASME)*, 110pp. 344-349.
- [10] Xiao, B., Li, K., and Rong, Y., 2010, "Automatic Determination and Experimental Evaluation of Residual Stress Calibration Coefficients for Hole-Drilling Strain Gage Integral Method," *Strain*, In Press, Accepted Manuscript.
- [11] Li, K., 1995, "Interferometric 45 and 60 Strain Rosettes," *Applied Optics*, 34(28) pp. 6376-6379.
- [12] Li, K., and Ren, W., 2007, "Application of Miniature Ring-Core and Interferometric Strain/Slope Rosette to Determine Residual Stress Distribution with Depth—Part I: Theories," *Journal of Applied Mechanics*, 74pp. 298.
- [13] Ren, W., and Li, K., 2007, "Application of Miniature Ring-Core and Interferometric Strain/Slope Rosette to Determine Residual Stress Distribution with Depth—Part II: Experiments," *Journal of Applied Mechanics*, 74pp. 307.
- [14] Luzin, V., Prask, H., and Gnaeupel-Herold, T., April 22, 2005, "Residual Stresses in GM aluminum Castings," NIST Center for Neutron Research, Gaithersburg, MD.
- [15] Hornbach, D., May 24, 2005, "X-ray Diffraction Determination of the Surface and Subsurface Residual Stresses in Two A356 Aluminum Castings," *Lambda Technologies*, 227-12260, Cincinnati, Ohio.

RESIDUAL STRESS ON AISI 300 SINTERED MATERIALS

C. Casavola, C. Pappalettere, F. Tursi

*Politecnico di Bari, Dipartimento di Ingegneria Meccanica e Gestionale,
Viale Japigia, 182 – 70126 Bari, e-mail: casavola@poliba.it*

ABSTRACT - Selective Laser Melting (SLM) is one of the most interesting technologies in the rapid prototyping processes because it allows to build complex 3D geometries. Moreover, full density can be reached and mechanical properties are comparable to those of bulk materials. However, the most important drawback is related to the thermal transient encountered during solidification which generates highly variable residual thermal stresses.

Parameters such as laser scanner strategy, laser velocity and power should be optimized also in order to minimize residual stresses that are strictly dependent on the manufacturing process and cannot be completely avoided. Geometry of parts should be optimized in order to keep residual stresses and distortions low.

This paper presents a study on residual stress distribution on SLM rectangular plates built by means of a new scanning strategy, implemented by dividing the fused zone in very small square sectors. Residual stresses measurement on SLM samples are performed by means of the hole drilling technique. Specimens made of AISI Maraging 300 steel are investigated and the residual stress profiles are compared with those related to previous measurements on SLM disks coming from the same process parameters.

INTRODUCTION

Selective Laser Melting (SLM), such as Laser Cladding (LC) and Laser Sintering (LS), represents a modern technology for building complex 3-dimensional parts. All these processes allow different layer of material to be combined and are especially used for the deposition of wear and corrosion protective coatings. Besides, powder metallurgy with SLM is capable to yields materials and components with a very wide range of properties. However, SLM is very similar to a welding process and it is necessary to understand the interaction between manufacturing parameters and mechanical and metallurgical properties of parts.

High precision in the dimension of SLM parts is strictly related to very high laser energy density. Large temperature gradients associated with the process, however, are the cause of high thermal stresses which may even lead to cracking, delaminating, and large bending distortion.

Developing of residual stress depends on thermal phenomenon [1-2]: when a new layer of powder is deposited onto the existing ones, temperature gradients develop because of the rapid heating of the upper layer induced by the laser. At the same time, heat conduction through previously solidified layers is comparatively slow. The heated top layer expands first and then cools and shrinks. In all cases, the surrounding material, whose yield limit is reduced by the high temperature, constrains these movements and produces plastic strains. In many cases these processes can lead to macroscopic curvature of the product (fig. 1) as each new layer is added into the structure.

Some studies demonstrate that the laser strategy used to melt the powder may affect significantly residual stresses and distortions [1-4]. In addition, product geometry, particularly the length and moment of inertia, affect the magnitude of residual stresses [5]. A base plate is generally used as rigid constraint welded to the part in order to reduce macroscopic distortions.

This paper presents experimental measurements of residual stresses in SLM specimens produced from AISI Maraging 300 steel. The strain gage hole drilling method (HDM) is used for measuring residual stress profiles in different position of a rectangular specimen. Non uniform stress field have been found into the thickness of specimens. Experimental strain released have been processed with different method (ASTM, power series, integral method) and discussed. Results have been compared with residual stresses on SLM specimens of circular shape, in order to evaluate the influence of geometry on SLM process.

MATERIALS

The SLM equipment used to built specimens is characterized by a Nd:YAG laser source with a wavelength of 1.064 μm , a spot diameter (d) of 200 μm and a maximum output power of 100 W in the continuous mode. Operation in pulsed mode in the 0-65 kHz band is also possible. Powder layers is deposited in one direction

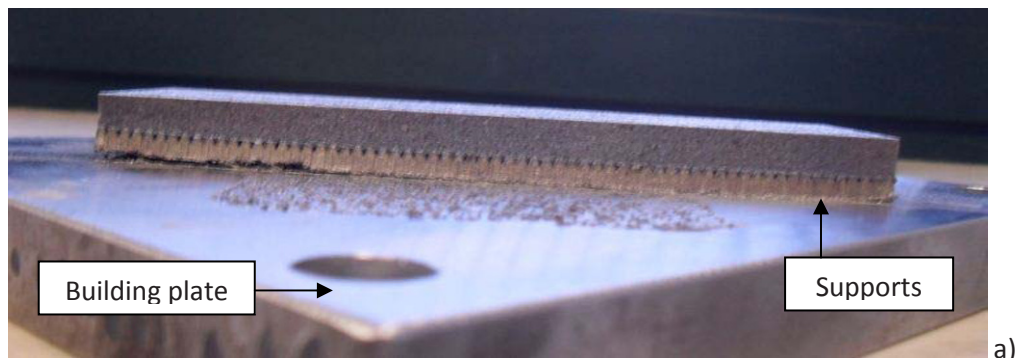
using a knife. The building chamber is filled with nitrogen to prevent oxidation of the parts. The layer thickness is set to 30 μm .

The powder used consists of spherical particles and has the composition of the AISI 18 Maraging 300 steel. The measured density of SLM parts is 8010 kg/m^3 . Mechanical properties are as follow: tensile strength 1152 MPa, Yield strength 985 MPa, Young modulus 166 GPa.

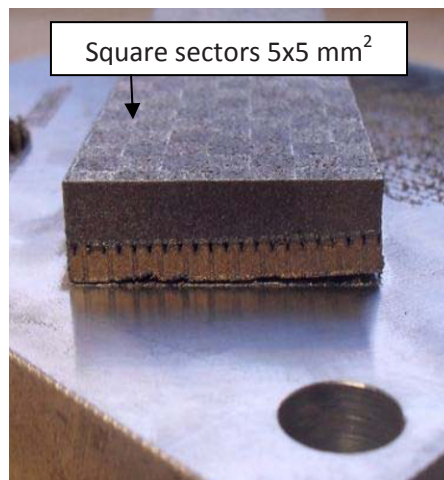
The laser sintering strategy used in the preparation of specimen is random, in order to distribute the fused zones over the whole surface of the component without localizing in some limited region high thermal gradients which may cause warping and generate residual stresses. Each layer is divided in small square sectors of $5 \times 5 \text{ mm}^2$ [6].

In order to reduce deformations that may lead to failures in the building process, specimens are manufactured onto a 15 mm thick substrate (building plate). Besides, parts are built using supports of 4 mm height in order to facilitate removal from the building platform. It has been observed that supports with a spare dimension of 2 mm cause the disengagement of the specimen from the building plate due to high thermal stress (Fig. 1). A spare dimension of 1 mm is recommended in order to avoid distortions of SLM parts.

Specimen geometry is reported in figure 2. The rectangular specimen is oblique on the building plates in order to facilitate the powder deposition by means of a knife. Positions 1, 2 and 3 indicate the locations of residual stress measurements. These locations are chosen in order to have a correspondence between disks studied in [7] and rectangular specimens made with identical material and process parameters. This should point out the influence of geometry on residual stresses generated by SLM.



a)



b)

Figure 1 – Distortion on SLM rectangular specimen

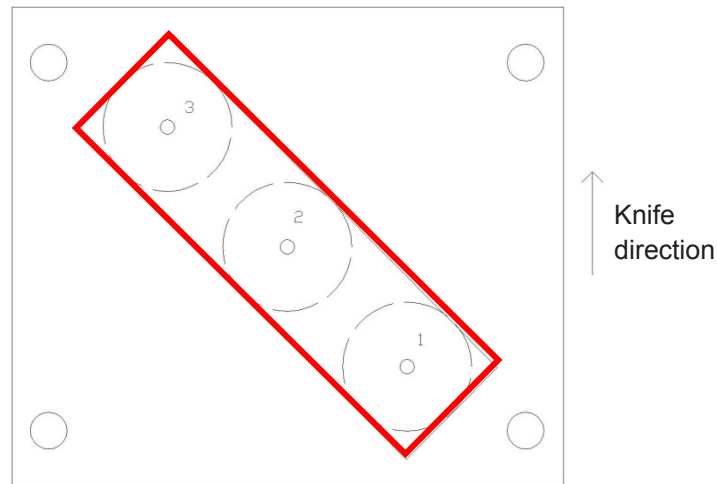


Figure 2 – Geometry of SLM rectangular specimens (127 mm x 35 mm) with holes location (1,2,3) and disks position (diameter 35 mm)

METHODOLOGY AND EXPERIMENTAL PLAN

The hole drilling method is utilized for the residual stresses measurements. It consists in drilling a very small hole into the specimen; consequently, residual stresses relax in the hole and stresses in the surrounding region change causing strains also to change; a strain gage rosette, specifically designed and standardized [8], measures these strains. Residual stresses can be calculated as suggested in [8]. The most recent version of ASTM standard contemplate a methodology for the very frequent case of non uniform stress field within the specimen thickness. *Power series* and *Integral method* [9-12] have also been considered in computing the experimental data.

The accuracy of residual stresses calculations from the measured strain values obviously depends also on the level of accuracy at which elastic modulus and Poisson's ratio are known. For this reason, E and ν values used in this work have been obtained from tensile tests on the same material.

Distribution and magnitude of residual stresses generated in SLM components depend on a number of factors. In order to reduce some of these factors, the dimensions of the building plate are much larger than the dimensions of the manufactured component which is rectangular. In addition, the scanning laser strategy has been optimized by trying to have scan vectors always oriented along the normal to the part's elongation. These facts should allow to maximize the adhesion between layers thus ensuring a nearly full density which limits the magnitude of residual stresses [13].

Specimens of circular geometry (disks of 35 mm diameter) studied in [7] exhibited very small warping effect which are instead very pronounced in specimens where one dimension predominates over the others (Fig. 1). The aim of the present work is to investigate on the influence of geometry (that is rectangular, with one dimension much larger than others, or circular) on residual stress values measured in the same location. As it can be observed in Fig. 2, the SLM rectangular specimens have been built so that SLM disks are comprised into its edge.

Three SLM rectangular specimens have been studied. In all cases residual stresses measurements have been executed by HDM at location 1, 2 and 3. Fig. 3 shows the drilling device utilized. Strain values have been measured with System 5000 by Micro Measurements.



Figure 3. Measuring device for HDM
(RS 200 Milling Guide by Micro Measurement)

EXPERIMENTAL RESULTS

Released strains have been measured and strain versus hole depth have been obtained for each measurements.

Figure 4 shows residual stresses values computed according to ASTM method (case of non uniform stress field), *Power series method* and *Integral method*. It can be observed the high variability of the ASTM results with respect to the others.

As with any other mathematical calculation, the quality of the calculated residual stresses depends directly on the quality of the input data. In this case, even if it should be observed that strain measurements are very sensitive to the effects of small experimental errors, the same data have been utilized for the 3 different computing procedures but results disagree: each of the 3 method utilize different approaches for stabilizing and smoothing the non uniform residual stress field. Since the strain variations during drill depends on many factors hardly predictable and checkable *a priori*, it seems that the best calculation method should be evaluated for each particular experiment. In the present work, the Power series method seems to be the most suitable for residual stresses calculations.

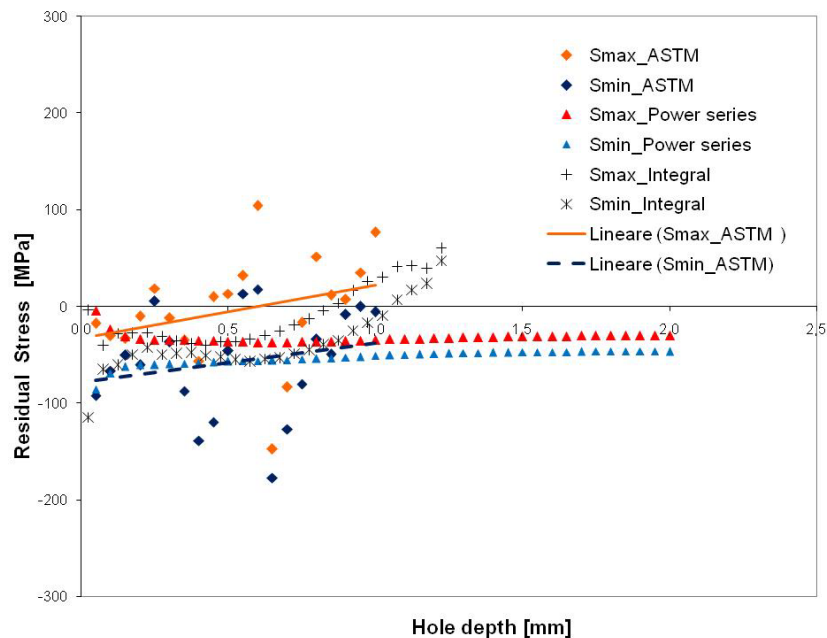


Figure 4 – Residual stresses values (specimen 2 – location 1)

Figures 5-7 show the trend of the calculated residual stresses in terms of Von Mises equivalent stress plotted versus the perforation depth. Measurements have been executed on 3 rectangular plates of the same geometry and manufacturing process.

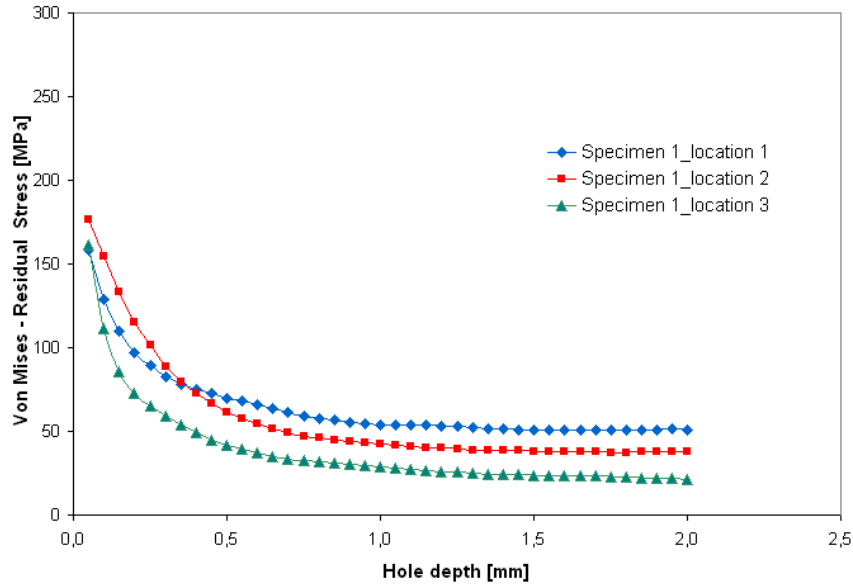


Figure 5 – Residual stress values on rectangular plate 1

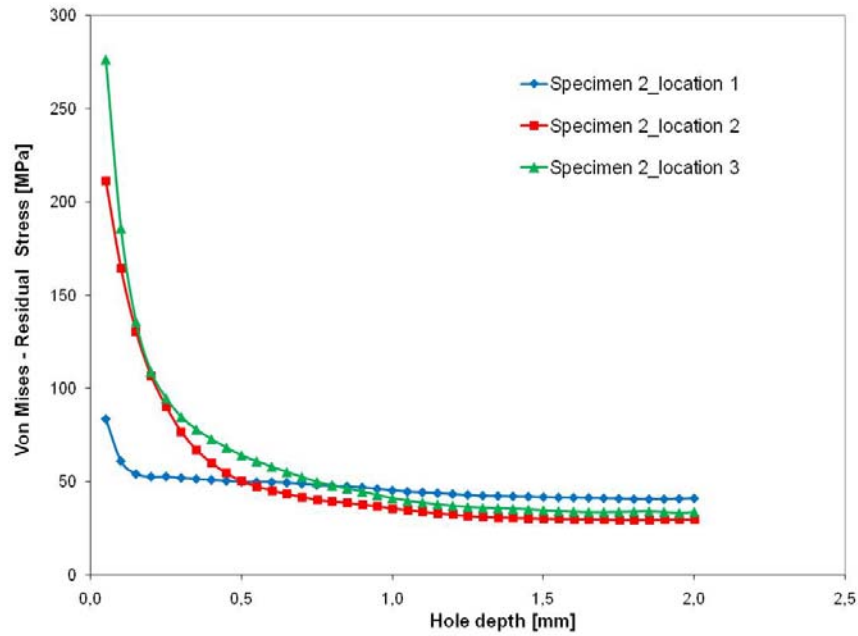


Figure 6 – Residual stress values on rectangular plate 2

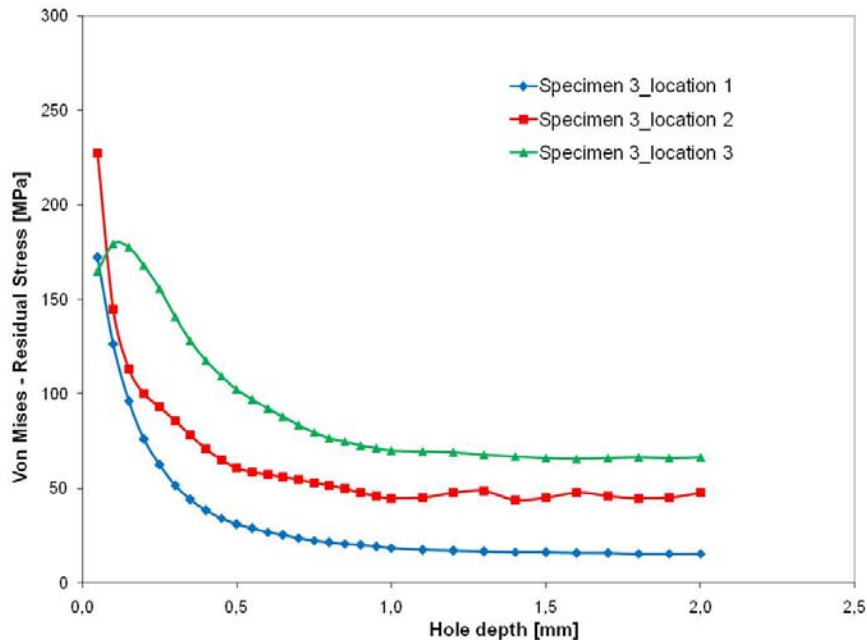


Figure 7 – Residual stress values on rectangular plate 3

Residual stresses are variable inside the tested components. For all considered specimens and regardless of the hole location on the rectangular shape, residual stress value decrease sharply as we move far from free surface.

In all cases, that is for each location, residual stress near the free surface are tensile and rather high (>100 MPa). Anyway, stress magnitude is lower than material yield point ($\sigma_y=990$ MPa). Residual stress values at a depth hole ranging from 0.1 mm (i.e., in the vicinity of the zones heated by the laser beam in the last stage of the SLM process) to 1÷1.5 mm are considered to be representative.

Results obtained at 1 mm hole depth, beyond which residual stress values do not change significantly, indicate that residual stresses are fairly small. This behavior probably occurs because the very large number of laser passes required to complete 7 mm thick parts may be considered to be equivalent to a sort of thermal treatment which relaxes internal stresses. This behavior seems to occur in the same way, both for rectangular plates and for disks: [figure 8](#) summarizes residual stresses on SLM disks [7]. It seems that in any case, both for rectangular specimens and disks, there is a strong reduction of residual stress through the thickness (about 1 mm depth) with respect to the surface. Moreover, residual stresses on location 2 are lower than in other locations.

[Table 1](#) summarizes Von Mises - residual stress values measured on rectangular plates. Let us consider the effect of residual stress location on the building plate: the comparison between values of residual stresses measured for specimens located the same on the build plate indicated that residual stresses corresponding to position 2 seems to be lower than other cases. It could be explained remembering that location 2 is in the centre of the building plate, where the scanning strategy makes it possible to line up the laser always orthogonally to the layer surface; location 1 and 3 have slope with respect to laser beam, so the density of energy in different location could be not uniformly distributed.

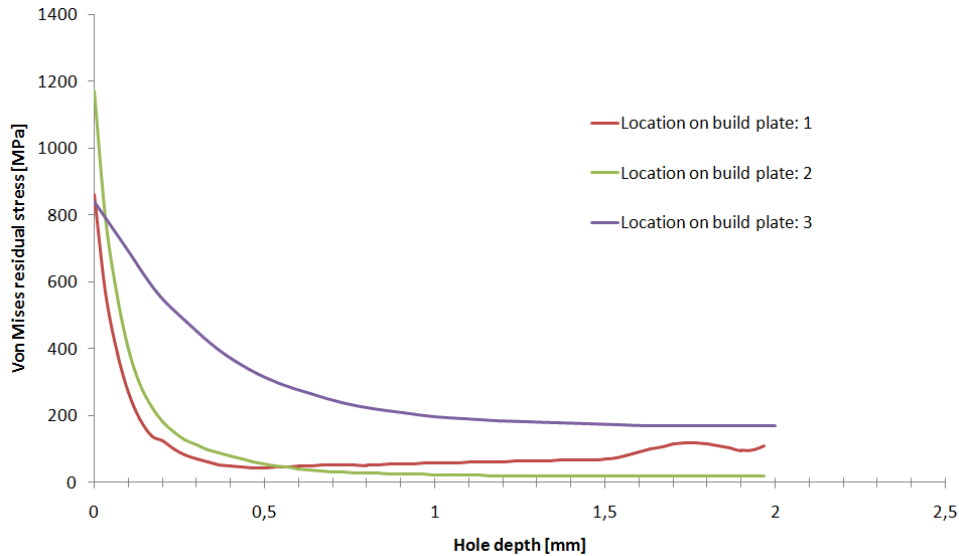


Figure 8 – Residual stress values on disks [7]

Rectangular plate	Position			Position		
	Hole depth 1,5 [mm]			Hole depth 0,1 [mm]		
	1	2	3	1	2	3
3	16	30	66	126	145	179
2	42	30	35	61	164	186
1	51	38	24	129	154	111
Mean	36	33	42	105	155	159
St Dev	18	5	22	38	10	41

Table 1 – Von Mises residual stress on rectangular plates

CONCLUSIONS

Selective laser melting (SLM) is a technological process which utilizes a laser beam to generate the energy for melting the powder and building parts of complicated geometry. However, this procedure may have some inherent drawbacks such as warping, cracking and residual stresses. The last melted layer generally shrinks during cooling while the layer underneath, already solidified constrains it and prevents further shrinking. Since this mechanism occurs for each layer at each step of the SLM process, residual stresses may develop inside the manufactured component. The whole phenomenon is very complicated and depends also on thermo-physical properties of the material (thermal expansion coefficient, thermal conductivity, density, etc).

This paper studied the magnitude of residual stresses developed in SLM-fabricated components of rectangular shape. Residual stresses were measured by means of the hole drilling method in three different locations on building plate (1, 2 and 3) and then compared with residual stresses measured on circular specimens in the same locations on building plate.

Experimental results were preliminary processed with ASTM, Power series and Integral method and then Power series method was chosen because of its ability in stabilizing non uniform stress field. Results of experimental tests provided the following indications: (i) residual stresses near free surface (i.e., at 0.1 mm hole depth) are tensile and higher than their counterpart measured at 1.5 mm. Stress magnitude decreased moving towards inner layers. This effect was more observed both for disks [7] and for rectangular specimens. (ii) Residual stress values became practically constant at 1.0 mm hole depth. (iii) The influence

of positioning on residual stresses: the position of the component on the build plate affects magnitude of residual stress, in fact the central position (i.e., Pos. "2") corresponds to the lowest stress values.

REFERENCES

- [1] Nickel A.H., Barnett D.M., Prinz F.B., Thermal stress and deposition patterns in layered manufacturing, *Mat. Science and Engineering A317*, 2001, pp. 59-64.
- [2] Shiomi M., Osakada K., Nakamura K., Yamashita T., Abe F., Residual Stress within Metallic Model Made by Selective Laser Melting Process, *CIRP Annals - Manufacturing Technology*, 2004, 53 (1), pp. 195-198.
- [3] Jacobs P., Rapid Prototyping and Manufacturing / Fundamental of Stereolithography, *Society of Manufacturing Engineers*, 1992, Dearbon (MI).
- [4] McIntosh J., Danforth S., Jamalabad V., *Proc. of Solid Freeform Fabrication Sym.*, University of Texas, Austin, 1997, pp. 159-166.
- [5] Klingbeil N., Beuth J., Chin R., Amon C., *Proc. of Solid Freeform Fabrication Sym.*, University of Texas, Austin, 1998, pp. 367-374.
- [6] Mercelis P., Kruth J.P., Residual stresses in selective laser sintering and selective laser melting, *Rapid Prototype J*, 2006, vol. 12, pp. 254-265.
- [7] C. Casavola, S.L. Campanelli, C. Pappalettere – Preliminary investigation on the residual strain distribution due to the Selective Laser Melting Process, *J of Strain Analysis* (Professional Engineering Publishing, London, UK), vol.44 (1), 93-104, 2009.
- [8] ASTM E 837 Standard method for determining residual stresses by the hole-drilling strain gage method, *Annual Book of ASTM Standards*, 2008.
- [9] Vishay Micro Measurements, Measurement of residual stresses by the hole drilling strain gage method, *Tech Note TN-503-6*.
- [10] Schajer G.S., Measurement of non-uniform residual stresses using the hole drilling method. Part I – Stress calculation procedures, *J of Engineering Materials and Technology*, 1988, vol. 110, pp. 344-349.
- [11] Schajer G.S., Measurement of non-uniform residual stresses using the hole drilling method. Part II - Practical Application of the integral method, *J of Engineering Materials and Technology*, 1988, vol. 110, pp. 344-349.
- [12] Ajovalasit, Rassegna del metodo del foro per tensioni costanti - Studi per una proposta di raccomandazione sull'Analisi Sperimentale delle Tensioni Residue con il Metodo del Foro, *Quaderno AIAS n. 3*, 1997, pp. 3-11 (in Italian).
- [13] Over, C., Meiners, W., Wissenbach, K., Lindemann, M., Hutfless, J., Laser Melting: A New Approach for the Direct Manufacturing of Metal Parts and Tools, *Proc. Euro-uRapid 2002 International User's Conf.*, A-5, 2002.

Practical Experiences in Hole Drilling Measurements of Residual Stresses

Philip S. Whitehead, Stresscraft Ltd, St Winefride's Chapel, Pick Street, Shepshed,
Leics., LE12 9BB, UK. stresscraft@btinternet.com

ABSTRACT

Strain gauge hole drilling is one of the most widely used destructive methods for measuring residual stresses. This paper describes hole drilling from 1987 to the present day at Stresscraft. Early procedures consisted of simple installations at readily accessible sites. In subsequent years, demands increased for hole drilling on more diverse component shapes and materials. Critical details of the methodology required for credible and reliable measurements are identified and discussed. These include strain measurements, the hole forming process and strain-to-stress calculation procedures. Developments were made to improve the reproducibility and reliability of the method and accessibility at difficult target sites. Significant developments have included implementation of the Integral Method in 1989 (after G. S. Schajer) and the introduction of PC-controlled miniature 3-axis drilling machines for orbital drilling in 1999. Two machines have been used over a 10-year period to drill approximately 15,000 gauges. While the fundamental elements of the method remain unchanged, in extreme cases, gauges can now be installed and drilled at sites that can only be viewed using miniature cameras. A number of examples of installations and results are presented and discussed to demonstrate the development of the method.

Introduction

Hole drilling is a popular method used for the determination of residual stresses in engineering components and structures. In this method, a 'target' strain gauge rosette is bonded to the test-surface. A hole is drilled into the test-surface relieving stresses at the hole boundary. Changes in strain output resulting from the drilling process are recorded; residual stresses are then calculated from the recorded strains using suitable coefficients. The equipment required for hole drilling is relatively simple; an operator working alone can complete a number of measurements in a day. Because of this simplicity and speed, hole drilling is an inexpensive method and, despite its destructive nature, this has led to its popularity. In many early instances of hole drilling, single sets of relaxed strains were measured at the end of the drilling process which were processed to generate residual stress values which refer to a single depth. In 1956, Kelsey [1] investigated the stresses which vary with depth using the hole drilling method; Rendler and Vigness [2] developed the method further on which later work was based.

During the early 1980s, Stresscraft Ltd was involved exclusively in the production and analysis of photoelastic models. In 1987, requests were received to tender for a number of hole drilling projects linked to photoelastic model work. A survey of current practices was carried out. These included a standard for the hole drilling method established by ASTM [3] and the Measurements Group Technical Note [4] which described the use of target strain gauges, a hole drilling machine and a stress calculation procedure. It was decided that it would be feasible to perform measurements of this type and that hole drilling would be a useful addition to the services we provided.

1987 – Type-1 Drilling Machine and Equivalent Uniform Stresses

It was observed that the requirements for hole drilling could be divided into three main activities, namely relaxed strain measurement, hole drilling and calculation of residual stresses from the relaxed strains. While strain gauge training was in progress, the company manufactured its own drilling machine so that the required features could be included. The machine is shown in Fig. 1 and includes :

- a combination of fixed and spring loaded rolling ball bearings in the drill guide for low friction linear motion without backlash or wear issues,
- an optical head for insertion into the drill guide for alignment and diameter measurement,
- a drill head (with micrometer feed attachment) for insertion into the drill guide for the drilling process.
- two methods of drill rotation – from a remote electric motor via a flexible drive cable drive (ca. 15,000 rpm) or from a dental air-turbine (ca. 250,000 rpm).



Fig. 1 Type-1 Drilling Machine

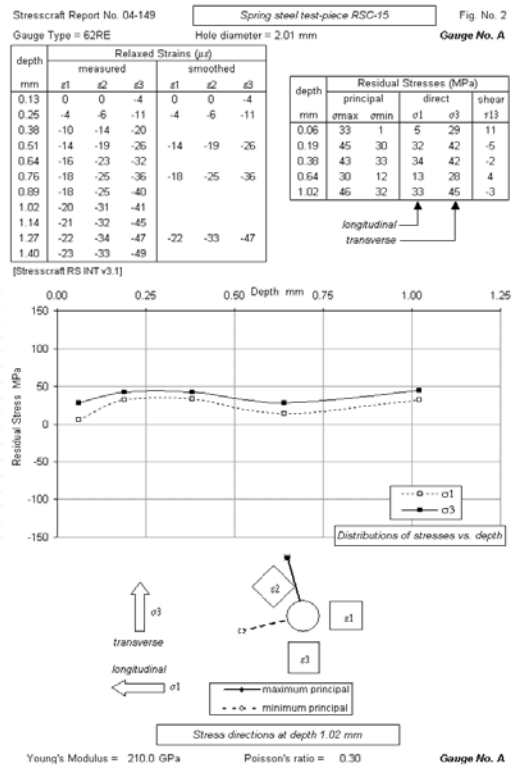


Fig. 2 Results Data Sheet

A BASIC language program was written for the calculation of residual stresses from relaxed strains. This was to be performed using the method described in the Technical Note [4] as required by customers. It was decided that results from each gauge would be presented on a single sheet for incorporation into the report to the customer. The sheet provides tables of depths, relaxed strains and calculated residual stresses, graphical distributions of stresses vs. depth, and a diagram of the gauge indicating the installation directions and principal stress directions. A typical results sheet is shown in Fig. 2; this type of layout remains little changed to this day. The program also provided for the recording and archiving of strain data in electronic format.

When hole drilling work was started it was understood that there was a need for close attention to all details of gauge installation, hole drilling and strain measurements. However, the importance of the choice of method used to calculate residual stresses from relaxed strains was not fully appreciated. Subsequently, stress calculation methods became the subject of much investigation within the company. One example of this work was based on a series of 6 mm thick alloy steel plate test-pieces pre-loaded to create a longitudinal tensile stress. Subsequently, parts of the plate surfaces were masked while other parts were shot-peened. Target gauges (type EA-06-031RE-120) were installed on the plates and drilled. Clear guidelines for the detection of stresses which vary with depth and the limitations of uniform stress calculations are given in ASTM E 837 [3]. The Technical Note [4] recommends that the equivalent uniform stress (EUS) is plotted against depth so that trends in distributions can be observed. The EUS is the stress which, if uniformly distributed from the surface to the bottom of the hole would produce the equivalent

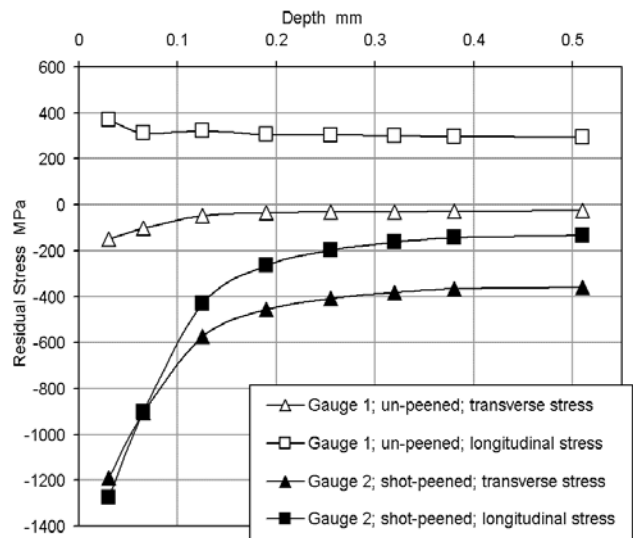


Fig. 3 Distributions of stresses in a steel plate (EUS)

strain at the surface. Results of the EUS calculation are shown in the distributions of stresses vs. depth in Fig. 3. Features of the stress distributions in Fig. 3 include :

- Residual stresses at gauge 1 (un-peened) are distributed in a generally uniform manner; tensile longitudinal stresses of ca. 300 MPa are calculated for the depth range 0.1 mm to 0.5 mm; transverse stresses are small.
- Intense near-surface compression was detected at the peened surface. However, at the final depth, residual stresses at gauge 2 are significantly smaller than at gauge 1; no tensile stresses were calculated for gauge 2. The apparent penetration of the shot-peening process is excessive; there is no trend for sub-surface stresses to revert to the un-peened state. This clearly demonstrates the severe limitation of the calculation method when applied to non-uniform stresses. In practice, it was not always possible to reconcile the concept of EUS with customers' requirements for results which could be confidently related to real levels of residual stresses.

At this stage in the development of hole drilling at Stresscraft, target gauges could be installed to a satisfactory standard and strain measuring equipment used to obtain reliable relaxed strain measurements. However, there was need for improvement in the hole driller design and, more importantly, the stress calculation method.

1989 – Type-2 Drilling Machine and Integral Method

A second drilling machine was manufactured. This machine was developed from the Type-1 driller but reduced in size for operation in confined situations. The guide (with rolling bearings) was configured so that the drill head could be removed sideways for operation within disc bores of $\phi 200$ mm. An electrical contact system was incorporated to aid drill / target datum depth detection, but this was not popular with drill operators who preferred to view the drilling cutter and gauge through a x10 magnification eyepiece. The drill collet was extended for operation as close as possible to step and shoulder features. A type-2 machine is shown in Fig. 4. With this machine the setting up time for hole drilling was reduced and the scope for hole drilling at positions which could not be accessed previously was significantly extended.



Fig. 4 Type-2 Drilling Machine

The limitations of the existing stress calculation method remained. A search was undertaken to find an alternative strain-to-stress calculation scheme. This revealed the papers by Schajer [5] in which the EUS Method, the Power Series Method, and the Integral Method were compared. Schajer describes in detail how stresses in any depth increment are relaxed as that increment is drilled and how further relaxation occurs during drilling of subsequent increments because of the change in compliance of the structure. The Integral Method appeared to have the properties required for the evaluation of residual stresses with the severe gradients encountered in the shot-peened example given above. It was decided to produce and test a BASIC program version of the Integral Method incorporating the coefficients provided. This program was first used to calculate residual stresses in the previously described steel plates. Fig. 5 shows the distributions of residual stresses calculated using strains from the

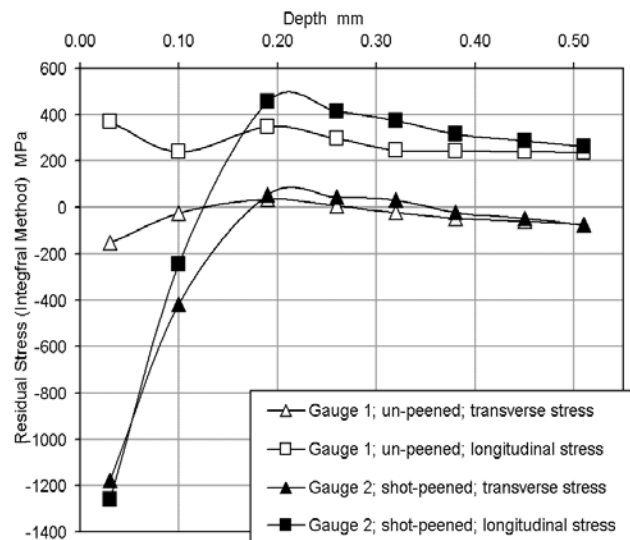


Fig. 5 Distributions of stresses in a steel plate (Integral Method)

same data set used for EUS results in Fig. 3, but on this occasion using the Integral Method. The gauge 2 results in Fig. 5 show the same intensity of near-surface shot-peening stresses as determined using the EUS method (Fig. 3). In the case of the Integral Method results, however, the rates of decay from the surface are more severe; a sub-surface tensile peak in excess of 400 MPa (greater than the un-peened stress) occurs at depth 0.2 mm. Values of sub-surface stresses from both gauges at depth 0.5 mm are very similar. This was seen to be a very encouraging result.

Prior to introduction of the Integral Method, it was decided to develop a better understanding of the behaviour of the relaxation of stresses caused by hole drilling. Models were created and processed (using Algor finite element software) to reproduce the Integral Method coefficients [5]. Coefficients were obtained by mapping displacements over the active gauge area. The level of agreement between coefficients from Stresscraft models and those from Schajer [5] was found to be good. In addition, hole drilling measurements were made on cantilever beams gauged and drilled in un-loaded and loaded conditions. Results from these tests confirmed the ability of the Integral Method to detect stress gradients, albeit at a reduced gradient from the shot-peening case. Following introduction of the Integral Method program (1989), it became apparent that the residual stresses calculated in this way were more sensitive to any deficiencies in the experimental procedure. A programme of testing was undertaken to enhance the quality of the relaxed strain data which would, in turn, reduce the levels of uncertainties in calculated stress values. This work included testing of :

- more rigorous gauge installation procedures: it was determined that swab etching target sites to a matt finish provided the most reliable installations,
- gauge adhesives: high-temperature cyano-acrylate types were found to be more reliable,
- gauge types: the use of flexible 'open' construction gauges produced thinner adhesive layers (and more reliable strain transfer) than encapsulated gauges for installations other than on completely flat surfaces,
- sourcing of inverted cone drilling cutters with 'sharp' corners (no chamfer) so that hole profiles were identical to those of FE models;
- 100% inspection and measurement of all drilling cutters for form, chips, size, etc.

Many details resulting from work of this type were incorporated into the NPL Good Practice Guide [6].

At this stage in hole drilling development at Stresscraft, it had been demonstrated that the use of the Integral Method for stress calculations had produced a significant advance in the credibility of residual stress results. In addition, the requirement for meticulous attention to detail in all procedures was made clear. During the period 1989 to 1998, four Type-2 drilling machines were constructed. Residual stress measurements were carried out for more than 30 customers on aerospace components, diesel engines, pressure vessels, racing engines, forgings and a wide variety of test-pieces and material samples. At Stresscraft, two machines and operators were used to drill, typically, 1000 to 1200 gauges per year.

1999 – 3-Axis Drilling Machine

For drilling tougher materials, it had sometimes been the practice to use a rotating eccentric ring between two elements in the drilling machines to provide an orbital motion during drilling. This addition was found to be very satisfactory in decreasing rates of drill wear and damage. It was also noted that the use of such a motion reduced the forces involved in the drilling process, the magnitudes of thermally induced strains and the length of the settling period between drilling and strain recording. In order to improve the performance of hole drilling, it was decided to build a new type of machine to achieve this type of motion. A machine design was evolved

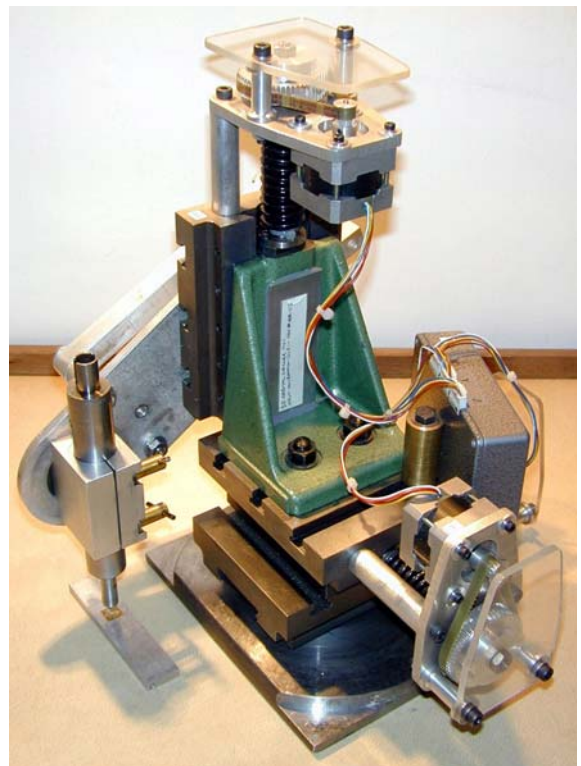


Fig. 6 3-axis hole drilling machine

which was built from 3 miniature dovetail slides. Motion for each slide was provided by a 1 mm pitch recirculating ball-screw driven by 200-step/rev stepper motor via a toothed belt. The machine is shown in Fig. 6. The drill head holder is fixed to a tee-slotted plate; this gives a more versatile arrangement for holding the tool than previous drillers. Step signals for the motors were provided by an input/output (I/O) card in a PC via power supply units. A program was written in MS Visual Basic to create a control panel linking mouse clicks to I/O card outputs. The stepper motor/ ball-screw drives were set to achieve a resolution of 1 μm per motor step.

A screen control panel is shown in Fig. 7; 'z' refers to the default drilling direction (vertically downward) and 'x' and 'y' to directions normal to the drill axis (in the horizontal plane). The LHS of the panel covers the selection of gauge size, orbit eccentricity, depth increment pattern and feed rate and provides a list of increment depths. The upper part of the panel centre shows the selected drill vector, the position of the drill head and controls for the movement of x, y and z directions. Beneath this section lie controls for movement along and normal to the selected drilling vector along with drill motor, orbit and increment drilling controls. A 'Cycle' control provides for datum depth detection; after the drill cutter has been set ca. 1000 μm above the gauge upper surface, a single mouse click advances the drill head by 1002 μm , completes a single orbit and then retracts by 1000 μm . By advancing 2 μm and retracting in this way, the operator can view the progress of the cutter through the gauge and adhesive layer and see the first contact with the target surface. The RHS of the panel provides for control of a P3 strain indicator; measured strains are recorded and tabulated for each depth increment. After setting up the drilling parameters and strain indicator, the 'Drill and Record' command allows the operator to drill through an entire increment pattern and record each set of strains on a single button click; after the final increment, strain values are written to an MS-Excel file for processing.

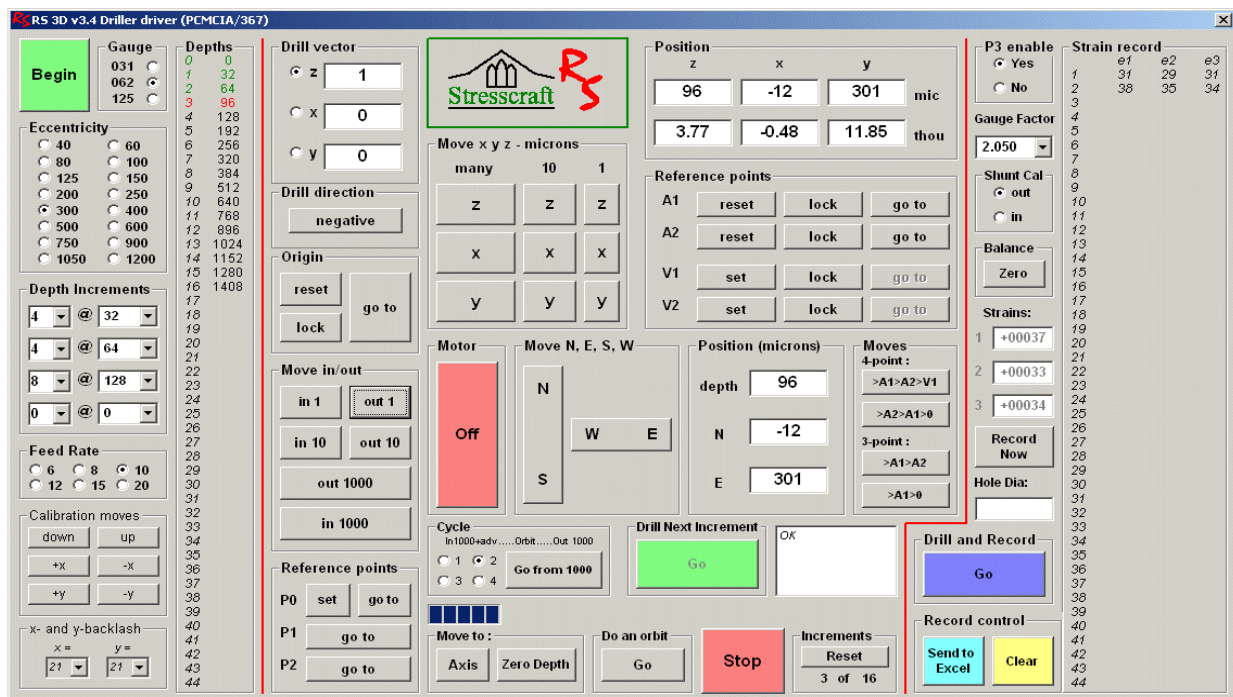


Fig. 7 PC control panel for the 3-axis hole drilling machine

It was clear from the first trials that results obtained using the 3-axis driller were very good and levels of consistency not previously seen were achieved because of the inherent characteristics of the machine :

- drilling cutter wear was significantly reduced; cutting edge chipping and damage were eliminated,
- settling times (from drill switch-off to strain recording) were reduced indicating a reduction in heat generated during the drilling process; forces generated during drilling were also found to be significantly reduced,
- control of the drill feed and orbit eccentricity size gives the operator a high degree of control over the process which can be suited to specific materials and installations. Settings can be recorded and all holes in a series of gauges can be drilled using the same parameters.

A second, identical 3-axis driller was completed to increase gauge throughput and allow further development work to be carried out. During driller calibration, it was determined that the accuracy of depths achieved was an order

of magnitude better than for conventional drillers. To exploit this, some test gauges were drilled in which the near-surface increments were divided into a number of sub-increments to extract more stress distribution detail from near-surface relaxed strains. Because of difficulties in interpolating Integral Method coefficients within the triangular matrix close to the zero depth point, the number of sets of increments at which coefficients were calculated for each hole diameter was increased to 11 (66 finite element models). This provided coefficients without the need for depthwise interpolation. Drill depth increment patterns were adopted which used 16 μm near-surface increments for 031-size gauges and 32 μm near-surface increments for 062-size gauges. Results from gauges drilled using finer increments are shown in Figs. 8 and 9

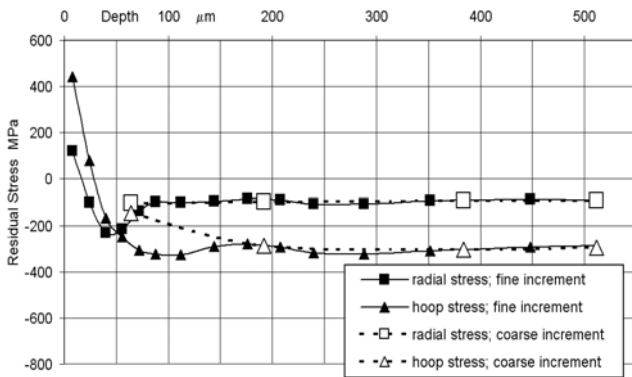


Fig. 8 Residual stresses in a nickel alloy disc; machined surface

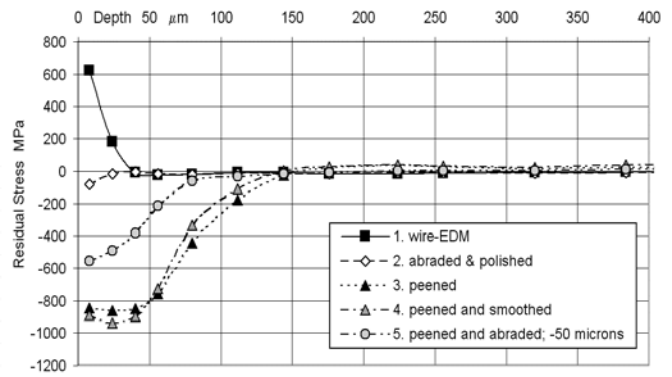


Fig. 9 Residual stresses in titanium alloy test-pieces

Fig. 8 shows an example of residual stresses obtained from hole drilling in a machined nickel alloy disc. The two sets of data show stresses obtained using both ‘coarse’ (64 μm) and ‘fine’ (16 μm) calculation increments. Stress distributions calculated using fine increment show near-surface tensile stresses and stress gradients which are not revealed by the coarser increment set. Fig. 9 gives a summary of residual stresses at 031-size gauges applied to a series of titanium alloy test-pieces and drilled using 16 μm near-surface increments. The conditions of the material surface for the five gauges are :

1. Wire-EDM cut surface
2. EDM surface; recast layer removed using a fine abrasive
3. Shot-peened
4. Shot peened (as 3) followed by smoothing using a fine abrasive to remove peening indentations
5. Shot-peened and smoothed (as 4) followed by further fine abrasion to remove ca. 50 μm .

The two following examples describe hole drilling measurements carried out on aerospace components.

Example 1; High-strength nickel alloy disc forging

This example is concerned with the determination of residual stresses in an aircraft engine disc forging following quenching, heat-treatment and ‘rough’ machining into the condition of supply (COS) shape. Such measurements are made to fulfil part of the aviation authorities requirements for engine certification. A section through a typical high pressure compressor disc forging for a Rolls-Royce Trent engine is shown in Fig. 10. Target strain gauges are to be installed and drilled at four positions on the disc; A and D at the hub flanks and B and C at the rim flanks, with four gauges equi-spaced around the circumference at each position (0°, 90°, 180° and 270°). Hole drilling results will determine the magnitudes of circumferential and radial stresses at each target site.

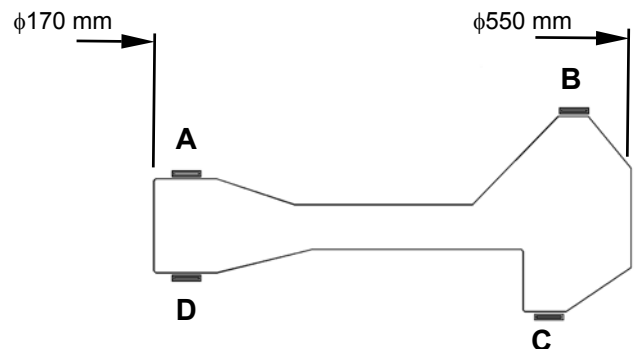


Fig. 10 Section through a compressor disc

Near-surface stresses are heavily influenced by the machining process and are not directly related to the state of stress within the disc structure. It is a requirement that the measurements demonstrate that the sub-surface stresses reported are not affected by the machining process. The gauge type used was the Measurements Group CEA-06-062UL-120 as shown in Fig. 11. Each gauge was drilled using a 3-axis machine at $11 \times 128 \mu\text{m}$ increments to give a final hole depth of 1,4 mm. This depth of penetration leaves an adequate machining allowance for subsequent processing; in this instance, the hole drilling procedure is not destructive. Stress distributions from the sixteen gauges are shown in Fig. 12; the scale of stress is σ/σ_y (where σ_y is the material yield strength).

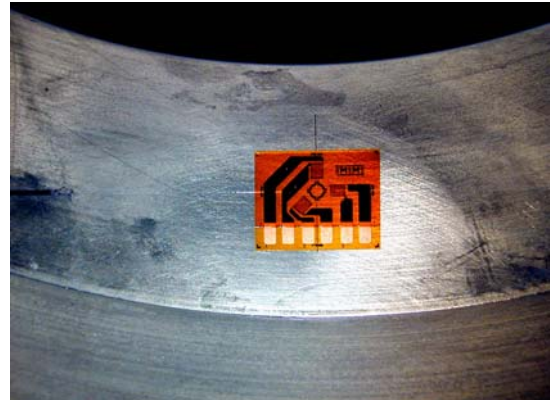


Fig. 11 Installation of a target gauge at the hub flank

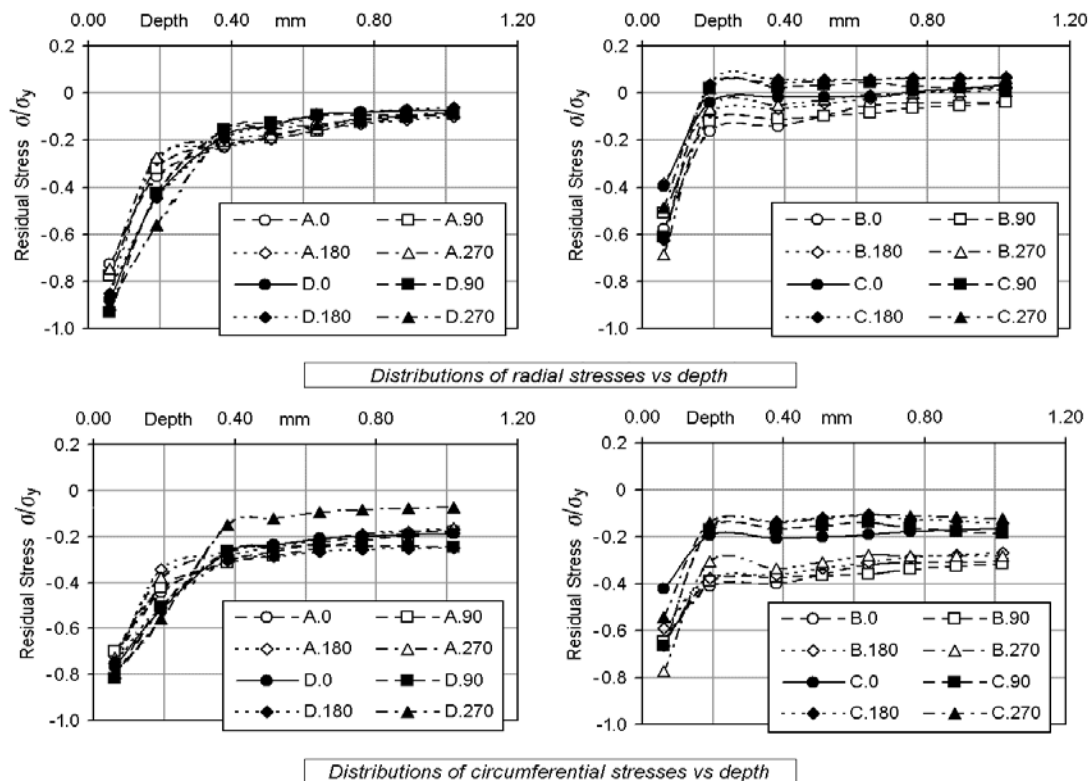


Fig. 12 Distributions of residual stresses in a nickel alloy disc forging

Residual stress results are examined for features including :

- The presence of compressive circumferential stresses at the hub flanks; as the disc is machined, there is a significant redistribution of stresses, but circumferential compression at the hub flanks is usually retained.
- The balance of stresses across the hub flanks. The top/bottom balance of the quenching process may give rise to a significant imbalance of front/rear stresses producing out-of-plane distortions during machining.
- The level of circumferential variation of stresses around the disc. Irregular temperature gradients during quenching or heat-treatment lead to circumferential variations in residual stresses and possible ovalisation distortions during machining.

Stress distributions in Fig. 12 confirm the maximum depth of machining-affected stresses as 0,4 mm; this depth differs at the four positions. Circumferential stresses at the hub flanks (A and D) are similar with the exception of those at gauge D.270 where the level of compression is less intense. In this case, the disc was subjected to a further assessment of hub flank stresses using additional target gauges near the 270° circumferential position.

Example 2; High-strength nickel alloy drum weld

Some measurement procedures require special attention because of considerations of the gauge installation, material machining, stress gradients and other features. The Rolls-Royce Trent HP compressor drum assembly (Fig. 13) presents an unusual set of challenges. The assembly is fabricated from two discs and a rear cone joined at two welds. The assembly material is a very tough high strength nickel superalloy and has been shot-peened in the measurement areas. In addition to conventional measurements at the disc hubs and diaphragms, etc, it was required to install and drill gauges in the region of the front and rear welds at the weld centre-lines and at positions displaced by - 1 mm and +1 mm from the centre-lines. Measurements were to be made at both the OD and ID at 3 equi-spaced circumferential locations. The wall thickness at the weld is ca. 6 mm.

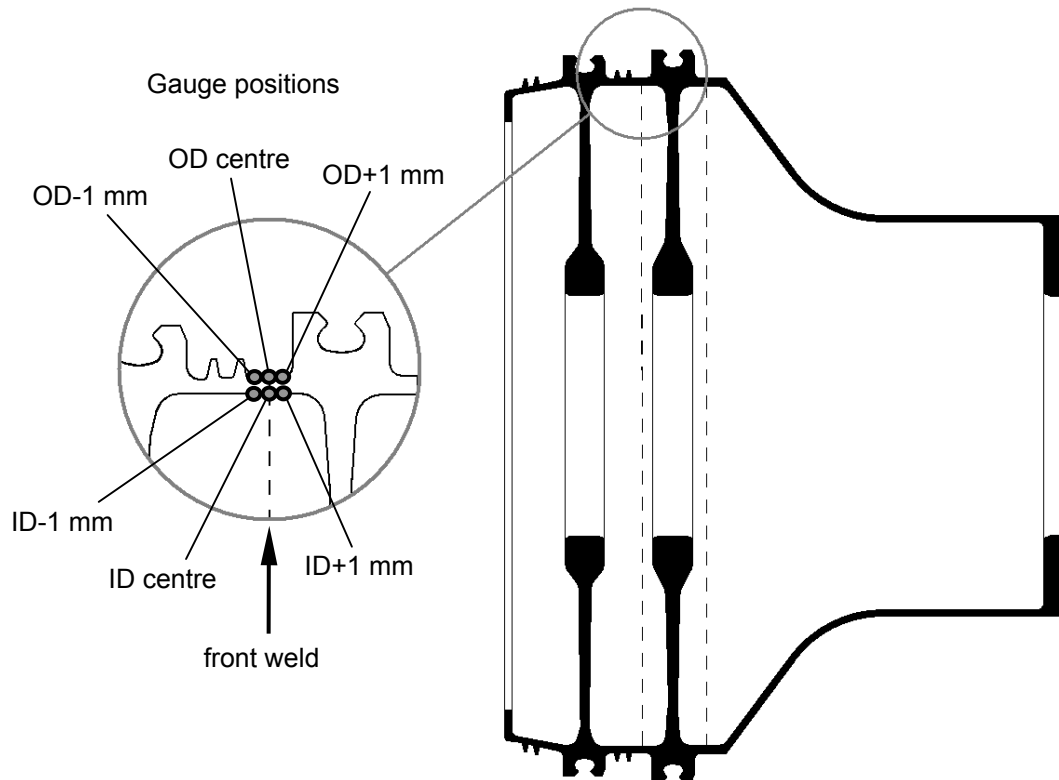


Fig. 13 Schematic view of HP compressor drum assembly and gauge positions

Outer diameter (OD) measurements were reasonably straightforward with easy access. Each target area was swab etched to reveal the weld centre-line; each gauge was installed with a circumferential offset to avoid any detectable interference from previously drilled holes (Fig. 14). The gauge type used was EA-06-031RE-120.



Fig. 14 Gauge and drilled holes at the OD



Fig. 15 Gauge and drilled holes at the ID

Gauges were drilled using near-surface drilling increments of $16\ \mu\text{m}$; sub-orbits used during machining (the feed rate) were set to $2\ \mu\text{m}$. The ID sites between the two discs are not visible directly; all etching, installation, soldering and drilling activities must be carried out while viewing using a miniature video camera and fibre light source. The radial distance between the hub bore and weld is ca. 160 mm while the axial distance between the adjacent hub flanks is 40 mm. An extended soldering iron and a number of other special tools were made to install the ID gauges. Fig. 15 shows a gauge installed at the ID and two previously drilled holes.

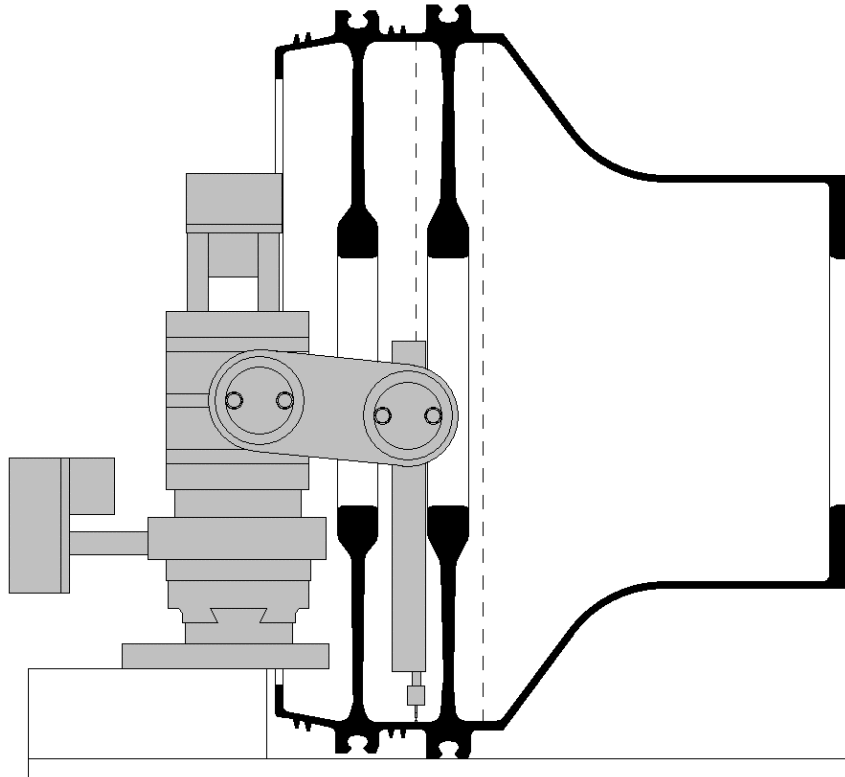


Fig. 16 Schematic view of the assembly and driller set up to drill at the front weld ID

The assembly and driller are shown in Fig. 16; the driller body (with eccentrically mounted air turbine) is assembled within the space between the two discs, inserted into the holder connected to the driller and then advanced towards the gauge and finally locked in position.

Final movements for the alignment of the drill and gauge are made using the driller x and y movement commands while viewing via the video camera.

Fig. 17 shows the driller at the front of the assembly during setting up.

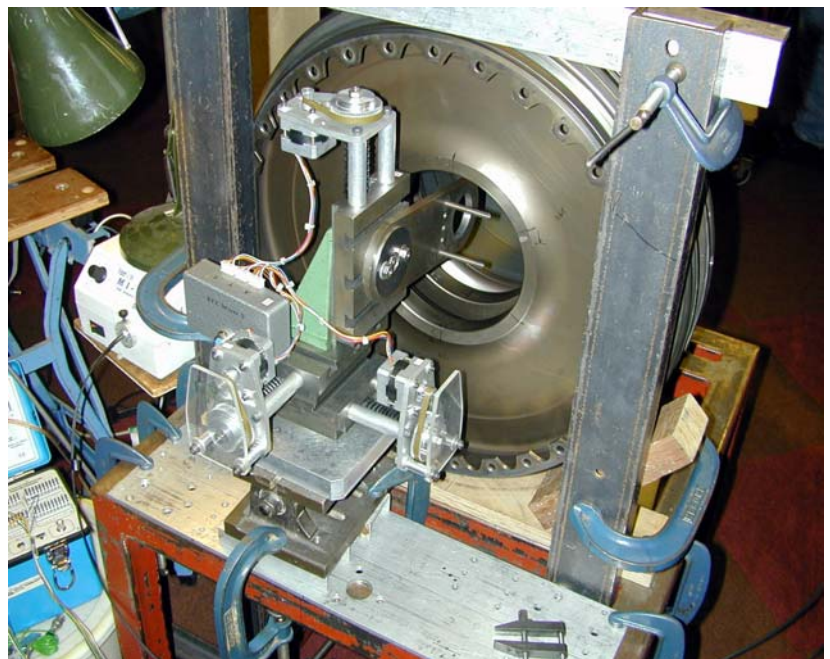


Fig. 17 Drilling machine at the front of the compressor assembly

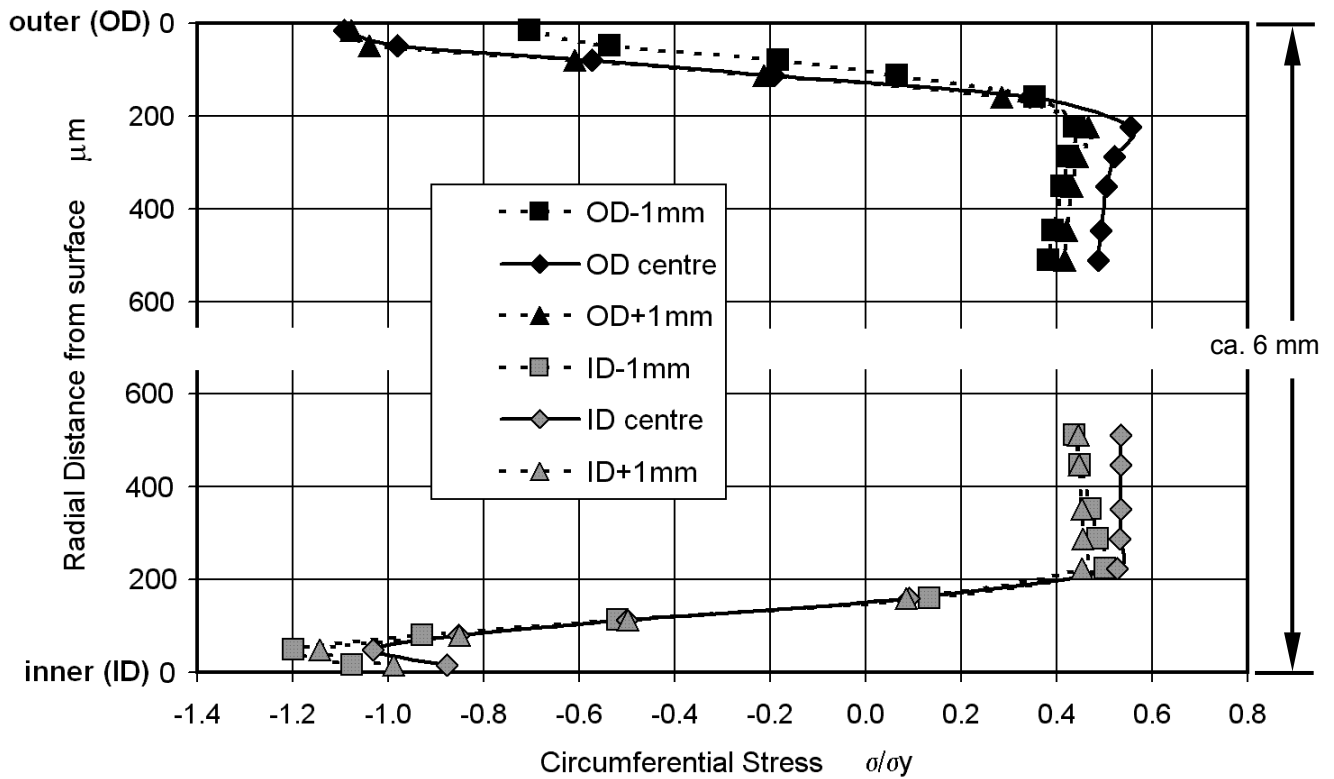


Fig. 18 Distributions of stresses at the weld OD and ID

Typical distributions of circumferential stresses from a group of gauges are given in Fig. 18; the scale of stress is σ/σ_y (where σ_y is the material yield strength). At each gauge, near-surface compression resulting from the shot-peening process is clearly shown; the peening process appears to be more intense at the ID than at the OD. Transitions from compression to tension occur between depths 100 μm and 200 μm . Tensile stress maxima occur immediately after the run-out of the peening effect (at depth ca. 200 μm). It has been demonstrated that sub-surface stresses at the weld centre are greater than at those at the -1 mm and +1 mm axial positions.

Conclusions

Over a period of 23 years, a number of developments have been applied to the hole drilling method which have added significantly to the value of the results produced. Throughout this time, the exemplary performance of commercially available target strain gauges and strain indicators has been a consistent feature. Early in this period, the introduction of the Integral Method transformed the way in which non-uniform stresses could be evaluated from relaxed strain data, while demanding a higher standard of gauge installation and hole drilling practice. It has been found that hole drilling to the required standard is best performed using an orbital drilling motion. At Stresscraft, this has been achieved using PC-controlled 3-axis drilling machines which can be configured to drill holes with a wide range of parameters and to enable gauges to be drilled in difficult locations.

Acknowledgements

The author wishes to thank the staff members at Stresscraft Ltd for their support and patient work in carrying out hole drilling measurements and manufacturing the drilling machines. Thanks are also due to Rolls-Royce plc for permission to publish the two examples included in this paper and to Gavin Baxter and Jim Orr for their assistance in the presentation of this material.

References

- [1] KELSEY, R.A., Measuring Non-uniform Residual Stresses by the Hole-drilling Method, Proc., SESA XIV (1), pp. 181-194, 1956
- [2] RENDLER, N.J. and VIGNESS, I., Hole drilling Strain-gauge Method of Measuring Residual Stresses, Exp. Mech., 6 (12), pp. 577-586, 1966
- [3] ASTM E 837-85 to -08e1, Determining Residual Stresses by the Hole drilling Strain-Gauge Method, 1985 to 2008
- [4] TECHNICAL NOTES TN-503-2 to -5, Measurement of Residual Stresses by the Hole drilling Strain Gauge Method, Vishay Measurements Group, 1986 to 1993
- [5] SCHAJER, G.S., Measurement of Non-Uniform Residual Stresses Using the Hole Drilling Method, J. Eng. Materials and Technology, 110 (4), Part I: pp.338-343, Part II: pp.3445-349, 1988
- [6] GRANT, P.V., LORD, J.D. and WHITEHEAD, P.S., The Measurement of Residual Stresses by the Incremental Hole Drilling Technique, NPL Good Practice Guide No. 53 Issue 2, February 2006

Destructive Methods for Measuring Residual Stresses: Techniques and Opportunities

Gary S. Schajer

Dept. Mechanical Engineering, Univ. British Columbia,
Vancouver, Canada V6T 1Z4
schajer@mech.ubc.ca

Abstract

Destructive methods are commonly used to evaluate residual stresses in a wide range of engineering components. While seemingly less attractive than non-destructive methods because of the specimen damage they cause, the non-destructive methods are very frequently the preferred choice because of their versatility and reliability. Many different methods and variations of methods have been developed to suit various specimen geometries and measurement objectives. Previously, only specimens with simple geometries could be handled, now the availability of sophisticated computational tools and of high-precision machining and measurement processes have greatly expanded the scope of the destructive methods for residual stress evaluation. This paper reviews several prominent destructive measurement methods, describes recent advances, and indicates some promising directions for future developments.

Introduction

Residual stresses greatly influence the service performance of practical engineering components, notably their strength, fatigue life and dimensional stability. Thus, it is important to know the size of these stresses and to account for them during the design process. The “locked-in” character of residual stresses makes them challenging to measure because there are no external loads that can be manipulated. Thus, residual stress measurement methods differ significantly from general stress measurement methods. Over the years, these methods have grown both in range and sophistication, and have collectively become a well-established specialty.

There are two general classes of residual stress measurement methods, destructive and non-destructive. The non-destructive methods [1] have the obvious advantage of specimen preservation, and are particularly useful for production quality control and for measurement of valuable specimens. However, they typically involve either very costly measurement equipment or they give empirically calibrated or comparative results. The destructive residual stress measurement methods generally have the opposite characteristics. While they either partially damage or fully destroy the specimen, they often require fairly simple equipment and generally give reliable and widely applicable results.

Many different destructive methods for measuring residual stresses have been developed for specific applications. They differ in specimen and material removal geometry, the measurement method and the required computations. However, they all share the same general principle, that is, they all determine the residual stresses from the deformations measured as some stressed material is cut or removed from the specimen. This approach mirrors the common method used for measuring stresses due to external loads, where the deformations are measured as the loads are applied or removed. The “load” associated with residual stresses is in the material itself, and is “removed” as the material is cut or removed. The challenge introduced by this process is that the stress is removed from one part of the specimen while the measurements are made in a different part. This feature significantly complicates the calculations required.

This paper gives an overview of the various destructive methods for measuring residual stress. The discussion focuses on the three main areas of development:

- specimen shapes and material removal geometry
- material cutting and deformation measurement technology
- stress calculation techniques

Substantial advances have been made in all three areas. It is the purpose here to describe the characteristics of the various techniques, give information on method selection, and to highlight recent developments and trends.

Specimen Shapes and Material Removal Geometry

The various destructive techniques for measuring residual stress have been developed on a mostly ad-hoc basis for particular applications and specimen shapes. Some of these methods have a wide range of application, and some are very specific. The more commonly used methods are described here.

Excision provides a simple quantitative method for measuring residual stresses. It involves attaching one or more strain gauges on the surface of the specimen, and then excising the fragment of material attached to the strain gauge(s). This process releases the residual stresses in the material, and leaves the material fragment stress-free. The strain gauge(s) measure the corresponding strains. Excision is typically used with thin plate specimens, where the cutting of a small material fragment around the strain gauge(s) is straightforward. Application on thicker specimens is also possible. Full excision is possible, but is not often done because the inconvenience of the undercutting process required to excavate the material fragment. Partial excision by cutting deep slots at each end of the strain gauge [2,3] is a more practical procedure.

Figure 1(a) illustrates the splitting method [4]. A deep cut is sawn into the specimen and the opening (or possibly the closing) of the adjacent material indicates the sign and the approximate size of the residual stresses present. This method is commonly used as a quick comparative test for quality control during material production. The “prong” test shown in Figure 1(b) is a variant method used for assessing stresses in dried lumber [5].

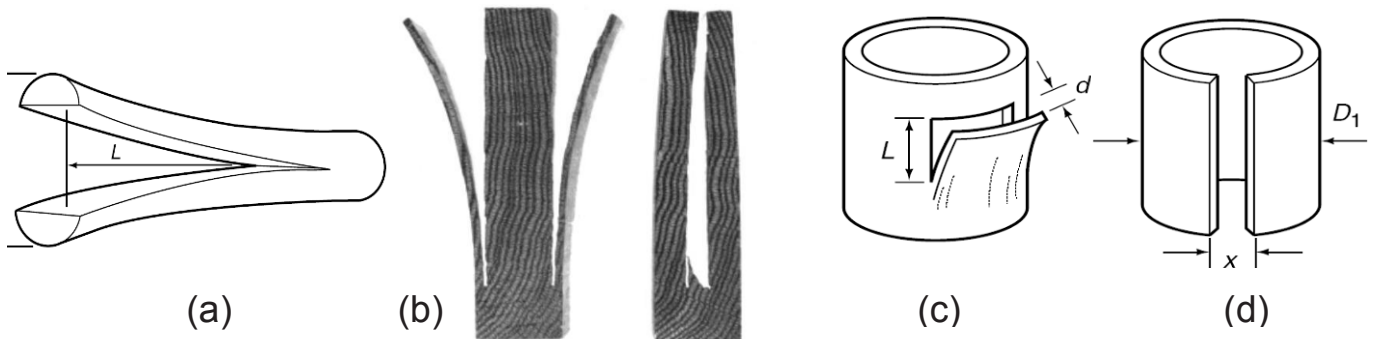


Figure 1. The splitting method, (a) for rods (from [4]), (b) for wood (from [5]), (c) for axial stresses in tubes [6], (d) for circumferential stresses in tubes [6].

The splitting method is often used to assess the residual stresses in thin-walled tubes. Figure 1 shows two different cutting arrangements [6], (c) for evaluating longitudinal stresses and (d) for circumferential stresses. The latter arrangement is commonly used for heat exchanger tubes, and is specified by ASTM standard E1928 [7].

The thin-wall tube splitting method illustrated in Figures 1(c) and (d) is also an example of Stoney's Method [8], sometimes called the curvature method. This method involves measuring the deflection or curvature of a thin plate caused by the addition or removal of material containing residual stresses. The method was originally developed for evaluating the stresses in electroplated materials, and is also used for assessing the stresses induced by shot-peening [9].

The sectioning method [10,11] combines several other methods to evaluate residual stresses within a given specimen. By choosing the combination and sequence of methods, a highly specific measurement can be made tailored to particular specimen. The sectioning method typically involves attachment of strain gauges and cutting out parts of the specimen. The strain reliefs measured as the various parts are progressively cut out provide a rich source of data from which both the size and location of the original residual stresses can be determined.

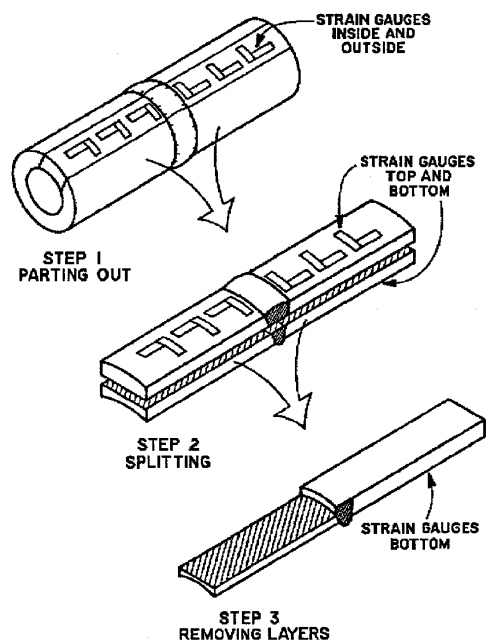


Figure 2. Sectioning method (from [10]).

Figure 2 shows an example of the sectioning method, where a sequence of cuts was made to evaluate the residual stresses in a welded pipe [10].

The layer removal method is a generalization of Stoney's method. It involves observing the deformation caused by the removal of a sequence of layers of material. The method is suited to flat plate and cylindrical specimens where the residual stresses are known to vary with depth from the surface, but to be uniform parallel to the surface. Figure 3 illustrates examples of the layer removal method, (a) on a flat plate specimen, and (b) on a cylindrical specimen. The method involves measuring deformations on one surface, for example using strain gauges, as parallel layers of material are removed from the opposite surface [12]. In the case of a hollow cylindrical specimen, deformation measurements can be made on either the outside or inside surface, while annular layers are removed from the opposite surface. When applied to cylindrical specimens, the layer removal method is commonly called "Sachs' Method" [13]. The method is a general one; it is typically applied to metal specimens, e.g., [14], but can be applied to other materials, e.g., paperboard [15].

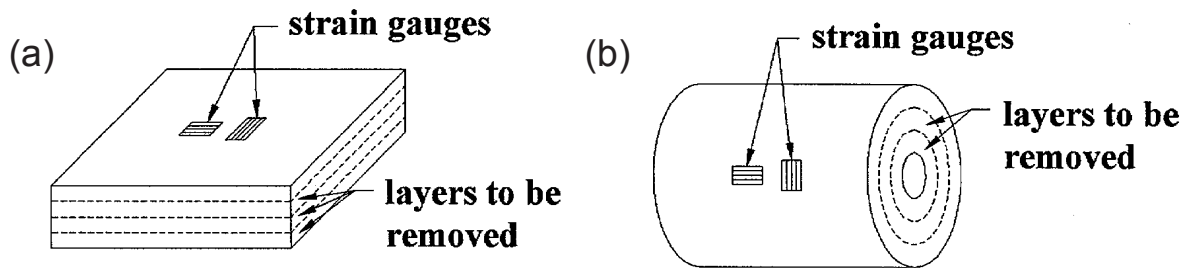


Figure 3. Layer removal method. (a) flat plate, (b) cylinder.

The hole-drilling method [16,17] is probably the most widely used destructive method for measuring residual stresses. It involves drilling a small hole in the surface of the specimen and measuring the deformations of the surrounding surface, traditionally using strain gauges [18], and more recently using full-field optical techniques such as Moiré interferometry [19], ESPI [20] and DIC [21]. Figure 4(a) illustrates the process. The hole-drilling method is popular because it gives reliable and rapid results with many specimen types, and creates only localized and often tolerable damage. The measurement procedure has been well developed [22] and is standardized as ASTM E837 [23].

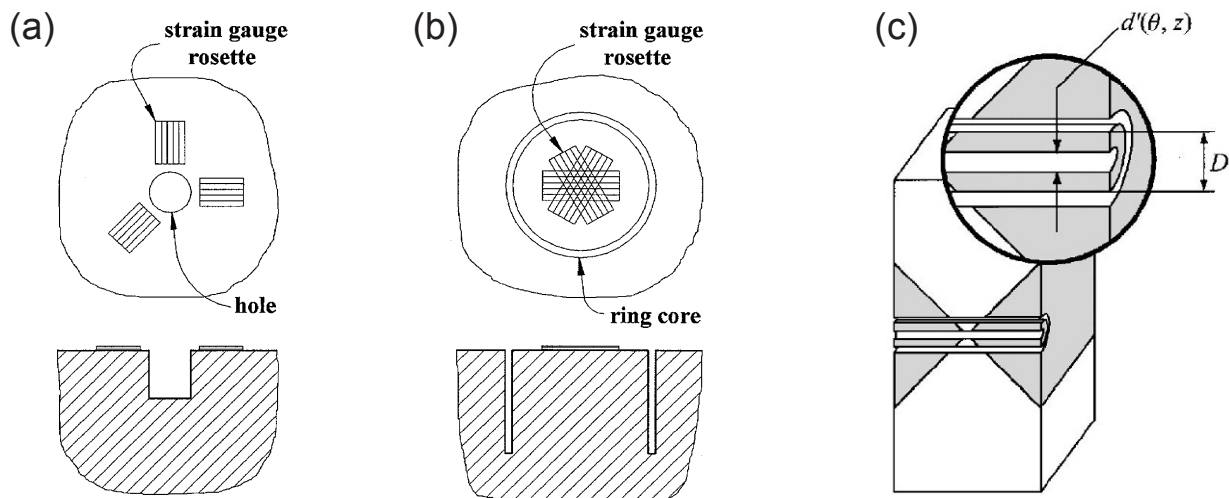


Figure 4. Hole-drilling methods: (a) conventional hole-drilling method, (b) ring-core method, (c) deep hole method (from [29]).

In the basic implementation of the hole-drilling method, the surface deformations are measured as the hole is drilled to a depth approximately equal to the hole radius. The in-plane stresses within the hole depth can

be determined from the surface deformations using tabulated calibration coefficients [23]. In a more detailed implementation of the hole-drilling method, the surface deformations are measured after each step in a series of small hole depth steps. This incremental procedure allows the stress profile within the hole depth to be determined [24].

The ring-core method [25,26] is an “inside-out” variant of the hole-drilling method. Whereas the hole-drilling method involves drilling a central hole and measuring the resulting deformation of the surrounding surface, the ring core method involves measuring the deformation in a central area caused by the cutting of an annular slot in the surrounding material. Figure 4(b) illustrates the geometry. The ring-core method is a circular generalization of the two-slots method [2]. As with the hole-drilling method, the ring-core method has a basic implementation to evaluate in-plane stresses [26], and an incremental implementation to determine the stress profile [27]. The ring-core method has the advantage over the hole-drilling method that it provides much larger surface strains. However, is less frequently used because it creates much greater specimen damage and is much less convenient to implement in practice.

The deep hole method [28,29] is a further variant procedure that combines elements of both the hole-drilling and ring-core methods. It involves drilling a hole deep into the specimen, and then measuring the diameter change as the surrounding material is overcored. Figure 4(c) illustrates the geometry. The main feature of the method is that it enables the measurement of deep interior stresses. The specimens can be quite large, for example, steel and aluminum castings weighing several tons. On a yet larger scale, the deep hole method is often used to measure stresses in large rock masses [30].

The slitting method [31,32] is also conceptually similar to the hole-drilling method, but using a long slit rather than a hole. Alternative names are the crack compliance method, the sawcut method or the slotting method. Figure 5 illustrates the geometry. Strain gauges are attached either on the front or back surfaces, or both, and the relieved strains are measured as the slit is incrementally increased in depth. The slit can be introduced by a thin saw, milling cutter or wire EDM. The residual stresses perpendicular to the cut can then be determined from the measured strains using finite element calculated calibration constants, in the same way as for hole-drilling calculations. The slitting method has the advantage over the hole-drilling method that it can evaluate the stress profile over the entire specimen depth, the surface strain gauge providing data for the near-surface stresses, and the back strain gauge providing data for the deeper stresses. However, the slitting method provides only the residual stresses normal to the cut surface, whereas the hole-drilling method provides all three in-plane stresses. Additional cuts can be made to find other stress components, in which case the overall procedure resembles the sectioning method.

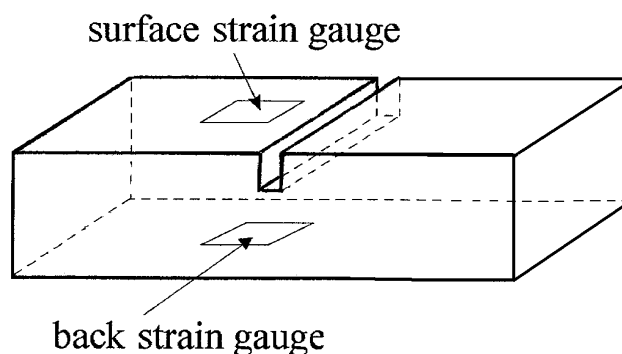


Figure 5. Slitting method.

The Contour Method [33] is a newly developed technique for making full-field residual stress measurements, typically within the cross-section of a prismatic specimen. It consists of cutting through the specimen cross-section using a wire EDM, and measuring the surface height profiles of the cut surfaces using a coordinate measuring machine or a laser profilometer. Figure 6 illustrates the process. The original residual stresses shown in Figure 6(a) are released by the cut and cause the material surface to deform (pull in for tensile stresses, bulge out for compressive stresses), as shown in Figure 6(b). The originally existing residual stresses normal to the cut can be evaluated from finite element calculations by determining the stresses required to return the deformed surface shape to a flat plane. In practice, to avoid any effects of measurement asymmetry, the surfaces on both sides of the cut are measured and the average surface height map is used.

The contour method is remarkable because it gives a 2-dimensional map of the residual stress distribution over the entire material cross-section. In comparison, other techniques such as layer removal and hole-drilling give one-dimensional profiles, while excision gives the residual stress only at one point. The contour method provides measurements of the stresses normal to the cut surface. If desired, stresses in other directions can also be determined by making additional cuts, typically perpendicular to the initial cut [34]. This approach effectively combines the contour method with the sectioning method. Taking a different approach, it is also possible to infer other stress components from the plastic deformations that original induced the residual stresses [35].

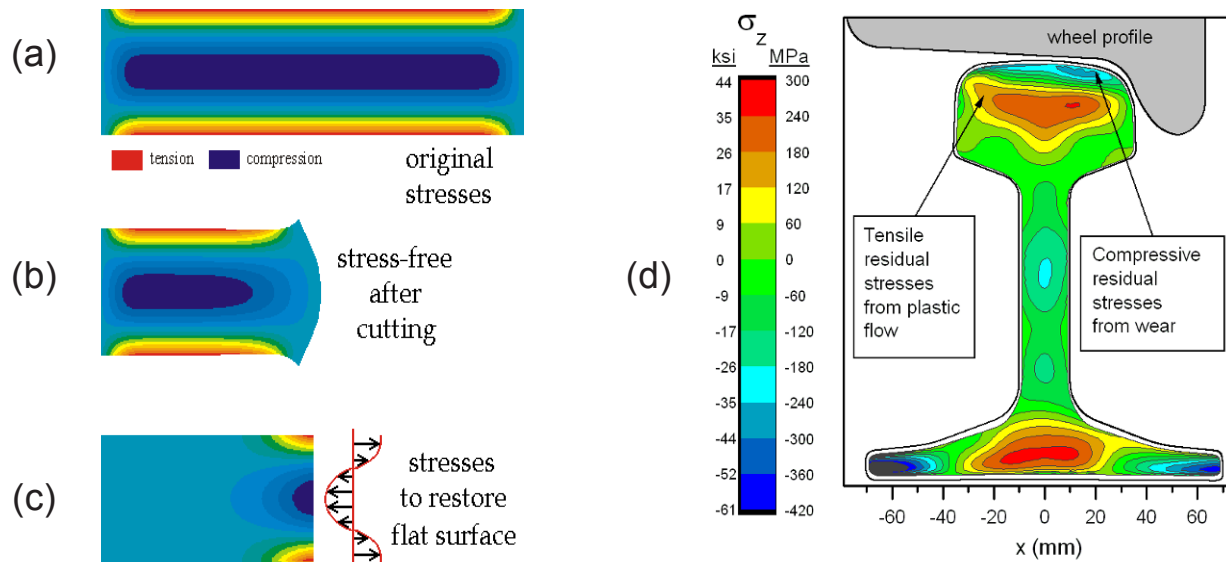


Figure 6. Contour Method (from Prime [33]). (a) original stresses, (b) stress-free surface after cutting, (c) stresses required to restore a flat surface, (d) an example measured stress profile of a railway rail.

Material Cutting and Deformation Measurement Technology

The majority of the destructive methods for measuring residual stress have histories that trace back over many decades. During their evolution, the various methods have greatly developed in terms of their practical implementations, notably the methods used for cutting the specimen material and for measuring the resulting deformations. Early implementations, e.g., [6], used saws and twist drills to cut material, and mechanical gauges to measure deformations. These were superseded by high-speed cutters and strain gauges, e.g., [17], while the most recent implementations use EDM and electronic optical metrology, e.g., [28,19]. Exceptionally, the Contour Method [33] is a recently developed method. However, its successful implementation is also critically dependent on the availability of modern high-precision material cutting and surface measurement techniques. Certainly, the advent of complementary modern technologies has substantially opened up, and will continue to open up, many new opportunities in terms of test materials, specimen shapes and detail/accuracy of the residual stress evaluations. The discussion here focuses on the more recent cutting and measurement technologies.

The two main requirements for a material cutting/removal technique are that the process should be accurate and should not induce additional residual stresses (“machining stresses”). The introduction of high-speed cutters [36] and abrasive machining [37] in the 1970s and 1980s, significantly advanced both these objectives. The more recent introduction of Electro-Discharge Machining (EDM) to residual stress measurements further advanced measurement capabilities to difficult-to-machine materials [38], deep-hole drilling [28] and to the Contour Method [33]. In the latter case, EDM can justifiably be described as an “enabling technology” because the Contour Method only became feasible with the advent of the very high accuracy cutting available from wire EDM.

A further example of an “enabling technology” is the application of Focused Ion Beam (FIB) instruments to make microscopic cuts [39], holes [40], rings [41], slots [42] etc., with dimensions in the low micron range. This development dramatically extended the dimension scale of the various residual stress measurement techniques into the micro and nano range. Figure 7 illustrates the application of FIB cutting to the splitting, ring core and slitting methods.

The measurement techniques used for residual stress measurements have followed the same developmental trend. In particular, optical methods have increasingly been applied [43], notably because of their full-field measurements and their adaptability to a wide range of machining geometries and size scales. The example applications shown in Figure 7 exemplify this adaptability, with three very different machining geometries applied at a microscopic scale.

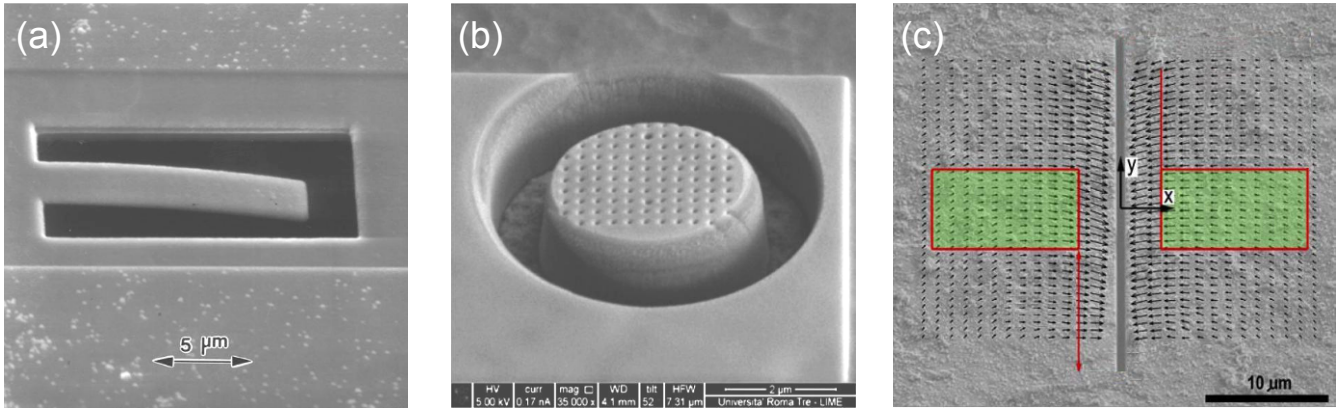


Figure 7. Focused Ion Beam machining. (a) splitting [39], (b) ring-coring [41], (c) slitting [42].

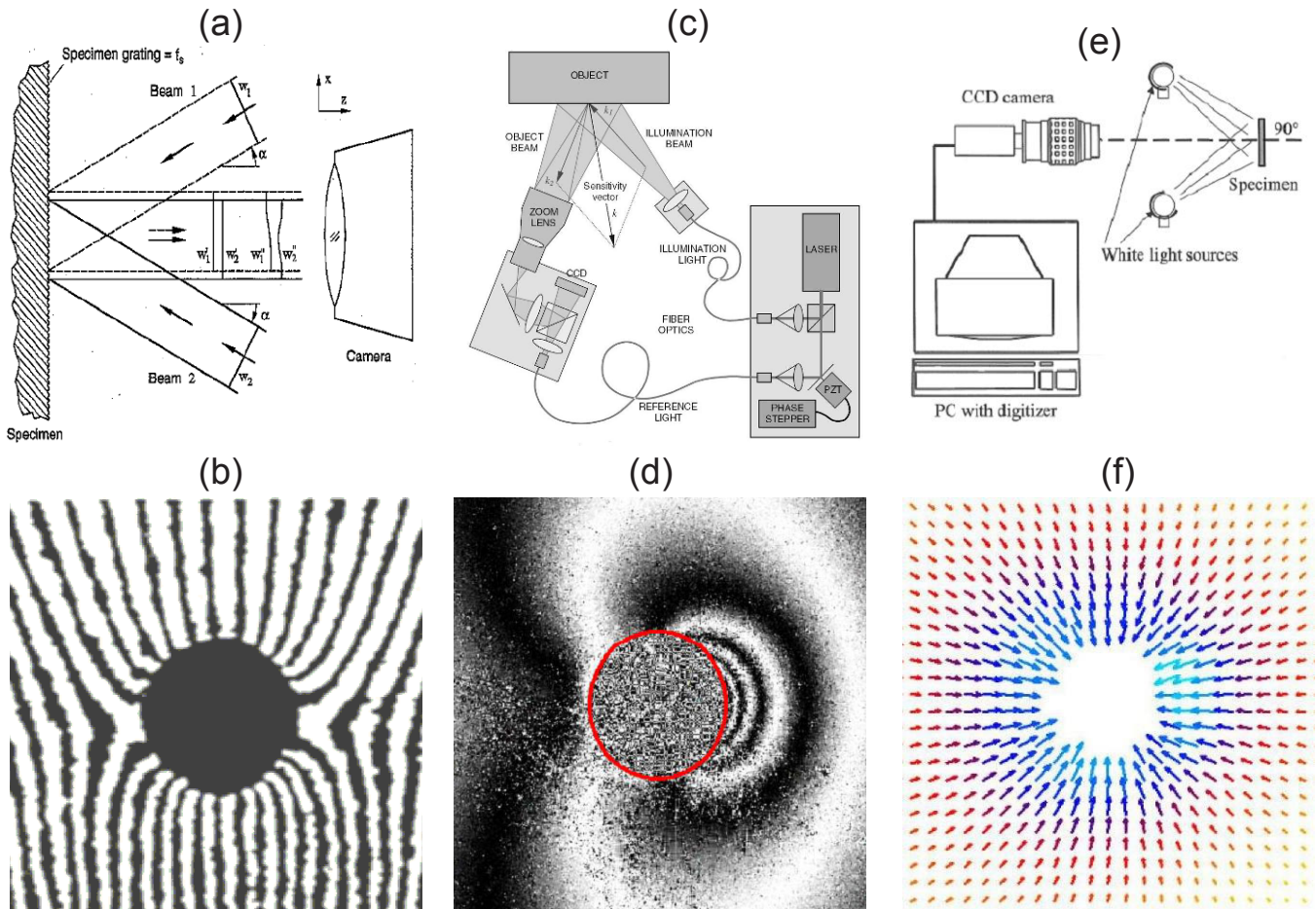


Fig. 8. Full-field optical techniques for surface deformation measurements. (a) Moiré interferometry (from [19]), (b) Moiré fringe pattern (from [45]), (c) ESPI (from [46]), (d) ESPI fringe pattern, (e) 2-D Digital Image Correlation (from [48]), (f) DIC vector plot (from [50]).

Moiré interferometry [19,44,45] provides a sensitive technique for measuring the small surface displacements that occur during residual stress measurements. Figure 8(a) schematically shows a typical optical arrangement [19]. Light from a single coherent laser source is split into two beams that illuminate the specimen surface with the symmetrical geometry shown in the diagram. A diffraction grating consisting of finely ruled lines, typically 600-1200 lines/mm, is replicated or made directly on the specimen surface. Diffraction of the beams creates a “virtual grating”, giving interference fringes consisting of light and dark lines. Figure 8(b) shows an example hole-drilling measurement [45]. Each light or dark line represents a contour line of in-plane surface displacement, in the x-direction in Figure 8(a). For typical optical arrangements, the in-plane displacement increment between fringe lines is about 0.5 μ m.

The full-field character of the measurements illustrated in Figure 8(b) provides opportunities not available from single point measurements. The availability of “excess” data provides the possibility to improve stress evaluation accuracy and reliability by data averaging, and to be able to identify errors, outliers or additional features. For example, the different fringe spacings in the upper and lower halves of Figure 8(b) show that the residual stresses are non-uniform within the surface plane.

Electronic Speckle Pattern Interferometry (ESPI) [20,46,47] provides a further important method for measuring the surface displacements around a drilled hole. It has several similarities to the Moiré method and also involves measuring the interference pattern that is created when mixing two coherent light beams. Figure 8(c) shows a typical ESPI arrangement [46]. The light from a coherent laser source is divided into two parts, one of which (the illumination/object beam) is used to illuminate the specimen surface so that it can be imaged by a CCD camera. The second (the reference beam) is fed directly to the CCD camera so that it creates an interference pattern on the CCD surface. Evaluation of this interference pattern provides a full-field map of the deformation of the measured surface, which can then be analyzed in a similar way as with Moiré interferometry. Figure 8(d) shows an example fringe pattern for a hole-drilling measurement.

Digital Image Correlation [21,48-50] is a versatile optical technique for measuring surface displacements in two or three dimensions. The 2-D technique, schematically illustrated in Figure 8(e), involves applying a textured pattern on the specimen surface and imaging the region of interest using a high-resolution digital camera. The camera, which is set perpendicular to the surface, records images of the textured surface before and after deformation. The local details within the two images are then mathematically correlated, and their relative displacements determined. The algorithms used for doing this have become quite sophisticated, and with a well-calibrated optical system, displacements of +/- 0.02 pixel can be resolved. Figure 8(f) shows an example vector plot of the measured displacements in a hole-drilling measurement.

The Moiré and ESPI techniques are based on the interference of coherent laser light, and they can measure surface displacements of fractions of a micron. Thus, they can provide sensitive measurements of the surface strains of structures ~1mm and larger. In contrast, Digital Image Correlation provides deformation measurements that are relative to the area being imaged. Thus, the DIC method can be applied over a wide range of length scales, for example on concrete structures measured in meters, e.g. [21], and on microscopic specimens measured in microns, viewed in a scanning electron microscope, e.g. [39-42]. In addition, the DIC method simultaneously provides displacement measurements in both axial directions, whereas separate Moiré and ESPI measurements must be made to resolve each direction. However, the strain sensitivity of DIC is typically about an order of magnitude less than with the Moiré and ESPI techniques, and is thus best reserved for measurements of large strains or small specimens.

Stress Calculation Techniques

Advances in stress computational methods, numerical techniques and computer hardware have also provided “enabling technologies”, analogous in supportive effect to the advances in material cutting and surface deformation measurement techniques. The computational challenge when doing a destructive measurement of residual stress arises because the measured deformations occur by stressed material removal rather than by load removal. This feature introduces two complicating factors, the geometry of the specimen is changed and the deformations are typically measured at a different location than the original residual stresses. Because of these factors, the relationship between the measured deformations and the corresponding residual stresses does not have the simple proportional stress/strain relationships typical when working with applied loads. Instead, it commonly has the form of an inverse equation, schematically shown in Equation (1) [51].

$$d(h) = \int_0^h G(H,h) \sigma(H) dH \quad (1)$$

where $d(h)$ are the data, typically strains or displacements, measured at position h , typically the radius or the distance from the measured surface, $\sigma(H)$ is the stress at position H , and $G(H,h)$ is the “kernel function” that relates the strains/displacements to the stresses. For simple specimen geometries, the kernel function $G(H,h)$ can be determined analytically. For example, the strains measured on the inside surface of a hollow cylinder, at radius = a , as concentric layers are removed from the outside surface, at radius = r (Sachs’ Method) are [52]:

$$\varepsilon_\theta(r) + \nu\varepsilon_a(r) = \frac{1-\nu^2}{E} \int_a^r \frac{-2r}{r^2 - a^2} \sigma(R) dR \quad (2)$$

Thus, it is seen that strain measured at any stage within the measurement sequence depends on the different stresses originally contained within all the removed material, and not just the stress at the last load removal point. This feature is the reason for the name “inverse equation”. The “forward” solution for the strains given the stresses is straightforward, but the “inverse” solution for the stresses given the strains is more difficult. The need for analytical deformation/stress relationships such as Equation (2) initially limited the types of tests that could be done to specimens with simple geometry, for example the planar and cylindrical layer removal methods illustrated in Figure 3. The advent of finite element calculations greatly widened the scope of possible measurements. For example, finite element calculations enabled stress/strain relationships to be determined for the hole-drilling method [37,24] with much greater accuracy than available through the previous experimental calibrations. In addition, the numerical calculations provided stress/strain results for cases where experimental evaluation of the kernel function $G(H,h)$ is not possible, thereby allowing substantial extensions of residual stress measurement capabilities. An example of this is the Integral Method [53,24] for measuring stress vs. depth profiles using the hole-drilling method.

The solution procedures for the various measurement methods were developed on an ad-hoc basis, and are as varied as the specimen geometries to which they refer. However, for the majority of cases the deformation/residual stress relationships have the same fundamental mathematical form as Equation (1), and thus can be solved by the same mathematical procedure [54]. This procedure is now specified in the ASTM Standard Test Method E837-08 [7] for hole-drilling, and is also effective for layer removal and slitting measurements [55]. A characteristic of solutions to inverse equations is that they tend to amplify noise. Thus, small measurement errors can create much larger relative errors in the stress solution. Although reflected in the mathematics, this characteristic has a physical origin. It is caused by the spatial separation of the locations of the measured data and the calculated residual stresses, the greater their separation, the greater the error sensitivity. Mathematical techniques such as regularization [56] can be used to stabilize the residual stress solution and reduce noise sensitivity.

The availability of large quantities of measured data from full-field optical measurements greatly extends the opportunities for residual stress evaluations. Every pixel within an image contains information, thus a typical image can provide thousands or millions of surface deformation data. Initial computation methods using optical data mirrored the previous procedures used with discrete sensors such as strain gauges, e.g., [57], and focused on selected data at a few specific locations. The performance of these methods can be significantly enhanced by including the contributions of the substantial quantity of additional data available beyond the few selected points. The challenge is to use the large amount of available data in an effective and compact way. Some desirable features of a residual stress computation method for use with optical data include:

- taking advantage of the wealth of data available within an optical image
- extracting the data from the image with a minimum of human interaction, preferably none
- using the available data in a compact and stable computation, preferably a linear one.

Least-squares [58,59] and orthogonalization [60] techniques have been developed that meet these criteria. The substantial data averaging that is implicit in the calculations substantially reduces measurement noise and enhances measurement accuracy. Error checking and outlier rejection also become possible [61]. In addition, the data quantity allows the calculations to take into account further behaviors in the measurements such as rigid-body motions, thermal strains, plasticity, material non-isotropy, etc. More complex residual stress fields can be assessed, for example, the slitting method has been extended so that the stress distribution along the length of the slit can be determined in addition to the stress distribution within the slit depth [47].

Concluding Remarks

The destructive methods for measuring residual stresses provide a versatile methodology that can be applied to a wide range of specimen and stress geometries. They are based on the elastic deformations that occur during residual stress release. This is a direct phenomenon, and thus, the methods generally give accurate and reliable results. This feature often makes them the measurement type of choice, even though some specimen damage is caused. The various specific methods have evolved over several decades and their practical applications have greatly benefited from the development of complementary technologies, notably in material cutting, full-field deformation measurement techniques, numerical methods and computing power. These complementary technologies have stimulated advances not only in measurement accuracy and reliability, but also in range of application; much greater detail in residual stress measurement is now available. A good example of this advance is the Contour Method. This full-field method relies on highly accurate material cutting and surface measurement technologies and individually evaluated finite element calculations.

Future developments in destructive residual stress measurement techniques are likely to follow present trends. The ongoing development of complementary technologies will continue to provide new opportunities for technical progress and sophistication. The research work cited here is but a small fraction of the output of an active and vibrant field; the number of researchers and the quantity of their published work continue to grow. These are signs both of practical interest and of opportunity to make advances. Most destructive methods have origins from the days of dial gauges, but the advent of ultra-high-precision cutting tools, laser interferometers, high-resolution cameras, etc. have substantially refreshed and advanced them. Certainly, a future review such as this should in just a few years be able to report many further advances and interesting applications.

Acknowledgment

This work was financially supported by a grant from the Natural Sciences and Engineering Research Council of Canada (NSERC).

References

1. Ruud, C. "A Review of Nondestructive Methods for Residual Stress Measurements", *Journal of Metals*, Vol.33, No.7, pp.35-40, 1981.
2. Schwaighofer, J. "Determination of Residual Stresses on the Surface of Structural Parts", *Experimental Mechanics*, Vol.4, No.2, pp.54-56, 1964.
3. Jullien, D. and Gril, J. "Growth Strain Assessment at the Periphery of Small-diameter Trees using the Two-grooves Method: Influence of Operating Parameters Estimated by Numerical Simulations", *Wood Science and Technology*, Vol.42, No.7, pp.551-565, 2008.
4. Walton, H. W. "Deflection Methods to Estimate Residual Stress", in *Handbook of Residual Stress and Deformation of Steel*, Totten, G., Howes, M., and Inoue, T. (eds.), ASM International, pp.89-98, 2002.
5. Fuller, J. "Conditioning Stress Development and Factors That Influence the Prong Test", *USDA Forest Products Laboratory, Research Paper FPL-RP-537*, 6pp, 1995.
6. Baldwin, W. M. "Residual Stresses in Metals", *Proc. American Society for Testing and Materials*, Philadelphia, PA, 49pp., 1949.
7. ASTM. "Standard Practice for Estimating the Approximate Residual Circumferential Stress in Straight Thin-walled Tubing", *Standard Test Method E1928-07*, American Society for Testing and Materials, West Conshohocken, PA, 2007.
8. Stoney, G. G. "The Tension of Thin Metallic Films Deposited by Electrolysis", *Proc. Royal Society of London, Series A*, Vol.82, pp.172-175, 1909.
9. Cao, W. Fathallah, R. Castex, L. "Correlation of Almen Arc Height with Residual Stresses in Shot Peening Process", *Materials Science and Technology*, Vol.11, No.9, pp.967-973, 1995.
10. Shadley, J. R., Rybicki, E. F. and Shealy, W. S. "Application Guidelines for the Parting out in a Through Thickness Residual Stress Measurement Procedure", *Strain*, Vol.23, pp.157-166, 1987.
11. Tebedge, N., Alpsten, G. and Tall, L. "Residual-stress Measurement by the Sectioning Method", *Experimental Mechanics*, Vol.13, No.2, pp. 88-96, 1973.
12. Treuting, R.G. and Read, W.T. "A Mechanical Determination of Biaxial Residual Stress in Sheet Materials", *Journal of Applied Physics*, Vol.22, No.2, pp.130-134, 1951.
13. Sachs, G. and Espey, G. "The Measurement of Residual Stresses in Metal", *The Iron Age*, Sept 18, pp.63-71, 1941.

14. Hospers, F. and Voegesang, L. B. "Determination of Residual Stresses in Aluminum-alloy Sheet Material", *Experimental Mechanics*, Vol.15, No.3, pp.107-110, 1975.
15. Östlund, M., Östlund, S., Carlsson, L.A. and Fellers, C. "Experimental Determination of Residual Stresses in Paperboard", *Experimental Mechanics*, Vol.45, No.6, pp.493-497, 1985.
16. Lu, J. (ed.) "Handbook of Measurement of Residual Stresses", Fairmont Press. Lilburn, USA, 1996.
17. Measurements Group. "Measurement of Residual Stresses by Hole-Drilling Strain Gage Method", Tech Note TN-503-6, Vishay Measurements Group, Raleigh, NC, 2001.
18. Rendler, N. J. and Vigness, I. "Hole-Drilling Strain-gage Method of Measuring Residual Stresses, *Experimental Mechanics*, Vol.6, No.12, pp.577-586, 1966.
19. Wu, Z., Lu, J. and Han, B. "Study of Residual Stress Distribution by a Combined Method of Moiré Interferometry and Incremental Hole Drilling." *Journal of Applied Mechanics*, Vol.65, No.4 Part I: pp.837-843, Part II: pp.844-850, 1998.
20. Nelson, D.V. and McCrickerd, J.T. "Residual-Stress Determination Through Combined Use of Holographic Interferometry and Blind-Hole Drilling", *Experimental Mechanics*, Vol.26, No.4, pp.371-378, 1986.
21. McGinnis, M. J., Pessiki, S. and Turker, H. "Application of Three-dimensional Digital Image Correlation to the Core-drilling Method." *Experimental Mechanics*, Vol.45, No.4, pp.359-367, 2005.
22. Grant, P. V., Lord, J. D. and Whitehead, P. S. "The Measurement of Residual Stresses by the Incremental Hole Drilling Technique", *Measurement Good Practice Guide*, No.53. National Physical Laboratory, UK, 2002.
23. ASTM. "Standard Test Method for Determining Residual Stresses by the Hole-Drilling Strain-Gage Method", *Standard Test Method E837-08*, American Society for Testing and Materials, West Conshohocken, PA, 2008.
24. Schajer, G. S. "Measurement of Non-Uniform Residual Stresses using the Hole-Drilling Method", *Journal of Engineering Materials and Technology*, Vol.110, No.4, Part I: pp.338-343, Part II: pp.344-349, 1988.
25. Milbradt, K.P. "Ring-Method Determination of Residual Stresses", *Proc. SESA*, Vol.9, No.1, pp.63-74, 1951.
26. Kiel, S. "Experimental Determination of Residual Stresses with the Ring-Core Method and an On-Line Measuring System", *Experimental Techniques*, Vol.16, No.5, pp.17-24, 1992.
27. Ajovalasit, A., Petrucci, G. and Zuccarello, B. "Determination of Non-Uniform Residual Stresses using the Ring-Core Method", *Journal of Engineering Materials and Technology*, Vol.118, No.2, pp.224-228, 1996.
28. Leggatt, R. H., Smith, D. J., Smith, S.D. and Faure, F. "Development and Experimental Validation of the Deep Hole Method for Residual Stress Measurement", *J. Strain Analysis*, Vol.31, No.3, pp.177-186, 1996.
29. DeWald, A. T. and Hill, M. R. "Improved Data Reduction for the Deep-Hole Method of Residual Stress Measurement", *Journal of Strain Analysis*, Vol.38, No.1, pp.65-78, 2003.
30. Amadei, B. and Stephansson, O. "Rock Stress and its Measurement", Chapman and Hall, London, 1997.
31. Prime, M. B. "Residual Stress Measurement by Successive Extension of a Slot: The Crack Compliance Method", *Applied Mechanics Reviews*, Vol.52, No.2, pp.75-96, 1999.
32. Germaud M., Cheng, W., Finnie, I., and Prime, M. B. "The Compliance Method for Measurement of Near Surface Residual Stresses - Analytical Background", *Journal of Engineering Materials and Technology*, Vol.119, No.4, pp.550-555, 1994.
33. Prime, M. B. "Cross-Sectional Mapping of Residual Stresses by Measuring the Surface Contour After a Cut", *Journal of Engineering Materials and Technology*, Vol.123, No.2, 2001.
34. Pagliaro, P., Prime, M.B., Clausen, B., Lovato, M.L., Robinson, J.S., Schajer, G.S., Steinzig, M.L., Swenson, H. and Zuccarello B. "Mapping Multiple Residual Stress Components Using the Contour Method and Superposition", *Intl. Conference on Residual Stresses*, Denver, CO, August 6-8, 2008.
35. DeWald, A.T. and Hill, M.R. "Multi-Axial Contour Method for Mapping Residual Stresses in Continuously Processed Bodies", *Experimental Mechanics*, Vol.46, No.4, pp.473-490, 2006.
36. Flaman, M. T. "Brief Investigation of Induced Drilling Stresses in the Center-Hole Method of Residual-Stress Measurement", *Experimental Mechanics* Vol.22, No.1, pp.26-30, 1982.
37. Beaney, E. M. "Accurate Measurement of Residual Stress on any Steel Using the Centre Hole Method", *Strain*, Vol.12, No.3, pp.99-106, 1976.
38. Lee, H.T., Rehbach, W.P., Hsua, F.C., Tai, T.Y. and Hsua, E. "The study of EDM Hole-Drilling Method for Measuring Residual Stress in SKD11 Tool Steel", *Journal of Materials Processing Technology*, Vol.149, No.1-3, pp.88-93, 2004.
39. McCarthy, J., Pei, Z., Becker, M. and Atteridge, D. "FIB Micromachined Submicron Thickness Cantilevers for the Study of Thin Film Properties", *Thin Solid Films*, Vol.358, No.1, pp.146-151, 2000.

40. Sabaté, N., Vogel, D., Keller, J., Gollhardt, A., Marcos, J., Gràcia, I., Cané, C. and Michel, B. "FIB-Based Technique for Stress Characterization on Thin Films for Reliability Purposes", *Microelectronic Engineering*, Vol.84, No.5-8, pp.1783-1787, 2007.
41. Korsunsky, A. M., Sebastiani, M., Bemporad, E. "Focused Ion Beam Ring Drilling for Residual Stress Evaluation", *Materials Letters*, Vol.63, pp.1961-1963, 2009.
42. Winiarski, B., Langford, R. M., Tian, J., Yokoyama, Y., Liaw, P. K. and Withers, P. J. "Mapping Residual Stress Distributions at the Micron Scale in Amorphous Materials", *Metallurgical and Materials Transactions A*, Vol.41, 2010.
43. Nelson, D.V. "Residual Stress Determination by Hole Drilling Combined with Optical Methods", *Experimental Mechanics*, Vol.50, No.1, pp.145-158, 2010.
44. McDonach, A., McKelvie, J., MacKenzie, P. and Walker, C. A. "Improved Moiré Interferometry and Applications in Fracture Mechanics, Residual Stress and Damaged Composites." *Experimental Techniques*, Vol.7, No.6, pp.20-24, 1983.
45. Nicoletto, G. "Moiré Interferometry Determination of Residual Stresses in the Presence of Gradients," *Experimental Mechanics*, Vol.31, No.3, pp.252-256, 1991.
46. Steinzig, M. and Ponslet, E. "Residual Stress Measurement Using the Hole Drilling Method and Laser Speckle Interferometry: Part I." *Experimental Techniques*, Vol.27, No.3, pp.43-46, 2003.
47. Montay, G., Sicot, O., Maras, A., Rouhaud, E. and François, M. "Two Dimensions Residual Stresses Analysis Through Incremental Groove Machining Combined with Electronic Speckle Pattern Interferometry", *Experimental Mechanics*, Vol.49, pp.459-469, 2009.
48. Sutton, M. A., McNeill, S. R., Helm, J. D. and Chao, Y. J. "Advances in Two-Dimensional and Three-Dimensional Computer Vision." Chapter 10 in "Photomechanics", ed. P. K. Rastogi, Springer-Verlag, Berlin Heidelberg, 2000.
49. Hung, M.Y.Y., Long, K.W. and Wang, J.Q. "Measurement of Residual Stress by Phase Shift Shearography", *Optics and Lasers in Engineering*, Vol.27, No.1, pp.61-73, 1997.
50. Lord, J.D., Penn, D. and Whitehead, P. "The Application of Digital Image Correlation for Measuring Residual Stress by Incremental Hole Drilling", *Applied Mechanics and Materials*, Vol.13-14, pp.65-73, 2008.
51. Parker, R. L. "Geophysical Inverse Theory." Princeton University Press, New Jersey, 1994.
52. Lambert, J. W. "A Method of Deriving Residual Stress Equations", *Proc. SESA*, Vol.12, No.1, pp.91-96, 1954.
53. Bijak-Zochowski, M. "A Semidestructive Method of Measuring Residual Stresses." *VDI-Berichte*, Vol.313, pp.469-476, 1978.
54. Schajer, G. S. and Prime, M. B. "Use of Inverse Solutions for Residual Stress Measurements." *Journal of Engineering Materials and Technology*. Vol.128, No.3, pp.375-382, 2006.
55. Schajer, G. S. and Prime, M. B. "Residual Stress Solution Extrapolation for the Slitting Method Using Equilibrium Constraints", *Journal of Engineering Materials and Technology*. Vol.129, No.2, pp.227-232, 2007.
56. Tikhonov, A., Goncharsky, A., Stepanov, V. and Yagola, A. "Numerical Methods for the Solution of Ill-Posed Problems," Kluwer, Dordrecht, The Netherlands, 1995.
57. Focht, G. and Schiffner, K. "Determination of Residual Stresses by an Optical Correlative Hole Drilling Method." *Experimental Mechanics*, Vol.43, No.1, pp.97-104, 2003.
58. Ponslet, E. and Steinzig, M. "Residual Stress Measurement Using the Hole Drilling Method and Laser Speckle Interferometry: Part II." *Experimental Techniques*, Vol.27, No.4, pp.17-21, 2003.
59. Baldi, A. "A New Analytical Approach for Hole Drilling RS Analysis by Full Field Method", *Journal of Engineering Materials and Technology*, Vol.127, No.2, pp. 165-169, 2005.
60. Schajer, G. S. and Steinzig, M. "Full-Field Calculation of Hole-Drilling Residual Stresses from ESPI Data." *Experimental Mechanics*, Vol.45, No.6, pp.526-532, 2005.
61. An, Y. and Schajer, G.S. "Pixel Quality Evaluation and Correction Procedures in ESPI", *Experimental Techniques*, (in press), 2010.

The Contour Method Cutting Assumption: Error Minimization and Correction

Michael B. Prime (prime@lanl.gov), Alan L. Kastengren*
Los Alamos National Laboratory, Los Alamos, NM 87545

* Now at the Energy Systems Division, Argonne National Laboratory

ABSTRACT

The recently developed contour method can measure 2-D, cross-sectional residual-stress map. A part is cut in two using a precise and low-stress cutting technique such as electric discharge machining. The contours of the new surfaces created by the cut, which will not be flat if residual stresses are relaxed by the cutting, are then measured and used to calculate the original residual stresses.

The precise nature of the assumption about the cut is presented theoretically and is evaluated experimentally. Simply assuming a flat cut is overly restrictive and misleading. The critical assumption is that the width of the cut, when measured in the original, undeformed configuration of the body is constant. Stresses at the cut tip during cutting cause the material to deform, which causes errors. The effect of such cutting errors on the measured stresses is presented. The important parameters are quantified. Experimental procedures for minimizing these errors are presented. An iterative finite element procedure to correct for the errors is also presented. The correction procedure is demonstrated on experimental data from a steel beam that was plastically bent to put in a known profile of residual stresses.

INTRODUCTION

Residual stresses play a significant role in many material failure processes like fatigue, fracture, stress corrosion cracking, buckling and distortion [1]. Residual stresses are the stresses present in a part free from any external load, and they are generated by virtually any manufacturing process. Because of their important contribution to failure and their almost universal presence, knowledge of residual stress is crucial for prediction of the life of any engineering structure. However, the prediction of residual stresses is a very complex problem. In fact, the development of residual stress generally involves nonlinear material behavior, phase transformation, coupled mechanical and thermal problems and also heterogeneous mechanical properties. So, the ability to accurately quantify residual stresses through measurement is an important engineering tool.

Recently, a new method for measuring residual stress, the contour method [2-4], has been introduced. In the contour method, a part is carefully cut in two along a flat plane causing the residual stress normal to the cut plane to relax. The contour of each of the opposing surfaces created by the cut is then measured. The deviation of the surface contours from planarity is assumed to be caused by elastic relaxation of residual stresses and is therefore used to calculate the original residual stresses. One of the unique strengths of this method is that it provides a full cross-sectional map of the residual stress component normal to the cross section. The contour method is useful for studying various manufacturing processes such as laser peening [5-10], friction welding [6,7,11-13] and fusion welding [14-21]. Some of the applications are quite unique such as mapping stresses in a railroad rail [22], in the region of an individual laser peening pulse [23], and under an impact crater [24].

The only common methods that can measure similar two-dimensional (2-D) stress maps have significant limitations. The neutron diffraction method is nondestructive but sensitive to micro-structural changes [25], time consuming, and limited in maximum specimen size, about 50 mm, and minimum spatial resolution, about 1mm. Sectioning methods [26] are experimentally cumbersome, analytically complex, error prone, and have limited spatial resolution, about 1 cm. A limitation of the original contour method is that only one residual stress component is determined. Recent developments have extended the contour method to the measurement of multiple stress components [27-30].

In an overly simplistic view, one might think that the contour method requires the assumption of a perfectly flat cut. Such an assumption is overly restrictive. In this paper, the actual assumptions about the cut are developed. Several potential error sources are shown to be removed by standard data processing. Other errors are explored in more detail numerically to establish procedure to minimize the errors. An experimental demonstration is given with a correction for errors arising because of the cut.

THEORY

This section reviews previously published theory for the contour method in order to allow for later detailed discussion of the assumption about the cut.

The contour method [2] shown in Figure 1 is based on a variation of Bueckner's superposition principle [31].

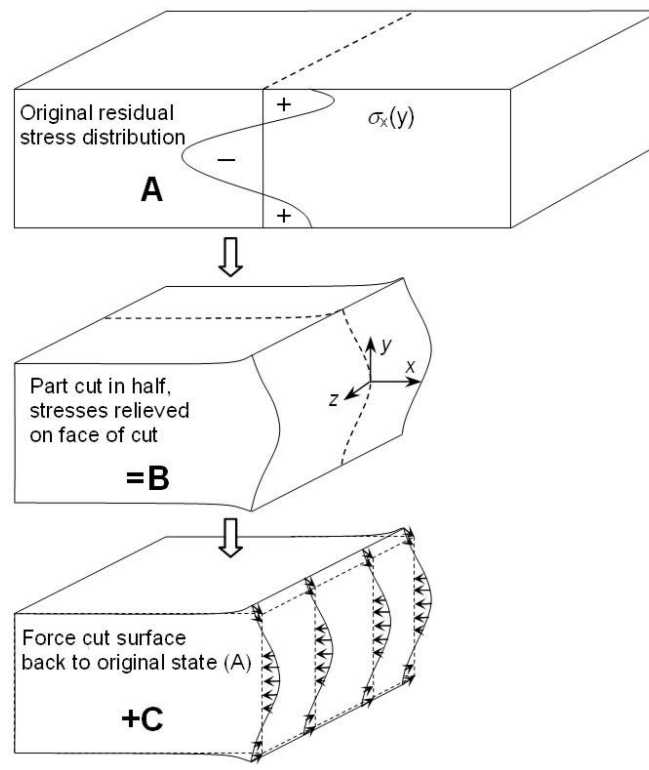


Figure 1 Superposition principle to calculate residual stresses from surface contour measured after cutting the part in two [28].

In **A**, the part is in the undisturbed state and contains the residual stress to be determined. In **B**, the part has been cut in two and has deformed as residual stresses were released by the cut. For clarity, only one of the halves is shown. In **C**, the free surface created by the cut is forced back to its original flat shape. Assuming elasticity, superimposing the partially relaxed stress state in **B** with the change in stress from **C** would give the original residual stress throughout the part:

$$\sigma^{(A)} = \sigma^{(B)} + \sigma^{(C)} \quad (1)$$

where σ without subscripts refers to the entire stress tensor.

This superposition principle assumes elastic relaxation of the material and that the cutting process does not introduce stress that could affect the measured contour. With proper application of this principle it is possible to determine the residual stress over the plane of the cut. Experimentally, the contour of the free surface is measured after the cut and analytically the surface of a stress-free model is forced back to its original flat

configuration by applying the opposite of the measured contour as boundary conditions. Because the stresses in **B** are unknown, one cannot obtain the original stress throughout the body. However, the normal and shear stresses on the free surface in **B** must be zero (σ_x , τ_{xy} and τ_{xz}). Therefore, **C** by itself will give the correct stresses along the plane of the cut:

$$\begin{aligned}\sigma_x^{(A)} &= \sigma_x^{(C)} \\ \tau_{xy}^{(A)} &= \tau_{xy}^{(C)} \\ \tau_{xz}^{(A)} &= \tau_{xz}^{(C)}\end{aligned}\tag{2}$$

The measured surface contour has an arbitrary reference plane, resulting in three arbitrary rigid body motions in defining the surface. These three arbitrary motions are uniquely determined by the need for the stress distribution over the cross section to satisfy three global equilibrium conditions: force in the x-direction and moments about the y and z axes. It is not necessary to explicitly enforce these constraints. In a finite element calculation, appropriate boundary conditions are applied to the cut plane, including three extra constraints to prevent rigid body motions. The remainder of the body is unconstrained. In the static equilibrium step used to solve for stress, the free end of the body will automatically translate and rotate such that the equilibrium conditions are fulfilled.

A small convenience is taken in the data analysis. Modeling the deformed shape of the part for **C** in [Figure 1](#) would be tedious. Instead, the surface is flat in the finite element model, and then the part is deformed into the shape opposite of the measured contour. Because the deformations are quite small, the same answer is obtained but with less effort.

CUTTING ASSUMPTION

From a theoretical point of view, the relevant assumption for the superposition principle in [Figure 1](#) is that the material points on the cut surface are returned in **C** to their original configuration. Experimental limitations results in two broad types of departures from that assumption. The first departure is that the surface contour measurement only gives information about the normal (x) displacement. So the material points are not returned to their original configuration in the transverse directions. The second departure is that in order for the measured surface contour to accurately return the material points to their original locations in the x-direction, those material points must have come from a common plane in the original configuration (**A**).

A transformation of this theoretical assumption into more practical assumptions can accommodate some of these issues without sacrificing any accuracy. This naturally leads to considering symmetric errors separate from antisymmetric errors, as explained in the following.

Anti-Symmetric Errors

The issues with both transverse displacements and anti-symmetric errors can be examined by considering the case of shear stresses [2]. The top of [Figure 2](#) shows a beam that was cut in half on a plane that had both normal and shear stresses. The two halves have different contours. The equivalent surface traction components for released stresses are given by $T_x = -\sigma_x n_x$, $T_y = -\tau_{xy} n_x$, where n is the surface normal vector. By a Poisson effect, the T_y from the released shear stress has an effect on the contour. As shown in [Figure 2](#) in reference [2], the tractions for releasing σ_x are symmetric about the cut plane, but the tractions for releasing τ_{xy} are anti-symmetric. Hence, the contours in [Figure 2](#) can be decomposed into the symmetric portion caused by normal stress and the anti-symmetric portion caused by shear stress.

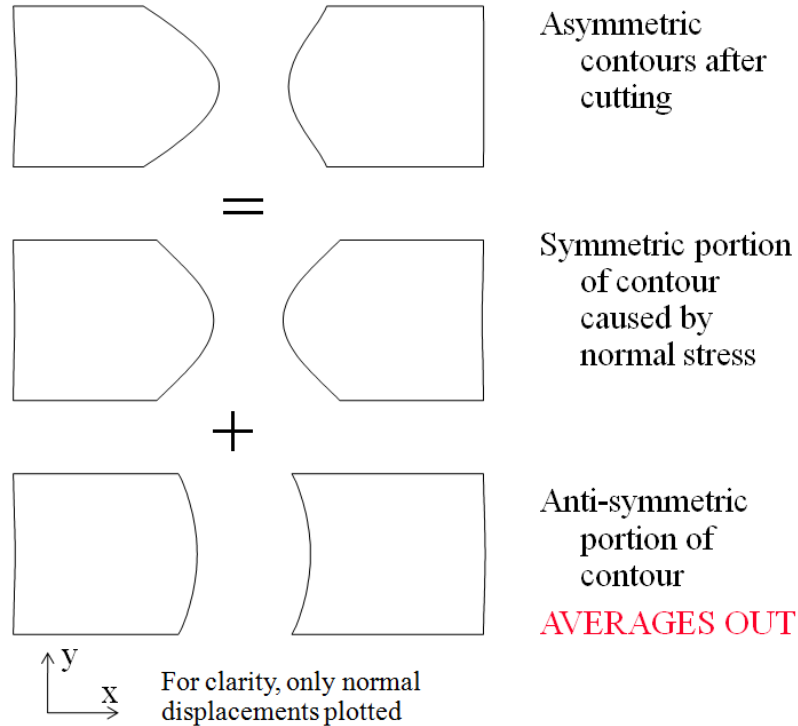


Figure 2. Asymmetric contours can be separated into the symmetric portion and the anti-symmetric portion, which averages away. Shown for the example of shear stresses.

The effect of shear stresses, and indeed all anti-symmetric errors, are removed by averaging the contours on the two halves.

The lack of information on transverse displacements also does not cause errors. In the analysis, the surface is forced back (step **C** in Figure 1) to the original flat configuration only in the x-direction, based on the average contour. The shear stresses (τ_{xy} and τ_{xz}) are constrained to zero in the solution. This stress-free constraint is automatically enforced in most implicit, structural, finite-element analyses if the transverse displacements are left unconstrained. Even if residual shear stresses were present on the cut plane, averaging the contours measured on the two halves of part still leads to the correct determination of the normal stress σ_x [2]. Even when there are no shear stresses, there are also transverse displacements from a Poisson-type effect when normal stresses are relaxed. Because there was no shear stress, there is no traction associated with those displacements. Therefore, the solution that constrains the shear stresses to zero on the cut surface, as described above, is still correct.

Averaging the contours on the two halves to remove anti-symmetric errors requires another assumption. The portion of the contour caused by the normal stress must be symmetric, which requires that the stiffness be the same on the two sides of the cut. For homogeneous materials, this assumption is certainly satisfied when a symmetric part is cut precisely in half. In practice, the part only needs to be symmetric about the cut within the region where the stress release has a significant effect. The length of this region is about 1.5 times the Saint Venant's characteristic distance. The characteristic distance is often as the part thickness, but is more conservatively taken as the maximum cross-sectional dimension unless specific information about the stress variation is known [12].

Figure 3 shows another example of an anti-symmetric error that averages away. If cut path is crooked in space, the resulting surface contours are anti-symmetric.

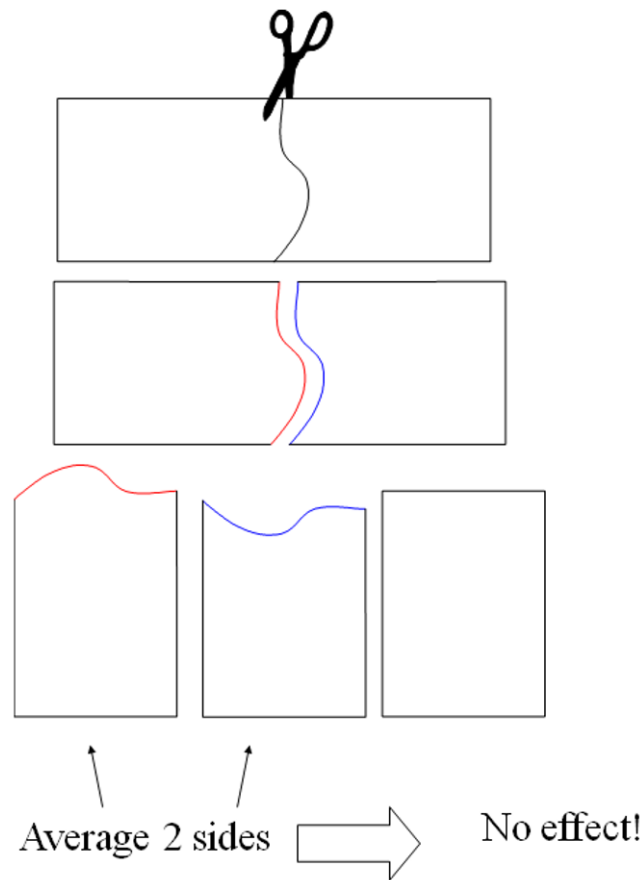


Figure 3. The effect of a crooked cut goes away when the two surfaces contours are averaged.

Figure 4 shows another anti-symmetric effect that in principle averages away, but that should be minimized anyway. This time the cut path is straight in space, but the part is moving as the stresses relax. In Figure 4, the movement occurs because the part is not clamped symmetrically. An experimental example later in this paper shows that the effect can be quite large. Averaging two very different contours can introduce some uncertainty, so both sides of the cut should be clamped to minimize such movement. It will be shown later that other errors are also reduced by good clamping.

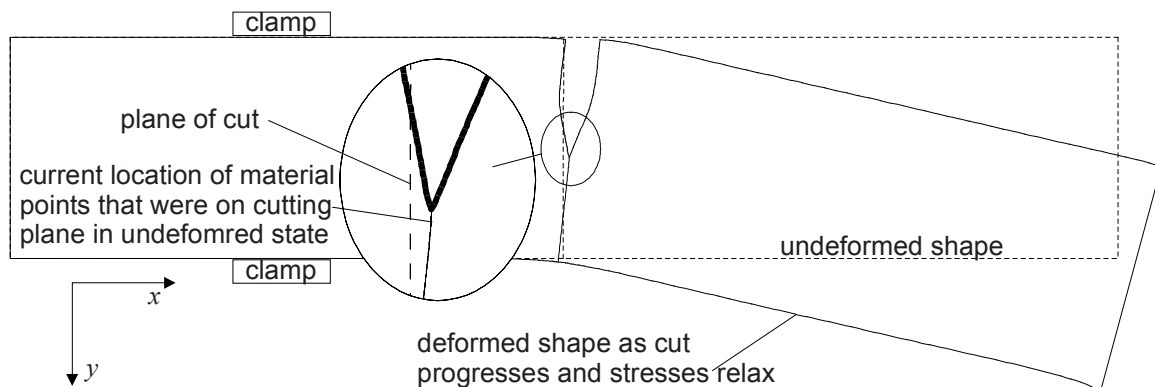


Figure 4. Movement of the cut plane as stresses relax during cutting. In this example, this is caused by asymmetric clamping.

Symmetric Errors

There are other errors that cause symmetric effects that do not average way. Before discussing those, realize that some cutting errors depend on how the cut is made. So far, the only method that has been successfully applied for the contour method is wire Electric Discharge Machining (EDM). Thus, this discussion focuses on EDM cutting.

Several of the symmetric error sources are relatively straightforward:

- Local cutting irregularities, such as wire breakage or overburning at some foreign particle. These are usually small length scale (order of wire diameter) and are removed by the data smoothing process or manually from the raw data
- Change in width of cut. This can occur in heterogeneous materials since the EDM cut width varies for different materials. Sometimes a change in the part thickness (wire direction) can also cause this.
- Wire vibration causing a “bowed” cut [2]. This can usually be avoided by using good settings on the wire EDM.
- Stresses induced by the cutting process can cause errors. Such errors have been studied for wire EDM cutting for use with incremental slitting (crack compliance) [32]. Such effects are generally negligible if “skim cut” or “finish cut” EDM settings are used. Those are low power settings that give higher accuracy and a better surface finish.

The symmetric error sources listed above do not depend on stress magnitude, which leads to a straightforward approach to the issue. A test cut in stress free material would have no contour caused by stresses but would show these errors. Any such error could then be corrected for by subtracting the error off of the measured contour. Most good practitioners make such a test cut standard practice. The simplest way to achieve a nearly stress free test cut is to use the actual test part. After surface contours are measured, one can cut a thin layer off of one of the cut surfaces. The relevant stress components are zero on the free surface and very small if the test cut occurs only a small distance from the original cut surface. The surface contour is measured on the new surface of the larger piece.

Some of those assumptions, primarily the constant cut width, may be less accurate near the edges of the cut surface. For example, the EDM cut width may flare out a little bit at the top and bottom of the cut. Contour results can therefore be quite uncertain near the edges of the cut and should not be generally be reported in that region. With special care, good results have been achieved very close to the edges [4,23].

The contour cut also cannot re-cut previously cut surfaces. This is one of the main reasons that EDM is used for the contour method. In principle, EDM might slightly recut the surface when cutting into a compressive stress. In practice, as sketched in [Figure 5](#), constraint at the cut tip minimizes the amount the cut surfaces can pinch in close behind the wire.

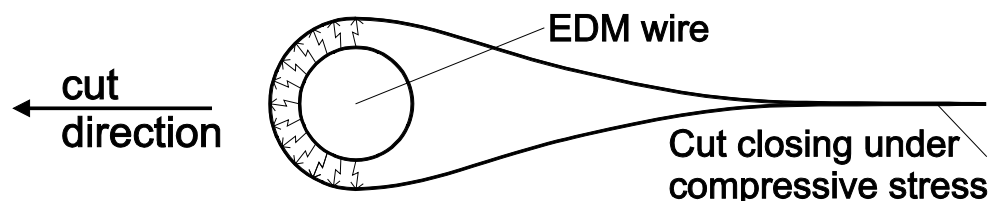


Figure 5. Even cutting into compressive stress, constraint limits the amount the cut surfaces can pinch in close behind the wire.

Most of the rest of this paper will concern a particular symmetric error that can cause significant bias in the contour method results if it is not dealt with. This error, called the “bulge” error, is illustrated in [Figure 6](#). The cutting process makes a cut of constant width w in the laboratory reference frame. As the cutting proceeds, stresses relax and the material at the tip of the cut deforms. The material at the cut tip that was originally w wide has stretched. However, the physical cut will still be only w wide, which means that the width of material removed has been reduced when measured relative to the original state of the body. Since the fundamental assumption is that step **C** of [Figure 1](#) returns the material points to their original configuration, this causes an error that will not

be averaged away. The effect is obviously dependent on the stress state at the cut tip relative of the original stress state. That change in stress can be minimized by securely clamping the part. Also, this effect is a result of the finite width of the cut; a zero-width crack causes only effects that average away, as shown in [Figure 4](#).

Considering anti-symmetric effects that average away as well as the bulge and other asymmetric errors, the fundamental assumption about the cut can be more compactly stated. The cutting process is assumed to remove a constant width of material when measured relative to the state of the body prior to any cutting.

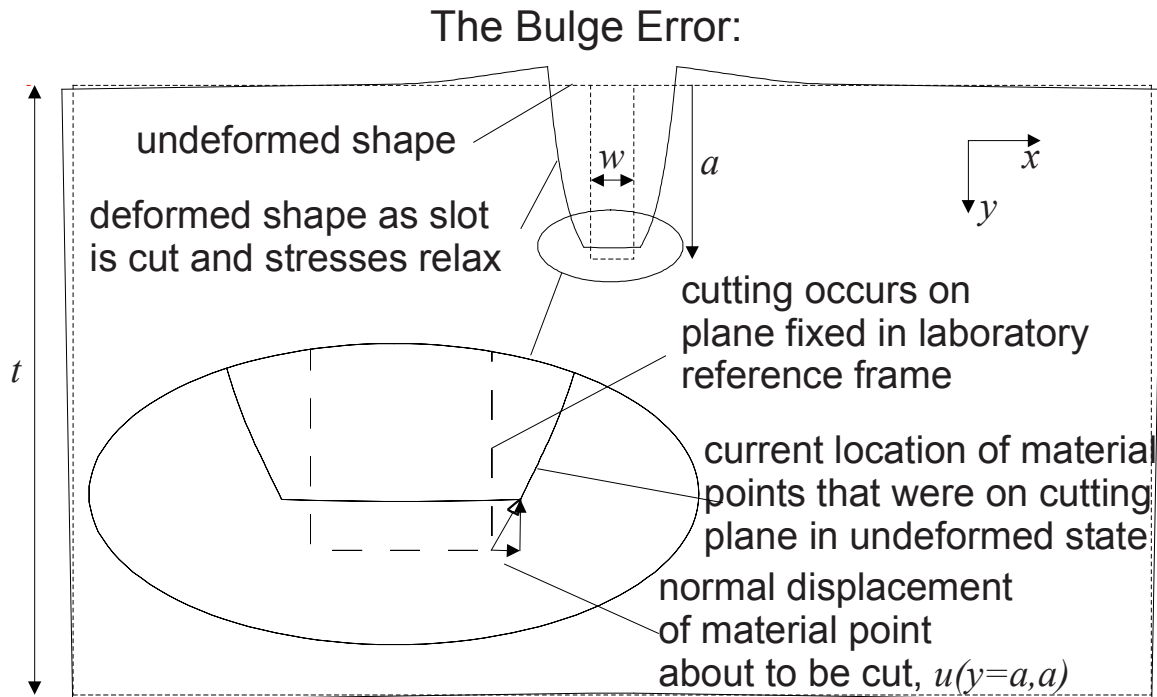


Figure 6. The “bulge” error. As cutting proceeds, the material at the tip of the cut deforms from stress relief. This changes the width of the cut relative to the original state of the body and causes errors.

Cut tip plasticity can also cause symmetric errors. Such errors violate the assumption that stress relaxation is elastic, rather than assumptions about the cut, but they cause very similar effects. Like the bulge error, this effect also depends on the stress state at the cut tip. Thus, any efforts to minimize the bulge error should also reduce plasticity errors. An FEM study showed that plasticity errors were generally small when clamping during cutting was secure [33]. Another study that looked at experimental results showed some significant errors that were explained, using FEM, by plasticity effects [34]. However, those experimental errors might have been a combination of both bulge and plasticity errors.

Summary of Assumptions

- The cutting process does not recut surfaces that have already been cut.
- The stiffness of the part is symmetric with respect to the cut within the regions where stresses are relaxed by the cut
- The cut removes a finite width of material when measured relative to the state of the body prior to any cutting.
- There is no plasticity at the cut tip

The ideal cut would be zero width, introduce no stresses, and allow no plasticity at the tip of the cut.

FINITE ELEMENT STUDY

Finite Element Models

The bulge error was estimated using two-dimensional ABAQUS [35] finite element simulations of sequentially cutting a slot into a beam, similar to Figure 6. A known field of residual stresses was used as an initial condition for the model using a user-defined subroutine. The cutting process was then simulated by sequentially removing elements. After each step, the displacement of appropriate material points originally on the cut plane were recorded to estimate errors in the planar cut assumption. Finally, residual stresses were calculated using the principle of Figure 1 but including the errors, and the difference between the calculated residual stresses and the known residual stresses were analyzed.

Several assumptions were used for the simulations. Isotropic, linear elastic material behavior is assumed throughout the analysis. It is also assumed that the cut is perfectly planar in space; hence, the deviations come only from deformation of the material. For meshing convenience, a square slot bottom was used. Since an EDM cut has a round bottom, this assumption may introduce errors. Dimensions of the beam were normalized to a beam thickness, t , of one unit. A total beam length of four units was chosen in order to minimize any effects from the free ends. Plane stress deformation was assumed.

Legendre polynomials were chosen for the residual stresses because Legendre polynomials of order two and greater automatically satisfy force and moment equilibrium over the beam cross section. For each simulation, the appropriate Legendre polynomial was used to initialize $\sigma_x(y)$ in the region of the cut. The other two stress components, σ_y and τ_{xy} , were initialized to zero in the region of the cut. The stresses elsewhere in the beam were specified such that local equilibrium and the stress-free boundary conditions were satisfied everywhere. The residual stress distributions were all normalized to a peak value of unity.

The choice of the elastic modulus E has no effect on the final stress values calculated from the displacements, since it proportionally affects both the error magnitude and the actual contour. Nonetheless, an E of 1000 was used rather in order to give reasonably scaled displacements; the σ_{max}/E ratio of 0.001 is consistent with typical residual stress magnitudes in metals. Since E has no effect on the final stresses calculated, plane strain can be simulated by replacing E with $E/(1-\nu^2)$; plane stress and plane strain will give the same results if the analysis is consistent.

The deviations from a planar cut assumption were estimated by considering the displacement of the material point where cutting is about to occur. Referring to Figure 6, the material point at the bottom corner of the slot is the next to be cut. The material point that was originally on the plane where cutting is occurring has displaced. In the actual cutting process, the wire will cut this point flush with the original cut plane. Therefore, the deviation from the flat cut assumption is given by the displacement of this material point normal to the cut plane, in the x direction. The y -displacement is not important.

A Lagrangian coordinate system is used to track the deformations. The displacements $u(x,y,a)$ refers to the x -direction displacement after the cut is at depth a of the material point that was at the coordinate (x,y) in the original configuration of the system. Because the only displacement that is relevant for this simulation is the displacement of points at the fixed value of x for the cut plane, the displacement is reported just as $u(y,a)$. The final contour of the cut surface is given by the displacements after the cut and is designated by $u(y,final)$. The results of the sequential cutting simulation were used as input to a subsequent analysis to calculate the effect of the cutting deviation on the residual stress measurements of the contour method. The final contour of the cut surface from the simulation was combined with the cutting error to give the displacement boundary conditions used to calculate the residual stress per the third part of Figure 1:

$$u(y) = -(u(y, final) - u(y = a, a)), \quad (1)$$

where the initial negative sign appears because calculating the original residual stresses requires applying the opposite of the measured contour.

This stress calculation makes two additional assumptions. The small displacements of the material on the cut plane were not accounted for in the material removed for the simulation. The simulation removed elements with edges that were originally on the cut plane but were no longer on the cut plane at the time of removal. Because the displacements are small, the difference has a negligible effect on the results of the stress calculations. An

exact simulation of the material removal would require adaptive remeshing or some other process, and such extra effort is not justified by the small changes that would result.

Simulation Results: General Features of the Contour Method and the Errors

There are several interesting features in almost all of these simulations. Typical deflection and cutting error profiles are shown in Figure 7 for a simple clamping arrangement: on the top and bottom surfaces of the beam at one thickness away from the cut, symmetric on both sides of the cut. The slot width is 0.01. The quadratic Legendre polynomial stress is used. The bulge error has a shape that is not the same as the stress profile. Rather, the bulge error is approximately proportional to the stress intensity factor, K_{Irs} , at the cut tip from the accumulated effect of releasing residual stress. Combining the bulge error with the theoretical contour gives the contour including the error. The general shape of the contour with cutting error closely parallels that of the deflection without cutting error. The deflection profile has a slightly smaller peak when the cutting error is included. It also shows a phase shift compared to the profile without cutting error, with the peak values shifted closer to the beginning of the cut. Near the end of the cut, the deflection error rises sharply, causing a large difference between the two profiles.

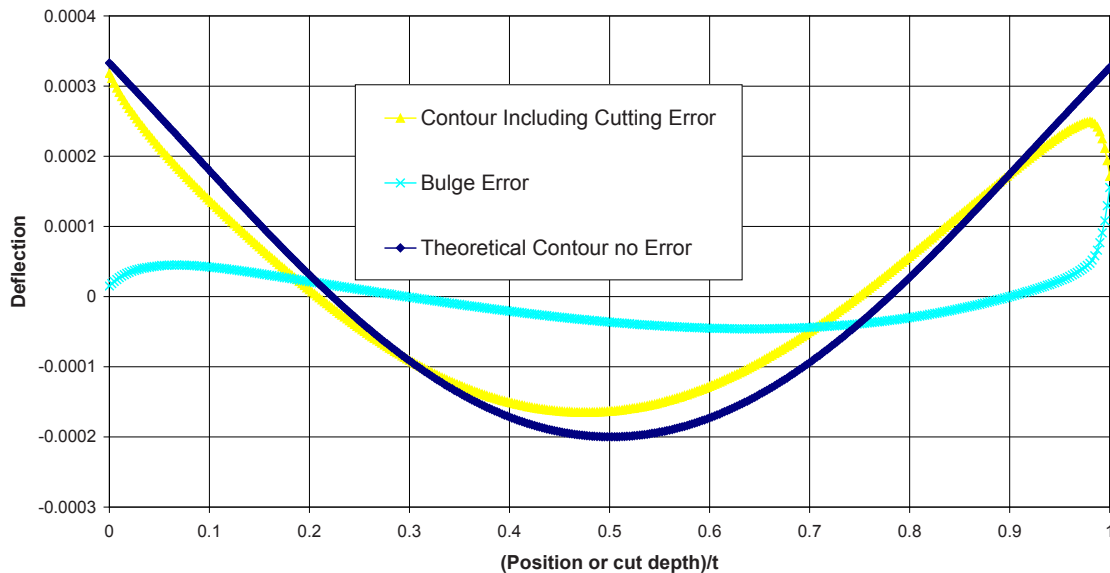


Figure 7. Bulge error for a FEM simulation of a quadratic stress profile.

The stress profiles in Figure 8 show most of the same features as the deflection profiles. The stress error is high near the beginning of the cut and very high near the end of the cut. This matches with the experiences in the actual measurement process, where the edges often show erratic behavior. However, the effect seems to be exaggerated in these simulations. More work is needed to improve the fidelity of the simulations at the beginning and end of the cut. Near the middle of the cut, the stress error is quite reasonable and seems to follow a smooth curve. Again, it does not seem to be simply related to the initial stress distribution, though a great deal of the error seems to be a phase shift between the profiles with and without cutting error. The peak compressive stress is slightly reduced in magnitude.

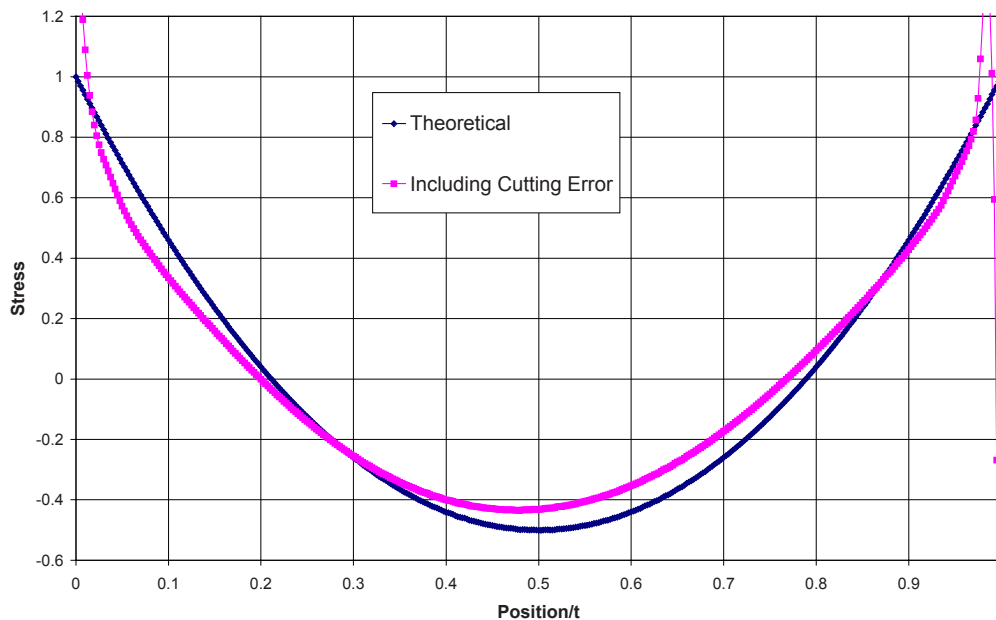


Figure 8. Stresses calculated from the contours of Figure 7 showing the stress error caused by the bulge error.

Effect of Clamping

A variety of clamping arrangements were simulated by constraining various nodes in the FEM model from moving. Because of the difficulty of achieving experimental clamping similar to the perfect constraint, only qualitative conclusions are presented:

- A significant benefit is achieved by going from clamping on one side of the cut to clamping both sides of the cut.
- In the simulations, a significant benefit is achieved by clamping the material all along the cut rather than just at the top and bottom surfaces. However, this is difficult to achieve experimentally.
- Modest but diminishing benefits are achieved by moving the clamping closer to the cut.

Effect of Slot Width

Another simulation examined the effect of slot width on the error. A zig-zag stresses profile typical of beam bending was used as the initial stress. The beam was clamped symmetrically on both sides of the cut. The FEM mesh was adjusted to give different slot widths. Figure 9 shows curves of bulge error as a function of cut depth relative to the beam thickness. The final contour (without error) is also plotted to illustrate the scale of the errors. The bulge error gets larger for larger cut width. The peak magnitude of the bulge error was extracted from each curve in Figure 9, normalized by the peak-to-valley magnitude of the contour, and plotted versus slot width in Figure 10. The peak error increases with slot width, with the slope being greater for narrow slots. A typical experimental slot width, taken from the beam tests to be discussed in the next section, is indicated in order to place the errors in proper context.

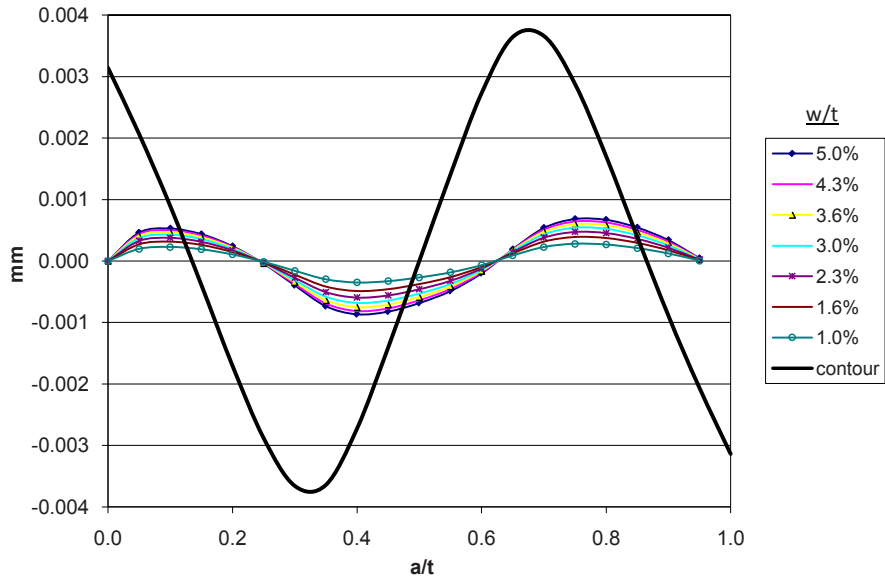


Figure 9. Bulge error as a function of cut depth for different slot widths relative to the beam thickness. The final contour (without error) is also plotted to illustrate the scale of the errors.

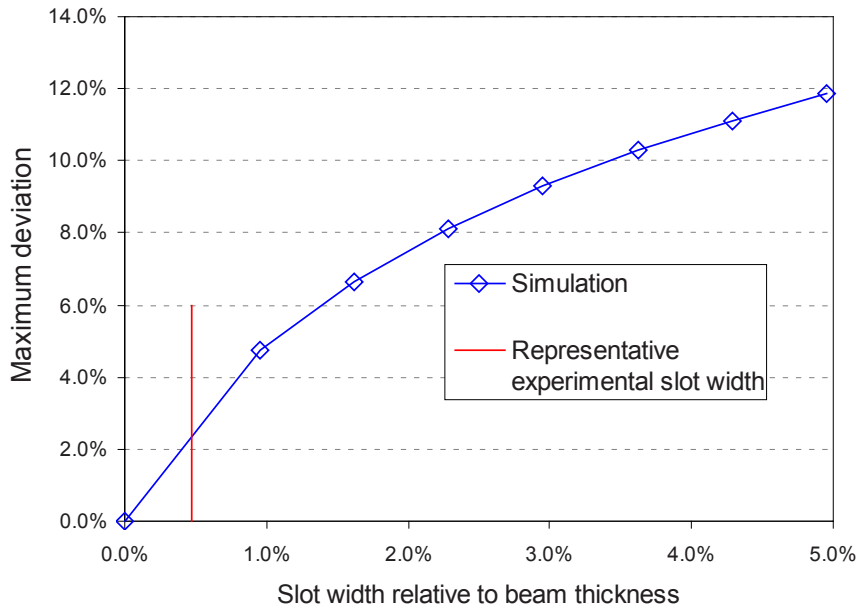


Figure 10. The peak values of bulge error from Figure 9 are normalized relative to the peak-to-peak amplitude of the measured contour and plotted versus slot width.

PROCEDURE FOR CORRECTING BULGE ERROR

The previous analysis, when applied to realistic slot widths, shows that the errors in the residual stress measurement are very reasonable, especially when compared to the errors in other residual stress measurement techniques. However, a method to correct these errors could improve the measurements by this technique.

An iterative finite-element analysis is proposed to correct the deflection error. The basic principle is to reverse the previous analysis technique. The experimentally measured or recorded profile is used to calculate residual stress. Since the errors in the contour method are relatively small, and the measurable deflection profile closely

parallels the theoretical profile, the calculated stress profile can be used as an initial guess for the theoretical profile. Then the FEM simulation described above is used to estimate the bulge error. The bulge error is used to correct the measured contour and then to calculate stresses now including an estimated bulge error. This process is then repeated until the stress converges.

EXPERIMENTAL

The bulge error and the iterative correction are examined on two bent beam specimens with known residual stress profiles. To prepare the specimen, strain gages were attached to the top and bottom of a stress-relieved stainless steel beam, 30.0mm deep. Residual stresses were induced in the beam by loading it into the plastic range using a four-point bend fixture. On removal of the load, the beam unloaded elastically, leaving permanent plastic deformations and substantial axial residual stresses. During this loading and unloading, the total load and corresponding strains were measured. The profile of the residual stresses was calculated from the measured strain data using the stress-strain curve identification method described by Mayville and Finnie [36]. More details on these specific beams are given elsewhere [2,37].

The first beam, beam A, was used as a known stress specimen for measurements using incremental slitting (crack compliance). As is standard with the slitting method [38], the beam was only clamped on one during the cutting as shown in Figure 11. The one sided clamping will make for a larger bulge error and different contours on the two halves of the beam. Before destructive measurement, the residual stresses in the beam were measured by neutron and x-ray diffraction, and within the associated uncertainty ranges, the results agreed with those of the stress-strain curve calculation [37,39]. A 200 μm diameter hard brass wire was used for the cutting. The cutting was done in 36 steps, at approximately 0.8mm intervals to a final depth of 29.26 mm, 97.5% of the beam depth. After cutting, the width of the cut was measured as 267 μm . Unfortunately, because the beam had not been cut all the way through, the remaining ligament was fractured by hand. That left the final 0.74 mm of the surface without a usable contour.

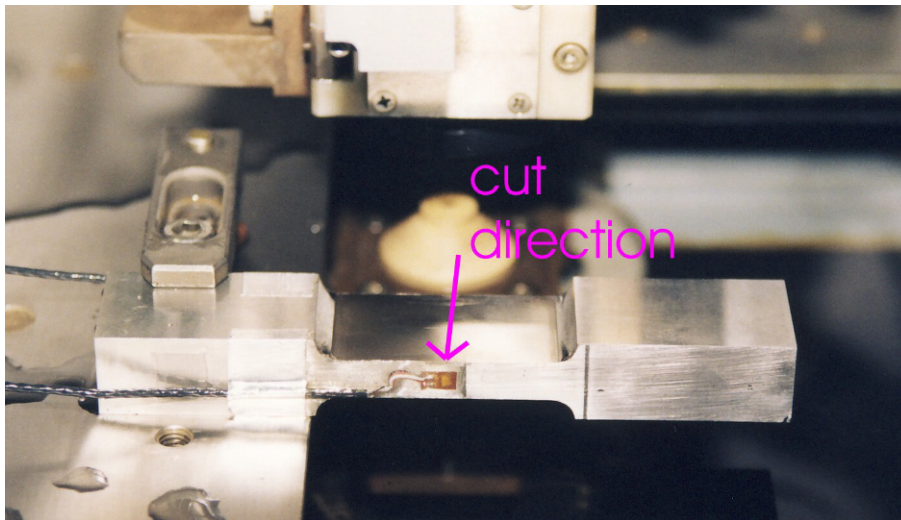


Figure 11. Beam A just prior to EDM cutting for the slitting method. The central section of the beam is 30 mm thick and 10 mm wide.

The second beam, beam B, was measured with the contour method [2]. As shown in Figure 12, it was clamped on both sides of the cut. This time the EDM cut used a 100 μm diameter zinc-coated brass wire and gave a cut width of 140 μm . The beam was cut all the way in half.

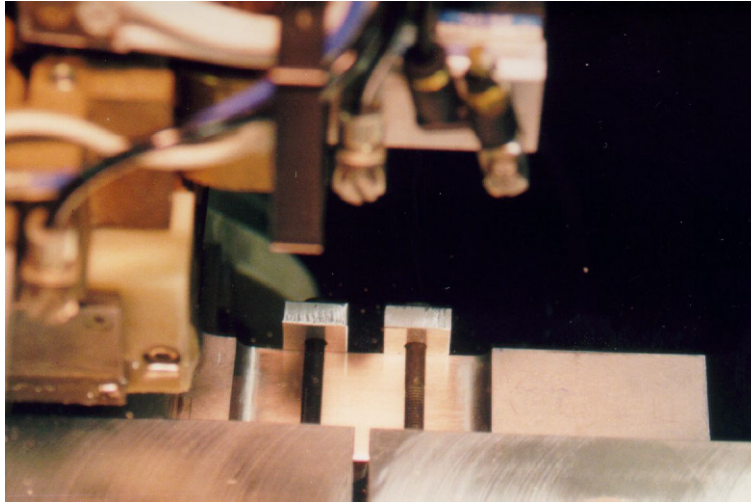


Figure 12. Beam B was clamped on both sides of the cut prior to EDM cutting.

Beam B

Beam B is examined first because it was cut under more ideal conditions: a narrow slot and clamped on both sides of the cut. The contours on the two halves of the beam were very similar, so the average was used for all subsequent calculations. By symmetry, only half of the beam was modeled (in 2D) with FEM. Displacement boundary conditions were applied on the top and bottom surfaces of the beam where the clamps from Figure 12 were located. Figure 13 shows the contours calculated with the iterative correction procedure. Because the correction is small, the correction has converged by the second iteration. Figure 14 shows the stress results compared with the stresses predicted in the bend test. The correction, while not large, has moved the contour results closer to the bend test prediction. Now the results generally agree within the uncertainty in the bend test prediction.

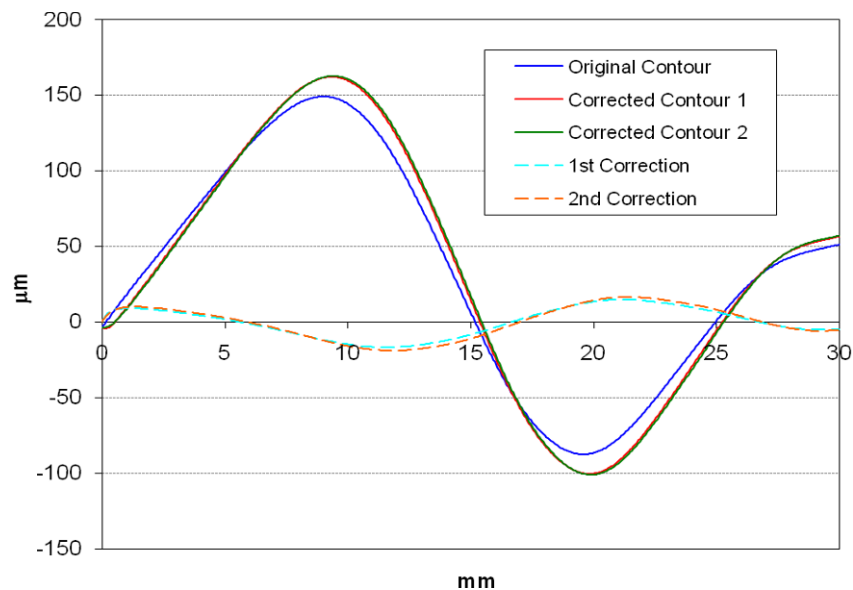


Figure 13. Iterative correction to measured contour on beam B.

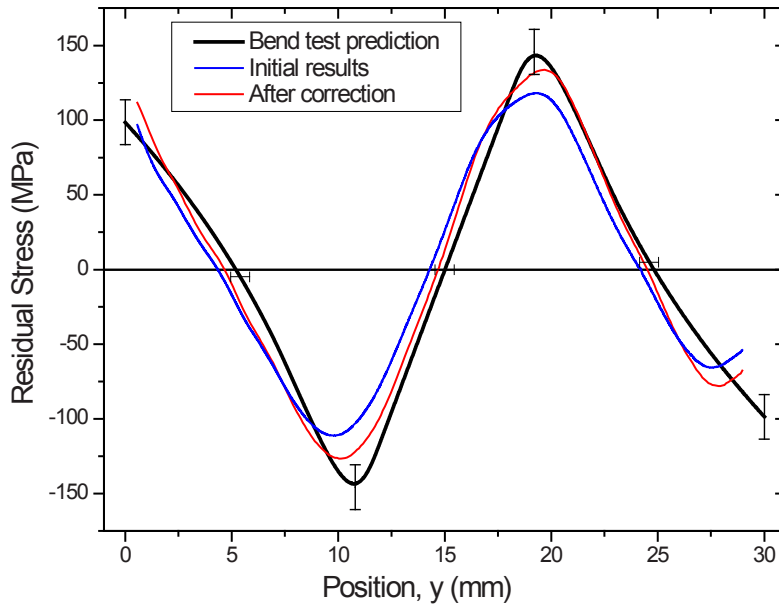


Figure 14. Contour method results before and after bulge correction compared with the prediction from the bend test.

Beam A

Because it was cut in such a non-ideal way for the contour method, with a wide slot and one sided clamping, beam A represents a challenging test for the iterative correction. Figure 15 shows the drastic difference between the contours measured on the two halves of the beam. Figure 16 shows results from beam A calculated using the average contour as well as using the contour from each half individually. The results are compared with bend test prediction and slitting and neutron diffraction measurements [39]. In spite of the large difference in the contours, the stresses calculated using the average contour do an impressive job of matching the bend test prediction and independent measurements.

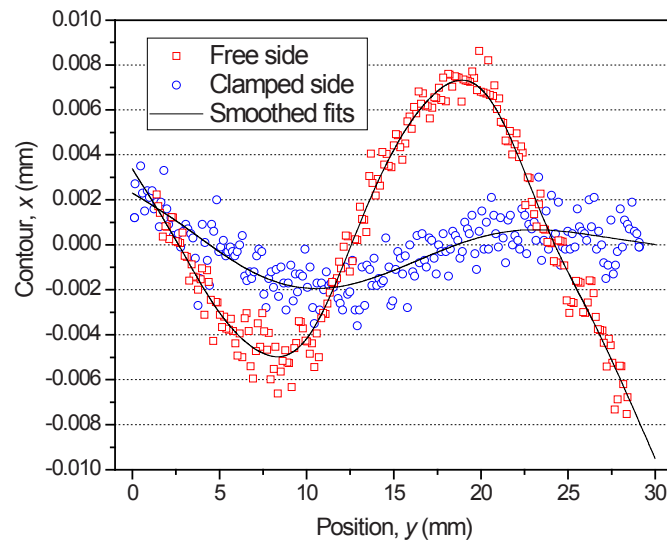


Figure 15. The surface contours measured on the two halves of beam A are very different.

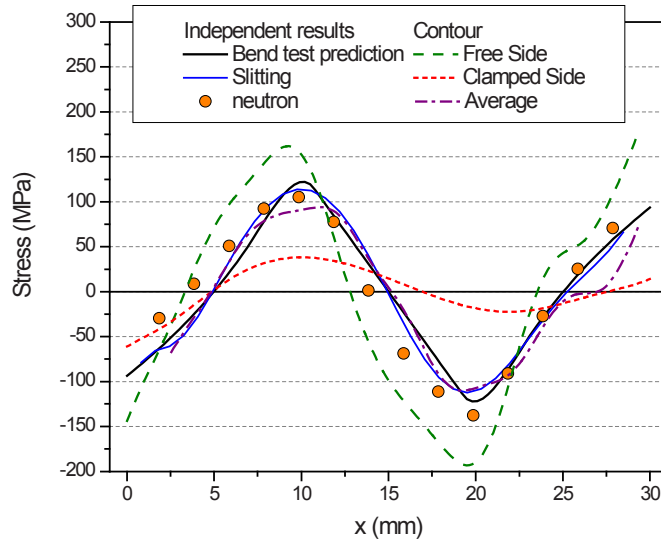


Figure 16. Stress results from beam A calculated using the average contour as well as using the contour from each half individually. Results compared with bend test prediction and slitting and neutron diffraction measurements.

A full 2D (no symmetry) FEM model was used to perform the iterative correction on the beam A results. Displacement boundary conditions were applied on the top and bottom surfaces of the beam where the clamps from Figure 11 were located. The contours had to be extrapolated to cover the final 0.74 mm of the surface that had been fractured off.

Because the contour on the free side of beam A over-predicted the stress magnitude, see Figure 16, the correction was also over-predicted, which led to a non-convergent solution. So for the first iteration only, half of the predicted correction was applied. Figure 17 shows that the correction was then reasonably stable and converged after several iterations. The average of the last two iterations compares quite well with the stresses predicted by the bend test.

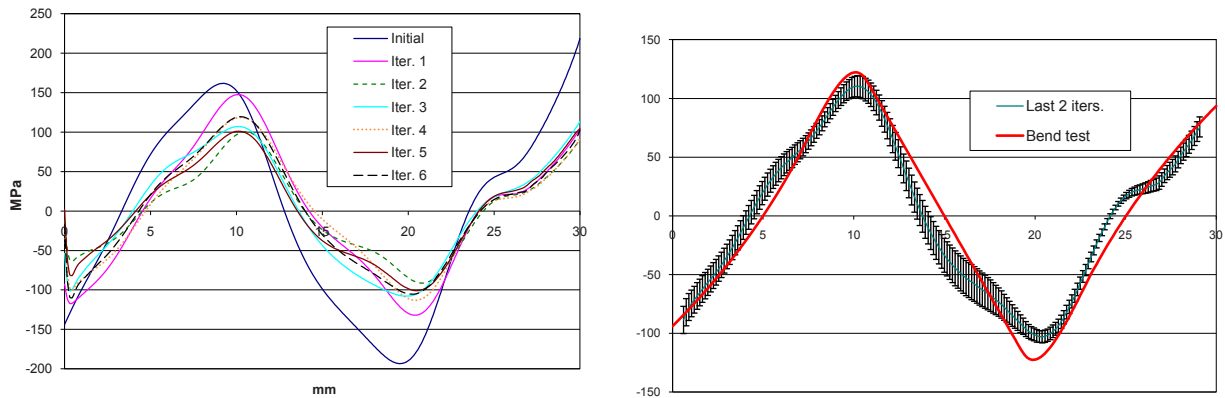


Figure 17. Iterative correction applied to the unclamped half of beam A.

Considering the starting point for the clamped half of beam A, a good result from the iterative correction was not expected. The results in Figure 15 and Figure 16 do not even have the correct shape. Figure 18 shows the iterative correction. Even though the results are poor at the ends of the beam, the central results slowly converge towards the expected results from the bend test analysis.

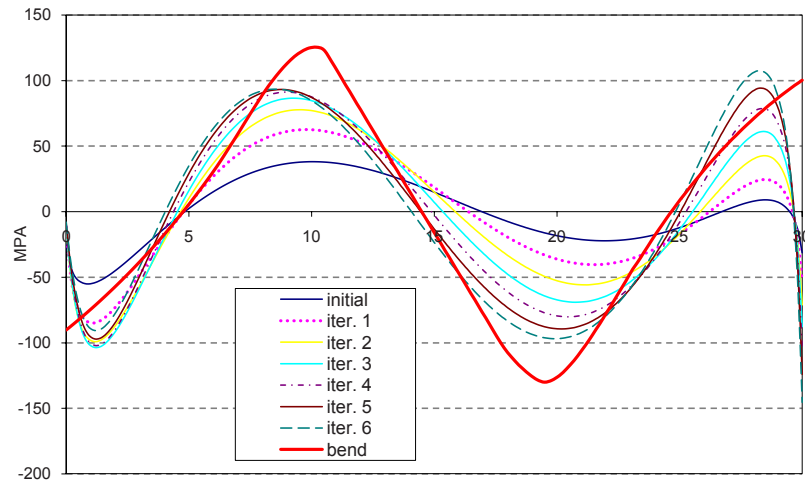


Figure 18. The iterative correction applied to the clamped half of beam A.

DISCUSSION

Both the bulge effect and plasticity errors (only briefly mentioned in this paper) are apparently dependent on the stress state at the cut tip, which can be characterized by the intensity factor, K_{IRS} , at the cut tip from the accumulated effect of releasing residual stress. Similar strategies could be used for both effects. More secure clamping, e.g., [20], would experimentally minimize the errors. Analytical corrections based on fracture mechanics analysis might be successful. Because of the dependence on K_{IRS} , such errors will depend on the direction of the cut.

Although the bulge error decreases for decreasing cut width, other errors might increase. Some difficulties getting good cuts with wire under 100 μm diameter have been observed.

The iterative correction procedure using FEM is promising. Some improvements need to be made on handling the beginning and end of the cut. The procedure is conceptually straightforward and was demonstrated in 2D. There is no conceptual difficulty in applying the procedure in 3D, but keep track of displacements at all the correct nodes for each cut depth would be tedious. A scripting procedure could simplify matters. Scripting interfaces are now available for many commercial finite element codes.

CONCLUSION

The assumptions about the cut for the contour method are

- The cutting process does not recut surfaces that have already been cut.
- The stiffness of the part is symmetric with respect to the cut within the regions where stresses are relaxed by the cut
- The cut removes a finite width of material when measured relative to the state of the body prior to any cutting.
- There is no plasticity at the cut tip

Deviations from these assumptions can cause errors:

- Cutting errors can be divided into errors that cause perturbations to the measured contours that are anti-symmetric with respect to the cut plane, and those that are symmetric. Anti-symmetric errors are removed by averaging the contours measured on the two halves of the part. Symmetric errors do not average away.
- The bulge error, a symmetric error, tends to cause stress profiles to show both a reduced peak stress magnitude and a spatial shift of the peaks
- The bulge error depends on the direction of the cut
- The bulge error is reduced the more securely material near the cut is clamped

- The bulge error decreases for decreasing slot width
- The bulge error can be modeled with FEM and an iterative correction is possible.
- Larger errors are expected at the beginning and end of the cut.

The ideal cut would be zero width, introduce no stresses, and allow no plasticity at the tip of the cut.

Some conclusions can be made about best practices for the contour method:

- The part should be clamped securely on both sides of the cut during cutting
- A stress-free test cut should be used as a control check on cutting assumptions. The test cut can be achieved after the contour measurement by cutting a thin slide off of the cut surface.
- Contour results are uncertain near the edges of the cut and should not be reported in that region unless special care is used to get better results there.

ACKNOWLEDGEMENTS

This work was performed at Los Alamos National Laboratory, operated by the Los Alamos National Security, LLC for the National Nuclear Security Administration of the U.S. Department of Energy under contract DE-AC52-06NA25396. By acceptance of this article, the publisher recognizes that the U.S. Government retains a nonexclusive, royalty-free license to publish or reproduce the published form of this contribution, or to allow others to do so, for U.S. Government purposes.

REFERENCES

- [1] Withers PJ (2007) Residual Stress and Its Role in Failure. *Reports on Progress in Physics* 70:2211-2264.
- [2] Prime MB (2001) Cross-Sectional Mapping of Residual Stresses by Measuring the Surface Contour after a Cut. *Journal of Engineering Materials and Technology* 123:162-168.
- [3] Prime MB, Sebring RJ, Edwards JM, Hughes DJ, Webster PJ (2004) Laser Surface-Contouring and Spline Data-Smoothing for Residual Stress Measurement. *Experimental Mechanics* 44:176-184.
- [4] Johnson G, (2008), "Residual Stress Measurements Using the Contour Method," Ph.D. Dissertation, University of Manchester.
- [5] DeWald AT, Rankin JE, Hill MR, Lee MJ, Chen HL (2004) Assessment of Tensile Residual Stress Mitigation in Alloy 22 Welds Due to Laser Peening. *Journal of Engineering Materials and Technology* 126:465-473.
- [6] Hatamleh O, Lyons J, Forman R (2007) Laser Peening and Shot Peening Effects on Fatigue Life and Surface Roughness of Friction Stir Welded 7075-T7351 Aluminum. *Fatigue and Fracture of Engineering Material and Structures* 30:115-130.
- [7] Hatamleh O (2008) Effects of Peening on Mechanical Properties in Friction Stir Welded 2195 Aluminum Alloy Joints. *Materials Science and Engineering: A* 492:168-176.
- [8] DeWald AT, Hill MR (2009) Eigenstrain Based Model for Prediction of Laser Peening Residual Stresses in Arbitrary 3D Bodies. Part 2: Model Verification. *Journal of Strain Analysis for Engineering Design* 44:13-27.
- [9] Liu KK, Hill MR (2009) The Effects of Laser Peening and Shot Peening on Fretting Fatigue in Ti-6Al-4V Coupons. *Tribology International* 42:1250-1262.
- [10] Hatamleh O, DeWald A (2009) An Investigation of the Peening Effects on the Residual Stresses in Friction Stir Welded 2195 and 7075 Aluminum Alloy Joints. *Journal of Materials Processing Technology* 209:4822-4829.
- [11] Woo W, Choo H, Prime MB, Feng Z, Clausen B (2008) Microstructure, Texture and Residual Stress in a Friction-Stir-Processed AZ31B Magnesium Alloy. *Acta Mat.* 56:1701-1711.
- [12] Prime MB, Gnaupel-Herold T, Baumann JA, Lederich RJ, Bowden DM, Sebring RJ (2006) Residual Stress Measurements in a Thick, Dissimilar Aluminum Alloy Friction Stir Weld. *Acta Mat.* 54:4013-4021.
- [13] Frankel P, Preuss M, Steuwer A, Withers PJ, Bray S (2009) Comparison of Residual Stresses in Ti6Al4v and Ti6Al2Sn4Zr2Mo Linear Friction Welds. *Materials Science and Technology* 25:640-650.
- [14] Zhang Y, Pratihari S, Fitzpatrick ME, Edwards L (2005) Residual Stress Mapping in Welds Using the Contour Method. *Materials Science Forum* 490/491:294-299.
- [15] Edwards L, Smith M, Turski M, Fitzpatrick M, Bouchard P (2008) Advances in Residual Stress Modeling and Measurement for the Structural Integrity Assessment of Welded Thermal Power Plant. *Advanced Materials Research* 41-42:391-400.

- [16] Kartal M, Turski M, Johnson G, Fitzpatrick ME, Gungor S, Withers PJ, Edwards L (2006) Residual Stress Measurements in Single and Multi-Pass Groove Weld Specimens Using Neutron Diffraction and the Contour Method. *Materials Science Forum* 524/525:671-676.
- [17] Withers PJ, Turski M, Edwards L, Bouchard PJ, Buttle DJ (2008) Recent Advances in Residual Stress Measurement. *The International Journal of Pressure Vessels and Piping* 85:118-127.
- [18] Zhang Y, Ganguly S, Edwards L, Fitzpatrick ME (2004) Cross-Sectional Mapping of Residual Stresses in a VPPA Weld Using the Contour Method. *Acta Mat.* 52:5225-5232.
- [19] Thibault D, Bocher P, Thomas M (2009) Residual Stress and Microstructure in Welds of 13%Cr-4%Ni Martensitic Stainless Steel. *Journal of Materials Processing Technology* 209:2195-2202.
- [20] Hacini L, Van Lê N, Bocher P (2009) Evaluation of Residual Stresses Induced by Robotized Hammer Peening by the Contour Method. *Experimental Mechanics* 49:775-783.
- [21] Turski M, Edwards L (2009) Residual Stress Measurement of a 316L Stainless Steel Bead-on-Plate Specimen Utilising the Contour Method. *International Journal of Pressure Vessels and Piping* 86:126-131.
- [22] Kelleher J, Prime MB, Buttle D, Mummery PM, Webster PJ, Shackleton J, Withers PJ (2003) The Measurement of Residual Stress in Railway Rails by Diffraction and Other Methods. *Journal of Neutron Research* 11:187-193.
- [23] Evans A, Johnson G, King A, Withers PJ (2007) Characterization of Laser Peening Residual Stresses in Al 7075 by Synchrotron Diffraction and the Contour Method. *Journal of Neutron Research* 15:147-154.
- [24] Martineau RL, Prime MB, Duffey T (2004) Penetration of HSLA-100 Steel with Tungsten Carbide Spheres at Striking Velocities between 0.8 and 2.5 km/s. *International Journal of Impact Engineering* 30:505-520.
- [25] Holden TM, Suzuki H, Carr DG, Ripley MI, Clausen B (2006) Stress Measurements in Welds: Problem Areas. *Materials Science and Engineering A* 437:33-37.
- [26] Schajer GS (2001) "Residual Stresses: Measurement by Destructive Testing." *Encyclopedia of Materials: Science and Technology*, Elsevier, 8152-8158.
- [27] DeWald AT, Hill MR (2006) Multi-Axial Contour Method for Mapping Residual Stresses in Continuously Processed Bodies. *Experimental Mechanics* 46:473-490.
- [28] Pagliaro P, (2008), "Mapping Multiple Residual Stress Components Using the Contour Method and Superposition," Ph.D. Dissertation, Università degli Studi di Palermo, Palermo.
- [29] Pagliaro P, Prime MB, Swenson H, Zuccarello B (2010) Measuring Multiple Residual-Stress Components Using the Contour Method and Multiple Cuts. *Experimental Mechanics* 50:187-194.
- [30] Kartal ME, Liljedahl CDM, Gungor S, Edwards L, Fitzpatrick ME (2008) Determination of the Profile of the Complete Residual Stress Tensor in a VPPA Weld Using the Multi-Axial Contour Method. *Acta Mat.* 56:4417-4428.
- [31] Bueckner HF (1973) "Field Singularities and Related Integral Representations." *Mechanics of Fracture* G. C. Sih, ed., 239-314.
- [32] Cheng W, Finnie I, Gremaud M, Prime MB (1994) Measurement of near-Surface Residual-Stresses Using Electric-Discharge Wire Machining. *Journal of Engineering Materials and Technology-Transactions of the ASME* 116:1-7.
- [33] Shin SH (2005) FEM Analysis of Plasticity-Induced Error on Measurement of Welding Residual Stress by the Contour Method. *Journal of Mechanical Science and Technology* 19:1885-1890.
- [34] Dennis RJ, Bray, D.P., Leggatt, N.A., Turski, M. , (2008), "Assessment of the Influence of Plasticity and Constraint on Measured Residual Stresses Using the Contour Method." *2008 ASME Pressure Vessels and Piping Division Conference*, Chicago, IL, USA, PVP2008-61490.
- [35] Abaqus 6.9, ABAQUS, inc., Pawtucket, RI, USA, 2009.
- [36] Mayville R, Finnie I (1982) Uniaxial Stress-Strain Curves from a Bending Test. *Experimental Mechanics* 22:197-201.
- [37] Schajer GS, Prime MB (2006) Use of Inverse Solutions for Residual Stress Measurements. *Journal of Engineering Materials and Technology* 128:375-382.
- [38] Cheng W, Finnie I (2007) *Residual Stress Measurement and the Slitting Method*, Springer Science+Business Media, LLC, New York, NY, USA.
- [39] Prime MB, Rangaswamy P, Daymond MR, Abeln TG, 1998, "Several Methods Applied to Measuring Residual Stress in a Known Specimen." *Proc. 1998 SEM spring conference on experimental and applied mechanics*, 1-3 Jun 1998, Society for Experimental Mechanics, Inc., 497-499.

Measurements of Residual Stress in Fracture Mechanics Coupons

Michael R. Hill¹, John E. VanDalen² and Michael B. Prime³

¹Mechanical and Aerospace Engineering Department,
University of California, One Shields Avenue,
Davis, CA 95616 USA, mrhill@ucdavis.edu

²Hill Engineering, LLC, McClellan, CA USA

³Los Alamos National Laboratory, Los Alamos, NM USA

ABSTRACT

This paper describes measurements of residual stress in coupons used for fracture mechanics testing. The primary objective of the measurements is to quantify the distribution of residual stress acting to open (and/or close) the crack across the crack plane. The slitting method and the contour method are two destructive residual stress measurement methods particularly capable of addressing that objective, and these were applied to measure residual stress in a set of identically prepared compact tension (C(T)) coupons. Comparison of the results of the two measurement methods provides some useful observations. Results from fracture mechanics tests of residual stress bearing coupons and fracture analysis, based on linear superposition of applied and residual stresses, show consistent behavior of coupons having various levels of residual stress.

INTRODUCTION

Fracture mechanics testing typically relies on test coupons being free from residual stress, though limited guidance is provided to ensure that coupons are stress free. For materials that cannot be tested in coupons free from residual stress, it may be that measured residual stress can be used to obtain a test outcome (i.e., fracture mechanics properties) independent of residual stresses.

The superposition of stress intensity factors provides a basis for residual stress corrections that might be applied for properties determined under generally linearly elastic, small scale yielding conditions, such as low-energy fracture (brittle or ductile in nature) or fatigue crack growth in metallic materials. Superposition of stress intensity factors (SIFs) under monotonic or cyclic loading can be expressed simply as

$$K_{Tot} = K_{App} + K_{RS} \quad (1)$$

where K_{App} is the SIF from applied loads, K_{RS} is the SIF from residual stress, and K_{Tot} is the total SIF. Testing standards (e.g., ASTM E399, E647, and so forth) provide expressions for K_{App} while K_{RS} would be determined using newly established standard procedures.

The objective of this work is to provide example measurements of the opening-direction residual stress on the crack plane, and the residual stress intensity factor, in fracture coupons containing various levels of residual stress. This paper is a follow-up to recently reported work that contains details of fracture tests on the same set of coupons [1].

METHODS

Material and geometry

Aluminum alloy 7075-T6 was selected for this test program due to its prevalent use in a variety of applications. This alloy exhibits low-energy ductile fracture with a rising R -curve. The material was received as clad plate 4.8 mm thick. Handbook [2] mechanical properties of 7075-T6 are listed in [Table 1](#).

Compact tension, C(T), coupons were used in this study, as described in several of the ASTM fracture toughness testing standards (e.g., ASTM E 561-98 – “Standard Practice for R -Curve Determination”). The C(T)

coupon is well suited for this work because of its accepted use in fracture toughness testing, simple geometry, and one-dimensional crack, characterized by the crack length a . Coupon geometry had thickness B of 3.81 mm and a characteristic width dimension W of 50.8 mm (Fig. 1). Coupons were cut such that crack growth occurred in the L-T orientation. To obtain the 3.8 mm coupon thickness from the stock material, material was machined in equal amounts from each side so that the coupons lay in the T/2 plane and the original clad layer was removed. A starter notch with integral knife edges for crack mouth opening displacement (CMOD) was cut into each coupon using a wire electric discharge machine (EDM). The EDM notch was 0.3 mm wide and had various lengths, as described below.

S_u (MPa)	S_y (MPa)	E (GPa)	ν	K_{Ic} (MPa m ^{0.5})
552	490	71	0.33	29.0

Table 1 – Mechanical properties of 7075-T6 plate [2]

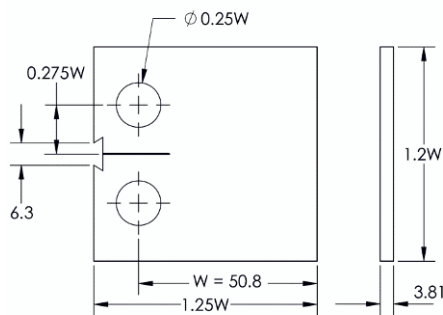


Fig. 1 – 7075-T6 C(T) Coupon (dimensions in mm)

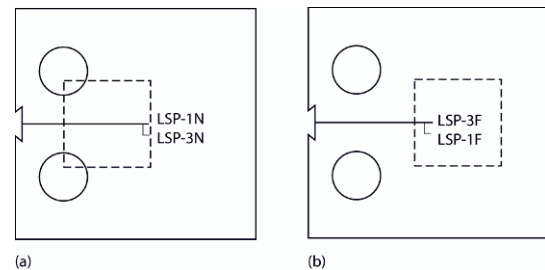


Fig. 2 – Location of LSP regions (square regions enclosed by dashed line, having side length of 22.9 mm) (a) near the front face (12.7 mm from the front face) and (b) far from the front face (12.7 mm from the back face) (also shown are initial crack lengths used for fracture tests of the coupon sets)

Residual stress treatment

Laser shock peening (LSP) was used to produce residual stress bearing coupons. In thin geometries, like the C(T) coupons used here, LSP can generate through-thickness compressive residual stress in the treated area. The LSP process uses laser-induced shocks to drive plastic deformation into the surface of a part [3,4]. For this work, LSP was applied using industrial facilities at Metal Improvement Company (Livermore, CA). LSP parameters were chosen to achieve high levels of residual stress in the C(T) coupons. Earlier work in high strength aluminum alloys found that deep residual stress was induced in 19 mm thick coupons using an LSP parameter set of 4 GW/cm² irradiance per pulse, 18ns pulse duration, and 3 layers of treatment (denoted 4-18-3) [5,6]. It was further found that 4-18-3 provided significant high-cycle fatigue life improvements in 19 mm thick bend bars.

For the present work, LSP was used to obtain two *amounts* of residual stress effect and either *positive* or *negative* residual stress effect on fracture toughness. To obtain sets of coupons with different amounts of residual stress, LSP was applied using a single layer, at 4-18-1, or using three layers, at 4-18-3, where three-layer LSP induces a greater amount of residual stress. To obtain sets of coupons with either positive or negative residual stress effects on fracture, LSP was applied in two different areas, each a square with side length of 22.9 mm and located either *near to* or *far from* the front face of the C(T) coupon (Fig. 2). Applying LSP near the front face results in compressive residual stress on the crack faces, providing a negative contribution to fracture (i.e., a negative residual stress intensity factor), while applying LSP far from the front face results in tensile residual stress on the crack faces, providing a positive contribution to fracture. In total, five coupon conditions were used in this study: as-machined (AM); one-layer LSP applied near the front face (LSP-1N); three-layer LSP applied near the front face (LSP-3N); one-layer LSP applied far from the front face (LSP-1F); and, three-layer LSP applied far from the front face (LSP-3F). LSP coupons were treated on both sides, alternating sides between each layer application until each side was treated with the desired number of layers.

Residual stress and K_{RS} measurements

Two-dimensional residual stress distributions were measured on the prospective crack plane of AM and LSP-3N coupon blanks using the contour method [7,8]. Measurements were made on C(T) blanks that had holes, but did not have initial notches. Wire EDM was used to cut the coupons in half and expose the crack plane. After cutting, an area-scanning profilometer was used to measure the resulting out-of-plane deformation of the cut surface, on both halves of the coupon. The measured deformations of the two halves were averaged and smoothed to remove effects of cut path wandering, shear stress, and surface roughness. The negative of the averaged and smoothed deformations were applied as displacement boundary conditions in a three-dimensional, linear elastic finite element model of one-half of the coupon. The stress resulting from the elastic finite element calculation provided the experimental estimate of residual stress in the coupon.

Thickness average residual stresses were measured in all coupon conditions using the slitting method. A strain gage with an active grid length of 0.8 mm was applied to the center of the back face of the coupon (opposite the crack mouth). Wire EDM was used to incrementally extend a slit through the coupon, with strain recorded after each increment of slit depth. Residual stress as a function of position across the coupon was determined from strain versus slit depth data using the approach recently described by Schajer and Prime [9] and adapted to the geometry of the C(T) coupon.

Measured residual stresses from slitting and contour are compared to one another to determine the degree of consistency among the methods employed. The comparison is made on thickness-average residual stress as a function of position across the crack plane, with the two-dimensional stresses from the contour measurements averaged at a set of positions across the crack plane.

The slitting method was also used to determine the residual intensity factor as a function of crack length, $K_{RS}(a)$, following Schindler's method for a thin rectangular plate [10]. $K_{RS}(a)$ was computed from the influence function $Z(a)$ provided in [10], the plane stress modulus of elasticity $E' = E$ (given in Table 1), and the derivative of strain with respect to slit depth

$$K_{RS}(a) = \frac{E'}{Z(a)} \frac{d\varepsilon(a)}{da}. \quad (2)$$

The influence function $Z(a)$ of [10] does not account for the holes present in the C(T) coupon, which was assumed to be of negligible effect. In addition, care was taken to account for the different definitions of crack size used by ASTM (measured from the load-line) and Schindler (measured from the front edge), which can cause error (or misinterpretation of results, as in [11]). The derivative of strain with respect to crack length was computed using a moving five-point quadratic polynomial, with slope evaluated numerically at the middle point.

Residual stress intensity factors were computed from measured residual stress using a Green's function for the C(T) coupon recently published by Newman, et al [12] and numerical integration, paying careful attention to the singularity of the Green's function [13]. Residual stress intensity factors computed from measured residual stresses are compared against those determined from Eqn. (2).

Fracture toughness tests were performed according to ASTM E 561-98 to determine the K-R crack growth resistance curve for each of the five coupon conditions. Replicate tests were run for each condition. Details can be found in our earlier work [1]. The K-R results are presented in terms of applied loading alone, and in terms of total residual stress intensity factor (Eqn. (1)). In addition, initiation toughness was determined in the coupons using data collected during K-R testing, but using the data reduction procedures of ASTM E 399 to determine K_{IQ} .

RESULTS

Residual stress fields on the crack plane determined using the contour method are illustrated in Fig. 3 for two AM and one LSP-3N coupons. Residual stress in the AM coupons have peak values around ± 20 MPa and have a similar through thickness distribution at all points across the coupon width, which is consistent with residual stress from plate rolling. The LSP coupon has a maximum compressive residual stress of -290 MPa that occurs on the surface near the middle of the coupon, and a maximum tensile stress of 350 MPa that occurs at the front face of the coupon. In the peened region (from $x = 12.7$ to $x = 35.6$ mm, where x is measured from the front face of the coupon), residual stress is compressive at the surfaces and grows more positive monotonically with position toward the coupon mid-thickness. Outside the peened region, residual stress is nearly uniform through thickness but varies with position across the width. The residual stress distribution features inside the LSP region are consistent with double sided peening and outside the LSP region are consistent with plate bending and axial stresses that arise in the coupon to achieve residual stress equilibrium (zero net force and moment across the contour plane).

Slitting residual stress measurements show that the location of the peened area significantly affects the stress distribution across the coupon (Fig. 4). LSP near the front face of the coupon (LSP-1N and LSP-3N) produces tensile stresses at the front face that give way to compression 12 to 16 mm from the front face. LSP far from the front face (LSP-1F and LSP-3F) creates tensile stresses at the front face and over a region extending 26 to 30 mm from the front face. For the same peened area, the shape of the stress distributions for one-layer and three-layer LSP are quite similar, with 3-layer LSP coupons having about twice as much residual stress.

Thickness average residual stress for the LSP-3N and one of the AM coupons is plotted in Fig. 5. AM coupons have a thickness-average stress of nearly 0 MPa at all points across the coupon, which is consistent with plate rolling. Thickness-average stress in the LSP-3N coupon has maximum tension at the front face (240 MPa) and maximum compression (-150 MPa) near the middle of the LSP area ($x = 28$ mm). The slitting residual stress measurement has a higher gradient near the right edge of the peened area ($x = 36$ mm) than shown for the contour residual stress, but the two measurements are in good agreement (Fig. 5). The difference may be due to surface fitting in the contour data reduction, which softens (spatial) stress gradients.

Estimates of K_{RS} were determined from strain versus depth data using two different procedures, and these are compared in Fig. 6. The first procedure used Eqn. (2), above, and results are shown as symbols in Fig. 6. The second procedure used the residual stress from slitting, reported in Fig. 4, the Green's function of Newman, et al [12], and numerical integration, and the resulting K_{RS} estimates are shown as lines in Fig. 6. There is good agreement between the two calculation procedures. For condition LSP-3N, K_{RS} was also computed using the Green's function and contour thickness-average residual stresses (Fig. 5). The estimates of K_{RS} show good agreement, except for the negative peak in K_{RS} , which appears softened when using the contour stresses and may be the result of surface smoothing (Fig. 7).

At initial crack lengths useful for fracture tests ($0.35W = 18$ mm $\leq a_o \leq 0.55W = 28$ mm), K_{RS} estimates show that $K_{RS}(a)$ is either negative or positive, depending on the location of the LSP area (Fig. 6). At these crack lengths, the far-from-front-face LSP coupons (LSP-1F, LSP-3F) have positive K_{RS} and the near-front-face LSP coupons (LSP-1N, LSP-3N) have negative K_{RS} . K_{RS} for the three-layer LSP coupons (LSP-3F, LSP-3N) are roughly double those for the corresponding one-layer LSP coupons (LSP-1F, LSP-1N). For LSP-3F, the positive K_{RS} reaches 35.9 MPa m^{0.5}, which is quite large, exceeding the material plane strain fracture toughness of 29.0 MPa m^{0.5} (Table 1). The magnitude of the most positive K_{RS} in coupons LSP-1F and LSP-3F (17.7 and 35.9 MPa m^{0.5}) is nearly twice the magnitude of the most negative K_{RS} in coupons LSP-1N and LSP-3N (-10.5 and -16.8 MPa m^{0.5}).

Based on the slitting results (Fig. 6), target initial crack lengths were selected for K-R fracture tests. The target crack lengths chosen for each condition are shown (to scale) with the LSP area in Fig. 2. Compression-compression precracking was performed for the LSP-1F and LSP-3F coupons due to the high magnitude, positive K_{RS} (for further precracking and other details of fracture testing, refer to our earlier work [1]).

Results of fracture testing showed significant and expected effects from LSP-induced residual stress. R -curves in terms of K_{app} are shown for all coupons in Fig. 8. Results for the two AM coupons exhibit typical elastic-plastic blunting behavior until about 30 MPa m^{0.5}, after which monotonically increasing (nearly linear) crack growth resistance is obtained. Compared with the AM results at a given crack length, the LSP-1N and LSP-3N coupons exhibit greater toughness (in terms of K_{app}) and the LSP-1F and LSP-3F coupons exhibit reduced toughness, with the 3-layer coupons having a larger effect in both cases. Comparing results for the two coupons within each coupon subset shows the data to be repeatable. Residual stress corrected R -curves were prepared using Eqn. (1) and using values of K_{RS} determined from Eqn. (2). The corrected R -curves for the different coupon subsets are similar (Fig. 9). The LSP-1N and LSP-3N results exhibit significantly greater elastic-plastic blunting than for the AM coupons, which is consistent with the higher level of applied loading at which they initiate crack extension. After blunting, the R -curves of all coupon subsets are in good agreement, though the LSP-3F coupons exhibit a significantly shallower R -curve.

Values of initiation toughness are very significantly affected by residual stress in terms of applied load (K_Q) but are nearly invariant in terms of total stress ($K_{Q,Tot}$) (Fig. 10). The mean K_Q for AM coupons was 33.1 MPa m^{0.5}, a value slightly greater than K_{Ic} (Table 1), which is expected given the limited coupon thickness. Mean K_Q values for residual stress bearing coupons ranged from 9.69 MPa m^{0.5} for LSP-3F coupons to 51.6 MPa m^{0.5} for LSP-3N coupons. Mean $K_{Q,Tot}$ values ranged from 32.1 MPa m^{0.5} (LSP-3F) to 37.4 MPa m^{0.5} (LSP-1N), with the latter value being somewhat of an outlier.

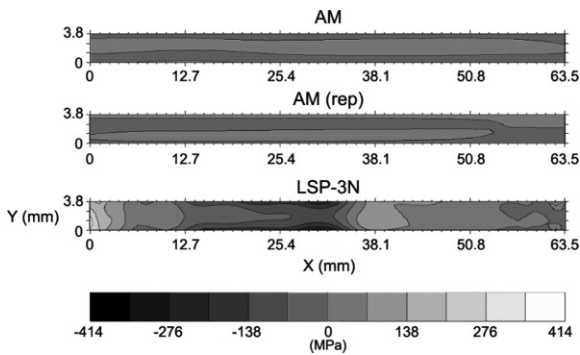


Fig. 3 – Contour measurement results illustrating the residual stress distribution on the plane of the crack for AM and LSP-3N coupons (“rep” indicates a replicate (identical) coupon)

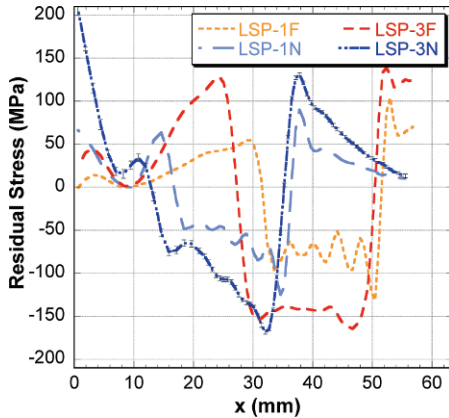


Fig. 4 – Slitting residual stress measurement results (AM condition not measured); one-sigma error bars are plotted for LSP-3N, other conditions exhibit similar levels of uncertainty

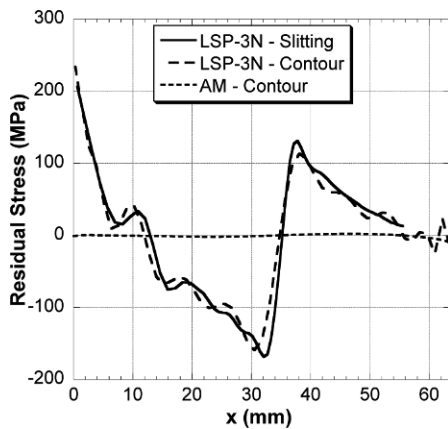


Fig. 5 – Slitting residual stress for LSP-3N plotted with contour through thickness average for LSP-3N and AM conditions

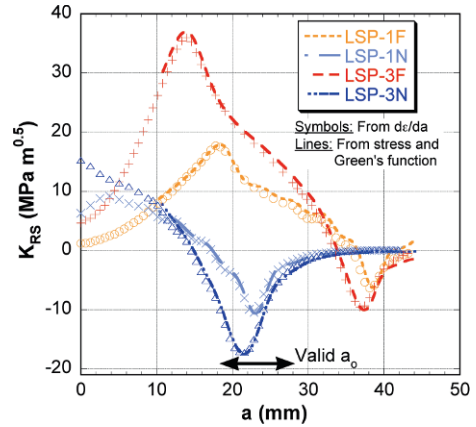


Fig. 6 – Comparison of K_{RS} determined from slitting strain data: symbols are determined from derivative of strain data (Eqn. (2)); lines result from integrating residual stress of Fig. 4 with the Green's function for the C(T) coupon published by Newman, et al. [12]

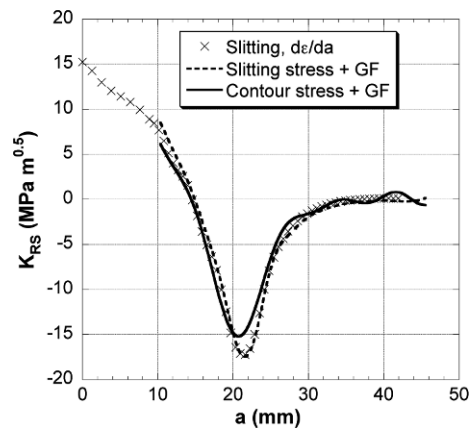


Fig. 7 – K_{RS} for LSP-3N condition computed from derivative of strain data (Eqn. (2)), and measured residual stress from slitting and contour thickness-average stress

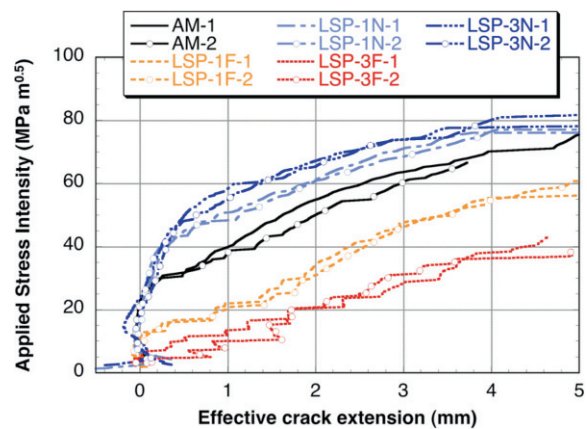


Fig. 8 – R-curve resulting from applied stress intensity factor

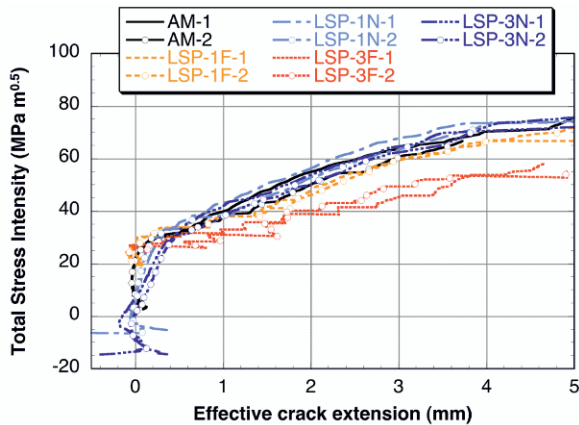


Fig. 9 – R-curve resulting from superposition of applied and residual stress intensity factors; $K_{RS}(a)$ from symbols in Fig. 6

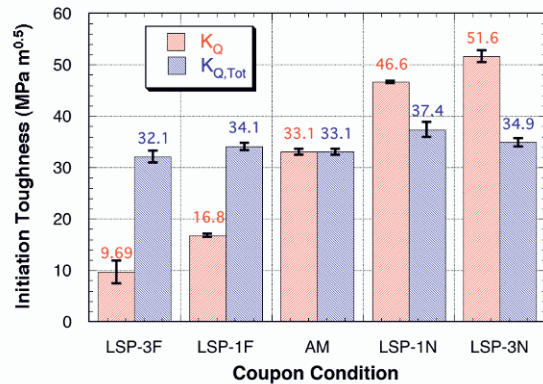


Fig. 10 – Comparison of K_Q and $K_{Q,Tot}$ for the five coupon conditions (bars and values provide mean, error bars indicate range from two coupons); $K_{RS}(a)$ from symbols in Fig. 6

SUMMARY

The present work describes measurements of residual stress in fracture coupons, the determination of residual stress intensity factors (as a function of crack length) from measured stress and more directly using Schindler's method [10], and correlation of observed fracture behavior in high-strength aluminum coupons. The results demonstrate consistent fracture property measurements in residual stress bearing coupons, where residual stress was taken into account; however, the consistency here was dependent on specific methodological choices. First, the material employed is one that exhibits low-energy fracture, and as such, has fracture behavior that is influenced directly (in fact, linearly) by K_{RS} . It remains to be determined whether consistent toughness data could be obtained in residual stress bearing coupons of a significantly more ductile material. Second, fracture toughness and K_{RS} measurements were performed on coupons prepared identically. A test program employing coupons with greater variability (e.g., hand-forgings or welded materials) likely would provide less-consistent results. Third, the coupon geometry had a large width-to-thickness ratio ($W/B \approx 13$), which allowed significant residual stress influence while avoiding complications arising from variations of K_{RS} along the crack front and the potential for non-straight crack fronts (e.g., as for welded joints [14]). While slitting was the best method for the present coupons, a significantly smaller width-to-thickness ratio might require accounting for through-thickness stress variation (e.g., measured by the contour method) and its affect on K_{RS} along the crack front. Follow-on work would need to determine the range of material, coupon geometry, and residual stress fields for which consistent fracture toughness properties can be obtained.

Method selection is an important step when making material property measurements, and the inclusion of residual stress in fracture property testing would require additional standardization activity. Here, the slitting method directly provided $K_{RS}(a)$ from Eqn. (2), which was readily combined with test data. The values of $K_{RS}(a)$ from Eqn. (2) were in very good agreement with those determined from residual stress and Green's function. Slitting was straightforward to implement and the method offers good repeatability (see replicate results for the present coupons reported in [1], as well as repeatability of residual stress reported in [15]). Active standardization of the slitting method, within ASTM Task Group E28.13.02, supports its potential use in fracture toughness testing standards. The good agreement for initiation toughness $K_{Q,Tot}$ and R-curve behavior shown here among coupons containing significantly different distributions of residual stress suggest a course of further work to extend standard fracture toughness tests so that they include residual stress effects for an appropriate range of material, coupon geometry, and residual stress fields.

REFERENCES

- [1] VanDalen, J. E. and Hill, M. R., "Evaluation of residual stress corrections to fracture toughness values," *Journal of ASTM International*, **5**(8), Paper ID JAI101713.
- [2] United States Department of Transportation – Federal Aviation Administration, 2003, *Metallic Materials Properties Development and Standardization*, Report DOT/FAA/AR-MMPDS-01.
- [3] Fabbro, R., Peyre, P., Berthe, L., and Scherpereel, X., 1998, "Physics and applications of laser-shock processing," *Journal of Laser Applications*, **10**, pp. 265-279.

- [4] Montross, C.S., Wei, T., Ye, L., Clark, G., and Mai, Y.-W., 2002, "Laser shock processing and its effects on microstructure and properties of metal alloys: a review," *International Journal of Fatigue*, **24**, pp. 1021-1036.
- [5] Pistochini, T., 2003, "Fatigue Life Optimization in Laser Peened 7050-T7451 and 300M Steel," M.S. Thesis, Department of Mechanical and Aeronautical Engineering, University of California, Davis.
- [6] Luong, H., 2006, "Fatigue life extension and the effects of laser peening on 7050-T7451 aluminum, 7085-T651 aluminum, and Ti-6Al-4V titanium alloy," M.S. Thesis, Department of Mechanical and Aeronautical Engineering, University of California, Davis.
- [7] Prime, M.B., 2001, "Cross-sectional mapping of residual stresses by measuring the surface contour after a cut," *Journal of Engineering Materials and Technology*, **123**, pp. 162-168.
- [8] Prime, M.B., Sebring, R.J., Edwards, J.M., Hughes, D.J., and Webster, P.J., 2004, "Laser surface-contouring and spline data-smoothing for residual-stress measurement," *Experimental Mechanics*, **44**, pp. 176-184.
- [9] Schajer, G.S., and Prime, M.B., 2006, "Use of Inverse Solutions for Residual Stress Measurements," *Journal of Engineering Materials and Technology*, **128**, pp. 375-382.
- [10] Schindler, H.J. and P. Bertschinger, 1997, "Some steps towards automation of the crack compliance method to measure residual stress distributions," in *Proceedings of the 5th International Conference on Residual Stress*, Linköping.
- [11] Ghidini, T., Donne, C. D., 2007, "Fatigue crack propagation assessment based on residual stresses obtained through cut-compliance technique," *Fatigue and Fracture of Engineering Materials and Structures*, **30**, pp. 214-222.
- [12] Newman, J.C., Yamada, Y., James, M.A., 2010, "Stress-intensity-factor equations for compact specimen subjected to concentrated forces," *Engineering Fracture Mechanics*, **77**, pp 1025-1029.
- [13] Wu, X.-R. and Carlsson, A.J., 1991, Weight function and stress intensity factor solutions, Pergamon Press, pp. 37-38.
- [14] Towers, O.L., Dawes, M.G., 1985, "Welding Institute research on the fatigue precracking of fracture toughness specimens," in *Elastic-Plastic Fracture Test Methods: The User's Experience, ASTM STP 856*, American Society for Testing and Materials, Philadelphia, PA, p. 23-46.
- [15] Lee, M.J., Hill, M.R., 2007, "Intralaboratory repeatability of residual stress determined by the slitting method," *Experimental Mechanics*, **47**, pp. 745-752.

Analysis of Large Scale Composite Components Using TSA at Low Cyclic Frequencies

Author: J. M. Dulieu-Barton, School of Engineering Sciences, University of Southampton,
Highfield, Southampton, SO17 1BJ, UK, J.M.Barton@soton.ac.uk

Co-Author: D. A. Crump, University of Southampton

ABSTRACT

Thermoelastic stress analysis (TSA) has been applied to large scale honeycomb core sandwich structure with carbon fibre face sheets. The sandwich panel was subjected to a pressure load using a custom designed test rig that could only achieve low cycle frequencies of 1 Hz. Two calibration approaches have been discussed and investigated to allow the use of the thermoelastic response as a validation tool for the stress distribution predicted by an FE model. The TSA data was calibrated using thermoelastic constants derived experimentally using tensile strips of the face sheet material. It has been shown that by using constants obtained from the tensile strips manufactured with the same lay-up as the face sheet of the sandwich panel it was possible to achieve a good correspondence between the predicted stress distribution and the measured TSA response.

1. Introduction

Thermoelastic stress analysis (TSA) [1] is a well established, non-contacting technique for the evaluation of stresses in engineering components, e.g. [2-5]. The technique uses an infra-red camera to obtain the small temperature change associated with the thermoelastic effect in a loaded component or structure. It is assumed that the small temperature change occurs isentropically; to eliminate heat transfer TSA is usually performed using a cyclic load. TSA has been successfully applied to realistic composite structures, e.g. large wind turbine blades [6] and to a marine tee-joint [7]. The aim of the current paper is to demonstrate that TSA can be used as an accurate and qualitative validation tool for finite element analysis (FEA) of complex sandwich structures with carbon fibre face sheets. In [8] TSA was applied successfully to a validation of FE models of sandwich beams with core junctions. The introduction of the core junction caused a large stress gradient to occur both through the

thickness and in the plane of the face sheet. In TSA, stress gradients drive the non adiabatic behaviour. In the case where the face sheets were manufactured from relatively low thermal conductivity material it was possible to obtain good results that compared well with strain gauge readings and therefore validated the FEA. For high conductivity aluminium alloy face sheets it was shown that adiabatic conditions could not be achieved. In the present paper, sandwich structure with carbon fibre face sheets are studied, which have a much greater thermal conductivity than the glass fibre face sheets used in [8]. This paper starts with a description of the TSA technique and its application to large carbon fibre sandwich structure representative of a secondary wing structure panel in an aircraft, known as a 'generic panel' [9]. The generic panels are subjected to a pressure load, representative of the aerodynamic pressure on the wing of an aircraft, using a specialist test rig [10]. Two different approaches are discussed for calibration of the thermoelastic response from the face sheet material. To achieve adiabatic behaviour in composite materials it is usually recommended that a frequency of at least 10 Hz is applied [11, 12]. The requirement for this relatively high loading frequency limits the use of TSA to laboratory experiments, and also the size of components that TSA can be readily applied to. Therefore, the calibration approaches are tested over a range of loading frequencies. However, to achieve a constant cyclic pressure the generic panels can only be loaded at a rate of 1 Hz using the test rig. Hence, this paper discusses the calibration of TSA data recorded using a low cycle frequency and the effect this has on the measured stresses.

2. Thermoelastic stress analysis (TSA) and experimental setup

The Cedip Silver 480M infra-red detection system manufactured by Cedip Infrared Systems was used to obtain the TSA data. The system comprises an infra-red camera with an InSb detector with 320 x 256 pixels at pitch of 30 μm and allows frame rates between 5 and 380 Hz. The images are recorded and processed using AltairLI software. This system is radiometrically calibrated so it is possible to obtain the temperature change directly as well as using the mean temperature field to correct for any changes in the specimen temperature. A 'lock-in' signal from the test machine is used to synchronise the TSA measurement, and in this way the structural response due to the loading can be averaged over a number of cycles and the accuracy improved. The output from the detector provides the change in surface temperature, ΔT , resulting from the change in the sum of the principal stresses on the surface of the material. For an orthotropic material, such as the composites investigated in this paper, ΔT can be related to the stresses in the material, σ_x and σ_y , as follows [7]:

$$\Delta T = \frac{-T}{\rho C_p} (\alpha_x \sigma_x + \alpha_y \sigma_y) \quad (1)$$

where α_x and α_y , are the coefficients of linear thermal expansion in the longitudinal and transverse material direction, σ_x and σ_y are the stresses in these directions, ΔT is the change in temperature, T is the ambient temperature, ρ is the density and C_p is the specific heat at constant pressure.

It is possible to combine the material constants in Equation (1), i.e. α_x , α_y , ρ and C_p into two thermoelastic constants K_x and K_y as follows [10]:

$$\Delta T = -T (K_x \sigma_x + K_y \sigma_y) \quad (2)$$

where $K_x = \frac{\alpha_x}{\rho C_p}$ and $K_y = \frac{\alpha_y}{\rho C_p}$.

In previous work [9], a generic sandwich panel was designed to capture some of the features representative of composite sandwich secondary wing structure (see Figure 1). Two generic panels were manufactured using Hexcel's 914C-TS-5-34% prepreg tape as the face sheet material, one with quasi-isotropic (QI) sheets $[0^\circ, 45^\circ, -45^\circ, 90^\circ, 0^\circ, 45^\circ, -45^\circ, 90^\circ, 0^\circ, 45^\circ, -45^\circ, 90^\circ]$ s about a core of Nomex honeycomb, and one with cross-ply (CP) sheets $[0^\circ, 90^\circ]_{6s}$ about the core. A custom designed rig was used to apply a pressure load, representative of aerodynamic loading, to the sandwich panel. The rig used the movement of the actuator in an Instron servo-hydraulic test machine to pull the sandwich panel over a water filled pressure cushion that is fully constrained by the rig and the panel. The rig has been designed to allow uninterrupted optical access to the top surface of the sandwich panel, thereby enabling the use of optical measurement techniques such as TSA. The panels were loaded cyclically at 1 Hz with a mean pressure of 10 kPa (1.5 psi) and an amplitude of 5 kPa (0.75 psi), thereby imparting a pressure range of 10 kPa (1.5 psi). The panel was attached to the test rig horizontally and therefore to measure the response from the surface it was necessary to mount the TSA detector vertically with the lens directed downwards; this would not have been feasible with the older bulk cooled infra-red detector systems. The detector was located at a distance that gave approximately 600 pixels across the 300 mm width of the panel. Therefore, the spatial resolution was approximately 2 pixels/mm, and the system recorded images at a frame rate of 100 Hz. To achieve this spatial resolution for the entire panel it was necessary to record 32 images per panel, and then 'stitch' the data together using a Matlab routine. This provided a full-field plot of the temperature change on the surface of the sandwich panel. This temperature field was then calibrated to obtain a full-field stress measure.

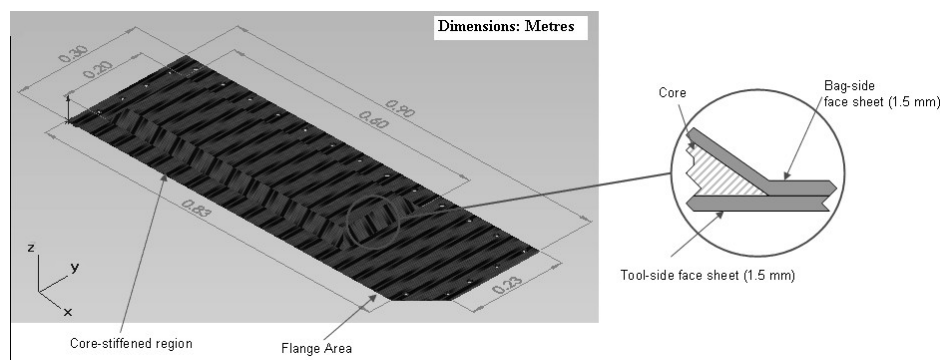


Figure 1: Design for generic sandwich panel [9]

3. Calibration approach

One of the major challenges in calibrating the thermoelastic response from composite materials is the requirement for accurate thermal and mechanical material properties both longitudinally and transversely. By using Equation (2) it is possible to calibrate the thermoelastic response using measured thermoelastic constants K_x and K_y . The uniaxial stress state in a tensile strip test provides the opportunity to measure the calibration constant, and by using longitudinal and transverse specimens it is possible to calculate K_x and K_y as follows:

$$K_x = \frac{-\Delta T}{\Delta \sigma_x T} \text{ and } K_y = \frac{-\Delta T}{\Delta \sigma_y T} \quad (3)$$

The values obtained from equation (3) inserted into Equation (2) and then by rearrangement the TSA data can be expressed in terms of a stress in such a way that it can be used for FEA validation:

$$\underbrace{\frac{\Delta T}{TK_x}}_{TSA} = \Delta \sigma_x + \underbrace{\frac{K_y}{K_x} \Delta \sigma_y}_{FE} \quad (4)$$

The left hand side of Equation (4) represents the TSA data calibration and the right hand side the form into which the FE data must be processed to make it comparable with the TSA data. In this paper two calibration approaches are investigated to establish if the stresses in equation (4) should be the global stresses or surface ply stresses in the face sheet. The key feature is to determine if this has an effect on the interpretation of the thermoelastic response. The first, 'global calibration', uses constants derived from tensile strips manufactured from material with the same lay-up as the face sheets of the generic panel, i.e. QI and CP depending on the panel. The second, 'UD calibration', uses constants derived from tensile strips manufactured with a unidirectional lay-up i.e. one with all plies aligned longitudinally or transversely. The surface ply in the panel faces sheets is orientated with the x-direction in all cases so the UD surface ply thermoelastic constants are the same for both the QI and CP generic panels. Tensile strips of 15 mm width were loaded in a servo-hydraulic test machine at both 1 and 10 Hz to investigate the effect of loading frequency on the derived thermoelastic constant. As a result of the different stiffness and strengths of the materials it was necessary to apply different loads to the longitudinal and transverse specimens than that used for the QI and CP strips. The longitudinal UD specimen was loaded at 10 ± 9.0 kN, the transverse UD specimen at 0.15 ± 0.1 kN whilst all the QI and CP specimens were loaded at 3.5 ± 3.0 kN. The specimens were not coated with paint as the response was sufficient in the uncoated condition.

Table 1 provides the thermoelastic constant for each of the tensile strips for both loading frequencies. The longitudinal UD 0° specimen provides a constant that is almost sixty times smaller than the transverse UD 90° specimen. The derived thermoelastic constants show increases in the response between the 1 and 10 Hz loading frequency of 11% for the UD 0° specimen and 5% for the UD 90° specimen. As all the plies are aligned in the same direction there is no through thickness stress gradient and hence little heat transfer. The small changes in response may be caused by the stress gradient between the surface resin rich layer and fibre reinforced substrate. This has been noticed in previous research [13] but is not considered in the present paper. For QI and CP specimen there is a considerable difference between the measured response at 1 Hz and 10 Hz; this is expected as there will be a stress gradient change ply by ply in these specimens. For the QI specimens at 1 Hz the longitudinal specimen provides a K value is around 50% less than that for the transverse specimen. At 10 Hz the transverse constant is more than three times greater. It is clear that at a 1 Hz loading frequency the QI specimens are not behaving adiabatically because of through thickness heat transfer from the subsurface plies. For the CP specimens at 1 Hz the longitudinal K value is practically the same as the transverse. Here it could be speculated the heat transfer through the thickness produces an almost homogenous material where the orientation of the surface ply is unimportant for the value of the calibration constant. When the loading frequency

is increased to 10 Hz the transverse K value is almost 3 times greater than the longitudinal in a very similar manner to the QI. The presence of $\pm 45^\circ$ plies in the QI specimen may be responsible for reducing the homogenising effect of heat transfer at low loading frequencies. It is important to note, particularly for the UD material, the data contains more than 50% noise. This is because ΔT is of the order 20 mK and very close to the minimum resolvable value of about 4 mK. This is because the α_x value is small for the UD 0° material and the applied stress must be small for the UD 90° material. There is clear non-adiabatic behaviour at 1 Hz for the materials that comprise the panel face sheets. As the loading rig can only operate at this level, then it must be established if applying the thermoelastic constants derived from these loading frequencies will provide a sufficiently accurate stress solution.

Table 1: Thermoelastic response and constants from calibration strips

Specimen	Loading at 1 Hz				Loading at 10 Hz			
	σ (MPa)	ΔT	T ($^\circ\text{K}$)	K ($\text{MPa}^{-1} \times 10^{-6}$)	σ (MPa)	ΔT	T ($^\circ\text{K}$)	K ($\text{MPa}^{-1} \times 10^{-6}$)
UD 0°	187.50	0.0175	294.0	0.32 ± 0.19	187.50	0.0197	294.0	0.36 ± 0.22
UD 90°	4.17	0.0235	295.1	19.12 ± 4.71	4.17	0.0247	295.1	20.09 ± 5.29
QI 0°	122.75	0.0576	295.6	1.59 ± 0.83	122.75	0.0351	295.6	0.97 ± 0.53
QI 90°	125.00	0.1161	298.5	3.11 ± 1.19	125.00	0.1388	298.5	3.50 ± 1.75
CP 0°	124.56	0.0710	295.0	1.93 ± 1.08	124.56	0.0643	295.0	1.75 ± 1.05
CP 90°	131.06	0.0783	295.0	2.03 ± 0.78	131.06	0.0991	295.0	2.56 ± 0.88

4. Analysis of generic panels – TSA vs FE

The generic panel was modelled using ANSYS 11. The relatively simple geometry of the panel is shown in [Figure 1](#). The face sheets were treated as orthotropic blocks of material using element Shell181 with material properties derived experimentally. The core was assumed to be a single anisotropic solid volume modelled using brick element Solid 185. After a convergence study using panel deflection, an element size of 0.01 m was selected [10]. The service constraints were represented in the model simply by imposing zero deflection on three edges of the model; i.e. the two short edges and one of the longer edges. The bolted connections used in the experimental work are not modelled so there will be differences between the FE and experimental results at the boundary. The pressure load of 10 kPa was treated in the FE model as a force perpendicular to each of the 2150 surface nodes, i.e. 0.96 N per node. As the panel is relatively thin in comparison to its length and width, and experiences a relatively large out-of-plane deformation a geometrically nonlinear solver was used.

The TSA data from the panels and stresses from the FE models were manipulated into the form in Equation (4) using both the UD and global values of K . [Figure 2](#) shows the full-field images for the CP panel as an example, although the images from the QI panel show similar trends. [Figure 2](#) (a and b) show the result of using the UD values on the FE model and TSA data respectively. There is very little correlation between the FE and TSA. This must be attributed to the fact that the surface ply in the TSA is not behaving in an adiabatic manner. However some trends are apparent, even though in general the FE model gives much larger stresses than the TSA, the

stress concentrations are still discernable. [Figure 2 \(c and d\)](#) show the result of using the global K values. Qualitatively there is obviously much better correlation between the images than for the UD calibration. The stress distribution appears to be in agreement, and the level of stress appears to be similar. To provide a quantitative comparison of the stress sum calibrated in this manner, a line of data is plotted through the stress concentration at the top right corner of the core for each of the panels and calibration approach. [Figure 3 \(a\)](#) plots the line of data for the CP panel calibrated with the UD approach comparing the FE and TSA. The FE model predicts a peak value of approximately 3200 MPa, whilst experimentally the TSA provides 1400 MPa. [Figure 3 \(b\)](#) shows the line for the CP panel calibrated using the global approach. The FE predicts a peak value of approximately 130 MPa, whilst experimentally the TSA provides 150 MPa. Using the global calibration approach the FE model under predicts the stress peak by only 15%. This indicates that using the thermoelastic constants derived from the global calibration experiments, at the actual loading frequency, provides a means of obtaining reasonable stress values from non-adiabatic thermoelastic data. [Figure 3 \(c and d\)](#) plots the line of data for the QI panel using the UD and global calibration approaches respectively. These plots support the conclusion from the CP panel that the global calibration can provide a means of deriving useful stress data from the thermoelastic response even if non-adiabatic conditions prevail.

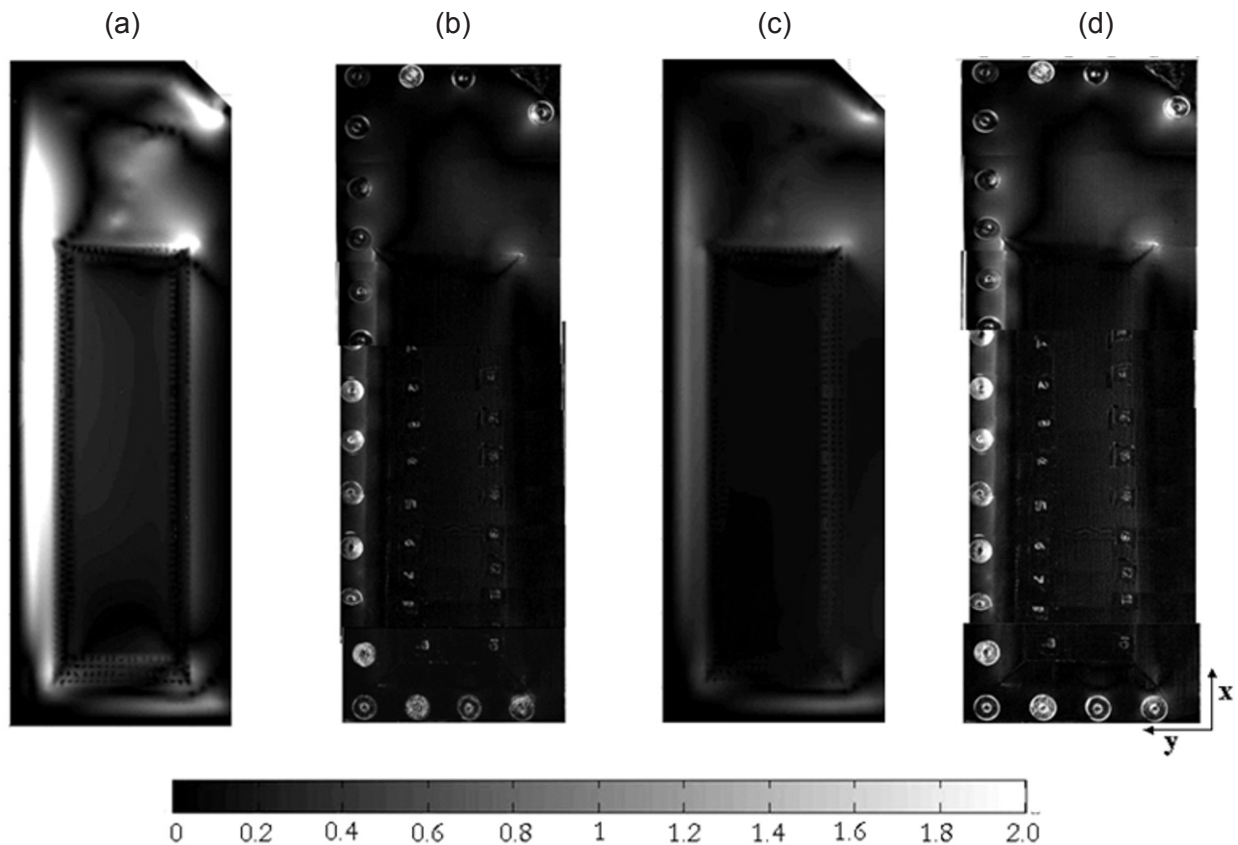


Figure 2: Full-field stress sum data for CP panel (a) FE model using UD calibration, (b) TSA using UD calibration, (c) FE model using global calibration and (d) TSA using global calibration

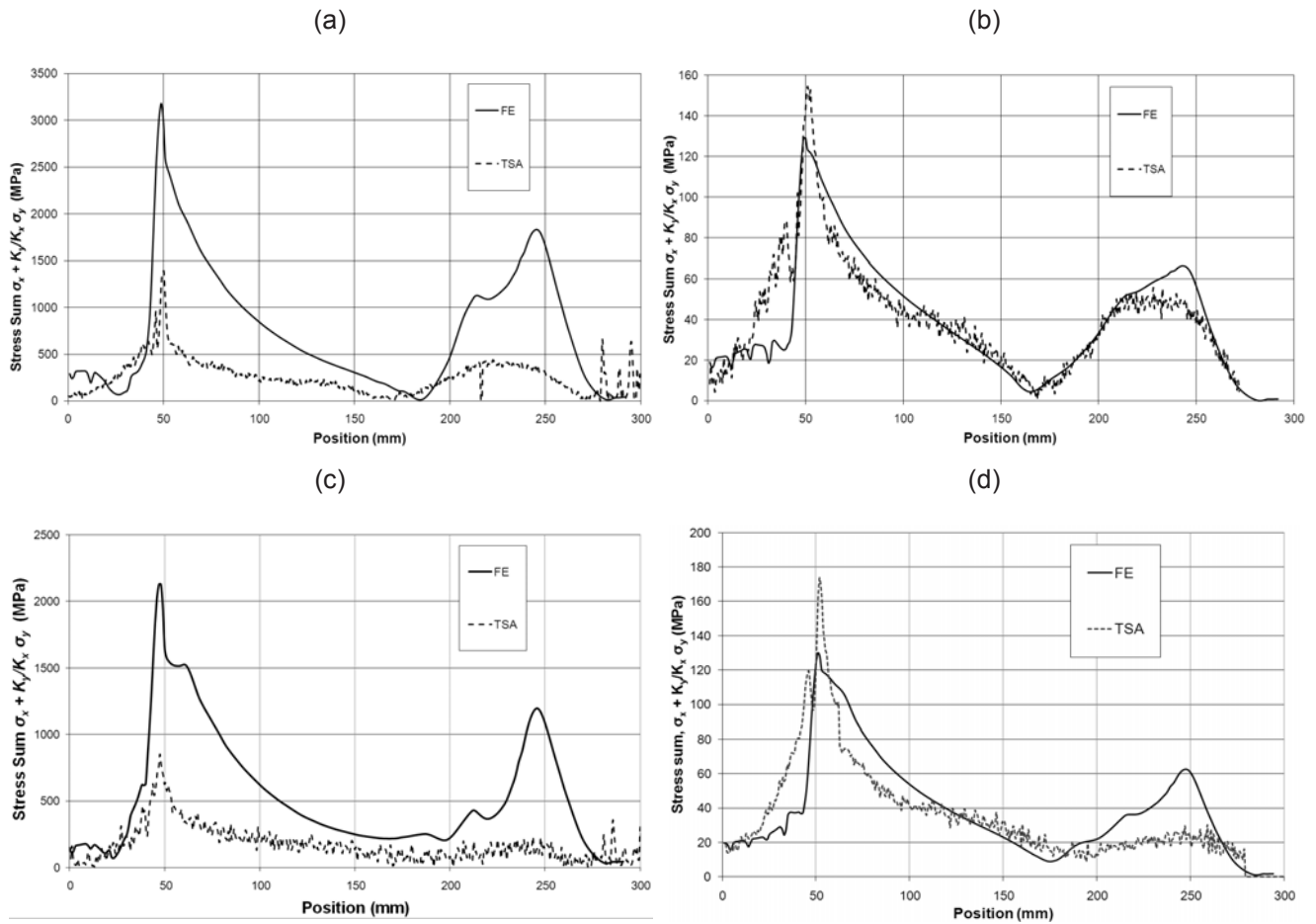


Figure 3: Line plot through stress concentration (a) CP panel with UD calibration, (b) CP panel with global calibration, (c) QI panel with UD calibration and (d) QI panel with global calibration

5. Conclusions

A method for validating FE models of large carbon fibre sandwich panels has been established using TSA. To ensure adiabatic conditions in a composite material it is usual to apply a cyclic load of at least 10 Hz. However, by obtaining calibration constants from tensile strips loaded at 1 Hz it has been shown possible to process full-field TSA data from a large representative carbon fibre sandwich panel loaded at just 1 Hz. The TSA data and stresses from an FE model were processed into a form that was comparable using two calibration approaches. The first used values measured from UD composite tensile specimens, whilst the second used values measured from composite specimens manufactured from the same layup as the face sheets of the generic panel. The processed TSA and FE data did not compare well when the UD calibration approach was applied in terms of both the stress distribution and the stress values. However, by applying the global calibration approach the stress obtained from the TSA and FE compared well in both distribution and value. The results are very encouraging in the sense that the idea of calibrating at the actual loading frequency provides a means of interpreting thermoelastic data from components that are subject to non adiabatic behaviour. However, the work presented in the paper represents only a small part of the overall picture regarding non adiabatic behaviour in laminated composite component. The work provides an initial indication that non adiabatic behaviour can be accounted for and that representative low loading frequencies can be used for TSA.

In future work the non adiabatic behaviour will be investigated further by using a ply-by-ply FE model and by evaluating the stress in the surface ply and thereby identifying when adiabatic behaviour is occurring. Further more detailed investigations into the effect of the loading frequency on the thermoelastic response of the tensile strips will be undertaken.

References

1. Stanley P, Chan WK. *The application of thermoelastic stress analysis to composite materials*. J Strain Anal Eng 1988; 23(3): 137-142.
2. Diaz FA, Patterson EA, Tomlinson RA, Yates JR. *Measuring stress intensity factors during fatigue crack growth using thermoelasticity*. Fatigue Fract Eng M. 2004; 27(7): 571-584.
3. Lin ST, Miles JP, Rowlands RE. *Image enhancement and stress separation of thermoelastically measured data under random loading*. Exp Mech 1997; 37(3).
4. El-Hajjar R, Haj-Ali R. *A quantitative thermoelastic stress analysis method for pultruded composites*. Comp Sci Tech 2003; 63(7): 967-978.
5. Emery, T. R., Dulieu-Barton. J.M., Earl, J., and Cunningham, P.R., *A generalised approach to the calibration of orthotropic materials for thermoelastic stress analysis*. Composites Science and Technology, 2008, 68(3-4), p 743-752
6. Paynter, R.J.H., Dutton, A.G., *The use of a second harmonic correlation to detect damage in composite structures using thermoelastic stress measurements*. Strain, 2003. 39(2): p. 73-78.
7. Dulieu-Barton, J.M., Quinn, S., Sheno, R.A., Read, P.J.C.L., and Moy, S.S.J, *Thermoelastic stress analysis of a GRP tee joint*. Applied Composite Materials, 1997. 4(5): p. 283-303.
8. Johannes, M., Dulieu-Barton, J.M, Bozhevolnaya, E., Thomsen, O.T., *Characterisation of local effects at core junctions in sandwich structures using thermoelastic stress analysis*. The Journal of Strain Analysis for Engineering Design, 2008. 43(6): p. 469-492.
9. Crump, D.A., Dulieu-Barton, J.M., and Savage, J, *The manufacturing procedure for aerospace secondary sandwich structure panels*, Journal of Sandwich Structures and Materials, 2009, 0, *In Press* (DOI:1099636208104531)
10. Crump, D.A., Dulieu-Barton, J.M., and Savage, J. *Design and commission of an experimental test rig to apply a full-scale pressure load on composite sandwich panels representative of an aircraft secondary structure*, Measurement Science and Technology, 2010, 21, 16pp
11. Cunningham, P.R., Dulieu-Barton, J.M., Sheno, R.A., *Damage location and identification using infra-red thermography and thermoelastic stress analysis*. Proceedings of SPIE, 2002. 4704: p. 93-103.
12. Cunningham, P.R., Dulieu-Barton, J.M., Dutton, A.G., Sheno, R.A., *Thermoelastic characterisation of damage around a circular hole in GRP component*. Key Engineering Materials, 2001. 204-205: p. 453-463.
13. Sambasivam, S., Quinn, S and Dulieu-Barton, J.M., "*Identification of the source of the thermoelastic response from orthotropic laminated composites*", 17th International Conference on Composite Materials (ICCM17), 2009, Edinburgh, 11 pages on CD

Determining Stresses Thermoelastically around Neighboring Holes whose Associated Stresses Interact

A. A Khaja¹ and R. E. Rowlands²

Department of Mechanical Engineering, University of Wisconsin, Madison, WI 53706

[1khaja@wisc.edu](mailto:khaja@wisc.edu)

[2rowlands@engr.wisc.edu](mailto:rowlands@engr.wisc.edu)

ABSTRACT

Since stresses at a geometric discontinuity can be influenced by the neighboring structural compliance, this paper emphasizes determining the individual components of stress in a finite tensile plate containing two different-size neighboring holes. Stresses associated with the respective holes interact. Relatively little information is available for such cases, purely analytical solutions are extremely difficult for finite geometries, and numerical approaches are challenging if the external loading is not well known. An effective method for determining stresses in perforated finite plane-problems is to synergize measured temperature information with a series representation of an Airy stress function. A separate stress function is employed here with each hole. The coefficients of the stress functions are evaluated from the recorded temperatures, imposing the traction-free conditions analytically at the edge of the holes, as well as satisfying stress compatibility between the holes. The number of Airy coefficients utilized is substantiated experimentally. TSA results agree with those from FEM and commercial strain gages. The technology has implications relative to reducing stress concentration factors.

1. Introduction

Numerous publications have been appeared investigating the effect of single geometric discontinuity in finite/infinite plate members, for example references [1-5]. Engineering members often contain holes whose tensile stress concentration factor can be reduced by introducing a nearby hole or notch such that their stress fields interact with each other. It is therefore important to investigate the effects on the stress field of an original hole of adding an auxiliary hole. The present study emphasizes determining the individual components of stress in a region containing two different-size neighboring holes in a finite tensile plate. Individually analyzing the stresses around each hole and due to stress compatibility between the two holes provide meaningful insight into how the stresses associated with each hole interact. These issues are pursued here by means of a finite tensile aluminum plate containing a circular hole plus a smaller neighboring hole, *figure 1*.

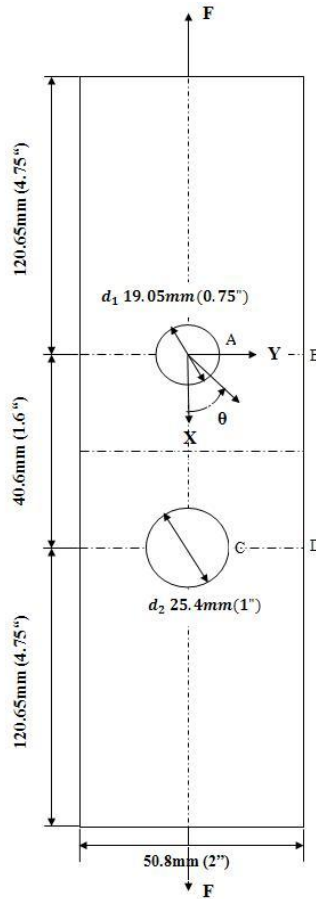


Fig. 1: Aluminum Plate .

2. Relevant Equations

For plane-stress isotropic TSA under cyclic proportional loading condition, the quantitative information of *figure 1* can be expressed as [4-6]

$$S^* = K\Delta S = K[\Delta(\sigma_1 + \sigma_2 = \sigma_{XX} + \sigma_{YY} = \sigma_{rr} + \sigma_{\theta\theta})] \tag{1}$$

where S^* is the thermoelastically-recorded signal, K is the thermomechanical coefficient (usually determined experimentally) and ΔS is the change in S , S is also called the isopachic stress or the first stress invariant.

TSA-wise, the doubly perforated plate of *figure 1* is analyzed by employing individual stress functions associated with the individual coordinate systems, these separate coordinate systems having their origins at the center of the respective holes. The longitudinal X-axis of *figure 1* is positive down in both cases (top small and bottom large hole) and in each case the angle θ is measured positive counter-clockwise from this downward X-axis. Based on the symmetry about X-axis, a relevant Airy's stress function in polar co-ordinates satisfying equilibrium and compatibility can be written as [6]

$$\begin{aligned} \phi = & a_0 + b_0 \ln r + c_0 r^2 + \left(a_1' r + \frac{c_1'}{r} + d_1' r^3 \right) \cos \theta \\ & + \sum_{n=2,3,\dots}^N \left[a_n' r^n + b_n' r^{(n+2)} + c_n' r^{-n} + d_n' r^{-(n-2)} \right] \cos(n\theta) \end{aligned} \tag{2}$$

where r is the radius measured from the center of a hole, angle θ is measured counter-clockwise from the longitudinal vertical X-axis (*figure 1*) and N is the terminating value of the above series (N can be any positive integer greater than one).

Individual components of stresses can be obtained by differentiating the stress function

$$\sigma_{rr} = \frac{1}{r} \frac{\partial \phi}{\partial r} + \frac{1}{r^2} \frac{\partial^2 \phi}{\partial \theta^2} \quad (3)$$

$$\sigma_{\theta\theta} = \frac{\partial^2 \phi}{\partial r^2} \quad (4)$$

$$\sigma_{r\theta} = -\frac{\partial}{\partial r} \left(\frac{1}{r} \frac{\partial \phi}{\partial \theta} \right) \quad (5)$$

Imposing the traction-free boundary conditions analytically on the boundary of the hole ($\sigma_{r\theta} = 0$ and $\sigma_{rr} = 0$ at $r = R$ (where $R = r_1$, radius of the small hole or $R = r_2$, radius of the large hole) and for all values of θ) results in some of the originally independent coefficients becoming dependent functions of other independent coefficients. The individual components of stresses become

$$\begin{aligned} \sigma_{rr} = & \left(\frac{1}{r^2} - \frac{3r}{2R^3} + \frac{r^3}{2R^5} \right) b_0 + \left[2 - \frac{3r}{R} + \left(\frac{r}{R} \right)^3 \right] c_0 + \left(\frac{-2R^4}{r^3} + 2r \right) \cos \theta d_1' \\ & + 3R^2 (1 - r^{-4} R^4) \cos(2\theta) b_2' + (R^{-2} + 3r^{-4} R^2 - 4r^{-2}) \cos(2\theta) d_2' \\ & + \left(\frac{24r}{R^6} - \frac{12r^3}{R^8} - \frac{12}{r^5} \right) \cos(3\theta) c_3' + \left(\frac{18r}{R^4} - \frac{8r^3}{R^6} - \frac{10}{r^3} \right) \cos(3\theta) d_3' \\ & + \sum_{n=4,5,\dots}^N \left\{ \left[(n^2 - 1)r^{-(n-2)} R^2 - (n+1)(n-2)r^n - (n+1)r^{-(n+2)} R^{(2n+2)} \right] \cos(n\theta) b_n' \right. \\ & \left. + \left[(n-1)r^{-(n-2)} R^{-(2n-2)} - (1-n^2)r^{-(n+2)} R^2 - (n-1)(n+2)r^{-n} \right] \cos(n\theta) d_n' \right\} \end{aligned} \quad (6)$$

$$\begin{aligned} \sigma_{\theta\theta} = & \left(-\frac{1}{r^2} + \frac{3r}{2R^3} - \frac{5r^3}{2R^5} \right) b_0 + \left(2 + \frac{3r}{R} - \frac{5r^3}{R^3} \right) c_0 + \left(\frac{2R^4}{r^3} + 6r \right) \cos \theta d_1' \\ & + \left[(-3)R^2 + 12r^2 + 3r^{-4} R^6 \right] \cos(2\theta) b_2' - (R^{-2} + 3r^{-4} R^2) \cos(2\theta) d_2' \\ & + \left(\frac{-24r}{R^6} + \frac{60r^3}{R^8} + \frac{12}{r^5} \right) \cos(3\theta) c_3' + \left(\frac{-18r}{R^4} + \frac{40r^3}{R^6} + \frac{2}{r^3} \right) \cos(3\theta) d_3' \\ & + \sum_{n=4,5,\dots}^N \left\{ \left[-(n^2 - 1)r^{-(n-2)} R^2 + (n+1)(n+2)r^n \right] \cos(n\theta) b_n' \right. \\ & \left. + \left[-(n-1)r^{-(n-2)} R^{-(2n-2)} + (1-n^2)r^{-(n+2)} R^2 + (n-2)(n-1)r^{-n} \right] \cos(n\theta) d_n' \right\} \end{aligned} \quad (7)$$

$$\begin{aligned}
\sigma_{r\theta} = & \left[-\frac{3r \cot(3\theta)}{2R^3} + \frac{3r^3 \cot(3\theta)}{2R^5} \right] b_0 + \left[-\frac{3r \cot(3\theta)}{R} + \frac{3r^3 \cot(3\theta)}{R^3} \right] c_0 \\
& - \left(\frac{2R^4}{r^3} - 2r \right) \sin \theta d_1' + (3R^2 - 6r^2 + 3r^{-4} R^6) \sin(2\theta) b_2' \\
& + (R^{-2} - 3r^{-4} R^2 + 2r^{-2}) \sin(2\theta) d_2' + \left(\frac{24r}{R^6} - \frac{36r^3}{R^8} + \frac{12}{r^5} \right) \sin(3\theta) c_3' \\
& + \left(\frac{18r}{R^4} - \frac{24r^3}{R^6} + \frac{6}{r^3} \right) \sin(3\theta) d_3' \\
& + \sum_{n=4,5,\dots}^N \left\{ \left[-(n^2 - 1)r^{(n-2)} R^2 + n(n+1)r^n - (n+1)r^{-(n+2)} R^{(2n+2)} \right] \sin(n\theta) b_n' \right. \\
& \left. + \left[-(n-1)r^{(n-2)} R^{-(2n-2)} - (1-n^2)r^{-(n+2)} R^2 - n(n-1)r^{-n} \right] \sin(n\theta) d_n' \right\}
\end{aligned} \tag{8}$$

and the isopachic stress is

$$\begin{aligned}
S = \sigma_{rr} + \sigma_{\theta\theta} = & -\frac{2r^3}{R^5} b_0 + \left(4 - \frac{4r^3}{R^3} \right) c_0 + 8r \cos \theta d_1' + 12r^2 \cos(2\theta) b_2' - 4r^{-2} \cos(2\theta) d_2' \\
& + \frac{48r^3}{R^8} \cos(3\theta) c_3' + \left(\frac{32r^3}{R^6} - \frac{8}{r^3} \right) \cos(3\theta) d_3' \\
& + \sum_{n=4,5,\dots}^N \left[4(n+1)r^n \cos(n\theta) b_n' - 4(n-1)r^{-n} \cos(n\theta) d_n' \right]
\end{aligned} \tag{9}$$

Unless stated otherwise (and although not needed), an additional twenty traction-free boundary conditions, $\sigma_{YY} = 0$ and $\sigma_{XY} = 0$, were also imposed at $h/2 = 10$ locations along the right edge of the vertical plate of [figure 1](#). Combining the measured temperature related data from TSA, $S = S^*/K$, and expressions for the isopachic stress at different values of r and θ , the following matrix equation can be written as

$$[A]_{(m+h) \times k} [c]_{k \times 1} = [d]_{(m+h) \times 1} \tag{10}$$

where matrix $[A]$ involves the m (m_1 for the small hole and m_2 for the large hole) Airy isopachic equations of [equation 9](#) and $h = 20$ expressions for $\sigma_{YY} = \sigma_{XY} = 0$ at the right edge of the vertical plate. Vector $\{c\}$ contains the k unknown coefficients. Vector $\{d\}$ consists of the m measured TSA data values of $S=S^*/K$ corresponding to the data points employed in the S to form matrix $[A]$ as well as the $h = 20$ zeros. [Equation 10](#) was solved using the '\ ' matrix division operator or 'pinv' pseudo inverse operator which uses the algorithm for least squares in MATLAB.

3. Experimental Details and Results

The tensile aluminum plate of [figure 1](#) ($E = 68.95$ GPa and Poisson's ratio $\nu = 0.33$) was sprayed with Krylon Ultra-Flat black paint to provide an enhanced and uniform emissivity. [Figure 2](#) is a photograph of the loaded aluminum plate. The plate was sinusoidally loaded between 1334.46 N (300 lb) and 5782.68 N (1300 lb) with a mean value of 3558.57 N (800 lb) at a frequency of 10 Hz. A separate uniaxial tension calibration specimen was used to determine the thermomechanical coefficient, $K = 210.3$ U/MPa (1.45 U/psi).

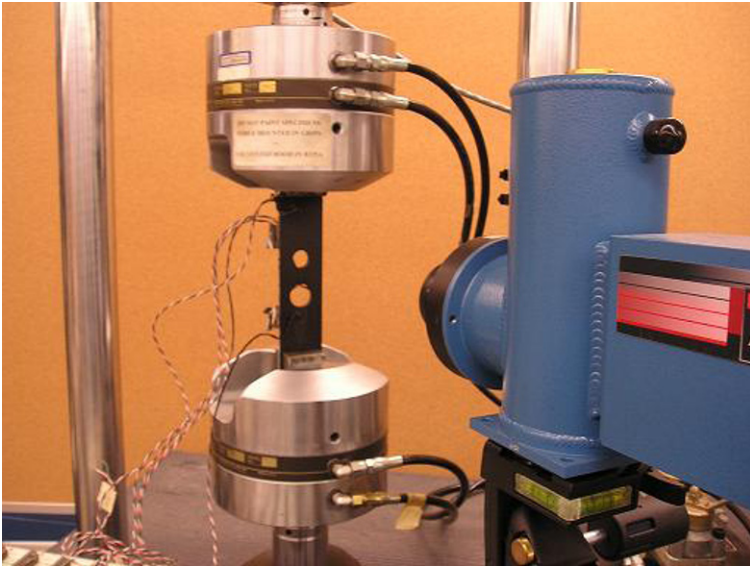


Fig. 2: Specimen loading and recording.

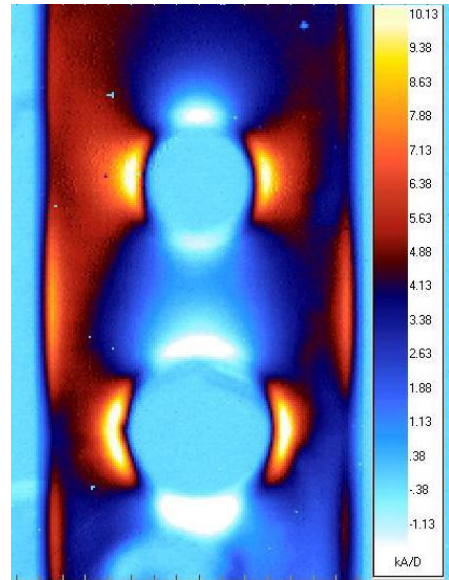


Fig. 3: Actual recorded TSA image, S^* , for a load range of 4448.22 N (1000 lb).

Figure 2 is a photograph of the loaded aluminum plate and mechanically cooled Delta Therm camera DT1410 having a sensor array of 256 horizontal x 256 vertical pixels, whereas *figure 3* is a recorded TSA image displayed using the commercially provided Delta Vision software. This image was averaged and recorded over a period of two minutes. As the plate is symmetrical about the longitudinal X-axis (*figure 1*), the recorded TSA data obtained were averaged about the longitudinal X-axis so that only one half of the plate is considered during thermoelastic stress analyses.

Individual analyses were carried-out for each of the large and the small hole and $k = 9$ was found to be an appropriate number of Airy coefficients for each of the small and large holes. For the analysis of the large hole of the plate of *figure 1* a total of $m_2+h = 2,517$ input values were used. Of these, 2,497 are measure TSA input values whose source locations as shown in *figure 4* and 20 are the traction-free conditions $\sigma_{YY} = \sigma_{XY} = 0$ imposed at the ten locations along the right edge of the vertical plate of *figure 4*.

After evaluating all the unknown Airy coefficients ($b_0, c_0, d_1', b_2', d_2', c_3', d_3', b_4'$ and d_4') from the measured S^* for each of the small and large holes from *equations 9 and 10*, the individual components of stress were obtained from *equations 6 through 8*. These TSA results are compared with those from finite element analysis (ANSYS) and commercial strain gages. Tangential stresses, $\sigma_{\theta\theta}$, are normalized with respect to the far field stress, σ_0 , and are plotted around the boundary of the large hole in *figure 5*. *Figure 6* compares the strains (static equivalent specimen load of $F = 4,448.22 \text{ N} = 1,000 \text{ lb}$) along the line CD extending from the large hole (*figure 1*) obtained from Thermoelastic Stress Analysis with those from finite element analysis (ANSYS) and strain gages.

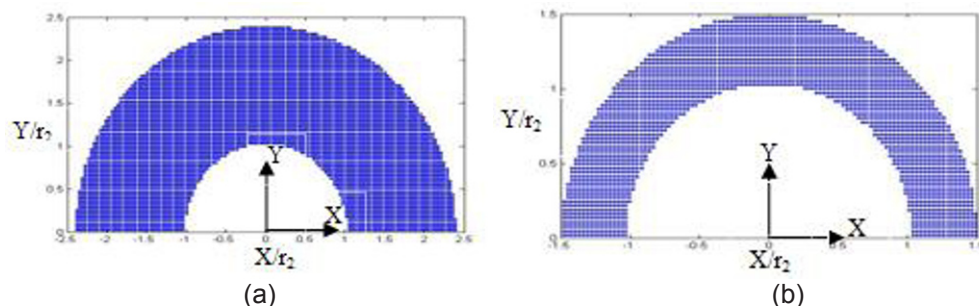


Fig. 4: TSA source locations (a) $m_1 = 5,350$ and (b) $m_2 = 2,497$ for the small and large hole.

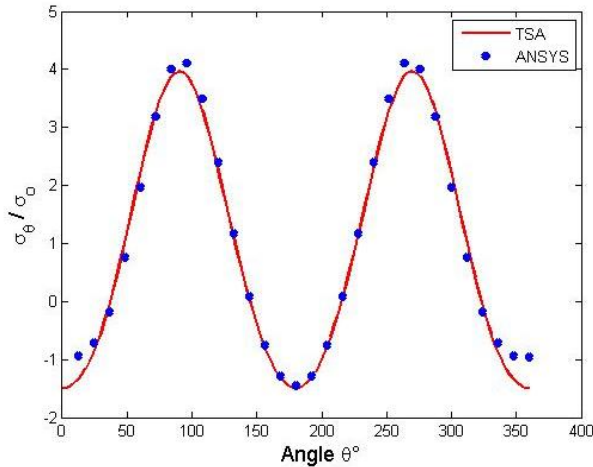


Fig. 5: Plot of $\sigma_{\theta\theta}/\sigma_0$ along the boundary of the large hole from TSA and ANSYS

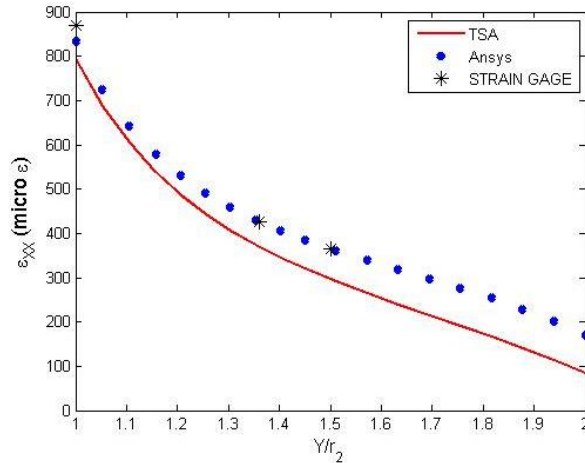


Fig. 6: Strain ϵ_{xx} along CD of *figure 1* from TSA, ANSYS and strain gages

4. Satisfying Stress Compatibility between the Holes

Although the measured input TSA data around either one of the holes automatically includes the consequences of the other hole, until now there was no attempt here to incorporate explicitly the consequence of the stresses associated with one hole on those of the other hole. This is now done so by imposing compatibility conditions for the analyses of the stresses associated with the large and the small holes, i.e., ensuring the stresses σ_{xx} , σ_{yy} , σ_{xy} given by the individual analysis for each of the small and the large hole are equal in the common region between the holes, *figure 7*. For this, the rectangular stress components, σ_{xx} , σ_{yy} , σ_{xy} , in the common overlapping area of *figure 7* associated with each hole were expressed in terms of their Airy coefficients according to *equation 10*. Additional conditions thus make use of the 406 discrete locations in this common region. Therefore, each stress component, σ_{xx} , σ_{yy} , σ_{xy} , provides 406 additional conditions i.e., $c = 406 \times 3 = 1218$ more conditions which were then employed to solve a matrix expression similar to *equation 10* by which to evaluate the unknown Airy coefficients. The total number of input values used now becomes $m_1 + h + c = 6,588$ for the small hole and $m_2 + h + c = 3,735$ for the large hole, where $c = 1,218$ conditions, $h = 20$ traction-free conditions at the longitudinal edge of the plate, $m_1 = 5,350$, and $m_2 = 2,497$ measured TSA values with $k = 9$ coefficients for the analysis of each hole.

The analysis associated with each of the small and the large hole of *figure 8* was again carried out individually, and enforced (in addition to the traction-free conditions at the respective hole and 10 locations at the edge of the plate) compatibility of the stresses by each of these analyses at the 406 points in the common region between the holes. The individual regions of the respective TSA source locations engulfing these separate holes of *figure 7* are those of *figure 4*. The inner radius for each of these regions is the [radius of hole + (4 x actual pixel size)] and the outer radius associated with the small and large holes are 22.86mm (0.9") and 19.05mm (0.75") or $X/r_1 = 2.4$ and $X/r_2 = 1.5$, respectively.

Figures 8 and 9 compare the normalized stress, σ_{xx}/σ_0 in the (loading) X-direction from ANSYS and TSA after having imposed stress compatibility between the holes.

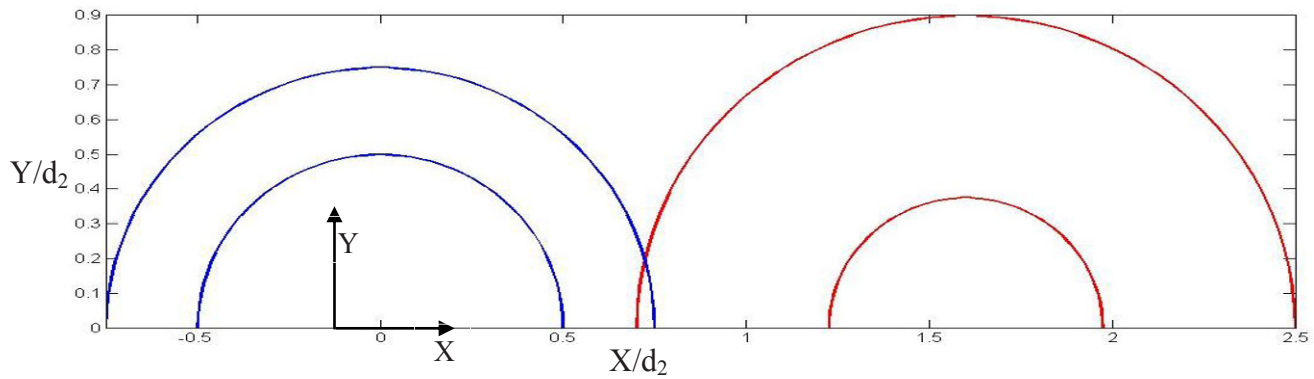


Fig. 7: Common area between small and large circles.

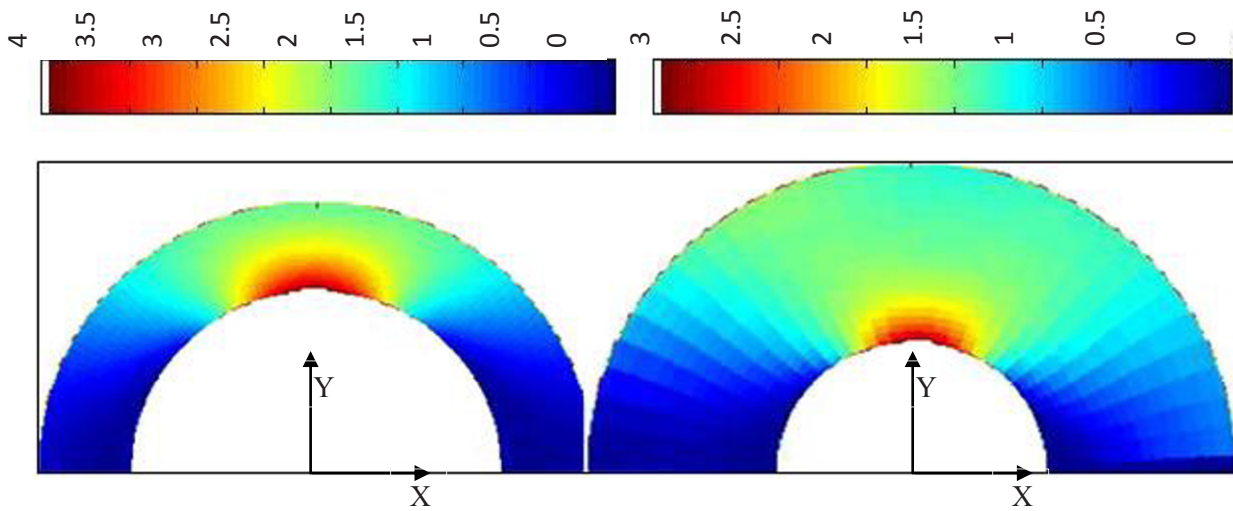


Fig. 8: Contour plots of σ_{xx}/σ_0 from ANSYS.

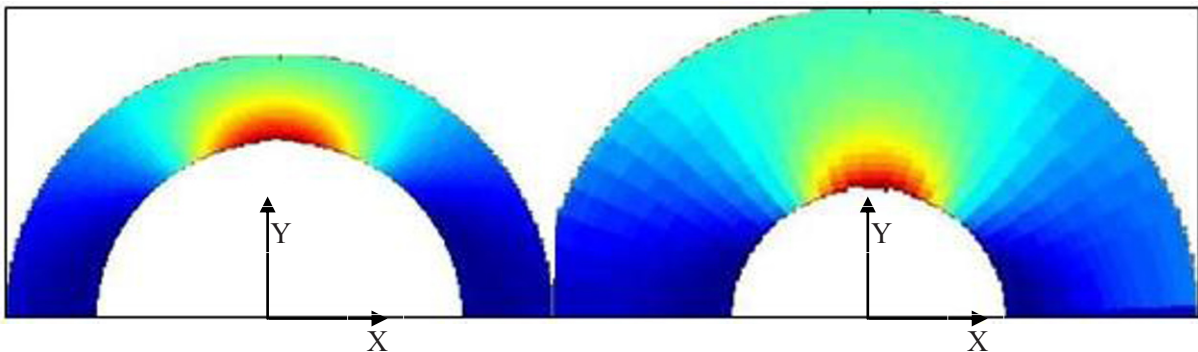


Fig. 9: Contour plots of σ_{xx}/σ_0 from TSA for small hole (right image) $m_1+h+c = 6,588$ input values, and $m_1 = 5,350$ TSA values, and for large hole (left image) $m_2+h+c = 3735$ input values and $m_2 = 2,497$ TSA values; $h = 20$, $c = 406 \cdot 3$, $k = 9$ coefficients.

5. Summary, Discussion and Conclusions

The present study was motivated by a relative lack of stress information in multiple-perforated *finite* members when the different size geometric discontinuities are sufficiently close together that their respective stress fields interact. Current TSA results correlate well with those from strain gages and FEM. While the details are omitted here for space reasons, force equilibrium is also satisfied.

Imposing the traction-free conditions ($\sigma_{rr} = \sigma_{r\theta} = 0$) on the edge of the holes analytically enables all of the Airy coefficients to be evaluated from measured TSA data without the need for any supplemental experimental stress analysis. That it is unnecessary to know the external boundary conditions is advantageous.

The present method of mathematically enforcing compatibility of the stresses which were associated initially only in the neighborhood of each of the individual holes involved averaging these respective stress components in a common region between the holes. The Airy coefficients are evaluated using least squares where the number of input values/equations (i.e., TSA measured temperature data, traction-free conditions and additional compatibility conditions) well exceeds the number of these coefficients, k . Under various conditions, $k = 9$ is found to be an appropriate number of Airy coefficients to use for the analyses of either the small or the large hole.

The technique gives the three individual components of ‘full-field’ stress, including on the edge of the holes, from only the measured temperature information and provides an enhanced understanding of how the stresses at a geometric discontinuity can be influenced by the neighboring structural compliance. This ability to determine the stress consequence of adding auxiliary holes or notches in the neighborhood of initial geometric discontinuities is important in engineering design. One could conceptually utilize photoelastic or measured displacement (moiré, speckle, digital image correlation) methods for such problems. However, unlike those approaches, TSA enjoys the advantages of neither having to differentiate the measured information, nor prepare a model or apply a birefringent coating to the component.

6. References

- [1] Rhee, J., Cho, H. K., Marr, R.J. and Rowlands, R. E., “On Local Compliances, Stress Concentrations and Strength in Orthotropic Materials”, *Society of Experimental Mechanics*, Portland, OR (2005).
- [2] Cho H. K. and Rowlands, R. E., “Reducing Tensile Stress Concentration in Perforated Hybrid Laminate by Genetic Algorithm,” *Composite Science and Technology*, **67**, 2877-2888 (2007).
- [3] Jindal, U.C., “Reduction of Stress Concentration around a Hole in a Uniaxially Loaded Plate”, *Journal of Strain Analysis*, **18**(2) (1983).
- [4] Lin, S-J., Matthys, D.R. and Rowlands, R.E., “Separating Stresses Thermoelastically in a Central Circularly Perforated Plate using an Airy Stress Function” , *Strain*, **45**, 516-526 (2009).
- [5] Foust, B. E., “Individual Stress Determination in Inverse Problems by Combining Experimental Methods and Airy Stress Functions”, Thesis, University of Wisconsin - Madison (2002).
- [6] Joglekar, N., “Separating Stresses using Airy Stress Function and TSA: Effects of Varying the Amount and Source Locations of the Input Measured TSA Data and Number of Airy Coefficients to Use”, Thesis, University of Wisconsin–Madison (2009).

Crack tip stress fields under biaxial loads using TSA

R. A. Tomlinson

*Department of Mechanical Engineering, The University of Sheffield,
Sheffield, S1 3JD, ENGLAND; email: r.a.tomlinson@sheffield.ac.uk

INTRODUCTION

The aerospace industry is striving to design less conservative and hence more efficient structures in order to meet weight reduction targets, and consequently give improvements in fossil fuel use. With this focus comes the need for the development of more accurate techniques for the assessment of the structural integrity of complex, lightweight, safety-critical components. Examples of such components are wing skin panels, which, with their array of stiffeners and holes, present a complex mixed-mode loading problem where cracks can change their growth direction. This paper focuses on the exploration of experimental mechanics methods which can be used to understand such mixed-mode fatigue failure problems.

BACKGROUND - TSA OF CRACKS UNDER BIAXIAL LOADS

In recent years considerable progress has been made using optical experimental mechanics techniques for the investigation of fatigue crack-tip strain fields^{1,2}. One of the most promising of these techniques is thermoelastic stress analysis (TSA), due to its simple surface preparation and non-contacting, full field, data collection capabilities. Thermoelasticity is based on the principle that under adiabatic and reversible conditions, a cyclically loaded structure experiences temperature variations that are proportional to the sum of the principal stresses. These temperature variations may be measured using a sensitive infra-red detector and thus the cyclic stress field on the surface of the structure may be obtained.

For over a decade, the Experimental Mechanics Research Group at the University of Sheffield has been performing significant work using TSA techniques for the understanding and description of crack-tip stress fields in mode I, and *some* work on mixed-mode applications. The initial work was by Tomlinson, who developed a methodology which she had used previously in photoelasticity, for the determination of stress intensity factors KI and KII using the Muskhelishvili approach³. Subsequent experiments were performed using this technique on biaxially-loaded slots and cracks (by Marsavina⁴), and mode I fatigue cracks through welds (by Diaz^{5,6}). The latter also explored the utilisation of the phase signal, which represents the phase shift between the thermoelastic signal recorded by the infrared detector and the reference signal from the test machine. The result of this research was to provide more information about the crack-tip stress field and plastic zones, and also the development of a method for tracking the crack tip. This work was particularly useful in the investigation of crack closure. Zanganeh used Diaz's bespoke software⁷ for investigating the interaction of crack tips, and then further developed the software to investigate T stresses. Other methodologies have been developed by other researchers and these are documented elsewhere⁸. One of the most active, however is Dulieu-Barton's team at the University of Southampton which has established a technique using a cardioid method^{9,10,11,12} to describe the relationship between the stress intensity factor, the crack-tip location and stress field surrounding the crack measured using TSA and the theoretical description proposed by Westergaard. The technique has been developed to allow estimations of the crack-tip stress intensity factors and crack-tip position by using genetic algorithms to aid direct curve-fitting of the cardioid (which mathematically describes the stress field) to the measured isopachics from TSA. This method appears to work well for mode I loaded cracks and slots, but for mixed-mode loads, the method to find the crack-tip from the cardioid patterns gives spurious results¹² which appear to be artefacts of the uniaxial loading regime. Thus it is proposed in the current study to investigate

mixed-mode cracks under controlled biaxial loads, where the crack will not change direction whilst data are being collected, thus preventing spurious results.

In addition to characterising the crack-tip stress field using the stress intensity factor, in recent years it has been shown that the T stress may be determined using TSA data. T stress is defined as the second non-singular term in Williams's¹³ crack-tip stress field solution. The T-stress is a constant stress parallel to the crack and is a measure of the constraint around the tip of a crack in contained yielding problems¹⁴ and can be used to identify how a crack growth will deviate from the perfect path due to irregularities in the microstructure¹⁵. The effects of the T-stress on the crack growth rate, crack-tip constraints, crack closure, and the shape and size of the plastic zone ahead of the crack-tip have also been assessed^{16,17}. Following successful use of TSA for stress intensity factor determination, a method was proposed to determine the T stress from such data¹⁸, however the T-stress results were found to be sensitive to crack-tip position. A new technique was proposed¹⁸ to find the crack-tip from thermoelastic images based on the Y or phase image, and this crack-tip location was used in the method to determine K and the T stress. This crack-tip location technique appeared to be more reliable than another similar technique proposed by Diaz⁶, especially in T-stress determination. The work by Zanganeh¹⁸ also investigated the use of higher order terms on the accurate determination of both K and T-stress, using methods based on both Williams's formulation and the Muskhelishvili technique. It was shown that Muskhelishvili and the two term Williams's solutions both give the same results and using them to determine the stress intensity factors does not affect the accuracy of the results significantly when compared to using three terms of Williams's solution. However, the two term Williams's solution was not sufficient to determine the T-stress accurately and the results for T-stress using this model were dissimilar to those predicted by a finite element method. It was shown that using up to three terms of the Williams's solution makes it possible to determine both the SIF *and* T-stress accurately. The majority of this work was carried out under Mode I loads and only one mixed-mode case was considered, thus there is great potential to continue this work under biaxial loading.

It was suggested by Hebb et al¹² that the inclusion of higher order terms in the theoretical description of the stress field could be more important for the accurate determination of the stress intensity factor in mixed-mode problems than in mode I. In previous work by Tomlinson which used the Mushkelishvili approach to determine K it was found that only three terms were needed to obtain convergence of the solution, however the values of KII determined still differed from the theoretical solution by up to 16%. It is now considered that the uniaxial loading, the location of the crack tip, and the resolution of the data recorded could have influenced the accuracy of these data. The subsequent work by Marsavina and Tomlinson⁴ using the Mushkelishvili approach on biaxially loaded slots and a single example of a fatigue crack concluded that the TSA technique had potential for investigating fatigue cracks under mixed-mode loads. Hence the availability at MSU of the TSA equipment together with a biaxial test machine presents the opportunity to explore this research further.

In addition to the determination of crack-tip parameters, it has been proposed by Patterson's group at Michigan State University¹⁹ that an understanding of the plastic zone size may be obtained from the TSA phase data. Diaz⁶ and then Zanganeh¹⁸ had already concluded that the maps of the phase difference between the applied load and the measured temperature contained important information which could be used to identify plasticity in the specimen, and used the signal to identify the crack-tip location. Patki¹⁹ has developed this idea further to measure the size of the plastic zone and used the information to document experimentally for the first time the effects of overloads. Again, these experiments have only been performed under Mode I conditions and so there is the potential to use this method for mixed-mode loading in order to gain greater understanding of such stress fields in a more practically relevant experimental arrangement.

Although the great potential of the TSA method has been demonstrated for Mode I fatigue cracks, it can be concluded that there is still not a full understanding of the meaning of the TSA data obtained from cracks under mixed-mode, and how these data relate to the crack-tip location, the crack-tip plasticity, the mathematical descriptions of the stress field, and subsequently the characterising parameters. Therefore it is proposed to combine the expertise of Tomlinson and Patterson in this area with the facilities at MSU in order to explore these aspects further.

PROPOSED EXPERIMENTS

The study will start by reviewing the methodology for quantification of the plastic zone size which has been developed by Patterson's team¹⁹. Experiments will be conducted in mode I on aluminium alloy 2024, with the application of larger overloads than those carried out by Patki, and then the technique will be applied using the biaxial test machine in mixed-mode loading. These experiments will provide additional understanding of the relationship between different load magnitudes, loading modes and the crack-tip behaviour, and further knowledge of the how the TSA data can characterise local crack-tip phenomena.

It is then proposed to use the bespoke software developed at the University of Sheffield for the determination of K and T stress in order to explore the TSA response of propagating mixed-mode fatigue cracks under biaxial loads. The bespoke software allows the number of terms to be varied easily, so the hypothesis that “the inclusion of higher order terms in the theoretical description of the stress field is more important for the accurate determination of K in mixed-mode problems than in mode I” will be explored. Both the Muskhelishvili approach and the Williams approach will be used.

It has already been suggested here that mode I crack growth from the slanted cracks under uniaxial loads caused spurious results in Hebb’s experiments¹², but it is also possible that specimen movement under such loads could distort the TSA data field collected. The mixed-mode methodologies for K and crack-tip location *may* be more sensitive to specimen movement under such loads than for mode I applications.

The biaxial test machine has four actuators which can be adjusted independently to minimise rigid body movement of a specimen. The ability to minimise such movement of the crack-tip will be crucial to quality data collection, an added advantage of biaxial loading.

The initial biaxial experiments will be performed using cruciform shaped specimens⁴ made from 150M36 steel which are identical to those used by Marsavina. This will allow direct comparison with previous results, but by using more modern machine control and data collection systems than these previous tests, better quality results are anticipated. It is then proposed to use the same cruciform specimen design with other materials such as the aircraft grade aluminium 2024 used by Patki¹⁹. This will allow the potential of the technique to be explored.

REFERENCES

- ¹ Olden E. J., Patterson E. A., Optical analysis of crack tip stress fields: A comparative study, *Fatigue and Fracture in Engineering Materials and Structures*, 277: 623-636, 2004.
- ² Sanford R. J., Determining fracture parameters with full-field optical methods, *Experimental Mechanics*, 29(3):241-247, 1989.
- ³ Tomlinson, R. A, Nurse, A. D. and Patterson, E. A., “On determining stress intensity factors for mixed-mode cracks from thermoelastic data”, *Fatigue and Fracture of Engineering Materials and Structures*, 20, (2), 217-226, 1997
- ⁴ Marsavina, L, and Tomlinson, R A, Thermoelastic investigations for fatigue life assessment, *Experimental Mechanics*, 44, 487 – 494, 2004
- ⁵ Diaz, F A, Patterson, E A, and Yates, J R, Some improvements in the analysis of fatigue cracks using thermoelasticity, *International Journal of Fatigue*, 26, 365–376, 2004
- ⁶ Diaz, F A, Patterson, E A, Tomlinson, R A, and Yates, J R, Measuring stress intensity factors during fatigue crack growth using thermoelasticity, *Fatigue and Fracture in Engineering Materials and Structures*, 27, 571 – 583, 2004
- ⁷ Yates J.R, Zanganeh, M., Tomlinson, R.A. Brown, M.W., and F.A. Diaz Garrido , Crack paths under mixed mode loading, *Engineering Fracture Mechanics*, 75, 319–330, 2008
- ⁸ Tomlinson, R A, and Olden, E J, Thermoelasticity for the analysis of crack tip stress fields - a review, *Strain*, 35, (2), 49-55, 1999.
- ⁹ Stanley P and Dulieu-Smith J M 1993 Progress in the thermoelastic evaluation of mixed-mode stress intensity factors *Proc. SEM Spring Conf. on Exp. Mech. Dearborn* 617–26, 1993
- ¹⁰ Dulieu-Barton, J M, Fulton, M C, and Stanley, P, The analysis of thermoelastic isopachic data from crack tip stress fields, *Fatigue and Fracture in Engineering Materials and Structures*, 23, 301-313, 2000
- ¹¹ Dulieu-Barton, JM and Worden, K, Genetic Identification of crack-tip parameters using thermoelastic isopachics, *Meas. Sci. Technol.* **14**, 176–183, 2003
- ¹² Hebb, R I, Dulieu-Barton, J M , Worden, K, and Tatum, P, Curve Fitting of Mixed Mode Isopachics, 7th *International Conference on Modern Practice in Stress and Vibration Analysis, Journal of Physics: Conference Series*, 181, 2009
- ¹³ Williams, M.L. On the stress distribution at the base of a stationary crack. *J. App. Mech.*, 24, 109–114, 1957
- ¹⁴ Ayatollahi, M.R., Pavier, M.J. and Smith, D.J. Determination of T -stress from finite element analysis for mode I and mixed mode I/III loading. *Int. J. Fracture*, 91, 283-298, 1998
- ¹⁵ Cotterell, B. Notes on the paths and stability of cracks. *Int. J. Fracture*, 2(3), 526-533, 1966
- ¹⁶ Roychowdhury, S. and Dodds Jr., R.H. Effect of T-stress on fatigue crack closure in 3-D small-scale yielding. *Int. J. Solids Struct.*, 41, 2581–2606, 2004
- ¹⁷ Smith, D.J., Ayatollahi, M.R. and Pavier, M.J. The role of T-stress in brittle fracture for linear elastic materials under mixed-mode loading. *Fatigue Fract. Engng. Mater. Struct.* 24(2), 137–50, 2001

¹⁸ Zanganeh, M, Tomlinson, R A, and Yates J.R., T-stress determination using thermoelastic stress analysis, *Journal of Strain Analysis for Engineering Design*, 43, 529-537, 2008

¹⁹ Patki, A S and Patterson, E A , Thermoelastic stress analysis of Fatigue Cracks subject to overloads, *Fatigue and Fracture of Engineering Materials and Structures*, submitted for special issue on *Experimental Fracture Mechanics*, 2009

Extending TSA with a Polar Stress Function to Non-Circular Cutouts.

A. A Khaja¹ and R. E. Rowlands²

Department of Mechanical Engineering, University of Wisconsin, Madison, WI 53706

[1khaja@wisc.edu](mailto:khaja@wisc.edu)

[2rowlands@enr.wisc.edu](mailto:rowlands@enr.wisc.edu)

ABSTRACT

This paper extends ability to thermoelastically stress analyze components containing other than circular discontinuities. Combining recorded temperatures with a stress function for stress analysis (i.e., TSA) has proven to be effective. Previous publications applied TSA to members having various shaped cutouts by employing a stress function in complex variables [1]. A shortcoming of such an approach is that one can typically evaluate the stresses only incrementally around the entire edge of a hole or notch. Real variables are also easier to use than complex variables and a general series-form of the Airy stress function exists in (real) polar coordinates which enables the stresses be determined simultaneously around an entire cutout. The TSA approach using polar coordinates is illustrated here for the case of an elliptical hole in a finite tensile plate. Little information is available for such finite situations, purely analytical solutions are extremely difficult for finite geometries, and both theoretical and numerical approaches are challenging if the external loading is not well known. The number of Airy coefficients to retain is evaluated experimentally, and the TSA results are substantiated independently.

1. Introduction

Holes of various shapes are frequently employed in engineering structures. Elliptical holes often occur in finite engineering components but such situations are difficult to stress analyze, particularly for finite components whose external boundary conditions are not well known. Relatively little information is available for finite members containing elliptical holes and even less for elliptical notches, [2-10]. This paper demonstrates the ability to thermoelastically stress analyze finite components containing a non-circular geometric discontinuity using a stress function in real (polar) coordinates. This is important because very few theoretical solutions are available for finite geometries, *figure 1* and strictly numerical (finite element or finite difference) methods necessitate knowing the external loading and geometry. The reliability of the present TSA results is substantiated by comparison with those from finite element analysis and commercial strain gages. The major contribution of this paper is the demonstrated ability to thermoelastically stress analyze finite components containing a non-circular geometric discontinuity using a stress function in real (polar) coordinates.

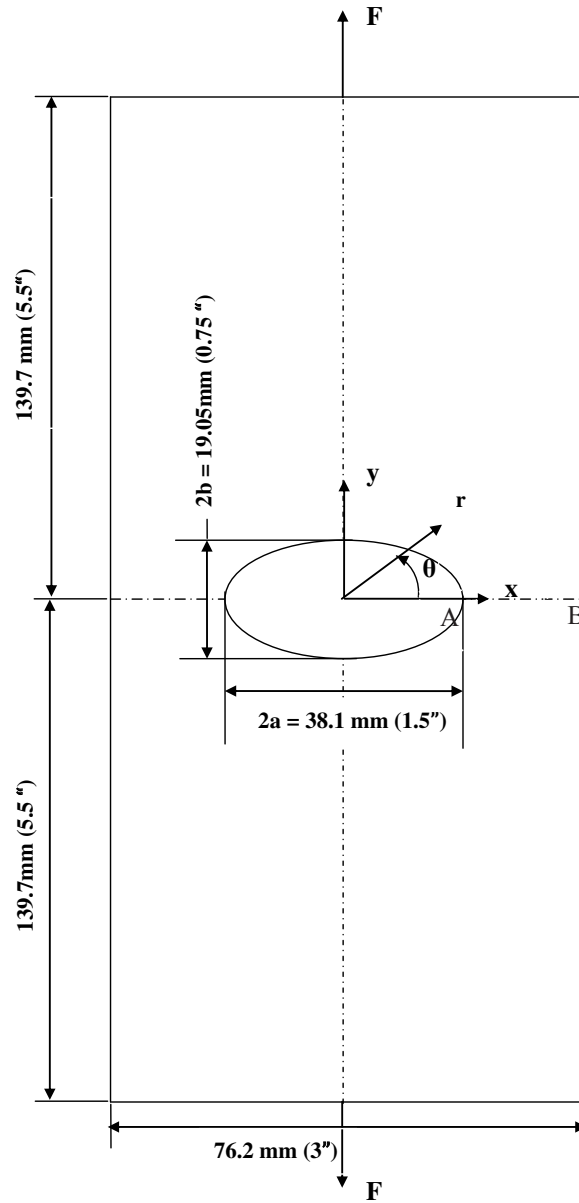


Fig. 1: Symmetrically-loaded tensile aluminum plate containing an elliptical hole.

2. Relevant Equations

Under proportional plane-stress isotropy, the measured TSA temperature signal, S^* , is related to the stresses by

$$S^* = K\Delta[(\sigma_1 + \sigma_2) = (\sigma_{rr} + \sigma_{\theta\theta}) = (\sigma_{xx} + \sigma_{yy}) = \sigma_{\xi\xi} + \sigma_{\eta\eta}] \quad (1)$$

where S is sometimes called the first stress invariant, the trace of the stress tensor or the isopachic stress value, K is the isotropic thermoelastic coefficient, and $(\sigma_1 + \sigma_2)$, $(\sigma_{rr} + \sigma_{\theta\theta})$, $(\sigma_{xx} + \sigma_{yy})$ and $(\sigma_{\xi\xi} + \sigma_{\eta\eta})$ are the sum of the stresses in the principal directions, in polar coordinates, in Cartesian coordinates and in elliptical coordinates, respectively, [figure 2](#).

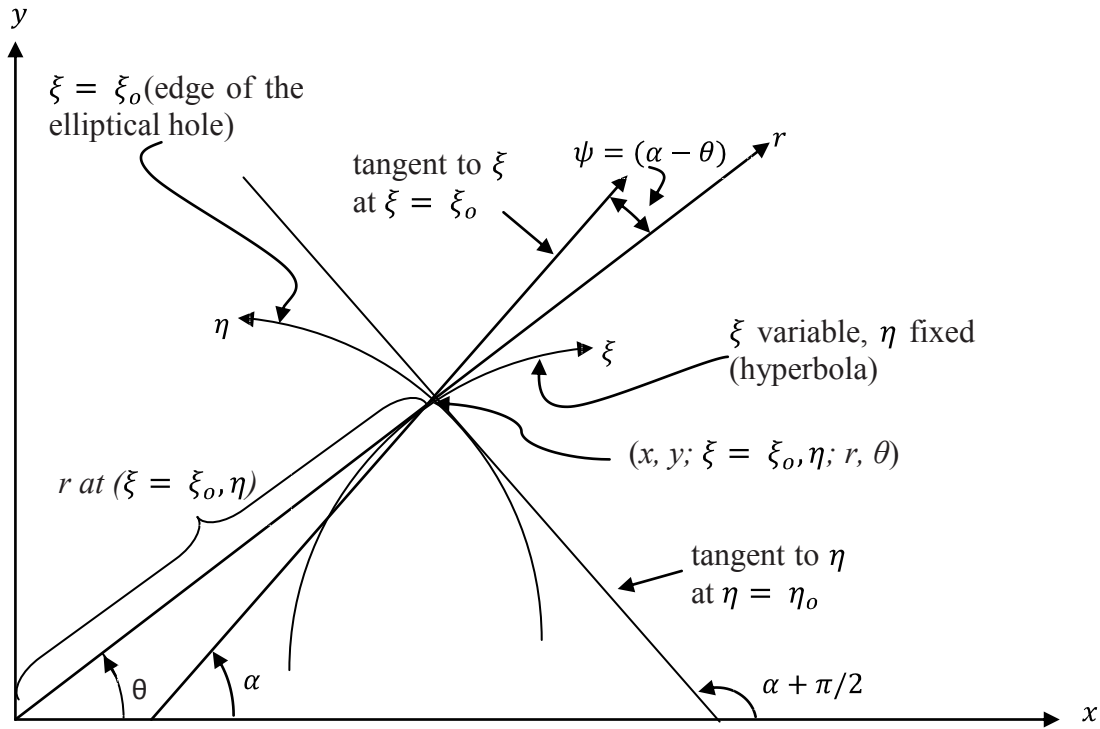


Fig. 2: Coordinate representations

For thermoelastically stress analyzing the elliptically-perforated vertically-loaded finite plate of [figure 1](#), one can utilize the Airy's stress function in polar coordinates. In this particular case the coordinate origin is at the center of the hole, [figure 1](#), such that the situation is symmetric about both x- and y- axes, thereby simplifying the stress function and hence the number of Airy coefficients needed. Since the plate of [figure 1](#), is symmetrical about both horizontal and vertical axes, the raw recorded TSA data were averaged throughout the four quadrants so as to eliminate any possible non-symmetry. In addition to the measured temperature data, the traction-free conditions are imposed *discretely* on the boundary of the elliptical hole. It is convenient to employ elliptical coordinates when satisfying the traction-free conditions at the edge of the elliptical hole. For the present case of [figure 1](#), a relevant Airy stress function is

$$\phi = a_0 + b_0 \ln r + c_0 r^2 + \sum_{n=2,4,6,\dots}^N \{(a_n r^n + b_n r^{n+2} + c_n r^{-n} + d_n r^{-(n-2)}) \cos n\theta\} \quad (2)$$

Individual components of stresses can be evaluated by differentiating the stress function of [equation 2](#) as shown in [equations 3 through 5](#):

$$\sigma_{rr} = \frac{1}{r} \frac{\partial \phi}{\partial r} + \frac{1}{r^2} \frac{\partial^2 \phi}{\partial \theta^2} \quad (3)$$

$$\sigma_{\theta\theta} = \frac{\partial^2 \phi}{\partial r^2} \quad (4)$$

$$\sigma_{r\theta} = -\frac{\partial}{\partial r} \left(\frac{1}{r} \frac{\partial \phi}{\partial \theta} \right) \quad (5)$$

Upon differentiating *equation 2* according to *equations 3 through 5*, the individual polar components of stress can be written as follows:

$$\sigma_{rr} = \frac{b_0}{r^2} + 2c_0 - \sum_{n=2,4,\dots}^N \left[\begin{array}{l} a_n n(n-1)r^{n-2} + b_n(n+1)(n-2)r^n \\ + c_n n(n+1)r^{-(n+2)} + d_n(n-1)(n+2)r^{-n} \end{array} \right] \cos(n\theta) \quad (6)$$

$$\sigma_{\theta\theta} = \frac{-b_0}{r^2} + 2c_0 + \sum_{n=2,4,\dots}^N \left[\begin{array}{l} a_n n(n-1)r^{n-2} + b_n(n+1)(n+2)r^n \\ + c_n n(n+1)r^{-(n+2)} + d_n(n-1)(n-2)r^{-n} \end{array} \right] \cos(n\theta) \quad (7)$$

$$\sigma_{r\theta} = \sum_{n=2,4,\dots}^N \left[\begin{array}{l} a_n n(n-1)r^{n-2} + b_n n(n+1)r^n \\ - c_n n(n+1)r^{-(n+2)} - d_n n(n-1)r^{-n} \end{array} \right] \sin(n\theta) \quad (8)$$

Quantity r is the radial coordinate measured from the center of the cavity and angle θ is measured counterclockwise from the horizontal x-axis, *figure 1*. N is the terminating index value of the series (since in practice one can only handle a finite number of terms) and it can be any positive even integer.

Using the transformation matrix, stresses acting in the polar co-ordinate system can be transformed to those in the Cartesian coordinates, *equations 9 through 11*, and in elliptical co-ordinates, *equations 12 through 14*, as follows:

$$\sigma_{xx} = \left[\begin{array}{l} \frac{b_0}{r^2} \cos 2\theta + 2c_0 \\ - \sum_{n=2,4,\dots}^N \left\{ \begin{array}{l} a_n n(n-1)r^{n-2} [\cos(n\theta - 2\theta)] \\ + b_n(n+1)r^n [n \cos(n\theta - 2\theta) - 2 \cos(n\theta)] \\ + c_n n(n+1)r^{-(n+2)} [\cos(n\theta + 2\theta)] \\ + d_n(n-1)r^{-n} [n \cos(n\theta + 2\theta) + 2 \cos(n\theta)] \end{array} \right\} \end{array} \right] \quad (9)$$

$$\sigma_{yy} = \left[\begin{array}{l} -\frac{b_0}{r^2} \cos 2\theta + 2c_0 \\ + \sum_{n=2,4,\dots}^N \left\{ \begin{array}{l} a_n n(n-1)r^{n-2} [\cos(n\theta - 2\theta)] \\ + b_n(n+1)r^n [n \cos(n\theta - 2\theta) + 2 \cos(n\theta)] \\ + c_n n(n+1)r^{-(n+2)} [\cos(n\theta + 2\theta)] \\ + d_n(n-1)r^{-n} [n \cos(n\theta + 2\theta) - 2 \cos(n\theta)] \end{array} \right\} \end{array} \right] \quad (10)$$

$$\sigma_{xy} = \left[\begin{array}{l} \frac{b_0}{r^2} \sin 2\theta \\ - \sum_{n=2,4,\dots}^N \left\{ \begin{array}{l} a_n n(n-1)r^{n-2} \sin(2\theta - n\theta) \\ + b_n n(n+1)r^n \sin(2\theta - n\theta) \\ + c_n n(n+1)r^{-(n+2)} \sin(n\theta + 2\theta) \\ + d_n n(n-1)r^{-n} \sin(n\theta + 2\theta) \end{array} \right\} \end{array} \right] \quad (11)$$

$$\sigma_{\xi\xi} = \left[\begin{array}{l} \frac{b_0}{r^2} \cos 2\psi + 2c_0 \\ - \sum_{n=2,4,\dots}^N \left\{ \begin{array}{l} a_n n(n-1)r^{n-2} \cos(n\theta + 2\psi) \\ + b_n(n+1)r^n [n \cos(n\theta + 2\psi) - 2 \cos(n\theta)] \\ + c_n n(n+1)r^{-(n+2)} \cos(n\theta - 2\psi) \\ + d_n(n-1)r^{-n} [n \cos(n\theta - 2\psi) + 2 \cos(n\theta)] \end{array} \right\} \end{array} \right] \quad (12)$$

$$\sigma_{\eta\eta} = \left[\begin{array}{c} -\frac{b_0}{r^2} \cos 2\psi + 2c_0 \\ \sum_{n=2,4,\dots}^N \left\{ \begin{array}{l} a_n n(n-1) r^{n-2} [\cos(n\theta + 2\psi)] \\ + b_n (n+1) r^n [n \cos(n\theta + 2\psi) + 2 \cos(n\theta)] \\ + c_n n(n+1) r^{-(n+2)} [\cos(n\theta - 2\psi)] \\ + d_n (n-1) r^{-n} [n \cos(n\theta - 2\psi) - 2 \cos(n\theta)] \end{array} \right\} \end{array} \right] \quad (13)$$

$$\sigma_{\xi\eta} = \left[\begin{array}{c} -\frac{b_0}{r^2} \sin 2\psi \\ \sum_{n=2,4,\dots}^N \left\{ \begin{array}{l} a_n n(n-1) r^{n-2} \sin(n\theta + 2\psi) \\ + b_n n(n+1) r^n \sin(n\theta + 2\psi) \\ - c_n n(n+1) r^{-(n+2)} \sin(n\theta - 2\psi) \\ - d_n n(n-1) r^{-n} \sin(n\theta - 2\psi) \end{array} \right\} \end{array} \right] \quad (14)$$

where angle $\psi = \alpha - \theta$, [figure 2](#).

Adding stresses in polar coordinates ([equations 6 and 7](#)) or in Cartesian coordinates ([equations 9 and 10](#)) or in elliptical coordinates ([equations 12 and 13](#)) gives the following equation for isopachic stress:

$$S = \sigma_{xx} + \sigma_{yy} = \sigma_{rr} + \sigma_{\theta\theta} = \sigma_{\xi\xi} + \sigma_{\eta\eta} \quad (1)$$

$$S = \left[\begin{array}{c} 4c_0 \\ \sum_{n=2,4,\dots}^N \left\{ \begin{array}{l} +b_n 4(n+1)r^n \cos(n\theta) \\ -d_n 4(n-1)r^{-n} \cos(n\theta) \end{array} \right\} \end{array} \right] \quad (15)$$

Comparing [equations 6 through 15](#) shows that coefficients present in the expression for isopachic stress are also present in the expressions for individual stresses. However, the individual components of stress also contain the Airy coefficients b_0 , a_n and c_n ([equations 6 through 14](#)) which are absent in the isopachic stress, [equation 15](#). Therefore the separate stress components cannot be determined from only thermoelastic data through the expression for the isopachic stress ([equation 15](#)). However imposing the traction-free conditions i.e., zero normal and shear stress around the boundary of the hole, together with measured temperature information, does enable all of the Airy coefficients to be evaluated.

Imposing the traction-free boundary conditions *discretely* on the boundary of the elliptical hole ($\sigma_{\xi\xi} = \sigma_{\xi\eta} = 0$ at $r = R$ (where R maps the boundary of the elliptical hole for $a = 19.05\text{mm}$ ($0.75''$) and $b = 9.525\text{mm}$ ($0.357''$))) and for all values of θ), together with measured TSA data, evaluates all the unknown Airy coefficients, such that

$$\begin{bmatrix} \sigma_{\xi\xi}(r=R) \\ \vdots \\ S \\ \vdots \\ \sigma_{\xi\eta}(r=R) \end{bmatrix} = \begin{bmatrix} \cos 2\psi / R^2 & \cdots & \cdots & (n-1)R^{-n} [n \cos(n\theta - 2\psi) + 2 \cos(n\theta)] \\ \vdots & \vdots & \vdots & \vdots \\ 0 & \cdots & \cdots & -4(n-1)r^{-n} \cos(n\theta) \\ \vdots & \vdots & \vdots & \vdots \\ -\sin 2\psi / R^2 & \cdots & \cdots & -n(n-1)R^{-n} \sin(n\theta - 2\psi) \end{bmatrix} \begin{bmatrix} b_0 \\ \vdots \\ \vdots \\ \vdots \\ d_n \end{bmatrix} = \begin{bmatrix} 0 \\ \vdots \\ S \\ \vdots \\ 0 \end{bmatrix} \quad (16)$$

Thus, by incorporating the boundary conditions around the central hole *discretely*, all the unknown Airy coefficients b_0 , c_0 , a_n , b_n , c_n , d_n for $n = 2, 4, 6, \dots, N$ can be evaluated from the measured TSA data. Equation 16 can be written in simplified form as follows:

$$[A]_{(m+h) \times k} \{c\}_{k \times 1} = \{d\}_{(m+h) \times 1} \quad (17)$$

where matrix $[A]$ also includes $h/2 = 73$ expressions for each of $\sigma_{\xi\xi} = \sigma_{\xi\eta} = 0$ imposed at the boundary of the elliptical hole. Vector $\{c\}$ of [equation 17](#) contains the k unknown Airy coefficients (i.e., b_0 , c_0 , a_n , b_n , c_n , d_n for $n = 2, 4, \dots, N$). The stress vector $\{d\}$ of [equation 17](#) therefore contains the traction-free normal and shear stresses at the boundary of the elliptical hole as well as measured values of S within the plate. Measured TSA data can be

noisy so it was advantageous to use more measured input values of S plus known boundary conditions than unknowns and to determine the Airy coefficients by least squares using the '\ ' matrix division operator or 'pinv' pseudo inverse operator in the commercial MATLAB software.

3. Experimental Details

Figure 1 shows the aluminum specimen (alloy 6061-T6, ultimate strength = 275 to 311 MPa (40 to 45 ksi) and yield strength = 241 to 275 MPa (35 to 40 ksi)), its geometry, dimensions, and orientation and location of the coordinate axes. The plate was sinusoidally loaded using a MTS hydraulic testing machine, at a mean value of 3558.57 N (800lb), maximum value of 5782.68 N (1300lb) and a minimum value of 1334.46 N (300lb) at a frequency of 10Hz, *figure 3*. The aluminum plate was polished with a 400 grid sand paper and then sprayed with Krylon Ultra-Flat black paint to provide an enhanced and uniform emissivity.

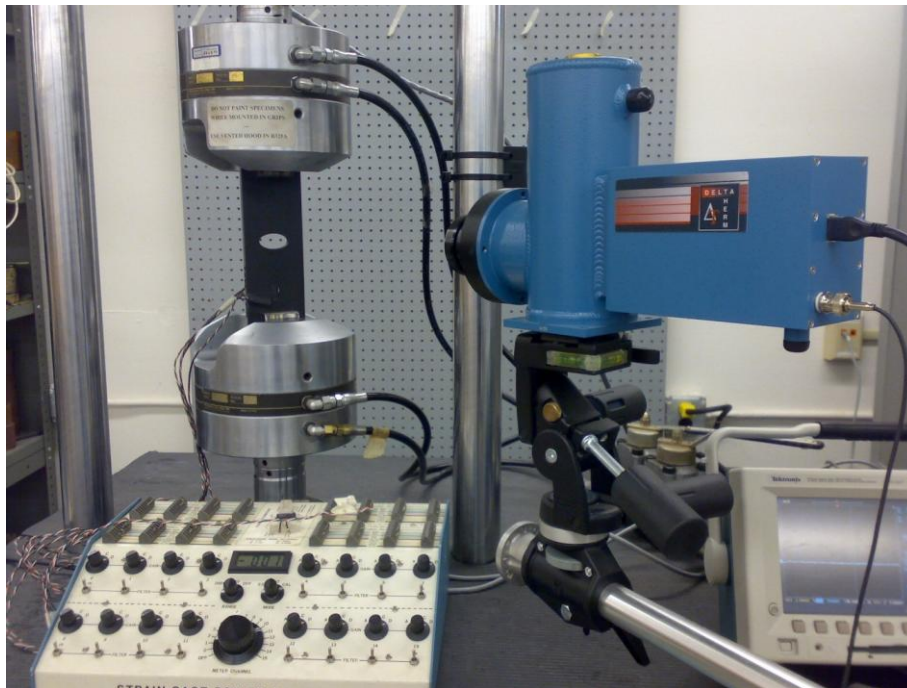


Fig. 3: Specimen in loading frame with Delta Therm DT1410 infrared camera

Figures 3 show the specimen loading, and the TSA and strain gage recording equipment. The load-induced temperature effect was recorded by a TSA Delta Therm model DT1410 camera which has a sensor array of 256 horizontal x 256 vertical pixels, *figures 3 and 4*. *Figure 4* shows an actual TSA image, S^* as recorded and displayed by the Delta Vision software which has data acquisition and interpretation tools. From a separately prepared and tested uniaxial tensile specimen (same material and "identical" (thickness, etc.) coating of flat black paint) and tested using the same TSA recording characteristics, the thermoelastic coefficient was found to be $K = 265.42 \text{ U/MPa}$ (1.83 U/psi).

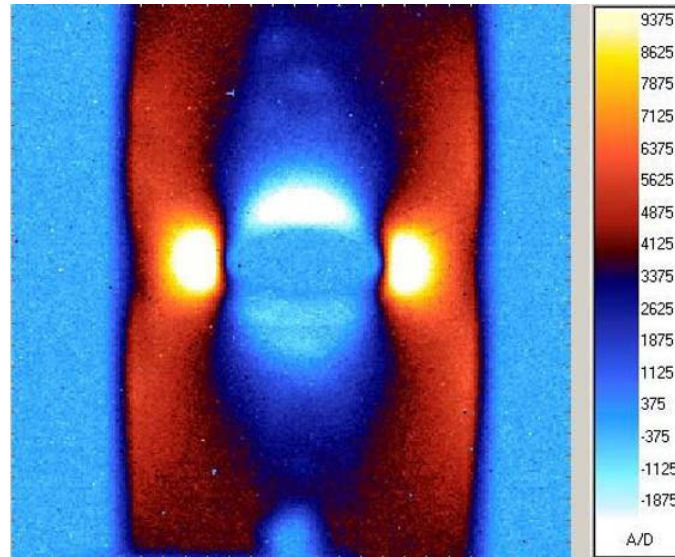


Fig.4: Actual recorded TSA image, S^* , for a load range of 4448.22 N (1000lb).

4. Analysis and Results

Since the plate is symmetrical about the both the x and y axes (figure 1), the recorded TSA data were averaged throughout the four quadrants. However, recognizing the typical unreliability of TSA data near an edge (figure 4), no measured information were utilized originating within at least two data positions (~ 0.96 mm or 0.0378 ") of the edge of the hole.

The $m = 1703$ measured TSA values of S^* utilized, figure 5, and the $h = 146$ traction-free conditions ($\sigma_{\xi\xi} = \sigma_{\xi\eta} = 0$) on the boundary of the hole (i.e. for a total of $m+h = 1849$ input values) were combined to evaluate the k unknown Airy coefficients, equation 17 for analyzing the elliptically perforated finite-plate of figure 1. In this analysis $k = 26$, was found to be a realistic number of Airy coefficients.

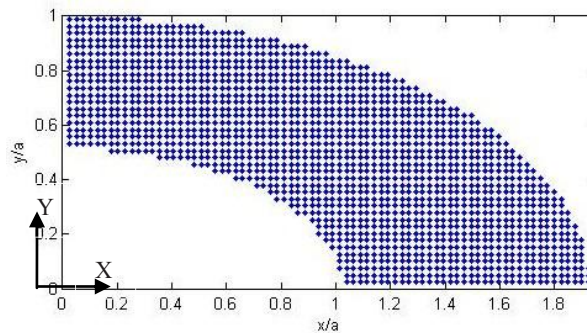


Fig.5: TSA source locations ($m = 1,703$) for 1,849 input values ($m+h = 1,849$).

After evaluating all of the unknown Airy coefficients ($b_0, c_0, a_n, b_n, c_n, d_n$ for $n = 2, 4, 6 \dots N = 12$) from the measured data, S^* , at the source locations shown in figure 5 along with the $h = 146$ traction-free conditions on the boundary of the hole of figure 1, the individual components of stress can be obtained from equations 6 through 14. TSA results are compared with the strain gages and finite element analysis in figures 6 through 8.

Figures 6 contain contour plots of the normalized Cartesian component of stress (σ_{yy}/σ_0) using the TSA (and imposed traction-free stresses on the edge of the hole) evaluated coefficients and from ANSYS. The x and y axes of figures 6 are normalized by $a = 19.05$ mm = 0.75 " (half of the major axis of the elliptical hole of figure 1). The normalized hoop stress in elliptical coordinates, $\sigma_{\eta\eta}/\sigma_0$, is plotted on the edge of the hole in figure 7. The stresses are normalized with $\sigma_0 = 9.19$ MPa (1333.33 psi) which is based on the applied tensile load, F , divided by the gross area. Angle θ of figures 7 is measured counter-clockwise from the positive x -axis, and the radial coordinate,

r , is measured from the center of the elliptical hole ($x = y = 0$) of *figures 1 and 2*. *Figure 8* compares the Cartesian components of strains $\epsilon_{\theta\theta} = \epsilon_{yy}$ from ANSYS, TSA and strain gages along line AB of *figure 1*. The x axis of *figure 8* is normalized by $a = 19.05 \text{ mm} = 0.75''$ (half of the major axis of the elliptical hole), *figure 1*.

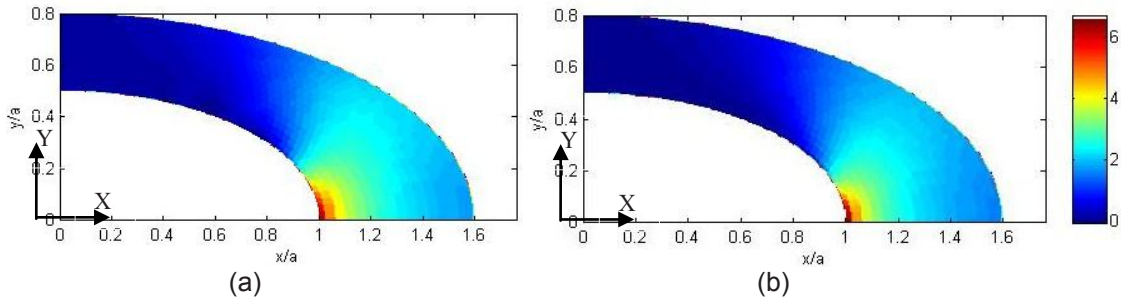


Fig. 6: Contour plots of σ_{yy}/σ_0 from TSA (a) and ANSYS (b).

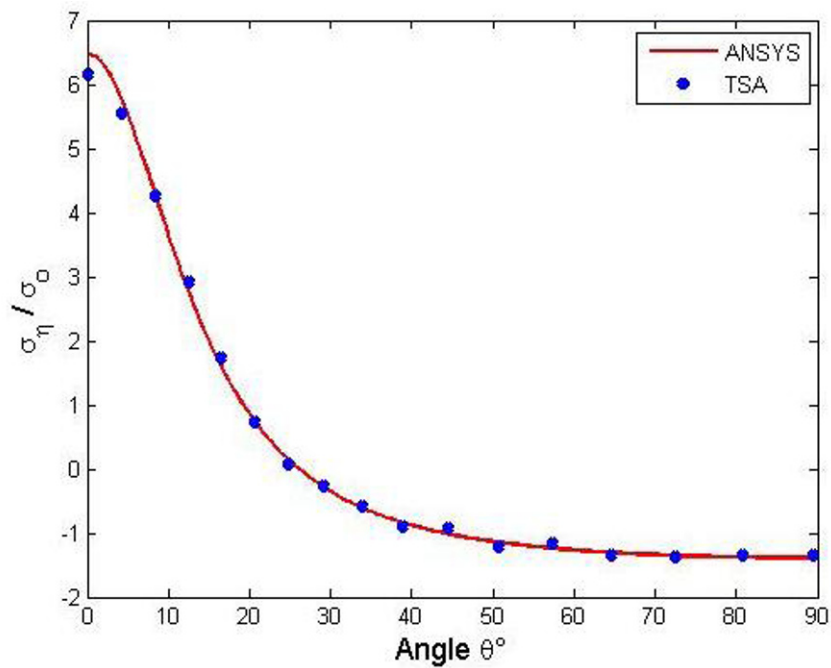


Fig. 7: Plot of hoop stress $\sigma_{\theta\theta}/\sigma_0$ on the boundary of the hole ($2a= 38.10 \text{ mm} (1.5'')$, $2b = 19.05 \text{ mm} (0.75'')$) from ANSYS and TSA ($m+h = 1,849$ input values, $k = 26$ coefficients and $m = 1,703$ TSA values).

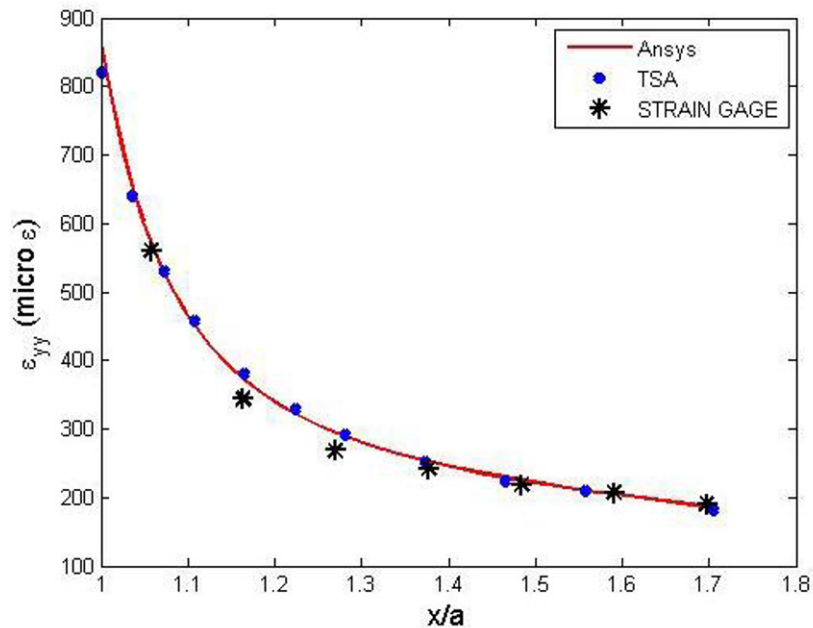


Fig. 8: Strain ε_{yy} along AB of *figure 1* from TSA, ANSYS and strain gages for $m+h = 1,849$ input values, $m = 1,703$ TSA values, $k = 26$ and $F = 4448.2$ N (1000 lb)

5. Summary

Combining a stress function with the recorded temperature information, plus perhaps some local boundary conditions, makes this general TSA approach amenable to a variety of engineering problems, thereby enhancing TSA's practical applicability. The demonstrated use of real variables (in polar coordinates) to evaluate the stresses in a finite plate containing an elliptical hole is particularly noteworthy. The TSA-based results agree with those from FEM and commercial strain gages. Summing σ_{yy} across twice the area associated with line AB of *figure 1*, i.e., $2 \int_A^B \sigma_{yy} t \, dy$ (where t is the thickness), gives a load of 4409.1 N (991.2 lbs), which agrees with the applied load of 4448 N (1000 lbs).

Since recorded TSA data are unreliable at edges, the described scheme employs temperature information only beyond at least two pixel locations from the boundary of the hole. Nevertheless, and in addition to giving individual components of stress full-field, the current technique provides accurate stress values at the boundary of the elliptical hole. Perhaps the most advantageous feature of the present approach is its ability to use a stress function in real (rather than complex) variables for other than a circular cut-out in a finite component. Stress functions formulated in terms of complex variables are mathematically more cumbersome. While the traction-free conditions at the hole are applied here discretely rather than analytically, the present approach also enjoys the advantage over the complex-variable technique of references [1] and [11] in that the latter method necessitates an iterative application for implementation around an entire hole.

Unlike the present TSA approach, strictly numerical and analytical methods require accurately knowing the far-field boundary conditions. Theoretical solutions to finite components are also extremely difficult, and few are available. The present general TSA approach is applicable to elliptical holes in more complicated components, under more complicated loading, as well as more complicated shaped cut-outs (holes, notches). In addition to not restricted to cases possessing symmetry, the current concepts could well find application to other areas of experimental mechanics.

6. References

- [1] S. T. Lin and R. E. Rowlands, "Thermoelastic Stress Analysis of Orthotropic Composites," *Experimental Mechanics*, **35**, 257-265 (1995).
- [2] Wang, J.T., Lotts, C.G., and Davis, D.D, JR., "Analysis of Bolt-Loaded Elliptical holes in Laminated Composite Joints" *Journal of Reinforced Plastics and Composites*, **12**(2), 128-138 (1993).
- [3] Oterkus, E., Madenci, E. and Nemeth. M. P., "Stress Analysis of Composite Cylindrical Shells with an Elliptical Cutout", *Journal of Mechanics of Materials and Structures*, **2**, 695-751 (2007).
- [4] Madenci, E., and Ileri, L., "An Arbitrarily Oriented, Rigid, Elliptic Inclusion in a Finite Anisotropic Medium", *Int'l Journal of Fracture*, **62**, 341-354 (1993).
- [5] Persson, E., and Madenci, E., "Composite Laminates with Elliptical Pin-Loaded Holes", *Engineering Fracture Mechanics*, **61**, 279-295 (1998).
- [6] Hwu, C., and Wen, W.J., "Green's Functions of Two-Dimensional Anisotropic Plates Containing an Elliptic Hole", *Int'l Journal of Solids and Structures*, **27**, 1705–1719 (1991).
- [7] Timoshenko, S., and Goodier, J.N., "Theory of Elasticity", McGraw-Hill Book Company, Inc. (1951).
- [8] Pilkey, W.D., and Pilkey, D.F., "Stress Concentration Factors", a Wiley-Interscience Publication, (2008).
- [9] Lekhnitskii, S.G., "Anisotropic Plates", Gordon and Breach, New York, (1968).
- [10] Savin, G.N., "Stress Concentration around Holes", Pergamon Press, London, (1961).
- [11] Huang, Y.M., and Rowlands, R.E., "Quantitative Stress Analysis Based on the Measured Trace of the Stress Tensor", *Journal of Strain Analysis*, **26**(1), 58-63 (1991).

Novel Synthetic Material Mimicking Mechanisms from Natural Nacre

Allison Juster, Felix Latourte, and Horacio D. Espinosa*

Dept. of Mechanical Engineering, Northwestern University, 2145 Sheridan Rd., Evanston, IL
60208-3111

* Corresponding author: espinosa@northwestern.edu

ABSTRACT

The biomimetics field has become very popular as Mother Nature creates materials with superior strength and toughness out of relatively weak material constituents. This concept is attractive because current synthetic materials have yet to achieve this level of performance from the same weak material constituents. Nacre, from Red Abalone shells, is among the natural materials exhibiting outstanding toughness, while being comprised of a brick and mortar structure of 95% brittle ceramic tablets and 5% soft organic biopolymer mortar. During loading, that tablets slide relative to each other. This generates progressive interlocking which constitutes nacre's primary toughening mechanism [1, 2]. We have translated this concept of tablet sliding and interlocking to create a novel composite material. Fabrication of the material will be discussed as well as design parameters. Results from tensile tests will be presented as well as comparison of the synthetic material to natural nacre. Implications to the synthetic materials community will be presented.

Introduction

Materials from Nature make use of hierarchical structures to yield high performance materials from weak material constituents (nacre, bone, wood [3-7]). Nacre is one of these natural materials found in Abalone shells that exhibit remarkable strength and toughness despite comprising of 95% brittle aragonite ceramic [3]. Because of its hierarchical structure, nacre is orders of magnitude tougher than the pure aragonite ceramic. At the microscale, nacre resembles a brick-and-mortar structure where the aragonite ceramic tablets are the bricks and the biopolymer lining of the tablets is the mortar [8, 9]. Under loading it has been shown that the brick tablets slide relative to each other, interlocking progressively as they slide to spread damage across the sample [1, 2, 10]. Because of nacre's damage spreading capabilities, it dissipates energy over large areas giving it superior toughness. Understanding the hierarchical mechanisms in natural materials, specifically nacre, will aide in the development of synthetic materials with extraordinary mechanical properties.

Through in-situ atomic force microscope (AFM) fracture experiments and digital image correlation (DIC), we are able to quantify tablet sliding at the nanoscale and elucidate the microscale mechanisms in the tablet geometry that generate progressive interlocking. Using this comprehensive nanoscale investigation of tablet sliding as a guide, we then translate these toughening mechanisms into a scaled-up composite material. We integrate the interlocking mechanism through a dovetailed structure that interlocks during loading, and use a soft polymer as the interface material to enable tablet sliding. We conduct a parametric analysis varying the geometry of tablets in the artificial composite material and arrive at an optimal design whose failure mode corresponds directly to that of natural nacre. Using the same DIC process as mentioned above, we see the same normalized degree tablet sliding as we observed in natural nacre.

Experiments

Natural nacre was tested in three-point bending using a pre-notched fracture sample [2]. To observe tablet sliding, the sample was imaged with an AFM during testing. With these images, we can observe the tablet sliding evolution of natural nacre. To quantify the tablet sliding, post processing was performed using DIC with sub-nanometer resolution (~1/10 pixel or 0.4nm) [11].

The artificial composite material was tested using a MTS Syntec 20/G tensile testing machine. Images were taken using a Navitar macro lens and CCD camera. The same DIC technique was used to quantify tablet sliding in the artificial material. Through this testing, we were able to analyze the effect of changing geometric parameters on the artificial material.

Results

By comparing the post processing from the natural nacre and artificial experiments, we have found that our optimized artificial sample has the same normalized failure mode as natural nacre. Furthermore, our artificial sample gives a 100% increase in energy dissipation, compared to the monolithic tablet material. We also see damage spreading throughout the sample which gives this increase in energy dissipation. With this study we can conclude that tablet sliding and interlocking is a major toughening mechanism in natural nacre.

References

1. Barthelat, F., et al., *On the mechanics of mother-of-pearl: A key feature in the material hierarchical structure*. Journal of the Mechanics and Physics of Solids, 2007. **55**(2): p. 306-337.
2. Barthelat, F. and H. Espinosa, *An experimental investigation of deformation and fracture of nacre–mother of pearl*. Experimental Mechanics, 2007. **47**(3): p. 311-324.
3. Sarikaya, M. and I.A. Aksay, eds. *Biomimetics, Design and Processing of Materials*. Polymers and complex materials, ed. AIP. 1995: Woodbury, NY.
4. Mayer, G., *Rigid Biological Systems as Models for Synthetic Composites Science*, 2005. **310**(5751): p. 1144-1147.
5. Buehler, M.J. and T. Ackbarow, *Fracture mechanics of protein materials*. Materials Today, 2007. **10**(9): p. 46-58.
6. Ashby, M.F., et al., *The Mechanical Properties of Natural Materials. I. Material Property Charts*. Proceedings: Mathematical and Physical Sciences, 1995. **450**: p. 123-140.
7. Gao, H.J., et al., *Materials become insensitive to flaws at nanoscale: Lessons from nature*. Proceedings of the National Academy of Sciences of the United States of America, 2003. **100**(10): p. 5597-5600.
8. Espinosa, H., et al., *Merger of structure and material in nacre and bone-Perspectives on de novo biomimetic materials*. Progress in Materials Science, 2009. **54**(8): p. 1059-1100.
9. Launey, M. and R. Ritchie, *On the fracture toughness of advanced materials*. Advanced Materials, 2009. **21**(2103-2110).
10. Tang, H., F. Barthelat, and H.D. Espinosa, *An elasto-viscoplastic interface model for investigating the constitutive behavior of nacre*. Journal of the Mechanics and Physics of Solids, 2007. **55**(7): p. 1410-1438.
11. F. Latourte, A.S., A. Chrysochoos, S. Pagano, B. Wattrisse, *An Inverse Method Applied to the Determination of Deformation Energy Distributions in the Presence of Pre-Hardening Stresses*. The Journal of Strain Analysis for Engineering Design, 2008. **43**(8): p. 705-717.

Mechanical Characterization of Synthetic Vascular Materials

AR Hamilton^{1,2}, C Fourastie^{2,5}, AC Karony¹, SC Olugebefola², SR White^{2,3}, NR Sottos^{2,4 *}

¹ Department of Mechanical Science and Engineering, ² Beckman Institute for Advanced Science and Technology, ³ Department of Aerospace Engineering, ⁴ Department of Materials Science and Engineering, University of Illinois at Urbana-Champaign, Urbana, United States
⁵ Arts et Métiers ParisTech, Paris, France

*1304 W. Green St., 61801, Urbana, Illinois, United States of America, 217-333-1041, n-sottos@illinois.edu

ABSTRACT

Biological materials in living organisms are furnished with a vascular system for the transportation and supply of necessary biochemical components. Many critical functions are supported by these vascular systems, including the maintenance of homeostasis, growth, autoimmune responses, regeneration, and repair. Synthetic materials with vascular systems have been created via a number of fabrication techniques in order to mimic some of these functionalities. The direct ink writing technique has been used to create polymer matrix, vascularized materials with micron-scale channels capable of autonomic repair. Liquid healing agents are delivered via the vascular system to sites of damage, where they polymerize in the crack plane, forming an adhesive bond with the surrounding material and recovering the mechanical integrity of the material. Characterizing the mechanical integrity of these materials is critical to optimizing their strength and toughness. The spacing between vascular conduits and the presence of locally-placed particle reinforcement have been shown to affect the local strain concentrations measured in these materials. In this work we study the effect of vascular geometry and local microchannel reinforcement on the bulk properties of the vascular material. Dynamic mechanical analysis is conducted to evaluate the stiffness of various vascular designs, and single edge notch beam (SENB) fracture samples are used to quantify the effect on fracture toughness.

SAMPLE PREPARATION

Epoxy matrix samples containing vascular networks were manufactured using direct ink writing. A fugitive organic ink (60% microcrystalline wax, 40% mineral oil, by weight) was deposited in a layer-by-layer manner with depositions made at each location where a microchannel was desired in the final sample. The resulting ink scaffold was then infiltrated with liquid epoxy and allowed to cure. The ink was subsequently removed by moderate heating (80°C) and applying vacuum to the microchannel outlets.

The resulting samples contained embedded microvascular networks of 200 μm diameter channels that were fully connected in three dimensions. The samples had a 0–90° stacking sequence between subsequent layers of channels, with connections from one layer to the next at the channel intersections. As detailed in [Fig. 1](#) and [Table 1](#), three different microvascular geometries (denoted Types I, II, III) were created for testing by varying the spacing between channels in the xy plane. Channel spacing in the yz plane was the same among all microvascular sample geometries.

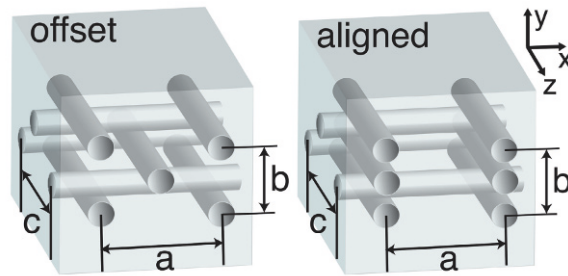


Fig. 1 Schematic of vascular system geometries.

Table 1 Vascular system dimensions

Label	Architecture	a (mm)	b (mm)	c (mm)
Type I	Offset	2.0	0.7	2.0
Type II	Offset	1.0	0.7	2.0
Type III	Aligned	2.0	0.7	2.0

Plain samples, with no vasculature, were produced using the same matrix material as vascular samples. This epoxy matrix was formed by mixing stoichiometric quantities (100:40) of Epon 828™ (DGEBA) and Epikure 3274™ (aliphatic amine). At a minimum, all samples were cured for the first 24 hours at room temperature, followed by 24 hours at 30°C.

DYNAMIC MECHANICAL ANALYSIS

Storage and loss moduli were measured by dynamic mechanical analysis over a range of frequencies from 0.01-10 Hz. Dynamic tests were performed using a TA Instruments model RSA III at a strain amplitude of 0.1%.

The storage modulus of plain epoxy samples was determined as a function of cure time beyond the minimum 48 hour cure cycle given above. The average storage modulus at 0.1 Hz for three samples is plotted in Fig. 2 as a function of cure time.

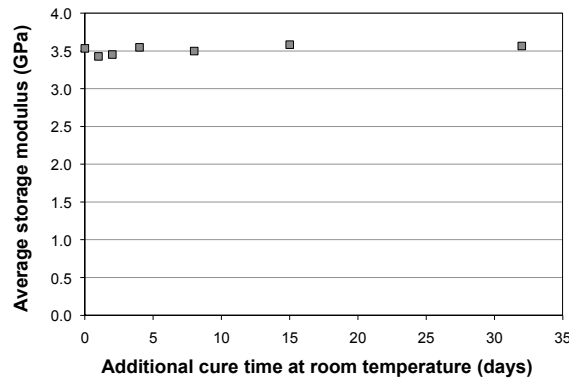


Fig. 2 Storage modulus measured at 0.1 Hz in plain epoxy samples as a function of cure time at room temperature beyond the first 48 hours. Each data point represents an average of three samples tested.

The data in Fig. 2 shows no significant change in the elastic modulus of the matrix material after the initial 48 hour cure cycle. Therefore, the moduli of vascular samples tested within a window of 5-30 days could reasonably be considered independent of cure time.

Microvascular samples were subjected to the same dynamic testing regime as plain samples. The storage modulus measured at 0.1 Hz was taken as an estimate of the elastic modulus. The average moduli for each vascular architecture (as defined in Fig. 1) are plotted as a function of microchannel volume fraction in Fig. 3.

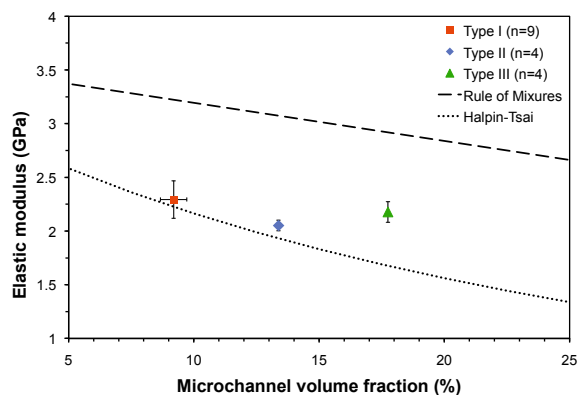


Fig. 3 Storage modulus measured at 0.1 Hz in microvascular samples plotted as a function of microchannel volume fraction. Each data point represents the average of the sample set (indicated for each sample type in the legend). Theoretical predictions, based on the rule of mixtures and the Halpin-Tsai equation, are plotted as dashed lines.

The elastic moduli obtained from dynamic mechanical analysis are compared with two theoretical predictions in Fig. 3. The theoretical curves were generated using either a rule of mixtures approximation or the Halpin-Tsai equation for particulate inclusions. For these calculations the elastic modulus of the matrix material was taken from the data plotted in Fig. 2. The Poisson's ratio of the matrix material was estimated as 0.40 for the Halpin-Tsai prediction, based on previous studies of this epoxy system [8]. All of the vascular sample types fall within the range of elastic moduli bounded by these model predictions. The Type I and Type II samples elastic moduli are better approximated by the Halpin-Tsai prediction, while the Type III sample elastic modulus lays between the two theoretical curves. The deviation of the Type III sample from the Halpin-Tsai trend may be an effect of the square lattice arrangement of microchannels, as opposed to the rhombic lattice in the Types I and II samples.

SINGLE EDGE NOTCH BEAM FRACTURE

Single edge notch beams (SENB) loaded in three-point bending were used to quantify the fracture toughness of the neat matrix material and of microvascular samples. The beam geometry detailed in Fig. 4 was determined based upon ASTM standard D5045-99 [9].

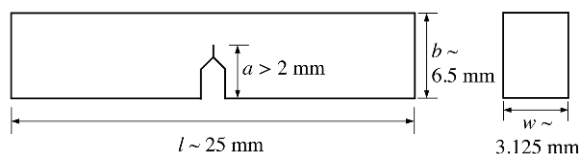


Fig. 4 SENB sample geometry and dimensions.

Sharp pre-cracks were initiated by loading the beams in cyclic fatigue until cracks extended from a notch that was scored with a razor blade. Pre-crack lengths were measured optically before monotonic loading to failure at a displacement rate of 10 $\mu\text{m/s}$. The average fracture toughnesses for the neat matrix material and vascular samples are tabulated in Table 2.

Sample	K_{IC} ($\text{MPa}\cdot\text{m}^{1/2}$)
Plain	1.18 ± 0.09
Vascular (Type I)	0.87 ± 0.08

Crack propagation occurred at lower loads in vascular fracture samples compared with plain samples, resulting in the reduced fracture toughness listed in Table 2. However, the reduced bending stiffness of the vascular samples was not taken into account in the calculation of K_{IC} . Furthermore, the effect of the initial position of the precrack relative to the microchannels has not yet been fully explored.

CONCLUSIONS AND FUTURE WORK

The elastic moduli of epoxy beams containing different microvascular network geometries were measured using dynamic mechanical analysis. The presence of microchannels reduced the overall flexural modulus of the material. The results are within the range of values predicted using the rule of mixtures and the Halpin-Tsai equation for particulate inclusions.

Preliminary fracture testing indicates a drop in the fracture toughness due to the presence of a microvascular network, however more analysis and testing are required to clarify this effect.

In a previous study, local reinforcement around a microchannel was shown to significantly reduce the level of strain surrounding a channel loaded in tension [10]. In the future, we intend to explore the effect of this locally-placed reinforcement on the bulk mechanical properties of vascular materials.

REFERENCES

- [1] Toohey KS, Sottos NR, Lewis JA, Moore JM, White SR (2007) Self-healing materials with microvascular networks. *Nat Mater* 6:581-585.
- [2] Toohey KS, Sottos NR, White, SR (2009) Characterization of microvascular-based self-healing coatings. *Exp Mech* 49:707-717.
- [3] Therriault D, White SR, Lewis JA (2003) Chaotic mixing in three-dimensional microvascular networks fabricated by direct-write assembly. *Nat Mater* 2:265-271.
- [4] Lewis JA (2006) Direct ink writing of 3D functional materials. *Adv Funct Mater* 16:2193-2204.
- [5] Hansen CJ, Wu W, Toohey KS, Sottos NR, White SR, Lewis JA (2009) Self-healing materials with interpenetrating microvascular networks. *Adv Mater* 21:1-5.
- [6] Williams HR, Trask RS, Bond IP (2007) Self-healing composite sandwich structures. *Smart Mater Struct* 16:1198-1207.
- [7] Williams HR, Trask RS, Bond, IP (2008) Self-healing sandwich panels: Restoration of compressive strength after impact. *Compos Sci Technol* 68:3171-3177.
- [8] O'Brien DJ, Sottos NR, White SR (2007) Cure-dependent viscoelastic Poisson's ratio of epoxy. *Exp Mech* 47:237-249.
- [9] ASTM D5045-99. *Standard Test Methods for Plane-Strain Fracture Toughness and Strain Energy Release Rate of Plastic Materials*. Annual Book of ASTM Standards, Vol. 08.01: Plastics (I) (ASTM International, West Conshohocken, Pennsylvania, USA, 2003).
- [10] Hamilton AR, Sottos NR, White SR (2010) Local strain concentrations in a microvascular network. *Exp Mech* 50:255-263.

MgO nanoparticles affect on the osteoblast cell function and adhesion strength of engineered tissue constructs

Morshed Khandaker and Kelli Duggan

Department of Engineering and Physics, University of Central Oklahoma, Edmond, OK 73034

Melissa Perram

Department of Chemical Engineering, Purdue University, West Lafayette, IN 47907

ABSTRACT

The objective of this research was to evaluate the influence of magnesium oxide (MgO) on the adhesion strength between hard tissue and soft tissue constructs. The scope of works for this research were: (1) to determine the viability of osteoblast cells in hydrogel and hydrogel with 22 nm MgO particles, (2) to design and construct a test setup for the measurement of adhesion strength of engineered tissue constructs, and (3) to determine if MgO nanoparticles affect on the adhesion strength of the engineered tissue constructs. Mouse osteoblast cells (MT3T3E1) were cultured on polycaprolactone (PCL) scaffold, hydrogel scaffold, as well as hydrogel scaffold with 22 nm MgO particles. The viability of cells was determined in: hydrogel and hydrogel with 22 nm MgO particles. Tensile test were conducted on: (1) PCL-hydrogel, (2) PCL-hydrogel with cells, (3) PCL-hydrogel with cells and MgO nanoparticles, and (4) PCL-hydrogel with MgO nanoparticles to measure the adhesion strength between these hard tissue and soft tissue constructs. This research found the increase of osteoblast cells adhesion on hydrogel scaffold containing 22 nm MgO particles and decrease of adhesion strength between PCL and hydrogel, when both PCL and hydrogel were seeded with cells and 22 nm MgO particles.

BACKGROUND

Each year, there are thousands of new injuries to soft tissue due to high energy impact [1]. Most of these injuries occur where soft tissue meets hard tissue in the body [2]. Several engineered tissue grafts have been developed for the reconstruction of the injured hard and soft tissues [3]. In this research, Polycaprolactone (PCL) based hard tissue and hydrogel based soft tissue grafts have been investigated. PCL scaffold is made using a precision deposition system which allows for the scaffold to have precise pore sizes and porosity, promoting an increase in cell adhesion [4-5]. The hydrogel resembles the mechanical properties of tissues in the body [6]. It has porous structure which allows the cells to grow [7]. Both of these scaffolds are biodegradable and biocompatible in the human body and can be used for bone-ligament or bone-cartilage reconstructions. The interface is the weakest place in the grafted bone-ligament or bone-cartilage reconstructions. There has not been much research done on improving the interface strength of the engineered tissue constructs. A strong bond of engineered tissue constructs will be beneficial for future tissue engineering. If this interface could be strengthened it would have great medical applications. MgO nanoparticles have been shown to improve osteoblast cell adhesion on bone cement [8]. But the influence of MgO nanoparticles on the interface strength on engineered tissue constructs is still unknown. This study hypothesized that the MgO nanoparticles could improve the osteoblast cell adhesion on hydrogel scaffold and the adhesion strength between PCL-hydrogel interfaces could be enhanced by the inclusion of nano sizes MgO particles on PCL and hydrogel tissue grafts. Both qualitative and quantitative cell viability test were conducted to examine the osteoblast cell adhesion on hydrogel scaffold. Mechanical test was conducted on PCL-hydrogel seed with MgO nanoparticles specimen using a custom made tensile test setup to the influence of adhesion strength between PCL-hydrogel interfaces. Materials and methods

MATERIALS AND METHODS

Cell viability tests

Cells were cultured in cell culture flask, and hydrogel with different percentages of MgO nanoparticles (2%, 1%, 0.5%, and 0.1%) for the cell viability tests (**Figure 1**). The viability testing of cells was conducted in these mediums both quantitatively and qualitatively. A hemocytometer is used to count cell density and cell viability of cells cultured on the flask. Trypan blue was mixed with the cells. It dyed the dead cells blue. The cells were

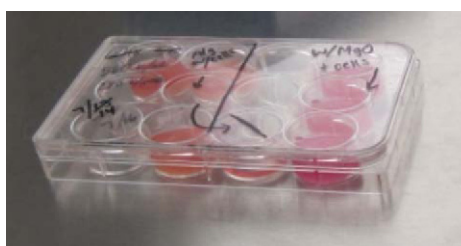
counted using the hemocytometer. The viability was evaluated by dividing the living cells by the total number of cells. A live/dead kit was used for the cell viability of cells on hydrogel samples. The samples were viewed under confocal microscope (Olympus BX61W1) for the qualitative measurement. Two different dyes were used in the kit to detect the live and dead cells. They are calcein AM and ethidium. Calcein AM entered the live cells and under blue light the cells turn to green. Ethidium entered the dead cell's nuclei and under green light, turns the cells to red. The ratio of live to dead cells was determined using the sliced confocal microscopic images. Fluorescent intensity tests were conducted on hydrogel with cells and hydrogel with nanoparticles using Fluostar Optima Microplate Reader (BMG Labtech) for determining the quantitative measurement the cell viability of cells on hydrogel samples.



Figure 1 Cell viability test on various kinds of hydrogel specimens: A. Control, Hydrogel with no cells. B. Hydrogel with cells C. Hydrogel with 2% nano D. Hydrogel with 1% nano E. Hydrogel with 0.5% nano F. Hydrogel with 0.1% nano.

PCL-Hydrogel specimen preparation

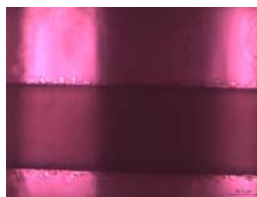
Mouse osteoblast cells (MT3T3E1) was obtained from the American Type Culture Collection (ATCC). The 5% sodium alginate was added to 5% CaCl_2 to make hydrogel scaffold ((height ~ 1.5 mm, scaffold diameter ~ 21 mm) independently in another well plate according to Lee *et al.* [9]. Osteoblast cells were cultured on hydrogel and hydrogel with MgO nanoparticles scaffolds according to ATCC instructions (Figure 2(a)). 3D Insert™ PCL scaffold scaffold (height ~ 1.5 mm, scaffold diameter ~ 21 mm, fiber diameter $\sim 300\mu$, fiber spacing $\sim 300\mu$) were purchased from 3D Biotek, LLC. The cells were cultured on the PCL well plate according to 3D Biotek instructions (Figure 2 (b to d)). The hydrogel scaffolds were carefully placed on top of the PCL and 3.9 Pascals of pressure was added on top using sterilized aluminum blocks. The hydrogel and PCL tissue constructs were cultured for 3 weeks.



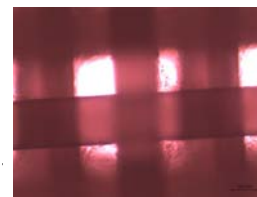
(a)



(b)



(c)



(d)

Figure 2 (a) Hydrogel samples in the sylgard mold, (b-d) PCL samples at different time periods: 2 days, 1 week and 2 weeks, respectively.

Design and manufacture of the setup and instrumentation

A custom made three point bend tester was used for the tensile experiment of the PCL-hydrogel samples. The complete setup is shown in Figure 3. A xyz stage was assembled with the test setup for microscopic viewing purposes of the samples. The PCL-hydrogel samples were carefully glued with two holders as shown in figure. A 250 gram load cell (Futek™ LCM300, model number FSH02630) with a sensor (Futek™ IPM500) was fastened to the one end of the holder. The other end of the loadcell was connected with a high precision microactuator (Newport™ LTA-HL[®] actuator) and motion controller (SMC 100). All instruments were calibrated before testing.

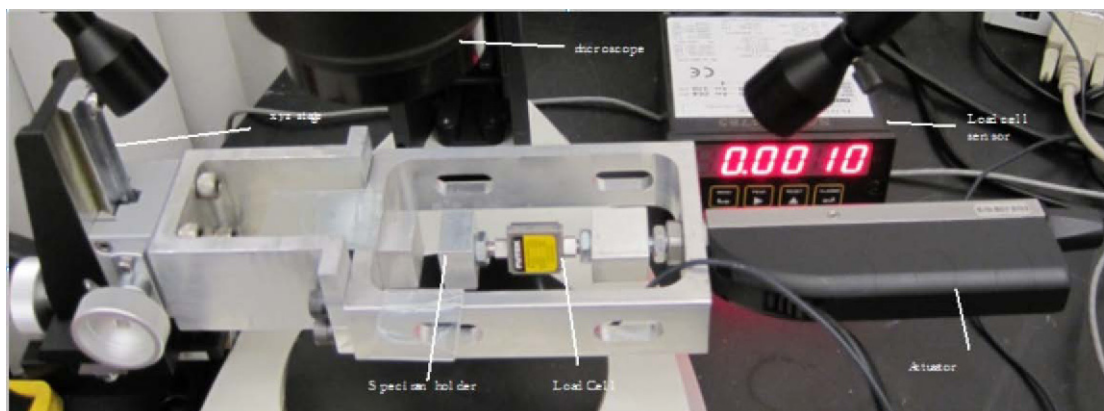


Figure 3 Experimental setup.

EXPERIMENT AND DATA ANALYSIS

Four different types of PCL-hydrogel tissue constructs were tested: PCL-hydrogel, PCL-hydrogel with cells, PCL-hydrogel with cells and MgO nanoparticles, and hydrogel with MgO nanoparticles. The PCL-hydrogel specimens were tested under moist condition using DMEM solution. The loading rate was 0.001 mm/s. The load and displacement data were continuously recorded until the failure of the PCL-hydrogel joint. The load and displacement data were processed to determine the critical interface tensile strength, σ_f , using the relationship [10]: $\sigma_f = P_{cr}/A$, where P_{cr} is the maximum value of the load-displacement curve and A is the cross-sectional area of interface ($A = \pi d^2/4$).

RESULTS

Absorbance tests were conducted (Figure 4) to determine an adequate amount of MgO nanoparticles to add to the hydrogel to increase adhesive strength, while not decomposing the hydrogel itself. The 0.5% and 0.1% were most closely compatible with the hydrogel with cells, so it was determined that the 0.5% would be sufficient to use in the hydrogel.

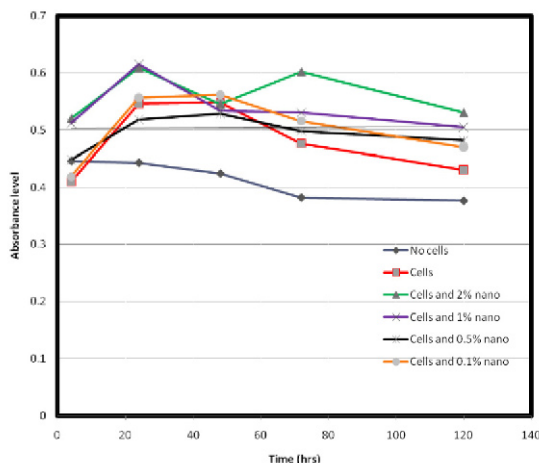


Figure 4 Absorbance test on cell seeded hydrogel with different percentage of 22 nm MgO additives.

Figure 5(a) compares the fluorescent intensity of hydrogel with cells and hydrogel with cells plus 22 nm MgO particles. Cell viability test shows that 36 μm MgO particles were detrimental to cell viability with 74% decrease in cells. Although increased cell adhesion of mouse osteoblast cells (MT3T3E1) to hydrogel-based soft tissue grafts with the use of 22 nm MgO particles. On the other hand, increased cell adhesion of mouse osteoblast cells (MT3T3E1) to hydrogel-based soft tissue grafts with the use of 22 nm MgO particles. The confocal microscope was used to see many different layers of the hydrogel and determine if the cells are living. Figure 5(b) shows that there are more alive cells (green color) than dead cells (red color).

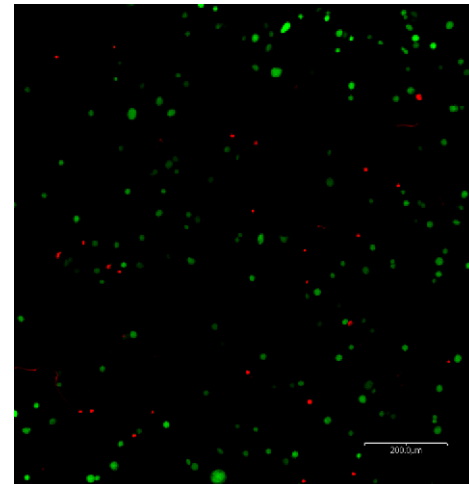
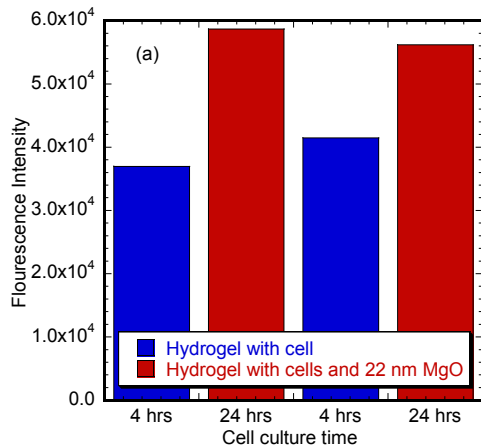


Figure 5 (a) Fluorescent intensity of hydrogel with cells and hydrogel with cells plus 22 nm MgO particles, and (b) confocal microscope image of the hydrogel samples with the cells.

Figure 6(a) compares the load-displacement curves among PCL-hydrogel, PCL-hydrogel with cells and PCL-hydrogel with cells plus 22 nm MgO. The load-displacement response of all specimens is characterized as initially elastic response, followed by a short inelastic region and then stable descending response. Figure - 5(b) compares the interface fracture strength values. Results shows decreased interface strength between cell-seeded PCL hard tissue graft and hydrogel when the MgO nanoparticles were mixed with hydrogel. The interface strength of PCL-hydrogel with no cells or nanoparticles was lower than PCL-hydrogel with cell samples but higher than PCL-hydrogel with cells and MgO nanoparticles.

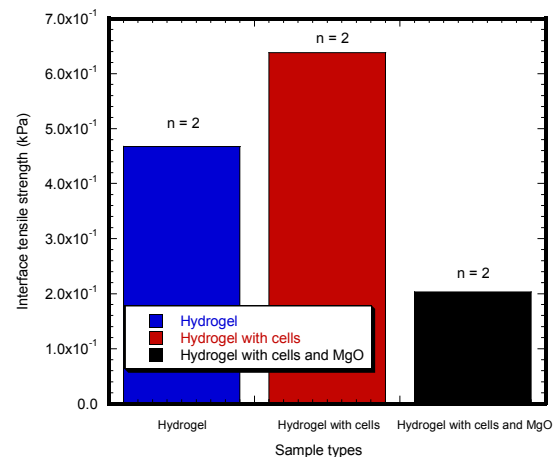
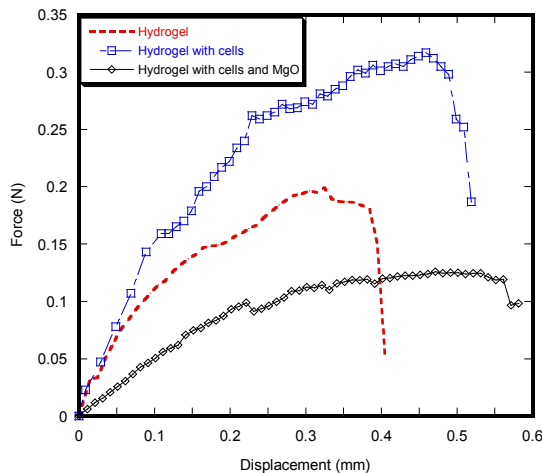


Figure 6 (a) Load vs. displacement plot of different kinds of PCL-hydrogel specimens, (b) variation of interface fracture strength for various kinds of PCL-hydrogel specimens.

CONCLUSIONS

Cells were successfully grown in hydrogel with MgO nanoparticles with no significant difference (p< .01) between samples of hydrogel with cells. The interface tensile strength of PCL-hydrogel with cells had 6% greater tensile

strength than PCL-hydrogel with cells and MgO nanoparticles. However, PCL-hydrogel with cells and MgO nanoparticles had the weakest tensile strength. This result showed that PCL-hydrogel tissue constructs had the strongest tensile strength when only cells were present in the tissue constructs and the addition of nanoparticles decreased the adhesion between PCL and hydrogel. This research concludes that appropriate amount of MgO nano additives is required for the proper cell function of the PCL-hydrogel tissue constructs.

ACKNOWLEDGEMENTS

This publication was made possible by 2009 OKEPSCoR summer research opportunity award.

REFERENCES

1. Hutmacher, D.W., "Scaffolds in tissue engineering bone and cartilage," *Biomaterials*, **21**(24), 2529-2543 (2000).
2. Lee, K.Y., Mooney D.J., "Hydrogels for tissue engineering," *Chemical Reviews*, **101**(7), 1869-1879 (2001).
3. Sun, W., Darling A., Starly B., Nam J., "Computer-aided tissue engineering: Overview, scope and challenges," *Biotechnology and Applied Biochemistry*, **39**(1), 29-47 (2004).
4. Kim, J.Y., "Fabrication of a sff-based three-dimensional scaffold using a precision deposition system in tissue engineering," *Journal of Micromechanics and Microengineering*, **18**(5), (2008).
5. Zein, I., "Fused deposition modeling of novel scaffold architectures for tissue engineering applications," *Biomaterials*, **23**(4), 1169-1185 (2002).
6. Shor, L., "Fabrication of three-dimensional polycaprolactone/hydroxyapatite tissue scaffolds and osteoblast-scaffold interactions in vitro," *Biomaterials*, **28**(35), 5291-5297 (2007).
7. Gleghorn, J.P., "Adhesive properties of laminated alginate gels for tissue engineering of layered structures.," *Journal of Biomedical Materials Research - Part A*, **85**(3), 611-618 (2008).
8. Ricker, A., Liu-Snyder P., Webster T.J., "The influence of nano mgo and baso4 particle size additives on properties of pmma bone cement," *International Journal of Nanomedicine*, **3**(1), 125-1 (2008).
9. Lee, C.S.D., Gleghorn J.P., Won Choi N., Cabodi M., Stroock A.D., Bonassar L.J., "Integration of layered chondrocyte-seeded alginate hydrogel scaffolds," *Biomaterials*, **28**(Compendex), 2987-2993 (2007).
10. An, Y.H., Draughn R.A., *Mechanical testing of bone and the bone-implant interface*. CRC (2000).

Mechanical Interactions of Mouse Mammary Gland Cells with a Three-Dimensional Matrix Construct

M.d.C. Lopez-Garcia, Graduate Research Assistant, Material Science Program,
Wisconsin Institutes for Medical Research

D.J. Beebe, Professor, Department of Biomedical Engineering,
Wisconsin Institutes for Medical Research

W.C. Crone, Professor, Department of Engineering Physics
University of Wisconsin – Madison,
1500 Engineering Dr, Madison, WI 53706
crone@engr.wisc.edu

Abstract

One risk factor associated with breast cancer is tissue or mammographic density which is directly correlated with the stiffness of the tissue. We undertook a study of mammary gland cells and their interactions with the extracellular matrix in a microfluidic platform. Mammary gland cells were seeded within collagen gels inside microchannels, using concentrations of 1.3, 2, and 3 mg/mL, along with fluorescent beads to track strains in the gel. The cells and beads were observed via four-dimensional imaging, tracking X, Y, Z positions over a three to four hour time frame. Three-dimensional elastic theory for an isotropic material was employed to calculate the stress. The technique presented adds to the field of measuring cell generated stresses by providing the capability of measuring 3D stresses locally around the single cell and using physiologically relevant materials properties for analysis.

Introduction

There are many risk factors related to breast cancer. One risk factor we would ultimately like to study is tissue or mammographic density. In a study by Boyd et al. it was found that women with a dense tissue are at four to six times greater risk of breast cancer than women with low density tissue [Friedl, et al, 2000]. This risk factor may account for as many as 30% of breast cancer cases. It was found that the increasing density in the mammogram was associated with increasing collagen and decreasing fat concentrations in the breast tissue [Cukierman, et al, 2001]. Increased density of this material correlates with an increase of stiffness in the tissue. Breast tissue is a multiphase material, in this case, mostly fat and collagen, exhibits the properties of both constituent phases. As the collagen concentration increases, the density of the tissue increases. Since the mechanical property of tissue stiffness increases with its collagen concentration [Jo, et al, 2000], we infer that the increase in density of the tissue is also related to the increase of stiffness in the material. This is one indicator of the role that mechanical properties has in the development of breast cancer.

In the research presented here we study the influence that a normal murine mammary gland cell has on its surrounding environment when encapsulated in a collagen matrix. Three different stiffnesses of collagen matrix materials were used in the broader study [Lopez-Garcia, et al, in press]. In the research discussed below we will focus on results obtained in the 2 mg/mL collagen gel.

Methods

This study was carried out in a microfluidic platform composed of PDMS fabricated via a photolithography technique [Jo et al. 2000; McDonald and Whitesides 2002]. Typically two channels per dish were assembled. [Figure 1i](#) shows a diagram of the glass bottom Petri dish with the channels, and [Figure 1ii-iii](#) shows the top and side views of the channel when seeded with the cells.

In brief, normal murine mammary gland cells transfected to express green fluorescent protein (GFP-NMuMG) were seeded in a collagen matrix within the microfluidic device. All experiments were carried out at passages less than Pn+18. The microfluidic channel walls were coated with a collagen solution 50 $\mu\text{g}/\text{mL}$ in PBS a few hours before the experiment. The cells were then suspended in collagen concentrations of either 1.3, 2.0, or 3 mg/mL. To this mixture, 0.2 μL of red fluorescent 1 μm carboxylate modified beads was added and mixed well. A 5 μL volume of the cell-gel mixture was poured into the channel. The channels were then covered and incubated. A droplet of media was added to the ports to feed the cells. They were incubated overnight, for 17 hours. Figure 1i-iii shows a diagram of cells and beads seeded into the channel.

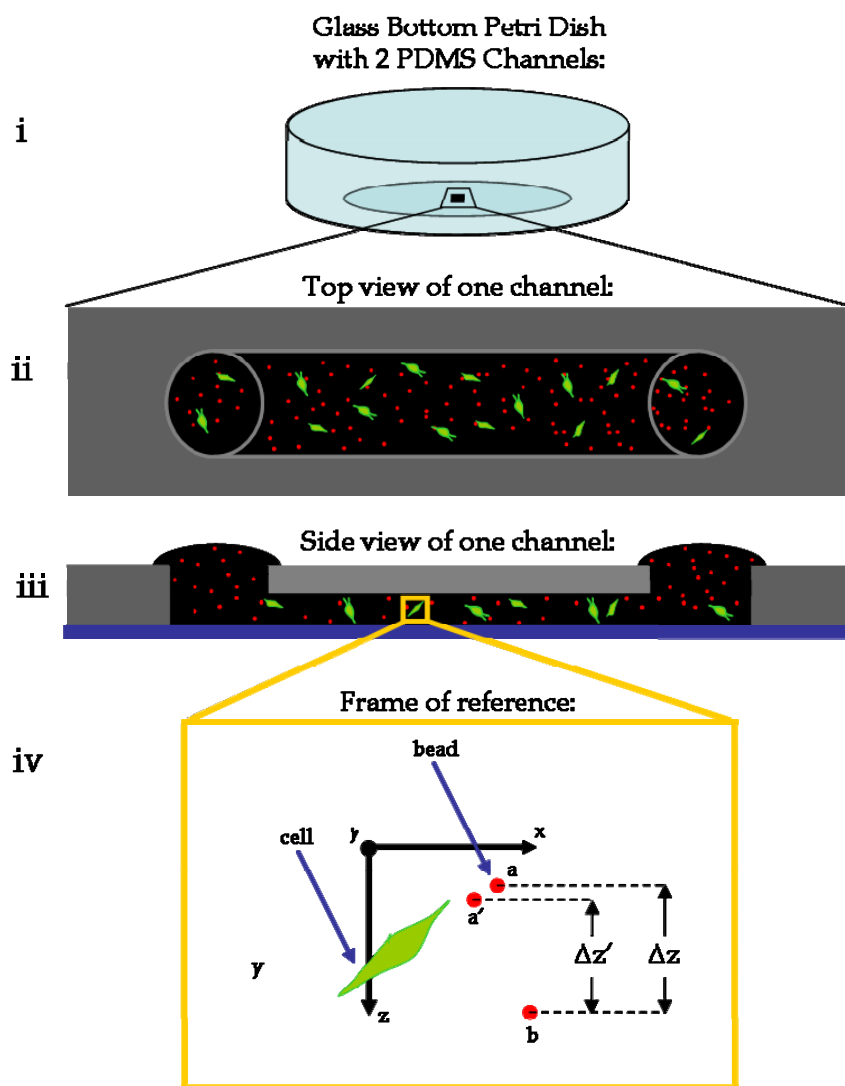


Figure 1 i) Schematic diagram of a glass bottom Petri dish with a PDMS straight channel. ii) Close up of the top view of one channel. Green objects are GFP fluorescing cells and red objects are red fluorescing beads. The channel has an inlet and outlet port on each end. iii) Close up of side view of one channel. iv) Frame of reference is shown with respect to the side view. Bead b has negligible displacement caused by the cell and is the reference bead. Bead a is being displaced by the cell. Bead a' is the position of bead a at a later time point. In the direction of the z axis, the strain that the cell has caused can be calculated by the distance between beads a and b at the later time point, $\Delta z'$, and dividing by the original distance between beads a and b, Δz . This analysis is done for all three directions, but is only shown here in z for clarity.

Results and Discussion

Although a number of different measures were made in the full study [Lopez-Garcia, et al, in press], here we will focus on one particular aspect observation: the fluctuation in the elastic stresses over time which was observed for many bead pairs. To determine if this fluctuation was produced by the cell and not an artifact of the technique the cell shape was studied as well as the path shapes and the behavior of the stress peaks. The area and the perimeter for cells in each concentration were measured and compared to the peaks in the stress graph. It was found that the shape of the cell changes throughout the experiment, but no strong correlation could be found with the stress peaks. On occasion, as shown in [Figure 2a, b, and c](#) for a cell in a 2 mg/mL collagen gel, the area and/or perimeter coincide with the peaks, but not consistently. One limitation, however, is that area and perimeter measurements of the cell can only be made in the XY plane. The path of the bead was also compared to the stress peaks. In the example shown in [Figure 2d](#) the peaks occur at times when the cell is pulling towards itself. Time between peaks was calculated for various tests as well as the relationship of the time between peaks and distance from cell as well as collagen concentration but no clear correlation was found. (Data not shown.)

[Figure 2d](#) also demonstrates how complex the displacement behaviors of the bead were throughout the observation period. The bead has backwards and forwards movement due to how the collagen was being displaced by the cell. This behavior was also seen in the Z direction. This information would not have been available if intermediate timepoints had not been obtained.

In [Figure 3](#) a cell moving in a 2 mg/mL gel is shown. The images shown are for the focal plane of the cell, the lines shown are paths of the beads that are adsorbed onto the collagen gel. There are 20 minutes between each image. The path between the first two timepoints is blue and change into turquoise, green, and then yellow as time progresses. The paths that are formed between the first and second timepoints tend in the opposite direction of the cell in the rear region; and they tend in the same direction of the cell in the frontal region. At this moment, the cell appears to move in a thrust between 0 – 20 minutes. During this thrust, the paths in the front are generally greater in length than the paths in the back of the cell. After the thrust, the paths in the front and in the back are of a similar size, and in the same direction.

Conclusion

In this work the strains generated by NMuMG cells in a three dimensional collagen matrix were measured using a microfluidic platform by tracking the displacements of beads that were embedded in the collagen. Fluctuations in the stress behavior over time were observed. Displacement of the material determined from the complex paths of the beads throughout the time of observation were also measured. This powerful tool can give way to future works in understanding 3D mechanical interactions between cells and their surrounding ECM and is an important step in that direction.

Acknowledgements

The authors would like to thank Patricia Keely's lab for allowing the use of their microscope, especially Dr. Matt Conklin for his time and assistance and Prof. Keely for helpful conversations. The authors would also like to thank Erich Zeiss for all of his help with the imaging and use of Slidebook Software. This work was possible via funding from the Harriet Jenkins Pre-doctoral Fellowship (JFPF-NASA); Graduate Engineering Research Scholars (GERS) of the College of Engineering, University of Wisconsin – Madison; and the Ruth Dickie Research Scholarship from the University of Wisconsin Beta Chapter of Sigma Delta Epsilon - Graduate Women in Science (SDE-GWIS).

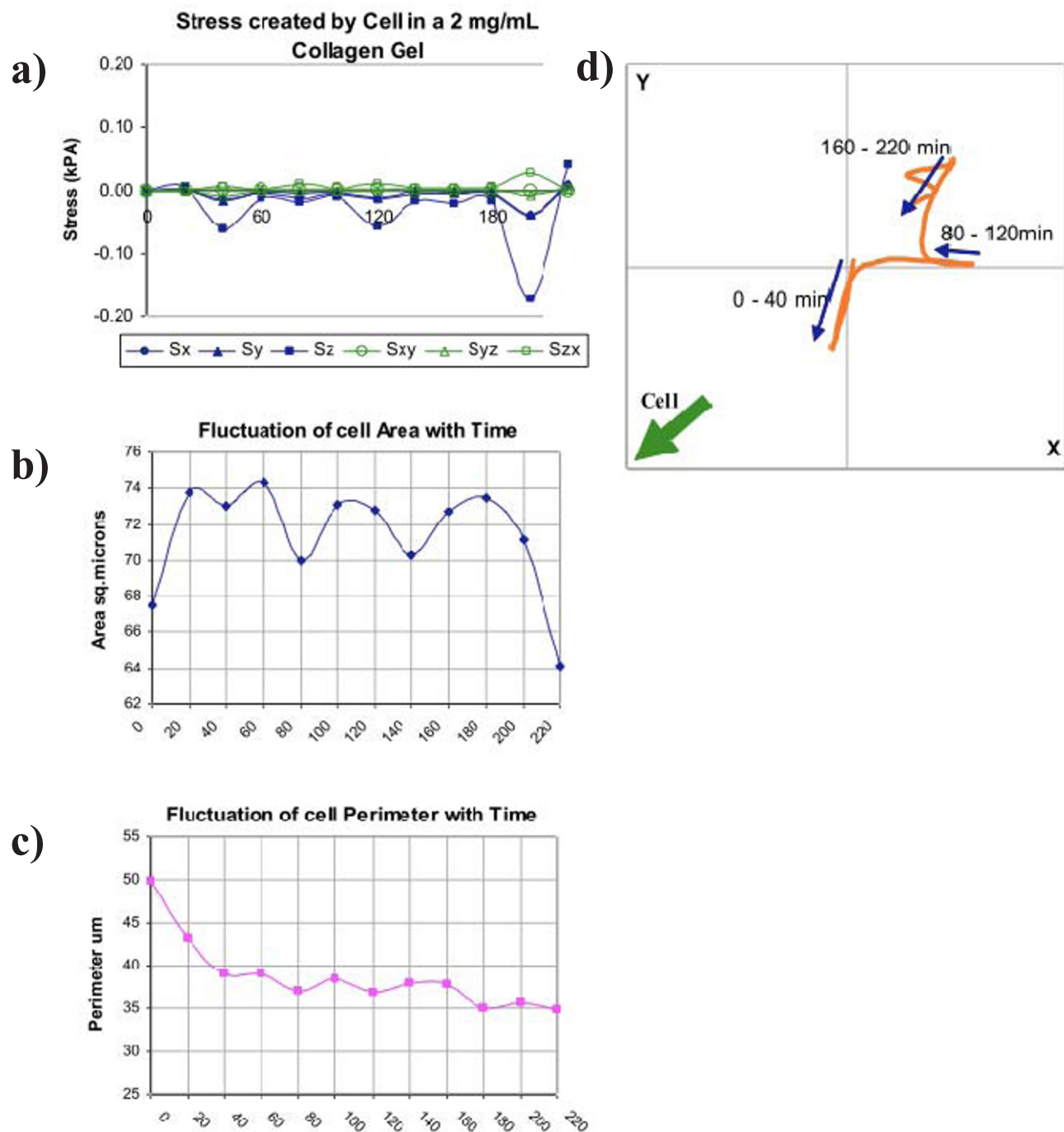


Figure 2 a) Graph shows the stresses generated by a cell in a 2 mg/mL gel. The cell b) area and the c) perimeter were measured at each time point and used to calculate the shape factor. The area, perimeter, and shape factor were used to compare to the stress behavior. On the top right c) the path in X and Y for the bead being studied is shown. The cell is in the direction in which the green arrow is pointing. The pulses in the stress graph all coincide with the times at which the cell is pulling the material marked by that bead towards itself.

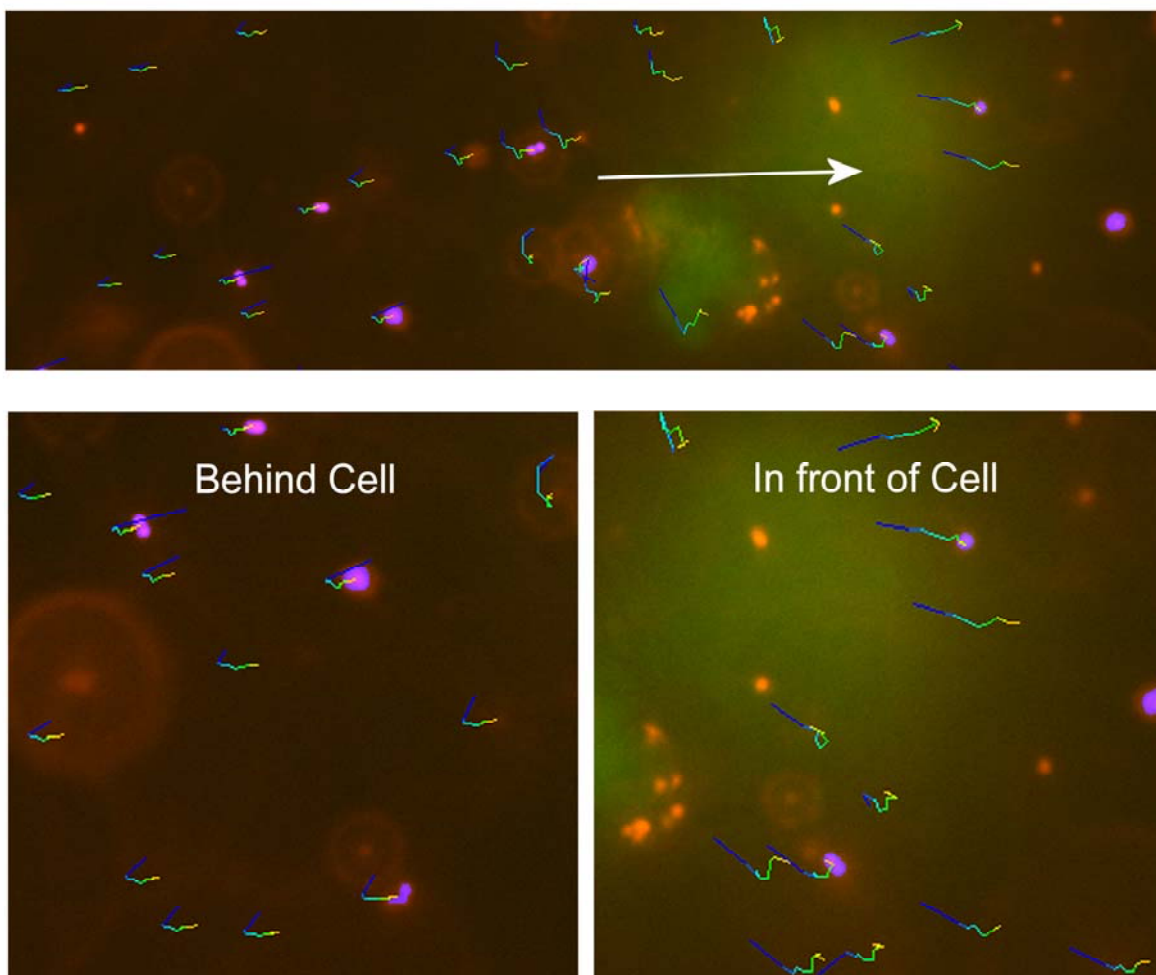


Figure 3. Cell moving in a 2 mg/mL collagen gel. Paths of beads adsorbed onto collagen are shown. The progression of the path is in chronological order by color: blue, turquoise, green, yellow. Each path section represents a 20 min interval. White arrow indicates direction of cell movement.

References

- Cukierman, E., et al., *Taking cell-matrix adhesions to the third dimension*. *Science*, 2001. **294**(5547): p. 1708-1712.
- Friedl, P. and E.B. Brocker, *The biology of cell locomotion within three-dimensional extracellular matrix*. *Cellular And Molecular Life Sciences*, 2000. **57**(1): p. 41-64.
- Jo, B.H., et al., *Three-dimensional micro-channel fabrication in polydimethylsiloxane (PDMS) elastomer*. *Journal Of Microelectromechanical Systems*, 2000. **9**(1): p. 76-81.
- Lopez-Garcia, M.d.C., D.J. Beebe, and W.C. Crone, "Mechanical Interactions of Mouse Mammary Gland Cells with Collagen in a Three-Dimensional Construct," accepted for publication in *Annals of Biomedical Engineering*, March 2010.
- McDonald, J.C. and G.M. Whitesides, *Poly(dimethylsiloxane) as a material for fabricating microfluidic devices*. *Accounts Of Chemical Research*, 2002. **35**(7): p. 491-499.

Tracking nanoparticles optically to study their interaction with cells

Jean-Michel Gineste¹, Peter Macko¹, Eann Patterson² and Maurice Whelan¹

¹Institute for Health and Consumer Protection, European Commission DG Joint Research Centre, Italy.

²Composite Vehicle Research Center, Michigan State University, East Lansing, MI48824, USA.
eann@egr.msu.edu

ABSTRACT

Nanoparticles are by definition too small to be visible in an optical microscope and devices such as scanning electron microscopes must be used to resolve them. However electron beams quickly lead to cell death and so it is difficult to study the interaction of nanoparticles with living cells in order to establish whether such interactions could be damaging to the cell. A simple modification to a conventional inverted optical microscope is proposed here which renders the location of nanoparticles readily apparent and permits tracking of them in three-dimensions. Particles in the range 100nm to 500nm have been tracked with a temporal resolution of 200ms. The technique, although motivated by the desire to study the interaction of nanoparticles with cells, has a wide range of potential applications in the fields of food processing, pharmaceuticals and nano-biotechnology.

1. INTRODUCTION

The Rayleigh limit defines the minimum resolution of an optical microscope based on the wavelength of light being employed so that most nanoparticles of interest are not resolvable in a conventional optical microscope. Nanoparticles are of interest for wide range of applications from colloidal systems in which they control the behavioral characteristics to cell biology where they may be associated with toxic effects. Consequently, significant research effort has been expended on inventing ways to image nanoparticles, identify their location and track their movement in an environment that permits the study of their interaction with living cells. Metallic particles are relevant easy to image since many of them can be designed to exhibit fluorescence and, or to produce large scatter patterns using dark-field microscopy. However, fluorescent-based techniques tend to suffer from photo-bleaching and dark-field microscopy works best in confocal microscopes where particles of diameter 80 to 180nm can be readily imaged [1, 2]. Metallic particles can be induced to generate both a plasmon resonance and a photothermal signature when excited by laser and then particles as small as 5nm diameter can be imaged using a scanning sensor [3].

An alternative approach is to defocus the microscope which magnifies the diffraction effects that most microscope users go to considerable effort and expensive to eliminate. These diffraction effects are based on forward scattering of the light from the particles which Ovaryn [4] in 2000 showed could be modeled for micro-spheres of diameter 5 to 10um using Mie theory. In 2006, Guerrero-Viramontes et al. [5] demonstrated the approach by tracking glass particles of diameter 20 to 30um using a 70mW He-Ne laser. In 2007 Kvarnstrom and Glasby used defocusing combined with local quadratic kernel estimates to locate particles of diameter 500nm and in the same year Toprak et al. [6] implemented a similar approach in a bifocal microscope and successfully tracked particles of diameter 200nm. Then in 2008, Patterson and Whelan [7, 8] defocused a simple optical inverted microscope and demonstrated that the location of both nominally opaque metallic particles and nominally transparent particles as small as 3nm in diameter could be identified. While finding the location of large nanoparticles using defocusing can be relatively straightforward, tracking them in three-dimensions is more challenging and the forward scattering from a small nanoparticle can be very faint so that even locating them can be problematic. The technique described here has been developed to overcome these difficulties without adding significantly to the complexity of the optical microscope or interfering with other capabilities which are of interest to those wanting to study cells.

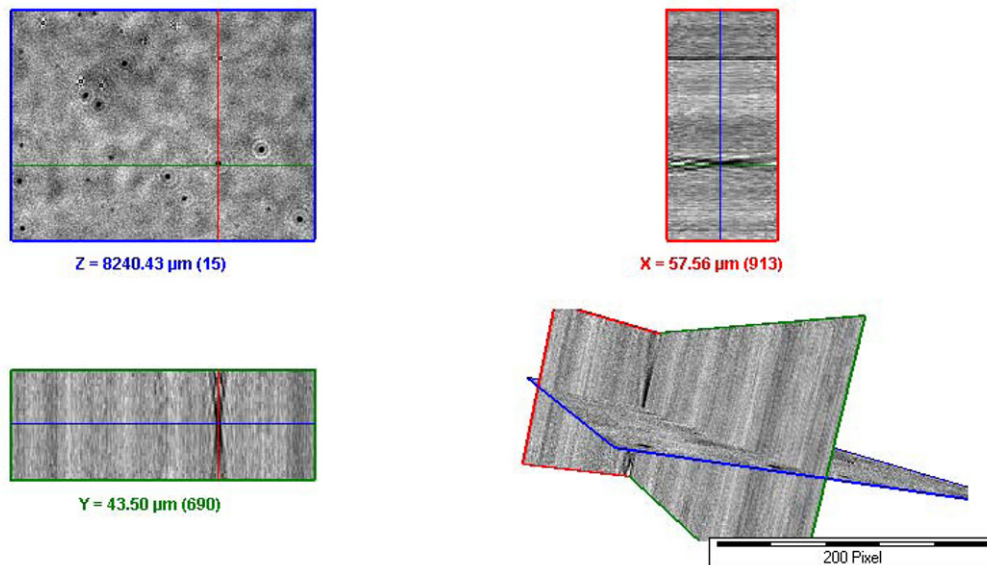


Figure 1: Image (top left), z-stacks for the xz- (top right) and yz- (bottom left) planes and a composite three-dimensional composite view (bottom right) for 300nm diameter polystyrene particles obtained by collecting images at 1 μ m steps of the objective over 30 μ m in the z-direction along the light path. [2008_01 experiments\tuesday22jan]

2. METHODOLOGY

The forward scatter pattern observed when small particles are viewed a conventional optical microscope is essentially a three-dimensional interference pattern consisting of a series of light and dark fringes as can be seen in the example in figure 1. The amplitude of this pattern is strongest along the light path (z-direction) through the center of a spherical particle. Thus, if the focal plane of the microscope objective is moved along this line then the pixels at the x,y position of the center of the particle would be expected to flash between bright and dark. This was arranged to occur by fitting a piezo actuator (Physik Instrumente GmbH & Co. KG. model Pifco P-725.4CD) with a servo controller (Physik Instrumente GmbH & Co. KG. model E-665) to an inverted optical microscope (Olympus IX71) with 100W halogen light source (Olympus U-LH100L-3) and narrow bandwidth filter (Olympus 43IF550W45). The microscope was fitted with an adjustable field aperture which was closed to its minimum diameter of 1mm in order to maximum the diffraction effects. The piezo actuator was oscillated with a peak-to-peak amplitude in the range 100 μ m to 150 μ m about a mean position that corresponded to the approximate center of the particle of interest. For pseudo-static investigations images were captured at 20 frames/second using a 12-bit monochrome CCD camera (Hamamatsu C8484-05G) with a resolution of 1344 \times 1024 pixels and for tracking motion a high-speed, 8-bit monochrome camera (Photron FASTCAM-PCI R2) was used with at a frame rate of 500 images/second and resolution of 256 \times 240 pixels. These cameras when combined with a \times 60 objective and \times 10 lens on the camera port gave a pixel size of 0.108² μ m and 0.127² μ m respectively at the objective plane.

Polystyrene particles of nominal diameters 100nm and 500nm (L0655-1ML and L05530-1ML respectively Amine-modified polystyrene, fluorescent blue, Sigma-Aldrich Inc., St Louis, MO) were used in this investigation and were diluted 1000-fold in phosphate buffered saline solution. Conventional glass microscope slides generate large diffraction patterns from the relatively low quality glass surface when used in a microscope set up in this mode and so the solution was sandwiched between glass slide covers (Menzil-Gläser, 21 \times 23mm #4).

The particles flash in real-time which allows the location of particles to be identify manually with ease. To allow automatic data processing a series of images were collected over several cycles of oscillation of the objective and the mean and standard deviation of the intensity as a function of time were calculated for each pixel in the field of view. The local maxima in the map of standard deviations were taken as the center of particles in the xy -plane and for these pixels the location of the particle in the z-direction, i.e. along the light path was identified by scanning along the z-direction to find the area of maximum intensity and the edge of it furthest from the objective was taken as the center of the particle as indicated in the model of Ovrin [4]. This process was repeated every 200ms when tracking a particle so that the x, y, z coordinates could be found as a function of time.

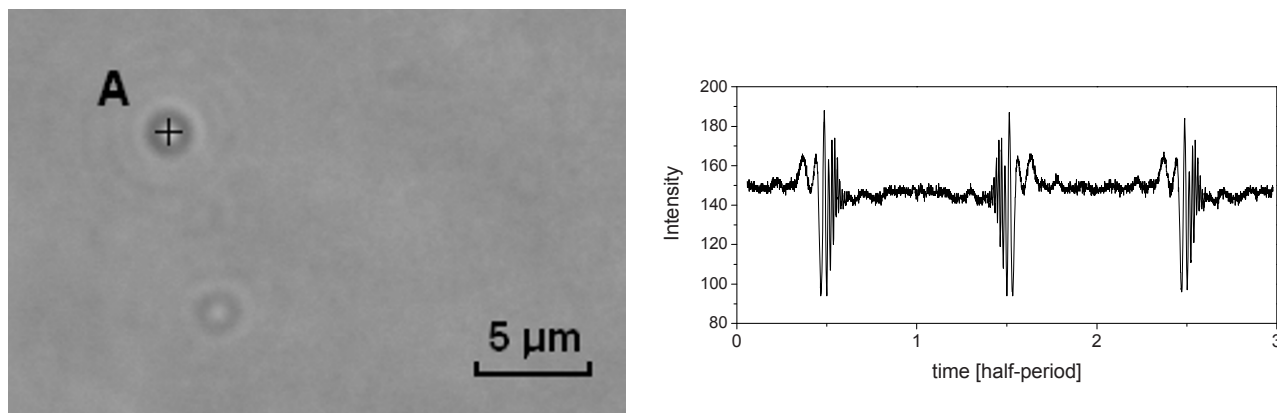


Figure 2: Image of 500nm diameter particles captured with the condenser aperture closed to a minimum with the objective stationary (*left*): and the variation of intensity with time (*right*) over a three half-periods of oscillation of the microscope objective for the pixel marked, A in the image which is approximately located at the center of a particle.

3. RESULTS

A typical image obtained with a static but defocused objective is shown in [figure 2](#) together with the time-varying intensity signal for the center of a particle of nominal diameter 500nm over three half periods of oscillation of the objective lens. A number of particles are apparent in the image and are at different depths in the solution and hence their forward scatter patterns appear to be different sizes because they are being sectioned at different distances from the center of the particles.

The maps of standard deviation for solutions of 500nm and of 100nm particles are shown in [figure 3](#) and the centers of the particles are distinctive against the background. In these grey scale maps the minimum standard deviation is close to zero and is shown white while the maximum standard deviation is black and occurs at the center of the particle. The size and intensity of the signature of a particle in these maps is both a function of the particle diameter but also its position relative to the center of oscillation of the objective. A particle whose forward scatter pattern is completely enveloped by the oscillation of the objective will appear much more distinct, such as the 500nm particle in the top left of the image, than one for which only part of the forward scatter pattern lies within the oscillation amplitude of the objective, such as in the bottom center and right of the image from the 500nm sample.

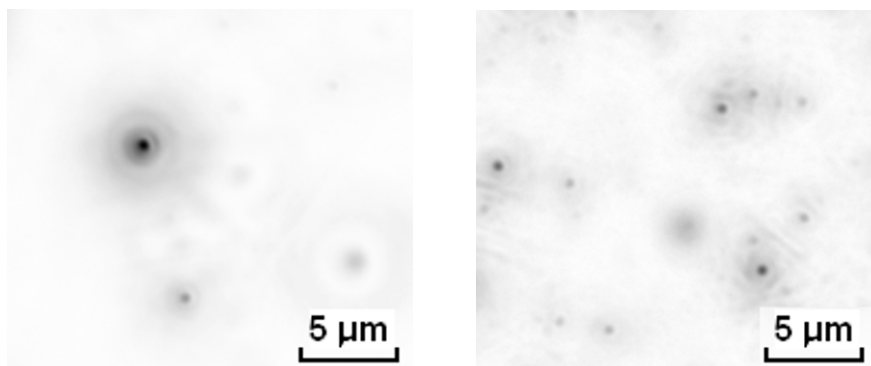


Figure 3: Grey-scale maps of the standard deviation of intensity as a function of time over five cycles of the motion the objective for solutions of 500nm (*left*) and 100nm (*right*) diameter particles.

The results in [figure 4](#) were obtained using the high speed camera to track the Brownian motion of a 500nm diameter particle using an objective amplitude of 100μm. When identifying the particle center in the z-direction a 3×3 patch of data centered on the particle center in the xy-plane was used rather than a single line of pixels in the z-direction. This strategy made the algorithm considerable more robust and less susceptible to noise and do not attenuate the resolution of the x, y or z coordinates.

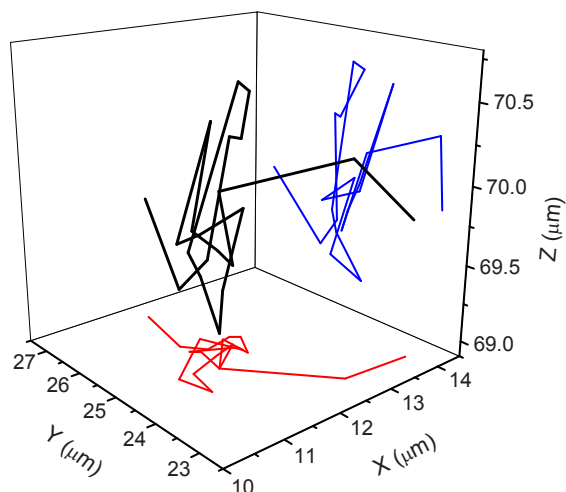


Figure 4: A typical trajectory (in black) of a 500nm particle illustrating the long-term, high resolution 3d tracking of the nanoparticle (in red and in blue are respectively the projections of the 3d trajectory onto the xy and yz planes).

4. DISCUSSION AND CONCLUSIONS

The results demonstrate that nanoparticles of the order of 100nm diameter can be readily tracked in three dimensions with respect to time with a temporal resolution of 200ms using an optical microscope with only a small modification that does not interfere with other functions of the instrument. This is a significant advance on other techniques for tracking in three-dimensions which require bifocal arrangements [6] or scanning sensors [1 – 3]. When used without the data processing, i.e. in manual mode but with the objective oscillating, the nanoparticles flash in the field of view rendering them far more apparent than in a simple defocused optical microscope [7, 8]. Consequently the technique has considerable potential in nanobiotechnology, nanoengineering, pharmaceuticals and food processing where introducing fluorescent particles or creating plasmons may not be compatible with the processes under observation.

REFERENCES

1. Xu, C.S., Cang, H., Montiel, D., Yang, H., Rapid & quantitative sizing of nanoparticles using three-dimensional single particle tracking, *J Phys. Chem.*, 111:32-35, 2007
2. Lout, G., Asahi, T., Tanaka, G., Uwada, T., Masuhara, H., Spectral and 3-Dimensional tracking of single gold nanoparticles in living cells studied by Rayleigh light scattering microscopy, *J Phys. Chem. C.*, 113:11766-11772, 2009.
3. Lasne, D., Blab, G.A., Berciaud, S., Heine, M., Groc, L., Choquet, D., Cognet, L., Lounis, B., Single nanoparticle photothermal tracking (SNaPT) of 5-nm gold beads in live cells, *Biophysical Journal*, 91:4598-4604, 2006.
4. Ovrjn, B., Three-dimensional forward scattering particle image velocimetry applied to a microscope field-of-view, *Experiments in Fluids* [Suppl.], S175-184, 2000.
5. Guerrero-Viramontes, J.A., Moreno-Hernandez, Mendoza-Santoyo, F., Funes-Gallanzi, M., 3D particle positioning from CCD images using the generalised Lorenz-Mie and Huygens-Fresnel theories, *Meas.Sci. Technol.*, 17:2328-2334, 2006.
6. Toprak, E., Balci, H., Blehm, B.H., Selvin, P.R., 'Three dimensional particle tracking via bifocal imaging', *Nano Letters*, 7(7):2043-2045, 2007.
7. Patterson, E.A., Whelan, M.P., Tracking nanoparticles in an optical microscope using caustics, *Nanotechnology*, 19:105502, 2008.
8. Patterson, E.A., Whelan, M.P., Optical signatures of small nanoparticles in a conventional microscope. *Small*, 4(10):1703-1706, 2008.

Coherent Gradient Sensing Microscopy: Microinterferometric Technique for Quantitative Cell Detection

M. Budyansky, C. Madormo, G. Lykotrafitis¹

Department of Mechanical Engineering, University of Connecticut
 191 Auditorium Road, UNIT 3139, Storrs-Mansfield, CT, 06269
¹gelyko@engr.uconn.edu

ABSTRACT

Micro-CGS, an integration of the interferometric optical method Coherent Gradient Sensing (CGS) [1-3] with an inverted microscope, is introduced. Micro-CGS extends the capabilities of Classical CGS into the cellular level. As such, it provides full-field, real-time, micro-interferometric quantitative imaging. Micro-CGS is based on the introduction of a microscope objective into the classical CGS setup. An experimental setup is detailed and resulting interferograms are shown. A digital image processing program is created to compute specimen curvature from the given fringe patterns. The experimental method is validated by the successful measurement of the curvature of 30-micron glass microspheres.

KEYWORDS: Micro-interferometer, Fringe pattern analysis, Optical system, Image processing, Phase

INTRODUCTION

A majority of the optical techniques currently used in microscopy, such as Differential Interference Contrast (DIC), Dark-Field (DF), and Phase Contrast (PC) microscopy, are qualitative in nature. Recently, there has been an emergence of quantitative optical techniques that obtain spatial and temporal information from living cells [4-5]. In this framework, we developed micro-CGS which offers an increased stability and direct measurement of the surface curvature of microstructures.

Classical CGS is a well-established large-scale quantitative optical interferometric technique which has been successfully used in the field of fracture mechanics as well as the measurement of residual stresses in thin films [1, 3]. CGS can be used in two operating modes, transmission and reflection. The working principle of transmission mode CGS is shown in Figure 1.

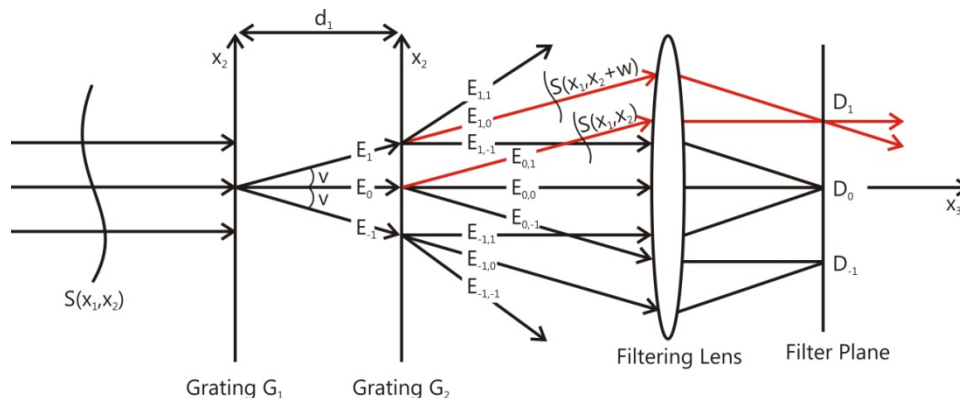


Fig. 1: Working principle of CGS

A collimated laser beam, or a nearly planar wavefront, passes through a specimen. Due to the refractive index of the specimen the planar wavefront is deformed. This deformation is directly correlated to the thickness of the specimen, assuming a constant refractive index throughout the specimen. Two high-density diffraction gratings, G_1 and G_2 , laterally shear the beam. The principle axis of the diffraction gratings is along the x_2 direction. When the incident wavefront, $S(x_1, x_2)$, encounters the first diffraction grating, G_1 , it is diffracted into several wavefronts E_0, E_1, E_{-1} , etc. For aesthetic purposes only E_{-1}, E_0, E_1 are shown. The resulting wavefronts are again diffracted at the second diffraction grating, G_2 . This produces an additional set of wavefronts, $E_{1,1}, E_{1,0}, E_{1,-1}, \dots$, from $E_1, E_{0,1}, E_{0,0}, E_{0,-1}, \dots$, from E_0 , and $E_{-1,1}, E_{-1,0}, E_{-1,-1}, \dots$, from E_{-1} , etc. A focusing lens is then used to combine parallel wavefronts at the filter plane. A diffraction pattern is produced consisting of several diffraction spots D_1, D_0, D_{-1} , etc. The single diffraction spot D_1 is isolated because it contains information on the curvature of the specimen [1, 3]. This diffraction spot is filtered out and imaged by a CCD camera.

EXPERIMENTAL SETUP

Micro-CGS is based upon the introduction of a microscopic objective into the Classical CGS experimental setup. A design schematic of the Micro-CGS setup can be seen in Figure 2. A 635-nm He-Ne collimated laser is spatially filtered and passed through a specimen. A microscope objective is introduced into the optical path for magnification purposes. The objective used is an Olympus 40x objective.

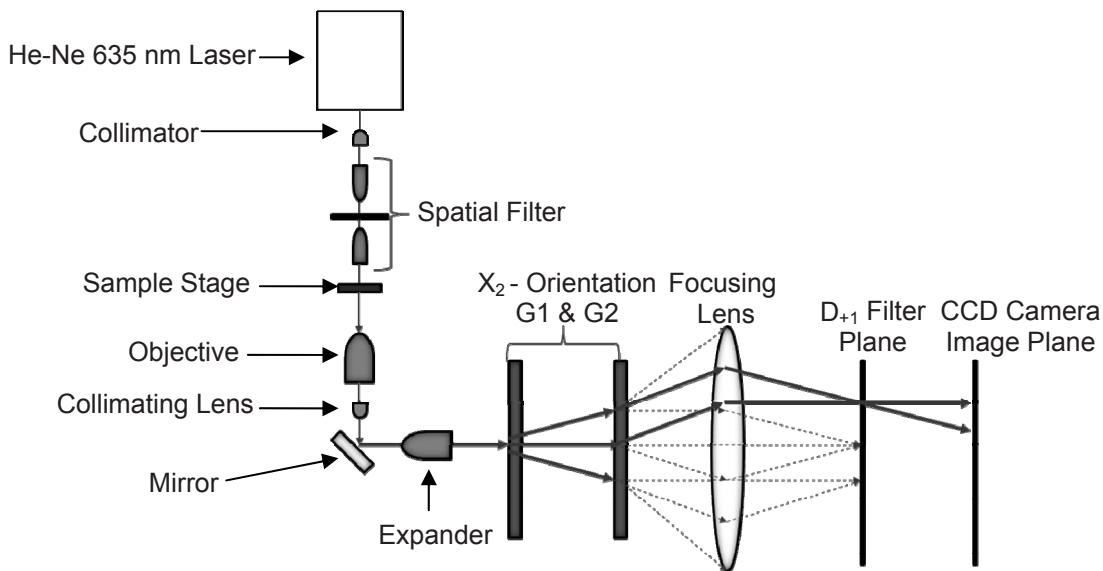


Fig. 2: Micro-CGS schematic

Upon exiting the microscope objective, the beam is re-collimated, expanded (10X) and directed through the pair of Ronchi diffraction gratings (1000 lines/inch) as in the classical CGS setup. A CCD camera, Casio EX-F1, focused onto the image plane is employed to capture the generated interferograms. The experimental optical setup is shown in Figure 3. The orientation of the diffraction gratings dictates the axis along which the setup will measure curvature. For the current setup the gratings are perpendicular to the x_2 direction and thus they provide surface gradient information along the x_2 axis. In order to acquire a complete description of the sample curvature, a second optical path with the pair of gratings oriented perpendicular to the x_1 direction has to be implemented.

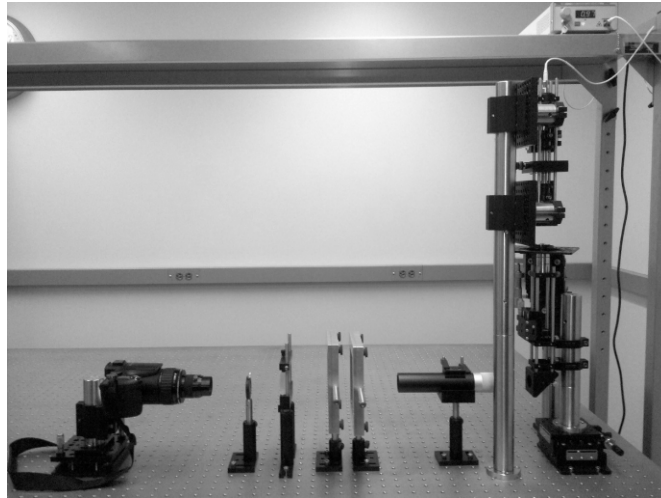


Fig. 3: Optical setup of Micro-CGS utilized in the experimentation

IMAGE PROCESSING

The software utilized to post-process the fringes was coded in MATLAB 2009. The algorithm begins by reading in the interferogram captured by the CCD camera [1]. The CCD camera records a pixel by pixel intensity distribution of the interferogram shown in Figure 4a. This interferogram corresponds to the x_2 axis surface gradients of a 75mm Plano-convex lens. The intensity distribution of the CGS interferogram can be described by Eq. 1

$$I(x_1, x_2) = a(x_1, x_2) + b(x_1, x_2) \cos \delta(x_1, x_2) \quad (1)$$

where $I(x_1, x_2)$ is the intensity of the fringe pattern at point (x_1, x_2) , $a(x_1, x_2)$ is the background intensity level, $b(x_1, x_2)$ is the fringe visibility, and $\delta(x_1, x_2)$ is the phase-angle term [1].

It can also be expressed in a complex form as Eq. 2

$$I(x_1, x_2) = a(x_1, x_2) + c(x_1, x_2) + c^*(x_1, x_2) \quad (2)$$

where $c(x_1, x_2) = \frac{1}{2}b(x_1, x_2)e^{i\delta(x_1, x_2)}$ and $c^*(\omega_1, \omega_2)$ is the complex conjugate of $c(\omega_1, \omega_2)$.

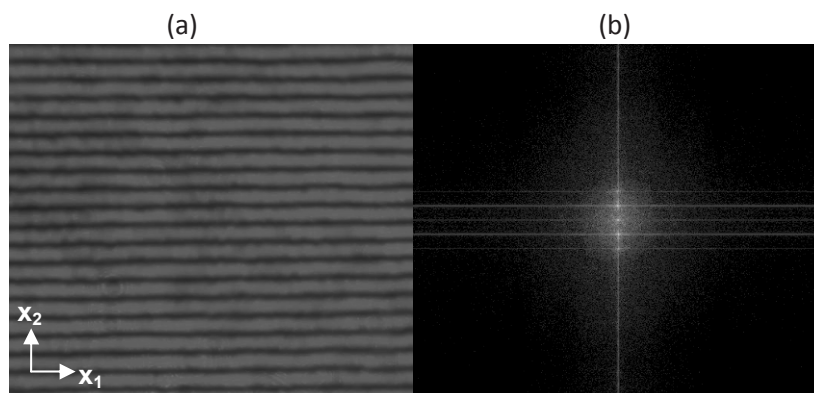


Fig. 4: (a) Interferogram for 75mm diameter Plano-convex lens, (b) corresponding frequency power spectrum after converting to Fourier domain

The program then converts the image to the Fourier domain by employing Fast-Fourier transform. The resulting frequency domain can be seen in Figure 4b. The intensity distribution in the Fourier domain is shown as Eq. 3

$$I(\omega_1, \omega_2) = A(\omega_1, \omega_2) + C(\omega_1, \omega_2) + C^*(-\omega_1, -\omega_2) \tag{3}$$

where ω_1 and ω_2 are the spatial frequencies in the Fourier domain, $A(\omega_1, \omega_2)$ contains low-frequency information, and $C^*(-\omega_1, -\omega_2)$ is the complex conjugate of $C(\omega_1, \omega_2)$. Bandpass filtering is used in order to eliminate $A(\omega_1, \omega_2)$ and either $C(\omega_1, \omega_2)$ or $C^*(-\omega_1, -\omega_2)$. The inverse Fourier transform of the remaining term is taken to obtain $c(\omega_1, \omega_2)$ or $c^*(\omega_1, \omega_2)$. The phase can then be found by using the following expression

$$\delta(x_1, x_2) = \tan^{-1} \frac{\text{Im}[c(x_1, x_2)]}{\text{Re}[c(x_1, x_2)]} \tag{4}$$

This is the full-field wrapped phase as seen in Figure 5a. A single column representation is provided in Figure 5b to display values oscillating between $-\pi$ and π .

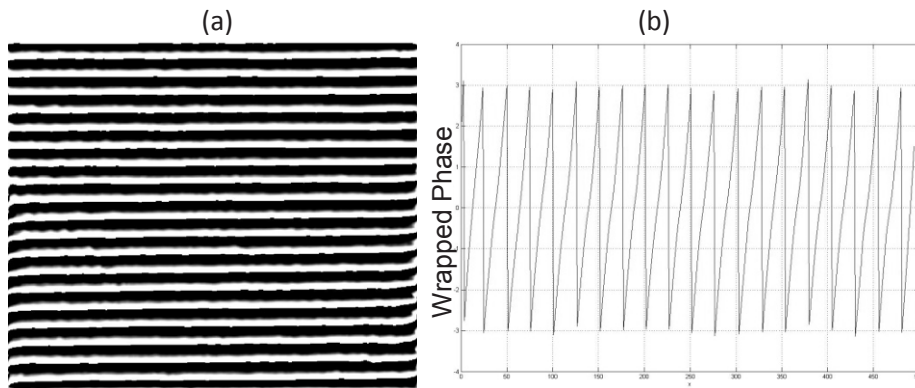


Fig. 5: (a) Full field wrapped phase of Fig. 4a, (b) Phase in radians vs. distance on y-axis of the Fig. 5a in pixels

After obtaining the wrapped phase, a phase unwrapping algorithm is used to unwrap the phase shown in Figure 5a. The resulting full field unwrapped phase is displayed in Figure 6a, accompanied by a single column representation shown in Figure 6b.

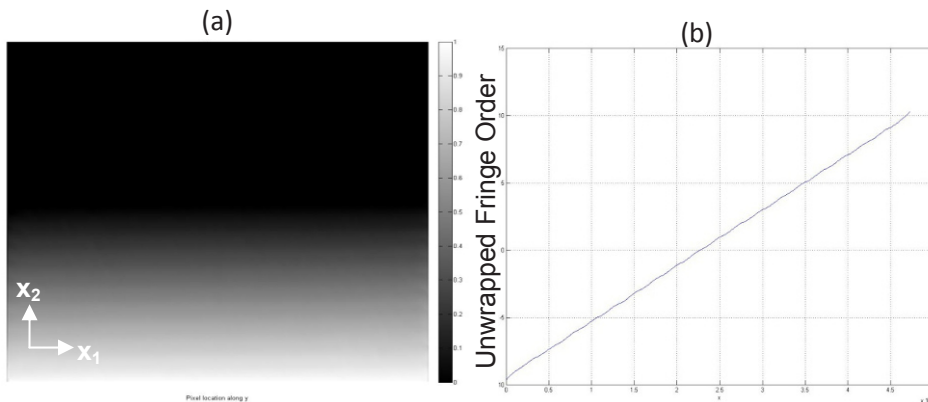


Fig. 6: a) Full field unwrapped phase, b) Unwrapped fringe order vs. distance on y-axis of Figure 6a in pixels

This particular case established linearity in fringe order for the plano-convex lens which has constant curvature. To approximate the curvature κ_{22} of the specimen, the unwrapped phase is differentiated with respect to x_2 direction according to Equation 5 [1-3] for CGS in transmission.

$$\kappa_{22} \approx \frac{\partial^2 S(x_1, x_2)}{\partial x_2^2} = \frac{\rho}{2\Delta} \frac{\partial n}{\partial D} \quad (5)$$

where ρ is the grating pitch, ∂n is the change in the number of fringes, Δ is the distance between the diffraction gratings, and ∂D is the distance between the fringes. Finally, a thickness profile is generated to obtain the thickness profile along the same direction as the curvature by integrating the unwrapped phase [6]

RESULTS

A sample of 30-micron glass microspheres ($\pm 1\%$), manufactured by Thermo-Scientific, in aqueous solution were imaged with the aforementioned experimental setup. The corresponding fringe interferogram of each bead captured in the CCD camera is shown in Figure 7a. The interferograms display a predicted constant curvature through the equidistant straight parallel fringes obtained about the y axis surface gradients. In addition, adjacent beads exhibit nearly the same fringe pattern and fringe spacing signifying identical curvature detection between these glass beads. For each of the labeled beads a rectangular cross section was isolated from Figure 7a, and analyzed by the currently in development image processing software. The results were averaged and presented in Figure 7b showing a calculated curvature ratio between numerical vs. analytical solutions $\kappa_{22} / \kappa_{bead}$. The average of the four beads has an average standard deviation of approximately 2.0% between the four beads. The numerical curvature values were also produced with an average difference of 1.5% from the analytical value (1/radius of curvature). The curvature was nearly constant along the x_2 -axis in the form of a reasonably flat plane in the field of the bead as exhibited in Figure 7b.

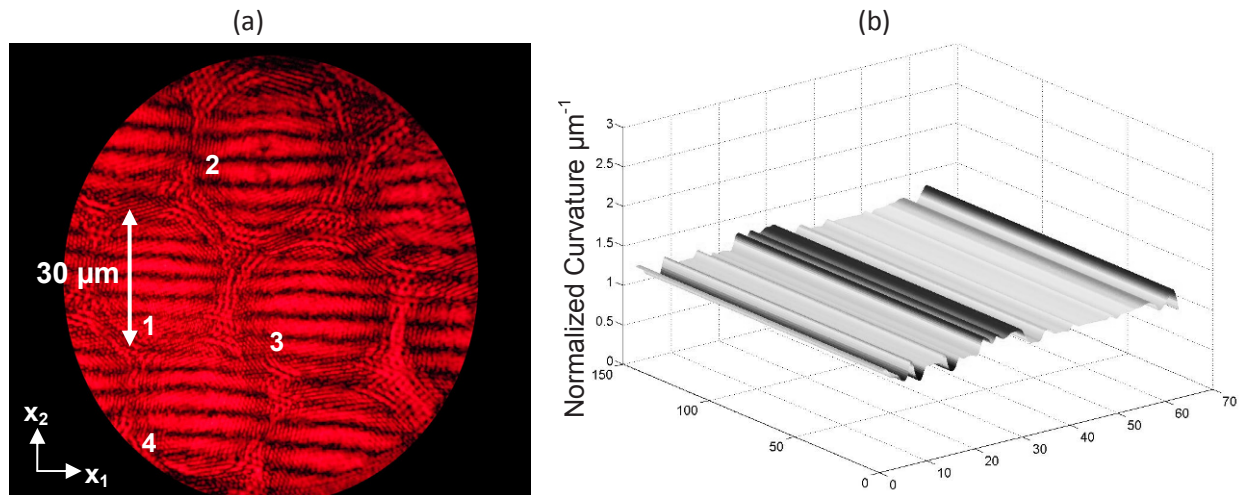


Fig. 7: a) Interferogram captured for 30-micron glass beads in aqueous solution
b) Curvature ratio of calculated vs. analytical bead curvature $\kappa_{22} / \kappa_{bead}$

CONCLUSION

A proposed adaptation to the optical method of Coherent Gradient Sensing (CGS), known as micro-CGS, has been presented. The constructed experimental setup was employed to produce interferograms from microbeads of known curvature. The preliminary curvature results obtained for a set of 30 micron beads produced an average error of 1.5% with respect to the known value. It is believed that with further refinements to the digital image processing program this result will become more accurate. The accuracy of the results signifies that micro-CGS can be used to successfully obtain curvature of static micro-specimens. In addition, the optical system produced repeatable fringe interferograms within the beads, signifying the successful detection capability of micro-CGS. Moving forward, the intention of the research is to further extend the capabilities of micro-CGS to cellular specimens. By characterizing the thermally induced surface vibrations of biological cells, their mechanical properties can be then determined.

ACKNOWLEDGEMENTS

We would like to acknowledge Ares J. Rosakis of the California Institute of Technology for very helpful discussions on Coherent Gradient Sensing and providing us with the Ronchi gratings used in the experimental setup. This work was supported by UCRF Large Grant J980.

REFERENCES

1. Lee H, Rosakis AJ, & Freund LB, Full-field optical measurement of curvatures in ultra-thin-film-substrate systems in the range of geometrically nonlinear deformations. *Journal of Applied Physics* 89(11):6116-6129. (2001).
2. Lee YJ, Lambros J, & Rosakis AJ, Analysis of Coherent Gradient Sensing (CGS) by Fourier optics. *Optics and Lasers in Engineering* 25(1):25-53. (1996).
3. Rosakis AJ, Singh RP, Tsuji Y, Kolawa E, & Moore NR, Full field measurements of curvature using coherent gradient sensing: application to thin film characterization. *Thin Solid Films* 325(1-2):42-54. (1998).
4. Ikeda T, Popescu G, Dasari RR, & Feld MS, Hilbert phase microscopy for investigating fast dynamics in transparent systems. *Optics Letters* 30(10):1165-1167. (2005).
5. Lue N, *et al.*, Live cell refractometry using Hilbert phase microscopy and confocal reflectance microscopy. *J Phys Chem A* 113(47):13327-13330. (2009).
6. Lambros J & Rosakis AJ, An experimental study of dynamic delamination of thick fiber reinforced polymeric matrix composites. *Experimental Mechanics* 37(3):360-366. (1997).

Rate effects in the failure strength of extraterrestrial materials

J. Kimberley¹, K.T. Ramesh¹, Olivier S. Barnouin². ¹Dept. of Mechanical Engineering, Johns Hopkins University, Baltimore, MD 21218 (jamie.kimberley@jhu.edu). ²Johns Hopkins University Applied Physics Laboratory, Laurel, MD 20723

Abstract—Most simulations of asteroid impacts use the properties of terrestrial analogs to approximate the behavior of the asteroid material because there is currently a lack of data for the mechanical properties of the materials that comprise asteroids. Since we do not have access to material retrieved from a specific asteroid, we investigate the mechanical response of a stony meteorite that is believed to be of asteroidal origin. We have measured, at strain rates ranging from 10^{-3} - 10^3 s⁻¹, the uniaxial (unconfined) compressive strength of specimens cut from an L5 ordinary chondrite, MacAlpine Hills 88118 (MAC88118). Quasistatic compression experiments were conducted using a servo-hydraulic load frame while dynamic compression experiments were conducted using a modified Kolsky bar. Images of the specimen were also recorded during the experiments for visualization of the failure process. A large increase (3-4X) in compressive strength is observed when the strain rate is increased from 10^{-3} - 10^3 s⁻¹.

Introduction—Limited data on the compressive strength of meteorites exist in the literature. Previous researchers have performed laboratory measurements on stony meteorites [1, 2, 3, 4, 5, 6], as well as iron meteorites [7, 8]. These studies were mostly designed to determine the strength of meteorites with regard to understanding the breakup of meteors entering the Earth's atmosphere. Despite the high entry velocities (typically 18 km/s) the process of traversing the Earth's atmosphere takes place on the time scale of seconds, and the strength under low rate (quasistatic) loading conditions is expected to be the relevant measure for predicting failure. Thus in previous studies the laboratory measurements performed were conducted at quasistatic loading rates. The only measurements performed at high strain rates to date were performed on specimens of an iron meteorite [8], which is expected to have a significantly different response when compared with stony meteorites.

For applications where the loading conditions are more dynamic (e.g. impact cratering), the quasistatic strength may not provide an accurate description of material response. Terrestrial rock specimens often exhibit an increased strength when compressed at strain rates higher than 10^2 s⁻¹ [9, 10, 11]. Stony meteorites are expected to exhibit similar rate dependence, but no measurements exist. To begin to fill this gap in data we have chosen to investigate the compressive strength of the meteorite MacAlpine Hills 88118 (MAC 88118) at strain rates ranging from 10^{-3} to 10^3 s⁻¹.

Specimen Description—Stony meteorites generally differ from terrestrial rocks in terms of composition and structure. Most meteorites recovered on earth are classified as chondrites, which are agglomerations of nearly spherical particles (chondrules) of silicate minerals, generally olivine, and pyroxene. These chondrules sit in a fine-grained silicate matrix that also surrounds grains of iron-nickel metal. MAC 88118 has been characterized as a L5 chondrite. The group "L" denotes that it has relatively low iron abundance, ~22% wt% total iron, with ~30% of the total iron content appearing as metallic iron. The petrologic type "5" denotes the level of thermal alteration on a scale of 3-6. At the low end of the scale chondrules are distinct and there can be large variations in chemical composition from grain to grain. At the high end of the scale chondrule boundaries tend to diffuse into the matrix and the chemical composition of the meteorite tends to homogenize. While there are terrestrial rocks with similar mineral composition (e.g. periodite), terrestrial rocks lack the chondritic texture and iron-nickel inclusions that are found in meteorites. These differences in structure and composition may lead to different mechanical response when compared with terrestrial rocks.

Experimental Method—For compression testing cube shaped specimens with edge lengths of approximately 5mm were cut from larger slabs of the meteorite specimen. Specimens were compressed in the direction normal to the surface of the parent plate to isolate any effects of specimen anisotropy [6]. Loading faces of the specimen were polished to ensure that the faces were parallel to within 5 μ m across the specimen. Specimens were measured to have a bulk density of 3240 kg/m³ and a porosity of 12%.

The quasistatic compression experiments were conducted using a MTS servo hydraulic uniaxial testing machine, while the dynamic compression experiments were conducted using a Kolsky (split-Hopkinson) bar [9, 12]. In all of the experiments the specimens were loaded until material failure. For all experiments images were recorded in real time to capture the evolution of failure in the specimen.

Experimental Results—The stress–time response of a specimen subjected to quasistatic compression (strain rate 10^{-3} s^{-1}) is shown in Fig. 1. The specimen was compressed in the vertical direction, and specimen stress was calculated from the recorded load data and the specimen cross sectional area. The images on the right side of the figure were captured during the experiment and the image numbers correspond to the stress–time pairs marked by the filled circles in the plot. One can clearly see the heterogeneous nature of the specimen, with the bright spots corresponding to metal inclusions and the light and dark gray areas corresponding to the matrix and chondrules. Here we see that the specimen stress increases to a peak value of 50 MPa before dropping off to zero. This peak corresponds to the quasistatic compressive strength of the meteorite. At times after the peak stress has been reached, several cracks (see arrows in frame 6) can be seen on the surface of the meteorite. In frames 7 and 8 these cracks have extended across the specimen in the loading direction (axial splitting failure mode) and the stress carried by the specimen has dropped to zero.

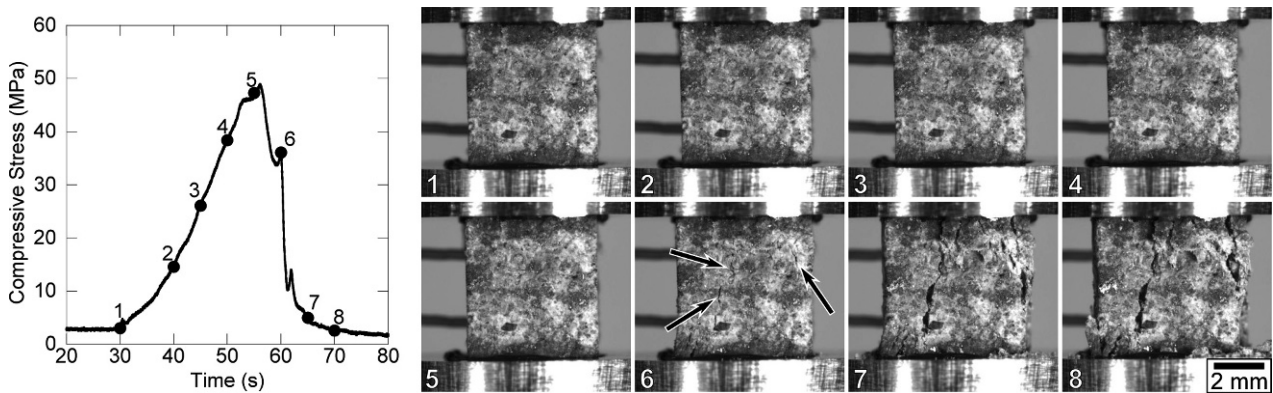


Fig. 1. Stress–time response of a specimen compressed to failure at a strain rate of 10^{-3} s^{-1} .

Similar experiments were conducted at high strain rates using the Kolsky bar. The stress–time response of a specimen compressed at a strain rate of 500 s^{-1} is presented in Fig. 2. The images on the right side of Fig. 2 show the specimen being compressed in the horizontal direction. The specimen stress was determined using the methods of Kolsky bar analysis for brittle materials [9]. Note that the time scale is now on the order of microseconds. As the stress in the specimen passes its peak value and begins to drop cracks appear on the surface of the specimen (arrow in image 4). In subsequent frames new cracks appear and are observed to extend across the specimen in the direction of loading (arrows in frame 8), and the stress in the specimen drops to zero.

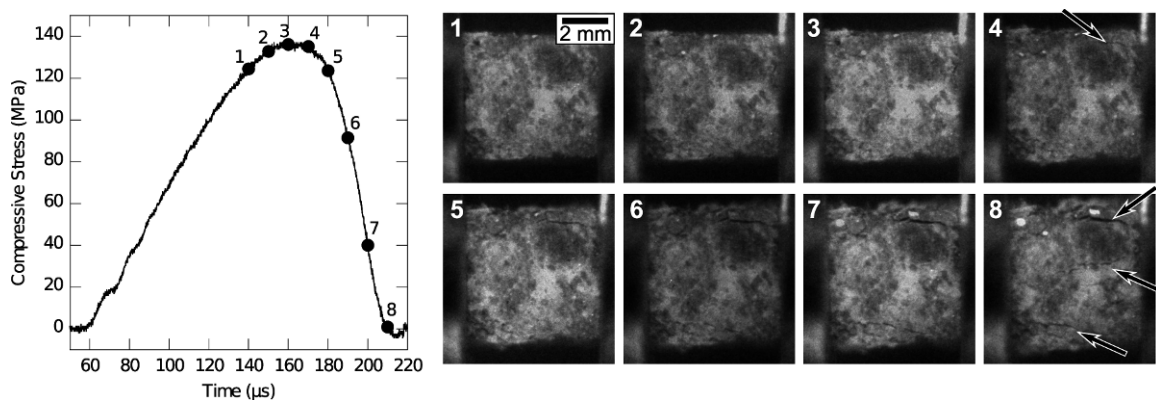


Fig. 2. Stress–time response of a specimen compressed to failure at a strain rate of 500 s^{-1} .

Comparing the results of the quasistatic and dynamic experiments we see a few similarities and differences. First, the failure mode of axial splitting dominates regardless of rate. This indicates that the failure is governed by the interaction and coalescence of microcracks that are present inside the specimen. The most notable difference between the two tests is the large increase in compressive stress observed in the experiment performed at the higher strain rate. The specimen compressed at a strain rate of $5 \times 10^2 \text{ s}^{-1}$ is almost 3x stronger than the specimen compressed at $1 \times 10^{-3} \text{ s}^{-1}$. Several more experiments were performed to verify that this was not due to specimen-to-specimen variations and the results of compressive strength as a function of strain rate are presented in **Fig. 3**. For rates greater than 10^2 s^{-1} there is a very steep increase in compressive strength with increasing rate. Similar trends have been observed in terrestrial rocks in which there exists a transition strain rate, above which significant increases in strength are observed with increasing rate [9, 10, 11]. One interesting observation is that these meteorite specimens show nearly a four-fold increase in strength whereas most terrestrial rock specimens typically show a factor-of-two increase in strength across a similar range of strain rates [9, 10, 11]. This may indicate that the transition rate in meteorite specimens is an order of magnitude lower than is typically observed in Earth rocks.

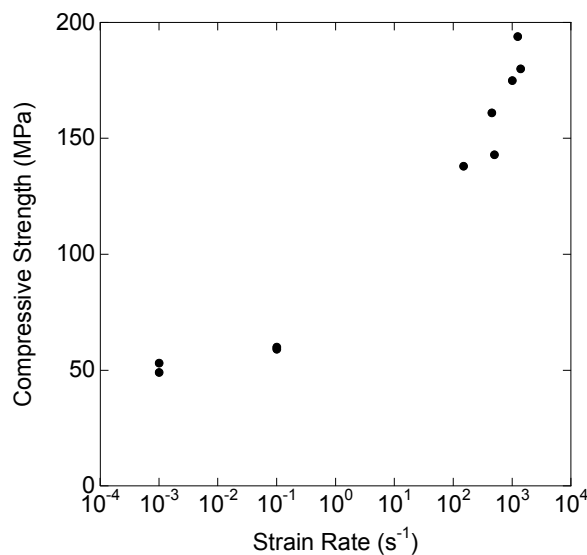


Fig. 3. Compressive strength as a function of applied strain rate for samples of MAC 88118.

Conclusions—We have performed the first high-rate compression experiments on material recovered from a stony meteorite. In addition to adding to the existing data sets for quasistatic compression strength of meteorite materials the results show that significant increases occur in the failure strength when specimens are compressed at higher strain rates. These rate effects may play an important role in determining the outcome of processes related to impact events, especially disruption of/impact cratering on asteroidal bodies

Acknowledgements—This material is based upon work supported by the National Aeronautics and Space Administration under Grant NNX09AE39G issued through the Planetary Geology and Geophysics Program. The authors thank Dr. Tim McCoy and Dr. Linda Welzenbach at the Smithsonian Institute for providing the meteorite samples, and performing the chemical composition analysis.

References:

- [1] Buddhue, J. D., The Compressive Strength of Meteorites, *Popular Astronomy*, 50, 390-391, (1942).
- [2] Baldwin, B. and Sheaffer, Y., Ablation and Breakup of Large Meteoroids during Atmospheric Entry, *J. Geophys. Res.*, 76(19), 4653-4668, (1971).
- [3] Svetsov, V. V., Nemtchinov, I. V., and Teterev, A. V., Disintegration of Large Meteoroids in Earth's Atmosphere: Theoretical Models, *Icarus*, 116(1), 131-153, (1995).
- [4] Flynn, G., Physical Properties of Meteorites and Interplanetary Dust Particles: Clues To The Properties of The Meteors and Their Parent Bodies, *Earth, Moon, and Planets*, 95(1), 361-374, (2004).

- [5] Miura, Y. N., Noguchi, T., Tsuchiyama, A., Yano, H., Yoshida, S., and Nagata, K., Compressive strength measurements of meteorites and terrestrial rocks: Implications for physical properties of asteroidal surfaces, In Proceedings of the Japan Geoscience Union Meeting, (P168-P002) (2008).
- [6] Nikitin, S. M., Korochantsev, A. V., Lorents, C. A., and Skripnik, A. Y., Strong Physical and Mechanical Anisotropy of Ordinary Chondrites, In 40th Lunar and Planetary Science Conference, (1051)(2009).
- [7] Gordon, R. B., Mechanical Properties of Iron Meteorites and the Structure of Their Parent Planets, Journal of Geophysical Research, 75(2), 439-447, (1970).
- [8] Furnish, M., Boslough, M., Gray, G., and Remo, J., Dynamical Properties Measurements for Asteroid, Comet and Meteorite Material Applicable to Impact Modeling and Mitigation Calculations, International Journal of Impact Engineering, 17(1-3, Part 1), 341-352, (1995).
- [9] Frew, D. J., Forrestal, M. J., and Chen, W., A Split Hopkinson Pressure Bar Technique to Determine Compressive Stress-Strain Data for Rock Materials, Experimental Mechanics, 41(1), 40-46, (2001).
- [10] Lindholm, U. S., Yeakley, L. M., and Nagy, A., The dynamic strength and fracture properties of dresser basalt, International Journal of Rock Mechanics and Mining Sciences & Geomechanics Abstracts, 11(5), 181-191, (1974).
- [11] Green, S. J. and Perkins, R. D., Uniaxial Compression Tests at Strain Rates from 0.0001/Sec. To 1000/Sec. On Three Geologic Materials, Technical Report: General Motors Technical Center Warren Mich Materials and Structures Lab MSL-68-6, 1-44, (1969).
- [12] Kolsky, H., An Investigation of the Mechanical Properties of Materials at Very High Rates of Loading, Proceedings of the Physical Society, Section B, 62, 676-700, (1949).

Determination of Dynamic Tensile Properties for Low Strength Brittle Solids

R. Chen^{1*}, F. Dai², L. Lu¹, F. Lu¹, K. Xia²

1. National University of Defense Technology, Changsha, China, 410073

2. University of Toronto, Toronto, Ontario, Canada, M5S 1A4

*Corresponding author: R_Chen@nudt.edu.cn

Abstract: We propose an indirect tensile testing method to measure the full dynamic tensile stress-strain curve of low strength brittle solids. In this method, we use the flattened-Brazilian disc (FBD) sample and apply the dynamic load with a modified split Hopkinson pressure bar (SHPB) system. Low amplitude dynamic loading forces are measured by a piezoelectric force transducer that is embedded in the transmitted bar. The evolution of the tensile stress at the center of the disc sample is determined via finite element analyses with the measured stress in SHPB as inputs. In a traditional Brazilian method, a strain gauge is mounted at the center of the specimen to measure the tensile strain, which is difficult to apply for low strength brittle materials. Therefore, a laser gap gauge (LGG) is used to monitor the expansion of the disc perpendicular to the loading axis, from which the average tensile strain is deduced. The numerical simulation reveals a linear relationship between the tensile strain at the center of the specimen and the average tensile strain and the relating factor is not sensitive to the material elastic parameters. The feasibility of this methodology is demonstrated with the SHPB-FBD experiments on a polymer bonded explosive (PBX).

INTRODUCTION

In studying brittle solids, conventional tension tests present difficulties both in specimen preparation and in alignment during the test. The Brazilian test involves compression of a disc along a vertical diameter [1], as shown in Fig. 1 (a). The compression induces a uniform tensile stress perpendicular to the loading axis which eventually causes failure by the formation of a vertical crack through the center of the disc. In the Brazilian test, the point contact between the loading platens and the circular boundary of a disc specimen, will lead to stress concentration at the loading end of the specimen. This may bring unexpected breakage of the specimen at the contact point.

Two types of attempts have been made to conquer this unreasonable failure mode of the disc specimen. One is to change the flat loading anvils in to curved anvils in order to fit the specimen [2], as shown in Fig. 1 (b). Curved anvils can prevent the formation of edge failure, but the match between the anvils and the periphery of a disc specimen is very complicated. The tensile strength is affected by the contact width between the specimen and anvil (2b), which is difficult to determine. Differently sized anvils must be required for discs with different diameters. The other solution to the problem is to machine two opposing flatten ends on the disc specimen in order to fit the loading anvils [3], as shown in Fig. 1 (c). By changing the regular Brazilian disc into the Flattened Brazilian Disc (FBD), the area of contacting surface is increased and local force concentration can be avoided.

In many applications, materials are stressed dynamically such as earthquakes, airplane crashes, projectile penetrations, rock bursts and blasts. The split Hopkinson pressure bars (SHPB) is widely used to measure the dynamic properties of materials [4]. But for the materials with the strength as low as 1MPa, the signals recorded from the strain gauges on the transmitted bar is too week to be detected. To accurately measure the dynamic loading force, a piezoelectric force transducer is embedded in the transmitted bar [5] to record the dynamic force directly. By the same token, instead of mounting a strain gauge on the specimen in a traditional Brazilian test, we use a recently developed laser gap gauge [6] to monitor the deformation of the material. The average tensile strain is deduced from the laser gap gauge (LGG) method. The tensile strain at the center of the specimen is

obtained by the average tensile strain times a scaling factor, which is deduced by the numerical simulation, and is not sensitive to the material elastic parameters. We demonstrate the feasibility of our modified system with tests on a polymer bonded explosives (PBX).

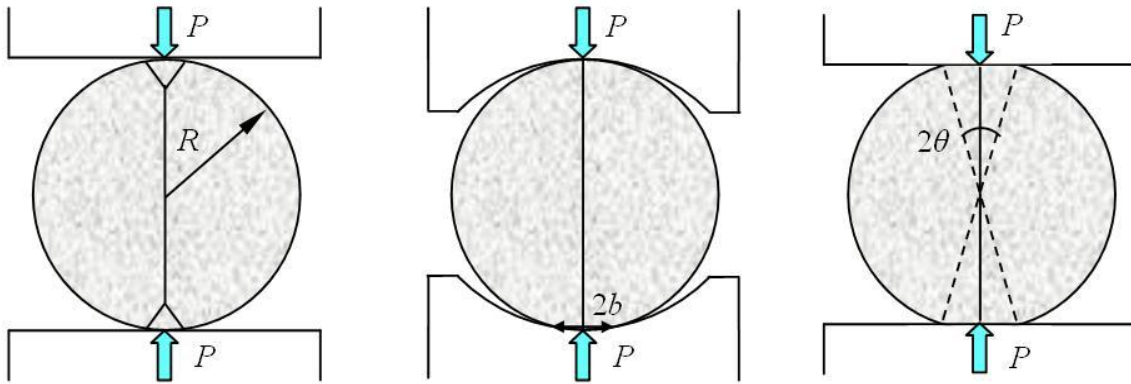


Fig. 1. (a) Brazilian test geometry. A disc, radius R , is loaded across a diameter between two flat anvils. The edge failures due to force concentration. (b) Schematic diagram showing tensile failure when using curved anvils. The contact width between the specimen and anvil is $2b$. (c) Schematic diagram showing the flattened Brazilian disc. The loading angle is 2θ .

EXPERIMENT

The geometry of a FBD specimen is used in our experiment, as shown in Fig. 2. Its radius $R = 10$ mm and thickness $B = 12$ mm, and the loading angle $2\theta = 20^\circ$. Wang showed that for a flattened disc specimen, the stress at the center is [3]:

$$\sigma_i = \frac{P}{\pi BR} \cdot Y(\theta) \quad (1)$$

where Y is the coefficient which is related to the loading angle. When $2\theta = 0$, $Y = 1$; and this case corresponds to the original Brazilian disc. For the given value of 2θ , Y can be calibrated by finite-element analysis [3]. In our case $2\theta = 20^\circ$, and $Y = 0.964$.

The 20mm-diameter aluminium SHPB system (Fig. 2) is used in the study. The length of the striker bar is 150 mm. The incident bar is 1800 mm long and the strain gauge station is 802mm away from the impact end of the bar. The transmitted bar is 1000 mm long and the quartz crystal is sandwiched between the transmitted bar and a 2mm-thick aluminium disc. A LGG is used to monitor the expansion of the disc perpendicular to the loading axis. An infrared detector system is used together with a two-channel TDS1021 digital oscilloscope to measure the velocity of the striker bar. A four-channel TDS5054B digital oscilloscope is used to record and store the strain signals collected from the Wheatstone bridge circuits after amplification. The pulse shape is used to shape the loading pulse and thus facilitates the force balance on both sides of the sample during tests [7].

When testing low strength materials using SHPB, the transmitted signal is too small due to the mismatch between the acoustic impedance of the bar and that of the materials. The X-cut quartz has been shown to be much more sensitive in detecting stresses in its X-direction than the strain gauge in SHPB tests, with three orders of magnitude increase in the sensitivity [5]. We use a piezoelectric transducer sandwiched between the specimen and transmitted bar to directly measure the dynamic loading force. The positive pole of the crystal is glued to the bars, and the negative pole of the crystal is glued to a thin aluminum disk, as shown in Fig. 2. The quartz crystal is calibrated by the strain gauge signal [5].

Conventional strain gauge methods are unsuitable for measuring strains on low strength samples with dimensions adopted in current studies. Strain gauges tend to reinforce the specimens at the point of attachment; a significant disturbance for low modulus materials. The adhesive may also react with the material, modifying its properties. To handle this, a non-contact method, LGG system, is used in this research to measure the tensile strain. The LGG

system has been used by the authors to monitor the notch opening during dynamic fracture tests[6]. The apparatus consists of four major components: diode line laser, a cylindrical lens, a collecting lens, a collecting lens, and a light detector (Fig. 2). In SHPB testing on a FBD specimen, LGG is mounted perpendicular to the bar axis. The specimen shadows part of the laser beam, and the expansion of the specimen is in inverse proportion to the output voltage of the detector (Fig. 2). Details of our LGG system were reported elsewhere [6].

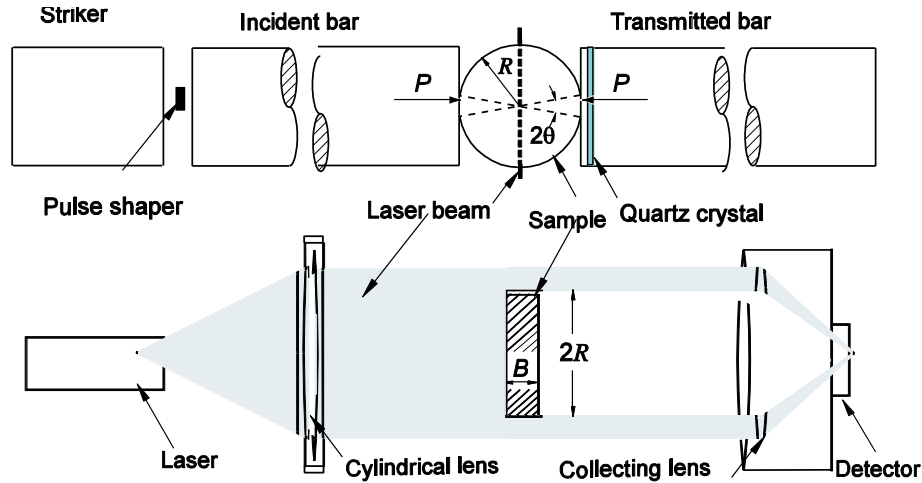


Fig. 2. Schematics of the split Hopkinson pressure bar (SHPB) system, the flattened Brazilian disc (FBD) sample, and laser gap gauge (LGG) system.

In this method, we can obtain the average tensile strain of the specimen rather than the tensile strain in the center. Do they have some relationship with each other? The strain distribution in a FBD specimen is only caused by the loading angle, no matter how much the loading force is, how much the elastic modulus or the Poisson's ratio of the specimen. We conduct finite element analysis to relate the average tensile strain to the tensile strain at the center of the specimen for a given specimen geometry. The forces applied on both sides of the sample during our SHPB tests are identical with the pulse shaping technique [7]. The inertial effects are eliminated because there is no global force difference in the specimen to induce inertial forces, so that the quasi-static analysis can be used here. This process is called numerical calibration. Taking advantage of the symmetry of the sample, quarter model is used to construct the finite element model. PLANE82 (eight-node) element is used in the analysis. Fig. 3 shows the schematic of the configuration for finite element analysis.

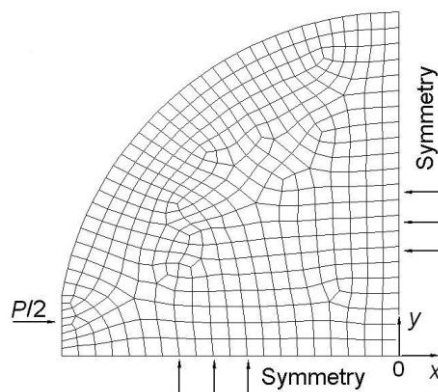


Fig. 3. Schematic of the configuration for finite element analysis.

We define the proportional parameter k_{FBD} as:

$$k_{FBD} = \varepsilon_{FBD} / \bar{\varepsilon}_{FBD} \quad (2)$$

where $\bar{\varepsilon}_{FBD}$ is the average tensile strain, and ε_{FBD} is the corresponding tensile strain in the center of specimen.

Fig. 4 shows that the strain distribution with different loading conditions, where y is the distance away from the sample center as shown in Fig. 3. The tensile strain is the largest at the center of the specimen, and decreases along y axle till zero in the edge. As the loading force increases from 0.5kN to 1.5kN, the strain increases proportionally. The distribution of the strain is similar to each other, and the proportional parameter k_{FBD} changes only 0.02 with the average value of 2.13, as shown in Fig. 4 (a). There are similar situations for different Young's modulus and different Poisson's ratios of the specimen, as shown in Fig. 4 (b) and Fig. 4 (c) respectively.

Further more, we validate whether the parameter k_{FBD} remains constant for non-linear materials. Set the multi-linear constitutions, shown in Fig. 4 (b), as the material model, we find that the varieties of parameter k_{FBD} still with in 7%, which is acceptable.

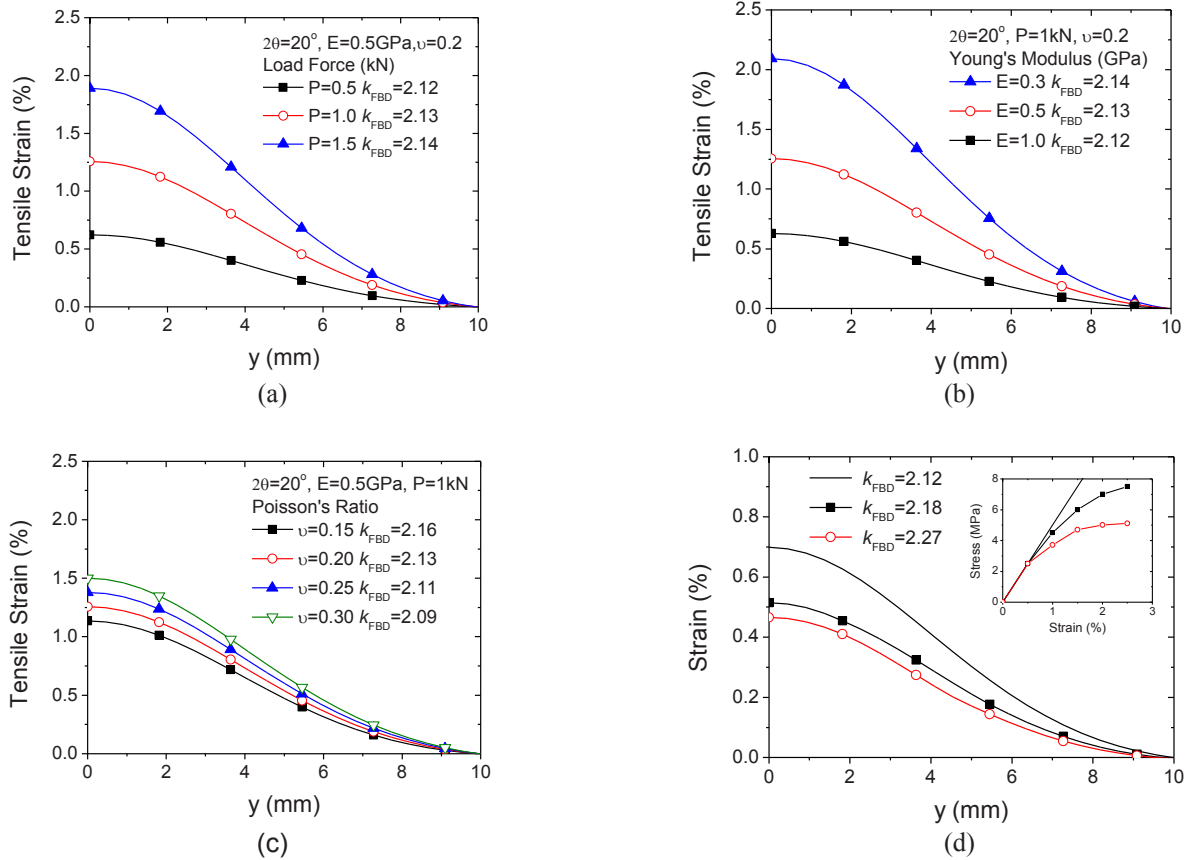


Fig. 4 The numerical calibration of k_{FBD} . Strain distribution with (a) different loading force, (b) different Yong's modulus, (c) different Poisson' ratio, and non-linear materials (d).

The movement of the specimen along the loading direction may lead to errors on the strain measurement. As shown in Fig. 5, the leaser beam is set to the center of the specimen before the experiment. When the incident wave arrives, the velocity of the loading anvils is:

$$v_1(\tau) = c_0(\varepsilon_i(\tau) - \varepsilon_r(\tau)), \quad v_2(\tau) = c_0\varepsilon_i(\tau) \quad (3)$$

where c_0 is the elastic wave velocity of the bar material, and $\varepsilon_i(\tau)$, $\varepsilon_r(\tau)$, and $\varepsilon_t(\tau)$ are incident, reflected, and transmitted wave respectively. Due to the huge impedance mismatch between sample and loading anvils, most of the incident wave will reflect back as the reflected wave, and the transmitted wave is very small. Then the displacement of the specimen center will be:

$$s(t) = \int_0^t \frac{v_1(\tau) + v_2(\tau)}{2} d\tau \approx c_0 \int_0^t \varepsilon_i(\tau) d\tau \quad (4)$$

The specimen displacement and the LGG error $\delta(t)$ can be related geometrically as follows:

$$\delta(t) = \frac{\sqrt{R'^2 + s^2(t)} - R'}{\sqrt{R'^2 + s^2(t)}} R' = \frac{s^2(t)}{\sqrt{R'^2 + s^2(t)}(\sqrt{R'^2 + s^2(t)} + R')} R' \approx \frac{s^2(t)}{2R'} \quad (5)$$

where R' is the radius of specimen after deformation. Finally, we can calculate the corrected average strain:

$$\bar{\varepsilon}_{FBD}(t) = \frac{k \cdot \Delta U(t) + 2\delta(t)}{2R} \approx \frac{k \cdot \Delta U(t)}{2R} + \frac{1}{2} \frac{s^2(t)}{RR'} \quad (6)$$

where $\Delta U(t)$ is the variation of LGG output voltage, and $k = 4.08 \text{ mm/V}$ is the calibrated coefficient of the LGG system [6]. The second part of equation (6) is the correction part caused by the movement of specimen. In a typical experiment, $k\Delta U = 0.5 \text{ mm}$, $s = 0.3 \text{ mm}$, $R = 10 \text{ mm}$, and set $R' = R$. The second part of (6) is second order small, and thus can be ignored.

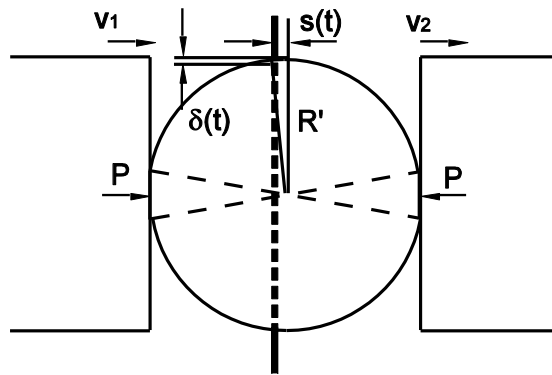


Fig. 5 The error caused by the motion of specimen along loading direction.

APPLICATION TO A PBX

To demonstrate the feasibility of the above methodology for measuring the dynamic tensile properties, we have performed SHPB-FBD tests on a polymer bonded explosives (PBX). Fig. 6 shows typical oscilloscope signals of the experiment. Channel 1 is the triggering signal, channel 2 is connected to the strain gauge on the incident bar, recording the incident and the reflection waves, channel 3 is connected to the quartz crystal, measuring the loading force, and channel 4 is connected to the LGG, monitoring the expanding of the specimen. Fig. 6 (a) shows the signals of a test when the specimen is cracked. The LGG signal stays constant after the loading ends, which means that the specimen stops expanding. Fig. 6 (b) shows the signals of a test when the specimen is fragmented. The LGG signal goes on decreasing after the loading ends, because there is surplus energy for fragment specimen, and the fragment specimen fly off each other.

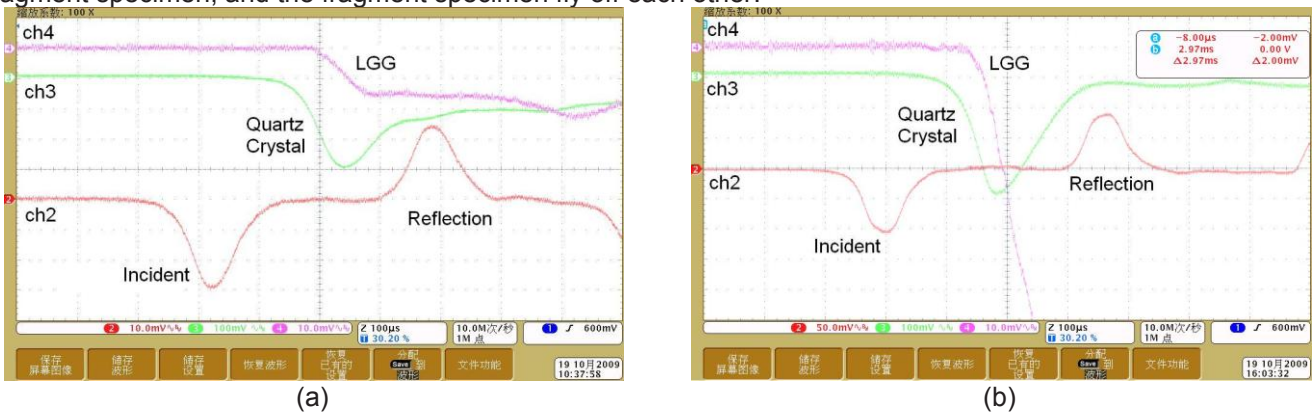


Fig. 6 Oscilloscope signals for two cases: (a) sample cracked and (b) sample fragmented.

As shown in Fig. 6 (a) for a typical test with outputs, we calculate the deformation and loads shown in Fig. 7 (a). The tensile strain at the center of the specimen is calculated by substituting Eq. (6) into Eq. (2), and the stress history is calculated using Eq. (1). There is a regime of approximately linear variation of strain with time from 100 to 200 μs . The slope of this region is determined from a least-squares fit as strain rate, shown as the dashed line in the figure. Fig. 7 (b) shows stress strain curves of a PBX with different strain rates. The strengths of the PBX increase linearly with increasing loading rates.

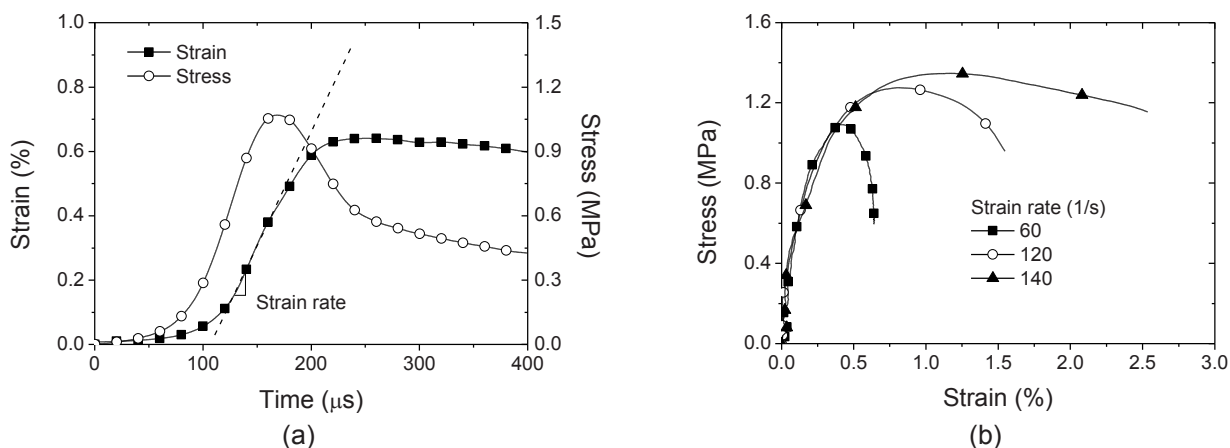


Fig. 7 (a) Stress and strain history of the specimen and the determination of strain rate. (b) Stress-strain curves of PBX with different strain rates.

CONCLUSION

We propose a modified SHPB testing technique with a FBD specimen to measure the full dynamic tensile stress-strain curve of low strength brittle solids. In this method, a piezoelectric force transducer is embedded in the transmitted bar in order to measure the loading force, and a LGG is used to monitor the expansion of the disc perpendicular to the loading axis, from which the average tensile strain is deduced. The numerical simulation reveals a linear relationship between the tensile strain at the center of the specimen and the average tensile strain. This scaling factor is not sensitive to the material elastic parameters. The feasibility of this methodology is demonstrated with the SHPB-FBD experiments on a PBX. This technique is readily implementable and can be applied to investigate dynamic tensile mechanics of low strength brittle materials.

ACKNOWLEDGMENTS

This work was supported by the Natural Science Foundation of China (NSFC) through Grant No. 10872215 & 10902100, and the Natural Sciences and Engineering Research Council of Canada (NSERC) through Discovery Grant No. 72031326.

REFERENCES

- [1] Berenbaum R. and Brodie I., "Measurement of the tensile strength of brittle materials", *British Journal of Applied Physics*. 10: 281-286 (1959).
- [2] Awaji H. and Sato S., "Diametral compressive testing method", *Journal of Engineering Materials and Technology-Transactions of the ASME*. 101(2): 139-147 (1979).
- [3] Wang Q.Z., Jia X.M., Kou S.Q., et al., "The flattened Brazilian disc specimen used for testing elastic modulus, tensile strength and fracture toughness of brittle rocks: analytical and numerical results", *International Journal of Rock Mechanics and Mining Sciences*. 41(2): 245-253 (2004).
- [4] George T. and Gray III., "Classic split-Hopkinson pressure bar testing". in: *ASM Handbook Vol. 8 Mechanical Testing and Evaluation*. 1027-1067 (2000).
- [5] Chen W., Lu F., and Zhou B., "A quartz-crystal-embedded split Hopkinson pressure bar for soft materials", *Experimental Mechanics*. 40(1): 1-6 (2000).
- [6] Chen R., Xia K., Dai F., et al., "Determination of dynamic fracture parameters using a semi-circular bend technique in split Hopkinson pressure bar testing", *Engineering Fracture Mechanics*. 76(9): 1268-1276 (2009).
- [7] Frew D.J., Forrestal M.J., and Chen W., "Pulse shaping techniques for testing brittle materials with a split Hopkinson pressure bar", *Experimental Mechanics*. 42(1): 93-106 (2002).

The Mechanical Response of Aluminum Nitride at Very High Strain Rates

Guangli Hu¹, K.T. Ramesh¹, J. W. McCauley²

¹ Department of Mechanical Engineering, Johns Hopkins Univ., Baltimore, Maryland 21218

² Army Research Laboratory, Aberdeen Proving Ground, Maryland 21078

Abstract

In previous work, we have used a modified compression Kolsky bar to determine the dynamic compressive strength of some ceramic materials, including aluminum nitride (AlN), at strain rates of approximately 10^3 s^{-1} . However, there is very limited experimental work on ceramics at higher strain rates (of the order of 10^4 s^{-1}) because of various technical difficulties. This work seeks to characterize the mechanical properties of AlN within the strain rate range ($10^3 \sim 10^4 \text{ s}^{-1}$) using the desktop Kolsky bar (DKB), taking advantage of the benefits of miniaturization. Our interest is in the influence of the loading rate on the compressive strength under uniaxial stress conditions. Microstructural analysis is performed to identify the failure mechanisms at different strain rates.

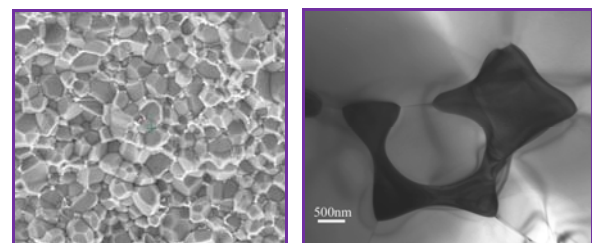
Introduction

AlN has received considerable attention due to its potential armor application. Heard and Cline [1] conducted quasi-static confined experiments using hot-pressed AlN at a confining pressure up to 820 MPa and observed the brittle to ductile transition. Subhash and Ravichandran [2] performed the uniaxial compression tests on hot-pressed AlN at different strain rates, and found that the peak stress exhibited a weak rate sensitivity at low strain rates ($10^{-6} \sim 10^{-2} \text{ s}^{-1}$) and a strong rate sensitivity at higher strain rates ($10^2 \sim 10^3 \text{ s}^{-1}$). Chen and Ravichandran [3] used a sleeve jacket to apply confining pressures up to 230 MPa on sintered AlN and studied the sensitivity of peak strength to pressure. Rosenberg et al. [4] and Grady et al. [5, 6] did the plate impact (strain rate around 10^5 s^{-1} [7]) experiments on AlN and observed the shear strength was independent of pressure at high pressure ranges. However, limited data is available at the strain rate range of $10^3 \sim 10^4 \text{ s}^{-1}$ due to the experimental technique limitation. Jia and Ramesh [8] developed a miniaturized Kolsky bar (DKB) which provided a technique to achieve a higher strain rate during the dynamic loading. In this paper, DKB is employed to probe the mechanical response of AlN at a strain rate of $10^3 \sim 10^4 \text{ s}^{-1}$. Real time failure process will be recorded by high-speed DRS Hadland Ultra 8 camera. Microscopic analysis will also be presented to identify the deformation and failure mechanisms under different testing conditions.

Materials and samples

The material in this study is sintered AlN, provided by the Dow Chemical Company. TEM pictures of the as-received AlN are below. The average grain size is

5 μm and about 3% volume fraction is sintering additive, Y_2O_3 . Fig.1 (a) is a Field Emission SEM picture of a cleaned fracture surface, showing the grain size is comparatively uniform and sintering additive phase. Fig. 1 (b) is a TEM picture of as-received AlN, nicely showing the AlN grains and the Y_2O_3 phase between the AlN grains. From TEM, we can also see the as-received material is free of dislocations. The cuboid samples are machined from the tile and sample size is 0.8 mm by 0.8 mm by 1mm. The loading direction is along 1 mm direction.



(a) (b)
Fig.1 (a) Field Emission SEM of a cleaned fractured surface showing 5-6 μm grain size (White phase is yttrium oxide and the grey phase are AlN grains) (b) As-received sintered AlN under TEM shows Yttrium Oxide phase (dark region) and grey region (AlN grain)

Experimental technique

Fig.2 shows the DKB setup will be used to test the AlN material. The diameter of the bars is 3.155 mm and the input and output bar lengths are 306 mm and 278 mm. Due to the small bar diameter size, heat-treated maraging steel (VascoMax C-350) is used to machine the platens instead of jacket WC platens to protect the end surface of the bars (red region in Fig.2). High speed camera will be

synchronized with experiments to record failure processes. Detailed experimental protocols are based upon Subhash and Ravichandran [9] and Jia and Ramesh [8].

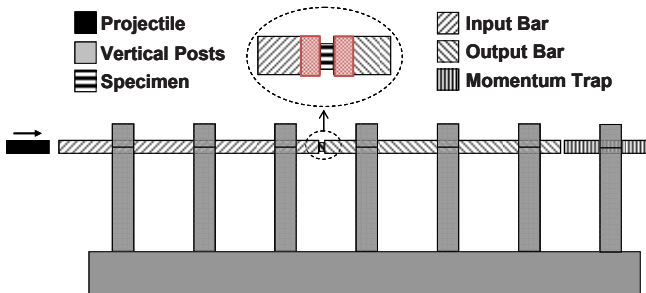


Fig.2 Schematic of the desktop Kolsky bar setup with the specimen sandwiched between the input and output bars.

Questions to answer

(a) Fig.3 shows a summary of existing data for AlN under quasi-static and conventional Kolsky bar technique. Stronger strain rate sensitivity is observed after 10^2 s⁻¹ strain rate. What is the behavior of AlN under strain rates 10^3 ~ 10^4 s⁻¹? Will the compressive strength of the material increase sharply as model predicted [10, 11]?

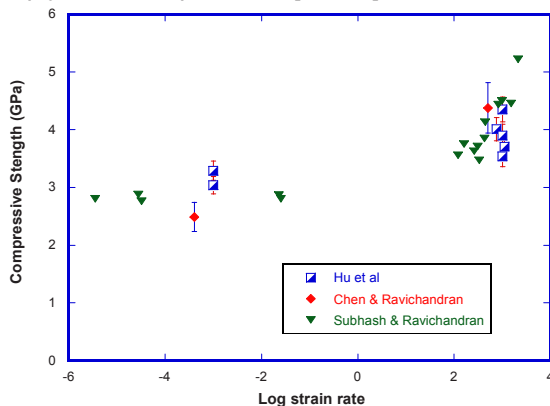


Fig.3 Strain rate effect on compressive strength of AlN. Note (i) Chen and Ravichandran's results [3] and current results [12] are for sintered AlN and Subhash and Ravichandran's results [2] are for hot-pressed AlN.

(b) Fracture mechanism map, Fig.4, has been constructed based upon the extensive microscopic observation on fracture surfaces of fragments from uniaxial quasistatic, dynamic compression (10^2 to 10^3 s⁻¹), and confined dynamic confined experiments. Map shows with increase of strain rate, transgranular fracture quickly dominate the fracture mechanism. Will the fracture mechanism change or stay the same under strain rate 10^3 ~ 10^4 s⁻¹ range?

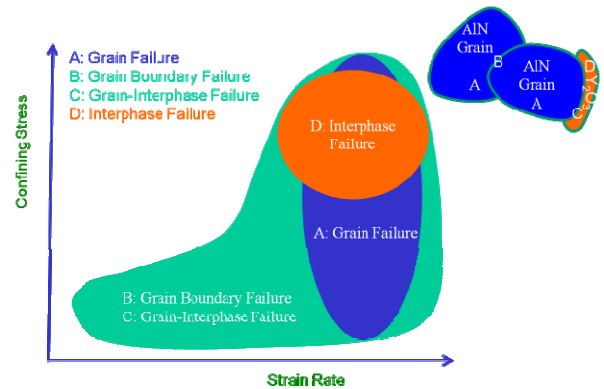


Fig.4 Fracture mechanism map as a function of strain rate and confining stress

Reference

- HEARD, H. and C. CLINE, *MECHANICAL-BEHAVIOR OF POLYCRYSTALLINE BEO, AL₂O₃ AND AlN AT HIGH-PRESSURE*. JOURNAL OF MATERIALS SCIENCE, 1980. **15**(8): p. 1889-1897.
- Subhash, G. and G. Ravichandran, *Mechanical behaviour of a hot pressed aluminum nitride under uniaxial compression*. JOURNAL OF MATERIALS SCIENCE, 1998. **33**(7): p. 1933-1939.
- Chen, W.N. and G. Ravichandran, *Static and dynamic compressive behavior of aluminum nitride under moderate confinement*. JOURNAL OF THE AMERICAN CERAMIC SOCIETY, 1996. **79**(3): p. 579-584.
- Rosenberg, Z., N.S. Brar, and S.J. Bless, *Dynamic High-Pressure Properties of AlN Ceramic as Determined by Flyer Plate Impact*. Journal of Applied Physics, 1991. **70**(1): p. 167-169.
- Kipp, M.E. and D.E. Grady, *Shock Phase-Transformation and Release Properties of Aluminum Nitride*. in *International Conference on Mechanical and Physical Behaviour of Materials under Dynamic Loading (EURODYMAT 94)*. 1994. Oxford, England: Editions Physique.
- Dandekar, D.P., A. Abbate, and J. Frankel, *Equation of State of Aluminum Nitride and Its Shock Response*. Journal of Applied Physics, 1994. **76**(7): p. 4077-4085.
- Grady, D.E., *Shock-wave compression of brittle solids*. Mechanics of Materials, 1998. **29**(3-4): p. 181-203.
- Jia, D. and K.T. Ramesh, *A rigorous assessment of the benefits of miniaturization in the Kolsky bar system*. Experimental Mechanics, 2004. **44**(5): p. 445-454.
- SUBHASH, G. and G. Ravichandran, *Split-Hopkinson Pressure Bar Testing of Ceramics*. Materials Park, OH: ASM International, 2000: p. 8.
- Huang, C.Y., G. Subhash, and S.J. Vitton, *A dynamic damage growth model for uniaxial compressive response of rock aggregates*. Mechanics of Materials, 2002. **34**(5): p. 267-277.
- Paliwal, B. and K.T. Ramesh, *An interacting micro-crack damage model for failure of brittle materials under compression*. Journal of the Mechanics and Physics of Solids, 2008. **56**(3): p. 896-923.
- Hu, G., et al., *The compressive failure of Aluminum Nitride considered as a model advanced ceramic*. In preparation, 2010.

Dynamic and Quasi-static Measurements of C-4 and Primasheet P1000 Explosives

Geoffrey W. Brown^{1,a}, Darla G. Thompson¹, Racci DeLuca¹, Philip J. Rae², Carl M. Cady², and Steven N. Todd³

¹High Explosives Science & Technology (DE-1), ²Materials Science & Technology (MST-8),
Los Alamos National Laboratory, Los Alamos, NM

³Energetic Systems Research (5916) and Systems Assessment and Research Center (5900),
Sandia National Laboratories, Albuquerque, NM

^aCorresponding author: MS C920, Los Alamos National Laboratory, Los Alamos, NM 87545.
email: geoffb@lanl.gov

ABSTRACT

We have measured dynamic and quasi-static mechanical properties of C-4 and Primasheet P1000 explosive materials to provide input data for modeling efforts. Primasheet P1000 is a pentaerythritol tetranitrate-based rubberized explosive. C-4 is a RDX-based moldable explosive. Dynamic measurements included acoustic and split-Hopkinson pressure bar tests. Quasi-static testing was done in compression on a load frame and on a dynamic mechanical analyzer. Split-Hopkinson and quasi-static tests were done at five temperatures from -50°C to 50°C. Acoustic velocities were measured at, above, and below room temperature.

INTRODUCTION

In this work we have measured the mechanical properties of C-4 and Primasheet P1000 explosive materials. The data will be used as input for a Damage-Induced Reaction Model [1] (DMGIR) that can predict non-shock-induced initiation. As in the development of other physics codes, the mechanical property data measured here contribute to constitutive relations that are used in equation-of-state models implemented in the code. P1000 and C-4 are relevant materials for DMGIR development and validation because they are used in a number of different explosives applications and because they can be considered representative “rubberized” and “moldable” explosive materials, respectively, to evaluate model capabilities. In previous work we have evaluated “pressed” and “cast” explosive materials for the same purposes [2].

EXPERIMENT

In this work we have measured dynamic and quasi-static mechanical properties of both materials. Dynamic measurements were made using split-Hopkinson pressure bar (SHPB) and acoustic testing. Quasi-static testing was carried out on mechanical load frames and on a dynamic mechanical analyzer (DMA). All quasi-static testing was done in compression.

Split-Hopkinson pressure bar (SHPB) tests were carried out with a custom made instrument [3]. The system has an environmental chamber that maintains the sample at various temperatures between -50°C and 50°C prior to testing. Maraging steel bars were used in these experiments. Over the +/- 50°C temperature range used in these experiments, the impedance of the Maraging steel changes negligibly. Molybdenum grease was used to lubricate the P1000 sample ends but no lubricant was used on the C-4. Samples were tested at -50°C, -15°C, 0°C, 21°C, and 50°C. SHPB samples for both materials were 0.125 inch thick disks, 0.25 inches in diameter. For P1000, the

strain-rates were typically 3000 s^{-1} except at $-50 \text{ }^\circ\text{C}$ where it was 2000 s^{-1} . For C-4, all strain-rates were approximately 5000 s^{-1} .

Quasi-static testing of P1000 at a strain rate of 33 s^{-1} was carried out on a commercial load frame (MTS model 810 with a high rate valve). Specimens were compressed between polished tungsten carbide platens lubricated with molybdenum grease to reduce end face friction. The platens were heated or cooled and surrounding insulation provided control of the sample temperature. Samples were tested at -50°C , -15°C , 0°C , 20°C , and 50°C . Quasi-static samples for both materials were 0.25 inch thick cylinders, 0.25 inches in diameter.

Quasi-static testing of both materials at strain rates of 0.025 s^{-1} and 0.0025 s^{-1} was carried out on a second commercial load frame (MTS Instron 5567). Specimens were compressed between stainless steel platens. Tests with and without lubricated end faces did not show significant differences. No lubrication was used on the C-4 samples. All testing was done in an environmental chamber using heated or cooled air flow to maintain the desired temperature. Samples were tested at -50°C , -25°C , 0°C , 25°C , and 50°C . For these tests, samples of both materials were 0.5 inch thick cylinders, 0.25 inches in diameter.

Acoustic wave velocities were measured using a time-of-flight method illustrated schematically in Figure 1. For each sample, the transit times of the initial peaks in the longitudinal and shear wave signals were measured both with and without the explosive sample in the transducer-delay bar stack. Knowing the sample thickness, the difference in transit times with and without the sample present then gives the acoustic wave velocity. An aluminum delay bar was used for all samples and all testing was done with commercial transducers having 1 MHz resonance frequencies. For both materials, we attempted to measure acoustic velocities at three different thicknesses and at temperatures below, at, and above room temperature. The actual sample sizes and temperatures are described in Table 1. For the P1000 material, thickened honey was used to couple the transducers to the samples. No couplant was used for the C-4 samples.

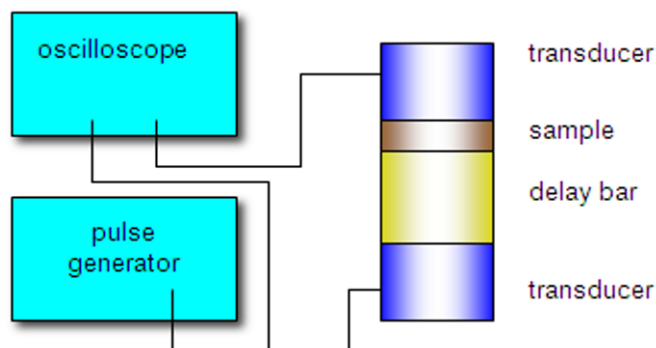


Figure 1. Schematic illustration of acoustic velocity measurement instrumentation.

Dynamic mechanical analysis (DMA) was carried out using a commercial instrument (TA Instruments Q800). The samples were held in stainless steel compression clamps inside the environmental housing with integral electric heaters. For the cold tests, liquid nitrogen vapor is flowed through the housing. P1000 samples were 0.25" diameter disks of thicknesses 2mm, 3mm, and 4mm. The C-4 samples were nominally 0.25" thick disks, 0.25" in diameter. No lubricant was used for any DMA samples.

SAMPLE MATERIALS

Primasheet P1000 is a rubberized explosive that is nominally 63% pentaerythritol tetranitrate by weight with 8% nitrocellulose and 27% binder. The binder was not specified for the samples used in this work. For all measurements, cylindrical samples were hand cored from sheets of P1000. Sample thicknesses were nominally 2mm, 3mm, and 4mm for acoustic and DMA tests and either 6mm or 12.5 mm for other tests. Thicker sheets were just stacks of the thinner sheets bonded together.

C-4 is a moldable explosive that is nominally 91% hexahydrotrinitrotriazine (RDX) in 9% oil or oil/polymer mixture. The material came in large prefabricated blocks and test samples were made by hand pressing small pieces of the block into molds. The density of the hand-pressed parts was less than that of the block but the composition of the material made it difficult to measure the dimensions or density of any samples. All results on C-4 should be considered typical of "worked" or "molded" material. Dynamic, quasi-static and DMA samples were all nominally 0.25" thick disks, 0.25" in diameter.

RESULTS

Primasheet P1000 Results

The SHPB results for P1000 at the temperature endpoints of $\pm 50^\circ\text{C}$ are shown in Figure 2. Each plot has traces from three different tests illustrating the sample-to-sample variability. The progression of the curves between these temperature endpoints can be seen in the right panel of Figure 3.

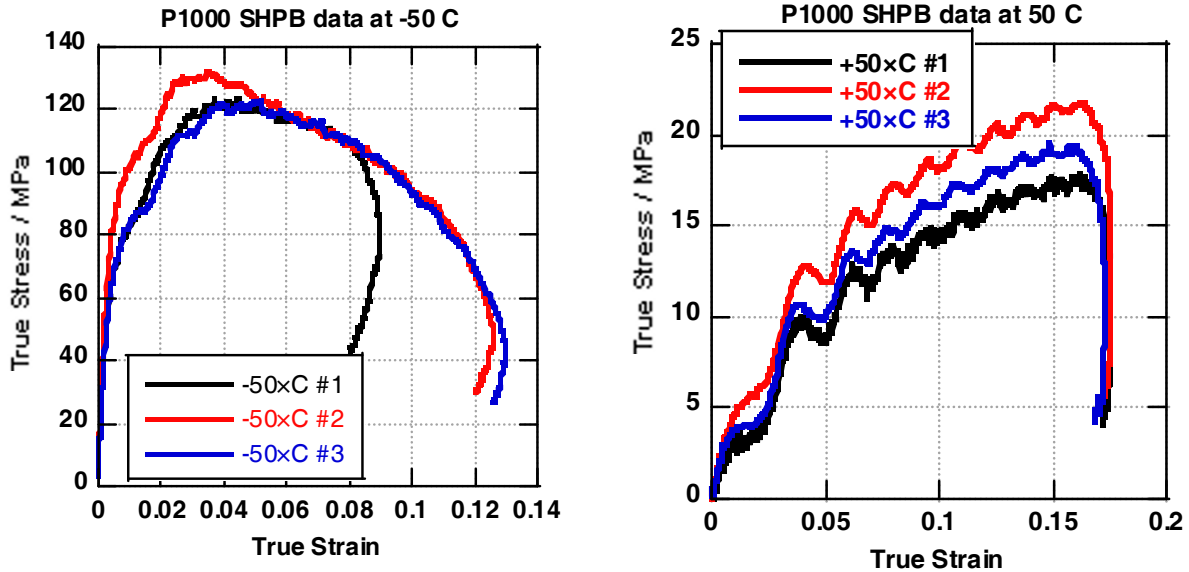


Figure 2. SHPB data from P1000 at -50°C and 50°C .

An example of the equilibrium region of the P1000 SHPB data can be seen from the “1-wave”, “2-wave” plots shown in the left panel of Figure 3. “1-wave” traces are the transmitted bar signals while “2-wave” traces are the sums of synchronized incident and reflected bar signals [4]. Typically, SHPB data is a valid measurement of the sample properties in regions where the 2-wave signal oscillates around the 1-wave signal and where the strain rate is roughly constant. For the P1000 data sets here, this region is roughly between 2% and 10% strain. Before 2% strain, the system has not reached equilibrium and after 10% strain, the signals are primarily related to damage accumulation in the sample. Example P1000 SHPB data for all temperatures is the right panel.

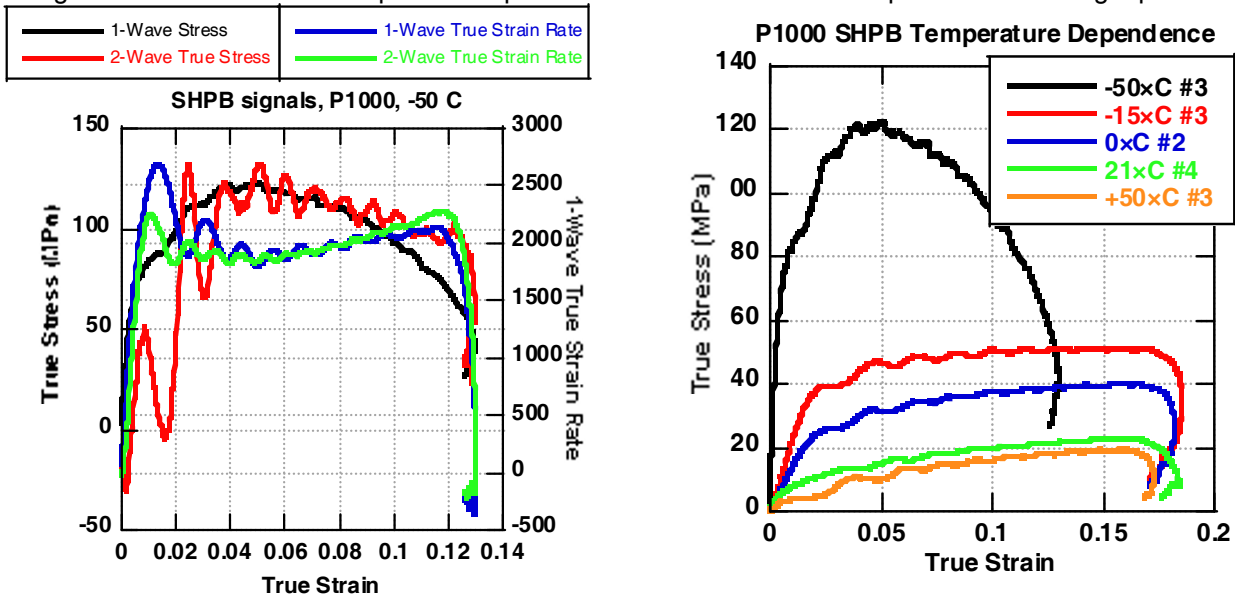


Figure 3. (left) SHPB stress and strains for one test on P1000 at -50°C . (right) Compilation of representative SHPB data for P1000 at all temperatures tested.

Quasi-static testing results for P1000 at 33s^{-1} and 0.025s^{-1} strain rates are shown in Figure 4. Tests at 0.0025s^{-1} were similar to those shown in the right panel. Details of the maximum stress values are in Figure 9.

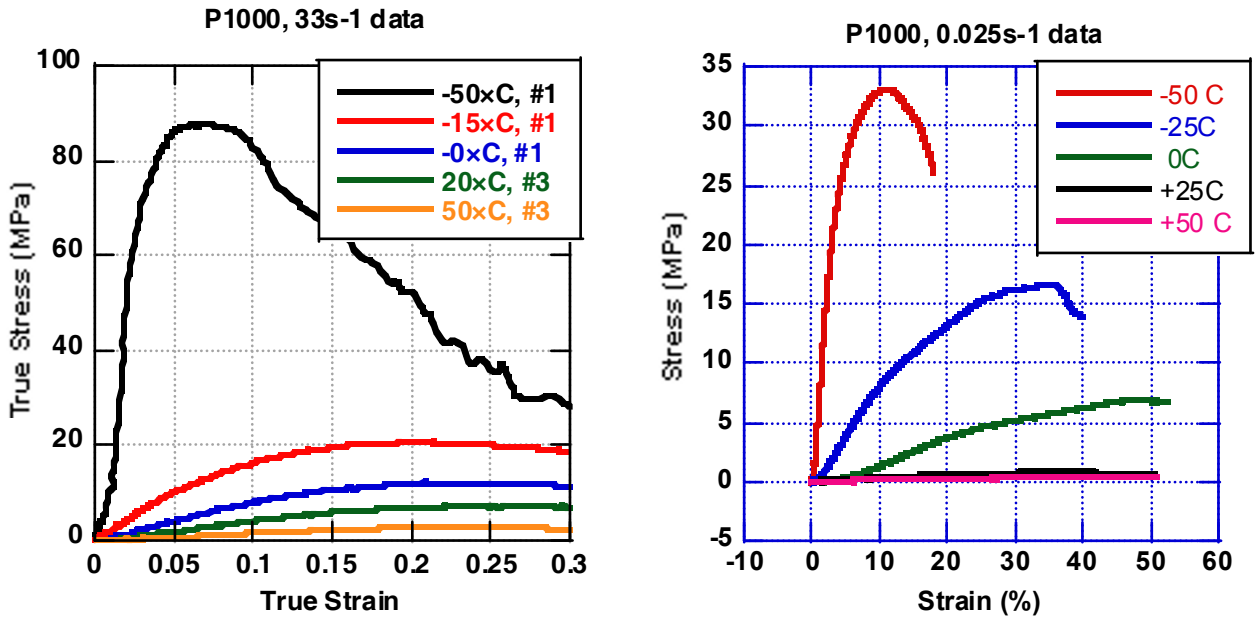


Figure 4. Quasi-static compression data for P1000 over the full temperature range.

DMA results are shown in the left panel of Figure 5. Samples were tested in compression disk platen fixtures at 1 Hz and 10 Hz with 5 micron amplitude setpoint and 0.2 N static applied force. A value of 0.44 was assumed for Poisson's ratio for calculations. In practice, the stiffness of the samples at low temperatures exceeded the instrument measurement capability. Samples were therefore ramped down in temperature from 50°C at a rate of 0.5°C/min until the instrument limit was reached. The right panel shows the thermal contraction during this cool down as measured in the DMA. The 2 mm and 4 mm thick samples behave similarly while the 3 mm samples exhibited somewhat different behavior. We examined all sheets of material with differential scanning calorimetry (data not shown) but did not observe any obvious compositional differences between the sheets.

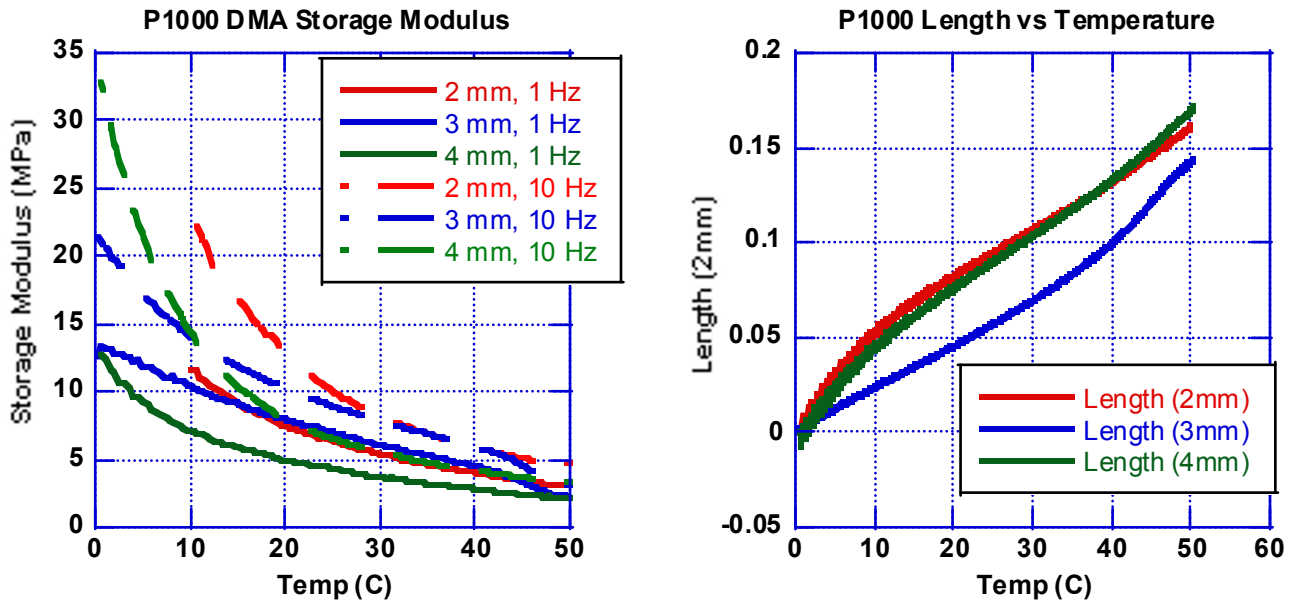


Figure 5. DMA results from P1000.

C-4 Results

The SHPB results for C-4 at the temperature endpoints of -50°C and 20°C are shown in Figure 6. Each plot has traces from three different tests illustrating the sample-to-sample variability. The variability is large for these hand pressed samples. Example plots at intermediate temperatures are shown in the right panel of Figure 7.

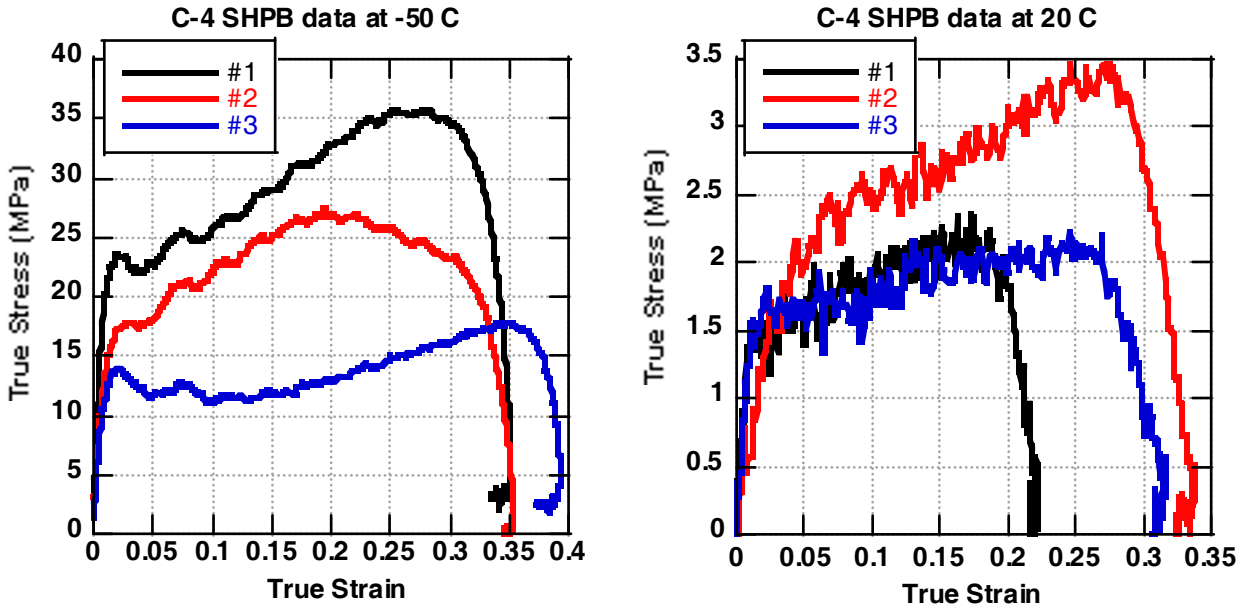


Figure 6. SHPB data from C-4 at -50°C and 50°C.

The equilibrium region of the C-4 SHPB data can be seen from “1-wave”-“2-wave” plots shown in the left panel of Figure 7 for the -50°C data set. For these soft samples, the equilibrium region is between around 1% and 3% strain. Example C-4 SHPB data for all temperatures is compiled in the right panel of Figure 7.

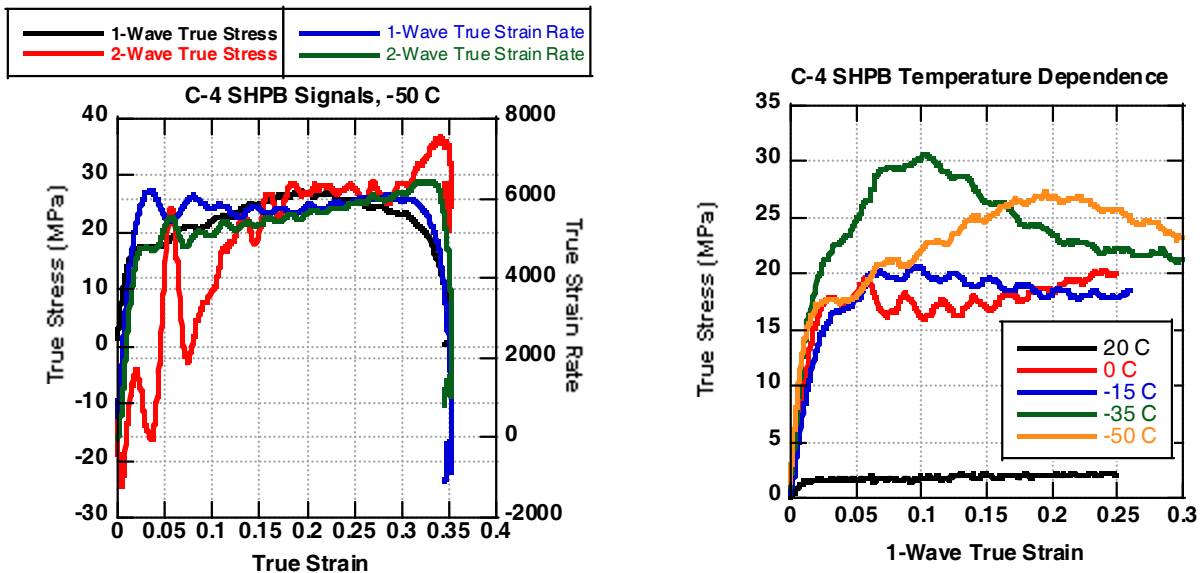


Figure 7. (left) SHPB stress and strains for one test on C-4 at -50°C. (right) Compilation of representative SHPB data for C-4 at all temperatures tested.

Quasi-static testing results for C-4 at all temperatures are shown in Figure 8. The load frame testing at the slowest strain rate is not shown but had similar characteristics to the curves in the left panel. The data in the right panel are constant force compression response plots acquired in the DMA instrument but without modulation. The softness of the material made it virtually impossible to sustain any appreciable stable modulation. Samples were compressed between the platens at rates of 0.8, 0.6, 0.4, 0.2, and 0.1 N/m from -50°C to 50°C. Variation of the ramp rate was necessary to maintain stable instrument control at each temperature. It was generally necessary to slow the ramp rate as the temperature was increased and the sample became softer. The first knee in the plots represents macroscopic failure of the pressed sample while the second upturn is the start of recompression of the material as the platens continue to move together.

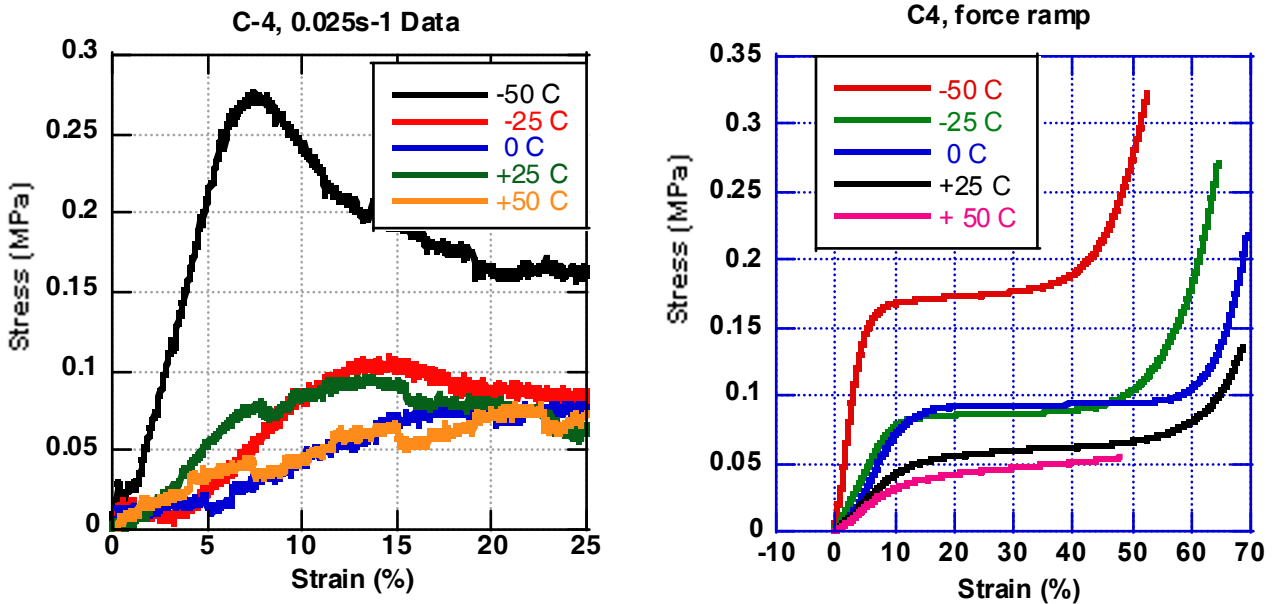


Figure 8. Quasi-static compression data for C-4 at -50°C and 50°C.

The maximum stress vs. temperature results for all constant strain rate tests are compiled in Figure 9.

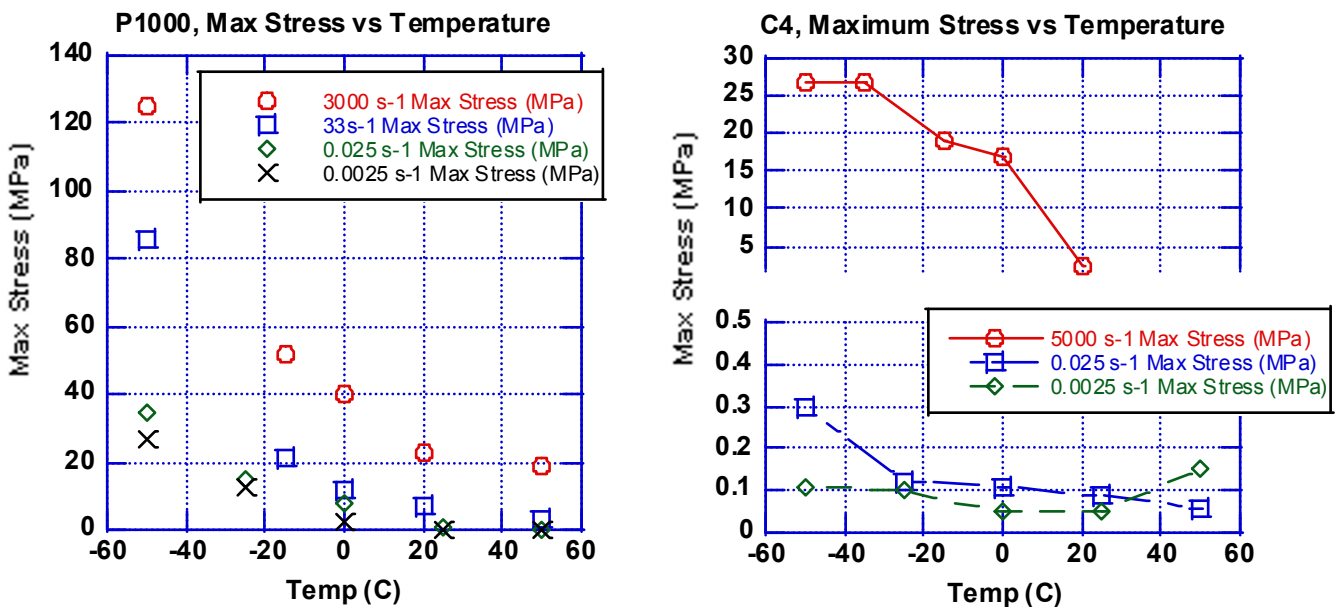


Figure 9. Maximum material stress for P1000 (left) and C-4 (right) as a function of temperature and strain rate for constant strain rate tests.

Acoustic Results

Table 1 shows the acoustic velocities measured for both materials. As with the thermal contraction results, the 3 mm thick P1000 samples were significantly different from the 2 mm and 4 mm samples and we have presented the two sets of results separately in the table. For all of the data in the table, the values are generally the average results of multiple measurements from at least three different samples. However, for the case of C-4 at 34°C, only the 0.9 mm thick samples provided data since the signal was too heavily attenuated in the thicker samples. In addition, for P1000 at 9°C and 23°C, the 2 mm samples were considered as part of the delay bar in order to calculate the shear wave velocities since the signal shape with any P1000 present was significantly different from the shape transmitted through the delay bar alone.

Table 1. Acoustic velocities measured for P1000 and C-4 materials.

Material	Temperature (C)	Thicknesses (mm)	V_L (km/sec)	V_S (km/sec)
P1000	9	2, 4	1.82	1.84
P1000	23	2, 4	1.71	1.68
P1000	34	2, 4	1.63	1.60
P1000	9	3	1.67	1.58
P1000	23	3	1.62	1.49
P1000	34	3	1.55	1.53
C-4	9	0.9, 1.8, 2.7	0.83	0.27
C-4	23	0.9, 1.8, 2.7	0.96	0.37
C-4	34	0.9	0.70	0.21

DISCUSSION

P1000

The dynamic and quasi-static test results for P1000 show changes in behavior over the temperature range examined. At -50°C and -25°C, the material is brittle and loads to failure in the SHPB and load frame tests. Above -25°C, however, there is indication of constant flow stress after the initial rapid loading followed by abrupt failure near 17% strain, regardless of temperature. In the load frame tests, above -25°C, abrupt failure is not observed and the sample is able to plastically deform over a large strain range. It is likely that the temperature dependence is due to a glass transition in the binder – the overall behavior is then what one would expect for a rubber material.

The 1 Hz and 10 Hz DMA storage moduli reflect the material's elastic response at low frequencies and small amplitudes. The peak strain rate during these tests is in the range of 0.0008s^{-1} to 0.008s^{-1} for 1Hz and 10 Hz tests, respectively. The maximum stress at these strain rates vs. temperature is also consistent with the data from the other testing methods plotted in Figure 9.

The thermal contraction differences provide the clearest indication that the 3 mm thick P1000 material differs from the 2 mm and 4 mm thick materials. In the absence of obvious compositional differences, the 3 mm thick P1000 samples may have a binder material with the same chemical composition but slightly different polymeric properties, such as molecular weight or cross-link density. This would also be consistent with the lower storage modulus of the 3 mm thick samples at lower temperatures – if they have a lower glass transition temperature, they will appear softer as the testing temperature drops nearer to the glass transition of the 2 mm and 4 mm samples.

C-4

The C-4 data are less straightforward to interpret because of the large amount of variability in the replicate tests. This is likely due to the variability inherent in hand forming these moldable materials. It does illustrate the possible range of response that may be encountered in tests made from materials that are very soft and easily deform during the handling necessary for mounting in the instruments. The data are also relevant to applications in which the prefabricated blocks must be deformed to match a specific shape.

In general the C-4 SHPB data shows rapid loading and ranges of constant flow stress at some temperatures before relatively abrupt failure. The load frame data shows similar results although the variability in the temperature dependent results above -50°C is large. The variability is less in the DMA compression data, which shows a decreasing elastic modulus with temperature and failure at around 10% strain.

An interesting observation is the point at which the temperature dependence has its largest change in the various tests. For the SHPB data, this occurs when going from 0°C to 20°C . For the load frame and DMA tests this occurs when going from -50°C to -25°C .

Acoustic Results

The acoustic velocities for P1000 are similar to what would be expected for other medium-soft rubber materials such as neoprene (typically 1.6 km/s). They are slightly higher due to the increase in density from the addition of PETN (1.77 g/cm³ compared to 1.23 g/cm³ for neoprene for example). The lower velocities in the 3 mm thick samples would indicate that they are slightly softer materials, consistent with the storage modulus results from DMA. The acoustic velocities of the C-4 samples likely reflect the low density and sample-to-sample variation resulting from hand pressing the parts.

REFERENCES

- [1] Todd, S.N., Vogler, T.J., Caipen, T.L., and Grady, D.E., "Non-shock initiation model for plastic bonded explosive PBXN-5: Theoretical Results", *Shock Compression of Condensed Matter – 2007*, CP955, pp. 1006 – 1009, 2007.
- [2] Brown, G.W., Tencate, J.A., DeLuca, R., Rae, P.J., Todd, S.N., "Dynamic and Quasi-static Measurements of PBXN-5 and Comp-B Explosives", *Society for Experimental Mechanics – 2009 SEM Annual Conference Proceedings*, Vol 2, pp. 731-738, 2009.
- [3] Gray III, G.T., and Blumenthal, W.R. "Split-Hopkinson pressure bar testing of soft materials", *ASM Handbook, Volume 8 – Mechanical Testing and Evaluation*, ASM International, pp. 488 – 496, 2000.
- [4] Gray III, G.T., Idar, D.J., Blumenthal, W.R., Cady, C.M., and Peterson, P.D., "High-and-low strain rate compression of several energetic material composites as a function of strain rate and temperature", *11th International Detonation Symposium*, 1998.

Dynamic Characterization of Mock Explosive Material Using Reverse Taylor Impact Experiments

*Louis Ferranti, Jr., Franco J. Gagliardi, Bruce J. Cunningham and Kevin S. Vandersall

*Engineering Technologies Division, Materials Engineering Group
Physical and Life Sciences Directorate, Chemical Sciences Division, Energetic Materials
Program Element

Lawrence Livermore National Laboratory
7000 East Avenue, Livermore, CA 94550
ferranti@llnl.gov

ABSTRACT

The motivation for the current study is to evaluate the dynamic loading response of an inert mock explosive material used to replicate the physical and mechanical properties of LX-17-1 and PBX 9502 insensitive high explosives. The evaluation of dynamic material parameters is needed for predicting the deformation behavior including the onset of failure and intensity of fragmentation resulting from high velocity impact events. These parameters are necessary for developing and validating physically based material constitutive models that will characterize the safety and performance of energetic materials.

The preliminary study uses a reverse Taylor impact configuration that was designed to measure the dynamic behavior of the explosive mock up to and including associated fragmentation. A stationary rod-shaped specimen was impacted using a compressed-gas gun by accelerating a rigid steel anvil attached to a sabot. The impact test employed high-speed imaging and velocity interferometry diagnostics for capturing the transient deformation of the sample at discrete times. Once established as a viable experimental technique with mock explosives, future studies will examine the dynamic response of insensitive high explosives and propellants.

INTRODUCTION

The safety and performance characteristics of insensitive high explosive and propellants are desirable for developing and validating computational models. Therefore, a systematic method for evaluating dynamic material parameters is needed for predicting the deformation behavior including the onset of failure and intensity of fragmentation resulting from impacts. Damage as a result of a sufficient insult alters the material's combustion response. This may range from a mild deflagration reaction to a violent explosion. The characterization of cumulative material damage and the threshold of these reaction extremes are needed for predicting energetic materials response to a variety of insults. These may include low-level insults, such as accidental handling impacts to more intense bullet and fragment impacts. A quantitative method for characterizing the damage evolution of explosive and propellant materials is necessary for constructing and validating physically based material models that predict fracture initiation and intensity of fragmentation.

The Taylor test [1] has become a customary method for developing and evaluating the constitutive behavior of materials. The average dynamic yield strength of a material is estimated as the consequence of an impact and based on the overall deformation imparted to the test specimen. The traditional experiment is performed with a rod-shaped specimen of a length, L_0 colliding against a rigid anvil at a velocity, U and making post impact measurements of the deformed shape. However, modified versions of Taylor impact experiments have been conducted in conjunction with velocity interferometry techniques to measure the material's response throughout dynamic loading up to and including fragmentation [2]. Taylor's original theory assumed an ideally rigid-plastic material model that exhibits rate-independent behavior and simple one-dimensional wave propagation concepts that neglect radial inertia. Upon impact, an elastic compression wave propagates through the axial length of the

rod followed by a much slower plastic wave. The deformed region propagates away from the contact surface, and the stress in this region is assumed to be constant and equal to the average yield stress of the material at a constant strain rate. The elastic wave continues to propagate the length of the specimen until it is reflected from the rear free surface and returns toward the propagating plastic wave. Upon reflection, the elastic wave interacts with the plastic wave and reduces the stress within the region to zero, thus bringing the deformation process to a conclusion.

Taylor's analysis was based on the behavior of metallic materials and neglects the minor elastic strains from a predominantly rigid-plastic material response. However, many energetic materials such as polymer bonded explosives (PBX) and propellants exhibit significant elastic strains prior to yielding. Energetic materials also behave non-linearly and are moderately dependent on both strain rate and temperature [3]. Additionally, PBX's contain an energetic component combined with a small quantity of a polymeric binder, generally 5-20 % by weight [4]. The addition of polymeric binder provides several potential advantages for the processing, performance and safety of PBX materials. These include making energetic materials mechanically rigid with better dimensional control and tolerance, improved pressing densities, the ability to machine complex geometries, and less sensitivity to accidental detonations such as a sudden shock.

Modified Taylor impact experiments have been successfully used to study the deformation behavior of polymer-bonded materials containing relatively hard inclusions [2]. Hutchings used a one-dimensional elastic/plastic wave propagation analysis and modified Taylor's rigid-plastic theory to account for the significant elastic strains encountered by polymeric materials prior to yielding [5]. Theories for the deformation of metallic materials predict some plastic deformation in the specimen at any finite, nonzero impact velocity. In contrast, Hutchings analysis accounts for an experimentally measured critical impact velocity where polymeric materials exhibit permanent deformation. Above this critical velocity, the change in specimen length increases as a function of impact velocity. The average dynamic yield stress can be calculated with knowledge of the specimen's length following impact and the critical velocity below which no plastic deformation occurs.

A complementary version of the Taylor test uses a reverse configuration where the specimen of interest is held stationary and a rigid anvil impacts the specimen at a high-velocity [2]. This configuration makes it possible to probe the specimen's free surface for obtaining a velocity-time signal to characterize the elastic wave behavior throughout the experiment. Furthermore, combining this analysis with transient deformation measurements using high-speed photography techniques provides a method for developing and validating constitutive models at discrete times throughout the deformation process.

In the present study, dynamic impact experiments were performed on mock explosive material using a reverse Taylor impact configuration. The mock explosive is an inert formulation used to replicate the density, mechanical and thermal properties of LX-17-1 and PBX 9502 insensitive high explosives [6]. The use of a mock explosive is advantageous, from a safety standpoint, for conducting initial experimental studies where specimen preparation techniques, experimental methods and design are still being developed. It is also of interest to characterize and eventually compare the mock explosive response with the actual explosive material. This work provides initial insight into the dynamic behavior of this class of materials.

The response of this material to dynamic loading was completely unknown and the mechanical behavior was characterized using a combination of diagnostics that include high-speed photography, to capture the transient deformation of the specimen, and photonic Doppler velocimetry (PDV), to measure the free surface velocity [7]. Digital image correlation (DIC) techniques [8] were also utilized for characterizing the mock explosive's response to an impact. The elastic wave speeds obtained from the DIC diagnostics were measured and compared to those obtained from the arrival of the wave at the free surface indicated from PDV. Insight into the critical fracture velocity for the mock was additionally revealed.

EXPERIMENTAL DETAILS

Reverse Taylor impact experiments were conducted on mock explosive specimens over an approximate 6-70 m/s impact velocity range. The specimens had a cylindrical geometry with a nominal diameter of 6.35 mm and 25.40 mm length. The experimental setup is shown schematically in [Figure 1](#). For this configuration, the specimen of interest was held stationary while a rigid anvil plate, mounted on the face of a polycarbonate sabot, was fired from a compressed-gas gun and collided with the specimen. The transient deformation of the specimen was observed throughout the entire deformation process up to the point of fragmentation using high-speed digital photography and PDV. Information regarding the experimental design and execution are described in the following section.

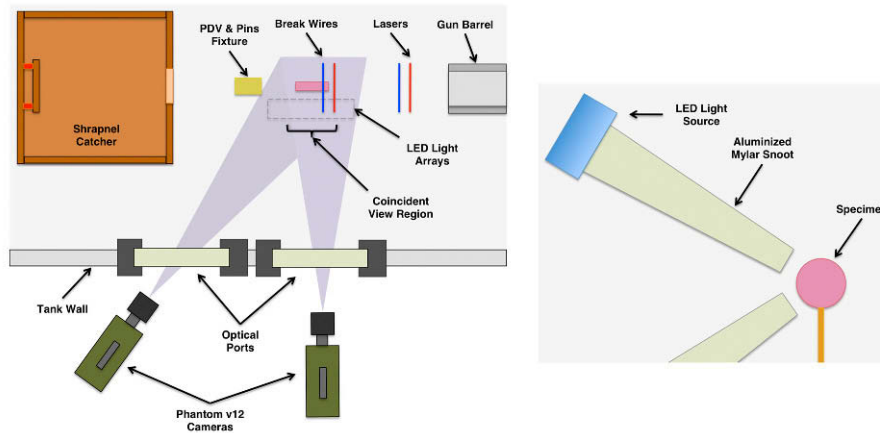


Figure 1. Top view schematic diagram of the reverse Taylor impact experiment (*left*) showing the cameras' orientations with respect to the specimen. The LED lighting system is also shown schematically in a vertical downrange orientation (*right*). Note both diagrams are not to scale.

EXPERIMENTAL SETUP

Reverse Taylor impact experiments were conducted using a newly acquired portable single-stage light compressed-gas gun (DEMII gun) that has three 1.8 m long interchangeable barrels with 25.4, 50.8 and 76.2 mm diameters [9]. The gun was operated within a large enclosed firing tank with a 5 kg explosive limit (TNT equivalent). An existing 100 mm diameter propellant-driven gun, in use mainly for studies on initiation and detonation of high explosives, operates over a velocity range (0.3-2.5 km/s) that exceeds the lower regime required for the reverse Taylor impact experiments. The 100 mm gun barrel was removed and the DEMII gun was placed in the firing tank for these experiments. Although the current work studies the dynamic response of an inert mock explosive, future experiments will be performed on energetic explosives and propellants in this firing tank.

The DEMII gun uses a simple ball valve breech design that incorporates an expendable shear pin with a gas actuator. The breech includes a 2 L accumulator volume with a 2.1 MPa maximum operation pressure that is sufficient for the approximate 10-100 m/s desired velocity regime. The 50.8 mm diameter barrel was used for these particular experiments and the gun was fired using dry air.

A shrapnel catcher was fabricated from two thick steel plates (25.4 mm) secured on either side of a steel pipe with an approximate diameter and length of 91.4 and 96.5 cm, respectively. The front of the shrapnel catcher, pictured in Figure 2, had a 17.8 cm hole that allowed the sabot and specimen debris to pass through the outer plate. A steel deflecting plate (30.5 cm square and 25.4 mm thick) was secured inside the vessel at the back with four heavy-duty springs. The plate was slightly angled for deflecting the debris downwards and bringing the materials to rest in the sand located at the bottom of the vessel.

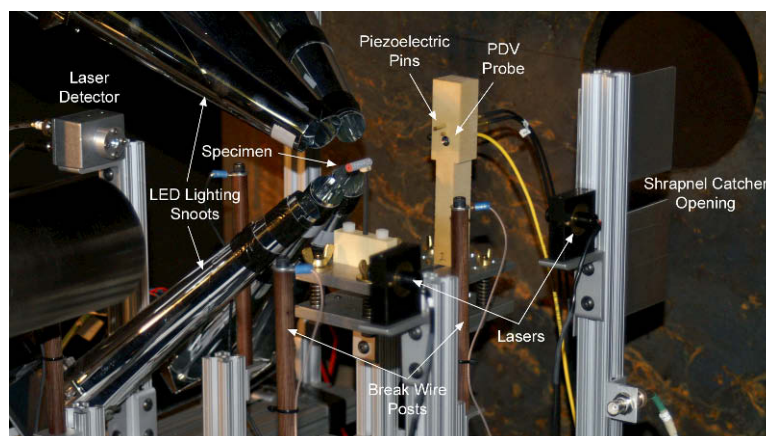


Figure 2. Image of the experimental setup featuring the specimen and associated diagnostics.

The sabot body was approximately 50.8 mm in diameter and made from polycarbonate. A steel anvil made from AISI 4140 steel (hardened to R_C 54-55) was attached to the front. The anvil was 10 mm thick with a slightly undersized diameter compared to that of the sabot. The back of the sabot had a medium density polyethylene obturator to form a tight seal with the barrel and two Viton[®] o-rings placed along the length. The complete assembly has a mass of approximately 500 g each and is shown in [Figure 3](#).



Figure 3. Image of the 50.8 mm diameter polycarbonate sabot assembly showing the AISI 4140 hardened steel anvil, polyethylene obturator and Viton[®] o-rings.

Since these experiments were the first use of the new gun, several redundant velocity-measuring techniques were utilized to obtain a precise impact velocity. The first technique used a laser-interrupt detection design with two laser/detector stations mounted down range from the gun muzzle. The system recorded the time interval between the two stations for computing the velocity. The laser/detector station closest to the specimen impact face (approximately 5 mm) was also used for triggering all of the diagnostics. The second method used a series of fine tungsten break wires (25.4 μm diameter) placed in the path of the sabot such that the wire breaks when contacted at the bottom edge of the anvil plate (approximately 5 mm). The break wires operated in a similar manner as the laser-interrupt system in that the distance between the two wires was measured and the arrival times of the sabot were detected for computing the velocity. The final technique used two piezoelectric crush pins with the impact faces offset approximately 10 mm and the arrival of the anvil at each provided a timed signal for computing the velocity. The piezoelectric pins were located behind the specimen and measured the velocity following the sabot's interaction with the target.

Two Vision Research[®] Phantom v12 high-speed digital cameras were used for the DIC measurements. The cameras were located outside the explosive firing tank and viewed the axial length of the specimen through two separate windows (3.81 cm thick quartz glass). The specimen was located in the center of the firing tank, which has an inside diameter of approximately 3.5 m. The camera's fields of view were approximately 32 by 16 mm and the cameras were fit with Nikon[®] 80-200 mm zoom lenses with Tamron[®] 2x teleconverters for imaging the specimen from a distance of approximately 2 m. The framing rate was approximately 120,000 fps (or 8.32 μs interframe time) with a 7.75 μs exposure time and the corresponding best available resolution of 256 x 128 pixel images.

The amount of light required for imaging the transient deformation of the specimen is related to the image acquisition rate. The DIC system additionally requires highly uniform light intensity over the entire surface to be measured. For these experiments, a total of six low voltage Lamina Titan[®] LED light sources were used to illuminate the specimen. Each light source is populated with multiple LED's to deliver approximately 1800 lumens of light. The light was focused on the specimen using reflective snoots, shown in [Figure 2](#), made from rolling aluminized mylar sheets. The ends of the snoots were positioned approximately 10 mm from the specimen, while the LED light sources were located approximately 40 cm from the specimen. This provided sufficient light to image the specimen and sufficient standoff distance to protect the lights from specimen fragmentation debris.

An adjustable three-point mounting fixture was used to secure the specimen perpendicular to the barrel, ensuring an impact normal to the anvil. A laser located at the up-range end of the barrel was focused toward the down-range direction through an optical collimator onto a small mirror placed on the impact face of the specimen. The three-point fixture was used to adjust the specimen's orientation and, once the laser reflected off of the mirror and projected a spot through the center of the barrel, the fixture was securely fastened.

SPECIMEN PREPARATION

The mock explosive material (RM-03-AG) was prepared from a mixture of 45 wt.% cyanuric acid, 44.5 wt.% magnesium silicate, and 10.5 wt.% PIBBMA binder, a copolymer of isobutyl and butyl methacrylate. The mock constituents were combined and isostatically pressed at approximately 138 MPa and 105 °C for three cycles of one minute each. The final mock explosive billet had a cylindrical geometry with approximately 24.1 cm diameter and 16.5 cm tall. Additional details regarding the development of mock explosive materials are available elsewhere [10].

Several right-circular cylindrical specimens with a nominal aspect ratio (L/D) of four-to-one were machined from the bulk billet of material. The specimens were measured at several locations and had an average length, L and diameter, D of 25.401 ± 0.001 mm and 6.342 ± 0.034 mm, respectively. The average density measured from eight specimens was 1.887 ± 0.020 g/cm³ and corresponded to 97.2 %TMD.

Each specimen was hand lapped using a lightly weighted fixture in preparation for the impact experiments. Lapping was conducted in two stages, first using 15 μ m and then 1 μ m silicon carbide sandpaper. The sandpaper was placed on a flat piece of glass and the specimens were lapped using a figure eight motion until the impact and rear surfaces were both parallel and planer to each other. The specimens were checked regularly during the lapping process until the desired overall length and surface finish was achieved. An aluminum reflector of approximately 5 mm diameter and 12.7 μ m thick was attached to the rear surface of the specimen using RTV silicon adhesive (Dow Corning®). The laser light from a PDV probe was reflected from the surface and used to measure the free surface velocity during the impact experiment.

The specimens were prepared with speckle pattern for DIC measurements. A thin layer of flat white Rust-Oleum® paint was applied to the radial surface of each specimen. The front and back surfaces of the rod-shaped specimens were masked with tape to prevent paint from adhering to these surfaces. After the white paint was allowed to dry, a flat black Rust-Oleum® paint was applied with a misting technique to form the fine black speckle pattern. An example of the final speckle pattern applied to each specimen is shown in [Figure 4](#).

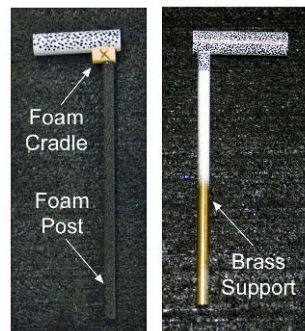


Figure 4. Examples of reverse Taylor specimens shown with a foam support assembly (*left*) and brass rod (*right*). Both support systems were attached approximately 1 mm from the free surface using a small amount of epoxy.

Two methods were used to secure the specimen and hold it aligned to the muzzle end of the barrel. Both attempt to hold the specimen adequately for handling and positioning purposes, but were designed to break away and provide the least amount of resistance during the impact experiment. The first assembly used a light foam cradle that had the same radius of curvature as the specimen and was secured to an upright foam post as shown in [Figure 4](#). The foam support was observed to deflect significantly during the experiment and was replaced in later experiments with a rigid brass rod. The rod had a 3.2 mm diameter that was machined at one end with the same radius of curvature as the specimen. [Figure 4](#) also shows an example of the specimen attached with a brass support rod. The foam cradle assembly and the brass rod were each located towards the rear surface of the specimen, approximately 1 mm from the edge and secured with a small amount of epoxy.

RESULTS AND DISCUSSION

Reverse Taylor impact experiments were performed on a mock explosive material at several impact velocities listed in [Table 1](#). The experiments were performed in a light vacuum level of less than 20 torr to eliminate the

possibility of an air blast interacting with the specimen before the anvil arrived. A total of seven experiments were completed for measuring the transient deformation and calculating the elastic wave speed of the material. In each experiment, great care was given to aligning the impact face of the specimen with the rigid anvil exiting the compressed-gas gun barrel using a laser alignment system. An indication of good alignment was observed from high-speed camera images acquired for each experiment. The planarity of impact was additionally measured, from an independent experiment with no target specimen in place, using a circular array of eleven piezoelectric contact pins. The array was aligned to the anvil in the same manner as the specimen using the laser alignment system. The planarity of impact had a measured tilt of 3.1 mrad and is expected to be similar for each reverse Taylor test conducted in this work.

Table 1 Summary of reverse Taylor impact experiments conducted for mock explosive material at several different impact velocities. Specimens fractured for shot numbers RT-001, RT-002, and Q-003.

Shot Number	Impact Velocity U [m/s]	Elastic Wave Velocity C_L [mm/ μ s]		*Free Surface Velocity U_{fs} [m/s]	
		PDV	DIC	PDV	DIC
RT-003	5.12	1.99	2.11	6.04 (11.16)	5.91 (9.91)
Q-001	8.83	2.09	1.95	15.46 (16.54)	14.53
RT-004	10.37	n/a	1.90	17.58 (20.49)	17.35
RT-005	10.83	2.00	2.05	18.89 (21.12)	18.59 (19.69)
RT-001	33.04	2.07	1.94	30.63 (36.10)	29.48
RT-002	47.94	n/a	1.86	n/a	25.79
Q-003	72.56	n/a	n/a	n/a	22.19 (60.71)

*Measured terminal velocities with peak free surface velocities shown in brackets.

The mock explosive had a highly brittle response to dynamic loading. This was expected since quasi-static measurements have shown similar behaviors for flexural three-point bend fracture toughness tests [11]. The specimens were observed to fracture for impact velocities of 33.04, 47.94, and 72.56 m/s corresponding to shots RT-001, RT-002, and Q-003, respectively. Selected images from experiment Q-003 are shown in [Figure 5](#). Fracture initiation was observed 21.64 and 13.08 μ s following impact for experiments RT-002 and Q-003, respectively. Both showed a typical double-frustum shape at the impact face [12]. However, experiment RT-001 exhibited a different behavior with essentially no radial deformation close to the impact face. This particular specimen fractured approximately 10 mm from the impact face at 31.18 μ s following impact. It does not appear that the fracture was initiated as a result of the impact (33.04 m/s), but rather the foam specimen support deflected significantly during the experiment. The deflection caused a bending moment on the specimen that was constrained at the impact face by the anvil. This was clearly observed from the high-speed camera images. Therefore, the actual critical fracture initiation velocity falls approximately between 33.04 and 47.94 m/s. The support deflection was also observed for shots RT-002 and Q-003, the latter illustrated in [Figure 5](#). However in both of these cases the specimen began to fracture at the impact face prior to appreciable deflection of the support and does not appear to influence the overall response of the mock. Axial and areal strain measurements quantify these observed differences in deformation behavior.

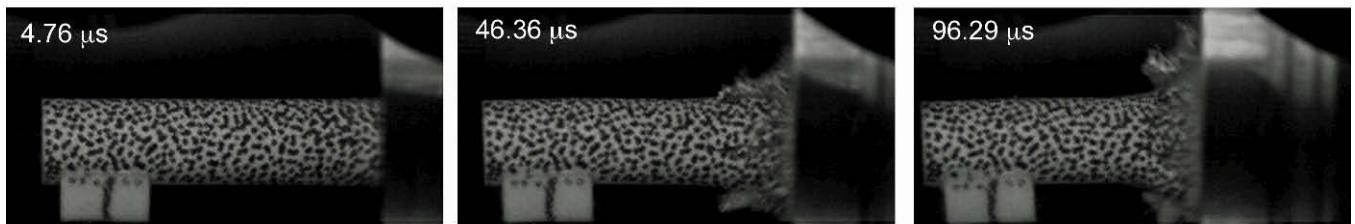


Figure 5. Select images from a reverse Taylor test showing the anvil impacting the specimen from the right at 72.56 m/s (shot Q-003). Images were taken (left to right) at 4.76, 46.36 and 96.29 μ s following impact. The specimen begins to fracture almost immediately at approximately 13.08 μ s.

Axial strain was calculated using $\varepsilon_L = \ln(L_0/L)$, where L_0 and L are the initial and incremental specimen lengths, respectively. Similarly, areal strain was calculated using $\varepsilon_A = 1 - (A_0/A)$, where A_0 and A are the initial and incremental cross sectional areas of the specimen, respectively. Areal strain measurements were taken at the impact face where the maximum deformation was typically observed. Shots RT-002 and Q-003 had areal strains measured at the moment of fracture and corresponded to 21.9 and 19.4 %, respectively. These represent the approximate maximum strain that the material could support before failure. However, shot RT-001 had a significantly lower areal strain of 5.7 %, thus indicating that the specimen did not have the characteristic deformation localized to the impact face of the specimen. All of these specimens had relatively small axial strains of 1.5, 1.0 and 3.1 % for RT-001, RT-002 and Q-003, respectively.

Specimens that were impacted at the lower velocities did not fracture and were observed to rebound from the anvil surface. These specimens were additionally recovered following the experiment and physically measured. All the specimens completely recovered elastically and had unchanged dimensions. The measured axial strains obtained during the experiment from high-speed camera images were typically less than 1%, while the specimens' diameters were unchanged.

The free surface velocity, U_{fs} was measured using PDV for each experiment. The PDV system detects a peak velocity rise once the elastic wave reaches the free surface of the specimen. For a purely elastic collision, the free surface velocity is expected to be twice that of the impact velocity. However, energy was typically consumed by the specimen deformation (elastically in this case) and breaking away from the support. Other energy dissipation mechanisms may also contribute, such as friction between the impact surfaces. The measured free surface velocities for specimens that did not fracture had an average coefficient of restitution of 0.70 ± 0.04 . The coefficient of restitution, C_R is a fractional value that represents the ratio of velocities following an impact. A perfectly elastic collision has a $C_R = 1$, while a $C_R = 0$ represents a perfectly inelastic collision where the two objects “stick” together. Impact experiments with velocities that resulted in the specimen fracturing had a C_R of less than zero, which indicated the anvil and specimen move closer together rather than bouncing apart during the impact. The computed C_R for shots RT-001, RT-002 and Q-003 with increasing impact velocities were - 0.08, - 0.48 and - 0.69, respectively. Thus indicating the C_R became more negative as the impact velocity increased.

The average velocity of the specimen following impact was also determined using DIC measurements. These are consistent with the free surface velocity measurements obtained from PDV. [Figure 6](#) compares the PDV and DIC velocities for two representative experiments with impact velocities of 5.12 and 10.37 m/s (shots RT-003 and RT-004, respectively). The figure shows that PDV has a significantly better response time and captured a much quicker rise to peak velocity for both experiments. This was typically observed for all the experiments performed in this study. Notice that the initial peak value for shot RT-003 was slightly greater from the PDV measure, but both measurements decay at the same rate to a similar terminal velocity of 5.91 and 6.04 m/s for the DIC and PDV curves, respectively. The PDV curve also exhibits a high frequency attenuation that was attributed to aliasing rather than a physical response of the material. The overall measured peak free surface and terminal velocity values from both types of measurements compare well and are listed in [Table 1](#).

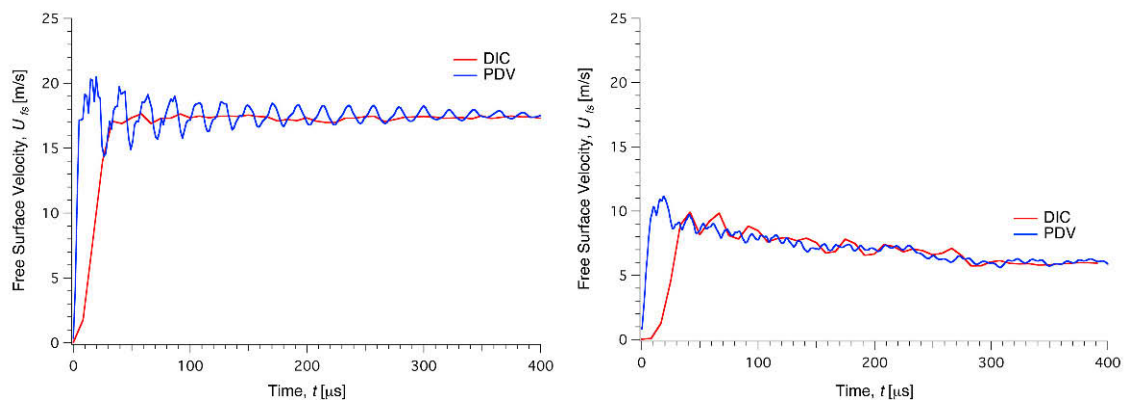


Figure 6. Comparison of PDV and DIC free surface velocity measurements for two experiments (shots RT-004 and RT-003, respectively) with impact velocities of 10.37 m/s (*left*) and 5.12 m/s (*right*).

The arrival of the wave at the free surface also permits the calculation of the elastic wave velocity. Knowing the impact time and the specimen length, the elastic wave velocity was computed for each experiment. These

values are also listed in Table 1. The average elastic wave velocity can also be obtained from the DIC measurements as depicted in Figure 7 for shot RT-003. The anvil was just out of sight, to the right of the image and moving at a velocity of 5.12 m/s. The color contour scale range was 0.01 to -0.02 mm of displacement, U . Each image was at the same scale and the negative displacement direction was to the left. The first image shows the displacement contour just following impact at 2.08 μs . Most of the specimen was within the middle range of the scale, which indicates zero displacement. The next image taken at 10.40 μs following impact shows the elastic wave moving towards the free surface. The front of the wave at this point was approximately 3.5 mm from the back surface. The color contour indicates that the free surface has not yet moved. The image shows the front of the wave was fairly dispersed and possibly reflects the resolution limits of the measurement. The next image taken at 18.72 μs indicates the entire specimen was moving at this point. The DIC measured elastic wave velocity was 2.11 mm/ μs and compares fairly well with 1.99 mm/ μs obtained from the PDV measurement. The average elastic wave velocity obtained from six experiments using DIC was 1.97 ± 0.09 mm/ μs and was not calculated for shot Q-003 due to a problem with the trigger timing that prevented the determination of the impact time. The average elastic wave velocity using PDV was 2.04 ± 0.05 mm/ μs . This value was obtained from only five experiments due to triggering problems for shots Q-003 and RT-002, which missed the arrival of the elastic wave at the free surface.

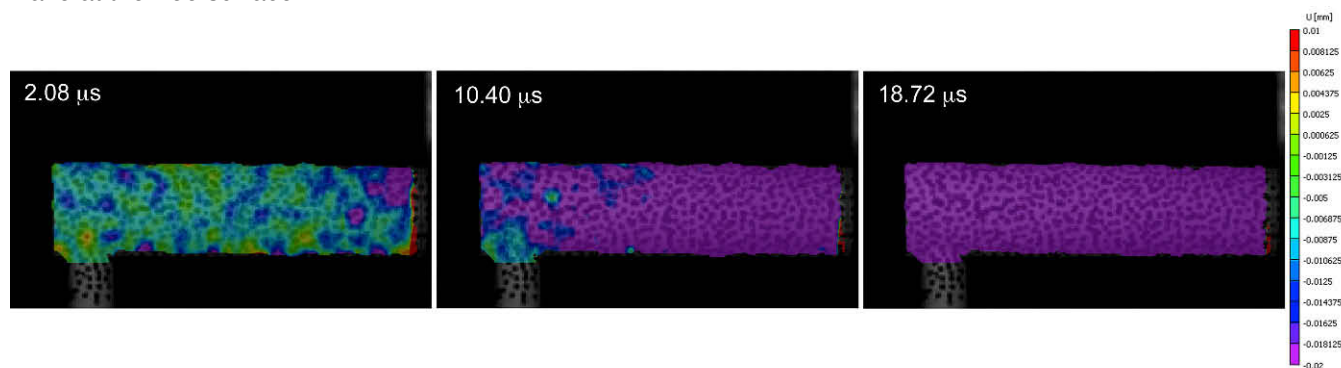


Figure 7. Select images from a reverse Taylor test showing the elastic wave propagating from right to left within the specimen using DIC calculated displacements, U . The anvil impacts the specimen from the right side and is moving at a velocity of 5.12 m/s (shot RT-003). The images were taken (left to right) at 2.08, 10.40, and 18.73 μs following impact. The middle image shows the elastic wave reaching approximately 3.5 mm from the free surface.

Ultrasonic elastic wave velocities were independently measured from an 8.76 mm thick rectangular plate obtained from the same batch of material used in the impact experiments. The measured ultrasonic velocity or bulk sound speed, C_0 was 2.92 ± 0.04 mm/ μs . The elastic wave travels at a slightly higher velocity through an unbounded medium than through a thin bar or rod [13]. The bulk sound speed was adjusted to account for this using elastic relations and an estimated Poisson's ratio of 0.420, to give $C_0 = 1.60 C_L$. After correction, the ultrasonic elastic wave velocity was 1.83 ± 0.04 mm/ μs and compares fairly well with the DIC and PDV measured values. Some uncertainty in determining the precise moment of impact could account for the slightly greater elastic wave speeds obtained in this study. The other possible cause could be that Poisson's ratio was slightly too high for the mock explosive. This value was experimentally determined for the insensitive explosive LX-17 [14]. A slightly lower value of 0.400 fits the mock explosive material better and corresponds to an elastic wave velocity of 1.99 mm/ μs .

SUMMARY AND CONCLUSION

This paper reports on the details regarding reverse Taylor impact experiments conducted for a mock explosive material. The motivation comes from the need for a quantitative method to measure the fracture and fragmentation behavior of explosives and other energetic materials. In doing so, it is important to measure the transient deformation state of the material up to and including its associated mechanical breakup. Once established, this capability will provide a method for developing and validating constitutive material models at discrete times throughout the entire deformation process.

The mock explosive has shown a highly brittle response to dynamic loading above a critical impact velocity. In contrast, sufficiently low impact velocities have also shown a viscoelastic material response that exhibited a small axial strain of less than 1 % and virtually no radial deformation. Experiments conducted at impact velocities of 33.04, 47.94 and 72.56 m/s have resulted in fracturing. The two highest velocity experiments showed the characteristic double-frustum deformation geometry before fracture initiation. However, the lowest velocity experiment exhibited a different response to loading with essentially no radial deformation upon impact. High-speed camera images show the specimen fracturing approximately 10 mm from the impact face due to a bending moment. A foam support assembly was used to hold the specimen aligned with the gun barrel. Upon impact, the support deflected and caused the specimen to fracture. Therefore, it is possible this is not the critical impact velocity for specimen fragmentation. Additional impact experiments over the approximate 33 to 48 m/s velocity range are planned to determine the actual critical velocity for the mock explosive material.

The first three experiments conducted in this study were at sufficient impact velocities to cause the specimen to fracture. All of the experiments used the foam support assembly where deflection was observed but did not influence the overall material response until the lowest velocity test (33.04 m/s) showed this contributed to the specimen prematurely fracturing. A rigid brass support rod was used for all subsequent experiments to remove this effect to dynamic loading. Following this modification to the experimental setup, the specimens were observed breaking cleanly away from the support at the epoxy joint and did not exhibit any noticeable deflection.

The reverse Taylor experimental configuration also provided useful data that was obtained from PDV and DIC diagnostics. Both techniques showed good agreement for measured free surface velocities of the specimen throughout the deformation process. However, PDV had a much faster response time to capture the specimen's acceleration than compared to the DIC measurements. This was evident by directly comparing free surface velocity-time plots for both techniques. The DIC measurements successfully captured the elastic wave propagating the length of the specimen and was used for computing the elastic wave speed of 1.97 ± 0.09 mm/ μ s. This value compared well with 2.04 ± 0.05 mm/ μ s obtained from the PDV measurements. Both techniques additionally compared fairly well with the ultrasonically measured elastic wave speed of 1.83 ± 0.04 mm/ μ s if Poisson's ratio of 0.420 is assumed.

Future reverse Taylor impact experiments will be designed for measuring the response of energetic materials to include explosives and propellants. Further refinement of this technique will permit the incremental measure of elastic/plastic transient deformation throughout the entire impact event, to characterize the elastic and plastic waves interactions within the specimen and measure mechanical properties for generating dynamic stress-strain response curves for energetic materials. Directly measuring the strain using DIC techniques is currently the largest challenge since significantly small deformations are taking place rapidly in a dynamic experiment. These effects require capturing the transient deformation of the specimen with high-speed cameras operating at significantly high framing rates and maximum resolution under ideal lighting conditions.

ACKNOWLEDGEMENTS

Many people have been essential for their technical support and assistance in this study. The authors would like to thank Randy Bonner, Tony Whitworth and Ted Strand for providing PDV support, Micha Gresshoff and Don Hoffman for their technical support working with Physics Application, Inc., John Scott, Adrian Godinez, Thomas Vi and Brian Cracchiola for HEAF facility support, Jan Batteux, Paul Chiao, Adriano Salamanca, Greg Silva and Jeff Wardell for mechanical support, Dan Greenwood for lighting design and camera operation, Frank Garcia for target design and assembly and the gas gun firing operations team James Jones, Rich Villafana and Jim Van Lewen. This work performed under the auspices of the U.S. Department of Energy by Lawrence Livermore National Laboratory under Contract DE-AC52-07NA27344.

REFERENCES

- [1] G.I. Taylor, "The Use of Flat-Ended Projectiles for Determining Dynamic Yield Stress: I Theoretical Considerations," *Proc. R. Soc. Lond. A*, **A194**, 289-299 (1948).
- [2] L. Ferranti, Jr. and N.N. Thadhani, "Dynamic Mechanical Behavior Characterization of Epoxy-Cast Al+Fe₂O₃ Thermite Mixture Composites," *Met. Trans. A*, **38A**, [11] 2697-2715 (2007).

- [3] W.R. Blumenthal, G.T. Gray III, D.J. Idar, M.D. Homes, P.D. Scott, C.M. Cady and D.D. Cannon, "Influences of Temperature and Strain Rate on the Mechanical Behavior of PBX 9502 and Kel-F 800," *Shock Compression of Condensed Matter* – 1999, Vol. 505, 671-674 (2000).
- [4] P.W. Cooper and S.R. Kurowski, Introduction to the Technology of Explosives; Wiley-VCH, New York (1996).
- [5] I.M. Hutchings, "Estimation of Yield Stress in Polymers at High Strain-Rates Using GI Taylor's Impact Technique," *J. Mech. Phys. Solids*, **26**, 289-301 (1979).
- [6] D.M. Hoffman, B.J. Cunningham and T.D. Tran, "Development of a Replacement Mock for the Insensitive High Explosives LX-17 and PBX 9502," LLNL Report, UCRL-JRNL-223040 (2006).
- [7] O.T. Strand, D.R. Goosman, C. Martinez, T.L. Whitworth, and W.W. Kuhlow, "A Novel System for High-Speed Velocimetry Using Heterodyne Techniques," *Rev. Sci. Instrum.*, **77**, 083108 (2006).
- [8] M.A. Sutton, J.J. Orteu and H.W. Schreier, Image Correlation for Shape, Motion and Deformation Measurements: Basic Concepts, Theory and Applications; Springer Press, New York (2009).
- [9] K.S. Vandersall, A. Behn, M. Gresshoff, L. Ferranti, Jr., and P.I. Chiao, "New Gun Capability With Interchangeable Barrels to Investigate Low Velocity Impact Regimes at the Lawrence Livermore National Laboratory High Explosives Application Facility," Proceedings of the 60th Aeroballistic Range Association, Baltimore, MD, September (2009).
- [10] D.M. Hoffman, B.J. Cunningham and T.D. Tran, "Development of a Replacement Mock for the Insensitive High Explosives LX-17 and PBX 9502," LLNL Report, UCRL-JRNL-223040 (2006).
- [11] L. Ferranti, Jr., F.J. Gagliardi, B.J. Cunningham and K.S. Vandersall, "Measure of Quasi-Static Toughness and Fracture Parameters for Mock Explosive and Insensitive High Explosive LX-17," Proceeding of the 14th International Detonation Symposium, Coeur d'Alene, Idaho 11-16 April (2010).
- [12] R. Balendra and F.W. Travis, "An Examination of the Double-Frustum Phenomenon in the Mushrooming of Cylindrical Projectiles Upon High-Speed Impact with a Rigid Anvil," *Int. J. Mech. Sci.*, **13**, 495-505 (1971).
- [13] M.A. Meyers, *Dynamic Behavior of Materials*; John Wiley & Sons, Inc., New York, 23-65 (1994).
- [14] B.J. Cunningham, F.J. Gagliardi, and L. Ferranti, Jr., "Low Strain Rate Measurements on Explosives Using DIC," SEM Annual Conference & Exposition on Experimental and Applied Mechanics, Indianapolis, Indiana 7-10 June (2010).

Mechanical Behavior of Hierarchically-structured Polymer Composites

A.L. Gershon and H. A. Bruck

Department of Mechanical Engineering, Univ. of Maryland, College Park, MD 20742

Abstract

As the engineering of hierarchically-structured polymer composites advances, so does the need for understanding the evolution of damage in these materials and their mechanical behavior. In natural systems, such as nacre, it is now well-understood that the damage accumulates across multiple length scales due to the nanoscale elastic biopolymers that bind together microscale aragonite crystals in a layered structure. The result is an extremely damage-tolerant microstructure that has a high hardness and fracture toughness. While it is difficult to duplicate this structure in synthetic polymer composites, it is still possible to alter mechanical behavior through structuring the material across multiple length scales. In this paper, the mechanical behavior of a hierarchically-structured polymer composite is studied by dispersing CNFs in a model epoxy system using sonication during solvent processing. A new nanomechanical characterization approach was used to characterize the multi-scale mechanical behavior in order to develop a model that was capable of determining the degree of dispersion and dispersion limit of CNFs that give rise to the hierarchical structure.

I. Introduction

With the current focus on nanotechnology and bio-inspired materials & systems, it is now possible to engineer materials at the smallest length scales using natural materials & systems for inspiration [1]. As a result, the development of advanced composite materials can now focus on the integration of various multi-scale ingredients in order to enhance the multifunctional behavior of the materials. However, one critical question involves the length scales and compositions at which the behavior of the composite material will transition to meet specific performance requirements. In nature, biological materials such as wood organize simple organic building blocks such as collagen molecules at various length scales (i.e., hierarchical-structures) to maximize the strength (MOR as high as 130 MPa), toughness (as high as 10 kJ), impact resistance (hammer drop heights of over 2 meters), and fatigue life (30 million cycles at 50% static strength) of these materials using the minimum amount of mass (ρ as low as 0.33 g/cc) [2]. Such a balance in properties has made wood a valuable structural material in marine applications, and it has proven difficult to achieve similar balances in polymer composites made from synthetic materials. Efforts to duplicate this behavior in synthetic materials has led to the use of nanoscale ingredients to create hierarchically-structured polymer composites, which have been characterized and modeled in polymers to determine transition length scales and compositions that will impact the development of processing-structure-property relationships in hierarchically-structured polymer composites (*Figure 1*) [3-6]:

These hierarchically-structured polymer composites are being developed for a variety of applications requiring lighter, more durable, blast resistant, and functional structures. Multi-layer structures consisting from carbon fiber-reinforced thermoplastics facing aramid fiber-reinforced thermoplastics are being used in new helmet designs for the Future Force Warrior (FFW) [7]. They are also being fabricated as fiber-reinforced composite sheets facing a foam core, reinforced with ductile polyurea layers that can stiffen under shock compression to protect the foam core from excessive crushing due to blast loading [8]. Advances in nanotechnology are enabling nanoparticles, such as nanoclay, to be added to phenolic foam cores in sandwich structures to enhance their mechanical behavior by controlling the cell size and distribution in the foam [9]. Similar improvement can be found by adding carbon nanotubes to fiber-reinforced polymer composites [10]. Therefore, it is anticipated that multifunctional structures consisting of hierarchically-structured polymer composites are of interest to support current large-scale initiatives in the development of protective structures for military vehicles and personnel.

In this paper, we investigate the mechanical behavior of hierarchically-structured polymer composites. In particular, we will be interested in characterizing and developing structure-property models. Three different model hierarchically-structured polymer composite systems are investigated: (1) an epoxy with CNFs, and (2) and a laminated polymer composite with a polymer interlayer enhanced with CNFs. Microtensile testing and nanoindentation are used to characterize the multi-scale mechanical behavior of (1), while three-point bend testing is used to characterize damage evolution of (2). Models of the damage evolution and mechanical behavior are then developed from the experimental data.

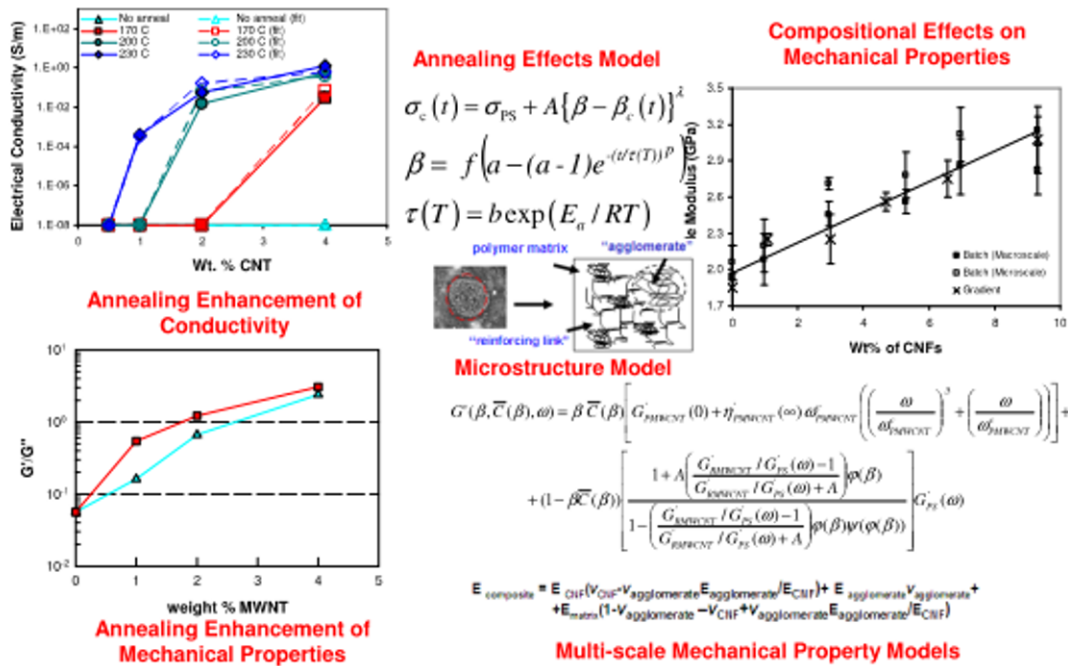


Figure 1. Transition length scales and compositions in nano-enhanced polymers [3-6].

2. Material Preparation

West System® 105 epoxy resin with 206 hardener was chosen as the matrix material due to its availability and ease of use. In order to create the nano-enhanced composite materials for tensile and compressive testing, the epoxy resin was thoroughly mixed with PR-19 grade Carbon Nanofibers (CNFs), with diameter 100200 nm, length 10-30 gm, and density 1.87 g/cm³, which were obtained from Applied Sciences — the same CNFs that were used as a nanoscale filler in the HIPS extrudate. Once thoroughly mixed, the resin-CNF mixture was placed in a VWR Aquasonic model 75D ultrasonic bath for 1.5 hours, 3 hours or 6 hours to help break up agglomerations of CNFs. The ultrasonic bath produced an average sonic power of 90 Watts, and a peak power of 180 Watts. A fourth set of composites was made with no sonication. After sonication, the resin-CNF mixture was placed in an ice bath to cool the mixture down to room temperature, which prolongs the useful working time after the hardener is added.

Once the resin-CNF mixture is at room temperature, West System 206 hardener was added in the ratio of 5:1 epoxy to hardener. Immediately after adding the hardener, the mixture was homogenized using a dual propeller mixing impeller. The mixing impeller was mounted on a drill press, and the epoxy, hardener and CNF mixture was mixed for 3 minutes. Mixtures containing CNFs were made with 1, 3, 5, 7 and 10 weight percent. After mixing, the nano-enhanced epoxy was degassed in a vacuum chamber at 560 mmHg for 5 minutes. The composite was sandwiched between two 0.020" thick sheets of Nylon 6/6, and sealed in a polyethylene bag fitted with a valve attached to a Gast ROC-R model ROA-P131- AA vacuum pump. A cotton mat was placed beneath the valve to prevent blockages in air flow, as well as to prevent excess polymer from entering the vacuum lines. The polyethylene bag containing the curing composites was placed between the platens of a Carver hydraulic unit model #3912 press using minimal force to ensure an even thickness throughout the material. These composites were cured at 450 mmHg vacuum at room temperature for 48 hours, and then cured for an additional 48 hours at 80°C at atmospheric pressure.

3. Microstructural Characterization

Optical micrographs of a specimen in *Figure 1a* clearly indicate the hierarchical structure of microscale agglomerates of CNFs, which were determined to be 10 vol. % through image analysis, in a polymer matrix with dispersed CNFs. Additional details of the structure of the agglomerates and the dispersion of the CNFs can be seen in *Figure 2a* from a backscattered SEM image of the specimen. This gives rise to the microstructural model of the hierarchical structure seen in *Figure 1b* that is formed by the interaction between the agglomerates and the polymer matrix reinforced by a percolated network of dispersed CNFs.

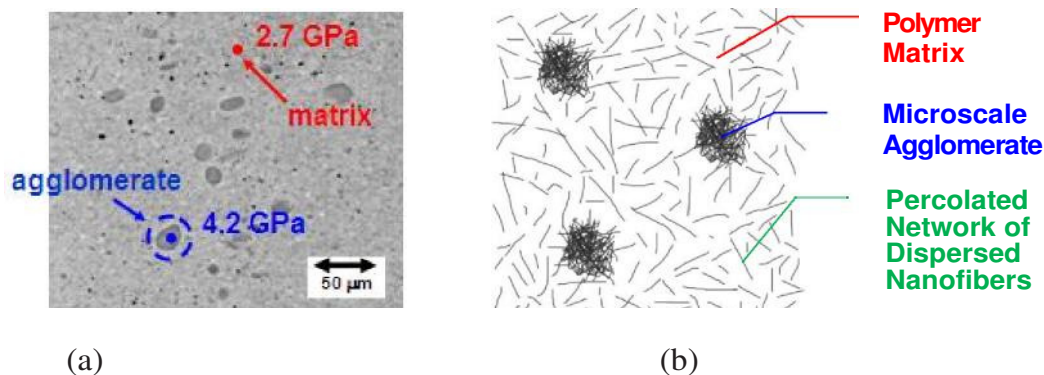


Figure 1. (a) Averaged nanomechanical characterization results from agglomerated CNFs and matrix with dispersed CNFs, and (b) the microstructural model of the hierarchical structure they form for modeling purposes.

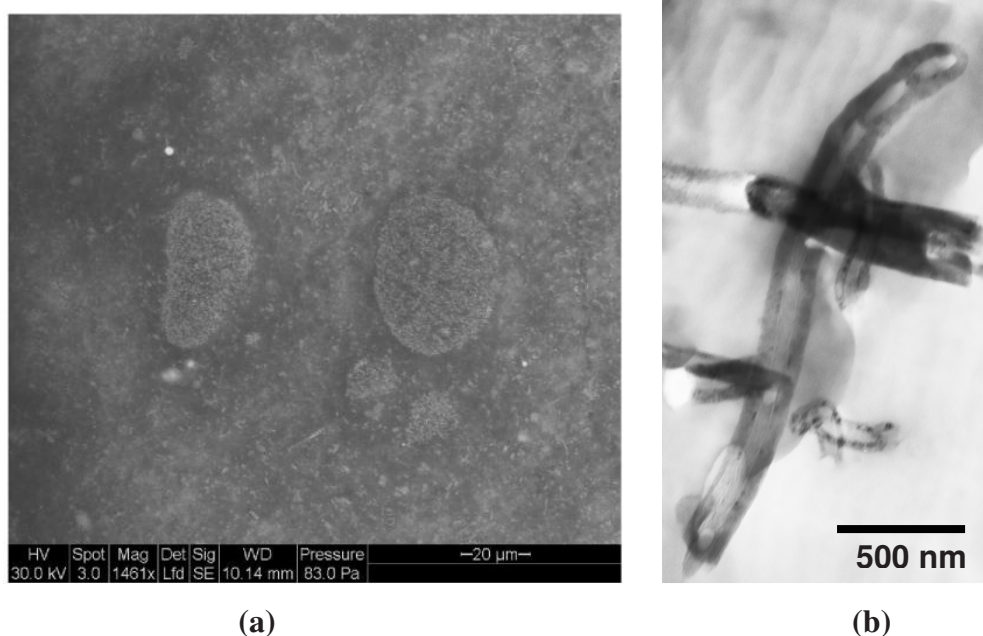


Figure 2. (a) Back-scattered SEM image of agglomerates and surrounding dispersed/percolated CNFs, and (b) TEM image of kinking in nanofibers.

Nanomechanical Characterization and Modeling

Using nanomechanical characterization, it was possible to isolate the modulus of microscale features represented by the agglomeration of CNFs from that of the matrix material reinforced by dispersed CNFs. By isolating the moduli of the microscale structures from the nano-reinforced polymer matrix, it is possible to develop a dispersion characterization model for the effects of nanofiber dispersion in a manner that is similar

to a model we previously developed for describing the effects of MWCNT percolation on rheological properties of the composite in the melt state [Kota07b].

In the dispersion characterization model, the percolated network of CNFs form an interpenetrating-phase microstructure with the remaining polymer matrix, similar to the previously developed model for rheological properties. The matrix is reinforced by the microscale agglomerates of nanofibers, which were found not to be fully infiltrated by the polymer and were thus considered to be highly filled CNF regions coated by the polymer. To determine the relative concentration of agglomerated CNFs, $v_{CNF\text{agglomerate}}$, in the composite, the volume fraction of the agglomerates, $v_{\text{agglomerate}}$, were directly determined from the optical micrograph, and then used with the modulus of the CNFs, E_{CNF} , and the modulus of the agglomerate determined from nanoindentation, $E_{\text{agglomerate}}$, in a linear Rule-of-Mixtures (ROM) formulation (i.e., isostrain) as follows:

$$v_{CNF\text{agglomerate}} = \frac{E_{\text{agglomerate}} v_{\text{agglomerate}}}{E_{CNF}} \quad (1)$$

In addition, the elastic modulus of the matrix determined from nanoindentation, E_{matrix} , was also used to determine the volume fraction of fibers in the matrix, $v_{CNF\text{matrix}}$, in a linear ROM formulation as follows since the resulting microstructure formed by the polymer and percolated CNFs was modeled as an interpenetrating phase composite:

$$v_{CNF\text{matrix}} = \frac{E_{\text{matrix}} - E_{\text{polymer}}}{E_{CNF} - E_{\text{polymer}}} \quad (2)$$

It was then possible to calculate the macroscale elastic modulus of the composite, $E_{\text{composite}}$, from the modulus of the matrix and the modulus of the reinforcing agglomerated CNF particles using an inverse ROM formulation (i.e., isostress) as follows:

$$E_{\text{composite}} = 1 / \left((1 - v_{\text{agglomerate}}) / E_{\text{matrix}} + v_{\text{agglomerate}} / E_{\text{agglomerate}} \right) \quad (3)$$

Experimental data can be seen in [Table 1](#). Since the nanoscale contribution to the modulus from the CNFs was not known, it was determined indirectly by fitting Equations (1) and (2) in the model to the data in [Table 1](#). The results can be seen in [Figure 3](#) and indicate that E_{CNF} is 30 GPa, which is at least an order of magnitude lower than typically assumed. One explanation for this is kinking along the nanofibers cause them to behave with a spring-like effect that reduces the effective stiffness (see TEM images of nanofibers from the nano-enhanced thermoplastic polymer in [Figure 2b](#)). The substantial reduction in modulus due to waviness of carbon nanofibers has been recently reported through direct measurements [11]. The nanomechanical moduli were then used with Equation (3) to compare with microtensile testing data in [Figure 4](#) that was obtained at different wt. % CNFs and different sonication times. This data indicated reasonable correlation that supported the assumed isostress reinforcement by the agglomerated CNF particles of the polymer matrix with the percolated CNF network.

Wt. % CNF	Sonication Time (hr)	Vagglomerate	Ematrix (GPa)	Eagglomerate (GPa)
1	0	0.02	2.9	4.2
1	1.5	0.01	3	4.4
1	3	0.01	3.1	4.3
1	6	0.00	3.3	n/a
3	0	0.06	3.1	4.0
3	1.5	0.04	3.2	4.5
3	3	0.02	3.3	4.6
3	6	0.01	3.4	4.3
5	0	0.10	3.2	4.4
5	1.5	0.06	3.5	4.1
5	3	0.02	3.6	4.8
5	6	0.01	3.8	4.7
7	0	0.14	3.5	5.1
7	1.5	0.10	3.8	4.8
7	3	0.06	3.8	4.7
7	6	0.04	3.8	4.9
10	0	0.18	3.6	5.2
10	1.5	0.16	3.9	5.0
10	3	0.14	3.9	4.9
10	6	0.12	3.9	4.7

Table 1. Constants obtained for the ROM formulation that quantifies effects of sonication time on tensile modulus of the hierarchically-structured polymer composite.

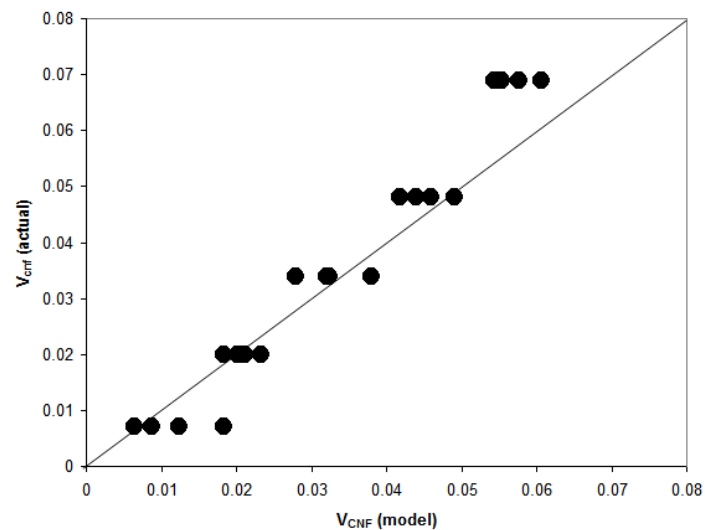


Figure 3. Fit of actual volume fraction of CNFs to the model using a modulus for CNFs of 30 GPa.

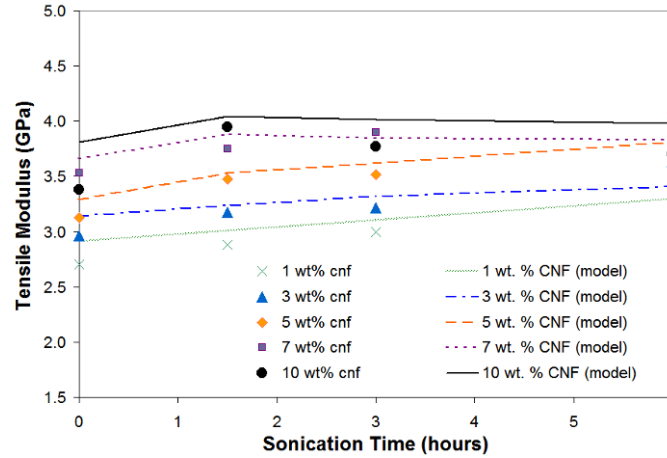


Figure 4. Tensile modulus as a function of sonication time of a hierarchically-structured polymer composite. Model predictions from Equation (3) for the tensile modulus of the nano-enhanced thermoset epoxy can be seen using E_{CNF} of 30 GPa.

From the data in Table 1, it was also possible to use Equations (1) and (2) to determine the *fraction of dispersed nanofibers* in the polymer matrix. The results can also be seen in Figure 3a. These results indicate that approximately 45-55% of the CNFs are dispersed before sonication, and increases to nearly 100% after 6 hours of sonication. However, as the loading is increased, the volume fraction of dispersed CNFs decreases after 6 hours. In fact, the decrease is consistent with a maximum volume fraction of dispersed CNFs of approximately 3.5 vol. %. Thus, it would appear that there is a *dispersion limit* to the amount of CNFs that can be dispersed in the polymer matrix using the TSE process. This dispersion limit corresponded to the percolation threshold previously determined for these polymer nanocomposites, and could explain why only limited quantities of nanoscale ingredients are typically used to nano-enhance polymers [3].

It was also possible to determine the *degree of dispersion*, D , as a function of sonication time, t , where the degree of dispersion is defined as the instantaneous concentration of agglomerated CNFs, $v_{CNFagglomerate}(t)$, relative to the dispersion limit, $v_{CNFagglomerate}(\infty)$, as follows:

$$D = 1 - \frac{v_{CNFagglomerate}(t) - v_{CNFagglomerate}(0)}{v_{CNFagglomerate}(\infty) - v_{CNFagglomerate}(0)} \quad (4)$$

The dispersion process itself can be modeled using the following conventional Avrami equation for nucleation and growth:

$$D = 1 - \exp\left(-\frac{t}{\tau}\right)^p \quad (5)$$

where τ is the time constant for the dispersion process and p is the Avrami exponent. Thus, the Avrami equation can be used to extract the time constant for the dispersion process associated with sonication. The degree of dispersion determined from the data in Table 1 and the resulting fit of the Avrami equation can be seen in Figure 8, along with the fraction of CNFs that are dispersed. The resulting time constant for the diffusion process was determined to be 2 hours, while the exponent was determined to be 1.2. Thus, the physics of the dispersion process for sonication is such that 2 hours would be the time required to achieve reasonable enhancements of dispersion. Also, as the weight fraction increases, the fraction of dispersed CNFs becomes insensitive to the sonication time. This is because there are enough CNFs at higher weight fraction to disperse without sonication close to the dispersion limit.

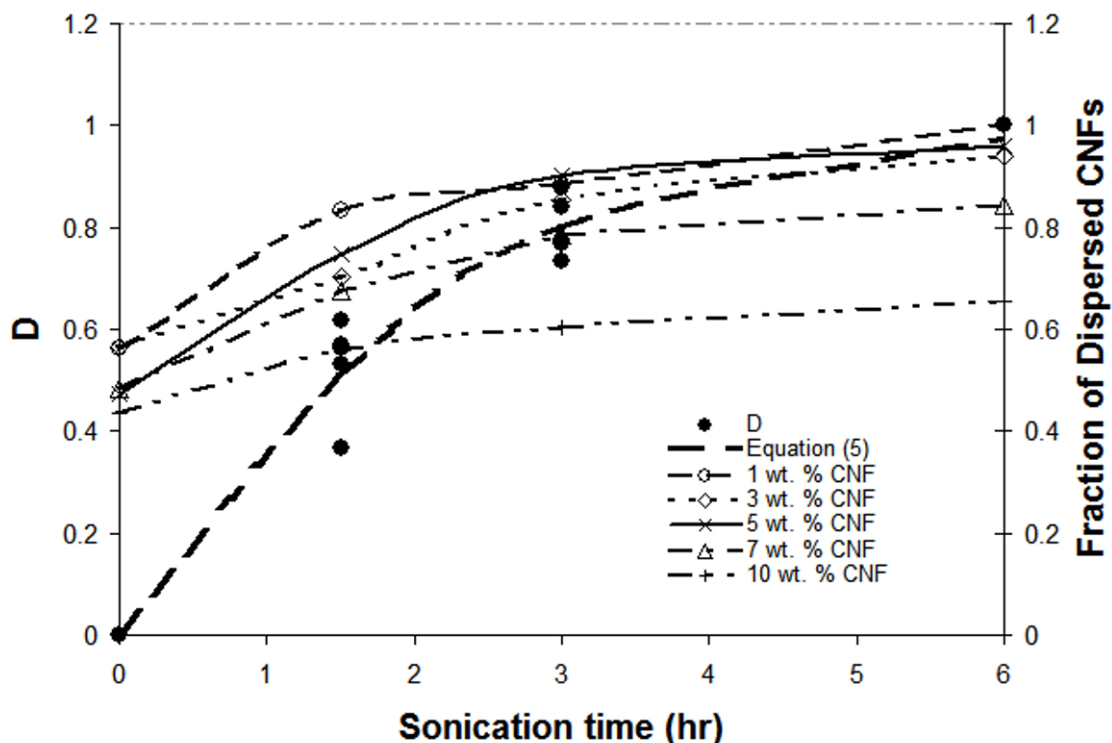


Figure 5. (left axis) The degree of dispersion versus sonication time with the Avrami fit to determine the time constant for processing the nano-enhanced thermoset epoxy, and (b) the fraction of dispersed CNFs at each weight fraction indicating saturation at higher weight fractions.

4. CONCLUSIONS

A new approach for mechanical characterization of hierarchically-structured polymer composites was developed. This approach was used to study the hierarchical structure in a model nano-enhanced thermoset epoxy using West System 105 as a model thermoset system processed using sonication to disperse CNFs during solvent processing in a long residence time, low shear rate batch mixing process. The new dispersion characterization approach enabled the *fraction of dispersed nanofibers*, *degree of dispersion* and *dispersion limit* for CNFs in the hierarchically-structured polymer composite to be determined.

The development of the new nanomechanical characterization approach involved the use of nanomechanical characterization to isolate the individual moduli of agglomerates from the polymer matrix reinforced by dispersed nanofibers. From these measurements, it was possible to develop a dispersion characterization model for quantifying dispersion. To develop the dispersion characterization model, the microstructure of the nano-enhanced polymer was modeled as a polymer matrix with a percolated network of dispersed CNFs forming an interpenetrating phase composite reinforced by microscale agglomerates that were considered to be highly filled regions of CNFs coated by the polymer. Based on the microstructural model, a ROM formulation could then be developed to relate the nanomechanical properties to the distribution of CNFs in the agglomerates and polymer matrix, as well as to the modulus determined using microtensile testing.

Using the nanomechanical characterization approach and model, the effective modulus of the CNF reinforcement was determined to be 30 GPa by correlating the volume fraction of CNFs predicted by the model to the actual volume fraction. Using this modulus, it was possible to quantify the degree of dispersion as a function of sonication time. By fitting an Avrami equation to the degree of dispersion results, a time constant of 2 hours for the dispersion process was identified. Furthermore, it was determined that there was a dispersion limit of approximately 3.5 vol. % CNFs.

ACKNOWLEDGEMENTS

This work was supported by ONR award number N000140710391.

REFERENCES

1. H.A. Bruck, "Implantable Biomedical Devices & Biologically Inspired Materials and Systems", Handbook on Experimental Mechanics, Ed. William N. Sharpe, Jr., Springer, New York, NY (2008)
2. D.W. Green, J.E. Winandy, and D.E. Kretschmann, "Mechanical Properties of Wood", Wood Handbook — Wood as an Engineering Material, Forest Products Laboratory, USDA, Madison WI (1999)
3. B. H. Cipriano, A. K. Kota, A. L. Gershon, C. J. Laskowski, T. Kashiwagi, H. A. Bruck, S. R. Raghavan, "Conductivity Enhancement of Carbon Nanotube and Nanofiber-based Polymer Nanocomposites by Melt Annealing", *Polymer*, 22, 4846-4851 (2008).
4. A.L. Gershon, A.K. Kota, and H.A. Bruck, "Characterization of Quasi-static Mechanical Properties of Polymer Nanocomposites using a New Combinatorial Approach", accepted for publication in *Journal of Composite Materials* (2008)
5. A. Kota, B. H. Cipriano, M. Duesterberg, D. Powell, D. I. Bigio, S. R. Raghavan, and H. A. Bruck, "Electrical and Rheological Percolation in Polystyrene/MWCNT composites", *Macromolecules*, 40, 7400-7406 (2007).
6. A. Kota, B. H. Cipriano, M. Duesterberg, D. Powell, S. R. Raghavan, and H. A. Bruck, "Quantitative Characterization of the Formation of an Interpenetrating Phase Composite in Polystyrene from the Percolation of Multiwalled Carbon Nanotubes", *Nanotechnology*, 18, 505705 (2007)
7. D.T. Campbell and D.R. Cramer, "Hybrid Thermoplastic Composite Ballistic Helmet Fabrication Study", *SAMPE Journal*, 44, 1-11 (2008)
8. G.J. Dvorak, Y.A. Bahei-EI-Din, and A. Suvorov, "Enhancement of Blast Resistance of Sandwich Plates", *Marine Composites and Sandwich Structures*, 2nd Edition, Office of Naval Research, 222-225 (2006).
9. V.K. Rangari, T.A. Hassan, Y.X. Zhou, H. Mahfuz, S. Jeelani, and B.C. Prorok, "Cloisite clay-infused phenolic foam nanocomposites", *Journal of Applied Polymer Science*, 103, 308-314 (2007).
10. D. Hui and M. Kireitseeu, "Nanoparticle-reinforced Multifunctional Materials", *Marine Composites and Sandwich Structures*, 2nd Edition, Office of Naval Research, 222-225 (2006).
11. T. Ozkan, M. Naraghi, and I. Chasiotis, 2010. "Mechanical Properties of Vapor Grown Carbon Nanofibers", *Carbon*, Vol. 48, pp. 239-244.

Composite Design through Biomimetic Inspirations

S.A. Tekalur, M. Raetz, and A. Dutta
Assistant Professor, Mechanical Engineering,
Michigan State University
2727 Alliance Dr, Suite B,
Lansing, MI 48910
Email: tsarjun@egr.msu.edu

Abstract

Biomimetics is a developing research field where principles of mechanics are used to both study existing natural systems and also design new systems incorporating the desirable attributes. In the current study, examples from nature that could be applied to design new composite materials and structures are presented. Mechanical characterization of bio materials such as Bivalves, bone and keratin were undertaken to understand the role of micro structure in determining the functionality of these bio-composites. Selected results such as failure in multi-layered structures, fracture properties in natural FGMs and functional attributes of layering will be discussed. Special attention provided to rational decision making in terms of choice of the materials and methods will also be presented.

Introduction

When it comes to load-bearing structures, engineers tend to prefer materials which are of high density, for example, steel, concrete, glass etc. However, when we look into nature, the same purpose is accomplished with the use of combination of layered, functionally graded or cellular solids. In this article, the bone of the cuttlefish (*Sepia Officinalis* L.) will be studied. It consists of two regions, namely the (outer) dorsal shield and an internal lamellar matrix. The microstructure of both the layers has been observed. A mechanics based analysis of coaxial cylinders was undertaken to provide insight into the performance of both the layers. This knowledge will be utilized in the design of efficient composite materials and structures. Additional studies on bivalves and bones will be presented in the talk.

Microstructure of Cuttlebone

Fig.1 shows the location of cuttlebone in a cuttlefish [1].

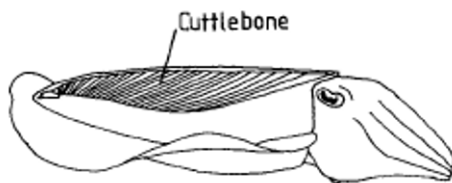


Fig.1. Position of cuttlebone [1]

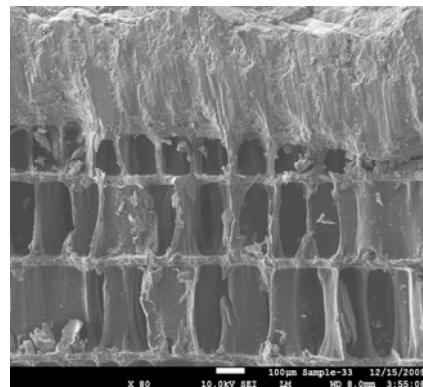


Fig.2. Dorsal shield & Lamellar matrix

The inner layer of the cuttlebone is known as the lamellar matrix. Figure 2 shows the scanning electron micrograph of the lamellar matrix and the dorsal shield in a cuttlebone. As it can be seen from the figure, the lamellar matrix consists of many chambers sealed from one another. However, gas or liquid is free to move within any chamber. Interlamellar spacing is approximately 200 μm . Pillars present between each of the chambers are approximately 10 μm thick. Inter pillar spacing is has been observed as approximately 150 μm . X-ray diffraction

studies on the calcereous material of the cuttlebone have confirmed the presence of aragonite [3]. The lamellar matrix comprising of the septa (layers) as well as the columns, are coated in an organic material, a protein-chitin complex. The outer layer of the cuttlebone is referred to as the dorsal shield. As it can be seen from the Fig.2, the top layer is a continuous layer, principally composed of sclerotized chitin [1] and hence is supposed to confer toughness and hardness to the structure. Cuttlefish are generally found at depths of approximately 300 meters below the sea surface. Thus we can say that the dorsal shield shields the lamellar matrix from the external pressures, and at the same time, seals off the separate chambers.

Failure

Compression tests were carried out on four rectangular blocks of lamellar matrix samples. The average sample size was approximately a cube of 10 mm edge length. The rate applied was 0.02 in/min and was in accordance with ASTM Standards. The maximum travel of the Extensometer (Clip Gage) was 0.15 in. The loading was applied both parallel as well as perpendicular to the lamellae. The compression stress-strain diagram is shown in Fig. 3. It was observed that the failure of the lamellar matrix was brittle in nature. A first look into Fig.3 might

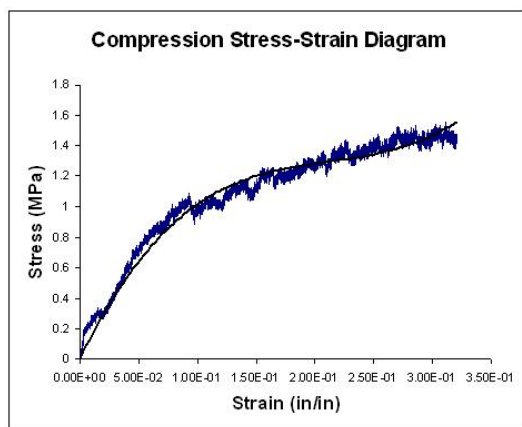


Fig.3. Compression stress-strain diagram of lamellar matrix

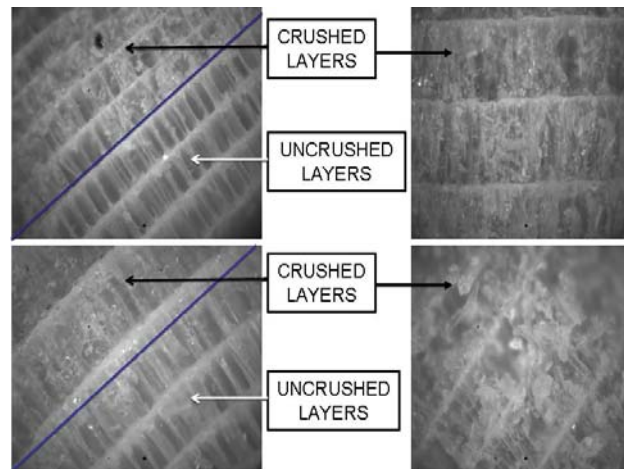


Fig.4. Crushed and uncrushed layers

appear to be the stress-strain curve as observed in the initial elastic and plateau region of foam type materials. The curve starts rising upward as it approaches the densification strain, which is a characteristic of foam materials; however, the characteristic hasn't been exhibited in the figure, because prior to reaching the densification strain, maximum travel of the test apparatus had already been attained, and hence, it was removed. As the compression proceeded, the individual layers as well as the pillars were crumbling down to powder form. Optical microscopy on the crushed samples confirms that failure occurs by the phenomenon of localized compaction. As per this phenomenon, as the crushing progressed from one side to another, remainder half of the layers were still uncrushed. This failure mode is illustrated in Fig.4. Deformation of the specimen occurs by progressive collapse from the free surface into the interior of the specimen.

Discussion

A simple mechanics based solution to concentric cylindrical surfaces was obtained. This represents a simplified model of a cuttlefish submerged in water. If the geometrical dimensions as well as the operating depth are fixed, the choice of the material in the two layers should be such that the outer layer should be of (i) greater density than the inner layer and, (ii) greater strength than the inner layer. The mean crushing strength of the lamellar matrix was observed to be approximately 1.2 MPa. The bending strength of the lamellar matrix is approximately the same as the compressive strength. From [1], bending strength of the dorsal shield is 170 MPa.

Cellular structures have the key feature of combination of high strength and stiffness with a low weight thus making them attractive subjects for mimicking these materials. The compressive stress strain plot for the lamellar matrix closely resembles [5] those of porous materials (elastic-brittle material). Initially, there is an elastic stage which reaches its limit when yield strength is reached. This is followed by the plateau stage and then the densification region. This characteristic can be attributed to structure where there is an existence of a dense, tough structure at the surface, followed by a lower dense material inside, which tend to lighten structural weight. Elastic-brittle porous materials tend to exhibit the same collapse mechanism and have significant load-carrying capacity. Drawing inspiration from these biological materials, we need to extend the idea of these biological

designs into the synthesis of novel composite materials so as to attain our ultimate objective on having a structure with minimum weight for a given strength of the material.

References

- [1]. Birchall J. D., Thomas N. L., 'On the architecture and function of cuttlefish bone', Journal of Material Science 18 (1983), pp. 2081-2086.
- [2]. M.F. Ashby, The Mechanical properties of Cellular Solids, Metallurgical Transactions, Volume 14A, September 1983-1755
- [3]. E.J. Denton and J.B. Gilpin Brown, J. Mar. Biol. Assoc. 41 (1961) 319
- [4]. Lakes, R. Composite Biomaterials, The Biomedical Engineering Handbook:Second Edition, Ed.Joseph D. Bronzino, CRC Press LLc, 2000
- [5]. Kang et. al., Compressive Behavior of Aluminum Foams Under Low and High Strain Rate, J. Cent. South Univ., Springer, 2007.

Nano-composite Sensors for Wide Range Measurement of Ligament Strain

Tommy Hyatt¹, David Fullwood, PhD^{1*}, Rachel Bradshaw¹,
Anton Bowden, PhD¹, and Oliver Johnson¹

¹ Brigham Young University

* Corresponding Author: 435 CTB, Brigham Young University, Provo, UT 84602, dfullwood@byu.edu

Abstract:

Biological tissues routinely experience large strains and undergo large deformations during normal physiologic activity. In order to quantify this strain, researchers often use optical marker tracking methods which are tedious and difficult. This paper investigates a new technique for quantifying large strain (up to 40%) by use of piezoresistive composite strain gages. The High Displacement Strain Gages (HDSGs) being investigated are manufactured by suspending nickel nanostrands within a biocompatible silicone matrix. The conductive nickel filaments come into progressively stronger electrical contact with each other as the HDSG is strained, thus reducing the electrical resistivity which is measured using conventional techniques. In the present work, HDSGs measured the strain of bovine ligament under prescribed loading conditions. Results demonstrated that HDSGs are an accurate means for measuring ligament strains across a broad spectrum of applied deformations. The technique has application to most biological tissue characterization applications.

Motivation

Biological tissues are quite unique in that they are capable of facilitating repetitive, dynamic physiological loads. Consider the anterior cruciate ligament of the knee, strains up to 12% are experienced during normal physiological motion [1], while the strains in the posterior longitudinal ligament of the spine routinely reach 34%[2]. From a research perspective, the strain experienced by a given material is useful to measure for quantifying and studying the mechanical behavior and response of a system. Strains of small magnitude (<1%) are easily measured through the use of commercially available strain gages which rigidly fixed to the surface of interest. However, high displacement systems cannot typically be quantified by conventional strain gages, due to the large strains experienced. As biological tissues have a viscous surface, low stiffness, and frequently experience large strains, the implementation of commercial strain gages is not a viable solution. To overcome this obstacle, researchers will typically use an optical technique such as photoelasticity [3-5], holography [6-8], or elastography [9-11]. The most common approach is an optical method known as Optical Marker Tracking (OMT), which fixes high contrast markers to an area of interest, and then tracks the deformation by recording the reaction to the applied loads throughout the deformation [12-15]. The position data can then be extracted from the recording, and used to calculate strain. Unfortunately, this process requires significantly more setup time, specialized equipment, does not provide real-time results, and is sensitive to numerical errors (both in the original position calculation and again in the strain calculation). Clearly, it would be advantageous to create strain gages with a higher range of measurable strain. Efforts in this direction have yielded only marginal results – piezoresistive polymers have been shown to be capable of the large deformations, but have not been able to provide accurate or repeatable results[16-18].

HDSG Background

The reason traditional strain gages fail to measure large displacements is because they plastically deform or otherwise fail upon experiencing relatively small deformations. This behavior is typical of naturally piezoresistive materials. To measure a wider range of strain, a High Displacement Strain Gage (HDSG) must (1) have greater flexibility and (2) experience a measurable change in resistivity throughout its motion. This apparent conflict of requirements can be satisfied through the use of a composite, whose properties can be designed by careful selection of

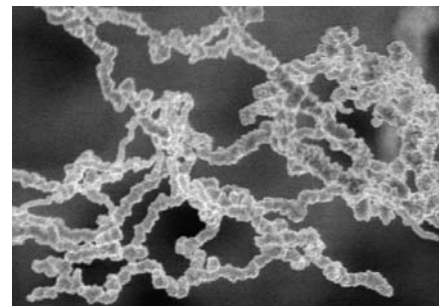


Figure 1 - SEM image of highly branched nickel nano-strands

matrix and reinforcement. The nano-composite that was developed for high displacement strain sensing is a synergistic combination of three different materials. The matrix is Dow Corning's® two part silicone elastomer, Sylgard 184. The reinforcement is a combination of nickel nano-strands (NiNs) and chopped nickel-coated carbon fiber (NCCF). The nano-strands are manufactured through a proprietary chemical vapor deposition (CVD) process that creates very high aspect ratios and a highly branched structure (see figure 1). The chopped nickel-coated carbon fiber is produced by CVD coating nickel onto unsized carbon fiber (see figure 2), and then chopping the coated tow to the appropriate length (approximately 2 mm). The constituent materials are combined using a double planetary mixer, cast into a CNC machined aluminum mold, and cured under vacuum [19].

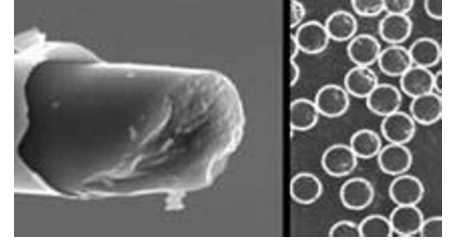


Figure 2 - SEM image of nickel coated carbon fiber and cross section of NCCF composite

HDSG Properties

As can be expected of any composite, the effective properties are related to the properties of the components. For gage material consisting of 11% NiNs and 2% NCCF, the effective strain to failure has been measured to be $50\% \pm 5\%$, and is limited by the strain to failure properties of the matrix. The electrical properties are more difficult to quantify. While none of the constituents of the nanocomposite are naturally piezoresistive, the composite behaves like a piezoresistive material with a negative gage factor. That is to say, in response to an applied load, the resistance goes down. This behavior is a result of the conductive nickel filaments and NCCF progressively coming into stronger electrical contact with each other as the HDSG is strained. Naturally, the improved electrical contact enhances the electrical conductivity, which corresponds to a reduction in resistance.

While it may be convenient to think of the electrical interaction as simple contact between conductors, the insulating silicone matrix fully wets all the reinforcement prior to curing, which prevents all classical electrical contact. The effect that governs the change in resistance is referred to as “quantum tunneling”. In short, the wave properties of the conduction electrons allow them to jump through or “teleport” past the thin potential energy barrier posed by the insulating matrix where the reinforcements are close to each other [20-22]. The maximum distance that the electrons can jump is related to the electrical properties of silicone, and proportional to the applied voltage. When the HDSG is unstrained, there are an equilibrium number of locations (or junctions) where quantum tunneling can take place. As the HDSG is strained, additional junctions are activated, thus reducing the overall resistance. This change in resistance is measured using a simple circuit known as a voltage divider. The HDSG is placed in series with a known resistor and an applied DC voltage. The voltage drop across the known resistor is measured with a voltmeter, and the change in resistance within the HDSG is then calculated at each point in time:

$$\Delta R_{HDSG} = \frac{R_1 * V_S}{V_{Drop}} - R_1 \quad (1)$$

Where R_1 is the resistance of the known resistor, V_S is the voltage of the source, and V_{Drop} is the measured voltage drop across the known resistor. The overall conductivity depends on the number of junctions that are activated during a deformation, meaning the change of magnitude in conductivity depends on the geometry of the particular gage being considered. This measured result is normalized by solving for resistivity, ρ .

$$\rho = R * \frac{A}{l} \quad (2)$$

Where R is the resistance as a function of strain, A is the cross sectional area, and l is the length. Another important property of strain gages is the “gage factor”. The gage factor (or strain factor) is the ratio of relative change in electrical resistance to the mechanical strain ϵ . That is to say,

$$GF = \frac{\Delta R}{R_0 * \epsilon} \quad (3)$$

Large gage factors are desirable as they allow for higher resolution measurement per unit strain. The gage factor of the HDSGs tested was found to be above 5, whereas commercially available metallic strain gages have a typical value of about 2.

HDSG testing on bovine tendons

The HDSGs were tested to validate the usability of the HDSG in biological applications, and assess their ability to measure a repeated strain accurately. Sectioned bovine achilles tendons were used as the test substrate onto which the HDSG and optical markers were attached on opposite sides (see figure 3). Cyanoacrilate glue (super glue) was used as the adhesive. In order to overcome the non-bonding characteristics of cured silicone, a hand held tesla coil was used to oxidize the glue surfaces of the HDSG. Contrary to standard strain gage attachment, the HDSG was only attached at the ends, in order to prevent modification of the tendon properties. Additionally, the HDSG needed to maintain electrical isolation from the ligament, because ligaments are both conductive and slightly piezoelectric. The conductivity of the ligament would effectively short out the voltage divider, and the piezoelectricity would cause a false reading on the voltage drop in the circuit. Lead shot was used for the optical markers, as they are small, reasonably consistent in size, and provide high contrast with the light background of the ligament. The optical markers were attached using a gel formulation of cyanoacrilate glue, in a 3x3 matrix pattern (see figure 3).

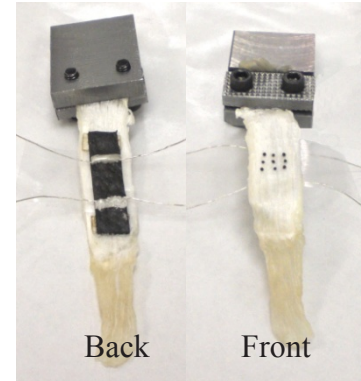


Figure 3 - Sectioned bovine ligament in test fixture with HDSG (left) and optical markers (right)

The changing resistance of the HDSG at each time step was measured with a voltage divider which was automatically recorded by a Data Acquisition system (DAQ). The positions of the optical markers were recorded by two orthogonal cameras equidistant from the sample, which were calibrated just prior to testing the prepared ligaments. The video feed from the cameras was also recorded by the DAQ using the same time interval as the voltage readings (10 Hz). The tendon was pulled in a load frame with a force of 50 pounds, which force was applied five times in a sine wave cycled at 1/20 Hz. The resulting resistance was recorded in a spreadsheet along with the force and displacement output by the load cell and crosshead respectively. The optical marker video was recorded as a sequence of jpeg images, which were processed in Matlab using Digital Linear Transformation to determine their xyz position in space.

Results

Having measured strain using two independent techniques, we can compare the resulting values to determine the validity of the new HDSG technique. Using OMT method, strain was calculated based on changing position of markers in the direction of the loadframe crosshead at each time step according to the equation:

$$\varepsilon = \frac{\Delta L}{L_0} \quad (4)$$

Where ΔL is the change in length, and L_0 is the initial length where the length is the distance between two rows of optical markers. It is recognized that strain has been calculated here as being one dimensional, whereas strain in soft tissue is frequently calculated as a two or three dimensional tensor. The one dimensional case was considered in order to compare directly with the HDSG measurements, which are currently limited to sensing strain in one dimension.

As with any strain gage, the changing resistance is meaningless without a calibration. Thus, the optical marker and resistivity data from the first test were used to calibrate the resistivity data from the subsequent tests. Considering the electrical nature of the composite material, it was not surprising to see that the magnitude of the resistivity significantly varied from test to test (nearly a factor of two). To compensate for this, the resistivity was normalized by the equation:

$$\rho = \frac{\rho_t}{\rho_0} \quad (5)$$

Where ρ_t is the value of resistivity at time step t , and ρ_0 is the resistivity at time step zero. The normalized ρ was then calibrated using an exponential curve fit with the strain data from the first set of optical marker data using the 'fminsearch' function in Matlab. The target exponential calibration was of the form:

$$A = Be^{Ct} - D \quad (6)$$

Where A, B, C and D were found to be 1.9998, -2.8269, 0.0281, and -1.8395 respectively. That calibration was then applied to the resistivity data from the other tests, resulting in strain data. The calibrated strain data is compared with the true strain as measured by the optical markers in the figures below. When superimposed, it is easily observed that there is some hysteresis and error. The average error for all the tests was calculated to be 7.1% (see figures 4-6).

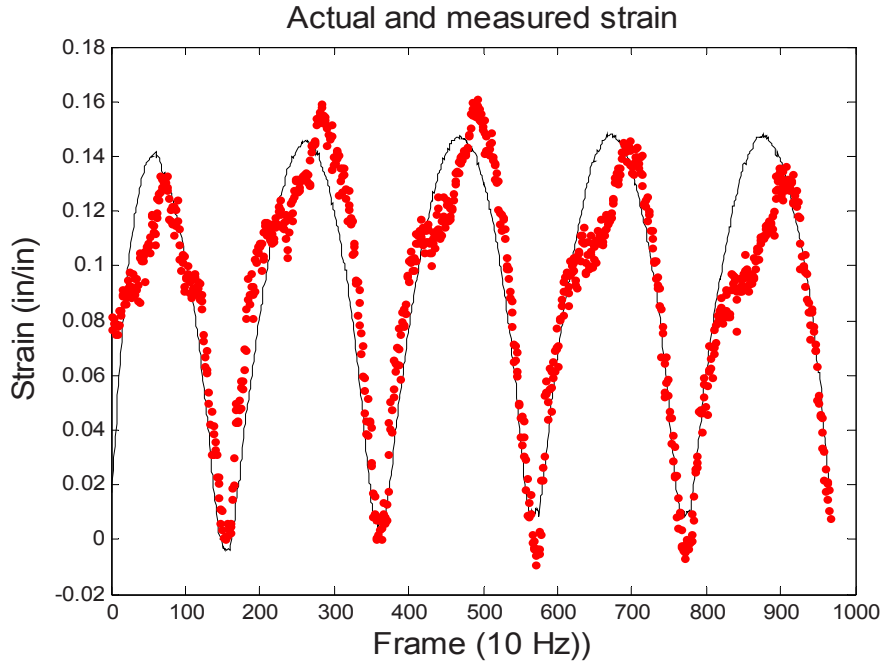


Figure 4 – Test 1: Calibration used to compare resistivity with strain. True strain (as measured by OMT) is the smooth black line, and strain as measured by the HDSG is show as red data points (error = 5.5%)

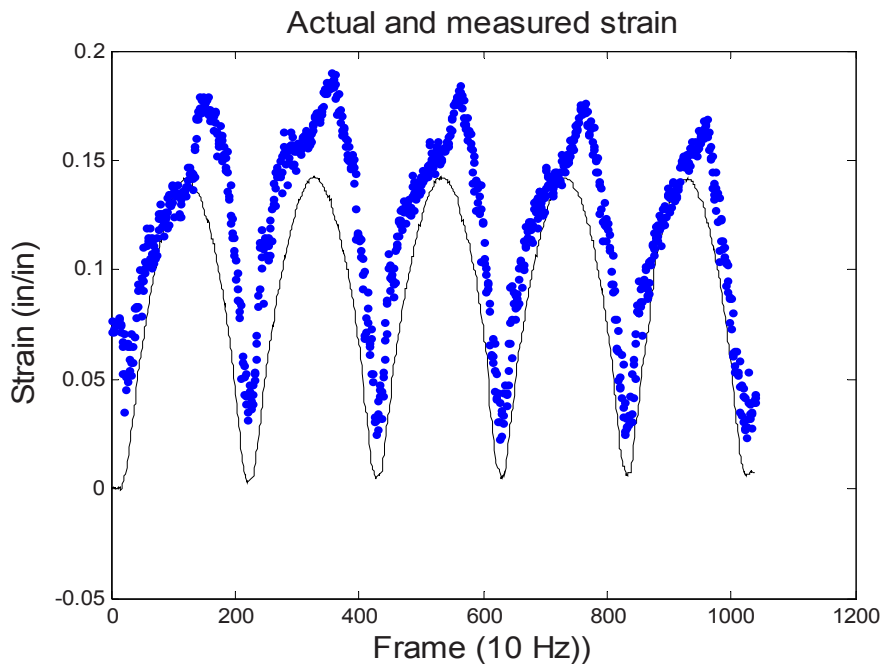


Figure 5 – Test 2: Strain as measured by resistivity vs. optical markers. True strain (as measured by OMT) is the smooth black line, and strain as measured by the HDSG is show as blue data points (error = 8.9%)

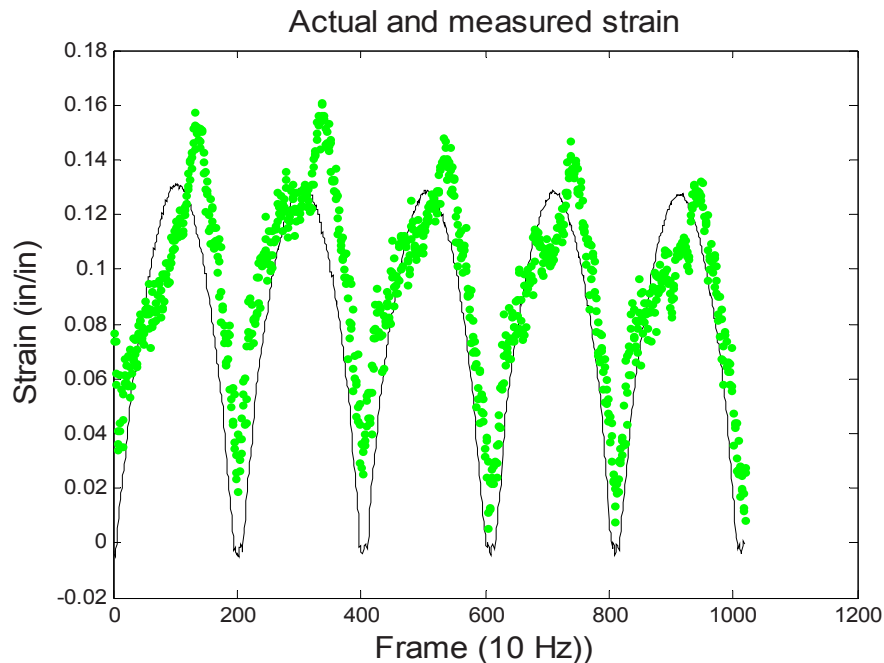


Figure 6 – Test 3: Strain as measured by resistivity vs. optical markers. True strain (as measured by OMT) is the smooth black line, and strain as measured by the HDSG is show as green data points (error = 6.9%)

Conclusion

The HDSG material being investigated is a viable option for measuring large strains in one direction. While the technology has room for improvement, it has been shown to provide accurate results measuring strain in one dimension without the expense, equipment, tedium and numerical singularities introduced by resorting to conventional OMT methods. The HDSG technique has application to most biological tissue characterization applications. This could include anything from strain monitoring on the skin of an athlete recovering from a muscle injury, all the way to research of spinal ligament characterization. This technique also has strong prospects in many other fields such as Human Machine Interface (HMI) applications; including touch-screens or position and motion sensors. Further work should be done to investigate HDSG strain gages performance over time and ways to reduce error.

References

1. Bach, J.M., M.L. Hull, and H.A. Patterson, *Direct measurement of strain in the posterolateral bundle of the anterior cruciate ligament*. J Biomech, 1997. **30**(3): p. 281-3.
2. Chazal, J., et al., *Biomechanical properties of spinal ligaments and a histological study of the supraspinal ligament in traction*. J Biomech, 1985. **18**(3): p. 167-76.
3. Nienhaus, U., T. Aegerter-Wilmsen, and C.M. Aegerter, *Determination of Mechanical Stress Distribution in Drosophila Wing Discs Using Photoelasticity*. Mech Dev, 2009.
4. Heller, W. and H. Oppenheimer, *Comparative studies on photoelasticity of elastomers and plastomers*. J Colloid Sci, 1948. **3**(1): p. 33-43.
5. Ainola, L. and H. Aben, *Fringe patterns in integrated photoelasticity*. J Opt Soc Am A Opt Image Sci Vis, 2009. **26**(7): p. 1714-20.
6. Rosso, V., et al., *Simultaneous strain and coherent imaging using coupled photorefractive holography and shearography through scattering media*. J Biomed Opt, 2008. **13**(4): p. 044010.
7. Matsumoto, T., T. Watanabe, and A. Kojima, *Deformation analysis of the human femur by holographic interferometry*. Conf Proc IEEE Eng Med Biol Soc, 2007. **2007**: p. 4699-701.

8. De la Torre-Ibarra, M., et al., *Detection of surface strain by three-dimensional digital holography*. Appl Opt, 2005. **44**(1): p. 27-31.
9. Chen, L., et al., *A quality-guided displacement tracking algorithm for ultrasonic elasticity imaging*. Med Image Anal, 2009. **13**(2): p. 286-96.
10. Rao, M. and T. Varghese, *Correlation analysis of three-dimensional strain imaging using ultrasound two-dimensional array transducers*. J Acoust Soc Am, 2008. **124**(3): p. 1858-65.
11. Tsubai, M., et al., *Development of an ultrasound system for measuring tissue strain of lymphedema*. Conf Proc IEEE Eng Med Biol Soc, 2008. **2008**: p. 5294-7.
12. Sato, K., et al., *Measurement of local strain on cell membrane at initiation point of calcium signaling response to applied mechanical stimulus in osteoblastic cells*. J Biomech, 2007. **40**(6): p. 1246-55.
13. Nicoletta, D.P., et al., *Machine vision photogrammetry: a technique for measurement of microstructural strain in cortical bone*. J Biomech, 2001. **34**(1): p. 135-9.
14. McCulloch, A.D. and J.H. Omens, *Non-homogeneous analysis of three-dimensional transmural finite deformation in canine ventricular myocardium*. J Biomech, 1991. **24**(7): p. 539-48.
15. Lujan, T.J., et al., *Simultaneous measurement of three-dimensional joint kinematics and ligament strains with optical methods*. J Biomech Eng, 2005. **127**(1): p. 193-7.
16. Bokobza, L., *Multiwall carbon nanotube elastomeric composites: A review*. Polymer, 2007. **48**: p. 4907-4920.
17. Zhou, J.F., et al., *Percolation transition and hydrostatic piezoresistance for carbon black filled poly(methylvinylsiloxane) vulcanizates*. Carbon, 2008. **46**: p. 679-691.
18. Yamaguchi, K., J.J.C. Busfield, and A.G. Thomas, *Electrical and mechanical behavior of filled elastomers. I. The effect of strain*. Journal of Polymer Science Part B: Polymer Physics, 2003. **41**(17): p. 2079-2089.
19. Johnson, O.K., et al. *Extreme piezoresistivity of silicone/nickel nanocomposite for high resolution large strain measurement*. in TMS 2010. 2010. Seattle.
20. Bloor, D., et al., *Metal-Polymer Composite with Nanostructured Filler Particles and Amplified Physical Properties*. Appl Phys Lett, 2006. **88**: p. 102-103.
21. *Peratech Limited: <http://www.peratech.com/>*. Quantum Tunneling Composites]. Available from: <http://www.peratech.com/>.
22. Palmer, J. (9 Feb 2010) *Quantum trick for pressure-sensitive mobile devices*. BBC News, <http://news.bbc.co.uk/2/hi/science/nature/8504373.stm>.

Advanced Biologically-Inspired Flapping Wing Structure Development

Lunxu Xie¹, Pin Wu² and Peter Ifju³
University of Florida, Gainesville, FL, 32611

ABSTRACT

This study examines the possibility to develop a manufacturing method to build a complicated composite structure comparable to insect wings. Stimulated by the research in flapping wing micro air vehicles, a wing structure that can be controlled with stiffness and mass distribution during manufacturing can enable complicated kinematics and efficient aerodynamics. Insects demonstrate superior flight performance and therefore their wings are good examples for building an artificial counterpart. Cicada wings are selected in this work for emulation. An artificial composite wing is built with computer numerical controlled tooling and manual fabrication, with similar vein pattern. The wings are compared with measurements of mass distribution in the spanwise direction. The results show that the composite reinforcement topology and cross section variation allow the two wings to have very similar property trends. Several difficulties are overcome in this work: replicating the cicada wing vein pattern, fabricating small composite structure components and measuring their weight distribution.

I. Introduction

In flapping wing aircraft research, researchers have paid much attention to understanding the mechanisms that govern flapping flight. Some researchers think that the wing flapping kinematics is a dominant factor in the lift generation[1], and others believe that the wing geometry and mechanical properties are critical [2][3]. The natural insect wing structure can be measured down to the minutest detail by a three dimensional curve-shaped measuring system [4], this provides a very good reference for the biologically inspired flapping wing fabrication process presented in this work.

The deformation of the flapping wing is a key factor in flight performance since it affects airflow around the wing and the consequent aerodynamic forces. Fabricating a biologically-inspired artificial flapping wing can be an effective way to understand the morphological function of the insect wing [5].

Flying insects in nature are the best example for a high performance artificial aircraft with flapping wings. A natural insect wing has very complex vein patterns, such as the cicada wing shown in [Figure 1](#).

If the vein of flapping wing skeleton is considered as a beam, its mechanical property would be dominated by the cross-section profile. The height variation of the cross-section determines the area moment of inertia, which consequently affect the bending/torsional performance of the wing. The area variation of the cross-section also results in non-uniform mass distribution across the wing. During flapping motion, therefore, this mass distribution would affect the wing deformation caused by inertia. In order to optimize the flapping wing aerodynamic performance, a method for creating an artificial flapping wing with complex vein pattern and variable cross-section needs to be developed.

¹ Research Assistant, 231 MAE-A, P.O. Box 116250, Gainesville, FL, 32611, email: Lunxu@ufl.edu.

² Research Assistant, 231 MAE-A, P.O. Box 116250, Gainesville, FL, 32611, email: diccidwp@ufl.edu.

³ Professor, 231 MAE-A, P.O. Box 116250, Gainesville, FL, 32611.

There are several biologically inspired wing fabrication methods available. Tanaka et al. have developed a three-dimensional insect-wing model by micromolding of thermosetting resin with a thin elastomeric mold [5]. Pornsin-sirirak et al. fabricated a insect wing frame made from titanium-alloy metal by using MEMS-based wing technology [6]. Kroninger et al. have developed a millimeter-scale flapping wing through a MEMS process and approved that this wing can produce similar lift and flight characteristics to those of insects in the same size class [7]. Shang et al. have developed a wing fabrication process by using a PDMS mold which is made from positive relief created by photolithography method [8]. Although these wing fabrication methods can be used for creating centimeter scale artificial wing, they are not suitable for building the wing structure with complex vein pattern and variable vein cross-section by using composite material.

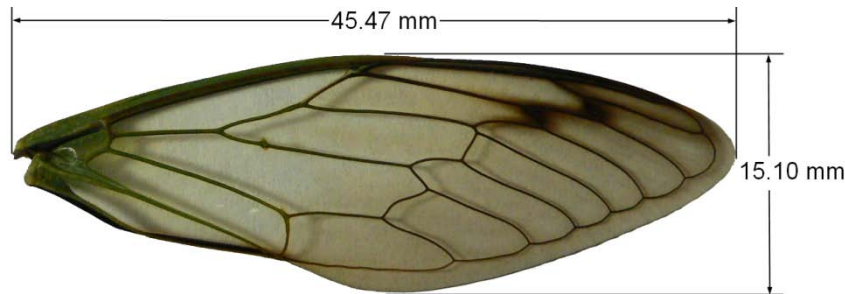


Figure 1. Natural cicada wing

The rest of this paper is organized as follows: the fabrication process that enables the complicated artificial structure is first explained. This is followed by the experimental method used in this work to compare the artificial cicada wing and a natural one. Finally, the result is presented.

II. Fabrication Process

For building a biologically-inspired wing, two things must be considered, one is the complex vein pattern, and the other is the vein cross-section changed continuously along each vein.

In this research, the vein pattern used for the artificial wing mimicks a natural cicada wing, and for simplifying the fabrication process, a planer wing is created. Because of the complex vein pattern, a Mikron UCP 600 Vario[®] CNC machine is used to cut the mold made from aluminum 6061 alloy (Fig.2(a)). Since the veins of a natural cicada wing has variable cross-section along each vein, a chamfer mill with 60° tip angle was selected as the cutting tool, this will generate an equilateral triangular vein cross-section, by changing the cutting depth, the cross-section's width will changed simultaneously with the cutting depth. As a result, wing mold with multiple grooves which have duplicated cicada vein pattern and variable cross-sections is generated(Fig.2(b)). Fig 3 shows the specification of groove depth variation. The depth varies linearly between adjacent nodes except the grooves for leading edge and trailing edge. The leading edge groove depth linearly varies from 0.7 mm at root to 0.3 mm at tip. The trailing edge groove keeps 0.05 mm constant depth. When determining the groove depth variation, the natural cicada wing vein size was used as reference. But one must consider that the artificial wing is made from different material, so the cross-section variation of artificial wing is no exactly duplicated from the natural wing.

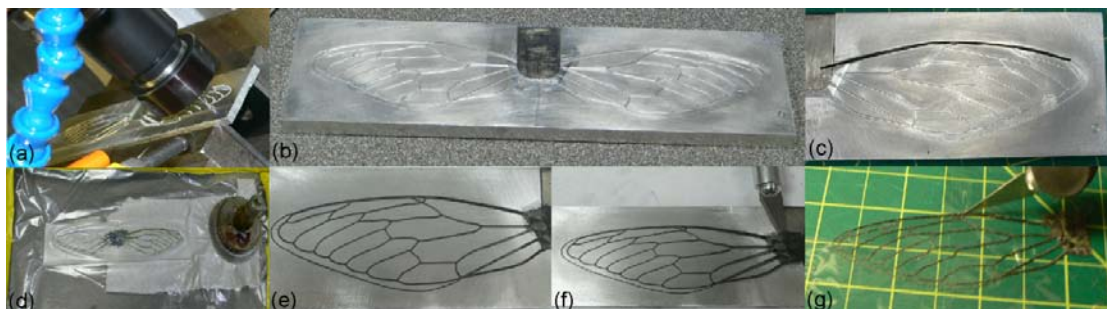


Figure 2. Wing fabrication process

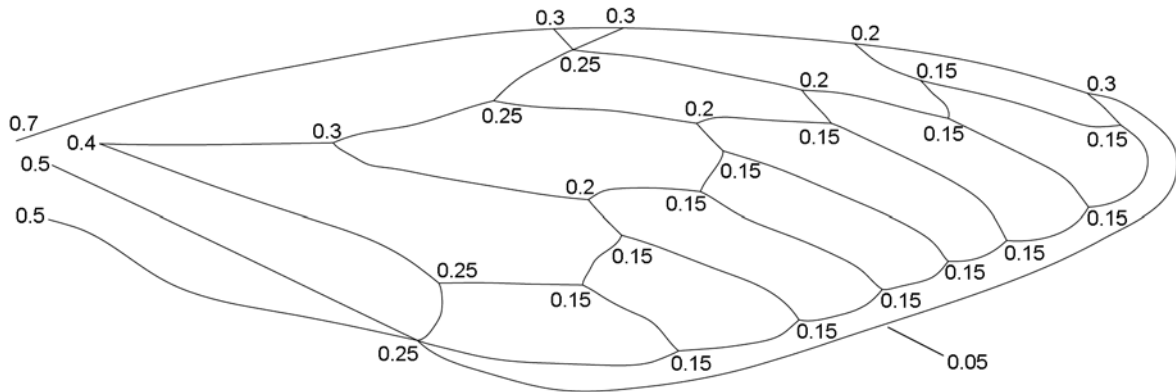


Figure 3. Wing mold groove depth specification (unit: mm)

The weight of natural cicada wing is very light, so the material for building the artificial wing skeleton must be lightweight and of high strength, so carbon fiber is selected for satisfying this requirement. Carbon fiber strips are cut from an unidirectional carbon fiber sheet by a razor knife and fill the grooves on the mold (Fig.2(c)). But the mold must be coated by release at least 2 times. In this research, FREEKOTE[®] 700-NC[™] release was used. After filling all the grooves with carbon fiber, the mold was covered by a layer of peel ply fabric and sealed by vacuum bag to ensure the carbon fiber will undergo uniform pressure during curing cycle (Fig.2(d)), and the peel ply can absorb the extra epoxy. The curing temperature cycle is shown in Fig.4.

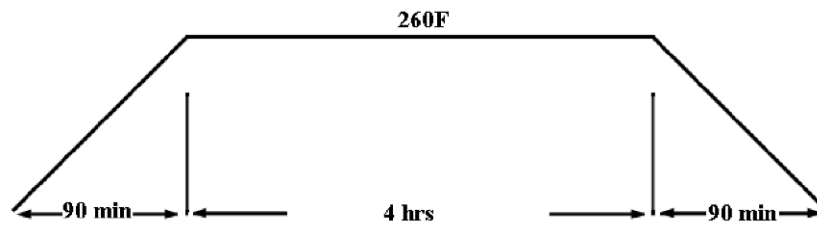


Figure 4. Carbon fiber curing temperature cycle

After the seven hour curing cycle, the excess carbon fiber is sanded off to the top surface of the mold on a flat sanding surface (Fig.2(e)) and take out the wing skeleton from mold carefully (Fig.2(f)). Although the natural cicada wing has non-uniform membrane thickness distribution in both spanwise direction and chordwise direction [9], this research is focus on the properties of vein structure. Therefore the membrane used here has uniform thickness. The material selected for wing membrane is Honeywell's Capran[®] Matt 1200 biaxially oriented nylon film [10]. It is combined with the wing skeleton by spray glue and trimmed along the wing's outside contour by a razor knife on a cutting mat (Fig.2(g)). The finished wing has 75.89 mm wingspan and 25.90 mm chord length is shown in Fig.5.



Figure 5. Finished artificial wing, (a) top view, (b) side view

As shown in Fig.5(a), the artificial wing made by this fabrication method has the same vein pattern as a natural cicada wing, and the vein width varies continuously along the vein. The side view of artificial wing shown in Fig.5(b) clearly shows that the height of each vein varies linearly from root to tip.

III. Experiment Method Exhibits

To examine whether the artificial wing built by this method exhibits comparable mass distribution as the natural cicada wing, they are divided to 32 sections from wing tip to the region nearby the root. As shown in Fig.6(a), the real cicada wing is fixed on reference plate with 1.2 mm line spacing by CA glue.

The reference plate for the artificial wing has 2.0 mm line spacing which is amplified from 1.2 mm by the amplification factor, and the wings are cut by a razor (Fig.6(b)). The horizontal line is for ensuring that the wings are placed in the wingspan direction. The remaining wing weight and length are measured after each cutting step. Weight is measured by Fisher Scientific accuSeries® accu-124 analytical balance which has 0.1 milligram readability and ±0.2 mg linearity. The length is measured by a caliper.

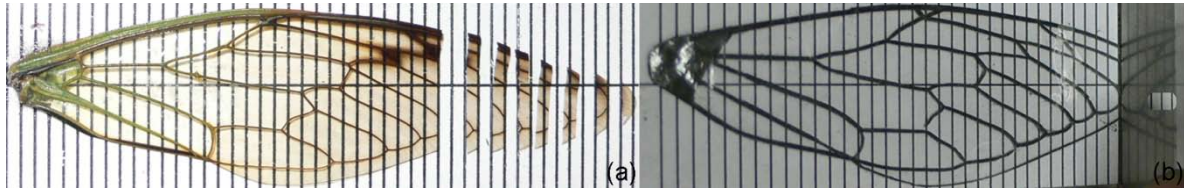


Figure 6. Wings fixed on reference plate

The weight of each wing section can be determined by the weight difference between two adjacent cutting steps, and the position of wing section along the wingspan direction can be calculated by the remaining wing length between adjacent cutting steps. In Figure 7, W_1 , W_2 present the remaining wing weight and L_1 , L_2 are the remaining wing length after corresponding cutting step, so the weight and center position of wing section in Fig.6 can be calculated by the following equations:

$$W = W_1 - W_2 \tag{1}$$

$$L = \frac{(L_1 - L_2)}{2} \tag{2}$$

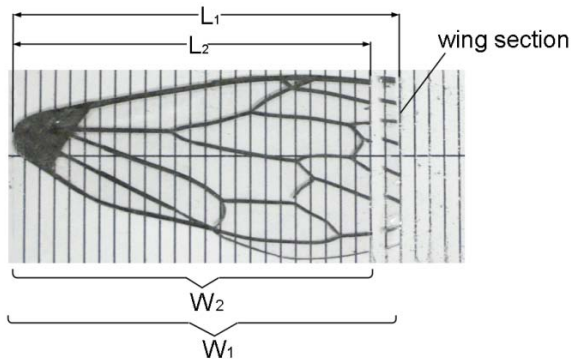


Figure 7. Determination of wing section's weight and center position

IV. Result

The spanwise wing section weight distribution of both wings is shown in Fig.8. The data of the artificial wing is scaled down to the same length dimension (divided by the cubed length ratio between the artificial and the natural wing). The comparison has shown that the similar vein pattern results in similar trends of weight distribution along the span direction for both wings: more material (therefore heavier) at the root and less material at the tip. If the cross section as well as the vein pattern were exactly the same, the section weight distribution could have been

the same. However, for the current available experiment equipment, significant measurement uncertainty is inevitable. The error bar of natural cicada wing section weight presents ± 0.17 mg weight measurement uncertainty, but for the artificial wing, the measurement uncertainty is scaled down based on the same reason above. Wings demonstrate some similarity of section weight distribution; this is caused by the big error in the section weight calculation.

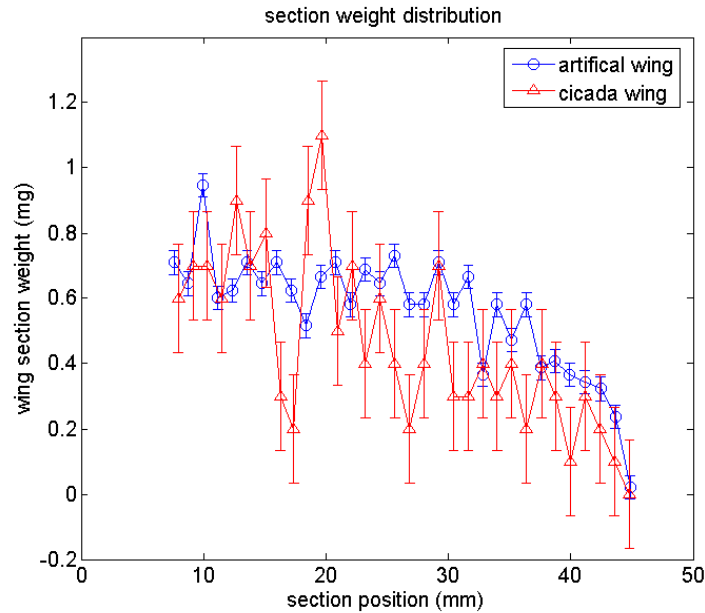


Figure 8. Wing Mass distribution

Similarly, the overall wing weight as a function of wing span location is shown in Figure 9. Again the data for the artificial wing have been scaled down to the same length dimension. The remaining wing weight distribution of these two wings show very good similarity from wing root to 50% of wingspan, but when the cutting position moves from 50% wingspan to the wing tip, the remaining weight of natural cicada wing decrease faster.

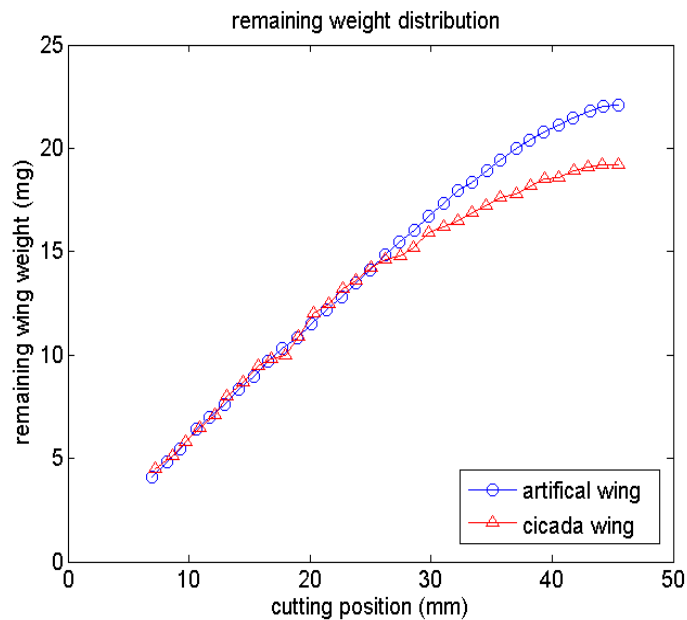


Figure 9. Remaining wing weight distribution

V. Discussion

In this experiment, wings are divided into 32 sections. This causes some sections nearby the wing tip region to have very small weight, close to the measurement uncertainty (± 0.17 mg). By increasing the section size (lowering the data special resolution), smaller overall uncertainty can be achieved. Figure 10 shows the wing section weight distribution when the wings are divided to 16 sections. Both wings are shown in the same length scale and the error bar represents ± 0.2 mg measurement uncertainty.

These two wings have very similar mass distribution pattern in the region from 50% wingspan to wing tip, this is because the artificial wing follows the same vein pattern as the natural wing, at the outside wing region, vein cross-section is very small compare to the vein at the inside region, weight distribution is dominated by the vein pattern, the difference between mass distribution is because these two wings are made from different material. As the section moves from 50% wingspan to wing root, the mass distribution pattern only shows limited similarity, because at the inside wing region (from wing root to 50% wingspan), the vein cross-section size is bigger and increases faster, the weight distribution is not only governed by the vein pattern but also affected by the cross-section variation. However, the natural cicada wing which was used in this experiment is a dehydrated wing. The dehydrated wing may have different weight distribution and mechanical performance than the fresh cicada wing. For further research, a fresh wing should be used.

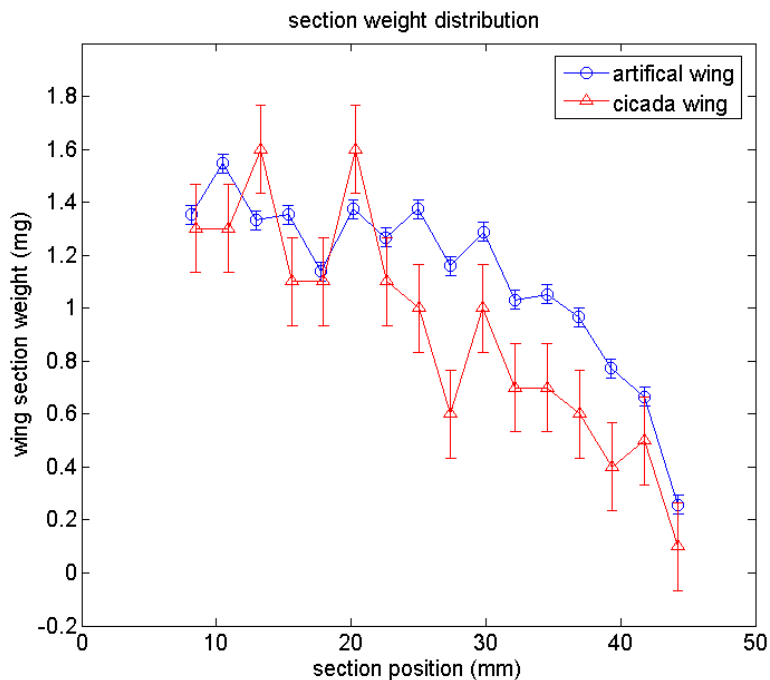


Figure 10. Mass distribution after increase sections' width

VI. Conclusion

This wing fabrication method provides an effective way to build an artificial flapping wing with complex vein pattern and variable vein cross-section by composite material. The artificial wing created here has comparable mass distribution to natural cicada wing. Better similarity of mass distribution or mechanical properties can be achieved by adjusting the cutting depth variation of the mold.

Though we have built a planner wing, the natural insect wings have camber and corrugation which may be important to thrust production. The artificial wing with 3-D structure can be built by using 3-D mold.

Acknowledgment

This work was supported by the Air Forced Office of Scientific Research under MURI #69726. The authors whole heartedly thank Professor Tony Schmitz and his graduate student Andrew Weston Riggs for their help during the manufacturing process. Also thank Professor Z. Hugh Fan for his help during weight measurement.

References

- ¹ Dickinson, M., Lehmann, F., Sane, S., "Wing Rotation and Aerodynamic Basis of Insect Flight," *Science*, Vol. 284, 1999
- ² Combes, S., Daniel, T., "Flexural stiffness in insect wings I. Scaling and the influence of wing venation," *J. Exp. Biol.* 206, pp. 2979-87. 2003
- ³ Combes, S., Daniel, T., "Flexural stiffness in insect wings II. Spatial distribution and dynamic wing bending," *J. Exp. Biol.* 206, pp. 2989-97. 2003
- ⁴ Tsuyuki, K., Sudo, S., Tani, J., "Morphology of Insect Wings and Airflow Produced by Flapping Insects," *Journal of Intelligent Material System and Structures*, Vol. 17, pp. 743-751, 2006
- ⁵ Tanaka, H., Matsumoto, K., Shimoyama, I., "Fabrication of a three-dimensional insect-wing model by micromolding of thermosetting resin with a thin elastomeric mold," *J. Micromech. Microeng.* 17, pp. 2485-2490, 2007
- ⁶ Pornsin-sirirak, T., Tai, Y., Nassef, H., Ho, C., "Titanium-alloy MEMS Wing Technology for A Micro Aerial Vehicle Application," *Sensor and Actuators A*, Vol. 89, pp. 95-103, 2001
- ⁷ Kroninger, C., Pulskamp, J., Bronson, J., Polcawich, R., Wetzel, E., "Bio-Mimetic Millimeter-Scale Flapping Wing for Micro Air Vehicles," <http://www.arl.army.mil/arlreports/2009/ARL-TR-4729.pdf>, 2009
- ⁸ Shang, J., Combes, S., Finio, B., Wood, R., "Artificial insect wings of diverse morphology for flapping-wing micro air vehicles," *Bioinsp. Biomm.* 4, 2009
- ⁹ Song, F., Lee, K., Soh, A., Zhu, F., Bai, Y., "Experimental studies of the material properties of the forewing of cicada," *J. Exp. Biol.* 207, pp. 3035-3052, 2004
- ¹⁰ Wu, P., Stanford, B., Ifju, P., "Passive Bending and Twisting Motion during the Flapping Stroke of a Micro Elastic Wing for Thrust Production," 47th AIAA Aerospace Sciences Meeting Including The New Horizons Forum and Aerospace Exposition, Orlando, FL, January 5-8, 2009

Characterization of Electrode-Electrolyte Interface Strengths in SOFCs

S. Akanda, M.E. Walter, The Ohio State University, Columbus, OH, 43210

ABSTRACT

Planar Solid Oxide Fuel Cells (SOFCs) are composed of multiple layers of dissimilar materials. Interfaces between the different components that make up an SOFC play an important role in the performance and robustness of the cells and stacks. The present study involves the characterization of electrode-electrolyte interfaces in solid SOFCs. Stud-pull test fixture was constructed and mounted on a servo-electric load frame to examine the anode-electrolyte interface. The stud-pull specimens were made of NiO-GDC/Ni-YSZ anodes and ScSZ electrodes and were reduced in either forming gas (5% H₂) or H₂ fuel. The test was not successful in separating anode from the electrolyte consistently and was inconclusive due to infiltration of glue into the porous anode which changed the interfacial strength significantly. In the Next step the notched four-point bend experiment was utilized to determine the fracture energy at the interface between the anode and the electrolyte. Crack propagation was monitored with acoustic emission and videography. Specimens for the bend experiments consist of unreduced NiO-GDC/Ni-YSZ anode and ScSZ electrolyte bi-layers sandwiched between steel stiffeners. The microstructure was studied using scanning electron microscopy (SEM).

Introduction

With their high efficiency and low emissions, solid oxide fuel cells (SOFCs) have the potential to radically alter the production and distribution of electricity. Although SOFCs operate at temperatures of 700-850°C, SOFCs have several advantages over other fuel cell types. The principal advantage is fuel flexibility. Because the ceramic membrane is an oxygen ion conductor, oxygen partial pressure gradients create the voltage that allows cell operation. Thus both H₂ and CO can be consumed as fuel, allowing a range of reformed hydrocarbon fuels to be considered. The high operating temperatures create advantages both by enabling catalysis of the fuels without special, expensive materials and by paving the way to enhanced efficiency within combined cycle systems (e.g., [1]). Another important advantage is the enhanced tolerance of SOFCs to fuel impurities. CO, which poisons proton exchange membrane (PEM) fuel cells, is a *fuel* for SOFCs. H₂S, another common contaminant in hydrocarbon and some biomass-derived hydrogen fuels, is tolerated in SOFCs currently being developed; competing fuel cell systems require large desulfurizers to assure high purity fuel. SOFCs are not without their own challenges, however. In particular, SOFC materials selection, cell and stack design, manufacturing, conditioning, sealing, and degradation/ failure are active subjects for research and development.

The main components of SOFC membrane electrode assemblies are thin, multi-layer ceramic oxide electrolytes, porous cermet composite electrodes, oxide-coated stainless steel interconnects, and glass or glass-composite seals. To date the specific materials for these components are selected primarily for their electrochemical properties, cost, and ease of manufacturing [2]. SOFC developers are beginning to consider materials, assembly, and operational issues associated with the integrity and mechanical robustness of SOFCs.

There are three main stack designs: tubular, planar anode-supported and planar electrolyte-supported. Especially for residential and mobile power systems, integrators have gravitated toward planar designs for ease of manufacturing, lower operating temperatures, simplified interconnects, and higher power densities [3]. Although significant resources have been invested in overcoming some of the manufacturing hurdles to anode-supported

cell production, planar anode-supported cell stacks continue to suffer from challenging drawbacks related to oxidation-reduction (redox) cycling, mechanical integrity, and seal complexity.

The process of reduction conditioning and unanticipated redox cycling has significant consequences for anode-versus electrolyte-supported designs. When the anode is reduced prior to operation, nickel oxide converts to nickel metal, creating stress in the cell that can result in significant warpage [4]. To restrain warpage and preserve cell-interconnect contact, designers use high compressive loads and thicker interconnect plates. Though the stacks developed with anode-supported cells are typically of considerable size and weight, they remain fragile [5]. In recent years there have been a number of microstructural ([6],[7],[8]) and mechanical [9] studies of the impact of anode redox cycling on cell performance and stability. The problems are related to volume changes from the NiO to Ni phase change and from microstructural coarsening (e.g., [9], [10]). Waldbillig *et al.* document a ~9% performance loss in fully re-oxidized anode supported cells [8].

To circumvent the challenges associated with anode-supported SOFC systems, efforts to develop electrolyte-supported systems have intensified. Simply thickening the electrolytes used in anode-supported designs leads to insurmountable trade-offs between mechanical strength and sufficient ion conductivity at intermediate temperatures. The electrolyte must be optimized for mechanical and electrochemical performance through materials selection and geometric design. Recent electrolyte-supported SOFCs have shown intermediate temperature efficiencies equivalent to the efficiencies of common anode-supported designs [11]. In addition, recent modeling has shown that oxidation expansion must be below 0.1% for an anode-supported cell while an electrolyte-supported cell with a 10 μm anode can sustain up to 0.5% oxidation strain [12].

For SOFCs, degradation and failure while operating and after anticipated or un-anticipated shutdowns and subsequent startups is largely a consequence of high operating temperatures. With such a range of materials within the stack monolith, challenges with spatially and temporally non-homogeneous high temperature environments are tremendous, and a direct result of a) widely varying thermal coefficient of expansion (TCEs), b) non-equilibrium and low temperature phases (especially at interfaces), and c) ceramic components with low toughness and low thermal conductivity. In SOFCs, thermal gradients associated with improper thermal balance between low temperature inlet gas streams and the exothermic oxidation reactions can result in catastrophic failure and loss of the stack. Even in normal operating conditions in a 10 x 10 cm cell, regions with large pO_2 gradients can be 250°C hotter than regions with depleted fuel and oxygen [5]. Difficulties associated with thermal gradients are compounded by homogenous temperature excursions involving materials that must maintain functional interfaces in the presence of dissimilar TCEs. To avoid thermally initiated failure during startup and shutdown, heating rates are kept low. Experimental prototype systems reported by the Department of Energy Solid State Energy Conversion Alliance (SECA) program use heating rates of ~3°C/minute and cooling rates of <1°C/minute. However, recent work at Forschungszentrum Juelich showed thermal cycling of anode supported stacks at rates of only 2°C/minute can lead to degradation of the stack performance [13]. For mobile and transportation markets, rates of 5-10°C/minute will be highly desirable. In all applications, commercially viable stacks must be able to withstand transients associated with events such as fuel supply or balance-of-plant interruptions.

The current approach to solving problems associated with thermal gradients and TCE mismatches is to increase the mechanical strength of various components. To some extent, this has been done; however, strengthening of anodes and electrolytes has exposed weaknesses at interfaces. Clear evidence from NexTech Materials Ltd (NTM) and the literature show that during thermal cycling electrode interfaces degrade and delamination occurs. Engineering solutions can protect the stack but there is no fundamental understanding of how material selection, assembly procedures, and thermal conditioning inter-relate to develop stresses at the electrode interfaces. The very expensive nature of experimental stack development guarantees that fundamental understanding of electrode interface stresses and degradation would have an immediate scientific impact and would help reduce development time and cost.

Materials

The necessary materials were supplied by NTM which is at the cutting-edge of electrolyte-support SOFCs. NTM has developed a family of planar cells designed to address shortcomings of anode supported designs, while

providing excellent performance under equivalent operating conditions. The NextCell™ shown in Fig.1 is a proprietary laminated electrolyte combining high conductivity 10 mol% Scandia (Sc) stabilized zirconia (ScSZ-10) layers with higher strength 6 mol% Sc stabilized zirconia (ScSZ-6) layers to provide a cell with combined properties that are particularly attractive. The thin (~120 μm) electrolyte layer allows excellent performance to be achieved in the electrolyte supported design.

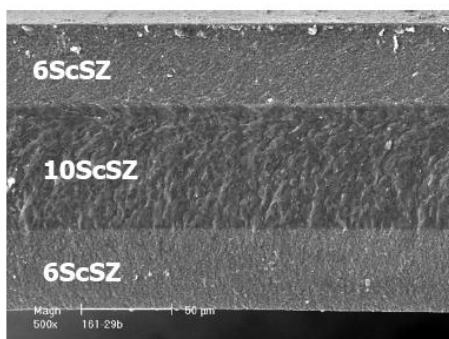


Figure 1: SEM micrograph of a laminated NextCell electrolyte.

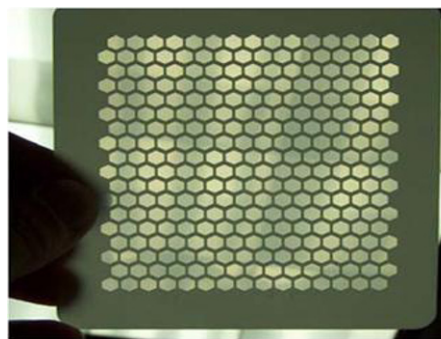


Figure 2: FlexCell™ Planar membrane cell.

NTM has further refined the NextCell™ into another proprietary design called the FlexCell™, which is shown in Fig.2. The FlexCell™ formed from thin electrolyte material sintered with a support layer consisting of slightly thicker electrolyte material that has hexagonal cut-outs. The resulting electrolyte membrane has a ~40 μm thickness under each hexagon. The thin electrolytes and ~50 μm screen-printed electrodes minimize the component thickness and results in mechanically flexible components that are compliant during stack assembly and operation. Electrochemical performance of the FlexCell™ is comparable to the best anode-supported cell design and enables a wider window of materials selection for the electrodes. This electrode material flexibility can enable lower operating temperatures and is more tolerant of the use of sulfur contaminated fuels. A top-view SEM micrograph of the electrolyte is shown in Fig.3.

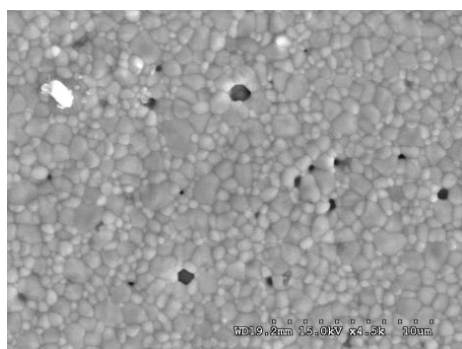


Figure 3: Stabilized grains of electrolytes.

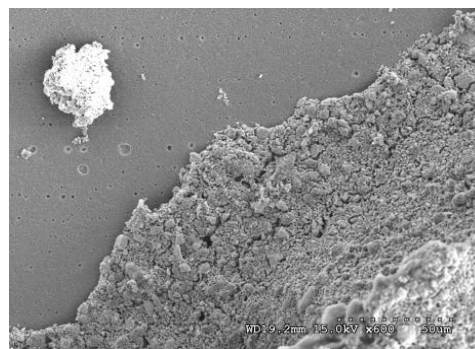


Figure 4: SEM micrograph of anode-electrolyte bi-layer.

Over the years NTM has found that a Ni-GDC/Ni-YSZ composite anode, where GDC refers to gadolinium doped cerium oxide, provides the best performance and stability. The anode material is produced by mixing controlled ratios of NiO, GDC, and YSZ (yttria stabilized zirconia) powders with well defined powder sizes and tape casting the powder slurry into sheets. The sheets are subsequently stacked and co-sintered with adjoining materials. Finally, exposure to an H₂ reducing environment converts NiO to Ni. Fig.4 shows an anode-electrolyte bi-layer where the anode is seen in the lower left half of the SEM micrograph.

As can be seen in Fig.5 and Fig.6, anode layer is separated in two parts a) Active anode layer b) Current collector layer. The active anode layer is 10 micrometer in thickness and the current collector layer is 25 micrometer in

thickness. In both the SEM images, a barrier layer can be seen between the active anode layer and the electrolyte. This barrier layer is known as bonding, catalytic or electrochemical interface layer. Barrier layer is fired separately in high temperature and screen printed or sprayed on top of the electrolyte. This layer is couple of micrometers in thickness.

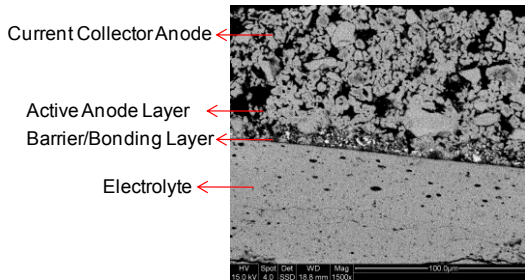


Figure 5: Backscattered SEM of reduced cross section.

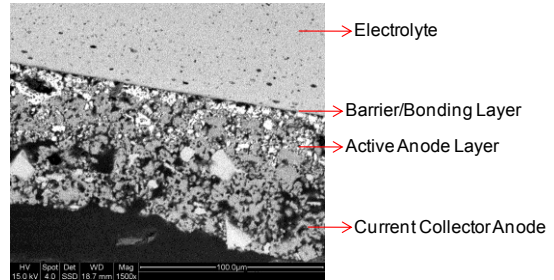


Figure 6: Backscattered SEM of unreduced cross section.

SOFC specimen for both the stud-pull test and four point bend experiment were provided by NTM. In Fig.7 and Fig.8 both the unreduced and reduced SOFC specimen for stud-pull test has been presented. The electrolyte substrate is 20 mm in diameter and 150 μm in thickness while the anode islands are 3/16” diameter and 750 μm thick.

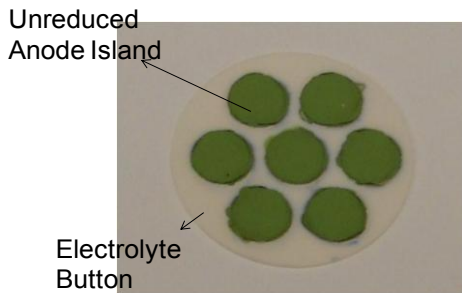


Figure 7: Unreduced SOFC specimen for stud-pull test.

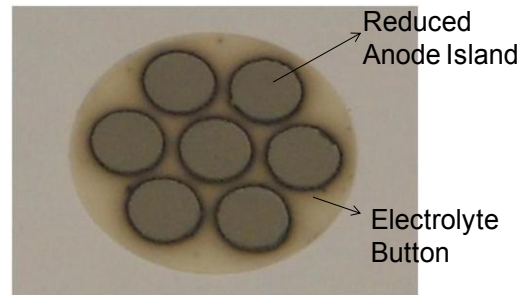


Figure 8: Reduced SOFC specimen for stud-pull test.

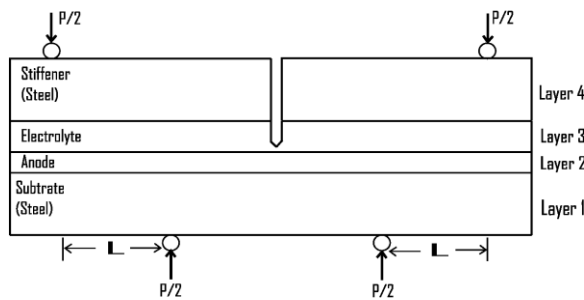


Figure 9: Test specimen for four point bending test.

Layer	Layer Name	Layer Material	Layer Thickness(μm)	Youngs Modulus (GPa)	Poissons Ratio
1	Substrate	Steel	1000	207	0.3
2	Anode	NiO/GDC	60	17	0.33
3	Electrolyte	YSZ	300	215	0.35
4	Stiffener	Steel	1000	207	0.3

Table 1. Thickness and mechanical properties of different layers of the test specimen.

The geometry of the test specimen used for four point bending experiment and shown in Fig.9 is a modification of the geometry suggested by Charalambides *et al* ([14],[15]). The test specimen is consisted of two stiffening steel layers on both sides of the specimen. The stiffening layers are used to suppress the segmentation of the brittle layers and as a result they increase the stored elastic energy and thus the driving force for delamination. A notch was created on the electrolyte prior to the test from which an initial crack was generated and propagated through the interface. The specimen is 70 mm in length and 10 mm in width. The mechanical properties and thickness of different layers of the specimen are given in Table 1.

Experimental

The present research utilizes both the stud-pull test and the four point bending experiment as an attempt to quantify the strength of adhesion between the anode and the electrolyte in SOFC. The stud-pull apparatus and the four point bend fixture were set separately in a servo-electric load frame from TestResources in their respective experiments. The load frame's accompanying software features real-time displays of the load and position of the load frame actuator. The software enables the user to program the actuator to follow the specific motions. Various data acquisition options are available and data was saved for subsequent analysis.

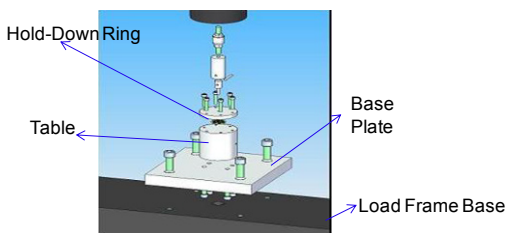


Figure 10: An exploded view of stud-pull apparatus.

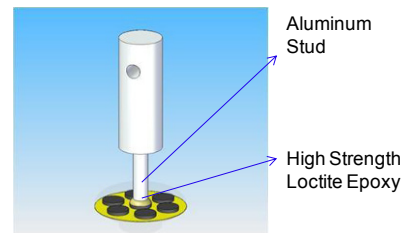


Figure 11: A schematic of multiple specimen and glue stud.

For stud pull testing with the apparatus shown in Fig.10, anode "islands" on electrolyte substrates were produced and are shown in a solid model in Fig.11. Epoxy (Loctite E-120HP) was chosen to glue the stud to the islands. The epoxy has a 2:1 resin to hardener mix ratio and fully cures after 24 hours. During the test, the stud was programmed to be raised at a rate of 0.01mm/s such that the time to reach maximum stress is no longer than 100 seconds. This rate is chosen based on the 1 MPa/s maximum stress rate indicated in the ASTM D4541 standard for pull-off strength testing. Failure occurs when a plug of material is detached within the system. The interface in which the failure occurred was noted.

Stud-pull test was performed on number of specimen and the peak load was recorded from the load-displacement curve in each case. SEM was conducted on the stud-pull surface and the cross section after the test. From the SEM images in Fig.12 and Fig.13 it can be concluded that the test was unsuccessful in separating the anode completely from the electrolyte in most of the cases. Also the results are inconclusive in respect to determining the peak load for separating anode from the electrolyte in both the unreduced and reduced cases as illustrated in Fig.14 and Fig.15. SEM images presented in Fig.16 and Fig.17 revealed the glue infiltration into the porous anode which is believed to strengthen the anode-electrolyte interface significantly. This was the reason for being

separated between the barrier/bonding layer and the active anode layer in most of the cases instead of being separated from the electrolyte interface.

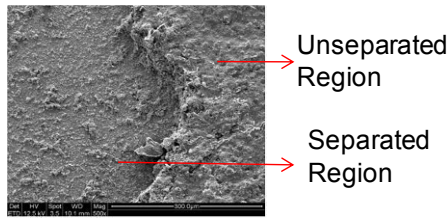


Figure 12: SEM image of stud-pull surface of unreduced specimen.

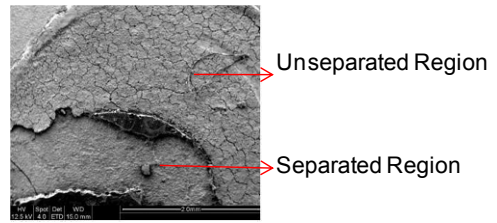


Figure 13: SEM image of stud-pull surface of reduced specimen.

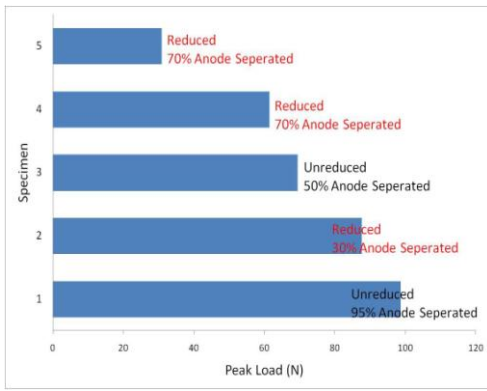


Figure 14: Stud-pull test results for separated anode.

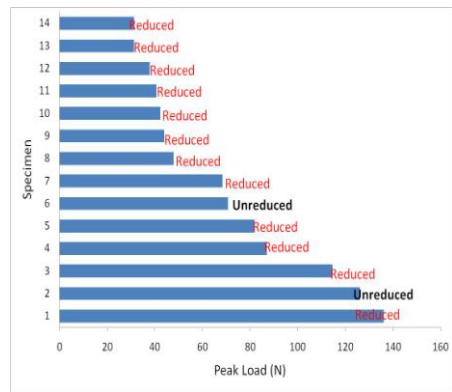


Figure 15: Stud-pull test results for un-separated anode.

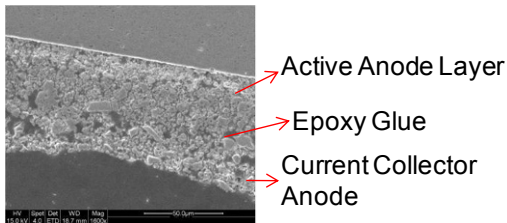


Figure 16: SEM image of unreduced cross-section after stud-pull test.

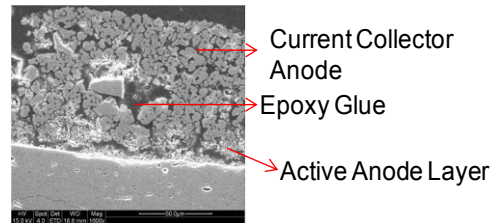


Figure 17: SEM image of reduced cross-section after stud-pull test.

In the next step, the four point bending experiment was performed as its ability to quantify the interfacial fracture energy between a coating and a substrate. The inner loading span distance was kept as 40mm and the outer span distance was 60mm. In the four point bending experiment, the delamination occurs due to the combined effect of residual stress present in the specimen and the effect generated by the application of an applied mechanical load. The energy release rate G is related by the equation [16], [17]

$$G = G_p + G_r + G_{pr} \tag{1}$$

where G_p is the residual stress independent contribution to the crack driving force, G_r is the contribution due to the relaxation of the residual stress, and G_{pr} is the contribution due to the interaction between applied load and residual stress.

From the theory of four point bending experiment for interface crack analysis, as long as the crack front remains between the inner loading span, it is subjected to the constant bending moment. The steady state energy release rate is achieved for the condition of the crack length being much larger than the free surface. The steady state energy release rate G_p can be obtained analytically under these circumstances by considering the difference between the strain energy under cracked beam and uncracked beam. There is always negligible strain energy in the beam above the crack and as a result G_p can be obtained by considering the energies in the uncracked section and in the section of the lower beam beneath the crack. From the Euler Bernoulli beam theory and plain strain condition, G_p can be calculated from reference ([16], [17]) as

$$G_p = \frac{M^2}{2b^2} \left(\frac{1}{E_{c,2}^* I_{c,2}^*} - \frac{1}{E_{c,4}^* I_{c,4}^*} \right) \quad (2)$$

With the constant bending moment $M = PL/2$. Here I is second moment of inertia, b represents the width of the specimen, E represents the Young's modulus and the subscript 1, 2, 3, 4 refer to the substrate, anode, electrolyte and stiffener respectively. The plateau in the load displacement curve indicates the stage of stable crack propagation through interface.

Residual stress is generated in bi-layer SOFC while cooling from the manufacturing temperature (1100°C) to room temperature due to thermal coefficient of expansion (TCE) mismatch between the anode and the electrolyte. The residual stress dependent contribution in energy release rate G_r can be calculated by the equation [16]

$$G_r = \frac{1}{2b} (E_2^* I_2 k_2^2 + E_3^* I_3 k_3^2 + E_2^* A_2 \varepsilon_2^2 + E_3^* A_3 \varepsilon_3^2) \quad (3)$$

where k_2 and k_3 are the curvatures of anode and electrolyte respectively due to residual stress present in the SOFC. The stress distribution in anode and electrolyte are calculated according to reference [18] and from that the curvatures of anode and electrolyte are calculated by reference [16].

The third term in equation 1 can be calculated by [16]

$$G_{pr} = -\frac{Pl}{2} k_2 \quad (4)$$

Results

In Fig.18 the analytical residual stress distribution in the anode and the electrolyte due to cooling from the elevated temperature (1100°C) to the room temperature has been presented. Stress is generated because of the difference of the Thermal coefficient of expansion (TCE) in both the anode and the electrolyte material. It has been found that the residual stress is tensile in brittle anode material which makes it more susceptible to fracture. From the figure it is also found that the stress gradient in the anode is negligible comparing to that of the electrolyte.

As stated in equation 1, the energy release rate has three terms corresponding to the contribution from the applied bending moment, from the residual stress and from interaction between the applied load and the residual stress. The relative significance of these three terms to the total energy release rate is presented in Fig.19. As illustrated in this figure, the residual stress plays an important role in the calculation of total energy release rate.

Fig.20 and Fig.21 show the parametric study of the energy release rate as a function of anode thickness and anode elasticity respectively. In Fig.20, R is ratio of anode thickness and electrolyte thickness whereas in Fig.21 it is defined as the ratio of anode elasticity and electrolyte elasticity. Fig.20 indicates that the interfacial fracture energy increases with anode thickness and from Fig.21 it can be concluded that the energy release rate decreases for more compliant anode as less strain energy is stored in the coating when it has a low stiffness.

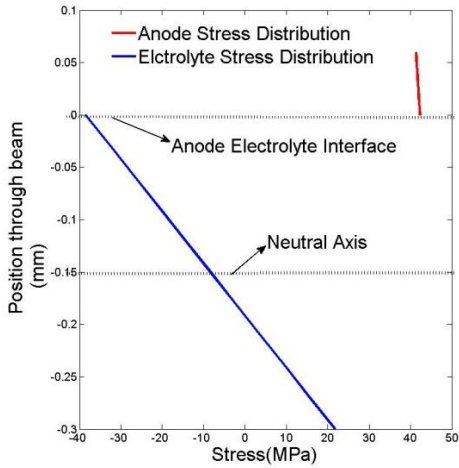


Figure 18: Residual stress distribution in anode and electrolyte.

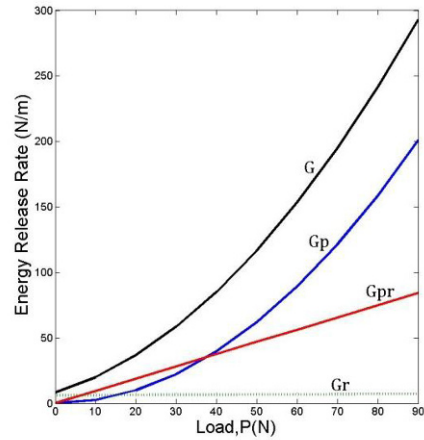


Figure 19: Interfacial fracture energy release rate vs load curve.

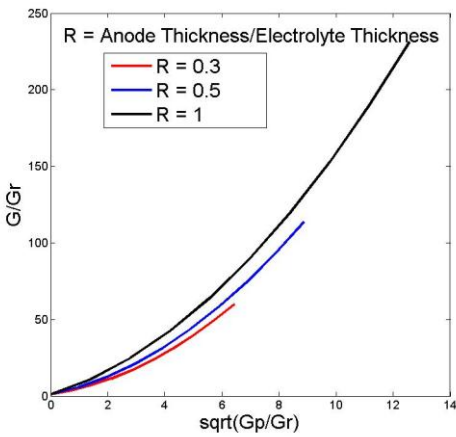


Figure 20: Fracture energy as a function of layer thickness.

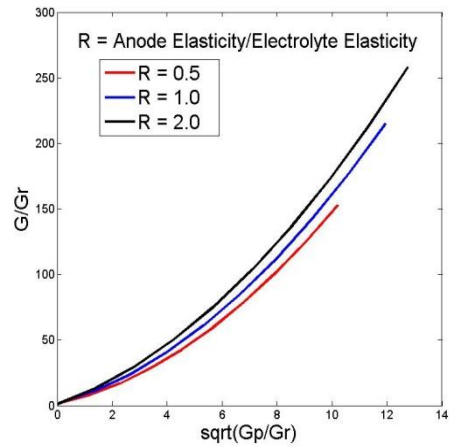


Figure 21: Fracture energy as a function of layer elasticity.

The four point bend experiment was performed and the interface was monitored with a microscope during the experiment. After the experiment the anode-electrolyte interface was analyzed using SEM. Fig.22 and Fig.23 represent the microscopic and SEM observation of the interface respectively. The images indicate that the crack initiated from the electrolyte propagated through the anode-glue interface instead of the anode-electrolyte interface. It is believed that the anode is too weak and thin (60 μm) to stop the crack at the interface and instead the crack went through the anode and delaminated the next interface. Further research is going on to purposely delaminate the interface just under the electrolyte crack by putting a weak carbon layer where the debond is intended to start. Another approach may be strengthening the anode under the crack by inserting viscous glue in the porous anode. Further experiments will be conducted using both the approaches.

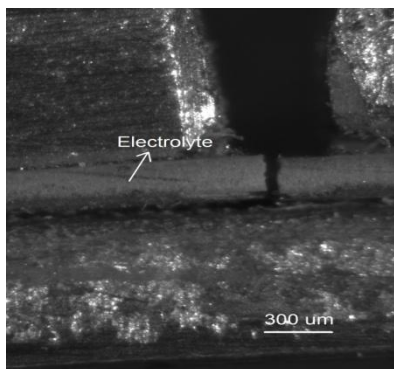


Figure 22: Microscopic image of the interface during experiment.

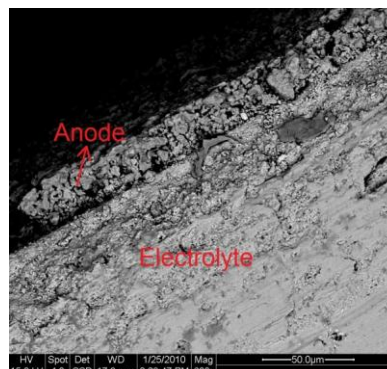


Figure 23: SEM observation of the interface after the experiment.

Conclusion

Stud-pull experiment was unsuccessful to provide any conclusive results to measure the interfacial adhesion strength. SEM images of the cross-section of specimen after the stud-pull test revealed that glue infiltrated into the porous anode which changed the interfacial strength significantly, making the test unsuccessful to separate the anode from the electrolyte. Next the four point bending experiment was performed to measure the interfacial fracture energy between the anode and the electrolyte interface in SOFC. However the experiment was not successful in delaminating the anode-electrolyte interface because of very thinness and weakness of the anode. The crack propagated through the anode-glue interface instead of the anode-electrolyte interface. In the future experiments, the approach of externally making defect in the anode-electrolyte interface and strengthening the porous anode with viscous glue will be applied so that the crack can propagate through the anode-electrolyte interface. The X-ray method will be used to validate the analytical residual stress distribution in different layers of SOFC.

Acknowledgement

This project was financially supported by National Science Foundation (NSF) grant no. 0825558. The technical support of NexTech Materials Ltd is also acknowledged.

References

- [1] Blum L., Buchkremer H.P., Gross S., Gubner A., de Haart L.G.J., Nabelek H., Quadackers W.J., Reisgen U., Smith M.J., Steinberger-Wilckens R., Steinbrech R.W., Tietz F. and Vinke I.C. Solid oxide fuel cell development at Forschungszentrum Juelich, *Fuel Cells*, 7, 204-210, 2007.
- [2] Haile S.M., Fuel cell materials and components, *Acta Materialia* 51, 5981-6000, 2003.
- [3] Wincewicz K.C. and Cooper J.S., Taxonomies of SOFC material and manufacturing alternatives, *Journal of Power Sources* 14, 280-296, 2005.
- [4] Li W., Hasinska K., Seabaugh M., Swartz S. and Lannutti J.J., Curvature in Solid Oxide Fuel Cells, *J Power Sources* 138, 145-155, 2005.
- [5] Recknagle K.P., Williford R.E., Chick L.A., Rector D.R. and Khaleel M.A. Three-dimensional thermofluid electrochemical modeling of planar SOFC stacks, *Journal of Power Sources* 113, 109-114, 2003.
- [6] Malzbender J., Wessel E. and Steinbrech R.W., Reduction and re-oxidation of anodes for solid oxide fuel cells, *Solid State Ionics* 176, 2201-2203, 2005.
- [7] Zhang Y., Liu B., Tu B.F., Dong Y.L. and Cheng M.J., Redox cycling of Ni-YSZ anode investigated by TPR technique, *Solid State Ionics* 176, 2193-2199, 2005.
- [8] Waldbilling D., Wood A., Ivey D.G., Electrochemical and microstructural characterization of the redox tolerance of solid oxide fuel cell anodes, *Journal of Power Source* 145, 206-215, 2005.
- [9] Fouquet D., Muller A.C., Weber A. and Ivers-Tiffée E., Kinetics of oxidation and reduction of Ni/YSZ cermets, *Ionics* 9, 103-108, 2003.
- [10] Cassidy M., Lindsay G. and Kendall K., The reduction of nickel-zirconia cermet anodes and the effects on supported thin electrolytes, *Journal of Power Sources* 61, 189-192, 1996.

- [11] Seabaugh M.M. (September 20, 2007) Personal Communication: *Discussion of Anode-Supported and Electrolyte-Supported SOFC Designs*.
- [12] Sarantaridis D. and Atkinson A., Redox cycling of Ni-based solid oxide fuel cell anodes: A review, *Fuel Cells* 7, 246-258, 2007.
- [13] Steinberger-Wilckens R., Haart L.G.J.d., Vinke I.C., Blum L., Cramer A., Remmel J., Blass G., Tietz F. and Quadackers W.J., Recent Results of SOFC Stack Development at Forschungszentrum Jülich. Proc. SOFC VIII, Proceedings of the 8th International Symposium on SOFCs, 98-104, 2003.
- [14] Charalambides P.G., Lunds J., Evans A.G., McMeeking R.A., A Test Specimen for determining the Fracture Resistance of Bimaterial Interfaces, *Journal of Applied Mechanics*, 56, 77-82, 1989.
- [15] Hofinger I., Oechsner M., Bahr H.A., Swain V.M., Modified four point bending specimen for determining the interface fracture energy for thin brittle layers, *International Journal of Fracture*, 92, 213-220, 1998.
- [16] Howard S.G., Tsui Y.C., Clyne W.T., The Effect of Residual Stress on the Debonding of Coating-I, Model for Delamination at A Bimaterial Interface, *Acta Metall. Mater.*, 42, 2823, 1994.
- [17] Yamazaki Y., Schmidt A., Scholz A., The Determination of the Delamination Resistance in Thermal Barrier Coating System by Four Point Bending Test, *Surface and Coating Technology*, 201, 744-754, 2006.
- [18] Tsui Y.C., Clyne T.W., An Analytical Model for Predicting Residual Stress in Progressively Deposited Coating Part 1: Planar Geometry, *Thin Solid Films*, 306, 23-33, 1997.

Die Separation Strength for Deep Reactive Ion Etched Wafers

D. A. Porter, Graduate Research Assistant, University of Louisville, Department of Mechanical Engineering, Louisville, KY 40292, daport02@gwise.louisville.edu

T. A. Berfield, Asst. Professor, University of Louisville, Department of Mechanical Engineering

Abstract

For the microfabrication industry, die separation is one of the most critical steps in producing an undamaged, stand-alone micro-scale device. Traditional separation methods include the use of dicing saws and/or backside grinding to dice-by-thinning. Excessive forces, vibrations, and surface contact involved with these methods can cause undesirable side-wall chipping and microcracking, which often translates to inoperable devices. Deep Reactive Ion Etching (DRIE) offers an alternative technique for die separation with less mechanical force. The DRIE process may be used to either introduce notches that allow for die separation via fracture in three-point bending, or to directly separate the dies by etching completely through the substrate.

This work presents an analysis of the stress concentrations due to DRIE etched notches and the bending stress required to achieve die separation. The defect rate and die strength associated with DRIE-based die separated is compared with traditional saw methods for a variety of notch depths. Results indicate that the DRIE-based separation technique offers modest advantages over the traditional methods, but can also greatly reduce strength if the protective mask is over etched.

1 Introduction

1.1 Background

Typical micro-scale devices made via cleanroom processes are often produced in bulk quantities on a single wafer. Depending on the lateral dimensions of a device, as many as a few hundred can be manufactured on an individual wafer. With expensive required facilities and raw materials, industrial manufacturing of silicon-based electrical and MEMS devices demands mass production to remain economical. Fabrication facilities can optimize throughput by performing batch processes on large diameter wafers containing many die. While larger diameter wafers contain more devices, they can require an extensive amount of time and effort to separate the die in a clean and effective manner.

Any improvements in the die separation process can translate to tremendous cost savings for manufacturers. Gains in efficiency may be achieved in a number of ways. In particular, the product yield can be increased by reducing the amount of material wasted between die, or by lowering the number of die typically damaged during the separation process. Additional concerns include the required separation time and any reduction in die strength due to flaws or micro-scale damage induced during separation.

1.2 Separation Methods

Separation methods for wafer-based devices can be time-consuming and traditionally involves a mechanical grinding process that can lead to lowered die strength. A single induced crack or ample flaw during manufacturing can immediately yield a bad device, or lead to premature failure. Currently most manufacturers separate die by means of mechanical grinding via the use of a diamond saw or more commonly, a "Dicing Saw." Problems that arise from use of a mechanical grinding technique include chipping and cracking on the top and bottom edges of the substrate near the sawn grooves. To lower the amount of damage done to the wafer, diamond tipped saws usually transverse the material at a very slow rate (10 to 15 mm/s) [1]. After completing all grooves along one direction, the wafer must be reoriented and the dicing saw must then repeat the process. Kerf widths, or the groove width dimension, for this type of separation technique are around 20 to 50 μ m for thin wafers [1].

In addition to edge chipping and cracking, dicing saws can also leave residual stresses on the sidewalls that can cause failure at low stresses when undergoing thermal cycling. Another problematic issue with dicing saws is the high-pressure cooling water, which in some systems is applied to cool the blade during the dicing process. The water stream can damage sensitive electrical devices via direct force or contaminate a device via diffusion. Many previous works have noted unacceptable chipping of die edges from dicing saws [2,3], the extent of which is dependent on the cutting rate, blade width, etc.

An alternative separation method of recent interest is dry etching. Although generally more time consuming than dicing, dry etching may offer benefits in the other areas of concern. During dry etching, the semiconductor material is removed through the bombardment of ions. In most cases, ions are supplied by a plasma of reactive gases. The gases are passed through a very high magnetic field alternating at a high frequency with a power of a few hundred watts. This effect causes the gas particles to rip apart, and thus becoming ionized (*i.e.* a plasma). The etch rate is dictated by the substrate material, the operating pressure, and the gas flow rates. Some common gases that are used for etching are CF_4 , O_2 , and Ar. Dry etching performed by ionized gases is almost always anisotropic and leaves very smooth surfaces. Reactive ion etching (RIE) is one form of dry etching in which plasma generated ions bombard a substrate that has been patterned with a photo-mask. Typical etch rates for RIE can vary from 1nm to $1\mu\text{m}$ per minute. Due to the anisotropic nature of RIE, extremely vertical sidewalls are very difficult to achieve, which makes RIE best suited for short etch depths.

A more advanced dry etch is called deep reactive ion etching or DRIE. In this method the substrate is etched as normal but with alternating passivation cycle inserted into the process. In the first phase of the process ions from plasma gas bombard the surface and bond with silicon while releasing it from the surface. This is the same process that RIE goes through when etching. During the second phase of the process the side walls and bottom of the notch are passivated with a polymer or oxide coating that prevents the etch cycle from cutting into the sidewalls. Here, the plasma ions are forced down in the vertical direction, causing the passivated bottom of the notch to be etched more quickly than the sidewalls.

The high aspect ratios (depth-to-width ratio of the etched feature) that are possible with the alternating etching/passivation cycles are what distinguish DRIE from scribing. Aspect ratios of around 25:1 are not uncommon for the DRIE process [4]. Depending on the substrate and processing conditions, the DRIE method can etch at rates from 50nm to $24\mu\text{m}$ per minute [5]. For silicon substrates using SF_6/O_2 (etching/passivation gas), etch rates up to $10\mu\text{m}/\text{min}$ can be achieved [6]. Another commonly used passivation gas is C_4F_8 .

The ability to construct vertical sidewall features uniformly over large areas is a very attractive tool for the patterning and manufacturing of MEMS devices. However, little is known about the effects of the passivation process on the sidewalls, the geometry effects of DRIE notches on die separation, and the effect on overall die strength. The objective of this research is to investigate the strength effect of separating wafers using deep reactive ion etching (DRIE) in comparison with standard separation methods. Most emphasis will be placed the effects that different DRIE trench geometries have on the bending stress required for die separation and also the corresponding defect rate via fracture stress for separated die.

2 Procedure

2.1 Standard Dicing Saw Notched Samples

The dicing blade used for all cuts had a nominal width of $70\mu\text{m}$. Five streets were cut aligned to the $\langle 110 \rangle$ wafer flat and then another five streets were cut perpendicular to the $\langle 110 \rangle$ wafer flat. Each street was placed 17.07mm apart, giving a die size of 17mm. Dicing speed was performed at a rate of 1 mm/s. The dicing depths for a wafer was 25, 50, 75, or 100% of the total wafer thickness. The initial total wafer thickness was $525 \pm 20\mu\text{m}$. For all specimens, P/Boron type, $\langle 100 \rangle$ wafers from the same lot were used (Silicon Valley Microelectronics, Inc.).

After dicing, the wafer package was carefully removed from the vacuum chuck. Then the wafer and tape were cut apart from the metal support ring. The dicing tape was then sheared at a 0 to 10° angle so that minimal normal force was applied to the wafer. In the case of 100% cut wafers the dies were simply pulled from the tape.

2.2 DRIE Etched Samples

The trench profiles on the <100> plane were the same for the DRIE samples as the diced samples: 17x17mm die with 70 μ m wide trenches. A thick layer of photoresist was used to protect the silicon that is not to be etched. The resist thicknesses were 3.2 μ m for the 25% and 50% etch depth depths and 4.25 μ m for the 75 and 100% etch depths. SF₆ and C₄F₈ were the etching and passivation gases used, respectively. The DRIE procedure was performed on an STS MESC Multiplex ICP.

After about 150 cycles (30 minutes) in the DRIE machine, the samples were removed and put on a hot plate at 115°C for 2 minutes. This helps harden and strengthen the photoresist so it can survive the deep etching process. Afterwards it is adhered to another wafer with Crystal Bond and placed back into the DRIE machine and etched the remainder of the desired depth. Before all DRIE samples used for fracture data were fabricated, the etch rate of the equipment was calibrated to determine the number of cycles required to reach each depth.

2.3 Die Separation and Fracture Strength

A 3-Point bending structure was designed in Solid Edge and machined in the University of Louisville's prototyping lab. [Figure 1](#) show an isotropic view and side view of the bending structure design. The length of the support structures on the base is 4.0 inches, to allow testing of full 4 inch diameter wafers. Aluminum was used for all components of the structure. To measure the exerted force on the samples, a 25 lb_f and a 100 lb_f load cell will be used and LabVIEW will acquire the data. [Figure 2](#) shows the machined 3-point bending structure fastened to a linear actuator and the LabVIEW program. A set of weight standards were used to calibrate the force transducers to ensure accuracy of the measurements. For all measurements, the adjustable bottom span was set to 15.0 mm.

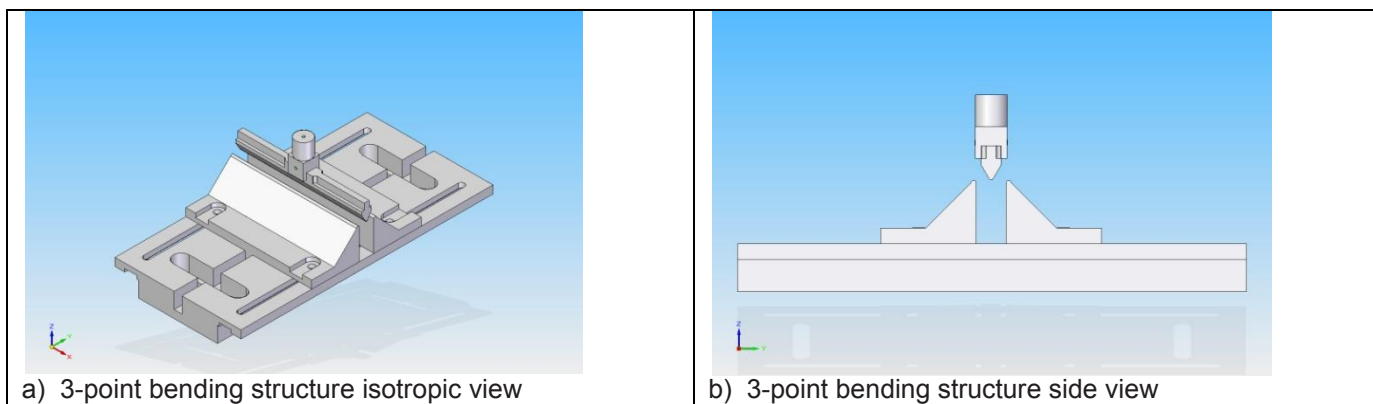


Figure 1. Assembled bending structure schematic, showing extra wide design to accommodate full 100 mm diameter wafers.

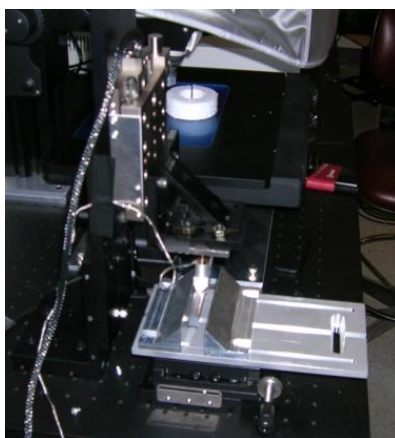


Figure 2. Machined 3-point bending structure and testing stage. A span width of 15.0 mm was used for all tests.

The die were separated sequentially in a consistent manner. [Figure 3](#) below shows the layout, labeling scheme, and the separation routine for the wafers. The first separation cleave of the wafer had a width of

97.4mm, the second and third cleave will had a width of 72.7mm, and the rest of the widths for cleaving were 17.0mm. After the die were separated by loading each notch in 3-point bending, each individual die was then tested in the 3-point bending structure to determine the failure strength.

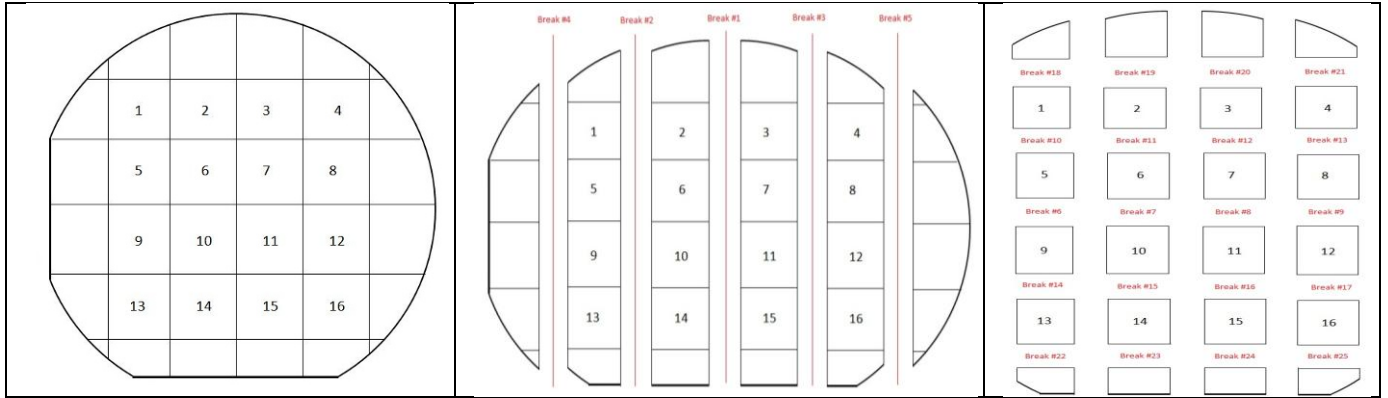


Figure 3. Layout, labeling, and cleaving scheme for the wafers.

The maximum normal bending stress was calculated for both the ultimate strength of each individual die, and the separation stress for the notched specimens by:

$$\sigma = \frac{Mc}{I} = \frac{3 FL}{2 wt^2} \tag{1}$$

where, M is the moment at the center of the beam, c is the distance to the neutral axis, I is the moment of inertia, F is the force applied to the beam, w is the width of the beam, and t is the thickness of the beam at the weakest point.

3 Results and Discussion

3.1 Stress Concentration Derivation

To derive the theoretical stress concentration factors for the bending separations, ANSYS 12 and Solid Edge were utilized. Before modeling the cross sections, the notch geometry formed by both the DRIE and dicing saw methods was inspected, [Figure 4](#). The geometries formed by the two vary significantly for various reasons. DRIE trench geometry varies by depth as this method of material removal depends on the gas flow and heat transfer about the sample. Shallow trenches have a much flatter base than the deeper etched trenches. Shallow features have a much flatter bottom as the etching gas has a more uniform flow pattern of fresh ionized gas. As trenches become deeper, the profile becomes more rounded due to the difficulty of the ionized gas flow to remain uniform. This is similar to having low flow velocity near sidewalls in pipe flow. Deep trenches and shallow trenches did show the same radii of curvature at the corner connecting the trench wall and the base. For the FEA modeling, it was assumed that the trenches are etched anisotropically, meaning that the walls are perfectly vertical. Dicing saw trenches had the same bottom radius and sidewall slope. To determine the radii of curvature for all specimens, images were taken of the cross-section and the curvature was fit to a circle ([Figure 4](#)).

With ANSYS 12 and the various models made in Solid Edge, stress concentration factors were derived for various depths while keeping the loading conditions, stiffness matrix, and loading magnitudes constant. Since silicon is an anisotropic material it has a 6x6 stiffness matrix $[C]$ which relates stress and strain. The Hook's law relationship and stiffness properties are given by [7]:

$$\begin{bmatrix} \sigma_x \\ \sigma_y \\ \sigma_z \\ \tau_{yz} \\ \tau_{xz} \\ \tau_{xy} \end{bmatrix} = \begin{bmatrix} c_{11} & c_{12} & c_{12} & 0 & 0 & 0 \\ c_{12} & c_{11} & c_{12} & 0 & 0 & 0 \\ c_{12} & c_{12} & c_{11} & 0 & 0 & 0 \\ 0 & 0 & 0 & c_{44} & 0 & 0 \\ 0 & 0 & 0 & 0 & c_{44} & 0 \\ 0 & 0 & 0 & 0 & 0 & c_{44} \end{bmatrix} \begin{bmatrix} \epsilon_x \\ \epsilon_y \\ \epsilon_z \\ \gamma_{yz} \\ \gamma_{xz} \\ \gamma_{xy} \end{bmatrix} \tag{2}$$

where σ , τ , and ϵ are normal stress, shear stress and strain respectively. The values of $[C]$ in the $[100]$ directions are $c_{11}=167.4$ GPa, $c_{12}=65.23$ GPa, $c_{44}=79.57$ GPa [7].

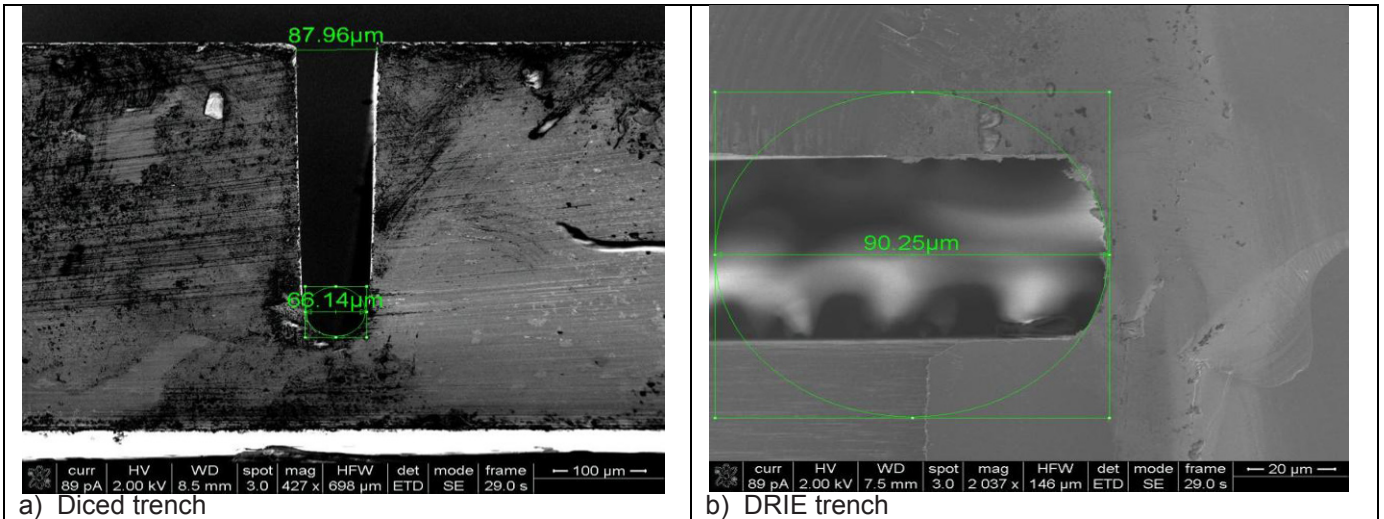


Figure 4. Comparison of diced versus DRIE trench profiles. Radii of curvature were fit for each of the notch depths tested.

The stress concentration factors were derived from the maximum 1st principal stress of the model and were found using:

$$SCF = \frac{1st\ Principal\ Stress}{Nominal\ Stress} \quad (3)$$

where, the nominal stress is the maximum bending stress calculated at the minimum cross section of the trench. [Figure 5](#) shows FEA results for a 70% etch depth for both the diced and DRIE notch geometry profiles.

Note that the maximum 1st principal stress is located in different places in the FEA analysis. For the dicing trench it is located at the very bottom of the profile while the maximum 1st principal stress for the DRIE is at the corner fillets. This was often observed to be the initiation point for cleavage in the separation test. For both trenching methods, profiles were modeled at 10 % increments of notch depth to derive the stress concentration factors over a range of geometries, the results of which are shown in [Figure 6](#).

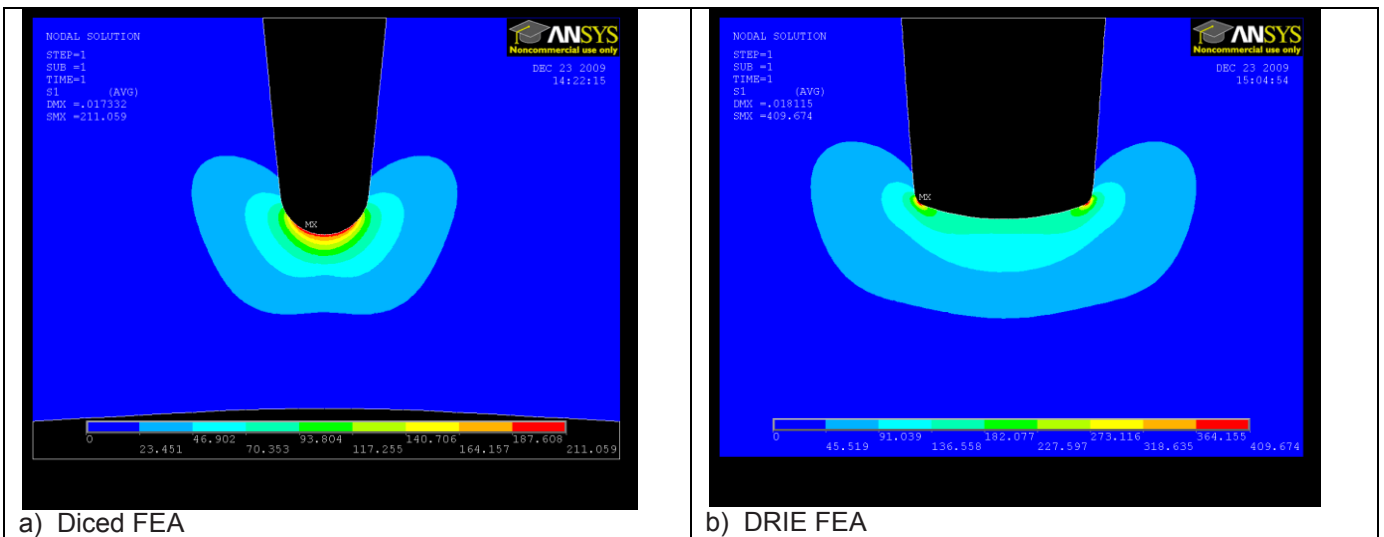


Figure 5. Finite element modeling results showing 1st principal stresses resulting from a 2 Newton force applied in 3-point bending.

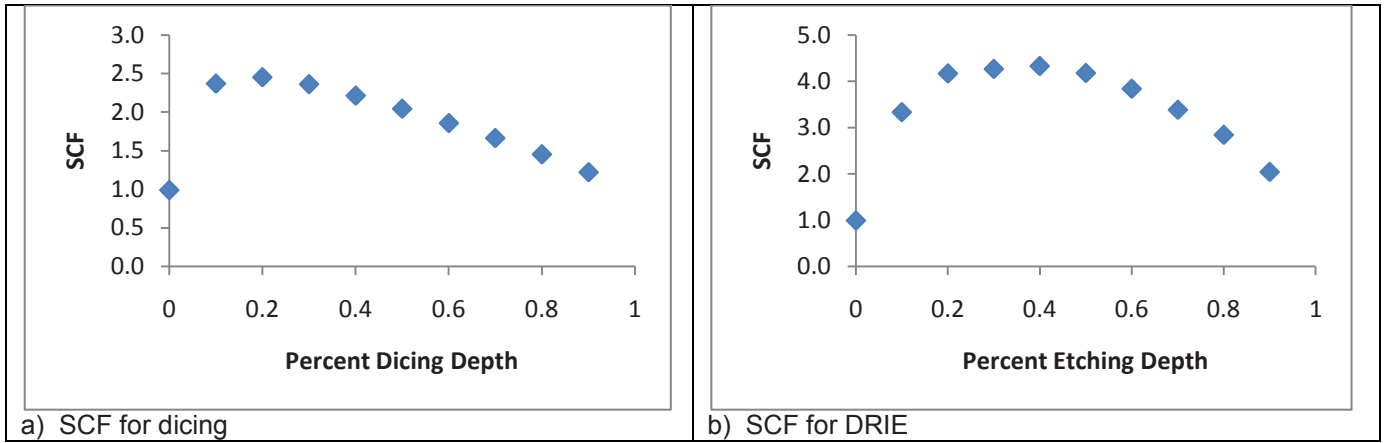


Figure 6. Stress concentration factors calculated from FEA modeling for a range of dicing and DRIE trench profiles.

3.2 Wafer Cleaving and Die Fracture Strength

Data results for the 25% diced samples are shown below. It was found that the Weibull fit was very effective at representing the cleaving (separation) stress for the samples. The Weibull parameters for the separation stress data were $\alpha=533.9$ MPa and $\beta=5.52$. Figure 7-9 show the cumulative distribution, probability distribution function, and the frequency versus cleave/fracture stress respectively.

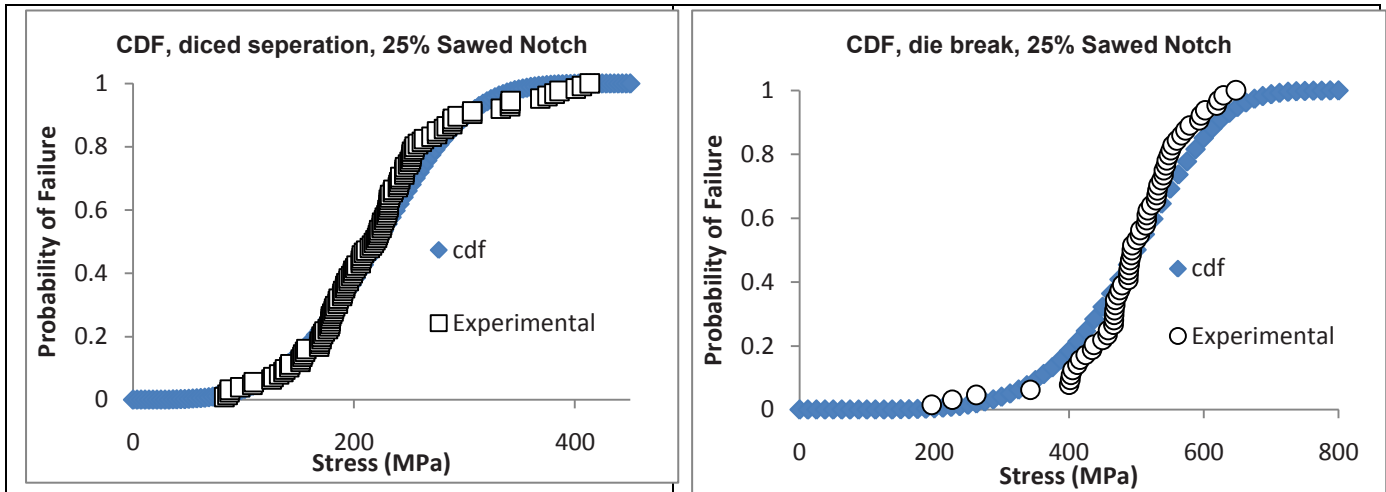


Figure 7. Cumulative distribution function for the cleave and die fracture tests regarding samples diced 25% deep.

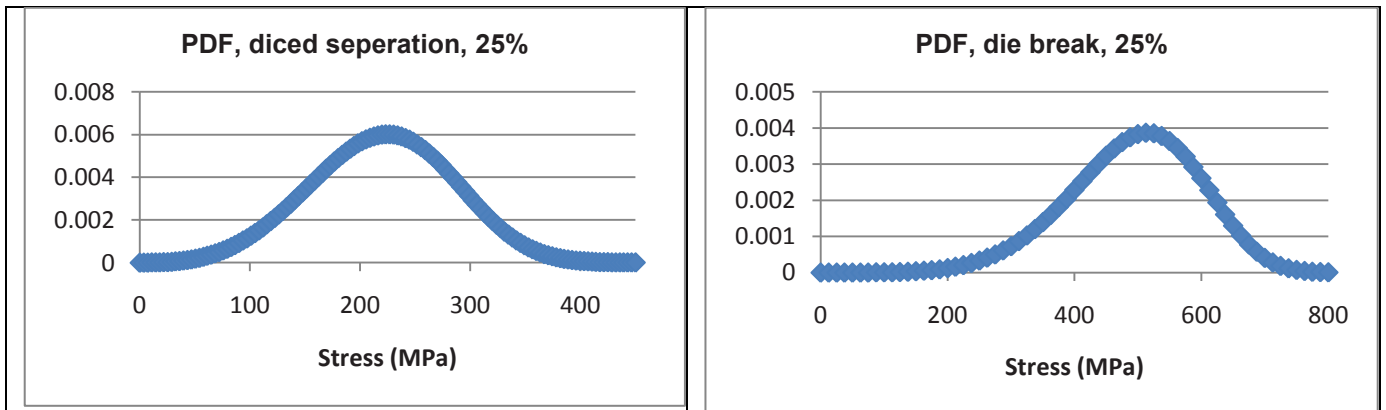


Figure 8. Probability density function (PDF) for the cleave and die fracture tests on samples saw diced 25% deep.

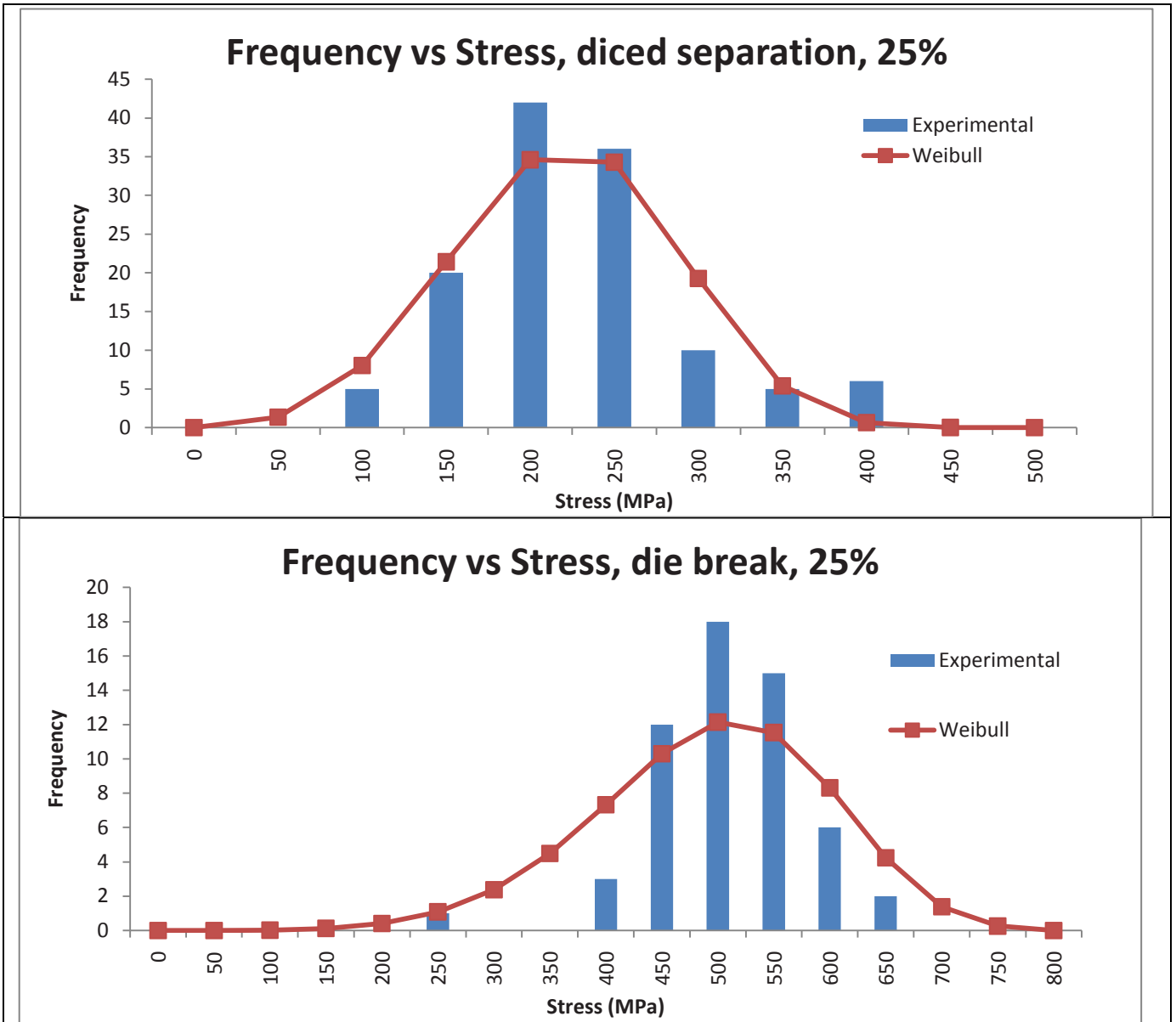


Figure 9. Frequency versus stress for the experimental data and the Weibull fit for the cleave and die fracture tests regarding samples diced 25% deep.

Wafer breaking stress for all of the diced and DRIE samples are shown in [Figure 10](#) below. The error bars represent one standard deviation. No 25% DRIE data is reported, as the energy released when the wafers were cleaved was very high, often resulting in crack propagation throughout the sample. Interestingly, the stress that the 50% wafers cleaved at was less than the stress at 75% and 25%. As the data shows, there is no conclusive dependence on trench depth versus the cleaving stress at separation, at least for this initial wafer thickness. This indicates that the flaw density and average flaw sizes remain relatively constant over the trench surfaces.

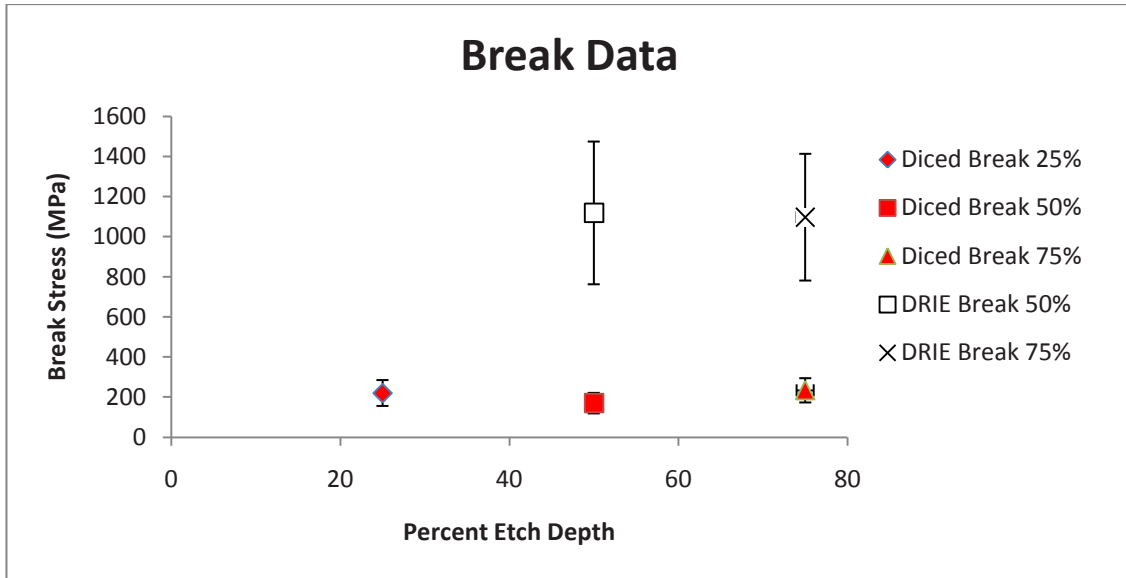


Figure 10. Maximum cleave stresses for the different sample wafers, calculated incorporating the modeled stress concentration factor for each notch geometry.

Die fracture stresses resulting from the different separation methods are shown in Figure 11 below. In the two figures below it is evident that the stresses at which die fracture decrease as trench depth increases. This could be explained by a smoother surface derived by the shear plane from separating the individual die. Also DRIE has problems when etching high aspect ratios. If the gas flow is not ultra pure then particles can deposit on the bottom of trenches and form micro-masks. These particles are not swept out easily the deeper the trenches are. This also happens when the flow rate of SF₆ is high. Micro-masks tend to form structures referred to as "grass" which appear like silicon stalagmites [8]. As the DRIE trench aspect ratio increases, the sidewalls become more rugged and flawed which can decrease the fracture stress. Figure 12 shows the formation of such "grass" on the sidewalls of a 100% DRIE separated sample and the micro-pitting of the top surface due to over etching.

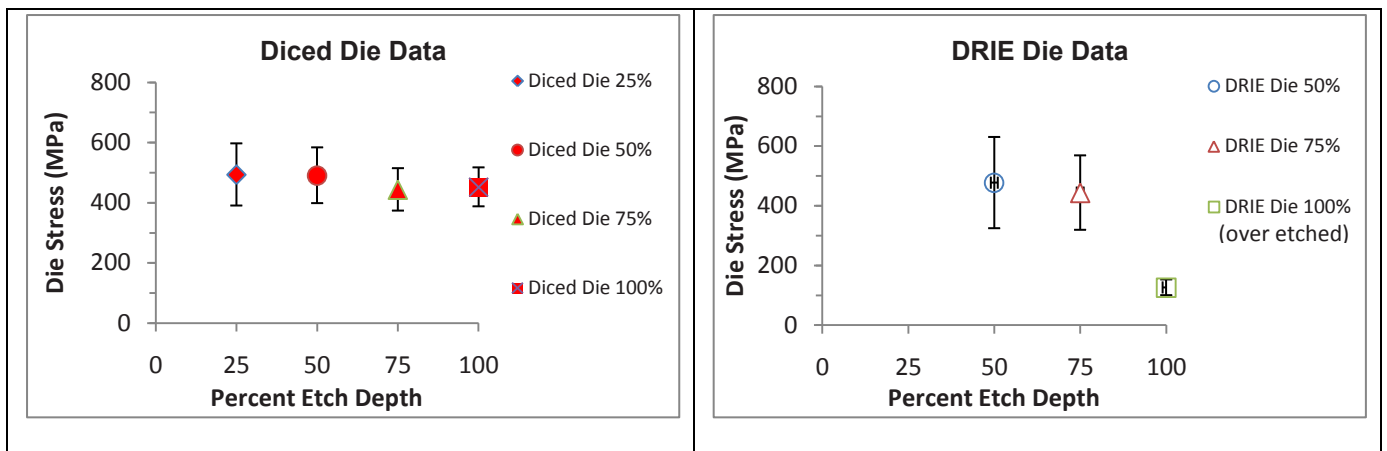


Figure 11. Die fracture stress for all samples tested. Note, the 100% DRIE separated die were slightly over etched, causing penetration of the protective mask and slight micro-pitting damage on the top surface.

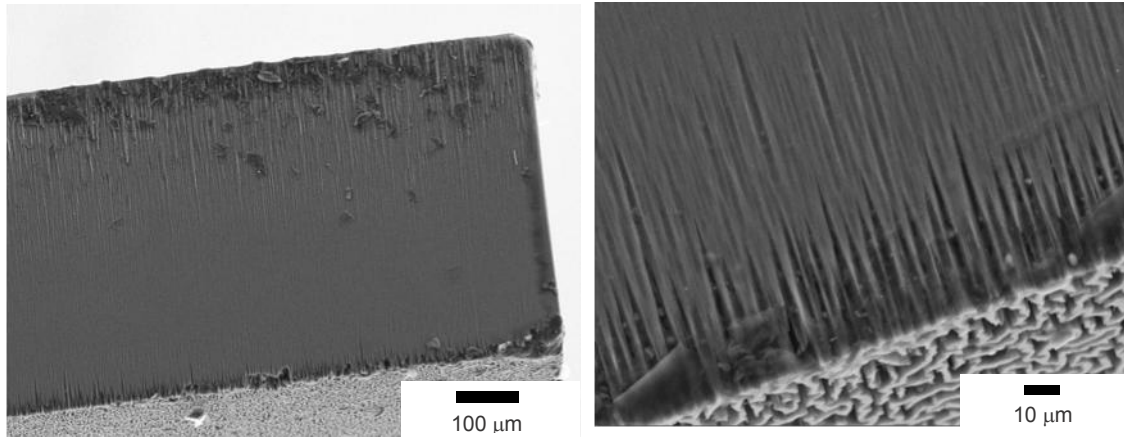


Figure 12. Grass formation along the sidewall of the 100% DRIE specimens, including micro-pitting on the top surface (bottom of right image).

SEM image of the 100% DRIE dies after fabrication show that the protective mask became compromised, resulting in micro-pitting of the top surface (Figure 12). As a result, the measured fracture strength for the 100% DRIE die was over three times lower than that observed for the other DRIE separation depths. The die strengths for the other (25, 50, and 75% trenched) specimens were fairly close, with the dicing saw specimens exhibiting a slightly higher average strength than the DRIE samples at each corresponding notch depth tested.

4. Conclusions

The stress concentration factors associated with notch profiles produced by both DRIE and dicing saw methods were determined with regard to trench depth. Additionally, the stress required to induce separation between die was much higher for the DRIE trenched specimens than the dicing saw notched samples. However, this did not result in a significantly lower final die strength. Finally, it was observed that any over etching of the protective mask during DRIE may result in micro-pitting of the sample surface, which dramatically reduces the die strength.

5. Acknowledgements

The authors wish to acknowledge the support of Mark Crain and the Micro- Nanotechnology Center at the University of Louisville for guidance with DRIE equipment. Additionally, the authors acknowledge the assistance of Scott Cambron with the wafer dicing saw.

6. References

- [1] Cooke, M. "Scribe and Dice", *The Advanced Semiconductor Magazine* **19**, No. 4, p. 20-24, 2006.
- [2] Magjeed, B., Paul, I., Razeed, K.M., Barton, J., and O'Mathuna, S.C., "Microstructural, mechanical, fractural and electrical characterization of thinned and singulated silicon test die", *J. Micromech. Microeng.*, **16**, p. 1519-1529, 2006.
- [3] Landesberger, C., Klink, G., Schwinn, G., and Aschenbrenner, R., "New Dicing and Thinning Concept Improves Mechanical Reliability of Ultra Thin Silicon", *Proceedings of the International Symposium on Advanced Packaging Materials Processes, Properties and Interfaces*, p. 92-97, 2001.
- [4] Jaeger, R.C., *Introduction to Microelectronic Fabrication*, 2nd, ed., Prentice Hall, p. 279, 2002.
- [5] Selbrede, S., Pilloux, Y., "DRIE Technology For MEMS", Tegal Corporation, Plasma Users Group, February 2009.
- [6] Laermer, F., Schilp, A., Funk, K., Offenbergl., "Bosch Deep Silicon Etching: Improving Uniformity and Etch Rate for Advanced MEMS Applications", *Proceedings of the IEEE Micro Electro Mechanical Systems*, p. 211-216, 1999.
- [7] Ikehara, T., Tsuchiya, T., "Effects of Anisotropic Elasticity on Stress Concentration in Micro Mechanical Structures Fabricated on (001) Single-Crystal Silicon Films", *Journal of Applied Physics*, **105** No 9., p. 093524-093534 2009.
- [8] Dixit, P. and Miao, J., "Effect of SF₆ flow rate on the etched surface profile and bottom grass formation in deep reactive ion etching process", *Journal of Physics: Conference Series*, **34**, p. 577-582, 2006.

Temperature Moisture and Mode Mixity Dependent EMC- Copper (Oxide) Interfacial Toughness

A. Xiao¹, G. Schlottig², H. Pape², B. Wunderle³, K M. B. Jansen¹, L. J. Ernst¹

¹Delft University of Technology, Mekelweg 2, 2628 CD Delft, the Netherlands

²Infineon Technologies AG, 81726 Munich, Germany

³Fraunhofer IZM, 13355 Berlin, Germany

Email: A.Xiao@tudelft.nl, Phone: +31 (0)15 278372

Abstract

An ongoing root cause of failure in microelectronic industry is interface delamination. In order to explore the risk of interface damage, FE simulations for the fabrication steps as well as for the testing conditions are generally made in the design stage. In order to be able to judge the risk for interface fracture, the critical fracture properties of the interfaces being applied should be available, for the occurring combinations of temperature and moisture preconditioning. As a consequence there is an urgent need to establish these critical interface fracture parameters. For brittle interfaces such as between epoxy molding compound (EMC) and metal (-oxide) substrates the critical energy release rate (or delamination toughness) can be considered as the suitable material parameter. This material parameter is strongly dependent on the temperature, the moisture content of the materials involved and on the so-called mode-mixity of the stress state near the crack tip. The present study deals with experimental investigation of the delamination toughness of EMC-Copper lead-frame interfaces as can directly be obtained from the production line. A small-scaled test setup was designed. The test setup is suitable for actualizing both pure mode I DCB (double cantilever beam) loading and pure mode II ENF (end notched flexure) loading and allows transferring two separated loadings (mode I and mode II) on a single specimen. The setup is flexible and adjustable for measuring specimens with various dimensions. For measurements under various temperatures and moisture conditions, a special climate chamber is designed. In this paper, the experiment and simulation procedure for establishing the interfacial fracture toughness from fracture test results at different temperatures, especially in the glass transition temperature region of epoxy molding compound (EMC) will be shown. In order to calculate accurate interface toughness, the material property of molding compound is characterized as a function of temperature. A detailed discussion of how EMC responses at its glass transition region will be provided. The influence of the material property on interfacial fracture toughness will be given.

Introduction

It is well known that semiconductor packages are fabricated from highly dissimilar materials. Usually, the fabrication processes take place at high temperature and then the products are cured to room temperature. For some typical processes and/or during the usage, the products have to be served under thermal cycling. Due to difference in thermo-mechanical properties of the dissimilar materials, interfacial delamination related failures appear to be one of the dominate reliability issues. Among other interface problems, EMC to copper interfaces seem to be very critical. In order to predict delamination at high temperature, especially in the glass transition region of the EMC, the material properties need first to be characterized as a function of temperature and time.

Up till now, much research has been contributed to interface characterization for various material interfaces as used in microelectronic applications. However, specially fabricated test specimens were generally used for establishing the critical fracture values and therefore usually those specimens do not have the identical surface conditions as real product interfaces. As a consequence there always remained an uncertainty on the applicability of critical fracture properties thus obtained. Therefore, in the present study, the test specimens are created and separated from real production line packages, such that they really are made with the identical fabrication processes and materials. During the sample production processes, residual stress is generated in the sample. In many literatures the residual stress is not well established or is even omitted when interpreting the interface fracture measurement results by means of FEM simulation. However, it turns out that the crack tip singularity is seriously influenced by the contribution due to residual stress. In the present study, the residual stress from the

fabrication process is well considered and predicted through experimental measurements and FEM analysis as well.

Generally, in delamination experiments an “infinitely sharp” initial crack should be present, that due to loading can propagate along the interface. Only then the fracture toughness and mode mixity can be adequately approximated through FEM-fracture mechanics simulations. In previous work researchers tried to initiate an “infinitely sharp” initial crack through adding a thin small weak layer on the interface (e.g. gold or Teflon), and subsequently applying a fatigue loading. It appears that with this procedure an “infinitely sharp” initial crack generally is not obtained. Testing the sample without a real “infinitely sharp” initial crack then would result into a different type of stress singularity at the onset of delamination. In those cases FEM-fracture mechanics simulation results can not reliably be used for interpretation of the measurement results at onset of delamination. In the present paper a new method to initiate an “infinitely sharp” initial crack is discussed. Since test samples are obtained from real production line packages, the old method, where a small weak layer on the interface is added for crack initiation is not even possible. The newly developed method can well be used for initiation of an “infinitely sharp” initial crack in test samples obtained from real production line packages.

Characteristic for the procedure of establishing the fracture toughness from fracture test results is that adequate FE simulations of the fracture test are required. A necessary first finite element (FE) analysis step is performed to establish the residual stress state due to chemical shrinkage (due to the cure of the EMC) and the subsequent cooling down to room temperature. Here it occurred to be quite important that suitable visco-elastic constitutive models are used for the EMC. It should be noted that in various literatures on fracture test interpretation this first step is completely omitted or just forgotten. It is found that this generally leads to erroneous results for the interface fracture toughness. After the residual stress state is established, the actually interface delamination experiment is simulated in a second step. Since the EMC behaves viscoelastic, in principle, the stress state in the sample is time-dependent, and so the stress singularity at the crack tip is. When the position of the crack tip is changing during the experiment, a second time dependency, related to the crack propagation rate is interacting with the visco-elastic time dependencies. This should be well accounted for in the FE simulations. The present paper will discuss the fracture propagation simulations that have to be used to account for both time-dependent effects.

It is also shown that for room temperature measurements, where the EMC is in the glassy-state, a simplification of the simulation procedure is allowed. In this simplified procedure the actual propagation of the crack during loading is not simulated. Instead, for a chosen crack tip position, step one is first performed using the complete visco-elastic constitutive model to (approximately) establish the crack tip singularity, due to cure and cooling down. Next in the second step the loading is added to the (already cracked) sample. The reason that this simplified procedure for room temperature appears to be admissible is the fact that at room temperature the EMC behaves elastic.

Study of Material Model of EMC

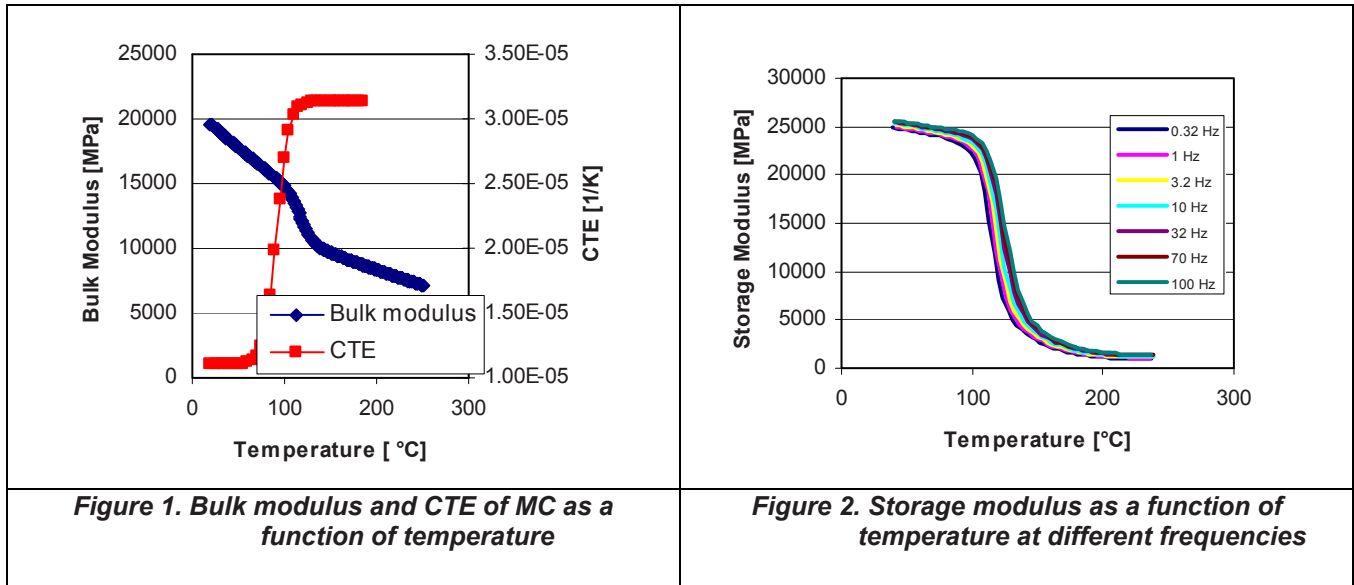
It is well known that the success prediction of delamination depends very much on the reliable material model to be used in the calculations. Further, the accurate material model is necessary to calculate stresses and strains during the cooling down of a package from the molding temperature.

Stresses which are present in an electronic package are partly caused by the thermal stresses during cooling down from the molding temperature. First of all, the warpage of a package during cooling down is caused by differences in CTE of the molding compound and the copper. Secondly, the amount and the direction of the warpage are affected by the mechanical properties of these materials. Next to thermal stresses also cure stresses are present in an electronic package, caused by cure shrinkage of the molding compound during cure. These stresses are building up during the formation of a 3 dimensional cross-linked network. The cure shrinkage of the molding compound causes a volumetric strain and thus it will increase the warpage. In this section, only the basic EMC material model characterization procedure is described. More detailed content can be found in [1]

The mechanical properties of molding compound are highly dependent on temperature and time in the temperature range at which the molding compound is cooled down from molding temperature to room temperature. DMA (Dynamic Mechanical Analyzer) tests are done to obtain the time and temperature dependent

Young's modulus. At the same time the bulk modulus is characterized by making use of a GNOMIX high pressure dilatometer.

A) *Bulk modulus* The bulk modulus and CTE of the MC are measured by making use of a high pressure dilatometer. With this instrument a hydrostatic pressure and or temperature loadings can be applied to a sample. By measuring the volume changes, the CTE and bulk modulus can be calculated. Figure 1 presents the bulk modulus and CTE as a function of temperature. Here it should be noted that as a realistic approximation the time dependency of the bulk modulus is assumed negligible.



As one can see in the above picture, the bulk modulus decreases when the temperature rises, with a clear change around T_g . The CTE increases at passing the T_g . The CTE is implemented in FE-software by making use of user-subroutines.

B) *Cure shrinkage* According to the dilatometer tests it turned out that cure shrinkage occurs. The volumetric cure shrinkage of this molding compound is 0.62 % which is low due to the high filler content. Cure shrinkage is applied in the model as an initial volumetric strain.

C) *Young's modulus* The visco-elastic Young's modulus of the MC is determined by dynamic mechanical analysis (TA instruments Q800). In this experiment a tensile bar [30 x 4 x 0.3 mm] is exposed to a sinusoidal strain with amplitude of 5 μm at different frequencies. During this frequency scan, the sample is heated with 1 $^\circ\text{C}/\text{min}$ to 200 $^\circ\text{C}$. The result of this scan is presented in figure 2. From the result, it turns out that the glassy modulus is around 25 GPa and the rubbery modulus is around 1.5 GPa.

D) *Shear modulus* For implementation of visco-elastic properties in FE-software, the shear modulus is required. However, it turned out that the visco-elastic shear modulus of MC is hard to be measured due to its high value. Therefore this property has to be calculated from the Bulk modulus and the Young's modulus. The following approximation formula is used to do so:

$$G(T, t) \approx \frac{3 \cdot K(T) \cdot E(T, t)}{9 \cdot K(T) - E(T, t)} \quad (1)$$

A master curve of the shear modulus is constructed by making use of time-temperature superposition. This master curve is normalized, due to the fact that the normalized Prony series of the normalized master curve have to be implemented in ABAQUS:

$$G(T, t) = G(T) \cdot \left[1 - \sum_{n=1}^N g_n \cdot (1 - \exp(-t / \tau_n)) \right] \quad (2)$$

Where $G(T)$ is the temperature dependent glassy shear modulus. The part between the squared brackets is the normalized master curve of the shear modulus. The Prony terms g_n and τ_n are found by using a fitting procedure. The same equation is used for the bulk modulus where the $G(T)$ and g_n terms are replaced by $K(T)$ and k_n terms respectively. For this case the k_n terms are set to zero due to the (approximate) time independency of this modulus.

The normalized shear master curve is calculated by dividing the original master curve by its temperature dependent glassy modulus. The normalized curve and the necessary shift-factors to obtain the master curve are presented in [figure 3](#). For temperatures above T_g a WLF shift-function is used. Below this temperature use is made of an Arrhenius shift-function. This model is implemented in ABAQUS by making use of user-subroutines.

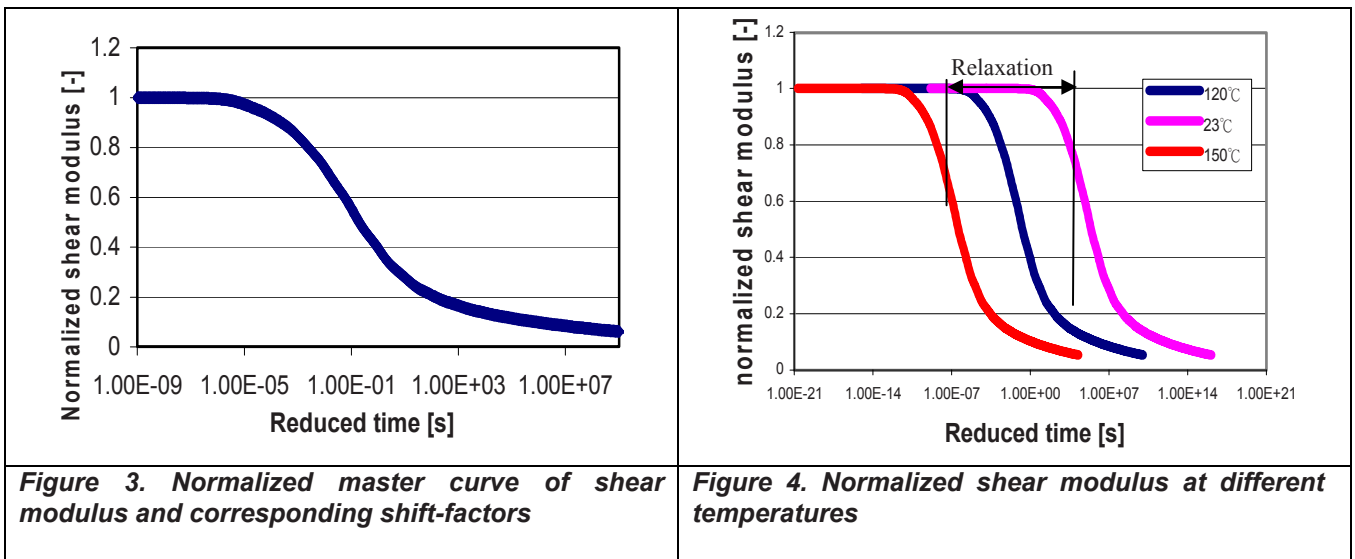


[Figure 4](#) shows the normalized shear modulus as a function of reduced time at different temperatures. It can be seen at 23°C, relaxation takes a very long time, meaning that during a fracture experiment the EMC still behaves elastic. Therefore, for the FE simulation for room temperature an elastic model is used for the EMC. At 150°C, the relaxation happens very fast, the EMC behaves more rubbery. Consequently, in the FE simulations for this temperature the rubbery modulus is used. However, at 120°C, the relaxation time and delamination experiment time are of comparable order of magnitude. This means that the visco-elastic model is necessary for the fracture calculation at this temperature.

From the calculations it turned out that the glassy shear modulus is about 9800 MPa. The temperature dependent bulk and shear modulus cannot straightforwardly be implemented in ABAQUS. These values are calculated from the glassy Young's modulus and glassy Poisson ratio and are presented in [figure 5](#).

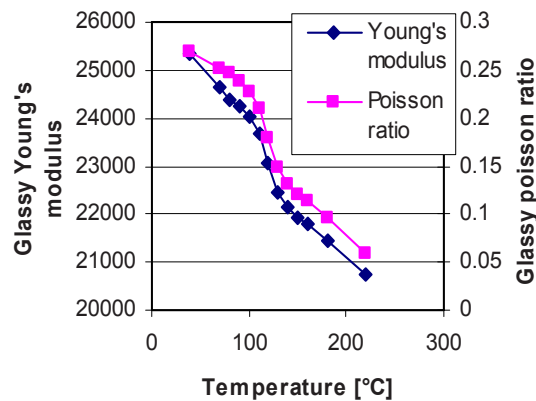


Figure 5. Implemented glassy values of the Young's modulus and Poisson ratio.

With these values, ABAQUS calculates the temperature dependent glassy bulk and shear modulus:

$$K(T) = \frac{E(T)}{3 \cdot (1 - 2\nu(T))}; \quad G(T) = \frac{E(T)}{2 \cdot (1 + \nu(T))} \quad (3)$$

The material model of the molding compound is validated by experimentally measuring sample warpage and calculating from both 2D and 3D simulations. The sample consists of a layer of EMC on a layer of copper. Samples are 35mm long, 1mm wide and 1.2 mm thick. It is first heated up to 175 °C which is the molding temperature of the molding compound and cooled down to room temperature as shown in figure 6. The warpage result is shown in figure 7. It can be seen that the warpage of the sample along the lateral direction from FE models matched quite well with the experiment result.

It is important to note that if the sample is stored for a long period, the internal stress in the structure may relax. Also the molding compound behavior then is influenced by physical ageing. Often the storage time is unknown. In order to establish a more realistic initial stress level in the sample, before the fracture experiment starts, an industrial cooling down process was applied to the sample and further added in the (pre-) fracture simulation.

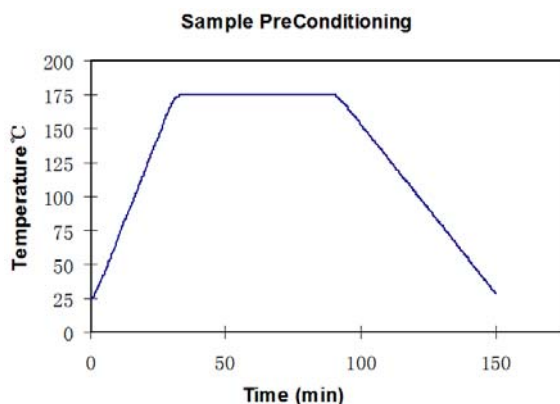


Figure 6. Sample pre-conditioning process

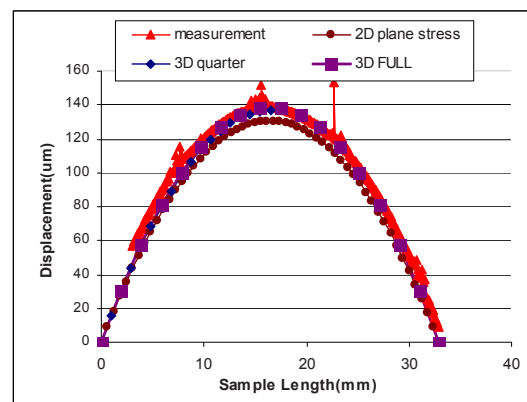


Figure 7. Result of Sample Warpage

Sample Preparation and Test Description

Samples used in this study are made from real product line parts. They are sawn along both sides from the runner on the copper lead pad of a matrix lead frame as partly shown in figure 8. In order to use these runners, several modifications were done as follows:

1. Leadframes without degating holes were used to get sufficient sample length.
2. The leadframe surface was treated with the same process as the real product.

A necessary sharp pre-crack for delamination testing was created by polishing a few millimeters at the side and bend the exposed copper downwards while the sample was compressed (figure 9).



Figure 8. Runner before out of a productive Lead-frame.

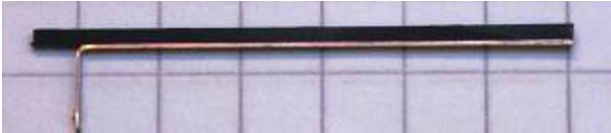
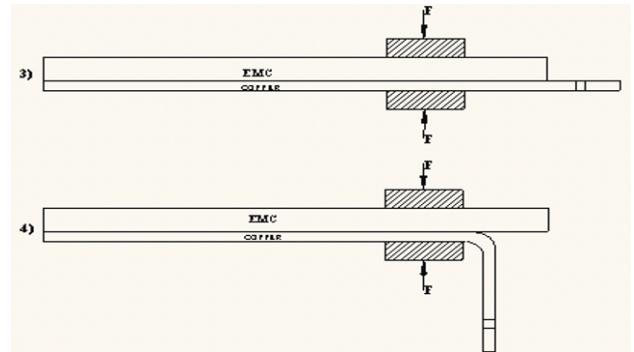


Figure 9. Illustration of creation of a re-arrested initial delamination and side view of the sample



Design of the Test Setup

The setup (shown in figure 10) consists of a loading beam, a lever, four frames, one hook and two clamps. The sample is supported by the two upper frames and the lever is used to transfer the load. The upper frames are first snapped on grooves in the beam. The sample is then inserted in the upper frames, while the mid frame is on the middle of the sample. The hook is crossed through the hole in the copper. Then the hook and the mid frame are subsequently connected with the lever, on which the lower frame is already positioned. The lower frame is finally connected to the lower clamp. By changing the loading position of the lower frame, various (loading) mode mixities can be controlled. The mode II three point bending (TPB) test occurs when not using the lever and directly connecting the middle of the sample with the lower loading frame. The Mode I double cantilever bending (DCB) test occurs when removing the lever, and connecting the hook with the loading frame.

The grooves in the beam and lever are used to provide the test abilities for different sample length and also to prevent frame sliding along the horizontal direction during the experiment. When inserting a sample in the setup, it seems that the sample is loaded immediately due to the gravity of the lever. However, the weight of this lever is very small. It is not expected that this mass will propagate the initial crack of the sample. The small load of this lever can simply be taken into account when interpreting the results by FE analysis (see later).

The advantages of the setup are: 1) It is a rather simple and flexible experimental tool. 2) The loading position and the position of the frames acting on the sample are very well adjusted. The distance between two grooves is accurately defined. For finite element analysis (FEA), it is very important that the modeling situation is exactly the same as in reality. 3) No additional material is used in this setup. Some researches used glues to attach samples on the frames. In this way, it is noted that the non elastic behavior of glues can influence the fracture test results. So it is necessary to include appropriate constitutive behavior of these glues in the FEA. Also these glues often do not survive at high temperatures.

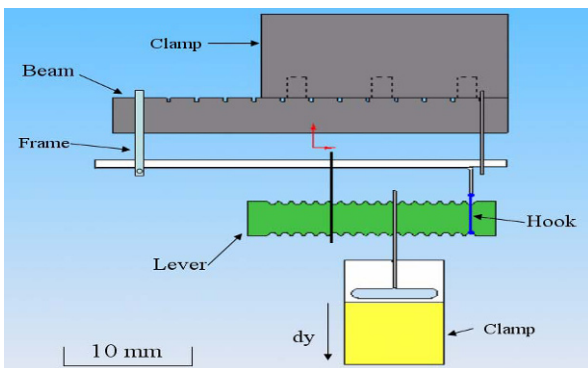


Figure 10. Schematic of the Experimental Setup



Figure 11. Temperature and Moisture Chamber

A special chamber is designed for testing samples at different temperature and moisture conditions (see also [figure 11](#)). The chamber consists of three Teflon parts and one aluminum part. Part number one is used for moisture inlet and part number two is used for moisture outlet. Part number 3 is an isolation layer. It is used for protecting heat loss during temperature testing. Four glass windows are mounted on this layer. The front window is used to observe crack growth inside the chamber and the remaining three windows are used for access with external light resources. These four windows are parallel to the windows bonded on part four. Part number four is a conduction layer. It is used for transferring heat into the chamber during temperature test. Several heating elements and thermal couples are mounted in this part.

Experiments were preformed as follows:

- 1) All the test samples were pre-conditioned as indicated in [figure 6](#).
- 2) Then the sample was clamped in a mixed mode bending tool ([figure 12](#)).
- 3) The sample was pre-heated to the ideal temperature in the setup for one hour.
- 4) Loading was performed at different loading mixities and different loading rates.
- 5) During experiment, a high speed camera was used to monitor the crack growth.

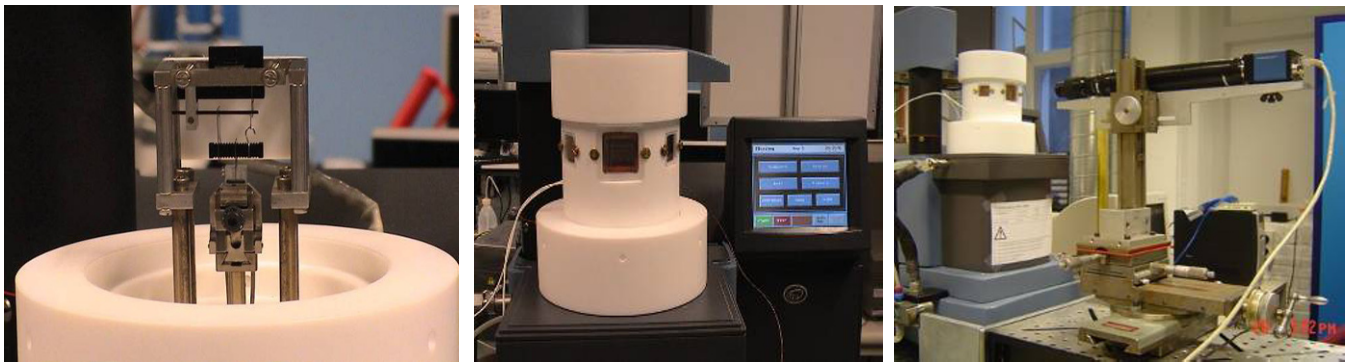


Figure 12. Setup Clamped in Tensile Tester with oven and camera

Experimental result

Experiments were done at different temperatures. [Figures 13](#) and [14](#) show the force-displacement results from DCB tests and MMB tests. From the test results, initially, the force-displacement increasing curve represents the opening of the crack. When the pre-crack starts to propagate, the force decreases. It is found that the crack growth is not stable. From the test results, it can be seen that if keep the experiment conditions as constant, the measured curves overlap. This proves the test setup is quite reliable and the experiments are reproducible. The mode I test results (shown in [figure 13](#)), are captured from two different pre-crack length samples. Because of the long plastic deformation zone, it is difficult to characterize the crack length during crack growth. Here, the samples were made with two different pre-crack lengths to observe crack length effect on DCB fracture toughness. A constant loading speed of 20 $\mu\text{m}/\text{min}$ was used to study the pre-crack effects on the fracture performance of the DCB specimens.

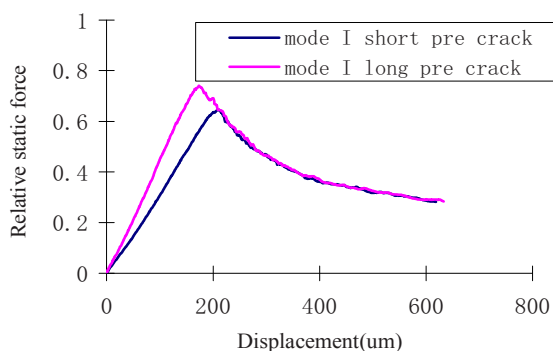


Figure 13. DCB Test Results

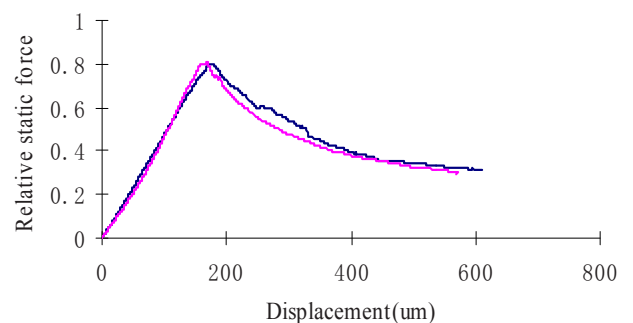


Figure 14. MMB Test Results

Evaluation experiments were performed at different temperatures and different loading rates. Figure 15 shows a test result in the glass transition temperature (T_g) region of the EMC. If we arrest the crack propagation by fixing the prescribed opening displacement at a certain moment, we observe that the force relaxes. This clearly indicates that at that temperature EMC behaves time dependant viscoelastic.

In order to properly investigate the fracture properties in the glass transition temperature region, the measurement procedure was modified, such that at certain time intervals the crack was resisted through unloading. After crack resist and unloading a certain relaxation time was applied. Subsequently, the sample was reloaded until crack propagation continued. This procedure is shown in Fig. 16 for a test at 120 °C, which is about the glass transition temperature of the EMC being considered.

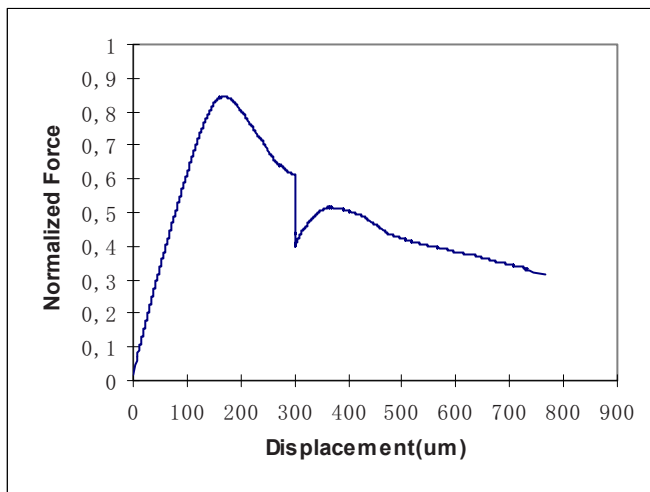


Figure 15. MMB test at 120 °C (arrested crack growth for 30mins)

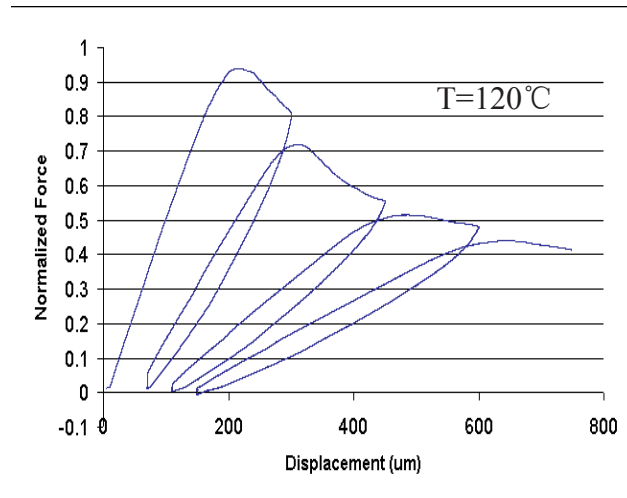


Figure 16. MMB test at 120 °C

As expected, it is observed that here the unloading and loading paths are almost identical and crack propagation restarts at forces slightly lower than at crack arrest level of a previous cycle. The FE simulations for 120 °C experiments are performed on FE models where the crack length corresponds to experimentally established crack tip positions at each cycle. It is known that during crack propagation, the stress state in the sample is changed due to time dependent behavior of EMC. It is found quite time consuming in FE analysis to simulate the real crack growth. Therefore, in the model, the crack growth is not simulated. Instead the force/displacement and the crack length of each loading cycle at the moment where the crack continues propagating after the arrest period are used. E.g. in the first loading cycle, the moment that the pre-crack starts to propagate is taken into account. For the second cycle, the moment that the extended (pre-) crack starts to grow is considered, etc. In between the two cycles, stress relaxation is considered in the FE analysis.

The same experiment procedure has also been performed at room temperature (The result is shown in figure 17); where the EMC is expected to be elastic. It can also be seen from this result that the unloading curve coincides with the re-loading line. This proves that for delamination measurements at room temperature and for the EMC under consideration, therefore simple continuous crack testing can be applied. This is because the material can be considered as “glassy elastic” during the crack propagation.

In this case a simplification of the simulation procedure is allowed. In this simplified procedure the actual propagation of the crack during loading is not simulated. Instead, for a chosen crack tip position, the previously discussed 1st step is performed using the complete viscoelastic constitutive model to (approximately) establish the crack tip singularity, due to cure, cooling down and preconditioning. Next in a 2nd elastic step the external loading is added to the already cracked sample. For verification the critical energy release rate established with this simplified procedure was compared to the result based on simulation of the complete cyclic test procedure.

This simplified procedure for establishing the critical energy release rate and mode mixity for a chosen crack tip position can also be used for temperatures far above the glass transition temperature. For example, at 175 °C the

relaxation of stress occurs within a fraction of a second. We thus can perform an elastic simulation in the 2nd step, this time while using the “rubbery modulus” values as quasi-elastic modulus.

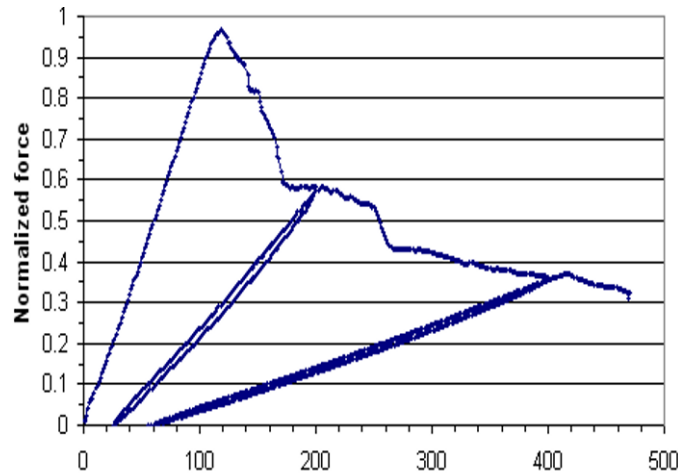


Figure 17. . The modified test procedure for delamination testing applied at room temperature (Force-displacement data at 23 °C)

Finite Element Model

It is found that for the present measurement setup with the bending sample, the lever system and “razor blade” load transfer, FEM-fracture mechanics simulations must be geometrically non-linear, while all the parts must be included in the model. This is because during loading and crack propagation, several parts of the system undergo a non-negligible rotation. As described before, a necessary 1st FE analysis step is performed to establish the residual stress state due to chemical shrinkage and the subsequent cooling down to room temperature. Here it occurred to be quite important that suitable viscoelastic constitutive models are used for the EMC.

The actual loading procedure (for testing in the glass transition temperature region, until crack re-propagation) is simulated in the 2nd step. Since the EMC behaves viscoelastic, in principle, the stress state in the sample is time-dependent, and so the stress singularity at the crack tip is. Therefore, it will be clear that the FE interpretation of the measurement results requires a dedicated viscoelastic constitutive model for the EMC, for which the temperature dependent relaxation data are established beforehand. When the position of the crack tip is changing during the experiment due to crack propagation, a second time dependency, related to the propagation rate is interacting with the viscoelastic time dependencies. This should be well accounted for in the FE simulations. For calculation at 120°C, FE simulations are performed on FE models where the crack length corresponds to experimentally established crack tip positions at each cycle.

We found that in many standard FEM packages used the calculation of the energy release rate through the implemented J -integral gave erroneous results in case of viscoelastic material behavior. Therefore, we used the following Griffith’s energy balance approach for post processing calculation. The energy balance for a crack of length a is given by the relation

$$W - U - S = 0 \quad (4)$$

Where W is the total input energy at the boundary, U is the strain energy density and S is the surface energy per unit area.

When the material is considered to be elastic, the equation (4) can be written as:

$$G = S \quad (5)$$

Where G is the energy release rate and is given by the well known relation

$$G = \left| \frac{\partial U}{\partial a} \right| \quad (6)$$

In the viscoelastic analysis, the process of crack propagation is assumed to be time dependent. Meaning, at any instant time t , the crack is assumed to have length a , and it is then assumed to further propagate by a small amount of Δa in a small time interval Δt . The Δt is assumed to be small enough such that the stress variations in the time interval can be considered to be negligible, so that the dissipation effects are neglected over this time step. During crack propagation, the temperature is assumed to be constant, so the other energy contributions like kinetic energy and heat energy are neglected. Therefore the elastic strain energy release rate relationship (3) can be used in this time step.

The energy release rate G is evaluated by calculating the strain energy change in the small time step. Consider a crack length a at time t which is further loaded in the next time interval ($t + \Delta t$), then strain energy at the end of this time is $U_1(a, t + \Delta t)$. Now consider the same crack length a at time t and let it grow by an amount Δa (a to $a + \Delta a$) in the time interval Δt (t to $t + \Delta t$), the strain energy at the end of this time is $U_2(a + \Delta a, t + \Delta t)$.

The energy difference $\Delta U = U_1 - U_2$ is the energy released in creating the new surface of length Δa and therefore the strain energy release rate G in this small time step is

$$G(t + \Delta t) = \left| \frac{\partial U}{\partial a} \right| \approx \left| \frac{\Delta U}{\Delta a} \right| \quad (7)$$

It can be rewritten as:

$$G(t + \Delta t) \approx \left| \frac{U_2(a + \Delta a, t + \Delta t) - U_1(a, t + \Delta t)}{da} \right| \quad (8)$$

In order to verify this approach, a benchmark study is done to compare G_c value from the energy approach with J -integral at room temperature and compare G_c from the energy approach with an analytical solution at high temperatures. It is found from the benchmark study that the energy approach is a suitable and accurate approach for G_c calculations when viscoelastic material has to be considered.

In our FE model, we chose Δa as 1/10 of the size of the adjacent crack tip element size. We calculate the energy change at the end of the loading in the same time interval.

Based on the experimental results, the critical energy release rate of copper-epoxy molding compound was calculated using 2D non linear simulation and the mode mixity was calculated using the crack surface displacement extrapolation method [9]. We chose 5mm as reference length.

The result of fracture toughness and mode mixity at different temperatures is shown in [figure 18](#). General speaking, at high temperatures in and above the glass transition temperature, the critical energy release rate and mode mixity have a similar relation to those at room temperature. When shifting the loading closer to mode II (corresponding from lower mode mixity to higher mode mixity in [figure 18](#)) the energy release rate and mode mixity increased. When looking at room temperature, the G_c is about 3 times higher at mode II loading than mode I loading. While, at high temperatures, the difference in G_c due to change in loading is getting smaller and smaller. At 175°C, G_c values of mode II loading are smaller than the mode I values.

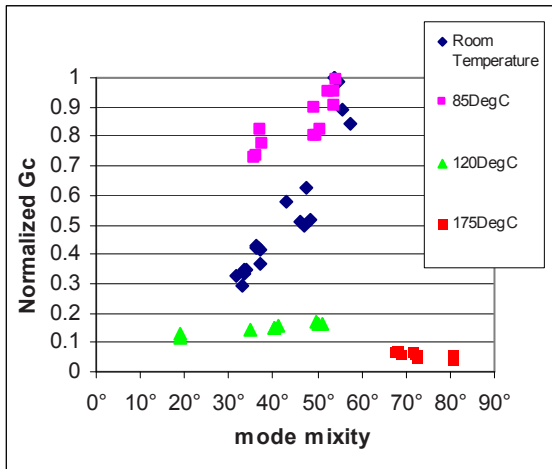


Figure 18. Fracture toughness as a Function of Mode Mixity at different temperatures.

MMB2	Normalized G_c [-]	Mode mixity
Room temperature	1	56°
85°	0.98	54°
120°	0.34	51°
175°	0.08	72°

Table1. Comparison of G_c and maximum load angle achieved in the setup at different temperatures

Compared with the previous room temperature result, G_c at 85°C is almost higher than at room temperature at all mode mixities tested here. It is found that at and above glass transition temperature, the fracture toughness is significantly reduced. At the highest mode mixity, let's consider the fracture toughness at room temperature to be at 100%, relative G_c reduces up to 70% at 120°C and further up to 90% at 175°C. We think the main reason for this phenomenon is that at 120°C or above, compared to the state at room temperature, the material strength is very much reduced and so is the interface fracture toughness,

Apart from G_c , looking at the temperature effect on the calculated load angle in a fixed load geometry of the setup, it seems that below 120°C, mode mixity is not much influenced by temperature. This can be seen in [table1](#). While at 175°C, mode mixity much shifted to very high load angles, i.e. shear loading is achieved, below 120°C the maximum is just 56° at room temperature.

Conclusion

In this study, the mixed mode bending test method was used to characterize the fracture toughness of EMC/copper as a function of mode mixity at the glass transition temperature of an EMC. The EMC material model was established through experimental investigation. The characterization procedure and results were shown. From a case study on warpage the material model was verified and shown to be necessary and accurate. The sample geometry and sample preparation was explained. It is worthwhile to mention that the fabricated test samples have identical surfaces as in the real product. The test procedure was built and the interfacial fracture toughness and mode mixity were calculated. It can be seen that at high temperature, the interface fracture toughness and mode mixity show a similar relation found at room temperature. Further, the toughness values at the glass transition temperature (and above) are tremendously reduced compared to the room temperature values.

Acknowledgment

We thank Olaf van de Sluis from Philips Applied Technologies for the discussion and input in the finite element analysis.

We thank the European Commission for partial funding of this work in FP7 under project NanoInterface (NMP-2008-214371)

References

- [1] J. de Vreugd et al, "Advanced viscoelastic material model for predicting warpage of a QFN panel" Proceeding Electronic Components and Technology conference, IEEE 2008, Pages: 1635-1640.
- [2] A. Xiao et al, "Mixed Mode Interface Characterization Considering Thermal Residual Stress" Proceeding Electronic Components and Technology conference, IEEE 2008, Pages: 937-943.

- [3] Andrew Tay, "*Application of fracture mechanics in microelectronics*" Lecture note of EuroSime 2006 short course.
- [4] W. D. van Driel et al, "*Driving mechanisms of delamination related reliability problems in exposed pad packages*" 6th. Int. Conf on Thermal, Mechanical and Multiphysics Simulation and Experiments in Micro-Electronics and Micro-Systems, EuroSimE 2005, PP 183-189.
- [5] W. D. van Driel et al, "*Characterization of Interface Strength as function of Temperature and Moisture Conditions*" 6th International conference on electronic package technology, page: 1-6, ISBN: 0-7803-9449-6.
- [6] Auersperg. J, B. Michel, "*Towards a Robust Design of Electronics Assemblies under Fracture, Delamination and Fatigue Aspects*" 2007 9th Electronics Packaging Technology Conference, pp. 476-481.
- [7] J. W. Hutchinson and Z. Suo, "*Mixed mode cracking in layered materials*" Advances in Applied mechanics, Vol.29, Academic, New York, 1991.
- [8] G. Q. Song et al, "*Effect of Loading Mode, Temperature and Moisture on Interface Fracture Toughness of Silicon/Underfill/Silicon Sandwiched System*" Intersociety Conference on Thermal and Thermomechanical Phenomena in Electronics Systems, pp. 1147-1152, May 2006.
- [9] Yuuki, R., and S.-B. Cho. "*Efficient Boundary Element Analysis of Stress Intensity Factors for Interface Cracks in Dissimilar Materials.*" Engineering Fracture Mechanics 34 (1989): 179–188.
- [10] Weidong Xie, Suresh K. Sitaraman, "*Investigation of Interfacial Delamination of a Copper-Epoxy Interface Under Monotonic and Cyclic Loading: Experimental Characterization*" IEEE Transactions on Advanced Packaging, Vol. 26, NO. 4, Nov 2003.

An Integrated Experimental and Numerical analysis on Notch and Interface Interaction in Same-materials

Arun Krishnan and L. Roy Xu¹
Department of Civil and Environmental Engineering
Station B 351831, Vanderbilt University, Nashville, TN 37235, USA

ABSTRACT

The theory of fracture mechanics has been extensively developed for cracks. However, notches are found a lot more than cracks in real life. Indeed, a crack is only a special case of a notch. Therefore, developing a generalized notch-interface failure criterion is very important for the field of fracture mechanics from a fundamental standpoint. In the current investigation, an integrated experimental and numerical analysis is conducted to determine the crack initiation load and to compare it with theoretical predictions. The angle of the notch (β), the loading point (S), and the interfacial adhesive are used as variables to understand their effect on the crack initiation load.

INTRODUCTION

The theory of fracture mechanics has been extensively developed for cracks (Anderson, 2004; Williams, 1952; Hutchinson and Suo, 1992 and several others). However, notches are found a lot more than cracks in real life structures. Indeed, a crack is only a special case of a notch (notch angle being 0° for a crack). Significant research has already been done on crack growth and several failure criterions have been proposed for the same (Qian and Fatemi, 1996). But, the problem of crack onset at a notched interface is still an open problem and only a few criterions have been proposed (Dunn et al., 1997; Leguillon, 2002). Recent experiments on composite laminates have indicated that impact-induced delamination will propagate under compressive loading (Krishnan and Xu, 2010). This delamination front is a notch and not a mathematically sharp crack (as shown in Fig. 1). Therefore, developing a generalized notch-interface failure criterion is very important for the field of fracture mechanics from a fundamental standpoint.

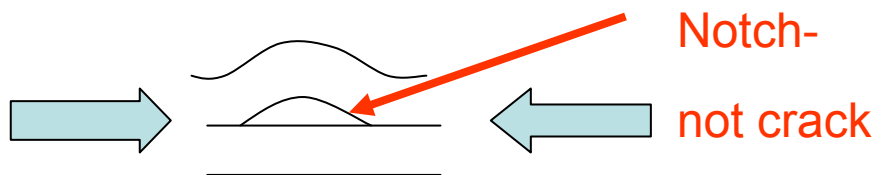


Fig. 1. Impact-induced delamination will propagate under compression load during CAI experiments. The delamination front is a notch, not a mathematically sharp crack

In the current investigation, a specimen as shown in Fig. 2 is designed and tested to determine the crack initiation load. This is used to compare with theoretical predictions developed by Leguillon (2002). The angle of the notch (β), the loading point (S), and the interfacial adhesive are used as variables to understand their effect on the crack initiation load. The specimen itself is made of two different parts which are bonded together. The above case is related to notch-interface failure in the same composite materials. A more general notch-interface stress and failure is observed in case of dissimilar materials. Two types of bonded PMMA-Steel specimens which were subjected to tension and compression load, showed large stress concentrations at the notch tips (notch angles are 180 and 90 degrees), and the notch tips were connected to interfaces. Using the Coherent Gradient Sensor (CGS) technique, severe stress concentrations can be found at the notch/interface tips leading to interface debonding when the applied load increases to a critical level. Therefore, a new failure criterion should be

¹ Corresponding Author, Tel: 615-343-4891, Fax: 615-322-3365. E-mail: l.roy.xu@vanderbilt.edu

developed in order to predict the critical load. Since the stress singularity order of a crack is always larger than that of a notch (Williams, 1952), it is an interesting failure mechanics problem to study the stress field/failure transition and very few researchers studied this problem before (Leguillon, 2002).

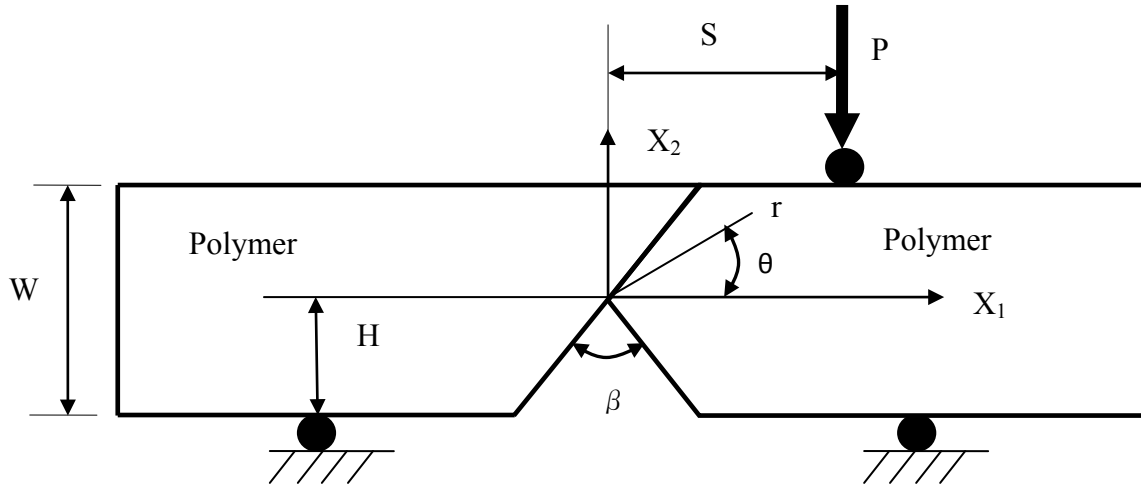


Fig.2 Schematic diagram representing notch-interface specimens

EXPERIMENTAL WORK

Specimens are made of polycarbonate as shown in Fig. 2. P is the applied load, W is the width of the specimen and H is the height of the notch. Each specimen had a total length of 254 mm, a width (W) of 50.8 mm and a notch height (H) of 19.05 mm. Every specimen was made of two individual halves which are bonded together to form a sharp notch. Material properties of bulk polycarbonate are as provided in Table 1. Two types of adhesives were used to understand the effect of strong/weak bonding on the interfacial failure strengths. Weldon-10 was used as a strong adhesive and Loctite 384 was used as the weak adhesive. The adhesives were chosen such that their elastic properties are close to bulk polycarbonate such that we can model the interface as a line without any thickness but with different bonding strength and fracture toughness (Krishnan and Xu, 2010). The properties of the bonded interfaces were obtained from Krishnan and Xu (2009). All the specimens are made of two separate parts enclosing a particular notch angle ($\beta = 30^\circ, 90^\circ$ and 120°). The reason to use different notch angles is that the stress around the notch tip and its singularity order vary with notch angle. Therefore, the critical load at the crack initiation will be different for different cases of notch angles. Meanwhile, using two bonded halves eliminates the need to machine a sharp notch which is physically impossible. Therefore, a mathematically sharp notch is produced in our case.

A three-point fixture is used to mount the specimen onto the MTS test machine. The specimens are designed such that the notch is always at the center of the specimen (length-wise) to make it easier for comparing with the variety in load cases. The crack initiation load P_c is measured by either the load-displacement curve or by observation of in-situ optical techniques. Also, the loading location S varies to change the local loading mixity of the notch tip (S from 30mm to 0mm, and -30 mm). The test set-up consists of three parts including a mechanical system to load the specimen, an optical system to develop fringe patterns and an imaging system to record the images. The mechanical testing system included an MTS 810 test machine and the three-point fixture. The fringe patterns developed only in case of the transparent Polycarbonate specimens, and the isochromatic fringe patterns are the contours of the maximum in-plane shear stress:

$$\tau_{\max} = \frac{(\sigma_1 - \sigma_2)}{2} = \frac{Nf\sigma}{2h} \quad (1)$$

where σ_1 and σ_2 are the in-plane principal stresses, N is the fringe order, f_σ is the stress-fringe constant, and h is the thickness of the specimen. The imaging system included a high-resolution digital camera to capture the fringe development and a density filter in front of the camera to reduce the laser intensity.

Table 1. Material properties for polycarbonate (PC)

	Polycarbonate
Density (kg/m ³)	1200
Elastic Modulus (GPa)	2.378
Poisson's Ratio	0.37
Tensile Strength (MPa)	62
Shear Strength	41
Mode-I Fracture Toughness (MPa m ^{1/2})	3.53

EXPERIMENTAL OBSERVATIONS

Effect of notch angle on crack initiation load

It is seen from our experimental results that there is a pronounced effect on the crack initiation load created by the notch angle. Theoretical results from Leguillon (2002) indicate that there should be an exponential increase in the value of crack initiation load with increase in notch angle. This prediction is exhibited in several cases in our study as presented below. Fig. 3 shows a variation of the crack initiation load with notch angle for loading at $S=0$. There is also a comparison between the strong and weak bonding. Both types of bonding show an increase in crack initiation load value (P_C) with increase in notch angle. However, it is clearly seen that the weak bond shows a linear variation with β and thus can be said to be relatively free from the effect of the notch angle. The strong bond on the other hand shows a distinct increase in P_C especially from 90° to 120° . This is consistent with earlier predictions (Leguillon, 2002). The results were repeatable and consistent failure loads, load-displacement plots and failure patterns were observed in each case. Also, the weak bonded specimens always show a lower crack initiation load value than the strong bond specimens which is as expected. Weak-bond specimens always show a sudden failure along the interface in case of all notch angles. These specimens seem to be independent of the notch angle. However, strong-bond specimens demonstrate crack kinking for higher notch angles. While $\beta=30^\circ$ shows failure along the interface, $\beta = 90^\circ$ and 120° show crack kinking into the bulk polycarbonate. The kinking is always towards the loading point which is $S=0$ in this case. The failure patterns for the three different notch angles (strong bonded polycarbonate specimens) are indicated in Fig. 4. The crack initiation load is found from in-situ optical techniques in case of specimens with kinking. This might be different from the loads shown from the load-displacement graphs.

The load-displacement plots also show a clear difference between crack initiation and final failure. A notch angle of $\beta=30^\circ$ shows a linear load-displacement curve and brittle failure. This indicates that the crack initiation and final failure occur almost simultaneously. This is different from $\beta=90^\circ$ and 120° when crack kinking is observed. A notch-angle of 90° and 120° show a distinct difference in failure pattern. A specimen with $\beta=90^\circ$ shows a brittle failure at a low displacement value followed by a sudden drop in load. Then the load again increases till failure. The first drop is due to crack initiation along the interface and crack kinking. The second part of the load-displacement curve is observed due to friction along the now-debonded interface. The applied load being very close to the interface, causes a small part of the interface (which is still bonded) to remain bonded due to friction. The remaining part of the interface was clearly seen from the optical experiments to be debonded. In case of $\beta=120^\circ$, the first drop in load is due to crack initiation along the interface. This is followed by crack kinking which is indicated by the second drop in the load-displacement curve. Now, the earlier mentioned phenomenon of friction

along the interface is responsible for the third part of the curve and ultimate failure. After crack kinking, there is a build-up of strain energy followed by explosive failure of the specimen. Photoelastic fringe patterns indicate interesting observations in the failure process. The fringes keep building and moving out from the crack tip until crack kinking when they remain constant indicating a build-up of strain energy. The experimental results obtained by testing the various specimens in three point bending are presented in Table 2. The experimentally measured crack initiation load is presented under the tables corresponding to the notch angles. The tensile, shear and fracture properties for each type of material bond are also presented in Table 2. It should be noted here that the shear strength, tensile strength and mode-I fracture toughness values are valid only for the bonded specimens which becomes relevant in our case. All the measured loads are in Newtons.

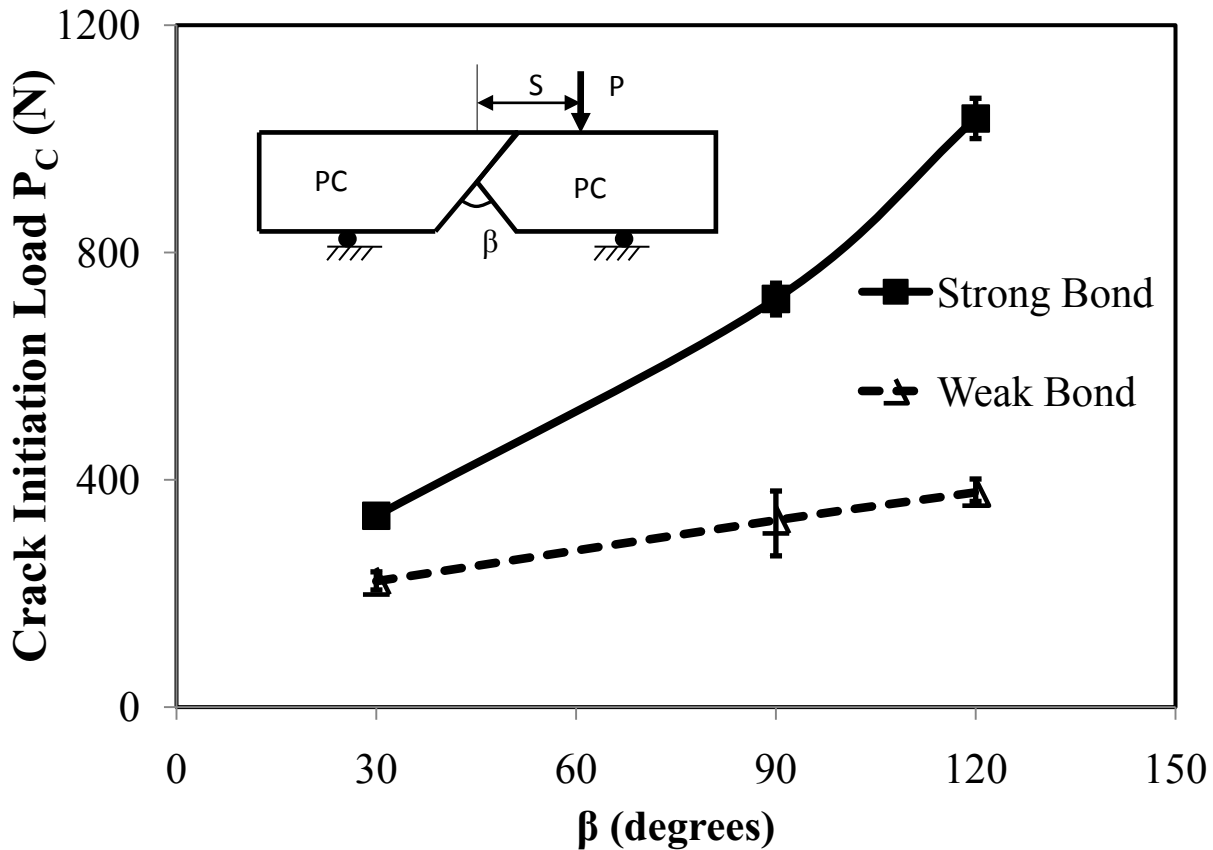
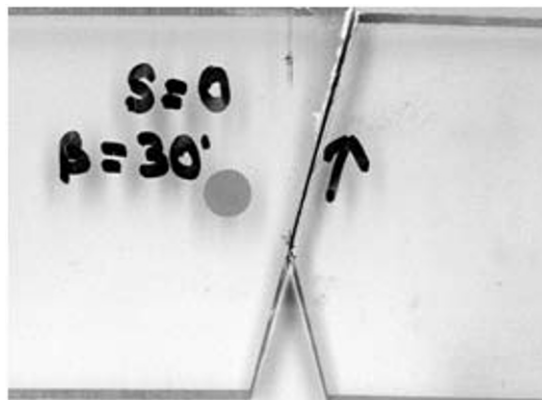


Fig. 3 Effect of notch angle on crack initiation load on same-material polycarbonate systems for $S=0$.



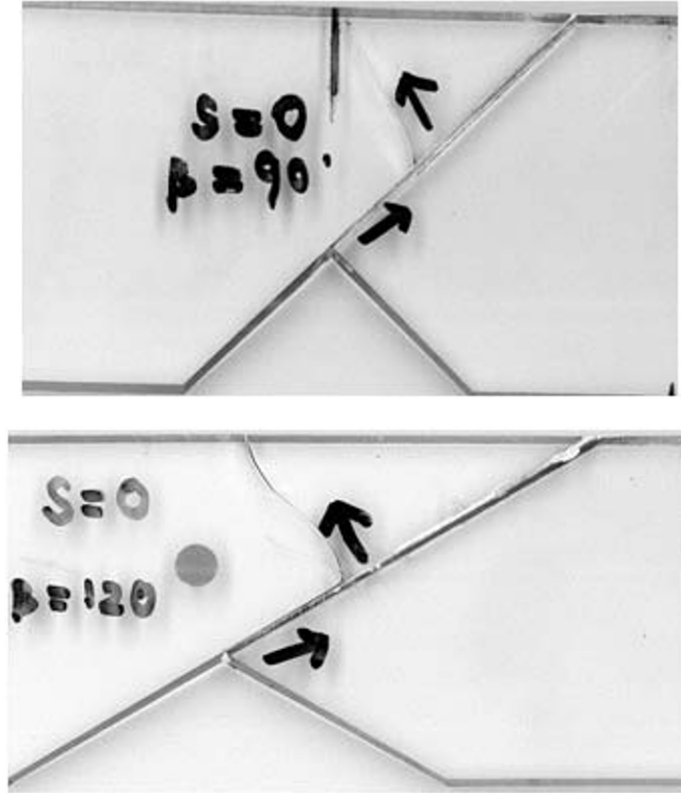


Fig.4 Failure patterns for same-material strong bonded polycarbonate specimens with $S=0$. Notch angles are illustrated in the pictures. (Circular dot is a mark of diameter 6.35 mm)

Table 2. Crack initiation loads for same-material polycarbonate systems

Notch Angle	S (mm)	30° (N)	90° (N)	120° (N)	Bonding tensile strength (MPa)	Bonding Shear Strength (MPa)	K_{IC} (MPa m ^{1/2})
Bonding							
Weak	0	222	329	378	6.06	10.99	0.64
	30	393	477	906			
	-30	536	964	1100			
Strong	0	337	718	1036	12.93	15.52	0.86
	30	1515	1358	1677			
	-30	1275	2857	2980			

Variation of crack initiation load with loading point S

The loading point for the three-point bending test was varied from $S=0$ to $S=-30$ and $S=30$ (all in mm) to produce interesting results. Fig.5 illustrates the variation in crack initiation load for the three different loading points for strong bonded same-material systems. A general trend observed in same-material systems is the increase in crack initiation load when the loading point is shifted away from the center. Thus, $S=30$ mm and $S=-30$ mm always show an increased load to initiate the crack. When $S=0$, the system is almost symmetric and is similar to mode I cracking. The presence of mode II component is limited in this case. However, moving the loading point to either $S=30$ or $S=-30$ brings about a significant mode II component which causes an increase in the load required to cause interfacial debonding. The failure pattern is also significantly different in the three cases with crack kinking dominating over interfacial debonding as the loading point is varied. This effect is especially pronounced in case of $\beta=120^\circ$ and the corresponding failure patterns are as indicated in Fig. 6.

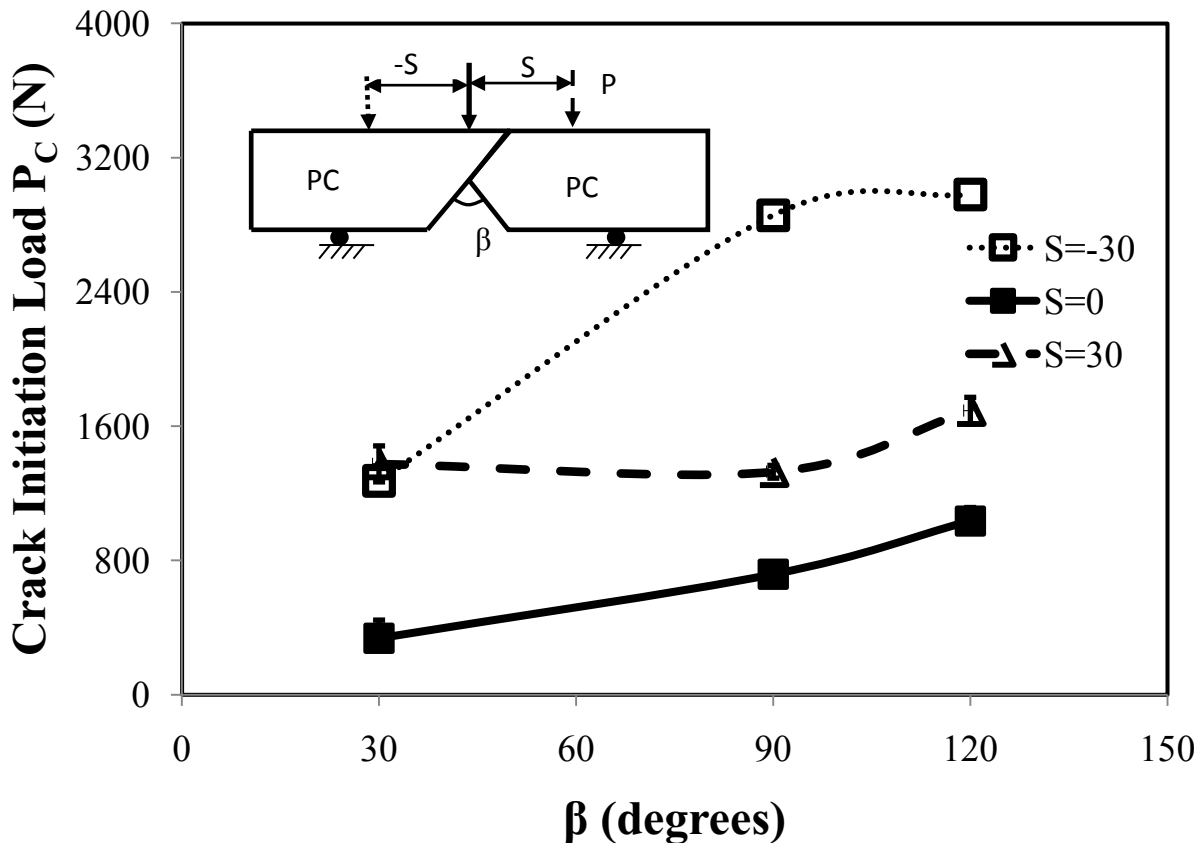


Fig. 5 Variation of crack initiation loads with notch angle for different loading points (S) for polycarbonate same-material strongly bonded systems.

The loading points of $S=30$ mm and $S=-30$ mm are symmetric with respect to the center of the geometry. In case of same-material systems, the materials also have the symmetry. This is as shown in Fig.7 which compares the three loading conditions for a notch angle of 120° . The $S=0$ mm loading point gives rise to a mode I component and hence has a lower load as discussed above. The $S=-30$ mm case has a higher initiation load than the $S=30$ mm case. This could be due a greater mode II component induced by the former. The load point corresponding to $S=-30$ mm is further away from the interface than $S=30$. Therefore, it induces more friction in the form of interfacial contact along the interface and hence produces a greater load. A similar trend is observed in case of notch angles of 90° and 120° . Also, the weak bond specimens exhibit a similar curve as the strong bond specimens albeit with a lower load. The loading point has a strong influence on the crack initiation load in case of notch-interface specimens. The mode mixity is influenced to a large extent by the loading point. Applying the load at the center or close to the center induces a strong mode I component. Moving away from the center induces a mode II

component along with the existing mode I component and increases the crack initiation load. Moving towards the interface produces lesser mode II component than moving away from the interface does.

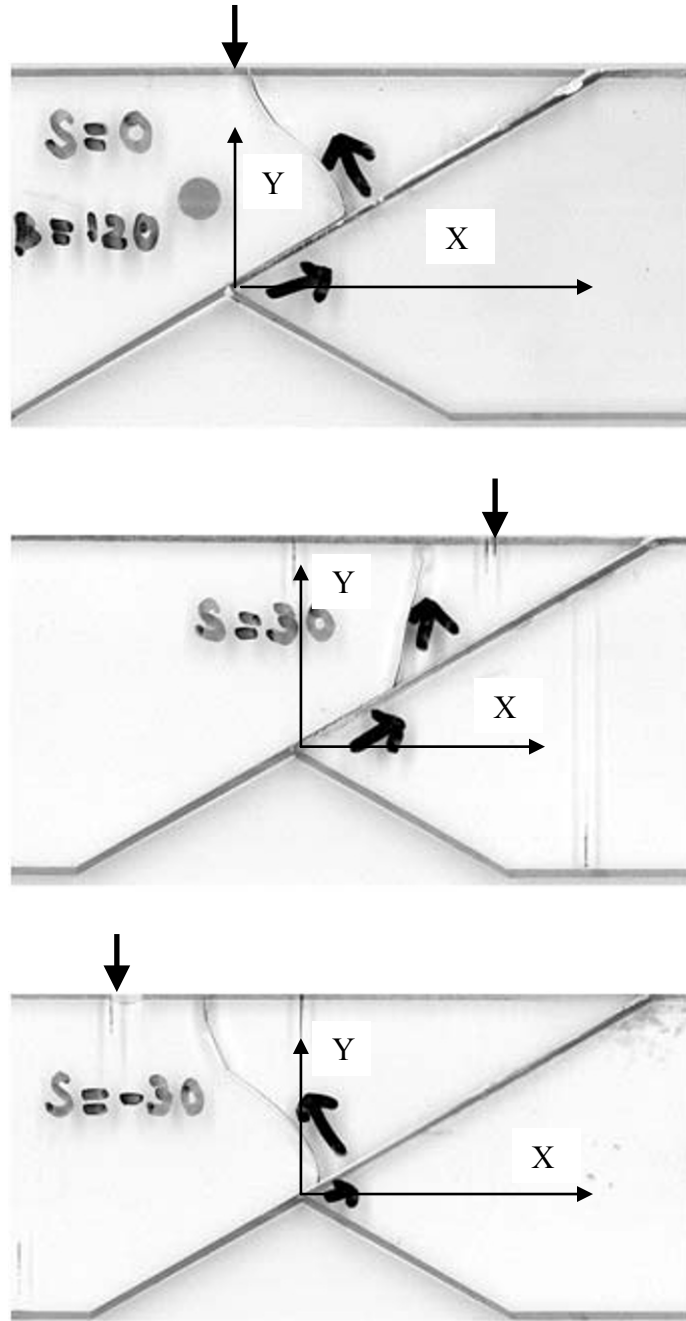


Fig.6 A comparison of the typical failure patterns for same-material strong-bonded polycarbonate specimens with $\beta=120^\circ$ and with variation in S .

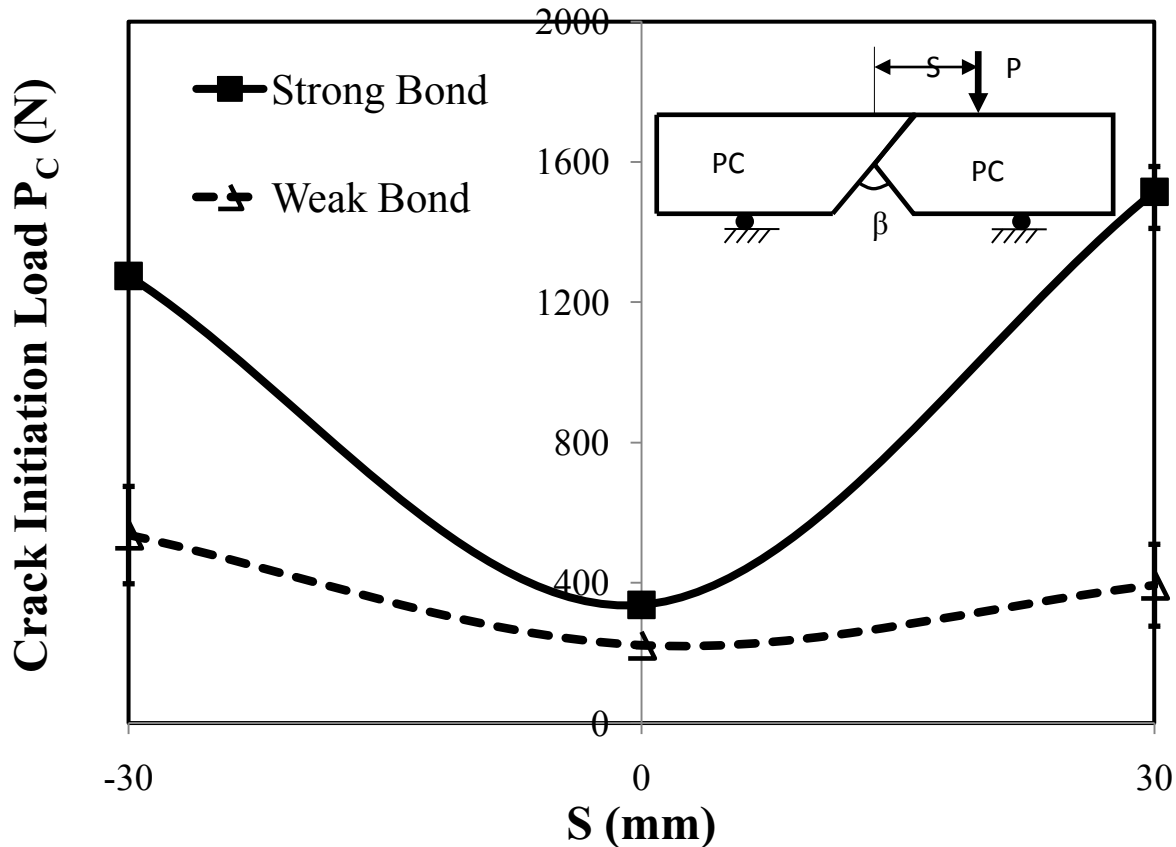


Fig. 7 Variation in crack initiation loads with loading points (S) for same-material systems with a notch angle of 30°

CONCLUSIONS

The same-material polycarbonate specimens are tested under three-point bending and the crack initiation loads are recorded. An in-situ photoelasticity experiment is used to obtain the correct crack initiation load. There is a significant difference seen between the strong and weak bonded specimens. Also, the effect of loading point and notch angle on the crack initiation load is studied.

ACKNOWLEDGEMENT

The authors acknowledge the support from the Office of Naval Research (Program manager Dr. Yapa D.S. Rajapakse) and the National Science Foundation.

REFERENCES

1. Anderson T.L., Fracture mechanics: Fundamentals and applications, 3rd Edn. CRC Press., 2004.
2. Dunn M.L., Suwito W., Cunningham S., Fracture initiation at sharp notches: correlation using critical stress intensities, *International Journal of Solids and Structures*, 34 (29), 3873-3883, 1997.
3. Dunn M.L., Suwito W., Cunningham S., Stress intensities at notch singularities, *Engineering Fracture Mechanics*, 57 (4), 417-430, 1997.
4. Hutchinson J.W., Suo Z., Mixed-mode cracking in layered materials, *Advances in Applied Mechanics*, 29, 63-191, 1992.
5. Krishnan A., Xu LR, Effect of the interfacial stress distribution on the material interfacial strength measurement, *Experimental Mechanics*, 50, 283-288, 2010.
6. Krishnan A, Xu LR, Systematic evaluation of bonding strengths and fracture toughnesses of adhesive joints, Submitted to *Journal of Adhesion*, 2009.

7. Leguillon D., Strength or toughness? A criterion for crack onset at a notch, *European Journal of Mechanics-A/Solids*, 21, 61-72, 2002.
8. Qian J., Fatemi A., Mixed mode fatigue crack growth: A literature survey, *Engineering Fracture Mechanics*, 55 (6), 969-990, 1996.
9. Williams M.L., On the stress distribution at the base of a stationary crack, *Journal of applied mechanics*, 24, 109-114, 1957.

Differentiation of Human Embryonic Stem Cells Encapsulated in Hydrogel Matrix Materials

Max Salick, Graduate Student, Engineering Mechanics Program,
University of Wisconsin – Madison

Richard A. Boyer, Graduate Student, Department of Biomedical Engineering,
University of Wisconsin – Madison

Chad H. Koonce, Senior Research Specialist, Department of Medicine,
University of Wisconsin – Madison

Timothy J. Kamp, Professor, Department of Medicine,
University of Wisconsin – Madison

Sean P. Palecek, Associate Professor, Department of Chemical and Biological Engineering,
University of Wisconsin – Madison

Kristyn S. Masters, Assistant Professor, Department of Biomedical Engineering,
University of Wisconsin – Madison

Wendy C. Crone, Professor, Department of Engineering Physics,
University of Wisconsin – Madison,

543 Engineering Research Building, 1500 Engineering Dr, Madison, WI 53706
crone@engr.wisc.edu

ABSTRACT

Prior work on many cell types, including stem cells, has definitively shown that mechanical stiffness of the neighboring material and the overall stress state influences cell behavior. There is also evidence that the topology (i.e. 2D vs 3D environment) impacts cell behavior. Our research involves controlling the differentiation of human embryonic stem cells (hESCs) through mechanical stimuli. We employ three-dimensional cultures to better understand how topology and mechanical properties of a surrounding matrix impact stem cell differentiation. For these experiments, H9 hESCs were embedded in hydrogels of varying Young's moduli with the target of differentiation toward cardiomyocytes. The amount of contractile behavior was quantified, and real-time polymerase chain reaction (qRT-PCR) tests were conducted at various time points. Results show a similar efficiency in cardiomyocyte generation to other methods with the advantages of a three-dimensional matrix environment more conducive to the needs of tissue engineering.

1.0 INTRODUCTION

It is well known that heart disease is a significant national health issue in the U.S. and in developed countries where it is the leading cause of death [1]. Coronary artery disease with associated acute myocardial infarction is the most common cause of heart disease, which results in the loss of functional myocardium and its replacement by scar tissue. The loss of functioning myocardium either from myocardial infarction or other insults can lead to adverse remodeling of the heart and a continuing spiral to congestive heart failure due to inadequate cardiac function. Fortunately, recent progress in the field of stem cells has provided hope that stem cell therapies may be available in the future that will allow for the regeneration or replacement of damaged cardiac tissues. There are still, however, many obstacles that stand between current research and clinical implementation.

A contributor to the limited tissue repair observed in humans and large animals is related to the challenges of keeping the transplanted cells in position near the site of injury and facilitating their development into useful tissue. Furthermore, the number of cells needed at the site of repair has been estimated to be in the range of 10^8 to 10^9 [2], thus a scaffold maintaining cells in location is a critical point in the pathway for development of any future treatment option of this type. In addition, the mechanical properties of cell culture environments have a profound influence on cell differentiation and function. Matrix stiffness can regulate cell adhesion, proliferation, migration, contractility, extracellular matrix production, and gene expression [3, 4]. Work by Engler et al, [5] has demonstrated the strong influence of stiffness on stem cell differentiation, where, in the absence of any other differentiation cues (i.e., media additives), substrate stiffness alone was able to direct the lineage of stem cell differentiation.

With this prior work in mind, it was clear that further studies exploring the connection between mechanical properties of a three-dimensional cultures and the differentiation of encapsulated stem cells could lead to a better understanding of stem cell behavior and potential lineage restriction. Thus, a combination of studies was conducted on various poly(ethylene glycol) (PEG) hydrogels to measure their mechanical properties and observe their influence on embedded embryoid bodies.

2.0 MATERIALS AND METHODS

2.1 Cell Culture

H9 hESCs were purchased from the National Stem Cell Bank (NSCB). Cells were maintained undifferentiated on mouse embryonic fibroblasts (MEFs) in DMEM/F12 culture medium supplemented with 19.6% KnockOut serum replacer, 0.1 mmol/L nonessential amino acids, 1 mmol/L L-glutamine (all from Invitrogen), and 0.1 mmol/L β -mercaptoethanol (Sigma). Routine G-band analysis was performed every 5 passages to confirm a normal karyotype as well as regular testing for mycoplasma contamination. In order to induce cardiac differentiation, embryoid bodies (EBs) were made from the hESC colonies by treating with 1 mg/mL Dispase (Gibco) at 37°C for 10-15 minutes then culturing in low attachment culture dishes (Corning). EBs were cultured for five days in cardiac differentiation medium (EB20) consisting of 78.8% DMEM/F12 (Invitrogen), 19.7% fetal bovine serum (FBS) (Invitrogen), 1% non-essential amino acids (Invitrogen), and 0.5% L-glutamine / mercaptoethanol solution (Invitrogen).

2.2 Encapsulation

After five days of culture in suspension, the EBs were encapsulated into large disks of diacrylated poly(ethylene glycol) (PEG-dA). These disks had a diameter of approximately 4 cm and were roughly 2 mm in thickness. Hydrogel mechanical properties were manipulated by adjusting the molecular weights of the PEG molecules and by altering the concentrations of the PEG-dA solution prior to polymerization. Lower molecular weights and increased concentrations of the PEG-dA lead to increased stiffness of the hydrogel. Three PEG-dA hydrogel compositions were used, as follows in order of increasing mechanical stiffness: 10kDa PEG at 15% w/v, 3.4kDa PEG at 15% w/v, and 3.4kDa PEG at 25% w/v. The PEG-dA solutions prior to crosslinking consisted of 88% phosphate-buffered saline (PBS) (Invitrogen) with respective dissolved PEG-dA, 0.8% CGRGDS peptide (Genscript), 4.8% Irgacure-2959 (Ciba) 0.1% w/v photoinitiator solution (final concentration of 0.05% w/v Irgacure-2959), and 6.4% cell solution containing EB20 and suspended EBs. To initiate crosslinking, the solution was exposed to UV light at 3.9 mW/cm² for five minutes.

2.3 Evaluation

Smaller disks of 8 mm diameter were sectioned out of the gels using biopsy punches. The small, EB-embedded disks were then placed in individual wells of 24-well plates and cultured with EB20 medium for the duration of the experiment. As portions of the EBs differentiated into cardiomyocyte populations over the course of several days, they began to exhibit spontaneous contractile behavior. Encapsulated EBs were observed at varying time points and the number of contracting EBs was then counted and recorded. In addition, live/dead staining was conducted using Calcein AM and Ethidium homodimer-1 (Invitrogen) to check for cell viability during days 1, 4, 9, and 21. Lastly, qRT-PCR analysis was conducted on multiple samples on days 0, 1, 4, 9, and 21.

As a control, EBs were plated onto 2-D culture surfaces at the same time as the 3-D encapsulation. These controls were kept on 6-well plates and treated with the same culture media as the encapsulated samples. Contractile behavior was similarly observed and qRT-PCR tests were conducted in parallel with the gel samples.

2.4 RNA Isolation and Reverse Transcription

Hydrogels were manually homogenized and treated with TRI Reagent (Sigma), and the manufacturer's directions were followed for isolation of RNA. Briefly, samples were treated with 750 μ l TRI reagent per well at 4°C. The homogenate was incubated for 5 minutes at room temperature. Chloroform was added to the homogenate at 0.2 ml / 1 ml TRI reagent and allowed to phase separate for 10 minutes. Centrifugation at 13,000 x g for 15 minutes completed separation. The aqueous phase was collected and RNA was then precipitated by adding 0.5 ml isopropanol / 1 ml TRI reagent. Incubation for 10 minutes was then followed by centrifugation at 13,000 x g for 8 minutes. The RNA pellet was washed with 75% ethanol (1 ml 75% EtOH / 1 ml TRI reagent) and centrifuged at 7,500 x g for 5 minutes. The RNA pellet was air-dried and resuspended in 500 μ l RNase-free H₂O. Samples were stored at -20°C until subsequent use. RNA was reverse transcribed using a High Capacity cDNA Reverse Transcription kit from Applied Biosystems. Methods were followed as described by the manufacturer. The cDNA was then used for qRT-PCR using a TaqMan Gene Expression assay (Applied Biosystems). Genes tested included peroxisome proliferator-activated receptor gamma (PPARG), runt-related transcription factor 2 (RUNX2), octamer-4 (OCT4), NK2 transcription factor related, locus 5 (Nkx2-5), natriuretic peptide precursor A (NPPA) and myosin regulatory light chain 2 (MYL2).

2.5 Mechanical Test Sample Preparation

To properly evaluate the connection between mechanical properties of the gels and the behavior of encapsulated EBs, mechanical testing was done on separate PEG hydrogel samples mimicking the properties of those used during the test cultures. The solutions examined consisted of the same molecular weights and concentrations, with modifications to account for the lack of cell solution and peptide: 10kDa PEG at 15% v/v, 3.4kDa PEG at 15% v/v, and 3.4kDa PEG at 25% v/v. A Teflon mold was used to create dogbone mechanical test samples. A small volume of 60-100 μ m diameter glass beads was embedded in the sample to allow optical strain data to be recorded during the mechanical tests. The samples were UV-polymerized at 3.9 mW/cm² for five minutes to simulate the polymerization of the biological samples. The samples were kept hydrated with PBS, and swelled to approximately 4.0 mm neck length, 2.5 mm neck width, and 3.0 mm thickness.

2.6 Mechanical Testing

Tensile testing of the samples was conducted using a MicroInstron 5548 Mechanical Test Machine. The samples were maintained in a hydrated environment and kept at 37°C throughout the tests via an environmental chamber.

Buoyancy tests were conducted simultaneously, and buoyant forces caused by changing water height were removed from the stress data. A 1 mm/min displacement was applied, and force measurements were recorded by a 10N load cell (Instron). During the tests, optical data was recorded by taking pictures at intervals of 11 seconds. The relative displacements of the embedded beads within the samples allowed strain data to be evaluated for each test. The tests were conducted purely in the elastic deformation region of the sample, so no plastic deformation was experienced by the sample. This allowed cross-sectional data to be gathered optically after mechanical testing was finished. The neck region of the sample was cut perpendicularly to

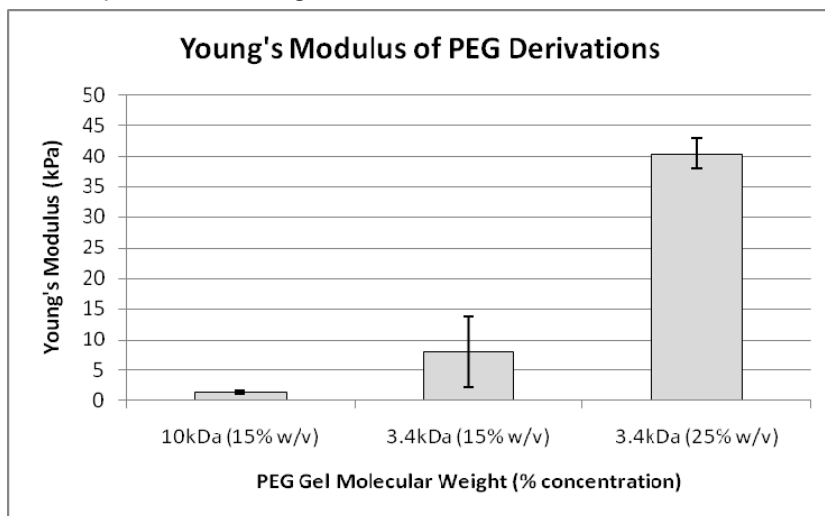


Figure 1. Young's modulus results from mechanical testing of hydrogels composed of varying PEG-dA molecular weights and concentrations (n=3).

the direction of tensile force and the cross-sectional area was measured using a phase contrast microscope.

3.0 RESULTS

3.1 Mechanical Testing Results

Stress and strain data gathered from the mechanical testing were analyzed to determine the Young's modulus (E) for each hydrogel composition. The Young's modulus was found by plotting stress vs. strain and measuring the slope of the linear portion of the relation. The values of E are representative of the materials' individual stiffnesses and were determined to be $E = 1.3\text{kPa}$ for the 10kDa (15% w/v) PEG, $E = 8.0\text{kPa}$ for the 3.4kDa (15% w/v) PEG, and $E = 40.4\text{kPa}$ for the 3.4kDa (25% w/v) PEG (see [figure 1](#)). As desired for the experiment, the examined stiffnesses covered a significant range of physiological stiffnesses observed in human tissue, with the 3.4kDa at 15% w/v most closely representing the mechanical properties of human cardiac tissue.

3.2 Live/Dead Staining Results

Live/Dead stains showed that all EBs were alive in all three types of gels during days 1, 4, 9, and 21. All fully-formed EBs survived the encapsulation process and remained viable throughout the experiment.

3.3 Contraction Observation Results

The observation of contractile behavior of embedded EBs did not show a distinct relation between percentage of contractions and PEG type. As expected, contractions began approximately 2-4 days after encapsulation, correlating to 8-10 days after EB formation. The percentage of contracting EBs reached a plateau after approximately 9 days within the gels, correlating to 15 days after EB formation. The three tested PEG hydrogel compositions and the 2-D control exhibited very similar behavior with regards to EB contraction, as shown in [figure 2](#).

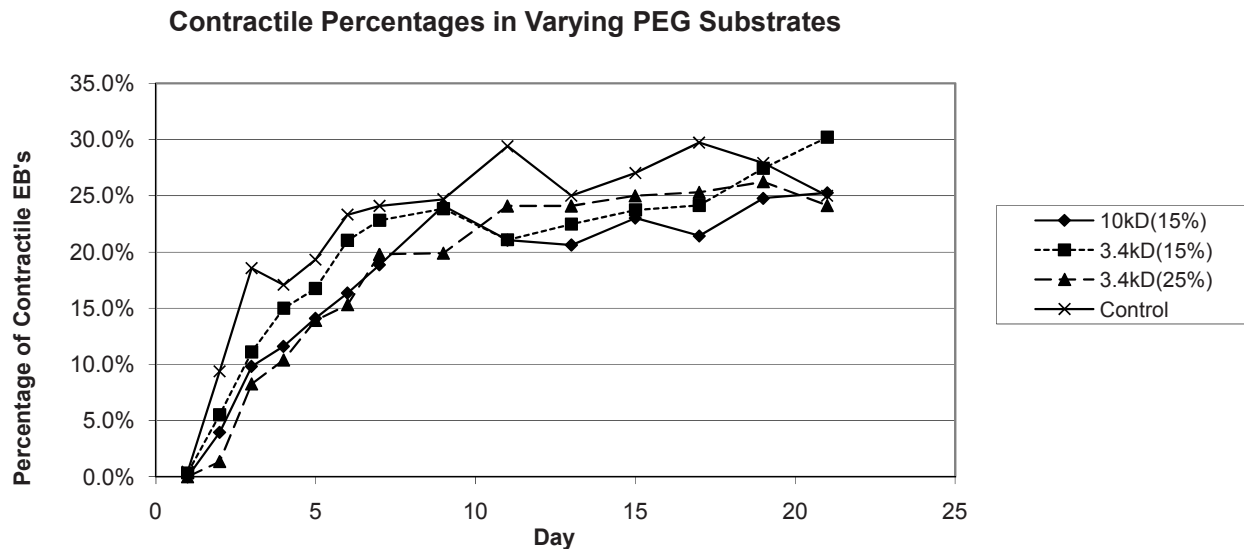


Figure 2. Percentage of contracting EBs versus time. The molecular weight and concentration of each PEG gel is identified in the legend.

3.4 qRT-PCR Results

The results derived from qRT-PCR analysis supported the hypothesis that PEG hydrogel mechanical properties influence the differentiation of embedded EBs. Expression of Oct4, RUNX2, PPAR γ , Nkx2-5, NPPA, and MYL2 all showed the trends for differentiating hESCs illustrated in [figure 3](#). Gene expression was normalized to the

housekeeping gene GAPDH (via the ΔC_T method). The control condition consisted of EBs cultured on 2-D fibronectin-coated tissue culture polystyrene.

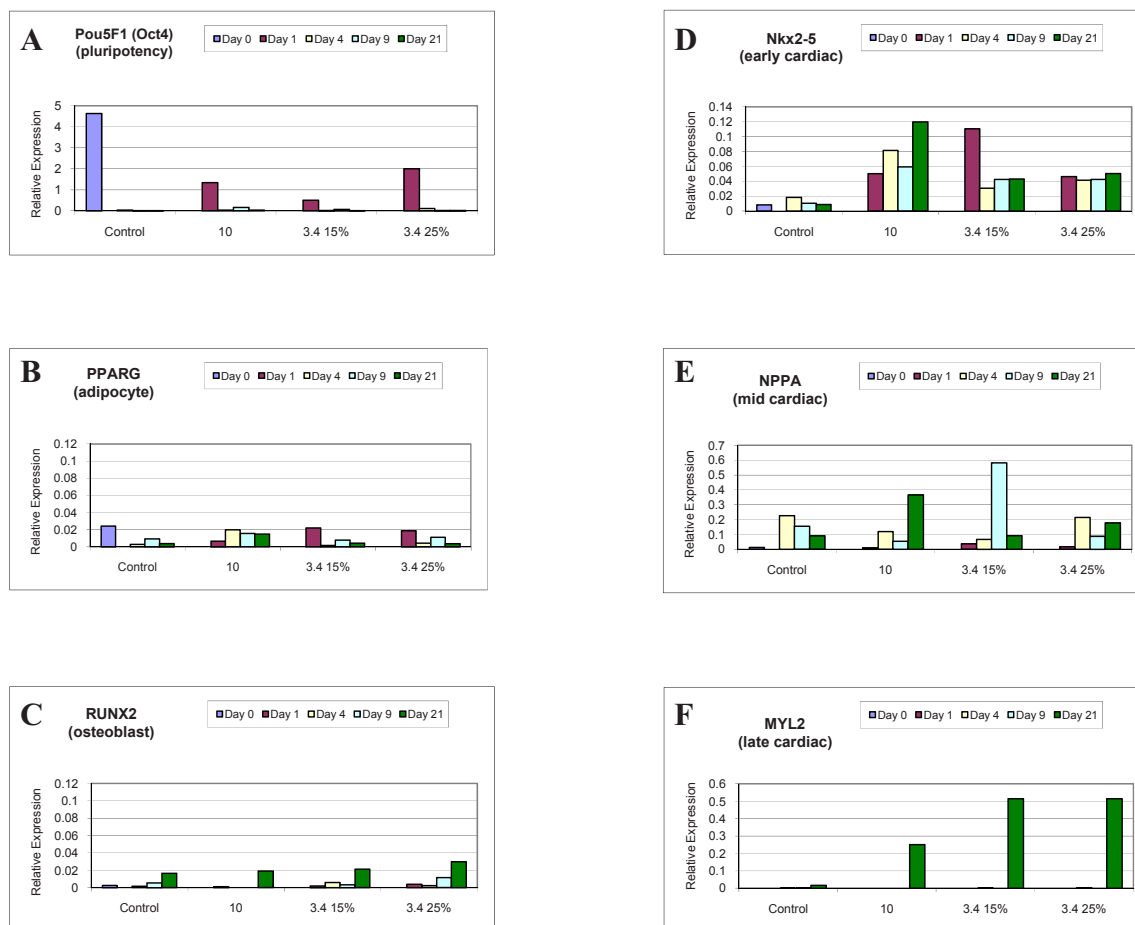


Figure 3. Relative expression of Oct4 (A), PPARG (B), RUNX2 (C), Nkx2-5 (D), NPPA (E), and MYL2 (F). Oct4 is a marker of pluripotency. PPARG is related to adipocyte development. RUNX2 is related to osteoblast development. Nkx2-5, NPPA, and MYL2 are cardiac markers for the early, mid, and late development stages (respectively).

4.0 DISCUSSION

Within the range covered by the Young's moduli of the tested PEG hydrogel compositions, it was expected that the middle stiffness gel, which most closely resembled the stiffness of native cardiac tissue, would support an increase in cardiomyocyte differentiation. Thus, it was expected that qRT-PCR results would show greater expression of Nkx2-5, NPPA, and MYL2 during their respective time-frames within the middle-stiffness gel. In addition, an increase in osteoblast formation was expected in the stiffer gel, and an increase in adipocyte formation was expected in the softer gel. Similarly, it was expected that the percentage of contracting EBs would be larger in the middle-stiffness than in the other derivatives and the 2-D control.

The results from observation of contractile behavior did not show distinguishable differences between the three hydrogel stiffnesses tested. This measure, however, is only one indicator of cardiomyocyte formation. There is inherent error in these counts if cells are distributed more evenly throughout the EB rather than having regions of high concentrations of cardiomyocytes.

Gene expression is another measure of cardiomyocyte formation and does show distinct differences between the three PEG hydrogel stiffnesses tested. The results gained from qRT-PCR analysis (see figure 3) agreed with expectations. The pluripotency marker Oct-4 was highly expressed during the first timestep and greatly declined in the following timesteps. This showed that the majority of differentiation occurred within the first 3 days after encapsulation.

PPARG, an adipocyte marker, did not show conclusive results. RUNX2, an osteoblast marker, was not clearly expressed until 21 days after encapsulation, and no significant trends in RUNX2 were noted across the different culture conditions.

Nkx2-5, NPPA, and MYL2 were the tested early, mid, and late cardiac markers, respectively. While most of the samples showed some level of expression of all of these genes at any given time, there was a clear upregulation in their expression within the middle-stiffness samples. During day 1 of testing, Nkx2-5 was expressed more in the middle stiffness samples than the other derivations, as was anticipated. Similarly, during day 9 of testing, NPPA was expressed much more in the middle stiffness than in the other samples. An increase in the expression of these genes suggests a relative increase in cardiomyocyte formation within the EBs comparable to that seen with other techniques. It is important to note that the expression of cardiac markers was substantially higher in all of the 3-D hydrogel conditions relative to the traditional 2-D tissue culture control. These results suggest that the three-dimensional PEG matrix in which the differentiation occurred provides a significant advantage for the control of spatial and temporal cues needed in the development of complex engineered tissues.

5.0 CONCLUSION

The greatest obstacles standing between stem cell research and potential treatments is the lack of consistent and effective means to restrict lineage pathways during cell differentiation and a three-dimensional environment in which a tissue engineered construct can be developed. Previous studies have shown that the mechanical properties of neighboring materials and tissues can have a drastic impact on the differentiation of stem cells in 2-dimensional environments. In this experiment, human embryonic stem cells were converted to embryoid bodies (EBs) and encapsulated within three-dimensional poly(ethylene glycol)-based hydrogels. The EBs survived encapsulation in the PEG gels with little damage to the hESCs. Contractile behavior was studied and gene expression was measured over a period of 21 days after encapsulation to measure how the surrounding material influenced the differentiation of the embedded cells. Pluripotency rapidly decreased after encapsulation due to cell differentiation. The qRT-PCR results indicate that the Young's modulus of the surrounding material had an impact on the lineage restriction of encapsulated EBs. Softer PEG gels with a stiffness of $E \approx 1.3\text{kPa}$ resulted in increased adipocyte formation, while both the midrange PEG gels with a stiffness of $E \approx 8.0\text{kPa}$ and the 1.3kPa softer gels resulted in increased cardiomyocyte formation. Moreover, the expression of early, mid, and late cardiac markers was significantly higher when EBs were cultured in any of the 3-D PEG scaffolds when compared against the 2-D tissue culture control. The encapsulation technique shown here provides a pathway for the development of constructs with better spatial and temporal controls over the cues that influence differentiating progenitor cells.

ACKNOWLEDGEMENTS

Support for this research was provided by the University of Wisconsin Graduate School Research Committee and WiCell Research Institute.

REFERENCES

- [1] C. H. Hennekens, "Increasing burden of cardiovascular disease: current knowledge and future directions for research on risk factors," *Circulation*, 97, 1095, 1998.
- [2] K. E. Healy, "Stem Cells, Biomimetic Polymers, and the Promise of Regenerative Medicine," *Materials Science Seminar, University of Wisconsin – Madison*, 2008.
- [3] W. H. Guo, M. T. Frey, N. A. Burnham, Y. L. Wang, "Substrate rigidity regulates the formation and maintenance of tissues," *Biophys J*, 90(6), 2213-2220, 2006.

[4] D. E. Discher, P. Janmey, Y. L. Wang, "Tissue cells feel and respond to the stiffness of their substrate," *Science*, 210(5751), 1139-1143, 2005.

[5] A. J. Engler, S. Sen, H. L. Sweeney, D. E. Discher, "Matrix elasticity directs stem cell lineage specification," *Cell*, 126, 677-689, 2006.

Nonlinear Viscoelasticity of Native and Engineered Ligament and Tendon

Jinjin Ma¹ and Ellen M. Arruda^{1,2,3,4}

1.Department of Mechanical Engineering, 2.Department of Biomedical Engineering, 3. Macromolecular Science and Engineering Program, University of Michigan. 4. Corresponding Author 2250 GGB 2350 Hayward Street, University of Michigan, Ann Arbor, MI 48109 E-mail: arruda@umich.edu

ABSTRACT

Ligaments and tendons are non-linear viscoelastic materials and their response functions are typically assessed using creep and stress relaxation tests. Non-linear viscoelastic models such as multiple Maxwell elements in parallel and the quasilinear viscoelastic model (QLV) used to capture the non-linear viscoelastic response of ligaments and tendons frequently employ multiple relaxation time constants determined from curve-fitting the entire available data set and generally lack a clear physiological relevance. Uniaxial load-unload tension tests on ligament and tendon also manifests the viscoelastic response and such experiments suggest that the bulk of the non-linearity in the response of these soft tissues is in the elasticity. We propose physiologically relevant non-linear viscoelastic models in which the response of the main structural proteins in ligament and tendon (e.g. collagen and elastin) are described using non-linear elasticity. Our approach using a three-element, non-linear solid micromechanical model captures this viscoelastic response in load-unload, stress relaxation and creep with a limited number of physically meaningful parameters. Previous research also shows different viscoelastic responses between native tendon and ligaments. In our model, by varying the properties of the non-linear springs, we are able to capture the differences in the viscoelastic responses of ligaments verses tendon. We will demonstrate the capabilities of our model by comparing to the experimental results from testing native and engineered ligament and tendon.

INTRODUCTION

Ligaments and tendons are non-linear viscoelastic materials. Characterization of the biomechanical properties of ligaments and tendons is of interest and numerical *ex vivo* experimental investigations are required in order to capture their responses. Currently, the biomechanical characteristics of ligament and tendon are not fully understood nor adequately characterized. The viscoelastic behavior of a material is normally characterized by conducting stress relaxation or creep tests from a given strain or stress, respectively. A uniaxial load-unload tension test on ligament or tendon also manifests the viscoelastic response from the energy dissipation shown as the area difference between the load and unload curves. Previous investigations have shown that ligament exhibits decreased relaxation rates with increased strain levels, whereas tendon exhibits increased relaxation rates with increased strain levels, demonstrating the inherently different mechanical properties of ligaments verses tendons. [1, 2].

Current non-linear viscoelastic models for ligament and tendon includes multiple Maxwell elements in parallel and the quasilinear viscoelastic model (QLV). The former employs multiple relaxation time constants determined from curve-fitting the entire available data set in order to capture non-linear behavior, and the many constants involved lack a clear of physiological relevance. Moreover, the separable QLV theory cannot predict the relaxation rate responses of ligament and tendon as shown in Provenzano et al. 2001.

MICROMECHANICAL MODELING OF TISSUE RESPONSE

Our approach is to use a three-element, non-linear solid micromechanical model to capture the viscoelastic response in load-unload, stress relaxation and creep of ligament and tendon with a limited number of physically meaningful parameters. As shown in **Figure 1**, in this model one non-linear spring B and linear viscous dashpot in series is in parallel with another non-linear spring A. To model the engineered and native ligament, a network of MacKintosh chains [4] is used for spring A and a Gaussian or neo-Hookean chain network (see Treloar for example [5]) is utilized in spring B. The MacKintosh network chain and the neo-Hookean chain are then switched

to capture the native tendon viscoelastic responses. For detailed descriptions of the micromechanical model, please refer to Ma.et al.2009 [3].

Briefly, as shown in **Figure 1 (a)** which demonstrates ligament mechanical behavior, \mathbf{F}^e is the elastic part of the deformation tensor and \mathbf{F}^v is the viscous part. From compatibility, the total deformation \mathbf{F} can be derived as $\mathbf{F} = \mathbf{F}^e \mathbf{F}^v$. The left Cauchy Green Tensor \mathbf{B} is $\mathbf{B} = \mathbf{F}\mathbf{F}^T$. From equilibrium of the system, the total Cauchy stress can be derived as $\boldsymbol{\sigma} = \boldsymbol{\sigma}_A + \boldsymbol{\sigma}_B$, where $\boldsymbol{\sigma}_A$ is the Cauchy stress generated from spring A and $\boldsymbol{\sigma}_B$ is the Cauchy stress generated from spring B. The MacKintosh chain network of the micromechanical model is embedded within an initially isotropic or anisotropic 8-chain framework [6,7,8] as in **Figure 2** to mathematically model the mechanical behavior of ligaments and tendons. This 8-chain MacKintosh chain network constitutive model equation was formulated and previously applied to capture the stress-strain behavior of an F-actin filament network. [12] The Cauchy stresses on each element can be represented as follows:

$$\boldsymbol{\sigma}_A = \frac{nk\theta_A r_0}{3a \lambda_c} \left(\frac{1}{4(1-\frac{\lambda_c r_0}{L_c})^2} \right) \left(\frac{\frac{L_c}{a} - 6(1-\frac{\lambda_c r_0}{L_c})}{\frac{L_c}{a} - 2(1-\frac{\lambda_c r_0}{L_c})} \right) \mathbf{B} - p\mathbf{I}, \lambda_c = \sqrt{tr(\mathbf{B})/3} \tag{1}$$

$$\boldsymbol{\sigma}_B = nk\theta_B \mathbf{B}^e - p\mathbf{I} \tag{2}$$

In these constitutive equations, n is the chain density of the Gaussian or neo-Hookean and MacKintosh network of chains, k is Boltzmann's constant, θ is temperature, and p is the hydrostatic pressure. For the MacKintosh chain network a represents the persistence length, L_c represents the contour length, r_0 is the initial vector chain length and λ_c is the chain stretch. The linear dashpot constitutive equation is $\mathbf{D}^v = \frac{\dot{\boldsymbol{\sigma}}_B}{\eta^*}$ where \mathbf{D}^v is the viscous shear strain rate, η^* is the constant shear viscosity and $\dot{\boldsymbol{\sigma}}_B$ is the equivalent shear stress. The network deformation is assumed to be isochoric and incompressible. A rate formulation is employed to compute the stress vs. strain responses of various tissues for multiple stress relaxation responses.

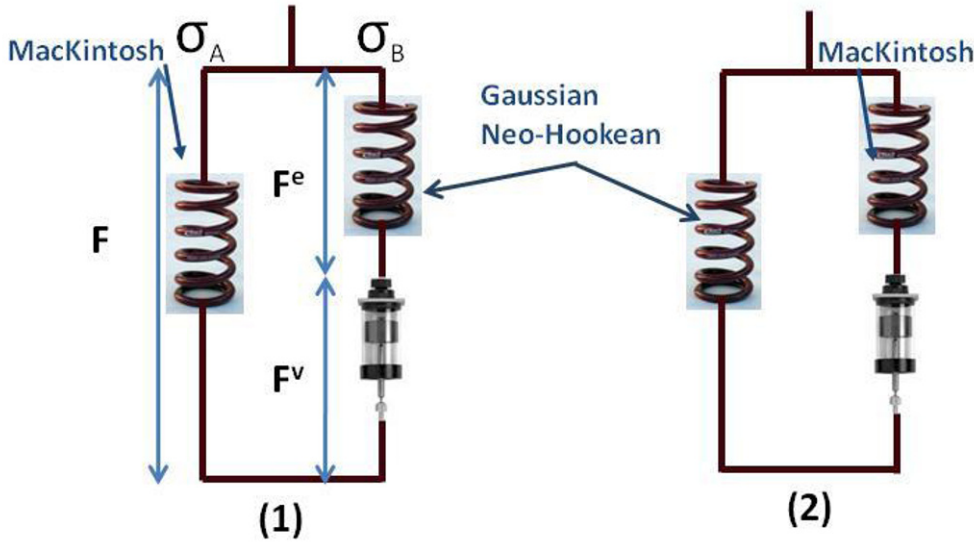


Figure 1. Micromechanical model of engineered and native ligament (1) and tendon (2).

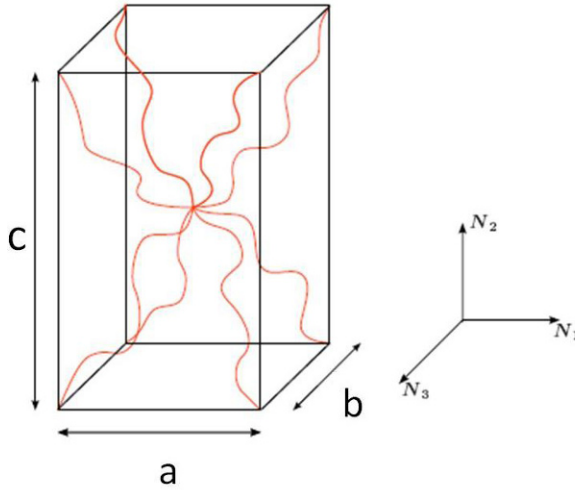


Figure 2. An anisotropic representative volume element for a network of semi-flexible chains. [7, 8]

RESULTS

The stress relaxation experimental responses of native ligament and tendon are obtained from literature. [1, 2] **Figure 3** compares the theoretical stress relaxation responses of ligament and tendon to experimental results. [1, 2] The response predicted from ligament model shows a decreased relaxation rate with increased strain. On the contrary, the response of tendon model shows an increased relaxation rate with increased strain. Both analytical responses predicted from the models relatively matches the experimental data below. **In figure 3 (1)**, by fitting the 2.38% strain response of ligament stress relaxation, the parameters in the current ligament model were found to be 20 for $nk\theta_B$, 5500 for $nk\theta_B$. The contour length and persistence length of the MacKintosh chains were found to be 10 and 20, respectively. Viscosity of the linear dashpot was found to be 1000. A similar procedure was used to capture the tendon responses using tendon literature results. Model parameters were found by fitting the 6% strain response of tendon stress relaxation. The parameters in the current model were found to be 90 for $nk\theta_A$, 2500 for $nk\theta_B$. The contour length and persistence length of the MacKintosh chains were found to be 10 and 9.8, respectively. Viscosity of the linear dashpot was found to be 1500.

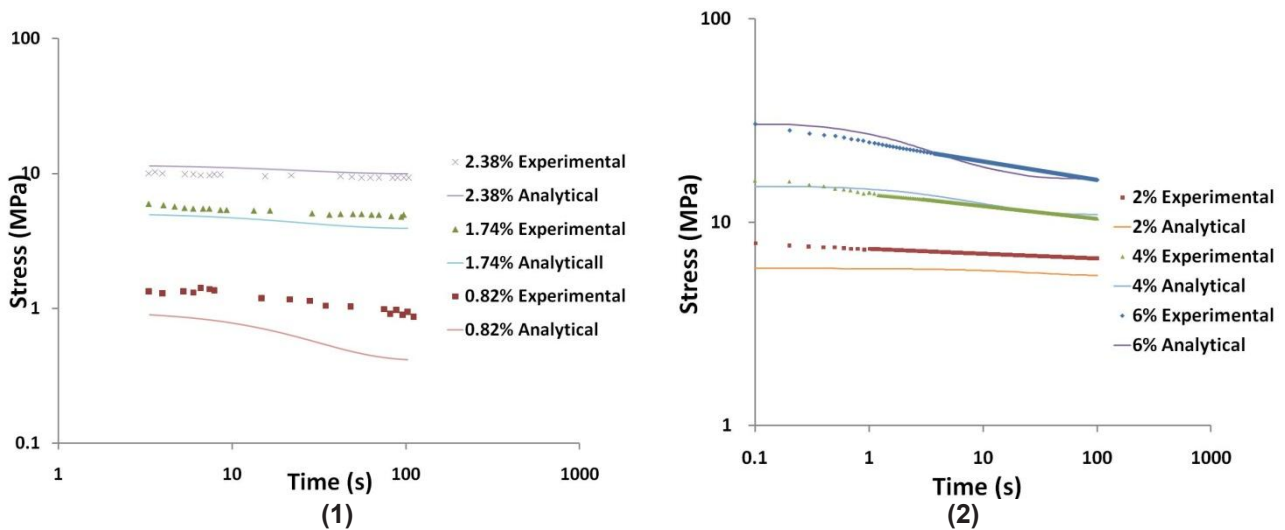


Figure 3. Analytical characterizations of ligaments (1) and tendons (2) compared to experimental results from the literature. [1,2]

The proposed ligament model is also used to capture the uniaxial load-unload mechanical response of the ligament region of an engineered bone-ligament-bone construct that has been designed and fabricated in our research lab [9] as shown in **Figure 4**. By varying the stiffnesses of the two nonlinear springs and the viscosity of the dashpot, the micromechanical model is robust enough to capture the mechanical responses of in vitro and in vivo engineered constructs.

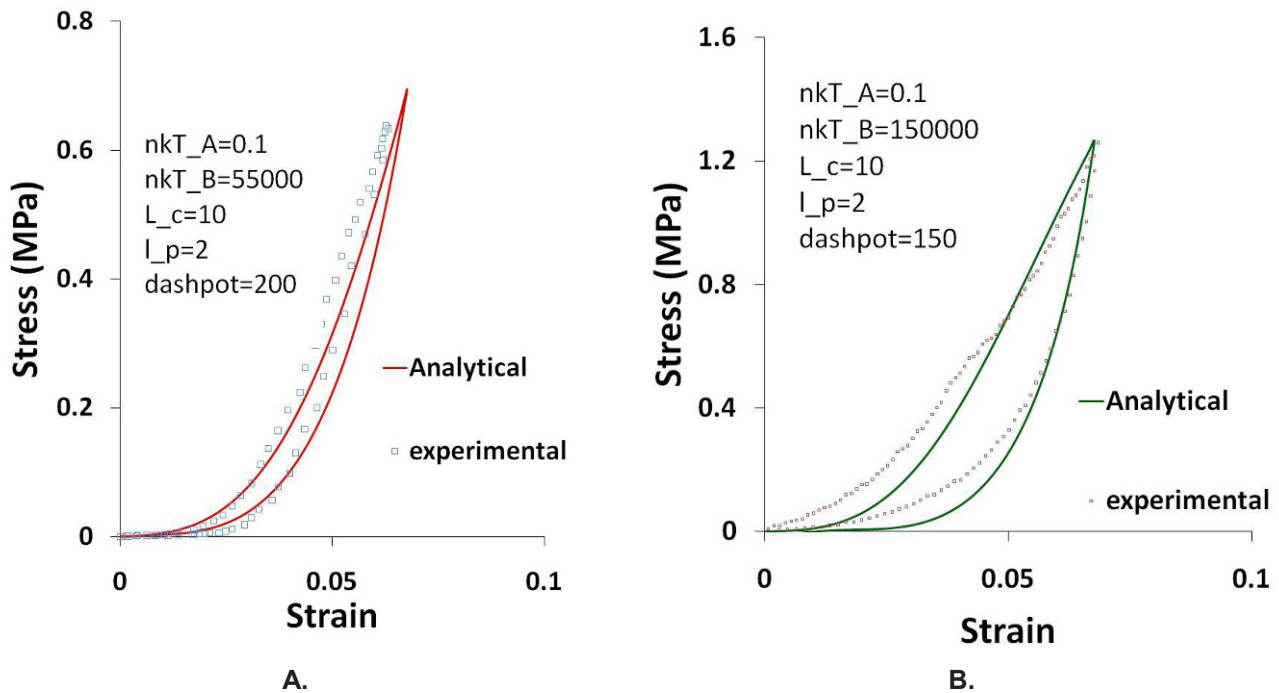


Figure 4. Micromechanical modeling of engineered in vitro BLB constructs (A) and engineered one-month in vivo BLB constructs (B).

DISCUSSION

ACL injuries are common injuries among athletes and usually ACL reconstruction is required in order for patients to maintain the same level of sport activity. During ACL reconstruction, PT and hamstring tendon are common grafts for ACL replacement. The outcomes of current reconstruction methods are successful with various limitations such as unmatched intra-articular biomechanical properties. For decades, the mechanical properties of ligament and tendon were described to be similar through the stiffness comparison measured from load to failure tests. A recent study has shown the differences in the stress-strain responses of an ACL and a patellar tendon (PT) from the same ex vivo subjects. [10] The ACL experiences a lower load at a given strain level than does the PT. Since the average strain level experienced by a human ACL during normal activities is less than 4% [11], uniaxial tension tests reveal vastly different mechanical responses between the ACL and PT in the physiological range. The viscoelastic responses of ligament and tendon are also fundamentally different. More recent studies have shown the mechanical responses of these two tissues to differ in important ways, suggesting limitations in the ultimate efficacy of a tendon as a ligament graft.

In linear viscoelasticity, a standard linear solid model is capable of capturing the linear viscoelastic behavior of materials. By changing the linear springs to nonlinear springs, the nonlinear solid model can theoretically capture the non-constant relaxation rates of ligament and tendons. As shown in **Figure 3**, we are able to qualitatively capture and predict the non-constant stress relaxation rates of ligament using a limited number of parameters that are physiologically relevant. Our previous work has shown ligament and tendon strain behaviors are heterogeneous. [9] In this paper, we are able to capture the average stress-strain response by assuming homogeneity. Our current work is investigating the nonlinear viscoelastic characteristics of patient-matched ligament and tendon behavior. We are also going to investigate the application of our micromechanical model to capturing the heterogeneity of ligament and tendon to assess the reliability and prediction of the model.

CONCLUSIONS

Our standard non-linear solid micromechanical model has been verified against low strain rate data of both ligament and tendon tissues as well as on engineered ligament, but the efficacy of this approach in capturing the high strain rate responses has not been determined.

REFERENCES

- [1] Provenzano P., Lakes R.S., Keenan T., and Vanderby R., Jr, Nonlinear Ligament Viscoelasticity, *Annals of Biomedical Engineering*, Vol. 29, pp.908-914, 2001
- [2] Duenwald S.E., Vanderby R., Jr, and Lakes R.S, Viscoelastic Relaxation and Recovery of Tendon, *Annals of Biomedical Engineering*, Vol.37, No.6, pp.1131-1140, 2009
- [3] Ma J., Narayanan H., Garikipati K., Grosh K. and Arruda E.M., "Experimental and Computational Investigation of Viscoelasticity of Native and Engineered Ligament and Tendon," *Proceedings of the IUTAM Symposium on Cellular, Molecular and Tissue Mechanics*, K. Garikipati and E. M. Arruda Eds, Springer, 2009(a).
- [4] MacKintosh F.C., Kas J. and Janmey P.A., Elasticity of semiflexible biopolymer networks, *Phys Rev Lett.*, 75-4425, 1995
- [5] Treloar L.R.G, *The physics of rubber elasticity*, Oxford University Press, 2005
- [6] Arruda, E. M. Boyce, M. C., A three-dimensional constitutive model for the large stretch behavior of rubber elastic materials, *Journal of the Mechanics and Physics of Solids*, Vol.41, No. 2, pages 389, 1993
- [7] Bischoff JE, Arruda EM, Grosh K, A microstructurally based orthotropic hyperelastic constitutive law, *J Appl Mech* 69:570–579, 2002a
- [8] Bischoff JE, Arruda EM, Grosh K, Orthotropic hyperelasticity in terms of an arbitrary molecular chain model, *J Appl Mech* 69 (4):198–201, 2002b
- [9] Ma J., Goble K., Smietana M., Kostrominova T., Larkin L. and Arruda E.M., "Morphological and Functional Characteristics of Three-Dimensional Engineered Bone-Ligament-Bone Constructs Following Implantation," *J Biomech Eng*, Vol. 131, Issue 10, 101017-1, 2009(b).
- [10] Chandrashekar N., Hashemi J., Slauterbeck J. and Beynon B., "Low-Load Behavior of the Patellar Tendon Graft and its Relevance to the Biomechanics of the Reconstructed Knee," *Clin Biomech*, 23:918, 2008.
- [11] Beynon B.D. and Fleming B.C., "Anterior Cruciate Ligament Strain in-Vivo: A Review of Previous Work," *J Biomech*, 31:519, 1998.
- [12] S.Palmer J.S. and Boyce M.C., Constitutive modeling of the stress-strain behavior of F-actin filament networks, *Acta Biomaterialia*, 4, 597-612, 2008

Spinal Ligaments: Anisotropic Characterization Using Very Small Samples

Rachel J. Bradshaw, Alison C. Russell, *Anton E. Bowden, PhD

* Corresponding author: abowden@byu.edu

Brigham Young University

435 Crabtree Building

Provo, UT 84602

ABSTRACT

Spinal ligaments exhibit a nonlinear, anisotropic, viscoelastic response, which has yet to be adequately characterized. Characterizing and modeling the material responses of spinal ligaments is essential to understanding both normal and pathological motion of the spine. Current methods for testing connective tissue require large volumes of sample and often experience difficulty in gripping, due to the texture of connective tissue. Consequently a mechanism capable of overcoming these barriers was developed, designated as the Anisotropic Small Punch Test (ASPT). The apparatus consists of a 6-mm diameter tissue sample clamped between two peripheral plates. The center of the sample is displaced by a 1mm rod and renders a multiaxial profile recorded by two cameras at orthogonal angles. The measured force and displacement experienced by the sample then serve as input for an optimization routine to derive constitutive coefficients that characterize ligament behavior. Bovine achilles tendon were used to validate that ASPT is an appropriate method for capturing the nonlinear, anisotropic, viscoelastic response of ligaments. This methodology has the potential to transform current methods of testing biological tissue in addition to quantifying mechanical properties of ligaments.

INTRODUCTION

Spinal ligaments are composed of closely packed parallel collagen fiber bundles embedded in a ground substance matrix composed of elastin, proteoglycans and water. This unique composition provides ligamentous stability to the spine, protecting the spinal cord from traumatic loading conditions, and facilitating physiological spinal motion. Spinal ligaments' unique microstructure generates nonlinear, anisotropic, viscoelastic material responses which have yet to be fully characterized. Current biomechanical methods for testing connective tissue often experience difficulty in gripping the sample, require large sample volume and are tested bi-directionally [1, 2]. These methods are poorly suited to test spinal ligaments—considering the tissues' minute size. Due to these conditions few studies have holistically characterized the properties of spinal ligaments. Consequently, the contribution of spinal ligaments towards spinal stability remains ambiguous and unclear.

The absence of this information affects clinical and academic applications in treating and understanding spinal pathology. The majority of spinal stability is often attributed to highly developed, dynamic neuromuscular control [3, 4]. Yet, this statement contradicts the conventional structural role of ligaments in the body; as shown in the knee, ligaments are primarily responsible for providing joint stability. Several studies have confirmed spinal ligaments mechanoreceptors are responsive to mechanical strain, serving as nociceptors in lower back pain [5, 6]. Likewise, several current spinal operative procedures damage ligaments' functional integrity, producing significant changes in ligament displacement ($p < 0.05$) under physiological loads (400N to 600N), and alter the inferior facet

motions ($p < 0.05$). This increase in spinal motion induces alternative loading patterns to adjacent spinal components (ligaments, intervertebral disc and musculature), potentially causing additional chronic pain [7].

Inherently, the stability of the spine depends on its constituents, including spinal ligaments. Quantifying the quasistatic properties of spinal ligaments is the first step to fully characterizing and understanding both physiological and pathological motion of the spine. The objective of the proposed work is to develop experimental methodology and optimization technique capable of characterizing quasistatic anisotropic properties of spinal ligaments.

BACKGROUND

The spinal column is unique as it consists of multiple joints, at each vertebral level, supported by six spinal ligaments: anterior longitudinal ligament (ALL), posterior longitudinal ligament (PLL), interspinous ligament (ISL), supraspinous ligament (SSL), facet joint capsule (FJC) and ligamentum flavum (LF); shown below in Figure 1.

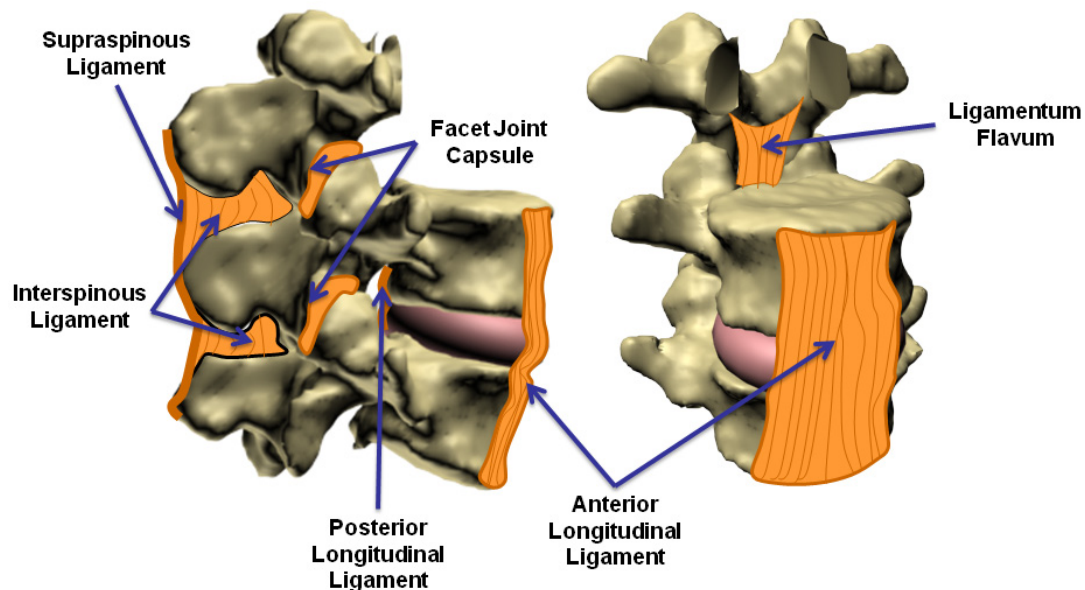


Figure 1. Diagram of the six spinal ligaments found in the human body.

Related literature has investigated variations in spinal ligament geometry, anatomy [8] and material properties [9, 10] with age, gender, postmortem weight, heights, causes of deaths and other related factors. The majority of these studies have obtained linear material responses (stress-strain) via bone-ligament-bone complexes or functional spinal units [9, 10]. However, these *linear* characterizations contradict the highly *nonlinear* response observed in ligaments due to collagen fibril crimping [2]. A notable exception is the work by Chazal, et. al. [11]. Chazal obtained nonlinear stress-strain curves associated with three different inflection points defined on the ALL, PLL, LF, SSL, and ISL ligaments. Additional efforts were made to consider the histology of the ISL and SSL ligaments to identify ligament integrity and mechanical patterns of collagen fibers at rest and rupture limits.

To fully define spinal ligament mechanics the development of adequate experimental and computational techniques are requisite. Recent literature identifies a multiaxial method capable of mechanically testing small isotropic samples. The Small Punch Test (SPT) has been used to assess mechanical properties of metals and polymers [12]. To our knowledge no literature indicates this technique has been used to test biological tissues or anisotropic materials.

METHODS AND MATERIALS

Three steps were executed to create and optimize the punch test ASPT (Anisotropic Small Punch Test). First, design objectives for the device were developed to initialize essential design processes and produce detailed generations of concept designs. Next, a working prototype was manufactured and assembled. Finally, using bovine Achilles tendons, experimental procedures were refined to obtain optical and numerical data to (1) validate the methodology and (2) obtain optimized constitutive coefficients using the developed system identification optimization routine. The selected constitutive model (Weiss model) has previously been used to evaluate nonlinear anisotropy of the medial collateral ligament of the knee, glenohumeral capsule of the shoulder and interosseous ligament of the forearm [13, 14, 15].

Design Objectives

The established objectives primarily sought to overcome current barriers of biomechanical testing, develop accurate components capable of testing very small samples (6mm diameter) and ensure the device did not significantly alter the integrity of the biological samples (i.e. hydration, temperature, altering the microstructure). Likewise the multiaxial testing of a transversely isotropic material requires a thorough and sophisticated: experimental techniques, data collection and optimization/constitutive models; in order to accurately predict the response of spinal ligaments to applied loads or displacements. Consequently the following design objectives were established:

Gripping of Sample — As mentioned before one of the greatest difficulties of testing connective tissue is gripping the sample. Previous testing methods have used assorted schemes to uniformly fixate a sample: direct fixation—tightly clamping or gluing the tissue sample, indirect fixation—testing existing tissues bone-ligament-bone complexes, or adjusted fixation—altering sample texture by either ‘drying out’ or ‘freezing’ the samples borders [1, 2]. However these options are not viable for testing spinal ligaments. Consequently a combination of techniques was proposed to increase the quality of ligament fixation. (1) To minimize the volume of sample required, a circular sample would be used, clamping the outer perimeter. (2) To enhance the mechanical hold, micro grips (~0.1mm) could to be machined on the device surfaces in contact with the sample. (See Figure 2) (3) Lastly, a peltier device could be attached to the outer wall of the device, freezing the outer perimeter of the sample.

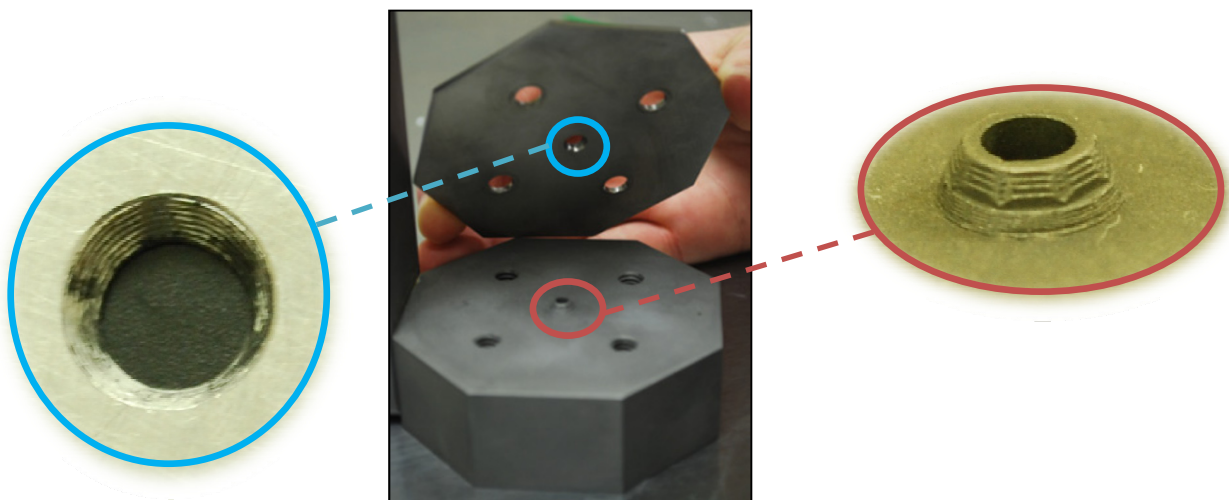


Figure 2. Zoomed images of micro grips: (Left) Top Plate Ridges (Middle) ASPT (Right) Etched Cone.

Numerical Data Collection — The force and displacement of the plunger reflects the force and displacement experienced by the tissue sample at the point of contact. It was essential to use extremely accurate methods to simultaneously capture this information, as the sample has a very small radius (3mm). The system for measuring displacement was a threaded lead screw, which when turned actuated a ‘piston’ plunger. A stepper motor or

linear actuator (piston) can provide a finer control of the plunger displacement. A Transducer Techniques® load cell was used for force measurement.

Optical Data Collection —Deriving displacement profiles, along the two orthogonal axes (soft and stiff), thus requires images be obtained simultaneously by two CCD cameras (scA640-70fm Basler Vision Technology) with CCTV lens (1/3" Tamron), with a 20-100mm focal length. This information can then derive the samples' reaction in nodal components; this can only be accomplished by combining optical and numerical data to determine the displacement of the sample at any given location.

Prototype

Concept designs went through series of reviews to optimize design components, dimensions and capabilities. The ASPT working prototype consists of a 6-mm diameter tissue sample which is set on a raised conical surface and clamped between two peripheral plates. Meanwhile a 1mm rod displaces the center of the sample to render a multiaxial profile, recorded by two CCD cameras at an orthogonal angle. Forces induced on the plunger are measured with a 25 lb load cell with an accuracy of ± 0.005 lbs. Precision threads on a lead screw vertically displace the plunger. Once the plunger contacts the sample the CCD cameras are calibrated and interfaced with a custom LabVIEW program to track profile slopes and record displacement simultaneously with the force induced by the plunger. Capturing orthogonal slope profiles is essential to quantifying anisotropic behavior as the profile slope is more nonlinear perpendicular (transverse) to the collagen fiber direction than along it (longitudinal). The ASPT orientation is illustrated in [Figure 3](#).



Figure 3. (Left) Experimental setup (Right) Calibration of ASPT.

Optimization Techniques

Experimental methodology was polished through a series of testing using bovine achilles tendon. The ASPT data was then input into a System Identification finite element analysis (FEA) Optimization Solver to quantify the samples material response. As shown below in [Figure 5](#), an inverse finite element (FE) method within the routine enables the optimization to generate model parameters to compare to experimentally obtained data by optimizing the selected numerical parameters ($C_1, C_2, C_3, C_4, C_5, \lambda^*$) and minimizing the residual error with respect to derived experimental obtained values.

Measured displacement and force exerted by the plunger, captured along the longitudinal and transverse axes, correspond to twenty equidistant nodes in the FE model, composed of hexahedral brick elements. The experimentally obtained nodal displacements and transitional crimp region (λ^* , found from the load displacement curve) then serve as analysis variables. Starting values for the material coefficients ($C_1, C_2, C_3, C_4, C_5, \lambda^*$) are assumed before initializing the optimization. The optimization continues to run until the sum of the square errors between the model and experimental profiles and plunger force have been minimized, and the resulting constitutive coefficients are found.

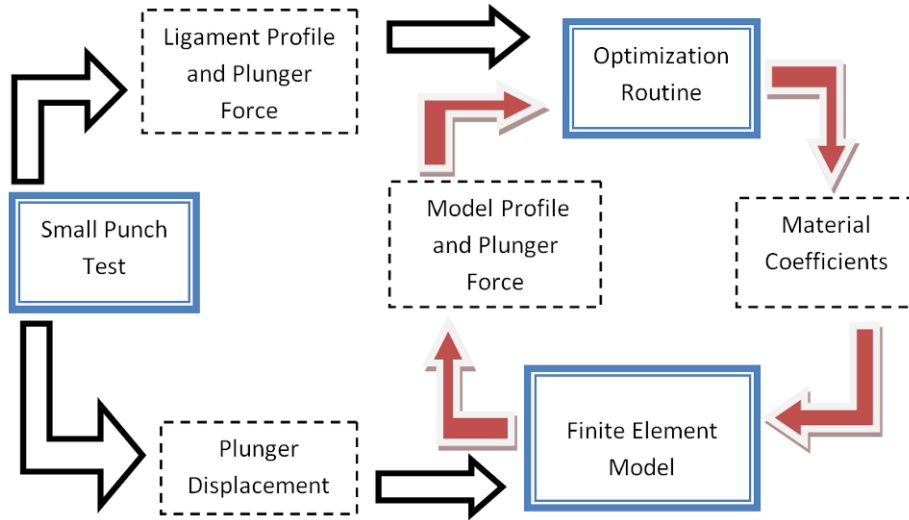


Figure 4. Schematic of ASPT system identification optimization routine.

RESULTS

Manufacturing of the device rendered a prototype that accomplished the established design objectives and was used for validating experimental punch test protocols. The Labview code output two CCD videos and synchronized data files of force and displacement readings with respect to time. As shown in Figure 5 the force varies with time and each sample is unique in its response. The stiff and soft side profiles and respective displacements are shown in Figure 6. The displacements are converted from units of pixels to millimeters, using an internal MatLab calculation. The three-dimensional plots chart the displacement of four equidistant nodes on the slope profile with respect to time.

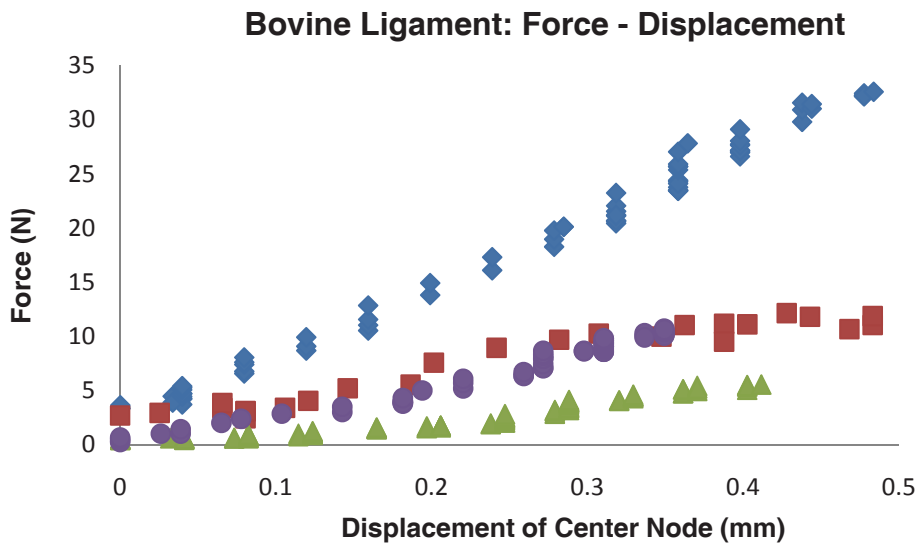


Figure 5. Force displacement plots of bovine samples.

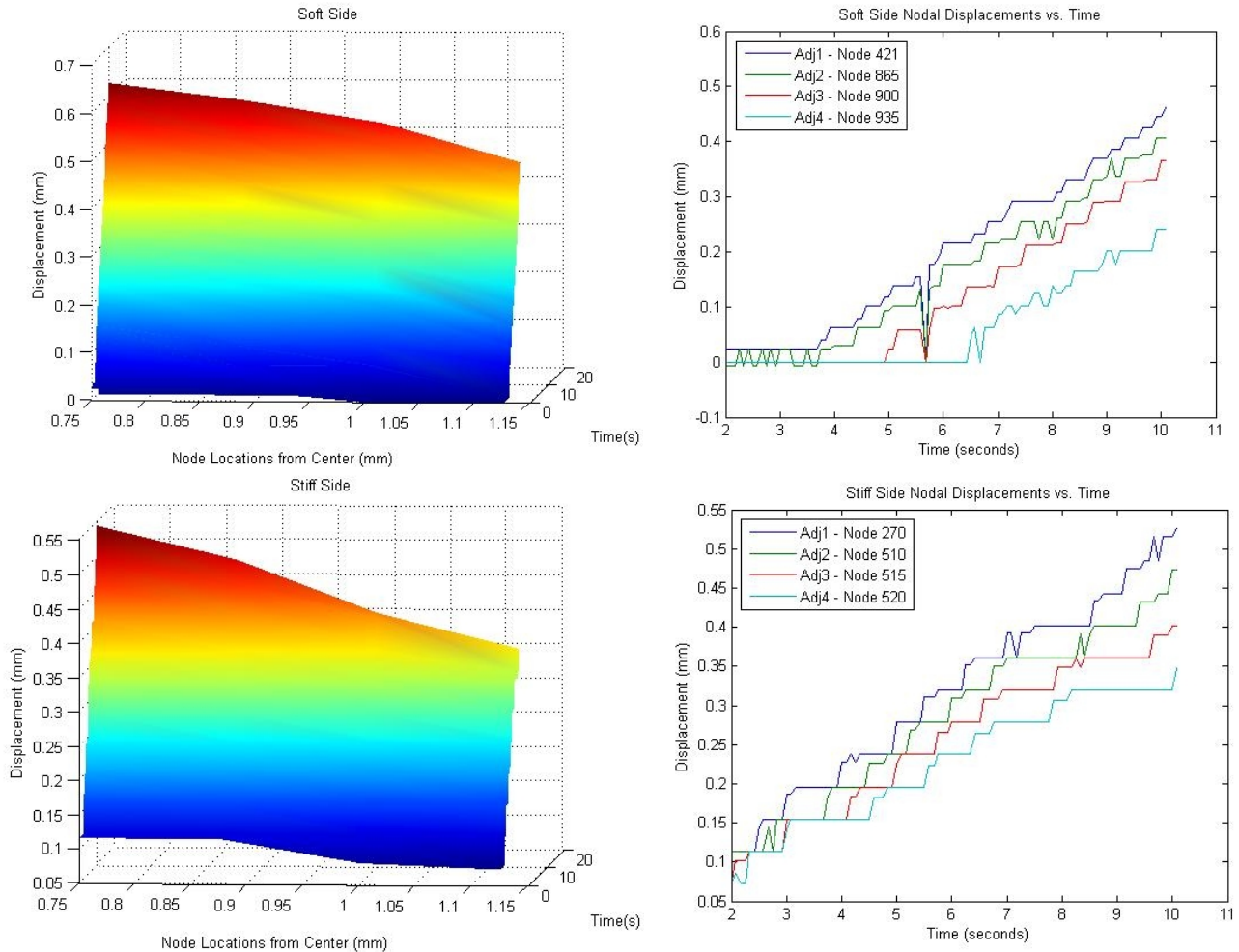


Figure 6. Slope profiles and correlating displacements of the (Top) soft and (Bottom) stiff side along seven nodes.

DISCUSSION

Combining the experimental capability of ASPT with system identification FEA optimization thus provides a fitting methodology for quantifying spinal ligaments' quasistatic, anisotropic, nonlinear response. The acquired data demonstrates the capability of this methodology for obtaining three-dimensional readings of displacement, force and the correlating slope profiles from very small samples. The ranges of force and displacement values vary due to bovine sample location, sample thickness, quality, and fiber orientation as demonstrated by Figure 5. The upper bound (sample 3) represents a marginally thicker ligament, while lower bound (sample 14) represents a notably thinner sample closer to the sample insertion site. These variations represent geometric differences in sample response, not constitutive differences. The optimization process takes into account the difference in sample thickness, yielding non-biased material constitutive parameters rather than geometry-specific structural properties.

Manufacturing of the prototype introduced several challenges, specifically in designing a system which accurately aligned and displaced the plunger through the center of the 6 mm sample. The mechanical micro grips proved to be very effective in holding the small samples; therefore a Peltier device was not used in this mechanism. In experimental setup, lighting of the sample introduced reflection into the camera views. However, high contrast lighting was necessary to capture of realistic slope profiles. To eliminate reflectance the mechanisms' top plate surface was painted black and a black backdrop was provided (Figure 3). It was found that best lighting was

provided by placing the lamp directly above the sample. Minor adjustments to the ASPT setup will prepare the system for testing and characterization of spinal ligament samples. Upon quantifying nonlinear anisotropic quasistatic properties of spinal ligament it is anticipated this methodology will be extended to characterize the viscoelastic constants supported by the Weiss model [13].

Research findings are anticipated to contribute to the field of spinal biomechanics by accurately identifying properties and roles of spinal ligaments. Likewise these findings may encourage clinicians to develop less invasive spinal surgery procedures, which currently compromise ligament functionality. Moreover, this novel methodology has the potential to transform current methods of testing biological tissue. Finally, we will use the obtained material coefficients as inputs to a lumbar spine FE model with validated three-dimensional ligament geometries and nonlinear material coefficients investigate ligament mechanics under physiological and pathological conditions. Clearly defining material properties of spinal ligaments is an essential step to expounding on probing uncertainties within the field of spinal biomechanics to understand and advance clinical treatments for chronic back pain.

ACKNOWLEDGEMENTS

Funding for this project provided by a BYU Mentored Environment Grant, a Fulton College of Engineering and Technology Supplemental Research Grant and a BYU Gerontology Research Grant.

REFERENCES

- [1] Hartright D., et al., *Orthopedic Biology and Medicine: Repair and Regeneration of Ligaments, Tendons and Joint Capsule*, Walsh W. R., Editor. 2006, Humana Press Inc.
- [2] Debski R.E., Moore S.A., and E.J. Rainis, *Encyclopedia of Biomaterials and Biomedical Engineering*, Bowlin G. L.; Walsh G. W., Editor. 2008, Informa Healthcare.
- [3] White, A.A. and M.M Panjabi, *Clinical Biomechanics of the Spine*. 2. Philadelphia: Lippincott Williams & Wilkins, 1990. Print.
- [4] Andersson C, Chaffin D, Herrin C, Mathews L. *A biomechanical model of the lumbosacral joint during lifting activities*. J Biomechanics, 1985. 18:571-84.
- [5] Cavanaugh, J. M., A. el-Bohy, et al. *Sensory innervation of soft tissues of the lumbar spine in the rat*. J Orthop Res, 1989. 7(3): 378-88.
- [6] Bogduk N, Wilson A, Tynan W. *The human lumbar dorsal rami*. J Anat, 1982. 134:383-97.
- [7] Cusick J.F., et al. *Biomechanics of Sequential Posterior Lumbar Surgical Alterations*, J Neurosurg 1992. 76:805-11.
- [8] Behrsin, J.F. and C.A. Briggs, , *Ligaments of the Lumbar Spine: A Review*, Surg Radiol Anat, 1988. 10:211-9.
- [9] Myklebust et al., *Tensile Strength of Spinal Ligaments*. Spine, 1986. 13(5):526-31
- [10] Pintar F.A. et al., *Biomechanical Properties of Human Lumbar Spine Ligaments*, J Biomechanics, 1992. 25(11): 1351-6.
- [11] Chazal J. et al., *Biomechanical Properties of Spinal Ligaments and a Histological Study of the Supraspinal Ligament In Traction*. J Biomechanics, 1985. 18(3): 167-76
- [12] Eskner M.E. and Sandstrom R., *Mechanical Property Evaluation Using the Small Punch Test*, J Testing Evaluation, 2004. 32(4):1-8.
- [13] Gardiner, J.C. and J.A. Weiss, *Subject-Specific Finite Element Analysis of the Human Medial Collateral Ligament During Valgus Knee Loading*. J Orthopedic Research, 2003. 21: 1098-106.
- [14] Moore, S.M. et. al, *The glenohumeral capsule should be evaluated as a sheet of fibrous tissue: a validated finite element model*. Ann biomed Eng, 2010. 38(1): 66-76.
- [15] Stabile, K.J. et. al, *Bi-directional mechanical properties of the human forearm interosseous ligament*. J Orthop Res, 2004. 22(3): 607-12.

In-Flight Wing-Membrane Strain Measurements on Bats

Roberto Albertani
Research & Engineering Education Facility (REEF), University of Florida
Department of Mechanical and Aerospace Engineering
1350 North Poquito Rd, Shalimar, FL, 32579, ralb@ufl.edu

Tatjana Hubel
Division of Engineering
Brown University, RI

Sharon M. Swartz
Department of Ecology and Evolutionary Biology
Brown University, RI

Kenneth S. Breuer
Division of Engineering
Brown University, RI

Johnny Evers
Air Force Research Laboratory, RWGN, Eglin AFB, FL

ABSTRACT

An efficient system for high-resolution measurements of a bat wing's membrane during flight is presented, proving the feasibility of dynamic strain measurements on bats wing membranes during flapping. Data were collected from wind tunnel wind-off flights of a Jamaican fruit bat, *Artibeus jamaicensis*, a nocturnal and frugivorous specie trained by Brown University team to fly back and forth in the test section. Visual image correlation was used for image post-processing providing spatial high-resolution three-dimensional displacements and strains on the bat's wing.

Temporal membrane surface-averaged strain analysis showed a level of strain in the X direction (spanwise) approximately three times larger than the Y direction (chordwise) with values around 10% and 3%, respectively. Strains are estimated from an unknown reference state at the beginning of each recorded sequence. Full surface membrane strain distribution shows a consistent strain-relief effect around the ring finger during downstroke in the X direction (spanwise). Temporal wing section shape analysis during a down stroke revealed a higher camber and a significant pitch-up twist of the ring finger respect to the free membrane between the little and ring finger.

INTRODUCTION

The aerospace engineering community is increasingly interested to the flight mechanics and dynamics of small flapping air vehicles, Fig. 1, and natural organisms in the low Reynolds number regime. Observing and studying leaving flying creatures could offer a significant source for bio-inspiration in several disciplines including mechanics of novel materials, highly dynamic adaptive structures, unsteady aerodynamics and guidance, navigation and control (GNC). Whereas flight measurements of biological systems are relative abundant, a high resolution recording of data mechanical data on specimen components and an efficient distillation of their results from a structural point of view is relatively rare. This paper presents the elastic deformations and in-plane strain on a wing's membrane of a bat flying in a wind tunnel collected using the experimental technique based on visual image correlation (VIC). The data presented were collected from a number of wind tunnel flights of different individuals of the Jamaican fruit

bat, *Artibeus jamaicensis*, Fig. 2. The experiments were conducted in the low-speed wind tunnel at the Division of Engineering at Brown University.

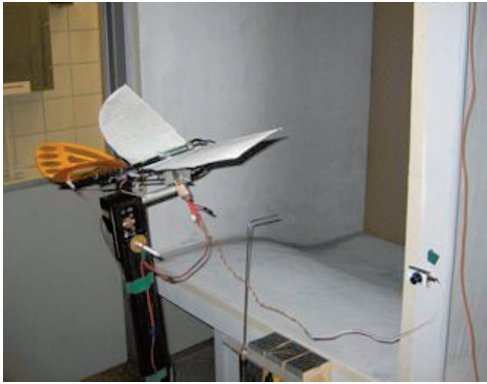


Figure 1. A 20 cm wingspan ornithopter with flexible wings in the University of Florida REEF small wind tunnel.



Figure 2. Example of the Jamaican fruit bat, *Artibeus jamaicensis*, the species used for the wind tunnel experiments.

Natural fliers demonstrate a diverse array of flight capabilities, many of which are poorly understood. NASA established a research project to explore and develop flight technologies inspired by biological systems [1]. Albertani et. al performed shape and strain measurements using visual image correlation (VIC) and aerodynamic coefficients evaluations for different configurations of elastic membrane micro air vehicles (MAV) wings in the wind tunnel in steady conditions [2], demonstrating the intimate relation between the membrane strain state and the aerodynamic characteristics. Decades of research in animal flight has given insights into the principles of flapping wing propulsion and led to some surprising discoveries such as the importance of unsteady mechanisms on lift generation in the low Reynolds number regime [3-5]. Multiple kinematic studies on bat flight have been conducted over the years with increasing accuracy [6-9] and recent simultaneous recordings of wake structure and wing motion by Hubel et al. provided new insight into the force generation on the wing [10,11]. Relevant research on the flight and structural behavior of bat wings was performed by Swartz, Bennett and Carrier [12]. The researchers, using strain gauges implanted on the right humerus and left radius bones, were able to collect *in vivo* strain data during controlled flight in a special cage demonstrating that torsion and shear are unique and crucial features of the skeletal biomechanics during flight.

The investigation of wing deformation on aerodynamic performance requires the ability to gain the information about the extent of the deformation over a large wing area and the course of a wing beat cycle. Nowhere is this as challenging as for the highly complex wing motion in bat flight. The skin of bat wings is exceptionally compliant. It consists of two very thin epidermis layers separated by a thin dermis layer that contains nerves, blood vessels and muscle fibers and has an anisotropic property with maximum elasticity parallel to the trailing edge and higher stiffness perpendicular to it [13]. Bat membrane wings are subjected to passive deformation due to inertial and aerodynamic forces and, contrary to insect wings that lack internal muscles, allow most likely active control of the wing deformation to a certain extent as well. However, although there is an increasing need to quantify membrane deformation and artificial latex wing have shown higher lift slopes, greater force magnitude and higher critical angles of attack, direct measurements of the deformation during flight remain largely elusive due to the lack of an appropriate measurement technique.

The scope of the work presented in this paper was to set an efficient system for high-resolution measurements of the three-dimensional shape and the strain state on a bat wing's membrane during flight. Results could support the characterization of the wing mechanics and kinematics used by bats for adapting their intricate control and elastic wings system to non-steady flight conditions. The results could originate new strategies for micro and nano air vehicles aerodynamic and aeroelastic design as well as novel GNC strategies. The results presented in this project show the feasibility of dynamic strain measurements on bats wing membranes during flight.

THE EXPERIMENTAL SET-UP AND POST PROCESSING

The experiments were performed in the Engineering Division of Brown University close-loop low-speed wind tunnel with a test section of 3.8 meters in length and a cross-section of 0.60 by 0.82 m (height x width) with optical access from the side-walls and the ceiling. In order to accommodate the wind tunnel for bat flight experiments doors were installed at the upper and lower end of the test section in order to introduce and retrieve the animals from the test section. Walls and ceiling of the test section consist of antireflective glass plates and Plexiglas windows allowing monitoring the animal constantly. A fine-meshed net that is installed at the upstream entrance in order to restrict the bats increased the turbulence level from 0.08% to 0.5%. All the experiments were conducted in wind-off conditions. Three Photron 1,024 PCI cameras, were used to record the wing motion of the bat while flying in the test section. The cameras had a resolution of 1,024 x 1,024 pixels and we recorded at 1000 fps with a shutter speed of 1/2000. The cameras were synchronized with each other and calibrated in two-pairs by moving a calibration target through the observation volume. The cameras were positioned above the test section looking down under different angles, as depicted in Fig. 3. In favor of high resolution the observation area was chosen to be rather small, concentrating on recording the dorsal side of the wing during mid up and downstroke. Three Halogen lights with red gel filters were used to illuminate the test section, keeping the light conditions favourable for the nocturnal flight behavior of the bats.

The data presented were collected from a number of wind-off flights of one individual of the Jamaican fruit bat, *Artibeus jamaicensis*, a nocturnal and frugivorous specie. Its distinctive features include the absence of an external tail and a minimal, U-shaped interfemoral membrane. The coat is gray-brown and has a mild, soap-like odor, and is slightly paler on the underside. It is known to have a nose that looks somewhat like a third ear, and it also has pointier ears than related bats. It is typically around 9 cm in length. The captive-bred male bat, illustrated in fig. 4 passing in the camera's field-of-view during a flight, was trained to fly back and forth in the test section prior to the experiment by offering a landing place at each end of flight space.

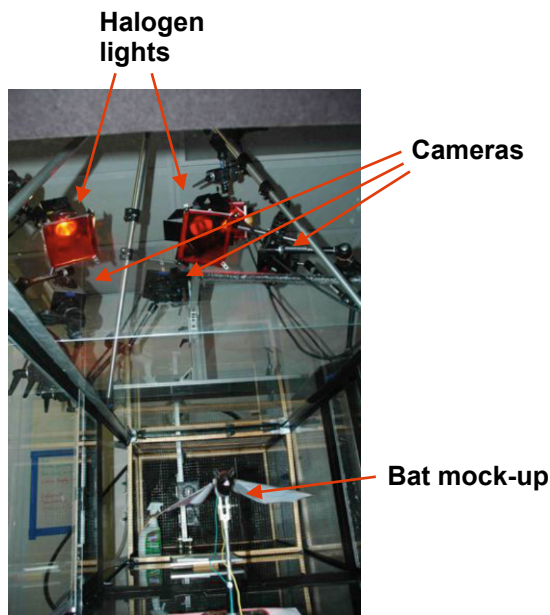


Figure 3. Front view of the three-camera set-up in the Brown University wind tunnel.



Figure 4. A Jamaican fruit bat flying in the Brown University wind tunnel.

Two nets were installed at each end of the test section in order to restrict the bats. The net at the downstream end of the test section served simultaneously as a landing place. An additional net was installed at the ceiling at the upstream location in order to provide the second landing place due to the inadequacy of the upstream restriction net to serve as such because of its very small mesh size. During the training process multiple bats were introduced to the test section at the same time taking advantage of their habit of roosting together. As soon as one bat discovered the roosting place the others usually followed suit. Once discovered the bats had no problem to fly back and forth between the two roosting places, often doing it without or very little outward encouragement. Only if the bat didn't change its roosting location for several minutes we intervened by opening the door of the test section or in addition reaching slightly towards it. A visual image correlation (VIC) system, originally developed and introduced

by researchers from the University of South Carolina [14, 15], was used to measure the bat's wing three-dimensional geometry, the in-plane and out-of-plane displacements. The principle of the VIC is to determine the displacements of the specimen under load by tracking the deformation of a random speckle pattern previously applied on the specimen's surface. The random pattern is digitally acquired by the cameras before and under load, and mathematically processed by finding the region in a deformed image that maximizes the normalized cross-correlation score with respect to a small subset of the image taken while no load was applied (reference image). The random speckle pattern was applied on the membrane of the dorsal side of the right wing using a skin-friendly and edible mixture of starch, cake icing and egg white. While the speckles were applied using a small stick the bat was anesthetized with isoflurane, Fig 5. Whereas the speckle pattern was prone to smear during the first five minutes and needed to be redone on two occasions its non-toxicity and easy removal that allowed the reuse of the same bat the next day made it highly beneficial. The limited time allowed for the speckling resulted in a relatively sparse pattern, illustrated in Fig. 6, resulting in a problematic correlation in several cases.



Figure 5. The anesthetized bat during the application of the speckle pattern on its right wing.



Figure 6. The bat's wing with the final speckle pattern.

The experiments typical procedure was to allow the bats randomly flight in the test section in wind-off conditions and manually trigger the cameras when the operator felt to have a good opportunity to capture useful images. Because of the inherent flight velocity of the bats and the limited field-of-view of the three cameras, it was possible to capture an average of 25 to 35 meaningful images per flight at a frame rate of 1000 frames per second. Post-processing of the images was conducted later and off-site due to the relevant amount of time devoted to the search of correct data among the thousands of images captured during the flight tests. The VIC post-processing could estimate the wing membrane displacements based on an initial state typically called reference image which, in wind tunnel experiments, is typically the wind-off conditions and the elastic membrane before application to the wing [2, 16]. In the case of the presented experiments, because of the lack of a truly relaxed wing's membrane reference state, the results are based on the first image of the sequence thus the displacements and strain represent the change in the membrane's state from an unknown initial condition represented by the first image in the sequence. Visual inspection of the pictures at the beginning of the events assured an initial state free of abnormalities on the membrane as buckling or other instability conditions. Furthermore, it appears that the membrane was always in tension in the reference state.

RESULTS AND DISCUSSION

The data analysis, consisting in running the VIC software in a selected area on the bat's wing, called area of interest (AOI), was performed for every test run using the first pair of images in the series as reference and proceeding with as many successive pair of frames as possible. While in ideal laboratory conditions and with controlled specimen it is possible to run the correlation algorithm for all the desired images, the combination of relatively short exposure of the bat in the cameras field-of-view and the extreme flapping motion of the wing limited the number of useful images to approximately 25-35 corresponding to 25 and 35 ms of data embracing a fraction of the wing stroke. Furthermore, for the above reasons, it was not possible to extend the AOI to the entire wing but only to a portion. The VIC software can provide contour plots, surface and temporal estimates of several parameters and solve for

the strains. The geometry and displacements from the output files are also used to estimate wing shape and kinematics. Using the displacement information, it was possible to calculate the discrete strain field in the AOI of the bat's wing through the classic large strain/displacement equations using the Lagrangian strain operator. The x, y, and z displacement fields are mapped onto an unstructured quadrilateral mesh resembling the specific topology of the wing. At each quadrilateral, the mapped displacement vectors at all four nodes are fit into appropriate shape functions. The strain field in each quadrilateral is then calculated as:

$$\varepsilon_{xx} = \frac{\partial u}{\partial x} + \frac{1}{2} \left[\left(\frac{\partial u}{\partial x} \right)^2 + \left(\frac{\partial v}{\partial x} \right)^2 + \left(\frac{\partial w}{\partial x} \right)^2 \right] \quad \varepsilon_{yy} = \frac{\partial v}{\partial y} + \frac{1}{2} \left[\left(\frac{\partial u}{\partial y} \right)^2 + \left(\frac{\partial v}{\partial y} \right)^2 + \left(\frac{\partial w}{\partial y} \right)^2 \right]$$

$$\varepsilon_{xy} = \frac{1}{2} \left[\frac{\partial v}{\partial x} + \frac{\partial u}{\partial y} + \frac{\partial u}{\partial x} \frac{\partial u}{\partial y} + \frac{\partial v}{\partial x} \frac{\partial v}{\partial y} + \frac{\partial w}{\partial x} \frac{\partial w}{\partial y} \right]$$

Figure 7 shows the typical AOI for one event superimposed to the image of the bat flying in the camera view. The example illustrates the reference frame and the coordinate reference system (X, Y, Z) in a body system. Considering one flight event labeled as aj07, flight number seven, and the distal part of the right wing, the membrane three-dimensional displacements data, wing shape and membrane strain were identified on the selected AOI. Figure 8 shows the AOI including the entire distal section of the wing and the specific points and sections where the data presented below were extracted. Section B coincides with the location of the ring finger whereas point B is on the joint on the same finger. The point and section A are randomly chosen on the wing's membrane.

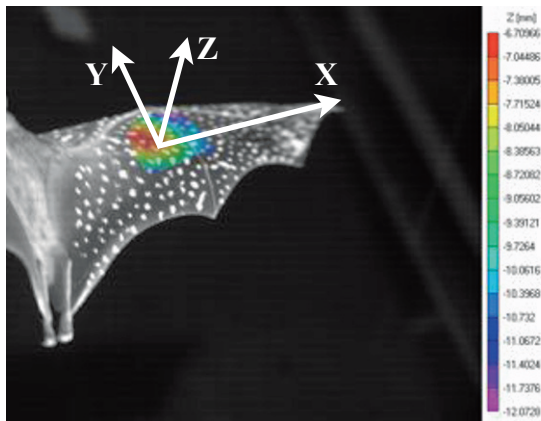


Figure 7. An example of the area of interest (AOI) on the bat's wing including the reference axes in the body frame.

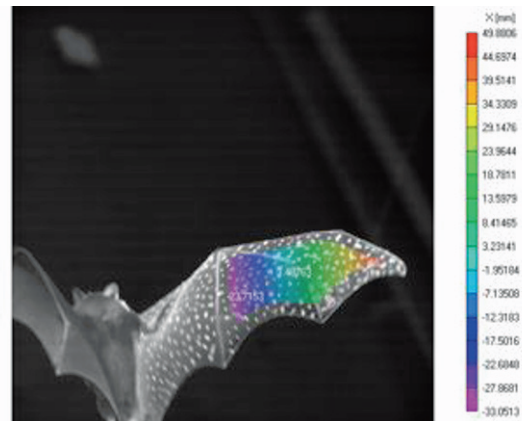


Figure 8. Positions of the points and the sections for the results presented in the paper. Section A represent the membrane; section B corresponds to the ring finger.

Figure 9 and Fig. 10 illustrates the displacements of the point B (joint on the ring finger) in the Y direction (v) and in the Z direction (w), respectively, during a portion of the downstroke. The motions of the above point could clearly be a combination of rigid body motion and elastic deformation nevertheless the linear behavior of v denotes a wing joint constant translational horizontal velocity of 1.625 m/s, probably the bat's flight velocity during the 25 ms of the flight data. The initial values for both variables are zero because by definition the reference is represented by the first position in the sequence. The temporal value of w shows a non-linear trend, indicating an acceleration of the flapping cycle and a possible combination with elastic deformation of the wing. Interestingly enough the wing's joint vertical acceleration is constant during the 25 ms of the recorded flight and the value is -0.19325 m/s^2 . Similar trend was observed in other flights showing negative values of vertical acceleration.

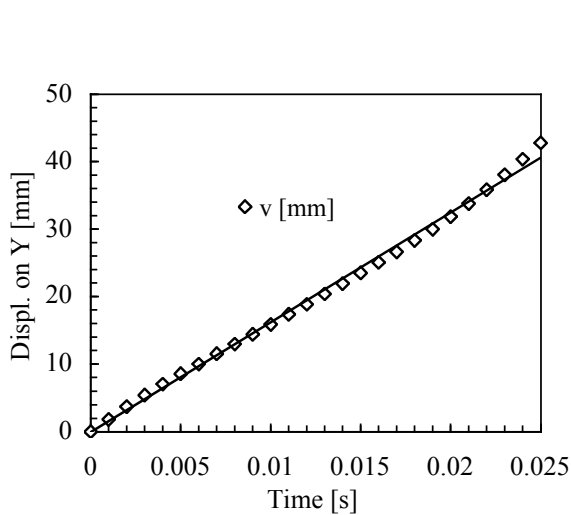


Figure 9. Temporal horizontal position in the flow direction of point B (joint on the ring finger).

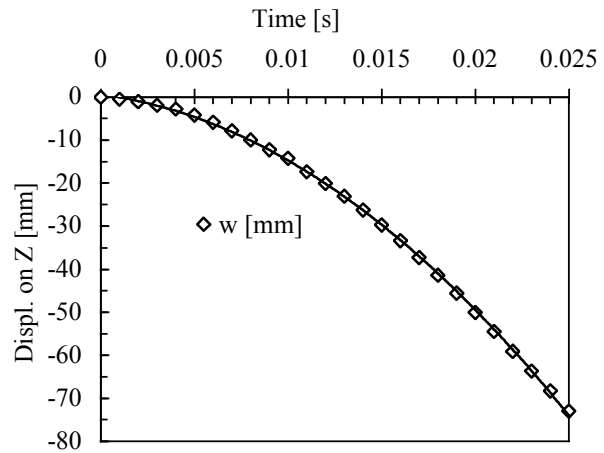


Figure 10. Temporal vertical position of point B (joint on the ring finger) during a portion of the wing down-stroke .

For every time interval, the averages values of the strains in the X and Y directions for the entire AOI illustrated in Fig. 8 were estimated and compiled in Fig. 11. In the same figure, the temporal values of the wing's joint vertical position showed in Fig. 10 is reported to give a visual relation of the membrane strains with the wing's position during the down-stroke. It is evident from an inspection of Fig. 11 that the strain in the X direction are larger in respect to the strain in the Y direction, a feature that was evinced in all the observed flights. It is important too emphasize again that the measured strains represent a change in respect to the first frame in the sequence therefore the absolute strain reference conditions of the wing's membrane is unknown.

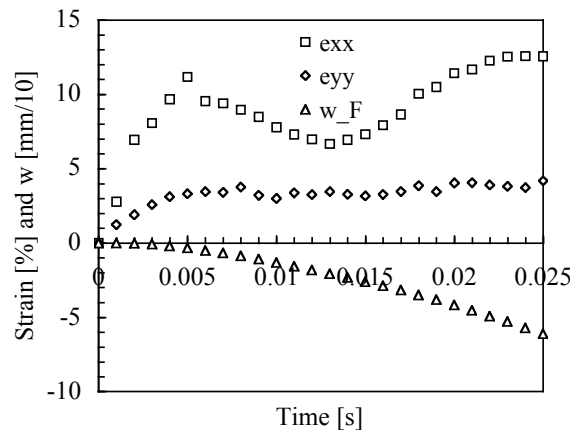


Figure 11. Temporal vertical position of point B (joint on the ring finger) and AOI surface averaged values of strains in X and Y directions during a portion of the wing down-stroke .

The strain-state with respect to the first frame on the distal portion of the right bat's wing, for the same sequence, is illustrated in Fig. 12 a-f. This progression shows contour plots with three snapshots of ϵ_x (a, b and c) and ϵ_y (d, e and f) at 5, 15 and 25 ms after the beginning of the sequence. Few observations could be infer from the plots in the Fig. 12. It is apparent the constant higher level of strain variation respect to the first image (omitted from the figure) along the X axis in respect to the Y axes. A feature showed also in Fig. 11 for a specific point on the wing's membrane and in all other flights. Furthermore, it is interesting to note the increase of strain in the X direction in the vicinity of the ring

finger, Fig. 12 sequence a-b-c, in respect to the free membrane. Such larger strain decreases with the progression of the flap in the down-stroke.

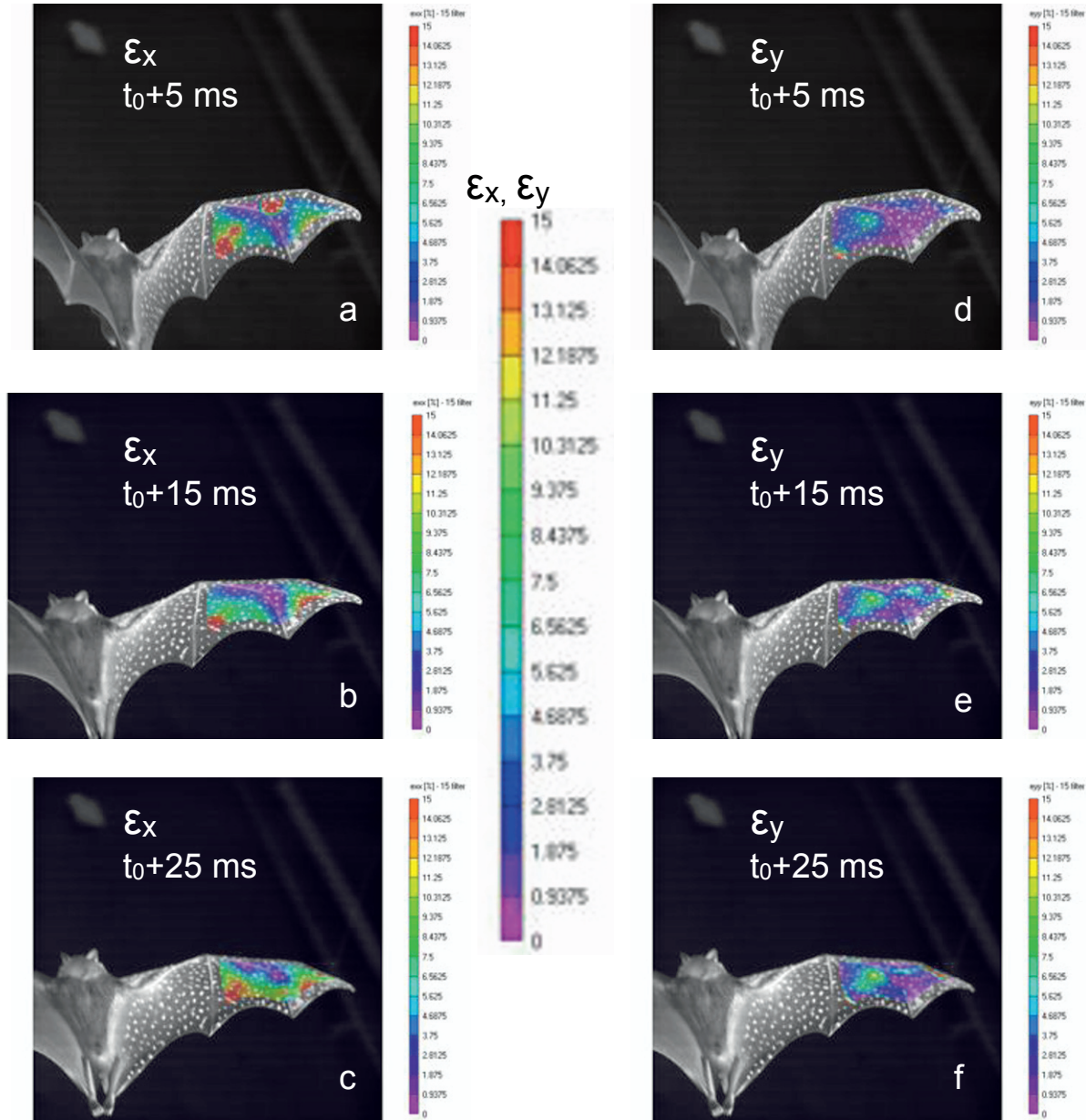


Figure 12. Snapshots of ϵ_x (a, b and c, left) and ϵ_y (d, e and f, right) in % at 5 (upper), 15 (median) and 25 ms (lower) after the start of the recorded flight.

The data acquired during the flight event within the AOI could also be used for kinematics analysis. Figure 13 and Fig. 14 show the position and shape of the two sections, on the membrane (A, Fig. 8) and the ring finger (B, Fig. 8) at the initial time and at 25 ms in the sequence, respectively. The positions of both sections are lower in Fig. 14, as expected from a downstroke motion. Interestingly the section with the larger camber is the finger instead of the free membrane. Furthermore the finger, a somewhat stiffer area in respect to the free membrane, changes significantly in camber (decreasing) and twist (pitching-up) during the flapping motion. Data are also available showing the shape and position of wing's sections in other areas and other flights.

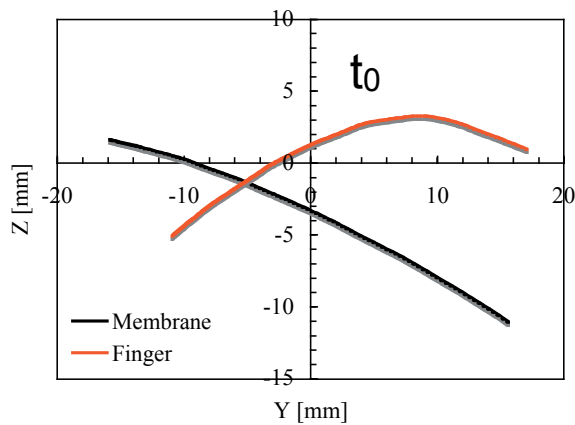


Figure 13. Sections on the bat's wing membrane and ring finger at the beginning of the sequence recorded during flight.

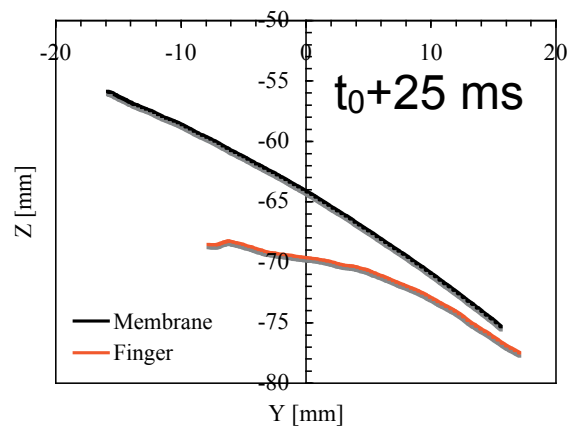


Figure 14. Sections on the bat's wing membrane and ring finger at the end of the sequence recorded during flight.

CONCLUSIONS

This paper has presented an efficient system for high-resolution measurements of the position and three-dimensional shape of a bat wing's membrane during flight proving the feasibility of dynamic strain measurements on bats wing membranes during flapping. The data presented were collected from a number of wind tunnel wind-off flights of one individual of the Jamaican fruit bat, *Artibeus jamaicensis*, a nocturnal and frugivorous specie with a typical length of 9 cm. The captive-bred male bat was trained by Brown University team to fly back and forth in the test section prior to the experiment by offering a landing place at each end of flight space. The data acquisition system, based on three high-speed digital cameras, used visual image correlation for images post-processing. The software represents a reliable method to obtain the global deformations and rigid body translations of a model during generic tests in wind tunnels, providing high-spatial resolution three-dimensional displacements and strains. The random speckle applied to the specimen's surface, a critical feature for the visual image correlation, consisted in a white solution based on egg white, sugar and starch. It is perfectly safe for the mammals and very easily washable from their skin.

Kinematics analysis of a point of the wing corresponding to the joint on the ring finger revealed a horizontal component of the flight velocity of 1.625 m/s. The same point showed a non-linear vertical velocity component due to flapping and elastic deformation of the wing with a constant acceleration of -0.19325 m/s^2 . A different flight exhibited a horizontal velocity of 3.784 m/s and a constant vertical component of 2.424 m/s (negative because of the down stroke) resulting in a reduced frequency k of 0.322. Surface-averaged strain data on the entire AOI showed a level of strain in the X direction (spanwise) approximately three times in respect the Y direction (chordwise). The strains are estimated from a reference state at the beginning of the recorded sequence, in this case 25 ms long. The state of the membrane at the reference is not known but a visual inspection of the images at and before the start of the sequence do not show any membrane surface abnormality as buckling or instability. The membrane seems to be in a fair tension state.

Strain levels are around 10% in the X direction and 3% in the Y direction. Surface snapshots of the membrane strain-state show in the X direction (spanwise) a consistent strain-relief effect around the ring finger during downstroke, with high-strain concentration areas on the membrane between the little finger and the ring finger. The estimates of the shape and positions of two section of the hand wing during the down stroke were evaluated and revealed a mild camber and a not significant twist of the section on the membrane. The section corresponding to the ring finger showed higher camber at the beginning of the sequence followed by a relevant pitch-up twist and decrease of camber at the end of the 25 ms event. The vertical motion of both sections was approximately 65-70 mm. Future work would consist of a smaller and higher density speckle application. Wind tunnel experiments would be run in wind-on conditions with the data acquisition of the bat in a still position in respect to the cameras thus allowing for the acquisition of longer flapping sequences.

ACKNOWLEDGEMENTS

The authors would like to acknowledge the support from the Air Force Research Laboratory at Eglin AFB, FL under contract F08635-03-D-0130 with Johnny Evers as project monitor. The authors would also like to thank the support for the data post processing from Joshua Martin, Department of

Electrical and Computer Engineering, University of West Florida, Shalimar, Florida and the students of the Biology Department at Brown University for their wonderful caring of the bats.

REFERENCES

- [1] Raney, D., L., Waszak, M., R., "Biologically Inspired Micro-Flight Research," SAE 2003-01-3042, 2003.
- [2] Albertani, R., Stanford, B., Hubner, J. P., and Ifju, P., "Aerodynamic Characterization and Deformation Measurements of a Flexible Wing Micro Air Vehicle," *SEM Journal*, DOI: 10.1007/s11340-006-9025-5, 2006.
- [3] Sane, S. P., "The aerodynamics of insect flight," *J. Exp. Biol.* 206, 4191-4208, 2003..
- [4] Muijres, F. T., Johansson, L. C., Barfield, R., Wolf, M., Spedding, G. R. and Hedenström, A. , "Leading-Edge Vortex Improves Lift in Slow-Flying Bats," *Science* 319, 1250-1253, 2008.
- [5] Warrick, D. R., Tobalske, B. W. and Powers, D. R., "Lift production in the hovering hummingbird.," *Proceedings of the Royal Society B: Biological Sciences* 276, 3747-3752, 2009.
- [6] Norberg, U. M., "Aerodynamics, kinematics, and energetics of horizontal flapping flight in the long-eared bat *Plecotus auritus*," *J. Exp. Biol.*, 65, 179-212, 1976.
- [7] Aldridge, H. D., "Kinematics and aerodynamics of the greater horseshoe bat, *Rhinolophus ferrumequinum*, in horizontal flight at various flight speeds," *J. Exp. Biol.*, 126, 479-497, 1986.
- [8] Riskin, D. K., Bahlman, J. W., Hubel, T. Y., Ratcliffe, J. M., Kunz, T. H. and Swartz, S. M., "Bats go head-under-heels: the biomechanics of landing on a ceiling," *J. Exp. Biol.*, 212, 945-953, 2009.
- [9] Riskin, D. K., Willis, D. J., Iriarte-Díaz, J., Hedrick, T. L., Kostandov, M., Chen, J., Laidlaw, D. H., Breuer, K. S. and Swartz, S. M., "Quantifying the complexity of bat wing kinematics," *Journal of Theoretical Biology*, 254, 604-615, 2008.
- [10] Hubel, T., Hristov, N., Swartz, S. M. and Breuer, K. S., "Time-resolved wake structure and kinematics of bat flight," *Exp. Fluids*, 46, 933-943, 2009.
- [11] Hubel, T. Y., Riskin, D. K., Swartz, S. M. and Breuer, K. (in review), "Wake structure and wing kinematics: the flight of the lesser short-nosed fruit bat, *Cynopterus brachyotis*".
- [12] Swartz, S., Bennett, M., Carrier, D. R., "Wing bone stresses in free flying bats and the evolution of skeletal design for flight," *Nature*, Vol. 359, 726-729, Nature Publishing Group, October 22, 1992.
- [13] Swartz, S. M., Groves, M. S., Kim, H. D. and Walsh, W. R., "Mechanical properties of bat wing membrane skin," *J. Zool.*, 239, 357-378, 1996.
- [14] Sutton, M. A., Cheng, M., Peters, W. H., Chao, Y. J. and McNeill, S. R., "Application of an optimized digital correlation method to planar deformation analysis," *Image and Vision Computing*, 4(3), pp. 143-151, 1986.
- [15] Sutton, M. A., Turner, J. L., Bruck, H. A., Chae, T. A., "Full field representation of the discretely sampled surface deformations for displacement and strain analysis," *Experimental Mechanics*, 1991:31(2): 168-77, 1991.
- [16] Babcock, J., Scheffer, R., Albertani, R., "Experimental Data for Micro Air Vehicles with Pliant Wings in Unsteady Conditions," *27th AIAA Applied Aerodynamic and Atmospheric Flight Mechanics Conference*, Chicago, IL, August, 2009.

The Mechanical Properties of *Musa Textilis* Petiole

Liou*, N.-S., Chen, S.-F., Ruan, G.-W.

Department of Mechanical Engineering, Southern Taiwan University
Yuang-Kang City, Tainan Hsien, Taiwan 710 R.O.C
email: nliou@mail.stut.edu.tw

ABSTRACT

From a structural point of view, banana leaf is an outstanding design of biological system. This work used a procedure based on finite element analysis and inverse problem method to estimate elastic moduli of different parts of banana petiole from compression test data. Two phase compression tests on petiole section specimens were performed to get the force-displacement data of petiole for inverse finite element analyses. The inverse analysis method was performed by using a MATLAB procedure to execute ABAQUS to obtain finite element results and read desirable data from finite element results for optimization procedure. The values of elastic moduli of skin and core of petiole estimated by current method are 28 MPa and 0.9 MPa respectively for the particular petiole section under test.

INTRODUCTION

Compared to other plants, banana (*Musa textilis*) has large leaf. From a structural point of view, banana leaf is an outstanding design of biological system. The light weight petiole is an efficient structure. Even lack of woody tissue, petiole still can provide sufficient rigidity to support the weight of large leaf lamina and resist dynamic wind load. The section of banana petiole is shown in Fig. 1. The outer layer tissues (skin) of petiole are similar to the petioles of other monocotyledonous plants. The skin of banana petiole composed of parenchyma reinforced by vascular bundles. The internal portion (core) of petiole is structure pierced by large air canals which are separated by parenchyma partitions which contain very few vascular bundles. In this study, the mechanical properties of skin and core parts of banana petiole are investigated. The skin and core parts of banana petiole are considered as linear elastic materials. The effective linear elastic material parameters of skin and core parts are identified by an inverse analysis procedure. The generalized pattern search method is used to extract the effective elastic moduli from the compression load-displacement data under compression test.

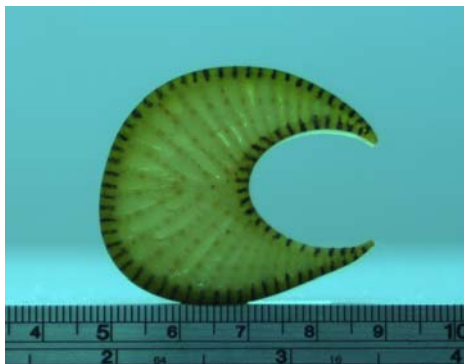


Figure 1: The section of banana petiole

MATERIAL AND METHOD

The current inverse analysis uses the generalized pattern search method [1] to estimate the elastic moduli of skin and core parts of banana petiole. The theory of the GPS method is based on minimizing an objective function with respect to the unknown parameters. For problems involving complex geometries, the calculation can only be obtained from numerical analyses such as finite element analyses. In this study, finite element calculations are conducted to simulate compression process of petiole section. Four material parameters, namely E_{skin} , ν_{skin} , E_{core} , ν_{core} , are required to define the linear elastic properties of banana petiole. For simplicity, the values of Poisson's ratios of skin and core parts are assumed to be constants and equal to 0.49 and 0.01 respectively. The values of Young's moduli can be extracted from the compression test load-displacement data by using finite element inverse analyses. In order to get the force-displacement data of petiole for inverse finite element analyses, petiole specimens were cut from fresh petiole for compression tests. Specimens were stored in room temperature fresh water before experiments. The compression tests were carried out by using Instron tensile test machine. In order to investigate the mechanical properties of skin and core parts separately, compression tests were performed in two phases. In first phase, compression test was applied to the full petiole section (Fig. 2a). In second phase, the core part of petiole specimen was removed and only the skin part was retained. Again, compression test was applied to the specimen contain the skin part only (Fig. 2b). Thus, the loading force is caused by the stiffness of skin part only. The compression displacement is 1.5 mm and the force was recorded after holding time of 300 sec.

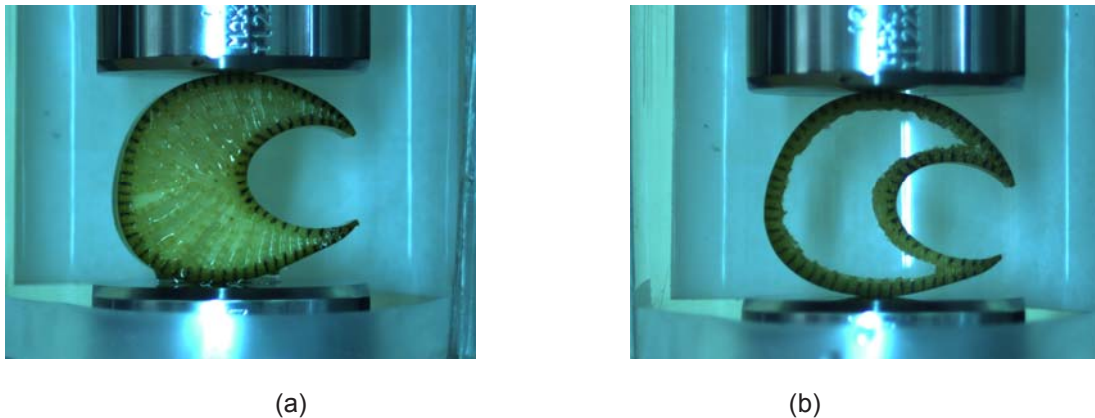


Figure 2 (a) full petiole section and (b) skin part of petiole

Plane strain finite element models were used to fit the compression test data. The contact between the compression plates and petiole specimen was assumed to be rough. This means no slip will occur once points are in contact. The compression was applied in the vertical direction (Fig. 3). Current GPS inverse analysis method was performed by using a MATLAB procedure to execute ABAQUS to obtain finite element results and read desirable data from finite element results for optimization procedure.



Figure 3: Finite element models of (a) full petiole section and (b) skin part of petiole

RESULT AND DISCUSSION

The finite element model with only skin part was used to estimate the elastic modulus of petiole skin. The value of elastic modulus of skin estimated by current method is 28 MPa for the particular petiole section under test. The finite element model with full petiole section was used to estimate the elastic modulus of petiole core. In this inverse finite element analysis of full petiole section model, the elastic modulus of petiole skin estimated by previous analysis was used. The value of elastic modulus of core estimated by current method is 0.9 MPa for the particular petiole section under test. The corresponding results of finite element analyses are shown in Fig. 4.



Figure 4: Finite element analysis results of (a) full petiole section and (b) skin section

This work used a procedure based on finite element analysis and inverse problem method to estimate elastic moduli of banana petiole from compression test data. It is known, in many inverse analyses, that when single compression or indentation procedure is used, the model could have problem with non-unique results if unknown parameters are more than one. In the future, the displacements of the tracking points shown in Fig. 1 will also be used in the optimization function to better identify the unknown material parameters.

ACKNOWLEDGEMENT

This research was supported by NSC 96-2221-E-218-048-MY3 from the R.O.C government.

REFERENCE

1. Wright, M.W.a.J., *COMPARISON OF A GENERALIZED PATTERN SEARCH AND A GENETIC ALGORITHM OPTIMIZATION METHOD*, in *Eighth International IBPSA Conference*. 2003: Eindhoven, Netherlands.

Analysis of Strain Energy Behavior throughout a Fatigue Process

Onome Scott-Emuakpor*, Tommy George, & Charles Cross
Air Force Research Laboratory
Wright-Patterson AFB, OH 45433

M.-H. Herman Shen
Department of Mechanical Engineering
The Ohio State University
Columbus, OH 43210

ABSTRACT

The dissipation of strain energy density per cycle was analyzed to understand its trend through a fatigue process. The motivation behind this analysis is to improve a fatigue life prediction method, which is based on a strain energy and failure correlation. The correlation states that the same amount of strain energy is dissipated during both monotonic fracture and cyclic fatigue. This means the summation of strain energy density per cycle is equal to the total strain energy density dissipated monotonically. In order to validate this understanding, the strain energy density per cycle was analyzed at several alternating stress levels with fatigue life between 10^3 and 10^5 cycles. The analysis includes the following: Alternating between high and low operating frequencies (50x difference), interruption of cyclic load during testing, and idle/zero-loading for intervals of 20-40 minutes between cyclic loading sequences. All experimental results show a consistent trend of cyclic softening as the loading cycles approach failure, which further validates the theories used in developing the energy-based fatigue life prediction method.

1. INTRODUCTION

In hopes of developing a physical quantity for component fatigue damage, the correlation between failure/fatigue and energy was studied [1]. Early results of this study showed minimal progress, until the introduction of the following hypothesis: There is a physical critical energy value dissipated during fatigue [2]. This hypothesis led to a more in-depth definition of the correlation between the fatigue life of a material and the energy dissipation during the fatigue process. The definition suggests that the energy required to fracture a material monotonically is the same as the energy dissipated during a fatigue process [3, 4]. Therefore, the critical energy value associated with fatigue is the total energy in a monotonic procedure.

Further investigation of the correlation between energy and failure showed that not all the energy dissipated during cyclic loading is a factor in the fatigue initiation process [5]. Energy dissipated through heat, vibration, surface defects and acoustics are omitted, and the energy/failure correlation is based only on strain energy. This means the strain energy in a monotonic fracture procedure, also known as the Modulus of Toughness, is the fatigue damage parameter (critical energy) needed for the assessment of failure. Based on this understanding, an energy-based method was developed to determine uniaxial fatigue life by dividing the total monotonic strain energy with the stabilized strain energy per cycle during fatigue [6, 7].

In order to validate the energy-based fatigue life method, the strain energy density trend during cyclic loading was analyzed. This analysis was necessary to prove the generalized procedure of the prediction method, which is influenced only by stress amplitude (i.e. strain energy only). Therefore, in the analysis, the effect of different factors on the behavior of strain energy density trend during cyclic loading are studied. The different factors include the effect of different alternating stress amplitudes, fluctuation between two operating frequencies, different material compositions, and the effects of test interruptions and unloaded idle time during fatigue testing. The experiments in the analysis were conducted on two different stocks of Aluminum 6061-T6. The results show that, for all analyzed stress amplitudes, there is a consistent trend of cyclic softening as loading cycles approach

* Corresponding author. Tel.: +1-937-255-6810; fax: +1-937-656-5532
E-mail address: onome.scott-emuakpor@wpafb.af.mil (Onome Scott-Emuakpor)

failure. Also shown is a need for an improved procedure that correlates experimental data to the strain equation used. Details of the results can be seen in the Sections that follow.

2. ENERGY-BASED FATIGUE LIFE PREDICTION METHOD

The energy-based fatigue life calculation system was developed from the stress-strain representations for monotonic and cyclic loading behaviors shown in Equation 1-3. Equation 1 and 2 represent the respective monotonic stress-strain relationship prior to and after the necking phenomenon, and Equation 3 is the expression for the cyclic strain [4, 6]. Equation 3 was created based on a simplified coordinate system, where the horizontal versus vertical axes represents peak-to-peak strain versus peak-to-peak stress, respectively. On this coordinate system, shown in Figure 1, the origin is defined as the minimum fully-reversed point of a hysteresis loop.

$$\varepsilon = \frac{\sigma}{E} + \varepsilon_o \sinh\left(\frac{\sigma}{\sigma_o}\right) \quad (1)$$

$$\sigma = \beta_1 \varepsilon + \beta_o \quad (2)$$

$$\varepsilon_{cycle} = \frac{\sigma_{pp}}{E} + \frac{1}{C} \sinh\left(\frac{\sigma_{pp}}{\sigma_c}\right) \quad (3)$$

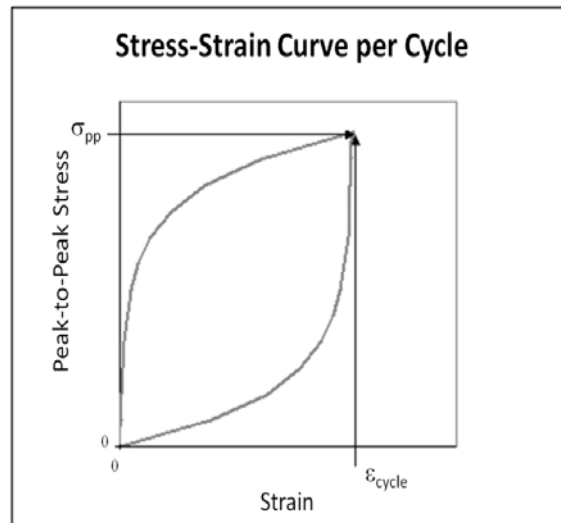


Figure 1. One fully-reversed cycle

The parameters for Equation 1-3 are defined as follows: σ is the nominal applied monotonic stress value, ε is the strain corresponding to the stress σ , β_1 & β_o are the respective slope and intercept of the stress-strain relationship in the necking region (From ultimate tensile to point of fracture), σ_{pp} is the generalized stress value corresponding to the generalized cyclic strain ε_{cycle} ($2\sigma_a$ replaces σ_{pp} in Equation 3 after all necessary derivations), E is the modulus of elasticity, and the variables σ_c , σ_o , ε_o , and C are curve fit parameters [6]. The curve fit parameters for the cyclic and monotonic representations (Equation 1-3) are statistically acquired by comparison between the equations and the respective experimental results.

The energy-based prediction method calculates fatigue life by taking the total monotonic strain energy density and dividing it by the strain energy density for one cycle. The total strain energy density dissipated during a monotonic process is determined as the area underneath the curve constructed by Equations 1 & 2, and the strain energy density for one cycle is represented by the area within the hysteresis loop formed by Equation 3. Calculating the monotonic strain energy density from experimental results is a straightforward task. The strain energy density in one cycle is determined by assuming the tensile stress-strain behavior of the hysteresis loop is the same as the compressive behavior. Therefore, cyclic strain energy density is expressed by Equation 4.

$$W_c = \sigma_{PP} \varepsilon_{cycle} - 2 \int_0^{\sigma_{PP}} \varepsilon_{cycle} d\sigma_{PP} \quad (4)$$

Using the energy-based understanding, fatigue life is calculated by Equation 5 [6], where σ_a is the alternating stress amplitude, σ_n is the necking stress, ε_f is the failure strain, and ε_n is the necking strain. The fatigue life calculations from Equation 5 are successfully compared to fully-reversed tension/compression Al 6061-T6 experimental results on the stress versus fatigue life (S-N) plot of Figure 2 [6].

$$N_f = C \frac{\sigma_n \left(\varepsilon_n - \frac{\sigma_n}{2E} \right) - \varepsilon_o \sigma_o \left[\cosh \left(\frac{\sigma_n}{\sigma_o} \right) - 1 \right] + \frac{\beta_1}{2} (\varepsilon_f^2 - \varepsilon_n^2) + \beta_o (\varepsilon_f - \varepsilon_n)}{2\sigma_c \left\{ \frac{\sigma_a}{\sigma_c} \sinh \left(\frac{2\sigma_a}{\sigma_c} \right) - \left[\cosh \left(\frac{2\sigma_a}{\sigma_c} \right) - 1 \right] \right\}} \quad (5)$$

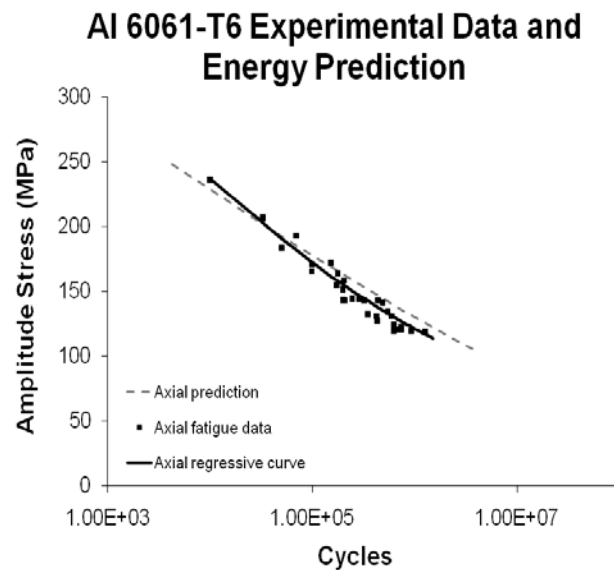


Figure 2. Fully-reversed tension/compression fatigue life comparison for Al 6061-T6 [6]

3. EXPERIMENTAL PROCEDURE

Experiments under cyclic loading were conducted at room temperature on flat dog-bone specimens, which were waterjet cut from plate stock. The cyclic load was applied with a MTS Systems Corporation axial servo-hydraulic load frame, located in the Turbine Engine Fatigue Facility of the Air Force Research Laboratory. Each test was load-controlled at operational frequencies between 0.005-20 Hz. The maximum frequency limit of 20 Hz was chosen to negate the effects of external energy dissipation factors and the experimental system instability.

Fatigue tests concluded when complete fracture of the specimen occurred. Though the fundamental nature of the energy-based fatigue life prediction method focuses on crack initiation, the number of cycles between initiation and complete fracture during tension/compression High Cycle Fatigue (HCF) is negligible [8]. Therefore, a method for distinguishing crack initiation from complete fracture was not necessary. Instead, the number of cycles to complete fracture is viewed as the number of cycles to crack initiation during tension/compression testing.

Test results were acquired with a Micro-Measurements Division CEA-13-062UW-350 strain gage, an extensometer strain reader (MTS model No. 634.12E-24), and the MTS TestStarII data acquisition system. The strain gage and the extensometer acquires experimental strain only and the TestStarII acquires and/or controls the applied load, displacement, and time. Strain results from the extensometer and the gage are compared with each other to ensure the precision of the extensometer throughout the duration of a fatigue test. This comparison is conducted at early cycles due to the low fatigue rating of the CEA-13-062UW-350 strain gage. Figure 3 successfully shows this comparison for the first 10 cycles of an experiment [9].

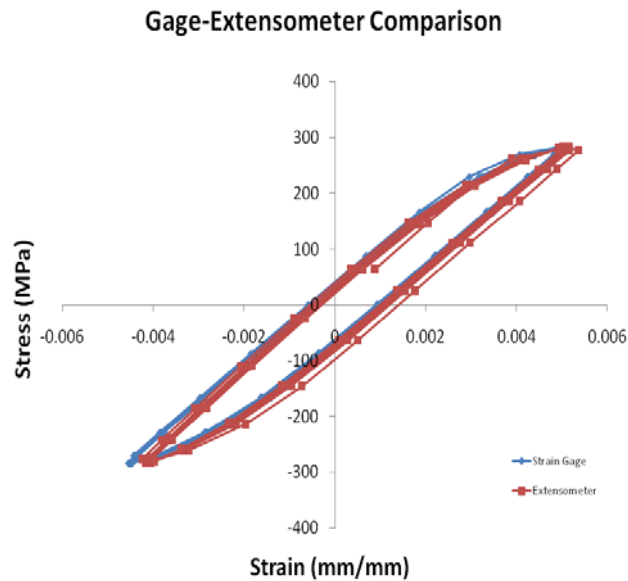


Figure 3. Extensometer and strain gage comparison for Al 6061-T6 [9]

4. STRAIN ENERGY PER CYCLE CALCULATION

In Section 2, there are two statements that were specified to simplify the characterization of cyclic experimental data: The minimum stress-strain point of a cycle is shifted to the origin of a peak-to-peak coordinate system, and the tensile half of the stress-strain behavior for one cyclic load is the same as the compressive half. Based on these statements, Equation 3 can be curve fit to experimental cyclic results, which then can be applied to Equation 4 to calculate the strain energy density in an individual cycle.

Curve fitting Equation 3 to cyclic experimental results is a tedious process due to the inevitable scatter of test results and the complex relationship between true stress versus strain (i.e. Equation 3). Since Equation 3 is a hyperbolic trigonometric function, the use of a simple Least Squared Approximation for curve fitting is discarded. Instead, the curve fitting process is a statistical optimization procedure, which is described as follows: Each experimental data point from a tensile curve of a cycle is compared to its corresponding analytical value, which is calculated by Equation 3. Then the standard deviation of the difference between each compared value is determined. These steps are conducted for numerous iterations, each with a specific combination of σ_c and C variables chosen from set parameter ranges, until the variable combination with the smallest standard deviation is found.

It was essential to find the experimental settings that provided the optimal data for calculating strain energy per cycle. Therefore, a series of tests were conducted at a fixed alternating stress amplitude of 241 MPa and operating frequencies ranging between 0.005-0.25 Hz on Al 6061-T6 specimens. Each of the conducted test acquired 20, 50, or 100 data points per cycle. The results of these tests are shown in Table 1. For each test in the table, 120 Total cycles were accumulated. Also, the outliers are defined as the individual strain energy values which lay outside 98% probability in a normal distribution. Observing Table 1, the acquired data concludes two key findings. First, due to the overwhelming amount of outliers, the inconsistency in the strain energy calculation from 100 points is too significant. Second, due to large gaps between the data points, acquiring only 20 experimental points per cycle is not enough data for an accurate calculation of the strain energy density value. Based on these findings, an analysis of frequency effect on strain was conducted only on the test acquisition setup with 50 data points per cycle. The reason for this analysis was to find a frequency that minimized the effect of anelasticity, viscoplasticity, and outside energy influence on the stress-strain relation. The analysis was conducted by comparing the variances of the strain energy per cycle at each operating frequency. This comparison is shown on the plot in Figure 4. From the plot, the optimal frequencies are 0.1 and 0.005 Hz. Since 0.1 Hz is a far less time consuming frequency than 0.005 Hz, it was used for strain energy calculation during the fatigue analysis in the following Section.

Test #	Data per cycle	Outliers	Average W_{cycle} (KJ/m ³)
1	20	4	72
2	50	6	117
3	100	29	139

Table 1. Strain energy density per cycle calculation for Al 6061-T6

**Al 6061-T6 Strain Energy Density Variance:
50 Points per Cycle**

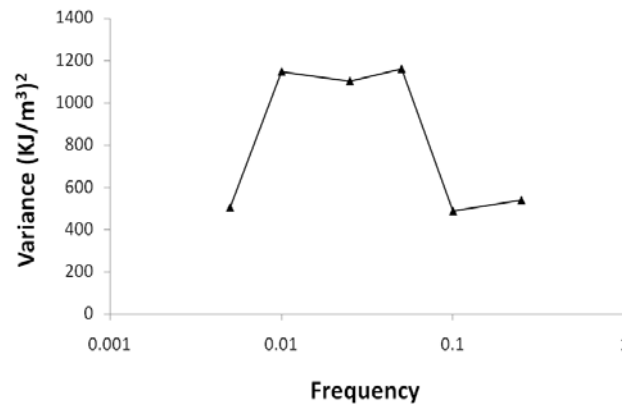


Figure 4. Strain energy density variance for Al 6061-T6, Stress=241 MPa

5. FATIGUE ANALYSIS AND RESULTS

Several experimental results were acquired from Al 6061-T6 to understand the effects of different testing conditions. A conventional fatigue test, run continuously at a fixed frequency, was compared to fatigue results of tests with frequency changes and loading interruptions. These results are shown on the normalized plot of [Figure 5](#), where N is the loading cycle, N_f is the cycle at failure (i.e. fatigue life), W_c is the strain energy density per cycle, and W_{sat} is the strain energy density in the steady-state/constant strain region ($N/N_f = 0.2$ through 0.6). In the legend of [Figure 5](#), *Continuous* refers to an uninterrupted fatigue test at 0.1 Hz. *3-Step* means the test started at an operating frequency of 0.1 Hz, moved up to 5 Hz, and then stopped for 20 minutes before starting again at 0.1 Hz, until failure. *5-step* is the same as the 3-Step, but the first two steps (at 0.1 and 5 Hz) are repeated before the final step to failure. *Stop-Start* means the test was conducted at 0.1 Hz, and then stopped and started back up every 0.23 N/N_f cycle, until failure. The results of [Figure 5](#) show that none of these testing conditions affect the strain energy density trend. This finding is essential due to the low operation frequency necessary to calculate strain energy density. Since there is no effect with changing frequencies, or stopping and starting a test, the duration of a fatigue test can be shortened and a specimen can be left idle during a multiple-day HCF experiment.

In a recently published paper, it is assumed that the strain energy density trend for a material is the same regardless of the stress amplitude of the cyclic load [9]. In an effort to prove this assumption true, an analysis of strain energy density trend was conducted at stress amplitudes of 283, 241, 207 and 179 MPa. Each test followed a multi-step procedure, similar to the 3-Step and the 5-Step, with operating frequencies of 0.1 and 20 Hz to reduce the duration of each test. The strain energy density results, which were only calculated for data acquired at 0.1 Hz, are compared on the normalized plot of [Figure 6](#). The comparison shows a consistent trend of cyclic softening as the loading cycles approach failure. Also shown in the comparison is that cyclic hardening only occurs on the fatigue test operating at 283 MPa. It is believed that this phenomenon occurred due to the stress amplitude being in the strain hardening stress range of a monotonic tensile curve. Nevertheless, the extra strain energy from cyclic hardening is negligible when compared to the total strain energy dissipated during a fatigue process.

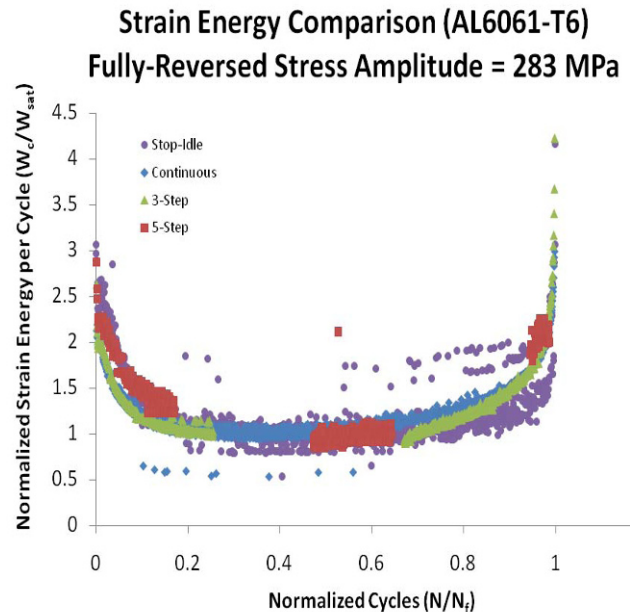


Figure 5. Strain energy density comparison during fatigue: Al 6061-T6, Stock I, 283 MPa

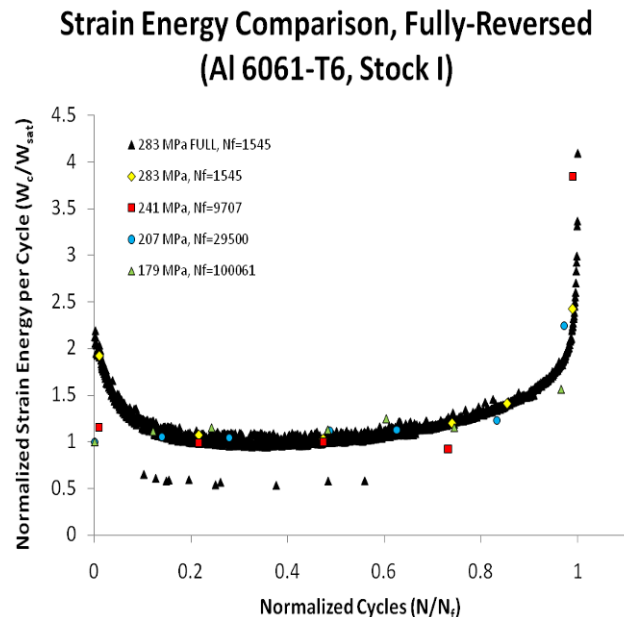


Figure 6. Strain energy density comparison at different stress levels: Al 6061-T6, Stock I

The strain energy analysis conducted in Figures 5 and 6 was repeated on a second stock of Aluminum with slightly different material properties, which are shown in Table 2. Figure 7 shows the comparison between a continuous and 3-Step test for stock II. The results concur with the first stock of Al 6061-T6, which means different test conditions do not affect the strain energy trend. Also, running cyclic experiments at an alternating stress amplitude in the linear monotonic tensile region prior to strain hardening eliminate the cyclic hardening witnessed in the previous stock of aluminum.

Validating the assumption that strain energy trend is the same for all stress amplitudes brought some energy calculation issues to surface. Strain energy density for fatigue data with alternating stress amplitudes of 276 and 241 MPa are successfully compared on Figure 8; however, accurate strain energy calculations for stress amplitudes less than 241 MPa could not be made. This inability to calculate strain energy density is either due to

inconsistent experimental strain data at low stresses, or a less effective method of curve fitting experimental results to the analytical expression at low stresses for some material properties. Determining which of these is the most hindering issue, and improving it, is a high priority in the efforts to understand strain energy behavior during cyclic loading.

Al 6061-T6	Stock I	Stock II
E (MPa) =	7.04E+04	6.63E+04
σ_y (MPa) =	310	303
δ (%) =	16.5	15.5
σ_{uts} (MPa) =	403	362

Table 2. Aluminum material properties

**Normalized Comparisons (Al 6061-T6, Stock II)
Fully-Reversed Stress Amplitude = 276 MPa**

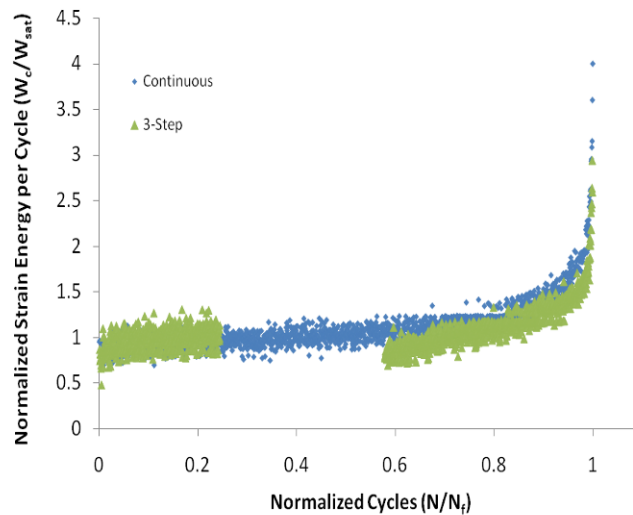


Figure 7. Strain energy density comparison during fatigue: Al 6061-T6, Stock II, 276 MPa

**Normalized Comparisons, Fully-Reversed
(Al 6061-T6, Stock II)**

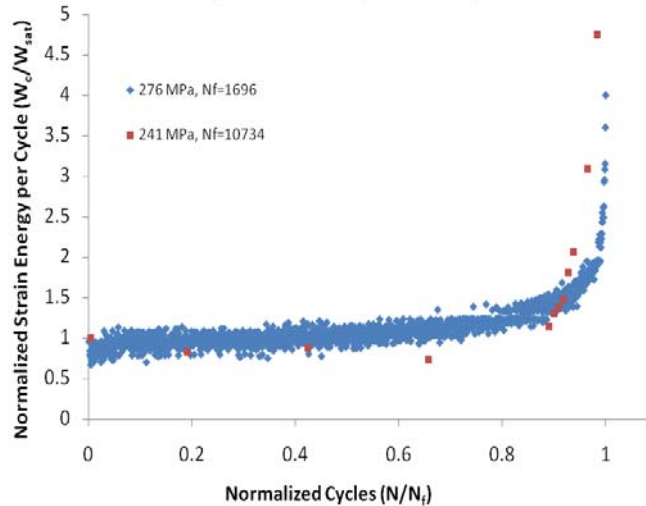


Figure 8. Strain energy density comparison at different stress levels: Al 6061-T6, Stock II

6. CONCLUSION

Analyzing the behavior of the dissipated strain energy density per cycle during fatigue led to a few discoveries for the case of aluminum. It was proven that a change in stress amplitude, alternating between two frequencies and cyclic loading interruptions show no effect on the strain energy trend during fatigue, within the range of $10^3 - 10^5$ cycles, for Al 6061-T6. Repeating this analysis for a second stock of aluminum, with slight different material properties, however, led to some unexpected results. There were difficulties calculating the strain energy density in each cycle for experiments operating at stress amplitudes below 241 MPa. The two assumed reasons for this are as follows: there is too much inconsistency in the experimental data, and the curve fit validation for the strain equation is not very effective at low alternating stresses. Each of these problems can be solved by either using a more precise measurement instrumentation to acquire stress-strain experimental data, or developing a procedure, similar to the coefficient of determination, for assessing the quality of the strain equation curve fit, which has a linear and nonlinear part. Despite the shortcomings from aluminum stock 2, the results of this study provide encouragement for the assumption of [9], stating that the strain energy density trend during fatigue is the same regardless of the stress amplitudes. Therefore, the energy-based life prediction method is further validated.

Acknowledgements

The authors would like to thank the Air Force Research Laboratories (AFRL), specifically the Turbine Engine Fatigue Facility (TEFF), for their financial support, facility and equipment access, and encouragement of this research.

REFERENCE

- [1] Jasper, T.M., "The Value of the Energy Relation in the Testing of Ferrous Metals at Varying Ranges of Stress and at Intermediate and High Temperatures," *Philosophical Magazine, Series. 6*, Oct. 1923; Vol. 46, pp. 609-627.
- [2] Enomoto, N., "On Fatigue Tests Under Progressive Stress," *American Society for Testing and Materials*, 1955; Vol. 55, pp. 903-917.
- [3] Feltner, C.E., and Morrow, J.D., "Microplastic Strain hysteresis Energy as a Criterion for Fatigue Fracture," *Journal of Basic Engineering Transactions, American Society of Mechanical Engineers*, New York, 1961; Vol. 83, pp. 15-22.
- [4] Stowell, E., "A Study of the Energy Criterion for Fatigue," *Nuclear Engineering and Design*, 1966; Vol. 3, pp. 32-40.
- [5] Xiao-Yan, T., De-Jun, W., and Hao, X., "Investigation of Cyclic Hysteresis Energy in Fatigue Failure Process," *International Journal of Fatigue*, 1989; Vol. 11, No. 5, pp 353-359.
- [6] Scott-Emuakpor, O., Shen, M.-H.H., George, T., Cross, C., and Calcaterra, J., "A New Energy-Based Uniaxial Fatigue Life Prediction Method for Commonly Used Gas Turbine Engine Materials," *Journal of Engineering for Gas Turbines And Power*, 2007; Vol. 129, Issue 1, pp. 162-169.
- [7] Scott-Emuakpor, O., Shen, M.-H.H., George, T., and Cross, C., "An Energy-Based Uniaxial Fatigue Life Prediction Method for Commonly Used Gas Turbine Engine Materials," *Journal of Engineering for Gas Turbines and Power*, 2008; Vol. 130, Issue 6, pp. 062504-1.
- [8] George, T., Shen, M.-H.H., Scott-Emuakpor, O., Nicholas, T., Cross, C., and Calcaterra, J., "Goodman Diagram via Vibration-Based Fatigue Testing," *Journal of Engineering Materials and Technology*, 2005; Vol. 127, Issue 1, pp. 58-64.
- [9] Scott-Emuakpor, O., George, T., Cross, C., and Shen, M.-H.H., "Hysteresis Loop Representation for Strain Energy Calculation and Fatigue Assessment," *Journal of Strain Analysis for Engineering Design*, 2010; Accepted for Publication, Paper No. JSA602.

Relating Fatigue Strain Accumulation to Microstructure using Digital Image Correlation

Jay Carroll^{1*}, Wael Abuzaid¹, Mallory Casperson¹, John Lambros¹, Huseyin Sehitoglu¹, Mike Spottswood², Ravinder Chona²

¹University of Illinois at Urbana-Champaign, ²Air Force Research Lab

*Corresponding Author Address: Department of Mechanical Science and Engineering, University of Illinois, 1206 W. Green St. Urbana, IL 61801, M/C 244, Email: Jcarrol2@uiuc.edu

Abstract

While fatigue has been studied extensively, fatigue life predictions are still phenomenological and relatively simple (e.g. Miner's rule, Paris relationship, etc.). Many improvements have been suggested to such models to incorporate newly discovered phenomena, but fatigue life predictions still have limited accuracy and scope. A quantitative understanding of fatigue at the grain level would lead to models with better predictive capability and/or broader applicability.

In this work, fatigue crack growth in Hastelloy X, a high-temperature nickel based alloy, was examined using an ex-situ digital image correlation technique. Electron backscatter diffraction (EBSD) was performed on a region of interest in front of the crack tip in a single edge notched tension specimen to obtain microstructural characteristics. The specimen was then fatigue loaded to advance the crack. At regular intervals of crack growth, the specimen was removed from the load frame and the region of interest was imaged with an optical microscope. By performing digital image correlation on these images, a full-field measure of the accumulated plastic strain was obtained as the crack approached and passed through the region of interest. Strain fields were compared to EBSD results to elucidate the relationship between microstructure and fatigue crack growth. The presence of strain concentrations at grain and (annealing) twin boundaries was seen to be instrumental in the evolution of plastic strain accumulation during fatigue.

Introduction

With the demand for more accurate material behavior predictions, microstructural-based material deformation models are being developed, particularly for fatigue situations. With these models comes the need for experimental data for model inputs and model validation. Experimental techniques for this purpose must provide full-field, quantitative experimental data that links microstructure to deformation behavior. This work focuses on linking fatigue strain accumulation, measured by digital image correlation (DIC) to microstructural measurements.

Several researchers have used DIC for microstructural investigations [1-4]. Padilla *et al.* [3] measured deformation behavior in dynamically loaded Zr specimens with an *in situ* DIC method. They also spatially overlaid strain fields with microstructural information from EBSD. This study provided valuable insight into the effects of grain orientation on dynamic deformation behavior of Zr. However, these experiments had relatively low spatial resolution (up to 1.2 $\mu\text{m}/\text{pix}$) which limited their ability to make precision pointwise comparisons between deformation and microstructure.

In Efstathiou *et al.* [4], grain level cyclic plasticity was observed in titanium by comparing *ex situ* strain fields (at magnifications from 1.36 to 0.087 $\mu\text{m}/\text{pix}$) to grain *geometry* that was revealed by etching the surface of the sample. While this work had high spatial resolution strain fields, microstructural information was limited to grain boundary locations.

In this work, an *ex situ* procedure was developed to spatially overlay high resolution DIC strain fields to grain geometry and orientation information obtained with EBSD. This procedure will be described and an example will be shown in which the technique is applied to fatigue crack growth. By comparing strain localizations to microstructural features such as grain boundary locations and grain orientation, we hope to advance the understanding of material deformation behavior and its relation to microstructure.

Procedure

The spatial resolution of DIC increases with magnification (see [figure 1](#)); however, field of view decreases with increasing magnification. By using the *ex situ* technique described here, high resolution measurements can be made over relatively large areas by stitching the results of many high magnification correlations. Furthermore, this procedure allows microstructural information to be compared with these high resolution strain measurements on a pointwise basis.

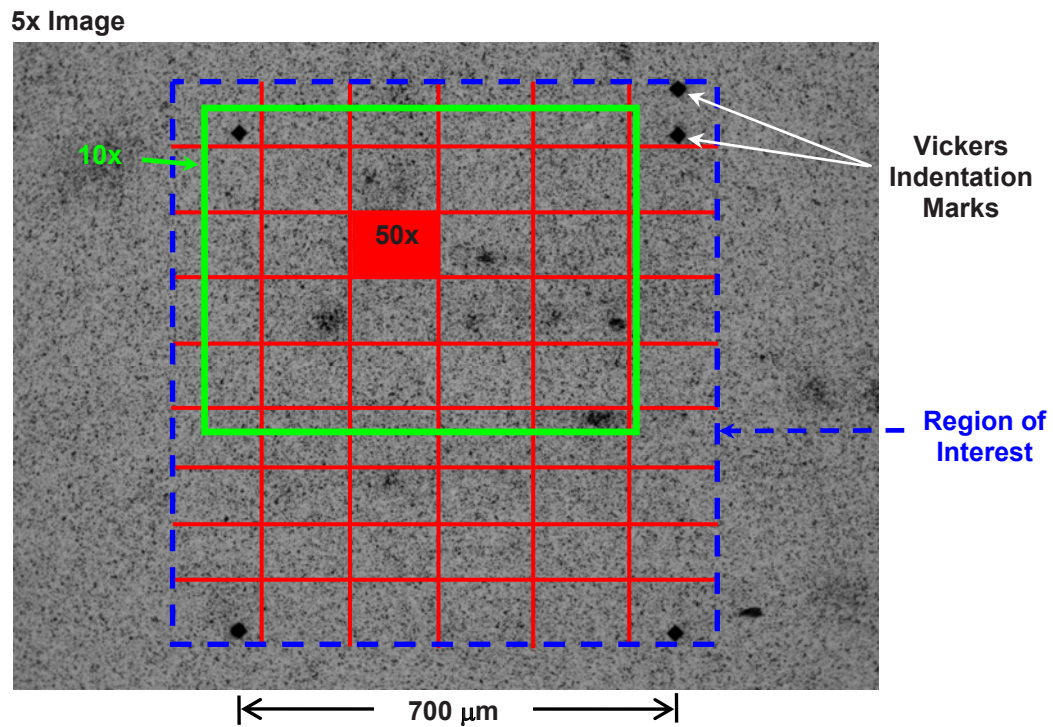


Figure 1. As magnification increases, the field of view decreases. In order to obtain DIC results with high spatial resolution over a sizeable area, results from many high magnification correlations were obtained and stitched together. Vickers indentation marks in the corners of the region of interest

The *ex-situ* DIC procedure developed in this work has six basic steps: (1) place fiducial markers on the sample to be used for spatial alignment of the various datasets to be collected; (2) gather microstructural information through EBSD measurements; (3) apply a speckle pattern to the specimen and capture reference images in the optical microscope; (4) load the specimen such that permanent deformation is achieved and capture images of the deformed specimen in the optical microscope; (5) perform DIC and stitch results together; (6) align the DIC strain field from step (5) with the microstructure obtained with EBSD from step (2) using the fiducial marks.

In this work, a single edge notched tension specimen made of Hastelloy X, a nickel-based superalloy was used. The notch was 1mm long and 0.15mm wide. After machining, the specimen was finely polished to obtain a smooth surface necessary for EBSD measurements. Vickers indentation marks were then used to outline a region of interest on the specimen ([Figures 1 and 2](#)). The specimen was placed in a scanning electron microscope and EBSD was performed to gather grain geometry and orientation within the region outlined by the indentation marks. As shown in [Figure 2](#), the average grain size of this material is around 95 μm . The grains appear to be randomly oriented and equiaxed. The EBSD plot also shows many annealing twins. One goal of this work is to investigate the effect of these annealing twins

Next, the specimen was speckled and loaded in fatigue until a fatigue crack initiated from the notch root. The specimen was then removed from the load frame and imaged in an optical microscope with 112 images at 50x magnification. The specimen was placed back in the load frame and fatigue loading resumed. Fatigue loading was such that the stress intensity factor amplitude was roughly constant at $\text{MPa}\sqrt{\text{m}}$. The specimen was imaged with the optical microscope at intervals of roughly 0.5 mm of crack growth as the specimen grew into and through the region of interest. Each image taken in the optical microscope was then correlated to its corresponding reference image (taken just after crack initiation) using DIC. Each displacement field was differentiated to obtain strain fields for each image. The resulting 112 strain fields were then stitched together to form a single strain field over the entire region of interest. Because the Vickers indentation marks are visible in both the optical microscope and EBSD results (Figure 2), it is possible to overlay the two data sets to relate strain to microstructure.

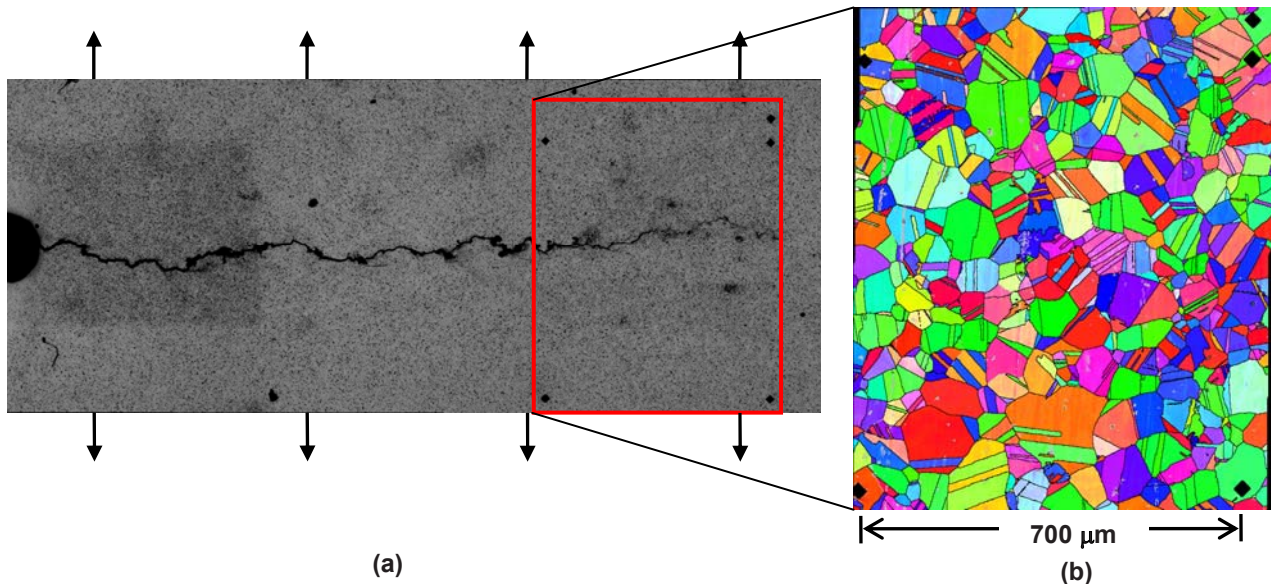


Figure 2. (a) A cracked specimen observed in the optical microscope. (b) Microstructure of the region of interest (from EBSD). Using Vickers indentation marks allows for alignment of DIC data taken from the load frame and optical microscope with microstructural data taken in the scanning electron microscope.

Results

This technique allows strain fields and microstructural data to be overlaid as shown in Figure 3. Reference images were taken just after crack initiation from the notch and the deformed images were taken after the crack had grown through the region of interest. The strain fields resulting from these correlations were stitched and aligned with microstructural measurements. Figure 3, on the next page, shows the resulting ϵ_{yy} strain field with grain boundaries overlaid onto the contour plot.

Many types of analyses can be done comparing strain to microstructure. While further studies of this data are planned, a few preliminary investigations have been made thus far. As can be observed in Figure 3, there are a few places where strain localizations occur on grain boundaries. There are also some grains with significantly higher strains than others. Future investigations will focus on the role of grain boundaries, annealing twins, and grain orientation on strain localizations in fatigue crack growth. Analysis of the microstructure in these strain localization regions will enhance the understanding of the role microstructure plays in fatigue crack growth.

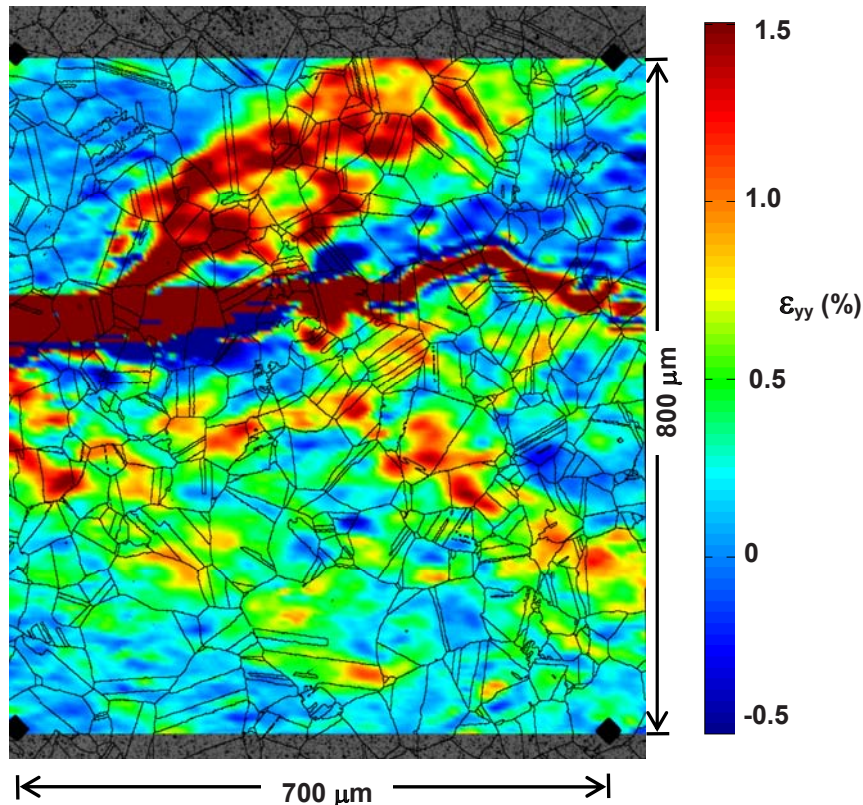


Figure 3. DIC strain field, ϵ_{yy} , resulting from crack growth through the region of interest. Grain boundaries, obtained from EBSD, are overlaid on top of the strain field. Overlaying strain accumulation and microstructure will provide insight for microstructure-based material deformation models.

Conclusions

Stitching multiple DIC results gives strain fields over sizeable areas with much higher spatial resolution than would otherwise be possible. By placing markers on the specimen, these high resolution DIC measurements could be spatially overlaid onto microstructural results. These EBSD microstructural measurements not only provide grain geometry information, they also full-field grain orientation information. With the overlaid data provided by this method, accumulated fatigue strains can be quantitatively compared to grain geometry and orientation on a full-field basis. Comparisons of this data will lead to a greater understanding of the influence of microstructure on fatigue.

Acknowledgements

This work was supported by the Midwest Structural Sciences Center (MSSC), which is supported by the Air Vehicles Directorate of the U.S. Air Force Research Laboratory under contract number FA8650-06-2-3620.

References

- [1] Tong W. "Detection of plastic deformation patterns in a binary aluminum alloy", *Exp Mech*, 2010
- [2] Zhao Z. Ramesh M. Raabe D. Cuitino AM. Radovitzky R. "Investigation of three-dimensional aspects of grain-scale plastic surface deformation of an aluminum oligocrystal", *Int. J. Plast*, 2004
- [3] Padilla H. Lambros J. Beaudoin A. Robertson IM. "Use of multiscale image correlation to study the relationship between inhomogeneous deformation and local texture in zirconium", *Submitted to Int. J. Solids and Struct*, 2010.
- [4] Efstathiou C. Sehitoglu H. Lambros J. "Multiscale strain measurements of plastically deforming polycrystalline titanium: Role of deformation heterogeneities", *Int. J. Plast*, 2010.

High Cycle Fatigue of Structural Components Using Critical Distance Methods

Somnath Chattopadhyay
Department of Engineering
The Pennsylvania State University
1 College Place
DuBois, PA 15801, USA
sc72@psu.edu

ABSTRACT

This study explores the high cycle fatigue strength of crack-like discontinuities in metallic structures as well as those made from powder metals using approaches that are based on theory of critical distances (TCD). The methods used in this study consist of (a) the point method, (b) the line method, and (c) the imaginary crack method. The effective parameter for the methods (a), (b), and (c) is the distance 'd' from the material surface, which is a material property and the reference parameter is the fatigue limit. The imaginary crack method involves introduction of a sharp crack at the root of a notch and the length of the crack, ' l_0 ' assumed a material constant. In the imaginary crack method, the effective crack length is taken as the sum of the actual crack and the material parameter ' l_0 '. It is concluded that the high cycle fatigue has a volumetric character and the proposed methods introduce the volume effect in the determination of stress and strain fields as well as the fatigue life. Using the material parameters from the various approaches, the number of cycles to initiate a fatigue has been determined for a number of materials and compared with experimental results.

NOMENCLATURE

a: crack length, m
 a_{th} : threshold crack size, m
d: distance parameter due to Roche [6], m
D: grain diameter, m
E: modulus of elasticity, GPa
K: stress intensity factor, MPa \sqrt{m}
 ΔK_{th} : threshold stress intensity factor range, MPa \sqrt{m}
 ΔK_{th}^I : long crack threshold stress intensity factor range, MPa \sqrt{m}
 l_0 : distance parameter due to El Haddad et al [5], m
N: number of cycles to initiate a crack
 ΔS : stress range, MPa (remote from crack)
 $\Delta \sigma$: stress range, MPa
 $\Delta \sigma_e$: endurance limit stress range, MPa

INTRODUCTION

The theories of fatigue initiation based on critical distance (or process zone) concepts have been used for many years. Peterson [1] considered that fatigue failure occurs when the stress at a constant distance beneath the surface equals the fatigue strength of the material. Neuber [2] related the stress concentration factor at the root of a sharp notch to the average stress over a certain critical distance. High cycle fatigue failures are not usually initiated by the large micro structural defects associated with low cycle fatigue failures, but often nucleate "naturally" at local regions of high stress. The damage

progresses through mechanisms starting with crack nucleation, and the growth of micro structurally small cracks. Each mechanism is associated with a characteristic size, and each characteristic size has its own geometric complexity, constitutive law, and heterogeneity. Fatigue behavior cannot be fully understood and predicted without obtaining information about each of the characteristic sizes. According to the observations of Kitagawa and Takahashi [3], fatigue crack growth behavior of short cracks differs in a non-conservative manner from expectations based upon long crack behavior.

The theory of critical distances as popularized by Taylor [4] attempts to predict the effect of notches and other stress concentration features by considering the stress field in the region close to the notch tip. This theory requires two parameters, a characteristic distance and a critical stress or strain characterizing failure. In one version of the critical distance theory, termed as the Point Method, the failure occurs when the stress becomes equal to the failure stress at a given distance from the notch root. In the other version of the critical distance theory, termed as the Line Method, the failure is assumed to occur when the stress becomes equal to the failure stress when computed as an average value over a line of given length. Early example of the use of the Point Method is found in the work of Peterson [1], and that of the Line Method in the work of Neuber [2]. Both these studies were directed at the high cycle fatigue of metallic materials. Another method which is related to the point method is the Imaginary Crack Method. This method due to El Haddad et al [5] introduces an effective crack length to predict the propagation behavior of short cracks. In this formulation the effective crack length is equal to the crack length plus an amount " l_0 ", which is related to the critical distance. This value " l_0 " was stated by the authors as a characteristic of the material and the material condition accounting for the non-continuum behavior of very small cracks. Roche [6] outlined a practical rule for fatigue initiation in steels based on the strain ranges at a distance " d " from the crack tip, where " d " is a material characteristic. This rule is based on Peterson's [1] hypothesis that fatigue failure does not occur when the peak surface stress reaches the endurance limit, but rather when the endurance limit is reached at some finite distance " d " below the surface. Thus according to this rule, for crack like discontinuities, no analysis is required for the material located less than a distance " d " from the surface. Furthermore the value of " d " was proposed to be 0.05 mm for steel whose maximum specified ultimate strength at room temperature is less than 600 MPa. This rule finds use in French nuclear pressure vessel code, RCC-MR [7].

BACKGROUND

Lanning et al [8] have investigated the effect of notch geometry on high cycle fatigue predictions for notched Ti-6Al-4V specimens using critical distance concepts. They hypothesized the critical distance as a single distance or depth in the vicinity of stress concentration over which a stress or a strain initiation. They have also come up with concepts similar to Point Method and Line Method due to Taylor [4]. In particular they have obtained a range of values of the critical distance based on Line Method from 20 μ m to 76 μ m for the material, and have observed no obvious effects of stress ratios on these values. Recently Ostash [9] has used the process zone size (a critical distance parameter) as the transition between the growths of a micro crack to a macro crack in a number of aluminum alloys, two steels, and two cast irons. However no specific initiation criterion has been provided for the nucleation of micro cracks. Chan [11] has developed a fatigue crack initiation model based on microstructure, which includes explicit crack size and microstructure scale parameters. Hanlon, Kwon, and Suresh [12] have studied the fatigue response of electrodeposited pure nickel and an ultra-fine crystalline Al-Mg alloy. They found that grain refinement leads to an increase in resistance to failure under stress-controlled fatigue accompanied by poor resistance to fatigue crack growth. Chu et al [13] have studied the cyclic deformation and crack initiation and propagation in α -iron polycrystals with particular reference to the orientation of grains. Krupp [14] in his recent treatise has identified the missing link between the microstructural dimensions of the fatigue process on the atomic scale and the engineering design concepts of structures subject to complex loading.

The stress intensity range required to propagate a crack must remain finite rather than become infinitely large when the length of the short crack is extremely small. The value of the critical distance is determined from experimental results. As such, it is an empirical parameter to be regarded as a material constant. El Haddad, Dowling, Topper, and Smith [5] demonstrated the need for a material constant (distance parameter) in dealing with short crack behavior. This parameter appears in different forms in a

number of theories of fatigue crack initiation. Mura and Tanaka [15] propose a theory of fatigue crack initiation dependent among other parameters, such as the grain size; the smaller the grain size, the higher the resistance to crack initiation. Miller [10] obtained a best-fit equation to the micro structural short crack growth data for medium carbon steels in the form of a fatigue crack growth parameter da/dN proportional to the stress range raised an exponent times the difference of the grain diameter and the crack length. The grain diameter is very close to the material parameter for metals as evident in the studies of Wilshaw et al [16] and that of Yokobori and Konusu [17]. In this work, therefore, the grain diameter “D” is the same as the distance parameter “ l_0 ” from the studies of El Haddad et al [5], which is also twice the distance parameter “d” of Roche [6]. The upper bound on micro structural short crack growth is considered to be equal to the grain diameter, “D.” If the threshold crack length exceeds “D,” then failure does not occur, but non-propagating cracks may be found. However, if, the threshold crack-length is less than “D,” then failure occurs. The concept of critical distance is used to obtain fatigue initiation characteristics of materials in terms of the S-N curves. For the nucleation of micro cracks we have employed the approach of Miller [10] that uses experimental data for medium carbon steels and assumes that micro crack initiation occurs immediately in fatigue. The nucleation period is characterized by the growth of micro crack from a zero length to the size corresponding to the threshold stress intensity factor range.

PROBLEM STATEMENT

In this work, fatigue crack initiation has been studied using the concept of distance parameter. The endurance limit is characterized by the maximum value of the local stress range, which generally occurs on the surface. For long cracks, the stress intensity factor range, ΔK , determines fatigue failure. This range is only an approximation to the stress field. For example, given two cracks of different lengths, both located in stress fields of uniform tension, if ΔK is the same for both, then their stress versus distance curves will be identical only at small radius. At large r , each curve will tend to the remote, applied stress value, which will be different for two cracks, and not equal to zero as expected from the definition of K . Therefore, it is not the entire stress field that is important, but only the stress field close to the crack tip. Traditionally, fatigue crack initiation has been treated by empirically determining the nominal stress amplitude that can be applied to a smooth specimen for an infinite number of cycles. This is the endurance stress range, $\Delta\sigma_e$ (twice the endurance limit, S_e). The application of fracture mechanics to fatigue has resulted in a definition of the threshold stress intensity factor range, ΔK_{th} , below which no detectable crack propagation occurs for cracked members. Measurement of ΔK_{th} establishes a range of crack sizes and stress amplitudes for which no further crack extension takes place.

METHODOLOGY

Following Roche [6], the stress range at a distance “d” from the crack tip is denoted as $\Delta\sigma$, a value that is less than the endurance stress range, $\Delta\sigma_e$ (twice the endurance limit, S_e). Denoting ΔS as the nominal stress range, for short cracks, an equation can be written as:

$$\Delta\sigma = \frac{\Delta K}{\sqrt{2\pi d}} + \Delta S \quad (1)$$

The criterion for initiation can then be expressed as:

$$\Delta\sigma_e = \frac{\Delta K}{\sqrt{2\pi d}} + \Delta S \quad (2)$$

Denoting ΔK_{th}^l as the long crack threshold stress intensity factor range, and recognizing the fact that for long cracks, ΔS approaches zero, equation (2) yields:

$$d = \frac{1}{2\pi} \left(\frac{\Delta K_{th}^I}{\Delta \sigma_e} \right)^2 \quad (3)$$

Denoting the crack length as “a”, and substituting $\Delta K = \Delta S \sqrt{(\pi a)}$, and the value of “d” from equation (3) into equation (2) we obtain the criterion for initiation as:

$$\Delta S = \frac{\Delta \sigma_e}{1 + \sqrt{\frac{a}{2d}}} \quad (4)$$

The corresponding distance parameter used in El Haddad's [5] work is denoted as l_0 and is given by:

$$l_0 = \frac{1}{\pi} \left(\frac{\Delta K_{th}^I}{\Delta \sigma_e} \right)^2 \quad (5)$$

and

$$\Delta S = \Delta \sigma_e \sqrt{\frac{1}{1 + \frac{a}{l_0}}} \quad (6)$$

FATIGUE CRACK INITIATION

The number of cycles to initiate a crack is determined by the small crack initiation stage followed by its growth to a long crack (from zero to initiation size, a_{th}). The initiation size (denoted by a_{th}) for a particular stress range is determined as:

$$a_{th} = \frac{1}{\pi} \left(\frac{\Delta K_{th}}{\Delta S} \right)^2 \quad (7)$$

For initiation, the equation provided by Miller [10] is employed. This is valid for medium carbon steels and will be assumed to apply for the material considered in this analysis.

The proposed equation is:

$$\frac{da}{dN} = 1.475 \times 10^{-41} (\Delta S)^{11.49} (l_0 - a) \quad (8)$$

In the above equation the grain diameter “D” appearing in the work of Miller [10] is assumed identical to the material parameter “ l_0 ” based on the results appearing in [16] and [17].

Integrating equation (8) from the crack lengths going from zero to a_{th} , we obtain the number of cycles to initiate a crack, N_i , as:

$$N_i = \frac{1}{1.475 \times 10^{-41} (\Delta S)^{11.49}} \ln \left(\frac{l_0}{l_0 - a_{th}} \right) \quad (9)$$

RESULTS AND ANALYSIS

For this assessment, the material A533B was selected for which the long crack threshold (ΔK_{th}^I) is 8 MPa \sqrt{m} . The material has an assumed endurance stress range ($\Delta \sigma_e$) of 1000 MPa (endurance limit of 500 MPa), the value of the Roche distance parameter “d” from equation (3) is calculated to be 70 μm or 0.07 mm and the El Haddad distance parameter “ l_0 ” from equation (4) is calculated to be 140 μm or 0.14 mm. With these values the limiting stress range for fatigue failure (ΔS) as a function of crack size (a) is obtained using equation (4). The corresponding values using the approach due to El Haddad et al [4] are also obtained using equation (5). A comparison of the two methods is shown in [Figure 1](#).

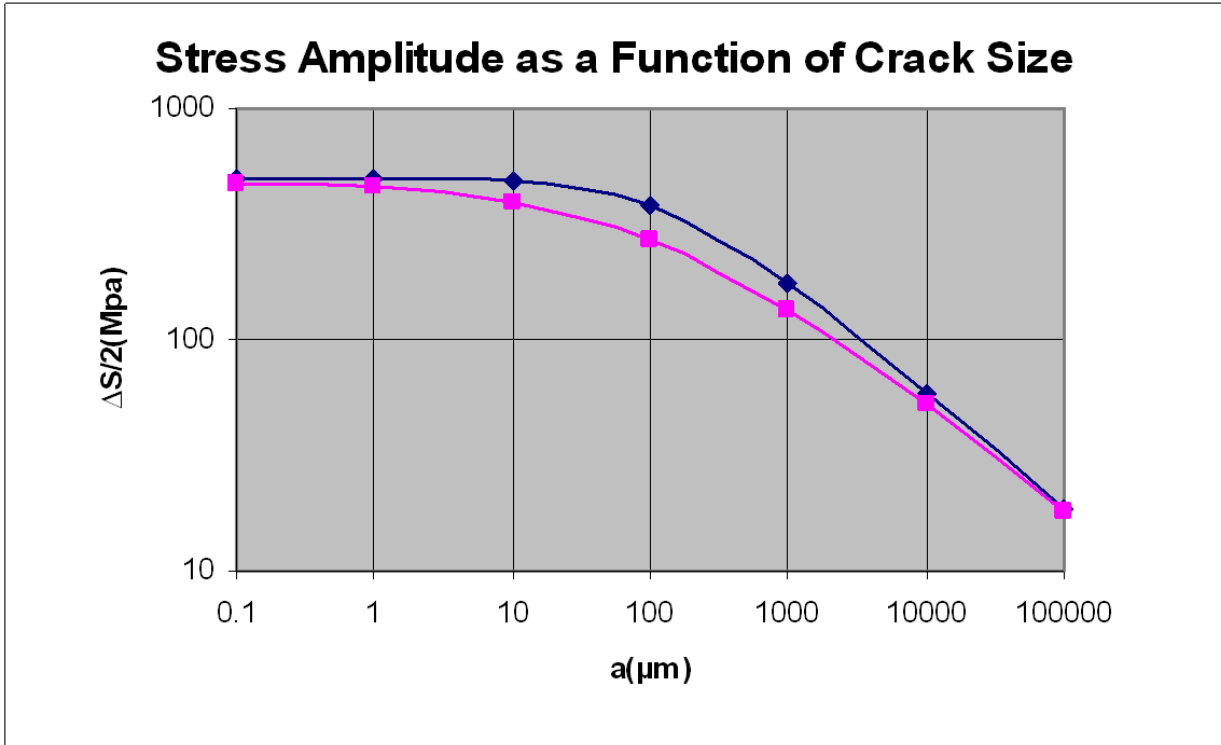


Figure 1: Comparison—Upper Curve El Haddad et al [5], Lower Curve Roche [6]

The number of cycles N_i , for initiating the crack and growing it from zero to a_{th} , is obtained from equation (9) and is shown in Figure 2.

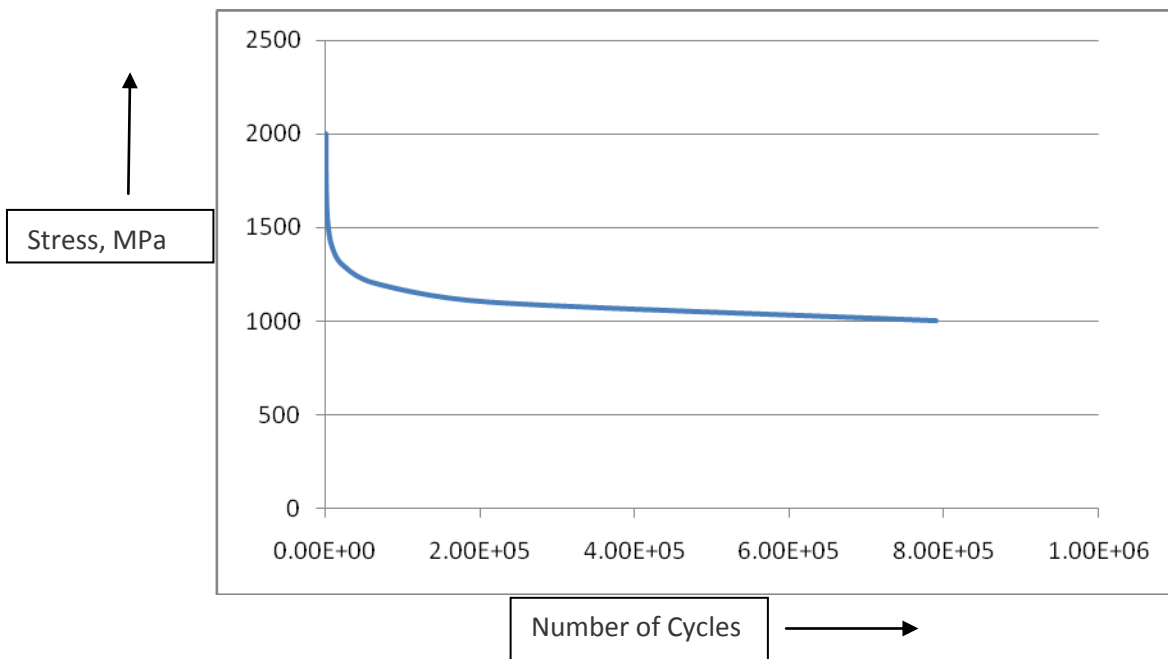


Figure 2: S-N Curve for Fatigue Initiation

CONCLUSIONS

Based on the studies due to Taylor [4] both the Point Method (akin to Roche [6]) and the Line Method (akin to El Haddad et al [5]) provide reasonable estimates for short crack growth. Generally the Point Method results are closer to the experimental data according to Taylor [4]. Therefore Figure 2 is the appropriate S-N curve for the material studied. Roche's [6] studies on a similar material also supports this conclusion. However for other materials experimental data are required to satisfactorily represent relationship similar to what appears in equation (8).

Most of the failures in the industrial world can be attributed to fatigue and is based on the response of the structural materials to alternating loads that are applied during service. The S-N curve, a graphical representation of the cyclic loading, is a plot of stress amplitude versus the number of cycles the material goes through before it fails. The greater the number of cycles in the loading history, the smaller the stress the material can withstand without failure. In keeping with the modern design philosophy of defect tolerant design, this work recognizes the presence of cracks in structural components. A rational process combining the nucleation of a crack on an assumed smooth surface (from a zero to the threshold value of crack length) and its subsequent growth to a characteristic dimension is assumed to govern the phenomenon of fatigue crack initiation. The number of cycles to initiate a crack is a feature that has been directly linked to the microstructure, and forms an important contribution of this study. By making use of an assumed crack initiation law, the S-N curve for a structural material has been obtained. Although most of the discussion in this work is directed to a typical pressure vessel steel material, the S-N curves for other materials can be obtained using a very similar approach.

REFERENCES

- [1] Peterson, R. E. (1959), "Notch Sensitivity," *Metal Fatigue*, Edited by G. Sines, J. L. Waismas, McGraw Hill, pp. 293-306.
- [2] Neuber, H. (1958), *Theory of Notch Stresses*, translation of 1957 Edition in German, Springer, Berlin.
- [3] Kitagawa, H., and Takahashi, S. (1976), "Applicability of Fracture Mechanics to Very Small Cracks in the Early Stage," *Proceedings of the Second International Conference on Mechanical Behavior of Materials*, ASM, Boston, 627.
- [4] Taylor, D. (2007), *Theory of Critical Distances: A New Perspective in Fracture Mechanics*, Elsevier Science.
- [5] El Haddad, M. H., Dowling, N.E., Topper, T. H., and Smith, K. N. (1980), "J Integral Applications for Sort Fatigue Crack at Notches," *International Journal of Fracture*, 16, 15.
- [6] Roche, R.L. (1990), "Fatigue Analysis of Crack-like Geometrical Discontinuities," *Res Mechanica*, 29, 79-94.
- [7] RCC-MR (1985): *Design and Construction Rules for Components of Fast Breeder Reactors*, AFCEN, Paris.
- [8] Lanning, D. B., Nicholas, T., and Palazatto, A. N. (2004), "Fatigue Failure Predictions in Stress Concentrations Using Critical Distance Methods," AIAA 2004-1999, *45th AIAA /ASME/ASCE/AHS/ASC Structures, Structural Dynamics and Materials Conference*.
- [9] Ostash, O. P. (2006), "New Approaches in Fatigue Fracture Mechanics," *Materials Science*, 42, 1, 5-19.
- [10] Miller, K. J. (1985), "Initiation and Growth of Short Fatigue Cracks," *Fundamentals of Deformation and Fracture*, (B.A. Bilby, K.J. Miller and J. R. Willis, eds), Cambridge University Press, 477-500.
- [11] Chan, K. S. (2003), "A Microstructure-Based Fatigue-Crack Initiation Model," *Metallurgical and Materials Transactions*, 24A, 43.
- [12] Hanlon, T., Kwon, Y.-N., and Suresh, S. (2003), "Grain Size Effects on the Fatigue Response of Nanocrystalline Metals," *Scripta Materialia*, 49, 675-680.
- [13] Chu, R.Q., Cai, Z., Li, S. X., and Wang, Z. G. (2001), "Fatigue Crack Initiation and Propagation in an α -iron Polycrystal," *Material Science and Engineering*, 313, 64-68.
- [14] Krupp, U. (2007), *Fatigue Crack Propagation in Metals and Alloys: Microstructural Aspects and Modelling Concepts*, WILEY-VCH Verlag GmbH & Co. KGaA, Weinheim.

- [15] Mura, T. and Tanaka, K. (1990), "A Theory of Fatigue Crack Initiation in Solids," ***Journal of Applied Mechanics***, 57, 1-6.
- [16] Wilshaw, T.R., Rau, C. A., and Tetelman, A.S. (1968), "A General Model to Predict the Elastic-Plastic Stress Distribution and Fracture Strength of Notched Bars in Plane Strain Bending," ***Engineering Fracture Mechanics***, 1, 191-211.
- [17] Yokobori, T., and Konusu, S. (1977), " Effects of Ferrite Grain Size, Notch Acuity and Notch Length on Brittle Fracture Stress of Notched Specimens of Low Carbon Steel," ***Engineering Fracture Mechanics***, 9, 839-847.

Crack Propagation Analysis of New Galata Bridge

Kadir Ozakgul, Res.Asst.Dr., Istanbul Technical Univ., Dept. of Civil Engineering,
Maslak 34469, Istanbul, Turkey, ozakgul@itu.edu.tr
Ozden Caglayan, Asst. Prof. Dr., Istanbul Technical Univ.
Ovunc Tezer, Res.Asst., Istanbul Technical Univ.
Erdogan Uzgider, Prof. Dr., Istanbul Technical Univ.

ABSTRACT

The New Galata Bridge links the two sides of the entrance of the Golden Horn and as a bascule-type bridge, the bridge has four wings, each having a span of 42 meters. The bridge has replaced the Galata Bridge which gave service from 1912 to 1985. After the new bridge has begun to give service, serious cracks located in steel stringers underneath the road surface and near the counterweight blocks were observed during maintenance. As a result, modifications around this area were made. Three dimensional finite element models of the third wing and cracked locations were prepared. Crack analyses were conducted around these points. Based on results, comments were provided.

Keywords: Crack propagation; Stress intensity factor; Crack analysis; Bascule-type bridge.

1. Introduction

Fatigue crack initiation and fatigue crack growth are important damage modes in bridge structures. Structural flaws can result from many sources, including initial fabrication and welding defects, life load induced fatigue cracking, corrosion, and impact damage. Improper weld procedures can result in weld cracking, low heat affected zone (HAZ) toughness, low weld metal toughness, and various types of voids and slag inclusions [1]. If uncontrolled, these defects greatly increase the potential for fracture and fatigue crack growth initiation. The fatigue resistance of welded details commonly used in bridge construction was characterized [2].

Three primary factors that control the susceptibility of a structure to brittle fracture are material toughness, flaw size and stress level [3]. Material toughness can be defined as the resistance to unstable crack propagation in the presence of a notch. Brittle fractures initiate from flaws or discontinuities of various kinds. These discontinuities can vary from extremely small cracks to much larger weld or fatigue cracks. Even though only small flaws may be present initially, repeated loading can cause them to enlarge, possibly to a critical size where brittle fracture can occur. For brittle fracture of a structure, tensile stresses are necessary.

2. Location and description of the bridge

The most recent Galata Bridge was installed on its current location in 1992 by replacing the old one as a result of decaying after 80 years of service life. The New Galata Bridge is one of the longest bascule bridges in the world, consisting of four flaps, each flap having a length of 42 meters. Each flap has an approximate width of 20 meters. The bridge has two main longitudinal beams and fourteen cross-girders lying in transverse direction. There are four towers beneath the longitudinal beams which contain the control rooms for opening the flaps for vessel crossing. Flaps are opened by hydraulic actuators which rotate the longitudinal beams around two main bearing points. Concrete counterweights of approximately 1600 tons help this opening and closing process. Then, cracks were observed on the steel plates which support the counterweight and connect these concrete blocks to cross-girders. A general view of the bridge is given in Fig. 1 below.



Fig. 1. General view of The New Galata bridge

3. Finite element modeling of existing bridge

Three dimensional finite element model of the third flap was prepared using COSMOS/M software [4] according to shop drawings obtained from the designer and consultant firms for both original and modified structural systems. The prepared finite element model has a total of 21477 shell elements, 171 isoparametric solid (8-node brick) and gap elements with a total of 19071 nodes and 114298 degrees-of-freedom. Figs. 2 and 3 below illustrate the 3D finite element model of the third flap. Steel beams were modelled using shell elements whereas concrete blocks were modelled using solid elements. At each side elements were used to tie the surrounding nodes to a single point which represents the axis of rotation of the bridge flap.

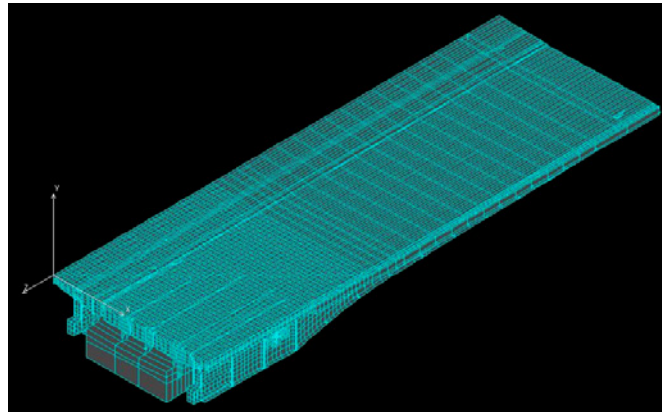


Fig. 2. Three dimensional finite element model of the third flap

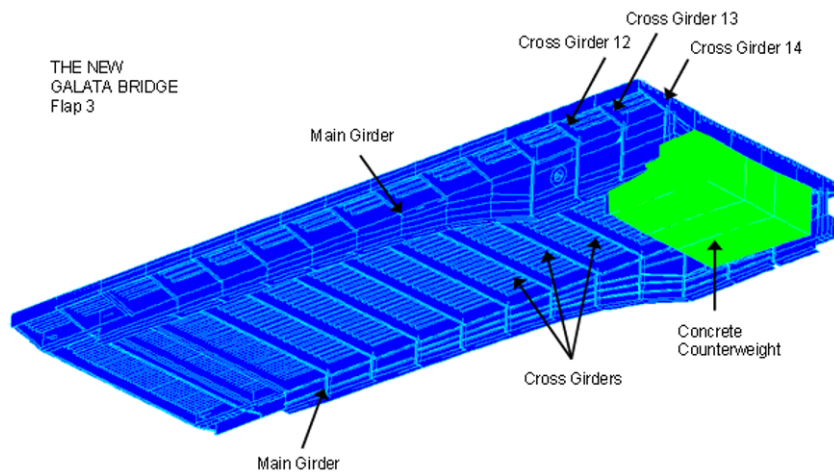


Fig. 3. Extruded view of the finite element model

4. Modal analyses

First four natural frequencies of the third flap, calculated with full finite element model by using Lanczos algorithm, are listed in [Table 1](#), and the first four mode shapes of the flap are shown in [Fig. 4](#).

Table 1. Natural frequencies of the third flap

Modes	1st	2nd	3rd	4th
Frequencies (Hz)	1.276	1.597	1.609	2.661

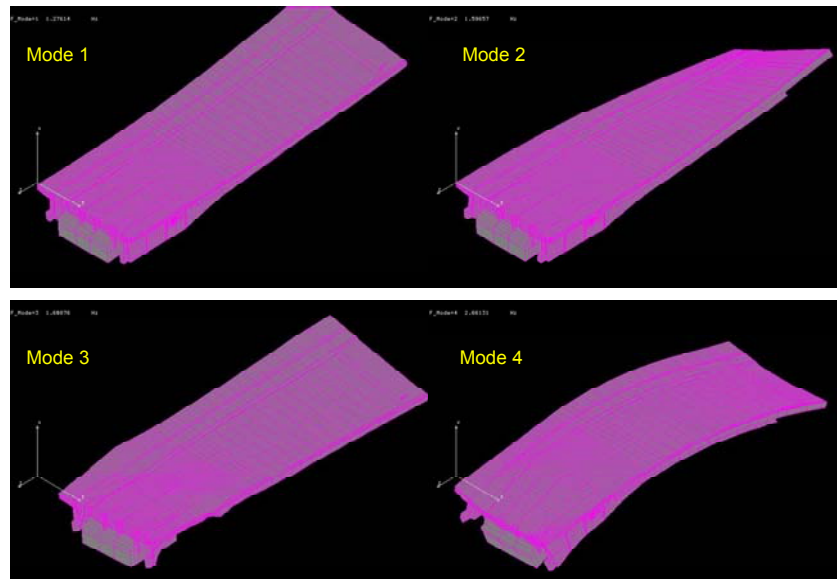


Fig. 4. Mode shapes of the third flap

5. Static analyses

Finite element analyses under static and thermal loads were conducted for various positions of the third flap, (0°), (45°) and (84°) positions according angle that is done with horizontal ground level. [Figs. 5 and 6](#) shows Von-Mises stress results belong to (84°) positions of the third flap.



Fig. 5. Stress results of the third flap subjected to static loads

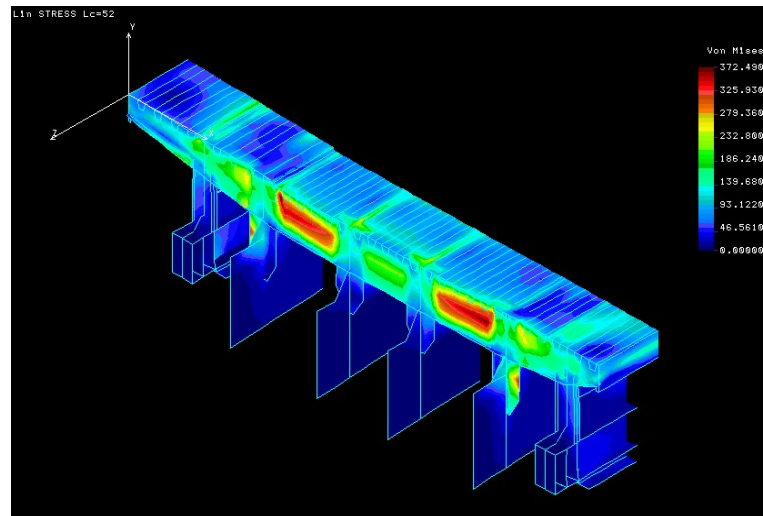


Fig. 6. Stress variation on the cross girder 14

6. Fracture analyses

A method of assessing the fracture toughness is to relate the Charpy V-notch (CVN) values to K_I . Charpy V-notch values were measured by the steel manufacturer. K_I , empirical formula based on CVN values, used for the critical crack size calculation was conservatively estimated following as [1,5],

$$K_I = \sqrt{0.64 \cdot E \cdot CVN} \quad (\text{kPa}\sqrt{\text{m}}) \quad (1)$$

where CVN is the standard Charpy V-notch energy in Joules and E is Young's modulus in kPa.

For stress analyses of cracks in solids, three types of relative movements of two crack surfaces are defined [1]. These displacement modes represented the local deformation ahead of a crack are given in Fig. 7. In analyses, it was assumed that the deformations at the crack tip can be treated as one or a combination of these local displacement modes [1,6].

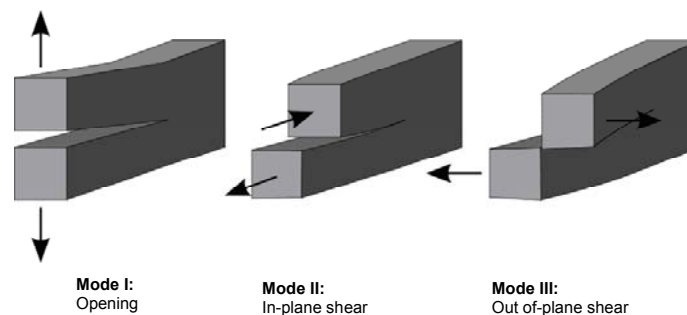


Fig. 7. The modes of crack surface displacements

A finite element model was prepared to examine cracks (see Fig. 8) at end cross girder 14, that is placed between sidewalk and roadway intersection line. Nodal displacements from global model were used as boundary displacement conditions for local finite element model (see Fig. 9). The local finite element model was obtained containing web frame with a slot that permits the longitudinal beam to pass through. Shell elements were used for the modelling with the mesh density concentrated in the vicinity of the slot edges (high accuracy is desired at this edge).



Fig. 8. Cracks at end cross girder web

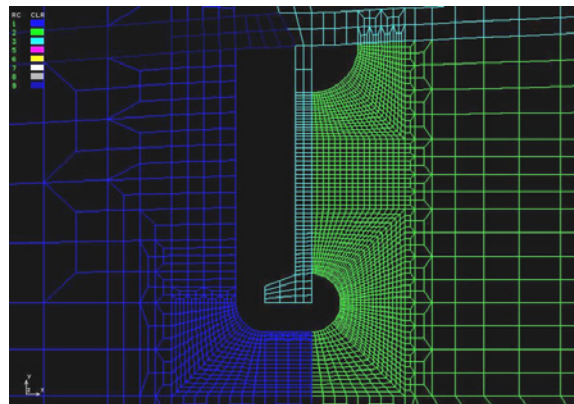


Fig. 9. Local finite element model

A set of boundary conditions for the model was determined by considering the deflection of a side shell under service loads. From the FE model of bridge, the boundary conditions for the local detail is obtained. By applying the boundary conditions to the local model, crack analyses were conducted using NISA-ENDURE software [7], and stresses and stress concentration points are found as shown Fig. 10. These points are known to be crack initiation locations.

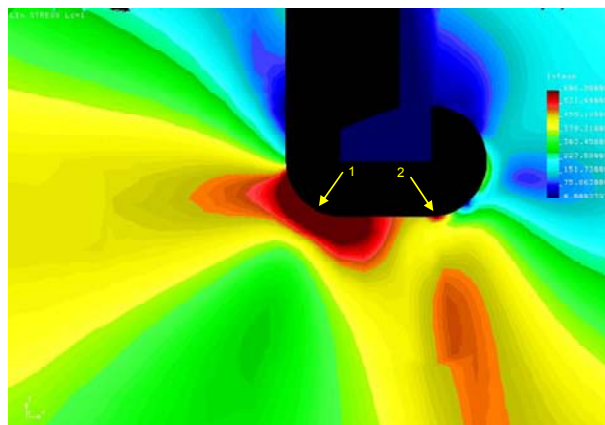


Fig. 10. Stress intensity factor values for the critical crack location

Two documents, one by the contractor and the other by an independent test laboratory revealed Charpy V-notch (CVN) toughness (K_I) values for S355 steel type used as 167 J ($148.38 \text{ MPa}\sqrt{m}$) and 170 J ($149.71 \text{ MPa}\sqrt{m}$) at -20°C , respectively. Charpy V-notch value of S355 steel material at -20°C according to DIN EN 10025 [8] is 27 Joules. Crack analyses were conducted using NISA-ENDURE software [8] for expected operating conditions. For the critical crack location (see Fig. 10), stress intensity factor (K_I) was found to be $40.12 \text{ MPa}\sqrt{m}$. Considering this value smaller than test results, it was concluded that the observed crack has formed due to an unpredicted and yet unidentified overloading condition.

In a similar fashion, cracks as seen in Figs. 11 and 12 at the welded connections of stringers to steel plates that carry concrete counterweights were also investigated in this study.

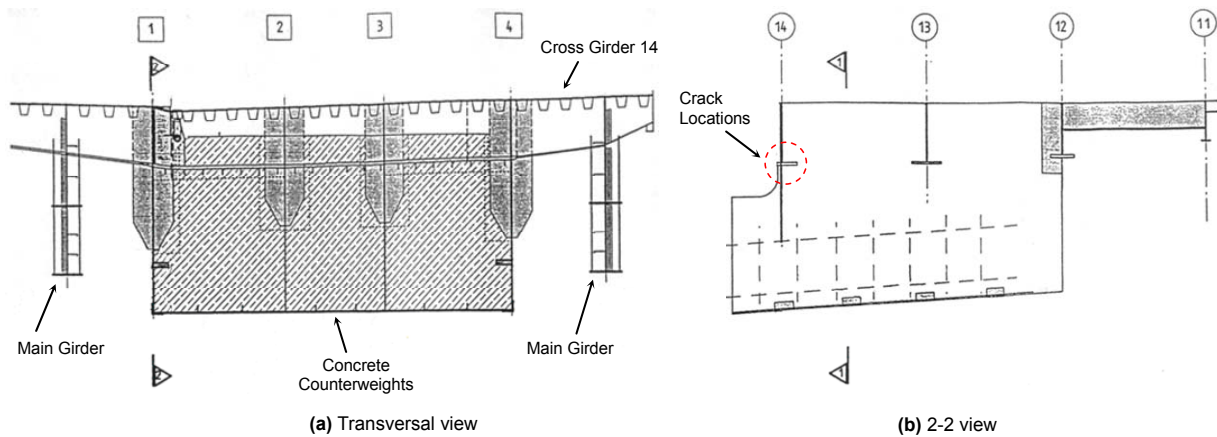


Fig. 11. Location of cracks at the welded connections

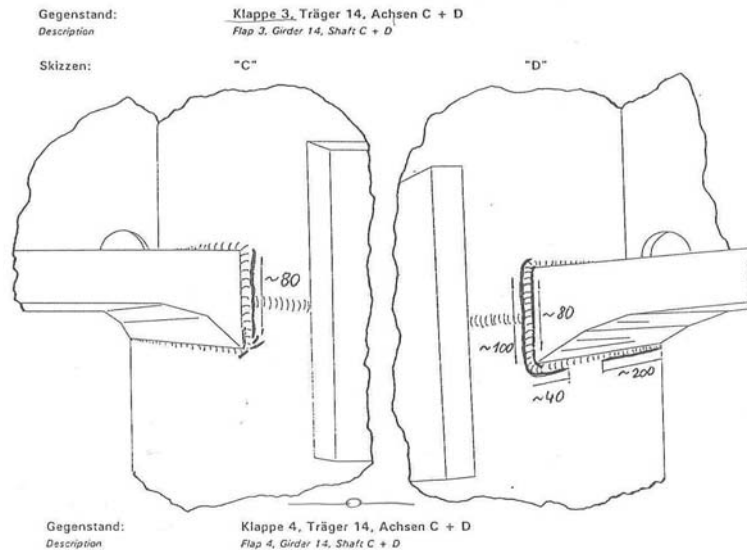


Fig. 12. Schematic description of the cracks

Nodal displacements obtained from finite element analyses of the global model were used as boundary displacement conditions for local finite element models given in Fig. 13. Stress intensity factors were computed at crack locations. Results were given in Table 2 and Table 3. Heat affected zones around these welds are thought to play an important role despite low number of load reversals.

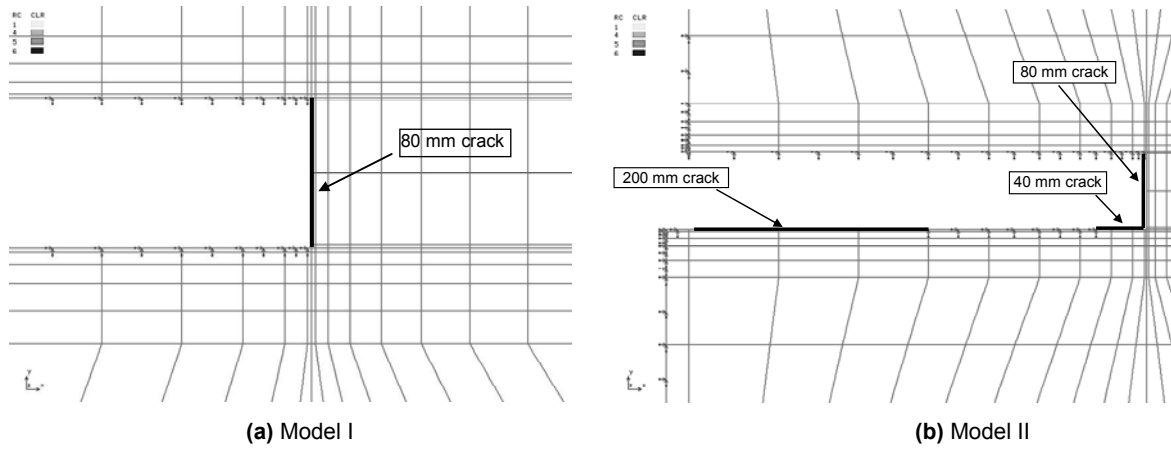


Fig. 13. Local finite element models of crack locations

Table 2. Stress intensity factor values for Model I

Crack finite element model	Nodes	Stress intensity factor ($MPa\sqrt{m}$)			
		for 0° position		for 84° position	
		Mode I	Mode II	Mode I	Mode II
	Node 1	43.10	26.70	61.65	91.89
	Node 2	28.12	42.57	84.81	34.38

Table 3. Stress intensity factor values for Model II

Crack finite element model	Nodes	Stress intensity factor ($MPa\sqrt{m}$)			
		for 0° position		for 84° position	
		Mode I	Mode II	Mode I	Mode II
	Node 1	54.86	26.23	88.48	93.50
	Node 2	11.66	27.68	11.82	33.97

7. Conclusion

In this study, serious cracks observed at the third wing of a bascule-type bridge having four wings are investigated. Finite element models of the third wing and cracked locations were performed and crack analyses were conducted around cracked points. Considering stress intensity factor values smaller than Charpy V-notch (CVN) test results, it was concluded that the observed crack has formed due to an unpredicted and yet unidentified overloading condition or heat affected zones around welds.

References

1. Barsom, J.M. and Rolfe, S.T., *Fracture and fatigue control in structures: Applications of fracture mechanics*, ASTM, Philadelphia, 1999.
2. Fisher, J.W., *Fatigue and Fracture in Steel Bridges: Case Studies*, Wiley, New York, 1984.
3. Rolfe, S.T., "Fracture and Fatigue Control in Steel Structures", *Engineering Journal, First Quarter*, 2-15, 1977.
4. COSMOS/M, *User's manual*, Solidworks Corporation, Dassault Systèmes, Massachusetts, 2008.
5. Wright, W.J., "Fracture toughness requirements for highway bridges: past and future trends", *Prog. Struct. Engng Mater.*, **4**, 96-104, 2002.
6. Wang, J.A. and Liu, K.C., "A New Approach to Evaluate Fracture Toughness of Structural Materials", *Journal of Pressure Vessel Technology*, **126**, 534-540, 2004.
7. NISA-ENDURE. *User's manual for fatigue and fracture analysis*, Engineering Mechanics Research Corporation, Michigan, 1993.
8. DIN EN 10025, *The EN standards for hot rolled products of structural steel*, Berlin, 2005.

Stress-Dependent Elastic Behaviour of a Titanium Alloy at Elevated Temperatures

Thomas K. Heckel^{1*}, Aimé Guerrero Tovar², Hans-Jürgen Christ¹

¹Institut für Werkstofftechnik, Universität Siegen, D-57068 Siegen, Germany

²Materials Science Department, Universidad Simón Bolívar, Apartado 89000, Caracas 1080A, Venezuela

*Corresponding author: thomas.heckel@uni-siegen.de

ABSTRACT

In this study the stress-dependence of the elastic modulus at elevated temperatures during fully-reversed low cycle fatigue of the titanium alloy Ti6242 is examined. The change of the elastic properties with stress manifests itself in a crescent-like shaped hysteresis loop of stress vs. plastic strain at very low amplitudes. A quadratic extension of Hooke's law with a second constant "k" is applied. The parameters are determined all along the unloading curve in tension and compression. The approach allows to align the branches of the hysteresis loop so that they become vertical, i.e. the elastic strain is accurately described. The value and sign of "k" depend whether the deformation occurs in tension or compression. Like the Young's modulus E_0 , "k" it also depends on temperature. The changes of "k" are correlated with the different mechanisms of dislocation movement activated at different temperatures. At temperatures up to 550°C the values of "k" in tension and compression do not change during fatigue life. However, at 650°C thermally activated slip processes lead to changes of both, E_0 and "k".

1 INTRODUCTION

Elastic deformation is associated with stretching, but not breaking, the chemical bonds between the atoms in a solid. If an external (elastic) stress is applied to a material, the distance between the atoms changes by a small amount that depends on the material and the details of its structure and bonding. These distance changes, when accumulated over a piece of material of macroscopic size, are called elastic deformations.

The distance between two atoms in a solid body is defined by the superposition of attractive and repulsive potential energies, U_A and U_R , respectively. The repulsive energy decreases faster towards larger atomic distances (x_a), but it increases more rapidly at short distances becoming larger than the attractive energy. The total atomic force is thus attractive at large distances, repulsive at short distances and zero at one particular distance, which is the equilibrium spacing. At this distance, the potential energy reaches a minimum. This relationship is illustrated in [Figure 1](#).

The total force F_T necessary to perturb the atoms from their equilibrium is given by

$$F_T = \frac{dU_T}{dx_a} \Rightarrow dU_T = F_T \cdot dx_a \quad (1)$$

For a specific potential energy, i.e. energy U_T per volume V or energy density, one finds the relationship

$$\frac{dU_T}{V} = du_T = \frac{F_T}{A} \cdot \frac{dx_a}{x_a} = \sigma \cdot d\varepsilon_{el} \Rightarrow \sigma = \frac{du_T}{d\varepsilon_{el}} \quad (2)$$

Where σ is the stress and ε_{el} is the elastic strain. From equation (2) one derives for the Young's modulus E_0

$$E_0 = \frac{d\sigma}{d\varepsilon_{el}} = \frac{d^2 u_T}{d\varepsilon_{el}^2} \quad (3)$$

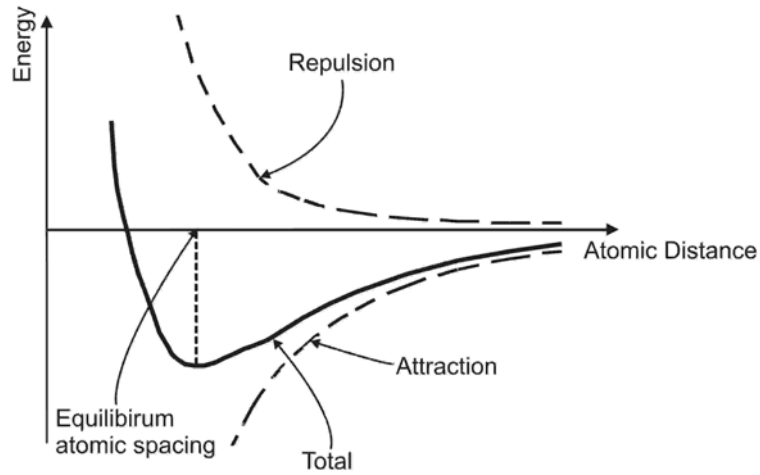


Figure 1: Variation with distance of the attractive, repulsive and total forces between atoms.

A constant, stress-independent, Young's modulus can thus only exist if U_T is described by a parabolic equation. Figure 1 indicates that this is true only for vanishing strains. It was already observed in the 19th century that the Young's modulus decreases for various metals and alloys when the stress is increased. A discussion of the various stress-strain formulas, proposed for materials which do not follow Hooke's law, was given by Mehmke [1]. In order to compensate the non-linearity of Young's modulus a third-order term may be added to the quadratic term to the expression of the specific potential energy, as has been suggested by [2]:

$$u_T = \frac{k}{3} \varepsilon_{el}^3 + \frac{E_0}{2} \varepsilon_{el}^2 + const. \Rightarrow \frac{du_T}{d\varepsilon_{el}} = \sigma = k\varepsilon_{el}^2 + E_0 \varepsilon_{el} \quad (4)$$

The inverse function of equation (4) yields

$$\varepsilon_{el} = \frac{\sqrt{E_0^2 + 4k\sigma} - E_0}{2k} \quad (5)$$

And for the non-constant, differential elastic modulus E_D one obtains

$$E_D(\varepsilon_{el}) = \frac{d\sigma}{d\varepsilon_{el}} = E_0 + 2k\varepsilon_{el} \quad (6)$$

or

$$\frac{1}{E_D(\sigma)} = \frac{d\varepsilon_{el}}{d\sigma} = \frac{1}{\sqrt{E_0^2 + 4k\sigma}} \Rightarrow E_D(\sigma) = \sqrt{E_0^2 + 4k\sigma} \quad (7)$$

2 MATERIAL and EXPERIMENTAL DETAILS

The alloy investigated is the near-alpha titanium alloy Ti-6Al-2Sn-4Zr-2Mo-0.1Si. It was developed in the late 1960s as an elevated-temperature alloy and is recommended for use up to 565°C [3]. The material was heat-treated in order to obtain a bi-modal microstructure, yielding a good balance between creep and fatigue properties. Further details about heat treatment can be found in [4].

Dog-bone shaped samples having a gauge diameter of 8 mm were used. Fatigue tests were carried out on a MTS servohydraulic test system. Specimens were tested in the temperature range of 350–650°C, both in air and in vacuum. Fully reversed low-cycle fatigue (LCF) tests were conducted in total strain control ($\Delta\varepsilon_t/2=0.7\%$) and

stress control ($\Delta\sigma/2 = 400$ and 600 MPa) applying a triangular command signal. Temperature was measured and controlled using a calibrated thermocouple attached to the centre of the gauge length. Elevated temperatures were generated using induction heating.

3 RESULTS and DISCUSSION

3.1 Dependence of Young's modulus on temperature and fatigue life

The temperature dependence of the Young's modulus $E_0(T)$ of Ti6242 can be described reasonable by the following equation [5]

$$E_0(T) = E_0(0K) \cdot \left(1 - m \cdot \frac{T}{T_m}\right) \quad (8)$$

Where $E_0(0K)$ is the Young's modulus at 0 Kelvin, m is the slope ($m = 0.9$ for Ti6242) and T_m the melting temperature (T_m (Ti6242) = 1978 K). In Figure 2 E_0 is plotted versus the temperature. The circles indicate the average values of the Young's modulus measured during fatigue testing at the respective temperatures.

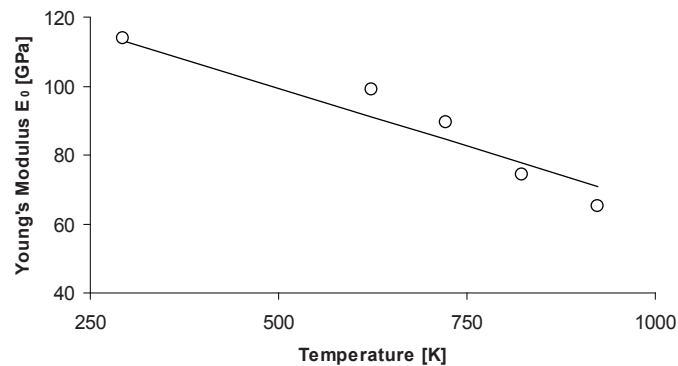


Figure 2: Young's modulus E_0 vs. temperature of Ti6242, circles represent average values measured during fatigue testing, line corresponds to equation (8)

The LCF tests have revealed that E_0 does not depend on the number of fatigue cycles at temperatures below 450°C , the Young's modulus remains saturated until the onset of fatigue crack growth. At 550°C and 650°C however, a continuous decrease of the elastic modulus can be observed, which is more pronounced at 650°C . For a better comparison of the modulus' behaviour, figure 3 describes the respective E_0 values at the different temperatures in relative coordinates relating E_0 to the value at the beginning of cyclic loading and N to the number of cycles to failure.. It can be seen that up to 450°C E_0 remains almost constant until the onset of unstable crack growth. At 550°C a slight decrease can be detected. This effect can be explained by the loss of strength due to microstructural changes, e.g. lamellar boundaries are not an effective barrier for dislocations anymore, leading to the deterioration of β -fringes [6]. Finally, at 650°C the degradation of microstructure becomes further pronounced and manifests itself in a continuous loss in stiffness during fatigue life.

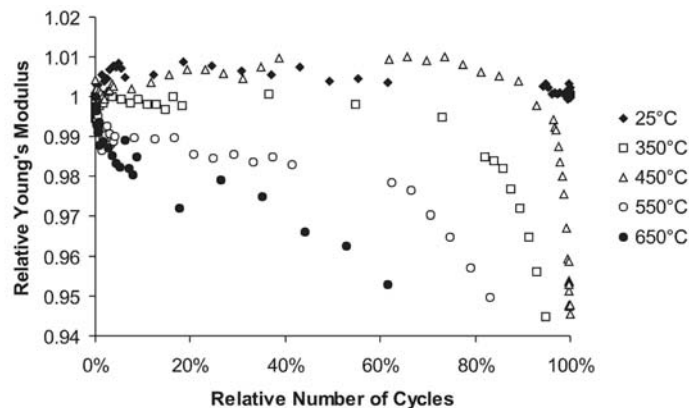


Figure 3: Dependence of Young's modulus on number of cycles during low cycle fatigue ($\Delta\varepsilon_f/2 = 0.7\%$) at different temperatures

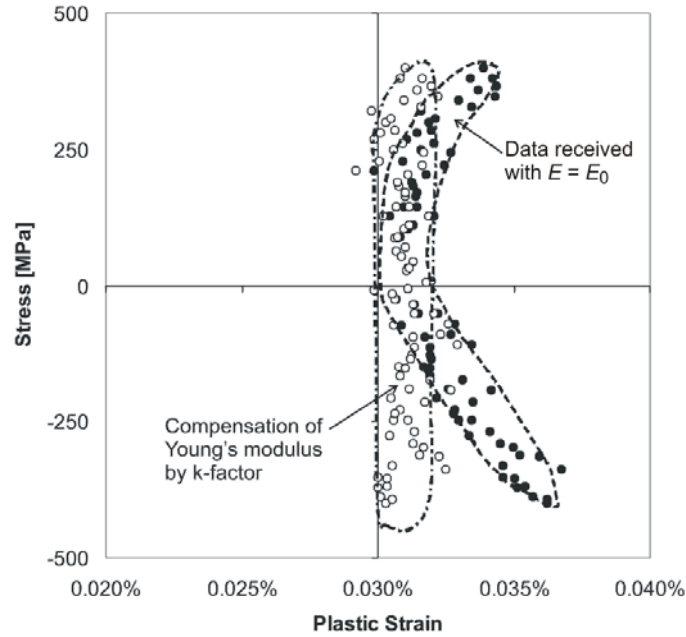


Figure 4: Crescent-like shaped hysteresis loop of Ti6242 at 350°C, $\Delta\sigma/2 = 400$ MPa (solid circles), and calculated compensation of stress-dependent Young's modulus (open circles)

3.2 Cyclic Behaviour of Stiffness

The stress dependence of the Young's modulus can be best visualised by plotting the hysteresis loop of stress vs. plastic strain at very low amplitudes. For this purpose, the calculated elastic strain was subtracted from the experimentally observed total strain. Fig. 4 shows a crescent-like shape of the hysteresis loop which was obtained in a LCF test at 350°C and $\Delta\sigma/2 = 400$ MPa using a constant Young's modulus.

Only in the vicinity of $\sigma = 0$ the branches of the as-received hysteresis loop show a vertical orientation. However, at higher stresses the deviation of the elastic behaviour from the ideal elastic behaviour becomes apparent. A description of the hysteresis loop by means of the k -concept as suggested in the introduction is able to compensate the stress-dependent deviations. The procedure to derive the specific k values is the following.

From the unloading data of total strain and stress after stress reversal the stress-dependent elastic modulus E (equation 6) can be calculated. The course of the modulus versus stress at 350°C for different control parameters is illustrated in figure 5.

It can be clearly seen that the Young's modulus becomes smaller the higher the stress and that it can approximately be described by a linear equation. However, the slopes in tension and compression are different, i.e. also the k factors are of different value in tension and compression. In compression the modulus decreases by about 7 MPa per 1 MPa increase in stress ($k^- = -350$ GPa), whilst in tension the slope is about -4 MPa ($k^+ = -190$ GPa).

3.3 Reconstruction of hysteresis loops with compensation of non-linear effects

The procedure described in this paragraph follows the route suggested in [2]. An integral elastic modulus E_I that describes the dependence of stress on elastic strain can be calculated easily from E_0 (linear contribution) and E_D (non-linear contribution)

$$\sigma = E_I(\sigma) \cdot \varepsilon_{el} = 0.5 \cdot (E_0 + E_D(\sigma)) \cdot \varepsilon_{el} \quad (9)$$

Since E_D is given by E_0 and k , the experimentally detected values of E_0 and k allow for the calculation of total (linear plus non-linear) elastic strain as a function of stress. Therefore it is possible to separate the measured total strain into elastic and plastic strains for every point of a hysteresis loop according to

$$\varepsilon_{pl} = \varepsilon_t - \frac{\sigma}{E_I(\sigma)} \quad (10)$$

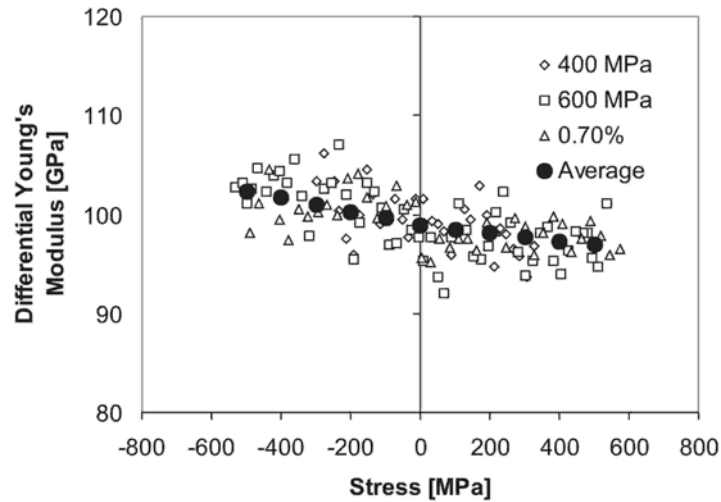


Figure 5: Dependence of differential Young's modulus E_D on stress for Ti6242 at 350 °C, $\Delta\sigma/2 = 400, 600$ MPa and $\Delta\varepsilon/2 = 0.7\%$, average values were obtained using equation (7)

The average values for E_0 and k are listed in table 1 and the shape change of the “plastic” hysteresis loops can be seen in figure 6.

Table 1: Average values of E_0 , k^+ and k^- at different temperatures.

T [°C]	E_0 [GPa]	k^+ [GPa]	k^- [GPa]	k^-/k^+	Number of tests evaluated
20	114.0	-90	-350	3.89	1
350	98.9	-190	-350	1.84	3
450	89.4	-275	-350	1.27	3
550	74.4	250	-650	-2.60	2
650	65.0	2000	-2175	-1.09	2

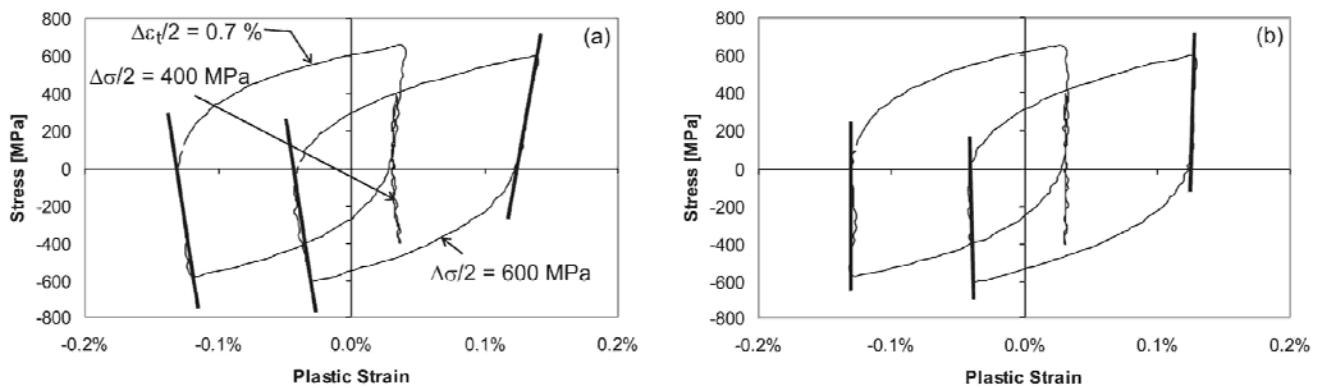


Figure 6: Hysteresis loops of stress vs. plastic strain of Ti6242 at 350 °C, (a) without considering non-linear effects, and (b) compensation of non-linear effects by extension of Hooke's law.

Sommer et al. [2] have shown that the extension of Hooke's law (equation 4) with a single constant k is sufficient to describe the elastic behaviour of a roller bearing steel properly. In their work, they were using small loading/unloading steps in order to assess the “true” elastic behaviour and not, as in this work and in the works by Hörnqvist and Karlsson [7] the unloading stiffness influenced by dislocation relaxation, which necessitates to introduce separate values of k for tension and compression.

It is evident from this investigation that the non-linear elastic behaviour can be described only if separate values of k in tension (k^+) and compression (k^-) are chosen. It is an interesting observation that the average value of k^- between room temperature and 450 °C remains constant at -350 GPa (cf. table 3). Thus, in compression the change in stiffness is only related to a change in temperature. In tension, however, the elastic modulus becomes more sensitive to a change of temperature. At room temperature, the Young's modulus is almost unaffected by a change of tensile stress (note the relatively small value of k^+ at room temperature in table 2).

A very surprising observation can be made at 550 and 650°C. At these temperatures the value of k^+ is greater than zero. Hörnqvist & Karlsson [7] also report about values of $k^+ > 0$ for aluminium. This behaviour can be understood in such a way that the amount of the elastic deformation becomes smaller in respect to the fraction of plastic deformation on total strain, i.e. flow stress and thus the critical resolved shear stress are reduced, which leads to activation of dislocation movement even at low strains. This behaviour is in accordance with the observations made by Paton et al. [8]. They note that the critical resolved shear stress of α -titanium alloyed with different amounts of aluminium reduces rapidly at temperatures above 600°C. A summary of E_D as a function of temperature and stress is given in figure 7.

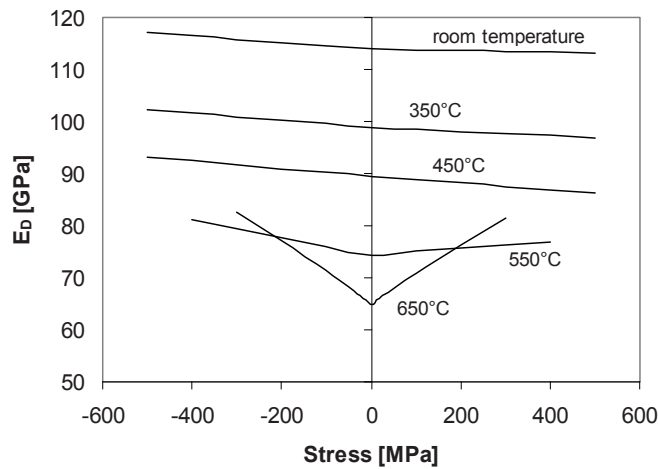


Figure 7: Calculated dependence of elastic modulus E_D on stress and temperature

3.4 Change of Unloading Stiffness during Fatigue Life

Figure 3 shows that at 650°C the Young's modulus decreases steadily. This behaviour also effects the values of k^+ and k^- as will be shown in this section. At low numbers of fatigue cycles, the absolute values of k^+ and k^- are about the same. At about half of the fatigue life (i.e. some 600 cycles for the specimen investigated) k^+ becomes smaller, while the absolute value of k^- rises. The behaviour of the two constants is shown in figure 8.

Some selected hysteresis loops are shown in figure 9. At 100 and 600 cycles the shape of the hysteresis loops is similar, however, due to the reduced Young's modulus the non-linear effects have to be compensated through different k -factors.

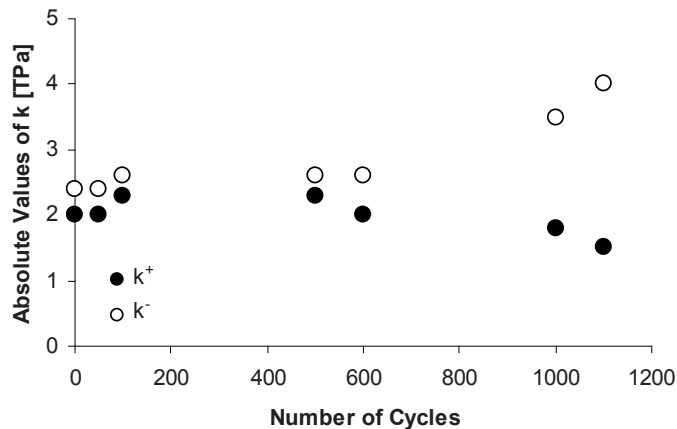


Figure 8: Evolution of the parameters k^+ and k^- with number of cycles, $T = 650^\circ\text{C}$, $\Delta\varepsilon/2 = 0.7\%$

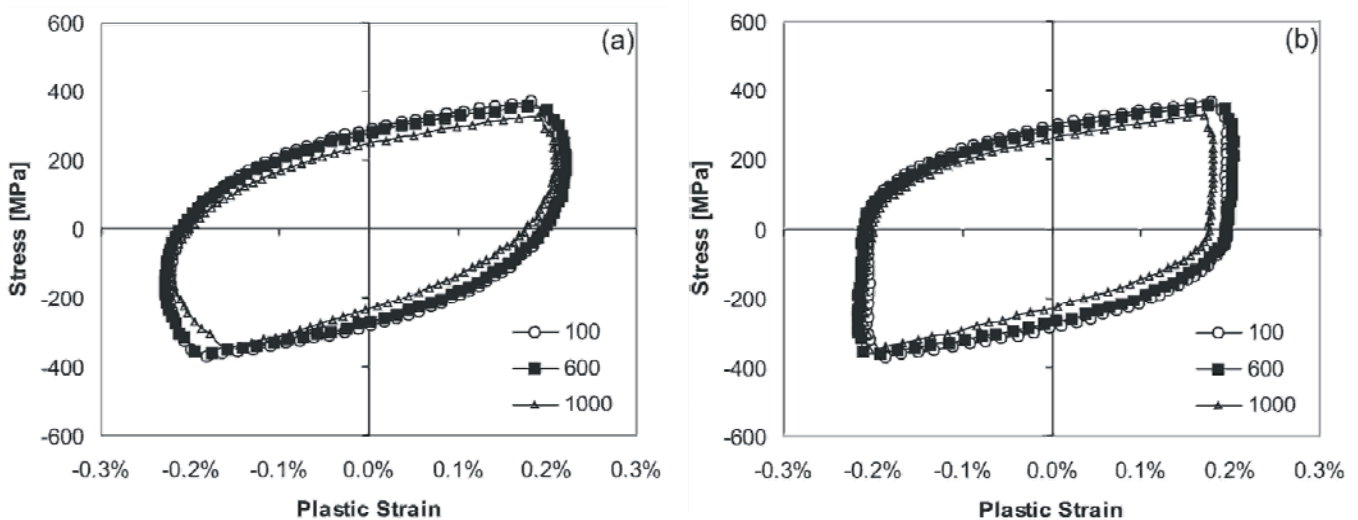


Figure 9: Measured (a) and k -compensated (b) hysteresis loops of Ti6242 for $N = 100, 600$ and 1000 cycles, $T = 650^{\circ}\text{C}$, $\Delta\varepsilon/2 = 0.7\%$

4 SUMMARY and CONCLUSIONS

The alloy investigated, Ti6242, possesses a high yield stress and a relatively low Young's modulus. Therefore, the deviation from the equilibrium atomic spacing at high elastic strains is relatively large, resulting in a distinct deviation of the linear Hooke's law. The stiffness behaviour has been evaluated during unloading from compressive and tensile peak stresses. The study has shown that the non-linear behaviour is different in tension and compression. It also changes with temperature. Up to 350°C one can observe constant values for the Young's modulus E_0 and the non-linear compensation factor k during fatigue life. However, in particular at 650°C increased thermally activated dislocation glide and grain boundary softening result in a continuous change of the k -values during fatigue life. The results suggest that the description of non-linear elastic effects through an extension of Hooke's law by a quadratic term lead to a reasonable description of the material's behaviour. Yet, it cannot be expected that this value is independent of (un)loading situation and temperature.

REFERENCES

- [1] Mehmke R: Zum Gesetz der elastischen Dehnungen. *Z Math Phys* **42**, 327-338, 1897.
- [2] Sommer C, Christ H-J, Mughrabi H: Non-Linear Elastic Behaviour of the Roller Bearing Steel SAE 52100 during Cyclic Loading. *Acta Met Mat* **39**, 1177-1187, 1991.
- [3] Boyer R, Welsch G, Collings EW: *Materials Properties Handbook: Titanium Alloys*, Materials Park, OH: ASM International. 337-375, 1994.
- [4] Heckel TK, Guerrero Tovar A, Christ H-J: Fatigue of the Near-Alpha Ti-Alloy Ti6242. *Exp Mech*, in print, doi: 0.1007/s11340-009-9238-5, 2010.
- [5] Rösler J, Harders H, Bäker M: *Mechanical Behaviour of Engineering Materials*. Berlin: Springer, 2007.
- [6] Singh N, Gouthama, Singh V: Low Cycle Fatigue Behavior of Ti Alloy Timetal 834 at 873 K, *Int J Fatigue* **29**, 843-851, 2007.
- [7] Hörnqvist M, Karlsson B: Development of the Unloading Stiffness during Cyclic Plastic Deformation of a High-Strength Aluminium Alloy in Different Temps. *Int J Mat Res* **98**, 1115-1123, 2007.
- [8] Paton NE, Williams JC, Rauscher GP: The Deformation of α -Phase Titanium. In: Jaffee RI, Burte HM, editors. *Titanium '72 Science and Technology*, New York, NY: Plenum Press. 1049-1070, 1973.

Numerical and Experimental Modal Analysis Applied to the Membrane of Micro Air Vehicles Pliant Wings

Uttam Kumar Chakravarty

Postdoctoral Fellow, School of Aerospace Engineering, Georgia Institute of Technology
Atlanta, GA 30332

and

Roberto Albertani

Affiliate Research Assistant Professor, Department of Mechanical and Aerospace Engineering
University of Florida, Research and Engineering Education Facility, Shalimar, FL 32579

E-mail: ralb@ufl.edu

ABSTRACT

Hyperelastic latex membrane is an integral structure of micro air vehicles and plays an important role in their wings performance. This paper presents finite element analysis (FEA) models for characterizing latex hyperelastic membrane at both static and dynamic loadings, validated by experimental results. The membrane at different pre-tension levels are attached with a circular steel ring and statically loaded using steel spheres of different sizes placed at the center of the membrane. The deformation of the membrane is measured by visual image correlation (VIC), a non-contact measurement system and strain energy is calculated based on Mooney-Rivlin material model. It is found that the deflection and strain energy of the membrane computed by experimental and FEA models are correlated well, although discrepancy is expected among experimental and FEA results within reasonable limits due to the variation of the thickness of the membrane. The experimental modal analysis is conducted by imposing a structural excitation to the ring for investigating the membrane vibration characteristics at both atmospheric pressure and reduced pressure in a vacuum chamber. The three-dimensional shape of the membranes during a burst-chirp excitation at different pre-tension levels is dynamically measured and recorded and the natural frequencies are computed by performing the fast Fourier transform of the out-of-plane displacement at several points of the circular membrane. Experimental results show that the natural frequencies increase with mode and pre-tension of the membrane, but decrease due to increase in ambient pressure. A preliminary FEA model is developed for the natural frequencies of the membrane at different isotropic and non-isotropic pre-tension levels at vacuum environment.

Keywords Micro air vehicle (MAV) · Hyperelastic membrane · Finite element analysis (FEA) · Visual image correlation (VIC) · Natural frequencies · Damping ratio

INTRODUCTION

The design and operation of micro air vehicles (MAVs) of similar proportions to natural fliers emphasizes the intricate but vital aeroelastic features mastered by biological systems. A particular form of these enhanced flying abilities benefit from the use of flexible lifting surfaces: either fixed or flapping. Birds and bats twist and bend their wings while maneuvering for optimal aerodynamics. Locusts use specialized dome shaped sensory organs (*campaniform sensillae*) within the structure of their wings [1]. These feedback sensors respond specifically to wing deformation in order to trigger the wing structure to operate at resonance frequency. Furthermore, bats can control their wing characteristics by changing the level of pre-tension in their wing membrane, thus effectively changing the wing camber and the passive aeroelastic dynamic feedback of the membrane to the aerodynamic loading [2].

Clearly, wing stiffness distribution and flexibility are essential aspects when considering natural fliers. The well-known class of materials which function in supportive systems through deformation have been classified by

biologists as pliant materials and include proteins, soft connective tissues and cartilage. Recently there has been significant progress in the understanding of the aerodynamics of low Reynolds number artificial and natural flight [3], though the structural intimate mechanical behavior is still under early numerical modeling efforts. The aerodynamic models and flight control design of fixed [3] and flapping wings [4] must include the wing flexibility and structural dynamics, an area where very little experimental data is available.

Many researchers [5-8] examine added mass effects on structural vibration. Yadykin et al. [5] review the added mass effects on a plane flexible plate oscillating in a fluid. Modal analysis of a taught, triangular membrane is given by Sewall et al. [9]. The membrane is excited with a shaker, and modal parameters are measured with an eddy current probe. Results are given with membrane pre-tension as a variable for vibration in both air and in a vacuum. Gaspar et al. [10] give similar data for a square membrane, with the eventual goal of progressing research in gossamer spacecraft. Excitation is provided with both an automated impact hammer and a shaker, and measurements are made with a scanning laser Doppler vibrometer (LDV). Modal parameters are reported as a function of membrane pre-stress and excitation locations. Jenkins and Korde [11] provide a comprehensive review of experimental analysis of membrane vibrations, as well as their own research on a circular membrane excited by a small audio speaker located at the membrane's center. A laser vibrometer is used to garner data, with good agreement to analytical results for highly localized mode shapes caused by the small speaker. Graves et al. [12] present dynamic deformation measurements of a MAVRIC-I semispan wing in a wind tunnel. Measurements from select locations over the wing are made with a high speed videogrammetric system operating at 60 Hz during flutter and limit cycle oscillations. Spectral analysis of the data indicates the prevalent wing modal frequencies. Similar work is presented by Burner et al. [13], with an extension of the videogrammetric technique to in-flight dynamic measurements.

Finite element simulations to explain the structural behavior of natural and artificial fixed and flapping wings is at an early stage of development. The large amplitude of wing deformations, the nonlinear interaction with the flow, and the lack of quantitative experimental results for validation limits the numerical models' applications. Critical experimental work showed the dependency of modal characteristics of microstructures with ambient pressure [14]. Experiments were conducted in the wind tunnel on a membrane sheet stretched between two rigid posts at a variety of angles of attack and Reynolds numbers [2]. Shape and strain measurements using visual image correlation (VIC) and aerodynamic coefficients evaluations for different configurations of membrane MAV wings in the wind tunnel have been performed in steady conditions [15, 16]. The flight performance of MAVs with flexible wings, shown in Fig. 1, has indicated several desirable properties directly attributable to the elastic nature of the wing: primarily, passive shape adaptation. Such adaptation also introduces a higher level of uncertainties in the structural dynamics.

The object of this work is to present results from experimental modal analysis techniques to evaluate the basic parameters of latex membrane of MAV thin flexible wing structures. This is an ongoing research project and as the first step, the latex membrane at different pre-tension levels is attached with the circular steel ring, as illustrated in Fig. 2, and characterized at static and dynamic loading environments. Different sizes spheres are placed at the middle of the membrane as the static load as shown in Fig. 2(b). The steel spheres are painted for avoiding the light reflection from the surface of the spheres so that deformation of the membrane specimen can be captured properly. The deflection is recorded using non-contact measurement technique and strain energy of the membrane is computed. The membrane is also vibrated for investigating the mode shapes (eigenfunctions), natural frequencies, and modal damping factors. The ambient pressure is varied to examine the added mass effect on the natural frequencies of the membrane. A static finite element analysis model is developed for computing the deflection and strain energy of circular membrane at different pre-tension levels. A preliminary numerical model for the dynamics of hyperelastic membrane is also proposed and validated with experimental data.

EXPERIMENTAL SET-UP AND PROCEDURE

Test Specimen

Rubber latex membrane at different pre-tension levels is attached with circular steel ring of inner and outer diameters 102.5 and 113.2 mm, respectively, as shown in Fig. 3. The thickness and density of the latex membrane are estimated 0.1016 ± 0.0508 mm and 980 kg/m^3 [17]. The average thickness of the membrane is measured by the authors and 0.15 ± 0.01 mm is a reasonable assumption for the FEA models. Mooney-Rivling material model [18, 19] is considered for this hyperelastic latex membrane. The Mooney-Rivling material

parameters are calculated based on the uni-axial tension experimental data, conducted by Stanford et al. [20], and the parameters are $C_1 = 18.088E4$ Pa and $C_2 = 18.088E3$ Pa, considering $C_1/C_2 = 0.1$. Three and two different pre-tension levels are considered for static and vibration tests, respectively. The average pre-tension levels of the membrane are shown in the [Table 1](#).

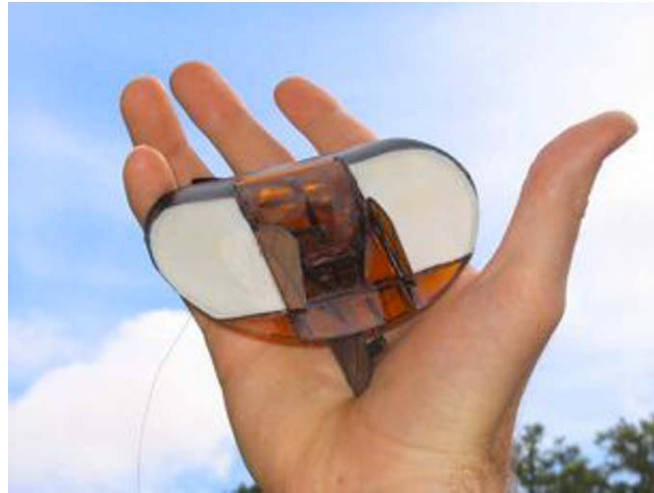


Fig. 1 Micro air vehicle with a flexible membrane wing from the MAV Lab at the University of Florida, Gainesville, Florida



Fig. 2 (a) Latex membrane specimen attached with circular ring subject of the experiments (b) The painted steel sphere of weight 0.66 N placed at the center of the membrane for static test

Table 1 Average pre-tension levels of the membrane specimen for static and vibration tests

Strain	Average pre-tension levels for static tests			Average pre-tension levels for vibration tests	
	Low	Medium	High	Low	High
ϵ_{xx}	0.0266	0.1009	0.1288	0.0541	0.0895
ϵ_{yy}	0.0136	0.0140	0.0380	0.0630	0.0305

Membrane Deformation Measurement

Because the measurements of the strains along a thin membrane must be performed using a non-contact method, a visual image correlation (VIC) technique is used. The VIC is a non-contacting full-field measurement technique originally developed by researchers at the University of South Carolina [21]. The underlying principle is to calculate the displacement field of a test specimen by tracking the deformation of a subset of a random

speckling pattern applied to the surface. Two pre-calibrated cameras digitally acquire this pattern before and after loading, using stereo-triangulation techniques. The VIC system then tries to find a region (in the image of the deformed specimen) that maximizes a normalized cross-correlation function corresponding to a small subset of the reference image (taken when no load is applied to the structure). Such a technique is known as temporal tracking.

Images are captured with two high-speed Phantom v7 CMOS cameras, capable of storing 2,900 frames in an in-camera flash-memory buffer. Typical data results obtained from the VIC system consist of geometry of the surface in discrete coordinates (x, y, z) and the corresponding displacements (u, v, w) . A post-processing option involves calculating the in-plane strains $(\epsilon_{xx}, \epsilon_{yy}, \epsilon_{xy})$. This is done by mapping the displacement field onto an unstructured triangular mesh, and conducting the appropriate numerical differentiation (the complete definition of finite strains is used).

Static Test

Wan and Liao [22] characterize thin circular flexible membrane by applying an external load to the film center via a rigid spherical capped shaft. Circular membrane is also characterized statically under the weight of a spherical ball [20, 23, 24]. Central alignment is ensured as the ball rolls to the membrane centre spontaneously by gravity.

For this paper, steel spheres of different sizes are also placed at the center of the membrane attached with the rigid ring for performing the static deformation tests (shown in Fig. 3). The membrane is stretched due to the weight of the spheres. The deformation of the membrane is recorded with the VIC system. Total strain energy stored in the membrane is calculated using the strain information from the VIC system and considering Mooney–Rivlin material model.

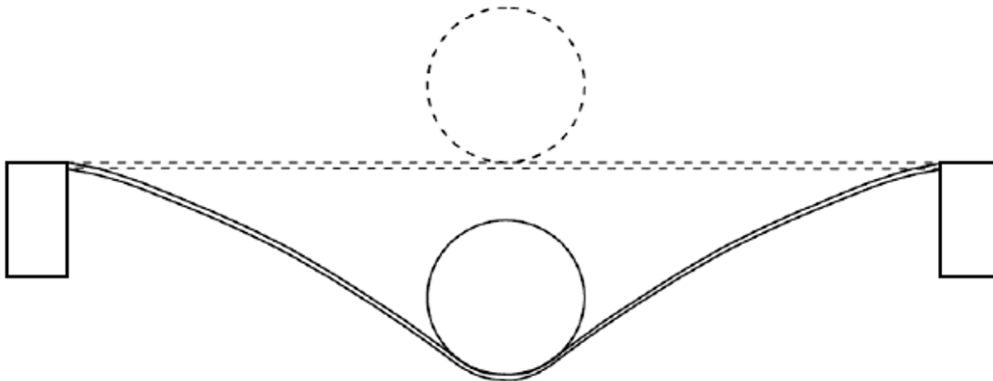


Fig. 3 Spherical indentation test setup of latex membrane attached with circular ring

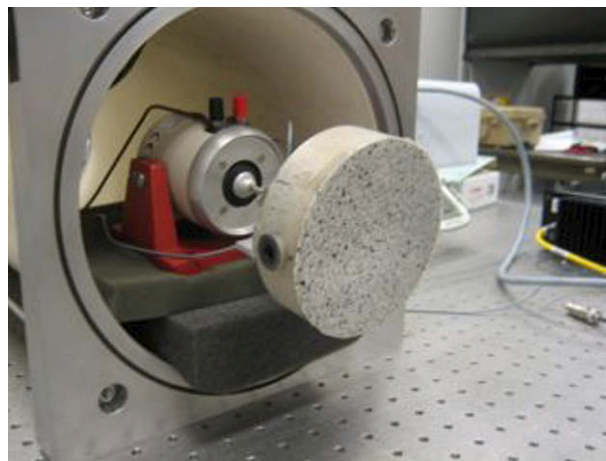


Fig. 4 Latex membrane attached with the circular steel ring mounted on the shaker

Vibration Test

Traditional experimental modal analysis techniques (such as an impact hammer in conjunction with an array of accelerometers) are not suitable for the testing of thin, lightweight membrane structures: non-contact measurement techniques must be applied. Since one of the key factors for modal analysis is generating frequency response functions (FRFs), an external system is needed to generate the input to the structures. The base excitation using external elements is considered the most promising excitation technique for microstructures [16] and is adopted in this work. The choice of excitation method is a very relevant factor affecting the quality of the computed FRFs. The application of white noise or a random sinusoidal sweep to the structure does not achieve the required structural excitation, especially in the membrane wings with low or no pre-tension (slack). The burst chirp is considered the best choice for all ranges of membrane pre-tension. Experiments on more rigid structures would most likely be able to make use of the random excitation methods, but the nature of our structures indicate that the complex burst chirp signal is the best method, with the cleanest results. Typical frequency sweeps range from 2 to 500 or 1,000 Hz. The specimen, mounted on the shaker (shown in Fig. 4), is placed in the vacuum chamber (shown in Fig. 5) where ambient pressure can be controlled for investigating the added mass effect on the membrane dynamics. The out-of-plane displacement (w) is recorded using VIC system [16]. Fast Fourier transform (FFT) is carried out for the natural frequencies of the circular membrane specimen at different pre-tension levels.

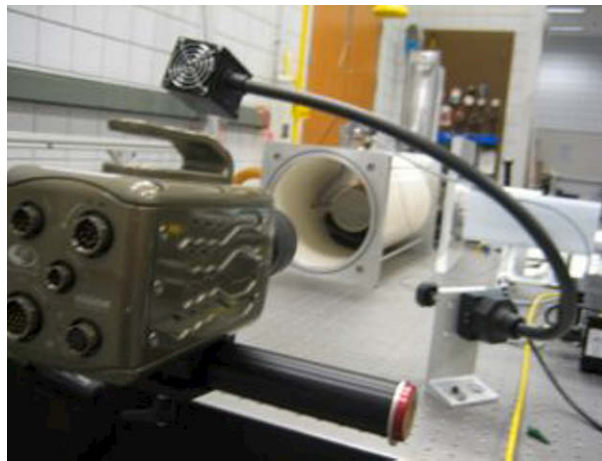


Fig. 5 Membrane specimen mounted on the shaker and positioned inside the vacuum chamber. Partial VIC system is also shown in the figure

Damping Ratio Calculation

The damping characteristic [25-28] of the circular membrane specimen at different pre-tension levels is investigated at atmospheric pressure. The out-of-plane displacement (w) of the specimen is recorded using VIC system due to the impact test by hammer. The amplitude of the picks decreases due to the presence of damping. The damping ratio (ζ) is computed based on the logarithmic decrement (δ) and from the following equation [25]:

$$\zeta = \frac{\delta}{\sqrt{(2\pi)^2 + \delta^2}}, \quad (1)$$

where $\delta = \frac{1}{n} \ln \frac{w_0}{w_n}$, w_0 and w_n ($w_0 > w_n$) are the amplitudes of two picks that are n periods away.

Post-Processing of Experimental Data

The strain energy density (W_{se}) of the latex membrane is computed based on Mooney–Rivlin material model [18, 19].

$$W_{se} = C_1(I_1 - 3) + C_2(I_2 - 3), \quad (2)$$

where C_1 , C_2 are Mooney-Rivlin material parameters; and I_1 , I_2 are strain invariants.

I_1 and I_2 can be calculated from the following equations:

$$I_1 = \lambda_1^2 + \lambda_2^2 + \lambda_3^2, \quad (3)$$

$$I_2 = (\lambda_1\lambda_2)^2 + (\lambda_2\lambda_3)^2 + (\lambda_3\lambda_1)^2, \quad (4)$$

where λ_i ($i = 1, 2, 3$) are principal stretches.

Total strain energy is estimated from the strain energy density, multiplying by volume of the membrane specimen.

COMPUTATIONAL MODEL

Computational models are developed for investigating both static and vibration characteristics of the latex membrane at different pre-tension levels, attached with circular ring. It is found that Stanford et al. [20] present a static numerical model for computing the deflection due to the indentation by sphere. In this paper, an axisymmetric static FEA model of circular membrane with fixed boundary condition and steel spheres of different sizes placed at the center is developed using finite element software, Abaqus 6.9[®] [29]. This problem is modeled considering axisymmetric due to geometrical symmetry and reducing the computational cost. Three different pre-tension levels (denoted as low, medium, and high in Table 1) and hyperelastic Mooney–Rivlin material model [18, 19] are considered for the membrane.

Gonçalves et al. [30] develop theoretical and Abaqus 6.5[®] [29] FEA models for investigating the dynamic behavior of a radially stretched circular hyperelastic membrane without added mass effect. In this paper, a finite element analysis (FEA) model is presented for studying the vibration characteristics of the circular membrane with fixed boundary condition and at different pre-tension levels using finite element software, Abaqus 6.9[®]. A 3-dimensional Abaqus[®] FEA model is developed for the membrane attached with circular ring specimen. A slice of 0.5⁰ 3-dimensional circular membrane specimen at two different pre-tension levels (denoted as low and high in Table 1) is chosen due to symmetry and reducing the computational cost. Mooney–Rivlin material model is also selected for the membrane. The membrane is vibrated inside vacuum environment and added mass effect is not considered for this preliminary FEA model.

This is an ongoing project work and FEA model for investigating the effect of the added mass on the vibration characteristics of membrane at different pre-tension levels will be developed and compared with experimental results as part of the future work.

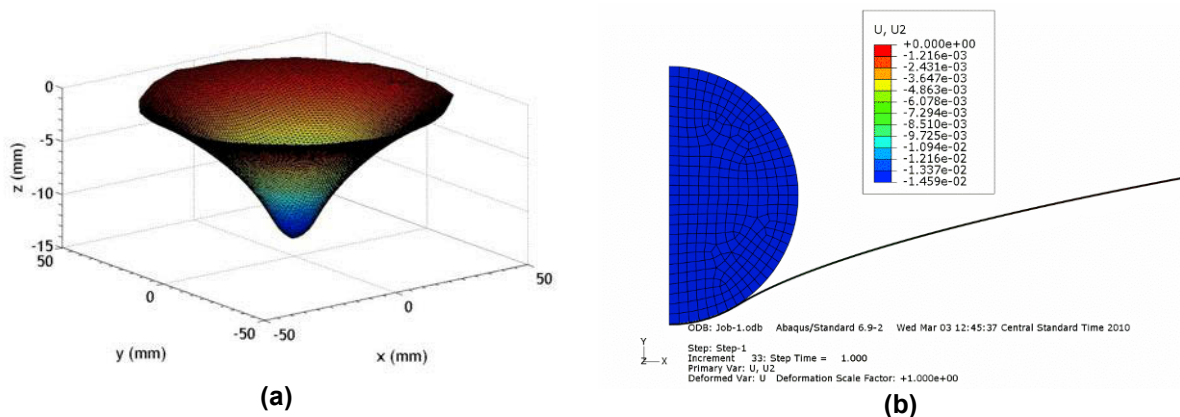


Fig. 6 Deformed shape plots of the low pre-tension membrane specimen from (a) Experimental VIC data and (b) FEA model due to 0.66 N weight of the sphere

RESULTS AND DISCUSSION

Static Test

The static test is performed using the steel spheres placed at the center of the membrane, as shown in Fig. 3. The deformation and strain states are captured using VIC system. The deformation of low pre-tension membrane from VIC data due to 0.66 N weight of the sphere is shown in Fig. 6(a). Finite element analysis (FEA) model of the latex membrane attached with the circular ring of the same geometry is also developed using Abaqus[®] software

for the static tests placing the steel spheres at the center of the membrane. CAX4H (4–node bilinear axisymmetric quadrilateral, hybrid, constant pressure) type of elements are considered for the membrane. But CAX4R (4–node bilinear axisymmetric quadrilateral, reduced integration, hourglass control) and CAX3 (3–node linear axisymmetric triangle) types of elements are selected for the steel spheres. The friction coefficient between the sphere and membrane surface is assumed 0.2. The deformation of low pre-tension membrane from axisymmetric FEA model at 4,880 degrees of freedom (DOF) due to 0.66 N weight of the sphere is depicted in Fig. 6(b). Mooney–Rivlin hyperelastic material model is selected for computing the deformation and total strain energy of the membrane specimen. The maximum deflection is occurred at the center of the membrane due to placing the sphere at that location. The experiment is repeated for several times for each sphere. The average maximum deflection and total strain energy with 95% confidence intervals are shown in Figs. 7 and 8, respectively. The strain energy at zero weight indicates the energy due to the pre-tension of the membrane in Fig. 8. The deformation and strain energy increase with the weight of the sphere and pre-tension level of the membrane. FEA and experimental results can vary within reasonable limits due to the variation of the thickness of the membrane [17].

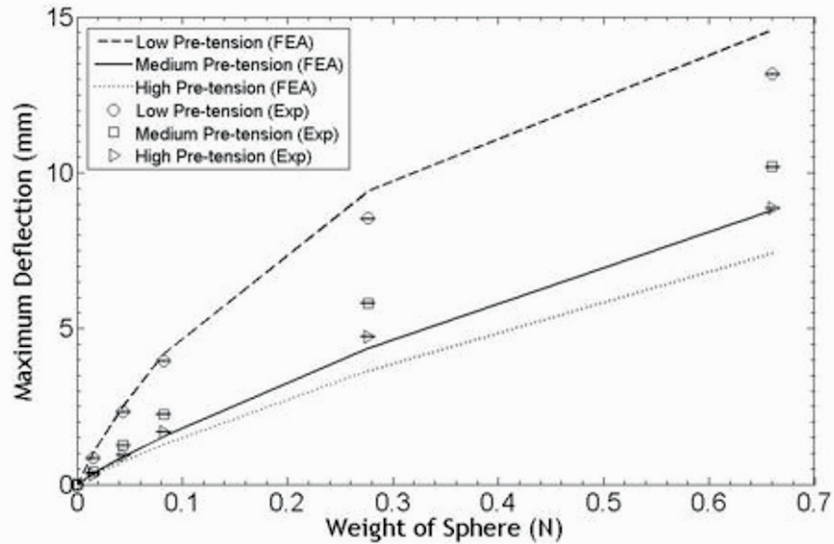


Fig. 7 Variation of maximum deflection of the membrane specimen due to the indentation of different weight spheres

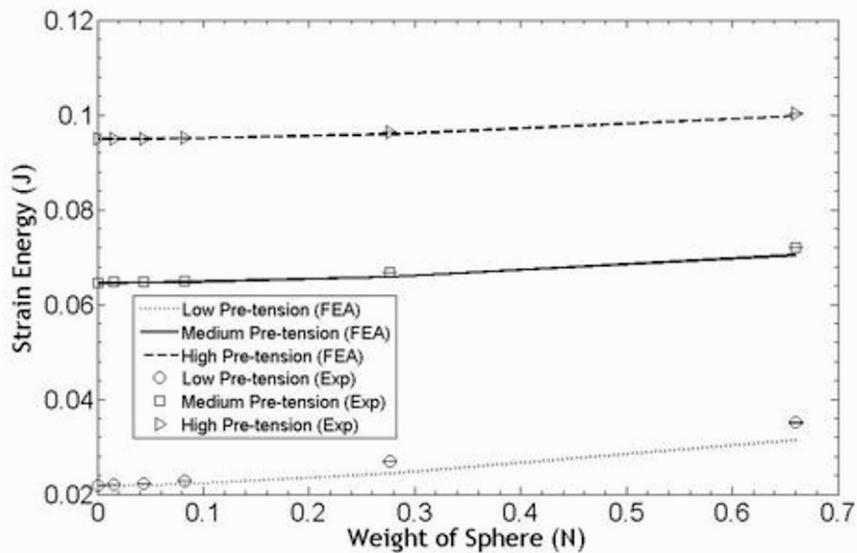


Fig. 8 Variation of total strain energy of the membrane specimen due to the indentation of different weight spheres

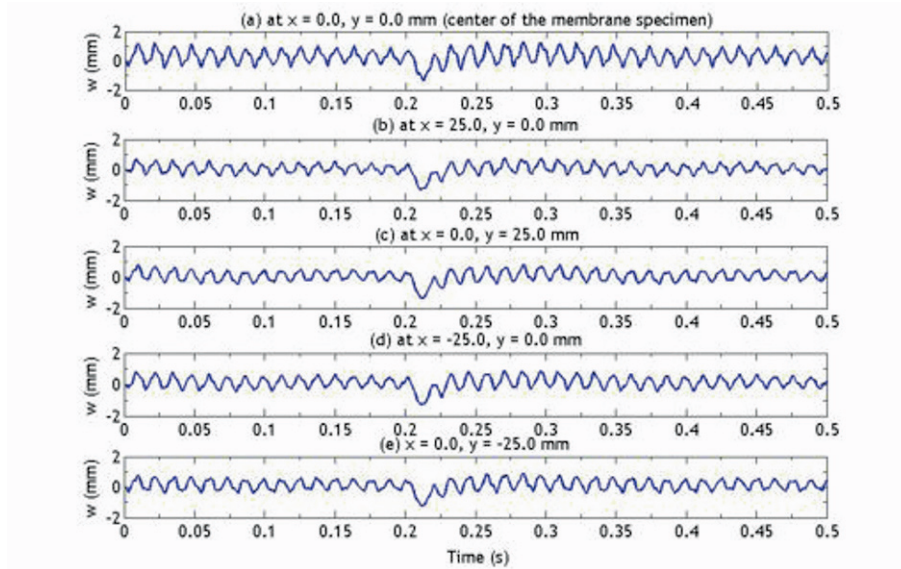


Fig. 9 Out-of-plane displacement (w) vs. time plots at five different locations for the high pre-tension membrane specimen from VIC data at atmospheric pressure

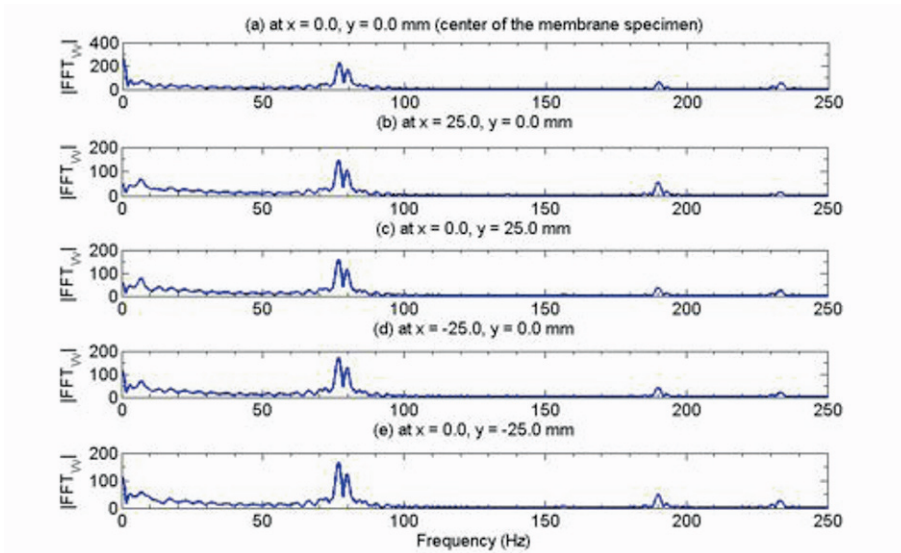


Fig. 10 FFT of Out-of-plane displacement (w) from Fig. 9

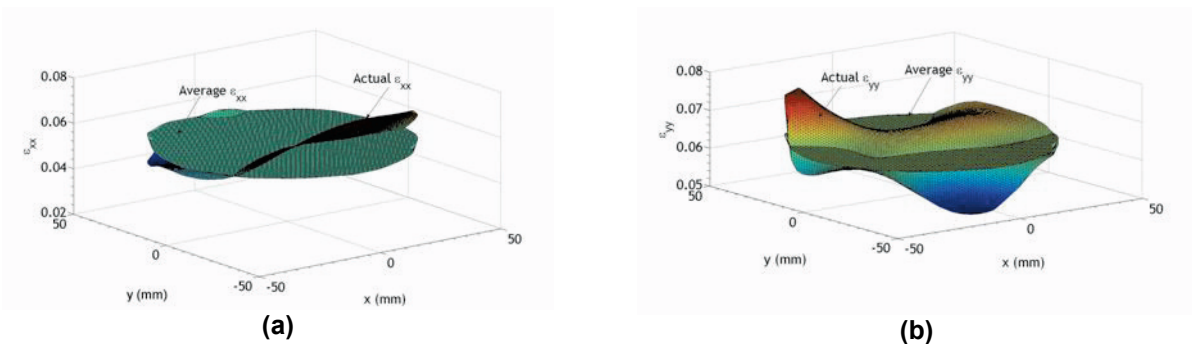


Fig. 11 Actual and average strains distribution over the low pre-tension membrane specimen

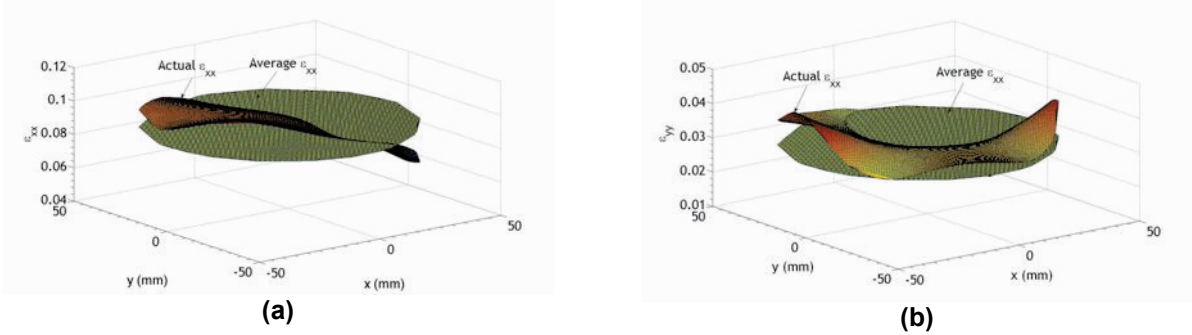


Fig. 12 Actual and average strains distribution over the high pre-tension membrane specimen

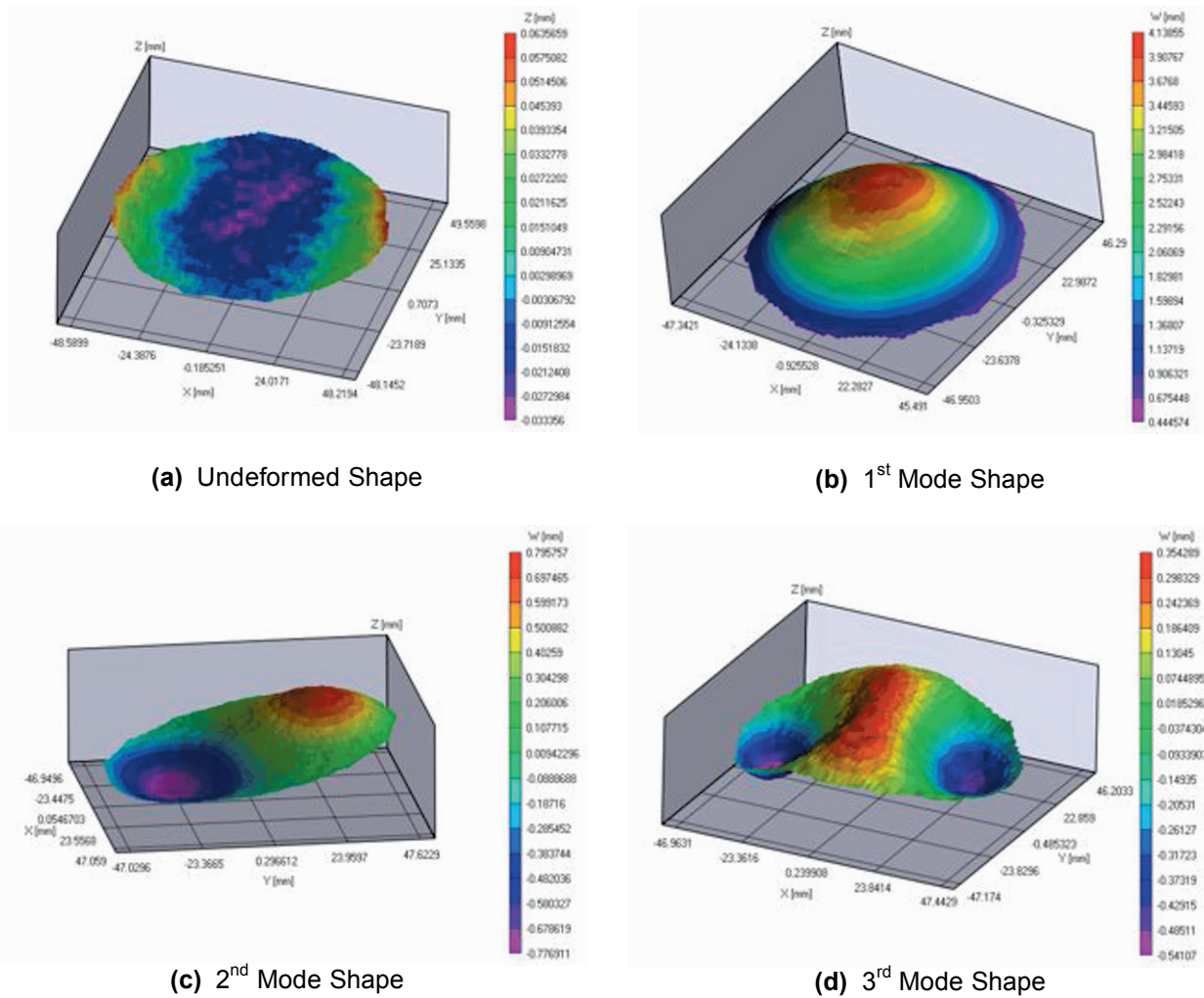


Fig. 13 Mode shapes of the high pre-tension membrane specimen from VIC data at atmospheric pressure

Vibration Test

The membrane specimen is mounted on the shaker and placed inside the vacuum chamber, shown in Fig. 5. The shaker is controlled using a complex burst chirp signal at ranges from 2 Hz to 500 Hz. The deformation images are captured using VIC system at the rate of 1,000 frames per second. The out-of-plane deformation (w) is computed at a specific location of the membrane for the fast Fourier transform (FFT). The variation of w with time at five different locations is shown in Fig. 9. FFT of w is carried out for the frequency plots and shown in Fig. 10.

The spikes in the figures indicate the natural frequencies. FFT is computed more than one location of the membrane so that all nature frequencies can be identified properly. For example, second modes and corresponding frequencies may not be captured if FFT is carried out at the center of the membrane only.

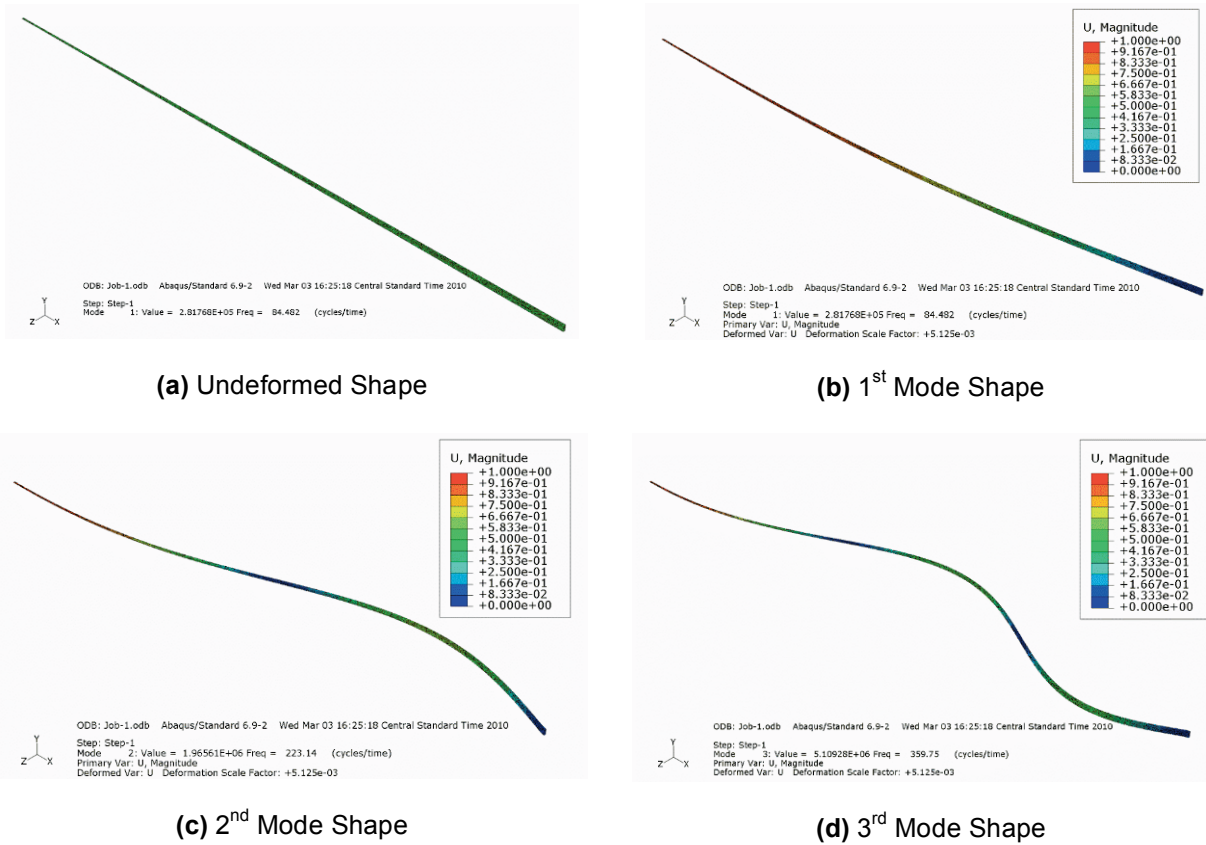


Fig. 14 Mode shapes of the high pre-tension membrane specimen from FEA model at vacuum environment

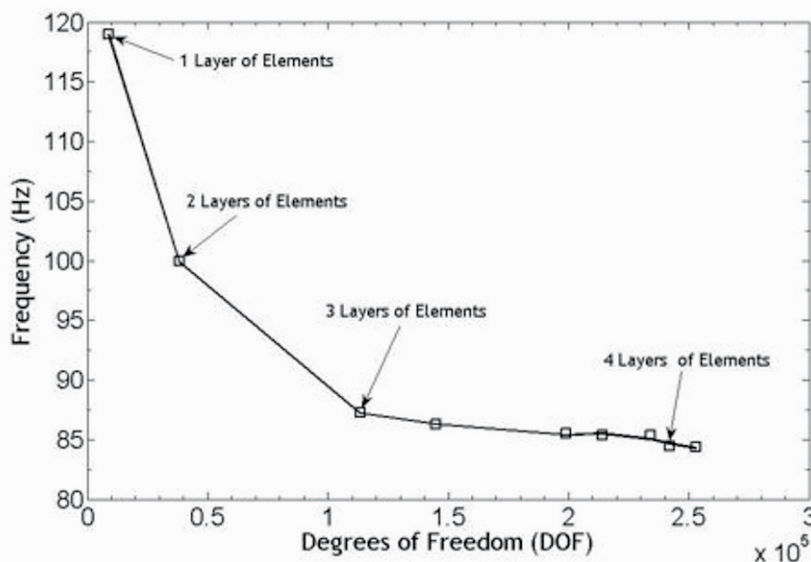


Fig. 15 Frequency of the first mode vs. degrees of freedom (DOF) plot for the high pre-tension membrane specimen. DOF are calculated based on among one-four layers of elements along the thickness direction of the membrane specimen

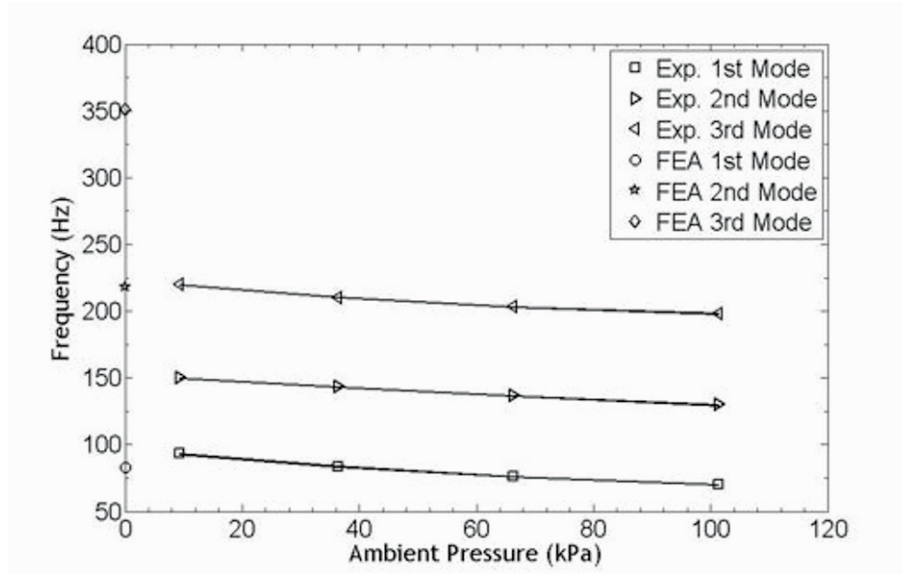


Fig. 16 Natural frequencies vs. ambient pressure plots for the low pre-tension membrane specimen

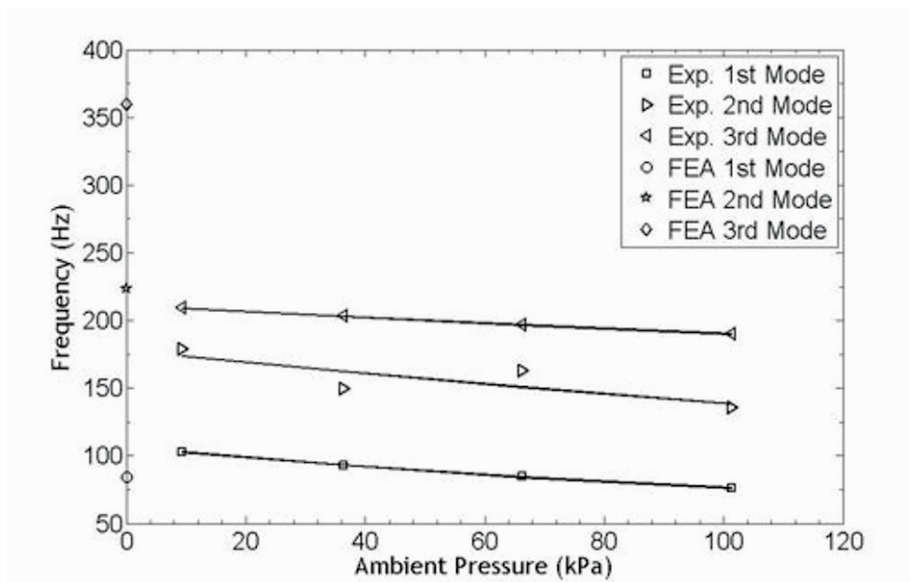


Fig. 17 Natural frequencies vs. ambient pressure plots for the high pre-tension membrane specimen

The actual and average strains distribution over the low and high pre-tension membrane specimens are shown in Figs. 11 and 12, respectively. The first three mode shapes of high pre-tension membrane from VIC experimental data and FEA model are shown in Figs. 13 and 14, respectively. C3D4H (4-node linear tetrahedron, hybrid, linear pressure) type of elements are selected for the FEA model of the membrane. The variation of the frequency of the first mode with DOF for the high pre-tension circular membrane specimen is depicted in Fig. 15. The frequencies of the first mode at different DOF levels are computed considering among one to four layers of elements at the thickness direction of the membrane specimen. It is found from Fig. 15 that the frequency converges at higher DOF. Natural frequencies and mode shapes are computed at 242,168 DOF for the FEA model inside vacuum environment (no added mass effect). The first three natural frequencies at two different pre-tension levels of the membrane are computed and shown in Figs. 16 and 17. The frequencies at zero ambient pressure in Figs. 16 and 17 indicate that the frequencies are computed at vacuum by the FEA model. The experiments in the vacuum chamber show the dependency of the modal frequencies on the membrane pre-tension and ambient pressure. Natural frequencies increase with the membrane pre-tension and decrease with ambient pressure. It is also found that the frequencies increase with the mode, as expected. The variation of first natural frequency (from FEA

model) with the uniform and non-uniform pre-tension levels of the membrane specimen is shown in Fig. 18. It is found from Fig. 18 that the frequency increases in a higher rate for non-uniform pre-tension membrane than that at uniform pre-tension.

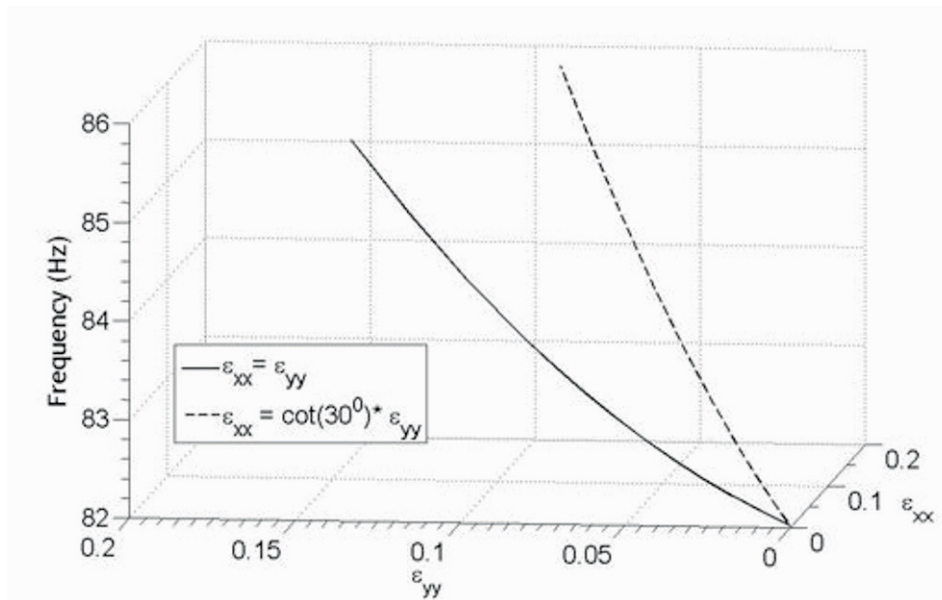


Fig. 18 The variation of first natural frequency (from FEA model) with the pre-tension levels of the membrane specimen

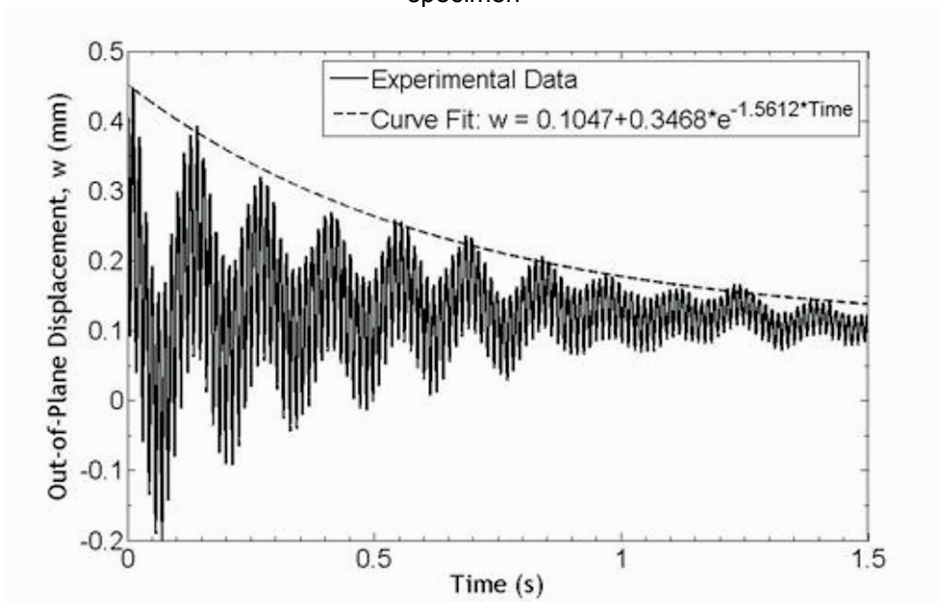


Fig. 19 Variation of the out-of-plane displacement (w) of the center of the high pre-tension membrane specimen with time due to impact test by hammer

Damping Ratio Calculation

The out-of-plane displacement (w) of the membrane specimen is recorded using VIC system due to the impact test by hammer. The variation of w with time at the center ($x=0$, $y=0$) location of the high pre-tension membrane specimen, caused by the impact test, is shown in Fig. 19. It is found from Fig. 19 that the picks of w decrease with time due to the damping. The exponential underdamped decay curve is also depicted in Fig. 19. It is found that the damping ratio of the high pre-tension membrane specimen at atmospheric pressure is 0.29%.

CONCLUSIONS

This paper presents the preliminary phase of an effort towards the theoretical and experimental characterization of the dynamics of an elastic latex membrane at different pre-tension levels. Experiments in static conditions are used for preliminary finite element analysis models validation. The elastic membranes with specific levels of pre-tension are attached to a rigid steel ring and loaded using steel spheres of different masses as dead weights. The VIC technique, a non-contact measurement system, is used for measuring the deformation of the membrane. The membrane-steel sphere system FEA model developed using Abaqus[®] exhibits a good correlation with experimental data in terms of the membrane displacement and elastic strain energy in function of the mass of the sphere and membrane pre-tension. The dynamic experiments are based on the base excitation of the steel ring using a shaker with a burst chirp control signal with frequency sweeps range from 2 to 500 or 1,000 Hz. The membrane specimen at a specific pre-tension level is placed inside a vacuum chamber, the three-dimensional dynamic shape is measured using the VIC technique and the natural frequencies are found from the FFT of the out-of-plane deformation time histories of selected points on the surface of the membrane. The chamber's ambient pressure is varied for investigating the added mass effect on the mode shapes and natural frequencies of the membrane. It is found from the experimental results that natural frequencies of the membrane decrease with the increase in ambient pressure of the vacuum chamber. As a result, added mass decreases the natural frequencies. Natural frequencies of the membrane increase with mode and pre-tension level.

A preliminary FEA model is developed with Abaqus[®] with the primary objective of estimating the natural frequencies of the membrane at different uniform and non-uniform pre-tension levels in the vacuum thus without added mass effect. The FEA model at vacuum (without added mass effect) can predict the first natural frequency reasonably well although second and third frequencies are quite high comparing to those calculated by experiments at different ambient pressures. Some sort of variation is expected among the frequencies predicted by experiments and FEA model due to the variation of the ambient pressure and the thickness of the membrane. It is not possible to perform experiments at ambient pressure less than 9.325 kPa with the available vacuum chamber set-up. So, the modal characteristics can not be found through experiments at vacuum (without added mass effect) to compare with the FEA results. The FEA model for investigating the effect of added mass on the modal characteristics is under progress and will be validated by experimental results when it should be available in future.

The out-of-plane deflection at the center of the membrane is computed due to the hammer impact test at atmospheric pressure and it is found that the amplitudes of the picks of the out-of-plane deflection decrease after ten periods away in exponential manner which indicate underdamped vibration behavior. The damping ratio of the membrane at atmospheric pressure is calculated from the logarithmic decrement of the amplitudes of two picks after ten periods away.

A computational model for investigating the added mass effect and damping on the vibration characteristics of the elastic membrane at different pre-tension levels will be developed and validated by experimental results as part of the future work. The added mass effect in relation to the size and mass of the membrane will also be investigated.

ACKNOWLEDGMENTS

The authors would like to thank the support from the Air Force Office of Scientific Research under contract FA9550-09-1-0072, with Prof. Victor Giurgiutiu (initiator) and Dr. David Stargel as project monitors. The continuing support for research activities from the Air Force Research Laboratories at Eglin AFB and Wright-Patterson AFB is also greatly appreciated. The authors would also like to thank the experimental support from Joshua Martin, Department of Electrical and Computer Engineering, University of West Florida, Shalimar, Florida.

REFERENCES

- [1] Raney, D., Slominski, E., "Mechanization and Control Concepts for Biologically Inspired Micro Air Vehicles," *Journal of Aircraft*, Vol. 41, pp. 1257–1265, 2004.
- [2] Song, A., Breuer, K., "Dynamics of a Compliant Membrane as Related to Mammalian Flight," *AIAA Paper* 2007–665, Jan. 2007.
- [3] Lian, Y., Shyy, W., "Laminar-Turbulent Transition of a Low Reynolds Number Rigid or Flexible Airfoil," *AIAA Journal*, Vol. 45, pp. 1501–1513, 2007.
- [4] Ho, S., Nassef, H., Pornsinsirakb, N., Tai, Y., Ho, C., "Unsteady Aerodynamics and Flow Control for Flapping Wing Flyers," *Progress in Aerospace Sciences*, Vol. 39, pp. 635–681, 2003.

- [5] Yadykin, Y., Tenetov, V., Levin, D., "The added mass of a flexible plate oscillating in a fluid," *Journal of Fluids and Structures*, Vol. 17, No. 1, pp. 115–123, 2003.
- [6] Noca, F., "Apparent mass in viscous, vortical flows," American Physical Society, 54th Annual Meeting of the Division of Fluid Dynamics, San Diego, California, Nov. 2001.
- [7] Deruntz, J. A., Geers, T. L., "Added mass computation by the boundary integral method," *International Journal for Numerical Methods in Engineering*, Vol. 12, pp. 531–550, 1978.
- [8] Han, R. P. S., Xu, H., "A simple and accurate added mass model for hydrodynamic fluid—Structure interaction analysis," *Journal of the Franklin Institute*, Vol. 333, No. 6, pp. 929–945, 1996.
- [9] Sewall, J., Miserentino, R., Pappa, R., "Vibration Studies of a Lightweight Three-Sided Membrane Suitable for Space Applications," NASA Technical Paper, TP 2095, 1983.
- [10] Gaspar, J., Solter, M., Pappa, R., "Membrane Vibration Studies Using a Scanning Laser Vibrometer," NASA Technical Memorandum, TM 211427, 2002.
- [11] Jenkins, C., Korde, U., "Membrane Vibration Experiments: An Historical Review and Recent Results," *Journal of Sound and Vibration*, Vol. 295, pp. 602–613, 2006.
- [12] Graves, S., Bruner, A., Edwards, J., Schuster, D., "Dynamic Deformation Measurements of an Aeroelastic Semispan Model," *Journal of Aircraft*, Vol. 40, pp. 977–984, 2003.
- [13] Burner, A., Lokos, W., Barrows, D., "Aeroelastic Deformation: Adaptation of Wind Tunnel Measurement Concepts to Full Scale Vehicle Flight Testing," NASA Technical Memorandum, TM 213790, 2005.
- [14] Ozdoganlar, O., Hansche, B., Carne, T., "Experimental Modal Analysis for Microelectromechanical Systems," *Experimental Mechanics*, Vol. 45, pp. 498–506, 2006.
- [15] Albertani, R., Stanford, B., Hubner, J., Ifju, P., "Aerodynamic Coefficients and Deformation Measurements on Flexible Micro Air Vehicle Wings," *Experimental Mechanics*, Vol. 47, pp. 625–635, 2007.
- [16] Albertani, R., Stanford, B., Sytsma, M., Ifju, P., "Unsteady Mechanical Aspects of Flexible Wings: an Experimental Investigation Applied on Biologically Inspired MAVs," MAV07 3rd US-European Competition and Workshop on MAV Systems & European Micro Air Vehicle Conference and Flight Competition 2007, ISAESUPAERO, Toulouse, France, Sept. 2007.
- [17] Technical data of The Extra Thin TAN Thera-Band® Band. The Hygenic Corporation, 1245 Home Avenue, Akron, OH 44310, USA.
- [18] Mooney, M., "A Theory of Large Elastic Deformation," *J. Appl. Phys.*, Vol. 11, pp. 582–592, 1940.
- [19] Macosko, C. W., *Rheology: principles, measurement and applications*, Wiley-VCH, NY, 1994.
- [20] Stanford, B., Albertani, R., Ifju, P. G., "Static Finite Element Validation of a Flexible Micro Air Vehicle," SEM Annual Conference on Experimental and Applied Mechanics, Saint Louis, MS, USA, June 2006.
- [21] Sutton, M., Cheng, M., Peters, W., Chao, Y., McNeill, S., "Application of an Optimized Digital Image Correlation Method to Planar Analysis," *Image and Vision Computing*, Vol. 4, pp. 143–151, 1986.
- [22] Wan, K., Liao, K., "Measuring mechanical properties of thin flexible films by a shaft-loaded blister test," *Thin Solid Films*, Vol. 352, No. 1–2, pp. 167–172, 1999.
- [23] Liu, K. K., Ju, B. F., "A novel technique for mechanical characterization of thin elastomeric membrane," *J. Phys. D: Appl. Phys.*, Vol. 34, pp. L91–L94, 2001.
- [24] Yang, W. H., Hsu, K. H., "Indentation of a Circular Membrane," *J. Appl. Mech.*, Vol. 38, pp. 227–230, 1971.
- [25] Alciatore, D. G., Hestand, M. B., *Introduction to Mechatronics and Measurement Systems*, 3rd ed., WCB/McGraw-Hill, Boston, MA, 2007.
- [26] Feldman, M., "Non-linear system vibration analysis using Hilbert transformation—I. Free vibration analysis method 'FREEVIB'," *Mechanical Systems and Signal Processing*, Vol. 8, No. 2, pp. 119–127, 1994.
- [27] Feldman, M., "Non-linear system vibration analysis using Hilbert transformation—I. Forced vibration analysis method 'FORCEDVIB'," *Mechanical Systems and Signal Processing*, Vol. 8, No. 3, pp. 309–318, 1994.
- [28] Wren, G. G., Kinra, V. K., "An Experimental Technique for Determining a Measure of Structural Damping," *Journal of Testing and Evaluation*, JTEVA, Vol. 16, No. 1, pp. 77–85, 1988.
- [29] Abaqus® FEA, SIMULIA, Rising Sun Mills, 166 Valley Street, Providence, RI 02909-2499, USA: <www.simulia.com>.
- [30] Gonçalves, P. B., Soares, R. M., Pamplona, D., "Nonlinear vibrations of a radially stretched circular hyperelastic membrane," *Journal of Sound and Vibration*, Vol. 327, pp. 231–248, 2009.

Objective Determination of Acoustic Quality in a Multipurpose Auditorium

B.Hayes, C.Braden, Undergraduate Students, Miami University, Hamilton, OH
R. Averbach, Conductor and Associate Professor, Miami University, Oxford, OH
V. Ranatunga, Associate Professor, Miami University, Middletown, OH
501 E. High St., Oxford, OH, 45056, hayesbm@muohio.edu

ABSTRACT

Significant differences in listening qualities have been reported by the audience attending wide varieties of functions ranging from orchestral music to stage drama and public announcements at the multipurpose auditorium of the Miami University Hamilton campus. Preliminary investigations have been conducted to examine the difference in sound qualities utilizing impulse responses at various seating sections throughout the auditorium, based on standardized measurement procedures. Detailed comparisons of measured acoustic quality parameters have been made against the available data in literature for statistically determined optimal acoustic conditions. Each measured range of parameter values has been analyzed to determine the distribution characteristics over a pre-determined set of locations on the audience seating area. Recommendations for improvements are presented throughout the paper.

INTRODUCTION

As a sub-discipline of classical mechanics, 'acoustics' is the science concerned with the study of sound. As a sub-discipline of acoustics, 'room acoustics' deals with the study of sound in enclosed spaces. In all rooms, acoustical conditions can be controlled. Usually this control is established within the architectural design and construction of the space. However, as with the auditorium studied in this research, that is not always the case. Some buildings are modified over time and as a result their design intent is altered. Other buildings may have not been intended for use in large varieties of functions, but have obtained a demand for such versatility over time. In the event that the quality of acoustics in a performance space is questionable, and/or a simple check-up is desired, this research will be particularly useful.

Using a multipurpose auditorium on the Hamilton campus of Miami University as an example, the aim of this research is to clearly describe a simple yet effective method of quantifying the quality of acoustics in a performance space for music, drama, and speech events, as it pertains to the audience perception only. (See reference [1] for an analysis of the 'stage acoustics' in this same auditorium). This 4500 cubic meter example auditorium is named Parrish Auditorium and will be referred to as such throughout the paper. Subjective and objective measures are employed to gain such an acoustic evaluation. Interviews and surveys are suggested to isolate subjectively perceived problems, while the ISO 3382 standard [2] defines several objective room acoustic parameters used as diagnostics. By studying subjective impressions and comparing objective measures to well accepted optimum parameter values, the acoustic quality of a space can be determined. Upon diagnosing the acoustic quality of a space using this research, a proposal for implementing acoustic improvements will have strong scientific support.

This study is an application of research by expert acousticians that can be implemented by those with a basic understanding of Physics, Integral Calculus, and basic Experimentation Techniques. Section 1 deals with acoustic modeling and experimentation, section 2 analyzes measurement results, while section 3 makes conclusions and recommendations for improving the example multipurpose auditorium.

1. Acoustical Modeling and Experimentation

1.1 Observing Subjective Impressions

Many studies have been done on subjective preferences as it relates to room acoustics for music, speech, and drama performances. Several acoustic attributes which are found to help describe such preferences are defined as followed (most definitions are obtained from table 19.1 reference [4]):

Intimacy – The sensation that music is being played in a small room.

Balance – Equal Loudness among the various orchestra and vocal participants.

Reverberation– The sound that remains in the room after the source is switched off.

Warmth – Low-frequency reverberation, between 75 and 350 Hz.

Liveness – Reverberation above 350 Hz.

Direct Sound – Sound which has not encountered any reflections before reaching the listener.

Reverberant Sound – Sound that has encountered at least 1 reflection before reaching the listener.

Auditorium Sound Projection – The ability of sound to be projected from the source to the audience area.

Blend - A harmonious mixture of orchestral sounds.

Brilliance – A bright, clear, ringing sound, rich in harmonics, with slowly decaying high-frequency components.

Clarity – The degree to which rapidly occurring individual sounds are distinguishable.

Speech Intelligibility – How well a speaker can be heard and understood in a room.

Envelopment – The impression that the sound is arriving from all directions and surrounding the listener.

Presence – The sense that we are close to the source.

Spaciousness – The perceived widening of the source beyond its visible limits.

Texture – The subjective impression that a listener receives from the sequence of reflections returned by the hall.

Timbre – The quality of sound that distinguishes one musical instrument from another.

Tonal Color – The subjective perception of a combination of sounds in sequence or played simultaneously.

Uniformity – The evenness of the sound distribution.

The weightings of acoustical attributes for music performances are reported by Marshall Long in reference [4]. This reported order of importance is given as; 1) Intimacy; 2) Liveness; 3) Warmth; 4) Loudness of direct sound; 5) Loudness of reverberant sound; 6) Balance and blend; 7) Diffusion; 8) Ensemble. As Long describes after reporting this order based on recollection, other parameters such as the Interaural cross correlation coefficient ($IACC_{E3}$), Early decay time (T_E), Surface diffusivity index (SDI), and Bass ratio (BR) act as better controls and allow for better repeatability in testing. If an adequate sample of musicians and listeners and appropriate instrumentation is available, such a study is more reliable than the subjective study described in this paper.

If an adequate sample of musicians/listeners is available, an effective method of analyzing subjective impressions is based on 2-sample T-tests done on various acoustical attributes. Each studied attribute is rated on a scale (possibly from 0 to 10) by listeners given various acoustic conditions (curtains open, curtains closed, orchestra enclosure in place, orchestra enclosure not in place, etc). In such a model, the null hypothesis (H_0) is that there is no change to the attribute as a result of changing the space. The alternate hypothesis (H_a) is that the attribute has increased as a result of implementing the acoustic control. By using the sample scores, a p-value can be calculated such as to reject or accept the null hypothesis. If the p-value < 5%, reject the null. Egan [5] uses a similar method, while also providing a survey sheet which can be utilized with the addition of a numeric scale.

Examining subjective impressions can frequently lead to the quick detection of acoustic strengths and weaknesses in a space. Results for Parrish Auditorium showed a very strong correlation between subjective impressions and the objective measurements. It was suggested by the Miami University and Hamilton-Fairfield Symphony orchestra conductors that; 1) the space lacked adequate reverberation; 2) sound projection from the stage to the audience is poor; 3) The musicians have trouble hearing themselves and each other during the performance. However, given this is a multipurpose auditorium, subjective impressions for other performances such as speech, drama, and amplified music were also investigated. For these performances, the acoustic quality was subjectively determined to be very good. Further comparisons and interpretations of these subjective results when compared to objective measurements are made in section 2.

1.2 Objective Measures

The ISO 3382 standard [2] defines and sets forth measurement procedures for objective parameters which closely relate to the subjective attributes mentioned. Each parameter could be measured and analyzed, but that is beyond the scope of this study. The focus here is on parameters which were determined to have strong correlations with the proposed subjective impressions. Using the subjective impressions from musicians, conductors, and staff at Miami University, five applicable parameters were selected for investigation. Table 1.2a below lists the selected parameters along with their related attribute(s).

Table 1.2a – Investigated objective parameters along with related subjective attribute(s).

Objective Parameters	Related Attribute(s)
Reverberation Time – RT_{60}	Reverberation, Liveness, Warmth,
Sound Strength - G	Sound Projection, Loudness
Clarity – C_{80}	Music Brilliance, Reverberation
Definition – D_{50}	Speech Intelligibility
Speech Transmission Index - STI	Speech Intelligibility, Clarity

Reverberation time (RT_{60}) is the time it takes for the sound level to drop 60 dB after a sound source stops. Preferred values in a multipurpose auditorium are suggested by Egan [5] as $1.6 < RT_{60} < 1.8$ seconds. Equation 1 is based on classic diffuse-field theory for estimation purposes. To calculate RT_{60} based on room impulse response measurements, backward integration of the decay curves was employed (ref. [2] section 5.3.3).

$$RT_{60} = 0.161 V / \sum_{i=1}^n \alpha_i S_i \text{ seconds} \quad (Eq. 1)$$

Where, V = Volume of the space (m^3), α = material coefficient of absorption, S = surface area of any material in the space (m^2), n = number materials in the space

Sound Strength (G) is the sound pressure level at any given location in an auditorium relative to the free-field level of an omni-directional source measured 10 m away [4]. This measure is dependent on distance from the source and is similar to our perception of loudness. Preferred range of G is $4 < G < 6$ dB given by Long[4].

$$G = 10 \log_{10} \left(\int_0^{\infty} p^2(t) dt / \int_0^{\infty} p_{10}^2(t) dt \right) \text{ decibels} \quad (Eq. 2)$$

Clarity (C_{80}) is a measure of balance between early- and late- arriving energy. It is the degree to which rapidly occurring individual sounds are distinguishable. Barron gives the preferred range as $-2 < C_{80} < +2$ dB.

$$C_{80} = 10 \log_{10} \left(\int_0^{80} p^2(t) dt / \int_{80}^{\infty} p^2(t) dt \right) \text{ dB} \quad (Eq. 3)$$

Definition (D_{50}) is the parameter which indicates the clarity of speech [10]. From 0 (bad) to 1 (excellent).

$$D_{50} = 10 \log_{10} \left(\int_0^{50} p^2(t) dt / \int_0^{\infty} p^2(t) dt \right) \text{ dB} \quad (Eq. 4)$$

Where p^2 = squared sound pressure measured in a room (Pa), p_{10}^2 = reference pressure in a free field 10m from the source (Pa), t = time (ms). An explanation of acquiring the G reference pressure is given in section 1.6.

Speech Transmission Index (STI). This is a machine measure of speech intelligibility whose value varies from 0 (completely unintelligible) to 1 (perfect intelligibility) [6]. An algorithm for the determination of STI is described in reference [7].

The ISO 3382 standard [2] gives clear definitions in A.2.1 and A.2.3 for equations 2 and 3. Both suggest that integrating the exponentially decaying squared sound pressure over time give quantities of acoustic energy. As a

confirmation of this statement, Miami University professor of Physics, Dr. Herbert Jaeger, states, “In the context of sound pressure and sound pressure level (dB), energy-like quantities are usually given as intensities. Intensity is the amount of energy that crosses a given surface area per unit time. So we are talking about energy/ time surface area or power/surface area. It also turns out that intensity = p^2/Z where Z is the characteristic impedance. In other words, the intensity is proportional to the square of the pressure, as the characteristic impedance is practically constant. So the ratio of p_1^2/p_2^2 is equal to the ratio of two intensities. But intensity integrated over time becomes energy per surface area. In that sense you can think of p^2 as an energy quantity.” Therefore, the squared pressure multiplied by time is equal to energy per surface area. Hence, ISO 3382 parameters are calculated using measured ratios of acoustic energy which vibrate the microphone membrane surface area as they are received from the source.

1.3 Various Architectural Acoustic Controls

In the same way that one might adjust a home theater or stereo equalizer, the previously defined attributes can also be adjusted through the usage of various architectural acoustic controls. The selection of such controls depends upon the nature of necessary improvement(s). Generally speaking, if speech is unintelligible in a space and unamplified music is good, the space requires more absorptive materials. These materials would reduce reverberation and allow the listener to perceive more of the direct sound. Such is the case in churches and other venues where speech intelligibility is desired.

The design and selection of effective architectural acoustic controls depends heavily on topics in sound transmission, absorption, and reflection. [Figure 1.3a](#) visually depicts these topics. In the case of the multipurpose Parrish Auditorium, having the ability to vary the acoustics is essential. Therefore, given the subjectively determined problems described above, controls were selected which reflect more acoustic energy from the stage to the audience. This is done by adding panels which surround the orchestra, called an orchestra enclosure or acoustic shell (shown in [figure 1.3b](#)). [Figure 1.3c](#) shows other types of controls.

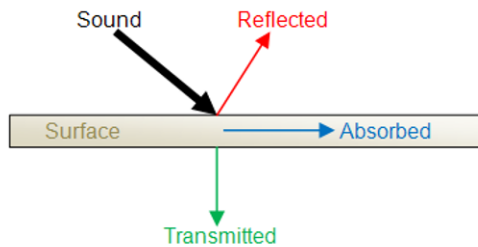


Figure 1.3a – Reflection, transmission, and absorption



Figure 1.3b – An orchestra enclosure (acoustic shell).

Figure was obtained from http://www.wengercorp.com/Acoustic/Shell_Diva.html



Figure 1.3c – Other types of acoustic controls. (top figure) is from reference [9] Fitzwilliam college auditorium. (bottom left and right) are from <http://www.wengercorp.com/Acoustic/Panels.html>

1.4 Modeling Objective Parameters

In this section, parameters RT_{60} and G are modeled using two methods: 1) Spreadsheet formulation; 2) Autodesk Ecotect software. Method 2 requires a 3D CAD model of the auditorium. Parameters C_{80} , D_{50} , and STI are only measured and compared to well-accepted optimum values in a later section.

Although not necessary in the calculation of RT_{60} (Eq. 1), a 3D CAD model was constructed using Solid Works prior to using either method. The 3D CAD model was found to be a convenient tool for quickly gathering accurate geometric information such as the volume of the room and surface area of each material. For example, from the architectural drawings it was found that the walls of the audience seating area are plaster. By measuring the area of all the plaster surfaces in the 3D model, one can quickly determine the total surface area associated with each material. The volume of the entire space was determined from the 3D model by extruding a separate body in the auditorium air space. This body was then measured using Solid Works evaluation tools. The volume and surface areas can also be determined by using the drawings. In this case, complex geometry can be simplified.

Using equation 1, the auditorium volume, the surface area of each material, and the coefficient of absorption for each material, a spreadsheet can be formulated from which to estimate RT_{60} . One can also estimate RT_{60} with and without the acoustic controls in place. Figure 1.4a reports estimated RT_{60} values of Parrish Auditorium with and without an acoustic shell on the stage. These values are averaged between the 500 Hz and 1000 Hz frequencies with a 0% auditorium occupancy. David Egan (reference [5]) states the optimum range for a multipurpose auditorium to be $1.6 < RT_{60} < 1.8$ seconds.

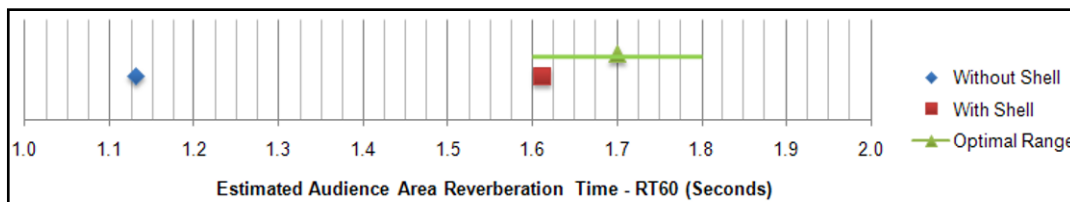


Figure 1.4a – Estimated RT_{60} with and without an acoustic shell

Clearly, RT_{60} without an acoustic shell is estimated to be quite low when compared to the suggested optimum range. However, for speech, drama, and amplified music the low reverberation is desired.

The objective parameter G is estimated using Barron's revised theory [3] given by the equation:

$$G = 10 \log_{10}(100/r^2 + 31200 (RT_{60}/V) \exp(-0.04 r/RT_{60})) \quad (\text{Eq. 5})$$

Where r = source to receiver distance (m), RT_{60} = reverberation time (dB), and V = Volume of the space (m^3). This relationship given by Barron's revised theory indicates G as a function of r , RT_{60} , and V . Reference [9] also describes several applications of using equation 5. Hence, with RT_{60} and V determined, and the source to receiver distance varying, G is estimated in figure 1.4b for the 'with shell' and 'without shell' acoustic states.

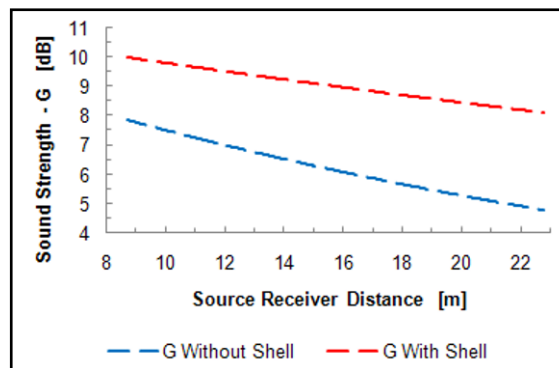


Figure 1.4b – Estimated G for with and without shell acoustic states

Predictions for both RT_{60} and G suggest a considerable increase as a result of implementing a full acoustic shell.

The next method of estimating RT_{60} and G was performed using the Autodesk Ecotect software. For this analysis, the 3D model was converted from its Solid Works file format into a stereolithography (stl) file for which Ecotect could open. Materials were then selected and assigned to their associated surfaces. With the geometry imported and materials defined, RT_{60} (averaged over 500 Hz and 1000 Hz frequencies with a 0% auditorium occupancy) without a shell was estimated by the Ecotect software using equation 1. The Ecotect estimated RT_{60} is **0.99 seconds**. The 'with shell' state was not estimated using this software.

Although G could not directly in itself be estimated using Ecotect, applying a 'Ray Tracing' analysis with and without the shell in place allows for a relevant simulation of how acoustic energy is projected in this space. With a 200 Watt sound source placed in the center of the stage, [figure 1.4c](#) and [1.4d](#) display how this acoustic energy would be projected 'without a shell' and 'with a shell' respectively. These simulated results give clear indications as to how sound strength would be increased. Note the highly increased density of acoustic energy in [figure 1.4d](#).

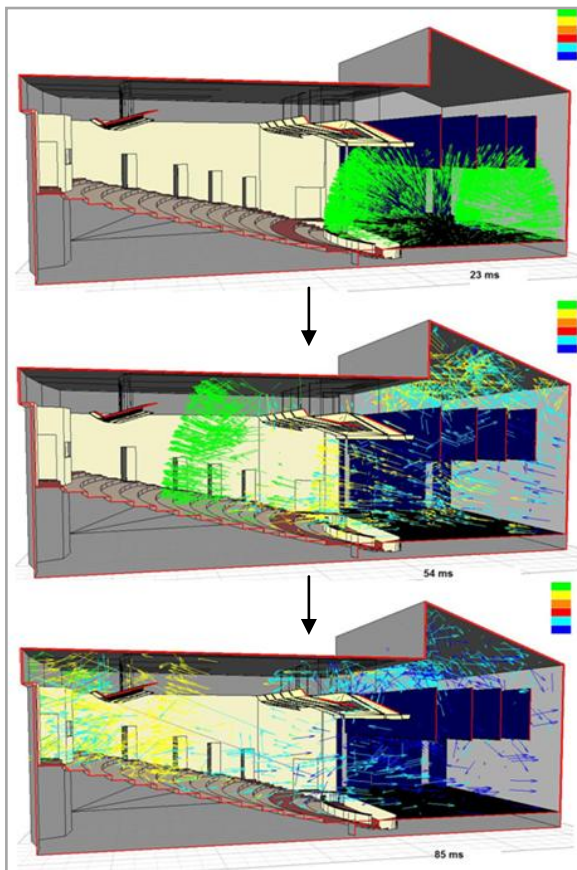


Figure 1.4c – Energy projection over time without shell

@25 ms

@55 ms

@85 ms

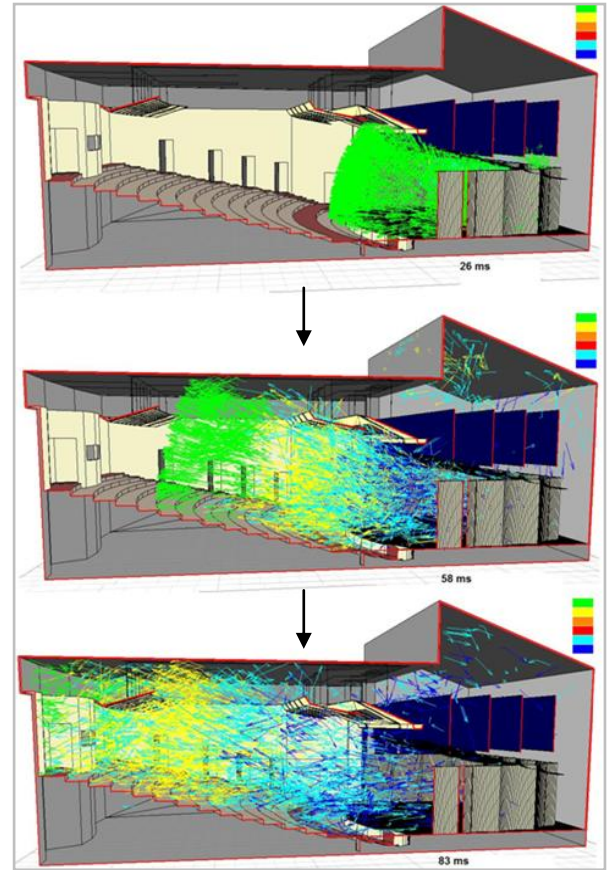


Figure 1.4d – Energy projection over time with shell

1.5 Hypothesis Formulation

Based on estimated objective parameters, gaining subjective impressions, and communicating with expert acousticians, it was understood that the suggested lack of sound projection and low reverberation time in the audience seating area of Parrish Auditorium is caused by a large surface area of 2 cm thick curtains and large fly space over the stage. These curtains make up 40% of the stage material composition and have the highest coefficient of absorption (shown in [figure 1.5a](#)). Therefore, because the musicians are surrounded by these materials during a performance, the sound waves are being absorbed and are losing much of their acoustic energy before ever leaving the stage. Thus, the hypothesis is that the stage materials are impeding upon the opportunity for quality auditorium and stage [1] acoustics for unamplified music performances.

Figure 1.5a shows the impact of the curtains as a result of their total surface area and high coefficient of absorption. Also note that the higher percentage of stage sound produced will strike these curtains.

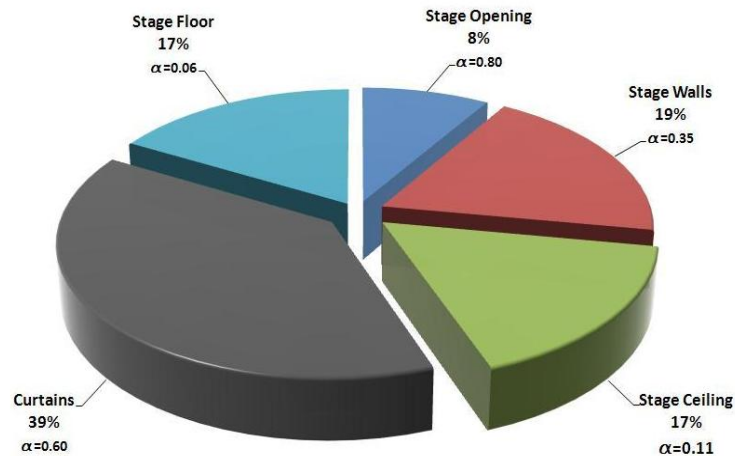


Figure 1.5a – Material composition of the stage area with coefficients of absorption

Thus, by surrounding an orchestra with reflective panels (an acoustic shell), this lost energy will be more efficiently distributed to the musicians and audience.

1.6 Measurement and Testing

The ISO 3382 standard [2] gives detailed instructions for measurement conditions, procedures, equipment, evaluating decay curves, determining uncertainty, spatial averaging, and stating results. Therefore, it would be redundant for the author to cover each topic. Section 9.2 of the standard also gives a template for reporting tests. The following list was populated using this suggested template:

- All measurements reported below conform to the testing procedures designated by ISO 3382.
- The tested space was Parrish Auditorium on the Miami University campus in Hamilton, Ohio.
- Sketch Plan of Parrish Auditorium along with selected source and receiver locations (figure 1.6a):

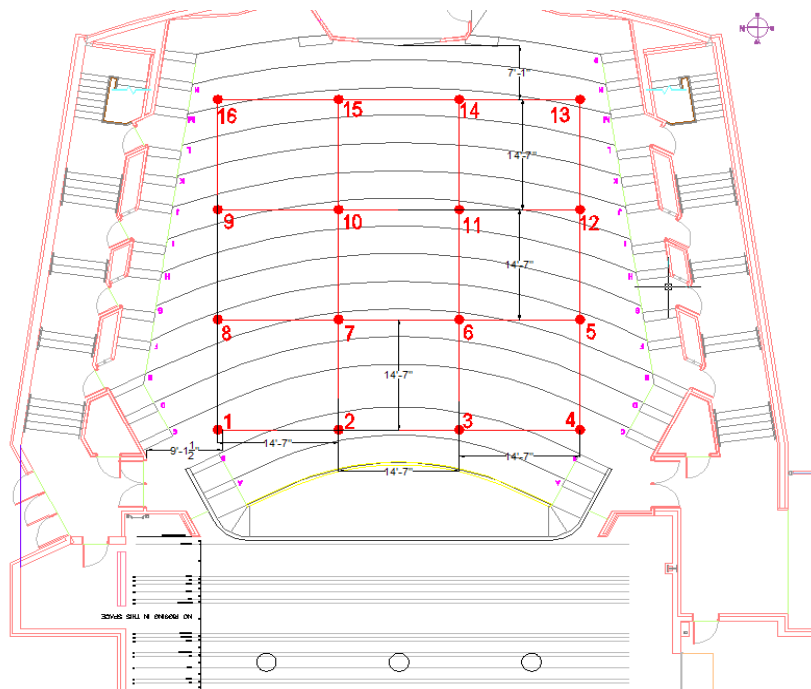


Figure 1.6a – Sketch plan of auditorium along with source and receiver locations

- d) Room Volume [V] = 4500 cubic meters = 158,916 cubic feet
- e) Total Capacity = 451 seats. Thick upholstered seats. Seats were raised during tests.
- f) Ceiling material is steel decking. Wall material is plasterboard and is angled in as you move away from the stage. Audience floor is cement with some carpet coverage. Stage floor is wood.
- g) There were 2 people in the auditorium during each test.
- h) There were 2 variable acoustic conditions tested: 1. Without an orchestra enclosure (shell) and 2. With an orchestra enclosure. It is a Wenger Legacy shell. Estimated age is 15-20 years old. The shell is located at Millet Hall on the Oxford campus and was borrowed for the test. 15 shell towers and 11 ceiling panels were used. The towers completely surrounded the area around an orchestra. The shell ceiling only covered about half of the area over the orchestra.
- i) All curtains and line batons were raised to their highest positions such as to maximize the acoustics of Parrish in the 'without shell' state. The auditorium blower system was switched off during each test.
- j) Stage furnishing conditions are described in section (h) above.
- k) The temperature was approximately 21 degrees Celsius during the test.
- l) Microphone used: Earthworks M30 Omni-Directional. Source Used: B&K – Type 4292 Dodecahedron. Power Amplifier: B&K – Type 2734-A. Sound Interface: Edirol UA-25EX. Recording Device: HP Notebook computer using WinMLS 2004 acoustic measurement and analysis software.
- m) The signal used was a sine-sweep from 125 Hz to 20 kHz.
- n) For the audience area, 3 source positions on stage were used (shown as circles in [figure 1.6a](#)). 16 microphone locations were selected in the auditorium (4x4 square grid).
- o) Measurements were taken from 2/15 through 2/19/2010. Miami University engineering students acquired these measurements.

The source and receiver sample size and locations were selected such that parameter distributions from auditorium front to back and left to right could be analyzed. Spatial averaging was applied in correspondence to ISO 3382 section 8. Results of this test are analyzed in section 2 of this paper.

Prior to obtaining more reliable instrumentation, simplified impulse response tests were performed in this space using similar source and receiver grid locations. In place of the B&K dodecahedron speaker, balloons were employed as an alternative sound source. [Figure 1.6b](#) shows a Miami University engineering student preparing to supply the auditorium with a sound impulse from which it will respond to (or in other words, he is going to pop the balloon with a needle).



Figure 1.6b – Balloon impulse tests

Such tests performed with balloons were found to be less reliable. Because not every balloon is created equally, varying thicknesses in the balloon latex membrane can cause equivalently sized balloons to provide different sound levels. If balloons are ones only means for producing a sound impulse, Miami University Physics professor, Dr. Herbert Jaeger, suggests the following: 1) Use balloons with tight manufacturing tolerances 2) Blow each balloon up to the same geometric size; 3) Apply the needle to the same location for each balloon pop. It was also suggested that by having two microphones recording for each balloon pop, corrections can be applied to compensate for balloon imperfections. One of the recording microphones would remain stationary throughout the entire process in order to gain correction data. Although not covered in this research, further investigations concerning the reliability of balloon impulse response tests would be useful.

Calibrating of the sound source level for measuring G

Calibrating the sound source level for measuring G was done without the use of an anechoic chamber. Normally this free field (without reflection) environment is subjected to identical impulse response tests as were performed on the diffuse space (auditorium). By taking 29 free field measurements around an omni-directional source (dodecahedron or balloon) and by using the same measurement settings as in the diffuse field, one can determine the reference pressure as an input for the denominator of equation 2. This is done by averaging the

total acoustic energy in all 29 measurements. This process is described in detail by the ISO 3382 standard. However, as is the case with the Parrish auditorium project, finding an appropriately sized free field environment (such as an anechoic chamber) can be challenging. Therefore, an In-Situ method of acquiring this reference pressure level was utilized. This method was suggested by Jens Jørgen Dammerud who is a Phd candidate at the University of Bath in England and is found in reference [8].

The system shown in Figure 1.6c was derived from the Dammerud [5] In-situ method. If this method is employed, the user must be certain to have an analysis system capable of calculating only the energy between the arrival of the direct sound and the first reflection from the floor. It should also be noted that this method is only proved valid at frequencies greater than 250 Hz. Figure 1.6d shows the time between the direct sound and the reflection

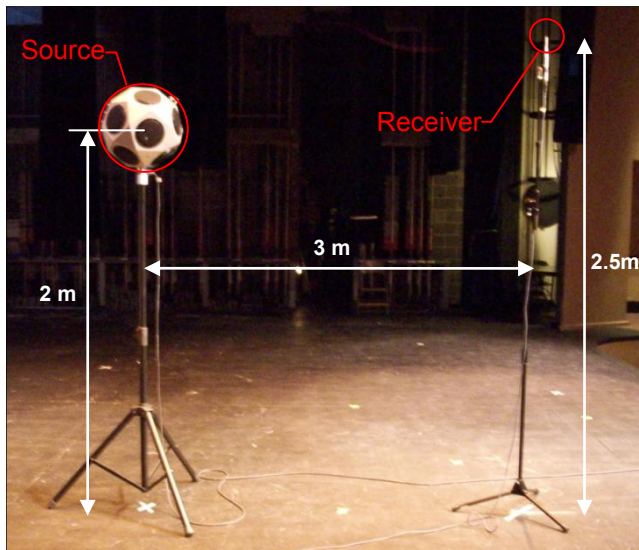


Figure 1.6c – Setup for calibrating G Measurements

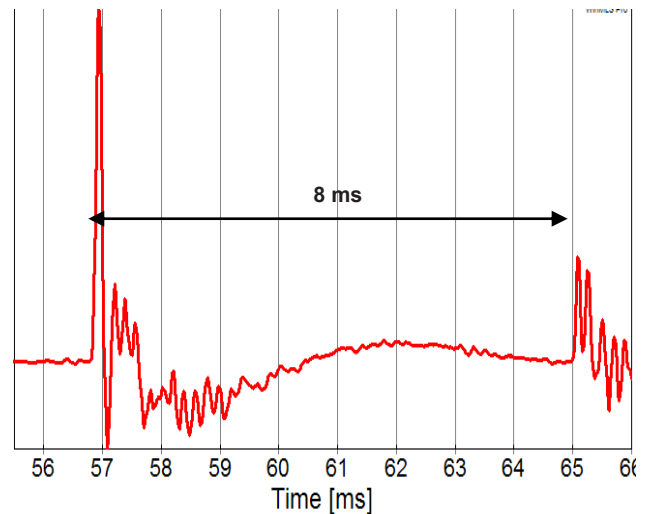


Figure 1.6d – Impulse response from direct sound to the reflection from the floor.

from the floor. The vertical axis is proportional to sound pressure (Pa) while the horizontal axis is time (ms). After squaring pressure, the integral sum of the area under the curve is acoustic energy.

In this study WinMLS 2004 software was used for sending the impulse signal to the source and for recording the auditorium response. The strength calibration menu in this software allows for the selection of all 29 measurement files upon which the calibration data is calculated. Before selecting the 29 files, in WinMLS 2004 the window type can be specified as 8 ms from the direct sound. This sets the lower limit of integration in the denominator of equation 2 as the direct sound, and the upper limit as being 8 ms after the direct sound. The point is to use only the energy which is measured between the direct and the first reflection.

2. Results

Section 2 is divided into two sections. Section 2.1 is concerned with the analysis of measurements pertaining to the quality of acoustics for unamplified music performances (orchestra, choir, etc), while section 2.2 concentrates on the quality of acoustics where speech intelligibility is desired. Parrish Auditorium is used as an example in both sections. All acquired acoustic data were recorded using WinMLS 2004. These data were then exported to MS Excel where data reduction and analysis was performed.

2.1 Acoustics for Unamplified Music Performances

The subjectively proposed problems with the acoustics in Parrish Auditorium are that the space lacks adequate reverberation, sound isn't being projected efficiently from the stage to the audience, and musicians cannot hear themselves and each other well (from section 1.1). Based on the hypothesis formulated in section 1.5, the objective parameters RT_{60} , G , and C_{80} are measured with and without an acoustic shell in place (Fig 2.1a, 2.1b).



Figure 2.1a – Measurements with shell



Figure 2.1b – Measurements without shell

Analysis of RT_{60} (Main subjective attribute is reverberation)

Figure 2.1c shows results for measured RT_{60} spatially averaged over frequencies, source, and receiver locations.

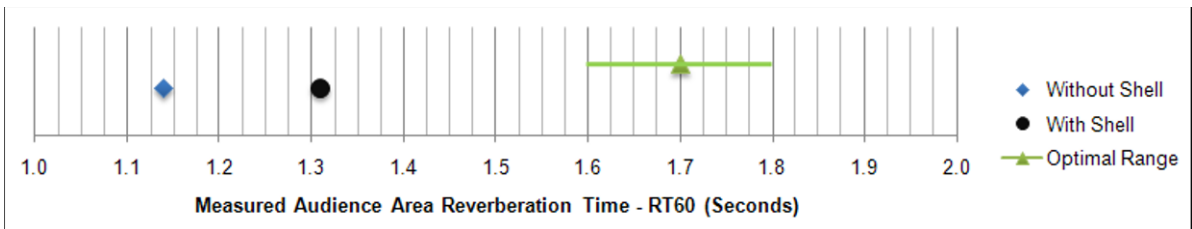


Figure 2.1c – Overall RT_{60} measured results

The % difference between theory and measured RT_{60} 'without shell' is less than 1%. However, results show the % difference between estimated (figure 1.4a) and measured RT_{60} 'with shell' is 20%. This difference is speculated to come from the 451 highly absorbent seats throughout the audience area. Such thick seats are very comfortable but provide difficulties when higher reverberation in a space is desired. These measurements are all performed relative to the 0% occupancy state of the auditorium. Therefore, when the auditorium is occupied the reverberation time (as well as other parameter values) will change further.

If it is desired to obtain optimal RT_{60} , 3 options are available: 1) Construct a new auditorium; 2) Do a major renovation to Parrish Auditorium; 3) Use artificial electro-acoustic enhancements. The electro-acoustic

enhancements would consist of phase shifted speakers placed throughout the space to provide the added reverberation. Such a system would provide a variable amount of artificial reverberation to the auditorium.

Excel generated contour surface plots are used to investigate distribution characteristics of RT_{60} (see 2.1d and 2.1e). These plots provide an overview as if the observer were on the ceiling looking down at the floor.

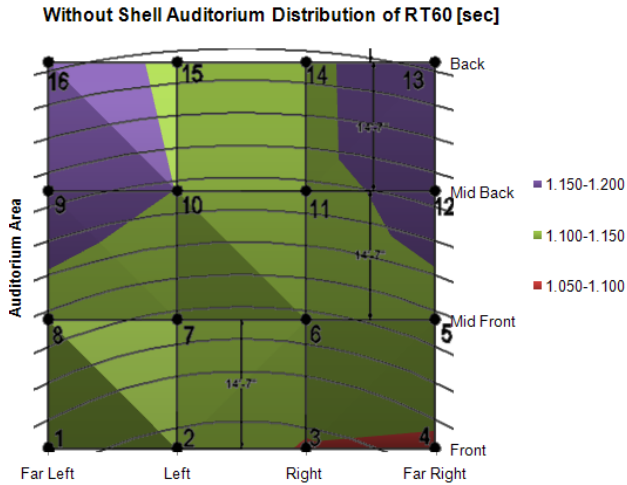


Figure 2.1d – Distribution of RT_{60} without shell

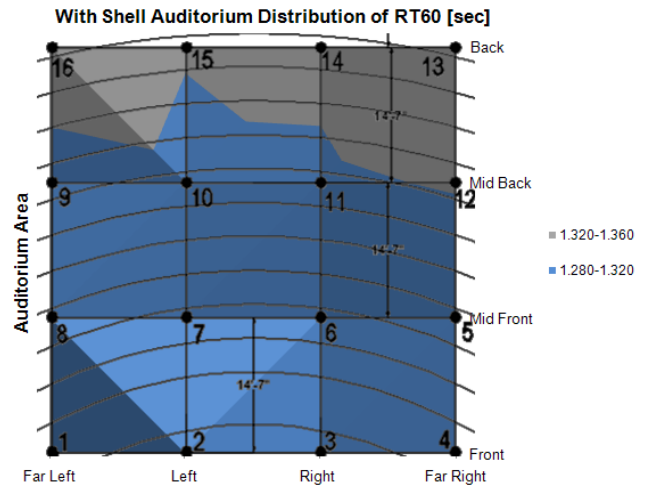


Figure 2.1e – Distribution of RT_{60} with shell

Although low, RT_{60} has good symmetry from left to right. Higher values in the back of the audience seating area are caused by an accumulation of acoustic energy from reflections against the rear wall and corners.

Analysis of G (Main subjective attributes are loudness and sound projection)

Figure 2.1f shows results for measured G_{mid} levels vs distance from spatially averaged over source and receiver locations. The preferred range of G suggested by Long [4] is given as $4 < G_{mid} < 6$ dB.

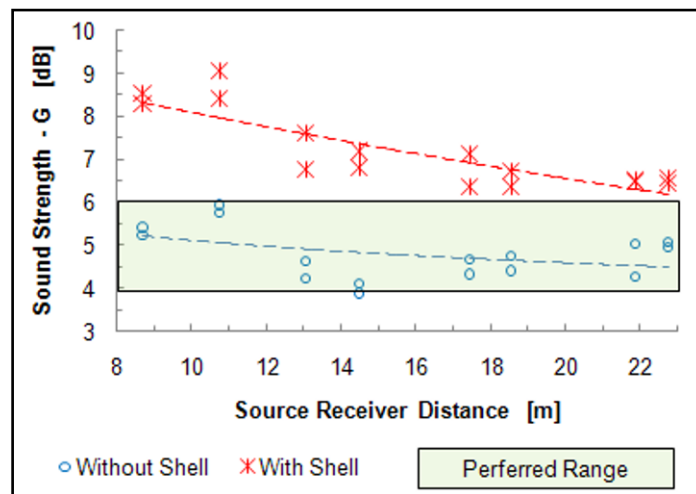


Figure 2.1f – Measured G vs distance from source

As predicted in section 1.4, G is increased as a result of the shell. Because the shell blocked off the large curtains and volume over the stage, and because the walls of the shell absorb very little sound, sound projected much more effectively to the audience. However, as can be observed from figure 2.1f, measured strength is above the preferred range of G . This would suggest that the addition of a full acoustic shell would amplify sound levels too much.

Figures 2.1g and 2.1h show distribution characteristics for G measured at the 16 microphone locations.

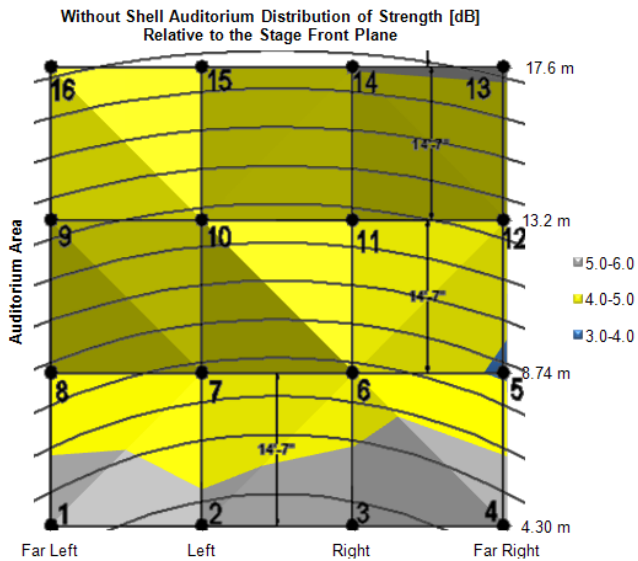


Figure 2.1g – Distribution of G without shell

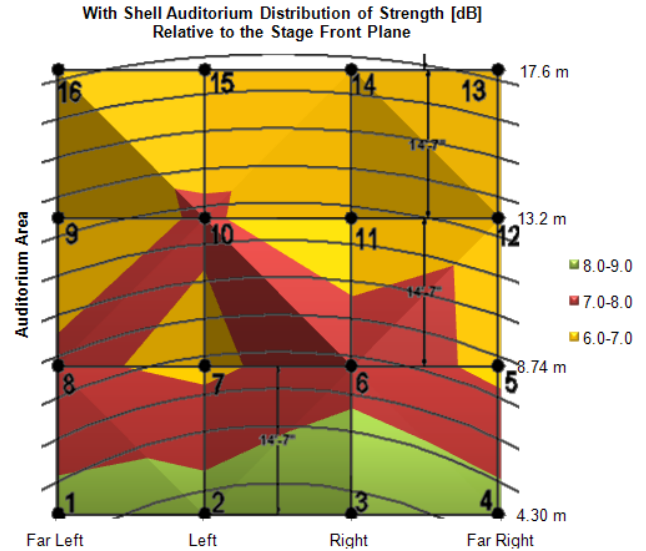


Figure 2.1h – Distribution of G with shell

Both figures show excellent symmetric distribution characteristics. Small anomalies in figure 2.1h could be due to details such as instrumentation tolerances. Both acoustic states clearly show a well diffused space, although as depicted in figure 2.1f, the acoustic shell increases strength above the preferred range.

Analysis of C₈₀ (Subjective attributes are musical brilliance and reverberation)

Figure 2.1i shows results for measured C₈₀ with and without an acoustic shell. The optimal range displayed

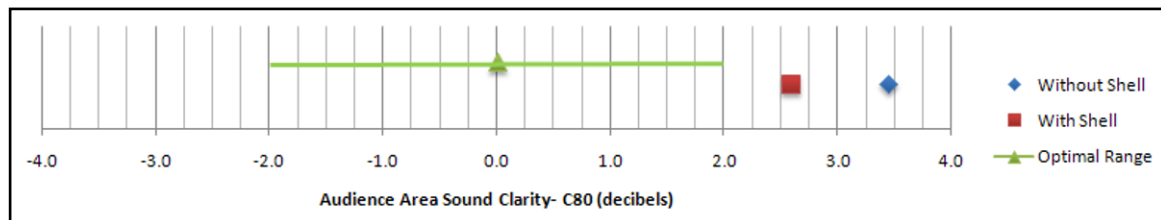


Figure 2.1i – Overall measured C₈₀

is suggested that for unamplified music the optimal range is $-2\text{dB} < C_{80} < +2\text{dB}$. C₈₀ is also inversely related to RT₆₀. Therefore, as the reverberation time increases (as was the case when the shell was implemented), C₈₀ will decrease. The shell only acts to decrease the intelligibility of speech in this space and would serve no practical purpose being used during these events. However, with the shell in place C₈₀ is shown to increase the quality of acoustics for unamplified music. As with RT₆₀, an optimal C₈₀ value in Parrish Auditorium could be achieved by incorporating an electro-acoustic reverberation enhancement system which was previously described.

2.2 Acoustics for Speech Intelligibility

Interviews with various subjects who attend wide varieties of functions at Parrish Auditorium indicate speech intelligibility to be very good in this space. Objective parameters D₅₀ and STI are measured and compared to well-accepted optimum values in literature.

Analysis of D50 (Subjective attribute is speech intelligibility)

Figure 2.2a shows results for measured D₅₀ ‘without shell’ when averaged and compared to optimal values.

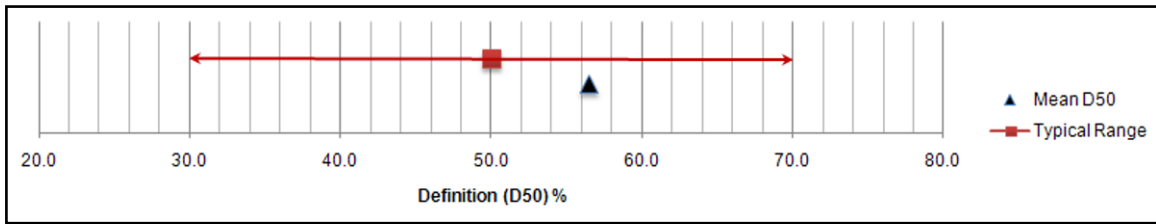


Figure 2.2a – Measured D₅₀ result

Clearly, definition in Parrish is leaning towards accurate subjective impressions of good acoustics. Figure 2.2b displays distribution of D₅₀ over the audience seating area.

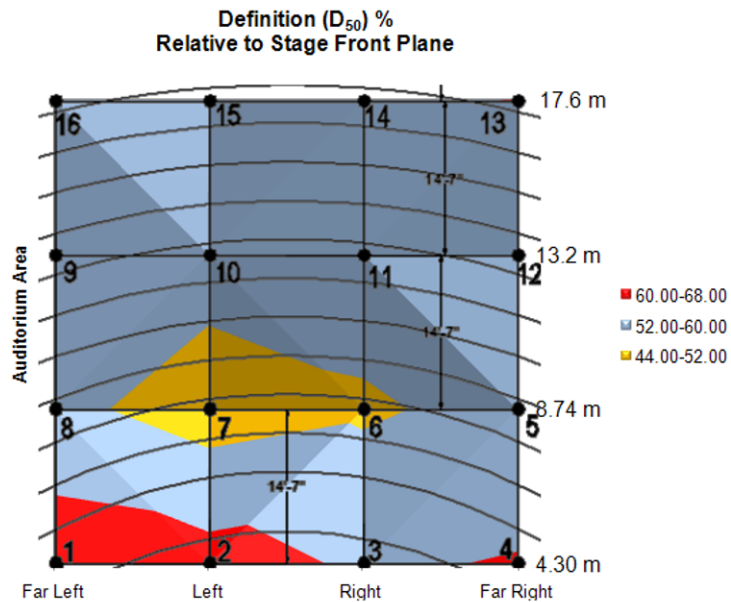


Figure 2.2b – Distribution of D₅₀

Overall distribution of D₅₀ is good with the exception of less than 50% between points 6 and 7. By selecting adaptable wall panels similar to the top of figure 1.3c, D₅₀ can be improved.

Analysis of STI (Subjective attributes are clarity and speech intelligibility)

Figure 2.2c shows results for measured STI values when averaged and compared to optimal values [6].

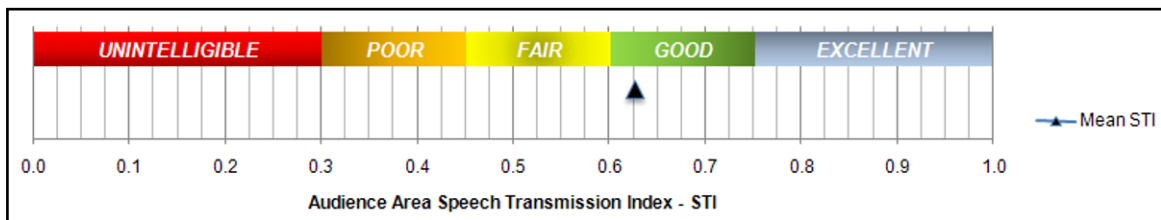


Figure 2.2c – Measured STI result

As with the analysis of D_{50} , incorporating adaptable absorbent wall panels in strategic locations would also place STI into the optimal range (between 0.75 and 1.0). However, the subjective impressions of the acoustics for speech intelligibility are objectively confirmed to be correct. That is, the acoustics are fairly good.

Figure 2.2d shows distribution characteristics for STI over the 16 measurement locations based on the ‘without shell’ acoustic state only.

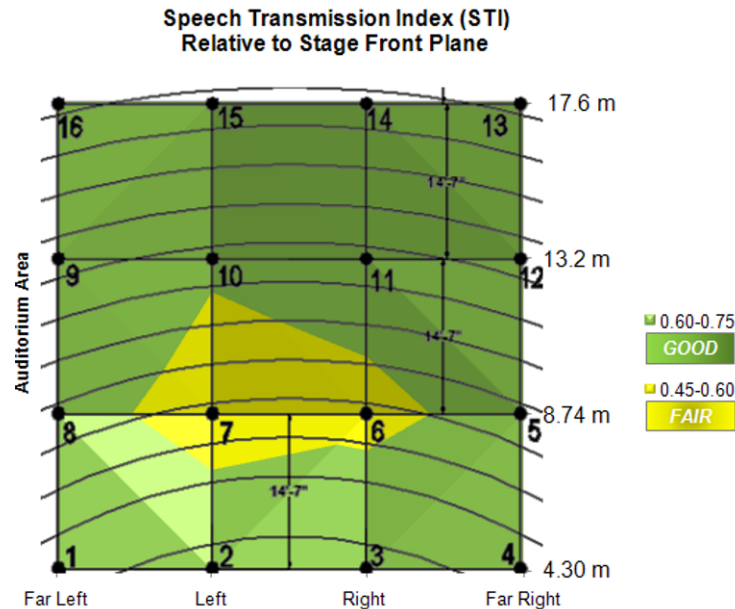


Figure 2.2d – Distribution of STI

The distribution of STI is highly symmetric relative to the source locations and side walls. Measurement locations 6 and 7 are points with the largest distance from any reflective surfaces. The STI distribution reaches its minimum value at a location between points 6 and 7. Therefore, one could postulate that because this surface minimum lies at a location centrally relative to the source, back walls, and side walls, there may be a need for more surfaces closer to this point. These surfaces could potentially be overhead as an extension to the auditorium’s existing acoustic clouds.

3. Conclusions

In conclusion, the summation of all the investigated acoustic characteristics of Parrish Auditorium makes the addition of adaptable acoustic equipment a significant enhancement. The main enhancements as a result of the acoustic shell would be improved musicians support on stage and an increase of sound strength (G) in the auditorium. Although the analysis of G in section 2.1 shows the full acoustic shell to increase G above the preferred limits, the author suggests that a partial acoustic shell (several towers and ceiling panels which do not enclose the musicians completely) would produce a significant improvement. This is because during an actual unamplified music performance the audience (which was not present in testing) will absorb acoustic energy. Therefore, when Parrish Auditorium has an audience and there is a partial acoustic shell present, G is expected to decrease to a preferable level. RT_{60} and C_{80} could also be greatly enhanced with the addition of an artificial electro-acoustic system as was suggested in section 2.1. This system would allow for variable control of the reverberation in Parrish upon demand. Although the shell would make the most impact to the acoustics in this space, one could fine-tune the acoustics by also adding adaptable or rotatable absorbent/reflective panels to the auditorium walls and ceiling. For this multipurpose auditorium, as well as many others, having the ability to adapt the acoustic environment to a variety of event functions would be a very desirable and potentially profitable characteristic to obtain.

ACKNOWLEDGMENTS

The author would like to thank Jens Jørgen Dammerud, Phd candidate at the University of Bath, and Brad Hoover, physicists and musician, for mentoring the research team in various aspects of acoustics. The author would also like to thank the Miami University administration and faculty from the many departments which helped in various aspects of research. The author would also like thank the Department of Engineering Technology for facility and financial support.

REFERENCES

- [1] Braden, C., Hayes, B., Ranatunga, V., Averbach, R., "*Identification and Enhancement of On-stage Acoustics in a Multipurpose Auditorium*". Society for Experimental Mechanics (SEM) conference proceedings paper #178, (2010)
- [2] ISO 3382. "*Acoustics-Measurement of room acoustic parameters*", Part One - Performance Spaces, International Organization for Standardization, (2009)
- [3] Barron, M., Lee, L.J., "*Energy relations in concert auditoria*", Acoustic Society of America, 84, 618-628, (1988)
- [4] Long, M., "*Architectural Acoustics*". Elsevier, Chapter 17, 666-682, 654-655, (2006)
- [5] Egan, D., "*Architectural Acoustics*". J.Ross Publishing, 64, 147-150, (2007)
- [6] Meyer Sound. "*Glossary of terms*". <http://www.meyersound.com/support/papers/speech/glossary.htm#sti>
- [7] IEC 60268-16. "*Sound system equipment – Part 16: Objective rating of sound intelligibility by STI*", International Electrotechnical Commission, (2004)
- [8] Dammerud, J.J., "*In-situ calibration of the sound source level for measuring G*". University of Bath Phd candidate paper, <http://home.no/jjdammm/stageac/insituGcalib.pdf>, (2008)
- [9] Aretz, M., Orłowski, R., "*Sound strength and reverberation time in small concert halls*". Elsevier, Applied Acoustics. 70, (2009)
- [10] Nittobo Acoustics. "*Definition of room acoustic parameters*", <http://www.noe.co.jp/en/product/pdt3/ot/ot03.html>

Identification and Enhancement of On-stage Acoustics in a Multipurpose Auditorium

C. Braden, B. Hayes, Undergraduate Students, Miami University, Hamilton, OH
R. Averbach, Conductor and Associate Professor, Miami University, Oxford, OH
V. Ranatunga, Associate Professor, Miami University, Middletown, OH
501 E. High St., Oxford, OH, 45056, bradencm@muohio.edu

ABSTRACT

The objective of this research is to identify the measurable sound quality parameters of an existing multipurpose auditorium in which the acoustics are not adequate for orchestral purposes. The major problems have been identified as the lack of sufficient projection of sound from the stage area, the inability of the musicians to hear themselves and each other, and the poor reverberation in the auditorium. Objective architectural acoustic parameters have been identified and analyzed by conducting acoustical measurements following standardized procedures. One of the measured objective parameters is 'Musician Support', which depends on the amount of early reflections available on stage for the musicians. An acoustic shell, which is a set of large panels that surround an orchestra, will increase the level of early reflections. The goal of this study is to assess the effectiveness of an acoustic shell in improving the on-stage acoustics of this particular auditorium. An objective analysis of these parameters is presented with and without the shell in place, in order to quantify the overall enhancement for the musicians provided by the acoustic shell.

INTRODUCTION

The acoustical analysis and enhancement of auditoriums is a subject which has been investigated by many researchers over the past few decades. The study of platform/stage acoustics for orchestras in particular was greatly affected by the findings of Gade, who introduced the parameter ST_1 (now referred to as ST_{early}) for quantifying 'Musician Support' [1]. This and other objective acoustical parameters are used in an attempt to assess the quality of acoustics for the musicians on stage. The particular stage in this study was analyzed using the following objective acoustic parameters:

Reverberation Time (RT_{60}) – The time required for the sound level in a room to drop 60 decibels after a source ceases to emit sound. A space is said to more “live” as RT_{60} increases. For multipurpose auditoriums, an optimal RT_{60} is within the range of 1.6 to 1.8 seconds [2]. An RT_{60} of closer to 2 seconds is preferred for orchestral performances.

Clarity (C_{80}) – The degree to which rapidly occurring individual sounds are distinguishable. For orchestral performances, a lower clarity provides sounds which flow more smoothly into one another. A study of eight concert halls showed that for the most preferred halls, mid-frequency C_{80} values on stage were in the range of approximately 2 to 4 dB [3].

Musician Support (ST_1 or ST_{early}) – A measure relating to how well musicians can hear themselves and others around them. This parameter depends on the amount of early reflections available from surrounding stage surfaces. The optimal range for ST_1 is between -13 and -11 dB [4].

Late Sound Level (G_{late} or $G_{80-\infty}$) – A parameter calculated from measured G (sound strength – closely related to “loudness”) and C_{80} values. It is a measure of the level of “reverberant sound”. G_{late} calculated for the auditorium and the stage indicates the ability of the auditorium to provide an audible level of reverberant sound to the musicians on stage. Based on the recent research of J.J. Dammerud of the University of Bath, the optimal range

for G_{late} in the auditorium is 1 – 3 dB [5]. G_{late} measured on-stage was found to be about 2 dB above G_{late} in the auditorium, for the most preferred halls in his study [3].

RT_{60} is calculated by the “integrated impulse response method” outlined in section 5.3 of ISO 3382-1:2009 [6]. In this case, RT_{60} is calculated based on “ T_{30} ”, the decay time over the range of -5 to -35 dB extrapolated to -60 dB. The equations for calculating C_{80} , G , and $ST1$ are stated in Annexes A and C of ISO 3382-1:2009 [6] and are also based on the integrated impulse response. $G_{\text{late, stage}}$ and $G_{\text{late, auditorium}}$ values were calculated based on G and C_{80} values. The equation for calculating G_{late} is below [7]:

$$G_{\text{late}} = G - 10 \log \left(1 + \log^{-1} \left(\frac{C_{80}}{10} \right) \right), \text{ dB} \quad (1)$$

BACKGROUND

An Engineering Perspective

The design of multipurpose auditoriums to cater to a wide variety of events is particularly demanding due to the varying acoustical needs of the venue. Motivation for this research originated from the accounts given by two area conductors on the orchestral acoustics of an existing multipurpose auditorium on the Miami University Hamilton campus in Hamilton, OH. Parrish Auditorium, shown in Figure 1, is relatively small with 451 seats, and is mostly used for theatre, lectures, and small amplified musical groups. The conductors’ subjective impressions were identical, and highlighted three main acoustical deficiencies in Parrish for orchestral purposes: 1) Low reverberation, 2) Lack of sufficient projection of sound from the stage to the audience area, and 3) Musicians struggling to hear themselves and each other.

The main objective of this paper is to quantify the improvement of the *on-stage acoustics for musicians* provided by the addition of an acoustic shell. From an engineering standpoint, this requires the identification and analysis of measurable objective architectural acoustic parameters related to musician perception (defined in the above section). Optimal ranges for these objective parameters have been identified based on subjective studies with musicians. The variation between the measured parameter values and the identified optimal ranges can then be compared, with and without the shell in place, in order to show the quantitative improvement of the acoustics provided by the shell.



Figure 1. Seating Area in Parrish Auditorium – View from Stage (Dodecahedron Loudspeaker at Center)

A Musical Perspective

Our observations on the importance of musicians being able to hear effectively while performing in an orchestra are significant in the conception of an acoustic setting. If musicians can better hear each other, and themselves, while playing, they can better adjust their intonation and manipulate tonal colors with ease. As in chamber music where musicians listen and interact with each other, the same holds true for a large ensemble. In both cases, an optimal acoustic setting is desirable.

With excellent acoustics, the sound will not only become richer and more resonant, but also more lively and varied due to the phenomenon of resonance. The phenomenon of resonance is a scientific explanation of the Physics of overtones; it is what is sensed by the musicians and the audience when the orchestra plays in tune. The sound becomes richer and multiplies due to many different pitches ringing within one predominant tone. Even after each musician tunes their instrument in relation to the A given by the oboe, they must be constantly aware of their intonation within the texture and adjust accordingly. Being “in tune” is not a solid, but rather having the buoyancy to float within the ringing tones of the overtone series.

Dynamic changes like *crescendo* and *diminuendo* should be observed within the context, as dictated by the musical score. These changes should be determined by the instruments that carry the main melodic line, and the accompanying instruments should subordinate the dynamic changes to this line in order that the main theme is always clearly heard. For example, if the strings are accompanying one or more woodwinds which carry the melodic line, their *crescendos* should never cover the solo woodwinds. What is most important in this case is that the strings always give the soloists space to breathe and soar above them.

Fugal passages should be performed in a way that the subject can always be followed and identified. This is particularly difficult when the subject is stated in the inner voices. Several solutions can be used, such as dynamic adjustments that are frequently not written in the music, the use of contrasting articulations, accents, etc. All of this can happen only if the musicians are able to clearly hear each other and themselves.

The strings are the most homogeneous section of the orchestra and should be thought of as a choir. String instruments can be particularly expressive especially when the homogeneity of sound, articulation and musical thought are achieved. They must blend as in a choir, or the purity of sound is missing. When the players are listening better to each other, it is possible for them to blend more effectively.

The trombones and tuba form another relatively homogenous group of instruments, however much smaller than the strings. The same holds true of the French horn section. These instruments form their own inner choirs within the brass section of the orchestra, which can be viewed as a larger choir encompassing all the brass instruments. The main challenge in dealing with the brass section is to achieve a similar homogeneous sound as with the strings. It is particularly challenging because of the many different timbres of the various instruments within the brass section.

In addition, it is more difficult for brass players to hear themselves in comparison to string instruments. Since the bells are facing away from the face and ears, these performers are usually hearing a reflected sound of their tone. The French horns are the most difficult instruments to blend with the others because their bells often face the back of the stage, while the bells of all the other instruments face the audience.

All brass instruments use a rather similar embouchure (formation of lips at the mouthpiece), something that cannot be said of the woodwind instruments. Woodwind instruments call for a wide variety of reeds, both single and double. In addition, the woodwinds, have at least three different registers that produce much more variance in timbre than in the other instrumental sections. Blending sounds and tone colors, the clarity of attacks, and homogeneity of various types of articulation is a significantly bigger challenge for the woodwind instruments.

The tone of each woodwind or brass instrument should positively relate to the others players in their section. Frequently there are dialogues or imitations of themes that go from one instrument to another. The players need to be able to listen to each other and try to find a logical way to phrase and articulate passages, so that the theme can flow artistically from one instrument to the other. Each player should find a unique voice and approach to the music, while yet maintaining a uniform style with the other instruments.

With the advent of recordings, standards for precision and tone quality in orchestras has increased significantly. Contemporary music presents significant technical challenges, and the treatment to orchestral performance is leaning more and more in the direction of a chamber music approach.

Because of this, there exists a constant demand to improve the acoustical environment where musicians perform so that the musicians can better hear each other and perform with the utmost accuracy. No matter how large the orchestra may be, players must be able to feel a sense of intimacy in order to communicate with one another and the audience. Herein, lies the key for an artistically effective performance.

EXPERIMENTAL SETUP

All measurements were performed in accordance with ISO 3382-1:2009, "Measurement of room acoustic parameters" [6]. Impulse responses were obtained using an Earthworks M30 Measurement Microphone (omni-directional microphone), Brüel & Kjær Type 4292 OmniPower Sound Source (dodecahedron loudspeaker), Brüel & Kjær Power Amplifier Type 2734-A (loudspeaker amplifier), Edirol UA-25EX Audio Capture (USB sound interface), and an HP Compaq 8510p Notebook PC using WinMLS 2004 acoustic measurement and analysis software (for sending output signal and analyzing input signal).

The output signal was a sine-sweep that began at 125 Hz and ended at 20 kHz. The acoustic shell used was a Wenger Legacy® Acoustical Shell. This is a portable-type shell with flat panels. For the "with shell" measurements, fifteen towers, 1.83 m wide by 4.88 m tall, were set up to enclose an area of approximately 100 m² on the stage (with the top sections angled downward). Eleven ceiling panels were used - each was 1.22 m by 2.44 m. Six ceiling panels were located near the back of the enclosure, and five were located near the front, as shown in Figure 2. They were at an average height of approximately 5 m above the stage. The ceiling panels were spaced such as to obtain the best ceiling coverage possible with the limited available line batons and rigging weight capacity. The ceiling panels covered about half of the area above the orchestra enclosure.

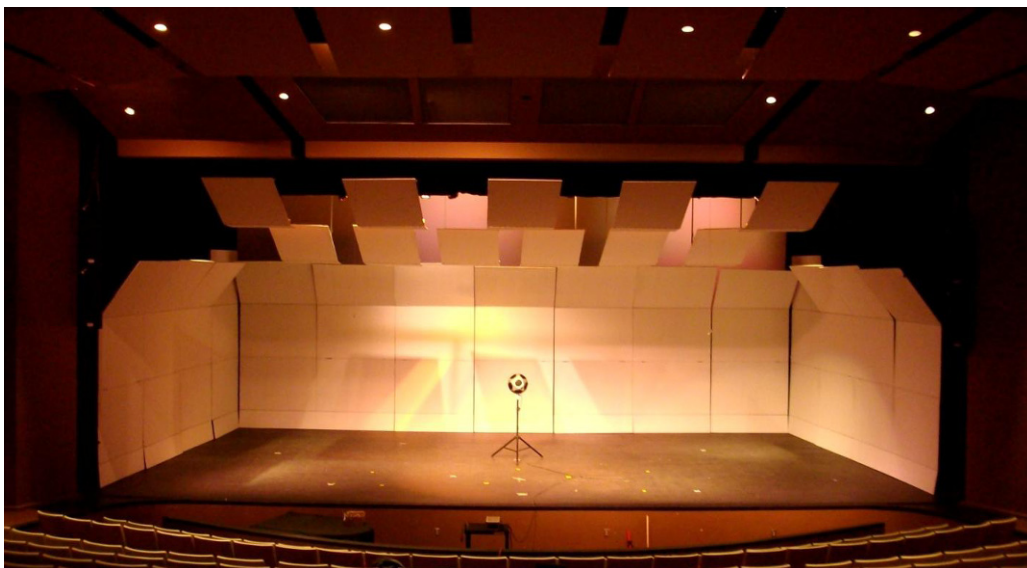


Figure 2. Acoustic Shell Setup with Loudspeaker Center-stage

The volume of Parrish Auditorium is approximately 4500 m³. During testing, the HVAC system was switched off in order to eliminate unnecessary ambient noise. In addition, all stage curtains were raised to their highest positions to provide the best possible stage acoustics for the "without shell" state. All access doors were closed, and there were two people present in the auditorium during testing. The temperature was approximately 21 degrees Celsius. The state of the platform was empty (except for the shell during the "with shell" measurements) – there were no chairs, music stands, or instruments present on stage during testing. The omni-directional microphone receiver was in a vertical position for all measurements.

Measurement positions for the corresponding objective parameters are shown below in [Figures 3 and 4](#). For RT_{60} , C_{80} , and G , source and receiver locations were chosen in an attempt to represent different instrumental groups. Locations for these measurements were also chosen to be at least 1 m away from reflecting surfaces (shell walls), as depicted by the pink line in [Figure 3](#). The height of the source was 1.5 m, and the height of the receiver was 1.2 m. For these measurements, 18 unique combinations of source-receiver locations were used, as follows:

Source @ 3, Receiver @ 7, 8, 9
 Source @ 4, Receiver @ 1, 7, 8, 9
 Source @ 6, Receiver @ 8
 Source @ 7, Receiver @ 1, 2, 3, 4, 5
 Source @ 8, Receiver @ 2, 3, 4, 5, 6

For the measurement of ST1, a different schematic was created (shown in [Figure 3](#)). ST1 requires that the source and receiver are 1 m apart. Gade also suggests keeping both source and receiver at least 4 m from walls to ensure that reflections from the walls are included in the support measure [8]. In this case, positions for the source were chosen to be at least 4 m from the shell walls, as depicted by the pink line in [Figure 3](#). Receiver positions were 1 m upstage from source positions. For ST1 measurements, the height of both source and receiver was 1 m. In total, 8 unique source-receiver locations were used.

In order to calculate G_{late} in the auditorium, a measurement system was required for obtaining G and C_{80} in the auditorium. The grid schematic used for the auditorium measurements, consisting of 16 receiver locations, is shown below in [Figure 4](#). The source remained at "[Figure 3](#) - position P6" during these measurements. The source height was 1.5 m and the receiver height was 1.2 m. A more detailed explanation of the acoustic assessment of the auditorium area is given in the paper by Hayes, et al. [9].

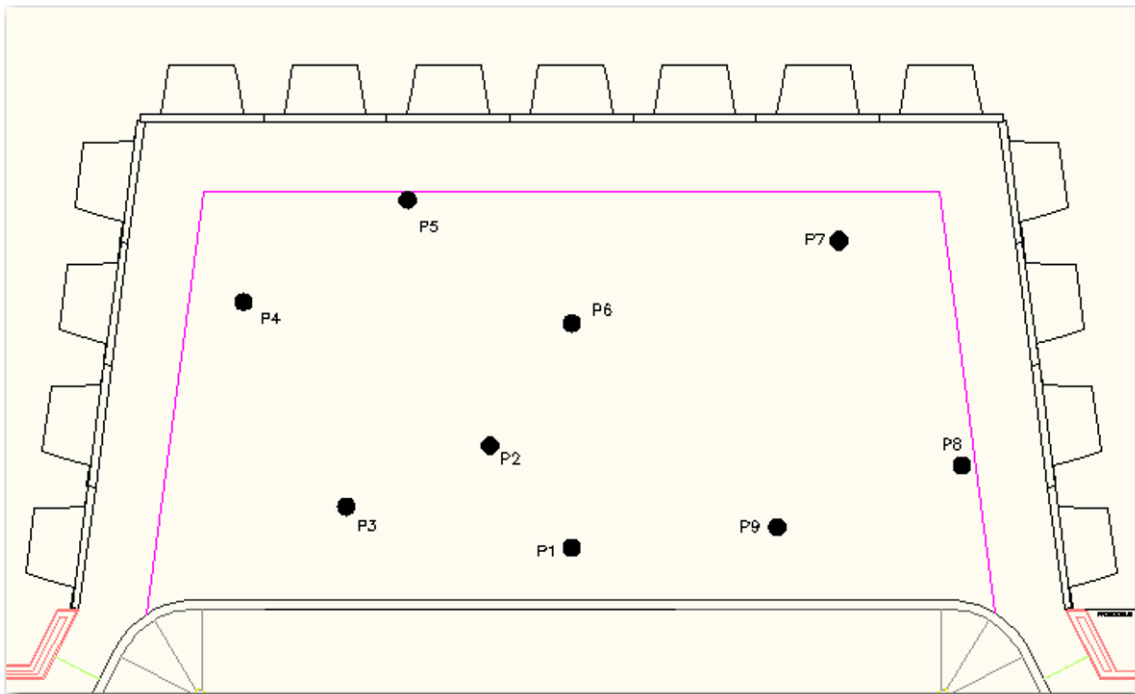


Figure 3. Measurement Positions for RT_{60} , C_{80} , and G on Stage

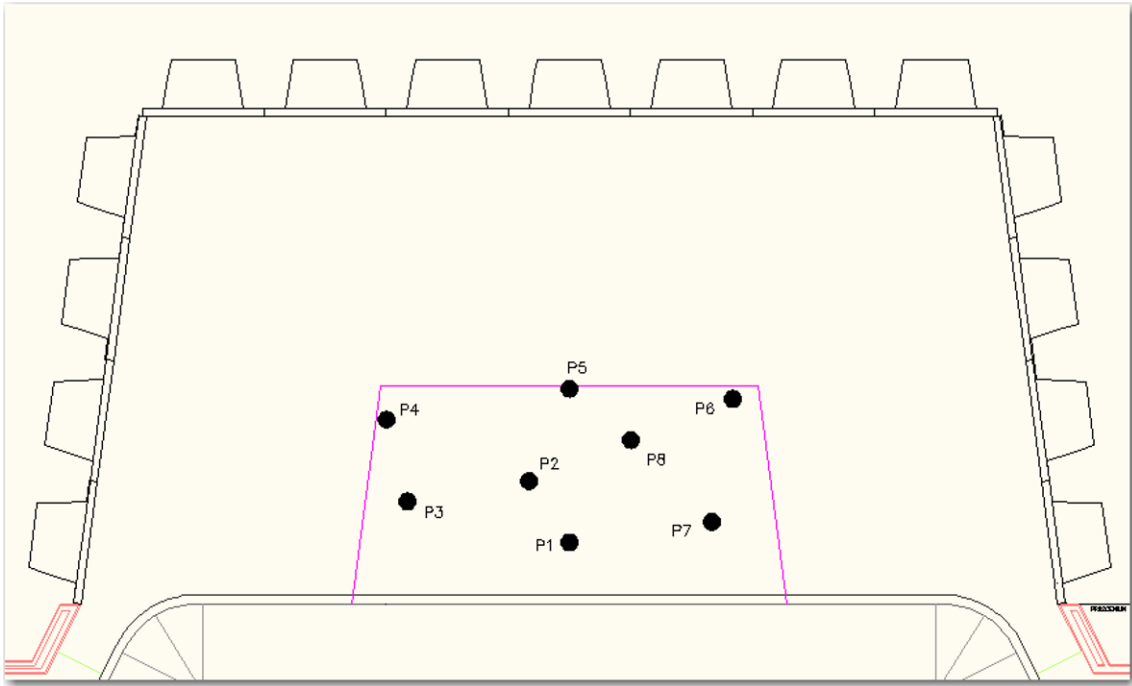


Figure 4. Measurement Positions for ST1 on Stage

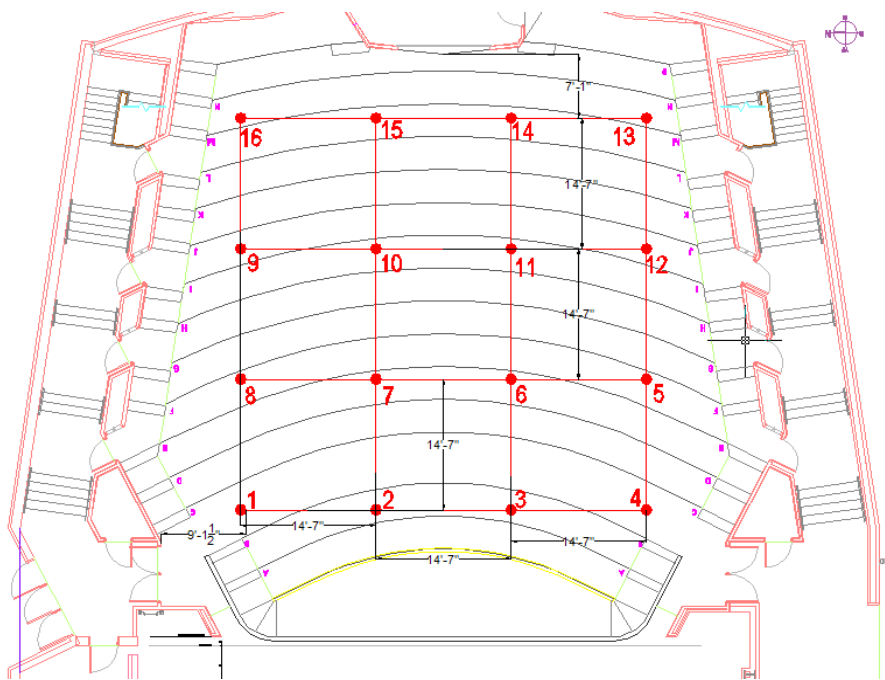


Figure 5. Measurement Positions for C_{80} & G in the Auditorium

Calibrating Sound Strength (G)

The calculation of G requires calibration measurements to be taken at a 10 m distance in a “free field” (an environment free of reflections). A true free field environment is hard to come by. One such possibility is the use of an anechoic chamber, which approximates a free field. However, anechoic chambers are also hard to come by. Therefore, an “in-situ” method described by Dammerud [10] was used for the purpose of calibrating the sound level without the use of a free field. This method simply requires defining a “reflection-free zone” around the loudspeaker and microphone, defined in Dammerud’s paper. The configuration used was a source height of 2 m, receiver height of 2.5 m, and a source-receiver distance of 2 m. In total, 29 measurements were taken – the source was rotated approximately 12.5° between each measurement. Hayes et al. further discusses the calibration of G [9].

RESULTS

The parameters RT_{60} , C_{80} , G, and ST1 were calculated from the measured impulse responses using WinMLS 2004 software. The results of G on stage, G in the auditorium, and C_{80} in the auditorium are not shown here, but were used to calculate $G_{late, stage}$ and $G_{late, auditorium}$ values. This was done using a spreadsheet created by Dammerud [11]. Mean values of the spatial averages over the 500-1000 Hz octave bands are presented in [Table 1](#). In the case of ST1, the mean spatial average is calculated over the octave bands from 250-2000 Hz. Spatial averages are also plotted in the four octave bands from 250 to 2000 Hz for each of the objective parameters. These results are shown in [Figure 6 \(a-e\)](#).

Table 1. Mean Spatial Averages of Objective Parameters

Parameter	Spatial Average: 500-1000 Hz Bands	
	<i>Without Shell</i>	<i>With Shell</i>
RT₆₀ (s)	1.03	1.29
C₈₀ (dB)	6.8	6.5
G_{late, stage} (dB)	0.0	4.4
G_{late, auditorium} (dB)	-0.3	2.7
Parameter	Spatial Average: 250-2000 Hz Bands	
	<i>Without Shell</i>	<i>With Shell</i>
ST1 (dB)	-15.0	-8.9

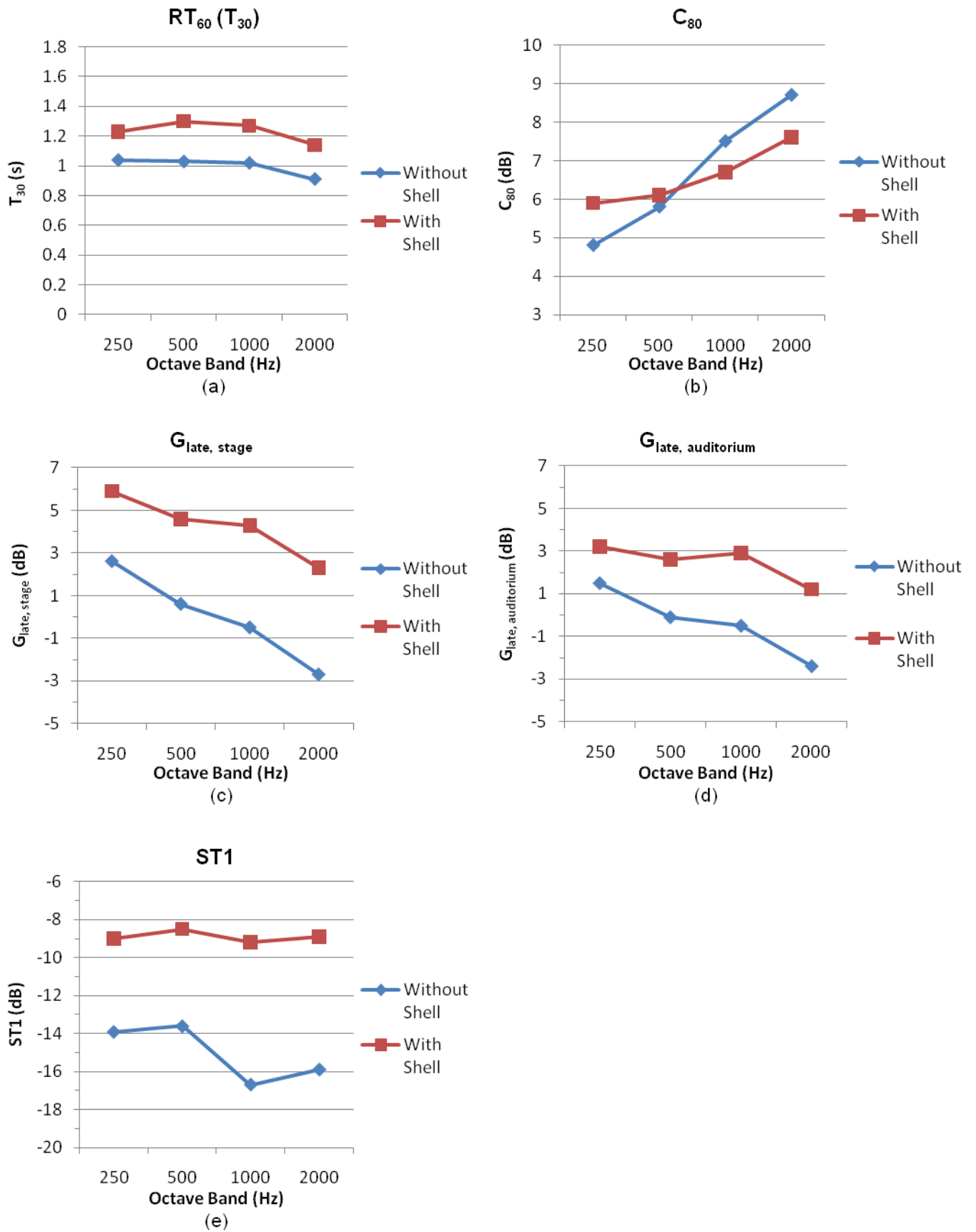


Figure 6 (a-e). Spatial Average Values in Octave Bands

DISCUSSION

Spatial Averaged Results

The addition of the shell on stage produced measurable differences in the objective parameters, most notably $G_{\text{late, stage}}$, $G_{\text{late, auditorium}}$, and ST1. An acoustic shell is not necessarily meant to increase the reverberation time as much as it is to provide early reflections for the musicians and also project sound from the stage to the audience. However, the addition of a shell increased the level of the reverberant sound (G_{late}) in both the auditorium and stage areas.

The shell increased RT_{60} on stage by 0.26 s. This is approximately a 25% increase, and brings the reverberation time approximately 50% closer to the optimal range of 1.6 to 1.8 seconds. The standard deviation of the mid-frequency average between individual measurement positions was only 0.04 s for “without shell” and “with shell”. According to Egan, RT_{60} on stage should be approximately equal to that of the auditorium, which was found to be the case, with and without the shell, based on comparisons with the auditorium area study by Hayes et al. [9].

The C_{80} spatial average value did not change much with the addition of the shell. The “with shell” spatial average values for the 1000-2000 Hz bands were lower than the “without shell” values. However, four of the nine measured locations show differences in the mid-frequency C_{80} (“without shell” vs. “with shell”) which exceed the JND (Just Noticeable Difference) of 1 dB. The measured differences in mid-frequency C_{80} values are by no means consistent across all stage locations – six of the nine locations showed a decrease in mid- C_{80} , while the other three locations showed an increase. One interesting thing to note is that the addition of the shell decreased the standard deviation of the mid- C_{80} between different positions from 1.4 to 0.9 dB. This is a standard deviation decrease of about 35%. Therefore, it can be said that the shell makes the clarity on stage slightly more uniform, which is desirable. However, even with the addition of the shell, the mid-frequency C_{80} values at all locations were still too high to be within the optimal range of approximately 2 to 4 dB.

As briefly described in an earlier section, G_{late} is simply the late-arriving portion of the sound strength (from 80 ms to ∞). The level of G_{late} measured in the auditorium must be high enough for the musicians on stage to perceive a sense of reverberance in the auditorium and a sense that their sound is being projected from the stage. The level of $G_{\text{late, auditorium}}$ is not the only concern, but also the difference between $G_{\text{late, auditorium}}$ and $G_{\text{late, stage}}$. G_{late} measured on the stage will be higher than G_{late} measured in the auditorium due to decreased source-receiver distances, based on Barron’s revised theory (discussed further in Hayes, et al. [9]). An acoustic shell further increases $G_{\text{late, stage}}$. If G_{late} measured on the stage is too much higher than that of the auditorium, the stage area may be acting as a separate acoustic space, creating its own reverberant response. This is undesirable, as it makes the sound on stage overwhelming and also prohibits the musicians from hearing the reverberant response from the auditorium. For the small set of popular stages investigated in Dammerud’s recent study, the average value of $G_{\text{late, auditorium}}$ was found to be within 1 – 3 dB [5], and the average value of $G_{\text{late, stage}}$ was found to be approximately 2 dB above the average $G_{\text{late, auditorium}}$ [3]. It should be noted that these suggested “optimal” values are currently more hypotheses than proven facts, as these topics have not been investigated much previously. In the “without shell” state, $G_{\text{late, auditorium}}$ was below the 1 – 3 dB range, and $G_{\text{late, stage}}$ was only 0.3 dB above $G_{\text{late, auditorium}}$. Comparing to the suggested optimal values, this would contribute to the initial perceived subjective problems of “lack of projection” and “lack of reverberation”. With the addition of the shell, $G_{\text{late, auditorium}}$ was increased to 2.7 dB, which is within the range proposed by Dammerud. $G_{\text{late, stage}}$ was increased to 4.4 dB, which is 1.7 dB above $G_{\text{late, auditorium}}$ – again, within the suggested optimal range.

In the “without shell” state, the average ST1 value was 2 dB below the optimal range. The addition of the acoustic shell greatly increased the ST1 value, to the point that it was approximately the same amount above the optimal range as it originally was below. It should be noted that the preferred height of overhead reflectors is approximately 7 m [12]. It is reasonable to assume that raising the overhead ceiling panels to the preferred height would decrease the ST1 value. According to O’Keefe [13], changing the height of overhead reflectors only produces ST1 changes in the range of 0.5 to 1.5 dB. However, assuming the upper end of that range, raising the overhead ceiling panels could bring the ST1 value very close to the optimal range.

Spatial Variation of C_{80} and G

The ISO standard states that the parameters C_{80} and G are normally not spatially averaged, as they “are assumed to describe local acoustical conditions” [6]. Although there is some relevance to spatial variations of these parameters, when quantifying stage acoustics, the typical method is to quote single position- and mid-

frequency-averaged values. As was mentioned above, the standard deviation of the mid-frequency C_{80} values on stage was 1.4 dB “without shell” and 0.9 dB “with shell”. The standard deviation of the mid-frequency G values on stage was 1.2 dB “without shell” and 0.5 dB “with shell”. This only resulted in a standard deviation of 0.5 dB for the calculated mid-frequency $G_{\text{late, stage}}$ values, “with shell” and “without shell”. The standard deviation of mid-frequency C_{80} in the auditorium was 0.9 dB “without shell” and 1.0 dB “with shell”. For mid-frequency G in the auditorium the standard deviations were 0.6 dB “without shell” and 0.9 dB “with shell”. This resulted in a standard deviation for $G_{\text{late, auditorium}}$ of 0.4 dB “with shell” and “without shell”. For a more detailed spatial analysis of C_{80} and G in the auditorium, see Hayes et al. [9].

Occupancy

It should be re-emphasized that these measurements were taken with the stage and auditorium in an unoccupied state. If measured in an occupied state, these parameter values would change. However, the optimal ranges for the studied objective parameters refer to unoccupied states. A scale model investigation by Dammerud showed a decrease in RT_{60} on stage by about 0.5 s when an orchestra was present on stage [14]. According to a discussion with Dammerud, C_{80} on stage will change significantly with the presence of an orchestra, but this change is difficult to predict because it is dependent upon the stage enclosure design. However, he states that C_{80} can be expected to decrease above 1000 Hz due to attenuation of the direct sound [15]. It is the suggested practice to measure ST1 with chairs, music stands, and instruments on stage, in order to better represent the platform conditions when an orchestra is present. Several researchers have found that ST1 decreases anywhere from 1 to 2.5 dB when chairs, stands, instruments, and even musicians are present (compared to an empty platform) [13, 14, 16]. According to Dammerud [17], $G_{\text{late, stage}}$ will decrease slightly with the addition of an orchestra – more so when an acoustic shell is present, and $G_{\text{late, auditorium}}$ should not decrease significantly with the addition of an audience, given adequate absorption characteristics of the audience seating.

CONCLUSIONS

The addition of the acoustic shell in this study proved a significant benefit based on observed changes in several objective acoustical parameters. The addition of the shell increased RT_{60} , $G_{\text{late, stage}}$ and $G_{\text{late, auditorium}}$, and also ST1. The increase in ST1 was slightly excessive, but by raising the ceiling panels to approximately 7 m above the stage, ST1 is expected to decrease to a level which would be close to optimal. This is expected to enhance the ability of the musicians to hear themselves play, as well as hear the other musicians around them. This, in turn, would have numerous beneficial effects on the ensemble, such as better intonation, resonance, blend, and homogeneity, as well as increased ability to make dynamic adjustments. The average C_{80} for the stage did not change by a significant amount. With the addition of the shell, RT_{60} was brought to within 0.3 s of the optimal range for multipurpose auditoriums. Taking into consideration the fact that $G_{\text{late, stage}}$ and $G_{\text{late, auditorium}}$ were increased to the suggested optimal state, the reverberance perceived by the musicians on the stage should be much improved, providing an enhanced sense of projection and acoustical response from the auditorium. Based on these results, the authors recommended that the Miami University Hamilton campus purchase an acoustical shell, similar to the one in this study, in order to enhance the orchestral acoustics of Parrish Auditorium. A future study with an orchestra present would prove beneficial to provide a subjective analysis of the state of the acoustics with and without the shell.

ACKNOWLEDGEMENTS

We extend our deepest thanks to Jens Jørgen Dammerud, PhD candidate from the University of Bath, who has so graciously offered his expertise in stage acoustics for the purpose of furthering this project. We would also like to thank Miami University and the Department of Engineering Technology for their financial and facilities support.

REFERENCES

1. Gade, A.C. “Investigation of musicians’ room acoustic conditions in concert halls. Part II: Field experiments and synthesis of results.” *Acustica* **69**, pp. 249-262, 1989.
2. Egan, M.D. *Architectural Acoustics*. Ft. Lauderdale, FL: J. Ross Publishing, 2007.
3. Dammerud, J.J., and M. Barron. “Concert hall stage acoustics from the perspective of the performers and physical reality.” *Proceedings of the Institute of Acoustics*. **30**, pp. 26-36, 2008.
4. Barron, M. *Auditorium Acoustics and Architectural Design*. London: E & FN Spon, 1993.

5. Dammerud, J.J. "EstimatingGI_fromTandV." *Stage acoustics for symphony orchestras in concert halls*. Updated 1 Oct. 2009. Accessed 25 Jan. 2010. <http://home.no/jjdammm/stageac/GI_fromTandV.xls>.
6. ISO 3382-1:2009: Acoustics – Measurement of room acoustic parameters – Part 1: Performance spaces, International Organization for Standardization, Geneva, Switzerland.
7. Beranek, L. "Concert Hall Acoustics – 2008." *J. Audio Eng. Soc.* **56**, pp. 532-544, 2008.
8. Jeon, J. Y. and M. Barron. "Evaluation of stage acoustics in Seoul Arts Center Concert Hall by measuring stage support." *J. Acoust. Soc. Am.* **117**, pp. 232-239, 2005.
9. Hayes, B., Braden C., Averbach R., Ranatunga, V. "Determination of Objective Architectural Acoustic Quality of a Multipurpose Auditorium." Paper presented at: SEM Annual Conference & Exposition on Experimental and Applied Mechanics; 2010 Jun 7-10, Indianapolis, IN.
10. Dammerud, J.J. "In-situ calibration of the sound source level for measuring G." *Stage acoustics for symphony orchestras in concert halls*. Updated 1 Oct. 2009. Accessed 2 Feb. 2010. <<http://home.no/jjdammm/stageac/insituGcalib.pdf>>.
11. Dammerud, J.J. "Ge_GI_fromGandC80." *Stage acoustics for symphony orchestras in concert halls*. Updated 1 Oct. 2009. Accessed 26 Jan. 2010. <http://home.no/jjdammm/stageac/Ge_GI_fromGandC80.xls>.
12. Barron, M. and J.J. Dammerud. "Stage Acoustics in Concert Halls – Early Investigations." IOA Proceedings, Copenhagen, Denmark, May 2006.
13. O'Keefe, J. "Acoustical Measurements on Concert and Proscenium Arch Stages." IOA Proceedings, London UK, Feb. 1995.
14. Dammerud, J.J. "Model investigations – preliminary." *Akutek.info*. Updated 3 Oct. 2009. Accessed 8 Mar. 2010. <http://www.akutek.info/Papers/JJD_Model_investigations.pdf>.
15. Dammerud, J.J. "Re: C80." Message to the author. 2 Mar. 2010. E-mail.
16. Skalevik, M. "Orchestra Canopy Arrays – Some Significant Features." Joint Baltic-Nordic Acoustics Meeting, Sweden, 2006.
17. Dammerud, J.J. "Re: Results of Glate." Message to the author. 11 Mar. 2010. E-mail.

Fractional Calculus of Hydraulic Drag in the Free Falling Process

Yuequan Wan

Department of Mechanical Engineering Technology,

Purdue University

Email: ywan@purdue.edu

Richard Mark French, Associate Professor,

Department of Mechanical Engineering Technology,

Purdue University.

138 KNOY, 401 N. Grant St, West Lafayette, IN47906, USA.

Email: rmfrench@purdue.edu

ABSTRACT: A new approach to describe the hydraulic drag received by a falling body has been developed through fractional calculus, and the analytical solution has been given. This new method treats the measurement of the hydraulic drag as the fractional derivative of the falling body's displacement. The existing methods could be classified into two categories. The first ones assume the drag could be described by a quadratic equation of the body's velocity and use the classical Newton law to describe the falling process. The second ones do introduce the fractional calculus to describe the dynamic process but still treat the drag as the quadratic of velocity, which make the physics meaning of parameters are obscure. Compared to existing methods, the new approach introduced in this paper is original from the perspectives of basic hypothesis and modeling. To evaluate the performance of this method, series experiments have been conducted with the help of high speed camera. The data fit the new method successfully, and compared to the existing approaches, the new one has the overall better performance on the accuracy to describe the dynamic process of the falling body and owns intuitive physical explanation of its parameters.

KEYWORDS: fractional calculus, hydraulic drag, falling process,

NOTATION:

F_H Hydraulic drag (Newton)

V Velocity (m/s)

m	Mass of the plug (kg)
β, p	Fractional order of derivative
F_G	Gravity of the plug (Newton)
F_B	Buoyancy of the plug (Newton)
a, b, K	Constant coefficients

1. Introduction

The fractional calculus, in which people consider the order of integral and derivative as any real number, has a history nearly as long as the ordinary calculus, which contains only integer orders^[1]. Recently, the applications of this technology have been successfully found in many fields, such as in viscoelasticity^{[2][3]}, control theory^{[4][5]} and electro-analytical chemistry^{[6][7]}

During a free falling process, traditionally people use quadratic function to approximate the hydraulic drag received by the falling body.^[8] When Reynolds number is low, the hydraulic drag is always described by a linear term of the falling speed, and when facing high Reynolds number situation, people consider the drag as the second order polynomial function of the falling velocity. This is considered to be the classic method which has existed for many years. Aided by the computation fluid dynamics (CFD), now people could simulate the hydraulic drag received at different velocity and fit the simulation result to facilitate further use such as estimating the falling position of an object at any given time. However, the CFD result depends on computational algorithm, environment parameters' setup, and model's quality. Besides, high quality CFD work, especially when dealing with 3-D problem, always consumes great amounts of CPU hours. And its result could still be quite different from the experiment, especially when using it to predict the falling position. Both the quadratic function and CFD methods are based on regular calculus method.

The application of fractional calculus in studying the hydraulic drag during a falling process could be categorized in the fractional viscoelasticity field. There have been scholars applied fractional calculus in the dynamical equation of the falling process, and gained high quality fitness to the historical data^{[9][10]}, however, this method still assume the hydraulic drag is quadratic of the falling velocity, and made modification to the Newton second law while involving terms which do not have intuitive physical interpretations.

In this paper, a new approach which assumes the hydraulic drag could be described by fractional calculus has been developed. And to support, series experiment under controlled environment have been conducted with the help of high speed camera. The result shows that, the new approach from this paper could fit the experiment data soundly, and the hydraulic drag received during this falling process could also be easily accessed. Compared with the existing methods, the advantages of the new approach based on fractional calculus are immediate evident.

2. Case Study and Experiment

In this paper, the free falling process has been studied is quite straightforward. It is a process that a polyurethane plug falling in a tube filled with water. Therefore this experiment could be conducted under fully control, and the results could be generalized into many more complex situations. By filling different materials into the plug, its mass could be modified while keeping the shape and surface unchanged. Different mass of plug lead to different falling process in terms of velocity's range, and provide more data to evaluate the performance of each method.

The high speed camera has been used to acquire the actual positions during the plug's falling. The camera used is a Casio Exillim Ex-F1, and the image processor is a Photron 1024. With respect to different falling process, the number of frames taken in one time unit could be changed to provide best accuracy.

The case studied in this paper and experiment setup could be described in the [figure 1](#). In [figure 1](#), frame (A) describes the case and frame (B) demonstrates the experiment setting. With repeated experiment, groups of data have been collected with respect to five different mass of the plug. [Table 1](#) shows the physics parameters and the falling process data for the first plug.

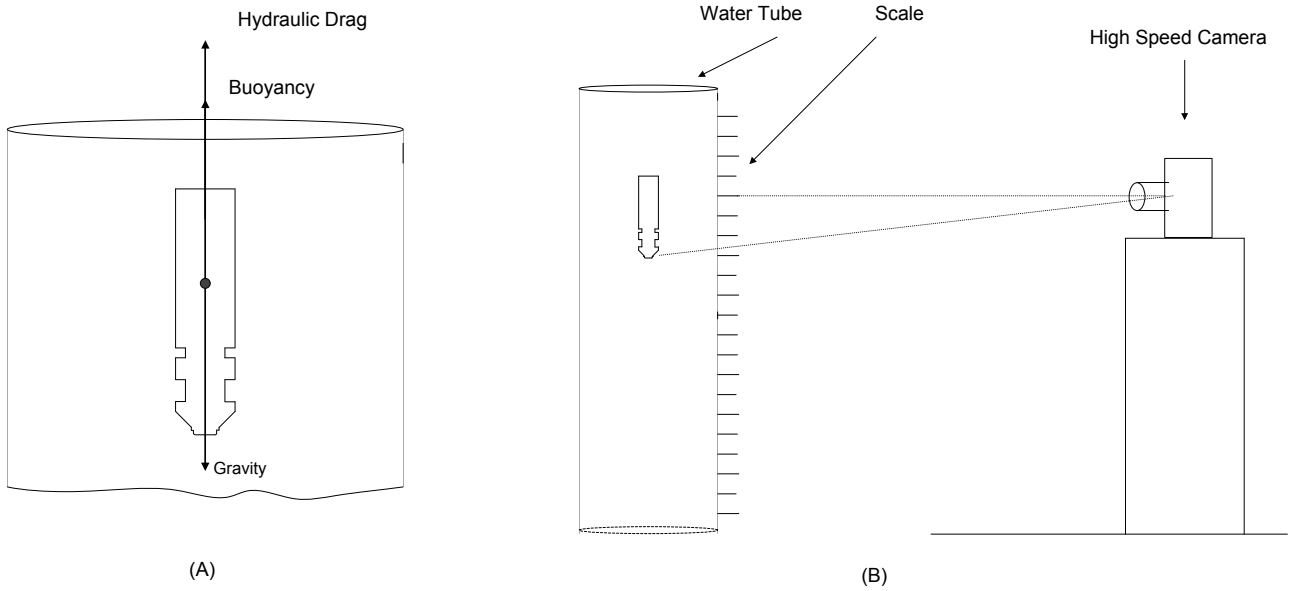


Figure 1, Case and Experiment Demonstration

Table 1: Physics Parameters and Falling Process of Plug#1									
Physics Parameters									
Plug Mass	Plug Volume	Water Density	Buoyancy	Plug Gravity					
0.16471 kg	1.5393e-004 m ³	998.2 kg/ m ³	1.5058 N	1.6142 N					
Falling Position (cm) Against Time (s)									
Position	Time	Position	Time	Position	Time	Position	Time	Position	Time
0	0	7.6956	0.6667	28.2317	1.3333	56.0366	2	88.4756	2.6667
0	0.0667	9.3293	0.7333	30.7927	1.4	59.1463	2.0667	91.5854	2.7333
0.2439	0.1333	10.9146	0.8	33.2927	1.4667	62.3171	2.1333	95	2.8
0.6404	0.2	12.7877	0.8667	35.9146	1.5333	65.4878	2.2		
1.2195	0.2667	14.5795	0.9333	38.7195	1.6	68.5366	2.2667		
1.8293	0.3333	16.8981	1	41.5244	1.6667	72.2355	2.3333		
2.7439	0.4	18.9024	1.0667	44.3293	1.7333	75.5484	2.4		
3.7195	0.4667	20.9431	1.1333	46.8825	1.8	78.3537	2.4667		
4.939	0.5333	23.3537	1.2	50.061	1.8667	81.5244	2.5333		
6.2846	0.6	25.6707	1.2667	52.8219	1.9333	85	2.6		

The physics parameters of the other four plugs are summarized in the [table 2](#).

Table 2, Physics Parameters of Plug #2~#5				
Physics Parameters of Plug #2				
Plug Mass	Plug Volume	Water Density	Buoyancy	Plug Gravity
0.15716 kg	1.56e-004 m ³	998.2 kg/ m ³	1.526048 N	1.5402 N
Physics parameters of Plug #3				
Plug Mass	Plug Volume	Water Density	Buoyancy	Plug Gravity
0.16062 kg	1.56e-004 m ³	998.2 kg/ m ³	1.526048 N	1.5741 N
Table 4, physics parameters and falling process of Plug #4				
Physics Parameters of Plug #4				
Plug Mass	Plug Volume	Water Density	Buoyancy	Plug Gravity

0.16206 kg	$1.56e-004 \text{ m}^3$	998.2 kg/ m^3	1.526048 N	1.5882 N
Physics Parameters of Plug #5				
Plug Mass	Plug Volume	Water Density	Buoyancy	Plug Gravity
0.16544 kg	$1.56e-004 \text{ m}^3$	998.2 kg/ m^3	1.526048 N	1.6213N

Figure 2 is a sample of the picture acquired during the falling process.

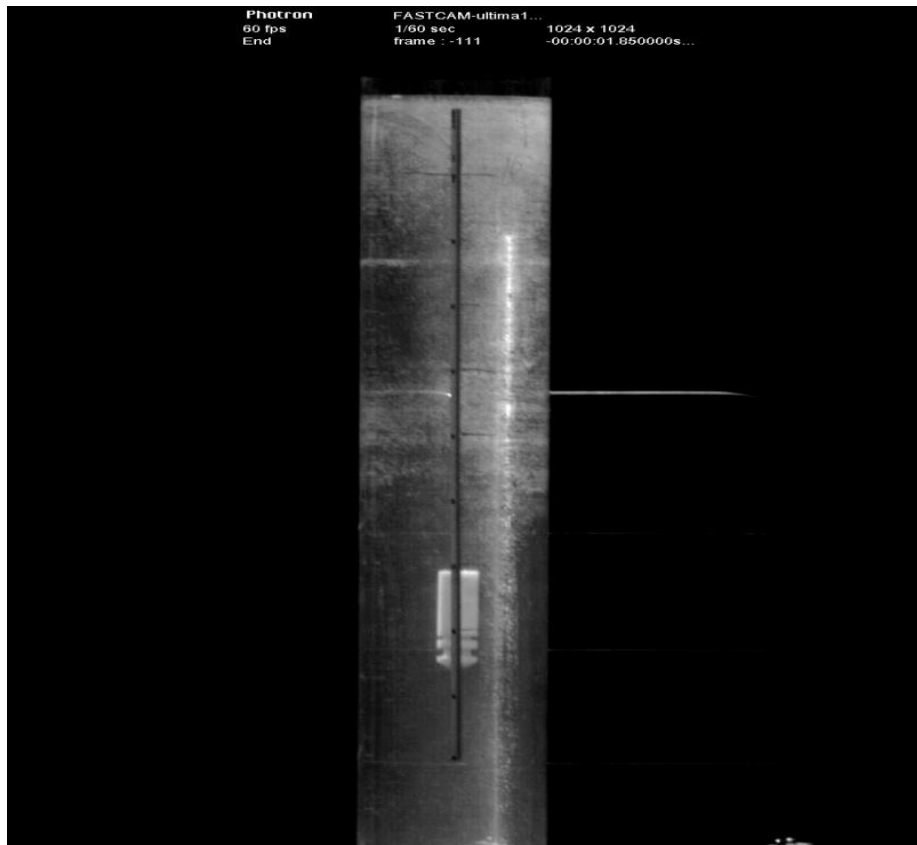


Figure 2, Sample of Picture Acquired

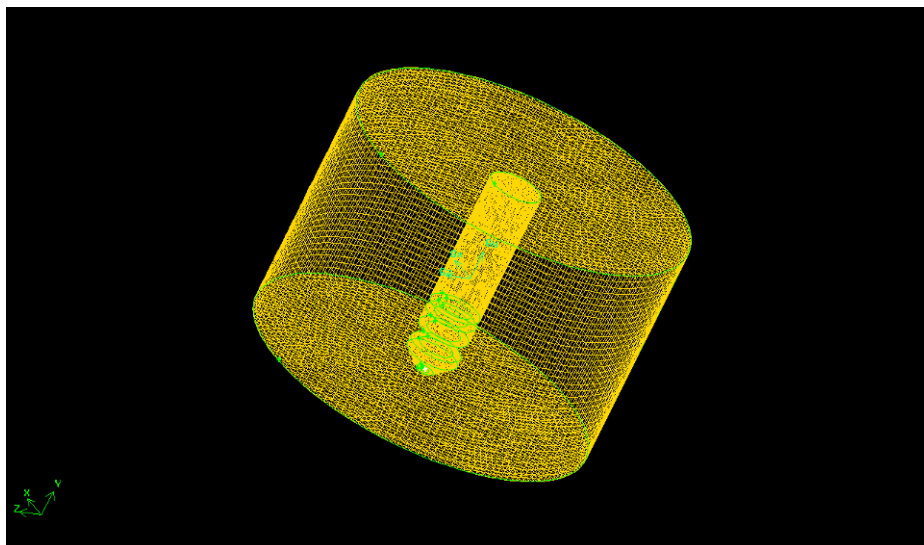


Figure 3, CFD Model Demonstration

For comparison purpose, a CFD model has also been built, and various simulation have been carried out under different flow velocities. The [figure 3](#) demonstrates the CFD model and the table 3 consists of the data collected during the simulation. Based on the simulation result of the drag force at different velocities, one could obtain a fine fit of the hydraulic force into a polynomial equation with no interception as the equation (1), and the fitted result is showed in the [figure 4](#).

$$F_H = 0.7785V^2 + 0.0317 V \tag{1}$$

Force	Velocity	Force	Velocity	Force	Velocity	Force	Velocity	Force	Velocity
0.000182	0.01	0.012472	0.11	0.041023	0.21	0.084929	0.31	0.143984	0.41
0.000593	0.02	0.014622	0.12	0.04473	0.22	0.090154	0.32	0.150709	0.42
0.001209	0.03	0.016932	0.13	0.048588	0.23	0.095522	0.33	0.157592	0.43
0.002015	0.04	0.019399	0.14	0.052598	0.24	0.101049	0.34	0.164649	0.44
0.003001	0.05	0.022024	0.15	0.056762	0.25	0.106729	0.35	0.171813	0.45
0.004162	0.06	0.024801	0.16	0.061078	0.26	0.112566	0.36	0.179128	0.46
0.005493	0.07	0.027735	0.17	0.065545	0.27	0.118547	0.37	0.186646	0.47
0.00699	0.08	0.030827	0.18	0.070164	0.28	0.124676	0.38	0.194274	0.48
0.008654	0.09	0.034071	0.19	0.074935	0.29	0.130949	0.39	0.202057	0.49
0.010482	0.1	0.037469	0.2	0.079856	0.3	0.137392	0.4	0.210005	0.5

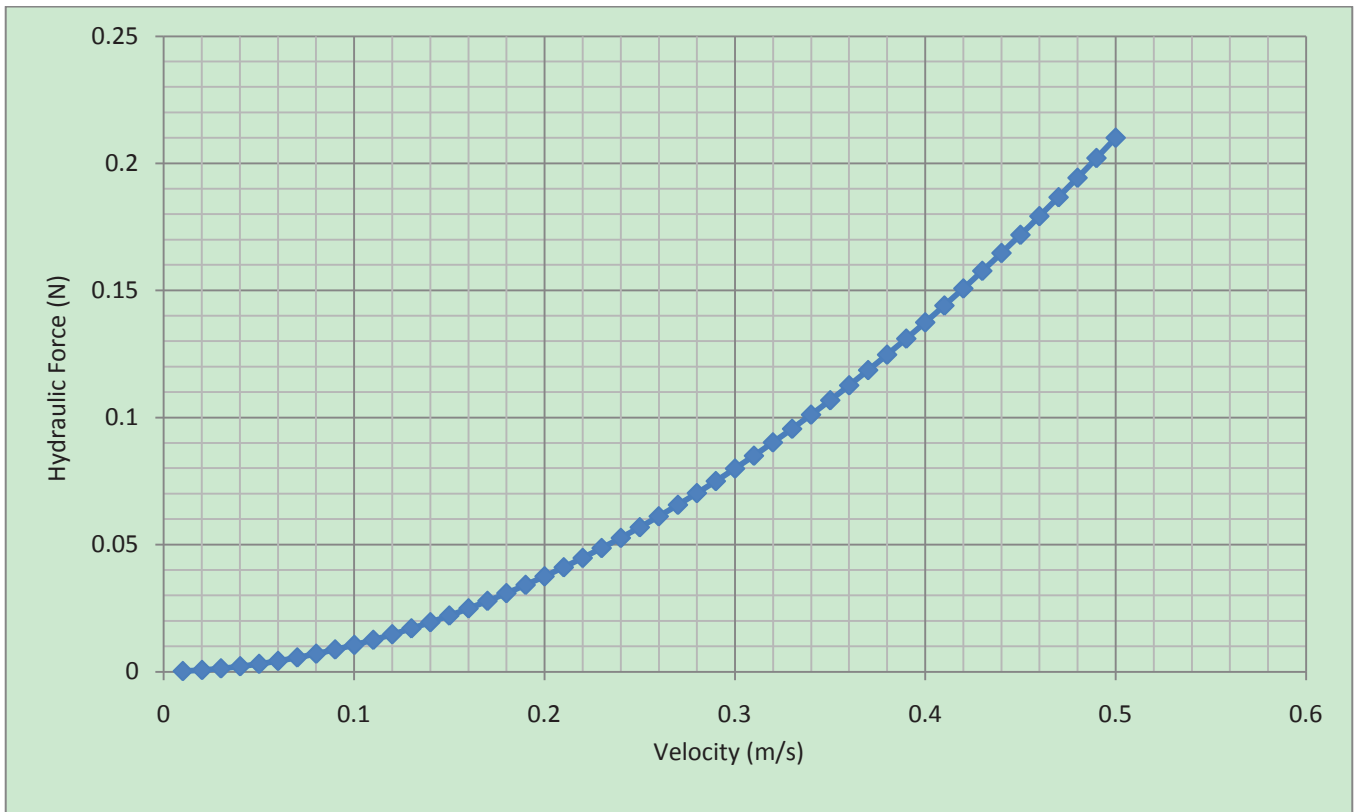


Figure 4, Fitted Hydraulic Force Received by the Plug at Different Velocities

3. Methodology

In this paper, the study is focused on the performances of the method which use fractional calculus to describe the hydraulic drag. To make comparisons, traditional method and CFD method are also involved.

Begin with the most classic quadratic method, which assumes the hydraulic drag could be described by a quadratic function as showed in equation (2)

$$F_H = a * V^2 + b * V \quad (2)$$

Apply the Newton second law in the studied case, one could get:

$$m * \frac{dV}{dt} = F_G - F_B - (a * V^2 + b * V) \quad (3)$$

And the solutions of (3) are:

$$V(t) = \beta + (\alpha - \beta) * \left(1 - \frac{\alpha}{\beta} * \exp\left(-\frac{a}{m} * (\alpha - \beta) * t\right)\right)^{-1} \quad (4)$$

$$Y(t) = \beta * t + \frac{m}{a} * \log\left(-\beta + \alpha * \exp\left(-\frac{a}{m} * (\alpha - \beta) * t\right)\right) + (\alpha - \beta) * t - \frac{m}{a} * \log(\alpha - \beta) \quad (5)$$

The $Y(t)$ in (4) represents the displacement of the falling plug, and the α and β in (4) and (5) are:

$$\alpha = \frac{1}{2*a} (-b + \sqrt{b^2 + 4 * a * F_G - 4 * a * F_B}) \quad (6)$$

$$\beta = \frac{1}{2*a} (-b - \sqrt{b^2 + 4 * a * F_G - 4 * a * F_B}) \quad (7)$$

Equations (2) through (5) are the classical method to describe the free falling process. The constant coefficients in (3) could be optimized by searching algorithm, such as the classic genetic algorithm^[11], the one has been used in this study.

Based on the CFD result, equation (1), one could obtain the constant coefficient in (3) immediately. However, as mentioned in introduction, the result based on CFD varies depending on the change of several factors. The coefficients find by CFD could be better if one optimized those factors, but tradeoff will include time and CPU hours.

For the fractional calculus method focused in this study, the basic assumption is that the hydraulic drag received by any falling body could be approximated through the fractional calculus, as described by (8)

$$F_H = K \frac{d^p Y(t)}{d t^p} \quad (8)$$

Apply the basic Newton law, one could have

$$m \frac{d^2 y(t)}{d t^2} = mg - F_B - K \frac{d^p Y(t)}{d t^p} \quad (K > 0) \quad (9)$$

There are several accepted definitions of the fractional derivative, $\frac{d^p Y(t)}{d t^p}$. And the one involved in this study is defined by Caputo^[12]. This definition gives the solid physics meaning of the initial condition^[13], which makes the application of equation (9) is straightforward. The figure 5 shows the trajectory of the hydraulic drag verses different p and K . For the purpose of better demonstration, the hydraulic drag is showed in its log formation in figure 5. And the calculation is based on the experiment data in table 1.

As showed in figure 5 (A), when the fractional order changes from 0 to 3 and the constant coefficient changes from 0 to 1, the hydraulic drag could vary roughly from e^{-6} to e^{10} Newton, a very large range. This shows the fractional calculus equation (8) could be very capable to describe the hydraulic drag that changing dramatically. One could fix the coefficient K and plot another trajectory as in the figure 5 (B), this figure demonstrates how the hydraulic drag changes with respect to the fractional order, and the plot implies that the variation of hydraulic drag mainly stems from the change of the fractional order.

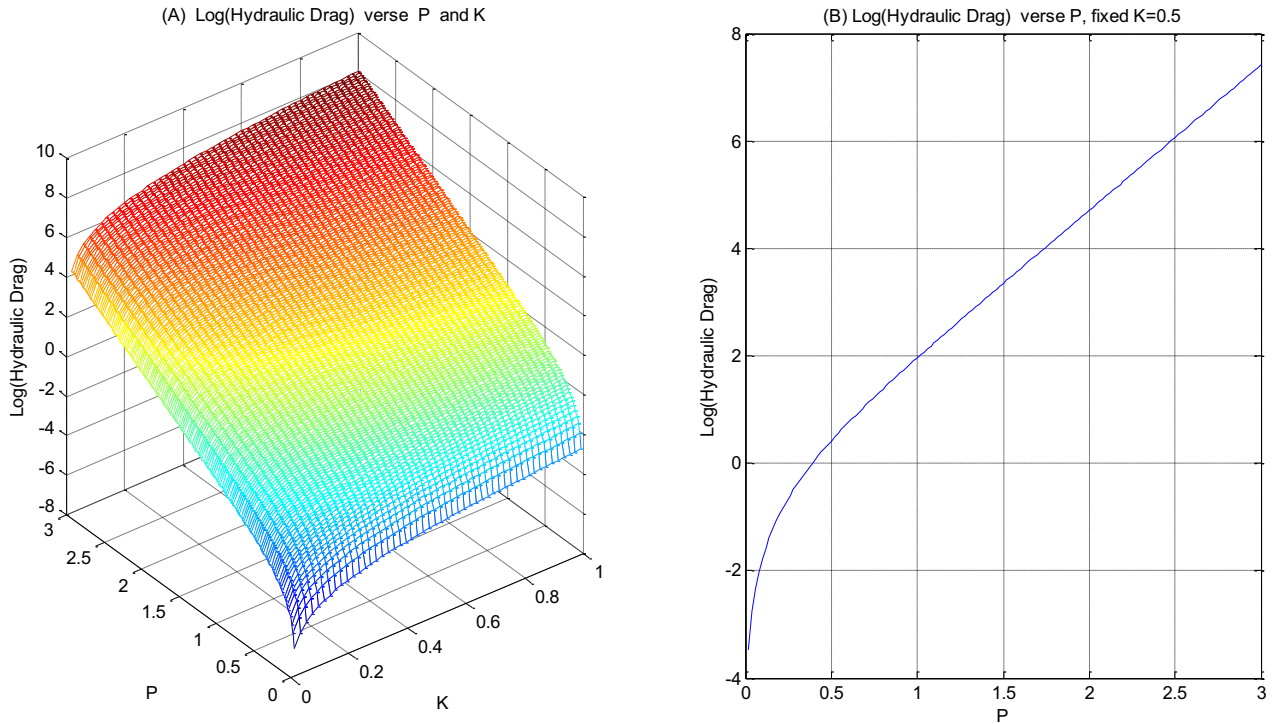


Figure 5, Hydraulic Drag Trajectory Based on Fractional Calculus

Following the Caputo's definition of fractional derivative, people could solve equation (9) in different ranges of the order p .

For $2 < p < 3$, the Fractional Laplace Transform^[14] of (9) is:

$$m[s^2 Y(s) - sY(0) - Y'(0)] = \frac{C_1}{s} - K[s^p Y(s) - s^{p-1} Y(0) - s^{p-2} Y'(0) - s^{p-3} Y''(0)] \tag{10}$$

In (10),

$$C_1 = mg - F_B \tag{11}$$

Take the notes that, $Y(0) = y_0$, $Y'(0) = v_0$, $Y''(0) = a_0$, people get (12) from (10)

$$Y(s) = \frac{1}{s^{p-2+r}} \left[\frac{C_1}{K} s^{-3} + r v_0 s^{-2} + r y_0 s^{-1} + y_0 s^{p-3} + V_0 s^{p-4} + a_0 s^{p-5} \right] \tag{12}$$

And in (12), $r = \frac{m}{k}$

Use the inverse Laplace transform to solve (12) term by term, one would obtain:

$$Y(t) = \frac{C_1}{K} t^p E_{p-2,p+1}(-rt^{p-2}) + r v_0 t^{p-1} E_{p-2,p}(-rt^{p-2}) + r y_0 t^{p-2} E_{p-2,p-1}(-rt^{p-2}) + y_0 E_{p-2,1}(-rt^{p-2}) + v_0 t E_{p-2,2}(-rt^{p-2}) + a_0 t^2 E_{p-2,3}(-rt^{p-2}) \tag{13}$$

In (13), $E_{\alpha,\beta}(z)$ is the two factors Mittag-Leffler function^[15] defined as in (14).

$$E_{\alpha,\beta}(z) = \sum_{k=0}^{\infty} \frac{z^k}{\Gamma(\alpha k + \beta)} \quad (\alpha > 0, \beta > 0) \tag{14}$$

Notice that, in (14) $\alpha > 0, \beta > 0$, this is the reason we have $p-2$ in (13) when $p > 2$, and the reason one needs to solve (9) in different ranges of p .

Similarly, note, $\tau = \frac{k}{m}$, one could have :

$$Y(t) = \frac{C_1}{m} t^2 E_{2-p,3}(-\tau t^{2-p}) + V_0 t E_{2-p,2}(-\tau t^{2-p}) + y_0 E_{2-p,1}(-\tau t^{2-p}) + \tau y_0 t^{2-p} E_{2-p,3-p}(-\tau t^{2-p}) + \tau v_0 t^{3-p} E_{2-p,4-p}(-\tau t^{2-p}) \quad (1 < p < 2) \tag{15}$$

and

$$Y(t) = \frac{C_1}{m} t^2 E_{2-p,3}(-\tau t^{2-p}) + V_0 t E_{2-p,2}(-\tau t^{2-p}) + y_0 E_{2-p,1}(-\tau t^{2-p}) + \tau y_0 t^{2-p} E_{2-p,3-p}(-\tau t^{2-p}) \quad (0 < p < 1) \tag{16}$$

Sum up the above equations from (13) to (16), and take the initial condition $v_0 = 0, y_0 = 0$, the solution to the fractional hydraulic equation (9) is as in (17) :

$$Y(t) = \frac{C_1}{m} t^2 E_{2-p,3}(-\tau t^{2-p}) \quad (0 < p < 2, p \neq 1) \tag{17}$$

$$Y(t) = \frac{m}{k^2} C_1 \left[\exp\left(-\frac{K}{m} t\right) - 1 \right] + \frac{C_1}{K} t \quad (p = 1)$$

$$Y(t) = \frac{C_1}{k+m} * \frac{t^2}{2} \quad (p = 2)$$

$$Y(t) = \frac{C_1}{K} t^p E_{p-2,p+1}(-rt^{p-2}) + a_0 t^2 E_{p-2,3}(-rt^{p-2}) \quad (2 < p < 3)$$

In section 4 of this paper, the equations (1), (5) and (17) are those fitted to the experiment data, and the results are used to evaluate the performance of the hydraulic drag methods, with respect to the CFD method, quadratic method, and the fractional calculus method.

4. Results and Analysis

This section is to analysis the methods described in section 3 in terms of their performance when fitting the experiment data. For equation (5) and equation (17), one could use optimization algorithms to find the optimum parameters which can provide the minimum of mean square errors (MSE), and then compare their performance. For the CFD method, one could use the result from equation (1), and find the mean square errors when fitting to the experiment data. The parameters and the qualities of the fitness to the experiment data of plug #1 are summarized in the [table 5](#).

Table 5, Fitting Result and Parameters of Plug # 1				
Quadratic Method		CFD Method	Fractional Calculus Method	
a	0.000127	0.7758	P	0.4174
b	0.262589	0.0317	K	0.2542
MSE	8.3352 cm ²	> 50 cm ²	MSE	0.3764 cm ²

The result shows that among the three methods studied, the fractional calculus method could provide the best fitness to the experiment data of the plug #1, and the CFD method provides the worst case of fitness. However, as mentioned above, the result of CFD is subject to improvement if one built more detailed models and set more accurate environment parameters.

The result of the quadratic method is more informative here. It implies that even with the optimized parameters the method which describes hydraulic drag by a quadratic equation is less capable to fit the data than the fractional calculus one. Therefore, even if people improved the CFD setups, it would still lacks accuracy to reality as long as the simulated result of drag falls into a quadratic function of falling velocity.

The fitness of equation (1), (5) and (17) to the experiment data of plug #1 is as in the [figure 6](#). Comparing the frame (A) and (B) with (C), the advantage of fractional method is evident. This method could be used to calculate the falling position of plug at a given time.

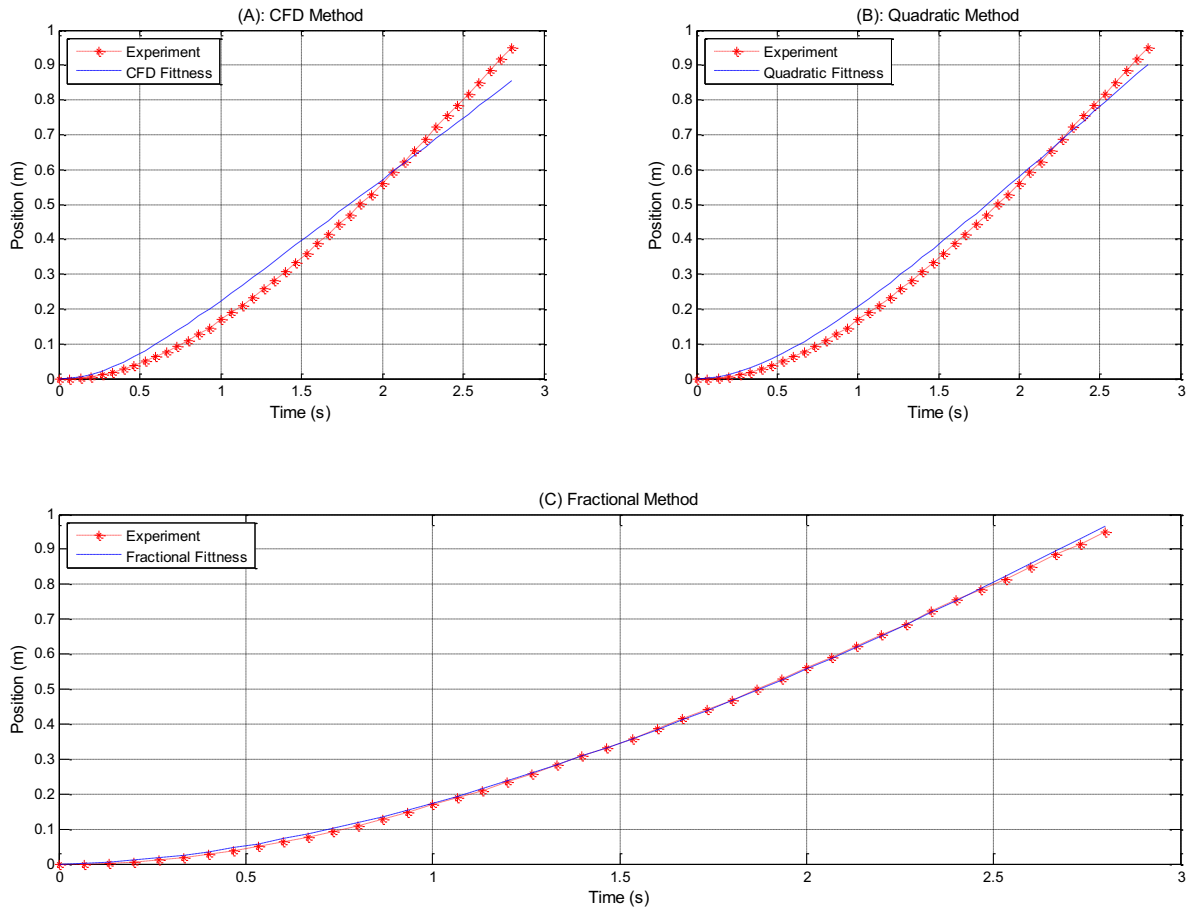


Figure 6, Comparison of Fitness among different method

Using the fractional method, now proceed to fit the experiment of plug #2 to #5. The physics parameters of those four plugs are listed in [table 2](#). The optimum parameters found and the corresponding mean square errors of fitness to each plug are summarized in [table 6](#).

By reading [table 5](#) and [table 6](#), people can conclude that the fractional method as demonstrated by equation (9) and solved by equation (17) is capable to describe the falling process of plug #1 to plug #5 in this study. And have advantages in terms of fitness when comparing with the classic methods.

Plug	# 2	# 3	# 4	#5
P	0.5132	0.2649	0.0244	0.0102
K	0.1857	0.1564	0.1466	0.1466
MSE	1.0913 cm ²	0.2785 cm ²	0.4109 cm ²	3.6966 cm ²

The fitness to plug #2~plug#5 are demonstrated by [figure 7](#) as in following.

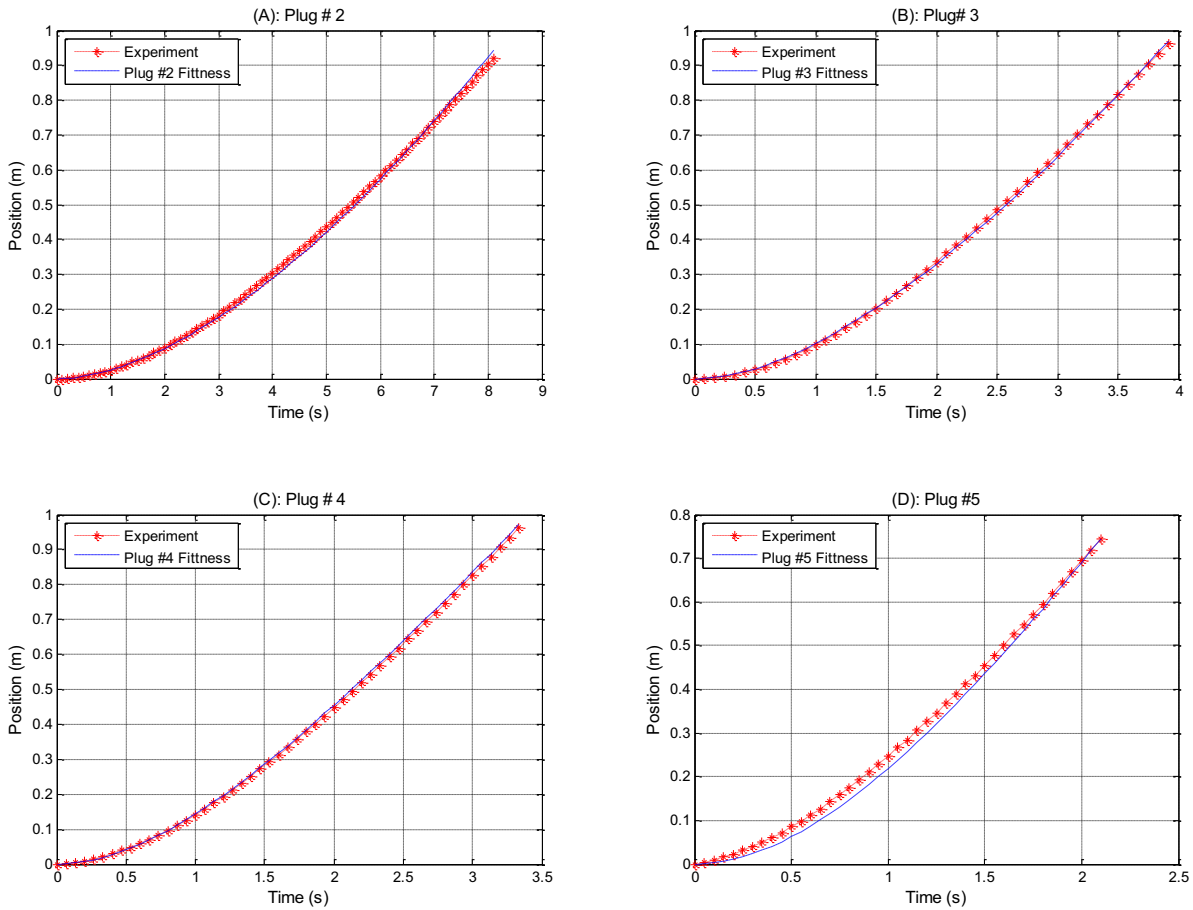


Figure 7, Fitness of Fractional Calculate Method to the Experiment Data, Plug #2~#5

5. Discussion and Conclusion

1. The fractional calculus method described in this paper is quite capable to describe the falling process studied in this paper, and the result could be generalized to other similar process.
2. In terms of fitness to the real following process, the fractional calculus method has advantages when compared to the classic methods, and the CFD method.
3. By changing the combination of the fractional order and the coefficient, the hydraulic drag provided by the fractional method will change dramatically.
4. The results of the fitness for the fractional calculus method implies that to obtain the best fitness to different plugs, the fractional order changes in a larger range than the coefficient do. This would lead to a following research question, which is to find the factors that influence the fractional order in the free falling process.

Proceed with the discovered new research question, the work will continue with more experiment and more crossover fitness to explore the influencing factors to the fractional order when describing the falling process by the fractional calculus method. And the proposed method will be used into more complex situations to evaluate its overall performance.

Reference

- [1] Loverro A., Fractional Calculus: History, Definitions and Applications for the Engineer, 2004
- [2] Mainardi F., Applications of Fractional Calculus in Mechanics, Transform Methods and Special Functions, Varna'96, SCT Publishers, Singapore, 1997.
- [3] Rossikhin Y.A, Shitikova M.V., Applications of Fractional Calculus to Dynamic Problems of Linear and Nonlinear Hereditary Mechanics of Solids, Appl. Mech. Rev. 50,15-67, 1997.
- [4] Bagley R.L. and Calico R.A., Fractional Order State Equations for the Control of Viscoelastically Damped Structures, J.Guidance, vol. 14, no. 5 pp.304-311, 1991
- [5] Makroglou A., Miller R.K. and Skkar S., Computational Results for a Feedback Control for a Rotating Viscoelastic Beam, J of Guidance, Control and Dynamics, vol. 17, no. 1, pp. 84-90, 1994.
- [6] Oldham K.B., A Signal Independent Electro-analytical Method, Anal. Chem., vol.72 pp.371-378, 1976
- [7] Goto M. and Ishii D., Semi-differential Electro-analysis, J. Electro anal. Chem. and Interfacial Electrochemical., vol.61, pp.361-365, 1975
- [8] Wiggins, C. H., and Goldstein R.E. "Flexive and Propulsive Dynamics of Elastica at Low Reynolds Number." Physical Review Letters 80.17 3879-3882, 1997
- [9] Fa, Kwok Sau, A falling body problem through the air in view of the fractional derivative approach, Physica A, Volume 350, Issue 2-4, p. 199-206. May 2005.
- [10] Davis H.T., Introduction to Nonlinear Differential and Integral Equations, Dover, New York, 1962
- [11] Eiben, A. E. et al, Genetic Algorithms with Multi-parent Recombination". PPSN III: Proceedings of the International Conference on Evolutionary Computation. The Third Conference on Parallel Problem Solving from Nature: 78-87, 1994
- [12] Caputo M., Linear Model of Dissipation Whose Q is Almost Frequency Independent - II, Geophys. J.R. Astr. Soc., vol. 13, pp.529-539, 1967
- [13] El-Sayed A. M. A., Multivalued Fractional Differential Equations, Applied. Math and Computer, vol. 80, pp. 1-11, 1994
- [14] Gorenflo, R. and Mainardi F., Fractional Calculus, Integral and Differential Equations of Fractional Order, Fractals and Fractional Calculus in Continuum Mechanics, 223-276, Springer Verlag. New York, 1997
- [15] Erdelyi A., Higher Transcendental Functions, vol.3, McGrawHill, New York, 1955.

Fatigue Cracks in Fibre Metal Laminates in the Presences of Rivets and Cold Expanded Holes

David Backman¹
Eann A. Patterson²

¹National Research Council
Institute for Aerospace Research
1200 Montreal Road, Building M14
Ottawa, Ontario Canada K1A 0R6

²Department of Mechanical Engineering
Michigan State University,
East Lansing, MI, USA
eann@egr.msu.edu

ABSTRACT

In order for new composite materials like fiber metal laminates (FML) to gain acceptance in the aerospace field, it is important to understand the effect on them of common manufacturing techniques such as riveting and cold expansion. A comprehensive research program was initiated using two advanced strain measurement techniques; digital image correlation and thermoelastic stress analysis, to understand the failure mechanisms in FML materials that had been fatigue cycled after having undergone hole cold expansion or riveting. Prior theoretical work has shown the potential for improvement in fatigue life of FMLs, so one standard grade of FML (FML 4-3/2) and a novel FML variant were manufactured and tested. Thermoelastic stress analysis was employed to measure strains on the mandrel exit face while digital image correlation was used to measure strains on the mandrel entry face in the coupons and additional insight was gained regarding the effect of the cold expansion process and of riveting on fatigue crack growth. The results also highlighted the effect of material design on fatigue life as well as the interaction between residual strains and fatigue crack growth.

INTRODUCTION

This study forms part of a larger research program with the overall objective of increasing the acceptance of fiber metal laminate (FML) materials in aerospace applications. This work focuses on fatigue cracks in FML resulting from cold expansion and riveting. In order for FML to be accepted as a direct replacement for aluminum alloys it is important to understand the static and fatigue properties of these materials when they undergo common procedures such as riveting or hole cold expansion. One potential issue with FML 4, when compared to standard aluminum alloys, is its orthotropic nature and the significant drop in stiffness at 45° to the longitudinal axis of the material. As a result, for this investigation both standard FML 4, comprised of three sheets of aluminum with a [90/0/90]_s glass prepreg, as well a new FML variant with more quasi-isotropic material properties were tested.

EXPERIMENTAL PROCEDURE

For this experiment, panels of FML-4-3/2 were produced in-house by the NRC composite fabrication facility. These panels measured 12 inches by 12 inches square and were water jet cut according to the cut plan in [Figure 1a](#) and then machined to the final dimensions shown in [Figure 1b](#). One coupon from each blank was set aside for static testing and the others were used for the fatigue test. For this test all fatigue coupons were cut with the long axis of the coupon oriented in the longitudinal direction.

For the cold expansion portion of the test, tension-tension fatigue testing of the FML coupons was performed at three stress levels (24, 26 and 29 ksi) with a stress ratio of 0.01. All coupons were center drilled with an open hole of 0.241 inches in diameter and half the coupons had this central hole cold expanded using split-sleeve cold-expansion tooling (Fatigue Technology Inc, Seattle WA). On the entry side of the coupon, a 2D digital image correlation system (Correlated Solutions Inc, Columbia SC) was used to measure the strain field during cold expansion as well as to monitor changes in the strain field during fatigue loading. An AVT Marlin camera (Allied Vision Technologies Inc.) with a C-mount lens and an extension tube provided a high magnification image that allowed image correlation to be performed without the need for any painting or speckling of the surface. This also allowed for optical tracking and measuring of crack growth. On the mandrel exit side of the coupon a thermoelastic stress analysis system (Deltatherm 1400, Stressphotonics Inc.) was used to measure the thermoelastic signal and provide a provide a strain map proportional to the first strain invariant.

For the riveting portion of this test, individual coupons were riveted using an instrumented arbour press (Figure 2a) with a squeeze force of approximately 3000 lb. Since the FML coupons were going to be used in fatigue, a special support fixture and loading platen were integrated into the arbour press (Figure 2b) to help standardize the riveting process and reduce any chance of bending the coupons. Standard 5/32 inch diameter aircraft grade rivets (MS20470AD-5) requiring a clearance hole of 0.161 inches diameter were used and all coupons were tested at a net stress of 38 ksi. On the driven head side of the riveted coupon the same image correlation system as above was employed to measure strain while on the manufactured head side of the coupon the same thermoelastic stress analysis system was used to provide a strain map proportional to the first strain invariant.

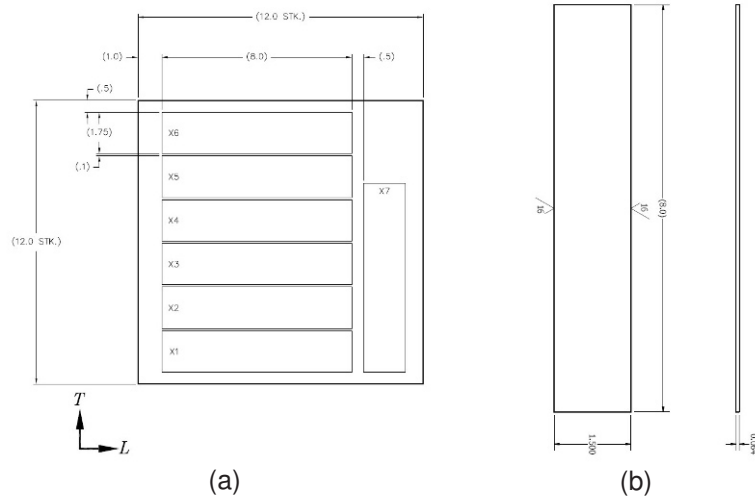


Figure 1: (a) Basic coupon dimensions and material orientations (b) coupon dimensions after machining

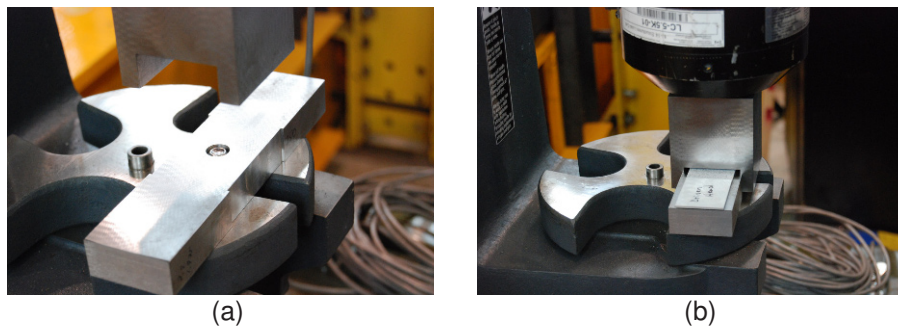


Figure 2: (a) Integral stop and support platen for the coupon during riveting with an (b) instrumented arbor press with load cell

RESULTS AND DISCUSSION

Static cold expansion

Before beginning the fatigue loading of the FML coupons, measurements were made of the strain resulting from the cold expansion process. One of the motivations for producing a more quasi-isotropic FML variant was to reduce the “butterfly” pattern (Figure 3a) seen in the maximum principal strain field following cold-expansion since ideally a more uniform radial strain distribution is desirable. The “butterfly” pattern is a direct result of the orthotropic nature of FML 4 and the new FML 4 variant showed a more uniform strain distribution (Figure 3c) except for the small strain discontinuity at 12 o'clock, resulting from the split sleeve used in the cold expansion process which is also observed in aluminium.

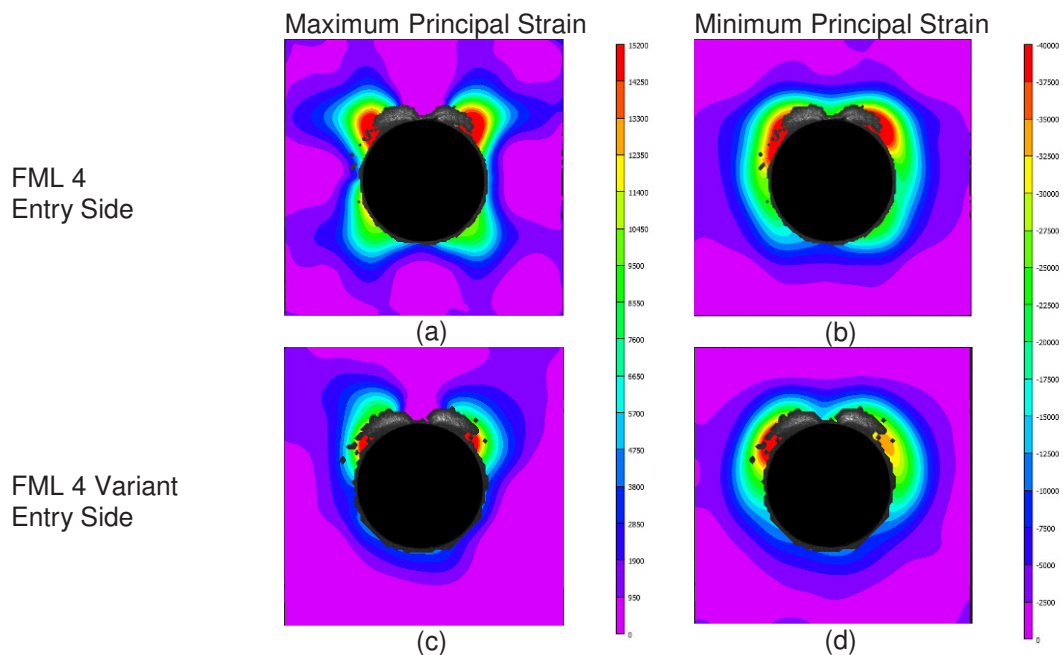


Figure 3: Maximum and minimum principal strains on the entry side of FML 4 and FML 4 variant coupons as a result of cold expansion

Fatigue cold expansion

For both FML materials similarities exist in the development of fatigue cracks, in both cases the crack begins propagating from the stress concentration on either side of the open hole (Figure 4a and Figure 5a) created by the tensile loading. The progressive development with crack growth of the maximum principal strain field is very similar for the two coupons, but it appears that the crack tip strains on the FML 4 variants are slightly higher than those on the standard FML (Figure 4b and Figure 5b). The image correlation results are taken on the entry face of the cold-expanded coupon and they clearly show visual evidence of crack growth. One of the issues with the cold expansion process in monolithic materials has been the three-dimensional nature of the strains imparted by cold expansion. Previous work by Backman et al [1] as well as others [2; 3] have shown that crack growth can differ significantly between the entry and exit faces of a coupon. The TSA results for both the FML 4 and FML 4 variant (Figures 6 and 7) show some gradual reductions in the magnitude of the TSA response around the stress concentration at the hole, but there is no evidence of a crack tip strain field moving away from the edge of the hole with increasing length of the crack. This may indicate that the residual stress generated on the exit face by the cold-expansion is higher and results in delayed or suppressed crack growth compared to the entry face as seen in aluminium specimens [1]. The overall fatigue results are summarized in Figure 8 and show a fatigue life advantage for FML 4 with this specific orientation of fatigue coupon.

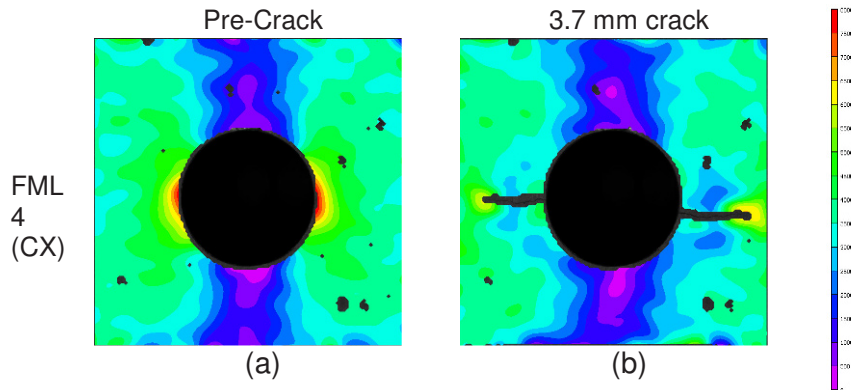


Figure 4: Variation in maximum principal strain with crack growth for FML 4 coupons (entry face)

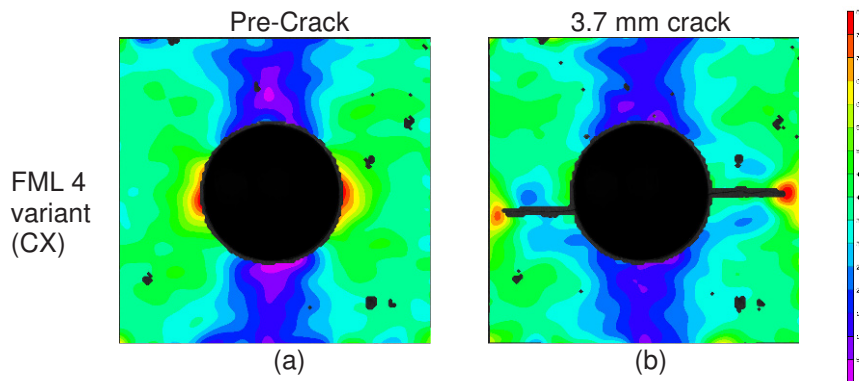


Figure 5: Variation in maximum principal strain with crack growth for FML 4 variant coupons (entry face)

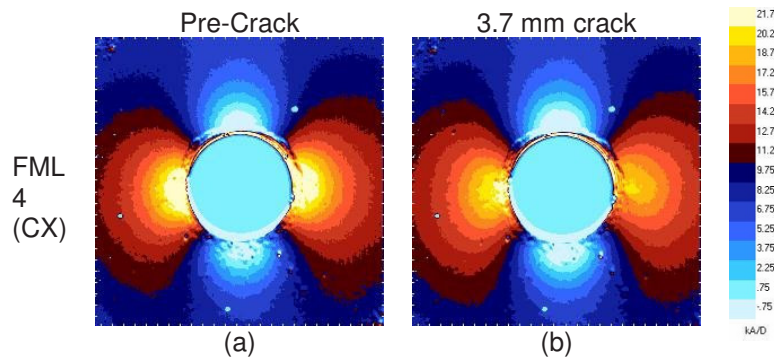


Figure 6: Variation in TSA signal (exit face) during crack growth for FML 4 coupons

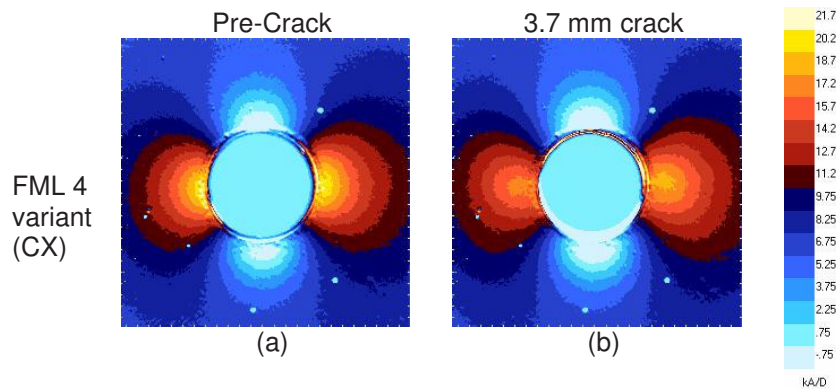


Figure 7: Variation in TSA signal (exit face) during crack growth for FML 4 coupons

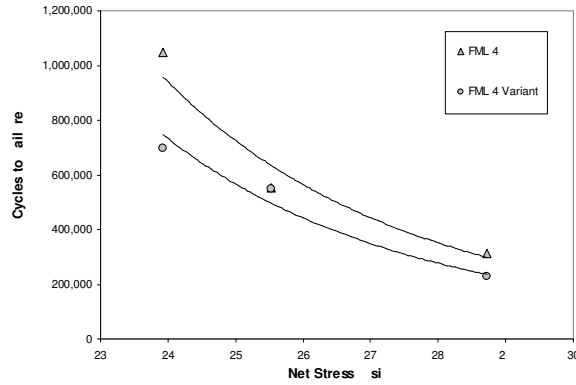


Figure 8: Cycles to failure for cold expanded FML 4 and FML 4 variant at various stress levels

Static riveting results

Measurement of the strain field during and after the riveting process is difficult due to the geometry of the formed rivet, which effectively obscures the region closest to the rivet shank. For this portion of the investigation, image correlation was used to measure strains on both the driven and manufactured head face of a riveted coupon in the region adjacent to the rivet body. The strains for the FML 4 coupon show a smaller version of the “butterfly” pattern with distinct maxima in the strain at 45° increments measured from the horizontal. As with the cold expanded coupons, these regions coincide with the location of the minimum elastic modulus of the material (Figure 9). The FML 4 variant, which was designed to reduce the orthotropy inherent in standard FML 4, shows a much more uniform strain field on both the driven and manufactured head faces (Figure 10) suggesting that the material is more quasi-isotropic in nature.

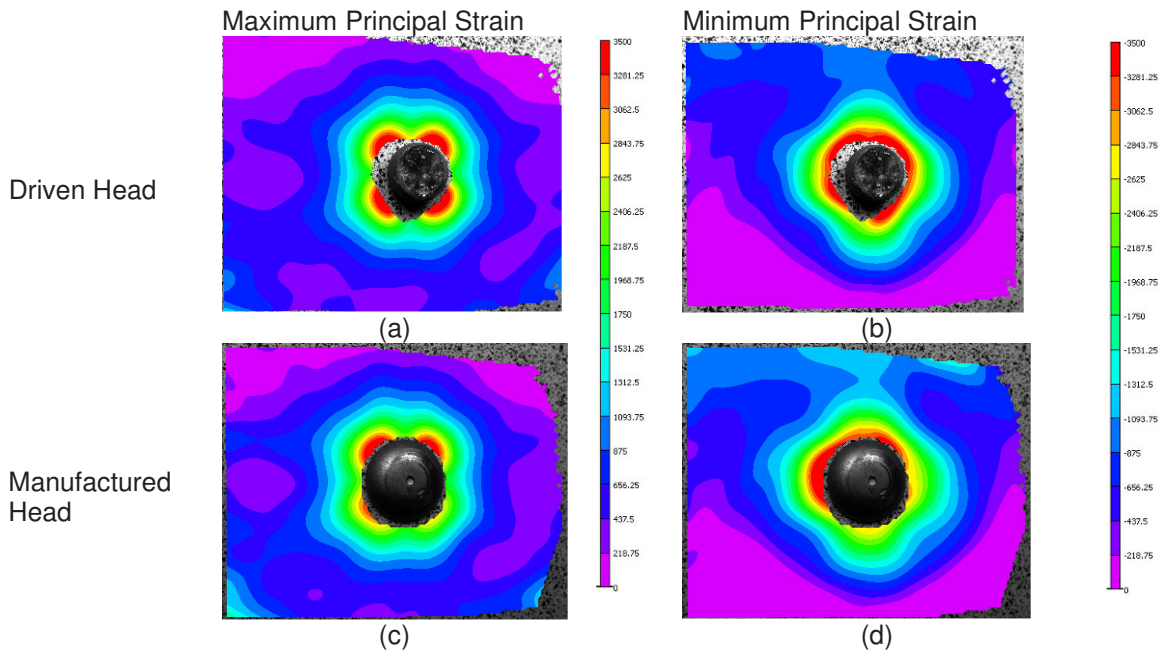


Figure 9: Riveting strains for FML 4 coupons on both driven and manufactured head faces

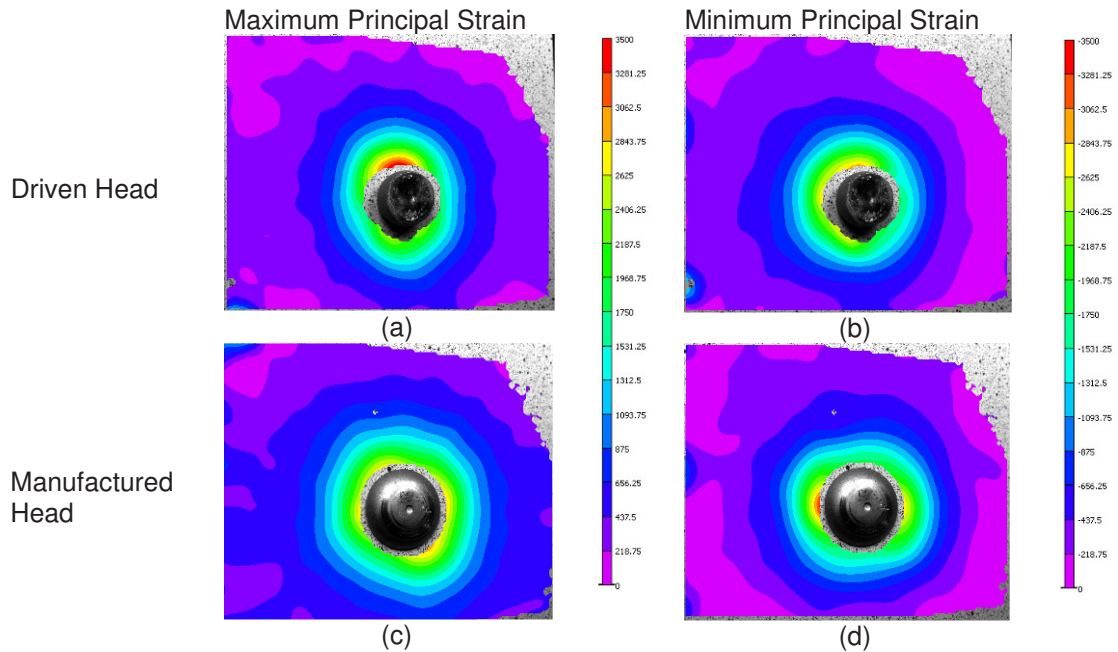


Figure 10: Riveting strains for FML 4 variant coupons on driven and manufactured head faces

Fatigue riveting results

The riveting and cold expansion process share several similarities in terms of the effect on the underlying material. In the case of riveting, there is no re-collapse of the material surrounding the hole, as the rivet shank remains in place, unlike with cold expansion. Another difference, is the clamping force generated around the hole as a result of the rivet process. In the case of a riveted joint, de Rijk et al [4] and others [5] have clearly outlined the positive role rivet clamping plays in reducing fretting fatigue. For the case of an open hole coupon with a rivet inserted, no clear indication existed in the literature regarding the effect on fatigue life. Fatigue testing performed with the riveted coupons at the same net stress levels used for the cold expanded coupons consistently resulted in run-outs in the fatigue test, i.e. no failure. A secondary pilot study showed that for a similar life the riveted coupons would need to be tested at a net stress of 38 ksi, almost 10 ksi higher than with the open hole coupons. Even at these higher stress levels, crack nucleation tended to occur away from the open hole, typically starting at the edges of the coupon and gradually moving inward. Since it was not possible to make standard crack growth measurements, the coupons were compared at the same relative number of cycles. The FML 4 coupon described in this paper failed at 184,301 cycles and the FML 4 failed at 95,501 cycles so comparisons were performed at an arbitrary percentage of the cycles to failure, in this case 75% of their cycles to failure (i.e 138,226 and 71,626 cycles respectively). Figure 11 shows the maximum principal strain field pre-crack initiation (Figure 11a) and at 75% cycles to failure (Figure 11b). Even with the apparent strain concentration centered on the rivet, no clear fatigue cracks have formed in this area. The TSA images obtained from the face with the manufactured head show even less change between the pre-crack condition (Figure 11c) and the coupon at 75% of its cycles to failure (Figure 11d).

For the FML 4 variants, the maximum principal strains, both pre-crack (Figure 12a) and at 75% of failure (Figure 12b) show slightly higher strains than with FML 4. The TSA images taken on the face with the manufactured head, show similar magnitudes pre-crack (Figure 12c) but at 75% of failure the TSA strain pattern is possibly indicative of the beginning of a micro-crack. The regions of low TSA signal centered at 12 o'clock and at 8 o'clock are artefacts caused by paint chipping as a result of fretting between the rivet manufactured head and the coupon face. Unlike with FML 4, fatigue cracks nucleated from under the rivet and propagated to the coupon edges. It is likely that the compression afforded by the rivet head is the main driver in changing the nucleation region from under the rivet head to the edge of the coupon. This effect is interesting in light of the consistent failure mode for the cold expanded coupons, where crack nucleation consistently occurred at the edge of the cold expanded hole and may suggest a mechanism for future improvements in fastener technology.

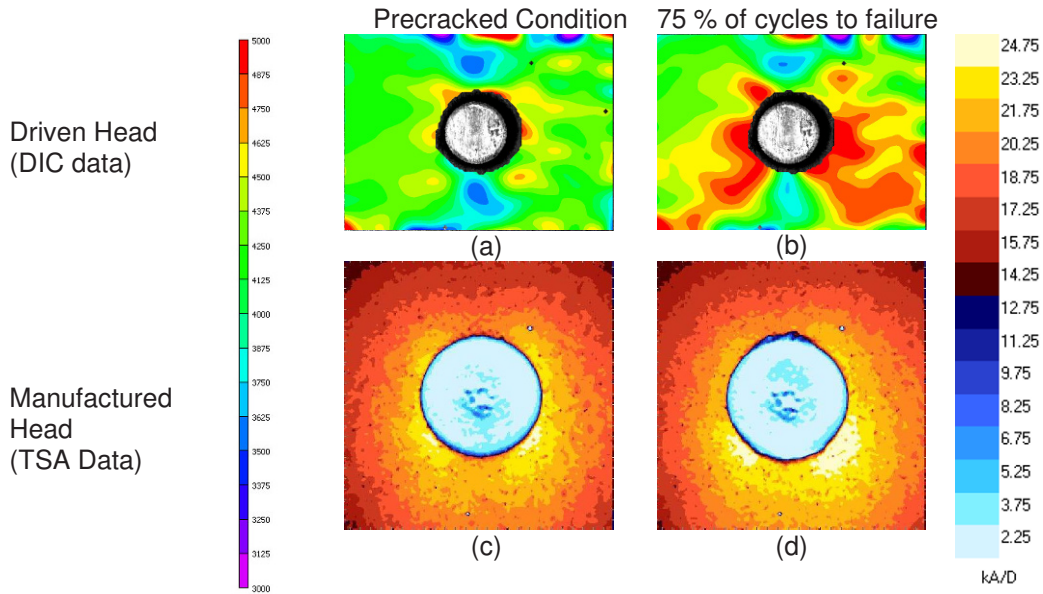


Figure 11: Strain information from faces with the driven and the manufactured head for the FML 4 coupon, at pre-crack formation and at 75% of the number of cycles to failure

The overall fatigue results shown in Figure 13 show that the FML 4 variant has a slightly lower life than standard FML 4. This result is not surprising given that theoretical analysis of the FML 4 variant shows that in the longitudinal direction the modulus of this FML 4 variant is slightly lower than standard FML 4. The true benefit of this FML 4 variant is its quasi-isotropic nature, and future testing will compare FML 4 and FML 4 variant materials at different orientations.

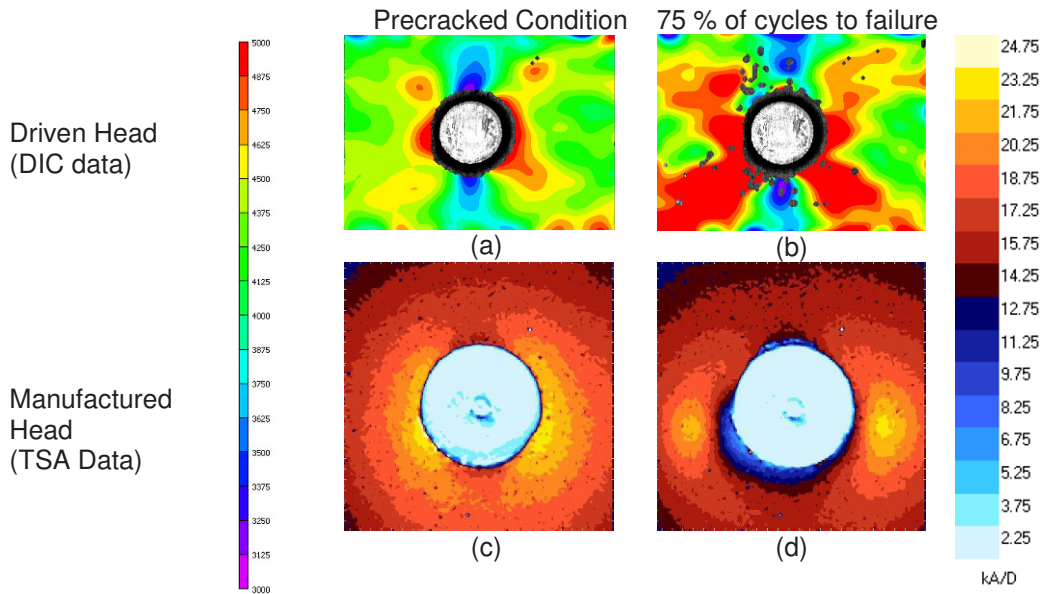


Figure 12: Strain information from the faces with the driven and the manufactured heads for the FML 4 variant coupons, at pre-crack formation and at 75% of the number of cycles to failure

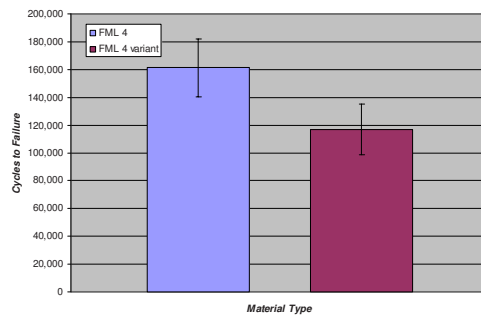


Figure 13: Cycles to failure for open hole and cold expanded FML 4 and FML 4B at various stress levels

CONCLUSION

A new, more quasi-isotropic FML 4 variant has been developed and tested against standard FML 4 after both hole cold expansion and riveting. Both grades of FML 4 show a significant improvement in fatigue life after either process, with standard FML 4 showing an increased fatigue life over that of the FML 4 variant. The static strain results support the conclusion that the new FML 4 variant is more isotropic and further fatigue tests with coupons aligned at the 45° or transverse direction may demonstrate a clearer benefit to using this new formulation. The surprising increase in fatigue life after riveting may suggest an avenue for the future development of interference fit fastener technologies.

ACKNOWLEDGEMENTS

The technical assistance of Mr. Stephan Cloutier and Mr. Richard Bos are gratefully acknowledged. Funding assistance for this project was provided by the Department of National Defence as well as the NRC-IAR New Initiative Funding Program.

REFERENCES

- [1] D.Backman, E.A.Patterson, C.Cowal, Analysis of the effects of cold expansion of holes using thermoelasticity and image correlation, *Fatigue and Fracture of Engineering Materials and Structures*, in press, (2010).
- [2] P.Beaver, J.Mann, J.Sparrow, Fatigue life enhancement by the cold expansion of holes - research and case study, in *Fatigue Prevention and Design* (edited by J.T Barnby), Chamelon Press, 1986, pp. 123-138.
- [3] X.Zhang, Z.Wang, Fatigue life improvement in fatigue aged fastener holes using the cold expansion technique, *International Journal of Fatigue* 25, (2003) 1249-1257.
- [4] J.de Rijck, J.Homan, J.Schijve, R.Benedictus, The driven rivet head dimensions as an indication of the fatigue performance of aircraft lap joints, *International Journal of Fatigue* 29, (2006) 2208-2218.
- [5] R.Muller, An experimental and analytical investigation on the fatigue behaviour of fuselage riveted lap joints, in: PhD Thesis, DELFT University of Technology, 1995

Effect of Nonlinear Parametric Model Accuracy in Crack Prediction and Detection

Timothy A. Doughty, Assistant Professor, University of Portland, 5000 N Willamette Blvd, Portland OR 97203, doughty@up.edu

Natalie S. Higgins, University of Portland, 5000 N Willamette Blvd, Portland OR 97203, higgins11@up.edu

Abstract

The use of nonlinear system identification has been applied to predicting and tracking cracks as they form and propagate through a vibrating cantilevered beam. Continuous Time based nonlinear system identification is used in application to the harmonically excited system. Model parameters are shown to vary as the beam transitions to failure, though no attention has been given to the accuracy of the parameters identified. In this application the effects of fixing sets of model parameters to their known, accurate values is explored as a method to enhance the health monitoring technique.

Introduction

In oscillating systems, damage is often the result of failure due to plasticity, crack initiation and growth as the system experiences fatigue. The ability to detect damage within simple vibrating structural elements is explored here as an obvious starting point for the health monitoring of more complex structures. Much has been done in recent decades to advance nondestructive damage identification in vibrating systems. See Doebling, et al [1] for a comprehensive review. While the phenomenon is highly nonlinear, linear analysis is often used. Among the most popular methods are those which identify cracks formation through changing natural frequencies and mode shapes, or through measured energy absorption [2-6], with the study of crack propagation due to pre-existing and pre-determined damage being well documented [7-9].

Nonlinear vibratory behavior in the presence of damage has long been studied [10]. The inclusion of nonlinearities in the study of crack detection continues to advance the field of modeling crack dynamics. The opening and closing or “breathing” of cracks and the associated system behavior has been the study of analytic, simulation, and experimental work [11-13]. Understanding how the nonlinear model of a system changes in the presence of a crack allows for the detection of crack initiation through observing this nonlinear phenomenon during regular system operation. Still, most experimental studies in this area involve looking for changes in the sub and super-harmonic system response to estimate the size and location of systems with pre-existing cracks. In many cases, impulse tests are used to induce vibration in an otherwise stationary system.

In this paper a cantilevered beam is excited near its second natural frequency. Terms in an established nonlinear model for the system are investigated, with parameter estimates plotted over time as the beam is allowed to oscillate from an initially healthy state through failure due to crack initiation and growth. Collected forcing and response data is used with the Continuous Time identification method, which has been shown to indicate the model’s nonlinear variations

[14]. The method has merit in comparison to more traditional linear approaches, as the nonlinear model explains the apparent change in natural frequency for a healthy system when its level of excitation is varied. The use of Continuous Time is also robust in that it can be applied to non-harmonic excitations and does not require an asymptotic approximation in implementation. In previous work, the method has been successful at detecting damage significantly prior to failure, even without a strong understanding of the model form or the accuracy of the values estimated by the system identification. A follow-up investigated sensitivity to the model chosen and to the number of records used in the identification process.

Emphasis here is given to the theory, identification, and use of the linear model parameters. Results indicate that fixing the actual linear model terms in a nonlinear model may actually hinder the methods ability to detect variations. When the model terms are allowed to vary from their known values, they are able to compensate for shortcomings in the chosen nonlinear model.

Theoretical Model Development

The study presented here is on a horizontally mounted cantilevered beam subjected to vertical excitation. The excitation is at a frequency which is near the beam's second natural frequency, allowing the spatial dependence of the model to be assumed. The theoretical configuration is shown in Figure 1.

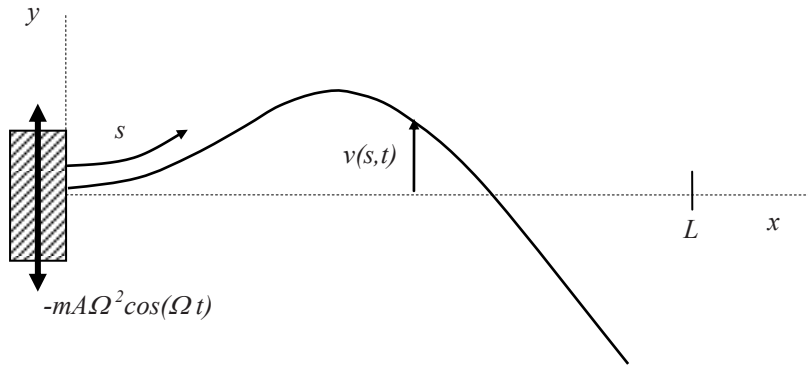


Figure 1. Theoretical Configuration for Base Excited Cantilevered Beam Demonstrating the Second Mode Shape.

In this representation v is the beam's vertical displacement, m is mass per unit length, c is damping per unit length, D_ξ is the bending stiffness, A is the amplitude of base displacement, Ω is the frequency of excitation, t is time, s is a reference variable, and L is the beam length.

The partial differential equation model for the transverse displacement of a cantilevered beam with nonlinear bending stiffness developed in [15] is given with the following partial differential equation and associated boundary conditions:

$$m\ddot{v} + c\dot{v} + D_\xi \left\{ v^{iv} + \left[v'(v'v'')' \right]' \right\} = -mA\Omega^2 \cos(\Omega t), \quad (1)$$

$$v(0,t) = v'(0,t) = v''(L,t) = v'''(L,t) = 0. \quad (2)$$

In the case of modal excitation, the spatial dependence is assumed known. Letting $v(s,t) = a(t) \cdot \phi(s)$, where $\phi(s)$ an orthonormalized mode shape which satisfies the stated boundary conditions, the nonlinear partial differential equation can be reduced to the form:

$$m\ddot{a} + c\dot{a} + ka + \alpha a^3 = F(t), \quad (3)$$

where:

$$k = \left\{ D_{\xi} \int_0^L \phi \phi^{iv} ds \right\}, \quad (4)$$

$$\alpha = \left\{ D_{\xi} \int_0^L \phi \phi^{n3} + 4\phi \phi' \phi'' \phi''' + \phi \phi'^2 \phi^{iv} ds \right\}, \quad (5)$$

and:

$$F(t) = \int_0^L \phi ds (-mA\Omega^2) \cos(\Omega t). \quad (6)$$

With this nonlinear model of the system, a collection of input $F(t)$ and response $a(t)$ can be used to estimate our system parameters. Note that if the nonlinear term, α , is set to zero, the result is the standard linear model for a forced mass-spring-damper system.

System Identification

The linear system parameters lend themselves to estimation through theoretical relationships or simple experimental validation. Both m and D_{ξ} can be estimated from tabulated material properties and the beam's geometry. With the mode shape, $\phi(s)$, known, stiffness k can be determined with Equation 4. Preliminary testing was done to determine the remaining terms in the linear model for the beam being studied. This includes an estimate of the beam's linear natural frequency and damping through the free decay of the beam excited in its second mode.

Nonlinear system identification is inherently more complex. In short, the system must be excited in a way that pronounces the nonlinearities so that information-rich data can be used in identification. Even with suitable data collected, the method of identification is not obvious. Nonlinear differential equations typically have no analytic solution, and so the formulation of algorithms is dependent on the method of approximating the solution to the governing model. While the methods of Multiple Time Scales and Harmonic Balance have both proven to be effective tools for identifying nonlinear model parameters [16], the Continuous Time method was chosen here for its ease of application and for its acceptance of transient time data.

For Continuous Time based system identification, the forcing and response signals are measured. An accelerometer is used in this study, and this is integrated to yield velocity and displacement vectors. The displacement vector is cubed and the state vectors are then collected in a matrix relation which can be solved in a least squares sense for parameter estimates.

Arranging Equation 3 we have:

$$\begin{bmatrix} \ddot{a}(t) & \dot{a}(t) & a(t) & a(t)^3 \end{bmatrix} \begin{bmatrix} m & c & k & \alpha \end{bmatrix}^T = F(t) \quad (7)$$

and

$$\begin{bmatrix} a(t)^3 \end{bmatrix} \begin{bmatrix} \alpha \end{bmatrix} = \{F(t) - m\ddot{a}(t) - c\dot{a}(t) - ka(t)\} \quad (8)$$

Equation 7 allows for the direct estimation of the parameter vector. With the linear parameters known, Equation 7 is easily rearranged to make α the only unknown in the matrix relation, which can then be estimated by solving Equation 8 in a least squares sense where the state vectors are concatenated steady state time responses from select excitation frequencies.

Though this approach does not correspond to curve fitting the nonlinear frequency response function, as the analytic form of this function is not known, it is useful to recognize that collecting steady state data for one sinusoidal forcing frequency would give poor parameter estimates as the data would only give one point along the frequency response trend line. For this reason,

steady state data records are collected over a range of frequencies so as to better define the system parameters. Here, we are using steady state input and response data from a harmonically excited system, though this is not necessary for application of this method. Data records were chosen at frequencies near the resonant frequency and on either side. Simulations have shown that data from these regions can be used to accurately identify similar nonlinear models [17, 18].

Streaming data from the periodic excitation at one near-resonance frequency is used to update one of the state entries in the system identification code. When this data indicates a fundamental change in the system, the result is a change in the estimated nonlinear term. In general application, changes in system response that are due to changes in system input will not notably change the estimation of the nonlinear parameters.

Experiment

The experimental configuration used for observing the initiation and failure of the cantilevered beam is given in Figures 2 and 3. 6061 Aluminum bar stock with dimensions 12.7 x 1.59 x 500mm was excited with a 45N shaker over a range of frequencies around the second natural frequency of the beam. LabVIEW was used in conjunction with National Instruments data acquisition to both excite the shaker and to record the accelerations at the base and on the beam. The beam's acceleration was differenced from the base acceleration, and then scaled according to the accelerometer's calibration and the spatial location along the beam; the accelerometer was located 0.045m from the clamped end. The base acceleration was multiplied by mass and then scaled with the mode shape in accordance with Equation 6. These were then treated as the system's output and input, respectively. The excitation signal from LabVIEW was low-pass filtered to smooth any effects associated with the digital to analog conversion, and signals from the accelerometers were amplified and filtered to remove any high frequency noise. The cut off for the accelerometer signals was chosen to allow for determination of signal content up to the seventh harmonic of the excitation frequency, in accordance with the nonlinear nature of the system being studied.

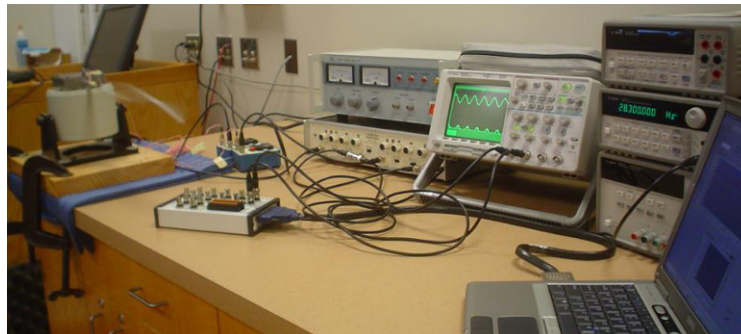


Figure 2: Experimental Staging for Fatigue Testing.

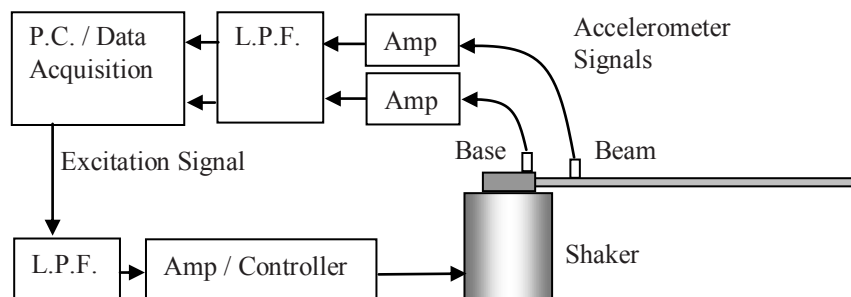


Figure 3: Experimental Configuration for Fatigue Testing.

The beam was secured to the base clamp and subjected to an impulse test, allowing for a rough estimate of the system's resonant frequencies. Exciting the system near its second natural frequency gave a sense of appropriate settings for data acquisition and, by removing the base excitation and recording the decay data, logarithmic decrement was used to estimate the damping associated with mode two. Mass and stiffness can be treated as known for the Aluminum used, leaving the cubic stiffness as the only remaining parameter to be estimated.

Initial sweeps of the excitation frequency indicated pronounced nonlinearities in the systems response for this level of forcing. Sweeping in both increasing and decreasing frequency allowed for identification of the nonlinear and two-solution regions of beam response. The sweep indicated the expected hardening spring effect, where the maximum response amplitude tends to the left as the excitation amplitude is increased.

For the fatigue test a single sine wave excitation was used to generate input and output data. The sample rate for all data collection was chosen to be 10 kHz. With the system resonance near 195 rad/sec, excitation frequencies were chosen at 182.21, 186.00, 189.75, 193.52, 197.29, and 202.32 rad/sec. At each of these frequencies, 0.10 seconds of data was recorded, corresponding to approximately three periods of steady state response. These acceleration signals were then scaled, according both to accelerometer calibration and dependence on the mode shape, and integrated appropriately for entry into the system identification matrices. The beam was then excited near resonance and allowed to shake until failure. The frequency chosen was 193.71 Hz, which produced a large amplitude response. Data from this excitation was collected continually and used to update the final entry in the system identification matrix, each time replacing the previous 0.1 seconds form the same excitation frequency.

Results

The seven records of steady state input output data used in the identification are used to generate the frequency response function seen in Figure 4. The entry at the fatigue excitation frequency of 193.71 rad/sec shows the change in the system's behavior. The linear system parameters have been used in conjunction with a linear model for the system, Equation 3 with the nonlinear stiffness removed, to generate the linear frequency response, which is superimposed.

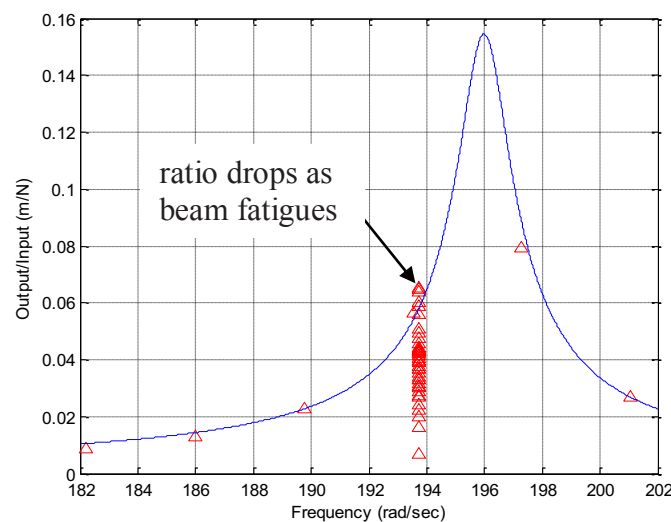


Figure 4: Experimental Nonlinear and Theoretical Linear Frequency Response Data.

In previous reports on this system, the Continuous Time identification was done following Equation 7, and the resulting estimates for the linear parameters were then used with Equation 8. In these applications the linear system parameters had no physical significance. In fact, the

condition of the matrix generated is troublesome as the ratio of displacement column and the acceleration column is nearly constant, owing to the harmonic nature of the response. This problem has been addressed in [17] and is not a concern here since the hope is that the detection of damage will not require the independent identification of linear parameters. In the previous study the methodology identified changes in system behavior approximately 120 minutes into its 218 minute life. The plot of the identified nonlinear coefficient as a function of time is repeated here as Figure 5 for comparison.

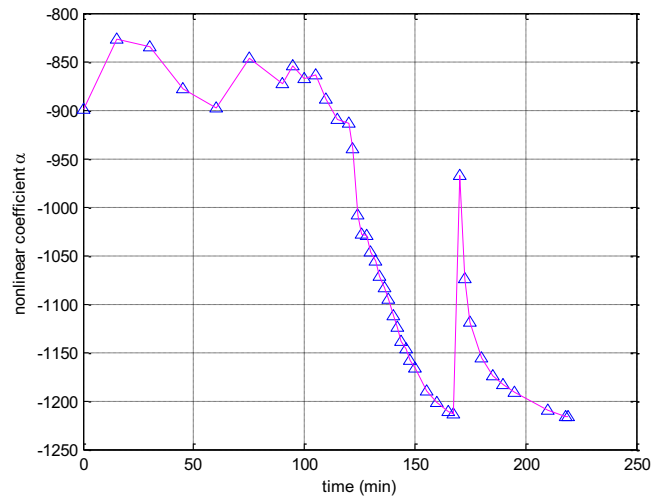


Figure 5: Mapping of Estimated Nonlinear Stiffness during Fatigue Testing with Linear Parameters from Continuous Time Identification. [18]

Updated with the accurate estimates of linear system parameter, Equation 8 is revisited. The result is shown in Figure 6. It is apparent that, with a fixed model and accurate linear model parameters, the behavior of the nonlinear coefficient provides a less clear indication of system changes. The variation over time is much more gradual and the trend that is not monotonic. A few discrete jumps in parameter estimate do exist, but it is not until after the notable change in the parameter estimated by the previous means.

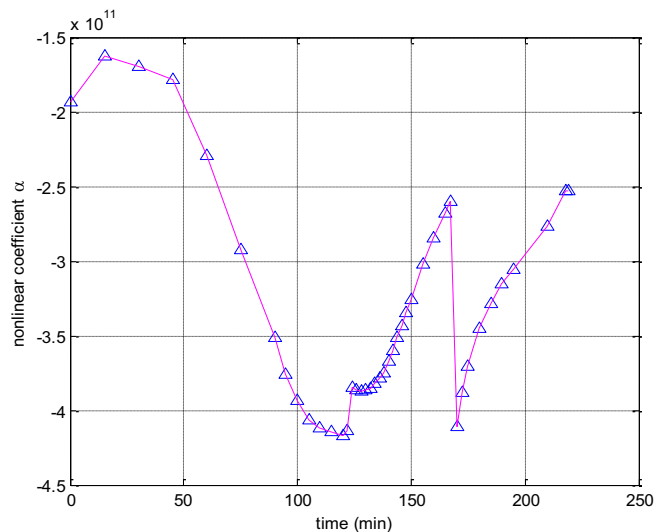


Figure 6: Mapping of Estimated Nonlinear Stiffness during Fatigue Testing with Accurate Linear Parameters.

It is speculated that the poorer performance is due to the mismatch of model to system. Any nonlinear phenomena associated with terms not included in the model can be compensated to some extent by the varying of the linear model parameters. When these parameters are fixed, all changes in behavior must be resolved in the nonlinear term included.

Conclusions

The application of Continuous Time based nonlinear system identification to detecting crack initiation and growth has been shown in previous work to be effective. Over the course of a fatigue test to failure the nonlinear system parameter was shown to initially remain constant with some observable error bound. Prior to the system's failure a shift in the nonlinear parameter was detected indicating the material properties were changing. Supplemental studies have helped establish the best regions from which to collect data, and the significance of model form. The study indicated that using a more complete nonlinear model does not provide any benefit, with some benefit noticed if the correct order of the primary nonlinearity is used in the model.

In the prior work, estimates for the linear parameters were the result of the general identification methodology and had no semblance to the actual model terms. This flexibility in model terms may have relaxed the need to have a thorough nonlinear model for the system being studied. In this most recent effort, the mass, stiffness, and damping were determined through traditional means and implemented in the identification algorithm. The resulting map of the estimated nonlinear stiffness term did not provide as clear an indication of changes in system behavior as the beam was excited to failure.

Though still in development, this method holds promise for systems requiring monitoring during use. Future studies will focus on different systems and time varying excitation.

References

- [1] Doebling, Scott W., Farrar, C. R., and Prime, M. B., "A Summary of Vibration-Based Damage Identification Methods," *Shock Vibration Digest* 30, 1998, pp. 91 -105.
- [2] Khiem, N.T., Lien, T.V., "Multi-Crack Detection for Beam by the Natural Frequencies," *Journal of Sound & Vibration* 273, May 2004, pp.175-185.
- [3] Loutridis, S. Douka, E., Hadjileontiadis, L.J., "Forced Vibration Behavior and Crack Detection of Cracked Beams Using Instantaneous Frequency," *NDT & E International* 38, July 2005: 411-419.
- [4] Lee, YY, Liew K. M., "Detection of Damage Locations in a Beam using the Wavelet Analysis," *International Journal of Structural Stability and Dynamics* 1, 2001, pp. 455-465.
- [5] Gudmundson, P., "Changes in Modal Parameters Resulting from Small Cracks," *Proceedings of the International Modal Analysis Conference and Exhibit* 2, 1984, pp. 690-697.
- [6] Kim, Jeong-Tae, Ryu, Yeon-Sun, Cho Hyun-Man, Stubbs, N., "Damage Identification in Beam-Type Structures: Frequency-Based Method vs. Mode-shape Based Method," *Engineering Structures* 25, 2003, pp. 57-67.
- [7] Leonard, F., Lanteigne, J., Lalonde, S., Turcotte, Y., "Free-Vibration of a Cracked Cantilever Beam and Crack Detection," *Mechanical Systems and Signal Processing* 15, May 2001, pp. 529-548.
- [8] Saavedra, P.N., Cuitino, L.A., "Crack Detection and Vibration Behavior of Cracked Beams," *Computers and Structures*. 79 (2001): 1451-1459.

- [9] Kim, J.T., Stubbs, N., "Crack Detection in Beam-Type Structures Using Frequency Data," *Journal of Sound and Vibration* 259, January 2003, pp.145-161.
- [10] Ding, J.L., Pazhouh, J., Lin, S.B., Burton, T.D., "Damage Characterization by Vibration Test," *Scripta Metallurgica et Materialia* 30, 1994, pp. 839-834.
- [11] Sih, G.C., Tzou, D.Y., "Mechanics of Nonlinear Crack Growth: Effects of Specimen Size and Loading Step," *Martinus Nijhoff Publications*, 1984, pp. 155-169.
- [12] Bovsunovsky, A. and Bovsunovsky, O., "Crack Detection in Beams by Means of the Driving Force Parameters Variation at Non-Linear Resonance Vibrations", *Key Engineering Materials*, v 347, *Damage Assessment of Structures VII*, 2007, pp. 413-420.
- [13] Andreaus, U., Casini, P., Vestroni, F., "Nonlinear Features In The Dynamic Response of a Cracked Beam Under Harmonic Forcing," *Proceedings of the ASME International Design Engineering Technical Conferences and Computers and Information in Engineering Conference - DETC2005*, v 6 C, 5th International Conference on Multibody Systems, Nonlinear Dynamics, and Control, 2005, pp. 2083-2089.
- [14] Wowk, V., *Machinery Vibration Measurement and Analysis*, McGraw Hill, Inc. New York, 1991.
- [15] Crespo da Silva, M. R. M. and Glynn, C. C., "Nonlinear Flexural-Flexural-Torsional Dynamics of Inextensional Beams, II. Forced Motions," *International Journal of Solids and Structures* 6, 1978, pp. 449-461.
- [16] Doughty, Timothy A., Davies, P., Bajaj, A. K., "A Comparison of Three Techniques Using Steady-State Data to Identify Nonlinear Modal Behavior of an Externally Excited Cantilever Beam," *Journal of Sound and Vibration*, 249(4), 2002, pp. 785-813.
- [17] Doughty, Timothy A., *System Identification of Modes in Nonlinear Structures*. PhD Thesis, Ray W. Herrick Laboratories, School of Mechanical Engineering, Purdue University, 2002.
- [18] Doughty, T. A. and Leineweber, M. J., "Investigating Nonlinear Models for Health Monitoring in Vibrating Structures", *ASME International Mechanical Engineering Congress and Exposition*, November 2009.

Optical Based Residual Strain Measurements

Jason Burnside*, William Ranson**, Dean Snelling*

*Direct Measurements Inc. and Graduate Student
Department of Mechanical Engineering
University of South Carolina
** Direct Measurements Inc.

Abstract

Residual stresses can occur due to either manufacturing, fabrication processes or intentionally engineered into structures in attempts to improve fatigue life. Equally important is that designers understand how to account for the potential effects of residual stresses on the life of structures or products.

This paper describes the theory and practice for residual strain measurements in friction stir welded joints in aluminum and cold worked holes using the split sleeve mandrel expansion for aircraft fasteners. The first application is based on the hole drilling method where a small hole is drilled in the central region of a measuring strain gage array. The optical method described in this paper makes use of a small circular gage that is rapidly applied through a peel and stick process. Once the gage is applied a reference reading is recorded and a second following the hole drilling. The circular gage is capable of measuring thirty-six tangential strain values around the circumference of the hole. This yields an over determined set of equations to calculate the residual strain components.

Cold-working of fastener holes is used extensively to increase the fatigue life and damage tolerance of mechanically-fastened joints in aircraft structural components. Life improvements of up to five or more are possible over a non cold worked hole. An optical method has been developed and presented to measure directly the hole diameters before and after cold working of holes. The diameter changes are then used as boundary conditions as input variables into a finite element code. This combined method of experimental and numerical techniques provide for a complete and accurate description of residual stress distributions around cold worked holes. Experimental examples are used to illustrate the application of each method.

Optical Based Residual Stress Using the Hole Drilling Method

The hole drilling technique involves measuring the change in strains produced when a small hole is drilled into a member with residual stresses usually due to a fabrication process. The strain (or stress) measurement is accomplished by several methods [1, 2]; however the strain gage method remains the most useful. The procedure outlined in the ASTM E 837-01 standard [3] specifies a strain rosette with three or more elements bonded to the material surface to be measured. A hole is drilled at the geometric center of the strain gage rosette to a depth of 0.4 of the mean diameter of the strain gage circle. Residual stresses in the vicinity of the hole relax and the resulting strains are measured. The method of calculating the residual stresses assumes an infinite, homogeneous plate under a state of biaxial stress which is defined as the original state of residual stress. The purpose of the hole drilling method is to open a small hole

thus creating a stress free hole. The resulting stress field is the Kirsch solution for a biaxially loaded infinite plate containing a hole with a finite radius [4]. The measured strains are then substituted into the Kirsch solution to calculate the biaxial residual strains. Many different techniques have been developed over the years to improve the accuracy of the measurements [1].

This paper presents an optical based technique based on a circular gage shown in [Figure 1](#). The gages are manufactured by a laser machining process and each gage contains a unique serialization number from 0-four billion. Furthermore the gage is marked so that thirty-six values of circumferential strains are measured around both the inner and outer boundaries of the circle. Solution of the Kirsch equations yields an over determined set of equations for the two unknown values of residual stress components. Only the inner boundary strains are needed to calculate the residual strain components. This experimental procedure was first to compare the measured values against the theoretical values of the Kirsch solution. A small central hole was drilled in an Aluminum 7075 plate subjected to uniform tension and the measured circumferential strains were compared to the theoretical strains. [Figure 2](#) shows the comparison of the measured values to the theory. Gages were then bonded to an Aluminum 7075 friction stir welded specimen at several locations in the weld zone. Small holes of one eighth inch diameter were drilled and the residual stresses were calculated from the thirty six measured strain values. The technique is accurate and gages are easy to apply either bonded as a conventional strain gage or using the peel and stick process.

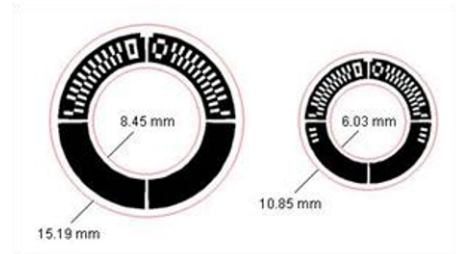


Figure 1. Circular Gage

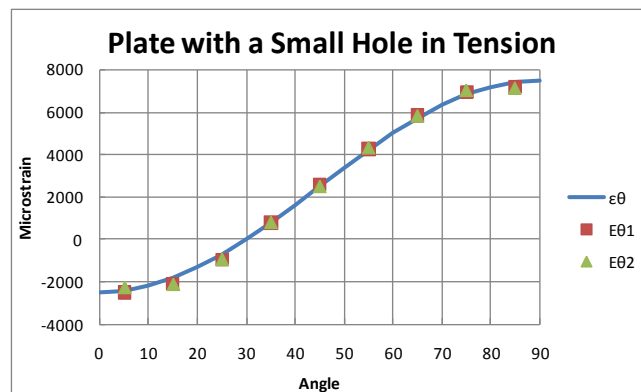


Figure 2. Circular Gage Measured Values Compared to Theory

Validation of a Residual Stress Field of a Cold Worked Hole

Cold work of fastener holes in aircraft structures has been an accepted method of enhancing fatigue life. The split-sleeve cold expansion method developed by Fatigue Technology [5] involves inserting a split sleeve and oversize mandrel within a hole and then drawing the mandrel through the hole. The radial expansion of the hole is large enough to cause plastic deformation in the material. After the mandrel is removed stress equilibrium is reached between the plastically deformed material and the material surrounding this zone. This creates a

compressive region around the hole approximately one radius from the edge of the hole. Although this method has been an accepted practice by the aircraft industry for many years some problems still exist. For example, approximately twenty thousand holes need to be cold work expanded for a typical aircraft. For each hole missed or not properly cold worked the fatigue enhancement is reduced. Thus a method needs to be developed which serializes the process and validates the degree of cold work for each hole and does not severely impact the manufacturing process. The most direct technique for validating the expansion is to measure the hole diameters before and after the expansion. The FTI [5] manual specifies that each hole must be reamed before and after cold work. Also a gage is used which insures that the diameters are within a specified tolerance but is a quality check and not an accurate measure of the expansion.

One method is to measure the retained expansion, I_r , which is a measure of the average diameters before and after expansion. This expression is given by [6] as

$$I_r = \frac{D_{cw} - D_o}{D_o} \quad (1)$$

Where D_{cw} is the diameter after expansion and D_o is the diameter before expansion.

A test was designed to determine the optical sensor accuracy compared to an optical measuring microscope with wire EDM machined holes. The wire EDM produces a clean and precise rim around the hole while still producing a cut to the accuracy of .0002 inches. The measuring microscope was a SmartScope ZIP® 250 with an accuracy of 1 μ m. At a magnification of 37.9x diameter readings are dependent upon the section of the hole that is measured. With a smaller deviation found using the SmartScope ZIP® 250, the more defined data can be correlated to the optical sensor device. Table 1 presents a parametric study conducted correlating the diameter readings of the optical sensor with the SmartScope ZIP® 250.

Hole Number	SmartScope Diameter Readings (in)					Sensor Readings (in)	SmartScope Sensor Deviation (in)
	Run 1	Run 2	Run 3	Run 4	Average		
CW0G	0.23671	0.23671	0.23674	0.23676	0.23673	0.2368	0.00007
CW0H	0.23685	0.23685	0.23698	0.23695	0.23691	0.2369	0.00001
CW0I	0.23684	0.23683	0.23689	0.23686	0.23686	0.2369	0.00004
CW0J	0.2369	0.2369	0.23691	0.23694	0.23691	0.2370	0.00009
CW0K	0.23692	0.2369	0.23693	0.23692	0.23692	0.2370	0.00008
CW0L	0.23678	0.2368	0.23678	0.2368	0.23679	0.2369	0.00011
CW07	0.23697	0.23696	0.23689	0.2369	0.23693	0.2370	0.00007
CW08	0.23718	0.23714	0.23715	0.23715	0.23716	0.2371	0.00005
CW09	0.23664	0.23664	0.23668	0.23668	0.23666	0.2368	0.00014
CW10	0.23683	0.23682	0.23684	0.23688	0.23684	0.2369	0.00006
CW11	0.23711	0.2371	0.23716	0.23717	0.23714	0.2370	0.00014
CW12	0.2369	0.23691	0.23697	0.23697	0.23694	0.2372	0.00026

Table 1. Data Correlation Between SmartScope ZIP® 250 and the Optical Sensor

Studies have shown that the split-sleeve cold expansion process created a complex three dimensional residual stress field due to axial material flow during mandrel pull through process and free edge effects during relaxation [7]. Furthermore the residual stress field is asymmetric around the hole where average diameter readings represent the best axisymmetric

measurement of the post cold work diameter. Equation (1) can be used as a rapid and inexpensive qualitative method to obtain cold work information and the retained expansion depends on the degree of plastic deformation produced by the process which controls the residual stress field. Therefore the retained expansion is a very good approximate measure of the magnitude of residual stress. Table 2 is a comparison of the pre and post expansion diameters measurements between the SmartScope and Optical Sensor. As can be expected some difference occur between the measurements which are a direct result of the asymmetric deformation around the hole.

For Holes 8 & 9	Smart Scope Average Readings (inches)			Optical Sensor Readings (inches)		
	Prior Coldworking	Post Coldworking	Post Reaming	Prior Coldworking	Post Coldworking	Post Reaming
CW08	0.23693	0.24491	0.28077	0.2368	0.2454	0.281
CW09	0.23706	0.24535	0.28003	0.2369	0.2451	0.2821

Table 2. Cold Work Comparison Between the SmartScope and Optical Sensor

References

- [1]. Rowlands, R.E. “ Residual Stresses”, Handbook on Experimental Mechanics Chapter 18, Second Revised Edition, Kobayashi, A.S. (Ed), Society for Experimental Mechanics, 1993.
- [2]. Kudryavtsev, Y.F., “Residual Stress,” Springer Handbook of Experimental Solid Mechanics, Chapter15, Sharpe (Ed), Springer, 2008.
- [3]. *Standard Test Method for Determining Residual Stresses by the Hole Drilling Strain-Gage Method*, ASTM Standard E 837-01, ASTM International, January 2002.
- [4]. Kirsch, G., ‘Theory of Elasticity and Applications in Strength of Materials,’ *J. Verz. Diach. Inge.*, 42,no.29 (1898), 797-807.
- [5]. *Cold Expansion of Holes Using the Standard Split Sleeve System (Cx) and Countersink Cold Expansion*, Engineering Process Specification 8101C, 1994 (Fatigue Technology Incorporated Limited, USA).
- [6]. Stefanescu, D.,” Experimental Study of Double Cold Expansion of Holes,” *J. Strain Analysis*, Vol. 38, No. 4, 2003.
- [7]. Kokaly, M.T., Ransom, J.S., Restis, J.H., Reid, L.F., “Predicting Fatigue Crack Growth in the Residual Stress Field of a Cold Worked Hole,” *Residual Stress Effects on Fatigue and Fracture Testing and Incorporation of Results into Design*, Bunch, J.O. and Mitchell, M.R. (Eds), ASTM STP 1497, Jan. 2007.

Correlating Fatigue Life with Elastic and Plastic Strain Data

Scott M. Grendahl and Daniel J. Snoha, Materials Engineers
U.S. Army Research Laboratory, Aberdeen Proving Ground, MD, USA
Beth S. Matlock, Sr. Materials Scientist
Technology for Energy Corp.
10737 Lexington Drive, Knoxville, TN, 37932
Beth.Matlock@tec-usa.com

ABSTRACT

It is widely accepted that residual compressive stresses in aerospace materials enhance fatigue performance. Conventional shot peening and the cold expansion of holes are two techniques for imparting beneficial compressive stresses. Stresses can be directly measured with x-ray diffraction (XRD), while the corresponding elastic and plastic strains are characterized with XRD peak shifts and widths. This paper presents elastic and plastic strain data, residual compressive stress state, and the resulting fatigue performance of aerospace materials shot peened over a range of common peening intensities. With few exceptions, the data correlated well in that higher intensities provided greater residual compressive stresses and strains. However, the greatest fatigue performance was observed on the lower end of the peening intensity range.

INTRODUCTION

Generating residual compressive stresses in aerospace materials can contribute significantly to the enhancement of fatigue performance. Conventional shot peening and cold expansion of holes are two techniques for imparting beneficial compressive stresses. X-ray diffraction is a direct method for measuring residual stress. Diffraction peak shifts are brought about by elastic strains, while peak widths are an indication of plastic strains. These elastic and plastic strains can be used to better assess the true condition of a component. This paper presents elastic and plastic strains from shot peened aerospace material as well as the corresponding axial fatigue data. Examination of surface data separated the samples in terms of compressive stresses. Together, they correlated well with the measured fatigue performance for each material.

EXPERIMENTAL PROCEDURE

Four aerospace materials were investigated in this program; 4340 (1100 MPa, 160 ksi) and 9310 (1310 MPa, 190 ksi) steels, titanium 6Al-4V (Ti 6-4), and 7075-T73 aluminum. Two separate suppliers provided specimens over a range of Almen intensity for each material on two specimen geometries at 200% coverage. A disk specimen for evaluating residual stress profiles and a threaded round, un-notched $K_t=1$, axial fatigue specimen for correlating fatigue performance were chosen. The fatigue performance was assessed with sinusoidal oscillation at a frequency of 20 Hz with an R-ratio of 0.1 on a 45 tf (100 kipf) test frame. All tests were conducted at room temperature.

X-ray diffraction (XRD) was used to evaluate the resulting shot peening-induced residual stresses in the disks and fatigue specimens. Surface measurements were made at the center of the gage section on the fatigue specimens in three equally spaced circumferential locations. The disks were measured at the center and near the edge of the flat surface at 0, 0.03, 0.05, 0.13, 0.18, and 0.25 mm (0, 1, 2, 5, 7, and 10 mils) depths. The subsurface residual stresses were characterized on the disks by alternately performing XRD measurements and electropolishing away layers of material.

RESULTS

A.1 Residual Stress and Peak Width Data

The residual stress (RS) and full width-half maximum (FWHM) data are shown in [Figures 1-5](#). These data represent the average of six separate measurements. V1 and V2 represent the two vendors, while 4A - 12A and 3N - 14N represent A- and N-scale shot peening intensities, respectively.

The 4340 steel surface residual stresses ranged from - 488.2 MPa (-70.8 ksi) for V2-12A to -593.0 MPa (-86.0 ksi) for V1-4A. For these samples, the maximum compressive stress occurred slightly subsurface at the 0.025 mm (0.001") and 0.051 mm (0.002"), and ranged in magnitude from -576.4 MPa (-84.6 ksi) to -610.2 MPa (-88.5 ksi) for V2-12A and V2-8A, respectively.

The depth of compression from maximum to minimum for the different shot peening conditions was V2-12A, V1-8A, V2-8A, V2-4A, and V1-4A, as one might expect with residual stress generally having a direct relationship with shot peening intensity.

The diffraction peak widths ranged from 2.84° to 3.17°. For all cases, the maximum FWHM was at the surface. The largest to smallest FWHM values for the different shot peening intensities were V2-12A, V1 and V2-8A, V2-4A, and V1-4A.

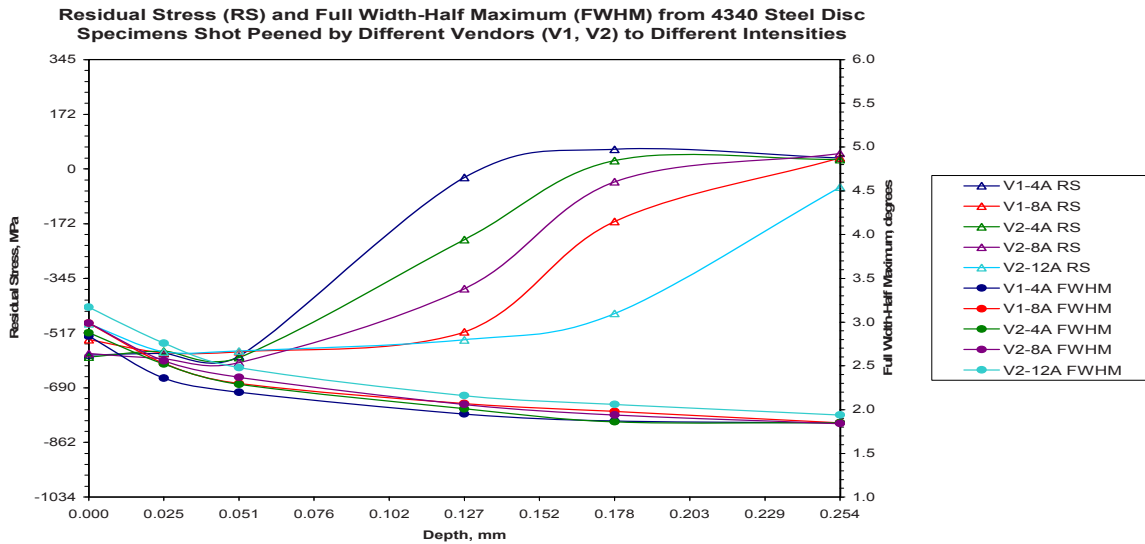


Figure 1. Residual Stress and Peak Width Profile for 4340 Steel

The trends for the 9310 steel followed the pattern for the 4340 steel; however, the compressive stresses were higher in magnitude. The depth of compression from maximum to minimum was V2-12A, V1-8A, V2-8A, V2-4A and V1-8A. At the surface, the maximum to minimum FWHM order was V2-12A, V2-8A, V1-8A, V2-4A, and V1-4A. Allowing for slight differences in vendor processing, the trend still followed the maximum to minimum shot peening intensities.

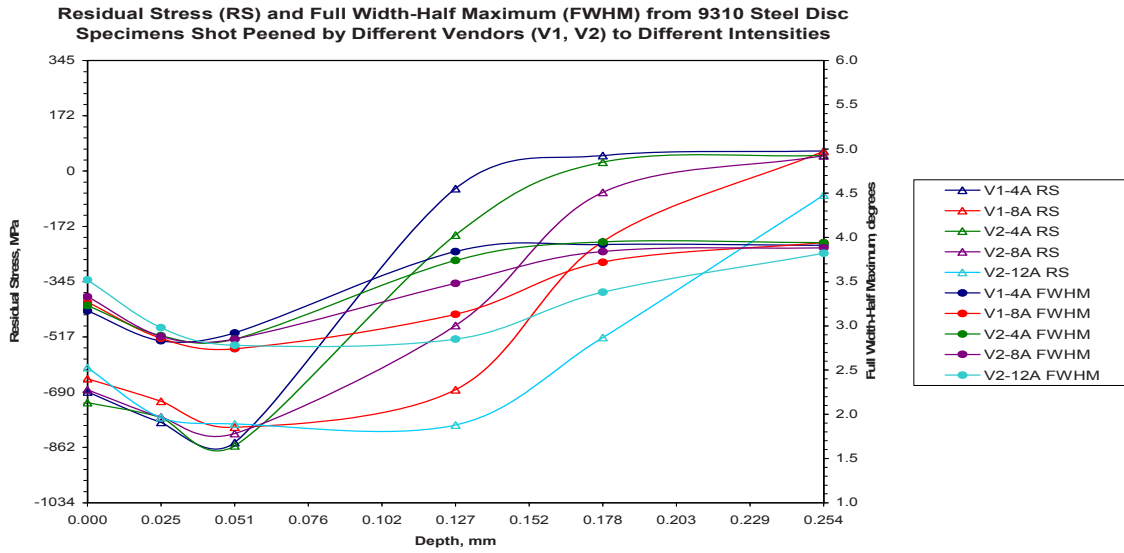


Figure 2. Residual Stress and Peak Width Profile for 9310 Steel

The Ti 6-4 samples were shot peened to both A- and N-scale intensities. The A-scale intensities resulted in deeper levels of compression with the maximum to minimum depth of compression order being V1-11.5A, V2-14A, V1-8A, and V1-4A. For these samples, the FWHM order was V2-14A, V1-11.5A and V1-8A, and V1-4A. There was a slight variation in depth of compression and FWHM trends that again can be attributed to vendor shot peen processing differences.

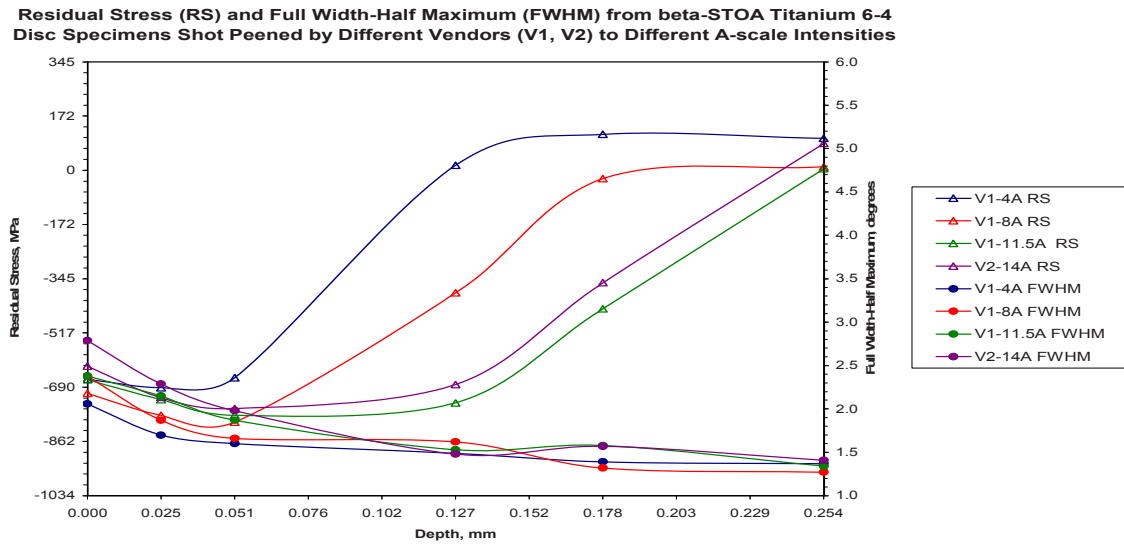


Figure 3. Residual Stress and Peak Width Profile for Ti-6-4, A-Scale

For the Ti 6-4 N-scale intensities data, the compressive stresses approached neutral between 0.025 mm (0.001") and 0.051 mm (0.002") for the lower intensity shot peening and prior to the 0.127 mm (0.005") depth for the higher intensity. The maximum to minimum compression level was V1-14N, V1-11N, V1-5N, and V1-3N. The FWHM data exhibited the same trend as the stress data.

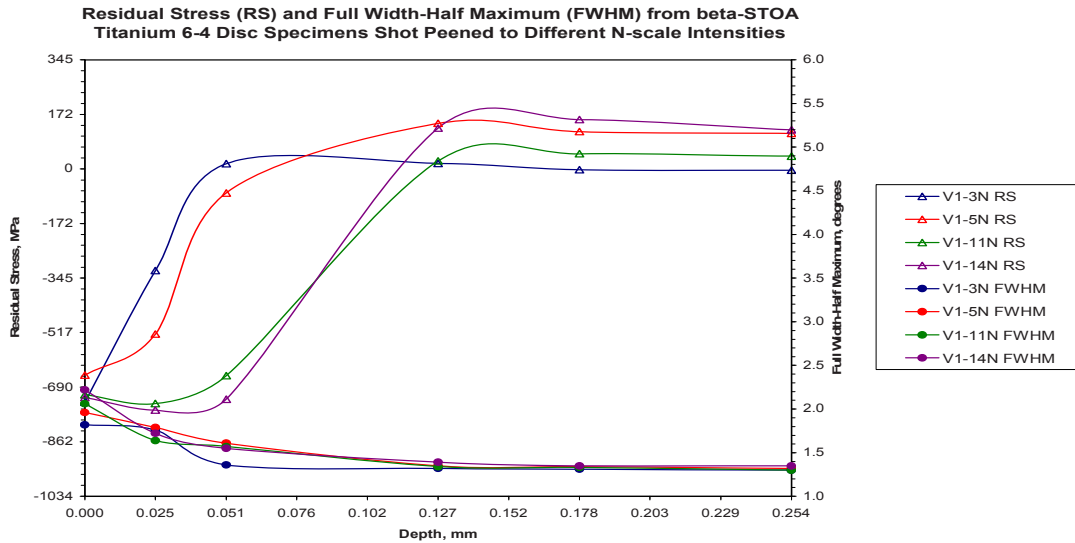


Figure 4. Residual Stress and Peak Width Profile for Ti-6-4, N-Scale

The 7075-T73 aluminum samples remained in compression to 0.254 mm (0.010"). At that depth, the residual stresses for the 10A, 12A, and 14A intensities ranged from -218.6 MPa (-31.7 ksi) to -295.8 (-42.9 ksi). Also at depth, the order of maximum to minimum compressive stresses was V1-14A, V1-12A, V2-10A, V2-12A, V1-10A, and V1-4A. Here the surface FWHM order was V1-14A, V1-12A, V1-10A, V2-10A and 12A, and V1-4A. Since there was no significant difference in the subsurface stresses for V1-12A, V2-10A and V2-12A, the trend of larger surface FWHM for more compressive depth holds.

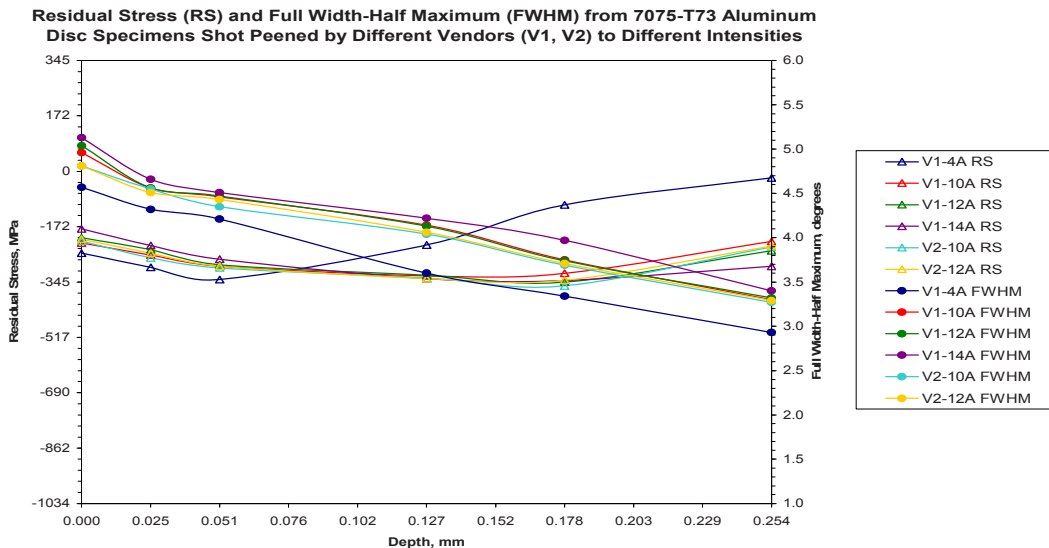


Figure 5. Residual Stress and Peak Width Profile for 7075-T73 Al

A.2 Fatigue Performance

The plotted data of cycles to failure versus fatigue maximum stress are shown in Figures 6-10. These data represent approximately 10 un-notched round axial fatigue specimens shot peened to various intensities at 200% coverage in comparison to an identical unpeened group. V1 and V2 represent the two vendors, while 4A - 12A and 3N - 14N represent A- and N-scale shot peening intensities, respectively.

The 4340 steel data demonstrated that in all cases the shot peening was beneficial. The 4A intensity (both vendors) had the best performance in terms of endurance limit and 12A had the poorest, while still showing an improvement over the baseline. There was clearly an inverse relationship between shot peening intensity and fatigue performance.

4340 Steel - Stress versus Cycles to Failure

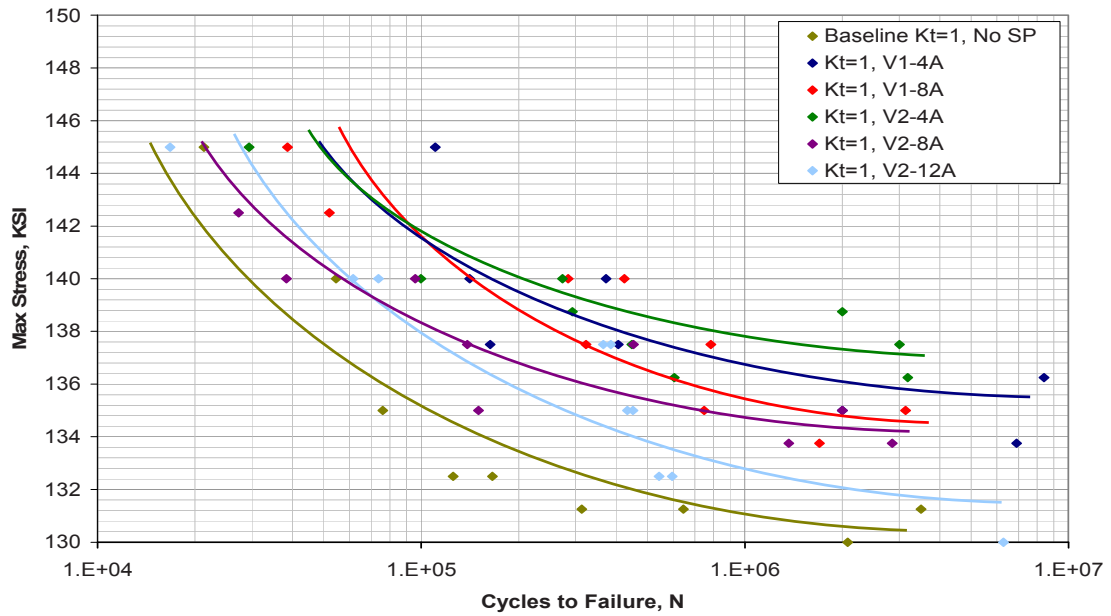


Figure 6. Fatigue performance of un-notched 4340 steel shot peened at 4A to 12A with 200% coverage

The 9310 steel data demonstrated similar trends. The 4A intensity (both vendors) had the best performance in terms of endurance limit, while 12A had the poorest. However, with this material, the 12A and even the 8A from one vendor has worse performance than the baseline. The inverse relationship between intensity and fatigue performance was still prevalent.

9310 Steel - Stress versus Cycles to Failure

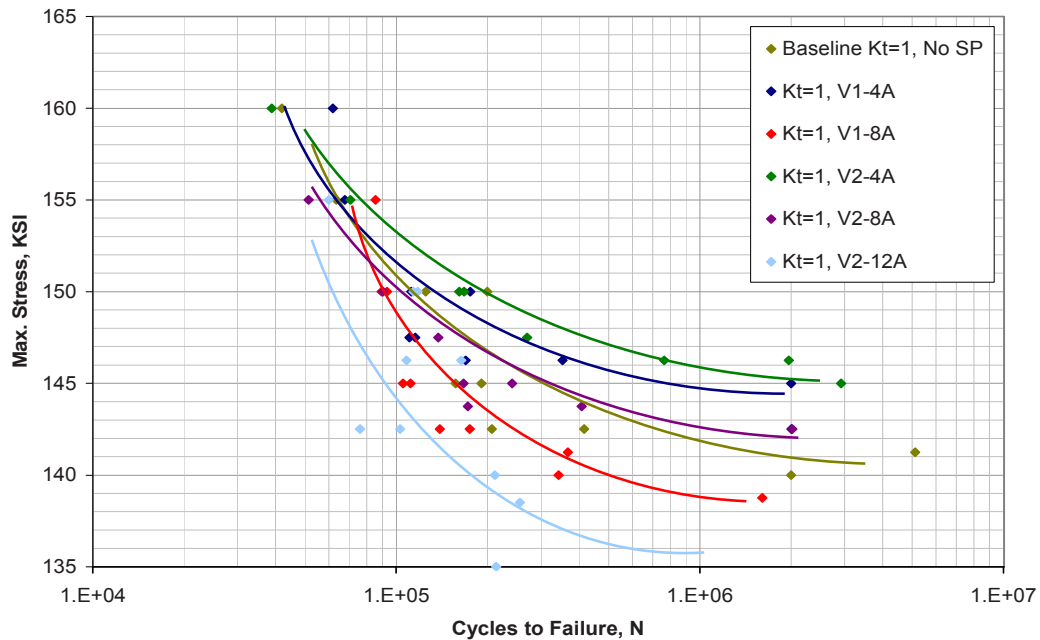


Figure 7. Fatigue performance of un-notched 9310 steel shot peened at 4A to 12A with 200% coverage

Titanium - Stress versus Cycles to Failure

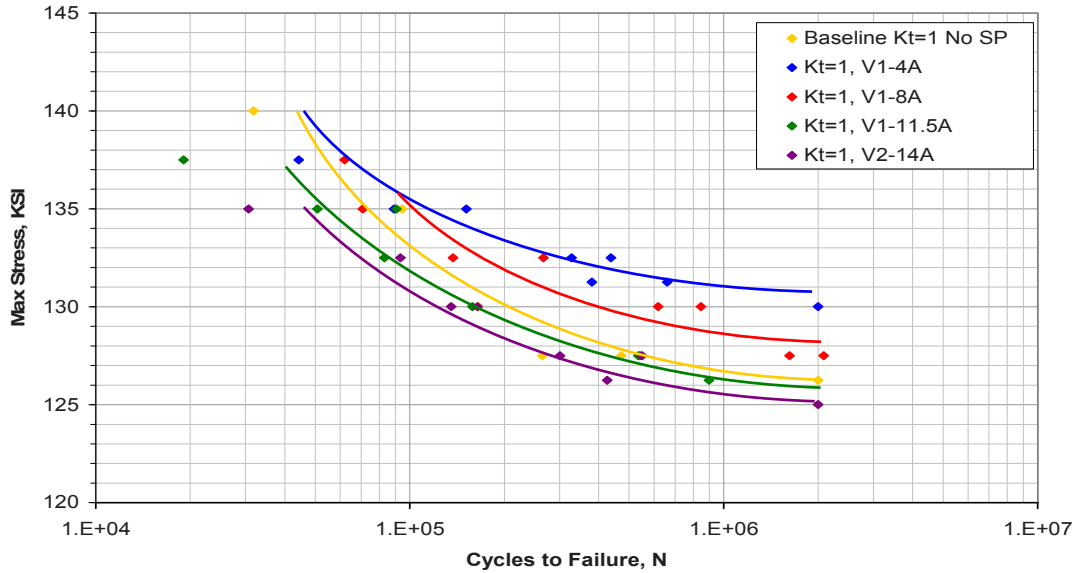


Figure 8. Fatigue performance of un-notched titanium 6-4 shot peened at 4A to 14A with 200% coverage

The titanium 6-4 material with the “A” scale shot peening intensity exhibited similar trends to the 9310 steel specimens. Low shot peening intensity proved beneficial to fatigue performance, while higher intensities proved detrimental when compared to the baseline. Uniformly, an inverse relationship of intensity and fatigue was observed.

The titanium 6-4 material with the “N” scale shot peening intensity exhibited a similar trend to that of the 4340 steel in that all shot peening intensities improved fatigue performance over the baseline samples. More scatter was observed in this data set, likely because the “N” scale is a very light peening intensity. The 5N and 14N groups provided the best performance. This was the only case where a clear trend was not observed in terms of both peening intensity and fatigue performance.

Titanium - Stress versus Cycles to Failure

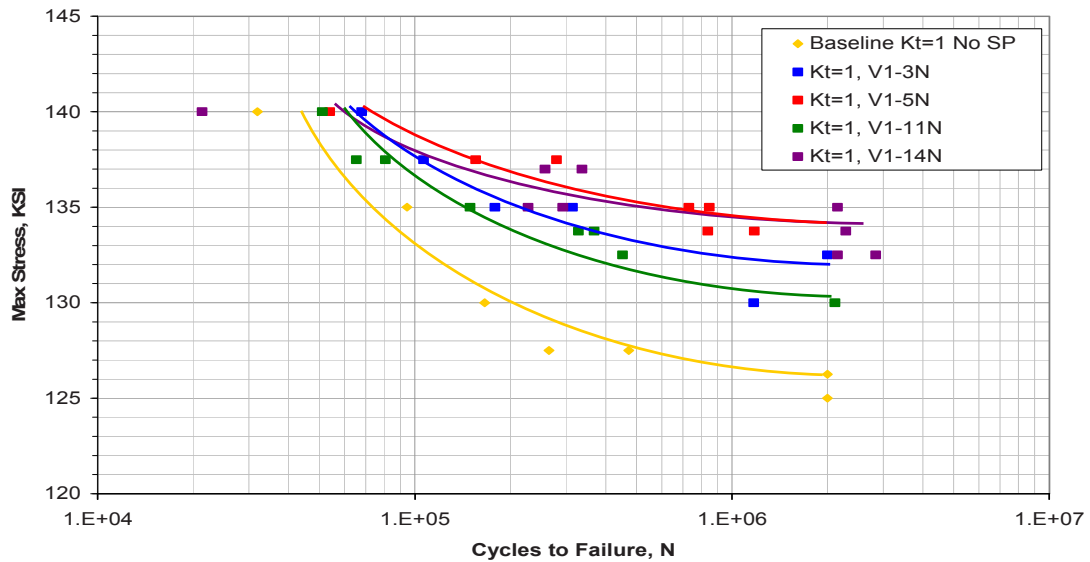


Figure 9. Fatigue performance of un-notched titanium 6-4 shot peened at 3N to 14N with 200% coverage

The aluminum 7075-T73 specimens demonstrated that shot peening, under the conditions selected, is not very beneficial to fatigue performance. Only the lightest peening intensity, 4A, approximated the performance of the baseline. This material did exhibit the inverse relationship of peening intensity with fatigue performance.

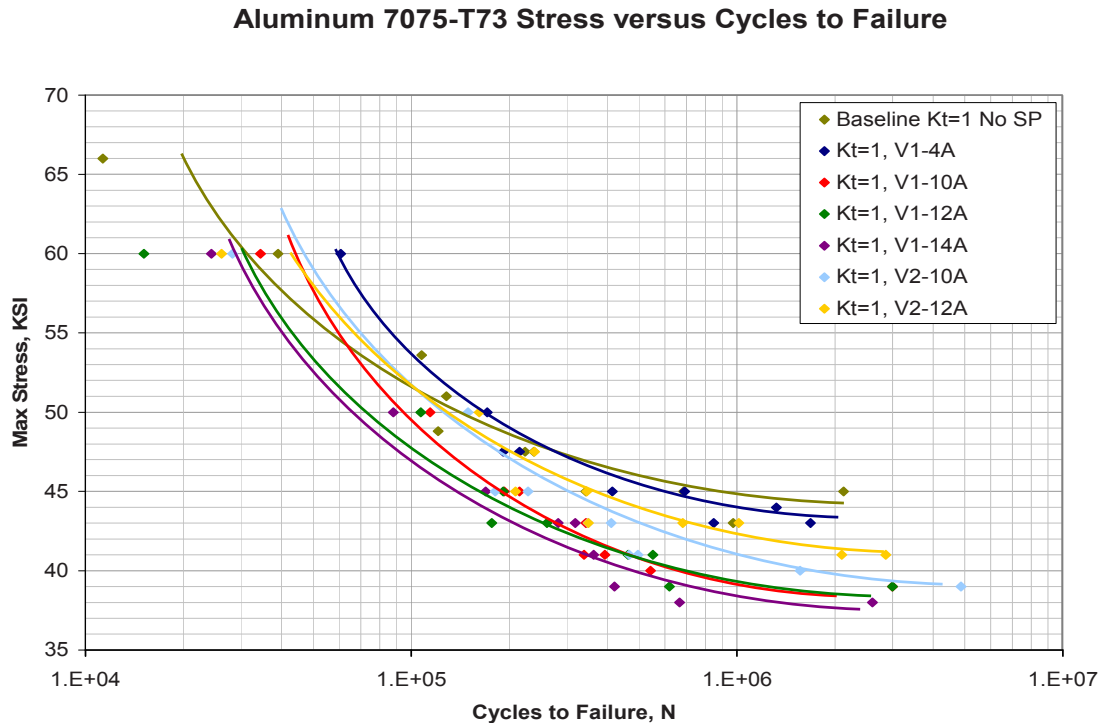


Figure 10. Fatigue performance of un-notched aluminum 7075-T73 shot peened at 4A to 12A with 200% coverage

DISCUSSION

Compressive residual stresses are generally associated with extending fatigue life. These stresses, however, must extend beneath the surface to be effective. Superficial compressive residual stresses can be negated by tensile stress spikes just beneath the surface if the surface stress fades or if a small crack or defect penetrates into the tensile region.¹ For these reasons, methods that impart a significant compressive layer beneath the surface or around a hole are important for improving fatigue life. A previous study on cold-worked hole samples showed the same correlation between the elastic and plastic strains relative to the degree of cold working.² It is generally assumed on these samples that the increased cold working would result in better fatigue properties although these data have not been generated.

X-ray diffraction can non-destructively measure surface stresses. This technique, however, effectively measures stresses in the first layers of a material, on the order of tens of microns. Residual stresses, by definition, are calculated from the elastic strains measured. The diffraction peak width indicates the amount of plastic strain in the part.³ Coupling surface residual stresses and diffraction peak width can provide information about the effective layer of compressive stresses.

¹ Ahmad et al (ed.), "Residual Stress Measurement by X-Ray Diffraction – SAE HS-784, Soc. of Auto. Eng., Warrendale, PA, 2003.

² Matlock et al, "Using XRD Elastic and Plastic Strain Data to Evaluate the Effectiveness of Different Cold-Working Techniques in Aerospace Materials," Powder Diffraction Suppl. **24** (S1), June 2009, pp.S51-S58

³ Noyan, I.C. and Cohen, J.B., Residual Stress: Measurement by X-ray Diffraction and Interpretation, Springer-Verlag, New York, 1987.

The shot peening study showed that deeper compressive stresses were regularly associated with the higher intensity shot peening. The exceptions were on the Ti 6-4 A-scale intensity samples and the 7075-T73 aluminum samples. For the Ti 6-4 samples, the V1-11.5A shot peening intensity produced a slightly greater residual compressive stress with depth than the V2-14A intensity. And for the 7075-T73 aluminum, the compressive stress in the V2-12A intensity sample was similar but not greater than the V2-10A sample. Although the number of samples tested was small, vendor shot peen processing differences may be the reason these particular samples did not follow the general trend.

Conventional thought with regard to residual compressive stresses and shot peening has often been that more is better. The data within this work suggests that while residual compressive stresses can be beneficial, it is quite possible that common higher shot peening intensities might become damaging from a fatigue standpoint even while providing greater compressive stress than a lighter treatment. It seems apparent that plastic strain and the associated dislocation entanglements at the atomic level, if excessive, would be beneficial to fatigue initiation and thus be detrimental to fatigue performance. Fatigue initiations are typically formed from cumulative dislocations associated with fine slip bands, as discussed by Dieter.⁴ The benefit of a small increase in magnitude in measured residual compressive stress induced by high intensity shot peening (as compared with the low intensity shot peening benefit) or by increased hole deformation might not outweigh the apparent costs of excessive permanent plastic strain which yields microscopic or even atomic level surface damage. It should be noted that the surface layers could be removed by various processes, and this might help alleviate the detriment. This postulate should be further examined. It is certainly true that shot peening at higher intensity and with greater coverage yields a rougher surface than the reverse. It is important to note that the 200% coverage in this work is typical of the aerospace industry. This study also focuses on surface (or slightly sub-surface) initiated failures and not damage tolerance applications.

CONCLUSIONS

Shot peening a sample or cold working a hole in a sample imparts residual compressive stresses. These plastic deformation processes increase the diffraction peak width relative to the amount of the plastic deformation. The XRD technique nondestructively measures elastic (residual stress) and plastic (diffraction peak width) strains at the surface of a sample. When the level of residual stress is compared to the peak width, the depth of compressive stresses can be qualified. These parameters should be jointly reviewed when determining the optimum conditions for resistance to the metal fatigue failure mechanism in either a surface related or a damage tolerance application.

This study shows direct correlation of shot peening intensity with the amount of resulting plastic strain, as might be expected. However, for the conditions examined, it appears that the lower peening intensities imparted a combination of residual compressive stresses and strains that were more fatigue resistant than the higher peening intensities, a rather surprising result.

ACKNOWLEDGMENTS

AMRDEC, Redstone Arsenal, AL funded this work.

The authors thank Benjamin Hardisky, US Army Aberdeen Test Center, APG, MD for his assistance in developing the data.

⁴ Dieter, G. E., Mechanical Metallurgy, 3rd Edition, McGraw-Hill, New York, 1986

Monitoring Crack Tip Plastic Zone Size During Fatigue Loading

Ying Du, Amol Patki, Eann Patterson

Composite Vehicle Research Center, Michigan State University, East Lansing, MI 48824, USA.

ABSTRACT

Digital image correlation has been used to obtain detailed strain maps around a propagating fatigue crack. The size of the plastic zone has been estimated from the maps and compared with the value calculated using Dugdale's and Irwin's models for crack tip yielding and from measurements made using thermoelastic stress analysis.

1. INTRODUCTION

It has been recognized for sometime that the plasticity generated at the tip of a crack during fatigue has an impact on the rate of crack growth [1, 2]. It is well-known that a plastic region is developed ahead of the crack tip during fatigue loading and is sometimes known as the plastic enclave or crack tip plastic zone. Dugdale [3] and Irwin [4] have provided models for assessing the size of this plastic zone based on the crack length, applied stress and material yield stress. When the crack tip moves forward it does so by connecting voids in the recently created plastic field ahead of the tip. So the crack grows through the recently created plastic field which then forms a plastic wake behind the crack tip. The material in the plastic wake is expanded relative to the surrounding elastic material so that during the unloading part of the fatigue cycle the crack flanks will make premature contact with one another, i.e. prior to the minimum load in the fatigue cycle. This phenomenon is recognized as a process of crack closure which tends to reduce the effective amplitude of the stress intensity factor experienced by the crack tip and hence retard crack growth based on the Paris relationship for crack growth rate [5]. It has also been suggested that the plastic enclave ahead of the crack tip shields the tip from the full effect of the applied load and thus also retards crack growth. However, it is difficult to measure these effects and in particular to quantify the extent of the plastic fields discussed above so that some have doubted the existence of shielding effects [e.g. 6] while others have proposed multi-parameter models to describe the shielding [7]. Thus, the direct measurement of the extent of plasticity is an important issue if the mechanisms associated with the shielding by both the plastic enclave and wake are to be resolved.

Often the radius of the plastic zone ahead of the crack are assessed using the expressions developed by Dugdale [3] and Irwin [4] while many efforts have been made to determine the extent of the plastic zone using numerical models. However, relatively little effort has been made at direct measurement. Earlier attempts using photoelasticity [8], moiré [9] and stereoimaging [10] lacked resolution. More recently techniques such as electronic speckle pattern interferometry [11], orientation gradient mapping and electronic channeling contrast imaging [12] have been used. Rajic et al [13] used the temperature of the plastic zone to define its extent while more recently Patki and Patterson [14] have shown that the phase difference between the applied load and thermoelastic response can be utilized to define the plastic zone quantitatively. In these studies the focus was on the plastic zone ahead of the crack tip in part due to the resolution and field of view of the measurement system. In this study digital image correlation is used to quantify the extent of the plastic enclave and wake associated with a crack growing in fatigue in an aluminum compact tension specimen. This builds on the approach employed by Lee et al [15] and Diaz et al [15] who used sub-image correlation of images of white light scattering from the surface of metallic specimens.

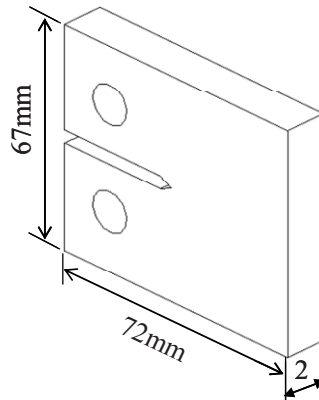


Figure 1: Geometry and dimensions in millimetres of specimen used in fatigue tests.

2. EXPERIMENTAL METHODS

Compact tension specimens were manufactured from 2mm sheet of aluminium alloy 2024-T3. The specimens were of height, $H = 67\text{mm}$ and width, $W = 72\text{mm}$ and conformed to the specification in ASTM E399 except with regard to thickness. The material has a yield strength of 345MPa and a modulus of 73GPa so that the yield strain is approximately $4720\mu\epsilon$. The CT specimens were loaded in fatigue at 10Hz using a minimum load of 500N and a maximum load of 1500N . The specimen surface was sprayed with black and then white paints at a density that was so low that bare metal was still visible and generated a fine speckle pattern. A single monochrome progressive scan $1/2''$ CCD camera with 1.4 Megapixels resolution (JAI, Glostrup, Denmark) fitted with an $\text{AF}90\text{mm F}/2.8$ Di $1:1$ macro lens (Tamron, Commack, NY) were used to collect images which were $19 \times 25\text{mm}$. A PL-800 fiber optic illuminator (Dolan-Jenner Industries, Boxborough, MA) with a fiber optic ring light guide ($2.37''$ inner diameter) were used to achieve the uniform illumination. The commercially available digital image correlation software, Istra4D (Dantec Dynamics, Ulm, Germany) was employed to process the images. The images were 1392×1040 pixels and for image correlation sub-images or facets 61×61 pixels were used and were overlapped by 59 pixels to give displacement vectors at a pitch of 0.038mm . Strains were calculated from the displacement data using the standard algorithms in Istra4D software, which is shown in equation (1).

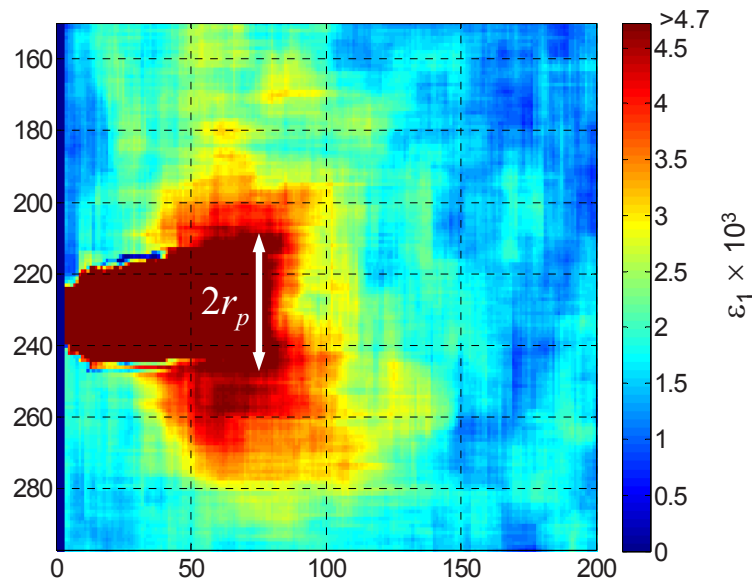


Figure 2: Distribution of maximum principal strain for an area $7 \times 6\text{mm}$ around the top of a crack of length 21.2mm with the color bar adjusted so that all strains above yield at $4720\mu\epsilon$ appear as the same dark red color. The diameter of the plastic zone was estimated as shown and $r_p = 0.76\text{mm}$.

$$\varepsilon_{ij} = \frac{1}{2} \left(\frac{\partial u_i}{\partial x_j} + \frac{\partial u_j}{\partial x_i} + \sum_{l=1}^3 \frac{\partial u_l}{\partial x_i} \frac{\partial u_l}{\partial x_j} \right) \quad (1)$$

Care was taken in selecting the size of sub frames, which needed to be big enough to carry out the correlation while not losing the detailed information of the deformation around the crack tip. The plastic zone diameter was defined as the maximum extent in the y-direction (perpendicular to the crack path) of the plastic region ahead of the crack as shown in figure 2.

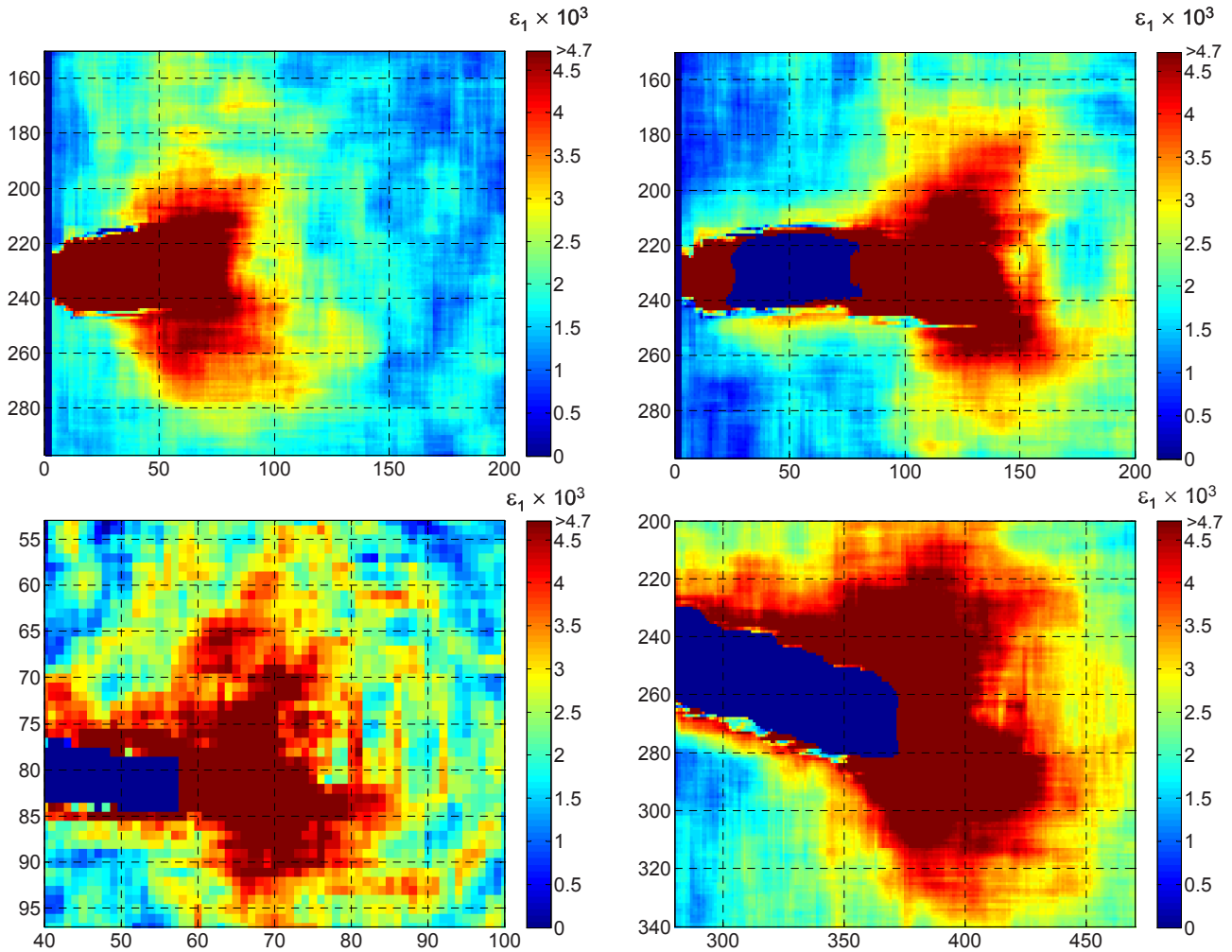


Figure 3: Distribution of maximum principal strain around the crack of length 21.2 (top left); 23.4 (top right); 25.8 (bottom left) and 32.8mm (bottom right) with strains above yield shown in dark red.

3. RESULTS AND DISCUSSION

The distribution of maximum principal strains around the crack is shown in figure 2 for four crack lengths. The development of the shape and extent of the plastic zone can be clearly seen. For one crack length ($a=25.8\text{mm}$) the pitch of the displacement vectors was changed from 0.038mm to 0.113mm by changing the overlap of the facets from 2 pixels to 6 pixels. The effect of the increase in pitch is a reduction in spatial resolution of the displacement data and significant reduction in the quality of the strain map.

Quantitative values for the radius of the plastic zone are plotted in figure 4 as a function of crack length together with results obtained in a similar specimen using thermoelastic stress analysis [14] and those obtained using Irwin's expression [4]:

$$r_p = \frac{1}{2\pi} \left[\frac{\Delta K_I}{2\sigma_y} \right]^2 \quad (2)$$

The plastic zone size was also evaluated based on the Dugdale's model of crack, for which the length of the plastic region d is given by [17]:

$$d = \frac{\pi}{8} \left[\frac{K_I}{\sigma_y} \right]^2. \quad (3)$$

It can be observed from figure 4 that the plastic zone sizes measured from DIC data were in a good agreement with the ones based on Dugdale's model. However, these plastic zones are larger than those obtained from thermoelastic stress analysis and using Irwin's model though they show the same trends.

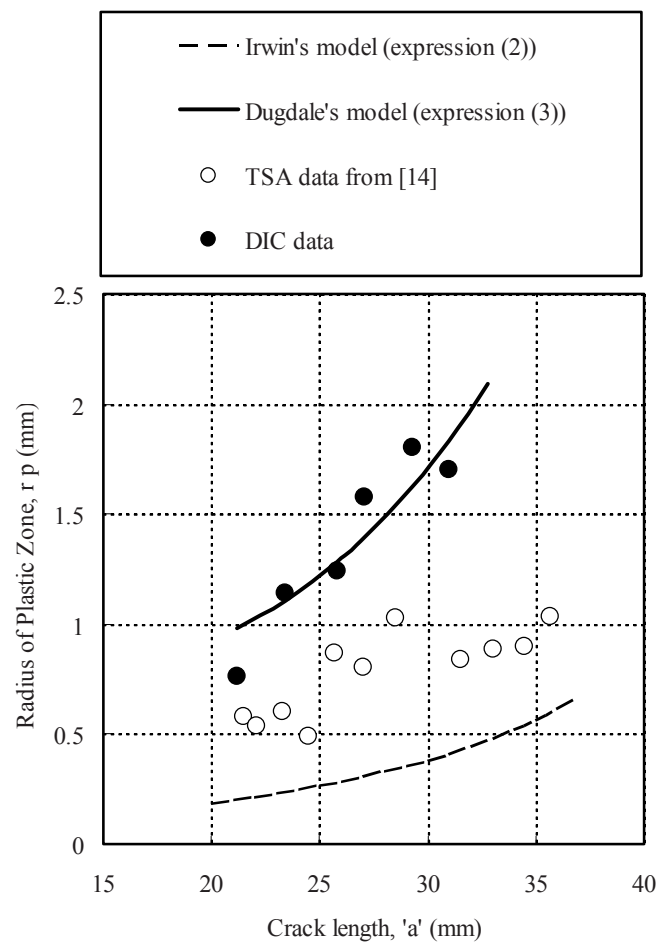


Figure 4: Plastic zone size as a function of crack length. The experimental data for comparison were taken from reference [14] and obtained using thermoelastic stress analysis.

4. CONCLUSIONS

A methodology has been developed for utilizing commercially-available digital image correlation software to quantify the form and extent of the plastic enclave associated with a propagating fatigue crack. It was found that a large facet size (61×61 pixels) with a large overlap of 59 pixels gave a sufficient high spatial resolution to allow

the plastic zone to be readily identified. The results were comparable to those obtained recently using the phase difference between the applied load and thermoelastic emission during fatigue loading and showed excellent agreement with Dugdale's model of crack tip yielding.

REFERENCES

1. Christensen RH, Fatigue crack growth affected by metal fragments wedged between opening-closing crack surfaces, *Appl. Mater. Res.* 2 4: 207-210, 1963
2. Elber W, Fatigue crack closure under cyclic tension, *Engng Fract. Mech.* 2, 37-45, 1970.
3. Dugdale, D.S., Yielding of steel sheets containing slits, *J. Mechs. & Phys. Solids*, 8(2):100-104, 1960.
4. Irwin, G.R., Linear fracture mechanics, fracture transition, and fracture control, *Engng. Fract. Mechs.*, 1(2):241-257, 1968.
5. James, M.N., Some unresolved issues with fatigue crack closure – measurement, mechanism and interpretation problems. *Proc. 9th Int. Conf. on Fracture*, Sydney, Australia, (eds. B L Karihaloo et al), April 1997, Pergamon Press, 5: 2403-2414.
6. Vasudevan, A.K., and Sadananda, K., Classification of fatigue crack growth behavior. *Metall. Mater. Trans. A: Phys. Metall. & Mater. Sci.*, 1995;26A(5):1221-1234.
7. Christopher CJ, James MN, Patterson EA, Tee KF, Towards a new model of crack tip stress fields, *Int. J. Fract.* 148:361-371, 2007
8. Gerberich, W.W., Swedlow, J.L., Plastic strains and energy density in cracked plates, *Experimental Mechanics*, 4(12):345-351, 1964.
9. Liu, H.W., Iino, N., Mechanical model for fatigue crack propagation, *Fracture 1969, Proc. 2nd Int. Conf.*, England, April 13, 1969, p.812-823.
10. Williams, D.R., Davidson, D.L., and Lankford, J., Fatigue crack tip plastic strains by the stereoimaging technique, *Experimental Mechanics*, 20:134-139, 1980.
11. Kim, Kyung-Su, Kim, Ki-Sung, Shim, Chum-Sik, A study of the measurement of plastic zone and crack growth length on the crack tip under cyclic loading using ESPI, *Structural Engineering and Mechanics*, 15(3):367-378, 2003.
12. Welsch, M.T., Henning, M., Marx, M., Vehoff, H., Measuring the plastic zone size by orientation gradient mapping (OGM) and electron channeling contrast imaging (ECCI), *Advanced Engineering Materials*, 9(1-2):31-37, 2007.
13. Rajic, N., Lam, Y.C., Wang, A.K., Plastic zone size determination by temperature measurement, *Trans. ASME. J. Engng. Materials and Technology*, 119(1):32-39, 1997.
14. Patki A, Patterson EA, Thermoelastic stress analysis of fatigue cracks subject to overloads, *Fatigue & Fracture of Engineering Materials & Structures*, in press, 2010.
15. Lee, C., Chao, Y.J., Sutton, M.A., Peters, W.H., Ranson, W.F., Determination of plastic strains at notches by image-processing methods, *Experimental Mechanics*, 29:214-220, 1989.
16. Diaz, F.V., Kaufmann, G.H., Armas, A.F., Galizzi, G.E., Optical measurement of the plastic zone size in a notched metal specimen subjected to low-cycle fatigue, *Optics and Lasers in Engineering*, 35:325-333, 2001.
17. Kanninen, M.F., Popelar, C.H., *Advanced fracture mechanics*, Oxford University Press, New York, 1985.

Studying Thermomechanical Fatigue of Hastelloy X using Digital Image Correlation

Mallory Casperson^{1*}, Jay Carroll¹, Wael Abuzaid¹, John Lambros¹, Huseyin Sehitoglu¹, Mike Spottswood², Ravinder Chona²

¹University of Illinois at Urbana-Champaign, ²Air Force Research Lab

*Corresponding Author. Address: Department of Aerospace Engineering, University of Illinois at Urbana-Champaign, 330 Talbot Lab, 104 S Wright St., Urbana, IL 61801, Rm. 330A, Email: mcasper2@illinois.edu

Abstract

Hastelloy X, a nickel based superalloy, has been extensively used in the past for high temperature applications. However, less is known about its thermomechanical fatigue response compared to other structural metals. Generally, the relation between microscale and macroscale is vital in order to identify specific phenomena that contribute to the cracked component fatigue lifetime. In this work, Hastelloy X notched samples were used to investigate fatigue crack nucleation near the notch and subsequent fatigue crack growth. Isothermal experiments at varying temperatures (up to 1,000 °C) were performed while the specimen was fatigue loaded to advance the crack. Macroscale Digital Image Correlation (DIC) was performed on images taken at various stages of crack growth. In addition, using images obtained directly behind the crack tip, microscale DIC was used to quantify the effects of crack closure. The interaction of crack closure and far-field loading was investigated as a function of temperature. The combination of full-field macroscale and near-tip microscale measurements will aid in the development and understanding of a multiscale fatigue crack growth model.

Introduction

The thermomechanical fatigue response of Hastelloy X is important for analyzing its structural capabilities at both room and high temperatures. Calculating stress intensity factors, K , at various temperatures and loads helps to predict the fatigue response of the material. In 1971, Elber discovered the relations between crack growth rates and crack closure. Determining the amount of crack closure present is therefore also vital to this lifetime prediction, as crack closure lowers stress intensity values and shields the crack from further propagation. In this work, full-field digital image correlation (DIC) of isothermal experiments provided a good method for determining displacement fields in order to calculate stress intensity factors. Comparing experimentally determined stress intensity factors to theoretical values allowed the amount of crack closure to be determined.

Experimental Methods

The specimen used in this experiment was a 75 mm by 7.0 mm by 1.28 mm piece cut from a plate of Hastelloy X using wire electrical discharge machining (EDM). Along one edge, a 1 mm long notch was cut using a 0.15 mm EDM wire at the center of the specimen. The specimen was then polished and painted with a speckle pattern of high temperature paint in order to create a pattern adequate for the use of DIC. Images were taken throughout the test using a 1600x1200 resolution CCD camera.

In the room temperature experiment, in order to initiate and grow a crack from the notch tip, the specimen was fatigued in axial tension at a frequency of 2 Hz. In order to maintain a stress intensity factor value, calculated from text book equation (1), between 18 and 24 MPa \sqrt{m} , the load amplitude was adjusted as the crack length grew. The stress ratio, R , was maintained at 0.05 as to facilitate the presence of crack closure. With the crack grown to a distance of about 2.4 mm from the edge of the specimen, loading was halted and the specimen was

subjected to several single cycles run at the same load amplitude but at a frequency of 0.125 Hz. The first of these cycles was captured at a magnification of 10x while the next cycle was captured at 2x magnification.

DIC analysis of the images was done using a commercially available digital image correlation software, Vic2D. The higher magnification cycle was analyzed using an extensometer method. In this method, DIC displacement gages, sets of individual subsets, were placed on either of the crack. With subset sizes of 71 pixels, these extensometers measured crack opening and crack closure at locations varying from 102 μm to 302 μm behind the crack tip along the length of the crack as shown by Figure 1. For the cycle run at the lower magnification of 2x, full-field DIC was utilized. Using subset sizes of 41 pixels at a spacing of 5 pixels in between subsets, stress intensity factors were calculated using a linear least squares regression method applied to the displacement field. In this regression method, plane stress is assumed and four different coefficients, those for stress intensity factor, rigid rotation, and rigid translation, and a higher order term, T , are applied in order to determine stress intensity factor.

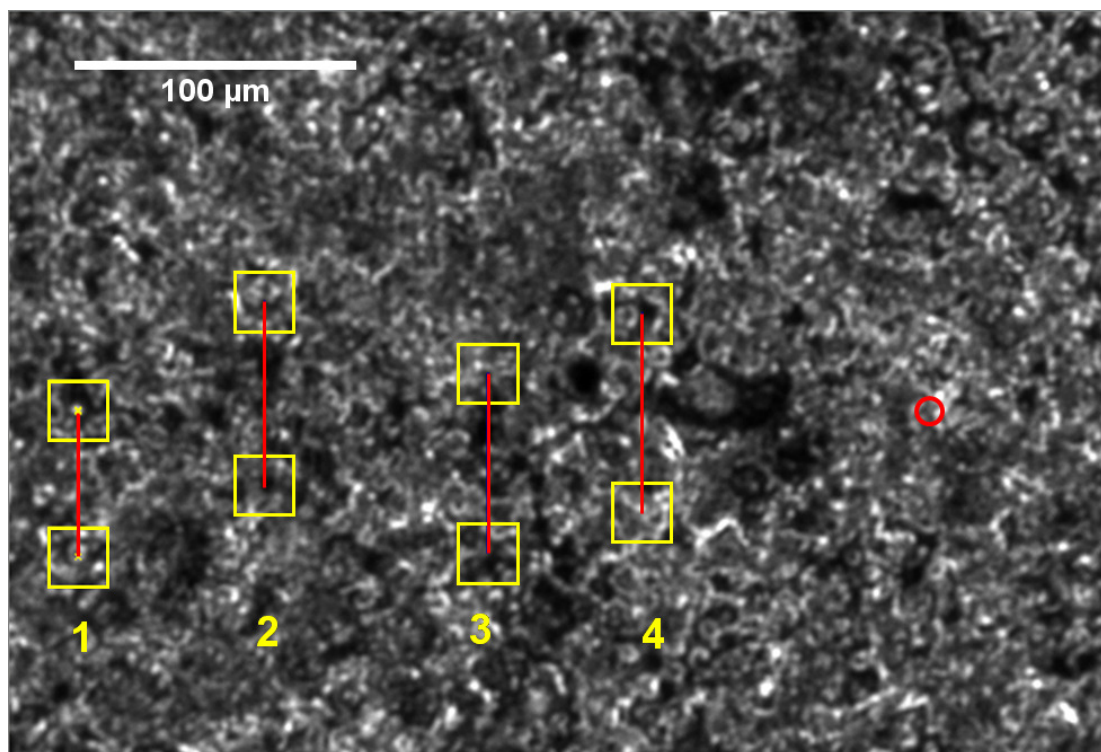


Figure 1. Schematic of the strain gages as placed along the crack length. The red circle shows the furthest point of crack propagation where the crack length, a , is approximately 2.4 mm.

Results and Discussion

The validity of the 2x magnification results were evaluated by comparing the KT regression contours to the experimental vertical displacement contours, vertical displacements being those perpendicular to the crack length. The plane-stress Von Mises plastic zone size was also estimated. Figure 2 displays these displacement contours at the point in the cycle of maximum loading.

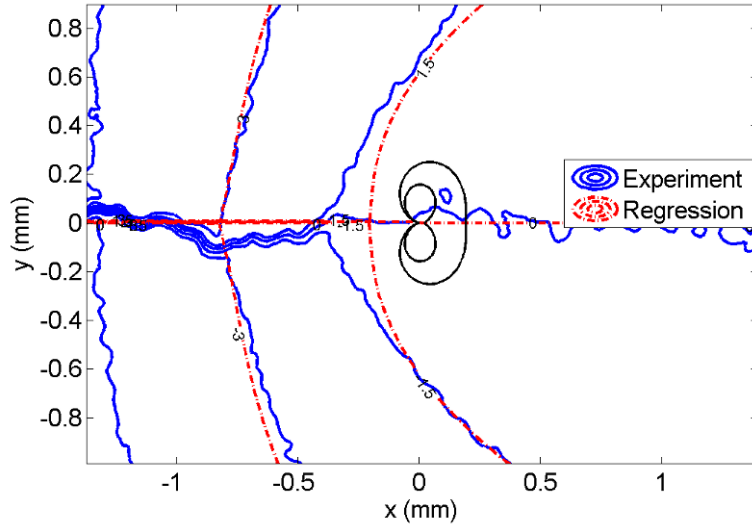


Figure 2. Comparison of experimentally determined and KT regression v -displacement contours. The solid black outline displays the approximate Von-Mises plastic zone size.

The KT regression also calculates the stress intensity factors from the experimental data recorded during loading of the specimen. The experimentally calculated stress intensity factor at the point of maximum loading was $13.3 \text{ MPa}\sqrt{\text{m}}$ while the theoretical value at this same point was $21.2 \text{ MPa}\sqrt{\text{m}}$. This discrepancy in stress intensity factor values, shown more readily in [Figure 3](#), was caused by the presence of crack closure.

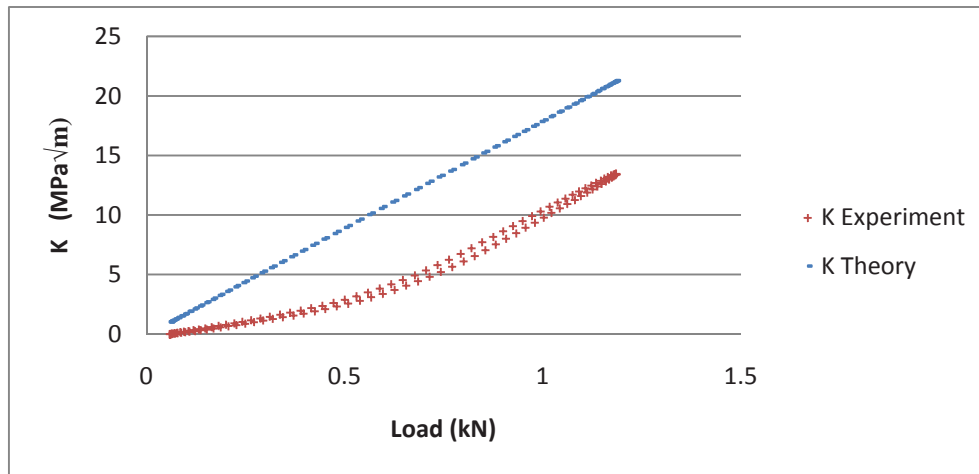


Figure 3. Comparison of theoretical stress intensity factors and those determined by the KT regression using experimental data.

[Figure 3](#) displays the experimental stress intensity values determined by KT regression compared with those calculated using the equation

$$K = F\sigma\sqrt{\pi a} \quad (1)$$

where F is 1.84 for the geometry of this specimen, σ is the far-field stress, and a is the length of the crack. The theoretical K values are consistently lower than those determined experimentally through the KT regression as crack closure tends to shield the crack tip with a plastic wake causing residual compression along the crack length [1]. Quantifying crack closure therefore becomes an important step in the analysis of fracture specimens. This is accomplished more readily by analyzing the experiments performed at higher magnifications than $2\times$.

The 10x extensometer experiment displays large levels of crack closure in Hastelloy X at room temperature. By analyzing the load where opening of the crack occurs (the opening load) and the peak load, the amount of crack closure can be quantified. The opening load is the load at which the gage displacement begins to increase more drastically [2]. The displacement gages, placed at 102 μm , 156 μm , 236 μm , and 302 μm from the crack tip, therefore track the amount of crack closure occurring as a function of distance from the crack tip and load amplitude. As shown in Figure , the gage furthest from the crack tip measured a crack closure level of 33.3% of the peak load, while the gage closest to the crack tip measured a crack closure level of 62.5% of the peak load. These large closure levels indicate that both plasticity induced and roughness induced crack closure are most likely involved.

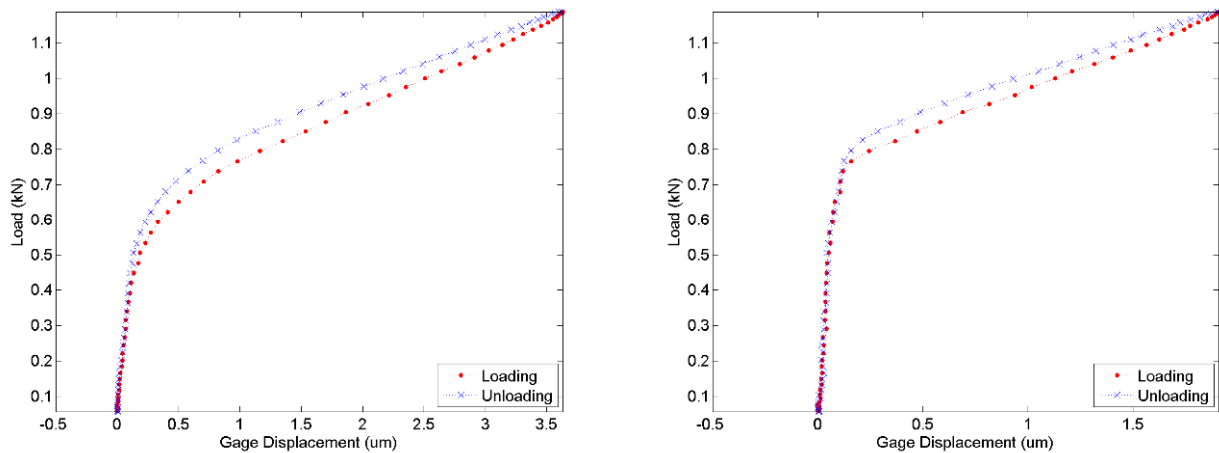


Figure 4. Gage Displacement vs. Load for the displacement gage located at 302 μm from the crack tip (left) and for the displacement gage located 102 μm from the crack tip (right).

High temperature applications are abundant in the aerospace industry; therefore the study of the fatigue response of Hastelloy X is important. Thermomechanical fatigue experiments, as well as the study of crack closure in these experiments, at high temperatures are forthcoming.

Conclusions

This work examined stress intensity factors determined by full-field DIC displacements. These stress intensity factors were shown to be consistently less than those theoretically determined due to the presence of crack closure at room temperature. Closest to the crack tip, opening and closure load levels were 62.5% of peak load. Results at high temperature are forthcoming.

Acknowledgements

This work was supported by the Midwest Structural Sciences Center (MSSC), which is supported by the Air Vehicles Directorate of the U.S. Air Force Research Laboratory under contract number FA8650-06-2-3620.

References

- [1] Elber, W. "The Significance of Fatigue Crack Closure." 486, ASTM STP. Damage Tolerance in Aircraft Structures. American Society for Testing and Materials, 1971. 230-242.
- [2] Carroll, J. et al. "Investigation of fatigue crack closure using multiscale image correlation experiments." Engineering Fracture Mechanics (2009).

Understanding Mechanisms of Cyclic Plastic Strain Accumulation under High Temperature Loading Conditions

Wael Abuzaid^{1*}, Huseyin Sehitoglu¹, John Lambros¹, Jay Carroll¹,
Mallory Casperson¹, Ravinder Chona²

¹University of Illinois at Urbana-Champaign, ²Air Force Research Lab

*Corresponding Author Address: Department of Mechanical Science and Engineering,
University of Illinois, 1206 W. Green St. Urbana, IL 61801, Email: abuzaid1@illinois.edu

Abstract

In-depth analysis of deformation mechanisms, such as slip deformation and slip/twin interaction, on the micro-level can greatly enhance the understanding of the physics behind thermomechanical fatigue damage accumulation in ductile metals. This improved understanding is essential for the development of new fatigue models that are not phenomenological, and have better predictive capability than the current ones. Hastelloy X, a nickel based superalloy has been experimentally studied using multiscale experimentation under different cyclic plasticity and thermomechanical fatigue loading conditions. High resolution *ex-situ* Digital Image Correlation (DIC) was used to measure plastic strain accumulation as a function of load and temperature. By performing DIC experiments with sub-grain resolution we can relate the measured strain fields to the underlying microstructure through comparison with EBSD scans of the same region of interest. The results reveal a highly heterogeneous material response at the grain level and even at the sub-grain level with high strain concentrations at regions such as twin boundaries and triple points, and with strain variations even within particular grains. By making such measurements at regular intervals of load, the evolution of plastic strain during loading was observed. As loading increased heterogeneity also increased (i.e. regions with high strain became more strained and regions with low strain remained relatively unstrained).

Procedure

To obtain accurate strain measurements with sub grain level resolution using DIC, it is necessary to increase the magnification at which reference and deformed images are captured. This reduces the field of view and thus imposes limitation on the area/number of grains that can be studied. The *ex-situ* technique that has been used in this study addresses this problem and enables high resolution measurements over relatively large areas by capturing and stitching enough high magnification images to cover the required area of interest (see [figure 1](#)). Fiducial markers on the samples surface allowed accurate alignment of the measured strain fields and the underlying microstructure obtained through EBSD.

In this work, plastic strain localization has been studied *ex-situ* using a dog bone specimen made of the nickel based superalloy Hastelloy X. The specimen was incrementally loaded in uniaxial tension to 2%, 3.8% and 5.6% nominal plastic strains. High magnification (31x) DIC measurements were obtained *ex-situ* at the end of each loading cycle, and lower magnification (5x) *in-situ* measurements were obtained real time throughout each loading cycle. A 1000 by 600 μm region of interest at the center of the specimen gage area was observed. Reference images were taken in the optical microscope at 31 x magnification (0.14 $\mu\text{m}/\text{pix}$). A total of 316 overlapping images were captured and stitched together to cover the area of interest.

In the first loading cycle, the specimen was loaded with a strain rate of $1.83 \times 10^{-4} \text{ s}^{-1}$ to 2.2% nominal strain (in position control) which corresponded to a stress of 465 MPa and then unloaded to 0 KN (in load control). The total residual strain accumulated was 2% nominal strain. Subsequently, 316 deformed images were captured and stitched following the same procedure used for the reference images. In plane displacements were calculated from DIC and results were differentiated to obtain strain fields. Grain boundaries from EBSD were overlaid onto the ϵ_{yy} strain field as shown in [figure 2a](#).

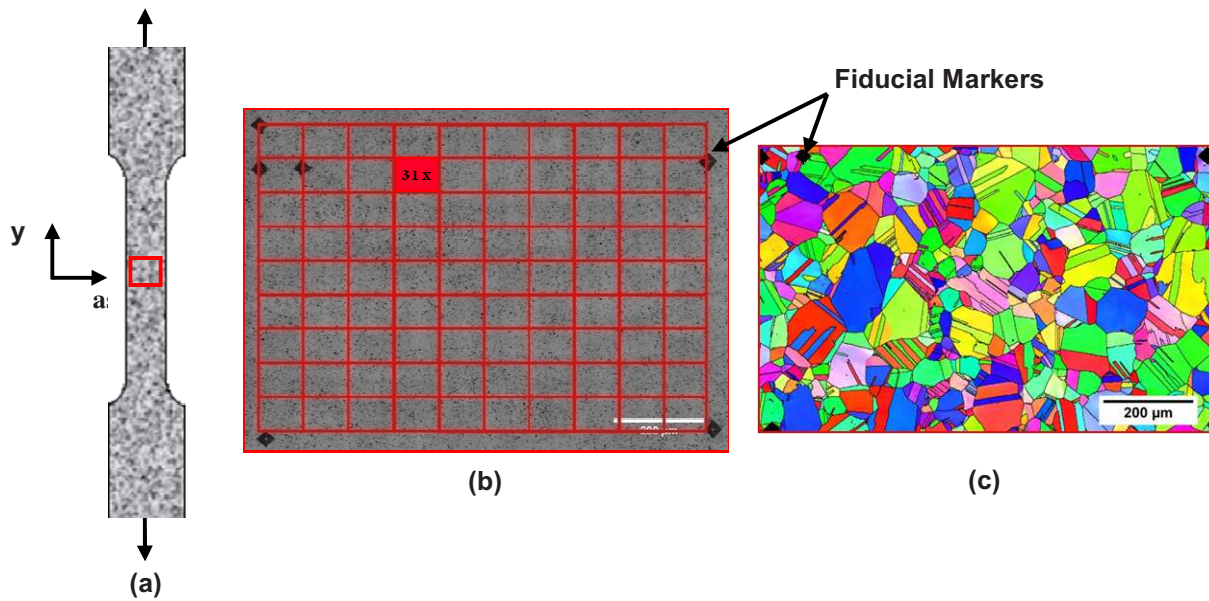


Figure 1. (a) A typical specimen showing the region of interest. (b) The region of interest is imaged using an array of high magnification images (31x) in the optical microscope. Vickers indentations are used as fiducial markers to delineate the region of interest. (c) Results of the EBSD scan showing grain orientations and location of microstructure in relation to the same Vickers indentation marks as in (b).

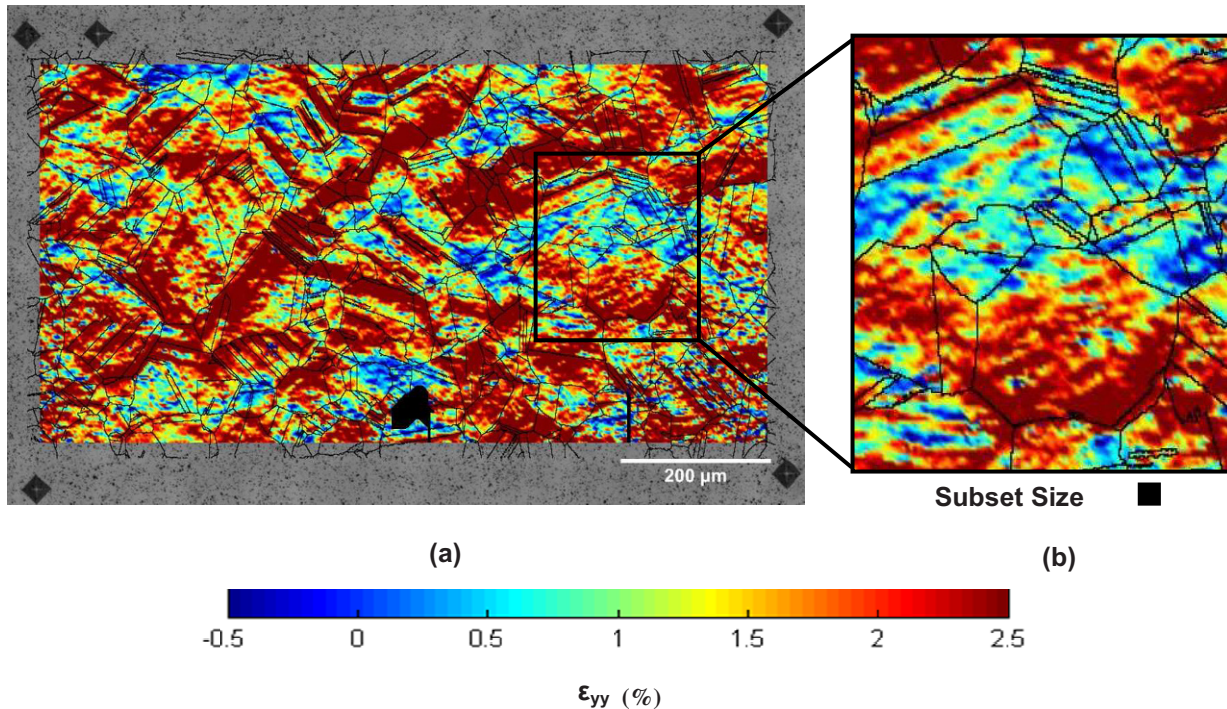


Figure 2. (a) Contour plot of the ϵ_{yy} strain field with overlaid grain boundaries. The reference and deformed images are a composite of 316 images at 31x magnification (*ex-situ*). (b) A portion of the contour plot in (a) is magnified to show the strain localizations that can be resolved with this technique. The subset size is shown as a black square in (b).

Results

The advantage of such a measurement procedure is that it enables quantitative analysis of the plastic strain fields in relation to the microstructure of the polycrystalline specimen. Different aspects of the microstructure, such as grain boundaries and grain orientation, and how they affect plastic strain accumulation, can then be investigated. Preliminary analysis of the results revealed a highly heterogeneous material response at the grain level, and even at the sub-grain level. Some regions accumulated more strain than the average nominal strain by a factor of three while other regions accumulated less or even no strain. Future investigations will focus on the role of different types of grain boundaries, grain orientations and temperature on the plastic strain localization.

Simulated Corrosion-Fatigue via Ocean Waves on 2024-Aluminum

E. Okoro, M.S. Student, Department of Mechanical Engineering
University of North Dakota

M.N. Cavalli, Assistant Professor, Department of Mechanical Engineering
University of North Dakota, 243 Centennial Drive, Stop 8359, Grand Forks, ND 58202-8359
matthewcavalli@mail.und.edu

ABSTRACT

The combined effect of corrosion and fatigue loading can be extremely detrimental to the service life of structures in and around bodies of salt water. 2000-series aluminum alloys are of special concern due to their tendency for pitting, which can lead to widespread crack initiation sites with relatively little loss in mass. In the current work, we present results from a series of experiments on 2024-T351 aluminum simulating the corrosive environment and wave loading of a structure in the North Sea. Details are presented about the method for constructing the simulated wave loading as well as the incorporation of periodic overloads. The effects of loading rate and grain orientation of the material on fatigue life are explored.

INTRODUCTION

Many aluminum alloys have been used in offshore structural applications such as ship building, offshore wind turbines, converted jack-up barges, fixed tower structures, tension leg platforms (TLPs), stationary floating spars, etc. The lower density of aluminum alloys and generally lower corrosion rate compared with steel alloys make aluminum a strong candidate for these applications. 2000-series aluminum alloys are of special interest due to their high specific strength [1]. The presence of both a corrosive environment (sea water) and variable loading cycles (due to wave action) tends to lead to failure in these structures much sooner than if either fatigue or corrosion were present alone [1-5]. Increased aluminum usage in marine environments has increased the need for increased corrosion-fatigue research.

To date, most of this research has concentrated on determining corrosion fatigue behavior using constant amplitude load cycles. In actuality, the amplitude of the loading cycles can vary significantly from wave-to-wave [2]. In the present study, the simulated water body (corrosive environment) is the North Atlantic Sea. Using actual wave amplitude data from the North Sea [2], a model wave is constructed consisting of a lower-amplitude, higher frequency portion and a higher-amplitude, lower frequency (overload) portion. An overload refers to the rare high wave height that sharply increases stress on the material. The resulting load history is expected to more closely mimic that seen by actual structures in service. The effects of changes in the maximum stress and the grain orientation of the samples being tested are investigated.

EXPERIMENTAL METHOD

Two sets of dogbone specimens were cut from a 305mm x 305mm x 3mm rolled 2024-T351 aluminum sheet according to ASTM E466. One set of the specimens had the rolling direction aligned with the loading direction and the other set had the rolling direction aligned transverse to the loading direction. Prior to testing, both sets were hand polished to a 220 grit finish to remove any machine marks might serve as stress risers and cause premature failure during testing. After polishing, the specimens were rinsed with alcohol and blown dry. Regions outside the gauge section were coated with Amercoat protective paint to ensure corrosion (and subsequent failure) occurred only in the gauge section. Several specimens of each orientation were tested under monotonic tensile loading in a Shimadzu AG-IS 50kN Universal Testing Machine to determine the stress-strain response of the material. This data was used to determine the appropriate loading levels for the fatigue tests.

Disposable tanks with dimensions 25 mm x 25 mm x 16 mm were attached to each fatigue specimen using silicone caulk. The tanks consisted of a 'U' shaped wooden section (coated with enamel to prevent water absorption) with a plexiglass front and bottom to allow for observation of the specimen being tested. After application of the tank, each fatigue specimen was clamped into the Bose ElectroForce 3500 fatigue testing machine, the tank was filled with 0.5M NaCl, and the fatigue testing began. A rubber top was placed over the tank to prevent evaporation of water during the test.

The fatigue loading was based on data from the North Atlantic Sea as presented by Cramer et al. [6] which is shown in Table 1. Data is presented in terms of the significant wave height, H_s , and zero crossing periods, T_z , for each observed wave along with how often that wave was observed. Using this information, the wave loading on a specified structural geometry can be modeled using Morison's equation [7]. However, inclusion of the full range of wave loading was not possible in the current investigation due to control software limitations. As a first step, the decision was made to divide the data from Table 1 into two regions, a 'normal loading' region and an 'overload' region. The normal loading region was taken to be all waves with a significant wave height of 7.5 m or less (comprising approximately 98% of all observed waves). The overload region comprised all waves with a significant wave height of 8.5m or higher. Within these two loading regimes, the most commonly occurring waves were identified, highlighted in Table 1. The highlighted waves represent over 50% of the observed waves in the each of the normal and overload regions and were used to construct the fatigue loading control signal. Scaling of the resultant forces was done to simulate a stress range of 275-340 MPa on the test specimens, chosen based on the measured yield strength of the 2024-T351 samples.

Table 1: Scatter diagram for North Atlantic Sea for use in fatigue computations [6]

H_s (m) \ T_z (s)	0.5	1.5	2.5	3.5	4.5	5.5	6.5	7.5	8.5	9.5	10.5	11.5	sum freq.
13.5	0	0	0	0	0	1	1	0	0	0	0	0	2
12.5	0	0	1	2	2	2	2	1	1	1	0	0	12
11.5	0	1	4	6	7	5	4	2	2	1	1	0	33
10.5	0	4	14	21	19	13	8	4	3	2	1	1	90
9.5	1	16	43	48	34	20	11	5	3	1	1	0	183
8.5	4	47	80	65	38	19	8	4	2	1	0	0	268
7.5	13	75	79	46	21	9	3	1	1	0	0	0	248
6.5	21	54	33	14	5	2	1	0	0	0	0	0	130
5.5	14	13	5	1	0	0	0	0	0	0	0	0	33
4.5	3	0	0	0	0	0	0	0	0	0	0	0	3
3.5	0	0	0	0	0	0	0	0	0	0	0	0	0
2.5	0	0	0	0	0	0	0	0	0	0	0	0	0
sum freq.	56	210	259	203	126	71	38	17	12	6	3	1	

Equation 1 (Miner's rule of linear cumulative damage) was used to account for contributions from each highlighted frequency domain in Table 1. This means that the overall wave loading is taken to be the sum of the individual loadings from each of the waves in the highlighted region, weighted with the relative frequency of occurrence for that particular wave [6,8]. The net loading for each region can be calculated as:

$$F_{t,net} = \sum_{i=1}^{I_{tot}} \frac{n_i}{I_{tot}} F_{t,i} \quad (1)$$

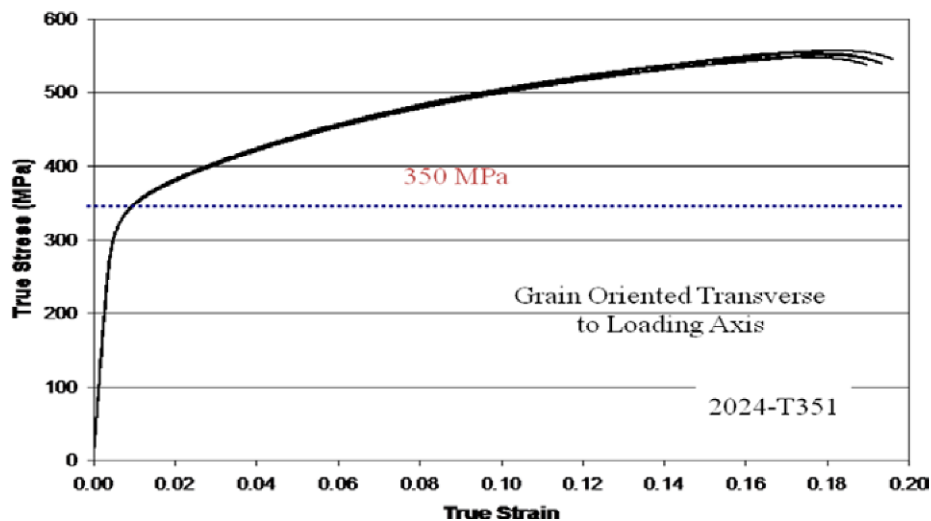
where I_{tot} is the total number of waves observed, n_i is the number of times the i^{th} wave was observed, and $F_{t,i}$ is the resulting force of the individual wave. The result of this analysis was two waveforms, one for the normal

loading region and one for the overload region. Two cycles of the overload wave were applied to the specimen for every 98 cycles of the normal wave, in keeping with the original wave distribution from Table 1.

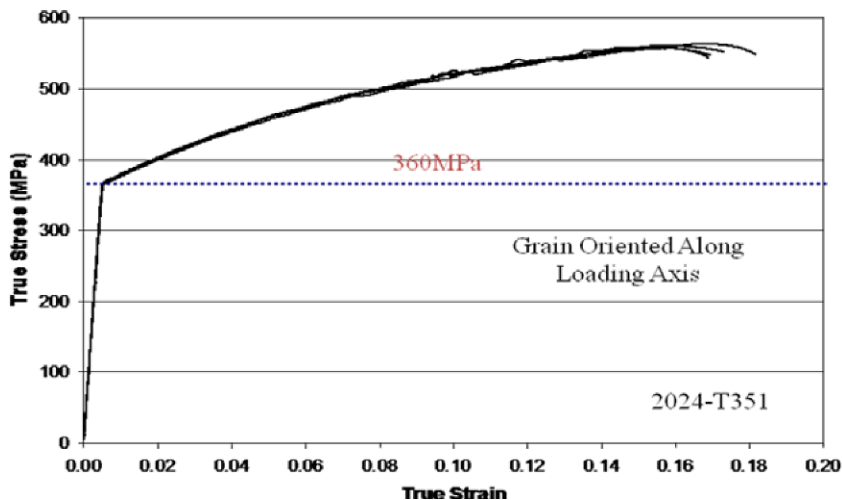
After failure, suitable samples were collected for fractographic analysis. Specimens were cut, mounted in epoxy, and lightly polished using $0.02\mu\text{m}$ silica as the abrasive. Polishing was done to enhance visualization of the failure process away from the surface of the specimens by optical microscope and scanning electron microscope. Imaging was also carried on some unpolished tested sample surfaces to allow for identification of crystallites on crack surfaces, in voids or on aggregate surfaces and effects such as hydrogen embrittlement and stress corrosion cracking which could be missed on polished samples.

RESULTS AND DISCUSSION

Cavalli and Okoro [9] presented the stress strain curves of Al 2024-T351 with grains oriented transverse to the loading axis and grains oriented along the loading axis as shown in Figure 1. Based on these results, an upper stress limit of 340MPa was chosen because it provides information for the behavior of the material when loaded close to its yield strength. A lower stress limit of 275MPa was chosen because at this level the specimen has stabilized enough withstand significant amount of fatigue phenomena such as crack ignition and nucleation.



(a)



(b)

Figure 1: Stress strain curve of Al 2024-T351 with rolling direction a) transverse to the loading axis and b) along loading axis [9]

Table 2: Summary of fatigue testing conditions [10]

Material orientation	Cyclic Max. Stress (MPa) at R = -1	Overload Stress (MPa)	Cyclic Stress/Overload	No. of tests performed
Longitudinal	256, 241, 229, 218, 207	340, 320, 304, 290, 275	0.753	13
Transverse				14

Figure 2 shows the plot of maximum stress versus fatigue life (cycles to failure) for both grain orientations. As expected, the life of the specimens increased as the stress amplitude was reduced. An interesting result is that the specimens loaded with overload stresses between 340-320 MPa failed at very low cycles for both loading directions, almost immediately after the overload was first applied. This phenomenon can be explained by the synergistic interaction between material, environment and stress. The effect is that the yield strength of the material is lowered causing the material to fail at a much lower overload stress than when tested in air [11]. This effect can be clearly observed in higher strength ductile materials [12]. As the maximum overload cyclic stress moves away from the yield stress region to 290 MPa, fatigue life increases significantly.

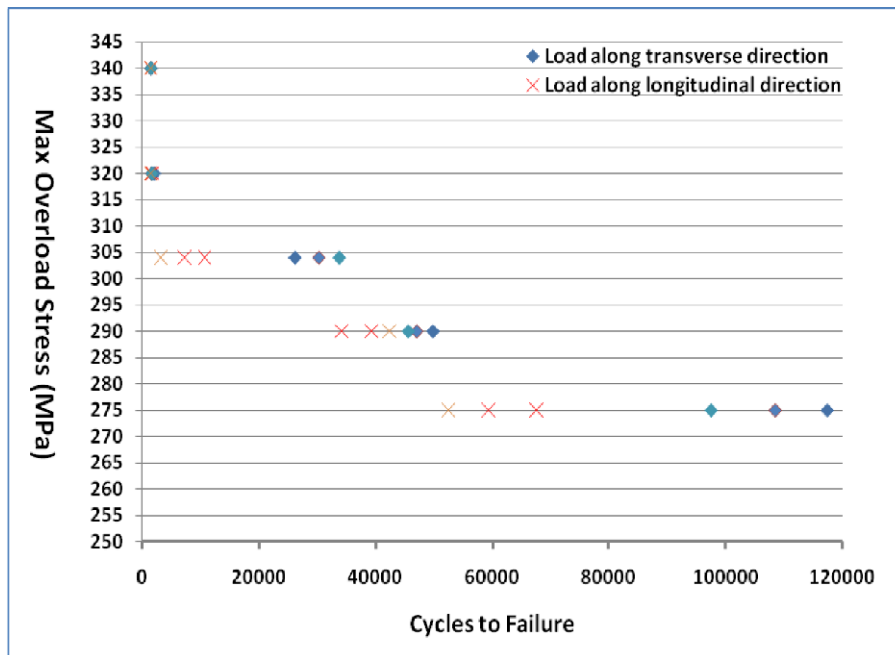


Figure 2: S-N plot for 2024-T351 with grain oriented along and transverse to the loading axis [10]

It can be observed that when load is applied transverse to the rolling direction there is marked improvement of fatigue life when compared to loading along the rolling direction. This is true for a maximum overload stress of 304 MPa or lower. In an attempt to understand the origin of this difference in fatigue lives for different grain orientations, fractographic analyses were performed.

Figure 3 is an optical micrograph of a specimen that failed after about 98,200 cycles loaded transversely to the grain orientation. Many pit nucleation sites were observed on the material surface. Figure 4 shows a differential interference contrast image of a specimen with the load applied in the rolling (longitudinal) direction which failed after 67,544 cycles. This specimen had significantly fewer pits but did exhibit extensive surface cracking. In both figures, the load was applied horizontally relative to the image. Based on these results, pit nucleation seems to be the primary cause of failure for loading transverse to the rolling direction while crack propagation appears to be the dominant cause of failure for loading in the rolling direction. In the latter case, pits appeared to act as crack initiators.

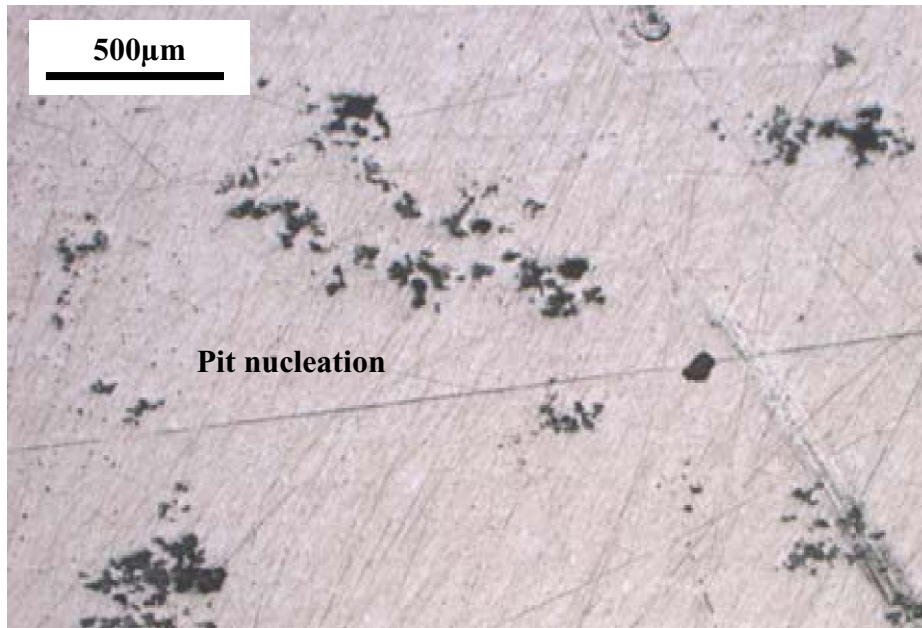


Figure 3: Optical microscope bright field image of transverse-loaded specimen, 275 MPa overload stress, showing pit nucleation [10].

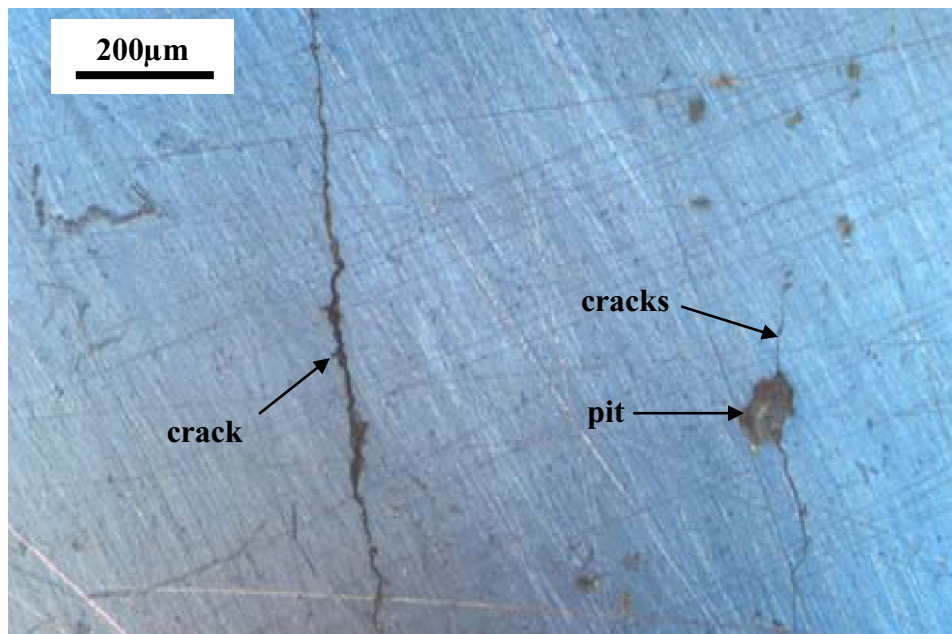


Figure 4: Differential Interference Contrast (DIC) micrograph of longitudinally-loaded specimen, 275 MPa overload stress, showing cracks apparently nucleated from pits [10].

For overloads of 290MPa and higher, slip bands and macrocracks were observed on the surface of failed specimens. This represents another failure mechanism. Slip is the movement of dislocations under an applied stress. Due to this slip mechanism, plastic deformation of real crystalline materials can occur at a much lower yield stress than for a theoretical perfect crystal [11,13]. Figure 5 shows a collection of slip lines. As mentioned previously, slip lines occur as a result of applied stress and intensify in depth and thickness as cyclic loading continues. With continual loading, there is increase in energy in the slip lines. But slip cannot set in until a stress value, known as the critical resolved shear stress, is reached. The critical resolved shear stress is the component of shear stress, resolved in the direction of slip, necessary to initiate slip in a grain. The value of the critical resolved shear stress depends on the atomic bonding, but the applied load needed to achieve this stress depends on the orientation of the crystal relative to the loading axis [13]. On an atomic level, plastic deformation

corresponds to the tearing of atomic bonds. In a perfect crystal each atom has many bonds with its surrounding atoms. For plastic deformation of a perfect crystal to take place all these bonds would need to be broken. At the site of a dislocation there is a line of free atoms (the dislocation line). The dislocation line can move through the polycrystalline material in the direction of the applied stress by breaking only one line of bonds at a time. This requires far less energy than breaking lots of bonds simultaneously, so the material can deform under a much lower applied stress. As the energy increases up to a critical value, crack initiates from the slip lines. From Figure 5, it can be seen that the slip band is at the surface of the specimen. Slip starts from the surface and slowly progresses into the material. The situation is made worse by the overloads. During the overloads, there is high driving force that causes material imbalance, as a result the energy in the slip bands increase faster, while the crack closure rate decreases, thus crack initiation and propagation occur faster causing more material damage that would normally have occurred if there was no overload [12]. This implies that the environment and surface finish play an important role in fatigue life. The life of the specimen can be significantly increased by surface treatment procedures such as polishing [11].

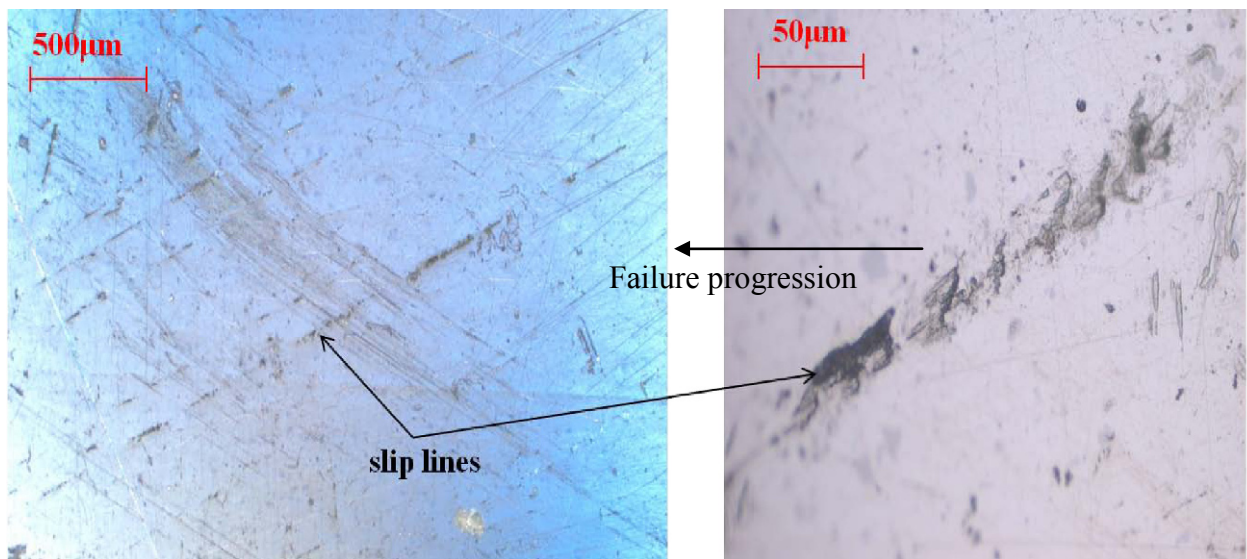


Figure 5: Slip lines observed on the surface of a longitudinally-loaded specimen, 290 MPa overload stress [10].

CONCLUSIONS

The main objective of this research was to evaluate the effects of load wave form and grain direction on the corrosion fatigue behavior of Al 2024-T351 in a simulated ocean environment. Results showed that the fatigue life of specimens loaded in the rolling direction tended to be less than that of specimens loaded transverse to the rolling direction for the same magnitude of overload stress. This difference in fatigue life seemed to originate from a change in failure mechanism from pit nucleation for the transversely-loaded specimens to crack propagation for the longitudinally-loaded specimens. At higher values of the overload stress, slip lines were observed to form on the surface of the specimens. These slip lines appeared to serve as pit nucleation sites.

ACKNOWLEDGEMENTS

The authors would like to acknowledge the support of Mr. Okoro by the UND Mechanical Engineering Department through a Graduate Teaching Assistantship and the aid of Mr. Jay Evanstad in machining the tensile test samples.

REFERENCES

- [1] Bernstein H. and C. Loebly (1988). Low-cycle corrosion of three engineering alloys in salt water, *Journal of Engineering Materials and Technology*, **110**(3), pp. 234-239.
- [2] Chlistovsky, R.M, P.J. Heffernan, et al. (2007). Corrosion fatigue behavior of 7075-T651 aluminum alloy subjected to periodic overloads, *International Journal of Fatigue*, **29**, pp 1941-1949.

- [3] Harvey C.V. and J. Min-Ten (1990). Fatigue of aluminum alloy 2024-T351 in humid and dry air, Journal of Materials Science, **25**, pp. 4708-4711.
- [4] Almar-Naess, A., et al. (1980). "Failure Analysis of Alexander L. Kielland. Examination of Fracture Surfaces and Materials," STFOI F80008, SINTEF.
- [5] Ramsamooj, D. and T. Shugar (2001). Modeling of corrosion fatigue in an aggressive environment, International Journal of Fatigue, **23**, pp. S301-S309.
- [6] Cramer E.H, R. Loseth, et al. (1995). Fatigue assessment of ship structures, Marine Structures **8**, Elsevier Science Limited, Britain, pp. 359-383.
- [7] Dean R.G. and R.A. Dalrymple (2008) Water wave mechanics for Engineers and scientists, Vol. 2, World Scientific Publishing Co., Singapore.
- [8] Van der Walde, K., J.R. Brockenbrough, et al. (2005). Multiple fatigue crack growth in pre-corroded 2024-T3 aluminum, International Journal of Fatigue, **27**, pp. 1509-2067.
- [9] Cavalli M. and H. Okoro (2009). Effects of Testing Parameters on Corrosion-Fatigue of 2024-T351 Aluminum, Proceedings of the SEM Annual Conference & Exposition, Albuquerque, NM, U.S.A.
- [10] Okoro, H.E. (2010). Effect of wave load form and grain direction on the corrosion fatigue behavior of Al 2024-T351 in salt-water environments. M.S. Thesis, University of North Dakota, U.S.A.
- [11] Stephens, R.I., A. Fatemi, et al. (2001). Metal Fatigue in Engineering, pp. 53–55, John Wiley and Sons, New York.
- [12] Barun Kanti Majumdar, B. (1986). Drill pipe fatigue analysis in offshore application. M.S. Thesis, Texas Tech University, U.S.A
- [13] Chawla, K. and M. Meyers (2009). Mechanical Behavior of Materials, 2nd edition, Cambridge University Press, United Kingdom.

The Effect of Processing Conditions on the Properties of Thermoplastic Composites

Frederick P. Cook, Virginia Tech, Department of Engineering Science and Mechanics, 106 Norris Hall, Blacksburg, VA 24060, fcCook@vt.edu
Scott W. Case, Virginia Tech, Department of Engineering Science and Mechanics

1 Abstract

Ultra high molecular weight polyethylene (UHMWPE) composites are produced from SpectraShield 3124 to evaluate the influence of the magnitude of the temperature and the pressure used to consolidate the composite on selected mechanical and physical properties. In this study, properties of composites processed using higher and lower temperatures and pressures than is the industry standard are examined. Differential scanning calorimetry (DSC) is used to examine differences in crystallinity, and dynamic mechanical analysis (DMA) is used to examine creep compliance response of the different materials. Tensile properties of the composites are also evaluated. Results indicate that higher processing pressure may result in more favorable tensile properties, but that the impact of processing temperature is relatively small.

2 Introduction

Ultra-high molecular weight polyethylene (UHMWPE) composites are used in applications requiring lightweight materials that are very strong and have favorable properties at high strain rates. The two primary UHMWPE fibers and laminates for high strain-rate applications are DSM (Dyneema) and Honeywell (Spectra and SpectraShield). The typical procedure for processing these materials involves stacking the desired number of sheets in a cross-ply lay-up, then placing them in a hydraulic press with heated platens for a certain period of time at a specified pressure and temperature [1]. Raising the temperature allows the matrix material to flow and adhere to the fibers. The pressure applied has been linked to composite interlaminar and fiber shear properties [1].

In this study, testing is completed on samples of UHMWPE processed five different pressure and temperature combinations. The tests completed include tensile strength, a creep compliance temperature sweep, and differential scanning calorimetry. Tensile properties of UHMWPE are very important to the designers of systems utilizing the material [1].

Creep compliance may be used in time-temperature superposition (tTSP) to estimate properties at high and low strain rates from intermediate strain-rate testing. tTSP is based on the principle that the properties of certain materials at various strain rates may be estimated by performing tests at corresponding (but differing) rates and temperatures. It is used on time-dependent materials to estimate their properties on time scales much longer or shorter than is convenient or possible to perform testing on. Stiffness or compliance data taken at different temperatures may be shifted left or right along a time scale to create a master curve. This master curve can then be used to predict the behavior of the material at time scales or strain rates that are not physically achievable on test equipment [2]. tTSP has also been applied to failure mechanisms by Miyano et al., who successfully shifted composite strength data over time to predict long-term durability in graphite fiber/vinyl ester (GFRP) laminates [4]. While tTSP is not applied in this text, differences in tensile creep compliance values are examined and may be indicative of tensile properties at different strain rates.

Differential scanning calorimetry (DSC) involves measuring the amount of energy needed to raise the temperature of a sample of a material by a certain amount. The results of these tests are used to measure the crystallinity of a sample [3].

3 Materials

3.1 Laminate processing procedure

Sheets of the Honeywell commercial SpectraShield 3124 product (which has a lay-up of [0,90]) were cut to the desired dimensions, most commonly 30.5 cm x 30.5 cm using a small computer-controlled circular saw. These sheets were then stacked in the desired configuration. In order to reduce processing time, multiple panels were consolidated in a single press cycle by placing a sheet of silicon paper between each. Panels were placed between two aluminum sheets (approximately 0.6 cm thick) and placed between the platens of the press. Panels were pressed at 4.79 MPa (with the sides unconstrained) and heated from room temperature to close to the desired processing temperature. Once the temperature stabilized there, the pressure was increased to the desired processing pressure and the temperature brought to the desired processing temperature. The panels were held at this temperature for approximately 15 minutes, and then were allowed to cool under pressure, which also took approximately 15 minutes. Once cooled to room temperature, the pressure was relieved and the panels were removed.

Five different sets of panels were processed in this way, such that panels processed as shown in [Table 1](#) were created.

Table 1: Processing conditions for various panels.

	Temp °C	Pressure, MPa
Panel 4	127	19.4
Panel 5	127	23.7
Panel 6	128	15.5
Panel 7	136	18.3
Panel 8	122	18.3

4 Testing Procedure

4.1 Creep Compliance Testing

A TA Q800 DMA was used to conduct creep compliance tests of lamina and laminates. Specimens were cut from larger panels using a razor blade to dimensions of approximately 20 mm by 6 mm. They were gripped using the thin film gripping mechanism on the DMA, with a gauge length of approximately 8 mm. A creep compliance temperature sweep program was set up for which the temperature of the sample was varied from -80°C to 40°C at 10°C increments. At each temperature, the chamber and the sample were allowed to equilibrate for 10 minutes, then a tensile load of approximately 15 N (corresponding to a stress of approximately 6 MPa) was applied and elongation of the sample was measured for 10 minutes.

4.2 Laminate Tensile Testing

For gathering tensile properties, the as-processed laminates were cut using a water-jet cutting machine at ARL-Aberdeen. A CAD program directed the machine to cut the 30.5 cm x 30.5 cm panels into 2.5 cm x 15.2 cm specimens. At Virginia Tech, aluminum extensometer tabs were glued to each specimen approximately 2.5 cm apart using an M-Bond 200 adhesive and catalyst.

Laminate testing was done using an MTS hydraulic piston-actuated load frame. A one-inch gage-length MTS 632.27E-20 extensometer with a one-inch gauge length was used for strain measurements, and was calibrated prior to each testing session. A 22-kip capacity MTS Force Transducer 661.20 was used for load measurements. MTS 647 Hydraulic Wedge Grips were used to grip each specimen at a pressure of 74 MPa. An in-house NI LabVIEW program was used to control the load applied to the sample during each test and to collect data.

4.3 Differential Scanning Calorimetry (DSC) Testing

A Netzsch STA 449F1 was used to complete differential scanning calorimetry on a sample of each material. For each test, a baseline run was completed with only the sample holders in place. Each sample test was run shortly after the completion of the baseline to keep the conditions as closely matching as possible. Figure 1 shows the temperature profile the sample was subjected to. The intention of the test was to completely melt the sample by raising the temperature to 150 °C, measuring the entropy required to do so, and then cool it to room temperature, 20 °C, such that it fully crystallizes. It was then melted and cooled once more, so that the heat needed to melt the sample was again measured. A rate of 1 °C per minute was used for both heating and cooling.

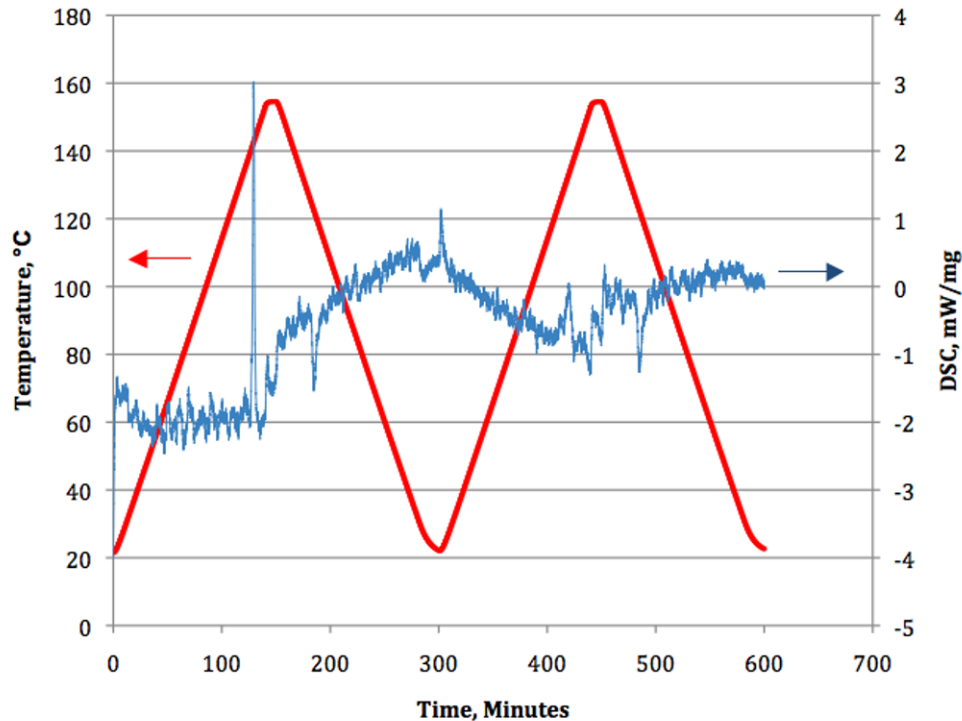


Figure 1: Temperature profile and DSC measurement for a sample from Panel 4.

5 Results

5.1 Creep Compliance Testing

A plot of shifted laminate creep compliance data is shown in Figure 2. The accompanying shift factors are shown in Figure 3.

As Figure 2 shows, the master curves do not transition smoothly between temperatures. The sample becomes more compliant as testing time increases. To determine shift factors, the slopes of the creep compliance curves at the beginning of the test are aligned.

This same method was used for several specimens for each set of processing conditions. The resulting shift factors are shown in Figure 4.

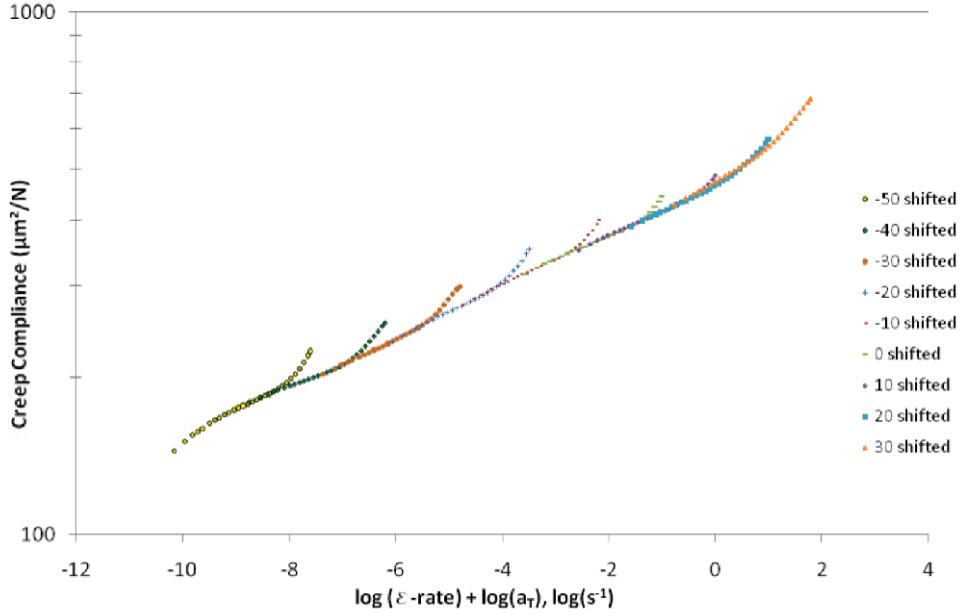


Figure 2: Shifted creep compliance of a laminate sample.

5.2 Laminate Tensile Testing

The tensile strength of each sample set is shown in Figure 5, with the horizontal axis representing the processing pressure. For panels five through eight, each point represents the average of ten tests, with error bars representing one standard deviation. For panel four, 18 tests are represented.

5.3 Differential Scanning Calorimetry Testing

Crystallinity was calculated as

$$X_c = (\Delta H_f - \Delta H_c) / \Delta H_f^\circ \quad (1)$$

where ΔH_f is the enthalpy of fusion of the original sample, ΔH_c is the enthalpy of crystallization as the sample is cooled, and ΔH_f° is the enthalpy of fusion of a 100% crystalline sample [3].

Each of these values was measured by integrating the area under the DSC-temperature curve as the material melted or crystallized. This area for the enthalpy of fusion of the original sample is shown in Figures 6. Table 2 shows the enthalpy, melting and recrystallization temperatures for each sample tested, as well as the calculated percent crystallinity, X_c .

Table 2: Enthalpy, melting and recrystallization temperatures, and calculated crystallinity, X_c for each sample tested.

	ΔH_f J/g	T_m °C	ΔH_c J/g	T_c °C	ΔH_f° J/g	T_m° °C	X_c %
Panel 4	8.90	142.2	-5.85	122.8	6.00	132.7	50.9%
Panel 5	8.42	142.0	-5.78	122.3	5.22	133.7	50.9%
Panel 6	2.18	142.6	-1.70	122.3	0.95	133.6	51.1%
Panel 7	2.96	142.6	-1.81	122.5	1.98	133.5	58.0%
Panel 8	11.44	142.6	-7.59	122.6	8.92	133.9	43.2%

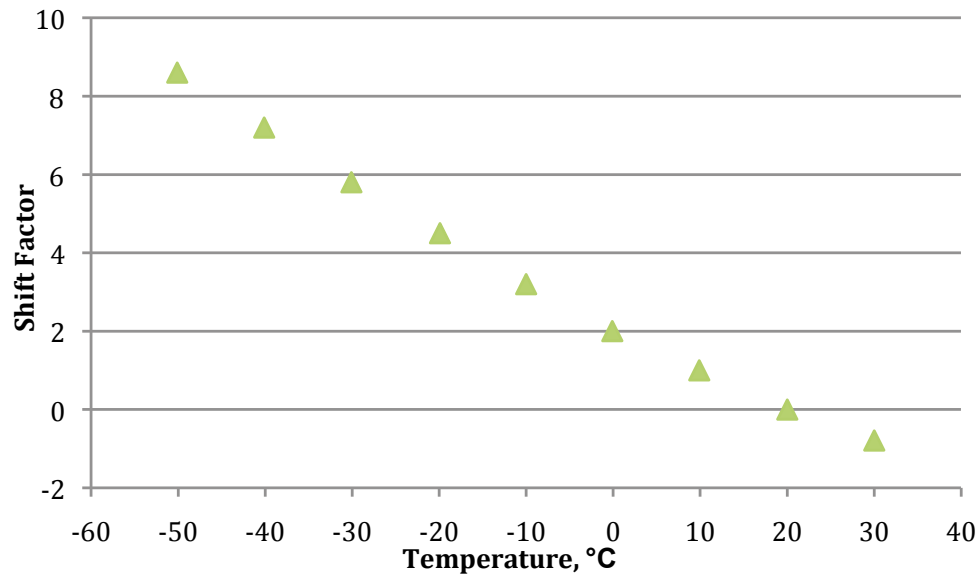


Figure 3: Shift factors associated with the master curve in [Figure 2](#).

6 Discussion

It was determined from k-sample Anderson-Darling testing that tensile strength of each sample set was from the same population as the panel processed under standard conditions. This analysis in addition to the similarity of the creep compliance data indicates that the tensile properties do not differ significantly at the various processing conditions.

Panels four, five, and six were all processed at approximately the same temperature, and have very close to the same computed crystallinity. Panel seven, which was processed at a higher temperature, exhibits a higher degree of crystallinity, while panel 8, processed at a lower temperature, exhibits a lower degree of crystallinity.

It is also noteworthy that the DSC measurements have many fluctuations close to the order of the increases seen during the melt phase of the test, bringing into question the precision of the test.

7 Conclusions

The lack of discernable difference in the tensile creep compliance or tensile strength, properties driven by fiber behavior, indicates that the fibers are largely unchanged by the heat and temperature applied during processing. This indicates that the changes are in the matrix rather than in the fiber, as any degradation in the fiber would likely have been evident in the tensile test results. Therefore, the higher crystallinity for the samples processed at a higher temperature is likely due to an increased degree of melting in the matrix material during processing. Likewise, the lower crystallinity for the samples processed at a lower temperature is likely due to less melting taking place in the matrix material at that temperature.

Future studies of the processing conditions should examine interlaminar shear strength of samples produced at different temperatures, as the matrix material largely determines these properties [1]. Additionally, through-thickness shear strength, which it is also believed is driven by matrix properties, should be examined in samples processed at different temperatures and pressures [1].

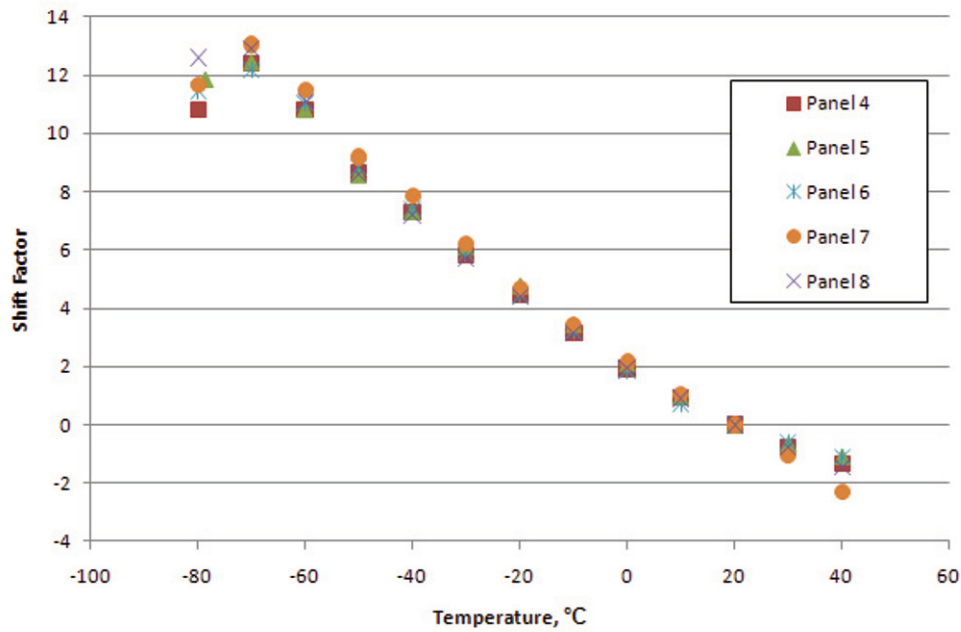


Figure 4: Creep compliance shift factors of panels at various processed at various conditions.

8 Acknowledgements

Research was sponsored by the Army Research Laboratory and was accomplished under Cooperative Agreement Number W911NF-06-2-0014. The views and conclusions contained in this document are those of the authors and should not be interpreted as representing official policies, either expressed or implied, of the Army Research Laboratory or the U.S. Government. The U.S. Government is authorized to reproduce and distribute reprints for Government purposes notwithstanding any copyright notation hereon.

Bibliography

- [1] Bhatnagar. *Lightweight ballistic composites: military and law-enforcement applications*. Woodhead, 2006.
- [2] Brinson L. Brinson H. *Polymer engineering science and viscoelasticity*. Springer, 2008.
- [3] Hay J.N. Kong Y. The measurement of the crystallinity of polymers by dsc. *Polymer*, 43:3873–3878, 2002.
- [4] Naoyuki S. Miyano Y., Nakada M. Accelerated testing for long-term durability of gfrp laminates for marine use. *Composites: Part B*, 35:497–502, 2004.

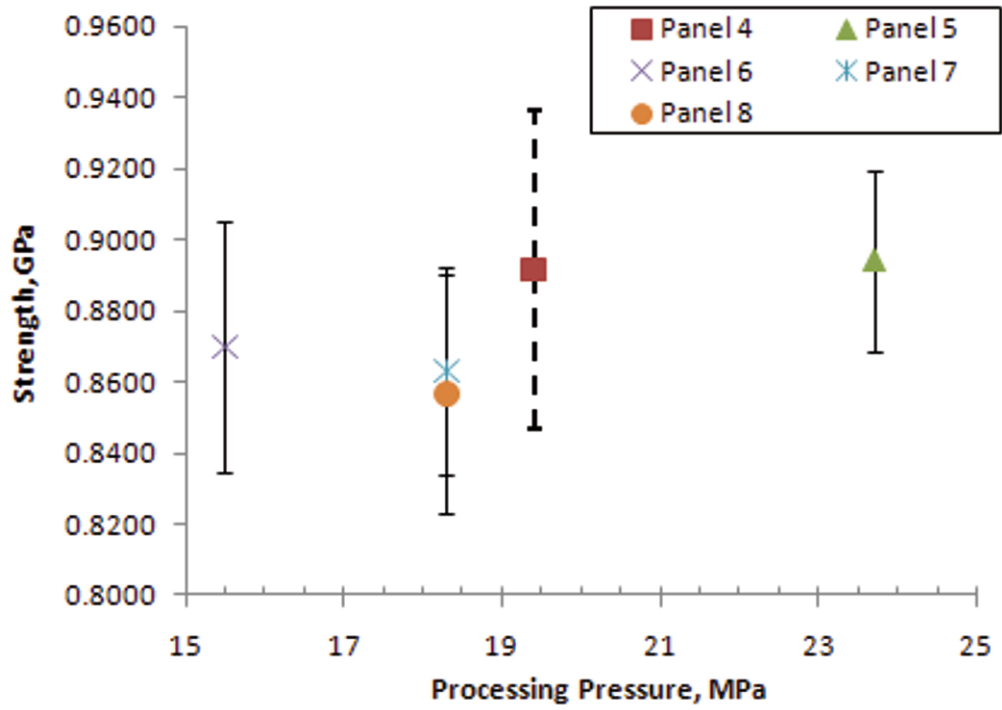


Figure 5: Laminate strength vs. processing pressure.

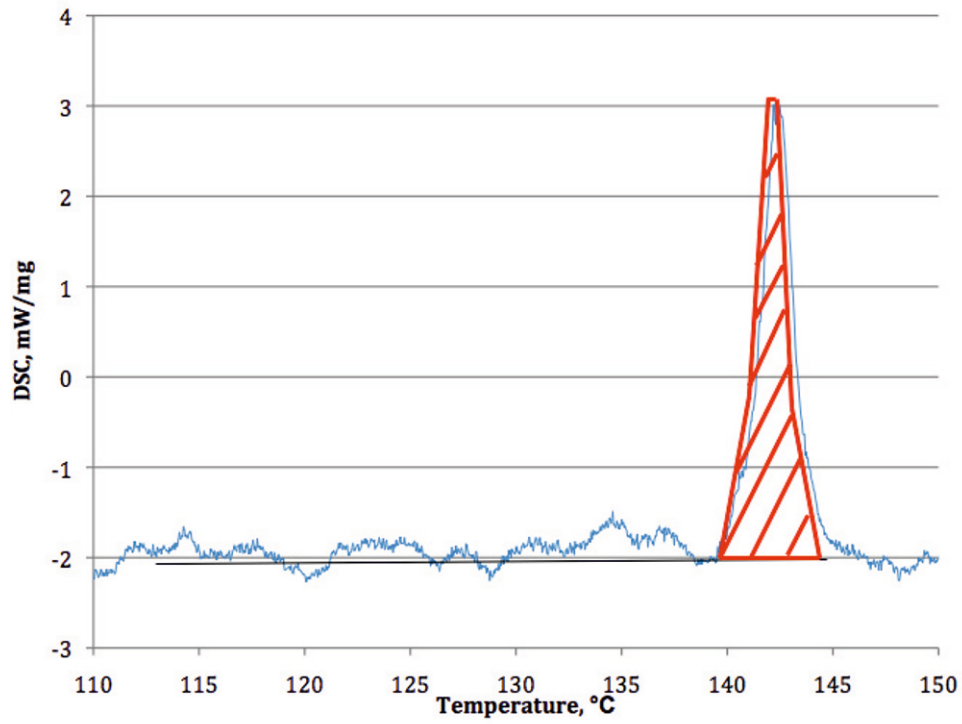


Figure 6: DSC vs. temperature for a sample from Panel 4, with the area approximating the enthalpy of fusion for the sample highlighted in red.

CALCULATION OF SHELLS AND PLATES CONSTRUCTED FROM COMPOSITE MATERIALS

R. Tskvedadze, G. Kipiani, D. Tabatadze

(Georgian Technical University , 77 M. Kostava str.,
Tbilisi, 0175, Georgia)

Abstract: *In the article is considered the analysis problem of having irregularity plates when the plate consists from the various strength separate elements which are connected with each other by ideal hinges. The simultaneous equations are solved by developed by Sh. Mikeladze for discontinuous functions generalized Maclaurin series which automatically considers in points of interfaces the values of functions and jumps of their derivatives.*

Keywords: plate; Maclaurin series; fiber; discontinuous; jump.

1. INTRODUCTION

It is possible to consider as classical example of composite materials the reinforced concrete constructions which the mankind applies already almost two centuries. Nowadays the large application was received by two versions of the reinforced fibers: Kevlar-29 and Kevlar-49. Physic mechanical properties of these fibers essentially differ from routine organic fibers. The material is characterized by high strength. The linear dependence between strain and stress takes place until of fibers break that from the mathematical point of view simplifies the problem solution within the linear theory. These materials differ also by high chemical stability. From composite materials are created typical load-bearing units - various plates and shells.

Such structures analysis is led to integration problem of such differential equations or simultaneous equations which variable coefficients undergoes the ordinary discontinuity in one or several finite points. Boundary conditions are expressed on border by desired function and its derivative. Certainly, the variety and specificity of problems of structural mechanics does not give the possibility of such universally super method development which would be effective in all cases. Therefore continuous development and perfection of computer facilities demand working out of essentially new algorithms, but on the other hand gives the chance to apply known algorithms which were earlier aren't realized or are less known.

2. BASIC PART

To the analysis problem of shells and plates with discontinuous parameters are devoted the works of many known scientists [1,2,3,4,5,] in which the basic accent is made on the possible account of caused jumps by cuts and apertures.

One of powerful mathematical methods of the given problem general solution is developed by Shalva and Zurab Mikeladze the general theory of design of discontinuous solutions [6, 7]. By basing on this theory

are considered such plate's analysis problems, which geometrical and physical characteristics undergo the ordinary discontinuity in one or several points.

Is considered the rectangular plate with sides length of $2a$ and b . The plate consists from separate orthogonal elements which are connected with each other by ideal joints. The plate undergoes influence of the distributed loading.

The co-ordinates (x_1, y_1, z_1) are selected as it is shown on Fig. 1. The differential equation of plate bending has the following form [8]

$$\frac{\partial^4 W}{\partial x_1^4} + 2 \frac{\partial^4 W}{\partial x_1^2 \partial y_1^2} + \frac{\partial^4 W}{\partial y_1^4} = \frac{q(x_1, y_1)}{D_n}, \tag{1}$$

where W is the value of deflection of a plate, $D = \frac{E_n h^3}{12(1-\nu_n^2)}$ - is the cylindrical rigidity, $q(x_1, y_1)$ is the distributed load intensity, E_n - is the separate elements modulus of elasticity, ν_n - is the Poisson's ratio, and h is the plate's thickness, which also would stepwise changed .

According to Hooke's law exists the following equalities [1]

$$\begin{cases} M_{x_1} = -D_n \left(\frac{\partial^2 W}{\partial x_1^2} - \nu_n \frac{\partial^2 W}{\partial y_1^2} \right), \\ M_{y_1} = -D_n \left(\frac{\partial^2 W}{\partial y_1^2} - \nu_n \frac{\partial^2 W}{\partial x_1^2} \right), \\ H = -D_n (1 - \nu_n) \frac{\partial^2 W}{\partial x_1 \partial y_1}, \\ Q_{x_1} = -D_n \frac{\partial}{\partial x} \left(\frac{\partial^2 W}{\partial x_1^2} + \frac{\partial^2 W}{\partial y_1^2} \right), \\ Q_{y_1} = -D_n \frac{\partial}{\partial y} \left(\frac{\partial^2 W}{\partial x_1^2} + \frac{\partial^2 W}{\partial y_1^2} \right), \end{cases} \tag{2}$$

where M_{x_1} and M_{y_1} are the bending moments, H - the torsion torque, Q_{x_1} and Q_{y_1} - the shearing or lateral forces.

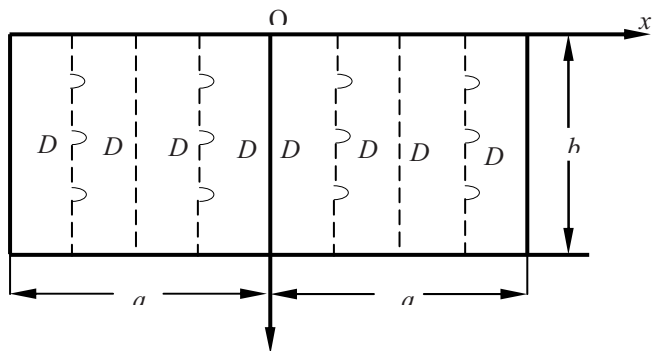


Fig. 1. Single span composite plate composed from Kevlar-49 longitudinal fibers and fine-aggregate concrete

Let's enter the dimensionless coordinates

$$\begin{aligned} x &= \frac{x_1}{a}, & -1 \leq x < +1, & \quad \eta = \frac{a}{b}, \\ y &= \frac{y_1}{b}, & 0 \leq y < 1. \end{aligned} \quad (3)$$

By taking into account the equalities (3) (1) will take the following form:

$$\frac{\partial^4 W}{\partial x^4} = +2\eta^2 \frac{\partial^4 W}{\partial x^2 \partial y^2} + \eta^4 \frac{\partial^4 W}{\partial y^4} = \frac{q(x, y) a^4}{D_n}. \quad (4)$$

Let's carrying out the separation of equation (4). With this purpose let's present the acting on the plate load $q(x, y)$ as the following trigonometric series:

$$q(x, y) = \sum_{m=1}^{\infty} q_m(x) \sin m\pi y, \quad (5)$$

where

$$q(x) = 2 \int_0^1 q(x, y) \sin m\pi y dy. \quad (6)$$

In this case is reasonable the deflection of plate $W(x, y)$ represents as similar series

$$W(x, y) = \sum_{m=1}^{\infty} W_m(x) \sin m\pi y, \quad (7)$$

If we will mean, that plate with sides of $y=0$ and $y=1$ is free supported then defined by equality (7) deflection function satisfies to the boundary conditions $y=0$ and $y=1$ along the edges.

In the case of uniformly distributed load (5) and (6) equalities gives:

$$\begin{aligned} q(x) &= 2 \int_0^1 q \sin m\pi y dy = \frac{4q}{m\pi}, \quad m = 1, 3, 5, \dots \\ q(x, y) &= \frac{4q}{m\pi} \sum_{m=1,3,5} \frac{1}{m} \sin m\pi y. \end{aligned} \quad (8)$$

By taking into account (7) and (8) (4) gives

$$W_m^{IV}(x) - 2\alpha_m^2 W_m^{II}(x) + \alpha_m^4 W_m(x) = \frac{q_m a^4}{D_m}. \quad (9)$$

where

$$\alpha_m = \eta m \pi, \quad q_m = \frac{4q}{m\pi}.$$

The equalities (2) by taking into account (6) gives:

$$\begin{cases} M_x = -\frac{D_n}{a^2}(W_m''(x) - \nu_n \alpha_m^2 W_m(x)) \sin m\pi y, \\ M_y = -\frac{D_n}{a^2}(\nu_n W_m''(x) - \alpha_m^2 W_m(x)) \sin m\pi y, \\ H = -\frac{D_n}{a^2}(1 - \nu_n) \alpha_m W_m'(x) \cos m\pi y, \\ Q_x = -\frac{D_n}{a^2}(W_m''(x) - \alpha_m^2 W_m(x)) \sin m\pi y, \\ Q_y = -\frac{D_n}{a^2}(\alpha_m W_m''(x) - \alpha_m^3 W_m(x)) \cos m\pi y. \end{cases} \quad (10)$$

Expression (9) represents the ordinary differential quartic equation which right part and derivatives of desired $W_m(x)$ function undergoes discontinuity of the first kind in conjugation points. Let's apply the generalized by Sh. Mikeladze Maclaurin series without remainder term and generate the discontinuous solution of (9) differential equation. The generalized Maclaurin series in our case takes the form

$$W_m(x) = \sum_{k=0}^n \frac{x^k}{K!} W_m^{(k)}(0) + \sum_{k=0}^n \frac{x^k}{K!} \sum_{\rho=1}^z \delta_\rho^{(k)} (x - x_\rho), \quad (11)$$

where x_ρ and $\delta_\rho^{(k)}$ accordingly denotes the break points and $W_m^{(k)}$ the function jump, n – is the remained in series terms number, and r – is the number of break points. Let's observe the $W_m^{(k)}$ function and its derivatives behavior in the x_ρ break points.

Due the plate elements hinged connections the $W_m^{(k)}$ function is continuous in $x = x_\rho$ break points, as for the $W_m''^{(k)}$ function it undergoes the discontinuity of the first kinds $x = x_\rho$ break points. In particular, angles of rotation in the hinge on right and left sides are different from each other that cause the $W_m^{(k)}$ function discontinuous. Thereupon that in the hinge bending moment is equal to zero from the first equality of (10) results, that $W_m''^{(k)}$ also didn't undergoes break in the $x = x_\rho$ points.

From the continuity condition of shear force Q_x in the break points from (10) is clear the character of discontinuity of $W_m'''^{(x)}$ function due the diversity of D_n value $(D_n)_+ \neq (D_n)_-$.

As in general the jump value $\delta_\rho^{(k)}$ in the $x = x_\rho$ break points k -th derivative $W_m^{(k)}(x)$ of $W_m(x)$ function jump value $\delta_\rho^{(k)}$ in the $x = x_\rho$ break points is defined by formula

$$\delta_\rho^{(k)} = W_m^{(k)}(x_\rho + 0) - W_m^{(k)}(x_\rho - 0),$$

where $W_m^{(k)}(x_\rho + 0)$ and $W_m^{(k)}(x_\rho - 0)$ accordingly represents the values of $W_m(x)$ function when we approximate to x_ρ point from the right and then from the left.

The value of 4-th derivative jump we find from the (9) equality

$$\delta_\rho^{(4)} = [W_m^{IV}(x_\rho + 0) - W_m^{IV}(x_\rho - 0)] = q_m a^4 \left(\frac{1}{D_{\rho+1}} + \frac{1}{D_\rho} \right) \text{ or}$$

$$\delta_{\rho}^{(k)} = \frac{q_m a^4}{D_{\rho}} \left(\frac{1}{D_{\rho+1}} - 1 \right).$$

If we differentiate term by term the equality (9) to the necessary order we can present the higher derivative $W_k^{(k)}(o)$ and also jump $\delta_{\rho}^{(k)}$ by lower derivatives. In particular all even derivatives $W_m^{(2i)}(o)$ ($i = 2, 3, 4, \dots, n/2$) would be expressed by combination of $W_m(o)$ and $W_m'(o)$ and $\delta_{\rho}^{(2i+2)}$ ($i = 2, 3, 4, \dots, n/2$) jumps by $\delta_{\rho}^{(k)}$, as for the jump of odd derivative functions they would be presented as combination of $\delta_{\rho}^{(1)}$ and $\delta_{\rho}^{(3)}$ values, and due the symmetry $W_m^{(2i+1)}(o)$ values are equal to zero.

Thus we will have:

$$W_m^{(2i)}(o) = (i-1)a_m^{2i-4} \frac{q_m a^4}{D_{\rho}} + ia_m^{2i-2} W_m''(o) - (i-1)a_m^{2i} W_m(o)$$

$$\delta_{\rho}^{(2i+1)} = ia_m^{2i-2} \delta_{\rho}^{(4)} \quad i=2, 3, 4, \dots, n/2.$$

$$\delta_{\rho}^{(2i+1)} = ia_m^{2i-2} \delta_{\rho}^{(3)} - (i-1)a_m^{2i} \delta_{\rho}^{(1)},$$

By the consideration of received equalities in the generalized Maclaurin formula we finally obtain:

$$\begin{aligned} W_m(x) = & W_m(o) \left[1 - \sum_{i=1}^{n/2} (i-1) a_m^{2i} \frac{x^{2i}}{(2i)!} \right] + W_m(o) \left[\frac{x^2}{2!} + \sum_{i=1}^{n/2} ia_m^{2i-2} \frac{x^{2i}}{(2i)!} \right] + \\ & + \frac{q_m a^4}{D_{\rho}} \sum_{i=1}^{n/2} (i-1) a_m^{2i-4} \frac{x^{2i}}{(2i)!} \left] + \sum_{\rho=1}^r \delta_{\rho}^{(1)} \left[(x-x_{\rho}) - \sum_{i=1}^{n/2} (i-1) a_m^{2i} \frac{(x-x_{\rho})^{2i+1}}{(2i+1)!} \right] + \\ & + \sum_{\rho=1}^r \delta_{\rho}^{(3)} \left[\frac{(x-x_{\rho})^3}{3!} + \sum_{i=1}^{n/2} ia_m^{2i} \frac{(x-x_{\rho})^{2i+1}}{(2i+1)!} \right] + \sum_{\rho=1}^r \delta_{\rho}^{(4)} \left[\sum_{i=1}^{n/2} (i-1) a_m^{2i-1} \frac{(x-x_{\rho})^{2i}}{(2i)!} \right]. \end{aligned} \quad (12)$$

The (12) equality includes unknown parameters $W_m(o)$, $W_m''(o)$, $\delta_{\rho}^{(1)}$ and $\delta_{\rho}^{(3)}$. For the purpose of its definition on the M_x $x = \pm 1$ edges we have the boundary conditions, and in their hinges condition of equal to zero the bending moments M_x .

in general for the boundary conditions we have:

a) the $x = \pm 1$ edges simply supported plate in this case: $W_m = 0$

$$\text{and } \frac{\partial^2 W_m}{\partial x^3} = 0 \text{ or } W_m(1) = 0, W_m''(o) = 0.$$

b) the sides $x = \pm 1$ are rigidly attached then $W_m = 0$ and $\frac{\partial W_m}{\partial x} = 0$ or $W_m(1) = 0, W_m''(o) = 0$.

c) the $x = \pm 1$ edges are free, in this case $M_x = 0$ and $\left(Q_x + \frac{\partial H}{\partial y} \right) = 0$ or $W_m''(1) - \nu \alpha_m^2 W_m(1) = 0$,
 $W_m''(1) - (2 - \nu) \alpha_m^2 W_m''(1) = 0$.

The condition of equal to zero the bending moment M_x gives to us:

$$W_m''(x_\rho) - \nu \alpha_m^2 W_m(x_\rho) = 0,$$

And the continuity condition of shear force Q_x

$$\delta_\rho^{(3)} - \alpha_m^2 \delta_\rho^{(1)} = \left(\frac{D_\rho}{D_{\rho+1}} - 1 \right) [W_m^m(x_\rho - 0) - \alpha_m^2 (x_\rho - 0)].$$

Thus we obtain the simultaneous equations by which we would defined all strength factors and components of deformation by the following equalities

$$W = W^0 \frac{q_m}{D_1} \sin m\pi\eta,$$

$$M_x = M_x^0 q_m \sin m\pi\eta,$$

$$M_y = M_y^0 q_m \sin m\pi\eta,$$

$$H = H^0 q_m \cos m\pi\eta,$$

$$Q_x = Q_x^0 q_m \sin m\pi\eta,$$

$$Q_y = Q_y^0 q_m \cos m\pi\eta.$$

In that particular case when plate consists from five orthogonal elements with different rigidity and along the $x = 0.2$ and $x = 0.6$ straight lines we have hinges (hinged connections) and in the series are remained two terms $m = 1$ and $m = 3$ and at the same time $\frac{D_1}{D_2} = \frac{D_2}{D_3} = 0.8$ and $\nu = 0.3$. For the W^0 , M_x^y , M_y^o , H , Q_x^0 ;

Q_y^0 values when the $x = \pm 1$ sides are rigidly attached in the some points of plate for their values we have following table

x	W^0	M_x^y	M_y^o	H	Q_x^0	Q_y^0
0.0	10.034	0.334	2.730	0.000	0.000	1.130
0.1	10.876	0.223	2.728	-0.100	-0.205	1.116
0.2	10.967	0	2.647	-2.240	-0.420	1.027
				1.870		
0.3	8.365	0.213	2.642	1.710	-0.410	1.149
0.4	7.016	0.305	2.005	1.625	-0.220	0.987
0/5	5.012	0.232	1.537	1.570	-1.117	0.710
0.6	3.105	0	0.940	1.527	-1.410	0.380
				1.256		
0.7	2.187	-0.525	0.613	1.160	-1.860	0.039
0.8	1.056	-1.420	-0.080	0.970	-2.466	-0.530
0.9	0.445	-2.308	-0.640	0.60	-3.168	-1.270
1.0	0	-4.439	-1.270	0.000	-4.140	-2.220

3. CONCLUSION

In work is raised and solved analytically the question of made from composite material rectangular plate calculation when the plate is presented from various rigidity elements which at the same time are connected with each other by cylindrical hinges. The question is solved by developed by Sh. Mikeladze for discontinuous functions Maclaurin generalized series.

REFERENCES:

- [1.] Mikhailov, B.K., Kipiani G.O. The spatial lamellar systems with discontinuous parameters deformity and stability. St. Petersburg. Stroyizdat SPB. 1995. - 442p.
- [2.] Ker V., Teodorevsky P. introduction in generalized function theory with application in engineering. Publishing "Mir", Moscow, 1978. -318 p.
- [3.] Bantsuri R.D., Isakhanov R.S. Some inverse problems of theory of elasticity // Transactions of Tbilisi Mathematical Institute, vol. 9, 87, 1987. pp. 3-20.
- [4.] Tskvedadze R. Variants of analysis of plates and shells with discontinuous parameters. Publishing "Technical University", Tbilisi, 2004. -115 p.
- [5.] Tabatadze D., Tskvedadze R. Plasto-elastic equilibrium of "stepped" plate // Transactions of Georgian Technical University , № 1(425), 1999
- [6.] Mikeladze Sh. E. Some problems of structural mechanics. Moscow-Leningrad, 1948. -267 p.
- [7.] Mikeladze M. Sh. Elasticity and plasticity of structures and machines elements. Tbilisi: Metsniereba. 1976. -157 p.
- [8.] Timoshenko S.P., Voinovsky-Kriger S. Plates and shells. Publishing of physical and mathematical literature. Moscow, 1963. -635 p.

Reducing Build Variation in Arched Guitar Plates

Eddy Efendy and Mark French
Department of Mechanical Engineering Technology
Purdue University
401 N. Grant St, West Lafayette, IN, 47909

Abstract

The objective of volume production is to produce identical products with little to no build variation in their parts. However, in instrument manufacture, this can be a challenging task due to the natural variation in wood properties. The purpose of this paper is to illustrate an approach to reduce build variation in the production of arched plates for acoustic guitars by using CAD/CAM software and the CNC machine. To accurately machine the arched plates, a family of curves called curtate cycloids was used during the design phase. The paper will also discuss the effort to reduce build variation during the manufacturing process by placing the arched plates under load while being machined. A series of arched back plates has been produced using this approach, and the build variation, as measured by resonant frequency, is notably reduced.

Introduction

One of the biggest challenges in volume production of stringed instrument manufacture is to produce identical sound quality for their product. Sound quality can be measured by comparing the first few resonant frequencies of parts or of whole instruments [1].

The ideal wood for a soundboard should be stiff, light and have closely spaced grain lines. Traditionally, only high grade wood of a few select species such as Sitka spruce, western red cedar and redwood have been used. Unfortunately, the availability of those types of woods is becoming limited because they are being logged faster than they can be replaced. Therefore, the manufacture of stringed instrument must adjust its practices if it wishes to maintain production.

One simple alternative is to use other species with roughly similar mechanical properties for soundboards [2]. Another, approach is to be less selective when choosing planks from the traditional species. In either case, the result can be increased variation in the mechanical properties of the raw materials. The purpose of this work is to develop a manufacturing process that can automatically compensate differences in material properties to achieve uniform dynamic response of the resulting components.

To do that, a correlation between resonant frequency and wood properties must be established. In the simplest sense, resonant frequency is a function of stiffness, k , and mass, m .

$$\omega = \sqrt{\frac{k}{m}} \quad (1)$$

Stiffness of a plate or beam is proportional to the cube of thickness, t , and mass is proportional to thickness as shown in equation (1) and (2) below,

$$k \propto t^3 = C_0 t^3 \quad (1)$$

$$m \propto t = C_1 t \quad (2)$$

Substituting equation (2) and (3) into equation (1) will make the resonant frequency, ω , to be proportional to thickness, t , as shown in equation (4) below,

$$\omega = \sqrt{\frac{k}{m}} = \sqrt{\frac{C_0 t^3}{C_1 t}} = \left(\sqrt{\frac{C_0}{C_1}} \right) (t) = C_3 t \quad (4)$$

Furthermore, within a species of wood, density and elastic modulus are roughly proportional. Thus plates or beams of differing thickness might have similar resonant frequencies if they were cut from separate, properly selected planks with differing stiffnesses and densities. If the thickness values could be chosen automatically given mechanical properties of the planks at hand, the relationships above could be used to reduce build variation in the top plates of guitars.

To test this idea, a series of arched guitar backs were machined using a CNC router while a partial vacuum was drawn on the wood blanks. Differences in the material stiffness would result in different deformations during machining process and, thus, differences in the final thickness. Since stiffness of wood (elastic modulus) is roughly proportional to density, the result should be machined plates with reduced variation in lower resonant frequencies.

Design process

In order to make sample plates using CNC machine tools, there has to be a clearly defined mathematical description for the nominal shape of the plate. Two mathematical models were utilized during the design process. First, the body outline was defined by a mathematical model in polar coordinates using curve fits [3]. [Figure 1](#) below shows the body outline, calculated from the curve fit function.

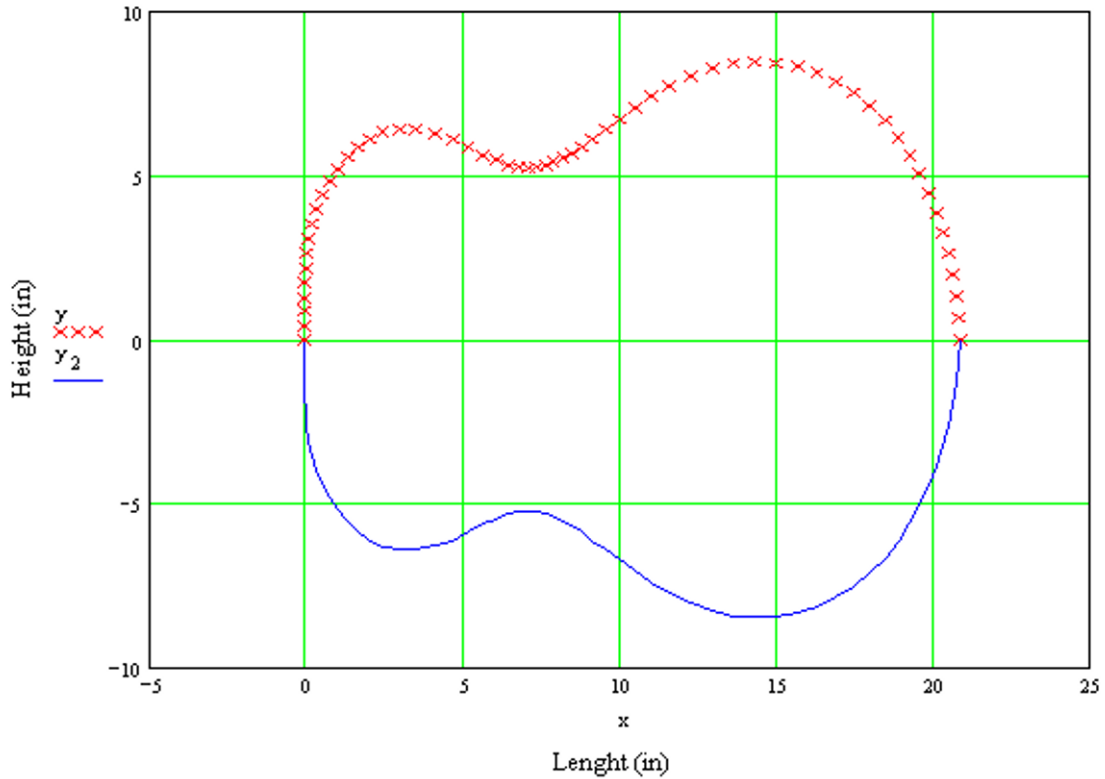


Figure 1. Classical Guitar curve Fit on Polar Coordinates

Meanwhile, for the arching designs, a different fundamental mathematical description known as the curtate cycloid curve is utilized. A curtate cycloid, as depicted in Figure 2, is the arch profile that is produced by the path of a fixed point at a radius that is less than the center point of a rolling circle. Quentin Playfair believed that curtate cycloid curves may have possibly been used since 1649 by Nicolo Amati for the back arches of a violin [4].

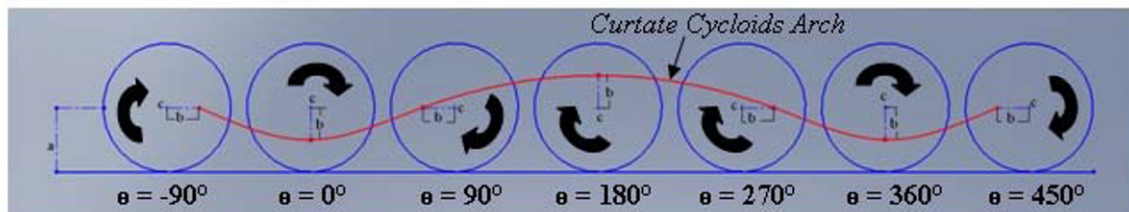


Figure 2. The Curtate Cycloid Arch

A curtate cycloid has parametric equations of

$$x = a\theta - b \sin(\theta) \quad \text{or} \quad y = a\theta - b \sin(\theta) \quad \text{Arch Length --- (5)}$$

$$z = b - b \cos(\theta) \quad \text{Arch Height --- (6)}$$

where a is the radius of the circle, b is a point at some distance from the center of a circle, and Θ (theta) the angular displacement. Notice that the highest point of the arch is always at $\Theta = 180^\circ$ and the arch is *always* symmetrical at $\Theta = 180^\circ$. By using different value for a , b , and c , (as long as $b < a$), an infinite variety of arches can be drawn accurately.

To draw an accurate soundboard model for arched guitar back, crucial dimensions for the arch thickness were taken directly from Robert Benedetto [5], as shown in Figure 3 below,

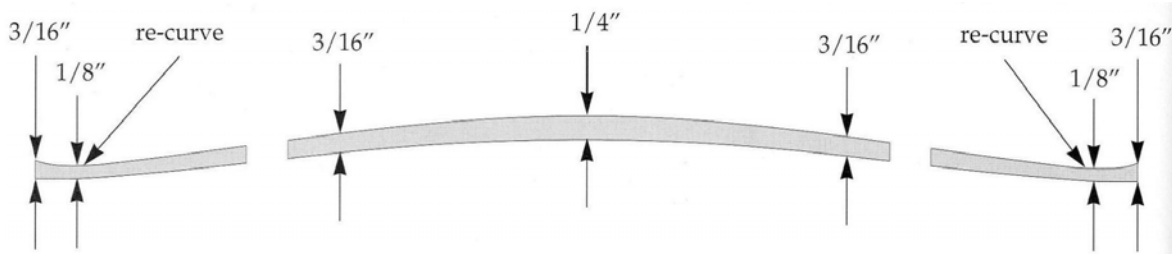


Figure 3. Longitudinal cross section of arched plates (Benedetto, 1994)

The highest point on the longitudinal arch is located at the bridge. The distance from heel to the bridge and the distance from tail to the bridge are not equivalent. Hence, four curtate cycloids are required when drawing the longitudinal cross section of the arched plates; two for the lower arch and another two for the upper arch.

Also notice how the cross section across the arched plates is irregular; the thickness at the edge is 1/8", whereas the thickness at the center is 1/4". Therefore, when calculating the upper longitudinal arched, an eighth inch offset is required for the arch height during the calculation, changing equation (6) to equation (7) shown below,

$$z = b - b \cos(\theta) + 0.125 \quad \text{Arch Height --- (7)}$$

Offset

The complete reproduction of longitudinal arch is shown in Figure 4 below. Note the re-curve of the upper right arch. This can be accomplished by setting the angular displacement for more than 360°.

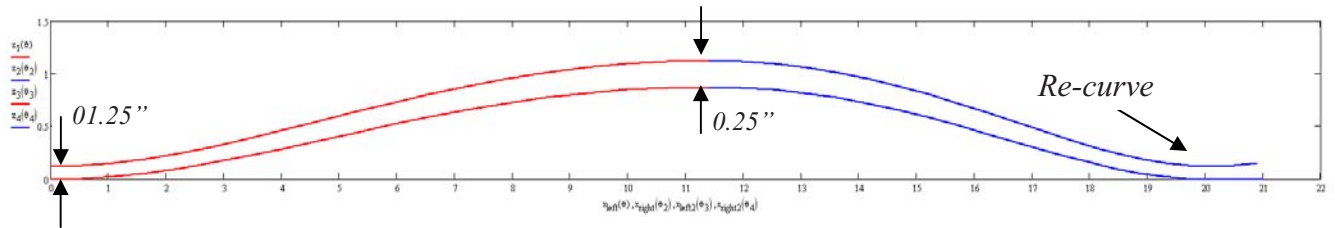


Figure 4. Longitudinal Arch

Once the longitudinal arch is established, the lateral arching can be set up. Since the guitar profile is symmetrical about the center, only half of the cycloids need to be created for the lateral arch, shown in Figure 5 below.

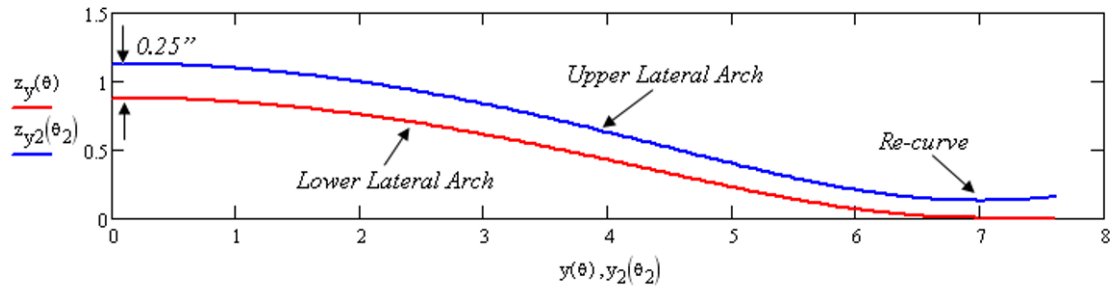


Figure 15. Lateral Arch

All the calculations can be performed using equation (1), (2), and (3) in math software such as Mathcad or even Microsoft Excel. Once the calculations are done, the values were transferred into SolidWorks software, sketching the guitar profile on the x-y axis, the longitudinal profile on the x-z axis, and the lateral profile on x-y axis, as depicted on [Figure 6](#).

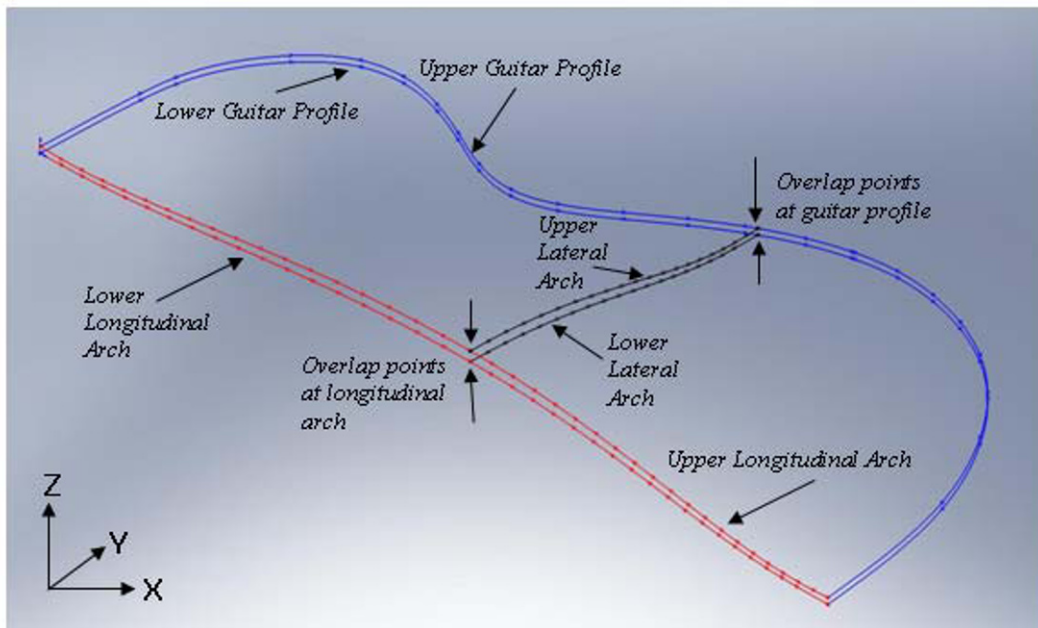


Figure 6 – Partial Arched Plate Outline

Using Loft and Mirror commands in SolidWorks were used to create the final solid model of the arched plate shown in [Figure 7](#) below.



Figure 7. Solid Model of the Complete Arched Plate

Manufacturing process

To test whether the effect of machining under partial vacuum can automatically compensate differences in material properties; two groups of arched plates were manufactured using kiln-dried, slab-sawn soft maple as wood blanks. During machining, the convex (outer) side was machined without a vacuum and the concave (inner) side was machined with a 0.5 psi vacuum, as shown in [Figure 8](#) below.

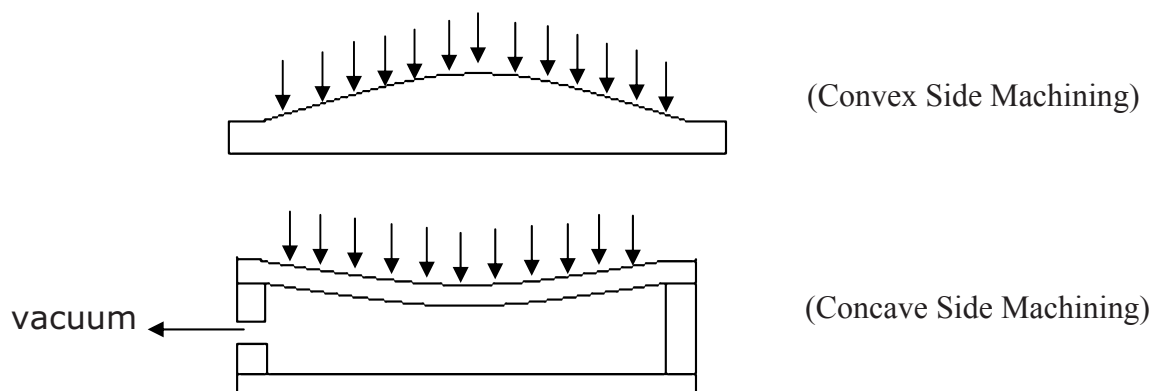


Figure 8 – Overview of Machining Process

This will let the part to pull away from the cutting tool, thus, giving a thicker top. How much the part will pull away from the cutting tool is depend on material stiffness. In the end, the vacuum pressure will assist to control the variation in tonal quality by increasing the thickness of the material.

Both convex and concave side will have roughing and finishing tool paths. [Figure 9](#) shows the configurations that are used in the machining process for this research paper. Keep in mind, that this configuration can be modified within the feed-speed limitations to speed up the processes.

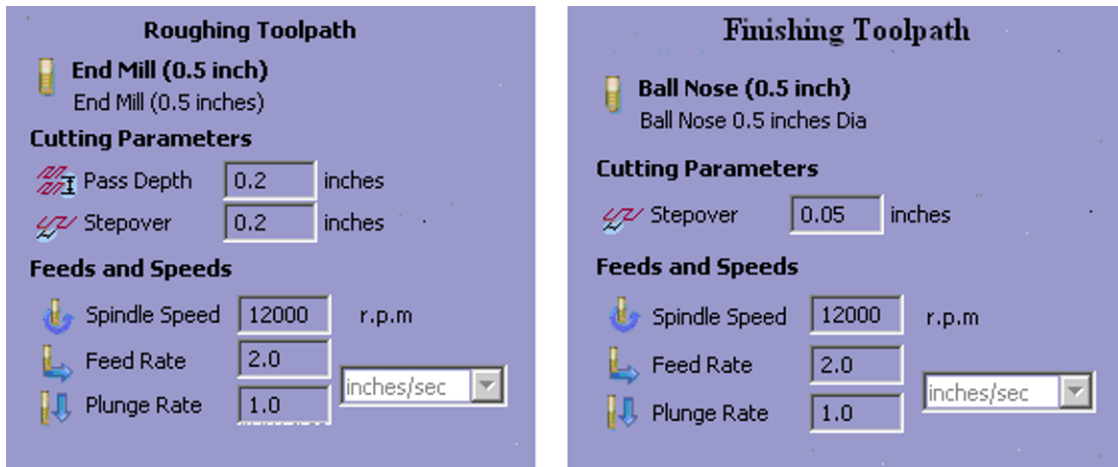


Figure 9. Machine configuration for Roughing and Finishing Cut

Figure 10 shows a CNC machining process of a rough cut and a finish cut for the convex (outer) arch of the archtop plate.



Figure 10 – Machining the Convex Side of the Plate

Testing

To determine the resonant frequencies, dynamic response measurements were taken as shown in Figure 11.

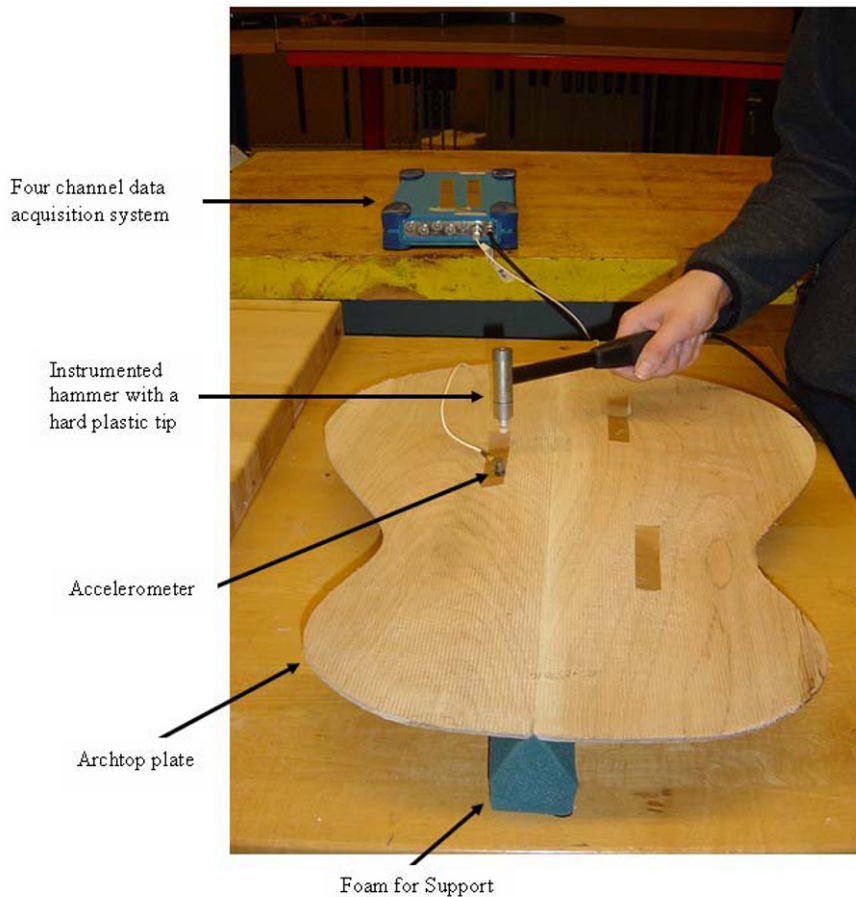


Figure 11 – Tap Testing the Completed Plate

In this dynamic response measurement test, the archtop plate was rested on foam blocks so the table won't interfere with the measured natural frequencies. Accelerometer was placed to the arched plate, and a standard hammer tap test was then performed. The hammer is equipped with a force gauge for measuring the input force. Both hammer and accelerometer are attached to channel data acquisition so the response from input force and accelerometer can be measured simultaneously. To ensure that all the lower frequency modes were captured, several hammer tap test was performed with accelerometers nearby in several location of the soundboard. The data was then recorded with the channel data acquisition. Only the first two natural frequencies (F_1 and F_2) were then compared to see if the new manufacturing process able to reduce the variation in resonant frequencies of the resulting parts.

Results and Analysis

A control chart is utilized to compare and monitor the build variation in the manufacturing process for both the experimental and control groups. The purpose is to measure the resonant frequency within three standard deviations, 3σ , of the mean value [6]. Control limits are added symmetrically above and below the mean to make it easier to interpret patterns in a run chart and draw conclusions about the state of control. The following figures (Figure 12 – Figure 15) show the data distribution for both the experimental and control groups.

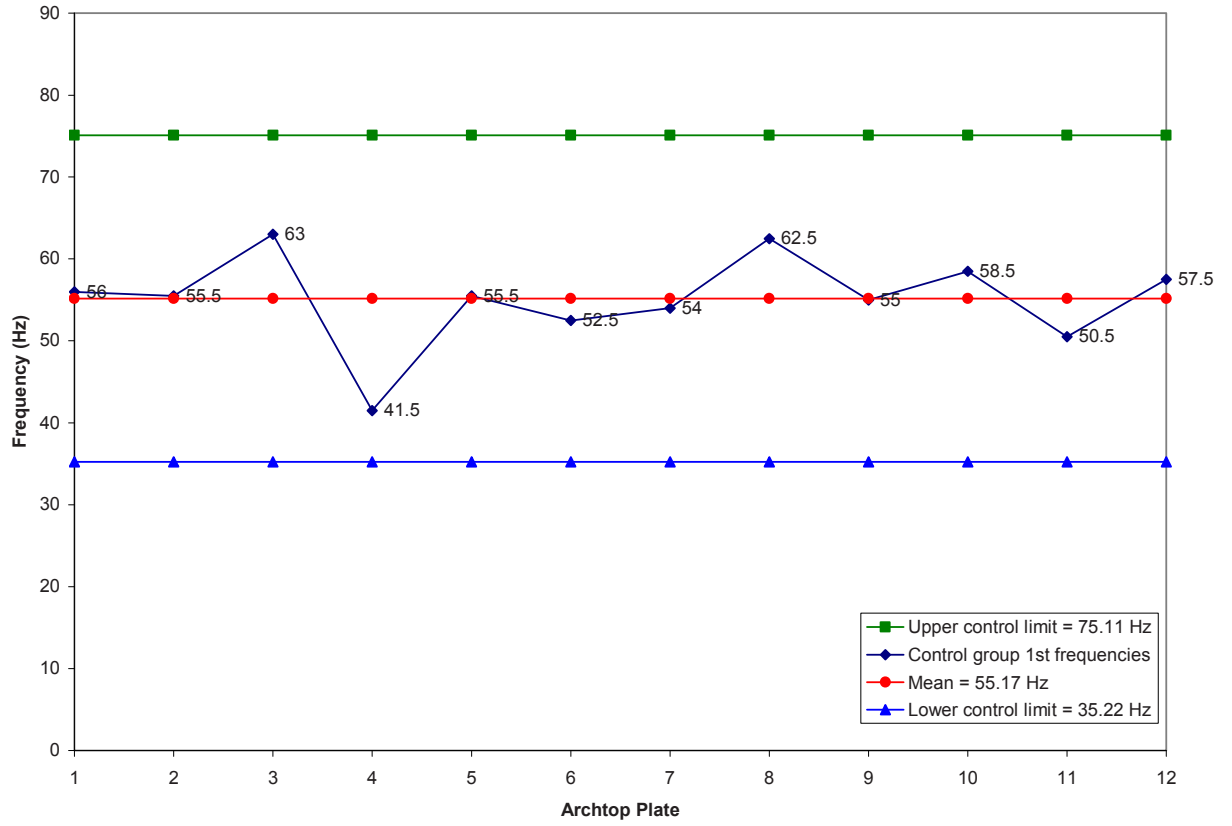


Figure 12 – Control Chart for 1st Frequencies (No Vacuum)

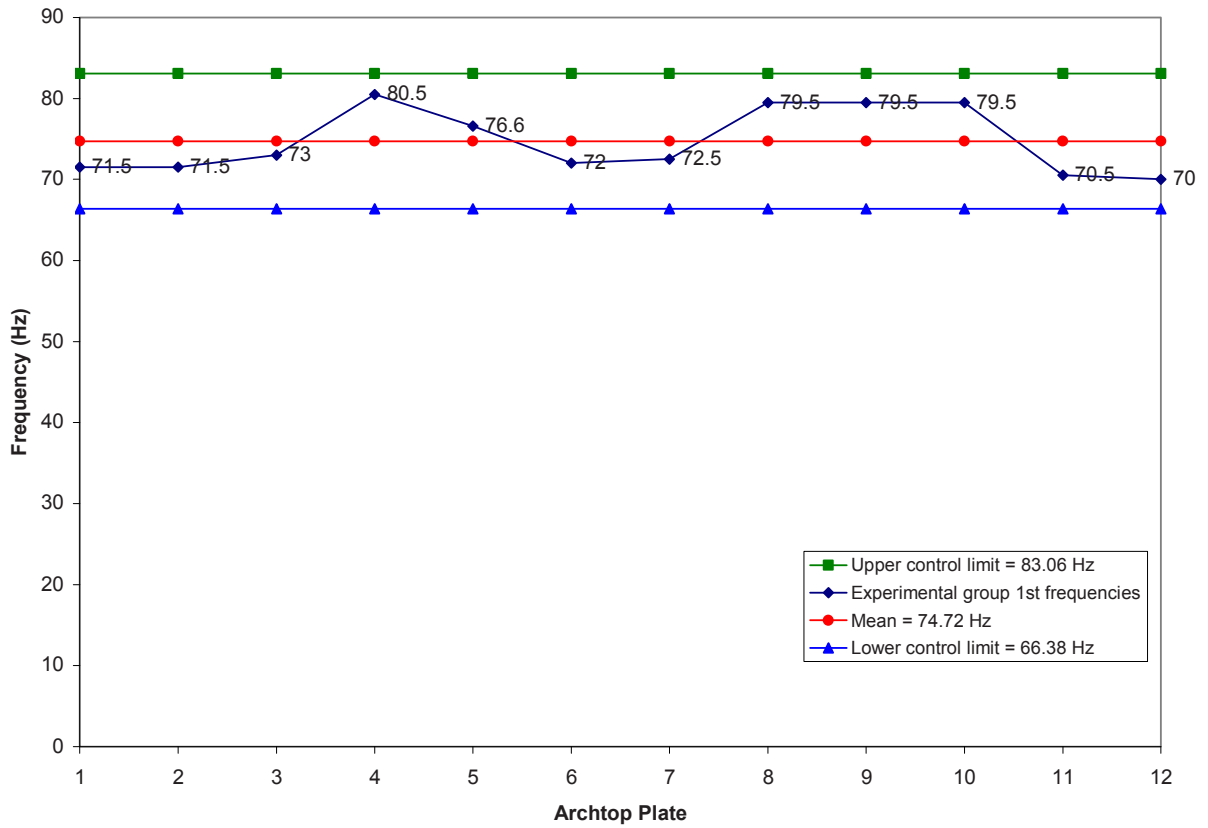


Figure 13 – Control chart for 1st Frequencies (Vacuum)

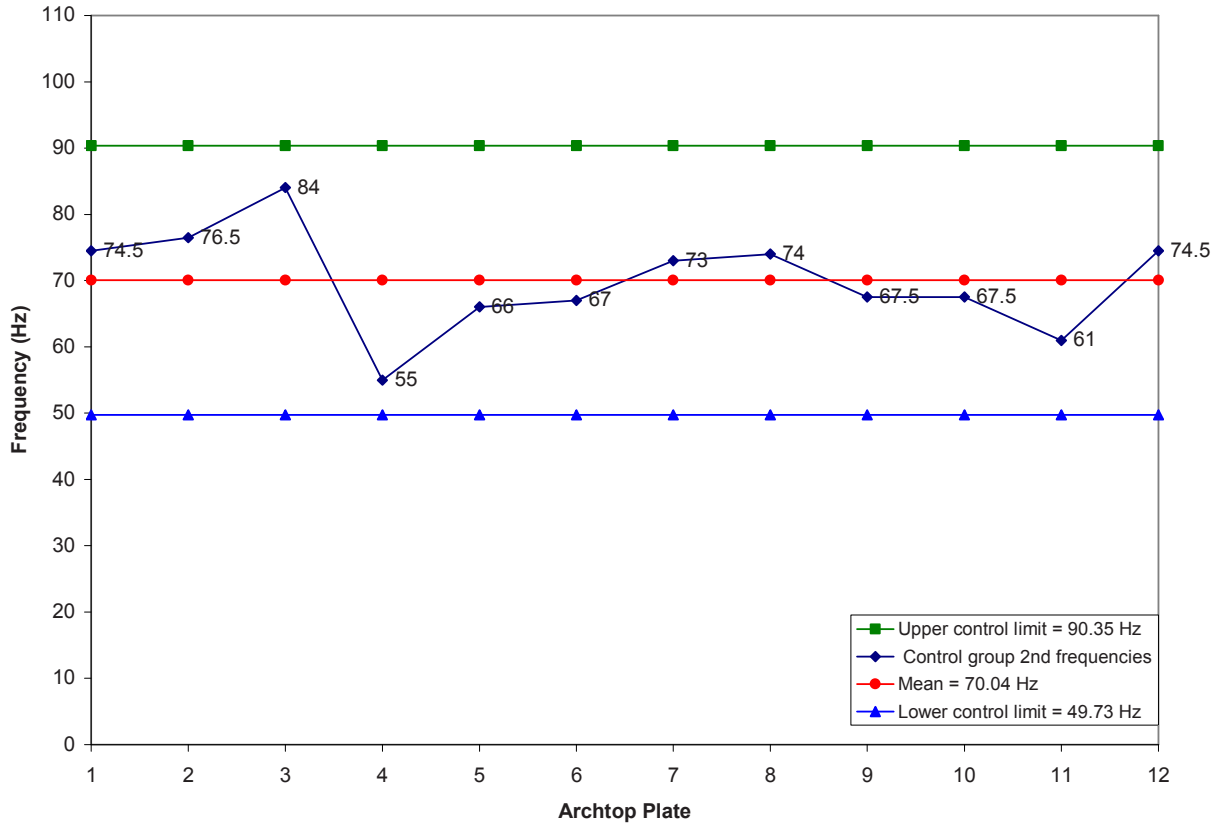


Figure 14 – Control Chart for 2nd Frequencies (No Vacuum)

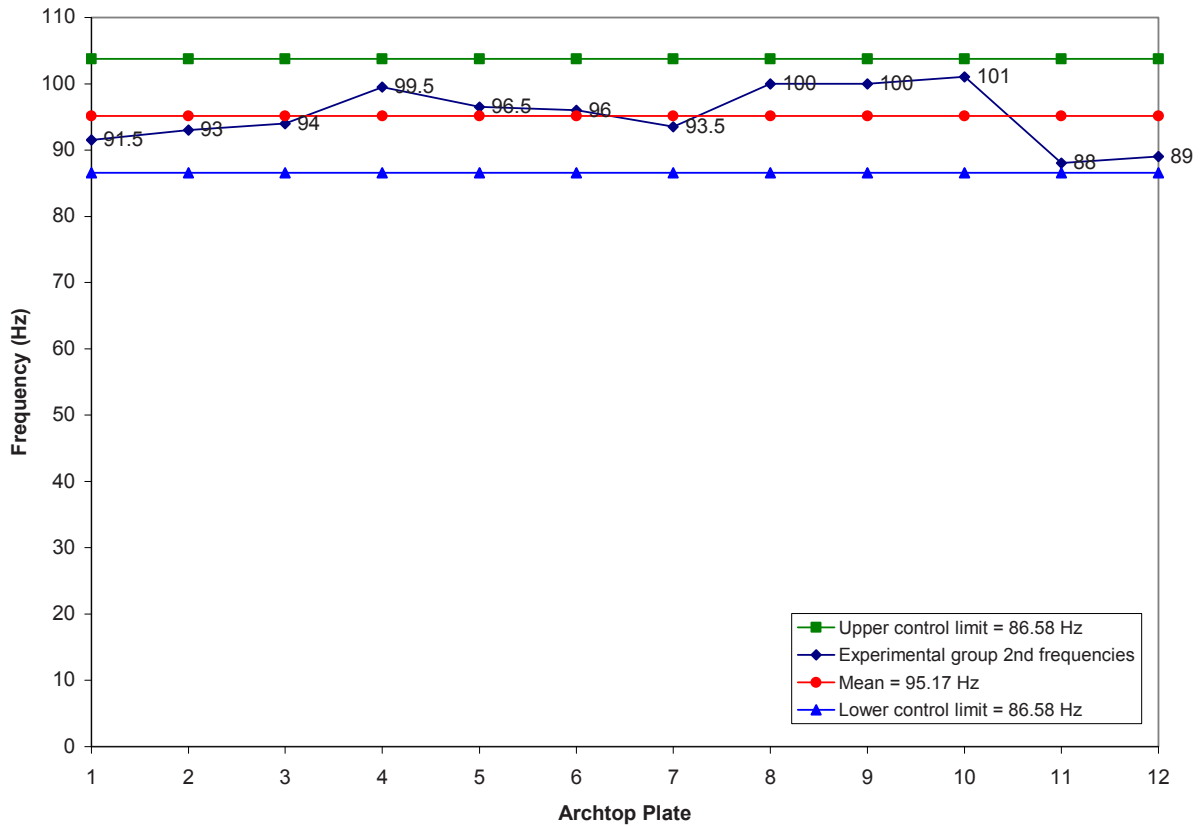


Figure 15 – Control Chart for 2nd Frequency (Vacuum)

Looking at the charts, both manufacturing processes groups are in statistical control because all the points are still within the control limits. The new manufacturing process proved to be a success in decreasing the build variation in resonant frequencies of the resulting parts. Notice how the resonant frequencies of the arched plates machined with vacuum are higher than those of the control group.

Even though these plates are curved, we assume they approximately follow basic trends for flat plates. Thus, we can assume resonant frequencies are proportional to the thickness of the plates [7]. In a production setting, this additional thickness would need to be accounted for in the design process.

Because of the different frequencies between the experimental and control groups, directly comparing standard deviation will be difficult. Therefore, we decided to compare the standard deviations as a percentage of the mean frequency. This is called the coefficient of variance. [Table 1](#) shows the results from the two groups of plates.

Table 1. Archtop plate result

	Mass (lb)	Frequency 1 (Hz)	Frequency 2 (Hz)	Frequency 3 (Hz)
No Vacuum 1	0.8775	56	74.5	108
No Vacuum 2	0.846	55.5	76.5	107.5
No Vacuum 3	1.0695	63	84	123
No Vacuum 4	0.538	41.5	55	65
No Vacuum 5	0.738	55.5	66	102.5
No Vacuum 6	0.8095	52.5	67	98.5
No Vacuum 7	0.7615	54	73	96.5
No Vacuum 8	0.864	62.5	74	116
No Vacuum 9	0.635	55	67.5	92
No Vacuum 10	0.7255	58.5	67.5	103.5
No Vacuum 11	0.6055	50.5	61	85.5
No Vacuum 12	0.859	57.5	74.5	108
Mean	0.7774	55.1667	70.0417	100.5000
Standard Deviation	0.1436	5.6381	7.6707	15.0710
Coefficient of Variance, %	18.47	10.22	10.95	15.00
	Mass (lb)	Frequency 1 (Hz)	Frequency 2 (Hz)	Frequency 3 (Hz)
Vacuum 1	1.033	71.5	91.5	128
Vacuum 2	0.9155	71.5	93	129.5
Vacuum 3	1.177	73	94	139
Vacuum 4	1.3715	80.5	99.5	157
Vacuum 5	1.0755	76.6	96.5	136
Vacuum 6	1.1625	72	96	133
Vacuum 7	1.076	72.5	93.5	129
Vacuum 8	1.1775	79.5	100	146
Vacuum 9	1.196	79.5	100	146.5
Vacuum 10	1.1225	79.5	101	145.5
Vacuum 11	1.007	70.5	88	129
Vacuum 12	0.955	70	89	125.5
Mean	1.1058	74.7167	95.1667	137.0000
Standard Deviation	0.1237	4.0631	4.4073	9.8258
Coefficient of Variance, %	11.18	5.44	4.63	7.17
Difference	7.29	4.78	6.32	7.82

Looking at [Table 1](#), all the coefficients of variance in the experimental group are much lower than the control group. Therefore, it is certain that the vacuum fixture helps to lower the build variation during the manufacturing process, which is a primary goal of this project.

Conclusion

Because of the natural variation in wood properties, producing identical sound quality in volume production of stringed instrument manufacture is proven to be a challenging undertaking. This project has successfully proven that the partial vacuum during machining can automatically compensate differences in material properties in wood, thus, controlling the build variation in tonal quality of the resulting parts. Perhaps the manufacture of stringed instrument might be able to employ this technique in other guitar manufacturing production.

References

- [1] French, Mark. Engineering the Guitar Theory and Practice. Springer 2009
- [2] U.S. Forest Product Lab. Handbook of Wood and Wood-Based Materials for Engineers, Architects and Builders. Hemisphere Publishing 1989. Also available in updated form electronically at: http://www.fpl.fs.fed.us/products/publications/pubs_interest.php
- [3] French, Mark. A Different Way of Defining Body Shapes. American Lutherie, No. 88, Winter 2006.
- [4] Playfair, Quentin. Cremona's forgotten curve. Strad, 110(1315):1194-1199, November 1999
- [5] Benedetto, Robert. Making an Archtop Guitar. Centerseam Publishing 1994
- [6] Evan, J., Lindsay, W. Managing for Quality and Performance Excellence. Thomson 2008
- [7] Leissa, A.W. Vibration of Plates, NASA SP-160, 1969

Biographical Information

MARK FRENCH received his B.S. from Va Tech in 1985, his M.S. in Aerospace engineering at the University of Dayton in 1988 and PhD there in 1993. He worked as a civilian engineer for the US Air Force from 1985 to 1995. He then worked in the auto industry as an engineer and lab manager from 1995-2004 before joining the Department of Mechanical Engineering Technology at Purdue University. His interests are experimental mechanics and musical instrument design. He especially likes making archtop instruments, but needs to practice his playing more (a lot more).

EDDY EFENDY received his B.S in Mechanical engineering at Purdue University in 2006. He is currently an M.S student in MET at Purdue University. His interests are design and manufacturing processes.

Rotation Angle Measurement Using an Electro-Optic Heterodyne Interferometer

Jing-Fung Lin^{1*} Chun-Jen Weng² Kuo-Long Lee¹ Yu-Lung Lo³

¹Department of Computer Application Engineering, Far East University,
No.49, Chung-Hua Road, Hsin-Shih Township, Tainan County 744, Taiwan ROC

²Department of Technology Management, Leader University,
No.188, Sec. 5, An-Chung Road, Tainan 709, Taiwan ROC

³Department of Mechanical Engineering, National Cheng Kung University,
No.1, Ta-Hsueh Road, Tainan 701, Taiwan ROC

*Corresponding author: jacklin@cc.feu.edu.tw

Abstract

An electro-optic heterodyne interferometer based on phase-locked extraction for measuring low optical rotation angle is successfully developed. The validity of the proposed design is demonstrated by a half-wave plate with the average relative error of 0.74%. When applied to the measurement of glucose solutions with concentrations ranging from 0 to 1.2 g/dl, the average relative error in the measured rotation angle of glucose solutions is determined to be 1.46%. The correlation coefficient between the measured rotation angle and the glucose concentration is determined to be 0.999991, while the standard deviation is just 0.00051 degrees. Overall, the current proposed system is capable of measuring glucose concentration as low as 0.01 g/dl with an error of 6.67%.

1. Introduction

When linearly polarized light passes through certain materials such as glucose or quartz, its plane of polarization may rotate. This phenomenon is referred to as optical rotation or circular birefringence and is a result of the asymmetric structure of the chiral materials. Obtaining accurate measurements of the rotation angles of optically active materials is a key concern in the optics, sugar-making, drug discovery, and many research fields. Owing to development of nanotechnology and diverse applications such as optical sensing of glucose concentration and chirality detection in nanograting, the precise measurement of optical rotation is increasingly important.

In the past, different modulated mechanisms in their interferometers were proposed for measuring the optical rotation [1-4]. For example, in 1997, Cameron and Côté [1] designed the glucose sensing digital closed-loop processing system. This measurement system was based on the common-path heterodyne interference technique. It utilized Faraday rotators (FR) for both modulation and compensation. This method used a closed loop processing system and lock-in amplifier to obtain the rotation angle of the glucose. This system required use of a feedback mechanism in order to reduce the system instability of FR modulator. Lin *et al.* [2] proposed a heterodyne Mach-Zehnder interferometer to enhance the measurement resolution about to 6×10^{-5} degrees in 2004. However, Lin's optical configuration and the associated algorithm were more complicated. In 2006, Lo and Yu [3] adopted a liquid crystal (LC) modulator to modulate the azimuth of the linearly polarization light in a sinusoidal signal and developed a new signal-processing algorithm for the

measurement of glucose concentrations. The standard deviation in rotation angle level of 0.00551° has been obtained, with a 0.998773 correlation coefficient between the reference and the measured values. However, the LC modulator has the drawback of slow frequency response. Recently, Lin *et al.* [4] proposed a circular heterodyne interferometer based on electro-optic (EO) modulation to measure the glucose concentrations with one phase-locked technique. The resolution of rotation angle is half that of the phase resolution obtained using the lock-in amplifier. The optical system is capable of measuring glucose samples with concentration as 0.2 g/dl.

In the proposed optical scheme, a polarimeter based on an electro-optic modulated linear heterodyne interferometer is successfully developed, and the proposed algorithm based on two phase-locked extractions is feasible to measure low rotation angle in a chiral medium. Overall, the current proposed system is capable of measuring glucose concentration as low as 0.01 g/dl with an error of 6.67% in the measured rotation angle.

2. Methodology

2.1 Optical Configuration

The optical configurations in Figs. 1(a) and 1(b) are based on the common-path linear heterodyne interferometer with EO modulation, and after first measurement in Fig. 1(a) when the principal axis of the linearly birefringent material is set to 45° and the analyzer is set to 0° , then both the linearly birefringent material and analyzer are rotated to add -45° increments to their principal axis and transmission axis, respectively, shown as in Fig. 1(b), and the second measurement is executed. In Fig. 1, a He-Ne laser light beam of wavelength 632.8 nm propagates initially through a polarizer and then through an EO modulator regulated by a saw-tooth waveform signal supplied by a function generator. The light beam then passes successively through the sample and a linearly birefringent material, and finally an analyzer. The output light intensity is then detected by a photodetector. Subsequently, the final signals I_1 and I_2 in Fig. 1 are processed by a lock-in amplifier, respectively, for extracting the rotation angle of the chiral medium.

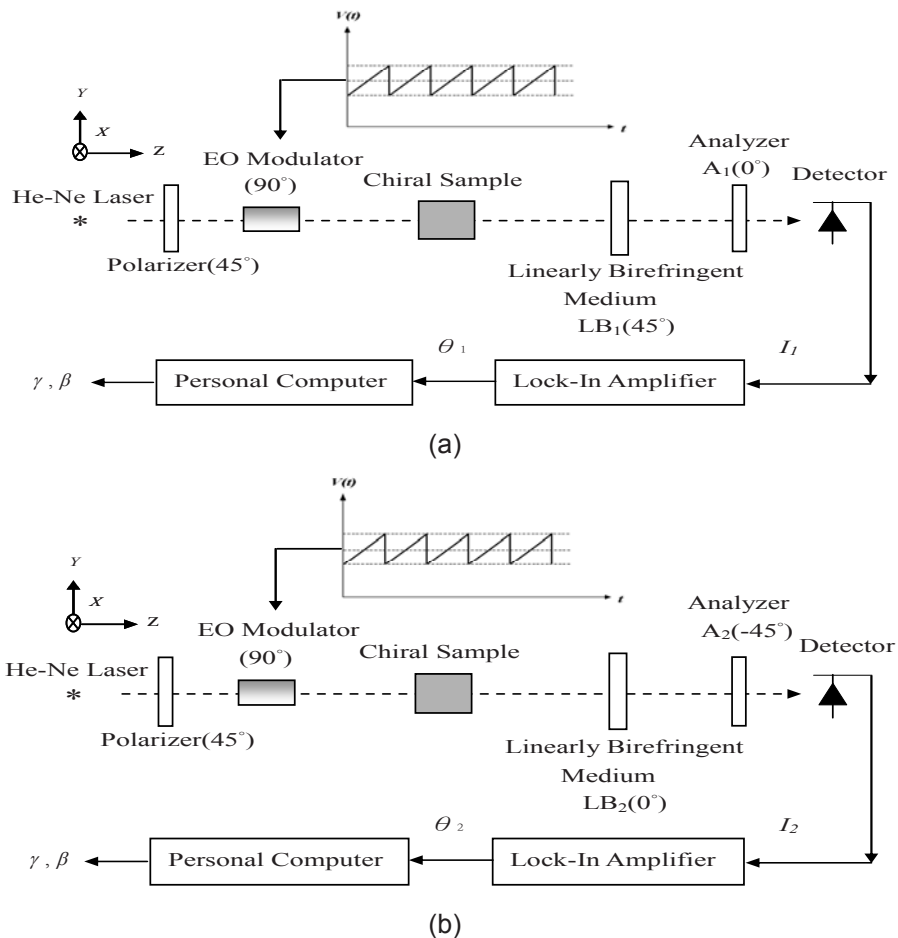


Fig. 1 Schematic diagram of a measurement system for the optical rotation angle.

2.2 Theoretical Description

According to the Jones matrix formalism, the vectors of electric field emerging from the first and second measurements in the common-path linear heterodyne interferometer as shown in Fig. 1 can be expressed, respectively, as:

$$E_1 = A_1(0^\circ).LB_1(45^\circ, \beta).S(\gamma).EO(90^\circ, \omega t).P(45^\circ).E_{in}$$

$$= \begin{bmatrix} 1 & 0 \\ 0 & 0 \end{bmatrix} \begin{bmatrix} \cos(\frac{\beta}{2}) & i \sin(\frac{\beta}{2}) \\ i \sin(\frac{\beta}{2}) & \cos(\frac{\beta}{2}) \end{bmatrix} \begin{bmatrix} \cos \gamma & \sin \gamma \\ -\sin \gamma & \cos \gamma \end{bmatrix} \begin{bmatrix} e^{-i\omega t} & 0 \\ 0 & e^{i\omega t} \end{bmatrix} \begin{bmatrix} \frac{1}{2} & \frac{1}{2} \\ \frac{1}{2} & \frac{1}{2} \end{bmatrix} \begin{bmatrix} 0 \\ E_0 \end{bmatrix} e^{i\omega_0 t}, \quad (1)$$

and

$$E_2 = A_2(-45^\circ).LB_2(0^\circ, \beta).S(\gamma).EO(90^\circ, \omega t).P(45^\circ).E_{in}$$

$$= \begin{bmatrix} \frac{1}{2} & -\frac{1}{2} \\ -\frac{1}{2} & \frac{1}{2} \end{bmatrix} \begin{bmatrix} \cos(\frac{\beta}{2}) + i \sin(\frac{\beta}{2}) & 0 \\ 0 & \cos(\frac{\beta}{2}) - i \sin(\frac{\beta}{2}) \end{bmatrix} \begin{bmatrix} \cos \gamma & \sin \gamma \\ -\sin \gamma & \cos \gamma \end{bmatrix} \begin{bmatrix} e^{-i\omega t} & 0 \\ 0 & e^{i\omega t} \end{bmatrix} \begin{bmatrix} \frac{1}{2} & \frac{1}{2} \\ \frac{1}{2} & \frac{1}{2} \end{bmatrix} \begin{bmatrix} 0 \\ E_0 \end{bmatrix} e^{i\omega_0 t}, \quad (2)$$

where E_0 is the amplitude of the incident electric field which is parallel to the y-axis, E_{in} , $A_1(0^\circ)$ is the Jones matrix of the analyzer A_1 parallel to the x-axis. Meanwhile, $LB_1(45^\circ, \beta)$ is the Jones matrix of the linearly birefringent medium LB_1 with unknown retardance β , whose principal axis is set at 45° to the x-axis, and $LB_2(0^\circ, \beta)$ is the Jones matrix of the linearly birefringent medium LB_2 with unknown retardance β , whose principal axis is set to the x-axis, and is considered as rotating the principal axis angle of LB_1 from 45° to 0° . $S(\gamma)$ represents the Jones matrix of the chiral sample, and γ is its rotation angle. Furthermore, $A_2(-45^\circ)$ is the Jones matrix of the analyzer A_2 , whose transmission axis is set at -45° to the x-axis, and is considered as rotating the transmission axis of A_1 from 0° to -45° . $EO(90^\circ, \omega t)$ is the Jones matrix of the EO modulator positioned with its fast axis parallel to the y-axis and driven by a saw-tooth waveform voltage at a frequency of ω , and $P(45^\circ)$ is the Jones matrix of the polarizer set at 45° to the x-axis.

As a result, the intensities for the two transmitted lights could be expressed, respectively, as:

$$I_1 = I_{dc1}(1 + \cos(\beta)\sin(2\gamma)\cos(\omega t) - \sin(\beta)\sin(\omega t))$$

$$= I_{dc1} + R_1 \cos(\omega t + \theta_1), \quad (3)$$

and

$$I_2 = I_{dc2}(1 - \cos(\beta)\cos(2\gamma)\cos(\omega t) - \sin(\beta)\sin(\omega t))$$

$$= I_{dc2} - R_2 \cos(\omega t - \theta_2), \quad (4)$$

where $I_{dc1} = I_{dc2} = E_0^2/4$ is the DC components of the output light intensities, respectively, I_1 and I_2 , and E_0^2 is the intensity of the input light. The notation R_1 represents $I_{dc1}\sqrt{(\cos(\beta)\sin(2\gamma))^2 + (\sin(\beta))^2}$, θ_1 represents $\tan^{-1}(\frac{\tan(\beta)}{\sin(2\gamma)})$, R_2 represents $I_{dc2}\sqrt{(\cos(\beta)\cos(2\gamma))^2 + (\sin(\beta))^2}$, and θ_2 represents $\tan^{-1}(\frac{\tan(\beta)}{\cos(2\gamma)})$.

From Eqs. (3) and (4), a lock-in amplifier can be employed to lock the AC components of the output intensities, I_1 and I_2 , respectively, at the reference frequency ω in order to measure the phase terms: i.e.,

θ_1 and θ_2 . Consequently, the optical rotation angle, γ , of the chiral sample can be determined from

$$\gamma = \frac{1}{2} \tan^{-1} \left(\frac{\tan(\theta_2)}{\tan(\theta_1)} \right). \quad (5)$$

From Eq. (5), the rotation angle can be estimated by two phase-locked extractions and is independent of the retardance of the linearly birefringent material. Above all, from the inspection of experimental results of glucose solution in front of a half-wave plate, the current system is capable of measuring low rotation angle corresponding to glucose concentration as low as 0.01 g/dl. When compared with Refs. [3-4], the proposed algorithm in this study is feasible to measure low rotation angle.

3. Experimental Results

The validity of the proposed system and analytical scheme was investigated using a sample as a half-wave plate (Casix Inc., Model WPF1225-633- $\lambda/2$) positioned in front of a quarter-wave plate (CVI Inc., Model QWP0-633-04-4-R10). In the verification experiment, the rotation angle was measured as the principal axis angle of the half-wave plate was rotated incrementally through a full 45° (from -22.5° to 22.5° in increments of 2.5°) while the principal axis angle of the quarter-wave plate was fixed at 45° in the first step of measurement and fixed at 0° in the second step of measurement, respectively.

Fig. 2 presents the optical rotation property of the half-wave plate. From inspection, the rotation angle measurements are found to have an average absolute error ($P_{measured} - P_{actual}$) of just 0.125° , with a standard deviation of 0.132° . Meanwhile, the average normalized error is determined to be 0.74%. It is noted that when $P_{actual} = 0$, the normalized error tends to infinity, and then is not included.

The correlation coefficient between the measured values of the rotation angle and the actual values is determined to be 0.999979. Thus, it is evident that the proposed metrology system has a highly linear response. Overall, the results presented in Fig. 2 confirm the ability of the proposed system to obtain highly accurate measurements of the rotation angle in chiral sample.

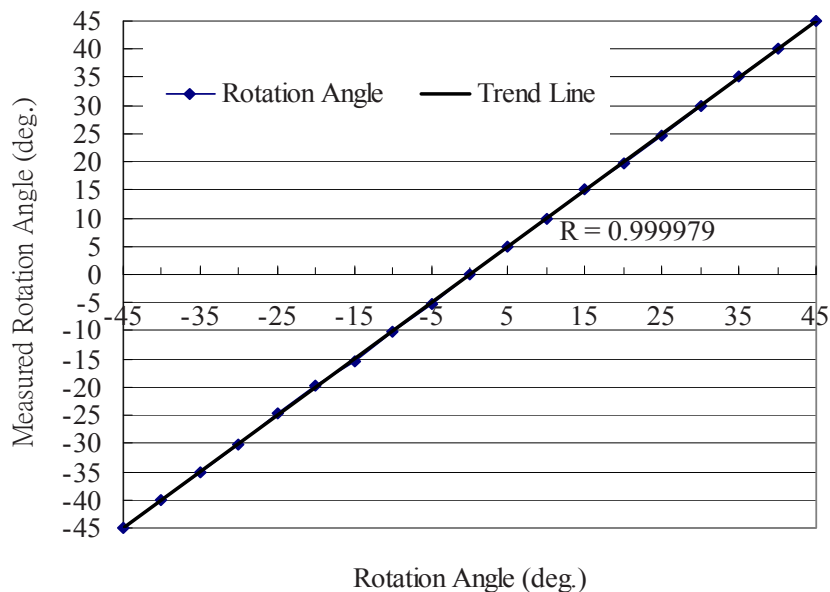


Fig. 2 Variation of measured rotation angle (sample: half-wave plate).

The feasibility of the proposed metrology system was further verified using a sample as a glucose solution of a specified concentration positioned in front of a half-wave plate with its principal axis angle set at 45° in the first measurement. Note that in this arrangement, the half-wave plate behaves as a linearly birefringent material. The glucose samples were prepared from a 60 mg/ml stock glucose solution produced by dissolving 6 g of D-glucose (Merck Ltd.) in a total volume of 100 ml of de-ionized water. Individual glucose samples with

concentrations ranging from 0 to 1.2 g/dl in 0.2 g/dl increments (0.1 g/dl, 0.05 g/dl, and 0.01 g/dl are included) were prepared by diluting the stock solution with an appropriate volume of de-ionized water. The glucose samples were injected into sample cells with a length of 50 mm and were then introduced individually into the optical measurement system in order to measure their respective rotation angles.

Further, the equation which describe the rotation of the polarization plane of light corresponding to the concentration of glucose is expressed as

$$C = \frac{100\gamma}{L[\gamma]}, \quad (6)$$

where the glucose concentration C in a liquid solution, expressed in grams per deciliter of the solution, γ is the observed rotation in degrees, L is the sample path in decimeters, and in general $[\gamma]$ is the specific rotation depending on temperature, wavelength, and pH level. Thus, optical path length, temperature, wavelength, and pH level have an uncertainty associated with their value and contribute to the total uncertainty of glucose concentration.

Fig. 3 presents the experimental relationship between the rotation angle and the glucose concentration for a driving signal with a frequency of 1 kHz. A correlation coefficient value of 0.999991 indicates a good linear response, with a standard deviation of 0.00051° , i.e., with a measurement deviation of 0.002 g/dl, which is lower than that of 0.075 g/dl in Ref. [5]. According to the 52.7° of the specific rotation angle in glucose solution at 633 nm and 20°C in Ref. [6], the average relative error in the measured rotation angles of glucose solutions is just 1.46%. Specifically, the measured rotation angle is 0.00246° for the glucose concentration of 0.01g/dl and the relative error of rotation angle is determined to be 6.67%.

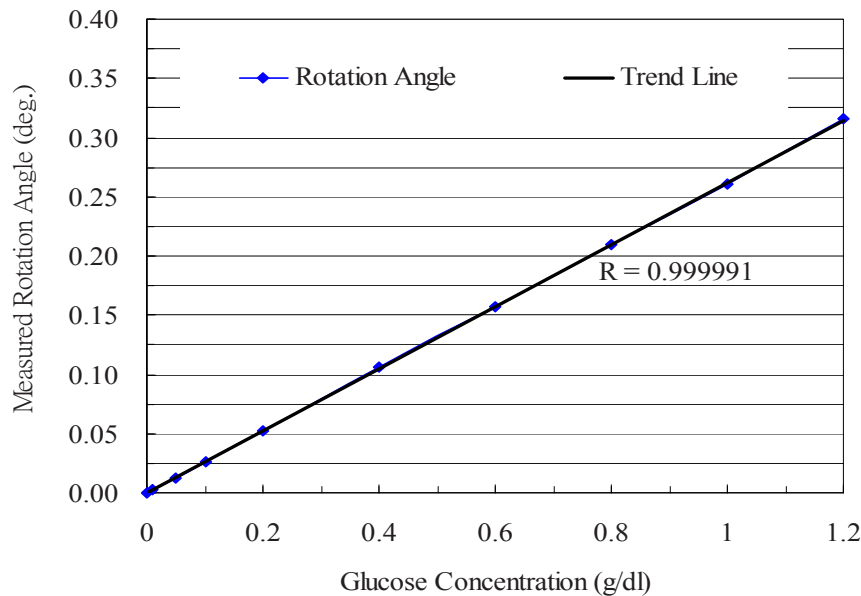


Fig. 3 Variation of measured rotation angle (sample: glucose solution).

To verify the repeatability of the measurement system, a glucose solution with a concentration of 0.01 g/dl was measured 13 times. The corresponding results are presented in Fig. 4. The average value of the measured rotation angle for glucose sample with a concentration of 0.01 g/dl is found to be 0.00254° , and the standard deviation σ to be 0.0001° , i.e., equivalent to a 1σ value of $\sim 3.94\%$ of the average value. The sensitivity for optical rotation detection is calculated at 2×10^{-5} deg/cm from the standard deviation and the length of sample cell. Furthermore, according to Ref. [6], the average relative error is determined to be just 3.70%, which is lower than 6.67% in Fig. 3.

From the experimental results, the phase instability of EO modulator due to the DC-biased voltage drift and thermal effect may mainly cause the variation of the measured rotation angle [7]. To stabilize the bias drift using PI control, the output from the PI controller is used to adjust the DC-biased voltage to the EO modulator via a GPIB power supply [8]. Therefore, the results confirm the ability of the optical system to obtain highly precise measurement and excellent repeatability characteristic in the optical rotation angle.

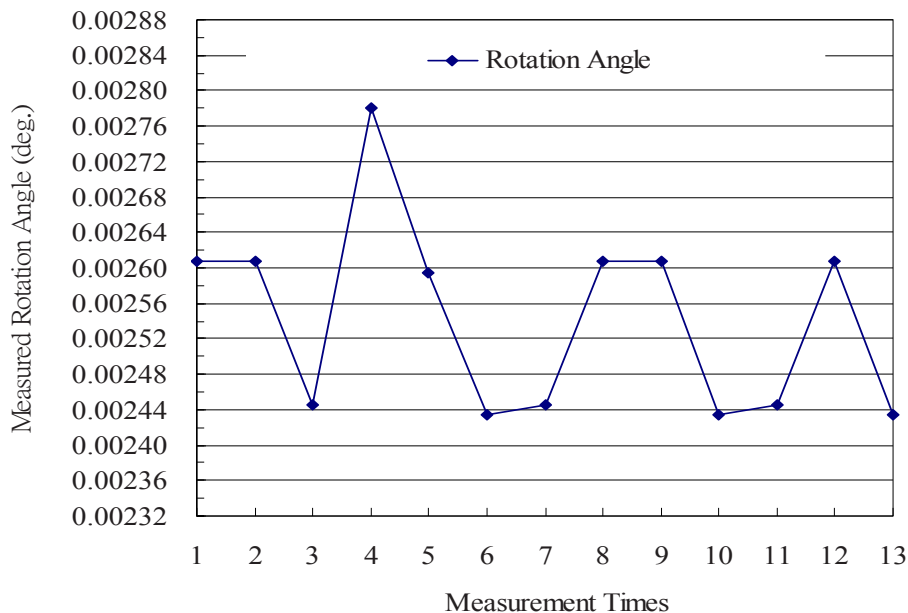


Fig. 4 Repeatability test (sample: glucose solution with concentration of 0.01 g/dl).

4. Discussions and Conclusions

A polarimeter for measuring low optical rotation angle in a chiral medium is developed successfully in this study. The system is based on an electro-optic modulated heterodyne interferometer and using the technique of two phase-locked extractions to measure the rotation angle precisely. From the inspection of a half-wave plate sample, the average relative error in rotation angle has been obtained as 0.74%. Further, a standard deviation in rotation angle level of 0.00051° has been obtained for glucose solutions with concentrations ranging from 0 to 1.2 g/dl, with a correlation coefficient value of 0.999991 between the reference and measured values. Moreover, the relative error of the rotation angle corresponding to 0.01 g/dl glucose concentration has been determined to be 6.67%. As compared to the others [3-4], the standard deviation of the developed system is superior to those in previous studies. The measurable low concentration of 0.01 g/dl is one order lower than 0.2 g/dl in Refs. [3-4]. As the glucose level of a normal human being is around 0.1 g/dl and for clinical use a relative concentration error of less than 15% is required [5], therefore the developed system has its potential in low glucose concentration measurement.

Acknowledgments

This research was partially supported by the National Science Council of Taiwan under contract NSC 98-2221-E-269-013.

References

- [1] Cameron B. D. and Côté G. L., "Noninvasive glucose sensing utilizing a digital closed-loop polarimetric approach," *IEEE Trans. Biomed. Eng.* Vol. 44, pp. 1221–1227, 1997.
- [2] Lin J. Y., Chen K. H., and Su D. C., "Improved method for measuring small optical rotation angle of chiral medium," *Opt. Commun.* Vol. 238, pp. 113–118, 2004.
- [3] Lo Y. L. and Yu T. C., "A polarimetric glucose sensor using a liquid-crystal polarization modulator driven by a sinusoidal signal," *Opt. Commun.* Vol. 259, pp. 40–48, 2006.
- [4] Lin J. F., Chang C. C., Syu C. D., Lo Y. L., and Lee S. Y., "A new electro-optic modulated circular heterodyne interferometer for measuring the rotation angle in a chiral medium," *Opt. Las. Eng.* Vol. 47, pp. 39–44, 2009.
- [5] Pu C., Zhu Z., and Lo Y. H., "A surface-micromachined optical self-homodyne polarimetric sensor for noninvasive glucose monitoring," *IEEE Photon. Technol. Lett.* Vol. 12, pp. 190–192, 2000.
- [6] Wang B., "Measurement of circular and linear birefringence in chiral media and optical materials using the photoelastic modulator," *Proc. SPIE* Vol. 355, pp. 294–302, 1999.
- [7] Compain E. and Drevillon B., "High-frequency modulation of the four states of polarization of light with a single phase modulator," *Rev. Sci. Instrum.* Vol. 69, pp. 1574–1580, 1998.
- [8] Snoddy J., Li Y., Ravet F., and Bao X., "Stabilization of electro-optic modulator bias voltage drift using a Lock-in amplifier and a proportional-integral-derivative controller in a distributed brillouin sensor system," *Appl. Opt.* Vol. 46, pp. 1482–1485, 2007.

Digital Shadow Moiré Measurement of Out-of-Plane Hygrothermal Displacement of TFT-LCD Backlight Modules

Wei-Chung Wang and Ya-Hsin Chang

**Department of Power Mechanical Engineering, National Tsing Hua University
Hsinchu, Taiwan 30013
Republic of China**

ABSTRACT

As the light source device of the thin film transistor-liquid crystal display (TFT-LCD), backlight modules (BLM) suffers not only the heat produced by itself own but also the possible high temperature and/or high humidity of the operating environment. In this paper, based on the specially designated hygrothermal reliability test conditions, the digital shadow moiré method was applied to inspect out-of-plane displacement fields of BLMs installed in 4.3" TFT-LCDs which are commonly employed in smart phones and navigators. Three hygrothermal reliability test conditions were selected in this paper, i.e. (1) high temperature storage; (2) high temperature operation; (3) high temperature and high humidity. In addition, test specimens of three different tolerances in the normal direction inside the BLMs were prepared to investigate the tolerance effects on the out-of-plane displacement. The current inspection procedures adopted in the TFT-LCD industry is to remove BLM periodically from the oven to measure the variation of the illumination of the BLM after experiencing the hygrothermal effects. With the whole-field and real-time inspection features, the digital shadow moiré inspection system developed in this paper can be employed to replace the current inspection procedures adopted by the TFT-LCD manufacturers. The experimental results showed that the out-of-plane displacement of the BLM under the high temperature and high humidity condition is the largest one among three conditions.

1. Introduction

Because of its advantages of light weight, thin size and low power consumption, in recent years, thin film transistor-liquid crystal display (TFT-LCD) has almost completely replaced the traditional cathode ray tube and

has been widely used in many commercial and industrial electronic products under different occasions and environments. Since TFT-LCDs may be used elsewhere in the world and worldwide climate differs significantly in different regions, the reliability and durability of TFT-LCDs are extremely challengeable. Backlight module (BLM) is the essential part of a TFT-LCD to provide the light source of the TFT-LCD. The optical films or components inside the BLM including prism sheet, diffuse sheet and light guide plate (LGP) are unavoidably deformed or warped after long period thermal effects of the light source. In addition, since the BLM is not perfectly sealed, warpage may also produce by the environmental humidity. Currently in TFT-LCD industry, hygrothermal reliability test conditions including high temperature storage, low temperature storage, high temperature operation, thermal shock as well as high temperature and high humidity, etc. During the tests, the BLM is taken out of the oven at selected intervals to inspect the variation of illumination. However, no inspection has yet been performed on the deformation of the components inside the BLM. In the past, researchers focused on finding new materials for the diffuse sheet to reduce the warpage. Kim [1] used the new diffuse sheet material polymethyl methacrylate (PMMA) to replace the formerly used material polyethylene terephthalate (PET). It was because that non-uniform illumination was caused by the warpage due to high temperature and high humidity in the PET. Similarly, Kim et al. [2] employed three-layer composite materials made of PET / polycarbonate (PC) / polybutylene terephthalate (PBT) to manufacture one diffuse sheet to give lower water absorption to reduce warpage in BLMs. In recent few years, the deformation of components inside the BLM and the non-uniform illumination of the TFT-LCD caused by the heat of the light source of the TFT-LCD are finally drawn attention to the researchers. In 2005, Chu et al. [3] measured the temperature variation and thermal stresses on the surface of the cell in a 23" LCD-TV. In 2005, Tseng [4] used ANSYS [5] to investigate the thermal deformation of the LGP of the BLM with cold cathode fluorescent lamp as the light source. He also used Pro/E [6] to plot the deformation and transfer it into the optical design software ASAP [7] to simulate the effect of the deformed LGP on the illumination of the BLM. In 2006, Hsu [8] integrated the shadow moiré method and phase-shifting technique to investigate the out-of-plane deformation of a four edge clamped BLM under high temperature and high humidity loading. The experimental results were also compared with the ANSYS results. To relieve the warpage produced by the temperature and humidity, today's common practice in TFT-LCD industry is to reserve certain amount of tolerances or gaps between optical films and plastic frame. The cross-sectional plot and the relative locations of the tolerance of the BLM used in this paper are shown in Fig. 1. The amount of reserved tolerance is determined purely based on trial and error. No systematic research has been done yet.

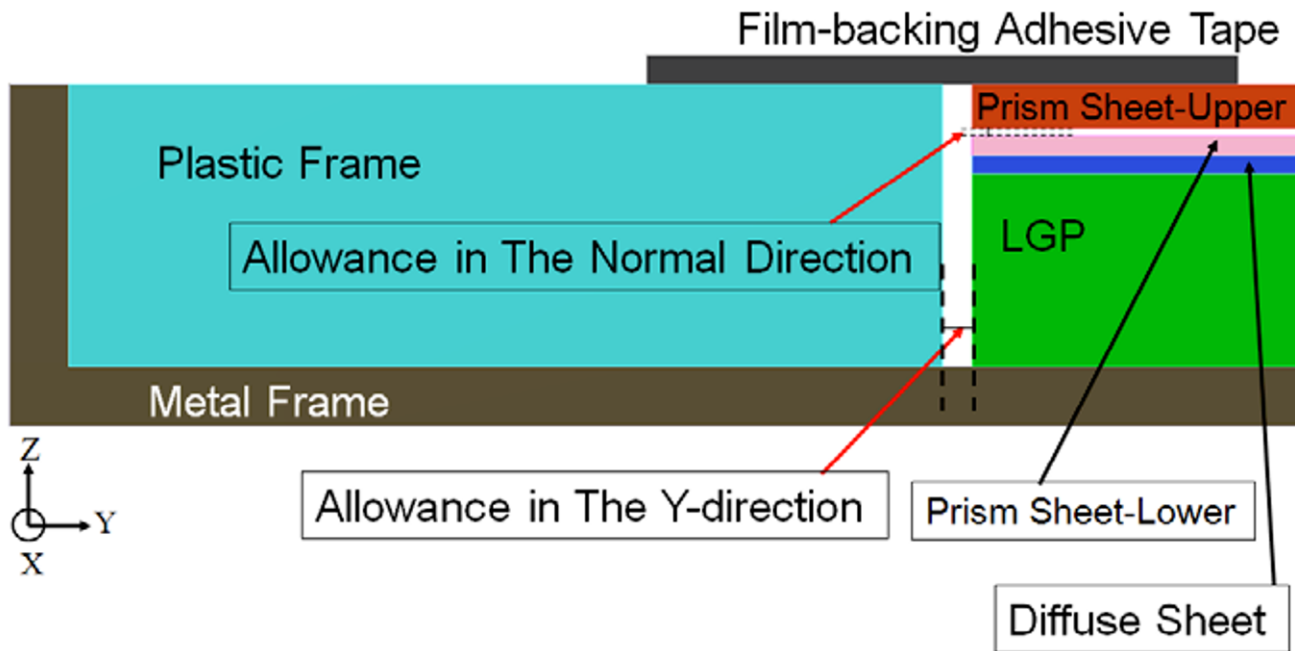


Fig. 1 Cross-sectional plot of components at different layers and tolerances at relative locations of a backlight module

Shadow moiré method is a whole-field real-time optical method for measuring the out-of-plane displacement. The interference fringe pattern obtained from the method is produced by superimposing the reference grating and its shadow on the object to be measured. The measurement accuracy of the method can be greatly enhanced by using the digital shadow moiré method, i.e. the symbiosis of the digital image analysis system and phase-shifting technique. Sullivan [9] used the phase-shift technique to increase the resolution of both the shadow moiré method and moiré interferometry to measure the surface contour variation of the thin aluminum plate subjected to slight torsion. A real-time phase-shifting shadow moiré system was setup by Stiteler and Ume [10] to detect directly the real-time surface warpage of printed wiring board assemblies (PWBA) at different time intervals in reflow of soldering process. By combining the shadow moiré method and high-speed continuous image taking device, Tay et al. [11] successfully measured time variation of surface contours of a hemispherical ball vibrating at 6Hz. By following the hygrothermal reliability test conditions used in the TFT-LCD industry, in this paper, the digital shadow moiré method was employed to measure the out-of-plane displacement under different arrangements of the tolerance in the normal direction of the BLM of 4.3" TFT-LCD commonly used in the smart mobile phone and GPS. In current inspection practice employed in the TFT-LCD industry, the BLM is necessarily taken out from the oven at regular intervals to measure its illumination variation during the hygrothermal reliability test period. It is not quite time and cost effective. With its whole-field and real-time inspection capability, the digital shadow moiré inspection system developed in this paper can be employed to replace the current inspection procedures adopted by the TFT-LCD manufacturers.

2. The shadow moiré method

As shown in Fig. 2 [12], the reference grating is placed at a small distance above the specimen of which the

out-of-plane displacement is to be measured. If the collimated light beam is incident on the reference grating at an angle α with respect to the normal while the observer or the image capture device is located on the other side of the normal and at an angle β with respect to the normal, the out-of-plane displacement of the specimen, W , at a point of the specimen can be expressed as

$$W(x,y) = \frac{NP}{\tan \alpha + \tan \beta} \quad (1)$$

where

P : the pitch of the reference grating counted in μm ;

N : the fringe order.

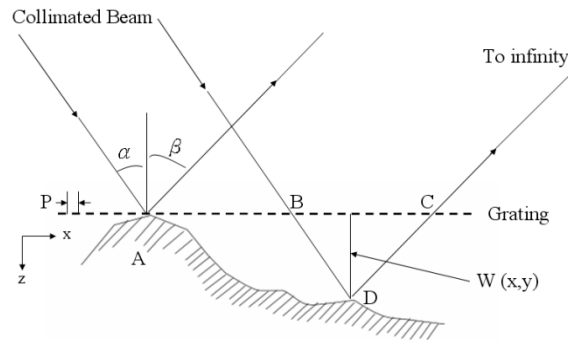


Fig. 2 Schematic diagram of the shadow moiré method

3. Experimental background

3.1. The arrangement of the tolerances inside the BLM

The dimensions of the optical films inside the 4.3" BLM used in this paper are 97 mm in length and 55 mm in width. From the bottom to the top of the BLM, the stacking sequence of the optical films inside the BLM is light guide plate (LGP); diffuse plate, lower prism sheet and upper prism sheet. The reserved tolerance in the normal direction is $28\mu\text{m}$. The cross-sectional plot of optical films at different layers and tolerances at relative locations of a BLM is shown in Fig. 1. Since the height of the plastic frame is fixed, the difference of the tolerance in the normal direction among three specimens was achieved by adopting different thickness combinations of optical films. In this paper, as listed in Table 1, three hygrothermal reliability test conditions were respectively used for specimens of three different tolerances in the normal direction. Hence in total 9 experiments on measurement of out-of-plane displacement were performed.

Table 1 Three hygrothermal reliability test conditions for specimens of three different tolerances. Stacking sequence of optical films is from bottom to top of the BLM

Test conditions	Stacking Sequence of Optical Films		
High Temperature Storage	LGP 650 μ m	LGP 650 μ m	LGP 650 μ m
High Temperature Operation	Diffuse Sheet 65 μ m	Diffuse Sheet 43 μ m	Diffuse Sheet 65 μ m
High Temperature and High Humidity	Prism Sheet-2 62 μ m	Prism Sheet-2 62 μ m	Prism Sheet-2 62 μ m
	Prism Sheet-1 150 μ m	Prism Sheet-1 150 μ m	Prism Sheet-1 62 μ m
Total Thickness	927 μ m	905 μ m	839 μ m
Tolerance in Normal Direction	28 μ m	50 μ m	116 μ m

3.2. Hygrothermal reliability test conditions

The three hygrothermal reliability test conditions used in this paper are:

- High Temperature Storage (Condition A): the specimen is heated from the room temperature up to 80°C, the heating time is 3 and 1/2 hours, the out-of-plane displacement is then measured.
- High Temperature Operation (Condition B): the specimen is heated from the room temperature up to 70°C with the light source of BLM is on, the heating time is again 3 and 1/2 hours, the out-of-plane displacement is then measured :
- High Temperature and High Humidity (Condition C): the specimen is heated from the room temperature up to 60°C with the relative humidity set at 90%RH, both the heating and the relative humidity were maintained for 3 and 1/2 hours, the out-of-plane displacement is then measured.

The power of the LED light source of the BLM tested is 64 mW. The LED light source is installed at the upper side of the LGP and lower prism sheet. The operation conditions are set at 22.4 V and 20 mA.

4. Specimen preparation

To assemble a BLM, the plastic frame was first installed into the metal frame. Next, the LGP was placed along the inner side of the plastic frame and the LED array was placed at the top of the LGP and attached to the plastic frame by adhesive. Diffuse plate and lower prism sheet were then placed at the top of the LGP by following the stacking sequence as indicated in [Table 1](#) and [Fig. 1](#). The final step is to adhere the upper prism sheet onto the plastic frame by film-back adhesive tape. The photograph of a BLM after assembly is shown in [Fig. 3](#). Since the optical films are high transparent materials, to obtain good contrast fringe patterns, a thin

layer white powder was sprayed on the surface of the specimens.

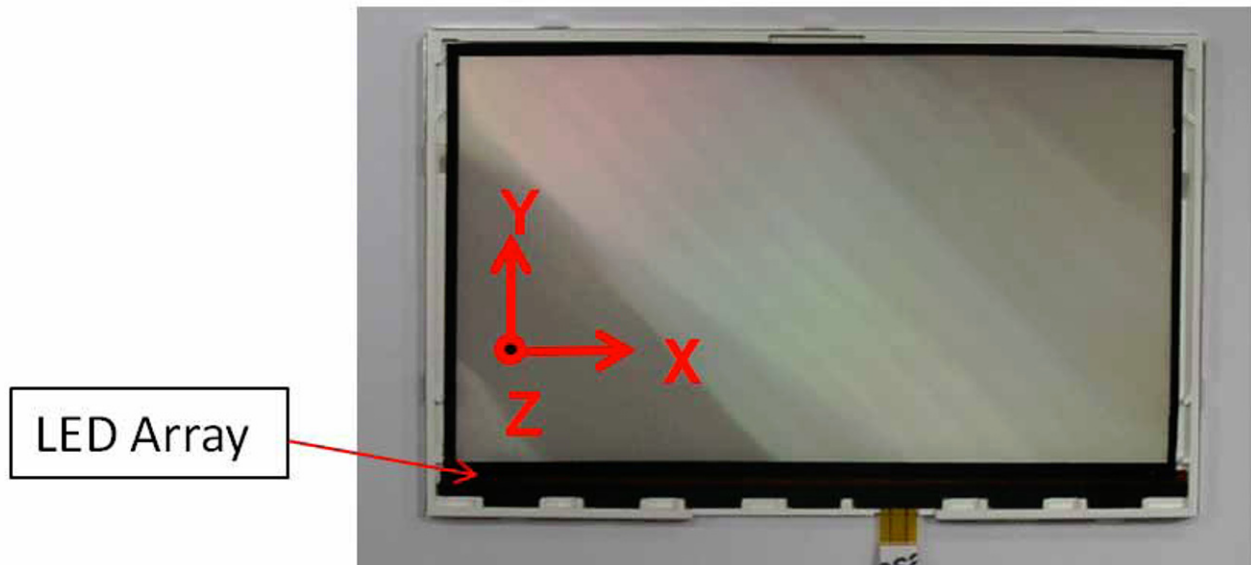


Fig. 3 Photograph of a 4.3" BLM

5. Arrangements of the digital shadow moiré system

The photograph of the digital shadow moiré system and hygrothermal test oven assembled in this paper is as shown in Fig. 4. To perform the phase-shift technique, a stepping motor was installed outside of the oven through an opening on the side wall of the oven to control the grating jig to an accuracy of $1\mu\text{m}$. The use of the stepping motor not only provides the accurate but also rapid control of the movement of the grating holder. Rapid movement of the grating holder is essential for executing the three step phase-shifting in the real-time inspection. The grating holder is manufactured from Invar. Invar is a material of high density and thus there exists a weight limit of the grating holder that the stepping motor can support. Weight reduction was achieved by removing the unnecessary parts from several portions of the grating holder. Four micrometer heads located at each corner of the grating holder can be individually adjusted to make sure that the grating is parallel to the specimen to avoid distortion of fringes for the very beginning. The incident angle of the single fiber optic light source (TechniQuip Co., USA) can be easily adjusted.

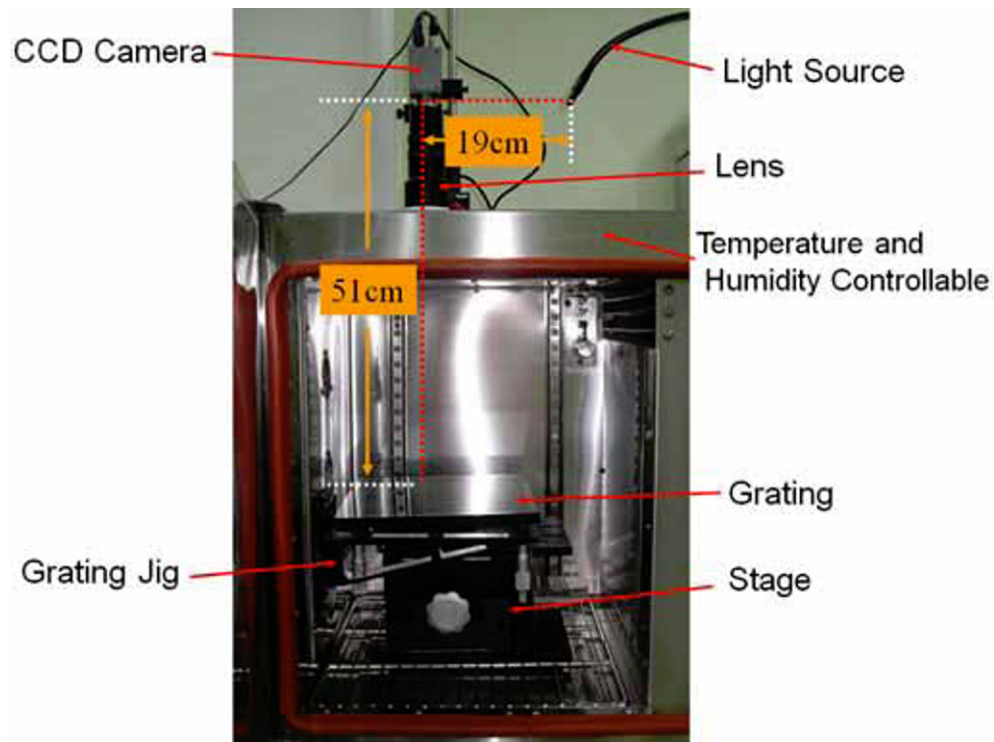


Fig. 4 Photograph of the experimental setup of the digital shadow moiré method and hygrothermal test oven

As shown in Fig. 4, the vertical and horizontal distances between the light source and the specimen surface and the CCD camera are 51cm and 19cm, respectively. Since the inclination angle of the CCD camera β is 0° and the pitch of the reference grating used in this paper is $48\mu\text{m}$, Eq. (1) can be rewritten as

$$W = \frac{48N}{19/51} = 128.842N \quad (2)$$

Therefore, the resolution of one fringe order of the out-plane-displacement measurement of the digital shadow moiré system assembled in this paper is $128.84\mu\text{m}$.

6. Results and discussions

6.1 Condition A: High temperature storage test

Wrapped phases diagrams and surface contours for tolerances $28\mu\text{m}$, $50\mu\text{m}$ and $116\mu\text{m}$ of high temperature storage condition are shown in Figs. 5-7, respectively. It is obvious from the wrapped phase diagram that the out-of-plane displacement is largest for the smallest tolerance.

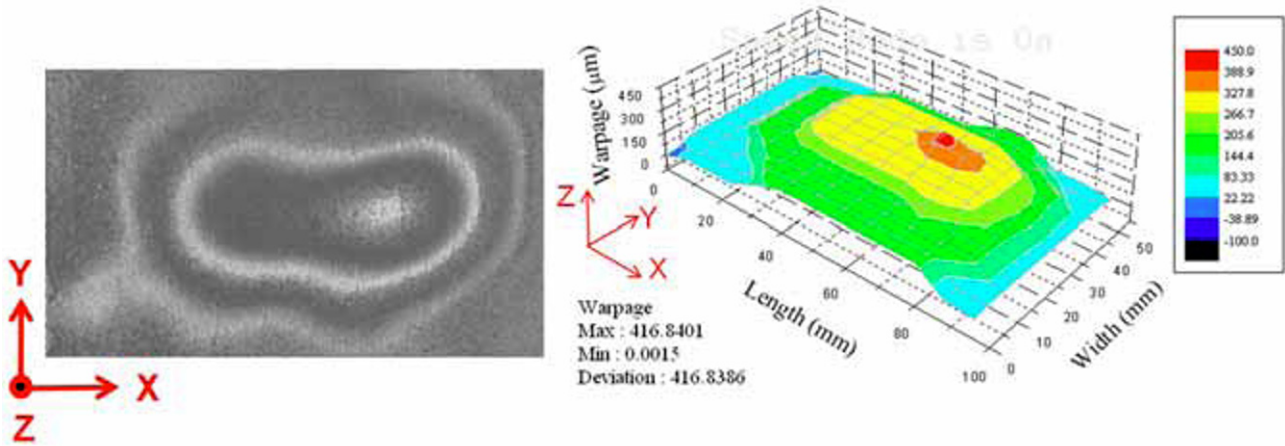


Fig. 5 Warped phases diagram and surface contour at tolerance 28µm of high temperature storage condition

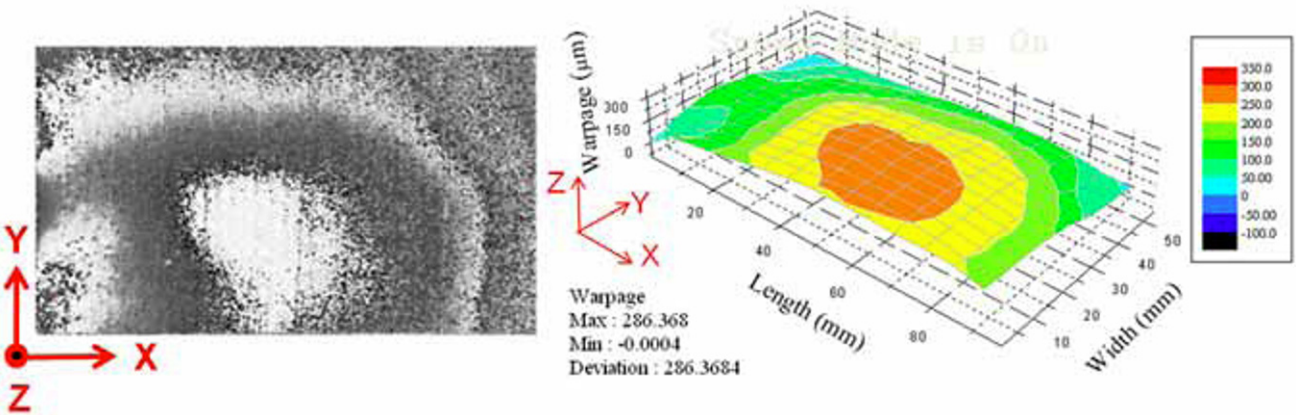


Fig. 6 Warped phases diagram and surface contour at tolerance 50µm of high temperature storage condition.

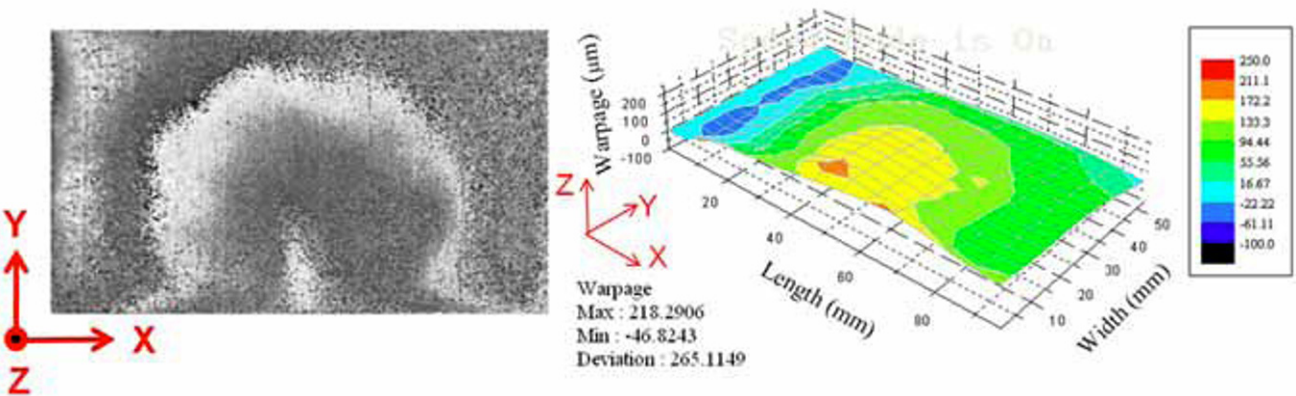


Fig. 7 Warped phases diagram and surface contour at tolerance 116µm of high temperature storage condition

As can be observed from the surface contours, the lowest point (i.e. the smallest out-of-plane displacement) is located at the left lower corner of the test specimen for tolerance 28µm and its magnitude is almost 0µm while the maximum displacement occurs close to the right of the center of the test specimen and its magnitude is 416.84µm. Therefore, the total displacement for tolerance 28µm occurs close to the right of the center of the test specimen and its magnitude is 416.84µm. Similarly, as listed in [Table 2](#), the total displacements for the test specimens of tolerances 50µm and 116µm are 286.37µm and 265.11µm, respectively.

Table 2 Total out-of-plane displacements of specimens under three different hygrothermal conditions (Unit: μm)

Test Conditions		High Temperature Storage	High Temperature Operation	High Temperature and High Humidity
28 μm	Maximum	416.84	440.98	787.75
	Minimum	~0	~0	~0
	Total Displacement	416.84	440.98	787.75
50 μm	Maximum	286.37	369.99	502.85
	Minimum	~0	~0	0.01
	Total Displacement	286.37	369.99	502.84
116 μm	Maximum	218.29	338.6	139.42
	Minimum	-46.82	~0	-166.14
	Total Displacement	265.11	338.6	305.56

The deformations of specimens of three tolerances are all rather symmetrical with respect to x-axis. In the cases of tolerance 28 μm and 50 μm , the out-of-plane displacement is completely toward the +z direction. At the same time, the minimum displacement values occur at the left front and back corners for 28 μm and 50 μm specimens, respectively. For the 116 μm case, most of the displacements are also toward the +z direction except the displacement in the vicinity of the left part region is toward the -z direction. It may be because the tolerance is too large so that wrinkles occur on the upper prism sheet. Similar result was obtained for the 116 μm case in the high temperature and high humidity test.

6.2 Condition B: High temperature operation test

Wrapped phases diagrams and surface contours for tolerances 28 μm , 50 μm and 116 μm of high temperature storage condition are shown in Figs. 8-10, respectively. Again, as can be observed from the wrapped phase diagram, the smallest out-of-plane displacement occurred for the smallest tolerance.

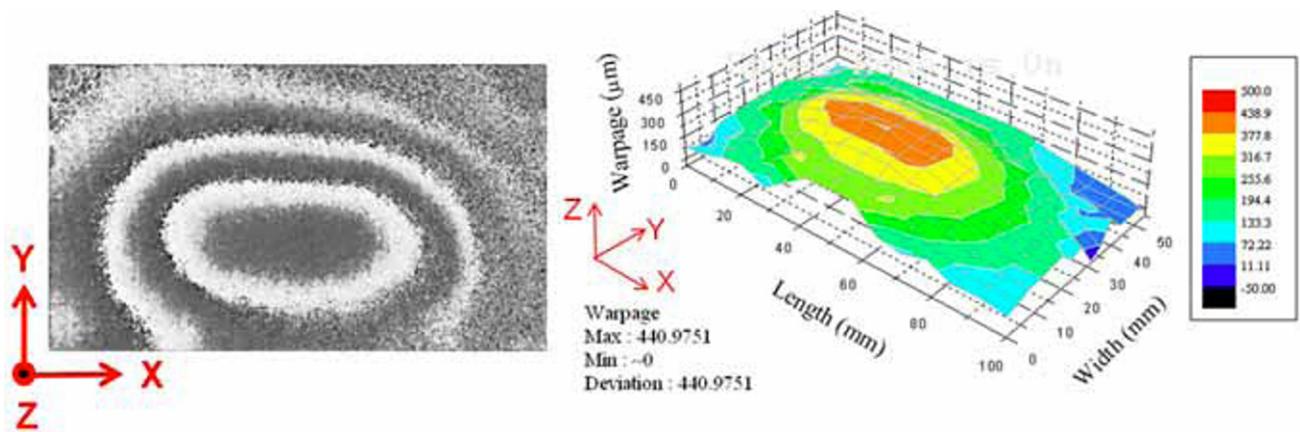


Fig. 8 Wrapped phases diagram and surface contour at tolerance allowance 28 μm of high temperature operation condition

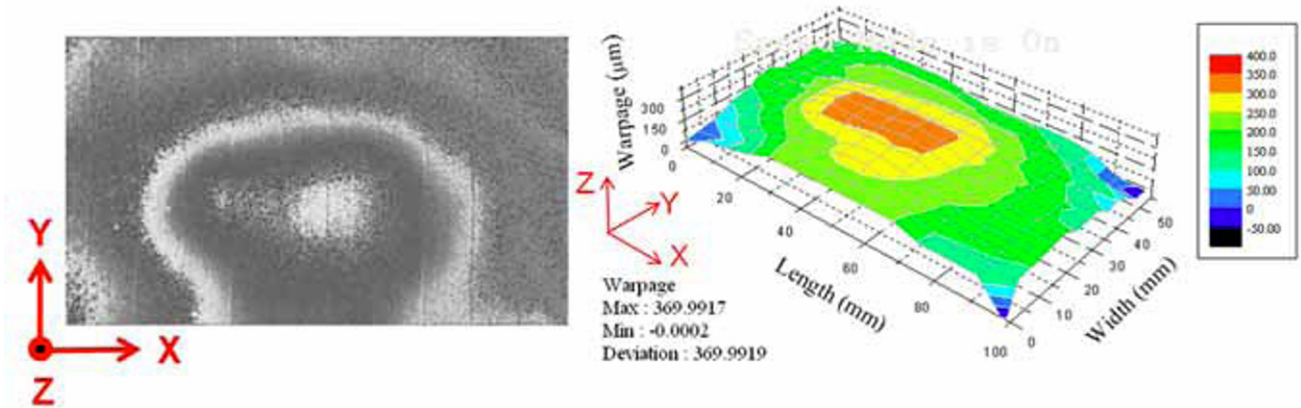


Fig. 9 Wrapped phases diagram and surface contour at tolerance 50 μm of high temperature operation condition

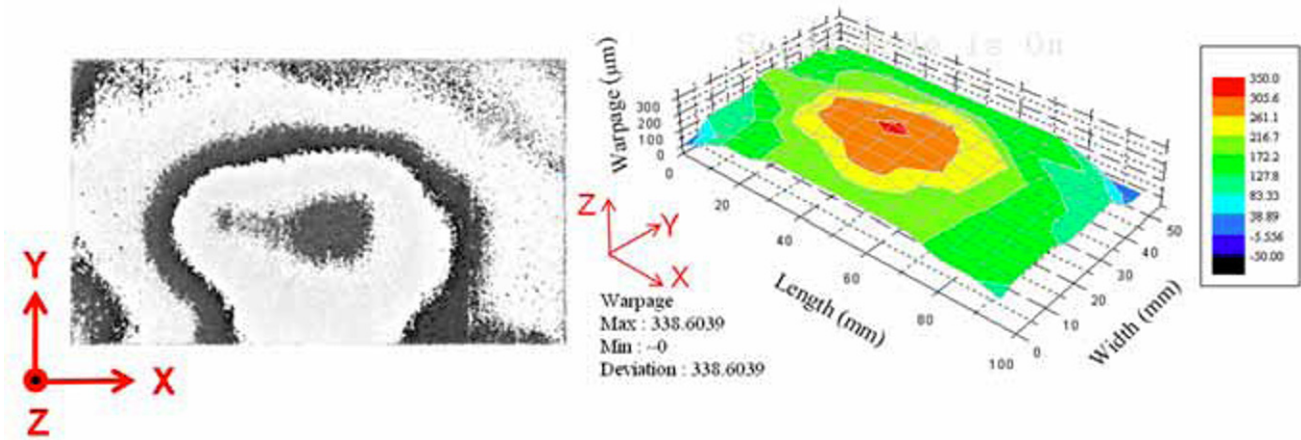


Fig. 10 Wrapped phases diagram and surface contour at tolerance 116 μm of high temperature operation condition

As listed in [Table 2](#), the total displacements obtained from the surface contours for test specimens of tolerances 28 μm , 50 μm and 116 μm are 440.98 μm , 369.99 μm and 338.6 μm , respectively. There is a tendency for the deformation contour to approach the left part for all three tolerances. This is not unexpected since the source of hygrothermal loading of the oven is on the left side of the specimen; the left edge is heated and deformed faster than the right edge. It should be noted that even the temperature loading of Condition B is 10°C lower than Condition A, the operation of the light source did make the temperature distribution inside the BLM become relatively non-uniform. Hence, in comparison with Condition A, the amount of out-of-plane is generally larger in Condition B. As can be observed from [Fig. 8-10](#), out-of-plane displacements of tolerances 28 μm and 50 μm are toward the +z direction and minimum displacement values are at corners or edges. In addition, the magnitude of the displacement of tolerance 28 μm is much higher than that of 50 μm . As mentioned earlier in Condition A, due to the much large tolerance, the ratio of displacements toward +z direction to -z direction is almost equal.

6.3 Condition C: High temperature and high humidity test

Wrapped phases diagrams and surface contours at tolerances 28 μm , 50 μm and 116 μm of high temperature and high humidity condition are shown in Figs. 11-13, respectively. Again, similar to the other two hygrothermal conditions, the smallest out-of-plane displacement occurred for the smallest tolerance.

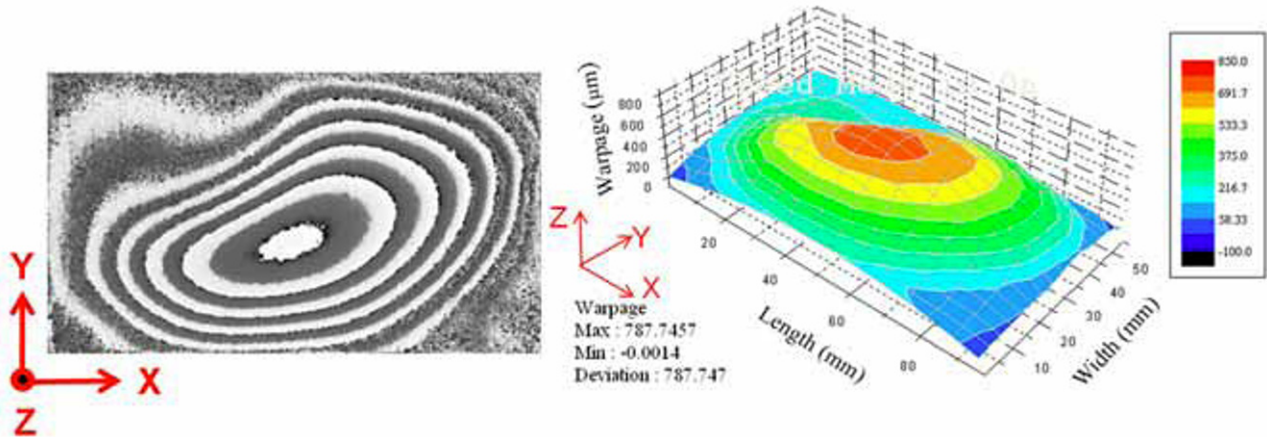


Fig. 11 Wrapped phase diagram and surface contour at tolerance 28 μm of high temperature and high humidity condition

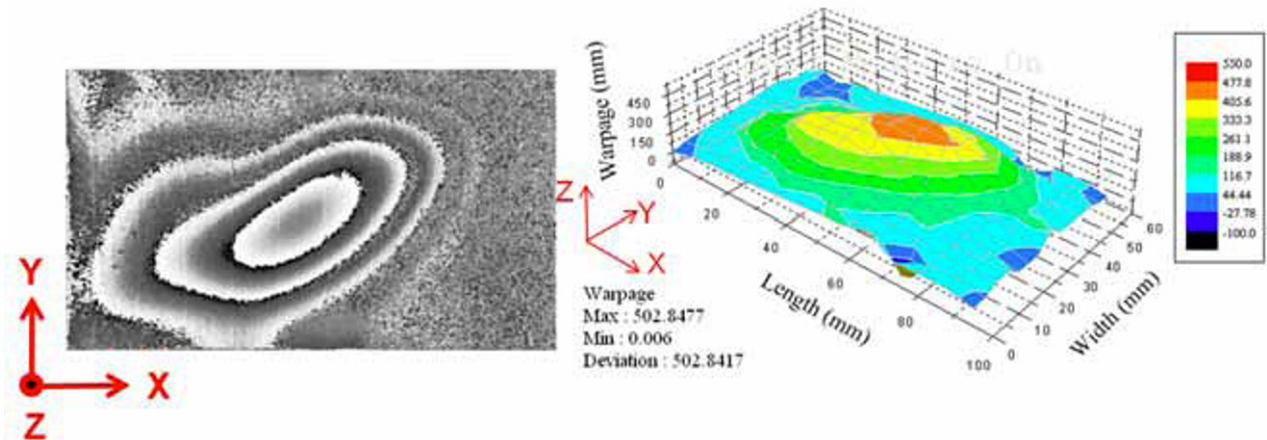


Fig. 12 Wrapped phase diagram and surface contour at tolerance 50 μm of high temperature and high humidity condition

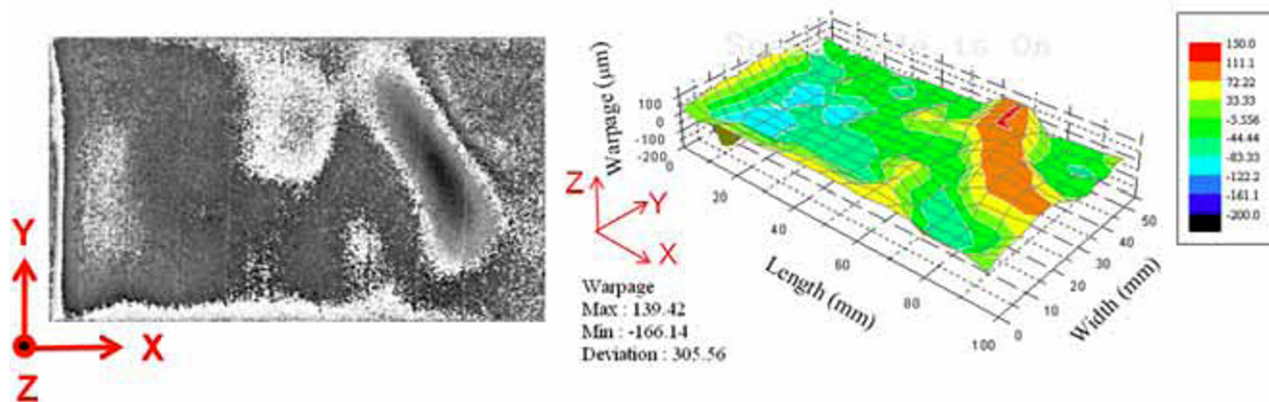


Fig. 13 Wrapped phase diagram and surface contour at tolerance $116\mu\text{m}$ of high temperature and high humidity condition

As listed in Table 2, the total displacements obtained from the surface contours for test specimens of tolerances $28\mu\text{m}$, $50\mu\text{m}$ and $116\mu\text{m}$ are $787.75\mu\text{m}$, $502.84\mu\text{m}$ and $305.56\mu\text{m}$, respectively. Similar to Condition B, there is a tendency for the deformation contour to approach the left part for all three tolerances. The out-of-plane displacement of the tolerance $28\mu\text{m}$ of Condition C is the largest one among all cases studied in this paper. There are 7 fringes appear in the wrapped phase diagram. The total out-of-plane displacement is twice of those in Condition A and Condition B for the same tolerance $28\mu\text{m}$. Similarly to the case of tolerance $50\mu\text{m}$, the magnitude of the out-of-plane displacement of Condition C is also larger than those of the other two Conditions. Even the heating temperature of Condition C is the lowest among three Conditions, the magnitude of the out-of-plane displacement is increased significantly due to the high humidity absorption of the optical film materials used in the BLM. As can be observed from Fig. 8-10, out-of-plane displacements of tolerances $28\mu\text{m}$ and $50\mu\text{m}$ are toward the $+z$ direction and minimum displacement values are at corners or edges. In addition, the magnitude of the displacement of tolerance $28\mu\text{m}$ is much higher than that of $50\mu\text{m}$. As mentioned earlier in Condition A, due to the much large tolerance in the case of $116\mu\text{m}$, the ratio of displacements toward $+z$ direction to $-z$ direction is almost equal. In addition, the magnitude of the displacement is much lower than the cases of $28\mu\text{m}$ and $50\mu\text{m}$. The out-of-plane displacements of all experiments are listed in Table 2. It is not unexpected that the smallest the out-of-plane displacement corresponds to the least tolerance in the normal direction. However, the increase amount of the magnitude of the out-of-plane displacement is not directly proportional to the increase amount of the tolerance. It is possible because that once the amount of reserved tolerance is sufficient enough to accommodate the out-of-plane displacement from the LGP and lower prism sheet produced by certain hygrothermal condition, the increase of the amount of out-of-plane displacement of the upper prism sheet due to other optical film components is significantly reduced.

7. Conclusions

In current hygrothermal reliability test procedures used in the BLM industry, the BLM has to move out from the test chamber to measure its illumination variation several times. The digital shadow moiré system introduced

in this paper provides a real-time, time-saving and cost-effective alternative solution. As the measurement range and accuracy depends on the pitch of the reference grating, the system also has the flexibility to adjust itself to be used for BLMs of different dimensions. Based on the experimental results obtained in this paper, it was found that the high temperature and high humidity condition is the one need to be most concerned for the reliability of the BLMs. The service life of a BLM could be longer if low moisture absorption polymeric materials are selected for manufacturing optical films. In addition, a proper choice of the dimension of the tolerance could also help reduce the out-of-plane displacement of the BLM. Furthermore, the out-of-plane displacement of the BLM is affected not only by the reserved amount of tolerance but also by the material properties of the film-back adhesive tape. If the adhesive strength is too large, the prism sheet 1 could be fully fixed to the plastic frame, however, the BLM may be rapidly deformed under certain hygrothermal condition. On the other hand, if the adhesive strength is not large enough, then the prism sheet 1 may be rather easily to get loose from the BLM even under slight deformation. Therefore, in addition to consider the amount of tolerance, the selection of the appropriate film-back adhesive tape might be another factor to be evaluated in designing the BLM.

ACKNOWLEDGMENTS

This research was supported in part by the National Science Council (project no.: NSC-95-2221- E-007-011-MY3), Taiwan, Republic of China.

REFERENCES

1. G. H. Kim., "A PMMA Composite as an Optical Diffuser in a Liquid Crystal Display Backlighting Unit (BLU)," *European Polymer Journal*, Vol. 41, No. 8, pp. 1729-1737, 2005.
2. G. H. Kim, W. J. Kim, S. M. Kim and J. G. Son., "Analysis of Thermo-Physical and Optical Properties of a Diffuser Using PET/PC/PBT Copolymer in LCD Backlight Units," *Display*, Vol. 26, No. 1, pp. 37-43, 2005.
3. C. Y. Chu, M. C. Pan and J. Ho., "Thermal Analysis and Experimental Validation on TFT-LCD Panels for Image Quality Concerns," *Electronics Packaging Technology Conference (EPTC)*, Grand Copthorne Waterfront, Singapore, Vol. 2, pp. 543-548, Dec.7-9, 2005.
4. Y. M. Tseng, "Thermal Deformation Effects on Characteristics of LCD Backlight Module", M. S. Thesis, Department of Mechanical Engineering, National Sun Yat-Sen University, Kaoshiung, Taiwan, 2005.
5. "ANSYS", Version 9.0, Swanson Analysis Systems Inc., Houston, PA, U. S. A., 2005.
6. "Pro/ENGINEER", Parametric Technology Corporation, Needham, MA, U. S. A., 2005.
7. "ASAP", Breault Research Organization, Inc., Tucson, Arizona, U. S. A., 2005.
8. H. H. Hsu, "Numerical Analysis and Experimental Investigation of Hygrothermal Deformation of Backlight Modules," M. S. Thesis, Department of Power Mechanical Engineering, National Tsing Hua University, Hsinchu, Taiwan, Republic of China, 2006.
9. J. L. Sullivan., "Phase-Stepped Fractional Moiré," *Experimental Mechanics*, Vol. 31, No. 4, pp. 373-381, 1991.
10. M. R. Stiteler and C. Ume., "System for Real Time Measurement of Thermally Induced PWB/PWA Warpage," *Journal of Electronic Packaging*, Vol. 119, No. 1, pp. 1-7, 1997.

11. C. Quan, Y. Fu and C. J. Tay., "Determination of Surface Contour by Temporal Analysis of Shadow Moiré Fringes," *Optics Communications*, Vol. 230, No. 1, pp. 23-33, 2003.
12. R. S. Sirohi and F. S. Chau., "Optical Methods of Measurement," Marcel Dekker, Inc., New York, U. S. A., 1999.

Theory and Applications of Universal Phase-shifting algorithm

Thang Hoang, Zhaoyang Wang* and Dung Nguyen

Department of Mechanical Engineering, The Catholic University of America, Washington, DC
20064,

*Corresponding author: wangz@cua.edu

Abstract

Phase shifting technique provides a fully automatic analysis for fringe pattern or interferogram processing. In practice, due to the imperfections of phase shifter, optical elements, experimental setup and other various reasons, typical phase-shifted interferograms generally contain nonlinear phase shifting errors, variations and fluctuations of background intensities and modulation amplitudes, optical nonlinearities between intensities and phases, and so on. These errors in practice severely violate the assumptions in the principles of the existing phase shifting algorithms. To cope with these problems in applications, this paper presents a simple, rigorous, precise yet unveiled universal phase-shifting algorithm for retrieving desired phase distributions with ultrahigh accuracies from actual interferograms. The algorithm is based on a least-squares approach and a generic governing equation for the description of practical interferograms. Computer simulation shows a perfect performance of the universal algorithm, and applications to selected experiments demonstrate its validity and practicability.

1. Introduction

Fringe projection profilometry (FPP) is one of the leading methods for acquiring three-dimensional (3D) shape information by projecting structured-light patterns onto the objects of interest [1-3]. Due to their numerous advantages such as low cost and high flexibility, digital projector as well as digital camera are usually employed in the FPP measurements. Furthermore, to obtain full-field 3D shape information with high accuracies, sinusoidal fringe patterns are typically used. Nevertheless, the luminance nonlinearity caused by the gamma encoding and decoding of the digital camera and projector brings unwanted intensity changes to the captured fringe patterns, which often lead to non-negligible errors in the 3D shape determination [4]. To overcome the nonlinear luminance problem, many approaches of phase (or fringe order) error compensation have been proposed, and they normally fall into two categories. The first one uses the transform techniques to extract the fringe phase, such as Fourier transform [5], wavelet transform [6], and Hilbert transform [7]. The transform techniques require complicated computation and cannot retrieve the desired phase map accurately for measurements involving multiple objects or an object with complex shape. On the contrary, the phase-shifting techniques classified into the second category are usually suitable for measuring objects with complex shapes; however, the phase-shifting algorithms generally face a trade-off between the accuracy of phase error compensation and computation time as well as complexity [8]. Despite the recent advances in retrieving phase distribution in real time with low aberration [9-11], a method that is not only very simple and easy to implement but also highly reliable in term of phase-error elimination for FPP system has not been unveiled. In this paper, a novel and robust scheme is presented by combining a universal phase-shifting algorithm and a generic gamma correction method, and the scheme is capable of providing high speed, high accuracy, and easy implementation for 3D shape measurements with FPP.

2. Universal Phase-shifting Algorithm

Mathematically, the existence of nonlinear luminance distortion in the FPP system brings high-order harmonics to the actual fringe patterns. Therefore, the intensity of the captured fringe image can be theoretically expressed as follows:

$$I^t(x, y) = a(x, y) + \sum_{j=1}^p b_j(x, y) \cos \{j[\Phi(x, y) + \delta]\} \quad (1)$$

where (x, y) denotes an arbitrary point in the image, a is the background or mean intensity, b is the intensity modulation amplitude, Φ is the fringe phase distribution, δ is the phase-shift amount, and p is the highest significant harmonic order of the captured fringe pattern. For convenience and simplicity, (x, y) will be omitted from the equations hereafter. Equation (1) involves $p+2$ unknowns: a, b_1, \dots, b_p , and Φ ; consequently, $p+2$ phase-shifted fringe patterns are required to solve for these unknowns. Defining a set of variables as $A_j = b_j \sin(j\Phi)$; $B_j = b_j \cos(j\Phi)$, each of the $p+2$ phase-shifted fringe patterns can be described as:

$$I_i^t = a + \sum_{j=1}^p B_j \cos(j\delta_i) - \sum_{j=1}^p A_j \sin(j\delta_i) \quad (2)$$

In the equation, $i = 1, 2, \dots, p+2$, and $\delta_i = \frac{i-1}{p+2} 2\pi$. The sum of squared differences between the theoretical pattern I_i^t and actual pattern I_i is:

$$S = \sum_{i=1}^{p+2} [a + \sum_{j=1}^p B_j \cos(j\delta_i) - \sum_{j=1}^p A_j \sin(j\delta_i) - I_i]^2 \quad (3)$$

To minimize S , the least-square approach $\frac{\partial S}{\partial B_1} = 0$. This yields

$$\sum_{i=1}^{p+2} \cos(\delta_i) [\sum_{j=1}^p B_j \cos(j\delta_i) - \sum_{j=1}^p A_j \sin(j\delta_i) - I_i] = 0 \quad (4)$$

Considering $\delta_i = \frac{i-1}{p+2} 2\pi$, it is easy to prove that $\sum_{i=1}^{p+2} \cos(\delta_i) = 0$, $\sum_{i=1}^{p+2} \cos(\delta_i) \cos(j\delta_i) = 0$ for any $j = 2$ to p , $\sum_{i=1}^{p+2} \cos(\delta_i) \sin(j\delta_i) = 0$ for any $j = 1$ to p . Consequently, Equation (4) can be simplified as:

$$[\sum_{i=1}^{p+2} \cos^2(\delta_i)] B_1 - \sum_{i=1}^{p+2} \cos(\delta_i) I_i = 0 \quad (5)$$

This give

$$B_1 = \frac{\sum_{i=1}^{p+2} \cos(\delta_i) I_i}{\sum_{i=1}^{p+2} \cos^2(\delta_i)} \quad (6)$$

Similarly, A_1 can be calculated from $\frac{\partial S}{\partial A_1} = 0$: (6)

$$A_1 = \frac{-\sum_{i=1}^{p+2} \sin(\delta_i) I_i}{\sum_{i=1}^{p+2} \sin^2(\delta_i)} \quad (7)$$

From Eqs. (6) and (7), and considering $\sum_{i=1}^{p+2} \cos^2(\delta_i) = 0 = \sum_{i=1}^{p+2} \sin^2(\delta_i)$ the phase can be retrieved as:

$$\Phi = \tan^{-1} \left(\frac{A_1}{B_1} \right) = \tan^{-1} \frac{-\sum_{i=1}^{p+2} \sin(\delta_i) I_i}{\sum_{i=1}^{p+2} \cos(\delta_i) I_i} \quad (8)$$

Equation (8) indicates that $p+2$ step uniform phase-shifting scheme can be employed to retrieve phase accurately from fringe patterns with nonlinear harmonics up to the p -th order.

In a recent research [10], Pan et al showed that the highest significant harmonic order in a practical FPP

image is five. Therefore, at least seven images are required in real FPP applications.

3. Generic Gamma Correction Scheme

The universal phase shifting algorithm is very simple and effective for extracting correct phase from real FPP images. However, taking more than three phase-shifted images is usually undesired in fast FPP measurements. To cope with this issue, a generic gamma correction scheme is described below.

In theory, the gamma effect of the projector and camera system can be described as:

$$I_n = I_0^{\gamma_o} \quad (9)$$

where I_n is the normalized intensity of captured or real image, I_0 is the normalized intensity of the computer-generated ideal sinusoidal pattern, and 0 is the gamma value of the entire system including projector and camera. It is noted that lately many research efforts have been focused on advancing simpler and more accurate techniques to detect the gamma value [12,13]. Nevertheless, an essential analysis that can detect the gamma quickly and correctly for the FPP system remains lacking.

It can be seen from Eq. (9) that applying an appropriate gamma encoding, $\frac{1}{\gamma_c} < 1$, during the generation of ideal image I_0 may help to attenuate the gamma effect and thus enhance accuracy even the number of images is minimum, i.e., three. In this case, $I_0 = I_n^{\gamma_c/\gamma_p}$; consequently,

$$I_n = I_0^{\gamma_p/\gamma_o} \quad (10)$$

In reality, considering the background effect, intensity amplitude, and system complexity, the desired intensity is determined by the following equation:

$$I_0 = AI^{\frac{\gamma_p}{\gamma_o} + \gamma'_o} + B \quad (11)$$

When three-step phase-shifting scheme is employed, the phase can be accurately determined by substituting Eq. (11) and the corresponding $p = 1$ in to Eq. (8)

$$\Phi = \tan^{-1} \left(\frac{-[I_2^{\gamma'} \sin(\frac{\pi}{3}) + I_3^{\gamma'} \sin(\frac{2\pi}{3})]}{I_1^{\gamma'} + I_2^{\gamma'} \cos(\frac{\pi}{3}) + I_3^{\gamma'} \cos(\frac{2\pi}{3})} \right) \quad (12)$$

Where
$$\gamma' = \frac{\gamma_p}{\gamma_o} + \gamma'_o \quad (13)$$

To detect γ' for the three-step phase shifting algorithm, the following equation can be used:

$$\tan^{-1} \left(\frac{-[I_2^{\gamma'} \sin(\frac{\pi}{3}) + I_3^{\gamma'} \sin(\frac{2\pi}{3})]}{I_1^{\gamma'} + I_2^{\gamma'} \cos(\frac{\pi}{3}) + I_3^{\gamma'} \cos(\frac{2\pi}{3})} \right) - C = 0 \quad (14)$$

where C is the correct phase value, which in practice is determined by using the universal phase shifting algorithm presented previously. It is noted that Eq. (14) is for one pixel only; to solve for γ' from the entire image to ensure high accuracy, a least-square approach is typically employed.

To simplify the phase calculation, it is desired to let $\gamma' = 1$ in Eq. (12). This can be done by determining γ_0 and γ'_o as follows:

$$\gamma_0 = \frac{\gamma_{p1} - \gamma_{p2}}{\gamma'_1 - \gamma'_2}$$

$$\gamma'_0 = \frac{\gamma_{p1}\gamma'_2 - \gamma'_1\gamma_{p2}}{\gamma_{p1} - \gamma_{p2}} \quad (15)$$

Once γ_0 and γ'_0 are obtained, setting $\gamma_p = (1 - \gamma_0)\gamma_0$ will yield $\gamma' = 1$. In this way, the conventional phase-shifting algorithm can be used.

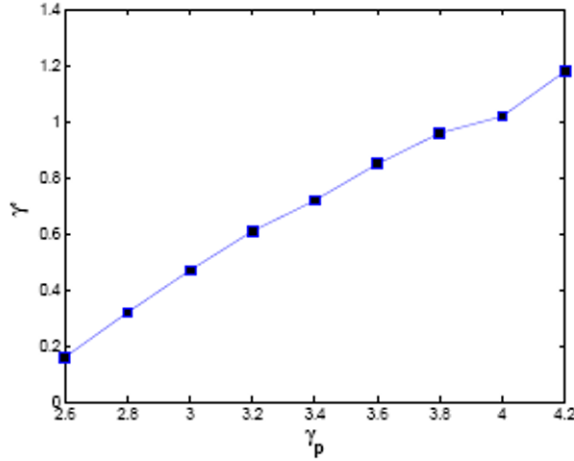


Fig. 1. plot of γ' over γ_p

Hence, an approach to simplify the process is presented:

Step 1: Using large number of phase-shifting interferogram (suggest $p > 15$), correct phase distribution is determined by Equation (8).

Step 2: With the first two initial encoded γ_{p1} , γ_{p2} , actual gamma γ_0, γ'_0 can be computed using Eq. (15).

Step 3: From Eq. (14) now we can estimate perfectly the real system gamma γ' by using Eq. (13) with γ_0, γ'_0 from Eq. (15).

Fig. (1) demonstrates the obtained experiment value of γ' and γ_p and validate the linear relationship between them in Eq. (15).

4. Experiment

Here, to verify the correctness the proposed method, an experiment on measuring the 3-D imaging of shell object is conducted. The structured light source is the commercial (Infocus PlusU4) projector. It projects the fringe patterns onto reference plane and shell object. The deformed patterns will be capture by digital camera (EPIX SV9T001C). The phase distribution originally is computed using conventional phase-shifting algorithm with 3 images using various gamma value in Eq. (8). Then, the phase error is introduced by subtracting that phase with real linear phase and shown in Fig. (2a). It shows that the least error with 0.01 rad at gamma is equal to 3. Fig. (2b) shows the phase error when large numbers of images are used without using gamma encoding. The error is substantially reduced when using large step phase shifting. For seven phase stepping, the phase error is around 0.01 rad. Nevertheless, the three-phase-stepping algorithm can achieve the same accuracy or even better with proposed approach. It is evident that the three-step phase shifting with appropriate gamma correction can extract the phase as accurate as large-step phase shifting (seven) does. Fig. (3d) illustrates the depth information of one arbitrary line on the flat box. It is noted that in real applications, where the small number of phase-shifting images is preferred and the non-linear property of both camera and projector occur, the presented technique provide not only high-speed due to minimum of images but also high accuracy as using high-number of images.

Fig. (3) illustrates the reconstruction of 3D imaging of sea-shell with the conventional 3 phase stepping, 7 stepping and our proposed 3 phase-stepping algorithm.

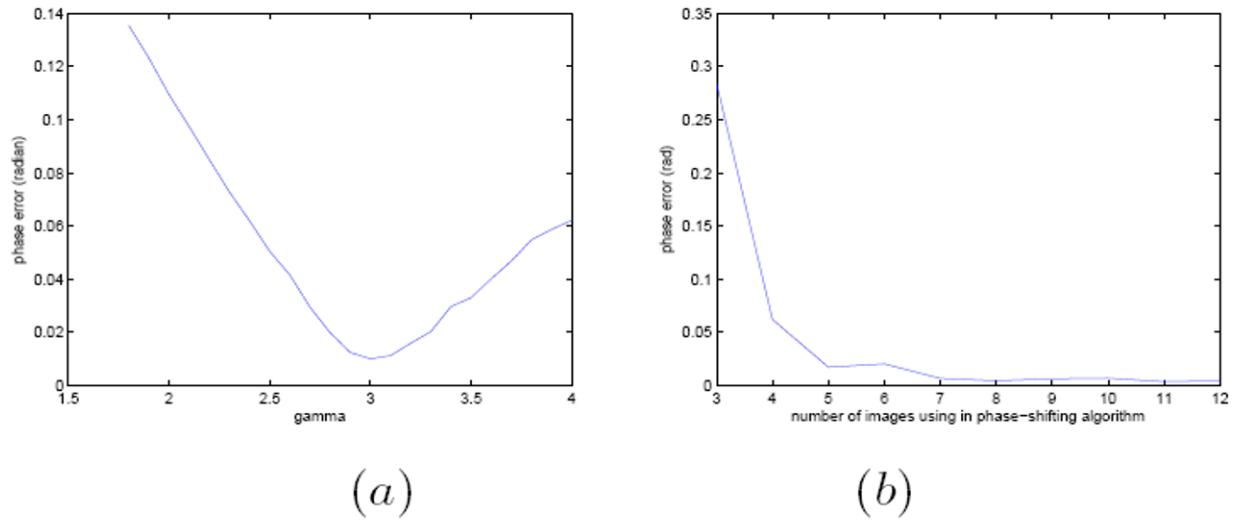
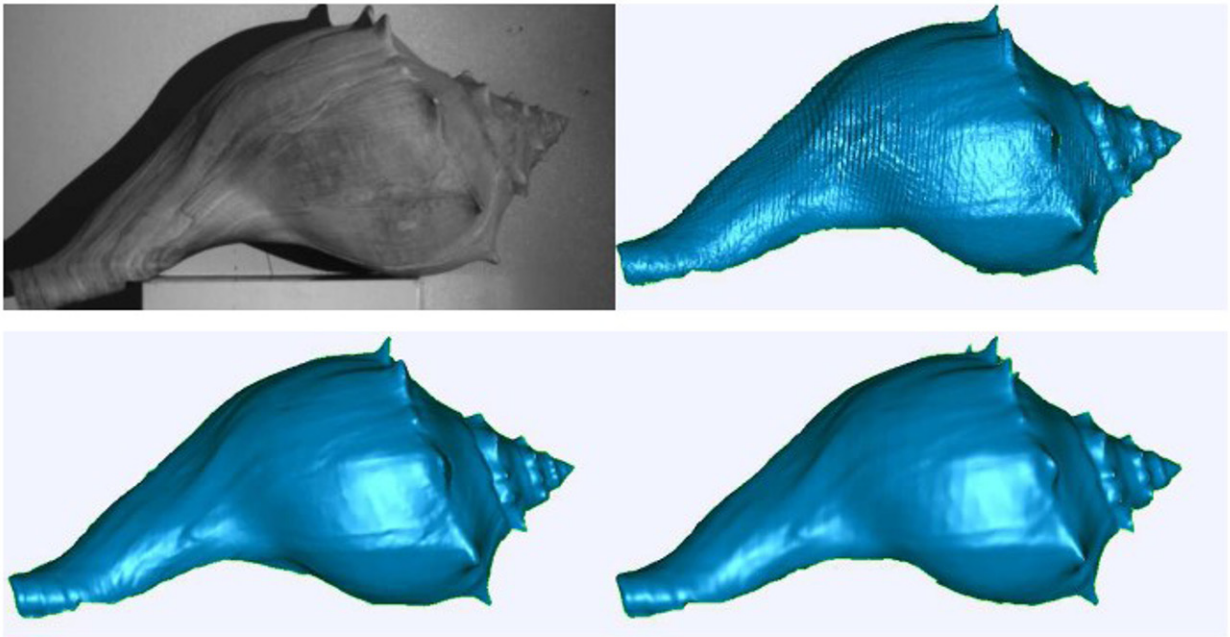


Fig. 2. mean phase error(rad) of an arbitrary line on pattern: (a)three-phase-shifting with multiple gamma encoded,(b)multiple-step-phase shifting without gamma encoded.



5. Conclusion

Due to flexibility and avoiding-phase-shift error, digital fringe projection profilometry has been intensively employed in 3-D measurement. Even so, the nonlinearity of the system, both camera and projector unavoidably reduce the correctness of the measurement. In this letter a simple, high accuracy but yet unveiled luminance nonlinear eliminating method has been proposed based on a combination of conventional phase-shifting algorithm and generic gamma correction technique for FPP systems. It is evident that the deviation from gamma estimating and phase error after using that estimated gamma value are reduced to almost zero. Therefore, the proposed technique can achieve the removing of luminance effect completely and high-speed as the same time.

References

1. F.Chen, G. M. Brown, and M. Song, "Overview of three-dimensional shape measurement using optical methods", *Optical Engineering*, Vol.39, Page10 (2000).
2. Z. Y. Wang, H. Du, and B. Han, "Out-of-plane shape determination in generalized fringe projection profilometry", *Optics Express*, Vol.14, Page 12122(2006).
3. P. S. Huang, C. Zhang, and F.-P. Chiang, "High-speed 3-D shape measurement based on digital fringe projection", *Optical Engineering*, Vol. 42, Page 163 (2003).
4. A. Asundi and C. S. Chan, "Phase shifted projection grid—Effect of pitch and profile", *Optics and Lasers Engineering*, Vol 21, Page 3 (1994).
5. M. Takeda and K. Mutoh, "Fourier Transform profilometry for the automatic measurement of 3-D object shapes", *Applied Optics*, Vol. 22, Page 3977 (1983).
6. J. Zhong and J. Weng, "Phase retrieval of optical fringe patterns from the ridge of a wavelet transform", *Optics Letter* , Vol.30, Page 2560 (2005).
7. L. Xiong and S.Jia, "Phase-error analysis and elimination for nonsinusoidal waveforms in Hilbert transform digital-fringe projection profilometry", *Optics Letter*, Vol.34, Page 2363 (2009).
8. Y. Surrel, "Design of algorithms for phase measurements by the use of phase stepping", *Applied Optics*, Vol.35, Page 51 (1996).
9. S. Zhang and S. Yau, "Generic nonsinusoidal phase error correction for three-dimensional shape measurement using a digital video projector", *Applied Optics*, Vol. 46, Page 36 (2007).
10. B. Pan, Q.Kemao and L.Huang, "Phase error analysis and compensation for nonsinusoidal waveforms in phase-shifting digital fringe projection profilometry", *Optics Letter*, Vol. 34, Page 416 (2009).
11. Z.Wang and B. Han, "Advanced iterative algorithm for phase extraction of randomly phase-shifted interferograms", *Optics Letter*, Vol.29, Page 1671 (2004).
12. H. Farid, "Blind inverse gamma correction", *IEEE Transaction on Image Processing*, Vol.10, Page 1428 (2001).
13. H. Guo, H. He and M. Chen, "Gamma Correction for Digital Fringe Projection Profilometry", *Applied Optics*, Vol.43, Page 2906 (2004).

Evaluation of Crash Energy Absorption Capacity of a Tearing Tube

Younki Ko¹⁾·Kwanghyun Ahn¹⁾·Hoon Huh^{*1)}·Wonmok Choi²⁾·Hyunseung Jung²⁾·Taesoo Kwon²⁾

¹⁾ School of Mechanical, Aerospace and System Engineering, KAIST

335 Gwahak-ro, Yuseong-gu, Daejeon 305-701, Republic of Korea

²⁾ Railway System and Safety Research Department, Korea Railroad Research Institute,

301-1 Wulam-dong, Uiwang-si, Gyeonggi-do 437-757, Republic of Korea

koyk@kaist.ac.kr, ankh1128@kaist.ac.kr, huh@kaist.ac.kr, wmchoi@krri.re.kr, jhs@krri.re.kr

and tskwon@krri.re.kr

ABSTRACT

This paper deals with the numerical prediction of energy absorption capacity of a tearing tube, which can absorb the crash energy through expanding and axial splitting processes. It is important to consider the dynamic material behavior and fracture characteristics of tube material in order to simulate the deformation behavior of a tearing tube accurately. Uniaxial tensile tests are performed in order to obtain the flow stress curve and the fracture strain of a tube material according to the strain rate. Quasi-static tensile tests were carried out in the range of strain rates from 0.001/sec to 0.01/sec using a static tensile testing machine. Dynamic tensile tests were conducted at strain rates ranged from 0.1/sec to 300/sec using a high speed material testing machine. These dynamic material properties are utilized to finite element analysis through a user material subroutine of ABAQUS/Explicit. Especially, ductile fracture criteria are adopted in order to describe the fracture characteristics of a tube material during axial splitting process. Dynamic tearing cases are simulated and the reliability of numerical results is verified by comparing them with the experimental results in dynamic tearing tests. The simulated results accurately predict the onset of fracture in axial splitting process and the energy absorption capacity has a good agreement with experimental results.

1. Introduction

Crash energy absorbing devices are used to protect human life as well as other important structures during collision of a heavy vehicle like a train. Since thin-walled structures are very efficient devices which dissipate the crash energy by plastic deformation, they attract much attention due to the wide range of deformation modes

generated.

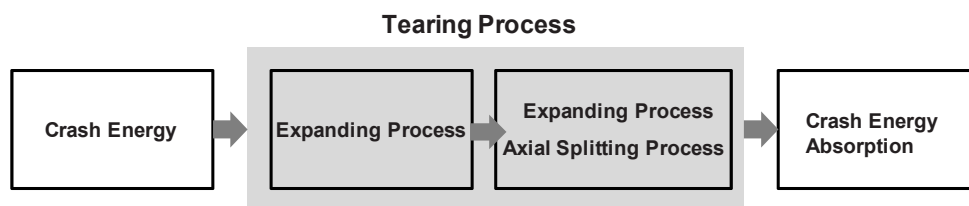
Especially, circular metal tubes are widely used as an energy absorbing device due to easy fabrication, installation and comparably well-known deformation behavior. Circular tubes may be axially crushed progressively in an axisymmetric or a non-axisymmetric mode by two flat plates. Plantema [1] suggested a theory to predict the plastic local buckling load and the theory was modified by Ahn and Huh [2] in order to consider dynamic characteristics of a material. Alexander [3] derive a prediction formula for axisymmetric collapse mode based on a balance of external and internal work done through simplification of wrinkle shapes. Afterwards, Abramowicz and Jones [4] improved the wrinkle shape model and carried out experiments for dynamic bucking effect of tubes and compared the result with the suggested theory.

Researches for another different deformation mode of circular tubes were carried out by many researchers. Reddy and Reid [5], and Huang et al. [6] investigated inversion modes of circular tubes through tube compression using a shaped die within a compatible range of parameters. Manabe and Nishimura [7] studied about forming characteristics according to tube and punch shapes, materials and lubrication in the ube expanding process. And Lu [8] carried out the numerical simulation according to the expanding ratio of a circular tube and the punch speed, and compared the result with results from tube expanding experiments. The splitting and curling behavior of a tube which occurs in an axially compression process between a plate and radius die was investigated by Lu et al [9]. Ezra and Fay [10] demonstrated circular tube splitting and curling as an efficient system based on specific energy dissipation. The mechanism has the advantage for a long stroke and steady reaction force during crushing process.

The present study is concerned with the energy absorbing device which is used in a head unit of a train in order to decrease the damage for other train structures and human safety during the train crash. A tearing tube was newly suggested as an energy absorbing device in order to maximize the crash absorbing energy through combining two different deformation modes which are expanding and axial splitting mode of a circular tube. The existing device uses an expanding tube as the energy absorbing device which absorbs crash energy only through expanding process. However, after expanding process, the expanded region of tube has the additive energy absorption capacity. In tearing process using a tearing tube, the expanded part will be utilized as the energy absorbing region which newly adopted through the axial splitting process. This paper will ascertain the possibility of the energy absorption process and suggest a method for the numerical simulation of the tearing process. Dynamic tearing experiments was also carried out in order to verify the reliability of simulation results.

2. Tearing Tube

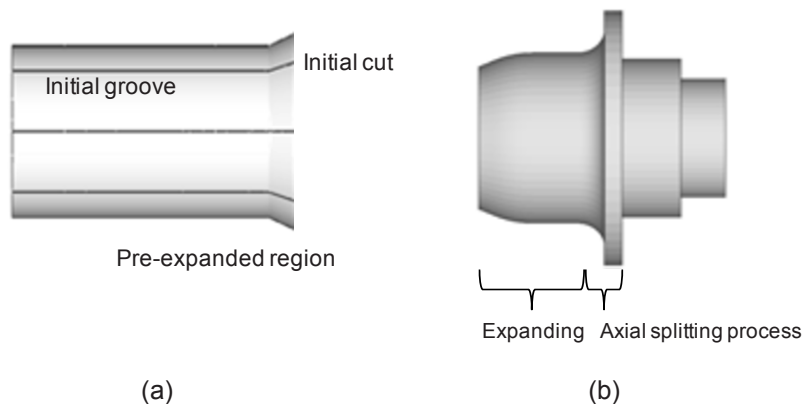
A tearing tube is devised to enhance the energy absorption capacity of a tube which absorbs the crash energy through the designed process. A tearing tube is similar to the expansion tube in the view point of energy absorption mode, which crash energy converts to deformation energy through tube expansion. However, the tearing tube is designed to maximize energy absorption of a material by inducing the axial split process and abrupt plastic deformation through the expansion of the tube over the allowable expansion ratio.



2.a. Conceptual figures of tearing process

Figure 2.a. shows conceptual flow chart of energy absorption mechanism of the tearing tube. At first, a tearing punch is moved toward the tube inlet and the punch makes the tube expand by the given expansion ratio. If the expanding process cannot absorb total crash energy, the punch moves continuously. And at next step, the tube is expanded over the given expansion ratio and is split from the inlet. The split part undergoes severe bending deformation along the boundary of the punch die shoulder. Therefore, the tearing tube has the additional energy absorption mechanism by axial splitting and bending deformation comparing to the existing expansion tube.

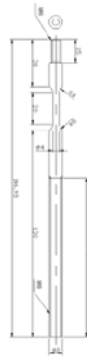
In order to achieve the tearing process successfully, some modification is needed to a simple circular tube. First of all, initial cuts should be processed at the tube inlet to bring in tear of the tube with constant spacing around the tube inlet. And initial groove should be made for uniform propagation in the longitudinal direction from the induced cracks around the tube inlet. However, these initial cuts and grooves are affected to the expanding process which is proceeded as the first energy absorption mechanism because cracks can occur at the initial cuts during the beginning of expanding process. The unexpected cracks will deteriorate the energy absorption capacity of the tube. For the sake of prevention of the deterioration, the pre-expanded region is designed at the tube inlet. The pre-expanded region is manufactured before processing the initial cuts and grooves and prevent from concentrating the plastic deformation at initial cuts and grooves during the expanding process. The designed tearing tube has 200mm diameter, 7mm thickness and 300mm length, and pre-expanded region of 35.0mm is manufactured at the tube inlet. 8 initial cuts with 1mm width and 5mm depth, and 8 initial grooves with 1mm width and 0.25mm depth are made on the inlet of the pre-expanded region. The conceptual shape of tube is represented in figure 2.b.(a). The tearing punch for tube expansion is shown in figure 2.b.(b). The punch is made to proceed expanding and axial splitting processes in sequence. The punch has expanding ratio of 1.15 for first expanding process and die shoulder radius of 100mm for the axial splitting process.



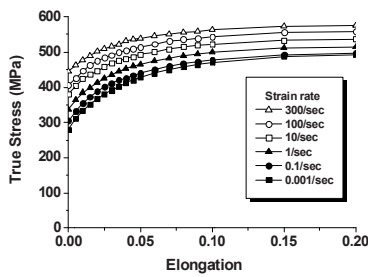
2.b. Schematic figures of : (a) a Tearing tube; (b) a Tearing punch

3. Experiment for Material Characterization

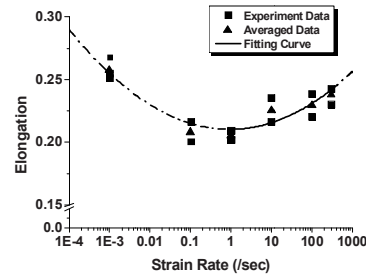
The tearing tube is a structure which undergoes dynamic deformation in train crash accident. The dynamic material characteristics should be obtained in order to simulate the dynamic behavior of a tube accurately because a material shows higher tensile strength and fracture characteristics in dynamic deformation comparing to the static case[11]. Uniaxial tensile tests for S20C which is used as a material of the tearing tube are carried out in static and dynamic condition. The specimen and high speed tensile testing machine for the experiment is represented in figure 3.a. The specimen has a cylindrical type with 8.0mm diameter and 20.0mm gage length. The range of strain rate of 0.001, 0.1, 10.0, 100.0, 300.0 /sec is imposed as considering the practical strain rate which the tube undergoes during expanding and axial splitting processes. Figure 3.b. shows the experimental results for the flow stress curves and fracture elongations according to strain rates. As shown in the figures, the flow stress curves are shifted up as strain rate increase, and the fracture elongation shows the tendency that the elongation decreases in lower strain rate and increases in higher strain rate centering around 1/sec strain rate.



3.a. Tensile specimen and High speed tensile testing machine



(a)



(b)

3.b. Result of uniaxial tensile experiment for various strain rates: (a) Flow stress curve; (b) Fracture elongation

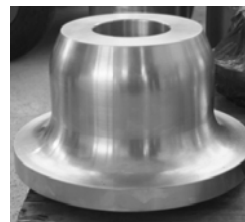
4. Tube Tearing Experiment

4.1. Experimental set up

Dynamic tearing experiments are carried out in order to verify the reliability of numerical simulation and performance of a practical tearing tube which is manufactured in the referred dimension. 2 tearing tubes and punches are used in the experiment as shown in figure 4.a. The moving barrier has 12.2 tons weight and it accelerates by 15.0 km/h before the crash.

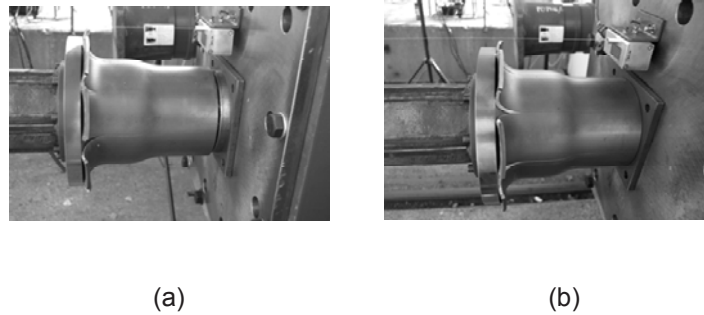


(a)

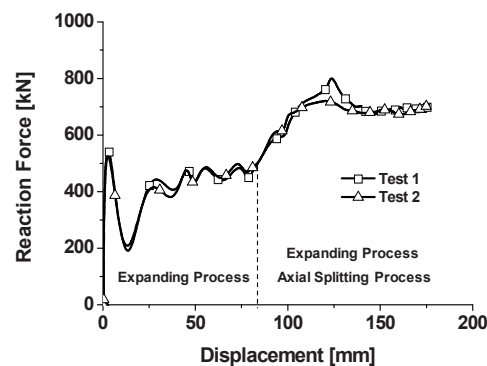


(b)

4.a. Preparation of specimen and equipment for tearing experiment: (a) Tearing tube; (b) Tearing punch



4.b. Deformation shape of tearing tube: (a) Test 1; (b) Test 2



4.c. Reaction force for dynamic tearing experiment and finite element analysis

4.2 Experimental result

Figure 4.b. shows the deformation shape of a tearing tube after the test. As shown the figures, the deformation shape denotes that fracture does not occur in the expanding process and that in the axial splitting process, cracks initiate at the initial cuts and propagate uniformly along the initial grooves due to abrupt expansion by a tearing die shoulder. Figure 4.c. is reaction forces for dynamic tearing tests, which are almost identical level and features for two trials. In beginning of the expansion process, load is fluctuated and slightly dropped. The phenomenon comes from load ringing by vibration of a fixed barrier system after the crash and after the phenomenon, reaction force has uniform level comparably. As the punch moves forward continuously, the abrupt tube expanding and axial splitting processes are proceeded, and the reaction force increases. By the characteristic of reaction force, it is ascertained that energy absorption capacity of the tube is enhanced due to the 30% increase of reaction force comparing to the expanding process.

5. Analysis for Tearing Process

5.1 Application of ductile fracture criteria

In ductile material, fracture occurs due to void growth and coalescence by plastic deformation of material. Many researchers had suggested the criteria in order to predict this ductile fracture of material since 1950's. In this

paper, 3 kinds of criteria are applied to evaluate the reliability of prediction of the crack initiation. These criteria are represented in equation (1)~(3). Especially, ductile fracture criterion by Ko and Huh [12] shows reliable result to predict hole expanding limit of a thick plate with a circular hole. The tearing process has basically similar deformation mechanism with the hole expanding process in the view point of stress state, which a material undergoes the stretch deformation along the circumferential direction. In order to apply the ductile fracture criteria, a user material subroutine (VUMAT) in ABAQUS/Explicit was constituted and calculated each ductile damage value of the criteria to judge the onset of fracture considering strain rate effect. In the calculation, fitting result of fracture elongation obtained from figure 3.b.(b) is used in order to consider the change of critical damage value by variation of strain rate. The fitting result is the as shown in equation (4). In the simulation, the fracture initiation and propagation can be described by means of eliminating the corresponding elements when the ductile damage calculated by each formulation reaches the critical value.

$$I_{Cockroft} = \frac{1}{D_{cock}} \int_0^{\bar{\epsilon}_f^p} \frac{\sigma_{\max}}{\bar{\sigma}} d\bar{\epsilon}^p \quad (1)$$

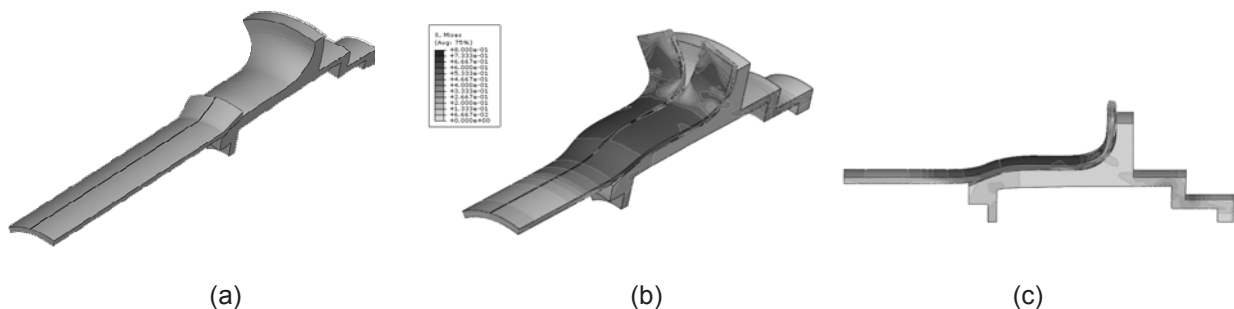
$$I_{Brozzo} = \frac{1}{D_{Brozzo}} \int_0^{\bar{\epsilon}_f^p} \frac{2}{3} \left(\frac{\sigma_{\max}}{\sigma_{\max} - \sigma_m} \right) d\bar{\epsilon}^p \quad (2)$$

$$I_{KH} = \frac{1}{D_{KH}} \int_0^{\bar{\epsilon}_f^p} \frac{\sigma_{\max}}{\bar{\sigma}} \left\langle 1 + 3 \frac{\sigma_{mean}}{\bar{\sigma}} \right\rangle d\bar{\epsilon}^p \quad (3)$$

$$\epsilon_f(\dot{\epsilon}) = 0.21 + 0.00025 \cdot \log(\dot{\epsilon}) + 0.005 \cdot \log(\dot{\epsilon})^2 \quad (4)$$

5.2 Finite element model and analysis conditions

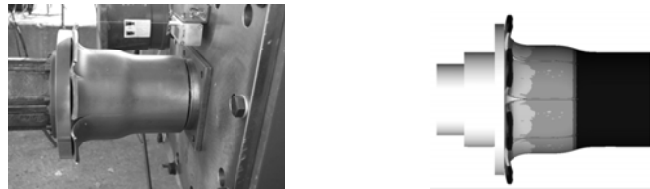
Figure 5.a.(a) is finite element model of the tearing tube and punch. As shown the figure, 1/8 part of entire shape is modeled and imposed the equivalent boundary condition at the symmetric section for the analysis efficiency. 3 dimensional continuum elements with a side length below 0.5mm are used in the region of initial cut and groove to describe the fracture propagation accurately. Flow stress curves in figure 3.b.(a) are imposed in the material of tube, and it is assumed that the material of punch has elastic behavior. The well lubricated friction condition of 0.05 friction coefficient is imposed at the contact surfaces between the punch and tube with Cr coating surface. The end nodes of the tube are constrained for all degree of freedom, and practical train crash conditions with 12.2 tons of train weight and initial velocity of 15.0 km/h are applied to the punch end.



5.a. Finite element models of a tearing tube and punch: (a) initial state; (b) iso view; (c) side view

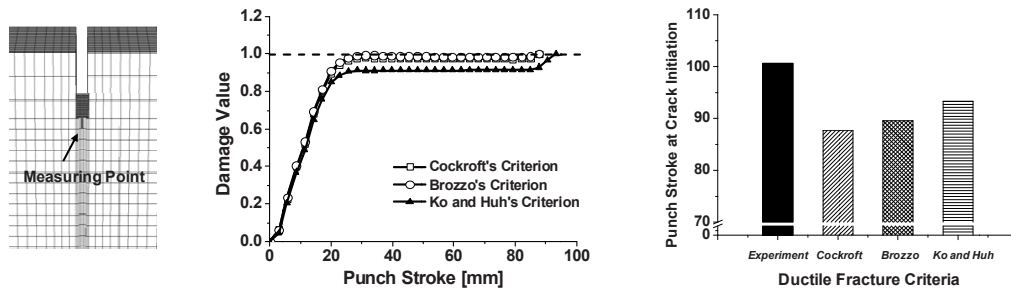
5.3 Analysis result for tearing process

In the simulation, the tearing punch come to stop after losing the entire crash energy at about 174.0 mm stroke, and the deformation shape with contour of effective stress level is represented in figure 5.a.(b)~(c). The result denotes that principal energy absorbing mechanisms are tube expanding process and bending deformation after the splitting process and that the corresponding elements over critical damage value was eliminated by ductile fracture criteria. Figure 5.b. shows the deformation shape of the tearing tube after the test and comparison with numerical result. As shown the figures, the deformation shape demonstrates that fracture does not occur in expanding process and that in axial splitting process, cracks initiate at the initial cuts and propagate uniformly along the initial grooves due to abrupt expansion by tearing die shoulder.

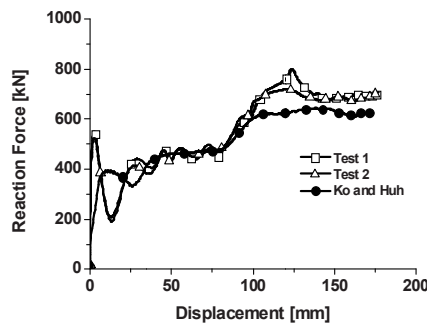


5.b. Comparison of deformation shape between experiment and simulation

Figure 5.c. represents the result for prediction of the onset of crack initiation at the tip of initial cut according to the criteria. As shown the figure, the criteria cannot predict the crack initiation accurately, but Ko and Huh's criterion shows better agreement with the experimental result comparing to Cockroft and Brozzo's criteria. Reaction force curve obtained during the process is shown in figure 5.d. and it represents detail deformation characteristics. Firstly, as expanding the tube, the reaction force rapidly increases. Continuously, the expanding process proceeds to about 81.0mm stroke maintaining the almost uniform reaction force level. Then, the tube is expanded abruptly and undergoes the severe bending deformation along the tearing die shoulder of the punch and cracks initiate from the initial cuts of the tube at the 105mm stroke.



5.c. Prediction of the onset of crack initiation in tearing process according to ductile fracture criteria



5.d. Reaction force during expanding and axial splitting process according to ductile fracture criteria

6. Conclusion

This paper deals with a tearing tube of the crash energy absorbing structure. Dynamic tearing experiments are carried out in order to verify the performance of tearing process for the tube designed. A method for numerical analysis of tearing processes is suggested in order to predict energy absorption capacity of tearing tube numerically. In the simulation, Crockroft, Brozzo, Ko and Huh's ductile fracture criteria are applied in order to describe axial splitting processes and their reliability is evaluated in the aspect of the onset of crack initiation and reaction force characteristic. The conclusion obtained by this research is as follow;

- 1) Dynamic material properties of tube material are obtained by high speed uniaxial tensile test in the range from 0.001/sec to 300/sec. From the experiment, flow stress curves and fracture elongation according to various strain rates are obtained and applied to the numerical simulation.
- 2) The dynamic tearing experiment demonstrates that the tearing process is effective to absorb the crash energy during the practical crash accident. The tearing tube absorbed the entire crash energy with expanding process and axial splitting process are proceeded in sequence
- 3) Ko and Hus's ductile fracture criterion shows better performance than the other criteria in the aspect of the onset of crack initiation and reaction force.
- 4) The numerical method suggested by this paper shows the reliability for prediction of the deformed shape of the tearing tube and energy absorption capacity comparing to tube tearing experiments.

Reference

- [1] F. J. Plantema, "Collapsing Stress of Circular Cylinders and Round Tubes", Nat. Luchtraart Lab. Rep., Amsterdam, 1946.
- [2] K. H. Ahn, J. S. Kim and H. Huh, "Energy Absorption of Expansion Tube Considering Local Buckling Characteristics", Int. J. Modern Physics B, Vol.22, No.31/32, pp.5993~5999, 2008.
- [3] J. M. Alexander, "An Approximate Analysis of the Collapse of Thin Cylindrical Shells Under Axial Loading", Q. J. Mech. Appl. Math., Vol. 13, pp. 10~15, 1960.
- [4] W. Abramowicz and N. Jones, "Dynamic Progressive Buckling of Circular and Square Tubes", Int. J. Impact Engng., Vol. 2, No. 2, pp. 263~281, 1984.
- [5] T. Y. Reddy and S. R. Reid, "Axial Splitting of Circular Metal Tubes", Int. J. Mech. Sci., Vol. 28, No. 2, pp. 111-131, 1986.
- [6] X. Huang, G. Lu and T.X. Yu, "On the Axial Splitting and Curling of Circular Metal Tubes", Int. J. Mech. Sci., Vol. 44, pp. 2369-2391, 2002.
- [7] K. Manabe and H. Nishimura, "Forming Loads in Tube-Flaring with Conical Punch – Study on Nosing and Flaring of Tubes V", J. Jpn. Soc. Technol. Plasticity, Vol. 24, No. 264, pp. 47~52, 1983.
- [8] Y. H. Lu, "Study of Tube Flaring Ratio and Strain Rate in the Tube Flaring Process", Finite Element Anal. Des., Vol. 40. Pp. 305~318, 2004.
- [9] G. Lu, H. Fan and B. Wang, " An Experimental Method for Determining Ductile Tearing Energy of Thin Metal Sheets", Metals and Materials, Vol. 4, pp. 432-435. 1998.
- [10] A. A. Ezra and R. J. Fay, "An assessment of Energy Absorbing Devices for Prospective Use in Aircraft Impact Situations", Dynamic Behavior Structures, pp. 225~246. 1972.
- [11] H. Huh, J.H. Lim, and S.H. Park, "High Speed Tensile Test of Steel Sheets for the Stress-Strain Curve at the Intermediate Strain Rate", International Journal of Automotive Technology, Vol.10, No.2, pp.195~204, 2009.
- [12] Y. K. Ko, J. S. Lee, H. Huh, H. K. Kim and S. H. Park, "Prediction of Fracture in Hub-hole Expanding Process Using a New Ductile Fracture Criterion", J. Mater. Proc. Tech. Vol.187-188, pp.358~362, 2007.

Fracture Studies Combining Photoelasticity and Coherent Gradient Sensing for Stress Determination

Sharlotte Kramer*

California Institute of Technology, Division of Engineering and Applied Science,
1200 E. California Blvd., Pasadena, CA 91125, slbkramer@gmail.com

*Present Address: University of Illinois at Urbana-Champaign, 405 N. Mathews Ave., Urbana, IL 61801,
sbkramer@illinois.edu

Abstract

An experimental study of in-plane tensorial stress determination from full-field phase-shifting photoelasticity and transmission Coherent Gradient Sensing (CGS) for stress intensity factor estimation is presented. Phase-shifting photoelasticity determines principal stress directions and the difference of principal stresses, while transmission CGS measures the x and y first derivatives of the sum of principal stresses. Combining these two methods for the same field of view allows for principal stress separation and, using the principal stress directions, the full in-plane stress tensor. The present study, which is the first experimental study for full-field tensorial stress determination around sharp cracks in a photoelastic material, applies this hybrid method for millimeter-scale fields of view including Mode I-dominant cracks in Homalite-100, a linear elastic brittle bulk polymer. The cases presented here range in Mode I stress intensity factor from about one-quarter of the fracture toughness to just below the fracture toughness. This experimental method can detect and determine mode-mixity ratios as small as 0.0043 with a range of -0.010 to 0.020 . The experimental stress fields have excellent global agreement with the full-field 2D asymptotic crack solution using the experimentally calculated Mode I and Mode II stress intensity factors.

1 Introduction

Complex loading geometries, particularly for fracture, can require determination of the full-field in-plane stress tensor (i.e., σ_{xx} , σ_{yy} , and σ_{xy}) near stress concentrations for failure characterization. Unfortunately, traditional stress analysis techniques provide only the sum or difference of principal stresses, σ_1 and σ_2 , so several researchers have developed hybrid stress analysis methods that combine either one experimental technique with a theoretical or numerical analysis component or two experimental techniques in order to separate the principal stresses and acquire the full stress tensor [1–10]. Most of these researchers focused on demonstrating their hybrid methods for well-known stress fields, such as the diametrically compressed disk [10], for relatively large fields of view on the order of centimeters. To the author's knowledge, Sakagami et al. [9] performed the only previous study of full-field tensorial stress determination in a cracked material, using thermoelasticity and reflection-photoelasticity applied to a mechanically loaded plate with a small central crack-like slit. This study determined the full-field stresses for an aluminum alloy plate, $450 \text{ mm} \times 80 \text{ mm} \times 6 \text{ mm}$ in dimension, with a central crack-like slit through the thickness, 16 mm in length and 0.2 mm in width. Their field of view was $200 \text{ mm} \times 80 \text{ mm}$ centered around the slit. Although qualitative comparison of their full-field experimental tensorial stress maps to their boundary element method simulation stress maps appears poor, they reported less than 5% error in their K_I calculation as compared to theory. The study by Sakagami et al. does demonstrate the capability for tensorial stress determination using their hybrid method for this situation, but only for a large field of view, for a crack-like slit, and for an opaque isotropic material.

The study presented here demonstrates full-field tensorial stress determination using the hybrid full-field phase-shifting transmission optical method developed by Kramer et al. [8] in photoelastic materials with a crack and for small fields of view around $4.6 \text{ mm} \times 4.6 \text{ mm}$, zoomed in very close around the crack. This study is the first to use a hybrid experimental method for full-field tensorial stress determination around actual *sharp* cracks in photoelastic materials. The hybrid method utilizes phase-shifting photoelasticity for the difference of the principal stresses ($\sigma_1 - \sigma_2$)

and the principal directions, meaning the angle between the Cartesian and principal coordinate systems known as the isoclinic angle, and transmission Coherent Gradient Sensing (CGS), a wavefront shearing interferometry technique, for the spatial first derivatives of the sum of the principal stresses ($\sigma_1 + \sigma_2$). The photoelastic material used here is Homalite-100, a brittle thermosetting polyester, often used as a model material for dynamic linear elastic fracture studies [11–14]. Straight pre-cracks in the Homalite-100 specimens are loaded via a wedge opening load, which simulates Mode I loading. Four different load cases are presented, with calculated K_I values ranging from about one-quarter to just below the fracture toughness, the critical value of K_I for crack propagation, of Homalite-100; a full analysis is provided for the highest K_I case, with the other three cases summarized to demonstrate the capabilities of the hybrid method to demonstrate stress determination for varied load cases. The experimental stress fields exhibit K -dominant stress behavior and show excellent comparison with the 2D asymptotic crack solution for mixed-mode fracture using the calculated K_I and K_{II} values from the experimental σ_{xx} and σ_{yy} . The experimental stresses indicate that the wedge loading is not purely Mode I, but can have a slight Mode II component, with measured mode-mixity K_{II}/K_I ranging from -0.010 to 0.020 , demonstrating that this experimental method is sensitive enough to capture slight mixed-mode fracture. Since these cases are for small fields of view, these experimental stress fields are for the local crack behavior, an important asset in studying small-scale specimens. This study of full-field tensorial stress determination around cracks in a photoelastic material lays a foundation for future research in using this hybrid experimental method for determining fracture criteria in anisotropic materials and for more complex loading geometries.

2 Experimental Method

2.1 Phase-Shifting Photoelasticity

Photoelasticity utilizes the stress-optic effect in certain materials that have a stress-induced birefringence proportional to the difference of the in-plane principal stresses: $n_1 - n_2 = C(\sigma_1 - \sigma_2)$, where C is the relative stress-optic coefficient. A photoelastic plate under stress acts as a linear retarder plate for polarized light with linear retardation δ with a fast axis at angle α relative to the x axis, also known as the isoclinic angle. The governing equation, the Stress-Optic Law, may be written as the following [15, 16]:

$$\sigma_1 - \sigma_2 = \frac{\delta\lambda}{2\pi Ch}, \quad (1)$$

where h is the thickness of the plate, and λ is the wavelength. A circular polariscope used to view the photoelastic effect includes a polarizer with axis at angle ρ , a $\lambda/4$ plate with fast axis at angle ξ , the photoelastic material, another $\lambda/4$ plate with fast axis at angle ϕ , and a final polarizer with axis at angle β as shown in Fig. 1. The six-step method used here has the input polarizer set to $\rho = 0$ and the input $\lambda/4$ plate set to $\xi = \pi/4$, but these input optics may also be set to $\rho = \pi/2$ and $\xi = 3\pi/4$ as done in [8]. With six combinations of the ϕ and β , the six-step method produces two images including only δ and four images including both δ and α , given in Table 1.

Image	Intensity	ϕ	β
I_1	$I_o[1 + \cos(\delta)]$	$\pi/2$	$3\pi/4$
I_2	$I_o[1 - \cos(\delta)]$	$\pi/2$	$\pi/4$
I_3	$I_o[1 - \sin(\delta) \sin(2\alpha)]$	π	π
I_4	$I_o[1 + \sin(\delta) \cos(2\alpha)]$	$\pi/4$	$\pi/4$
I_5	$I_o[1 + \sin(\delta) \sin(2\alpha)]$	$\pi/2$	$\pi/2$
I_6	$I_o[1 - \sin(\delta) \cos(2\alpha)]$	$3\pi/4$	$3\pi/4$

Table 1: Photoelasticity phase shifting for either $\rho = 0$ and $\xi = \pi/4$ or $\rho = \pi/2$ and $\xi = 3\pi/4$ [Angles refer to fast axes of optics]

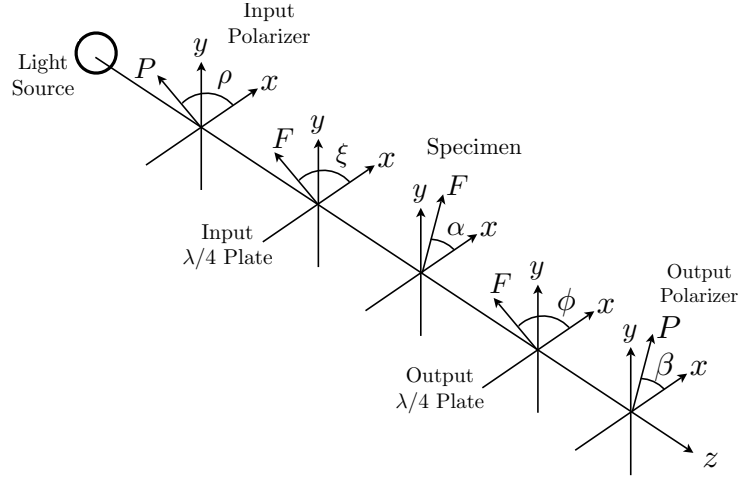


Figure 1: Schematic of circular polariscope with fast axes of optics labeled.

The isoclinic angle emerges from I_3 through I_6 in Eq. (2) with wrapped phase range of $-\pi/4 \leq \alpha < \pi/4$:

$$\alpha = \frac{1}{2} \arctan \left(\frac{I_5 - I_3}{I_4 - I_6} \right) = \frac{1}{2} \arctan \left(\frac{\sin(2\alpha) \sin(\delta)}{\cos(2\alpha) \sin(\delta)} \right), \text{ for } \sin(\delta) \neq 0. \quad (2)$$

This wrapped α is carefully unwrapped to remove the isoclinic ambiguity [17] and to deal with artificial discontinuities in the wrapped data in regions near $\sin(\delta) = 0$, as discussed in detail by Kramer et al. [8, 18]. Some of these artificial discontinuities can be due to a slight rotational misalignment of the polarization optics, particularly of the first $\lambda/4$ plate by error e_1 on the order of $\pm\pi/180$ radians [see [18]]. These artificial discontinuities can be modeled and compared to the experimental and theoretical photoelastic data, as shown in Section 4.2.2. In general for this analysis, the artificial discontinuities in the wrapped α field are removed via interpolation across user-defined regions prior to unwrapping α . The data-quality driven phase unwrapping algorithm, implemented in MATLAB[®], is a weighted preconditioned conjugate gradient (PCG) method developed by Ghiglia and Romero [19]. The weight function \mathbf{W} is a combination of a wrapped data quality weighting presented by Baldi et al. [20] and of zero weight values for physical boundaries like the crack across which data can be discontinuous. The implementation of this algorithm is described in detail in [8, 18, 21]. The isochromatic phase in Eq. (3) uses all six images and the unwrapped isoclinic angle, producing a wrapped phase with range $-\pi \leq \delta < \pi$:

$$\delta = \arctan \left(\frac{(I_5 - I_3) \sin(2\alpha) + (I_4 - I_6) \cos(2\alpha)}{I_1 - I_2} \right). \quad (3)$$

The isochromatic phase is also unwrapped using the PCG algorithm and then converted to a full-field map of $\sigma_1 - \sigma_2$.

2.2 Coherent Gradient Sensing for Photoelastic Materials

CGS is a full-field lateral shearing interferometry technique that may be used in transmission or reflection [22]. The resulting fringe pattern from reflection CGS may be related to in-plane derivatives of displacement, while that from transmission CGS may be related to in-plane derivatives of the sum of principal stresses ($\sigma_1 + \sigma_2$). Fig. 2 is a schematic of the CGS optics. The working principle of transmission CGS is that a plane wave of coherent light passes through a deformed specimen of thickness h , assuming plane stresses, such that the plane wave is slightly perturbed by the Poisson effect thickness change. This perturbed wave is then laterally sheared by passing through pair of Ronchi gratings, G_1 and G_2 , with known pitch p and grating separation $\tilde{\Delta}$. The ± 1 diffraction order is chosen

by filtering. The angle of the first order diffraction, γ , is related to p and λ such that $\gamma = \sin^{-1}(\lambda/p) \approx \lambda/p$ for small γ . The lateral shearing distance is $d_{shear} = \gamma\tilde{\Delta}$. The lateral shearing produces an interference pattern with intensity $I_1 = 2A^{\pm 1}(1 - \cos(\varphi))$, where φ is the phase of the interference pattern and $A^{\pm 1}$ is the amplitude of the ± 1 diffraction order. Assuming linear elasticity and optical isotropy, the interference phase φ is related to the stresses by

$$h\left(D_1 - \frac{\nu}{E}(n_o - 1)\right) \frac{\partial(\sigma_1 + \sigma_2)}{\partial x_i} \approx \left(\frac{p}{2\pi\tilde{\Delta}}\right)\varphi, \quad (4)$$

where D_1 is the absolute stress optic constant for an optically isotropic material, ν is Poissons ratio, E is the elastic modulus, n_o is the refractive index, and subscript i denotes the derivative variable, depending on the Ronchi grating orientation [22, 23]. The sensitivity of transmission CGS, which is $p/\tilde{\Delta}$, may be adjusted by the changing the pitch or separation of the gratings.

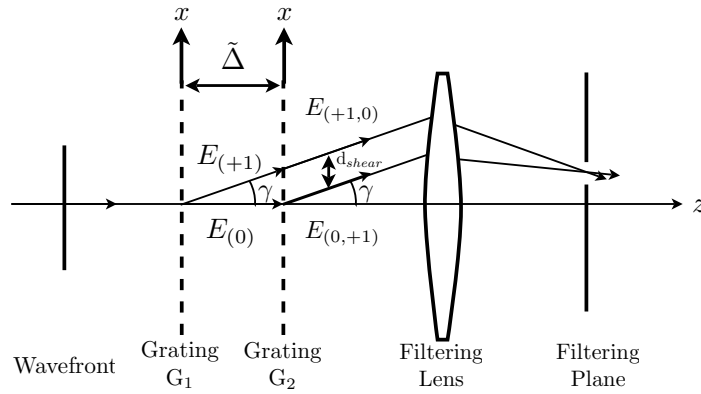


Figure 2: Schematic of horizontal shearing experimental setup for transmission CGS: the +1 diffraction order electric field wavefronts ($E_{(0,+1)}$ and $E_{(+1,0)}$) are selected.

Eq. (4) holds for linear elastic, optically isotropic materials only, so further analysis was developed to extend this to linear elastic, optically anisotropic materials, which is the case here since photoelasticity requires a photoelastic material, which is an optically anisotropic material when stressed. The derivation for the governing equation of transmission CGS for a photoelastic material involves following the electric field through the CGS system, noting that the optical anisotropy in the specimen leads to unequal phase gains along the principal directions. The resulting image I^{image} is a superposition of two interference patterns, which both are functions of the sum and difference of the principal stresses and of α , the isoclinic angle. Given a general electric field incident to the photoelastic material, the phase related to $\sigma_1 + \sigma_2$ cannot be separated from the phase related to $\sigma_1 - \sigma_2$; however, with specific polarization and amplitudes of the incident electric field, these two phases may be separated using phase shifting. A full analysis of transmission wavefront shearing interferometry for photoelastic materials is described by Kramer et al. [21].

If the incident light to the specimen is circularly polarized, then the resulting image has an intensity

$$I^{image} = I_o\{2 + \cos[\varphi_{sum} + \varphi_{diff}] + \cos[\varphi_{sum} - \varphi_{diff}]\}, \quad (5)$$

where I_o is the uniform background intensity, and

$$\varphi_{sum} = \frac{2\pi\tilde{\Delta}D_3h}{p} \frac{\partial(\sigma_1 + \sigma_2)}{\partial x_i} \quad (6a)$$

$$\varphi_{diff} = \frac{2\pi\tilde{\Delta}D_3h}{p} D_4 \frac{\partial(\sigma_1 - \sigma_2)}{\partial x_i}, \quad (6b)$$

where, for plane stress,

$$D_3 = \frac{D_1 + D_2}{2} - \frac{\nu}{E}(n_o - 1) \quad (7a)$$

$$D_4 = \frac{D_1 - D_2}{D_1 + D_2 - 2\nu(n_o - 1)/E}, \quad (7b)$$

and where D_1 and D_2 are the two absolute stress optic coefficients such that $C = D_1 - D_2$. The analysis for an optically isotropic material is equivalent to the analysis for a photoelastic material when $D_1 = D_2$, resulting in $D_4 = 0$, $\varphi_{diff} = 0$, $\varphi_{sum} = \varphi$, and Eq. (6a) for a +1 diffraction order matching Eq. (4), transmission CGS governing equation.

The phase shifting interferometry technique used for CGS is a four-step technique with $\pi/2$ phase steps, induced by a lateral shift of $p/4$ in one Ronchi grating in the direction of the dominant lateral shearing, resulting in four phase shifted interference patterns. For initially circularly polarized light through optically anisotropic materials, the four phase shifted images based on Eq. (5) are

$$I_1 = I_o \{1 + \cos[\varphi_{sum}] \cos[\varphi_{diff}]\} \quad (8a)$$

$$I_2 = I_o \{1 + \cos[\varphi_{sum} + \frac{\pi}{2}] \cos[\varphi_{diff}]\} \quad (8b)$$

$$I_3 = I_o \{1 + \cos[\varphi_{sum} + \pi] \cos[\varphi_{diff}]\} \quad (8c)$$

$$I_4 = I_o \{1 + \cos[\varphi_{sum} + \frac{3\pi}{2}] \cos[\varphi_{diff}]\}. \quad (8d)$$

Using the phase shifted images in Eq. (8) in the standard $\arctan()$ formula for a four-step method, φ_{sum} may be separated from the φ_{diff} :

$$\varphi_{sum} = \arctan \left[\frac{I_4 - I_2}{I_1 - I_3} \right] = \arctan \left[\frac{\sin(\varphi_{sum}) \cos(\varphi_{diff})}{\cos(\varphi_{sum}) \cos(\varphi_{diff})} \right], \text{ for } \cos(\varphi_{diff}) \neq 0. \quad (9)$$

The wrapped φ_{sum} for the vertical and horizontal shearing directions are unwrapped using the PCG algorithm with $h_d = \pi$ since the $\arctan()$ formula with a range of $(-\pi/2, \pi/2]$ must be used. The unwrapped phases are then converted to the first x and y derivatives, in specimen coordinates, of $\sigma_1 + \sigma_2$. These derivatives are numerically integrated by a global minimization algorithm similar to the PCG method described above to give the full-field $\sigma_1 + \sigma_2$ after using a traction free boundary condition (e.g. $\sigma_{\theta\theta} = 0$ at $\theta = \pm\pi$) to determine the constant of integration, as discussed in [8, 18].

As described above, an advantageous polarization choice for this application is circularly polarized light, which may be achieved by several combinations of angles of the input polariscope optics. Since the input photoelasticity optics with the input polarizer at angle 0 and input $\lambda/4$ plate at angle $\pi/4$ leads to circularly polarized light, then the input polariscope optics may remain the same for both the photoelasticity and CGS images.

2.3 Hybrid Experimental Setup

Experimentally, as shown in Fig. 3, CGS and photoelasticity can be employed simultaneously by sending a plane wave of coherent monochromatic light through the input polarizer, the input $\lambda/4$ plate, and the specimen, after which the light is split by a non-polarizing beamsplitter into two identical wavefronts sent along two separate sets of analyzing optics, one for CGS and the other for photoelasticity. Identical imaging optics and CCD cameras are used to capture the same field of view of the specimen for each technique. To avoid issues with slight changes in amplitude due to unequal x and y transmission and reflectance through a non-polarizing beamsplitter, as described in detail in [8, 18], a translating mirror may replace the beamsplitter such that when it is in the beam path, the light is directed along the CGS optics, and when it is translated out of the beam path, the light continues straight through to the photoelasticity optics. This secondary solution requires some short time delay between CGS and photoelasticity imaging, but is acceptable for quasi-static loading conditions. For this paper, the translating mirror

setup is used instead of the non-polarizing beamsplitter to remove possible errors due to the transmission and reflectance coefficients of the beamsplitter. Use of a beamsplitter with well-matched transmission and reflectance coefficients should not change the applicability of this experimental method to fracture studies.

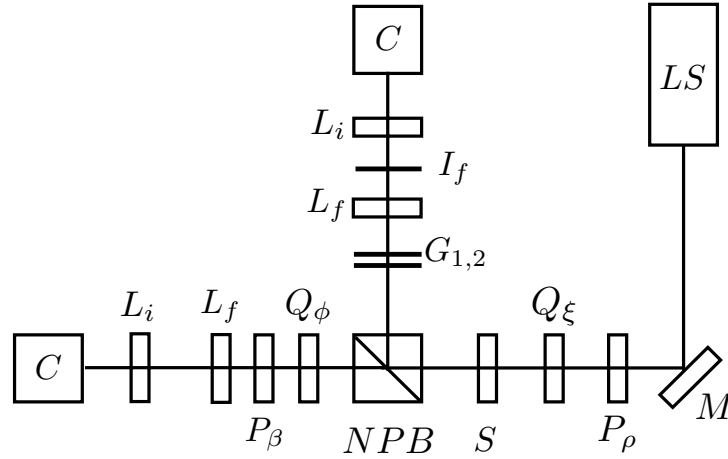


Figure 3: Schematic of the experimental setup: LS =Light Source; M =Mirror; P =Polarizer; $Q=\lambda/4$ plate; S =Specimen; NPB =Non-polarizing beamsplitter or translating mirror; $G_{1,2}$ =Gratings 1&2; L_f =Filtering lens; I_f =Filtering iris diaphragm; L_i =Imaging lens; and C =Camera.

2.4 Mode I-Dominant Wedge Opening Setup

The experimental loading configuration is a symmetric wedge with an angle of $\pi/9$, symmetrically opening a straight notch of length a_1 that is at the tip of a V-shaped notch and that has a sharp crack of length a_2 emanating from the straight notch tip, as shown in Fig. 4(a). The sharp crack is formed in two steps. First, a straight razor blade is pressed into the tip of the straight notch, initiating two sharp, short, crack-like defects, one on each face of the specimen moving partly through the thickness. Second, the loading condition for the experiments is used to gently and slowly open the notch to fill in the crack through-thickness from these two defects as shown in Fig. 4(b); the crack generally propagates and then arrests a few millimeters from the straight notch tip. Fast loading of this notch leads to sudden and complete fracture of the specimen, so modest displacement rates of the wedge around $50 \mu\text{m/s}$ produce cracks that do not propagate the length of the specimen. The specimen is then unloaded before the experimental loads are applied in order to adjust the specimen height such that the crack tip is in the field of view of the optical setup. This precracking method is useful for brittle photoelastic materials such as Homalite-100, but may be less successful in ductile photoelastic materials such as polycarbonate because the defects made by the razor blade do not coalesce, but plastically deform, when wedged open. [Note: In the experimental configuration, the crack is along the vertical optical direction such that the optical coordinate system is the $\pi/2$ rotation of the conventional crack-plane coordinate system. The x and y axes generally refer to the optical coordinate systems, (such as $E_x \hat{i}$ is the optical- x component of the electric field, and vertical shearing CGS is shearing in the optical- y axis), unless the x and y are in direct reference to the derivatives or to the crack. Therefore, CGS vertical shearing corresponds to the specimen x derivative, while horizontal shearing corresponds to the specimen y derivative. Any other possible confusion is clearly denoted as either relative to the optical or specimen coordinate systems.] During experimental loading, the wedge can be slightly misaligned with the x axis of the specimen, and therefore the downward motion of the wedge can impart a slight Mode II load to the crack, evident in slight asymmetry about the crack plane in the stress fields. For these experiments, the theoretical model is a straight crack along the x axis of the specimen with superposed dominant Mode I and slight Mode II loadings. The mode-mixity is characterized by the stress intensity factor ratio $\mu_{SIF} = K_{II}/K_I$.

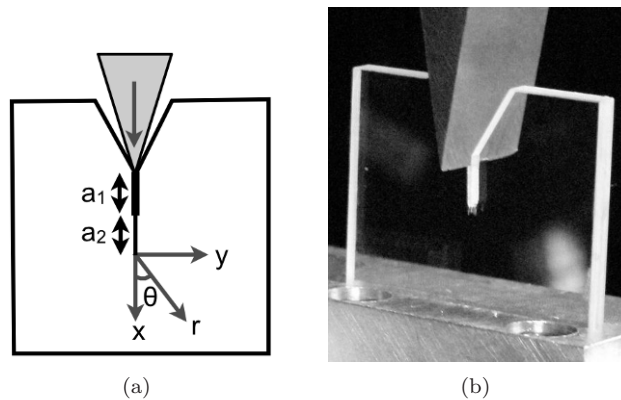


Figure 4: Experimental loading configuration for wedge opening: (a) schematic; and (b) pre-cracking setup prior to growth of the sharp crack of length a_2 from cut notch of length a_1 and razor blade-induced crack-like defects.

3 Analysis Method: Determination of Stress Intensity Factors

Assuming that the loaded crack has both symmetric and antisymmetric stress components and that the stresses are characterized by singular terms with constant stress intensity factors K_I and K_{II} , the stress field is the sum of the Mode I and Mode II stress field components as follows [24]:

$$\sigma_{\alpha\beta} = \frac{K_I}{\sqrt{2\pi r}} f_{\alpha\beta}^I(\theta) - \frac{K_{II}}{\sqrt{2\pi r}} f_{\alpha\beta}^{II}(\theta). \quad (10)$$

The mixed-mode stress intensity factors K_I and K_{II} may be determined from the interference patterns of both photoelasticity and CGS, assuming the field of view contains K -dominant points, i.e., points where the stresses may be characterized by Eq. (10). From inspiration from Smith and Smith [25], Sanford and Dally [26], and Smith and Olaosebikan [27], who used photoelastic interference patterns, and from Mason et al. [28], who used CGS interference patterns, an iterative nonlinear least-squares approach using many points from both photoelastic and CGS phase data has been developed for calculating K_I and K_{II} for mixed-mode fracture.

The approach starts with relationships between the interference phases from both techniques and the variables K_I , K_{II} , r and θ . Using Equations (1) and (10), the photoelastic isochromatic phase for mixed-mode K -dominant fracture is

$$\delta(r, \theta) = \left(\frac{2\pi Ch}{\lambda} \right) \frac{1}{\sqrt{2\pi r}} \sqrt{[K_I \sin(\theta) + 2K_{II} \cos(\theta)]^2 + [K_{II} \sin(\theta)]^2}, \quad (11)$$

and using Equations (6a) and (10), the CGS phases related to the x and y derivatives of the sum of principal stresses for mixed-mode K -dominant fracture, $\varphi_{sum}^{\partial x}$ and $\varphi_{sum}^{\partial y}$, respectively, are

$$\varphi_{sum}^{\partial x}(r, \theta) = \left(\frac{2\pi \tilde{\Delta} D_3 h}{p} \right) \frac{1}{\sqrt{2\pi r^3}} \left[-K_I \cos\left(\frac{3\theta}{2}\right) + K_{II} \sin\left(\frac{3\theta}{2}\right) \right] \quad (12a)$$

$$\varphi_{sum}^{\partial y}(r, \theta) = \left(\frac{2\pi \tilde{\Delta} D_3 h}{p} \right) \frac{1}{\sqrt{2\pi r^3}} \left[-K_I \sin\left(\frac{3\theta}{2}\right) - K_{II} \cos\left(\frac{3\theta}{2}\right) \right]. \quad (12b)$$

The errors at any point i for the three phases are dimensionless so that the errors from different types data are comparable and, therefore, may be used in the same nonlinear least-squares algorithm; the errors are defined as the difference between the experimental phases and their theoretical values, normalized by the range of experimental data of the M points used in the algorithm for that phase:

$$\epsilon_i^\delta = \frac{\left[\delta(r_i, \theta_i) - \left(\frac{2\pi Ch}{\lambda} \right) \frac{1}{\sqrt{2\pi r_i}} \sqrt{[K_I \sin(\theta_i) + 2K_{II} \cos(\theta_i)]^2 + [K_{II} \sin(\theta_i)]^2} \right]}{(\max[\delta] - \min[\delta])} \quad (13a)$$

$$\epsilon_i^{\partial x} = \frac{\left[\varphi_{sum}^{\partial x}(r_i, \theta_i) - \left(\frac{2\pi \tilde{\Delta} D_3 h}{p} \right) \frac{1}{\sqrt{2\pi r_i^3}} \left[-K_I \cos\left(\frac{3\theta_i}{2}\right) + K_{II} \sin\left(\frac{3\theta_i}{2}\right) \right] \right]}{(\max[\varphi_{sum}^{\partial x}] - \min[\varphi_{sum}^{\partial x}])} \quad (13b)$$

$$\epsilon_i^{\partial y} = \frac{\left[\varphi_{sum}^{\partial y}(r_i, \theta_i) - \left(\frac{2\pi \tilde{\Delta} D_3 h}{p} \right) \frac{1}{\sqrt{2\pi r_i^3}} \left[-K_I \sin\left(\frac{3\theta_i}{2}\right) - K_{II} \cos\left(\frac{3\theta_i}{2}\right) \right] \right]}{(\max[\varphi_{sum}^{\partial y}] - \min[\varphi_{sum}^{\partial y}])}, \quad (13c)$$

where the errors for the isochromatic phase and the CGS phases related to the x and y derivatives of $\sigma_1 + \sigma_2$ are denoted ϵ^δ , $\epsilon^{\partial x}$, and $\epsilon^{\partial y}$, respectively. The normalization is done by the range of the experimental data instead of the theoretical data in order to avoid dividing the differences between the experimental and theoretical phases by zero, a situation that could arise during the iterative nonlinear least-squares algorithm, described below, at an iteration where K_I and K_{II} are zero.

Since the experimental phases used in the error calculations come from an unwrapping process that incorporates a data-quality weight functions \mathbf{W} , the errors ϵ_i^δ , $\epsilon_i^{\partial x}$, and $\epsilon_i^{\partial y}$ are multiplied by the appropriate weight functions calculated for the PCG unwrapping algorithm for every point i , such that the higher quality data points receive more weight in the least-squares minimization algorithm. The weight functions for the isochromatic phase and the CGS phases related to the x and y derivatives of $\sigma_1 + \sigma_2$ are denoted W_i^δ , $W_i^{\partial x}$, and $W_i^{\partial y}$, respectively.

The iterative nonlinear least-squares algorithm minimizes the function $f(K_I, K_{II})$, which is a vector function incorporating these error definitions and appropriate weight functions described above, by iteratively choosing K_I and K_{II} values using the trust-region-reflective algorithm based on the interior-reflective Newton method, which is a standard nonlinear least-squares algorithm; this algorithm has been implemented in MATLAB[®]. The function $f(K_I, K_{II})$ and the minimization of the squared L_2 norm is as follows, for M points of δ , N points of $\varphi_{sum}^{\partial x}$, and P points of $\varphi_{sum}^{\partial y}$:

$$\mathbf{f}(K_I, K_{II}) = \left[\frac{1}{\sqrt{2}} W_1^\delta \epsilon_1^\delta, \dots, \frac{1}{\sqrt{2}} W_M^\delta \epsilon_M^\delta, \frac{1}{2} W_1^{\partial x} \epsilon_1^{\partial x}, \dots, \frac{1}{2} W_N^{\partial x} \epsilon_N^{\partial x}, \frac{1}{2} W_1^{\partial y} \epsilon_1^{\partial y}, \dots, \frac{1}{2} W_P^{\partial y} \epsilon_P^{\partial y} \right]^T \quad (14)$$

$$\begin{aligned} \min_{K_I, K_{II}} \left\| \mathbf{f}(K_I, K_{II}) \right\|_2^2 &= \min_{K_I, K_{II}} (f_1^2 + f_2^2 + \dots + f_{M+N+P}^2) \\ &= \min_{K_I, K_{II}} \left(\frac{1}{2} \sum_{i=1}^M (W_i^\delta \epsilon_i^\delta)^2 + \frac{1}{4} \sum_{j=1}^N (W_j^{\partial x} \epsilon_j^{\partial x})^2 + \frac{1}{4} \sum_{k=1}^P (W_k^{\partial y} \epsilon_k^{\partial y})^2 \right). \end{aligned} \quad (15)$$

The constant coefficients in front of the elements of the vector function \mathbf{f} in Eq. (14) and the constants in front of the summation symbols of Eq. (15) are present to equally weight the contributions of the two experimental techniques to the minimization algorithm since photoelasticity gives only one stress-related phase and CGS gives two, i.e., the photoelasticity data set receives twice the weight in the minimization algorithm as each of the CGS data sets.

Another consideration in the determination of K_I and K_{II} is the assumption of plane stress in these specimens; the mixed-mode fracture stress fields in Eq. (10) are only valid for plane stress K-dominant regions. The stresses determined by transmission interference techniques are inherently through-thickness averages of the stresses, so if the specimen is under plane stress, then the measured stresses are constant through the thickness. Since the field of view is small (mm -scale) in the cases presented in this study, a notable portion of the field of view of the interference patterns are subject to 3D (triaxial) stress effects around the crack tip. According to Rosakis et al. [29] and Krishnaswamy et al. [30], who studied 3D effects in elastodynamic crack problems, the extent of the 3D zone has a radius around 0.4 – $0.5h$. Using this as a general guideline for excluding points in the field of view that may be subject to 3D effects, all of the points inside a circle of radius $0.5h$ centered around the crack tip are excluded from the points used in calculating K_I and K_{II} . Additionally, all points that have been excluded by a user-defined mask

in the unwrapping algorithm are also excluded from consideration. In the spirit of having full-field phase maps, all the remaining points not excluded for the three phases in the field of view are used in the nonlinear least-squares minimization algorithm to determine K_I and K_{II} .

4 Results

4.1 Summary of four cases

Experimental results from four different quasi-static wedge loads, with two loads each for two specimens, are summarized here, with a detailed presentation of results for the largest load just below crack propagation. The specimens are made of Homalite-100 with Young's modulus $E = 4.55$ GPa, refractive index $n_o = 1.561$, Poisson's ratio $\nu = 0.31$, and photoelastic constants $D_1 = -9.058 \times 10^{-11}$ m²/N, $D_2 = -1.143 \times 10^{-10}$ m²/N, $D_3 = -1.41 \times 10^{-10}$ m²/N, and $D_4 = -0.0844$ [14, 15]. The monochromatic CCD cameras used are IMPERX model IPX-1M48-L with a 1000×1000 pixel chip. Table 2 gives the specimen geometry and pertinent parameters for the optical setup; the main difference between the two specimens are the thicknesses and the crack length. With these small thicknesses relative to the outer dimensions of the specimens, plane stress is assumed. Ultimately, the measured stresses in these small fields of view indicate local through-thickness average stress information around the crack tip.

Specimen	h (mm)	L (mm)	d_V (mm)	a_1 (mm)	a_2 (mm)	FOV (mm \times mm)	p (mm)	$\tilde{\Delta}$ (mm)	λ (nm)	d_{shear} (μ m)
S1	2.19	25.48	6.25	4.01	4.05	4.60×4.60	1/40	8.87	632.8	225
S2	3.43	25.46	6.25	3.53	8.84	4.57×4.57	1/40	8.84	632.8	224

Table 2: Specimen geometry and parameters for the experimental setup [Note: L is the length of the square specimen, d_V is the depth of the V-notch, and FOV is the field of view imaged onto the camera sensor.]

Table 3 summarizes the calculated stress intensity factors and their ratios for the four loads, which have a range of K_I from 0.145 MPa \sqrt{m} to 0.514 MPa \sqrt{m} . Given the small, but detectable, K_{II} values ranging from -2.9 kPa \sqrt{m} to 5.0 kPa \sqrt{m} , the mode-mixities μ_{SIF} are also small from -0.010 to 0.020 . The static initiation fracture toughness K_{Ic} values for Homalite-100 vary in literature and can vary for the same set of experiments. Bradley and Kobayashi [11] reported fracture toughness values ranging from 0.593 MPa \sqrt{m} to 0.690 MPa \sqrt{m} with an average of 0.636 MPa \sqrt{m} . Irwin et al. [13] and Dally [12] state that Bradley and Kobayashi overestimates the initiation fracture toughness and report a value of only 0.445 MPa \sqrt{m} . The largest calculated K_I value at 0.514 MPa \sqrt{m} in this current study, which did not result in crack propagation, is around the reported fracture toughness values; since the next load increment for specimen S1 resulted in crack propagation, then this calculated K_I value seems reasonable to be close to reported fracture toughness values.

Specimen	K_I (MPa \sqrt{m})	K_{II} (kPa \sqrt{m})	μ_{SIF}
S1	0.259	5.0	0.020
S1	0.514	4.4	0.0085
S2	0.145	0.63	0.0043
S2	0.289	-2.9	-0.010

Table 3: Summary of calculated stress intensity factors and mode-mixities for the four load cases. [Note: the units for K_I and K_{II} are different in magnitude by $\mathcal{O}(10^3)$.]

4.2 Crack with $K_I = 0.514 \text{ MPa}\sqrt{\text{m}}$ and $K_{II} = 4.4 \text{ kPa}\sqrt{\text{m}}$

Fig. 4.2 shows the specimen S1 before loading with the experimental field of view indicated on the specimen. The mm-scale field of view is far from the boundaries of the specimen, so the measured stress fields are free of boundary effects, allowing for the use of the 2D asymptotic crack solution as a model.

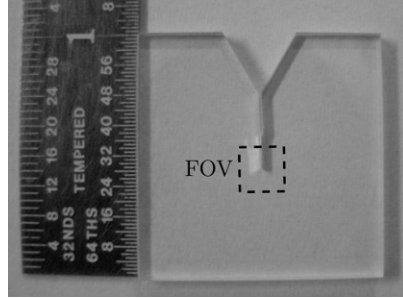


Figure 5: Specimen S1 before loading with field of view (FOV) indicated.

4.2.1 Experimental and Theoretical Phase-Shifted Interference Images

Figures 6 and 7 show the experimental and theoretical six phase-shifted photoelasticity images for specimen S1. The features of the experimental images match remarkably well with the theoretical images, taking into account for the slightly Gaussian behavior of the background intensity field I_o in the experimental images as opposed to the uniform theoretical I_o . The experimental images have high-frequency, low-amplitude Fizeau fringes on top of the underlying photoelastic fringes, which are the interference of the reflected wavefronts from the front and back of the specimen and are not related to photoelasticity. This noise source is minimized using a Wiener filter with window size of $[25 \times 25]$ pixels before processing the data. Additionally, as expected, the high stresses at the crack tip result in caustic shadows in the experimental images; these caustic shadows are not modeled in the theoretical fields. The caustic shadows are present in all of the experimental images for both experimental techniques in the data presented because the imaging method used here is unable to capture the highly divergent light rays at the crack tip.

Figure 8 show the first image, I_1^{image} of Eq. (8), of the set of four phase-shifted images for experimental and theoretical vertical and horizontal shear CGS. Since Homalite-100 has a modest value for D_4 of -0.0844 , which dictates the relative strength of secondary CGS phase φ_{diff} related to $\sigma_1 - \sigma_2$ in Eq. (6b), then φ_{sum} phase dominates the images. For the vertical shear CGS, the experimental and theoretical images have the dominant circular features of φ_{sum} with some slight modulation of the intensity near the crack tip where $\cos(\varphi_{diff})$ is close to zero. The vertical shear experimental images tend to be stretched along the shearing direction as compared to the theoretical images because the experimental phases cannot capture the large changes in the derivatives of stress near the crack tip with a finite shearing distance $d_{shear} = 225 \mu\text{m}$ that is 5% of the field of view. As with the vertical shear, the horizontal shear experimental image compare well with the theoretical image, with slight differences near the crack tip due to the finite shearing distance issue described above. The circularly polarized light result in the expected circular lobes to the side of the crack for the horizontal shear case. The finite shearing distance is visible in the horizontal shear; the crack appears to be doubled in the experimental images. Data points between the crack are not reliable because these arise from interference of light on opposite sides of the crack, and therefore this data is masked in the analysis. Despite this finite shearing distance, the experimental and theoretical images compare well in fringe density, shape, and contrast.

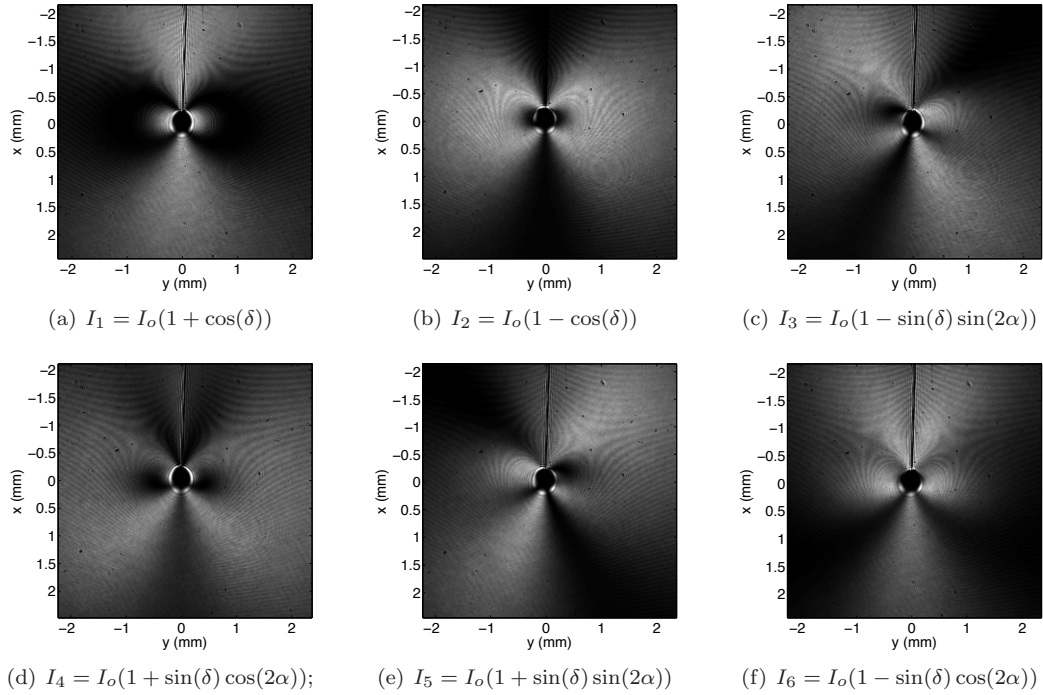


Figure 6: Experimental mages from six-step phase-shifting photoelasticity for specimen S1 for $K_I = 0.514 \text{ MPa}\sqrt{\text{m}}$ and $K_{II} = 4.4 \text{ kPa}\sqrt{\text{m}}$: Caustic shadows obscure the data at the crack tip due to the stress concentration, and the weak high density fringes overlaying the photoelastic fringes are due to the interference of the reflections from the front and back faces of the specimen.

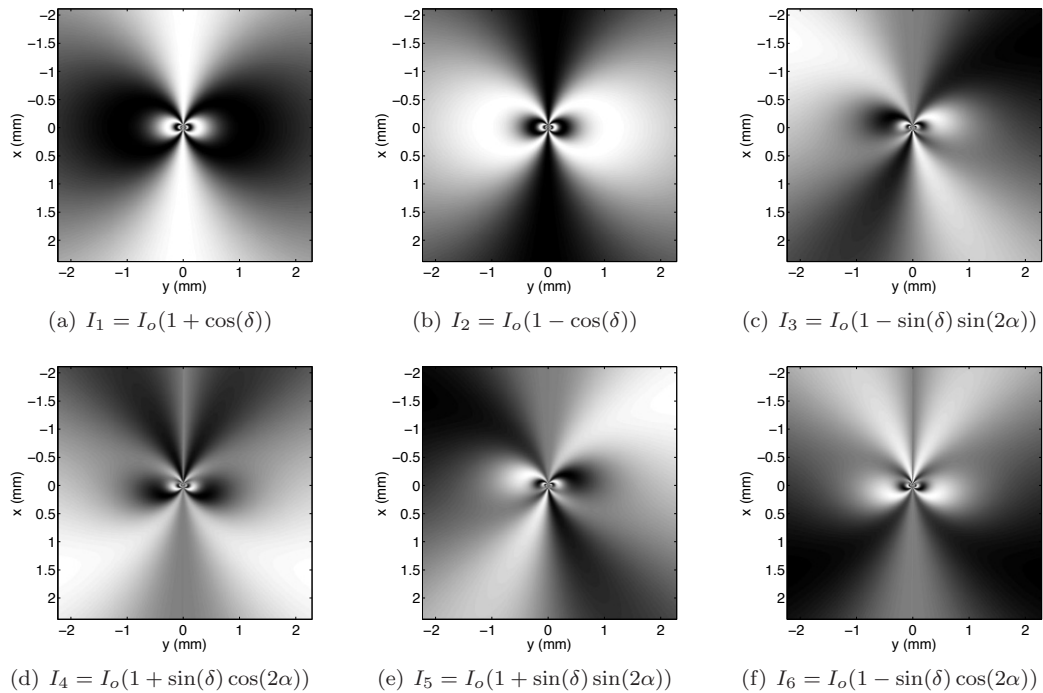


Figure 7: Theoretical mages from six-step phase-shifting photoelasticity for specimen S1 with $K_I = 0.514 \text{ MPa}\sqrt{\text{m}}$ and $K_{II} = 4.4 \text{ kPa}\sqrt{\text{m}}$, where I_o is uniform over the field of view, unlike the experimental images, where the intensity is Gaussian.

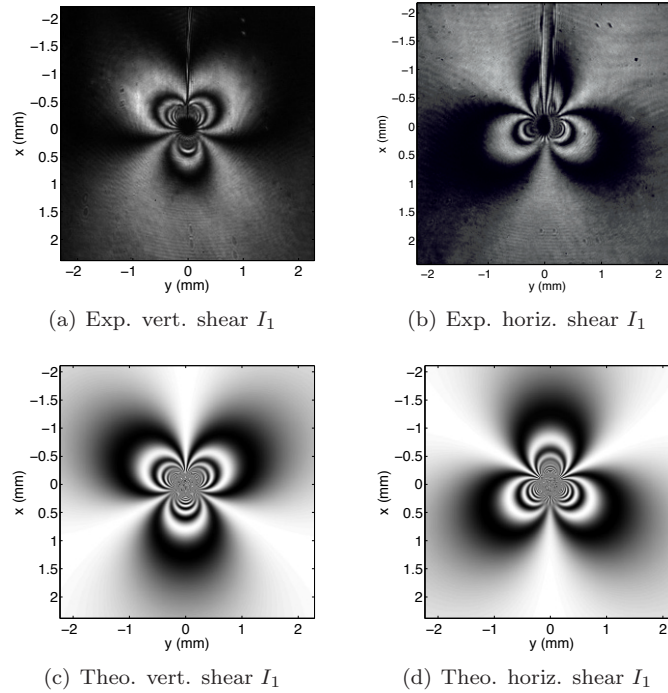


Figure 8: Experimental and theoretical first images I_1^{image} of the vertical and horizontal shearing CGS sets of four phase-shifted images for specimen S1 for $K_I = 0.514 \text{ MPa}\sqrt{\text{m}}$ and $K_{II} = 4.4 \text{ kPa}\sqrt{\text{m}}$.

4.2.2 Photoelastic Data Analysis

Figures 9 and 10 present the isoclinic angle analysis from photoelastic images I_3 through I_6 and the isochromatic phase analysis from all six images. As mentioned in Section 2.1, the rotational alignment of the first $\lambda/4$ plate relative to the first polarizer has a prominent effect on the wrapped isoclinic angle data; figures 9(a) and 9(d) show how the isoclinic angle measurement is sensitive to the misalignment of the first $\lambda/4$ plate, resulting in false discontinuities and regions that incorrectly sweep through zero. These features, which are near regions where $\sin(\delta) = 0$, are not apparent in the theoretical wrapped isoclinic angle from well-aligned optics in Fig. 9(e). The theoretical field in Fig. 9(d) incorporates a small misalignment in the first $\lambda/4$ plate of $\pi/180$ from the ideal position of $\xi = \pi/4$, resulting in similar error features as the experimental field in Fig. 9(a). The false discontinuities and regions that incorrectly sweep through zero are corrected manually, focusing on regions near $\sin(\delta) = 0$. The ambiguous wrapped isochromatic phase generated from the wrapped isoclinic angle, given in Fig. 9(c), informs the user-defined regions for correction, as described in [18]. All of these manual changes of the wrapped isoclinic angle are guided by some basic *a priori* knowledge of the general trend of α , keeping in mind that α does not often have large gradients, though the 2D asymptotic crack problem is unusual with a large gradient across the crack plane. The crack problem is ideally radially symmetric, so the phase discontinuities should be radial in nature. The corrected wrapped α in Fig. 9(b) is close to this expectation, with slightly more variance from radial symmetry near the interpolated regions near the crack tip. The corrected wrapped α in Fig. 9(b) unwraps well, as shown in comparing the experimental and theoretical values in Figures 10(a) and 10(d) with the largest errors near regions where $\sin(\delta) = 0$.

Fig. 10 also shows the experimental and theoretical wrapped and unwrapped isochromatic phase with excellent agreement globally. Both experimental and theoretical fields are slightly rotated in the $-\theta$ direction due to the slight Mode II component, have similar lobe shapes, and have similar locations for the 2π phase discontinuities in the wrapped phase. Due to the slight error in the isoclinic angle near $\theta = 0$, the experimental field does not reach to the low values close to zero as the theoretical field does in this region, but the general trend of smaller phase values does hold.

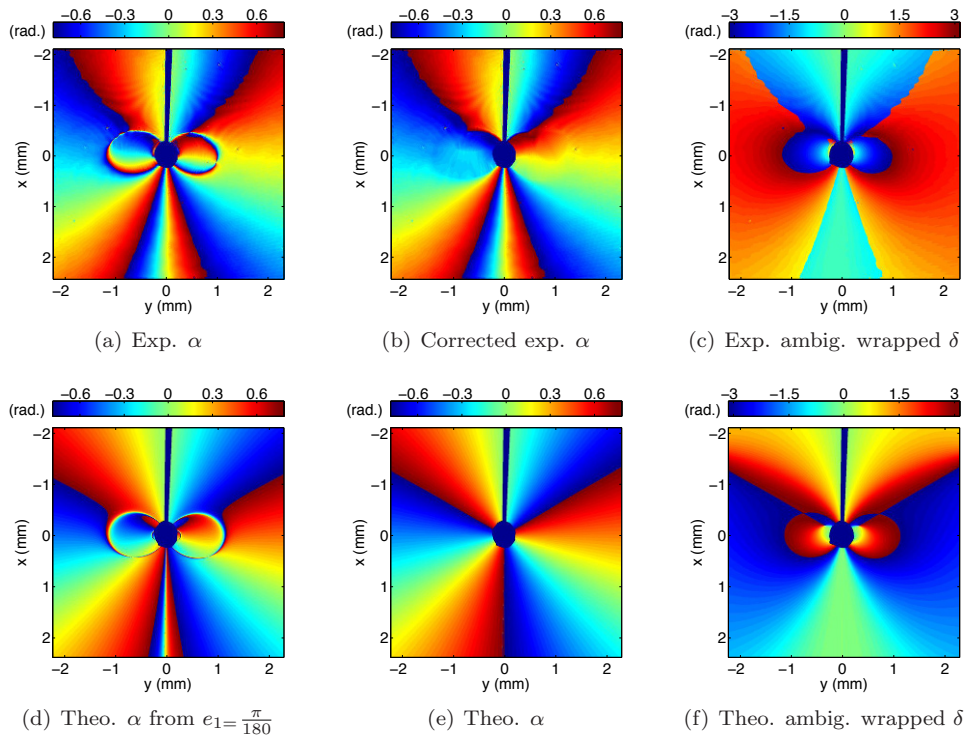


Figure 9: Experimental and theoretical data for the wrapped isoclinic angle for specimen HomC1 for $K_I = 0.514 \text{ MPa}\sqrt{\text{m}}$ and $K_{II} = 4.4 \text{ kPa}\sqrt{\text{m}}$ with crack region masked in blue.

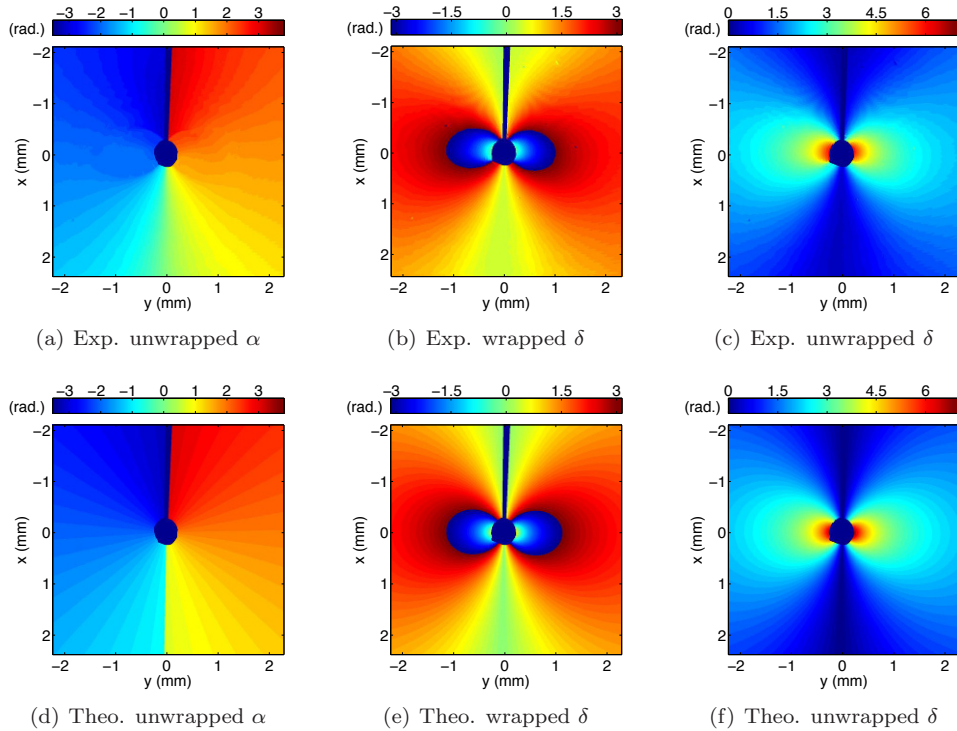


Figure 10: Experimental and theoretical α and δ with crack region masked blue.

4.2.3 CGS Data Analysis

Fig. 11 shows the experimental and theoretical wrapped and unwrapped vertical shearing CGS data from the circularly polarized electric field input and the theoretical $\cos(\varphi_{diff})$ field that modulates the interference pattern, as explained in Section 2.2. The experimental and theoretical wrapped φ_{sum} from the circularly polarized electric field input data in Figures 11(a) and 11(c) have similar fringe density and shape, though the lobes behind the crack tip of the experimental data are slightly larger than the theoretical. The experimental fringes have slight errors in a four-leaf clover pattern around the crack tip near where $\cos(\varphi_{diff})$ is close to zero. As expected, data near $\cos(\varphi_{diff}) = 0$ is prone to higher error since the $\arctan()$ function for φ_{sum} in Eq. (9) is indeterminate at $\cos(\varphi_{diff}) = 0$. Since Homalite-100 has a small value for the photoelasticity-related constant $g = -0.0844$, which is related to the magnitude of φ_{diff} as defined in Section 2.2, the effect of the φ_{diff} phase is generally confined to very close to the crack tip even for this case with significant K_I loading; many of these errors are masked by the user-defined crack tip mask, and therefore do not have large influence on the data. Since the $\cos(\varphi_{diff})$ field is fairly uniform, the φ_{sum} has few unwrapping errors and is thus a good measure for the derivative of stress. The unwrapped phase in Fig. 11(b) is able to capture the theoretical change in phase globally except that the negative phase lobes are slightly further back from the crack tip than in the theoretical fields. The experimental and theoretical wrapped and unwrapped φ_{sum} data for the horizontal shearing direction in Fig. 12 compare well but with smaller lobes along the crack in the experimental data. The φ_{sum} field nearly matches the theoretical phase in Fig. 12(d), except on either side of the crack where the phase is rather large theoretically. Since $\cos(\varphi_{diff})$ for the horizontal shearing direction is only close to zero just in front of the crack, and the wrapped phase is easily masked there to reduce unwrapping errors, the φ_{sum} data has good comparison to the theoretical phase.

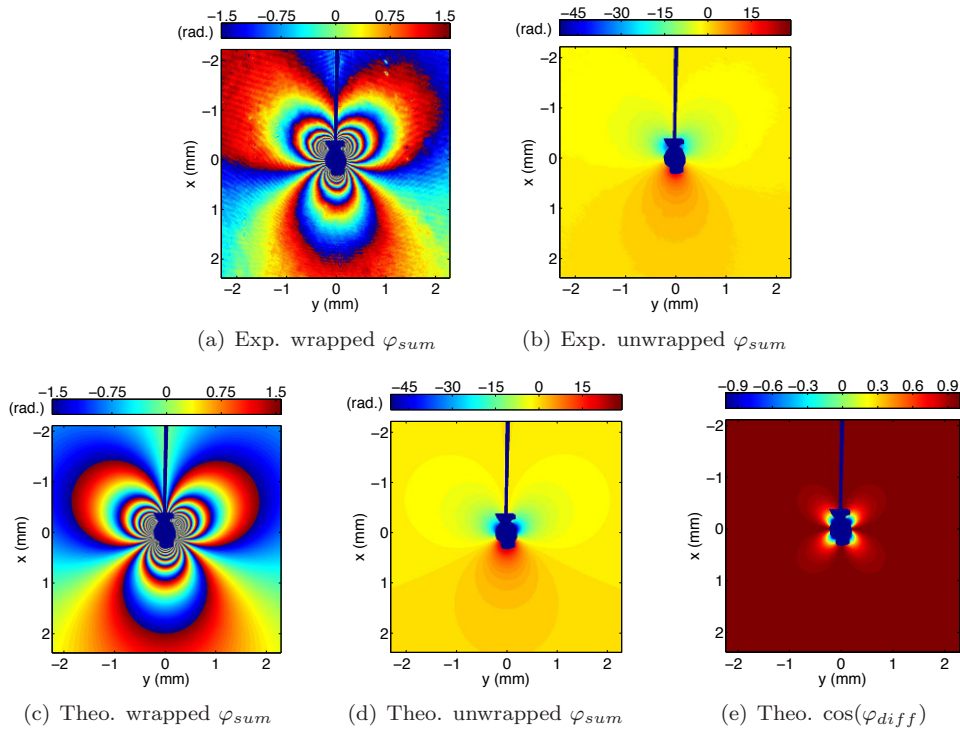


Figure 11: Experimental and theoretical φ_{sum} data for vertical CGS for specimen S1 for $K_I = 0.514 \text{ MPa}\sqrt{\text{m}}$ and $K_{II} = 4.4 \text{ kPa}\sqrt{\text{m}}$ with crack region masked in blue.

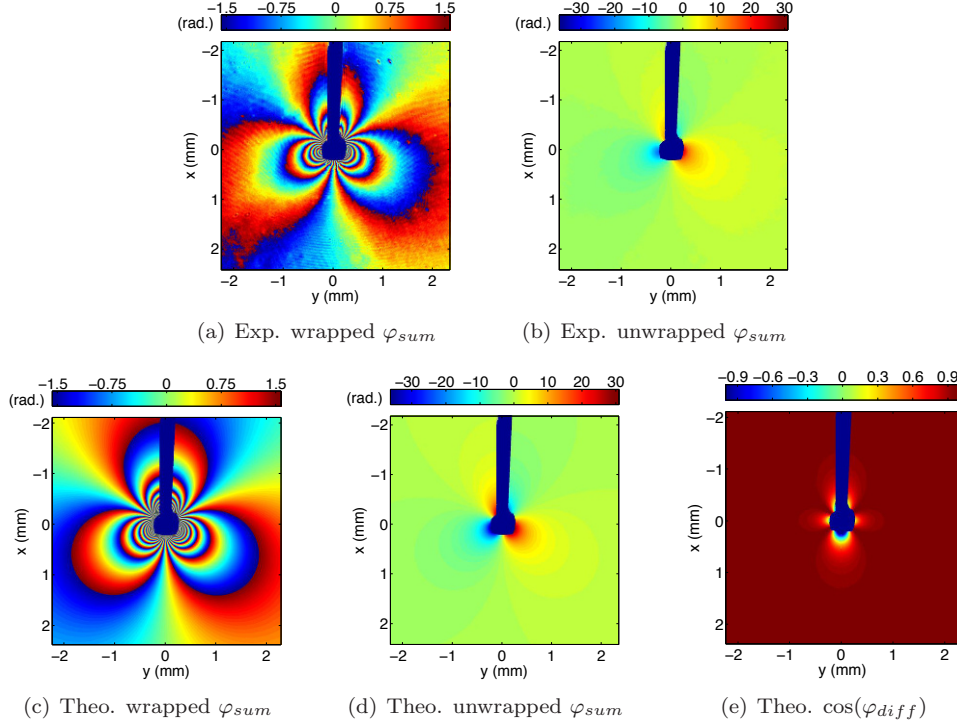


Figure 12: Experimental and theoretical data for horizontal CGS for specimen S1 for $K_I = 0.514 \text{ MPa}\sqrt{\text{m}}$ and $K_{II} = 4.4 \text{ kPa}\sqrt{\text{m}}$ with crack region masked in blue.

The initial assumption for using CGS to determine derivatives of the principal stress sum is that the shearing distance is small enough to approximate a finite difference as a first derivative. Bruck and Rosakis [31, 32] considered the accuracy of this assumption for CGS in fracture mechanics applications. They calculated the error of this assumption for a K_I -dominant field for both shearing directions around a loaded crack, using the following expression for the x direction (with an equivalent expression for the y direction shear):

$$\epsilon^{CGS} = 1 - \frac{\frac{\partial(\sigma_1(x, y) + \sigma_2(x, y))}{\partial x}}{\left[\frac{(\sigma_1(x + \frac{d_{shear}}{2}, y) + \sigma_2(x + \frac{d_{shear}}{2}, y) - \sigma_1(x - \frac{d_{shear}}{2}, y) - \sigma_2(x - \frac{d_{shear}}{2}, y))}{d_{shear}} \right]}. \quad (16)$$

If the loading condition only has a K_I component, as was the only case considered by Bruck and Rosakis [31, 32], then the error field plots for the vertical and horizontal shearing directions for the $4.6 \text{ mm} \times 4.6 \text{ mm}$ field of view and lateral shearing distance of $d_{shear} = 225 \text{ }\mu\text{m}$ are given in Figures 13(a) and 13(b). These plots indicate regions with error less than 1%, 1%–5%, and greater than 5%, showing symmetry across the crack plane. The regions with greater than 5% error are concentrated around the crack. Since these plots only include a K_I component, then the value of K_I does not affect the error calculation in Eq. (16), which is only affected by d_{shear} and the field of view; therefore, these plots hold for any K_I -dominant field with pure K_I loading for this field of view.

Given mixed-mode loading conditions, the actual values of K_I and K_{II} do play a role in the error calculated with Eq. (16). For this case where $K_I = 0.514 \text{ MPa}\sqrt{\text{m}}$ and $K_{II} = 4.4 \text{ kPa}\sqrt{\text{m}}$, the error plots for both shearing directions in Figures 13(c) and 13(d) show different behavior than for the K_I -only error plots, where the symmetry across the crack plane is lost, the error in the horizontal shearing direction is very similar to the K_I -only case, and the error in the vertical shearing direction is larger behind the crack with more area with greater than 1% error. These plots indicate why the experimental vertical shearing data appears to be different than the theoretical data behind the crack in Fig. 11. This error analysis shows the potential regions of higher error in the $\sigma_1 + \sigma_2$, such as behind the crack and close to the crack tip, which may give rise to higher error in the separated stresses in those regions.

Fortunately, [Figures 13\(c\)](#) and [13\(d\)](#) indicates that the majority of the field should have less than 5% error (indicated by the light gray and dark gray regions in print and by the yellow and green regions online), so the CGS data may confidently be used to determine the derivative of stress in a global sense.

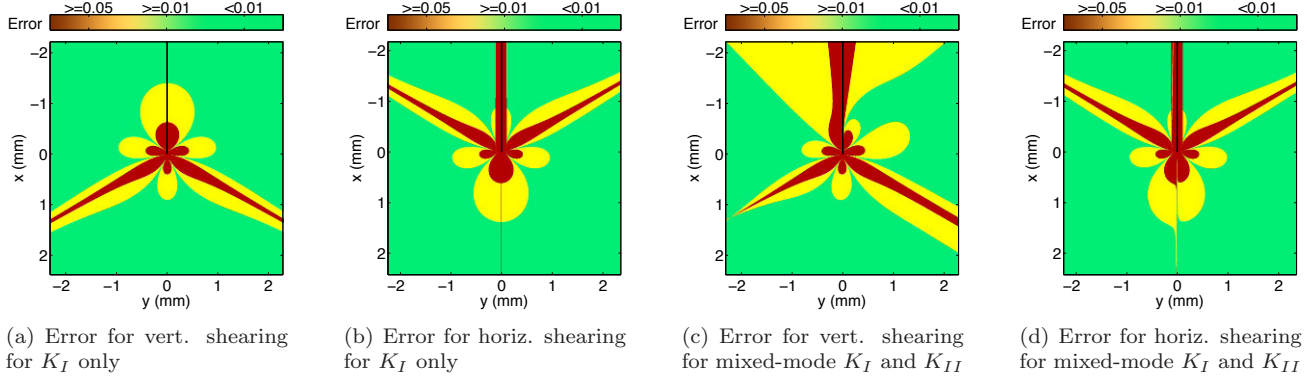


Figure 13: Theoretical error for CGS approximating the derivatives of $\sigma_1 + \sigma_2$, assuming K_I loading only or assuming $K_I = 0.514 \text{ MPa}\sqrt{\text{m}}$ and $K_{II} = 4.4 \text{ kPa}\sqrt{\text{m}}$, for the $4.6 \text{ mm} \times 4.6 \text{ mm}$ field of view and lateral shearing distance of $d_{shear} = 225 \text{ }\mu\text{m}$ [crack indicated in black].

4.2.4 Stress Field Determination

[Fig. 14](#) shows the experimental and theoretical sum and difference of principal stress fields. The $\sigma_1 - \sigma_2$ field is calculated from δ using the Stress-Optic Law in Eq. (1); the experimental $\sigma_1 - \sigma_2$ compares to the theoretical field with the double lobes about the x axis. For the analysis of $\sigma_1 + \sigma_2$, the constant of integration c_i is determined from the boundary condition of $\sigma_{\theta\theta} = 0$ along $\theta = \pm\pi$, which requires α , $\sigma_1 - \sigma_2$, and $\sigma_1 + \sigma_2 + c_i$ to calculate. In this case, due to the horizontal spreading of the crack region of the horizontal shearing direction data, the actual location of the crack is under the mask. Therefore a pixel very close to the crack just to the side of the masked region, is chosen as the the location to apply the boundary condition. Here $\sigma_{\theta\theta}$ is taken to be zero at $(r, \theta) = (2.06 \text{ mm}, -3.08 \text{ rad.})$. The experimental $\sigma_1 + \sigma_2$ in [Fig. 14\(b\)](#) matches the rounded fan-like shape originating about the crack tip as in the theoretical field. From the experimental $\sigma_1 + \sigma_2$ and $\sigma_1 - \sigma_2$, full-field σ_1 and σ_2 can be calculated. From the isoclinic angle and the separated principal stresses, the Cartesian stresses in [Fig. 15](#) are determined. Though the experimental Cartesian stresses have some slight differences from the theoretical fields near the crack tip, due to the error in the isoclinic angle, the experimental fields have similar shape and values as the theoretical. Unfortunately, the small local errors in α propagate through the analysis to the stress fields, as seen in the differences in the experimental and theoretical stress fields near $\theta = 0$. These errors propagated from the isoclinic angle demonstrate that the current analysis of the wrapped α field is not perfect, but the generally good comparison of the stress fields demonstrates that the isoclinic angle analysis does enable the experiment to yield reasonable data. These Cartesian stresses, though with some local error, do demonstrate good global agreement with theory, showing the slight asymmetry of the stresses about the x axis due to the small K_{II} loading component. The excellent global agreement of the experimental and theoretical fields can be quantified, as seen in [Table 4](#), which reports the root mean squared deviation (RMSD) and the normalized RMSD. The low NRMSD values range from 0.019 to 0.049. The lower errors are generally for the fields directly related to the experimental phases such as the derivatives of $\sigma_1 + \sigma_2$, α , and $\sigma_1 - \sigma_2$, with the higher errors in stress fields from combining different fields, like the Cartesian and polar stresses. These higher errors are due to accumulation of errors locally around the crack tip and along the x axis.

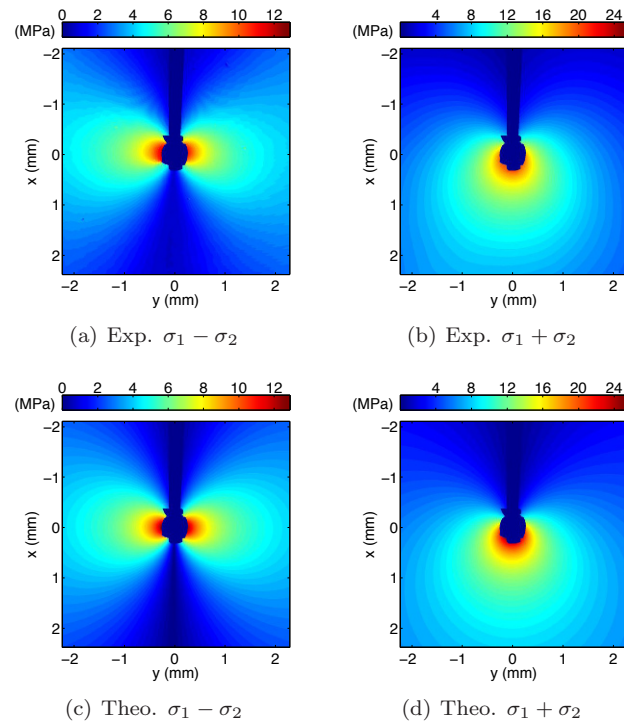


Figure 14: Experimental and theoretical data for $\sigma_1 - \sigma_2$ and $\sigma_1 + \sigma_2$ for specimen S1 for $K_I = 0.514 \text{ MPa}\sqrt{\text{m}}$ and $K_{II} = 4.4 \text{ kPa}\sqrt{\text{m}}$ with crack region masked in blue.

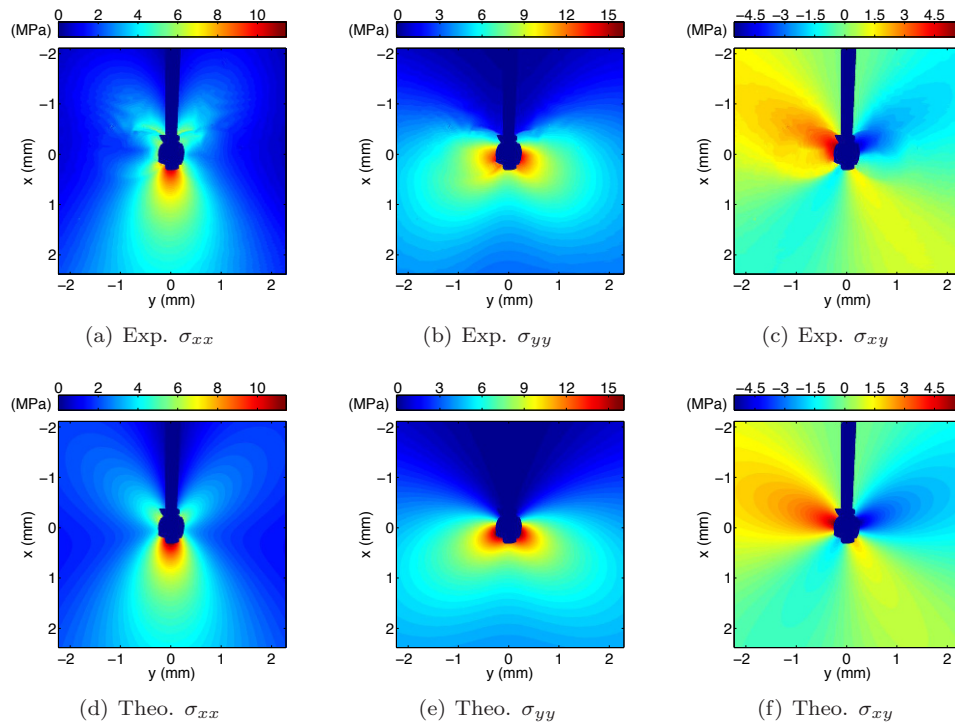


Figure 15: Experimental and theoretical data for the Cartesian stresses for specimen S1 for $K_I = 0.514 \text{ MPa}\sqrt{\text{m}}$ and $K_{II} = 4.4 \text{ kPa}\sqrt{\text{m}}$ with crack region masked in blue.

Quantity	Units	RMSD (in Units)	Data Range (in Units)	NRMSD (No Units)
α	rad.	0.17	7.33	0.023
$\partial(\sigma_1 + \sigma_2)/\partial x$	MPa/mm	1.47	80.8	0.019
$\partial(\sigma_1 + \sigma_2)/\partial y$	MPa/mm	1.33	64.2	0.021
$\sigma_1 + \sigma_2$	MPa	0.60	20.1	0.030
$\sigma_1 - \sigma_2$	MPa	0.25	12.3	0.020
σ_1	MPa	0.36	15.4	0.023
σ_2	MPa	0.29	10.4	0.028
σ_{xx}	MPa	0.48	10.5	0.046
σ_{yy}	MPa	0.62	14.4	0.043
σ_{xy}	MPa	0.30	10.7	0.028
σ_{rr}	MPa	0.42	14.1	0.030
$\sigma_{\theta\theta}$	MPa	0.44	11.8	0.037
$\sigma_{r\theta}$	MPa	0.44	9.0	0.049

Table 4: Error analysis for various experimental fields for specimen S1 for $K_I = 0.514 \text{ MPa}\sqrt{\text{m}}$ and $K_{II} = 4.4 \text{ kPa}\sqrt{\text{m}}$.

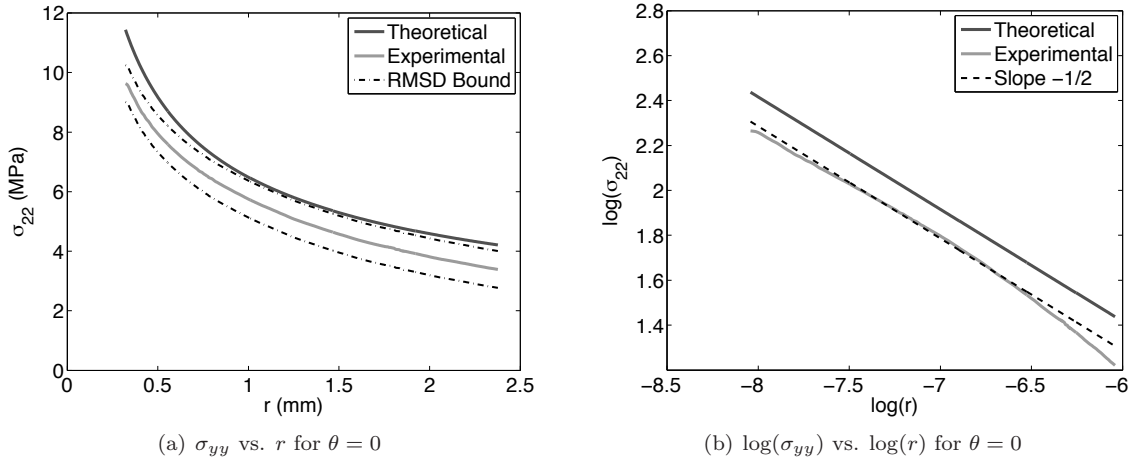


Figure 16: Experimental and theoretical data for σ_{yy} along $\theta = 0$ for specimen S1 for $K_I = 0.514 \text{ MPa}\sqrt{\text{m}}$ and $K_{II} = 4.4 \text{ kPa}\sqrt{\text{m}}$: The experimental data is slightly lower than the theoretical data, but with similar $r^{-1/2}$ dependence seen by the near $-1/2$ slope on the log-log plot of σ_{yy} versus r .

A measure of the comparison of the experimental data with the theoretical fracture model is to consider σ_{yy} behavior versus r along the crack plane, since $\sigma_{yy} = K_I/(2\pi r)$ for $\theta = 0$. Fig. 16 shows the experimental and theoretical σ_{yy} versus r plot and the $\log(\sigma_{yy})$ versus $\log(r)$ plot for $\theta = 0$. The experimental σ_{yy} is slightly smaller than the theoretical, implying a smaller K_I value of $0.442 \text{ MPa}\sqrt{\text{m}}$ on average, but this is most likely due to the small errors in the isoclinic angle near $\theta = 0$. The theoretical values fall around the upper error bar, which is $\sigma_{yy} + \text{RMSD}_{\sigma_{yy}}$, showing that this difference along $\theta = 0$ is around the global difference. Despite the smaller absolute values, the experimental σ_{yy} has the correct $r^{-1/2}$ behavior, evident in the nearly uniform $-1/2$ slope of the experimental $\log(\sigma_{yy})$ versus $\log(r)$ plot in Fig. 16(b). This $-1/2$ slope also implies that most of the field of view, excluding the masked regions, is in a K_I -dominant region [24].

5 Discussion

The four Mode I–dominant, mixed-mode crack cases presented above demonstrate the ability of the hybrid experimental method to determine the in-plane tensorial stress around a crack in a photoelastic material. The different cases represent a significant range of K_I values for Homalite-100, whose fracture toughness is around $0.445 \text{ MPa}\sqrt{\text{m}}$ to $0.636 \text{ MPa}\sqrt{\text{m}}$ [11–13]: $K_I = 0.145 \text{ MPa}\sqrt{\text{m}}$, $K_I = 0.259 \text{ MPa}\sqrt{\text{m}}$, $K_I = 0.289 \text{ MPa}\sqrt{\text{m}}$, and $K_I = 0.514 \text{ MPa}\sqrt{\text{m}}$, which are from about $0.25K_{Ic}$ to $\sim K_{Ic}$. Each of these cases demonstrate K -dominant stress behavior, allowing for excellent comparison to the 2D asymptotic crack solution for a mixed-mode crack. The full analysis of the highest K_I case establishes the validity of the experimental method to determine stress near a crack close to initial crack propagation, while analysis of the smallest K_I case demonstrates stress determination for loads closer to that of high-cycle fatigue. The other two cases listed in the case summary in Table 3 demonstrate the moderate K -dominant loading of the two cracked specimens. The K dominance allows for calculation of the Mode I and Mode II stress intensity factors from a nonlinear least-squares fitting algorithm, excluding data points in the masked regions along the crack and a circle of radius $0.5h$ around the crack tip to remove points that may have 3D stress effects. Even though the K_I and K_{II} values come from full-field data from two different experimental techniques, these values lead to theoretical data that compare well with all of the experimental data, implying that CGS and photoelasticity are compatible for use in this hybrid method. If the K_I and K_{II} values only allowed for good agreement in a few fields, then the experimental method would be suspect. Across all of these cases, the NRMSD ranges from 0.012 to 0.078 with most of the fields below 0.05, indicating excellent global error for all of these cases. This experimental method also allows for determination of not only K_I values, but small K_{II} values as well, and therefore is able to detect small mode-mixity μ_{SIF} from -0.010 to 0.020 . These small mode-mixities have a noticeable affect on the stress fields, giving rise to asymmetries in the stress fields that are apparent in the experimental data. Exclusion of K_{II} would lead to larger errors in the data by a few percent.

The four cases illuminate consistent error sources in the data. The rotational misalignment of the polarization optics, particularly the first $\lambda/4$ plate, lead to false discontinuities and zero-crossings that require manual correction. These corrections generally work, allowing for the determination of the isoclinic angle without detrimental and completely incorrect unwrapping. The isoclinic angle is a key component to the experimental method, so the manual corrections to the wrapped α field enable the method to work even with some localized errors in the subsequent stress fields. Obviously, a robust algorithm for correcting these errors due to polarization optic misalignment would improve confidence in the method, especially for fracture studies where the theoretical stress field solution is not known. In the cases presented here, the experimental isoclinic angle has error along the crack plane because the polarization optic misalignment leads to discontinuities near $\theta = 0$ that appear to be real discontinuities. Corrections here would not be simple and would require a variety of experiences with this method; hence, leaving the discontinuities as they are leads to α fields with known error sources, but with acceptable error levels. One way to reduce this need for corrections in the first place is to introduce strict polarization optic alignment techniques. Another error source in the data is the Fizeau fringes, but these are easily removed with anti-reflective coatings on the specimen.

The CGS assumption that the phase is related to a stress derivative is pushed to its limit due to three factors in this study: the small field of view, the finite shearing distance, and small mode-mixity. The first two factors work together to push the limit of the derivative assumption in that having a small field of view and requiring a reasonable phase sensitivity over a wide range of K_I cases requires a shearing distance that is a significant size relative to the field of view like the 5% of the side of the field of view in the cases presented above. Evident in the ϵ^{CGS} error analysis in Section 4.2.3, larger shearing distance produces more error in the derivative assumption over more area of the field of view. Also, the addition of a small K_{II} component appears to increase the ϵ^{CGS} error, particularly behind the crack for the shearing direction related to the x derivative, as the mode-mixity increases for the range of mode-mixity. The effect of this on the stress fields is higher error behind the crack, seen with increasing severity with increasing mode-mixity. A full error analysis of the effect of mode-mixity on CGS derivative measurements is required if this method is applied to mixed-mode fracture cases. Characterization of these error sources explains the differences between experiment and theory in the cases presented here, but should not detract from the overall ability of this experimental method to determine full-field stresses around cracks in a photoelastic material. The experimental data have remarkable agreement with theory and allow for calculation of a range of stress intensity factors for Mode I–dominant cracks.

6 Conclusion

The hybrid CGS-photoelasticity experimental method is demonstrated for in-plane tensorial stress determination around Mode I-dominant cracks in Homalite-100 for a range of stress intensity factors for small fields of view, the first experimental study for full-field tensorial stress determination around cracks in photoelastic materials. Four cases across a range of $K_I = 0.145 \text{ MPa}\sqrt{\text{m}}$ to $K_I = 0.514 \text{ MPa}\sqrt{\text{m}}$, which is near the fracture toughness of Homalite-100, show K -dominant behavior, allowing for excellent comparison of the experimental stress fields with the 2D asymptotic crack solution for mixed-mode loading; the global error is less than 5% for most fields and no greater than 7.8%. The experimental method allows for calculation of K_I and small K_{II} values based on experimental data derived from both CGS and photoelasticity, showing that the two techniques work well together for stress determination and that this hybrid method is sensitive enough to detect small stress intensity factors. Common error sources have been characterized and can be mitigated with careful experimentation and with improved analysis algorithms. Overall, this study demonstrates the goal of applying a hybrid experimental method for full-field in-plane tensorial stress determination suitable for fracture studies in photoelastic materials with the ability to view local stresses around a crack for small (mm-scale) fields of view for small specimens, laying a foundation for using this method for stress determination around a crack in more complicated loading conditions.

Acknowledgements

I gratefully acknowledge the support of the National Science Foundation (DMR # 0520565) through the Center for Science and Engineering of Materials (CSEM) at the California Institute of Technology, of the American Society for Engineering Education National Defense Science and Engineering Graduate (NDSEG) Fellowship Program, and of the National Science Foundation Graduate Research Fellowship Program. I also thank Professors G. Ravichandran and K. Bhattacharya of the California Institute of Technology for their advisement during this project.

References

- [1] S. Barone and E. A. Patterson. Full-field separation of principal stresses by combined thermo- and photoelasticity. *Exp. Mech.*, 36(4):318–324, 1996.
- [2] S. Barone and E. A. Patterson. Polymer coating as a strain witness in thermoelasticity. *J. Strain Anal. Eng.*, 33(3):223–232, 1998.
- [3] D. Berghaus. Combining photoelasticity and finite-element methods for stress analysis using least squares. *Exp. Mech.*, 31(1):36–41, 1991.
- [4] R. J. Greene, A. B. Clarke, S. Turner, and E. A. Patterson. Some applications of combined thermoelastic-photoelastic stress analysis. *J. Strain Anal. Eng.*, 42:173–182, 2007.
- [5] S. J. Haake, E. A. Patterson, and Z. F. Wang. 2D and 3D separation of stresses using automated photoelasticity. *Exp. Mech.*, 36(3):269–276, 1996.
- [6] Y. M. Huang, H. H. Abdel Mohsen, and R. E. Rowlands. Determination of individual stresses thermoelastically. *Exp. Mech.*, 30(1):88–94, 1990.
- [7] Y. M. Huang, R. E. Rowlands, and J. R. Lesniak. Simultaneous stress separation, smoothing of measured thermoelastic isopachic information and enhanced boundary data. *Exp. Mech.*, 30(4):398–403, 1990.
- [8] S. L. B. Kramer, M. Mello, G. Ravichandran, and K. Bhattacharya. Phase shifting full-field interferometric methods for determination of in-plane tensorial stress. *Exp. Mech.*, 49(2):303–315, 2009.
- [9] T. Sakagami, S. Kubo, Y. Fujinami, and Y. Kojima. Experimental stress separation technique using thermoelasticity and photoelasticity and its application to fracture mechanics. *JSME Int. J. A*, 17(3):298–304, 2004.

- [10] S. Yoneyama, Y. Morimoto, and M. Kawamura. Two-dimensional stress separation using phase-stepping interferometric photoelasticity. *Meas. Sci. Tech.*, 16:1329–1334, 2005.
- [11] W. B. Bradley and A. S. Kobayashi. Fracture dynamics—a photoelastic investigation. *Engr. Fracture Mech.*, 3(3):317–332, 1971.
- [12] J. W. Dally. Dynamic photo-elastic studies of fracture. *Exp. Mech.*, 19(10):349–361, 1979.
- [13] G. R. Irwin, J. W. Dally, T. Kobayashi, W. L. Fourney, M. J. Etheridge, and H. P. Rossmannith. Determination of the A-K relationship for birefringent polymers. *Exp. Mech.*, 19(4):121–128, 1979.
- [14] K. RaviChandar. *An experimental investigation into the mechanics of dynamic fracture*. PhD thesis, California Institute of Technology, 1982.
- [15] C. P. Burger. *Handbook of Experimental Mechanics*, chapter Photoelasticity, pages 165–266. Wiley, 2nd edition, 1993.
- [16] T. S. Narasimhamurty. *Photoelastic and Electro-optic Properties of Crystals*. Plenum Press, 1981.
- [17] P. Siegmann, D. Backman, and E. A. Patterson. A robust approach to demodulating and unwrapping phase-stepped photoelastic data. *Exp. Mech.*, 45(3):278–289, 2005.
- [18] S. L. B. Kramer. *Phase-shifting full-field interferometric methods for in-plane tensorial stress determination for fracture studies*. PhD thesis, California Institute of Technology, 2009.
- [19] D. C. Ghiglia and L. A. Romero. Robust two-dimensional weighted and unweighted phase unwrapping that uses fast transforms and iterative methods. *J. Opt. Soc. Am. A*, 11(1):107–117, 1994.
- [20] A. Baldi, F. Bertolino, and F. Ginesu. On the performance of some unwrapping algorithms. *Opt. Laser Eng.*, 37:313–330, 2002.
- [21] S. L. B. Kramer, G. Ravichandran, and K. Bhattacharya. Transmission wavefront shearing interferometry for photoelastic materials. *Appl. Opt.*, 48(13):2450–2460, 2009.
- [22] H. V. Tippur, S. Krishnaswamy, and A. J. Rosakis. A coherent gradient sensor for crack tip deformation measurements: analysis and experimental results. *Int. J. Fracture*, 48:193–204, 1991.
- [23] A. J. Rosakis. *Experimental Techniques in Fracture*, chapter Two Optical Techniques Sensitive to Gradients of Optical Path Difference: The Method of Caustics and the Coherent Gradient Sensor (CGS), pages 327–425. Society of Experimental Mechanics, 1993.
- [24] T. L. Anderson. *Fracture Mechanics: Fundamentals and Applications*. CRC Press, 3rd edition, 2005.
- [25] D. G. Smith and C. W. Smith. Photoelastic determination of mixed mode stress intensity factors. *Engr. Fracture Mech.*, 4:357–366, 1972.
- [26] R. J. Sanford and J. W. Dally. A general method for determining mixed-mode stress intensity factors from isochromatic fringe patterns. *Engr. Fracture Mech.*, 11:621–633, 1979.
- [27] C. W. Smith and O. Olaosebikan. Use of mixed-mode stress-intensity algorithms for photoelastic data. *Exp. Mech.*, 24(4):300–207, 1984.
- [28] J. J. Mason, J. Lambros, and A. J. Rosakis. On the use of coherent gradient sensing in dynamic mixed-mode fracture mechanics experiments. *J. Mech. Phys. Solids*, 40(3):641–661, 1992.
- [29] A. J. Rosakis, S. Krishnaswamy, and H. V. Tippur. On the application of the optical methods of caustics to the investigation of transient elastodynamic crack problems: Limitations of the classical interpretation. *Opt. Laser Eng.*, 13:183–210, 1990.

- [30] S. Krishnaswamy, A. J. Rosakis, and G. Ravichandran. On the extent of dominance of asymptotic elastodynamic crack-tip fields, part ii: A numerical investigation of three-dimensional and transient effects. *J. Appl. Mech.*, 58 (1):95–103, 1991.
- [31] H. A. Bruck and A. J. Rosakis. On the sensitivity of coherent gradient sensing: part I—a theoretical investigation of accuracy in fracture mechanics applications. *Opt. Laser Eng.*, 17:83–101, 1992.
- [32] H. A. Bruck and A. J. Rosakis. On the sensitivity of coherent gradient sensing: part II—an experimental investigation of accuracy in fracture mechanics applications. *Opt. Laser Eng.*, 18:25–51, 1993.

Strength and Fracture Behavior of Diffusion Bonded Joints

A.H.M.E. Rahman, Ph.D. Student, Department of Mechanical Engineering
University of North Dakota

M.N. Cavalli, Associate Professor, Department of Mechanical Engineering
University of North Dakota, 243 Centennial Drive, Stop 8359, Grand Forks, ND 58202-8359
matthewcavalli@mail.und.edu

ABSTRACT

Current high temperature alloy systems for turbines and powerplant heat exchangers are typically titanium-, nickel- or iron-based. The extreme performance environments in these applications demand exacting control of both alloy composition and microstructure. This can be problematic when fabrication or repair requires the joining of multiple parts. Traditional welding processes destroy the desirable microstructure in the region of the weld and may lead to the formation of undesirable phases. Diffusion bonding has been gaining increasing interest in this area as a means of both preserving the joint microstructure and controlling second phase formation. The current paper presents the results of initial experimental studies on diffusion bonding of commercially pure titanium, iron and nickel samples.

INTRODUCTION

Producing high quality joints requires extensive knowledge of the intended application, the properties of the materials being joined and the effects of available joining processes on those materials. Ignoring any of these factors can lead to premature joint failure and loss of time, money, and in extreme cases, life. For example, joints with good stiffness at room temperature may become too compliant as the temperature increases (e.g. adhesive joints), leading to excessive deflections at high temperatures. Joints with good strength may also be very brittle (e.g. arc welds without proper post-weld treatments), leading to brittle fracture. Many other problems can arise from poor joint design. Yet despite these limitations, joining remains essential for both fabrication and repair of advanced engineering structures. For example, consider the components of the newest Integrated Gasification Combined Cycle (IGCC) power plants. Whether joints comprise the regions of a turbine blade assembly [1,2] or connect segments of a high temperature heat exchanger [3,4], they must withstand high temperatures under applied stress in potentially corrosive conditions. Exacting control must be maintained over both chemistry and microstructure during the joining process to produce joints that can perform well in these environments. Properly executed, diffusion bonding allows this degree of control [5,6].

Diffusion bonding is a general term for any joining process in which bonding is primarily due to atomic diffusion. Transient liquid phase (TLP) bonding refers to diffusion bonding in which a filler metal with a relatively low melting temperature is used. This leads to local melting during bonding. An excellent overview of the TLP bonding process has been presented by Gale and Butts [7]. Joints may also remain solid throughout the diffusion bonding process. The final joint morphology will depend on the thermodynamics and kinetics of the materials involved in the joining process.

Several examples of diffusion-bonded joints are shown in [Figure 1](#). In [Figure 1a](#), the filler material tends to diffuse evenly away from the joint, altering the surrounding composition but in a fairly continuous manner [8]. In [Figure 1b](#), the filler material reacts with the surrounding metal to form two layers of intermetallics at the bond region as well as additional second-phase regions away from the joint [9,10]. The brittleness of most intermetallics would typically make this an undesirable situation, especially if creep strength or toughness were design considerations. Finally, [Figure 1c](#) shows a joint in which both diffusion and recrystallization have been used to create a nearly continuous microstructure across the bondline [6,11,12].

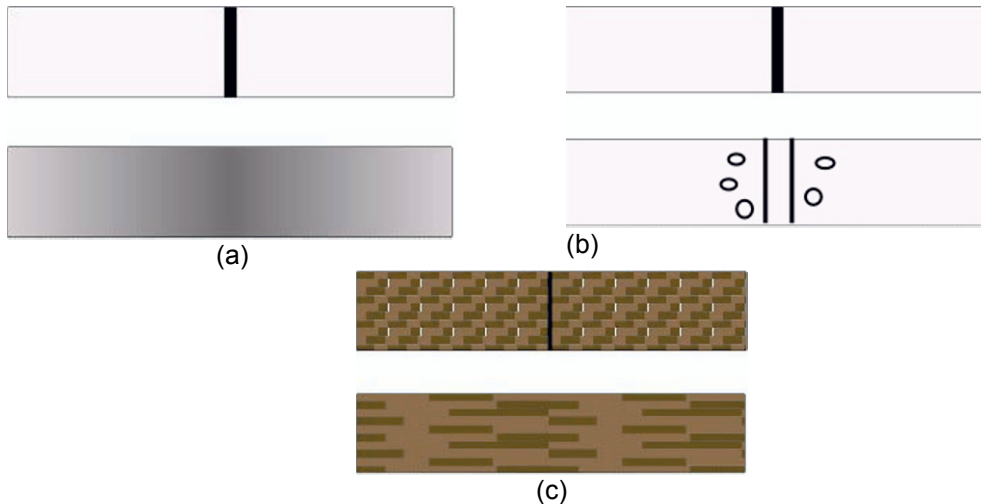


Figure 1: Examples of three types of compositions/microstructures that have been observed from as a result of the diffusion bonding process.

Titanium-, iron- and nickel-based alloys are extensively used for structures that must withstand applied loads at elevated temperatures. Titanium and its alloys have high specific strength and can retain appreciable strength at temperatures found in the chemical and aerospace industries [13-15]. Iron-based alloys (particularly with significant chromium and nickel contents) can be used to even higher temperatures and exhibit good corrosion resistance for a number of environments typically found in turbine engines and combustion chambers. Nickel superalloys generally exhibit the best temperature/corrosion resistance of the group. The strength and corrosion resistance of these alloys depends not only on their chemistry but also on their microstructure. Joining processes such as arc welding which disrupt the microstructure can lead to the presence of undesirable phases and premature failure of the joints. For example, Ti and Ti alloys are difficult to weld with traditional methods because they are highly chemically reactive and oxidize at very low partial pressures of oxygen. As a result, diffusion bonding is a preferred joining method for Ti and Ti alloys [16].

In the present study, diffusion-bonded joints have been fabricated using commercially pure titanium, iron and nickel. A variety of bonding conditions have been used (temperature, time and brazing foils). The resulting microstructures are presented along with some data about the strength of the resulting joints. A limited amount of data from numerical simulations using the DICTRA/ThermoCalc software package is also presented and compared with the experimental results.

EXPERIMENTAL METHOD

Two axisymmetric sample geometries have been fabricated, 6.35mm diameter / 8mm length (cylindrical) and 9mm diameter / 118mm length (dogbone, ASTM E8M). The former geometry was used for investigations of the microstructure formed during bonding. The latter geometry was used to measure the tensile strength of the joints. The bonding faces of the larger tensile specimens were ground to a 120 grit finish and ultrasonically polished prior to bonding. Sample preparation for the smaller samples began with polishing the bonding surface to a 600 grit finish and then cleaning the samples in an ultrasonic bath (isopropyl alcohol). Samples were then stored in alcohol until being bonded. Bonding was performed in a tube furnace under argon gas. Titanium samples were clamped in titanium jigs to prevent thermal expansion mismatch. Kovar jigs were used for bonding iron and nickel joints. Figure 2 shows a schematic of the samples during bonding. Table 1 shows the bonding conditions used for each material type.

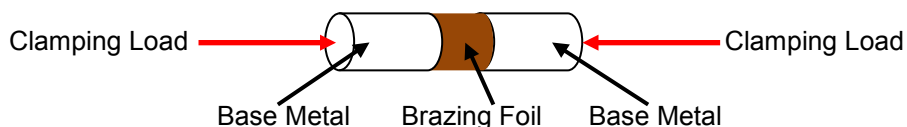


Figure 2: Schematic of diffusion bonding process

Table 1: Summary of joint geometries and bonding conditions investigated

Base Metal	Sample Type	Surface Finish	Temp (°C)	Time (h)	Brazing Foil
Titanium	Small, Large	600 grit, 120 grit	980, 1000, 1030	10, 20, 30	None, Ag, Cu
Iron	Small	600 grit	1100	10	Cu
Nickel	Small	600 grit	1100	10	Cu

Following bonding, the smaller samples were sectioned and polished to a $1\mu\text{m}$ finish (Al_2O_3 suspension). Microstructural examination was performed using a Hitachi S-3400N scanning electron microscope (SEM). Chemical compositions in the bonding region were analyzed using via energy dispersive spectroscopy (EDS). The strength of the larger samples was measured using a Shimadzu AG-IS 50kN universal testing machine. Samples were tested under displacement control at a rate of 1mm/min. Following fracture, observations of the failure surface were used to estimate the total bonded area.

RESULTS AND DISCUSSION

Microstructures

Titanium Base Metal

At 1030°C , Ti can dissolve approximately 29 wt% Ag in a solid solution. At room temperature, this decreases to about 1 wt%. Fig. 3 shows the SEM images of diffusion bonded Ti using an interlayer of Ag. Bonding occurred at 1030°C for 10h. The bottom of the figure corresponds with the midline of the joint. In the central region of the joint, submicron-to-micron AgTi_2 particles in a matrix of AgTi were observed. Approximately $80\mu\text{m}$ from the bond centerline, a eutectic structure of $\alpha\text{-Ti}$ and AgTi_2 formed. At about $160\mu\text{m}$ from the centerline, the microstructure consisted solely of a solid solution of Ti and Ag. For longer bonding times (30h), a similar overall structure was seen with some general increase in the dimensions of each region being observed. Some regions of Ti-Ag solid solution were found in the AgTi matrix at the bond centerline for longer binding times.

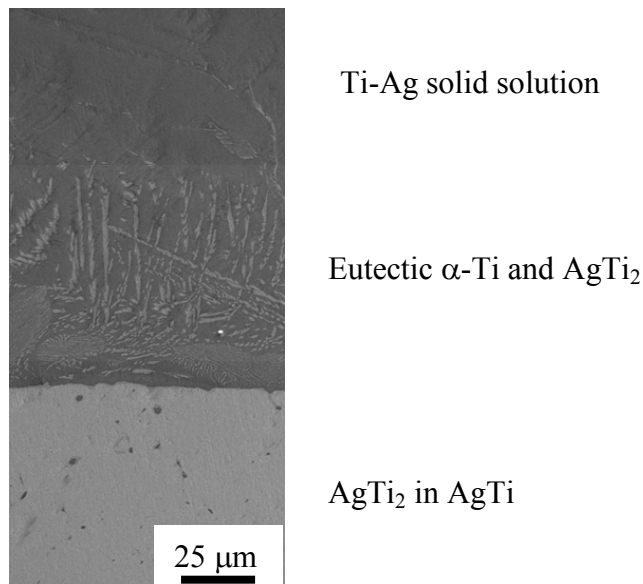


Figure 3: Microstructure of Ti bonded with Ag interlayer for 10h at 1030°C [17].

At 900°C , Ti can dissolve about 12 wt% Cu in a solid solution. This decreases to less than 1 wt% at room temperature. Figure 4 shows several images from a joint made with titanium base metal and a copper interlayer, diffusion bonded at 900°C for 10 h. In Figure 4a, the midline of the joint is seen to consist of a region of Cu-Ti solid solution surrounded by a region of different intermetallics (TiCu_4 , Ti_2Cu_3 , TiCu). Bounding the intermetallics is a eutectic region of $\alpha\text{-Ti}$ and Ti_2Cu (Figure 4b). The spacing between adjacent lamellae is much finer in this joint than that seen in the Ti-Ag joint (Figure 3). The outermost region is a solid solution of Cu in Ti. For a higher bonding temperature (1000°C), no intermetallics were observed near the centerline, only a eutectic mixture of Ti

and Cu. For much higher bonding temperatures ($>1050^{\circ}\text{C}$), macroscopic pores appeared in the bond region; pore size increased with increasing temperature.

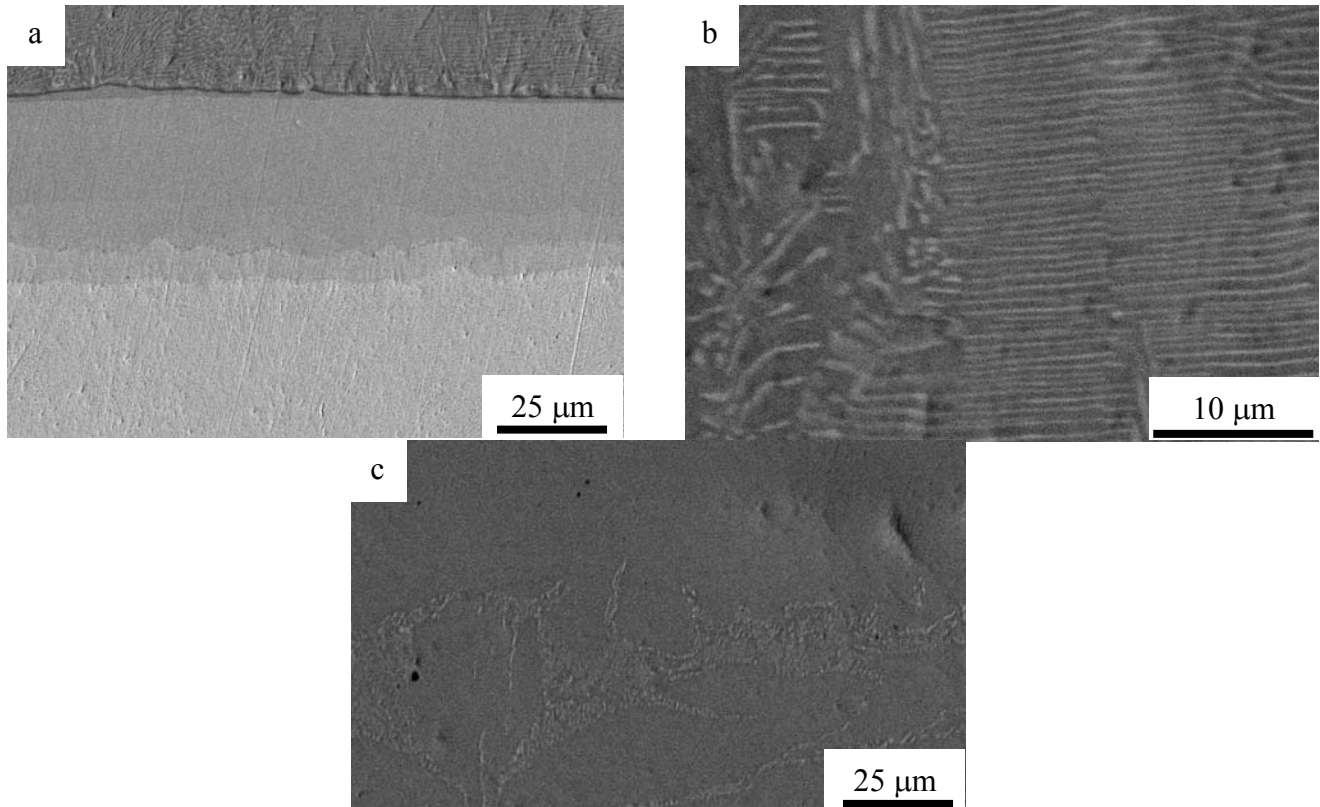


Figure 4: Microstructures observed a) at the midline, b) in an intermediate region and, c) near the base metal in a joint made with Ti and an interlayer of Cu at 900°C for 10h [17].

Iron Base Metal

Figure 5 shows the concentration profile recorded for a joint made with Fe base metal and a $100\mu\text{m}$ Cu interlayer, bonded at 1100°C for 10h. The SEM images showed two distinct regions, which is supported by the concentration profile shown in Figure 5. Near the bond midline, a very small amount of iron has diffused into the copper interlayer. Approximately $45\mu\text{m}$ from the centerline ($\sim 1/2$ the initial interlayer thickness), a step in the concentration to a region primarily composed of iron with a small amount of copper is observed. Despite the fact that iron can dissolve approximately 8 wt% Cu in a solid solution at 1100°C , relatively little Cu has diffused away from the midline, indicating that the kinetics for diffusion of Cu in Fe are much slower than those for Cu in Ti, even at a significantly higher bonding temperature.

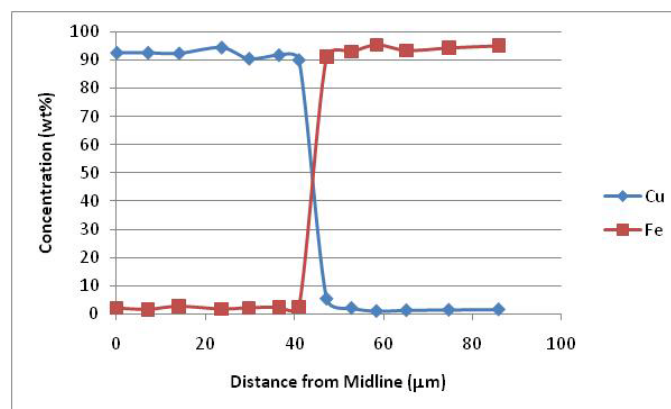


Figure 5: Concentration profile for Fe-Cu joint bonded at 1100°C for 10h

Nickel Base Metal

Figure 6 shows the concentration profile for a joint fabricated from Ni base metal and a 100 μm Cu interlayer, bonded at 1100 $^{\circ}\text{C}$ for 10h. Unlike the Fe-Cu joint, the Ni-Cu joint shows a relatively continuous variation in concentration for both elements from the bond midline to the surrounding base metal. Copper and nickel are completely miscible in one another, which explains the absence of any second phases. It appears, however, that the kinetics of the diffusion in this system, while faster than those seen in the Fe-Cu joint, are still slower than those of the Ti-Cu system.

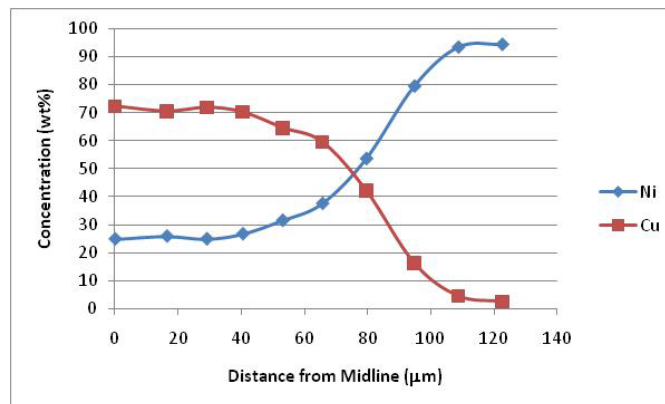


Figure 6: Concentration profile for Ni-Cu joint bonded at 1100 $^{\circ}\text{C}$ for 10h

Mechanical Properties

Tensile testing showed that the strongest Ti joints were those fabricated with a Cu interlayer. Average joint strengths of 502 MPa were achieved for a bonding temperature of 1030 $^{\circ}\text{C}$ for 10h. This compares to an average tensile strength of 511 MPa for dogbone specimens made from unbonded Ti. The strengths of the Ti-Cu joints increased with bonding temperature with average strengths for bonding at 980 $^{\circ}\text{C}$ and 1000 $^{\circ}\text{C}$ measured to be 460 MPa and 468 MPa, respectively. In contrast, the strongest Ti-Ag joint (bonded at 1030 $^{\circ}\text{C}$ for 30h) only achieved an average tensile strength of 160 MPa. The measured joints strengths tended to be higher for bonding conditions for which no intermetallics were observed near the bondline (the highest bonding temperatures with Cu as an interlayer). In addition, the scatter in the tensile strength data tended to decrease in the absence of intermetallics, consistent with the tendency of intermetallics to fracture in a brittle manner. No tensile data is yet available for the Fe-Cu or Ni-Cu joints.

CONCLUSIONS

This study has investigated the microstructure and mechanical properties of diffusion bonded joints made from Ti, Fe and Ni base metals. For Ti-based joints, the best results were found using a Cu interlayer at a bonding temperature of 1030 $^{\circ}\text{C}$. Joints fabricated using these conditions achieved approximately 98% of the strength of the base material. This is thought to be due to the absence of intermetallic phases after bonding. Ti-Ag joints, in contrast, were found to have intermetallic phases in the bond region under all bonding conditions and achieved less than 30% of the strength of the base material. Initial concentration data for Fe-Cu and Ni-Cu joints have been presented but no mechanical data is yet available.

ACKNOWLEDGEMENTS

The authors would like to thank both the UND Senate Scholarly Activities Committee and the National Science Foundation (Award #DMR-0907616) for their financial support of this work.

REFERENCES

- [1] Lingenfelter, A. C. (1997). *The Welding Metallurgy of Nickel Alloys in Gas Turbine Components*. D. o. Energy.

- [2] Pollock, T. M. and S. Tin (2006). "Nickel-Based Superalloys for Advanced Turbine Engines: Chemistry, Microstructure, and Properties." Journal of Propulsion and Power **22**(2): 361-365.
- [3] Aquaro, D. and M. Pieve (2007). "High temperature heat exchangers for power plants: Performance of advanced metallic recuperators." Applied Thermal Engineering **27**: 389-400.
- [4] Hurley, J. P., D. J. Seery, et al. (2003). "Experience with an ODS High-Temperature Heat Exchanger in a Pilot-Scale HiPPS Plant." Materials at High Temperatures **20**(1): 39-44.
- [5] Wei, S. (1996). "Diffusion Brazing of Mechanically Alloyed Oxide Dispersion Strengthened Materials." Rare Metals **15**(1): 16-22.
- [6] Moore, T. J. and T. K. Glasgow (1985). "Diffusion Welding of MA 6000 and a Conventional Nickel-Base Superalloy." Welding Journal **64**(8): 219s-226s.
- [7] Gale, W. F. and D. A. Butts (2004). "Transient Liquid Phase Bonding." Science and Technology of Welding and Joining **9**(4): 283-300.
- [8] Khan, T. I., M. J. Kabir, et al. (2004). "Effect of transient liquid-phase bonding variables on the properties of a micro-duplex stainless steel." Materials Science & Engineering A: Structural Materials: Properties, Microstructure and Processing **372**: 290-295.
- [9] Juan, W., L. Yajiang, et al. (2005). "Study of Diffusion Bonding of Fe-28Al Alloy with Austenitic Stainless Steel in Vacuum." Vacuum **79**: 45-51.
- [10] He, P., J. C. Feng, et al. (2002). "Microstructure and Strength of Diffusion-bonded Joints of TiAl Base Alloy to Steel." Materials Characterization **48**: 401-406.
- [11] Khan, T. I. and E. R. Wallach (1996). "Transient Liquid Phase Diffusion Bonding and Associated Recrystallization Phenomenon When Joining ODS Ferritic Superalloys." Journal of Materials Science **31**: 2937-2943.
- [12] McKimpson, M. G. and M. T. Kling (2006). Diffusion Bonding Studies on Incoloy® MA956. MS&T 2006, Cincinnati, OH.
- [13] Sheng, Z.G., X.E. Hu, et al. (2009). Materials Science and Engineering A **499**: 101-105.
- [14] Lee, H.K., H.S. Han, et al. (2006). Materials Science and Engineering A **415**(1-2): 149-55.
- [15] Peng, H., Z. Jiu Hai, et al. (1999). Materials Characterization **43**(5): 287-92.
- [16] Kahraman, N., B. Gulenc, et al. (2007). International Journal of Impact Engineering **34**: 1423-32.
- [17] Rahman, A.H.M.E. and M.N. Cavalli (2010). Strength and Microstructure of Diffusion Bonded Titanium Using Silver and Copper Interlayers. Manuscript in preparation.

Fabrication and Characterization of Novel Graded Bone Implant Material

Bender, S., El Wakil, S.D., Chalivendra*, V.B., Rahbar, N., Bhowmick, S.
285 Old Westport Rd, North Dartmouth MA, 02747, University of Massachusetts Dartmouth
*corresponding author: 508-910-6572, vchalivendra@umassd.edu

ABSTRACT

A solid structure and porous core graded porosity materials were fabricated and characterized for potential bone replacements. Stainless steel is considered as a model material for generating graded porosity structure in this study. Powder metallurgy concepts were employed to generate constant porosity metallic implant materials and later they were sintered using a high temperature furnace with inert gas environment. Sintered materials were densified on the surface using a novel indentation tool. To verify the feasibility of our methodology, pure iron powder was used in preliminary studies. Preliminary results obtained using scanning electron microscopy images and image analysis of MATLAB indicated that the densification process generated gradation of porosity from the surface. The gradation of porosity is continuous and the gradient is high for higher densification depths. Preliminary results also indicated that hardness values changed gradually from the surface to certain depth. To control the process parameters of densification process in the fabrication, a numerical model is developed using a flow rule associated with porous materials. Micro-indentation tests will be conducted to study variation mechanical properties along the porosity gradation. Both quasi-static flexure and fracture experiments will also be conducted to understand the effect of gradation on fracture toughness and flexure strength.

1 INTRODUCTION

This paper describes the process of fabrication, characterization and mechanical evaluation of functionally graded specimens for the use as a bone implant. Methods for creating functionally graded bone structures have involved many techniques and materials. Pelletier et al.[1] studied poly(methyl methacrylate) (PMMA) bone. Results showed the curing temperature effected the porosity distribution and at elevated temperatures there was an increased pore density toward the center of the material. Zeming et al.[2] investigated a sip-casting process for alumina ceramics. The specimens produced had a two part structure of dense material and porous material. Most of the investigations of metallic structures like that of Gradzka-Dahlke et al.[3], are homogeneously porous. The specimens described in this paper are metallic structures with a porosity gradation from a solid surface layer to a homogeneously porous core. Powder metallurgy techniques were used to create the initial porous structure and a novel surface densification technique was used to produce a solid surface with a graded porosity structure to a porous core.

2. MATERIALS AND EXPERIMENTAL METHODOLOGY

2.1 Initial Compacts using Powder Metallurgy Technology

To familiarize with Powder Metallurgy technology, iron powder was used in the initial phase for producing specimens. Iron was chosen because of its relatively inexpensive cost as well as its superior compacting and sintering properties in comparison to those of the accepted bio-materials such as stainless steel, Co-Cr alloys, and titanium. Through the use of iron powder the methodology for densification and characterization of the degraded porous structure was developed. The iron powder was purchased from ISP Technologies Inc. (Mountain View, NJ). It has a purity of 99.7% and an average particle size of approximately 16 microns. Samples of the iron powder, each amounting to 50g, were compacted in a cylindrical die with a 57mm diameter, at pressures in the range of 310 to 450 MPa by means of a Tinius-Olsen hydraulic press. The die walls were lubricated through the use of a solution of zinc stearate in acetone. Allowing the acetone to evaporate left a thin layer of lubricant which enabled the compact to be safely ejected from the die using a force of a small magnitude exerted by the hydraulic press. The green compacts sintered in a Sentrotech tube furnace to a temperature of 1300 C at a rate of 4 C/min and held at that temperature for 30 minutes It was then allowed to slowly cool back to room temperature. To prevent oxidation the furnace was first vacuumed and then backfilled with argon. A gentle argon flow of 0.4gal/min was used while the furnace temperature was below 1000 C and then decreased to

0.1gal/min until 1300 C. This was done to maintain consistent temperature throughout the furnace. After sintering the compacts, they were then measured and massed to obtain their densities and corresponding porosities.

Iron is not a feasible material for biological applications because it has poor corrosion resistance in an electrolytic solution. Therefore, upon completion of the processing and characterizing of the iron powder, it was necessary to begin working with a material more suitable for biomedical applications. Type 302 stainless steel was chosen because it was one of the first metals used for bone implants [4]. Also, it is less expensive than 316 stainless steel, Co-Cr Alloys, and titanium. It was initially thought that the compaction methods previously described would still be applicable to 302 stainless steel. However, even after annealing the powder and use of a larger particle size, the powder still showed very poor compactability. Loose sintering was adopted as the consolidation technique to obtain initial compacts having various porosity levels [5]. That process involved filling cylindrical ceramic tubes with the stainless steel powder and placing them in the sintering furnace at a specific elevated temperature for 60 minutes, before allowing them to cool down to room temperature. The porosity level in the porous consolidated body could be controlled by selecting the sintering temperature, the higher the sintering temperature the lower the porosity level.

2.2 Surface Densification

The surface of the sintered compact had to undergo a densification process to reduce the porosity at the outer surface while maintaining a porous center. To achieve this, a custom tool was designed. It consisted of a hardened steel alloy ball which is allowed to rotate freely within its housing. The ball protrudes from one end of the tool while the other end was designed to fit in the tool post of a lathe. at one end, and the other end has a hemispherical pocket that holds part two, a ball. The protruding ball is used to indent the porous specimen. The ball-point tool is shown in [figure 1](#). The sintered compact could then be mounted in the chuck of the lathe, the densification tool was firmly mounted in the tool post perpendicular to the surface of the sintered porous compact. The spindle of the lathe was set to rotate at 50 rpm. The tool post vernier guage was zeroed when the ball just touched the center of the surface of the compact. The tool was then forced to penetrate 0.125mm into the surface of the compact. By cranking the handle of the cross slide the tool was then moved laterally, forth and back, to sweep and densify the whole surface. Once the tool is back at the center it could be forced 0.125mm deeper into the surface. This process could be repeated until the desired depth of indentation is achieved.



Figure 1. Ball-point tool for densification

2.3 Porosity Gradation Analysis

To view the gradation of porosity from the surface to the porous core of the compact after densifying the surface, a cross section had to be prepared following the known metallurgical procedures. This was done by rough cutting the sample with an abrasive disk. Followed by machining and finally by grinding, polishing and etching.

Optical microscopy images were taken of the densified region of the specimens cross section. The images were analyzed in MATLAB using a code created to plot the intensity of the image versus the distance from the densified surface. The Pores appear darker in the image. That enabled a correlation between porosity and image intensity to be established [6]. The MATLAB analysis was verified by machining thin layers of the densified surface and subsequently calculating the density of the layer that was removed by measuring the mass and height of the remaining specimen and subtracting them from the previous mass and height of the specimen.

Pore structure and morphology was carefully examined along the cross section with the use of SEM technology. SEM images of the densified cross section were taken at interval depths below the densified surface.

3 RESULTS AND DISCUSSION

3.1 Porosity Gradation in Iron Compacts

The compacting pressure vs. sintered density curve for iron compacts of 310 to 450 MPa of compacting pressure are shown in Figure 2. The sintered densities of the iron compacts are in the range of 85 to 95%. Green compacts of 65 to 70 % density were too weak and cracked upon ejection of the die, so the target range of porosity for bone replication was not achievable [7]. Because iron was used as a “proof of concept” for the densification process measures were not taken to lower the density of the sintered compacts to 70 % and the 85 % density compacts were used for densification process. Iron powder of 100g samples that were compacted to 310MPa and sintered as described above were densified to 0.64mm, 1.0mm, 1.27mm, and 1.78mm by means of the previously described process. Figure 3 shows the results of the MATLAB image analysis of the four indentation depths used for the densification process for the iron compacts.

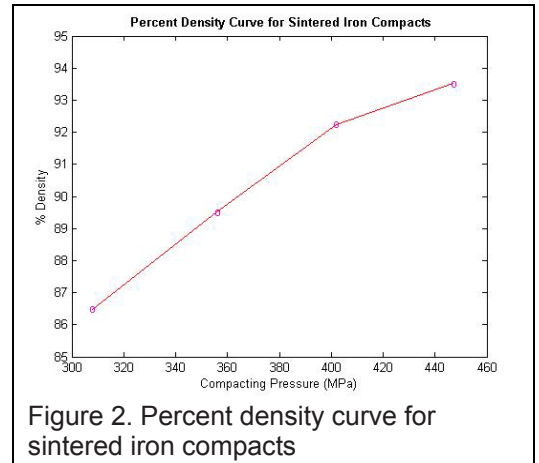


Figure 2. Percent density curve for sintered iron compacts

This analysis reveals that there are three distinct regions of the indented specimen. The first is the solid surface layer directly at the indented surface. A porosity gradation region follows, and finally the porosity increases till it equals that of the homogeneous core. The core region consists of the porosity developed by the initial compacting and sintering. It was observed that an increased depth of indentation increased both the density in the solid layer as well as the total depth of that layer into the specimen. Figure 4 illustrates these results.

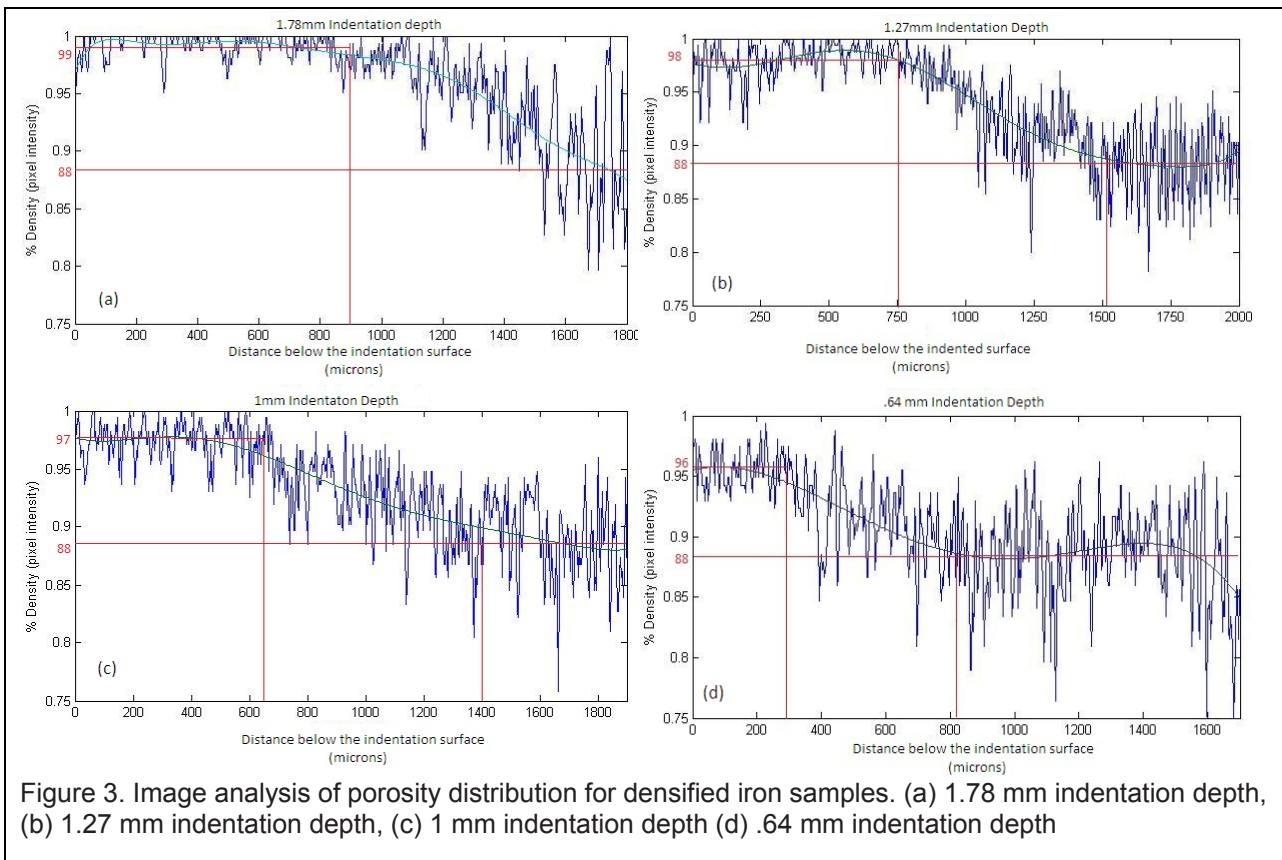
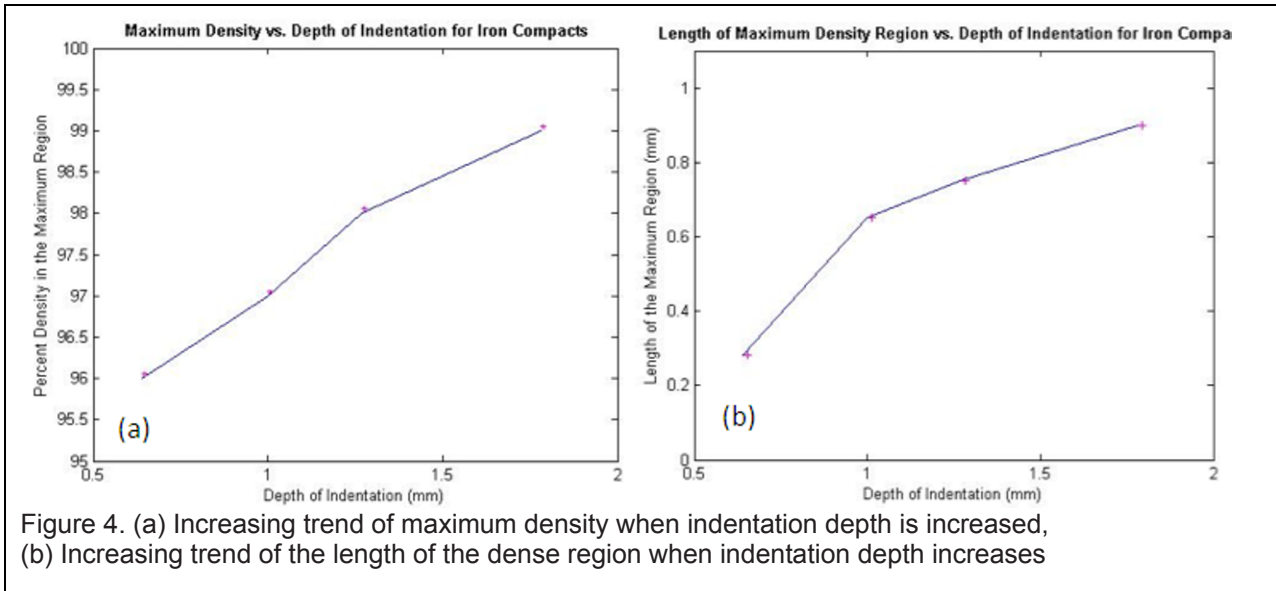


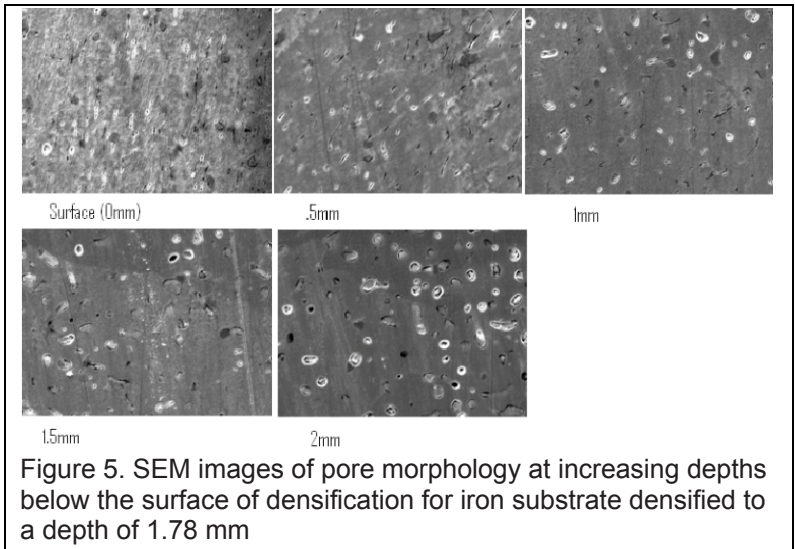
Figure 3. Image analysis of porosity distribution for densified iron samples. (a) 1.78 mm indentation depth, (b) 1.27 mm indentation depth, (c) 1 mm indentation depth (d) .64 mm indentation depth



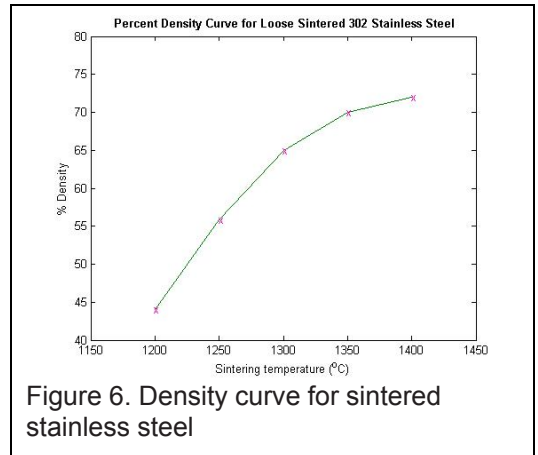
SEM images of the 1.78 mm densification depth on an iron substrate were taken at increasing depth below the surface of densification. In the region of the solid surface it was observed that the pores were mostly collapsed. Images toward the core region revealed a decreased ratio of collapsed pores to rounded pores. The SEM images at 0.5 mm intervals below the densified surface are shown in figure 5.

3.2 Porosity Gradient of Porous Stainless Steel Samples

The stainless steel powder was massed into 100g samples, poured into pure alumina tubes of diameter of approximately 50 mm and lightly shaken to produce a level surface. No pressure was applied to the powder. To achieve the desired initial density of 70%, the sintering temperatures were varied between 1200C and 1400C, the temperatures were held for 60 min. Figure 6 shows the percent density curve for loose sintered stainless steel.



The densification of the stainless steel samples were preformed differently then the iron samples. Indentation depth was held constant at 1mm for the stainless steel and the initial porosity was varied. Samples chosen for desification were sintered at 1300C, 1350C, and 1400C resulting in porous samples having percent densities of 68%, 70%, and 72%, respectively. The process for densification The stainless steel sample was the same as that of the iron compacts. For the stainless steel densified samples a filter was used to reduce the noise in the image analysis. To verify the image analysis with physical data, a density gradient was obtained by calculating the mass and volume of the sample with surface densification and the machining away a thin layer of the densified surface, and recalculating the new mass and volume of the



remaining sample. From these two sets of values the density of the thinly machined layer can be calculated. This process was performed on the 68% density (1300C sintering temperature) sample. Tolerances of the measuring devices induce some inaccuracies. However, the data shows a similar trend as the image analysis. The comparison between the MATLAB data and the machining process data is shown in figure 7.

Figure 8 shows the filtered data from the image analysis of the three sintering temperatures. The data suggests a more gradual density degradation for the high sintering temperature. It also suggests that the depth of the fully dense region is consistent for all three temperatures. There is no correlation between the density of the fully dense region and the initial porosity.

4 EXPERIMENTS IN PROGRESS

Micro-indentation experiments using a Vickers indentation tip are in progress to determine the mechanical properties of the solid surface and the graded porous region. Theory for obtaining Young's modulus from the load deflection curves with a Vickers indentation tip is described by Antunes et al [8]. Quasi-static fracture and flexure tests are also in progress. Both homogeneously porous and densified samples are used to determine the porosity gradient's effect on fracture toughness and flexure strength. A numerical model of the indentation process is being developed with the use of ABAQUS finite element software to control and optimizes process parameters such as the radius of curvature of the densification tool tip [9]. The results of these experiments will be presented at the conference.

5 CONCLUSIONS

Functionally graded materials can be created from sintered powder metals. Surface densification through the use a ball end tool will create a densification degradation with three distinct regions a fully dense region closes to the surface a graded region below that, and the core region consisting of the initial density. By varying the initial density of the specimen and the indentation depth during densification, the properties of these three regions can be controlled and optimized in order to mimic the properties of natural bone as best as possible.

ACKNOWLEDGEMENTS

The authors would like to acknowledge Dean Robert E. Peck of the College of Engineering, University of Massachusetts Dartmouth, for support of the project. The authors would also like to acknowledge William Moore, Mark Janson, and Bob Bergeron for their support with fabrication and specimen preparation.

REFERENCES

1. Pelletier M. H. et al., "Pore Distribution and Mechanical Properties of Bone Cement Cured at Different Temperatures", *Acta Biomaterialia*, Actbio 995, 2009
2. Zeming He et al, "Dynamic Fracture Behavior of Layer Alumina Ceramic", *Materials Letters*, 59, 901-904, 2005
3. Gradzka-Dahlke M. et al., "Modification of Mechanical Properties of Sintered Implant Materials," *Journal of Materials Processing Technologies*, 204, 199-205, 2008
4. Park J.B. et al., *Metallic Biomaterials*, Biomaterials, 1.1-19, 2007
5. El Wakil S.D., Khalifa H., "Cold Formability of Billets by Loose Powder Sintering", *The International Journal of Powder Metallurgy and Powder Technologies*, 19, 1, 21-27, 1983

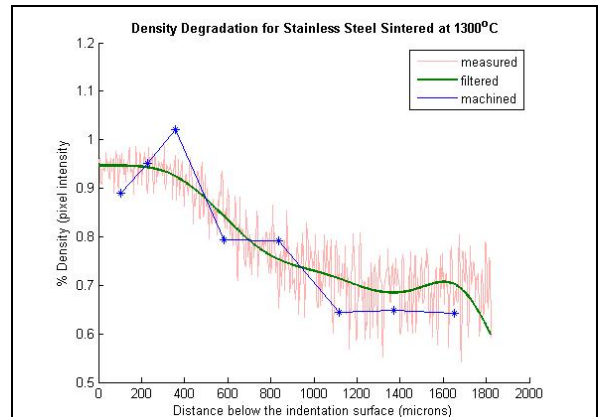


Figure 7. Comparison of Image analysis to machining analysis of density degradation

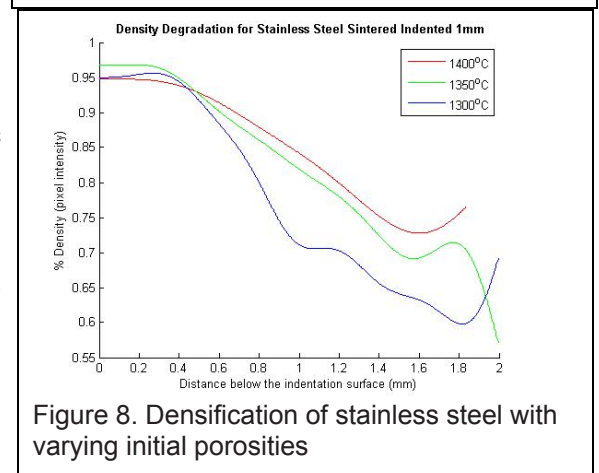


Figure 8. Densification of stainless steel with varying initial porosities

6. Spowart J.E. et al, "Multiscale characteration of spatially heterogeneous systems", *Material Science and Engineering*, A307, 51-66, 2001
7. Vasconcellos et al., "Porous Titanium Scaffolds Produced by Powder Metallurgy for Biomedical Applications", *Materials Research*, 11, 3, 275-280, 2008
8. Antunes J.M. et al., "Ultra-micro harness testing procedure with Vickers indenter", *Surface Coating Technology*, 149, 27-35, 2002
9. Cheng-Chao Huang et al., "Forging simulation of sintered powder compacts under various frictional conditions", *International Journal of Mechanical Sciences*, 44, 489-507, 2002

A Dynamic Design Model for Teaching

T.K.Kundra
Emeritus Fellow, Former Professor and Chair
Mechanical Engineering Department, Indian Institute of Technology
New Delhi 110016. India.
tkkundra@mech.iitd.ernet.in

ABSTRACT

There is a need to include inverse design problems of vibration engineering into undergraduate and postgraduate education of mechanical and structural engineers. It has not been hitherto possible due to lack of economical dynamic testing equipment and absence of several of dynamic design technologies. With the emergence of laboratory compatible modal testing equipment and the emergence of technologies like those of finite element model updating, structural dynamic modification, operational modal analysis and laser vibrometry it is now feasible to include dynamic design procedures into curriculum. The present paper proposes a dynamic design model based on three decades of research in the area. The paper discusses several cases of application to vibration engineering design employing the above mentioned emerging technologies. It then proposes a vibration design model which is well integrated with satisfaction of other design requirements and constraints of machines/ structures based on yield strength, fatigue strength, surface fatigue strength and other modes of failure. The concept of concurrent mechanical/ structural design to include dynamic soundness of the equipment/ structure is also discussed.

INTRODUCTION

The texts on Mechanical Engineering Design [1-4] and the like enable the learners to incorporate adequate strength including fatigue and surface aspects, in the designed structural/ machine components. These components are also subjected to vibrations leading to failures of several kinds. The forced vibrations include failures like those of disastrous resonance and unacceptable levels of vibration and noise. The self excited vibrations encompass all the performance failures due to dynamic instability. 'Vibration-Designing' is critical in mechanical structures and machines for achieving ever increasing demands of high accuracy and productivity from them. For example while vibration levels of a machine tool limit its accuracy, the chatter vibration or dynamic instability of a machine tool limit its productivity by constraining width/ depth of cut or by limiting the level of its operating speed. A global challenge is how to go about vibration designing so that cost of mechanical equipment is still competitive in spite of additional costs of vibration designing. Equipment manufacturers are scared of the costs of vibration designing and its frustrating nature, and rightly so. The fear is primarily rooted in the traditional repeated prototype vibration testing and evaluation coupled with cut and tries of prototype modifications to achieve the above-mentioned objective of a desired robust sound vibration design. This 'craftsman' era method has hitherto been highly time consuming and expensive. Further, the high hopes placed in Finite Element Modeling of machines for the low cost drawing board/ computer level vibration design have also been belied.

Are there any effective vibration designing routes today? Several vibration engineering design technologies based on the research in the area like modal testing [5], finite element model updating [6], structural dynamic modification [7,8] and operational modal analysis have emerged during last three decades. These methods are not purely theoretical but they do replace the expensive and time consuming repeated prototype modification to a

great extent say by more than 90%. Thus these methods hold the hope of making vibration designing highly economical and effective.

In sixties and seventies fatigue design models based on several decades of research in the area of fatigue failures research were included in the mechanical engineering design texts books thus raising the level of design expertise of the students. In view of the above mentioned vibration engineering technologies there is a need to include vibration/ dynamic design models based on this research especially in the inverse design problems of vibration engineering. Further there is an ever increasing knowledge on concurrent mechanical design strategies like those of systematic design methods and design for X including design for manufacturing and assembly. These also need to be integrated with the teaching of Mechanical Engineering Design which should be learnt as a problem solving capability.

VIBRATION ENGINEERING TECHNIQUES

(Major part of this section has been adapted from reference [11])

Modal Testing is currently the state of the art vibration testing technology. By modal testing of a machine tool one can obtain natural frequencies, mode shapes and damping of a structure relatively quickly, efficiently and accurately. The time taken by modal testing to determine vibration characteristics today is a matter of few days compared to the months spent on dynamic testing for the same results about four decades ago. Details of a typical test setup used for vibration testing of a machine tool structure (Figure 1) are shown in Figure 2.

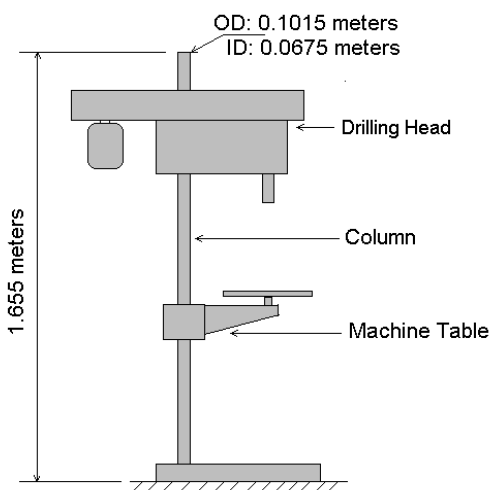


Figure 1: A typical drilling machine

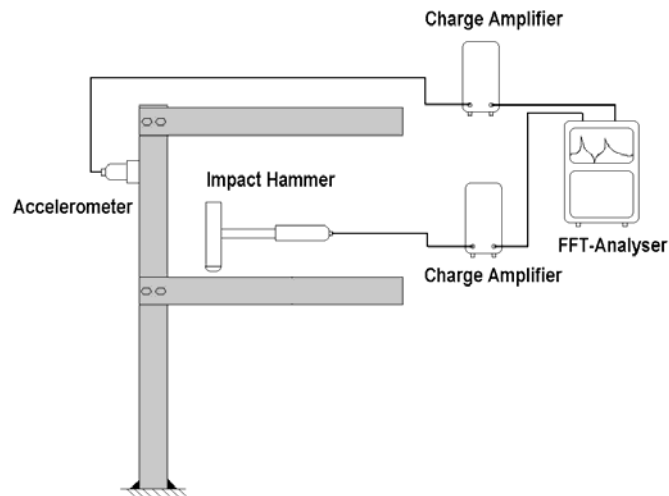


Figure2 : Modal Testing of Fig.1 like machine

Major equipment required is a Vibration or Modal Exciter/ Impact hammer, an FFT [Fast Fourier Transform] analyzer, vibration pick ups like accelerometers and charge amplifiers. Also required is a desktop computer or workstation loaded with programs/ algorithms to extract above mentioned vibration parameters namely natural frequencies, mode shapes and damping from the dynamic test data. The latter is not shown in the Figure 1 but FFT, which is also microprocessor based stores the vibration test data, is connected to the computer to transfer the data for analysis by the above-mentioned software programs. Several such software packages are now available. LMS, B&K, EDS, ICATS is to name only few vendors who can provide these packages off the shelf for dynamic test data acquisition and extraction of modal parameters of a structure. The textbook by Ewins [5] is the most widely used reference for the details of the theoretical and the experimental aspects of modal testing. Currently the above-mentioned software and hardware in a package form like that of MODENT [12] can be obtained at an affordable price by the Institutes for educational purposes.

Finite element model updating: Finite Element Method (FEM) is a powerful technique for obtaining a discrete mathematical model of a structure however complex. Due to its accurate prediction of static stress, strain it has

become a well-established procedure for static design/ analysis in industry. On the other hand when a finite element model of a complex machine structure is used to predict theoretically its vibration characteristics like natural frequencies and vibration levels, the errors in results are unacceptable. The sources of error in the FE model can also not be completely eliminated. For example nature and distribution of damping in the machine structure, unlike mass and stiffness parameters cannot be obtained theoretically. Further, accurate stiffness and damping modeling of the joints, which assemble various parts of a machine, is another important factor affecting the accuracy of the FE model. Type of the mesh, the nature of the chosen finite element and coordinates of interest in the FE model are some other sources of error. These uncertainties get reflected in the significant differences, at times, between the dynamic predictions based on a finite element model, like natural frequencies, mode shapes, damping ratios and frequency response functions [vibration levels], and the experimentally obtained test data. It is also observed that predictions of the dynamic behavior made on the basis of an FE model constructed by several individuals independently may not always agree. Variation in the choices with regards to the number and type of finite element selected, the mesh employed, the software used and some other decisions that one may have to make during the modeling process could be some of the reasons for the above lack of agreement. Numerical predictions of structural dynamic properties are not always as reliable as they are generally believed to be [10]. Therefore, it is experienced that an FE model is not always a reliable model to be used in Vibration design. This has given rise to the techniques of Finite Element Model Updating for correcting or updating an FE model in the light of actual modal test data of the prototype of the machine tool. The algorithm of this updating is shown in [Figure3](#).

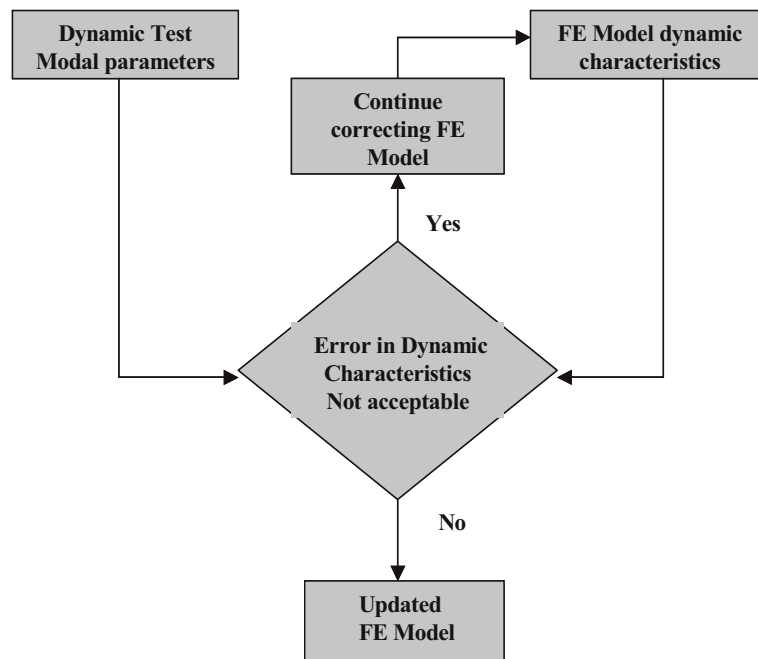


Figure3: Finite Element Model Updating flow chart

In view of the above it is required to correct an FE model so that the resulting updated FE model is able to predict dynamic characteristics of the structure with acceptable accuracy. Extensive research has been going on in the area of finite element model updating for the last two decades and several procedures of correcting FE models have been proposed. The text on model updating by Friswell and Mottershead [6] discusses various principles involved in model updating. All updating procedures require vibration test data of the prototype of the machine structure, obtained by Modal testing and its FE model. Before undertaking the actual step of correcting or updating the FE model, its correlation with the experimental data is carried out.

Correlation aims at assessing the quality of an FE model by providing an idea of degree of correlation that exists between the FE model and the measured data of a structure. In case of an acceptable level of correlation an FE

model can be used as it is, otherwise fresh measurements or rebuilding of FE model may have to be undertaken so that a reasonable agreement exists between the two sets of data. In general the number of measured coordinates are typically much less than the degrees of freedom in an FE model chiefly due to the difficulties encountered in measuring rotational degrees of freedom and due to inaccessibility of some degrees of freedom that are inside the body of the structure. Further, the coordinates of interest that are generally small also limit the number of coordinates that one would like to measure. Correlation of related modes in FE model and measured data can be established by visual comparison and by quantifying it using a correlation coefficient. Modal assurance criterion (MAC) is generally employed to quantify degree of correlation between a measured mode and an analytical mode. A MAC-value close to 1 indicates good correlation while a value close to zero indicates poor correlation. Accordingly, MAC is also used for the pairing of analytical and experimental modes.

Structural Dynamic Modification [SDM] and Dynamic Design: SDM techniques are computer based methods by which dynamic behaviour of a structure is improved by predicting its modified behaviour brought about by adding modifications like mass, stiffeners, dampers or by changing structural configuration, material and processes. Dynamic design is the process that aims at obtaining desired dynamic characteristics of the structure of the equipment being designed. Several of the SDM techniques for dynamic design are described in references [7,8]. Use of an updated FE model of a structure in the process of vibration design is perceived to be a potential replacement to the conventional prototype testing so that the cost and the time involved in the design and development could be significantly reduced. SDM methods are the techniques used to determine the changes in the dynamic characteristics as a result of a certain design modification like addition of a mass, spring, stiffener or damper. Thus, these techniques form the basis for performing vibration design employing updated FE model at the computer level. It may be noted that these modifications and prediction of resulting changes in the vibration behavior of the structure are now conducted theoretically with the help of a computer. It does not involve any more of prototype[s] building with actual hardware changes as it is required to be done traditionally and is so time consuming and expensive. At computer level one can see the effect of several changes using the updated FE model very quickly and economically and select the optimal modification to be implemented in the current design of the structure.

DYNAMIC DESIGN STUDIES

Dynamic design of several structures like beams, combination of beams (as the F type shown in [Figure2](#)) including real life automotive and machine tool structures typically shown in [Figures 4 and 5](#) [9,11,13,14] is



Figure4: A drilling machine with stiffener SDM

Figure5: automotive bonnet with mass SDM

conducted. Modal testing and FE Modelling of each of the structure has been conducted followed by correlation and FE Model Updating. In all the cases the modal parameter natural frequency predicted with the updated FE model is found to be acceptable with error from the experimental values to be less than 5%. The updated model is used to conduct SDM and therefore dynamic design at the computer level. SDM is usually preceded by sensitivity analysis and followed by optimal SDM. The dynamic design is observed to be conducted successfully for the constraints (or requirements) of the modal parameter of the natural frequencies. The flow chart based on these successful studies is shown in Figure6. For accurate prediction of vibration levels with updated models Incorporation of damping into model updating has been reported by Arora et al [18].

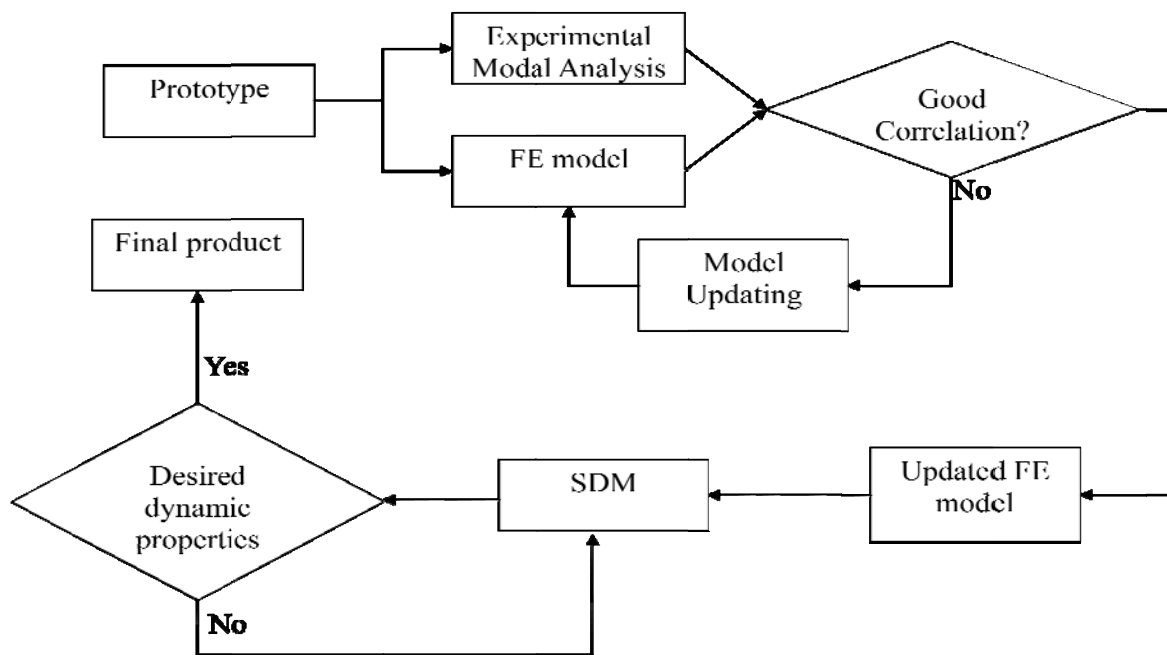


Figure6: A flow chart of vibration or dynamic design via modal testing, model updating and SDM

PROBLEM SOLVING AND A DYNAMIC DESIGN MODEL FOR TEACHING

Problem solving or designing is recommended by several designers [15-17] to be conducted in an iterative four step flow as shown in Figure7. In the author's experience the hierarchy of the steps is flexible. Further in author's observation the third step of detailing in case of mechanical equipment or machine structures is not similar to the design of a machine component subjected to simple static loading where a design equation provides straight away the size parameters of the component. Real life mechanical equipment including fatigue type of loading of shafting, cases require an initially estimated design or solution. It is so because several fatigue situations including surface failure cases require factors which depend upon the solution itself. For example size factor in fatigue cannot be determined until and unless the size (or the solution) is not known before hand. This gives rise to the classical chicken-egg problem in design or inverse problem solution in complex loading situations. The vibration loading is not an exception. The author suggests in Figure8 the detailing process in all these situations where initial solutions have to be estimated empirically including designer's experience of the solutions in similar situations. This initial solution is then evaluated in the light of constraints or requirements. Further the requirements which are quantified into constraints at the first step of problem solving should simultaneously or concurrently take care of all the personnel who are a part of the design cycle. For that reason management, designer, manufacturing, assembly, marketing, shipping, after sales support people, and above all the customer need to be taken care of. An engineering solution is a failure which takes care of only the strength or stiffness

requirements of a problem. Mechanical engineering designers have also not been taking care of vibration requirements in many of the problems. A recent study of mechanical equipment esp. machine tools reveals that

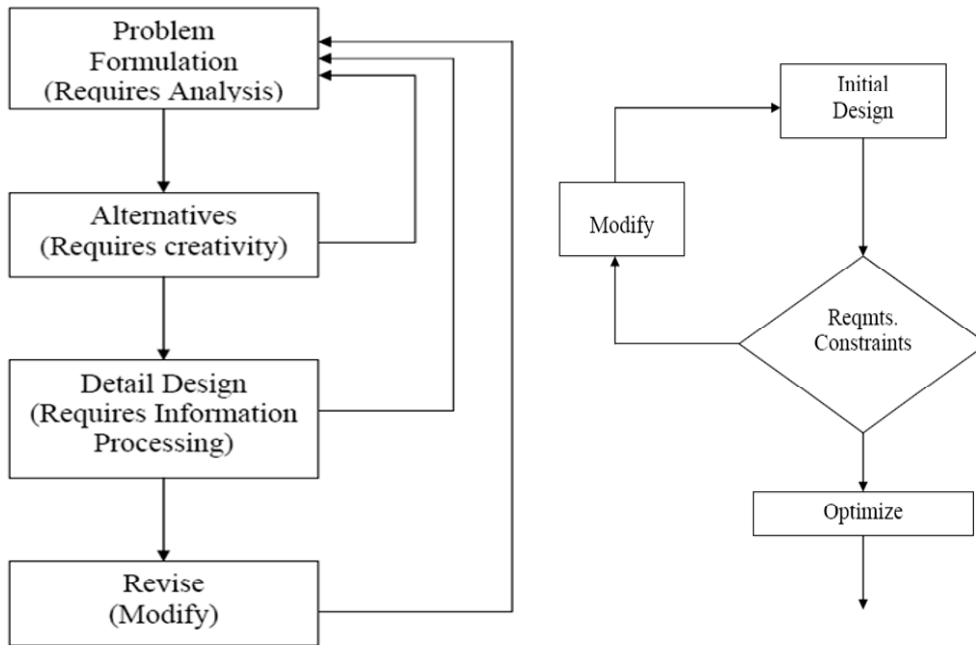


Figure7: 4 step problem solving or designing

Figure8: Steps in detailing of the third step of [figure7](#)

the designs are more than adequate and significantly away from being lean. The redundancy to a great extent is occurring due to uncertainties hitherto involved in the dynamic design. The uncertainties are always to be covered through higher factors of safety leading to over design. The solution lies in making younger minds, being trained to solve engineering problems especially in mechanical engineering, aware of the fact that vibration or dynamic design like fatigue design is of critical importance in all mechanical equipment. It is difficult to visualize any machine or mechanical equipment to be without vibrations due to inherent nature of moving parts and manufacturing tolerances. Resonance, unacceptable levels of vibration and dynamic instability must be prevented to avoid disasters and raise performance in terms of productivity, efficiency and accuracy of the equipment. In view of the foregoing discussion in view of the new economical dynamic design technologies and the need for concurrency or totality in problem solving it is possible to integrate dynamic design method like other methods to avoid failures into design process. For example one possibility to include the steps of dynamic design shown in [Figure6](#) can be integrated into the detail design step of [Figure7](#). A chapter on dynamic design like fatigue design need to be included into design text books. The curriculum in this case naturally demands vibration engineering to be taught before the design courses like mechanics of solids is taught before such a course as a prerequisite. Further the design courses need to emphasize the quantification of requirements into constraints so that feasible solution(s) can be found at detail design level shown in [Figure7](#). The feasible solution(s) can be optimized in the light of the universal objective of engineering namely the economy (combining cost & performance/quality). An example of a list of typically quantified constraints is given below:

Designer's Constraints [including some dynamic design constraints]: Principal stress or von Mises stress \leq Yield point strength or UTS/Factor of safety; Deflection of shaft \leq 0.005mm; Natural frequency \leq 2.5 times [or \geq 2.5 times] excitation frequency; Negative part of real receptance \leq acceptable limit to raise dynamic stability; Integral lighting \geq 500 lux; others.....

Management Constraints: Profits \geq 10%; Launch period \leq 3 months; others...

Customer Constraints: Cost≤\$200, Weight≤120N; Others...

Manufacturing and assembly: Number of components≤23; Wall thickness ≥5mm; others...

After Sales Support: Replacement time for a failed part ≤10 minutes; others

Others... like Constraints of State, of Shipping, of Marketing, of Industrial, International and national standards..

ACKNOWLEDGEMENTS

Several of the studies referred/ reported in this paper have been funded by DST- Govt of India including an ongoing one on Indo-German associated study on lean design of machine tools. The related research has been conducted with the help of co-researchers namely Prof B.C.Nakra, Prof P.V.Madhusudan Rao, Dr S.V.Modak and several PhD and M.Tech project students. The author wishes to record his gratitude for the support provided by the DST and the co-researchers.

REFERENCES

1. Budynas, R.G. and Nisbett, J.K., Shigley's Mechanical engineering Design, McGraw Hill, 2010.
2. Norton, R.L., Machine Design: An Integrated Approach, Prentice Hall, 2010.
3. Hamrock, B.J. et al., Fundamentals of Machine Elements, McGraw Hill, 2007.
4. Juvinall, R.C. and Marshek, K.M., Fundamentals of Machine Component Design, John Wiley, 2005.
5. Ewins, D.J., Modal Testing: Theory, Practice and Application, Research studies press, 2000
6. Friswell, M.I. and Mottershead J.E., Finite Element Model Updating in Structural Dynamics, Kluwer Academic Publishers, 1995.
7. Kundra, T.K. and Nakra, B.C. [Ed], Optimum Dynamic Design, Allied Publishers Ltd., 1997.
8. Kundra, T.K., "Structural Dynamic Modifications via models", Sadhana-the Indian Academy of Sciences proceedings in Engineering Sciences, 25(113), Vol 25 Part 3, June 2000, pp 261-276.
9. Modak, S.V., Kundra, T.K. and Nakra, B.C., Use of an updated finite element model for dynamic design, Mechanical Systems and Signal Processing, Vol.16, No.2, pp 303-322, March 2002.
10. Ewins, D.J. and M. Imregun, M., 1988 On the reliability of computational dynamic response prediction capabilities [DYNAS], Journal of the Society of Environmental engineers, Vol27-1 (Issue 116) pp 3-13, 1988.
11. Kundra, T.K., Vibration-designing of Machine Tools, Modern Machine Tools, pp 38-44, Jan. 2004.
12. MODENT: ICON Suite, 58 Prince's Gate, Exhibition Road, London SW7 PG, UK, [www.icats.co.uk], 2008R.
13. Bais, S., Gupta, A.K., Nakra, B.C., and Kundra, T.K., Studies in dynamic design of drilling machine using updated finite element models, Mechanism and Machine Theory 39(2004) 1307-1320.
14. Gondhalekar, A.C., Kundra, T.K. and Modak S.V., Dynamic Design of a Complex Automobile structure via Finite Element Updating, Proc. IMAC XXV conference held in Florida in Feb 2007
15. Gerhard Pahl, W. Beitz, Jörg Feldhusen, and Karl-Heinrich Grote., Engineering Design: A Systematic Approach, Springer, 2007
16. Haik, Y., Engineering Design Process, Thomson, Brooks/Cole, 2003
17. Dixon, J.R. and Poli, Corrado, Engineering Design and Design for Manufacturing, Field stone publishers, 1995
18. Arora, V., Singh, S.P., and Kundra, T.K., Comparative study of damped FE model updating methods, Mechanical Systems and Signal Processing, Volume 23, Issue 7, October 2009, Pages 1113-1219

Video Demonstrations to Enhance Learning of Mechanics of Materials Inside and Outside the Classroom

Michael Dietzler, Undergraduate Student, Engineering Mechanics Program,
University of Wisconsin – Madison
Wendy C. Crone, Professor, Department of Engineering Physics,
University of Wisconsin – Madison,
1500 Engineering Dr, Madison, WI 53706
crone@engr.wisc.edu

ABSTRACT

Using video to present demonstrations holds a significant number of advantages, particularly when class size or demonstration complexity prevents students from having hands on access. In video format delivered via the web, students have the capability to pause and repeat videos. Used in a classroom setting, the video provides the instructor more ease in set up and ensures high quality viewing in a large lecture hall forum. We have created videos of mechanics of materials demonstrations from a collection used in both introductory and advanced mechanics of materials courses. A wide range of topics are represented in the video collection, but three topics in particular (thermal effects, transverse shear in bending, combined loading) have been identified for use teaching where an assessment of learning outcomes can be measured.

Introduction

A host of introductory mechanics of materials textbooks now provide on line tools such as course organizers [1], tutorials [2], and virtual laboratories [3]. Interactive, animated exercises and review materials that give students immediate feedback about their work have also been developed by authors such as Philpot [4]. In order to provide a simple and technologically advanced approach for presenting visual demonstrations of concepts taught in a mechanics of materials course, we have developed and implemented video content using previously developed demonstrations, some of which are described in [5].

Demonstrations captured in video provide many advantages to the instructor and students in the learning environment by having concrete laboratory examples that can be referenced at any time without loss of experimental consistency. By creating these video demonstrations the data is guaranteed to be accurate and uniform every viewing. Because the goal of these demonstrations is ultimately for downloading via the internet, they are aimed to be, at maximum, three minutes in length. This target time limit is based on file size considerations for web-based dissemination [6]. This length is a reasonable target in most cases given that the demonstrations are not naturally long. In cases where it's necessary to exceed this time limit significantly, a series of demonstrations are best. Special considerations must be taken when creating these videos in order to make the process of downloading and viewing the end result as easy as possible. Outlined below are the main issues involved in creating the demonstrations, including the use of storyboarding concepts from well developed demonstrations, video capturing methods and hardware, software and editing methods, and output format.

Storyboarding

The first step in creating these video demonstrations is to develop an outline using storyboarding techniques. The components that are generated from a general storyboard include: an outline of all important aspects of the demonstration to be filmed, a feel for suitable physical interactions while handling the equipment during filming,

and confirmation on any measurable data to be discussed within the demonstration. We sought similar quality and length to the successful Nanoscale Science and Technology Video lab Manual developed by the University of Wisconsin - Madison MRSEC [6], so the procedure for storyboarding used in creating these mechanics of materials demonstrations most closely follows that format.

The experiments are first conducted prior to video-taping where equipment handling and measurements are optimized so that every aspect of the demonstration is shown in its best working order when video-taped. This process involves running through the experiment, sometimes more than once, while taking notes on measurements and key shots of the equipment during operational use. A smooth method for gathering good data from the equipment, an insight into what the experiment as a whole is to accomplish and how it will be done, and finally what aspects of the operational equipment will be pertinent for video-taping are sought.

Video Capturing Methods and Hardware

During videotaping, the capabilities and limitations of the video recording device must be well understood. The main considerations with the video recorder itself are the brightness and color settings. Not all cameras have these options, but if available they should be adjusted before recording. The speed at which the video recorder is set to record at is important as well, as some mini DV tape decks, especially high end ones, only capture tapes recorded in LP mode.

The outline from the storyboarding exercise may need to be modified to accommodate the limitations of the equipment, space, and editing software. The main goal during the recording process with the storyboards is to allow a flow of clips to be made quickly and in the proper order that the experiment requires. Where possible it is desirable to have a constant running video while the equipment is being modified or measured. This technique provides a better viewer experience and limits the number of fade in/out transitions needed during editing, because transitions can have a significant impact on video file size. It is also helpful to have options for scenes while editing, so recording important scenes more than once is wise.

The video camera in use for creation of the mechanics of materials demonstrations discussed below was a Sony DCR-HC85 model. Videotaping these lab experiments requires that the video camera be mounted to a tri-pod with at least one, ideally two, stage lights that are also mounted to tri-pods. Ambient lighting conditions cannot be used to create quality demonstrations. One must be able to control the lighting effects within the demonstration so shadows can be lightened or removed and a near-constant illumination of all equipment can be attained. To accommodate the desire to outline the equipment and experiment at hand and take advantage of file compression routines, a chroma-key, or blue screen, is necessary as well. Since no audio is used in these demonstrations, audio capturing equipment is not a concern as the audio tracks were deleted in the editing process. The video camera utilizes mini DV tapes that are sixty minutes long. These mini DV tapes are captured to a hard drive via a tape deck to a computer capable of connecting through a firewire connection.

Computer Hardware, Software and Editing Methods

The computer hardware required for effective means of editing work to be done is based on the minimum system requirements to run the editing and video compression software. A variety of options are available for editing video, and in this case the facilities of the University of Wisconsin - Madison Digital Media Lab were employed. The editing software used was Sony Vegas Pro version 8 and the video compression software was Sorensen Squeeze version 5. In order to properly capture the mini DV tapes to a computer or external hard drive, a firewire connection is necessary with a minimum of 1 GB of RAM in the computer hardware. This reduces the likelihood of losing or corrupting the data for the video clips during the capturing process.

In producing these demonstrations for use to download online, an optimum approach to creating a file that will be easily downloaded and viewed by anyone with an internet connection speed comparable to DSL or higher was sought [6]. It was decided that in order to have the demonstrations viewed on a Mac or PC platform, they needed to be in a format compatible with both Windows Media Player and Apples' iTunes QuickTime Player. This format is MPEG-4 with the .mp4 extension. It allows for a good quality video to be viewed on both platforms while keeping the file size small and is capable of delivering media at any data rate.

Components of the demonstrations that are implemented during editing include the use of text along with black pointing arrows and occasional figures imported from Adobe Illustrator or Photoshop as .png files. The text, coupled with arrows and figures, helps to explain the important concepts and steps of the demonstration being shown. Examples of some of these components are shown in Figures 1 and 2 from the “Transverse Shear” and “Temperature Effects” demonstrations, respectively. Note the use of a plain black arrow and white text to provide a clear visual distinction between equipment and these explanation components. Also note the constant color of the background via use of a chroma-key backdrop.



Figure 1: Use of text and box outline highlights an important aspect of this portion of the “Transverse Shear” demonstration.



Figure 2: Use of black arrow with text and blue chroma-key background. This image shows the beginning of the demonstration where the equipment is defined.

Other aspects of the editing process include outlining collection of data from lab equipment and placement of thought provoking questions, as shown in Figures 3 and 4 from the “Temperature Effects” demonstration. While collecting data it is optimal to create a constant running scene without having to stop the experiment and start again from a second take. However, when editing these long scenes it’s necessary to cut them between segments of uneventful activity then paste them back together, so the same experimental trial is being shown while skipping the unimportant segments. This strategy was used extensively in the “Temperature Effects” demonstration while the temperature is being measured along with the deflection of the cooling bimetallic strip.



Figure 1: An image during data collection of temperature vs. deflection of the bimetallic strip is shown here.

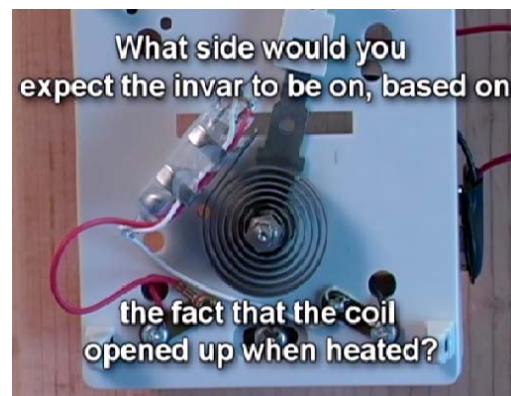


Figure 2: Thought provoking question used in the final scene of the “Temperature Effects” demonstration.

The files produced by video editing are not rendered in .mp4 format using Sony Vegas Pro 8, as the compressor built in to the editing software is not an optimum one. Instead the videos are rendered in full .avi format, which

keeps the quality of the video high. These .avi files are then compressed by a separate program, Sorensen Squeeze, to the .mp4 format where the file size drops from around 250MB to an average 15MB. These 15MB videos are easily downloaded even with a DSL connection, approximately 1 minute on average. The link to a site where a free player can be downloaded is made available for users on the same page as the demonstrations.

Example of Demonstration Use in Teaching Mechanics of Materials

The first method of using these demonstrations is in a classroom setting with a computer-projector set-up. The demonstrations can be downloaded prior to the start of class for confirmation that the file will play with the video player. In this case of use, the instructor can provide supplementary explanation of equipment and demonstration goals along with the text provided in the demonstration. Data provided in the demonstration can also be utilized in class as a reliable example exercise. This ultimately gives the student an opportunity to clearly view the demonstration, hear an explanation from the instructor integrated within the lecture setting, and utilize the data shown with the appropriate model being covered in the topic discussion.

A second method of use is through assigning the video demonstrations as a homework exercise. In this case the demonstration can be downloaded and viewed at the students' leisure to supplement the material covered in their textbook and in class experiences. In cases where data is collected, the student can apply it to the mathematical models developed on the topic and compare measured values with calculated solutions to help prove the underlying model and test the experimental accuracy. This method provides students with complete lab demonstration visualizations and data manipulation without having to set-up the experiment and measure data for every student or group of students in a class. It is not meant to replace the component of hands on experimental procedures for undergraduate engineering students, however it can expand their exposure to a broader range of opportunities to make connections between theory and experiment.

The third method deals with the compatibility of these demonstrations with online course delivery used in distance and asynchronous learning. These demonstrations can be used as described in the previous section as one component of an online lesson. Although they were originally constructed with no audio to keep them as flexible as possible in their ultimate use, an audio track can be overlaid with a variety of methods. This has been successfully accomplished with Camtasia, a screen and audio capture software that can be used to create a variety of file types. In addition examples can be worked right next to the video from the data collected in the demonstration.

Evaluation Results

These videos have been used as part of an introductory "Mechanics of Materials" course taught at the University of Wisconsin – Madison with all three methods described in the previous section. In the case of the "Temperature Effects" and "Transverse Shear" video demonstrations described above, the videos were incorporated within an online lessons composed of five to seven segments ranging in length from 2 to 12 minutes. The "Temperature Effect" demonstration was supplied without an audio track, whereas the "Transverse Shear" demonstration was presented with an audio overlay narrating the demonstration. The lessons were created for students to view outside of class time in preparation for special in class active learning experiences.

A quiz based on the online content encouraged completion of the lesson prior to class. After the quiz the students were asked to complete a brief questionnaire evaluating the lesson content and delivery. Students were asked to rate the usefulness of the content in each lesson component on a scale that ranged from -1 to 4 point scale, where -1 = Unable to access, 0 = Chose not to access, 1 = Not at All Useful, 2 = Somewhat Useful, 3 = Useful, 4= Very Useful. [Figure 5](#) and [6](#) show the survey results obtained from the surveys presented in Weeks 3 and 7 of the Spring 2010 semester of EMA 303 "Mechanics of Materials". The main difference between these two videos was the creation of an audio track for the "Transverse Shear" video. This is likely to account for the significantly higher ratings this video received.

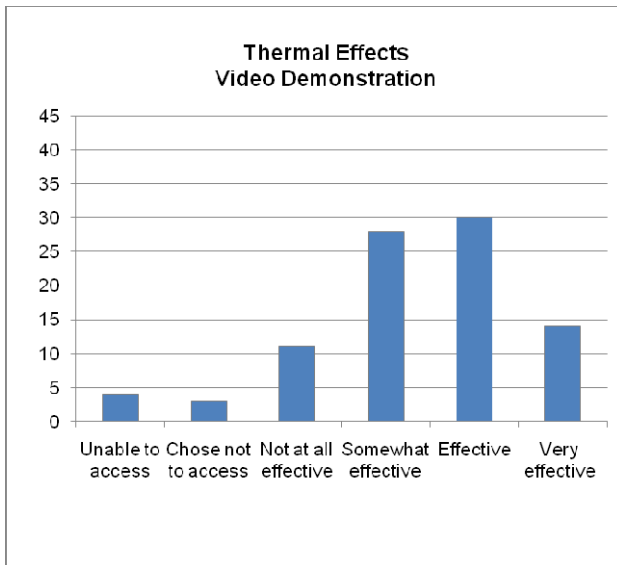


Figure 5: Survey results for the “Temperature Effects” video used in a preclass assignment in Week 3 of Spring 2010.

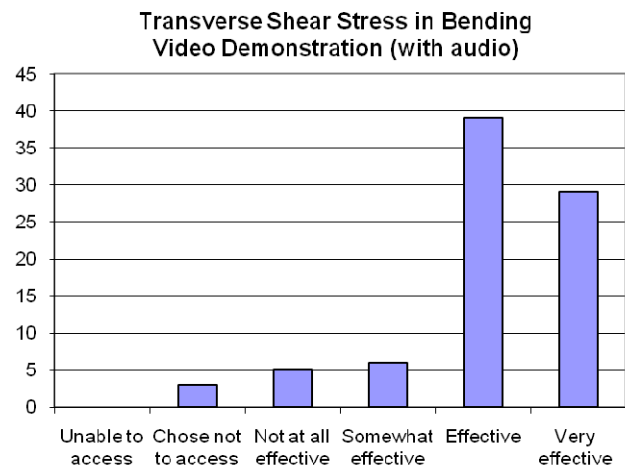


Figure 6: Survey results for the “Transverse Shear” video used in a preclass assignment in Week 7 of Spring 2010.

Conclusion

The use of video demonstrations to supplement other content in a course such as mechanics of materials has advantages for both the instructor and student. The instructor has a higher level of assurance that the demonstration will work successfully every time and can implement the demonstration in a wider range of ways. The ultimate goal is to enhance student learning of the content by providing a range of delivery methods and giving the student the control to stop, rewind, and replay a demonstration to meet their own learning pace.

Acknowledgements

This work was supported by the University of Wisconsin – Madison College of Engineering through a *COE 2010: Transforming Undergraduate Education in the College of Engineering 09-10* grant. We would also like to thank the staff of the University of Wisconsin - Madison Digital Media Lab for their advice on editing techniques and Barbara Calcagno for tabulation of the evaluation results.

References

- 1 Course Compass associated with Hibbeler, R. C. (2008). *Mechanics of Materials* (7th ed.). Upper Saddle River: Pearson/Prentice Hall. <http://www.pearsonhighered.com/educator/product/Mechanics-of-Materials/9780132209915.page>
- 2 S.M.A.R.T tutorial associated with Beer, F. P., Johnston, Jr, E., DeWolf, J. T., & Mazurek, D. F. (2009). *Mechanics of Materials* (5th ed.). New York: McGraw-Hill: http://highered.mcgraw-hill.com/sites/0072980907/information_center_view0/s_m_a_r_t_tutorial_sample.html
- 3 Virtual labs associated with Jenkins, C. H., & Khanna, S. K. (2005). *Mechanics of Materials*. Burlington, MA: Elsevier. <http://www1.us.elsevierhealth.com/books.elsevier/companionsites/JenkinsKhanna/index.html>
- 4 MecMovies associated with Philpot, T. A. (2008). *Mechanics of Materials: An Integrated Learning System*. Hoboken, NJ: John Wiley and Sons. <http://web.mst.edu/~mecmovie/>

- 5 W. C. Crone (2002) "Using an Advanced Mechanics of Materials Design Project to Enhance Learning in an Introductory Mechanics of Materials Course," *ASEE Annual Conference and Exposition Proceedings*, 2268, 1-7.
- 6 George G. Lisensky, K. Lux, and W.C. Crone "A Web-based Video Lab Manual for Nanoscale Science and Technology," in *Nanoscale Science and Engineering Education: Issues, Trends and Future Directions*, Aldrin E. Sweeney and Sudipta Seal, Editors, American Scientific Publishers (2008).

Experimentation and Product-making Workshop Simplified for Easy Execution in Classroom

Tsuyoshi NAKAZAWA¹, Masaaki MATSUBARA², Sumiyoshi MITA³, Katuo SAITOU²

¹ Faculty of Engineering, Gunma University, 1-5-1 Tenjincho, Kiryu, Gunma, Japan
e-mail: nakaza-t@gunma-u.ac.jp

² Graduate School of Engineering, Gunma University, 1-5-1 Tenjincho, Kiryu, Gunma, Japan

³ Faculty of Education, Gunma University, 4-2 Aramaki, Maebashi, Gunma, Japan

Abstract

In this study, we introduced the students to experimenting with and manufacturing of real products. The products are a "Model Car" and a "Walking Model." With this specific objective and using no special equipment, students can learn and utilize mechanics which is one of the fundamental discipline in engineering. We introduced these two products in a lecture format and evaluated the effectiveness of the learning process. Results of the evaluation administered before and after the class showed that the students obtained a greater understanding of mechanics by using the two products. A resulting concept map and survey questionnaire showed that the students had improved their ability to apply scientific knowledge through their practical experiences in experimental and manufacturing processes. Moreover, detailed analyses including factor analysis suggest an improvement in the students' confidence in their scientific knowledge and activities in product making.

Introduction

Creativity in science and technology is promoted in Japan as a national policy due to her scarcity in natural resources, and an extremely dense population. Therefore, engineering education is extremely important for the future of Japan. A problem of the Japanese engineering education is that the students do not have sufficient opportunities to learn actively through real experiences of experimental and manufacturing processes. Their knowledge are increasingly derived from lectures given within an overcrowded schedule. The scientific literacy of Japanese students is decreasing according to an international academic ability survey, results, such as those of the Program for International Students Assessment (OECD's PISA). That in some fields is not good when compared with results from other OECD countries. Moreover, a survey of engineering education at the university level described the education with too many lecture classes. Therefore, students have not obtained a sufficient chance to touch and think about practical subjects. Opportunities to use practical ability to apply knowledge are few [1]. A new educational approach is thus required to alter this current state.

Originally, we have been able to acquire technological knowledge through a repeatable spiral cycle comprising of four processes: concrete experience, abstract conceptualization, reflective observation, and active experimentation [2]. Especially, university students, who have already finished learning basic knowledge, should not only acquire knowledge but also build a basis of intellectual creativity. The students can effectively acquire such basic ability, by conducting experiments to support the study of an actual phenomenon and grapple with the problem. Therefore, we inferred the following: when the students try to complete a product with a target performance, they must perform experiments, consider a problem by using the scientific knowledge learned in the lectures, and use a trial-and-error method to arrive at the optimal product. Through such activities, students will acquire engineering knowledge with an improved ability to apply the knowledge. In this study, we develop two teaching procedures to support such learning activities.

Specifically, we produce the following two teaching materials: a "Model Car" and a "Walking Model." Using those two

teaching materials, students can learn mechanics, which is an important basic discipline in engineering. Using the model car, the students can learn “statics,” such as static equilibrium. Using the walking model, the students can learn “kinetics,” such as oscillation. For this study, we introduce two developed teaching materials into the class intended for the first-year students at Gunma University.

The intentions of using these two teaching materials are three. The first objective is to make the students firmly understand mechanics related to the teaching materials. As previously stated, the students have received much knowledge from the lectures but with few opportunities to use that knowledge in real experience. Therefore, as the second objective, we strive to improve the students’ abilities and innovative mind to apply the knowledge of mechanics by using the experimental and design capability with teaching materials. Moreover, we want students, after using the teaching materials, to associate independently various design with real activity including the manufacturing process. Consequently, as the third objective, we seek to improve the students’ confidence in their scientific knowledge and real activities such as product making through the use of our teaching materials.

To date, high costs and labor were necessary when we tried to establish such classes. For instance, we had to prepare special equipment and had to arrange an instructor to guide the use of the equipment according to the number of students. Additionally, we had to adjust the equipment before the class and put it back in order after the class. With this learning exercise, we tried to remove such load. Using the developed teaching materials, students conducted experiments and produced these teaching materials in the classroom without using any special equipment. We introduced to the class for the freshman of Gunma University the developed teaching materials and evaluated their learning process with these teaching materials in this class. In the following, we describe specific contents of the developed teaching materials and a teaching plan of class with these teaching materials.

“MODEL CAR” TEACHING MATERIAL

We developed the model car shown in Fig. 1 as a teaching material. Students were able to learn basic mechanics of statics through the experiment. Students are interested in automobiles and the mechanisms involved through driving. They need to acquire more knowledge and perform the experiments related to the technology for designing automobiles. Students can easily produce this model car using light tools such as a screwdriver. The main design subject was the transmission of mechanical power. A model car that can raise a 150-g mass is the assigned design subject. This design includes knowledge of mechanics and technology, including force, moment of force, friction, center of gravity, motors, and gears.

The main points for the students’ consideration are the following two.

- (1) Decide the design of the reduction gear necessary to raise a mass when the power of the motor is known.
- (2) Obtain the frictional force between the model car’s tire and the road to raise the mass,

Next, we explain these two subjects in detail.

(1) REDUCTION GEAR DESIGN

For the model car to defy gravity and to raise a 150-g mass, students must consider the design of a reduction gear. With sufficient gear reduction, the force of the tire is expected to be adequate to raise the mass. We assembled a transmission of a model gear box (No.93; Tamiya Inc.) and two brass gear wheels in the model. The students can

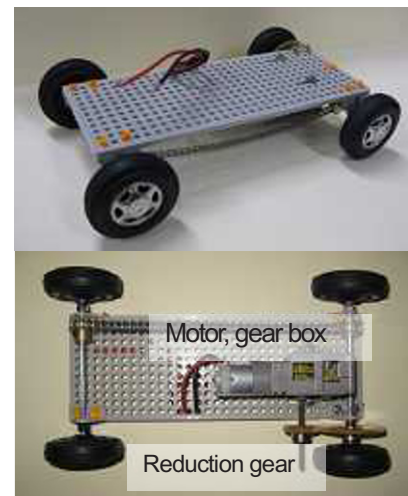


Fig. 1 A model car.

Table 1 Learning contents of “design of reduction gear.”

Contents the student should consider	Instructional elements
Gravity on the mass	Force, Gravity, Law of reciprocal actions
Power of motor	Electric power, rotational frequency, Torque, Power
Reduction gear	Work, Energy, Power transmission, Moment, Equilibrium
Force generated by tire	Work, Torque, Force

change the combination of two brass gear wheels. The students are given the power of the motor (RE-130; Mabuchi Motor Co., Ltd.) for this model car. The students obtained the desired force and experiment for raising a mass through various combinations of the gear wheels. Through such activity, students learn about the transmission of power by a gear wheel. Table 1 shows the summarized contents of the mechanics that the students considered in this process along with instructional elements of related mechanics.

(2) FRICTION BETWEEN THE TIRE AND THE ROAD

Sufficient force does not act on the road and tire if the model car's tire slips. In this case, even if the tire generates sufficient force, the model car cannot raise the mass. To raise the mass, the frictional force between the tire and road must be greater than gravity on the mass.

First, students should investigate the frictional properties of the tire and the road. Furthermore, the students should consider how much body weight is necessary to obtain a sufficient frictional force. In this model, two-wheel drive and a four-wheel drive are switched easily so the students can consider the working frictional force for each drive system. Especially for the two-wheel drive, the frictional force of the propulsion wheel between the road changes greatly depending on the body's center of mass. Students should consider which position of the center of mass is necessary for raising the mass.

The students repeat the experiment and design change to obtain the frictional force sufficient to raise the mass. The students can change the weight and the center of the body mass by adding mass to the body. In addition, the students can switch the model car's drive system. Students can conduct experiments under various conditions. By repeating the experiment and design, students can learn the mechanics which includes the law of reciprocal action.

Table 2 summarizes the contents of the mechanics that the students consider in this process and the instructional elements of mechanics that relate to the design.

Table 2 Learning contents of "friction between tire and road."

Content that students should consider	Instructional elements
Frictional force between tire and road	Gravity, Friction, Normal force
Center of mass for model car	Center of mass, Equilibrium of Moment
Normal force of propulsion wheel	Gravity, Law of reciprocal actions Equilibrium of Moment
Friction force between road and model car	Gravity, friction, law of reciprocal actions

TEACHING PLAN FOR THE CLASS INTRODUCING THE MODEL CAR

First-year students of Gunma University attended the class which included the production of this model car. Table 3 presents a teaching plan for this class.

First, students received an explanation of the class and assembled a trial model car. Through this process, students became interested in the model car and understood the class objective.

Next, the students studied statics as a preparation for designing the model cars. This lesson has a lecture which includes observations of the experiment. In addition, the students can effectively learn through conceptual mapping using the KJ method in this process [3].

Later, the students are assigned a specific design subject which is "a model car which can raise the mass of 150 g." The students consider it through experimentation related to the center of the mass position and transmission.

Subsequently, students choose the design of a model car. In this process, they experiment and study it in the form of group learning. Exchanging opinions with classmates improves their understanding.

Finally, the students produce the model car, and confirm whether the model car can raise the mass of 150 g in the experiment. Students can experience the results of their

Table 3 Flow chart of this class.

1. Introduction	Outline explanation, Assembling teaching materials as introduction
2. Lecture	Lecture about mechanics, Review of high school physics, Explanation of progressive content
3. Experiment (design)	Consideration and experiment for concrete target, Design of teaching materials, Exchange opinions with other students
4. Production performance test	Produce teaching material, Performance test of teaching material

experiment and design consideration through this performance test. Students also compose a report explaining the design, which brings the results together.

EVALUATION OF THE LEARNING PROCESS WITH THE MODEL CAR

We evaluated this learning process of 25 students who attended the class. Students executed achievement tests before and after the class. All students had learned physics in high school. The students took the achievement test before this class (pre-test), and took the achievement test after the end of the class (post-test). The purpose of the achievement test was to measure the students' level of understanding of statics related to the model car. This achievement test has 13 questions. The test contents are about statics that relate to the model car shown in Tables 1 and 2. The questions are different, but the contents are the same in the pre-test and post-test.

Table 4 Results of achievement tests about model cars.

	Average accuracy rate	Standard deviation	Significance level
Pre-test	50.8	17.7	p<0.01
Post-test	77.5	16.6	

Table 4 presents results of the achievement test. The accuracy rate of the post-test is higher than that of the pre-test. We compared the accuracy rate using a paired t-test, and obtained a statistical significance for p<0.05. This result shows improvement in the students understanding of statics through this learning process.

“WALKING MODEL” TEACHING MATERIALS

We developed the “Walking Model” as another teaching material. Students can learn about oscillation, which is the basis of kinetics, through the use of this teaching material. Figure 2 presents one example of the walking model that students produced. Parts of this model are fabricated with paper and resin, which are commercially available. The student can produce this walking model in the classroom using light tools. The model walks on a slope by oscillation of the body. The walking cycle changes concomitantly with the period of oscillation in the body. The students can learn oscillation as an important basis of engineering through experimentation and design of the walking model.

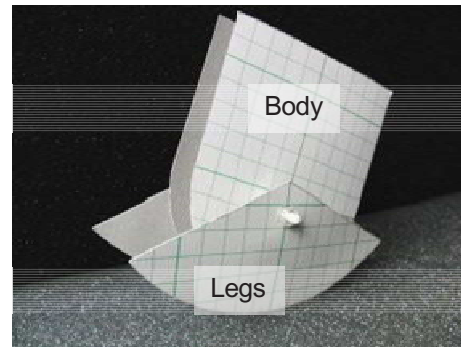


Fig. 2 A walking model.

The body oscillation, which is the basis of the operation of this walking model, is shown in Fig. 3. The period of oscillation of this model T [s] can be expressed using the equation below. The author confirmed that this equation relates well with the result of the experiment [4]. In the equation below, k [m] is the radius of gyration, g [m/s²] is the gravitational acceleration, R [m] is the radius of the bottom circular arc, and ℓ [m] is the distance of the grounding point and center of mass when standing upright.

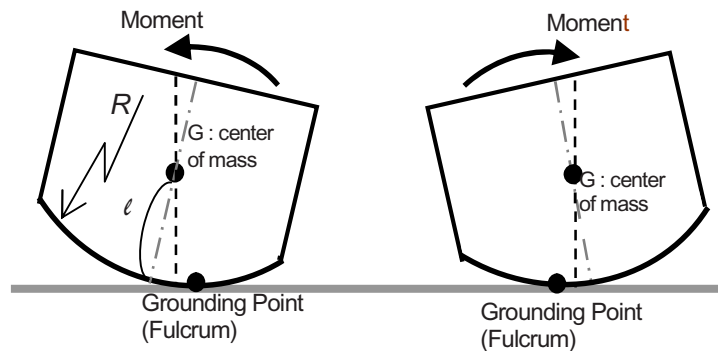


Fig. 3 Waving model.

$$T = 2\pi \sqrt{\frac{(\ell^2 + k^2)}{g(R - \ell)}}$$

When we regard the oscillation of the walking model as a physical pendulum for which the center of mass oscillates about a grounding point, we note that this equation is equivalent to the equation showing the cycle of a physical pendulum, with the exception for the quantity in the parentheses of the denominator in the square root. The students conducted experiments on a simple waving model and confirmed the change of waving model's cycle. As a result,

the students considered where to install two heavy masses in the light walking model.

In addition, as the students designed and produced the walking model, students applied the basic kinetic theory including the learned physical

pendulum to the walking model. Through such activity, students improved their basic knowledge of the oscillation and their ability to apply this knowledge. Students can confirm from the experiment that the walking cycle changes as the position of the mass changes. Moreover, the students can consider the cause by applying the knowledge related to the position of the center of mass and the moment of inertia. Table 5 presents contents that can be learned in relation to the walking model. The Walking model's cycle is shown in Fig. 4 as a concept map [5].

Table 5 Learning contents of "Walking Model."

Content that students study	Instructional elements
Height of center of mass of walking model	Center of mass, Moment, Equilibrium
Radius of gyration of walking model	Rotation of a rigid body, Angular velocity, Moment of inertia
Walking cycle of walking model	Harmonic oscillation, physical pendulum

TEACHING PLAN AND EVALUATION OF THE LEARNING PROCESS OF A WALKING MODEL

We introduced this walking model into the same class as the model car. Table 3 is a teaching plan for using a walking model also. We evaluated the learning process of the walking model using an achievement test and the concept map. We evaluated this learning process for the same 25 students as those who produced the model car. The evaluation is described as follows.

(1) ACHIEVEMENT TEST

We evaluated the learning process using the pre-test and post-test. This achievement test has 10 questions. The contents of the test are kinetics, specifically oscillation related to the walking mode. The questions in the pre-test and post-test differ, although the contents are the same. Table 6 shows results of the achievement test. The accuracy rate of the post-test is higher than that of the pre-test. We compared the accuracy rate using the paired *t*-test, and confirmed the statistical significance ($p < 0.01$).

Table 6 Results of achievement test about walking model.

	Average accuracy rate	Standard deviation	Significance level
Pre-test	62.4	14.2	$p < 0.01$
Post-test	84.4	13.3	

Regarding the result described above, the understanding of kinetics (oscillation) was improved through this class using this walking model teaching material.

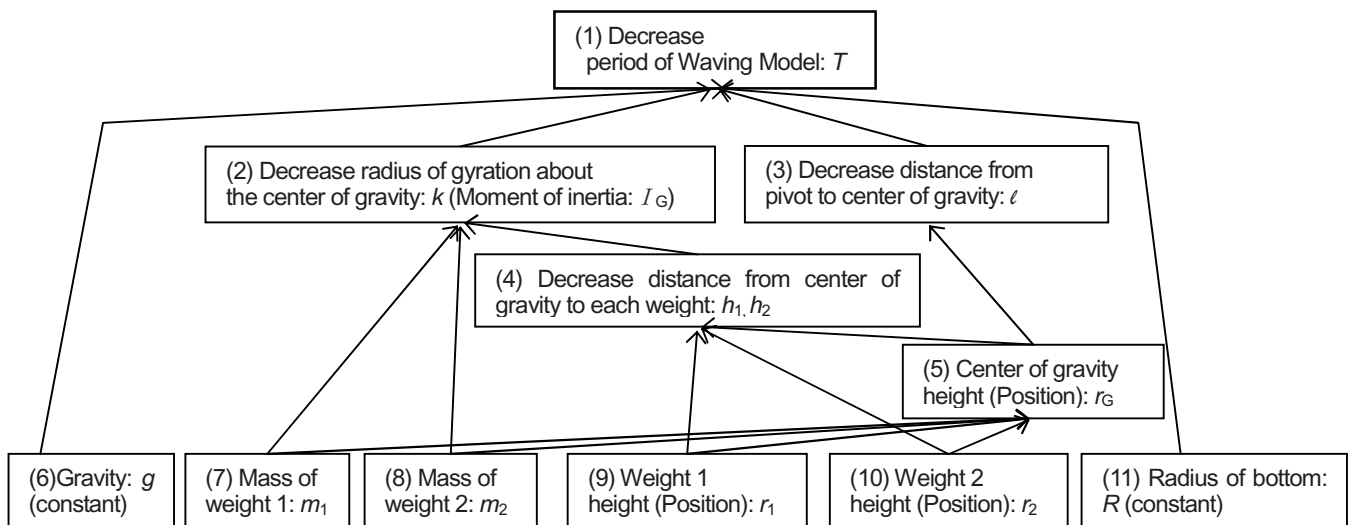


Fig. 4 Concept map for students' study (Effect of two weights in waving and walking).

(2) CONCEPT MAP

The students drew up the concept map shown in Fig. 4 during the lesson. Students tied each element text in a rectangle with a directional line. The students can sort their thoughts by drawing up the concept map. In addition, the teacher can understand whether the students can apply their learned knowledge correctly from the concept map that is drawn up. We used the ratio of the correct line shown in the equation below.

$$\text{Ratio of the correct lines} = \frac{\text{Number of (student's) correct lines}}{\text{Total of correct lines}} \times 100[\%]$$

The concept map was drawn up three times in all. The first time is after "2. The lecture" in Table 3, the second time is after "3. Experiment (design)", the third time is after "4. Production, Performance test ." Table 7 presents the total result of the concept map that the students drew up.

Table 7 shows that students were able to draw up the map correctly through their experience of the experiment, the production and the performance test. We confirmed the statistical significance at each ratio of correct line. The result described above shows that students came to use the knowledge correctly through their experience of the experiment, production, and the performance test. We were able to confirm that the students had improved their ability to apply knowledge from the concept map.

Table 7 Ratio of correct lines of student concept maps.

	Ratio of correct line	Standard deviation	Significance level
First time	30.1	31.3	$p < 0.01$
Second time	62.4	34.6	
Third time	72.0	27.9	$p < 0.05$

QUESTIONNAIRE SURVEY

Students answered the questionnaire survey before and after this class of the model car and the walking model. This questionnaire survey was intended to clarify the students' perception of how their application of knowledge changed. This questionnaire survey is based on research for scientific literacy [6]. The students evaluate themselves using each question. Questionnaire survey scores were determined according to a five-point scale by which one

Table 8 Contents of questionnaire survey.

Q1	When there are questions that you do not know the answer to or which are necessary for life, do you usually investigate it soon?
Q2	Do you want to investigate topics in the news in society?
Q3	Do you often visit museums, science pavilions, and courses open to the public?
Q4	Can you solve problems well through discussion with others?
Q5	Do you want to participate in evaluation activities of science and technology as adults?
Q6	Are you good at repairing broken items?
Q7	Do you want to buy or receive electrical appliances that used a new science and technology immediately?
Q8	Can you master the use of new electric equipment quickly?
Q9	Do you like product making (including cooking, gardening, and handicrafts)?
Q10	Is your knowledge of science and technology abundant?
Q11	Are you good at imagining a solid from a projection?
Q12	Are you good at grasping the points of long sentences and lectures?
Q13	Are you good at thinking theoretically?
Q14	Are you good at grasping common features of things?

point was given for "No" and five points for "Yes." Table 8 shows the question contents. The questions are 14 items. Some questions show a strong ceiling effect or floor effect. However, we judged that as acceptable.

The result of the questionnaire survey is presented in Table 9. In the post-survey, the mean value of the answer rose compared with the pre-survey. The statistical significance in the mean value of the survey was ($p < 0.01$). This result shows improved students skill in their application of scientific knowledge.

In addition, we tried to clarify why some answers to questions changed remarkably. Therefore, we assessed the statistical significance of the mean value of an

Table 9 Result of questionnaire survey.

	Mean value of answer	Standard deviation	Significance level
Pre-survey	3.07	0.607	$p < 0.01$
Post-survey	3.36	0.570	

answer for each question in Table 8 for the pre-survey and post-survey. The mean value of answers in four questions showed statistical significance: question 10 related to richness of knowledge ($p < 0.01$); question 5 related to participation in science evaluation ($p < 0.05$); question 6 related to work such as repair ($p < 0.05$); question 11 related to the ability to read drawings ($p < 0.05$). In every one of the four questions, the mean value of the post-survey answers is higher than that of the pre-survey answer. This result suggests the following: through this class, students came to have greater confidence in their knowledge of science; they came to take a positive stance toward science; and they improve their confidence in real activities such as repairing and reading drawings.

To evaluate the changes in the aptitude of the students in greater detail, we conducted a factor analysis of 14 measurement items presented in Table 8 using the Principal Factor Promax Rotation. Table 10 shows the factor analysis of the pre-survey. Table 11 shows the factor analysis of the post-survey. We thought that three factors were appropriate in both factor analyses based on the change in the eigenvalue. The cumulative contribution at the third principal component was about 65.0% in the pre-survey and 68.9% in the post-survey.

Tables 10 and 11 show the items that composed each factor and factor loadings. Questions that composed each factor are the same in Tables 10 and 11, but the factor loadings differ. Tables 10 and 11 present that factor loadings of "6. Repairing" and "11. Reading drawings" are higher as the first factors of the post-survey. These questions are related to the confidence in the actual product-making activities and showed individual statistical significance. Differences in the first factor suggest that students, who were interested in product making before the class, improve their confidence in the actual product making.

We named each factor based on the item with high factor loadings. Then we summarized the factors in the pre-survey and post-survey in Table 12. We added Cronbach's α values as indicators of internal consistency.

We can summarize the contents described above as follows. Table 9 shows that the class which introduced our teaching

Table 10 Pattern matrix of factors in the pre-survey.

Content of Item		I	II	III
9	Preference to product making	0.823	0.051	-0.129
3	Visiting the museum	0.797	-0.137	0.167
11	Good at reading drawings	0.732	-0.169	0.145
6	Good at repairs	0.609	0.401	-0.039
5	Intention to participate in evaluation of science	0.500	0.389	-0.008
4	Good at discussion	0.458	0.231	0.05
2	Investigating news	-0.229	0.818	0.359
8	Good at using equipment	0.048	0.719	-0.072
1	Investigating usual questions	0.041	0.650	0.430
7	Interest in new products	0.023	0.620	-0.500
10	Confidence of science knowledge	0.088	0.423	-0.134
13	Good at thinking logically	0.062	-0.225	0.945
12	Good at grasping points	0.250	-0.034	0.607
14	Cognitive ability	-0.111	0.308	0.492
Corr. Coeff.		I	II	III
		I	—	0.331
		II	—	0.098
		III	—	—

Table 11 Pattern matrix of factors in the post-survey.

Content of Item		I	II	III
6	Good at repairs	0.878	-0.067	-0.037
11	Good at reading drawings	0.863	-0.051	-0.323
4	Good at discussion	0.691	0.268	0.027
3	Visiting the museum	0.665	-0.155	0.251
9	Preference for product making	0.615	0.185	-0.103
5	Intention to participate in evaluation of science	0.561	0.037	0.123
7	Interest in new products	-0.206	0.839	-0.406
8	Good at using equipment	-0.022	0.740	0.284
10	Confidence of science knowledge	0.073	0.727	-0.063
2	Investigating news	0.103	0.651	0.181
1	Investigating usual questions	0.207	0.560	0.252
13	Good at thinking logically	-0.327	0.048	0.973
12	Good at grasping points	0.191	-0.074	0.809
14	Cognitive ability	0.011	0.090	0.619
Corr. Coeff.		I	II	III
		I	—	0.323
		II	—	0.237
		III	—	—

Table 12 Results of factor analysis.

Pre-survey	
First Factor ($\alpha=0.857$)	Interest in product making, Active participation
Second Factor ($\alpha=0.751$)	Investigation and Proof
Third Factor ($\alpha=0.724$)	Logical understanding
Post-survey	
First Factor ($\alpha=0.850$)	Confidence in product making, Active participation
Second Factor ($\alpha=0.815$)	Scientific investigation and Proof
Third Factor ($\alpha=0.814$)	Logical understanding

materials improved students' aptitude to apply scientific knowledge. Moreover, results of factor analysis and statistical significance of each item suggest that improvement in student confidence for doing real activities, such as repairing and reading drawings.

CONCLUSION

We summarize the results of this study as follows.

We developed two teaching materials: "Model Car" and "Walking Model." These teaching materials enabled students to learn mechanics through experiment and producing items in the classroom.

We introduced these two teaching materials in a lecture course and evaluated the learning process and its outcomes. The results of the evaluation tests showed that improvement in the student understanding of mechanics through this class. The results of the concept map and questionnaire survey showed that the students had improved their ability and aptitude to apply scientific knowledge. In addition, the results of the detailed analysis and the factor analysis suggest that the students improved their confidence in their scientific knowledge and real activities such as product making.

REFERENCES

- [1] Kougaku kyouiku renraku iinkai (Japan National Committee for Engineering Education), Science Council of Japan "Global jidai ni okeru kougaku kyouiku (Engineering Education in the Global Age), "*Kougaku kyouiku renraku iinkai houkoku (Report from Japan National Committee for Engineering Education)*. (2000).
- [2] Kolb, D.A., *Experimental Learning*, PTR Prentice Hall, (1984).
- [3] Kawakita, J., *Hassou Hou (Conceiving Method)*, Tyuou Kouron Sya, (1967).
- [4] Nakazawa, T., Mita, S., "Development of a Walking Model for Teaching Material and Application to Mechanical Engineering Introductory Education", *Journal of Japanese Society for Engineering Education*, vol. 55, No. 2, pp. 230-236, (2007).
- [5] Sato, T., *ISM kouzou gakusyuu hou (ISM Structural Learning Method)*, Meiji Tosyo Syuppan, (1987).
- [6] Kawamoto, S., Nakayama, M., Saijo, M., "A Questionnaire Designed for Proposing an Educational Program by Literacy Cluster," *Japanese Journal of Science Communication*, vol. 3, pp. 40-60, (2008).

Illustrating Essentials of Experimental Stress Analysis Using a U -Shaped Beam

Mark E. Tuttle, Professor and Chair
Department of Mechanical Engineering
University of Washington
Seattle, WA 98195
tuttle@uw.edu

Abstract

A graduate-level homework assignment and follow-on laboratory experiment involving a flat U -shaped specimen is described. The base of the U can be considered a curved beam. The specimen is loaded such that a known bending moment M and shear force V are applied to the curved beam. Closed-form elasticity solutions exist for these two loading conditions. The homework assignment is to superimpose these two solutions and plot the in-plane principal stresses and orientation angle of the principal stress coordinate system along a specified radial line within the curved section. During the follow-on lab experiment an aluminum U -shaped beam is instrumented with several 3-element strain gage rosettes along the specified radial line. The rosettes are used to measure principal strains and orientation of the principal strain coordinate system. The corresponding principal stresses are then calculated using the plane stress form of Hooke's law and compared with theory. Together the homework assignment and lab experiment illustrate many essential elements of the experimental stress analysis process.

I. Introduction

A first-year graduate-level course entitled "Experimental Stress Analysis I" has been offered for many years by the Mechanical Engineering Department at the University of Washington. Students enrolled in this course are typically beginning their graduate studies, and often require a review of undergraduate course materials before proceeding with understanding towards more advanced studies.

This paper describes a coupled homework assignment and follow-on laboratory experiment that in the author's experience result in a good review and integration of several concepts critical to the field of experimental stress analysis. The concepts include the principle of superposition, the proper use of Hooke's law, recognizing the nature of the stress tensor at a free boundary, interpretation of data obtained using a 3-element strain gage rosette, and relating local principal coordinate systems to global coordinate systems.

II. The Test Specimen

Both the homework assignment and the follow-on lab experiment are concerned with the 'curved beam' portion of the flat U -shaped specimen shown in [Figure 1](#). The overall specimen geometry ([Fig 1a](#)) is defined by specifying the thickness h , distance l , inner radius a , outer radius b , and the diameters of two holes c , which are centered on the beam arms and located a distance d from the curved base of the specimen. During the lab experiment an in-plane load P acting transverse to the arms is applied via pins inserted in the two holes. Since h is small compared to other dimensions, plane stress conditions may be assumed.

A free-body diagram ([Fig 1b](#)) shows that the external load P causes both an internal shear force $V = P$ and an internal bending moment $M = Pd$ to be applied to the curved end of the specimen.

III. Background Information

The following information is discussed during class lecture, prior to assigning the homework problem or conducting the lab experiment. Although first-year graduate students have typically been exposed to most of this material during previous studies, in the author's experience a brief review is beneficial for many.

Elasticity solutions for a curved beam: Two closed-form solutions for curved beams pertinent to the present discussion can be derived using the theory of linear elasticity [1]. The first solution is for a curved beam

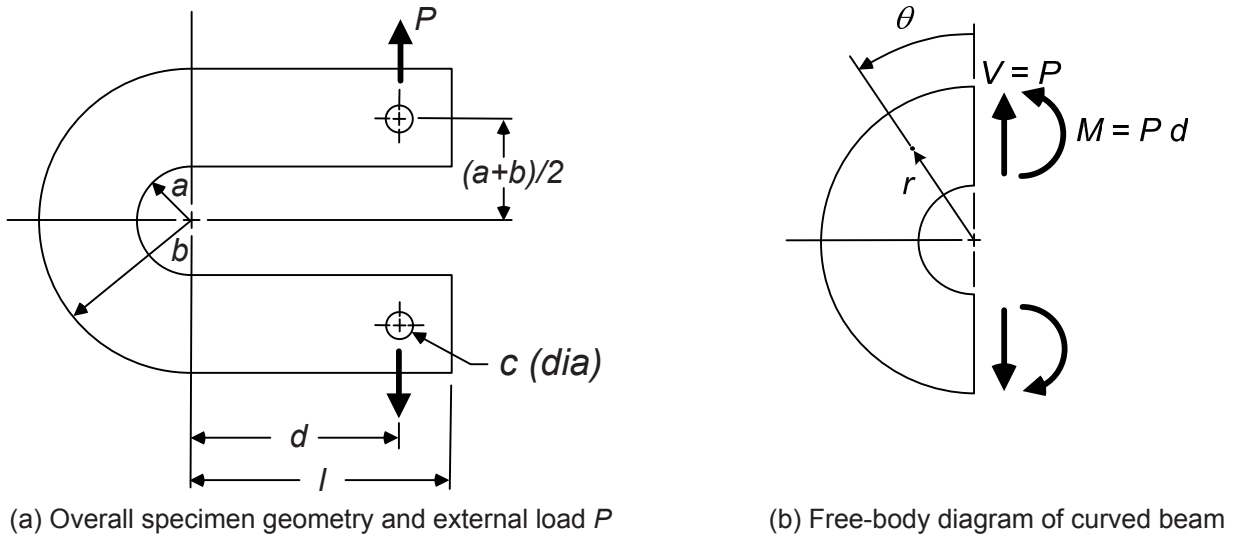


Figure 1: Thin flat test specimen of thickness h , subjected to external loads P

subjected to a pure bending moment M (see article 29 of [1]), and the second is for a curved beam subject to a shear force V (see article 33 of [1]).

Stresses induced in a curved beam by a pure bending moment M are given by:

$$\begin{aligned}\sigma_r &= \frac{-4M}{Nh} \left[\frac{a^2 b^2}{r^2} \ln\left(\frac{b}{a}\right) + b^2 \ln\left(\frac{r}{b}\right) + a^2 \ln\left(\frac{a}{r}\right) \right] \\ \sigma_\theta &= \frac{-4M}{Nh} \left[\frac{-a^2 b^2}{r^2} \ln\left(\frac{b}{a}\right) + b^2 \ln\left(\frac{r}{b}\right) + a^2 \ln\left(\frac{a}{r}\right) + b^2 - a^2 \right]\end{aligned}\quad (1)$$

$$\tau_{r\theta} = 0$$

where:

$$N = (b^2 - a^2)^2 - 4a^2 b^2 \left(\ln \frac{b}{a} \right)^2$$

Note that since $\tau_{r\theta} = 0$, for the case of pure bending the radial and tangential axes are everywhere the principal axes. Also note that stresses vary only with r and do not depend on θ .

In contrast, stresses induced in a curved beam by a pure shear load V are given by:

$$\begin{aligned}\sigma_r &= \left(2Ar - \frac{2B}{r^3} + \frac{D}{r} \right) \sin \theta \\ \sigma_\theta &= \left(6Ar + \frac{2B}{r^3} + \frac{D}{r} \right) \sin \theta \\ \tau_{r\theta} &= - \left(2Ar - \frac{2B}{r^3} + \frac{D}{r} \right) \cos \theta\end{aligned}\quad (2)$$

$$\text{where: } A = \frac{-V}{2Eh} \quad B = \frac{Va^2b^2}{2Eh} \quad D = \frac{V}{Eh}(a^2 + b^2) \quad E = a^2 - b^2 + (a^2 + b^2) \ln\left(\frac{b}{a}\right)$$

Note that since $\tau_{r\theta} \neq 0$ (in general), when a shear load is applied to the beam the radial and tangential axes are not the principal axes (in general). Also note that in this case stresses vary with both r and θ .

Principal Stresses: Since plane stress conditions are assumed $\sigma_z = \tau_{rz} = \tau_{\theta z} = 0$ and the out-of-plane normal stress is a principal stress equal to zero; $\sigma_3 = 0$. The two in-plane principal stresses are given by [2,3]:

$$\sigma_{1,2} = \frac{1}{2}(\sigma_r + \sigma_\theta) \pm \left[\frac{1}{4}(\sigma_r - \sigma_\theta)^2 + \tau_{r\theta}^2 \right]^{1/2} \quad (3a)$$

Having determined the in-plane principal stresses σ_1 and σ_2 , the angle between the r -axis and the principal 1-axis, ϕ_1 , is given by:

$$\phi_1 = \tan^{-1} \left(\frac{\sigma_1 - \sigma_r}{\tau_{r\theta}} \right) \quad (3b)$$

Rosette Equations: Rectangular three-element strain gage rosettes are used during the laboratory experiment. A schematic representation of a rectangular rosette referenced to a r' - θ' coordinate system is shown in [Figure 2](#). Denoting the strains measured by the three independent gage elements as ε_{0° , ε_{45° , and ε_{90° , the in-plane strains referenced to the r' - θ' coordinate system are [2,3]:

$$\begin{aligned} \varepsilon_{r'} &= \varepsilon_{0^\circ} \\ \varepsilon_{\theta'} &= \varepsilon_{90^\circ} \\ \gamma_{r'\theta'} &= 2\varepsilon_{45^\circ} - (\varepsilon_{0^\circ} + \varepsilon_{90^\circ}) \end{aligned} \quad (4)$$

Having determined the three in-plane strain components relative to the r' - θ' coordinate system, the principal strains and orientation of the principal strain coordinate system *relative to the r' -axis* can be determined through the use of Mohr's circle or equivalent. Alternatively, the principal strains and the principal angle ϕ_1 can be calculated from the measured strains as follows [2,3]:

$$\begin{aligned} \varepsilon_1 &= \frac{1}{2}(\varepsilon_{0^\circ} + \varepsilon_{90^\circ}) + \frac{1}{2} \left[(\varepsilon_{0^\circ} - \varepsilon_{90^\circ})^2 + (2\varepsilon_{45^\circ} - \varepsilon_{0^\circ} - \varepsilon_{90^\circ})^2 \right]^{1/2} \\ \varepsilon_2 &= \frac{1}{2}(\varepsilon_{0^\circ} + \varepsilon_{90^\circ}) - \frac{1}{2} \left[(\varepsilon_{0^\circ} - \varepsilon_{90^\circ})^2 + (2\varepsilon_{45^\circ} - \varepsilon_{0^\circ} - \varepsilon_{90^\circ})^2 \right]^{1/2} \\ \phi_1 &= \tan^{-1} \left\{ \frac{2(\varepsilon_1 - \varepsilon_{0^\circ})}{2\varepsilon_{45^\circ} - (\varepsilon_{0^\circ} + \varepsilon_{90^\circ})} \right\} \end{aligned} \quad (5)$$

Note that ϕ_1 is the angle between the r' -axis and the +1-axis, as shown in [Figure 2](#), and is defined positive in accordance with the right-hand-rule.

Plane stress form of Hooke's law: According to the traditional definition a state of plane stress exists when the magnitudes of all out-of-plane stress components are zero. Hence a plane stress state is defined by specifying the magnitudes of the remaining three in-plane stress components. For present purposes it is convenient to

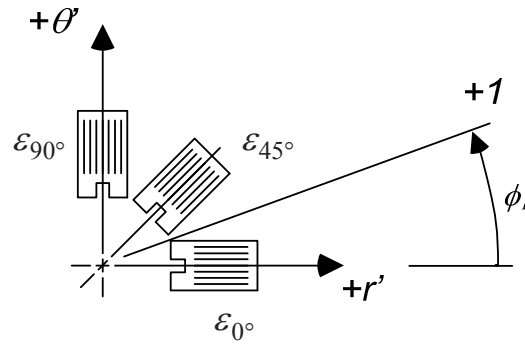


Figure 2: Three-element rectangular rosette referenced to a r' - θ' coordinate system

describe stress and strain using a cylindrical (r, θ, z) coordinate system. Assuming $\sigma_z = \tau_{rz} = \tau_{\theta z} = 0$, the non-zero stress components that may exist are σ_r , σ_θ , and $\tau_{r\theta}$, and the plane stress form of Hooke's law can be written:

$$\begin{Bmatrix} \sigma_r \\ \sigma_\theta \\ \tau_{r\theta} \end{Bmatrix} = \begin{bmatrix} \left(\frac{E}{1-\nu^2}\right) & \left(\frac{\nu E}{1-\nu^2}\right) & (0) \\ \left(\frac{\nu E}{1-\nu^2}\right) & \left(\frac{E}{1-\nu^2}\right) & (0) \\ (0) & (0) & \left(\frac{E}{2(1+\nu)}\right) \end{bmatrix} \begin{Bmatrix} \varepsilon_r \\ \varepsilon_\theta \\ \gamma_{r\theta} \end{Bmatrix} \quad (6)$$

If principal strains have been calculated, then the plane stress form of Hooke's law can be written:

$$\begin{Bmatrix} \sigma_1 \\ \sigma_2 \end{Bmatrix} = \begin{bmatrix} \left(\frac{E}{1-\nu^2}\right) & \left(\frac{\nu E}{1-\nu^2}\right) \\ \left(\frac{\nu E}{1-\nu^2}\right) & \left(\frac{E}{1-\nu^2}\right) \end{bmatrix} \begin{Bmatrix} \varepsilon_1 \\ \varepsilon_2 \end{Bmatrix} \quad (7)$$

IV. The Homework Problem

The homework assignment is to develop a computer-based procedure to automatically generate plots of the following quantities within the curved region of the beam at any a user-specified angular position θ , assuming linear elastic behavior:

- The maximum principal stress, σ_1 , vs radial position, r .
- The minimum principal stress, σ_2 , vs radial position, r .
- The angle α vs radial position, r , where α is defined as the angle between the line of action of force P and the $+1$ -axis.

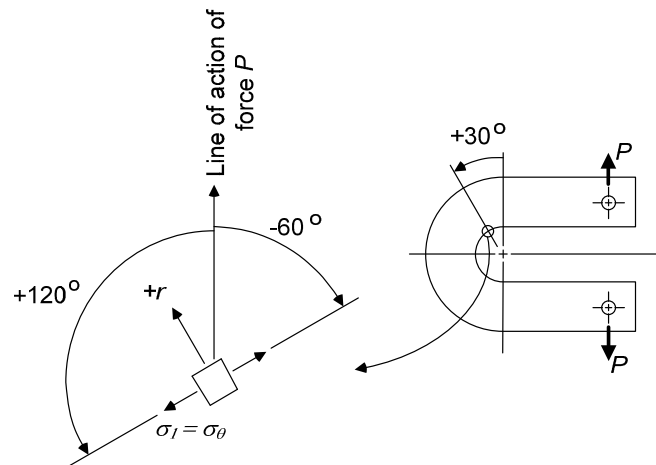


Figure 3: Stress element at the point $r = a$ and $\theta = 30^\circ$

As already noted a simple free-body diagram (Fig 1b) reveals that the curved beam portion of the specimen is subjected to both a bending moment $M = Pd$ and shear load $V = P$. Hence, by invoking the principle of superposition the radial, tangential, and shear stresses present at any point (r, θ) can be obtained by adding the solutions represented by eqs (1) and (2) together. The principal stresses can then be calculated using Eqs (3a) and plotted.

Proper generation of plot (c) requires additional considerations, however. Specifically, the angle returned by Eq (3b) is the angle between the r -axis and the 1 -axis. In contrast, part (c) of the homework problem specifies that a plot of the angle between the line of action of force P and the 1 -axis, angle α , must be generated. Therefore a constant representing the angle between the line of action of force P and the r -axis must be added to angle ϕ_1 calculated using Eq (3b).

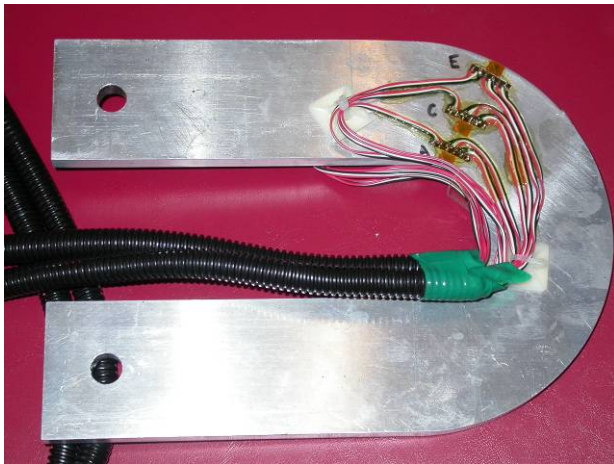
A specific example will be used to illustrate this latter point. Suppose that a plot along the radial line defined by $\theta = 30^\circ$ is required. A stress element at the inner radius for this case (i.e., for $r = a$, $\theta = 30^\circ$) is shown in Figure 3. At this point the orientation of the principal stress coordinate system is known by inspection. That is, the tangential stress is clearly tensile, whereas the radial and shear stresses are both zero (since the boundary is unloaded). Hence, at this point it can be concluded by inspection that

$$\sigma_1|_{r=a} = \sigma_\theta|_{r=a} \quad \sigma_2|_{r=a} = 0$$

Therefore, at this point the angle between the 1 -axis and the r -axis is $\phi_1 = \pm 90^\circ$, whereas the angle between the line of action of force P is $\alpha = 120^\circ$, or (equivalently) $\alpha = -60^\circ$. Angle α is related to angle ϕ_1 according to $\alpha = \phi_1 + 30^\circ$ or $\alpha = \phi_1 - 30^\circ$. Either convention can be used to define angle α , as long as the same convention is used for all radial positions $a \leq r \leq b$. No restrictions are placed on the computer software used to complete the assignment, beyond the statement that a “computer-based procedure to automatically generate plots” is required. Students have completed the assignment using several widely-available software packages, including Excel, Maple, Matlab, or Mathematica, for example.

V. The Lab Experiment

The goals of the lab experiment are to (a) measure principal strains in a curved beam using rectangular 3-element strain gages rosettes, (b) to convert these measured strains to principal stresses, and (c) to compare these experimental results with the elasticity solution previously described.



(a) Specimen side with rosettes A, C, and E



(b) Specimen side with rosettes B and D

Figure 4: A 7075-T6 aluminum specimen instrumented with five stacked strain gage rosettes

The 7075-T6 aluminum specimen shown in Figure 4 is used for this purpose. Dimensions (refer to Figure 1) and elastic properties are:

$a = 31.8 \text{ mm (1.25 in)}$	$b = 88.9 \text{ mm (3.5 in)}$	$l = 152 \text{ mm (6.0 in)}$
$d = 127 \text{ mm (5.0 in)}$	$c = 12.7 \text{ mm (0.5 in)}$	$h = 9.53 \text{ mm (0.375 in)}$
$E = 71.7 \text{ GPa (10.4 Msi)}$	$\nu = 0.32$	

Five stacked rectangular rosettes (M-M type WA-13-060WR-120) are bonded along the radial line defined by $\theta = 30^\circ$. Since each rosette consists of three gage elements, a total of fifteen individual strain gage elements are used. Due to the large number of leadwires involved rosettes A, C, and E are bonded on one side of the specimen (Fig 4a), while rosettes B and D are bonded on the opposite side (Fig 4b). The radial position of each rosette is listed in Table 1.

Load is applied using an Instron Model 8511 load frame, and increased monotonically from zero to about 2225 N (500 lb_f). All strain gages are monitored using a Vishay System 5000 data acquisition system equipped with the StrainSmart software package. This software package accounts for gage factor and transverse sensitivity of each individual gage element. Typical strains measured using the 15 gage elements are plotted in Figure 5.

The slope of strain versus load was calculated for each gage element using linear regression and is included in Table 1, along with the intercept b and correlation coefficient R^2 . Linear-elastic behavior is maintained at the load levels employed, as evidenced by the very small intercepts as well as the fact that R^2 exceeds 0.99 in all cases.

The slopes for each gage element are combined with the rosette equations, eqs (5), to determine the normalized principal strains and the orientation of the principal strain coordinate system at each rosette site. Results are summarized in Table 2. Note that the orientation angle listed is the angle between the line of action of force P and the $+r$ -axis, rather than the angle between the $+r$ -axis and the $+1$ -axis.

Finally, the normalized principal strains listed in Table 2 are combined with the plane stress form of Hooke's law, eqs (7), to calculate the principal stresses at each rosette site. Principal stresses inferred from experimental measurements are included in Table 2, along with principal stresses and orientation angle calculated using the elasticity solutions. A summary plot of measured and predicted stresses and orientation of the principal axes for all rosette locations is shown in Figures 6 and 7. The obvious agreement reinforces student's confidence in both the experimental and analytic topics presented during class lecture.

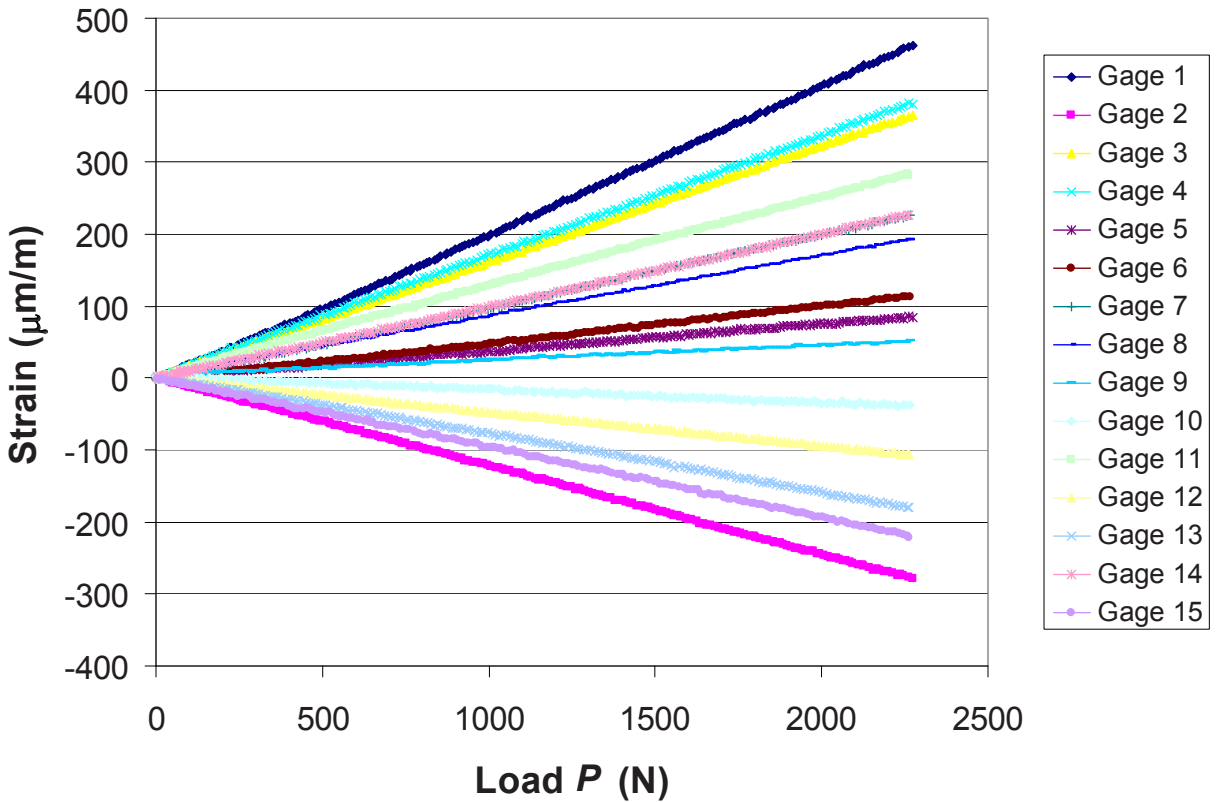


Figure 5: Strains measured with increasing load P , using five 3-element strain gage rosettes

Table 1: Linear regression of strain data shown in [Figure 5](#)

Rosette	Radial Position (mm)	Gage Element Number	Slope m ($\mu\text{m}/\text{m}\cdot\text{N}$)	Intercept b ($\mu\text{m}/\text{m}$)	R^2
A	34.9	1	0.205	-5.40	0.999866
		2	-0.123	0.865	0.999932
		3	0.161	1.10	0.999945
B	44.4	4	0.168	2.07	0.999843
		5	0.037	1.18	0.99861
		6	0.051	-3.37	0.999233
C	52.3	7	0.101	-3.29	0.999717
		8	0.084	2.81	0.99989
		9	0.021	3.69	0.996243
D	69.8	10	-0.018	2.19	0.994283
		11	0.125	2.46	0.999733
		12	-0.047	-0.124	0.999579
E	86.4	13	-0.080	2.56	0.999553
		14	0.100	-0.489	0.999721
		15	-0.097	0.573	0.999689

Table 2: Measured and predicted principal strains and principal stresses

Rosette	Radial Position (mm)	Experimental Measurements				Predictions	
		Normalized Principal Strains ($\mu\text{m}/\text{m}/\text{N}$ or degs)		Normalized Principal Stresses (kPa/N or degs)		Normalized Principal Stresses (kPa/N or degs)	
A	34.9	ε_1/P	0.488	σ_1/P	35.8	σ_1/P	36.1
		ε_2/P	-0.123	σ_2/P	2.64	σ_2/P	3.66
		α	-57.9	α	-57.9	α	-57.6
B	44.4	ε_1/P	0.202	σ_1/P	16.6	σ_1/P	16.4
		ε_2/P	0.0167	σ_2/P	6.51	σ_2/P	7.15
		α	-40.5	α	-40.5	α	-42.8
C	52.3	ε_1/P	0.107	σ_1/P	8.99	σ_1/P	9.34
		ε_2/P	0.014	σ_2/P	3.88	σ_2/P	3.34
		α	0.1	α	0.1	α	2.0
D	69.8	ε_1/P	0.125	σ_1/P	5.12	σ_1/P	4.87
		ε_2/P	-0.190	σ_2/P	-11.9	σ_2/P	-11.2
		α	27.3	α	27.3	α	25.1
E	86.4	ε_1/P	0.100	σ_1/P	0.884	σ_1/P	0.63
		ε_2/P	-0.277	σ_2/P	-19.5	σ_2/P	-21.0
		α	29.5	α	29.5	α	29.5

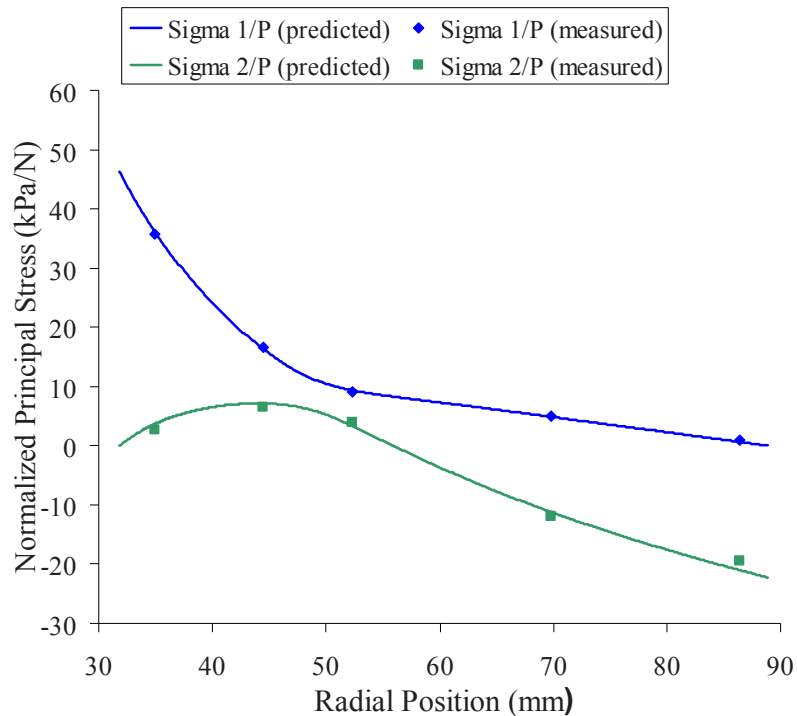


Figure 6: Comparison of Measured and Predicted Principal Stresses

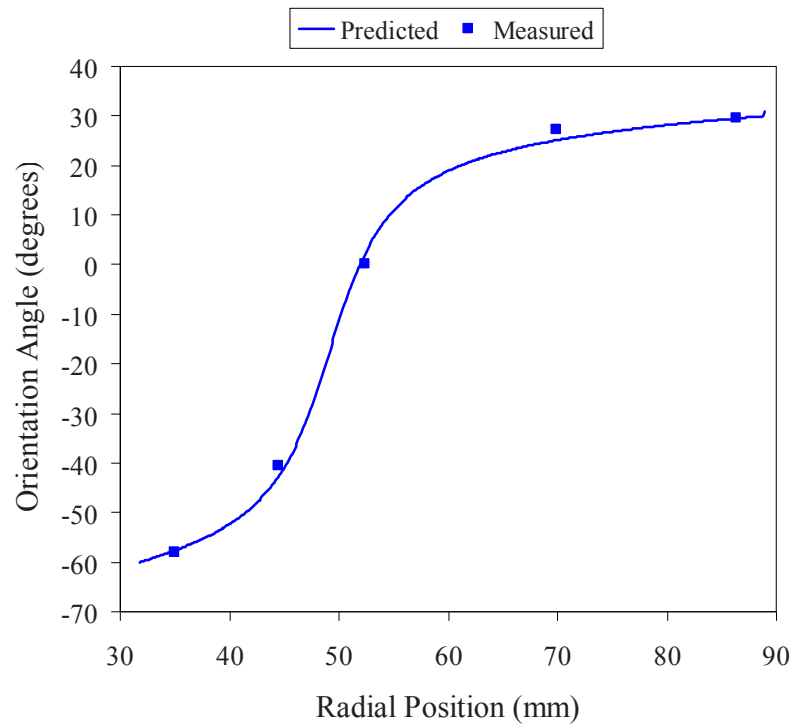


Figure 7: Comparison of Measured and Predicted Orientation Angle of the Principal Axes

VI. Summary

A homework assignment and follow-on laboratory experiment involving a flat *U*-shaped specimen has been described. Together the homework assignment and lab experiment illustrate many essential elements of the experimental stress analysis process. This includes the principle of superposition, the proper use of Hooke's law, recognizing the nature of the stress tensor at a free boundary, interpretation of data obtained using a 3-element strain gage rosette, and relating local principal coordinate systems to global coordinate systems. The *U*-shaped test specimen is simple to fabricate and is easily loaded, and yet the stress and strain fields induced are relatively complex and are therefore reminiscent of those encountered in real structures. The author has found the assignment and lab experience to be ideally suited to a course devoted to experimental stress analysis.

Demonstration of Rod-Wave Velocity in a Lecture Class

*Dulal Goldar, Former Principal
Delhi College of Engineering*

Abstract:

There was a discussion of Wave Propagation in Solids in a Graduate Class of Structural Engineering. Propagation of Longitudinal Wave (Rod-wave) was demonstrated by the author using a piece of Chalk and Wooden Duster.

Introduction:

The dynamic response of materials and structures due to impact loading is complex phenomenon. For isotropic solids it indicates propagation of two types of waves from elastic theory. Dilatational (or longitudinal) waves are those in which the particle motion induced by disturbance is normal to wave front. Distortional (or transverse or shear) waves are those wherein material particles move in a plane at right angle to that in which wave front propagates.

Expression for the velocities of propagation for the two types of disturbances, denoted by c_L and c_s given for bounded media are $(E/\rho)^{1/2}$ and $(G/\rho)^{1/2}$ respectively, where E and G are Young's Modulus and Shear Modulus respectively and ρ is mass density (i.e. density/ acceleration due gravity).

When either a dilatational or distortional wave impinges on a boundary of the solid, waves of both types are generated. For the present situations impact is the normal impingement of strong compressive pulse on a free surface. The pulse reflected as a tensile wave. If the magnitude of the tensile stress wave is greater than the tensile strength of the material, fractures occur causing material separation. Simple analyses predict reasonable well the location of the fracture plane and the size and speed of the ejected material. If after fracture the magnitude of stress pulse still exceeds the material tensile strength then multiple fractures may occur.

Fracture due to stress waves:

The material failures near a free surface remote from the point of application of the impact load have been studied extensively. For materials strong in compression but weak in tension (Concrete, rock, chalk, brass and cast- iron etc) scabbling or spalling at free surface expected due reflection of incident-compression pulse generated due to impact/ impulsive loading.

It may be treated such impulse as triangular in shape. In one dimensional treatment, the stress pulse is propagated without change in shape or intensity. It also assumed that if material undergoes fracture when tensile stress reaches the critical value i.e. σ_F , then fracture will occur instantaneously in a plane of geometry being considered where σ_F is first reached.

Let σ_m = magnitude and λ = pulse length of incident- compressive pulse. The wave will be reflected from the free surface (Fig.1) with net- maximum tensile stress = σ_T which will always occur at the leading edge of the reflected wave and can be defined as $\sigma_T = \sigma_m - \sigma_i$ ----(1)

Where, σ_i is the compressive incident stress at the same point as leading edge of the reflected wave.

Equation (1) will be valid at any given point of time during the reflection of the wave.

Now if $\sigma_m > \sigma_F$ fracture will occur instantly when $\sigma_T = \sigma_F$

At instant $\sigma_F = \sigma_m - \sigma_i$ where, σ_T can now be defined by geometry as $\sigma_T / (\lambda - 2t_1) = \sigma_m / \lambda$

Or, $\sigma_i = \sigma_m (\lambda - 2t_1) / \lambda$

And to eliminate σ_i gives $\sigma_F = \sigma_m - \sigma_m (\lambda - 2t_1) / \lambda$

Now to get spall thickness, $t_1 = (\sigma_F / \sigma_m) (\lambda / 2)$

Fracture occurs at a distance $\lambda / 2$ from rear face, it occurs at all, if $\sigma_F = \sigma_m$.

If $\sigma_m < \sigma_F$ no fracture will occur.

If $\sigma_m > \sigma_F$, multiple fractures will occur.

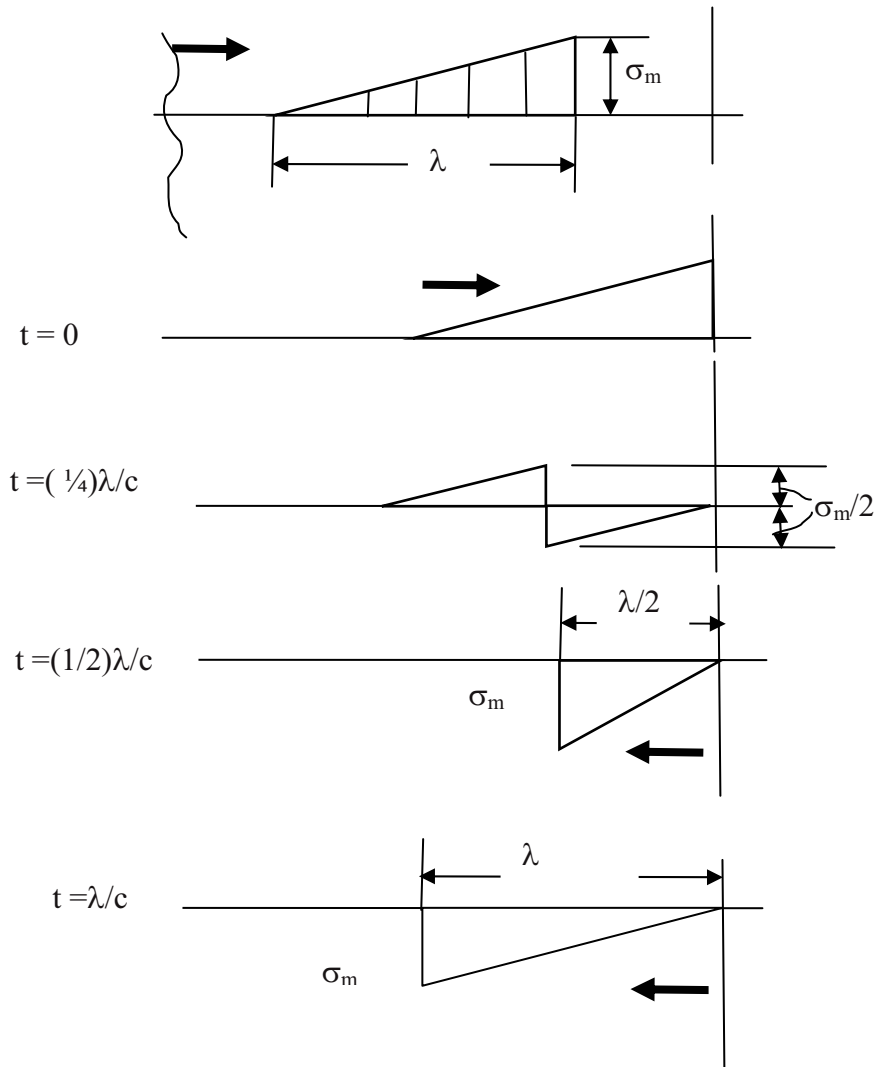


Fig.1. Net Stress for reflection of saw tooth pulse at various

Experiment in the Class Room:

The author used a piece of Chalk and Wooden Duster. The chalk piece was kept in left hand vertically. The wooden duster was struck on the top of the chalk piece with right hand to create a compression pulse on the top of cylindrical bar of brittle material like a chalk piece (80 mm long of 8mm diameter). The compression pulse traveled longitudinally until it will hit the end of chalk piece. The moment the compression hit the end it created a tension pulse. The chalk piece was broken with impulse as brittle and tension failure and broken part fell with force on the floor/ table of the class room.

Conclusion;

The simple experiment demonstrated the behavior of longitudinal wave (Rod-wave) characteristic.

References:

1. Zukas, A.Jonas et.al. "Impact Dynamics" John Wiley & Sons, 1982 pp. 1-40.

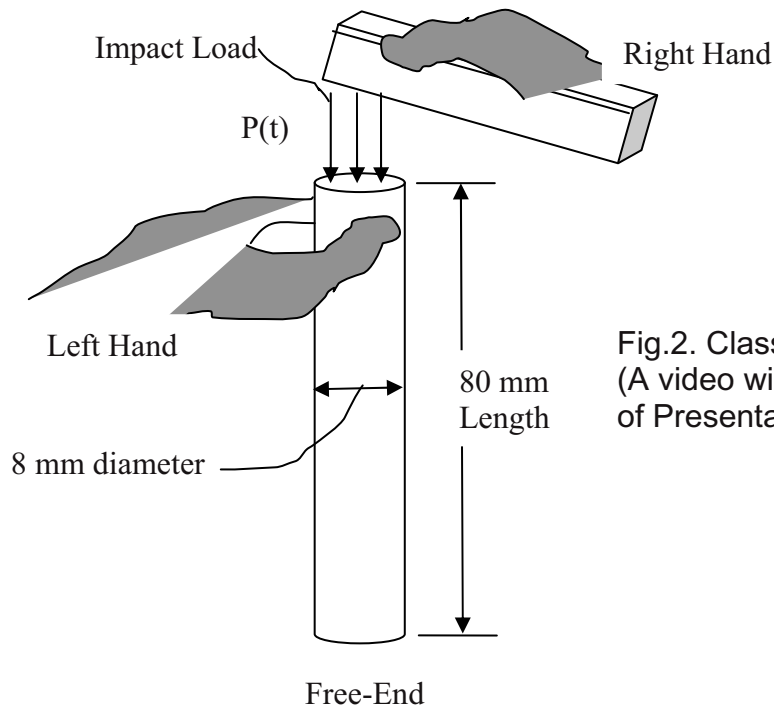


Fig.2. Class Room Experiment
(A video will be provided at the time of Presentation)

Influence of Friction-Stir-Welding Parameters on Texture and Tensile Behavior

Zhenzhen Yu¹, Hahn Choo¹, Wei Zhang², Zhili Feng², and Sven Vogel³

1. Department of Materials Science and Engineering, University of Tennessee, Knoxville, TN 37996, USA
2. Materials Science and Technology Division, Oak Ridge National Laboratory, Oak Ridge, TN, 37831, USA
3. Los Alamos Neutron Science Center, Los Alamos National Laboratory, Los Alamos, NM, 87545, USA

ABSTRACT

A series of friction stir welding (FSW) was conducted on AZ31B Mg alloy plate by varying its key parameters, i.e., rotation speed and travel rate of the weld tool, to investigate the influence of thermo-mechanical input during welding process on the resulting texture and tensile behavior. Neutron diffraction texture measurements show that, with the systematic changes in the thermo-mechanical input during welding, there are corresponding changes in crystallographic texture that correlates well with the expected changes in deformation and recrystallization mechanisms. Furthermore, tensile behavior along the longitudinal direction was examined as a function of FSW parameters, and the results show dramatic changes in the strength and ductility in a way that is consistent with the changes in texture.

1. INTRODUCTION

During friction stir welding (FSW), a cylindrical threaded tool pin rotates and plunges into the workpieces and produces a stirring action that joins the workpieces together, while the shoulder part of the tool forges down the workpiece providing frictional heating as shown in Fig. 1. The joining is accomplished by running the rotating tool along the weld line. Significant heat is generated mainly from the friction between the tool shoulder and workpiece, while a severe plastic deformation occurs in the softened material by the stirring pin. As a result, a severely-deformed 'stir zone' (SZ) with fine grains is produced through dynamic recrystallization (DRX). To date, the challenge remains in the fundamental understanding of the governing mechanisms for the grain refinement, texture formation, and the resulting mechanical behavior after FSW of Mg alloys. It is noted that, for hcp crystalline structure, deformation condition dominates the active deformation modes (slip vs. twinning), and, hence, the development of texture ^[1]. In this study, the objective was to investigate the influence of thermo-mechanical input during FSW on texture development and the corresponding mechanical behavior after FSW of AZ31B Mg alloy. A series of FSW experiments were designed to cover a wide range of deformation conditions by varying the rotation and travel speeds of the tool. The changes in texture of the SZ were investigated using neutron diffraction technique. The tensile behavior of the FSW plates was also examined. Finally, the relationship among the processing parameters, texture evolution, and the mechanical behavior of the FWP Mg alloy plate is discussed.

2. EXPERIMENT DETAILS

A commercial AZ31B Mg alloy wrought plate with a thickness of 6.5 mm was used in the FSP experiment. The processing tool made of H-13 tool steel has a shoulder with 19.05 mm diameter, and a threaded pin with 6.35 mm diameter and 5.72 mm height. In order to design FSW processes covering a wide thermo-mechanical input range, two empirical equations are used to estimate the maximum temperature ^[2], T , (Eq. (1)) and average strain rate ^[3], $\dot{\epsilon}$, (Eq. (2)) in SZ during FSW, respectively.

$$\frac{T}{T_m} = K \left(\frac{\omega^2}{2.362v \times 10^4} \right)^a \quad (1);$$

$$\dot{\epsilon} = \frac{R_m \cdot 2\pi r_e}{L_e} \quad (2),$$

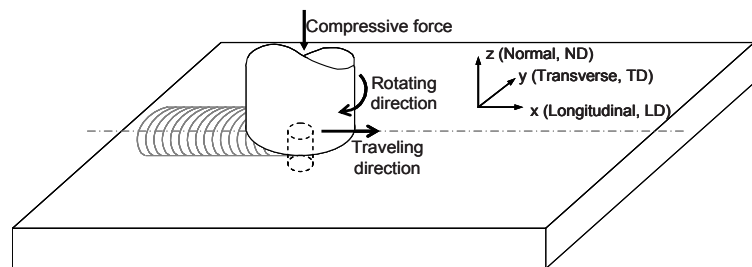


Fig. 1 Schematic (not to scale) of friction stir welding (FSW) in Mg plate.

where T_m is the melting temperature, ω is the tool rotation speed, and v is the travel speed. K and a are constants. r_e and L_e are the effective radius and depth of the SZ. R_m is the average flow rate, which is about half of the pin rotational speed, ω . Six different FSW cases were investigated. Then, the two primary deformation

parameters, strain rate ($\dot{\varepsilon}$) and temperature (T), are incorporated into Zener-Hollomon parameter, Z, which is defined as below^[1, 3]:

$$Z = \dot{\varepsilon} \exp(Q/RT) \quad (2),$$

where R is the gas constant, Q is the activation energy for diffusion, which is 135 kJ/mol^[3]. When deformed at lower Z values, slip mode should be the dominant deformation mechanisms. On the other hand, when deformed at higher Z, twinning should play an important role during DRX, which would strongly influence the texture of the SZ. For low Z (LZ) cases 1 to 3, ω was set to be 1200rpm, as v varies from 0.25, 0.64, and 1.1 mm/s, Z increases from 6.37×10^{10} , 2.19×10^{11} to $4.52 \times 10^{11} \text{ s}^{-1}$. In high Z (HZ) cases 1 to 3, v was kept at 1.1 mm/s, while ω decreases from 600, 400, to 300 rpm, and therefore Z further increase from 1.50×10^{12} , 3.07×10^{12} to $5.15 \times 10^{12} \text{ s}^{-1}$. The crystallographic texture of the SZ was measured from all 6 cases using neutron diffraction at the HIPPO beamline at the Los Alamos Neutron Science Center. The results provide volume-averaged ($5 \times 5 \times 6.4 \text{ mm}^3$) texture analysis from the SZ. In order to study the tensile behavior of the SZ, subsize tensile samples were prepared from the six FSW cases in longitudinal direction (LD), with a gage section of 25mm in length, 6mm in width and 4.8mm in thickness. Tensile tests were conducted at an initial strain rate of $5 \times 10^{-4} \text{ s}^{-1}$ at room temperature.

4. RESULTS AND DISCUSSION

Fig. 2 shows the {0002} texture measured from base metal and two representative texture measurements of SZ of FSW Mg plates from LZ and HZ cases, respectively. The as-received hot-rolled Mg plate shows a typical strong basal texture parallel to normal direction (ND) of the plate. After FSW, systematic changes in crystallographic texture in SZ corresponding to different FSW parameters were observed. In LZ cases 1-3, at lower Z input, a two-component-texture was developed, as shown for the case LZ-1 in Fig. 2. The near- $\langle 0001 \rangle // \text{LD}$ texture component is a texture generated from shear deformation when material flows with the rotating tool by slip. In HZ cases 1-3, the near- $\langle 0001 \rangle // \text{LD}$ component disappears, as shown for the case HZ-1 in Fig. 2. The possible reason is with high Z input (less heat input), twinning mode should be more easily activated in the early stage of deformation, and dramatically influence the DRX process and corresponding texture development, which could lead to a $\sim 90^\circ$ rotation of the near- $\langle 0001 \rangle // \text{LD}$ shear component towards ND. Fig. 3 shows the tensile behavior of SZ along LD measured on FSW samples with different Z parameter. Clear changes in the strength and ductility are observed, which is consistent with the changes in the texture. Specimens with two-component-texture (LZ 1-3) shows high tensile strength with low ductility, while specimens with near-normal basal texture (HZ 1-3) exhibits a relatively low yield strength and better ductility when tested along the LD.

In summary, this study shows a good correlation among the processing parameters, texture development, and deformation mechanisms for the FSWed Mg alloy AZ31B. The results could be useful for the design of desired final properties in FSWed Mg alloys.

Acknowledgements: This research is supported by NSF Major Research Instrumentation (MRI) program under contract DMR.0421219. The authors are grateful to staff in Materials Science and Technology Division in Oak Ridge National Laboratory, and Los Alamos Neutron Science Center for their great help in performing the experiments.

References: [1] Galiyev A., Kaibyshev R., Gottstein G., Correlation of Plastic Deformation and Dynamic Recrystallization in Magnesium Alloy ZK60. *Acta Mater.* 49, 1199-1207, 2001. [2] Arbegast W.J., Modeling Friction Stir Joining as a Metalworking Process. *Hot Deform. of Aluminum Alloys III*, Z. Jin, ed. TMS, 2003. [3] Chang C.I., Lee C.J., Huang J.C., Relationship between Grain Size and Zener-Hollomon Parameter during Friction Stir Processing in AZ31 Mg Alloys. *Scripta Mater.* 51, 509-514, 2004.

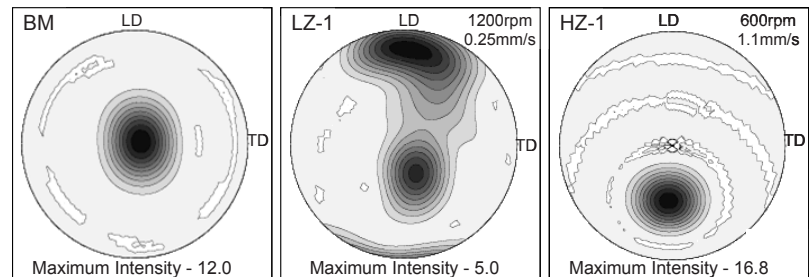


Fig.2 {0002} pole figures for base metal (BM) and two different FSW cases are plotted using gray scale with the maximum intensity marked at the bottom of each figure. LD is longitudinal direction (parallel to travel direction of the tool during FSW as well as the rolling direction of the plate), and TD is transverse direction.

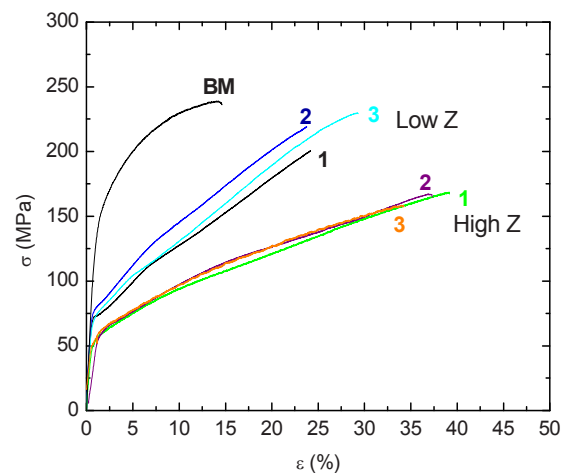


Fig.3 Tensile test results of the SZ for six FSW cases tested along LD compared to the behavior of base metal.

Comparing Two Different Approaches to the Identification of the Plastic Parameters of Metals in Post-necking Regime

Antonio Baldi, Andrea Medda and Filippo Bertolino

Dipartimento di Ingegneria Meccanica, Piazza d'Armi, 09123 Cagliari - ITALY

e-mail: baldi@iris.unica.it

ABSTRACT

In the past 20 years the growing computation power availability encouraged experimental mechanics specialists to couple full field measurements with FE methods to raise the so called hybrid experimental-numerical methods. A typical example is the identification of the plastic parameters of metals starting from experimental data.

In this work a comparison of two different inverse approaches is presented. A global method, called Kali, identifies the parameters of a plastic law (e.g. Ramberg-Osgood, Hollomon,...) fitting the global experimental data (load, clip-gauge) with FE results obtained using the trial parameters. Instead a full field method, called PlastFemDIC, prescribes DIC measured displacement data of the specimen surface as well as the global ones.

To judge the best approach, the silhouette of a round axial-symmetric specimen is compared at various load levels with the FEM results obtained with the parameters identified by the global and local approaches.

1. Introduction

Since costs and weight reduction are being the main target in modern mechanical design and generically in each manufactured product, the need of better mechanical performance is gradually growing. For this reason the knowledge of mechanical behavior in post-necking and large strain field is unavoidable at all. Besides during machining and assembling phase, many technological processes give rise to large strains of material, due to the need of "look and feel" design or to other specific design needs, so the know-how of mechanical performances is important both in early and far-strain fields.

In spite of the fact that metal alloys are used safely from long time, also in mission critical situations (nuclear vessel, oil and gas piping, aircraft and automotive industry), the complexity of parameters identification of many descriptive models [1] from a bare experimental point of view, leads to the adoption of simple models, which in some circumstances perform quite poorly. The result is a notable disagreement between theoretical and real performances of products, that leads to adoption of large safety factors, and require long and expensive experimental verifications.

Nowadays, the standard approach to the design of mechanical components in the large strain field is a numerical analysis using a FEM code. One of the most important prerequisites for a successful simulation is the availability of reliable true stress - true strain curve. Building the true stress - true strain curve up to necking is quite simple and can be done under the hypothesis of constant volume deformations, which leads to the well known logarithmic strain (and stress) formulation. However, after necking, when large triaxial stress components are present and strains are highly localized in the necking area, the curve identification is not so straightforward. In fact, when localized necking begins, the strain distribution at the minimum cross-section becomes highly non-uniform. The average axial strain $\varepsilon = \ln(A_0) - \ln(A) = \ln(1 + e)$, where e is the engineering strain, is considerably smaller than the maximum axial strain at minimum cross section; in parallel, the (true) stress distribution near necking is highly nonuniform and correction methods, like the Bridgman's one [2], are known to be not valid for flat samples [3].

To face these problems two tools, able to numerically estimate the true yield function by inverse calibration, have been developed by the authors [4,5]. The first one, called Kali, tries to identify the parameters of the true stress -

true strain curve on the basis of the data which can be extracted from a standard tension/compression test; the second one (PlastFEMDIC) couples these data with the surface displacement field measured during testing. Since the point of view of the two approaches is completely different (global versus local minimization) and their usage implies different levels of complexity (both from the experimental and the numerical point of view), in this work we try to compare their performance in terms of accuracy, and execution time.

2. Kali

Kali tries to identify the parameters of a yield model by exploiting their influence on appropriate global quantities coming from experimental tests. These quantities (in this case, the engineering stress and strain) are chosen so that they can be measured easily and with great accuracy. Thus the method mainly consists in a minimization of an error function which represents the difference between experimental (engineering) global data and the same quantities obtained, as a parameter-dependent response, from a finite element model simulating the experimental setup:

$$\Delta_i = \int_0^{e_m} |s^{\text{exp}} - s_i^{\text{fem}}| de \cong \frac{1}{2} \sum_{j=1}^{m-1} \left| (s_{j+1}^{\text{exp}} + s_j^{\text{sp}}) - (s_{i,j+1}^{\text{fem}} + s_{i,j}^{\text{fem}}) \right| (e_{j+1}^{\text{exp}} - e_j^{\text{exp}})$$

where s_i and e_i are respectively the engineering stresses and strains at the i^{th} step.

To summarize the full process, the main steps are: **a)** Execution of the test, taking care to acquire the global quantities to be fitted. **b)** Set-up of the FEM analysis corresponding to the experimental test and implementation the model to be investigated, so the simulation outcomes will be depending on model parameters. **c)** Iterative minimization of the error function varying the hunted parameters. The final set of parameters can be considered the best fit set. The entire procedure is quite straightforward, but several practical points have to be faced (e.g. error function derivatives are not available, thus the range of the minimization algorithms available is quite small; software must be able to interact with FEM code to modify simulation parameters and extract final results; some set of parameters could lead to a failed simulation, ...) and may require some time both in set-up and data processing. Moreover a good first guess set of parameters is needed do avoid the algorithm to fall in a local, erroneous, minimum.

2.1 Plastic models available in Kali code

Kali implements several plastic models which are tested in succession seeking the best performing theoretical formulation.

2.1.1 Hollomon model

The Hollomon model implements the classic Hollomon's power law [6]:

$$\sigma = \sigma_0 + H \varepsilon^n$$

where σ_0 is the initial yield (true) stress ($\sigma_0 = \sigma|_{\varepsilon_p=0}$) and ε is the total (true) strain. The model requires fitting 2 or 3 parameters, depending on the assumption made on the initial yield stress (user defined or fitted by code).

2.1.2 Ling model

Ling model extends the Hollomon model by using, in the post-necking area, a weighted sum of the power-law and a linear extrapolation [7].

$$\left\{ \begin{array}{ll} \sigma = \left(\frac{\sigma_u}{\varepsilon_u^{\varepsilon_u}} \right) \varepsilon^{\varepsilon_u} & \varepsilon \leq \varepsilon_u \\ \sigma = \sigma_u \left[w(1 + \varepsilon - \varepsilon_u) + (1 - w) \left(\frac{\varepsilon^{\varepsilon_u}}{\varepsilon_u^{\varepsilon_u}} \right) \right] & \varepsilon > \varepsilon_u \end{array} \right.$$

where $\sigma_u = s_u(1 + e_u)$, s_u being the ultimate engineering stress. The model relies on the correct identification of the ultimate engineering values (s_u and e_u) and requires fitting only 1 parameter (w).

2.1.3 Ramberg - Osgood model.

The Ramberg Osgood model differs from the Hollomon's one for using the plastic component of strain only [8]:

$$\sigma = \sigma_0 + H \varepsilon_p^n$$

It requires fitting 2 or 3 parameters depending on the assumption made on the initial yield stress.

2.1.4 Bld₁ model

The Bld₁ model extends the Ramberg - Osgood model in the same way the Ling model does with the Hollomon model. However the formulation does not rely on the correct identification of the ultimate point and introduces an extra parameter (ε_l) to control the switch point:

$$\left\{ \begin{array}{ll} \sigma = \sigma_0 + H \varepsilon_p^n & \varepsilon_p \leq \varepsilon_l \\ \sigma = w(\sigma_0 + H \varepsilon_p^n) + (1-w)\sigma_l(1 + \varepsilon_p - \varepsilon_l) & \varepsilon_p > \varepsilon_l \end{array} \right.$$

where $\sigma_l = \sigma_0 + H \varepsilon_l^n$. The model requires fitting up to 5 parameters, depending on the assumption made.

2.1.5 Bld₂ model

The Bld₂ model integrates the damage concept in the yield law. Thus, starting from the ideal Ramberg-Osgood law of the not-damaged material, it is easy to obtain $\sigma = (\sigma_0 + H \varepsilon_p^n)(1 - D^\beta)$, where D is the damage and β the damage exponent. By assuming the damage to be proportional to the plastic component of strain, we finally get

$$\sigma = (\sigma_0 + H \varepsilon_p^n) \left[1 - \left(\frac{\varepsilon_p}{\gamma} \right)^\beta \right]$$

Thus γ is the plastic strain at unitary damage (the critical plastic strain). The model requires fitting 4 or 5 parameters depending on the assumption made on the initial yield stress.

2.1.6 Roux model

The Roux model combines an exponential formulation with a linear (and optionally) a parabolic term:

$$\sigma = \sigma_0 + A[1 - \exp(-B\varepsilon_p)] + C\varepsilon_p + D\varepsilon_p^2$$

The model requires the identification of either 3, 4 or 5 parameters depending on the inclusion of the optional parabolic term and on the assumption made on the initial yield stress.

3. PlastFemDIC

PlastFemDIC uses the surface displacement field, measured during loading up to failure by Digital image correlation, to estimate the parameters of an elasto-plastic constitutive equation in order to best match the computed and measured displacements. The FEM code allows to compute displacement fields at each time step for all values of the internal parameters. Only the set of nodes at the surface of the specimen where displacement is measured, will be considered in the sequel, although the model is three-dimensional.

The start-up value of parameters in the minimization algorithm is not based on a Finite element computation. It simply consists in trying to estimate stresses and strains from elementary volumes of the material. The most difficult part to estimate is obviously the stress since no local measurement is available. The specimen geometry is used through the assumption that the stress state is homogeneous in each section of the sample. Thus the domain of interest is "sliced" into small thickness parallelepipeds. In each of them the stress is assumed to be uniaxial and equal to the total force divided by its real cross-section. The mean strain is obtained from the image correlation algorithm for the in-plane components. Moreover, due to the large strains involved in the striction area, we

used an isochoric plastic flow assumption in order to infer the transverse component of the strain needed for estimating the real cross-section. The same procedure is performed repeatedly and independently for all slices in the domain of interest, and for all loading stages.

Collecting all those mean stress-mean strain, an admittedly crude estimate of the constitutive law, independent of a specific choice of its algebraic form, is obtained.

The main minimization approach consists in modeling the specimen with its natural boundary conditions, i.e. free surface along the observation face, and by imposing a uniform purely tensile stress at the two ends of the specimen, adjusted to the measured tensile force scaled by the area of the cross-section.

One obvious difficulty is due to the striction. Indeed, it is an instability which numerically does not set in naturally, or if it does, it has no chance to coincide with the actual localization of the striction. To give a hint to the code, the FEM model is modified in such a way to create, at the location of the striction zone, a somewhat narrower section (relative reduction of order 10^{-3}). This is enough to initiate the striction where it is observed. The sensitivity to this perturbation was studied by amplifying it to 10^{-2} . This ten-fold increase was shown to have a very small impact on the overall behavior.

The optimization of the error function is performed using an ad hoc Matlab procedure, called PlastFEMDIC-core-direct, that uses the down-hill (or amoeba) search algorithm.

The objective function can be read as a time and space sum of a local discrepancy. Thus it is interesting to observe where the difference is maximum.

Alternatively to this approach, one may try to impose the measured displacement field as a specific boundary condition to the FEM computation. In this case, the in-plane displacement is prescribed at nodes. The out-of-plane component of the displacement can be estimated from the prescription of this surface being load free. If f is the nodal force at the surface, its component normal to the free surface is set to zero. As the in-plane displacement is imposed, corresponding in-plane nodal forces can be computed, at each surface node. For the surface to be free, one has to impose that tangential forces f must be equal to zero. Exploiting this condition is the basis of the equilibrium gap method, used previously in two dimensions for this purpose. The main difference of the proposed scheme is that only surface measurements of a 3D computation are used. In addition, the measured tensile force is imposed as in the previous case through a uniform (uniaxial tension) stress being applied at the specimen grip level. This approach is implemented in a different Matlab subroutine, called PlastFEMDIC-core-dual, using the same non-derivative amoeba method.

The advantage of this formulation is that striction is naturally initiated and the vanishing the resisting surface forces is a natural way to adjust the constitutive law so that this striction would indeed correspond to a genuine instability.

The difficulty of this approach is that axes of the tensile force, and that of the displacement field may not coincide exactly since one is linked to the testing machine, while the other pertains to the image acquisition. If a small angle exists in between the two frames of reference, then this would correspond to having a tangential force being applied at the grips. If the latter is not introduced, then it may be compensated by a distribution of surface forces which then would not be a measure of the proper account of the constitutive law, but would be polluted by an inaccurate modelling of the boundary conditions.

4. Experimental Procedure

As previously described, Kali relies on the results of a "standard" tensile tests. This data have to be augmented

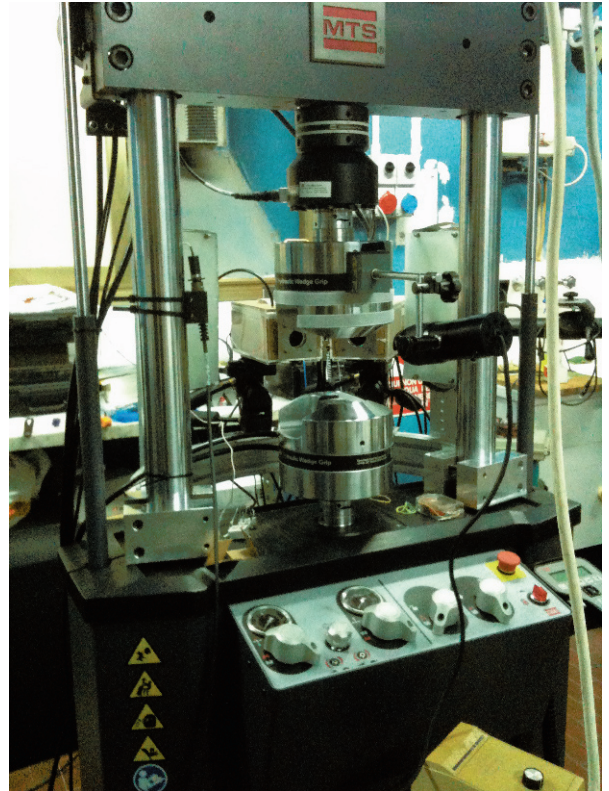


Fig. 1: the acquisition system. Cameras and lights are mounted on a circular frame centered at the axis of the testing machine (back). An extra illumination system is clamped to the fixed head of the testing machine to lit up the background during silhouetting.

whit full field surface displacements to enable PlastFEMDIC processing. Thus a standard servohydraulic testing machine (MTS Landmark model 370.10) was equipped with two digital cameras (AVT Pike 421f) and an illumination system to allow acquiring the displacements field using the Digital Image Correlation technique (Fig. 1). To ensure reliable results (we expected very large strains, at least in the necking zone), some test were performed to find the best type of paint which must be able to endure very large local strains (up to 100%) without detaching from the surface of the specimen. The two cameras are positioned in a non-symmetrical configuration: one directly in front of the specimen, the other at about 30 degrees from the normal. This allows to perform both a standard bi-dimensional and a three-dimensional Digital Image Correlation analysis. To ensure a contemporaneous acquisition of the images by the cameras, the shutters are driven by a hardware trigger. A home made LabView code generates the trigger signal at a user specified rate via the digital output channels of a multipurpose acquisition card (National Instrument PCI-6229) and log the signal of the load cell and of the extensometer generated by the testing machine to allow synchronizing the acquired images with the applied load (to this aim, we use the output channels of testing machine control board and the analogue input channels of the NI card). Figure 2 shows the engineering stress - strain graph and the last images acquired during the test.

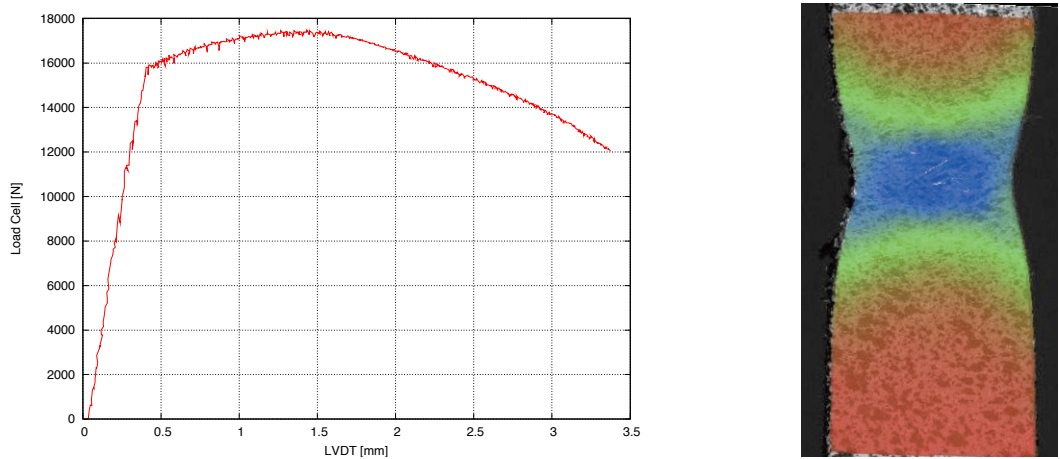


Fig. 2. Left: the experimental stress/strain engineering curve. Right: the V displacement field of last image of the sequence acquired during the test.

The acquired data were processed using both Kali and PlastFEMDIC. Figure 3 shows the engineering FEM-reconstructed stress-strain curves (left) and the related work hardening laws. It is worth noting that the work hardening curve estimated by PlastFEMDIC is quite different from those ones estimated by Kali. As a reference, tab.1 reports all the estimated parameters of the various laws.

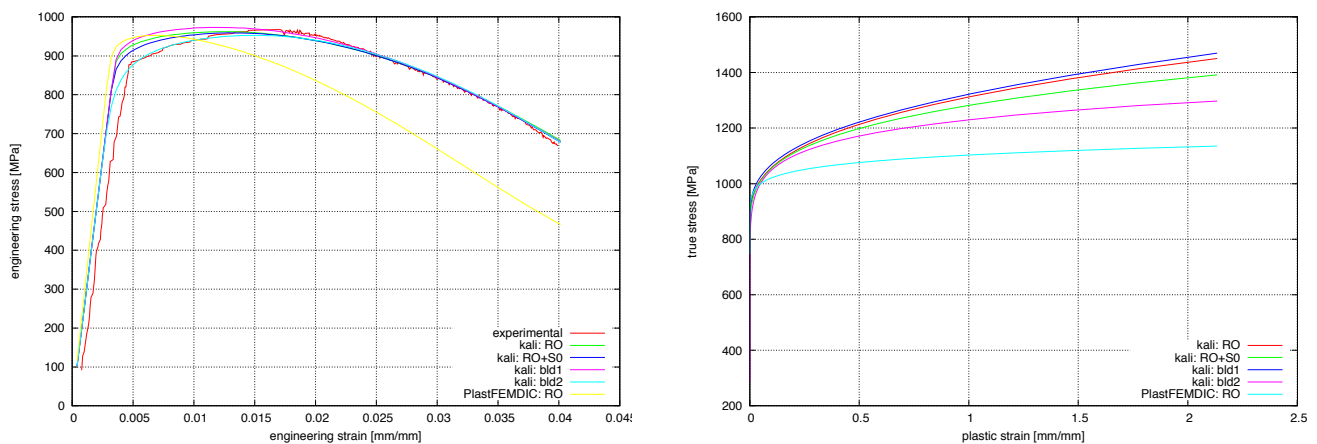


Fig. 3. Left: the experimental and the FEM-estimated stress/strain engineering curve. Right: the estimated work hardening curves.

Table 1: Estimated Parameters

R.O. (Kali)	σ_0 : 850	H : 462.44473	n : 0.34593
--------------------	------------------	-----------------	---------------

R.-O. (Kali)	σ_0 : 785.5	H : 496.40861	n : 0.26415		
Bld₁ (Kali)	σ_0 : 855.8	H : 452.85910	n : 0.32552	w : 0.02144	ε_f : 0.01909
Roux (Kali)	σ_0 : 850.0	A : 138.676	B : 379.998	C : 572.803	
Bld₂ (Kali)	σ_0 : 284.25	H : 945.97	n : 0.09182	γ : 5.4308	β : 8.9065
R.O. (PlatFEMDIC)	σ_0 : 745.76	H : 357.25	n : 0.11344		

5. Result Validation by Silhouette Technique and Conclusions

A silhouetting test was performed to estimate the best agreement to the experimental results. The final contour of the specimen was easily extracted using a standard tool (public domain ImageJ software). Two silhouettes were also extracted from final step of FEM simulations related to model Bld₂ (Kali) and Ramberg-Osgood (PlastFEMDIC). Finally all the contours were superimposed to have a qualitative check of the performances of the plastic models (Fig. 4). The final geometries resulting from both plastic models generally agree quite well to the experimental one, with the exception of the striction area where the Bld₂ model seems to match better the real shape.

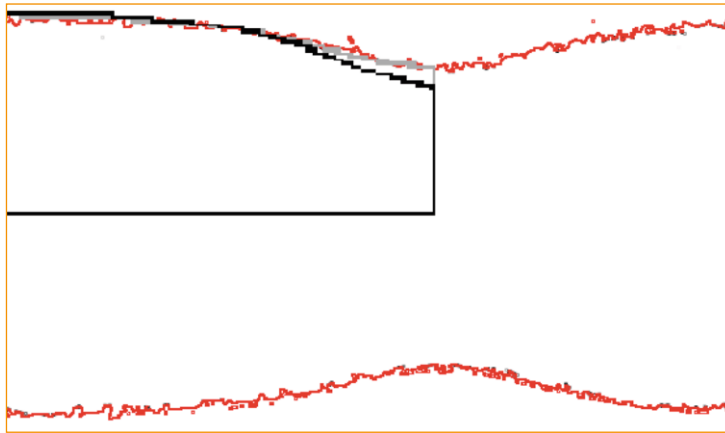


Figure 4: Comparison of the final shape of simulated and experimental tension test. Red: experimental contour. Black: FEM simulated contour related to Ramberg-Osgood model fitted using PlastFEMDIC. Gray: Bld₂ model fitted by Kali.

From these experimental results, it seems that a global fitting procedure is accurate enough to correctly identify the work hardening law in the post-necking field. However it should be noted that the Bld₂ model was not implemented in PlastDicFem thus at the moment it is not possible to separate the contribution of the model from that one of the calibration algorithm (the Kali-fitted Ramberg-Osgood curve does not perform particularly better than that one of PlastDicFem).

References

- [1] R. Hill, *The Mathematical Theory of Plasticity*, Clarendon, Oxford, 1950.
- [2] Bridgman P.W., *Studies in Large Plastic Flow and Fracture*, McGraw-Hill, New York, 1952.
- [3] Aronofsky J., Evaluation of Stress Distribution in the Symmetrical Neck of Flat Tensile Bars, *J. App. Mech.*, March 1951, 75-84, 1951.
- [4] A. Baldi, A. Medda, F. Ginesu, Kali: un algoritmo di calibrazione inversa della curva true stress-true strain. , *AIAS 2009, Atti del XXXVIII Convegno Nazionale*. Torino, 9-11 settembre 2009, p. 211-212, 2009.
- [5] Medda A., Bertolino F., Roux S., Hild F., Experimental identification of a plastic constitutive law from digital image correlation, *In press*.
- [6] Zener C, Hollomon J.H., Effect of Strain Rate Upon Plastic Flow of Steel, *J. Appl. Phys.* 15, 22, 1944.
- [7] Ling Y., Uniaxial true Stress-Strain after necking, *AMP Journal of Technology*, vol. 5, pp.37-48, 1996.
- [8] Ramberg W., Osgood W.R., Description of stress-strain curves by three parameters, *National Advisory Committee for Aeronautics, Washington, D.C., Technical Note No. 902*, 1943.

Determination of hardening behaviour and contact friction of sheet metal in a multi-layered upsetting test

S. Coppieters¹, P. Lava¹, H. Sol³, P. Van Houtte² and
D. Debruyne^{1, 2}

¹ Department of Mechanical Engineering, Catholic University College Ghent, Association K.U. Leuven,
Gebroeders Desmetstraat 1, B-9000 Gent

² Department of Metallurgy and Materials Engineering, K.U.Leuven
Kasteelpark Arenberg 44, B-3001 Herverlee

³ Department of Mechanics of Materials and Constructions,
Vrije Universiteit Brussel, Pleinlaan 2, B-1050 Brussels
sam.coppieters@kahosl.be

ABSTRACT

This paper describes the identification of hardening parameters of DC05 sheet metal and contact friction coefficients using a multi-layered upsetting test (MLUT), the modified two specimen method (MTSM) and a finite element based inverse method. The MLUT is an alternative compression test that is based on the stacking of small circular specimens on top of one another. This test was designed in order to identify frictional and material behavior under severe local forging of sheet metal as encountered during a clinching operation. The MTSM is adopted in order to identify the friction coefficient between the tools and the stacked circular specimens which are cut from the base material by spark erosion. Next, the hardening behavior is identified inversely by combining the results of a MLUT and finite element simulations of the test setup. Finally, the results are compared with standard tensile tests and it is shown that the MLUT is a viable alternative for the identification of the local hardening behavior of sheet metal where standard test specimens cannot be prepared due to size limitations of the specimen.

1 Introduction

In this paper the possibility of identifying frictional and material behaviour under severe local forging of sheet metal as encountered during a clinching operation [14] is explored. Clinching is a mechanical joining technique which involves severe local plastic deformation of two or more sheet metal parts. The optimization of such a connection can be investigated with the aid of the finite element method provided that accurate material data is available. Due to the forming process of the sheets, the local material properties in the clinch area can be substantially altered compared to the initial flat sheet. As the metal flow during the clinching process is limited to a very small region around the tools [6], an optimisation of the geometry using FEA requires accurate local hardening properties of the material. In general, several sheet forming operations, such as deep drawing, bending or stretching, precede clinching of the semi-finished or final product and it is not always possible to produce conventional tensile test specimens. Moreover, experimental data from a simple tensile test would only be useful up to the ultimate tensile strength. Since plastic strains in the order of 2-3 occur during the forming of a clinch the experimental stress-strain curve needs to be extrapolated by a certain hardening law. A compression test would be a much better test for measuring the flow stress since there is no problem with necking. However, it would be very difficult to conduct on a thin sheet. This paper presents an alternative compression test that is based on the stacking of small circular specimens on top of one another, which can be easily removed from the base geometry. An increasing interest in related set-ups for small scale testing for the identification of parameters of constitutive laws has, in

recent years, resulted in a number of papers. Recently Cheon et al.[4] reported about their research on flow stress determination by a small punch test using a hybrid inverse method. On a much smaller length scale, Beghini et al.[3] addressed the mechanical characterization of metallic materials by instrumented spherical indentation testing. Although these tests have different objectives, the same philosophy is followed. However, these small scale tests do not enable the identification of material behaviour at high plastic strains. Other authors [10, 11] have proposed to retrieve the extended yield curve using a tensile test and the finite-element-based inverse technique. The plane strain compression test [2] is also a suitable test to obtain stress-strain curves of sheet metal at high plastic strains. Unfortunately, both the tensile test and the plane strain compression test are not feasible when the sheet pieces are too small. The material test presented in this contribution was designed in such a way that stacked circular sheet metal specimens of arbitrary size are compressed between two identical punches. Of main interest in this Multi-Layered Upsetting Test (MLUT) is to reveal the local hardening behaviour of the sheet metal at high plastic strains, i.e. beyond the ultimate tensile strength of the material. During this type of experiment one has to take into account that there is substantial friction between the tools and the specimens on the one hand and between the specimens themselves on the other hand. This requires that the frictional properties also have to be identified in order to separate them from the hardening behaviour.

Section 2 presents the experimental setup. Next, in Section 3, the Coulomb friction coefficient between the tools and the stack is determined via the Modified Two Specimen Method (MTSM). Section 4 embarks on the identification of the hardening behaviour using a finite-element-based inverse method. Finally, some conclusions can be found in Section 5.

2 Multi-layered Upsetting Test

The multi-layered upsetting test consists of the simultaneous application of two identical punches to a number of stacked circular sheet metal specimens which can be removed from a base geometry by using spark erosion or any other suitable method. In principle, there is no restriction on the geometry of the samples save that the height must be limited to avoid buckling. This test allows the stacked cylinder of thin metal sheet to be forged, where the bottom punch can be seen as the anvil while the top punch represents the forging tool. In order to compress the stack, the test apparatus, schematically drawn in Figure 1, is mounted into a tensile machine. The dimensions of the circular specimens used in this study can also be found in Figure 1. The height of the stack depends on the number of circular specimens and can be varied. During the upsetting of the stack, the loading force and the punch displacement are measured using a load cell and an extensometer.

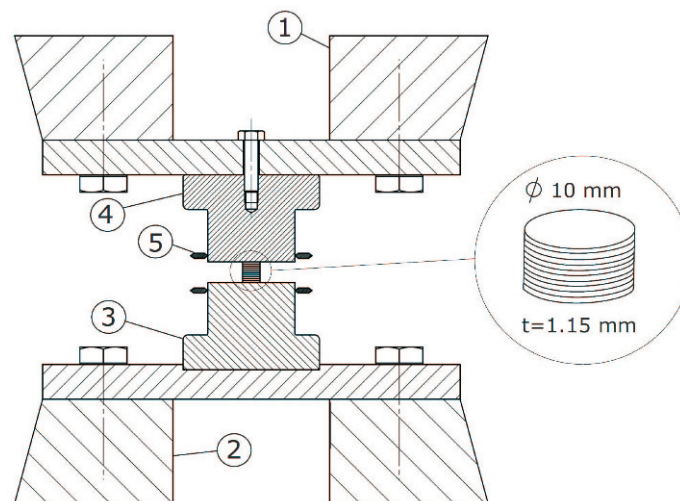


Figure 1: Setup of the MLUT: 1. Upper clamp of the tensile bench, 2. Lower clamp of the tensile bench, 3. Anvil, 4. Punch and 5. Extensometer

Figure 2 shows different possible deformation modes of the stack due to varying friction conditions as can be obtained in a FE simulation. Three examples are shown: (A) frictionless contact between tools and the stack (perfect

lubricant) in combination with Coulomb friction between adjacent specimens $\mu_i=0.4$, (B) Coulomb friction between tools and stack $\mu_t=0.2$ and $\mu_i=0.4$ and, finally, (C) shows upsetting assuming $\mu_t=0.2$ and $\mu_i=0.1$. However, the latter situation is not likely if there is dry contact between adjacent circular specimens and the interface between stack and tools is lubricated adequately. Therefore, it is assumed for all tests that μ_i is constant and $\mu_i > \mu_t$. It can be inferred from Figure 2 that the decrease in layer thicknesses may be either proportional or non-proportional depending on the assumed friction condition. The force-displacement data, measured during the multi-layered upsetting test, can be used to identify the hardening behaviour of the sheet metal provided that friction conditions are more or less known or that they can be determined simultaneously. As lubrication deteriorates due to thinning of the film and extension of the surface, the friction may actually vary during the MLUT. Zone-Ching et al. [15] inversely identified plastic material properties through an upsetting test assuming the change of friction to be known a priori (see also [16, 17]). However, it is assumed that the frictional shear stress at the surface of the stack is directly and constantly proportional to the normal stress due to the presence of the lubricant. μ_t was identified by the modified two specimen method (MTSM) which requires additional testing.

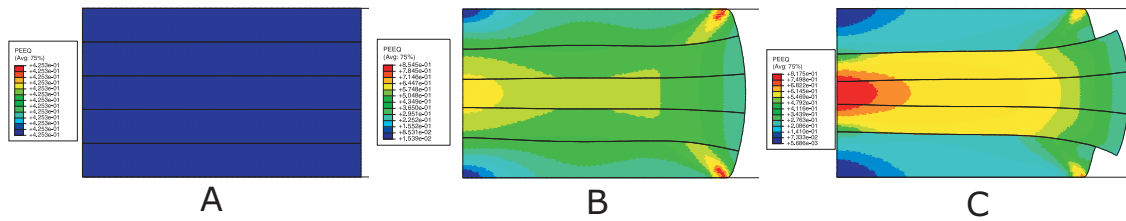


Figure 2: Axisymmetric deformation modes obtained by FEA. A. Frictionless contact between tools and the stack in combination with Coulomb friction between adjacent specimens $\mu_i=0.4$ B. Coulomb friction between tools and stack $\mu_t=0.2$ and $\mu_i=0.4$ C. $\mu_t=0.2$ and $\mu_i=0.1$

3 The modified two specimen method

The most common method used to determine friction for a forging process is the ring compression test. This test uses a thin ring with dimensions (outer diameter : inner diameter : thickness) in the ratio (6 : 3 : 1) [7]. As the thickness of the sheet is normally rather small, the dimensions of the ring become very small. Sheet metal friction testing methods do exist, but these tests are based on a low interface pressure and large sliding lengths. In this paper the friction between the stack and the tools is studied by a modified two specimen method. The MTSM is based on the hypothesis that the material behaviour is independent of the specimen's geometry, in contrast to the flow resistance. In addition one assumes that the material is plastically incompressible and the coefficient of friction is an average value on the contact surface. In certain situations, it is possible to derive a mathematical model which expresses the relationship between the flow resistance (or loading force), the flow stress and the friction coefficient in a test setup. If two experiments are conducted adopting similar conditions in terms of temperature, boundary conditions and strain rate, but, using a different specimen geometry, an objective function or cost function $C(\mu)$ can be constructed where the flow stress is eliminated. The minimization of $C(\mu)$ enables the estimation of the friction coefficient μ . For further details we refer to Han Han [8, 9]. In this contribution, the MTSM is adopted to estimate the Coulomb friction between the tools and the stacked circular specimens. In order to use the mathematical model of cylinder upsetting the stack is glued together thereby preventing frictional dissipation between the stacked specimens. $C(\mu)$ then reads as:

$$C(\mu_t) = \sum_{i=1}^m (P_{2,i} - P_{1,i} \left(\frac{h_{2,0}}{h_{1,0}}\right)^2 \frac{\exp(\mu_t X_{2,0} - 1 - \mu_t X_{2,i})}{\exp(\mu_t X_{1,0} - 1 - \mu_t X_{1,i})})^2 \quad (1)$$

with

$$X_{k,i} = \frac{2r_{k,0}(\exp(\bar{\epsilon}_{k,i}))^{1.5}}{h_{k,i}} \quad (2)$$

where m is the number of measurements, $P_{k,i}$ a 1-dimensional vector containing the measurements of the flow resistance, h_i the instantaneous height of the stack and r_i the radius. The above strategy was adopted in order to determine the Coulomb friction coefficient condition between the upper and the lower circular specimen of the stack and the forging tools. Experimental data was obtained by conducting upsetting experiments using two geometrical different stacks. Only the number of the circular specimens differed, yielding two stacks with heights $h_{1,0} = 5.75$ mm and $h_{2,0} = 10.35$ mm, respectively. The actual upsetting of the stacks was carried out using two flat, mirror finished open dies made of 42CrMoV4 which were mounted on a Zwick tensile machine with a capacity of 250 kN. A mixture of high pressure grease and WS_2 was applied in order to reduce friction. The compression was conducted with a punch travel velocity of 0.01 mm/s, assuming quasi-static conditions and constant temperature. The cost function $C(\mu)$ (Equation 1) is then minimized using a Levenberg-Marquardt algorithm; this yields a Coulomb friction coefficient $\mu_t = 0.19$. Friction is closely related to surface roughness and Figure 3 shows the average surface roughness R_a of an undeformed specimen, a deformed specimen, a deformed top specimen and the punch. As can be inferred from this figure, R_a decreases significantly after deformation of the stack ($\ln(\frac{h_o}{h}) = 0.2$) and a clear difference can be noticed between the top specimen's surface and the surface of adjacent specimens. Figure 3 shows also the final axisymmetric geometry: top half of this figure is the FEA result, while the bottom half is a cross section of the encapsulated specimen.

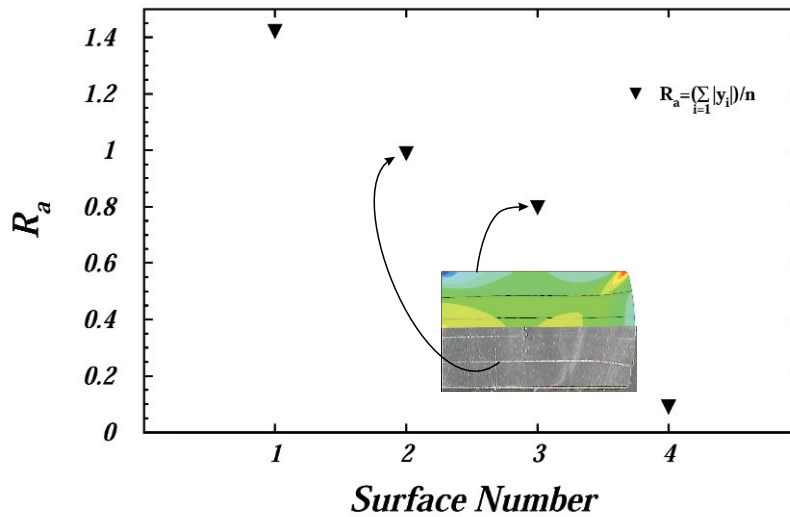


Figure 3: Average Roughness. 1. Undeformed specimen surface 2. A surface of adjacent Specimens 3. Top Specimen surface 4. Punch Surface

4 Finite-element-based inverse method

The present work focuses on a multi-layered upsetting test where only load-displacement data is available. Therefore, plastic material parameters are adjusted until the predicted load-displacement curve matches the experimental one as close as possible. In other words, a procedure is needed to minimize a cost function $C(\mathbf{q})$ expressing the error between the experimental results and the simulation:

$$C(\mathbf{q}) = \frac{1}{2} \sum_{i=1}^m (r_i(\mathbf{q}))^2 = \frac{1}{2} \mathbf{r}^T \mathbf{r} \quad (3)$$

where m is the number of measurements, \mathbf{q} the set of unknown model parameters and \mathbf{r} the residual vector defined as

$$\mathbf{r} = \mathbf{f}^{\text{exp}} - \mathbf{f}^{\text{num}} \quad (4)$$

where \mathbf{f}^{exp} and \mathbf{f}^{num} are the column vectors of the experimentally measured forces and the numerically computed forces, respectively. The minimization of the cost function $C(\mathbf{q})$ requires an appropriate optimisation method which

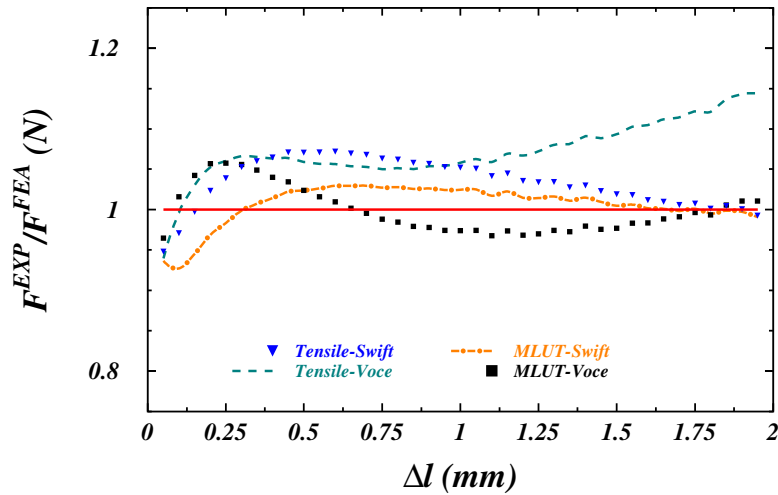


Figure 5: Deviation between sample results and the simulation.

is encountered in the MLUT in case of a stack-height reduction of 35%. Whereas the average logarithmic strain in the thickness direction is equal to 0.43 ($= \ln(1/0.65)$), the FE simulations predict a local maximum equivalent plastic strain of 0.6. These strain values are significantly higher compared to the maximum uniform strain of 0.23 in the tensile test. As can be inferred from Figure 4, the identified Swift laws correlate quite well up to the maximum plastic equivalent strain in the MLUT. Clearly, the accuracy of the MLUT combined with the inverse procedure highly depends on the a priori chosen hardening law. The right panel of Figure 4 shows the identified laws extrapolated up to high plastic strains. The identified laws are used to simulate the multi-layered upsetting test and it can be concluded from Figure 5 that the error between the sample results and the simulation using a Swift type hardening law with the parameters deduced from the multi-layered upsetting, is minimal.

5 Conclusions

This paper studied the identification of hardening parameters and friction coefficients of sheet metal (DC05) using a multi-layered upsetting test. This test consists of the forging of stacked circular sheet metal specimens that can be cut from base material by spark erosion or some other method. The purpose of this material test is to provide an alternative small scale test for the determination of local hardening properties at significantly higher strains as encountered during tensile testing. The first part of this work focussed on the identification of the friction between the stack and the open dies. For this purpose, geometrically different stacks were compressed in order to apply the Modified Two Specimen Method (MTSM). Next, the parameters of two hardening laws were identified using a finite element based inverse method, thereby using the earlier identified friction coefficient. The results were compared to those obtained by standard tensile tests. The Voce law derived by the tensile test predicts a lower saturation level than the one obtained by the MLUT; as a result it leads to an underestimation of the compression force during the MLUT. However, the two Swift laws converge with increasing equivalent strain, indicating that the Swift law is better suited to describe the large strain behaviour of the studied deep drawing steel DC05. Thus, the MLUT allows to identify which of the tensile test hardening laws is most appropriate for higher strains.

6 Acknowledgements

The help of Kris Hertschap (Arcelor Mittal R&D Industry Gent, OCAS NV) in providing the materials used in the MLUT is gratefully acknowledged. The authors also like to thank Renaat van Hecke (Catholic University College Ghent) for the construction of the experimental setup.

guarantees the convergence to a global minimum. Here, the Gauss-Newton algorithm was adopted, for which the update equation can be written as

$$\Delta \mathbf{q} = [\mathbf{S}^T \cdot \mathbf{S}]^{-1} \cdot [\mathbf{S}^T \cdot ((\mathbf{f}(\mathbf{q}))^{\text{exp}} - (\mathbf{f}(\mathbf{q}))^{\text{num}})] \quad (5)$$

In this work the sensitivity matrix S_{ij} contains the sensitivities of the computed forces to the unknown hardening parameters. Finite differentiation was used to compute this matrix. In this approach the partial derivative of the punch force with respect to the unknown model parameters is numerically approximated from responses calculated with a set of slightly modified parameters. The numerical model of the MLUT was built using the commercial implicit finite element code *Abaqus/Standard*, which applies a hypoelastic-plastic constitutive model. The material is assumed to be elastically and plastically isotropic. The elastic behaviour is characterized by a Young's modulus $E = 200$ GPa and a Poisson coefficient $\nu = 0.3$. Strain rate dependence was not considered. The axisymmetric FE model was built using 4-node bilinear axisymmetric quadrilateral elements with reduced integration and enhanced hourglass control. Furthermore, the model assumes quasi-static equilibrium and takes into account the nonlinear effects from the plastic material behaviour and contact with friction. The Coulomb friction model using the identified value (see Section 3) is adopted to model friction between tools and stack. The model used to simulate the friction between adjacent specimens was extended with a shear stress limit τ_{max} . This shear stress limit is introduced because the high contact pressure could cause the Coulomb theory to provide a critical shear stress at the interface that exceeds the yield stress in the material beneath the contact surface [1]. The isotropic hardening was modelled using two phenomenological hardening laws which are commonly adopted to extrapolate the stress-strain behaviour obtained in a tensile test:

$$\bar{\sigma}(\epsilon_{eq}^{pl}, q_i) = K(\epsilon_0 + \epsilon_{eq}^{pl})^n \quad (6)$$

$$\bar{\sigma}(\epsilon_{eq}^{pl}, q_i) = A - B \exp(-C \epsilon_{eq}^{pl}) \quad (7)$$

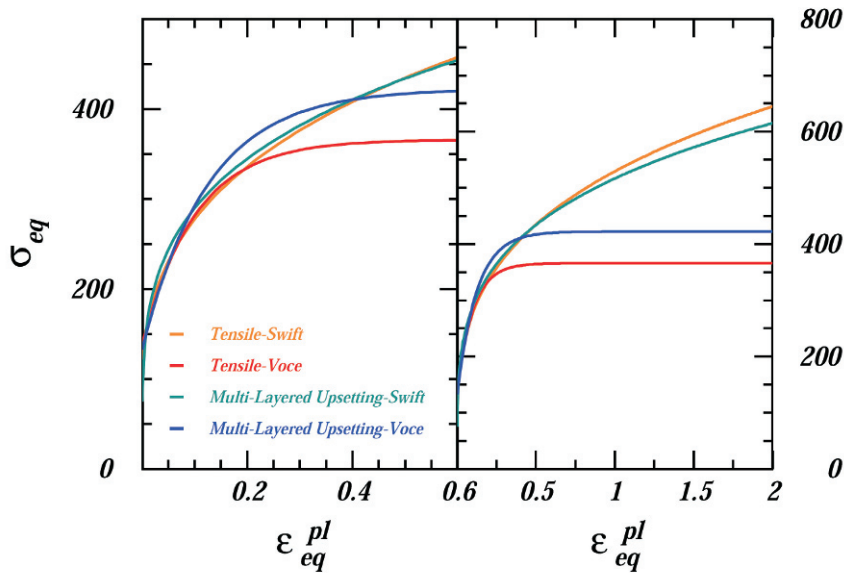


Figure 4: Left panel: experimental flow curves deduced from standard tensile test and multi-layered upsetting. Right panel: identified laws extrapolated up to high plastic strains

The results of a simple compression test on a specimen of ductile metal are virtually identical to those of a tensile test if Cauchy stress is plotted against logarithmic strain [13]. Due to friction, however, the state of stress cannot be one of simple compression and deviations from tensile test results are expected. The experimental data used to identify the parameters of the hardening laws Equation (6) and (7) was obtained by the upsetting of a stack comprising 5 circular specimens. The left panel of Figure 4 shows the strain hardening in the strain range that

References

- [1] Abaqus Theory Manual Version 6.7
- [2] Becker, N., Phlandt, K., 1989. Improvement of the plane strain compression test for determining flow curves. *Annals of the CIRP* Vol. 38/1/1989
- [3] Beghini, M., Bertini, L., Fontanari, V., 2006. Evaluation of the stress-strain curve of metallic materials by spherical indentation. *International Journal of Solids and Structures*. Vol. 43, Issues 7-8. pp. 2441-2459.
- [4] Jin-Sik Cheon and Cheol-Hong Joo, 2008. Small punch test for determining a flow stress by using hybrid inverse procedure. *Computational Materials Science*. Vol. 43, Issue 4. pp. 744-751.
- [5] Cooreman, S., Lecompte, D., Sol, H., Vantomme, J., Debruyne, D., 2008. Identification of mechanical material behavior through inverse modelling. *Experimental Mechanics*. Vol. 48, Issue 4. pp. 421-433.
- [6] de Paula, A.A., Aguilar, M.T.P., Pertence, A.E.M., Cetlin, P.R., 2007. Finite element simulations of the clinch joining of metallic sheets. *Journal of Materials Processing Technology* Vol. 182, Issues 1-3. pp. 352-357.
- [7] Dieter, G.E., 1987. *Mechanical Metallurgy*. McGraw-Hill Book Company. London.
- [8] Han Han, 2005. Determination of mean flow stress and friction coefficient by the modified two-specimen method in cold-rolling. *Journal of Materials Processing Technology*. Vol. 159, Issues 3-10. pp. 401-408.
- [9] Han Han, 2002. The validity of mechanical models evaluated by two-specimen method under the unknown coefficient of friction and flow stress. *Journal of Materials Processing Technology*. Vol. 122, Issues 2-3. pp. 386-396.
- [10] Koc, P., Stok, B., 2004. Computer-aided identification of the yield curve of a sheet metal after onset of necking. *Computational Materials Science*. 31 pp. 155-168.
- [11] Kajberg, J., Lindkvist, G., 2004. Characterisation of materials subjected to large strains by inverse modelling based on in-plane displacement fields. *International Journal of Solids and Structures* 41 pp. 3439-3459
- [12] Lecompte, D., Cooreman, S., Coppieters, S., Vantomme, J., Sol, H., Debruyne, D., 2009. Parameter identification for anisotropic plasticity model using digital image correlation: Comparison between uni-axial and bi-axial tensile testing. *European Journal of Computational Mechanics*. Vol. 18, Issues 3-4. pp. 393-418.
- [13] Lubliner, J., 2008. *Plasticity theory*. Dover Publications. New York. pp. 77-78.
- [14] Varis, J.P., 2003. The suitability of clinching as a joining method for high-strength structural steel. *Journal of Materials Processing Technology*. Vol. 132, Issues 1-3. pp. 242-249.
- [15] Zone-Ching Lin, Chang-Cheng Chen, Hsin-Ho Wang, 2009. The determination of material strength coefficient and strain hardening constant by inverse method. *Journal of Materials Processing Technology*. Vol. 209, Issue 5. pp. 2393-2401.
- [16] Zone-Ching Lin, Chun-kung Chen, 2006. Inverse calculation of the friction coefficient for upsetting a cylindrical mild steel by the experimental load. *Journal of Materials Processing Technology*. Vol. 178, Issues 1-3. pp. 297-306.
- [17] Zone-Ching Lin, Ven-Huei Lin, 2006. Friction coefficient of upsetting with a procedure of combining the inverse model and the Tikhonov method. *International Journal of Mechanical Sciences*. Vol. 48, Issue 7. pp. 717-725.

Measuring the Elastic Modulus of Soft Thin Films on Substrates

M.J. Wald^{1*}, J.M. Considine², K.T. Turner³

¹Dept. of Engineering Physics, University of Wisconsin, Madison, WI

²US Forest Service, Forest Products Laboratory, Madison, WI

³Dept. of Mechanical Engineering, University of Wisconsin, Madison, WI

*1513 University Avenue, Madison, WI 53706; wald@wisc.edu

Abstract

The use of instrumented indentation to measure the mechanical properties of thin films supported on substrates where the Young's modulus of the film (E_1) is substantially less than that of the Young's modulus of the substrate (E_2) with modulus ratios from $E_1/E_2 = 0.0001$ to 1 is important for investigating materials such as soft polymers, cellulosic sheets, and biological materials. Most existing models for determining the elastic properties of films or sheets on substrates from indentation measurements were developed for the analysis of metal and dielectric films on semiconductor substrates and thus have been used in cases where E_1/E_2 is ~ 0.01 to ~ 10 . In the present work, flat punch indentation of systems with $E_1/E_2 = 0.0001$ to 1 is investigated via finite element (FE) modeling and experiments. A FE parametric study in which E_1/E_2 was varied from 0.0001 to 1 was performed to quantify the effect of substrate stiffness on the measurement of the elastic film properties. A semi-analytical model that treats the thin film and substrate as two springs in series was fit to the FE results to allow for use of the results presented. Preliminary experiments, in which a series of film/substrate systems with various modulus mismatch (E_1/E_2 from ~ 0.0005 to ~ 1) were characterized using instrumented indentation, were performed to evaluate the effectiveness of the model for extracting films properties from indentation measurements. The results of the parametric FE study show that for very stiff substrates, the measured stiffness becomes insensitive to changes in substrate modulus. The analytical model and FE model agree to within 7% for E_1/E_2 values between 0.0001 to 1 and a/t ratios from 1 to 100. Comparison of the preliminary experimental results and FE model show reasonable agreement, but further investigation is required to obtain better correlation.

Introduction

Instrumented indentation is a common method for characterizing the mechanical properties of a thin film on a substrate. A widely accepted method for determining the modulus of an elastic halfspace from indentation was presented by Oliver and Pharr [1]. For films on substrates, the Oliver-Pharr method has been shown to produce reliable measurements of film properties for indentation depths up to approximately ten percent of the film thickness for certain indenter geometries [2]. This limit on indentation depth is an approximation as the size of the contact area and thickness of the film both influence the role that the substrate will have on stiffness measurements. Regardless, when indenting films on substrates, even to shallow depths, the measurement and standard data analysis often yields an effective modulus that depends on the elastic properties of both the film and substrate. Numerous mechanics models [3-7] have been developed to determine the Young's modulus of the film from the effective modulus measurements obtained using the standard Oliver-Pharr approach. Most of these models, however, have only been rigorously tested and shown to be effective for film modulus to substrate modulus ratios of 0.1 – 10, which are typical of systems that involve combinations of metals, ceramics, and semiconductors. It is unclear if these models can be applied to cases where the indenter has a large contact area and the film/substrate system has a high elastic mismatch, such as a polymer film or biological material supported on much stiffer substrate like metal or glass.

In the present work, cylindrical flat punch indentation of an elastic thin film on an elastic substrate is investigated for cases in which E_1/E_2 varies from 0.0001 to 1. Cylindrical flat punch indentation is investigated here because many soft materials of interest have complex and porous structures and larger contact areas are required to

suitably sample the average elastic properties. Specifically, we investigate flat punch indentation cases where the contact radius, a , to film thickness, t , ratio, a/t , varies from 1.0 to 100. Indentation over this range of E_1/E_2 and a/t ratios was investigated using a 2-D axisymmetric finite element model. A simple analytical model based on treating the film-substrate system as two springs in series is presented to capture the response predicted by the FE model. Finally, instrumented indentation experiments were used to examine the properties of a thin low density polyethylene (LDPE) film on several substrates with different elastic moduli in order to examine the effectiveness of the model. We note that LDPE is not a particularly soft material ($E \sim 100$ MPa) compared to gels and biological materials, however LDPE allows specimens with a large range of moduli mismatch (E_1/E_2 from ~ 0.0005 to ~ 1) to be easily prepared and tested and thus was chosen for this initial work.

Background

Analysis of Flat Punch Indentation

Results from instrumented indentation tests are typically analyzed assuming the specimen is a homogeneous isotropic elastic halfspace. From the load-displacement history recorded in a test, a stiffness k is measured. For an axisymmetric indenter, the effective modulus is related to the measured stiffness via

$$E_{eff} = \frac{\sqrt{\pi}}{2} \frac{1}{\sqrt{A}} k, \quad (1)$$

where A is the area function of the indenter and, in general, is a function of indentation depth [1]. For flat punch indentation, the indenter area is constant with depth and $A = \pi a^2$. Thus, Equation (1) reduces to

$$E_{eff} = \frac{k}{2a}. \quad (2)$$

The effective modulus is defined as

$$\frac{1}{E_{eff}} = \frac{1}{E_s^*} + \frac{1}{E_i^*}, \quad (3)$$

where $E_s^* = E_s/(1-\nu_s^2)$ and $E_i^* = E_i/(1-\nu_i^2)$ are the reduced moduli of the specimen and the indenter respectively. The above equations are valid for cases in which the substrate is an elastic halfspace or in cases in which a film is sufficiently thick such that the substrate does not affect the stress distribution in the film. However, for most practical applications of cylindrical flat punch indentation in which the properties of a thin film on a substrate

(Figure 1) are measured, the specimen cannot be treated as a halfspace and k , and subsequently E_{eff} , depend on the elastic properties of the film and substrate, film thickness, and indenter geometry.

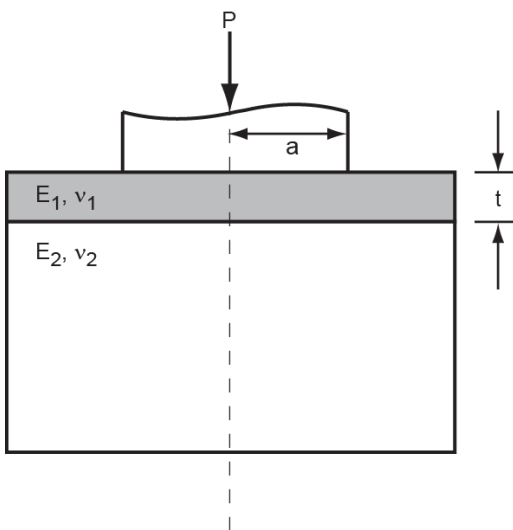


Figure 1 - Schematic of indentation problem considered. The system consists of an elastic thin film on a thick elastic substrate being indented by a rigid cylindrical flat punch

Previous Analyses of Indentation of Films on Substrates

Several models have been proposed to describe the relationship between the film and substrate elastic properties, indenter geometry, and film thickness in order to extract the elastic modulus of a thin film on a substrate from instrumented indentation measurements. A complete review of all the models is not possible here, thus the more commonly cited models are briefly summarized. Gao, *et al* [3], King [7], and Sakai [6] have all presented analytical models for the indentation of a film supported on a halfspace. Gao *et al* employed weight functions with no undetermined constants to determine the elastic properties of films from measured effective moduli. This method is only applicable for cases where the E_1/E_2 ratio is between 0.5 and 2. An analysis from Rar *et al*. [4] extended Gao's model apply to cases with a modulus mismatch from 0.1 to 10 and a/t between 0.1 and

10. King's model describes the relationship between film and substrate modulus using exponential functions and an undetermined constant and has been used to determine the modulus of an aluminum film on silicon substrate [8]. Sakai used Boussinesq's Green function to determine film modulus from E_{eff} and presented results for E_1/E_2 from 0.2 to 10 and a/t from 0.01 to 10.

In the present work, we use an analytical model similar to that presented by Bec *et. al* [5] in which the film and substrate are treated as two springs in series. The stiffness of one spring is determined by considering the stiffness of the film deformed by a uniform displacement by a rigid cylindrical flat punch. The stiffness of the second spring is the stiffness of an elastic halfspace under a uniform displacement with the substrate's elastic properties. Combining these springs in series gives

$$\frac{1}{k} = \frac{t}{f\left(\frac{a}{t}\right)\pi a^2 E_1^*} + \frac{1}{f\left(\frac{a}{t}\right)2aE_2^*}, \quad (4)$$

where k is the measured stiffness, t is the film thickness, a is the indenter radius, and E_1^* and E_2^* are the reduced moduli of the film and substrate, respectively. Bec *et. al* [5] used $f\left(\frac{a}{t}\right) = 1 + \frac{2t}{\pi a}$. Cases where E_1/E_2 varied from 0.1 to 10 and a/t varied from 0 to 3 were examined in [5].

Methods

Finite Element Modeling

A finite element (FE) model was developed to systematically investigate the effect of indenter contact radius, film thickness, film modulus, and substrate modulus on the effective modulus measured via indentation. The basic model geometry consists of a thin elastic layer on a thick elastic substrate indented by a cylindrical flat punch as shown in Figure 1. The model was axisymmetric and the film and substrate were meshed with eight-node elements. The indenter was modeled as a rigid body and displaced into the surface. The indenter-film surface interaction was modeled using contact elements. The model was developed and solved using the commercial package ABAQUS [9]. Two studies were performed using the model. In the first, the modulus ratio, contact radius to film thickness ratio, and film thickness were parametrically varied across the range shown in Table 1. In all of these cases, the Poisson's ratio for the film and substrate was fixed at 0.3. In the second study, the sensitivity of the measured stiffness to changes in film modulus was evaluated by investigating the percent change in the effective stiffness when the film modulus is changed from $E_1 = 100$ MPa to $E_1 = 110$ MPa on substrates with moduli ranging from 100 MPa to 1 TPa (corresponding to E_1/E_2 from ~ 1 to ~ 0.0001). Again, Poisson's ratio for the film and substrate was fixed at 0.3.

Instrumented Indentation Experiments

Indentation tests were conducted on a TA Q800 DMA in controlled force mode using a 900 μm diameter steel cylindrical flat punch. The specimens were loaded at a rate of 10 mN/s up to maximum load of 1 N. The maximum load was held for 1 minute. Following the hold period, the specimens were unloaded at a rate of 10 mN/s. The stiffness, k , is determined from the slope of the unloading curve. Machine compliance was measured through indentation tests on a fused silica sample, yielding a machine compliance of 0.668 \pm 0.091 $\mu\text{m}/\text{N}$. The stiffnesses measured from the unloading curves were corrected using this machine compliance.

Table 1 - Parameters for FE simulations

Fixed Parameters	Parameters Varied
$t = 80 \mu\text{m}$ $E_1 = 100 \text{ MPa}$ $\nu_1 = \nu_2 = 0.3$	$E_1/E_2 = 0.0001 - 1$ $a/t = 1 - 100$
$t = 100 \mu\text{m}$ $E_1 = 100 \text{ MPa}$ $\nu_1 = \nu_2 = 0.3$	$E_1/E_2 = 0.0001 - 1$ $a/t = 1 - 100$

Table 2 - Summary of film and substrate properties used in experiments

	Young's Modulus	Ref.
Film		
LDPE	55.1 - 172 MPa	[10]
Substrate		
LDPE	55.1-172 MPa	[10]
PMMA	3.3 GPa	[10]
Aluminum	70 GPa	[11]
Steel	204 GPa	[11]

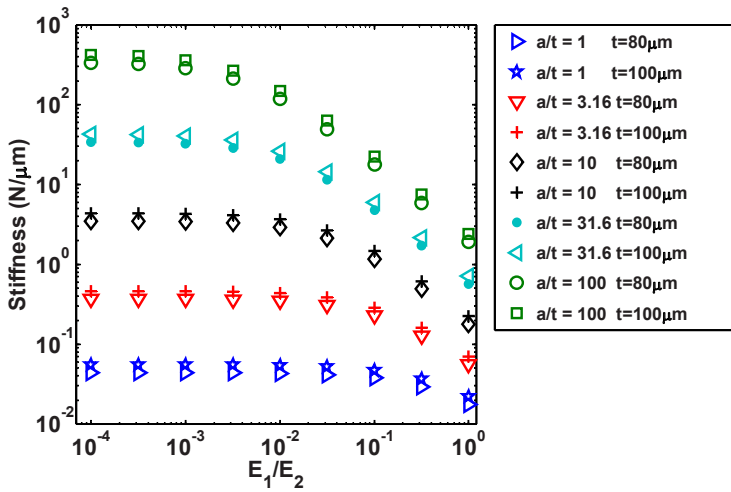


Figure 2 - Effective stiffness of a film on a substrate for various E_1/E_2 and a/t ratios calculated via FE modeling. For all cases, $E_1 = 100$ MPa and $\nu = 0.3$

increases and as the substrate modulus increases. At low values of E_1/E_2 (i.e. substrate modulus \gg film modulus), the stiffness is relatively insensitive to substrate modulus.

A study to assess the sensitivity of film-substrate systems to changes in film modulus was also performed. The percent change in stiffness that occurs due to changing the film modulus from 100 MPa to 110 MPa is shown in Figure 3 as a function of a/t and substrate modulus. The sensitivity to changes in the film modulus increases as the substrate modulus increases, approaching a 9% change when $E_1/E_2 \sim 0.0001$ for the cases shown. However, as the a/t ratio increases, the change in measured stiffness decreases. This is especially apparent when comparing the $a/t = 1$ case and the $a/t = 100$ case at $E_2 = 100$ MPa where there is a 4.3% change in stiffness for the $a/t = 1$ case, but 0.1% change when $a/t = 100$.

Analytical Model

The indenter substrate system shown in Figure 1, in which $a/t > 1$, lends itself to the development of a simple analytical model.

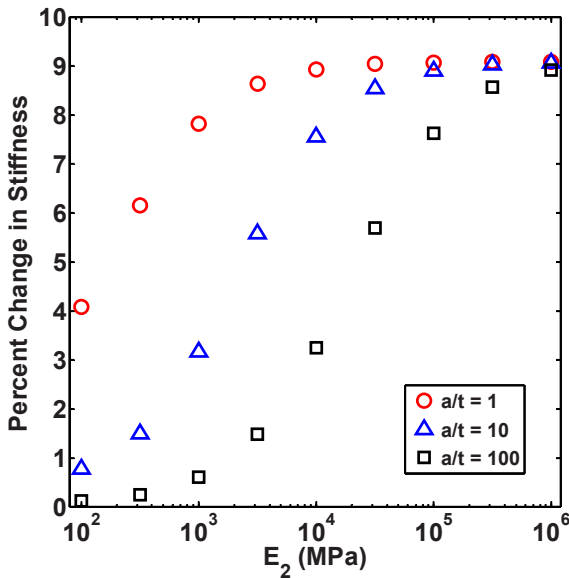


Figure 3 - Percent change in effective stiffness between two films ($E_1=100$ MPa and $E_1=110$ MPa) on substrates of varying modulus (E_2)

The stiffness of a LDPE film ($t = 100 \mu\text{m}$) on several different substrates with various elastic moduli were measured. The elastic properties of the film and the substrate are summarized in Table 2. All values shown in Table 2 are nominal values taken from the references listed. Tensile tests to verify the properties of actual materials used are currently being performed.

Finite Element Results and Analytical Model

FE Results

Results from FE simulations over the range of parameters in Table 1 are summarized in Figure 2, which shows the indentation stiffness as a function of modulus and a/t ratio. For a fixed film modulus, the stiffness of the system increases as the contact radius

increases and as the substrate modulus increases. At low values of E_1/E_2 (i.e. substrate modulus \gg film modulus), the stiffness is relatively insensitive to substrate modulus. A study to assess the sensitivity of film-substrate systems to changes in film modulus was also performed. The percent change in stiffness that occurs due to changing the film modulus from 100 MPa to 110 MPa is shown in Figure 3 as a function of a/t and substrate modulus. The sensitivity to changes in the film modulus increases as the substrate modulus increases, approaching a 9% change when $E_1/E_2 \sim 0.0001$ for the cases shown. However, as the a/t ratio increases, the change in measured stiffness decreases. This is especially apparent when comparing the $a/t = 1$ case and the $a/t = 100$ case at $E_2 = 100$ MPa where there is a 4.3% change in stiffness for the $a/t = 1$ case, but 0.1% change when $a/t = 100$.

The stiffness of the spring representing the film is estimated as the stiffness of an elastic cylinder of radius a under uniform axial displacement. As the layer is thin relative to the cylinder radius, the in-plane strain is constrained and the uniaxial-strain modulus is used in place of Young's modulus. The degree of constraint will be a function of a and t and thus a constant, C_1 , that is assumed to be a function of a and t is introduced. With these assumptions, the stiffness of the film is given as:

$$k_f = \frac{C_1 \pi a^2 E_1'}{t}, \tag{5}$$

where $E_1' = \frac{(1-\nu)E_1}{(1+\nu)(1-2\nu)}$.

The stiffness of the spring representing the substrate is determined by calculating the stiffness of an elastic halfspace loaded by a constant pressure over a circular area of radius a [12]. A constant pressure distribution assumes the thin film evenly distributes the pressure from the indenter onto the substrate. The radius of the area over which the pressure is distributed will be slightly larger than the contact radius and will depend on a/t , thus a constant C_2 , that is a function of a/t is introduced in the stiffness equation yielding

$$k_2 = \frac{C_2 \pi a E_2^*}{2}, \quad (6)$$

where $E_2^* = E_2 / (1 - \nu^2)$. The overall stiffness of the system was found by combining Equations 5 and 6 assuming the springs are connected in series:

$$k = \frac{k_1 k_2}{k_1 + k_2} = \frac{C_1 C_2 \pi a^2 E_2^* \xi}{(2 C_1 a \xi + C_2 t)}, \quad (7)$$

where $\xi = \frac{E_1'}{E_2^*}$.

As noted earlier, constants C_1 and C_2 are unknown, but are assumed to be a function of a and t . The values of C_1 and C_2 are determined through fits to the FE simulations in the present work. During fitting, the following dimensionless stiffness is used:

$$\frac{k}{E_2^* \sqrt{A}} = \frac{C_1 C_2 \sqrt{\pi} \xi}{2 C_1 \xi + C_2 \cdot \left(\frac{t}{a}\right)}. \quad (8)$$

Calibration of Analytical Model using FE Results

Values of C_1 and C_2 were determined by fitting the model given by Equation (8) to the FE results shown in Figure 2. A comparison between the analytical model fit and the FE data is shown in Figure 4a. The error between the FE model and the analytical model is shown in Figure 4b. There is good agreement between the FE results and

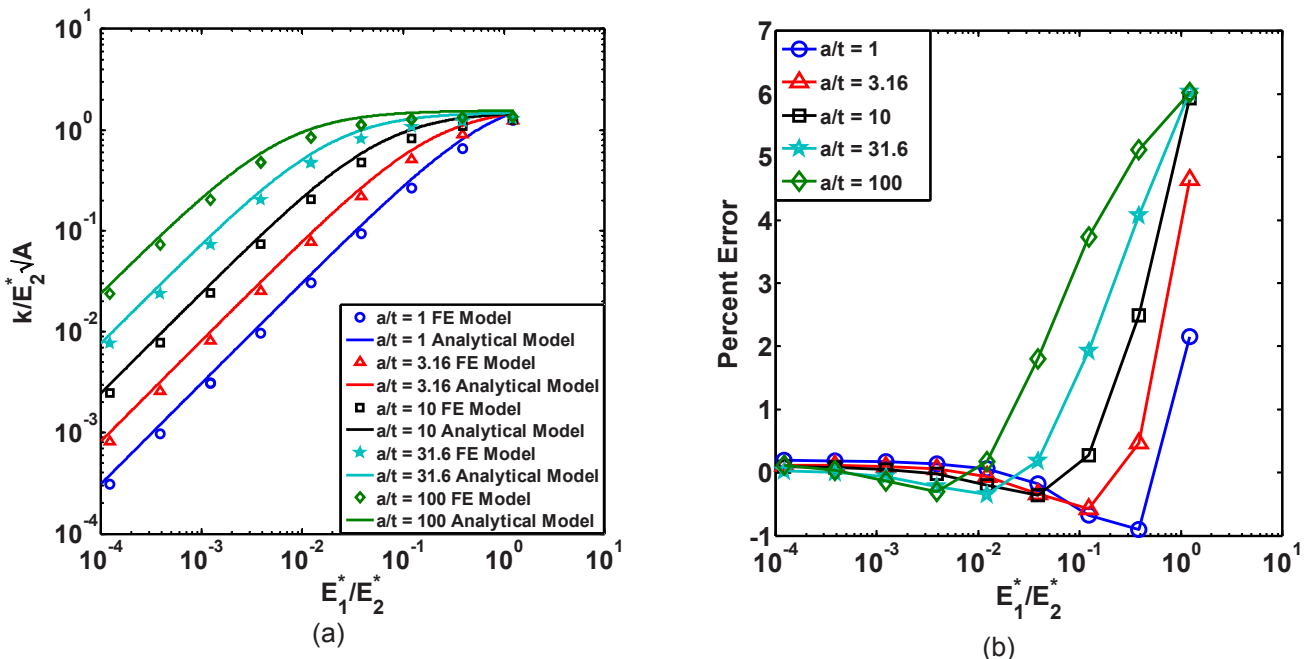


Figure 4 - (a) Results of the FE simulations and the analytical model fit to the FE results. Nondimensional stiffness as a function of modulus ratio is shown. (b) The error between the analytical model fit and the FE results. As the substrate modulus increases, the error between the models decreases.

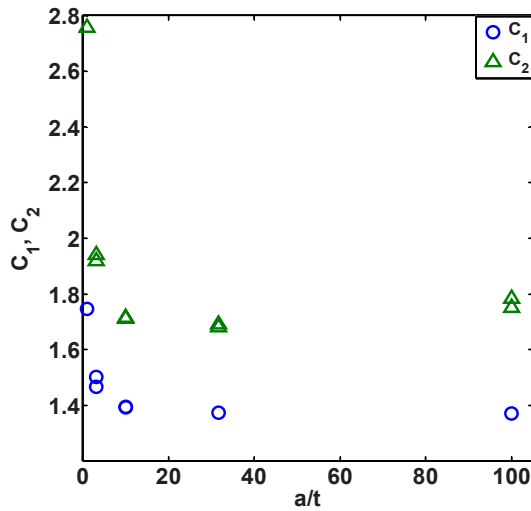


Figure 5 - Values of C_1 and C_2 parameters in the analytical model as a function of a/t determined through fitting to FE results.

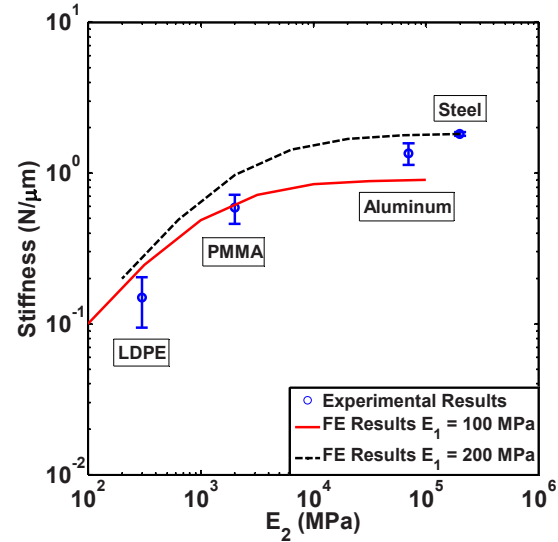


Figure 6 - Measured stiffness of an LDPE film on LDPE, PMMA, aluminum, and steel substrates. For each substrate, 5 measurements were performed at 5 locations. The mean values are plotted and the error bars correspond to \pm one standard deviation. The solid lines show the FE calculated stiffness for a film with $E_1 = 100$ MPa and $E_2 = 200$ MPa.

the fit, with errors of less than 7% over the range examined. The agreement is best in cases where the substrate is much stiffer than the film. When the substrate modulus is at least 100 times larger than the film modulus, the difference between the FE and fit is less than 1%. The C_1 and C_2 values calculated during the fitting procedure vary as a function of a/t and are shown in Figure 5. For both parameters, much of the variation occurs for low a/t ratios ($a/t < 20$). The analytical model differs from the model presented by Bec *et al.* [5] in two ways: (1) Bec *et al.* assumed the substrate was subjected to a uniform displacement rather than a uniform pressure, (2) Bec *et al.* derived analytical expressions for the constants as functions of a/t .

Preliminary Experimental Results

The effective stiffnesses of the LDPE film on several substrates are shown in Figure 6 as a function of the modulus ratio. As expected, the measured stiffness of the system increases as the substrate modulus increases.

Figure 6 also shows finite element results for cases where the film modulus is 100 MPa and 200 MPa. For both cases, the maximum load was 1 N and Poisson's ratio was assumed to be 0.3. While the modulus of the LDPE film is not known precisely, the finite element simulations provide boundaries that suggest that the modulus of the film is between 100 and 200 MPa, which is consistent with the nominal values given in Table 2. Although most of the experimental data lies within the boundaries of the 100 MPa and 200 MPa cases, the trend shown by the data does not follow either set of FE results as function of substrate modulus.

There are several potential causes for the discrepancy between the experimental data and FE simulations. First, the elastic properties of the materials in the experiments are not precisely known and literature values were used. Second, for the FE simulations it was assumed that Poisson's ratio was 0.3 for all cases, whereas the materials tested do not all have a Poisson's ratio of 0.3. Finally, the compliance of steel indenter may need to be considered, particularly in the cases where E_2 is high, as the model currently assumes a rigid indenter. Additional FE simulations and experiments are underway to establish better correlation between the model and experimental results.

Conclusion

Finite element studies were conducted to determine the effect that the a/t ratio, the E_1/E_2 ratio and the film thickness have on the measured stiffness of a thin film on a substrate indented using a cylindrical flat punch. For substrates that are very stiff relative to the film, the measured stiffness is insensitive to changes in the substrate modulus. When $a/t = 1$, this occurred for $E_1/E_2 < 0.1$.

To better understand the relationship between the film and substrate properties and to facilitate the use of the results from the FE model, an analytical model of the film-substrate system was developed. The system was modeled as two springs connected in series. The FE results were used to determine the values of two unknown constants in the analytical model. With the values of these constants that were determined through fitting, the analytical and FE model agree to within 7% over E_1/E_2 values from 0.0001 to 1 and a/t ratios from 1 to 100.

The stiffness of an LDPE film resting on LDPE, PMMA, aluminum, and steel substrates was experimentally characterized using instrumented indentation and compared to model results. Preliminary experimental results show reasonable agreement with the model, but clear discrepancies exist and further investigation is required.

Acknowledgments

We acknowledge financial support from the United States Postal Service and the US Forest Service, Forest Products Laboratory.

References

- [1] Oliver, W. C., and Pharr, G. M., 1992, "An Improved Technique For Determining Hardness And Elastic-Modulus Using Load And Displacement Sensing Indentation Experiments," *Journal of Materials Research*, 7(6), pp. 1564-1583.
- [2] Pharr, G. M., and Oliver, W. C., 1992, "Measurement Of Thin-Film Mechanical-Properties Using Nanoindentation," *Mrs Bulletin*, 17(7), pp. 28-33.
- [3] Gao, H. J., Chiu, C. H., and Lee, J., 1992, "Elastic Contact Versus Indentation Modeling Of Multilayered Materials," *International Journal of Solids and Structures*, 29(20), pp. 2471-2492.
- [4] Rar, A., Song, H., and Pharr, G., 2002, "Assessment of New Relation for the Elastic Compliance of a Film-Substrate System," *Materials Research Society Symposium Proceedings*, pp. 431-436.
- [5] Bec, S., Tonck, A., Georges, J. M., Georges, E., and Loubet, J. L., 1996, "Improvements in the indentation method with a surface force apparatus," *Philosophical Magazine a-Physics of Condensed Matter Structure Defects and Mechanical Properties*, 74(5), pp. 1061-1072.
- [6] Sakai, M., 2006, "Elastic and viscoelastic contact mechanics of coating/substrate composites in axisymmetric indentation," *Philosophical Magazine*, 86(33-35), pp. 5607-5624.
- [7] King, R. B., 1987, "Elastic Analysis Of Some Punch Problems For a Layered Medium," *International Journal of Solids and Structures*, 23(12), pp. 1657-1664.
- [8] Bec, S., Tonck, A., and Loubet, J. L., 2006, "A simple guide to determine elastic properties of films on substrate from nanoindentation experiments," *Philosophical Magazine*, 86(33-35), pp. 5347-5358.
- [9] 2010, "ABAQUS," Version 6.7, SIMULIA.
- [10] Brandrup, J., Immergut, E. H., Grulke, E. A., Abe, A., and Bloch, D. R., 2005, *Polymer Handbook*, John Wiley & Sons.
- [11] Cook, R. D., and Young, W. C., 1999, *Advanced Mechanics of Materials*, Prentice Hall, Upper Saddle River, NJ.
- [12] Johnson, K. L., 2003, *Contact Mechanics*, Cambridge, New York.

CHARACTERIZATION IN BIREFRINGENCE / DIATTENUATION OF AN OPTICAL FIBER IN A FIBER-TYPE POLARIMETRY

Thi-Thu-Hien Pham, Po-Chun Chen, *Yu-Lung Lo

Department of Mechanical Engineering, National Cheng Kung University, Tainan, 701, Taiwan
[*loyl@mail.ncku.edu.tw](mailto:loyl@mail.ncku.edu.tw)

ABSTRACT: An analytical technique based on the Mueller matrix method and the Stokes parameters is proposed for extracting five effective parameters on the principal axis angle, phase retardance, diattenuation axis angle, diattenuation and optical rotation angle of anisotropic optical materials. The linear birefringence (LB) / circular birefringence (CB) properties and linear diattenuation (LD) properties are decoupled within the analytical model. The analytical method is then integrated with a genetic algorithm to extract the optical properties of samples with linear birefringence property using a fiber-based polarimeter. The result demonstrates the feasibility of analytical model in characterizing five effective parameters of anisotropic optical material. Also, it confirms that the proposed fiber-based polarimeter provides a simple alternative to existing fiber-based probes for parameter measurement in the near field or the remote environment. A low birefringence fiber-based polarimeter based on effective parameters and genetic algorithm without using a fiber polarization controller is first proposed confirmatively.

1. INTRODUCTION

Anisotropic optical materials are used for a diverse range of applications [1], and thus many methods have been proposed for measuring their fundamental optical properties including the linear birefringence (LB), circular birefringence (CB), linear diattenuation (LD), and circular diattenuation (CD). In [2-3], a technique to measure LD and LB spectra of infrared materials in transmission was proposed. The intensity modulation that resulted from the rotation of the sample was Fourier analyzed, and the LD and LB of the sample were calculated from the Fourier series coefficients for each wavelength. However, in extracting the sample parameters, an assumption was made that the principal birefringence and diattenuation axes were aligned.

Several methodologies have been proposed for measuring the LB and LD properties of optical samples using near-field scanning optical microscopy (NSOM) with a near-field optical-fiber probe. Fasolka *et al.* [4] and Goldner *et al.* [5, 6] used a photo-elastic modulator (PEM) and a Fourier analysis scheme to measure the principal axis angle, retardance, diattenuation axis angle, and diattenuation of the local optical properties of photonic block copolymers and polystyrene-b-polyisoprene block copolymers, respectively. Also, Campillo and Hsu [7] measured the birefringence and diattenuation properties of SiN membranes using a NSOM technique in which the polarization of the input light was adjusted using a PEM and the detected signal was processed using a Fourier analysis scheme. However, a fiber polarization controller with the three paddles allows any retardance added by the fiber to be cancelled out [7]. It is found that without knowing properties of a near-field optical fiber probe and compensating for its polarization effects, the signal will be easily contaminated. However, the algorithms developed in [4-7] were overly complex for practical use.

Chenault *et al.* [8] proposed one method using an infrared Mueller matrix spectropolarimeter to measure a retardance spectrum for the electro-optic coefficient of cadmium telluride. Also, a Mueller matrix spectropolarimeter was used to measure an achromatic retarder in transmission, a reflective beamsplitter, and the electro-optic dispersion of a spatial light modulator by Sornsins and Chipman [9]. In a recent study, Chen *et al.* [10] proposed a technique for measuring the LB and LD of an optical sample using a polarimeter based on the Mueller matrix formulation and the Stokes parameters. Unlike the existing methods introduced above, the LB and LD parameters were decoupled within the analytical model. However, certain anisotropic materials have not only the LB and LD, but also CB.

The present study proposes a method based on the Mueller matrix formulation and the Stokes parameters for determining the effective optical parameters of an anisotropic material on the LB, LD, and CB. The feasibility of the proposed method is demonstrated by extracting the five effective optical parameters of an optical fiber. Also, the feasibility of the proposed low-birefringence fiber-based polarimeter is demonstrated by measuring the LB property of a quarter-wave plate.

2. METHOD OF MEASURING FIVE EFFECTIVE OPTICAL PARAMETERS OF AN ANISOTROPIC MATERIAL

This section proposes an analytical method for determining the effective LB, LD and CB properties of an anisotropic optical material utilizing the Mueller matrix formulation and the Stokes parameters. According to [11], the Mueller matrix for a LB material such as a waveplate or retarder with a slow axis principal angle α and a retardance β can be expressed as

$$M_{lb} = \begin{pmatrix} 1 & 0 & 0 & 0 \\ 0 & \cos(4\alpha)\sin^2(\beta/2) + \cos^2(\beta/2) & \sin(4\alpha)\sin^2(\beta/2) & \sin(2\alpha)\sin(\beta) \\ 0 & \sin(4\alpha)\sin^2(\beta/2) & -\cos(4\alpha)\sin^2(\beta/2) + \cos^2(\beta/2) & -\cos(2\alpha)\sin(\beta) \\ 0 & -\sin(2\alpha)\sin(\beta) & \cos(2\alpha)\sin(\beta) & \cos(\beta) \end{pmatrix} \quad (1)$$

Meanwhile, the Mueller matrix for a LD material with a diattenuation axis angle θ_d and diattenuation D has the form

$$M_{ld} = \begin{pmatrix} \frac{1}{2}\left(1 + \frac{1-D}{1+D}\right) & \frac{1}{2}\cos(2\theta_d)\left(1 - \frac{1-D}{1+D}\right) & \frac{1}{2}\sin(2\theta_d)\left(1 - \frac{1-D}{1+D}\right) & 0 \\ \frac{1}{2}\cos(2\theta_d)\left(1 - \frac{1-D}{1+D}\right) & \frac{1}{4}\left(\left(1 + \sqrt{\frac{1-D}{1+D}}\right)^2 + \cos(4\theta_d)\left(1 - \sqrt{\frac{1-D}{1+D}}\right)^2\right) & \frac{1}{4}\sin(4\theta_d)\left(1 - \sqrt{\frac{1-D}{1+D}}\right)^2 & 0 \\ \frac{1}{2}\sin(2\theta_d)\left(1 - \frac{1-D}{1+D}\right) & \frac{1}{4}\sin(4\theta_d)\left(1 - \sqrt{\frac{1-D}{1+D}}\right)^2 & \frac{1}{4}\left(\left(1 + \sqrt{\frac{1-D}{1+D}}\right)^2 - \cos(4\theta_d)\left(1 - \sqrt{\frac{1-D}{1+D}}\right)^2\right) & 0 \\ 0 & 0 & 0 & \sqrt{\frac{1-D}{1+D}} \end{pmatrix} \quad (2)$$

Finally, the Mueller matrix for an optically active material with an optical rotation angle γ can be expressed as

$$M_{cb} = \begin{pmatrix} 1 & 0 & 0 & 0 \\ 0 & \cos(2\gamma) & \sin(2\gamma) & 0 \\ 0 & -\sin(2\gamma) & \cos(2\gamma) & 0 \\ 0 & 0 & 0 & 1 \end{pmatrix} \quad (3)$$

Thus, for an anisotropic material, a total of five effective optical parameters (α , β , θ_d , D , and γ) need to be extracted. Figure 1 presents a schematic illustration of the model setup proposed in this study for characterizing the LB, LD and CB properties of an optically anisotropic material such as an optical fiber. As shown in Fig. 1, P is a polarizer, Q is a quarter-wave plate, and \hat{S}_c and S_c are input and output Stokes vector, respectively. The CB component of the sample is in front of the LB and LD components.

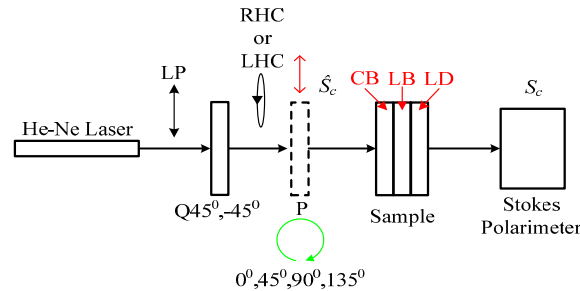


Fig. 1. Schematic diagram of model used to characterize anisotropic material.

The output Stokes vector S_c in Fig.1 can be calculated as

$$S_c = \begin{bmatrix} S_0 \\ S_1 \\ S_2 \\ S_3 \end{bmatrix}_c = [M_{ld}][M_{lb}][M_{cb}]\hat{S}_c = \begin{pmatrix} m_{11} & m_{12} & m_{13} & m_{14} \\ m_{21} & m_{22} & m_{23} & m_{24} \\ m_{31} & m_{32} & m_{33} & m_{34} \\ 0 & m_{42} & m_{43} & m_{44} \end{pmatrix} \begin{pmatrix} \hat{S}_0 \\ \hat{S}_1 \\ \hat{S}_2 \\ \hat{S}_3 \end{pmatrix} \quad (4)$$

Given a knowledge of the input polarization state and the measured values of the output Stokes parameters,

namely m_{11} , m_{14} , m_{21} , m_{24} , m_{31} , m_{34} , m_{42} , m_{43} , and m_{44} provide the means to solve the five effective optical parameters of the anisotropic material. It should be noted here that the other complex terms are not required to solve the effective optical parameters of the anisotropic material. In the methodology proposed in this study, the five effective optical parameters of the anisotropic material, i.e. α , β , θ_d , D , and γ , are extracted using six input polarization lights, namely four linear polarization lights (i.e. $\hat{S}_{0^\circ}=[1, 1, 0, 0]^T$, $\hat{S}_{45^\circ}=[1, 0, 1, 0]^T$, $\hat{S}_{90^\circ}=[1, -1, 0, 0]^T$, and $\hat{S}_{135^\circ}=[1, 0, -1, 0]^T$) and two circular polarization lights (i.e. right-handed $\hat{S}_{RHC}=[1, 0, 0, 1]^T$ and left-handed $\hat{S}_{LHC}=[1, 0, 0, -1]^T$).

Therefore, α , β , θ_d , D , and γ of the sample can be obtained, respectively, as

$$2\alpha = \tan^{-1} \left(\frac{C_3 [S_{RHC}(S_2) - S_{LHC}(S_2)] - C_2 [S_{RHC}(S_3) - S_{LHC}(S_3)]}{C_2 [S_{RHC}(S_2) - S_{LHC}(S_2)] - C_1 [S_{RHC}(S_3) - S_{LHC}(S_3)]} \right) \quad (6)$$

$$\beta = \tan^{-1} \left(\frac{S_{45^\circ}(S_3)}{\cos(2\alpha + 2\gamma) \cdot S_{RH}(S_3)} \right) \quad (7)$$

$$2\theta_d = \tan^{-1} \left(\frac{S_{45^\circ}(S_2) + S_{135^\circ}(S_2)}{S_{0^\circ}(S_1) + S_{90^\circ}(S_1)} \right) \quad (8)$$

$$D = \frac{S_{0^\circ}(S_1) + S_{90^\circ}(S_1)}{\cos(2\theta_d) \cdot [S_{0^\circ}(S_0) + S_{90^\circ}(S_0)]} \quad (9)$$

$$2\gamma = \tan^{-1} \left(\frac{-S_{0^\circ}(S_3)}{S_{45^\circ}(S_3)} \right) - 2\alpha \quad (10)$$

where

$$C_1 = \frac{1}{4} \left(\left(1 + \sqrt{\frac{1-D}{1+D}} \right)^2 + \cos(4\theta_d) \left(1 - \sqrt{\frac{1-D}{1+D}} \right)^2 \right) \sin \beta \quad (11)$$

$$C_2 = \frac{1}{4} \left(\sin(4\theta_d) \left(1 - \sqrt{\frac{1-D}{1+D}} \right)^2 \right) \sin \beta \quad (12)$$

$$C_3 = \frac{1}{4} \left(\left(1 + \sqrt{\frac{1-D}{1+D}} \right)^2 - \cos(4\theta_d) \left(1 - \sqrt{\frac{1-D}{1+D}} \right)^2 \right) \sin \beta \quad (13)$$

In summary, α , β , θ_d , D , and γ can be extracted using Eqs. (6) ~ (10), respectively. It is noted that the proposed methodology does not require the principal birefringence axes and diattenuation axes to be aligned. Moreover, while the LB and CB properties are coupled within the analytical model, the LB/CB and LD properties are decoupled. Thus, the LB/CB properties of the sample can be solved directly without any prior knowledge of the LD properties.

3. ANALYTICAL SIMULATIONS

In this section, the ability of the proposed analytical model to extract the five effective optical parameters of interest over the measurement ranges defined in the previous section is verified using a simulation technique. In performing the simulations, the theoretical values of the output Stokes parameters for the six input lights were obtained for a hypothetical anisotropic sample using the Jones matrix formulation based on known values of the sample parameters and a knowledge of the input Stokes vectors. The theoretical Stokes values were inserted into the analytical model derived in Section 2 and the effective optical parameters were then inversely derived. Finally, the extracted values of the effective optical parameters were compared with the input values.

The ability of the proposed method is evaluated by extracting α , β , θ_d , D , and γ of an anisotropic sample, respectively. It is noted that which parameter is extracted the input of that parameter is changed over the full range of $0 \sim 180^\circ$ (except input values of β : $0 \sim 360^\circ$). The other input parameters were specified as follows (except the extracting parameter): $\alpha = 50^\circ$, $\beta = 60^\circ$, $\theta_d = 35^\circ$, $D = 0.03$, and $\gamma = 15^\circ$. Figure 2(a) ~ (e) plots the value of α , β , θ_d , D , and γ extracted using Eq. (6) ~ (10) against the input value of α , β , θ_d , D , and γ over the range $0 \sim 180^\circ$ (β : $0 \sim 360^\circ$), respectively. Good agreements are observed between the two values of α , β , θ_d , D , and γ , respectively and thus the ability of the proposed method to obtain full-range measurements of α , β , θ_d , D , and γ are confirmed.

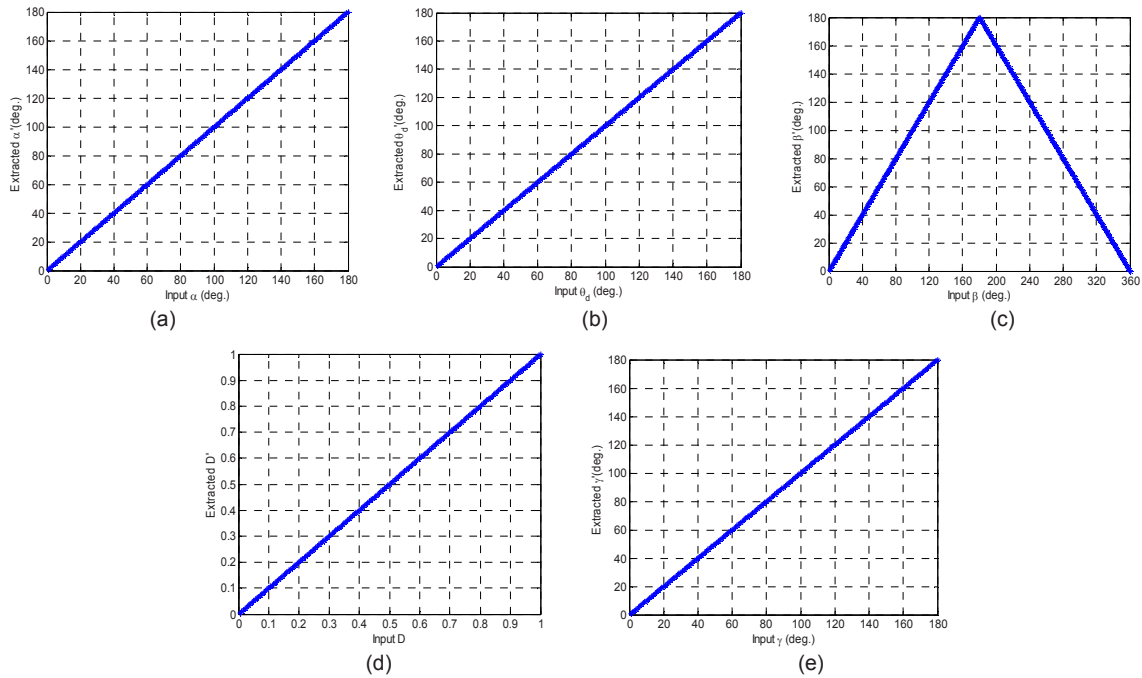


Fig. 2. Correlation between input value and extracted value of (a) principal axis angle α & α' , (b) phase retardance β & β' , (c) diattenuation axis angle θ_d & θ_d' , (d) diattenuation D & D' , and (e) optical rotation angle γ & γ' , respectively.

Overall, the results presented in Figs. 2(a) ~ (e) demonstrate that the proposed analytical method yields full range measurements of all the optical parameters of interest other than the phase retardance. In other words, the method proposed in this study enables both the LB/LD and the CB properties to be obtained.

4. EXPERIMENTAL SETUP AND RESULTS FOR MEASURING EFFECTIVE PARAMETERS OF OPTICAL FIBER

Figure 3 presents a schematic illustration of the experimental setup proposed in this study for characterizing the LB, LD and CB properties of an optically anisotropic material such as an optical fiber. Initially, the LB and LD properties of a single-mode optical fiber (630HP, Thorlabs Co.) with a length of 47 cm were measured using a commercial Stokes polarimeter (PAX5710, Thorlabs Co.). The transmitted light is provided by a frequency-stable He-Ne laser (SL 02/2, SIOS Co.) with a central wavelength of 632.8 nm. In Fig.3, P is a polarizer (GTH5M, Thorlabs Co.) and Q is a quarter-wave plate (QWP0-633-04-4-R10, CVI Co.), which are used to produce linear polarization lights using 0° , 45° , 90° , 135° , and right/left handed circular polarization light. As shown, the polarized light is coupled into an optical fiber by a fiber coupler. Note that the neutral density filter (NDC-100-2, ONSET Co.) and power meter detector (8842A, OPHIT Co.) are used to ensure that each of the input polarization lights has an identical intensity.

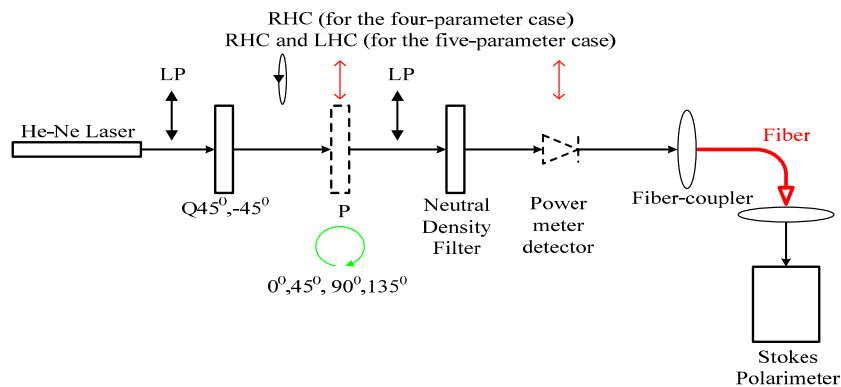


Fig. 3. Schematic illustration of measurement system used to characterize an optical fiber.

The experiments are conducted in two different cases of four and five effective parameters being assumed in an optical fiber. Tables 1 illustrates the extracted four and five effective optical parameters of the optical fiber,

respectively. First case, the values of the four effective optical parameters of the optical fiber extracted using Eqs. (6) ~ (5) (Note that γ is set equal to 0 since the optical fiber is assumed to have LB and LD parameters only). In this case, the optical fiber was illuminated by five input lights (i.e. four linear polarization lights on 0° , 45° , 90° , 135° and one right-hand circular polarization lights, respectively). The standard deviations of the measurements of α , β , θ_d , and D were determined to be 0.98° , 0.95° , 2.12° , and 0.01° , respectively. It is noted that one hundred data points are used to calculate the standard deviation and the average data in experiments. Second case, the values of the five effective optical parameters of the optical fiber extracted using Eqs. (6) ~ (10) in Section 2, respectively. In this case, it is noted that the optical fiber was illuminated by six input lights (i.e. four linear polarization lights on 0° , 45° , 90° , 135° , and two right-/left-hand circular polarization lights, respectively) rather than five. The standard deviations of the α , β , θ_d , D , and γ , measurements were found to be 1.37° , 1.01° , 13.76° , 0.02 , and 1.80° , respectively.

Table 1. Calculated values of five effective optical parameters of optical fiber

Measured effective parameters	Calculated results	
	Four effective parameters	Five effective parameters
α (deg)	98.46°	123.78°
β (deg)	40.52°	22.55°
θ_d (deg)	25.54°	102.44°
D	0.06	0.04
γ (deg)	#	-24.35°

5. EXTRACTION OF LB SAMPLE PARAMETERS USING FIBER-TYPE POLARIMETER AND GENETIC ALGORITHM

In Fig. 3, one sample was placed behind fiber-coupler to measure the parameters of a LB sample using a fiber-type polarimeter, a genetic algorithm (GA), and the Stokes method. The light emerging from the fiber is passed through the LB sample and is then coupled into a Stokes polarimeter. During the experimental procedure, the slow axis of the LB sample is rotated to 0° , 30° , 60° , 90° , 120° , 150° or 180° , and the corresponding values of the principal axis angle and phase retardance are extracted using a GA. For comparison purposes, the parameters of the LB sample are extracted using two different treatments of the optical fiber parameters, namely (1) the optical fiber is assumed to have LB and LD parameters only, and (2) the optical fiber is assumed to have both LB / LD and CB parameters. It is noted that the case where the optical fiber is assumed to have just LB and LD parameters can be obtained simply by replacing the Mueller matrix used to simulate the optical rotation of the fiber, i.e. $[M_{cb}]$, by a unit matrix.

5.1 Genetic algorithm (GA) for extracting sample parameters

A genetic algorithm is a search technique used in computing to find exact or approximate solutions to optimization and search problems [12-14]. In the present study, the quality of the optical parameters obtained using the GA is evaluated using an error function (fitness function) defined in terms of the distance between the computed values of the Stokes parameters and the experimental values. Thus, the error function can be defined as [12]

$$Error = \sum_{i=1}^9 (\phi_{i,Experiment} - \phi_{i,Compute}) \quad (14)$$

where $\phi_{i,Experiment}$ represents the experimental values of the nine Stokes and $\phi_{i,Compute}$ represents the corresponding values of the Stokes parameters computed using the Mueller matrix method based upon the estimated values of the sample parameters. In other words, the objective of the GA is to determine the LB parameters of the optical sample (α_s , β_s) which minimize the distance between the computed values and the experimental values.

Figure 4 presents a flow chart showing the major steps in the GA optimization procedure. As shown, the GA commences by generating an initial population of random solutions (α_s , β_s). The Mueller matrix method is then used to calculate the corresponding set of Stokes parameters Φ (α_s , β_s) for the three input lights. The calculated values of the Stokes parameters are then substituted into Eq. (14) to determine the corresponding error value. This process is repeated iteratively until the error distance falls within the acceptable range and the specified number of iteration loops has been completed. In performing the present simulations, the maximum number of iteration loops was set as 500, and the initial range of the candidate solutions for α_s and β_s were specified in the ranges $0^\circ \leq \alpha_s \leq 180^\circ$ and $0^\circ \leq \beta_s \leq 180^\circ$, respectively.

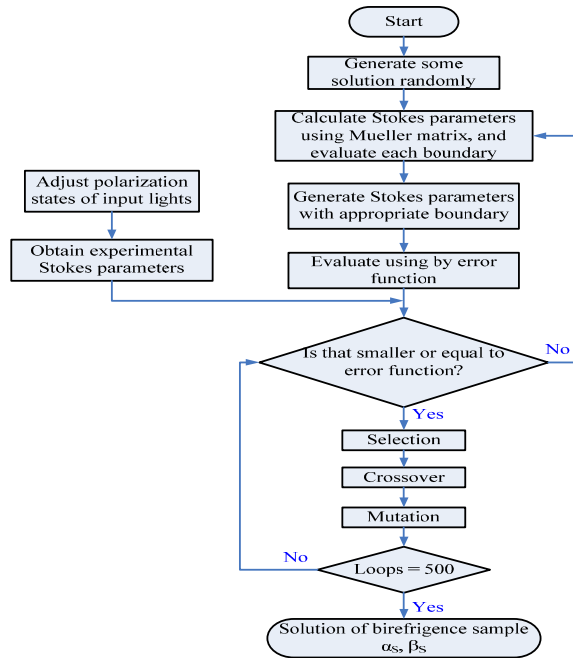


Fig. 4. Flowchart of GA optimization procedure used to extract LB sample parameters.

5.2 Experimental results for LB sample parameters based on four/five effective parameters of optical fiber

The LB parameters of a sample (a quarter-wave plate: QWP0-633-04-4-R10, CVI Co.) were initially extracted using the GA optimization procedure subject to the assumption that the optical fiber was characterized by four or five effective optical parameters. Note that the polarizer, quarter-wave plate, neutral density filter and power meter detector were the same as those used to measure the effective properties of the optical fiber.

First case, the four effective optical parameters of the fiber and the three sets of normalized Stokes were inserted into the GA in order to extract α_S and β_S of the LB sample. As shown in Fig. 5(a), a relatively poor agreement is obtained between the extracted values of the LB sample parameters and the known values. Specifically, the experimentally-derived values of α_S have a linear correlation with the true values, but are shifted slightly compared to the actual values, while the experimental values of the retardance have a significant non-linear correlation with the true values. The standard deviations of the measured α_S and β_S values were found to be 10.49° and 6.04° , respectively. In other words, the results suggest that the use of just four effective parameters is insufficient to fully characterize the optical performance of the fiber used in the polarimeter.

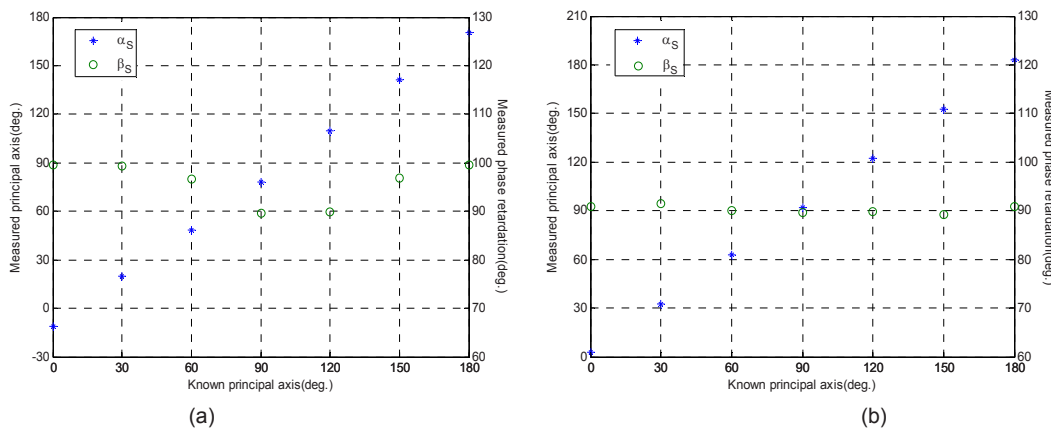


Fig. 5. Experimental results for birefringence of quarter-wave plate (a) without considering the optical rotation angle, and (b) with considering the optical rotation angle.

For comparison purposes, the optical parameters of the LB sample were also extracted for the case in which the optical fiber was assumed to have five effective optical parameters. The five effective optical parameters of the fiber and the three sets of normalized Stokes parameters obtained using the setup were inserted into the GA in order to extract α_S and β_S of the LB sample. Figure 5(b) plots the extracted values of α_S and β_S of LB sample at

various values of the known principal axis angle. It is observed that a good correlation exists between the experimental values of the sample parameters and the true values. From inspection, the standard deviations of the α_S and β_S measurements were determined to be 2.55° and 0.69° , respectively. The standard deviations of the α_S and β_S measurements shown in Fig. 5(b) are notably smaller than those of the measurements shown in Fig. 5(a), in which the CB properties of the optical fiber are ignored. Thus, the results imply that in utilizing the GA optimization method to extract the sample parameters, the Mueller matrix of the optical fiber used to calculate the Stokes parameters should be based on all five effective optical parameters, namely α , β , θ_d , D , and γ .

6. CONCLUSIONS

This study has proposed an analytical method based on the Mueller matrix method and the Stokes parameters for extracting the LB, LD, and CB effective properties of an anisotropic optical material. The proposed method enables all of the effective parameters other than the phase retardance to be extracted over the full range. Moreover, the LB/CB and LD properties are decoupled within the analytical model. The experimental values obtained using the proposed method for the principal axis angle, retardance, diattenuation axis angle, diattenuation, and optical rotation angle of a single-mode fiber have standard deviations as 1.37° , 1.01° , 13.76° , 0.02 , and 1.80° , respectively. It has been shown that the analytical model can be integrated with a GA to construct a scheme for extracting the optical parameters of birefringent samples using a fiber-type polarimeter. Without using a fiber polarization controller and selecting only optical fiber probes with minimal difference in extinction ratios of two orthogonal polarizations, in general, the results have confirmed that the proposed polarimeter design provides a straightforward and practical alternative to existing optical-fiber based probes for optical parameter measurement in the near field or the remote environment.

ACKNOWLEDGEMENTS

The authors gratefully acknowledge the financial support provided to this study by the National Science Council of Taiwan under grant no. NSC96-2628-E-006-005-MY3.

REFERENCES

- [1] G. F. Smith, *Constitutive equations for anisotropic and isotropic materials*, (North-Holland, 1994).
- [2] D. B. Chenault and R. A. Chipman, "Measurements of linear diattenuation and linear retardation spectra with a rotating sample spectropolarimeter," *Appl. Opt.*, 32, 3513-3519, (1993).
- [3] D. B. Chenault and R. A. Chipman, "Infrared birefringence spectra for cadmium-sulfide and cadmium selenide," *Opt. Lett.* 17, 4223-4227 (1992).
- [4] M.J. Fasolka, L.S. Goldner, J. Hwang, A.M. Urbas, P. Swager, T. DeRege, and E.L. Thomas, "Measuring local optical properties: near-field polarimetry of photonic block copolymer morphology," *Phys. Rev. Lett.*, 90, 016107 (2003).
- [5] L.S. Goldner, M.J. Fasolka, S. Nougier, H.P. Nguyen, G.W. Bryant, J. Hwang, K.D. Weston, K.L. Beers, A. Urbas, and E.L. Thomas, "Fourier analysis near-field polarimetry for measurement of local optical properties of thin films," *Appl. Opt.*, 42, 3864-3881, (2003).
- [6] L.S. Goldner, M.J. Fasolka, and S.N. Goldie, "Measurement of the local diattenuation and retardance of thin polymer films using near-field polarimetry," *Applications of Scanned Probe Microscopy to Polymers*, 897, 65-84, (2005).
- [7] A. L. Campillo and J. W. P. Hsu, "Near-field scanning optical microscope studies of the anisotropic stress variations in patterned SiN membranes," *J. Appl. Phys.* 91, 646-651 (2002).
- [8] D. B. Chenault, R. A. Chipman, and S. Y. Lu, "Electro-optic coefficient spectrum of cadmium telluride," *Appl. Opt.*, 33, 7382-7389, (1994).
- [9] E. A. Sornsin, and R. A. Chipman, "Visible Mueller matrix spectropolarimetry," *SPIE*, 3121, 156-160, (1997).
- [10] P. C. Chen, Y. L. Lo, T. C. Yu, J. F. Lin, and T. T. Yang, "Measurement of linear birefringence and diattenuation properties of optical samples using polarimeter and Stokes parameters," *Opt. Exp.*, 17, 15860-15884, (2009)
- [11] I.C. Khoo and F. Simoni, *Physics of Liquid Crystalline Materials*, (Gorden and Breach Science Publishers, 1991), Chap. 13.
- [12] H.C. Cheng and Y. L. Lo, "The synthesis of multiple parameters of arbitrary FBGs via a genetic algorithm and two thermally modulated intensity spectra," *J. Light. Tech.*, 23, (2005).
- [13] T. C. Yu and Y. L. Lo, "A novel heterodyne polarimeter for the multiple-parameter measurements of twisted nematic liquid crystal cell using a genetic algorithm approach," *J. Light. Tech.*, 25, (2007).
- [14] W. L. Lin, T. C. Yu, Y. L. Lo, and J. F. Lin, "A hybrid approach for measuring the parameters of twisted-nematic liquid crystal cells utilizing the Stokes parameter method and a genetic algorithm," *J. Light. Tech.*, 27, (2009).

Predictive Fault Detection for Missile Defense Mission Equipment and Structures

Jeffrey S. Yalowitz, Instrumental Sciences, Inc.
P.O. Box 4711, Huntsville, AL 35815, email yalowitz@insciences.com
Roger K. Youree, Instrumental Sciences, Inc.
Aaron Corder, Missile Defense Agency
Teng K. Ooi, Missile Defense Agency

Abstract

Equipment failures in defense systems result in loss or reduction of operational capability, impacting system readiness. Faults in critical equipment can impact system performance and reliability, as can structural failures. Predictive fault detection (PFD) provides prognostic capability to identify components and internal structures that exhibit either degradation or increased variability of parameters, in advance of actual faults occurrences. It has the power to reduce facility down times significantly, enhancing system availability and reducing maintenance costs. PFD enables maintainers to take corrective action before actual failures occur, thus improving system availability and reducing maintenance costs for the covered facility. The authors have applied an integrated approach to PFD, including multiple-phenomenology sensing and data acquisition; generalized multivariate statistical treatment of waveform shapes, continuous variable values, and discrete event occurrences; and maintenance decision-making techniques that balance performance and cost factors. An engineering prototype PFD product has been developed and tested under an MDA-sponsored Small Business Innovative Research project sponsored by the Missile Defense Agency.

Introduction

This paper describes the architecture and design of a system that the authors have developed and tested to perform fault prediction functions in health monitoring of mission equipment, industrial equipment, and facilities. The system employs generalized multivariate statistical analysis methods to establish nominal characteristics of monitored parameter sets in operating equipment and to recognize significant departures from the nominal characteristics. Statistical assessments of nominal and anomalous conditions provide bases for prediction of impending equipment failures. This technique is especially useful in health-monitoring situations where equipment physical models are unavailable or of limited fidelity.

The automated PFD system described in this paper integrates the statistical techniques with multiple types of sensors, data acquisition hardware, and a cognitive processing architecture to produce timely maintenance action recommendations in advance of actual failures. The PFD capability enables maintainers to minimize downtime and use resources efficiently, and to replace schedule-based preventive maintenance, which is costly and impacts readiness.

Equipment and Facility Health Monitoring Scenarios

In general terms, the products of equipment and facility health monitoring consist of equipment condition estimates inferred from measured values of selected equipment and environmental parameters. Sensor devices are available to measure health-related effects in various domains. For example, shock and vibration characteristics can be measured using accelerometers. Mechanical and optical distance-measuring

devices can be used to measure displacements. Electronic sensors can be used to measure electrical voltage, current of components, resistivity of structural materials, and surface temperatures. Some types of equipment incorporate internal sensors for fault detection, but the internal monitoring provisions typically do not output fault/failure prediction information. In some systems values of certain performance parameters are collected by embedded processors and preserved in log files for later retrieval. Regardless of the sensor device, the sensor information relevant to health monitoring and PFD typically falls into only a few categories, including [1]:

- Variation in a quantitative parameter over time
- Variation in the shape of a recurrent transient waveform or in identifiable features of the waveform
- Frequency of occurrence of a defined event type.

Fault-related effects are often difficult to characterize in terms of a priori physical models, because of the myriad possible fault modes that can occur in most structures and the complexity of structures typically used in military and industrial systems. However, statistical models of expected behaviors can be compiled empirically for many types of effects, using sensor data collected over time and maintaining statistical representations of key waveform characteristics.

Concurrent measurements from multiple sensors result in parallel data streams, as do extractions of parameters representing multiple features of a recurrent transient waveform. Information relevant to PFD often resides in the relationships among the concurrent data streams. The multivariate statistical methods applied in this project provide the implicit means to capture both the relationships among data streams and temporal relationships between successive segments of given data streams. The multiple data streams, while differing in source phenomenology and specific information content, have common characteristics as sequences of vector quantities. These common characteristics permit the present development of the generalized multivariate statistical algorithms described in the following sections, and the application of the same set of algorithms to a variety of health monitoring scenarios.

PFD System Architecture

The architecture we employ for the PFD system is based on the cognitive processing model, which has been applied successfully to military decision support systems and a variety of industrial processes. A typical form of the cognitive processing structure consists of a sequential flow through the following subprocesses:

- Sensor observations/measurements
- Signal/data acquisition
- Data fusion
- Interpretation
- Assessment
- Planning
- Decision-making

The PFD system is tasked with conducting prognostic health evaluations of communications terminals that incorporate radio equipment and antennas, processors, electrical power distribution circuits, and environmental control units. Determination of the future operational condition of the overall terminal requires prediction of the health of the included mission and support equipment items. We selected sensor types to monitor key dynamic electrical, mechanical, and thermal characteristics of the equipment items and the terminal environment. As an example, electrical current clamp probes applied to AC power inputs of the air conditioning units provide means of indirectly estimating mechanical loading of the compressor motors. As another example, triaxial accelerometer sets mounted on frames of rotating machines yield vibration measurements that may indicate shaft balance or bearing wear problems, or presence of potentially destructive vibration conditions in the environment. In addition to using measurements from sensors provided in the PFD hardware complement, the PFD system includes data interfaces to the host system processor(s) management information bases (MIBs) and log files to permit acquisition of status and self-test measurements already made by the host system.

For PFD the data acquisition portion of the process consists of monitoring selected aspects of covered equipment operation. The monitoring functions acquire relevant data using signals either available at the equipment

interfaces or supplied by external sensors installed for that purpose. Monitoring takes place over extended periods of time, or over many operations of discrete actions of the equipment, producing streams of data with significance in magnitude variations or event occurrence statistics. Conditioning of the data (e.g., via scaling, compression, enhancement of signal-to-noise ratio) to facilitate archiving or downstream processing is performed as part of the data acquisition subprocess. Acquired data samples are time-stamped accurately to support multisensor data fusion and multivariate statistical analysis functions subsequently performed on the data streams. Data fusion consists of cross-correlating parameters of multiple data streams to produce synthetic streams that highlight coincident patterns of the streams. Data fusion can also be performed on a single data stream, in which case autocorrelation is used to search for multiple events that are related but separated in time.

Interpretation is the extraction of useful information from acquired (and fused, if applicable) data streams. In the PFD process, interpretation involves searching for patterns in the data. Of particular interest are patterns that have significance in quantifying component wear, cumulative effects of resource depletion, or too-frequent occurrence of errors or transient faults. However patterns that indicate normal operation (i.e., healthy equipment) are of interest for accumulation of statistical measures of normal operating limits. The basis of interpretation is either a priori engineering experience or theoretical knowledge of the behavior of the subject equipment. Assessment is the subprocess of evaluating significant interpreted information in the context of the covered equipment and the communications facility, to determine the future impact, if any, on operability of the facility. The PFD system employs multivariate statistical similarity testing and trend evaluation techniques for assessment and uses assessment results for prediction of impending failure conditions.

Planning is the generation of alternative courses of action in response to an assessed situation and the evaluation of the generated alternatives. For PFD, alternatives may include recommending specific maintenance actions, declining to make such recommendations, postponing action until confirming data arrives, and invoking self-tests to force acquisition of additional data. The evaluations include estimation of benefits and costs of the respective alternative courses, with costs in terms of economics and impact on availability. Decision-making, the final portion of the process, consists of comparing the planning results and formulating a recommendation for maintenance action if warranted. The set of maintenance actions may include component replacement, detailed inspection/testing by maintenance personnel, or addition of spare parts to the appropriate support base inventory. [Figure 1](#) illustrates the PFD system hardware architecture.

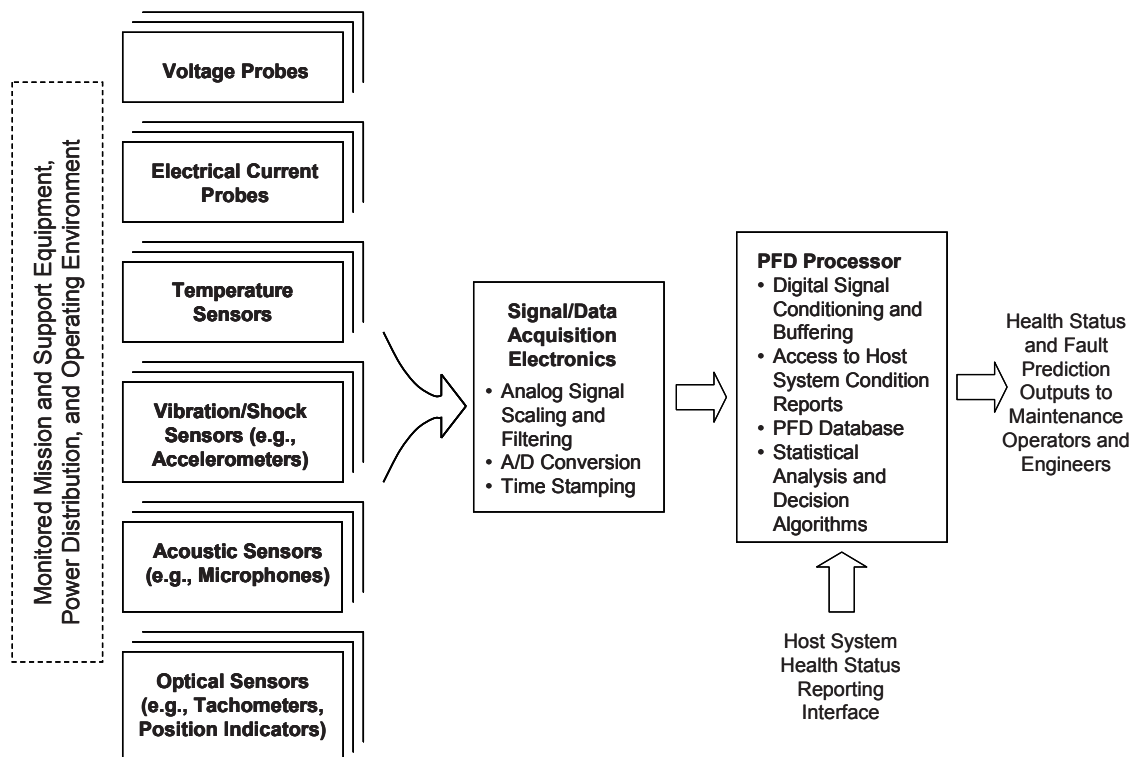


Figure 1. PFD Architecture

PFD Statistical Analysis and Decision Functions

Figure 2 is a block diagram of the PFD statistical analysis and decision functions, which are implemented in software. The inputs to the process consist of signals that have been measured by sensor suites tailored to the specific installation and converted to numerical data streams by computer-based data acquisition modules. The desired outputs from the process are maintenance-action recommendations with associated statistical rationale.

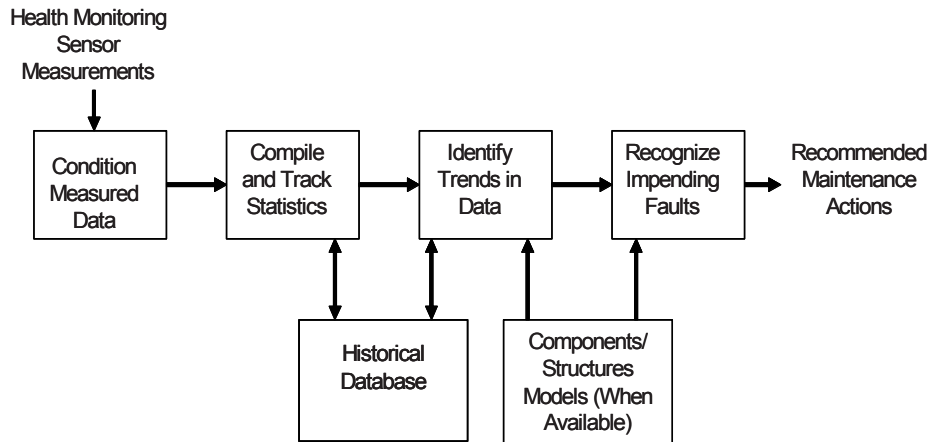


Figure 2. PFD statistical analysis process block diagram

The PFD algorithms determine if the current data from the hardware appear to be statistically different from what the data are expected to be, and if so, predict what state the hardware will likely be in at various future times. To do this, one or more test points on the hardware are monitored. The algorithms assume that there will be an opportunity to collect baseline data from these test points, i.e., prior to the time period when the hardware begins to show signs of failure, and that we will have monitored the data streams from these test points and collected statistically significant amounts of data to determine what the specifically-monitored hardware looks like when working correctly. Many types of hardware have enough variance from unit-to-unit to make a generic baseline insufficient to accurately assess the future state of the hardware and therefore data from the specific instance of hardware are needed.

The algorithms assume that the system continues to collect data from the same test points after the baseline data are collected. After the baseline data are collected, however, we call the collected data test data, because the algorithms use these data to test if the hardware has changed from the baseline data in a statistically significant way. If the algorithms used to do this indicate that the test data are sufficiently close to the baseline data, no further actions are taken and the algorithms repeat this process when the next test data are available. If, however, the algorithms determine that the test data are sufficiently different, then the algorithms to determine the future state of the hardware are invoked. These algorithms trend data to the future and use the trended data to determine the future state of the hardware. This determination of state is based on minimizing the “cost” to the system, whether that cost by dollars or downtime, or some other cost.

Similarity Testing

The first major set of tests performed by the PFD algorithms is for statistical similarity. Tests used depend on whether the data are single or multidimensional. For a single dimensional data stream, part of the similarity testing involves a Kolmogorov-Smirnov (KS) test. The similarity test for multidimensional data involves statistical tests designed for multidimensional data. The KS test is a nonparametric test, meaning that it does not assume a known underlying distribution. It takes one of the data streams from the baseline data and the associated stream from the test data and creates an empirical cumulative distribution function for each. The value of such a distribution function as a function of a variable x is the number of observed values less than or equal to x , divided by the total number of samples. The maximum absolute value of the difference between these two distributions

also has a probability distribution, which is used by the KS test to determine if the baseline and test distributions are the same to a user-specified confidence. See [2] or [3] for more details. For multi-dimensional data, several efficient statistical methods such as Hotelling's T-Squared test are used. (See, for example, [4] or [5].) For this test, multiple test data streams and the associated multiple baseline data streams are used to create the Mahalanobis distance between the baseline and test data. The Mahalanobis distance can be measured for statistical significance by considering the Hotelling T-square statistic, or more commonly by converting this statistic to an F-test. Hence, we can determine if the baseline data and the test data means are the same to a user-specified confidence level.

Trend Evaluation and Decision

If the test data are not sufficiently similar to the baseline data, trending is called for. Since the trended data will be tested via a Bayes risk criterion, these trended data should relate to predicting impending failures. In some cases, this criterion may call for additional feature extraction prior to trending. The algorithms calculate one or more features to trend. A curve fitting function is used to curve fit these feature curves to a variety of function forms. Several types of information from the following list are computed as needed and considered in determining how well data fit a given curve:

- Residual Noise
- Sum of Squares due to Error
- Degree-of-Freedom Adjusted R-Square
- Confidence Bounds for the Coefficients
- Slope of the Fitted Curve

Results of these tests are combined to formulate a decision as to which fit best represents what the data will do in the future. If the curve fit fails the residual noise test or the slope test, it is rejected out-right. If the confidence in the coefficients is low, the fit is rejected unless no other fit has sufficiently tight bounds on the coefficients. The SSE is subtracted from a maximum SSE, as is the coefficient confidence maximum difference. These differences, along with the quality of the fit from the residual noise test and the adjusted R-square are suitably weighted and then added, the largest sum being the curve fit chosen as best. Details of the trending algorithms are provided in [1].

After it has been determined that the test data are sufficiently different from the baseline data and trending has been performed, the results of the trending are evaluated to determine what the most likely future state of the hardware will be. A Bayes risk criterion [6] is used to choose the state which results in the minimum expected cost. This cost may be in dollars (based on number or location of spares and on number of repair personnel and their work hours), or is may be in terms of hardware down time and hence hardware availability. Other costs can also be constructed to suit different needs.

Example Equipment Health Monitoring Applications

Vibration Monitoring

A sensor suite consisting of three triaxial accelerometer sets from the PFD system was installed on an SHF communications antenna positioner mounted on the deck of a sea-based radar platform vessel. Each triaxial accelerometer set, or triax, incorporates three linear accelerometer devices mounted on adjacent surfaces of a rigid cube to produce three-dimensional vibration vector components. The antenna positioner uses servo-driven mechanical assemblies atop a solid pedestal to rotate parabolic reflector antennas about azimuth and elevation axes. The vessel vibration environment includes effects of multiple large diesel motor-generators, propulsion units, and ventilation systems, in addition to effects of water on the vessel hulls.

The PFD system data acquisition unit was configured to take sample readings from each of the nine accelerometer devices at three-hour intervals. Each reading consisted of 20,000 samples at 3000 samples/second. The data acquisition unit sensor channels were coordinated to permit simultaneous sampling of selected accelerometer device pairs on separate triaxes to support computation of rotational vibration component amplitudes, in addition to the directly-measured translational components. Rotational vibration levels are

important to antenna positioner health prediction because the positioner gimbal bearings are sensitive to off-axis rotational mechanical loading. Data was collected over a period of three months. A record of vessel operating conditions (e.g., at port, under way, on station) during the period was provided by the vessel crew for use in off-line correlation of the vibration data with vessel activities.

The vibration data was transmitted to the ISI facility for statistical analysis using the PFD system. The analysis included application of time-domain and spectral techniques to individual sensor outputs and vector combinations of outputs. [Figure 3](#) is a discrete Fourier transform plot of the vibration acceleration power spectral density for an accelerometer measuring the vertical component of vibration at the base of the pedestal.

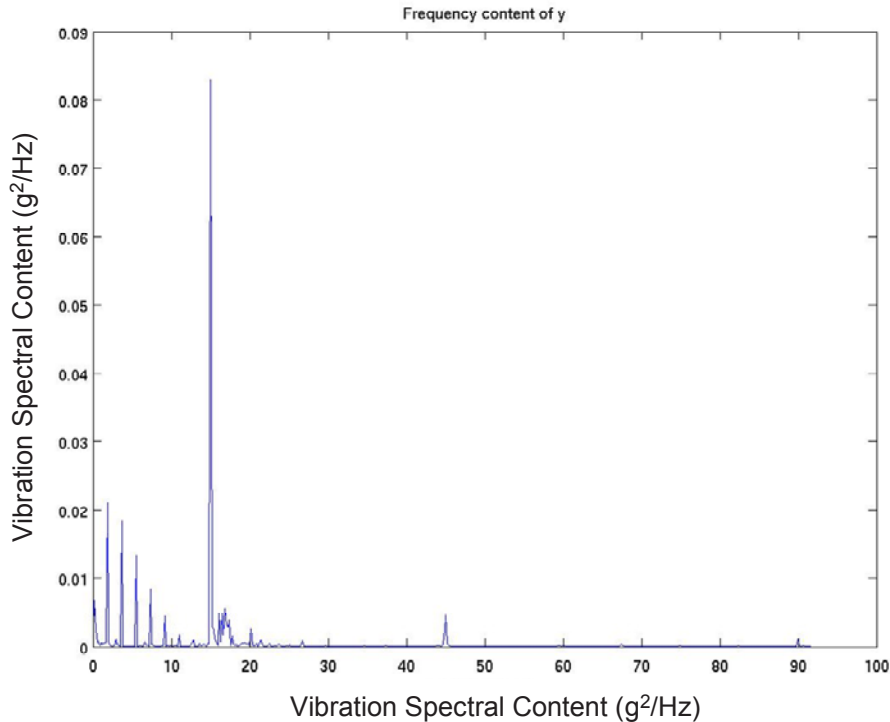


Figure 3. Vibration Power Spectral Density Plot Computed from PFD Vibration Sensor Data

This vibration spectrum is comprised primarily of discrete lines. The equally spaced lines at frequencies below 10 Hz were determined to result from a series of pulses recurring at a 1.8 Hz rate. The other lines are believed to have originated in large rotating machines on board the vessel. The statistical analysis technique applied to this spectrum for PFD processing is to maintain histories of magnitudes and frequencies of significant spectral lines that recur in sample measurements over time, then perform similarity testing and trend evaluation to recognize adverse changes.

Induction Motor Input Current Monitoring

An example PFD application is the monitoring and evaluation of the input electrical current drawn from the AC power distribution circuit by an induction motor under load. Significant prognostic information about the motor and its load can be deduced through measurements of the transient characteristics of the current waveform. [Figure 4](#) [7] identifies several explicit features of an induction motor AC current input waveform, which serve together as components of a feature vector characterizing the waveform. After many repetitions of the transient waveform have been acquired, the multivariate statistical analysis and trending algorithms operate to determine similarity of the waveform instances and classify trends in later instances which fail the similarity tests.

Depending on characteristics of the load equipment, monitoring the steady-state current can also provide information of prognostic value. For example, if the motor drives a refrigeration or air conditioning compressor, an

increase over time in the steady-state current level can be indicative of an adverse change in refrigerant pressure. Changes in thermostat-controlled compressor on time can indicate a loss in cooling system efficiency.

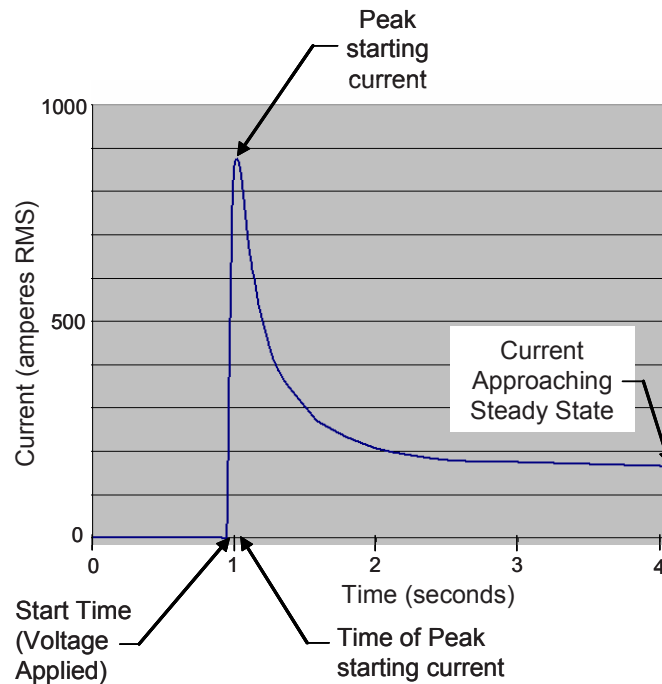


Figure 3. Induction motor startup current waveform, illustrating features usable for statistical analysis

Conclusions

In this paper we have described the architecture and implementation of a predictive fault detection system for prognostic health monitoring of complex missile defense facilities that incorporate a variety of equipment types. The PFD system features multiple sensor types to measure relevant electrical, mechanical, thermal, and optical signals, multiple-input signal conditioning/data acquisition capability, and a generalized multivariate statistical analysis system capable of concurrent processing inputs from many sensors. The techniques presented take advantage of advanced statistical methods to provide health assessments in the basis of empirical data collected from the monitored system over time, thus enabling prediction of faults even in the absence of detailed physical models of the covered structures in normal and anomalous states. The analysis algorithms employ similarity tests, data trending, and statistical distance comparisons, and Bayes cost decision criteria. A prototype implementation of the system described in the paper is undergoing continuing laboratory and field testing.

Acknowledgement

This work was supported in part by the U.S. Department of Defense, Missile Defense Agency under Contracts FA8750-04-C-0220 and W9113M-05-C-0162.

Approved for Public Release
10-MDA-5399 (29 April 10)

References

- [1] Yalowitz, Jeffrey S.; Youree, Roger K. and Gregory J. Romanowski Gregory J.; "Predictive Fault Detection for Unmanned Communications Facilities, Final Technical Report," Instrumental Sciences, Inc., December 2004.
- [2] Press, William H.; *Numerical Recipes in C*, Cambridge, UK: Cambridge University Press 1988.

- [3] Kokoska, Steven and Zwillinger, Daniel; *Standard Probability and Statistics Tables and Formulae*, New York: Chapman and Hall/CRC 2000.
- [4] Rencher, Alvin; *Methods of Multivariate Analysis*, New York: John Wiley and Sons, Inc. 1995.
- [5] Manly, Bryan F. J.; *Multivariate Statistical Methods: A Primer*, New York: Chapman and Hall 1986.
- [6] Melsa, James L. and Cohn, David L.; *Decision and Estimation Theory*, New York: McGraw-Hill 1978.
- [7] McGranaghan, M. and Kinder, F; "Evaluating Motor and Transformer Inrush Currents", http://ecmweb.com/mag/electric_evaluating_motor_transformer/, December 2006

Portable Maintenance Support Tool Enhancing Battle Readiness of MDA Structures and Vehicles

Trevor Niblock, John O'Day, Duane Darr, and Bernard C. Laskowski
Anatom Incorporated
562 E. Weddell Drive, Suite 4
Sunnyvale, CA 94089-2108

Tel: (408) 734-9392 Fax: (408) 734-8335
Email: bernard.laskowski@anatom.com

Harsh Baid and Ajit Mal
Mechanical and Aerospace Engineering Department
School of Engineering and Applied Science, University of California
Los Angeles, CA 90095-1597

Teng K. Ooi and Aaron Corder
Missile Defense Agency, 7100 Defense Pentagon, Washington, DC 20301

ABSTRACT

Handheld Portable Maintenance Support Tool (PMST) incorporates microcontroller unit providing a wireless interface between a sensor node network, consisting of Anatom micro-LPR corrosion sensors combined with off-the-shelf sensors, and portable computer databases for high value asset monitoring and matériel management. PMST will be able to provide the user real-time capability to evaluate health status and operability of future MDA hardware including structures and vehicles such as Launch Platform, and Future Interceptor. This assessment capability provides early warning of structural and component deterioration or failure traditionally encountered during time of use. PMST system results in reduced maintenance, maintenance costs, downtime, and vulnerability of MDA's stockpile, while increasing inventory condition-awareness and battle readiness. Clear benefits are improvements in safety and security while expanding field readiness and operational capacity. Future extensions to PMST system will provide new prognostics, readiness predictions, matériel inventory management, and mobilization capabilities.

INTRODUCTION

Anatom has developed the basic technology for a Portable Maintenance Support Tool (PMST). The device is unique and novel in that it uses a Micro Controller Unit (MCU) in a handheld device to perform data analysis whilst maintaining a link with a Personal Computer (PC) based database for further support. The system is using an established Anatom Inc. interface module that can communicate with most sensors and machine subsystems. It can accommodate any sensor operating in the range 0V to 5 V and 4mA to 20mA, which includes most off-the-shelf commercially available sensors. Sensor data uploaded to the device are presented on a Graphical User Interface (GUI) on the unit.

An input option allows for new scenarios in maintenance to be both cross referenced on the main database and any new action to be recorded. This allows for technical logic and experience to be assimilated over time into a main database to produce an intelligent system. The PC based interface is programmed to allow for further in-depth analysis of data and allow new systems to be analyzed using an easily programmable object based interface. This is formulated so that it can be downloaded to the hand held unit, i.e. as new scenarios, equipment, systems and sensors are added appropriate interface modules can be developed.

The PC based interface is a development of the Analatom Inc. interface for its Data Acquisition (DAQ) system. The software interfaces with the DAQ via either wired or wireless means. It also has a modular interface to Extensible Markup Language (XML) data base systems such as Oracle and Access. The system allows for a larger knowledge base to be accumulated over time on parallel systems all feeding a central database.

The technology is in the development path of a Structural Health Monitoring (SHM) system that Analatom Inc. engineers have been building over the last half-decade. The system provides maintenance engineers with not only a flash image of the state of the system they are examining, but also a comparison of the system's behavior or properties over its life. The Analatom PMST system is easy to use and to interact with. Additionally, the PMST is able to compare the state of the system under review with other systems and where necessary recommend appropriate action on maintenance and repair.

The SHM system that Analatom Inc. has developed to date has been engineered to be part of a greater PMST system; it has generic interfaces on both ends. For example, it interfaces to most sensors and monitoring suites and communicates across a broad range of media to most diagnostics and prognostics systems. As a product the PMST system is market pulled, i.e. many potential customers who operate and maintain high value structures have expressed a desire for such a system if available. Potential commercial markets for the PMST system include but are not limited to the aerospace, shipping, petrochemical and civil engineering industries.

SENSOR SUITE

The concept with the PMST is to have a tool that will give the reader information on a structure or system and that will relay its present status. Additionally the system has to provide the user with all appropriate documentation and specifications of the area of the structure (component) they are examining. At this point in the development of the system the type of data that is provided to the user, how it is tagged and rated is not of concern—it will be assumed that for each structure, system and sub-system all the appropriate information will be provided and the PMST will simply make it available to the user as and when required.

Getting sensor data to the PMST is critical. Data processing will not be performed on the PMST, but remotely on a server with results being relayed back to the PMST. In this paper we examine the systems that are being put in place to allow the PMST to collect data from analog sensors. Most analog sensors are three wire devices with a common ground, a supply voltage and an output channel. The output channel can either be voltage or current controlled. Typical output channel voltages are listed below in [Table 1](#).

Output type	Current	Voltage
Typical Values	4-20 mA	0 to 1, 1.5, 2.5, 3.3, 5 & 10 V

Table 1: Typical Analog Sensor Outputs

Analatom Inc. also produces the μ LPR (Linear Polarization Resistance) corrosion sensor which plays a key role in SHM. This sensor will also be included into the suite of analog sensors with which the PMST interacts. The μ LPR sensor requires more than a 'simple' sensor interface. As this sensor has an offset corrosion potential that needs to be scanned around, the PMST nodes will use the onboard microcontroller to interact with the μ LPR sensors. In addition, strain needs to be monitored and this too is not a simple voltage reading as it requires a Wheatstone bridge. By using two tangential SGs (Strain Gauges) the system's sensitivity can be enhanced. However, for the present only one arm of the bridge will contain a strain gauge.

PMST INTERFACE SYSTEM REQUIREMENTS

The concept for the PMST system that Analatom Inc. is designing is to produce a hand held unit that has an interactive Graphical User Interface (GUI). This GUI has to represent the structure being monitored and offer intuitive access to information on the structure through 'point and click' interaction. In this paper the interface developed to date will be covered. The PMST interface needs to provide the following functionality.

Warnings. The system needs to be able to set off an alarm on the PMST if an event occurs that is outside of pre-set limits on the structure. Ideally, this warning system is not limited to the PMST but activates warnings on the structure itself and at remote monitoring locations where action can be taken or the information is required.

General SHM Data. The system needs to be able to provide the user with usage data of the structure in a simple to understand format. Hence, an engineer using the PMST should be able to ‘pull up’ historical and real-time data on nearby data acquisition nodes. A remote user without a PMST should ideally have access to the same data so that reports can be generated and the general usage of the structure examined.

Manuals. The system should provide access to manuals on any system or component that the SHM system is monitoring. In this manner, a PMST user who is on location should have instant access to operational information.

Spare Parts Lists. Either as part of the user manual or as a separate module the PMST should provide an interactive manual where systems and subsystems can be examined with spare parts lists, ordering information and (ideally) lead times.

Text Input. The system needs to allow for notes on the structure to be input to the system via the PMST or a remote location. These notes need to be searchable; hence the system either needs to have a standardized form that is completed (which would be arduous) or be automatically cataloged according to the actual text.

Image and Video Input. The architecture of the PMST has not been specified to have a camera. However, the ideal system would allow for an engineer who is on location to take images and video of events and occurrences on the structure and load them onto the ‘system’ so that engineers who are not on location could actually see events. Likewise, it would be ideal if the system allowed for remotely placed engineers to be able to upload images to the system to (e.g.) give support to an engineer at the structure.

Contact Details. The system should have a separate location that gives instant access to the correct support personnel.

PMST INTERFACE IMPLEMENTATION

Different architectures have been examined for the PMST interface. Initially when the project was conceived the concept was to develop the Analatom Inc. DAQ node so that it included a ZigBee wireless module, and a hand-held derivative of the unit would contain a screen to allow communication with any Analatom Inc. node. The initial designs were for wireframe drawings that had interactive links. This developed into 3D models with ‘clickable’ nodes on them aimed at representing the actual location of nodes and/or sensors on the structure. But in conjunction with this project’s development has been rapid development in the hand-held Personal Digital Assistant (PDA) market. Today these units offer full 3G cellular, WiFi and Bluetooth connectivity. At the same time the units have powerful processors, GPS, accelerometers and have a myriad of functionalities. In addition, the PDA units are set up with operating systems that make programming and addressing the on-board functionality relatively simple. Therefore, the objective of the PMST project is now shifting to utilize this technology. As these devices (cellular smart PDA’s) are internet enabled, it is now possible to develop the PMST system on ‘standard’ web based systems.

For example, in developing a PMST application to work on the Google Android PDA platform, it is important to set out the system’s required objectives. These objectives are to “Demonstrate functional access, seamless data acquisition and storage from sensor through data archival and retrieval”. In context this means that an operator/technician needs to be able to go to a sensor location and be able to retrieve all the available information on the sensor and the location that is available. In addition, the PMST platform needs to be able to offer the operator the ability to record input (data) on any observations that they make and feel need to be input into the SHM system. It should be noted that this last requirement is an ‘additional’ criteria to the original specification. What it offers is a dynamic two-way portal for the technician; during maintenance and inspection the same tool can be used to gather data on a component, schedule maintenance, and report completed maintenance or any additional information on the structure (input through the tool by the technician).

Selection of the appropriate cellular PDA platform was relatively simple. The Google Android platform was selected as it offers the same functionality as any other unit with the additional advantage of being open source. The task has therefore been to compile an application for the Android that shows the functionality of the system. To this aim the following criteria have been delineated:

1. The application should be 'just another application' on the platform. It should still allow full functionality of the PDA Cell.
2. Security should be ensured. Standard password protection has to be added
3. Location is important; the application needs to be able to bring up a viewable map of sensor and node locations. Ultimately other (GPS) applications can be used to bring the technician to the correct location if they have never visited a site before.
4. Using the map a technician needs to be able to access sensors remotely and bring up data on that node. I.E., if on route to a location, the technician should be able to see which nodes in the area are showing a problem so they can be visited first.
5. Alternative to a map the technician should be able to bring up a list of sensors/node that details activity and output. Note, that in the list form the sensor only needs an Active/Alert status.
6. From the unit it should be possible to download all node data.
7. The technician should also be able to communicate with the node, i.e. activate or deactivate the node, a device, system or sensor. This includes being able to set a node to 'alert' for a problem or condition spanning multiple sensors or sensor types.
8. A 'find' function. In practice scenarios will arise where a technician may not know where the node(s) currently are. For example, they could have been moved to a new location, or a new vehicle could arrive at a hanger. In this case, a find function for local nodes would be very desirable.

The points listed above will now be covered in their implementation on the Android platform. The application is run on an emulator provided by Google. The first point to address was to ensure that the application ran on the platform in conjunction with the phone's applications; i.e. 'just another application' on the PDA cell. The second point was to ensure system security. All data through the (cell) system is encrypted by default. Hence, it is the interface that needs protecting and a login password is necessary and has been implemented. Once logged in one sees the home page with Map and Sensor Menu buttons at the top as outlined in the third point. The ability to locate a particular node or sensor as described in the fourth point is included in the functionality of the system. Point five requires that the sensors in an area be listed. Note that the sensors and node can be virtual, i.e. a sensor's output file is generated which the android addresses over the web. Rather than numbering the sensors and nodes, they can be named to give more detail on their location and operation. The node data can be updated remotely as specified in point six. Note this is all being done through the cell network. As such the technician can be local to the node or in a remote location. In a situation where a technician is on a structure and finds a fault that has not been picked up by the local sensors, the local node can still be updated. For point seven a node can be set to an alert level. In further development of the system, notes and reports can be tagged to the alert. In this manner a technician who visits the site at a later point in time will be able to understand why there is an alert and an engineer monitoring the site remotely will be able to understand the position on the ground. Any alert data with notes is also of high value to the Artificial Analysis (AI) software system as it is possible to create virtual sensors for the problem. For example, if excess humidity and temperature cause a component to fail, the AI system can call for an inspection on the component if it has been abnormally hot and humid. The final eighth point was for a find function. For this the application presently can give cross streets and a map view using Google maps. Ultimately, for locations such military bases the screen can be altered to give a vector (arrow and distance) pointing to the node.

DEMONSTRATOR OVERVIEW

The variety of SHM applications is wide and vast, covering a number of structures from e.g. rotary winged aircraft to large fixed structures such as bridges and highways. Within each structure there are a number of phenomena that need to be monitored from e.g. strain to corrosion with accompanying sensors and systems having sampling and data rates in the high speed e.g. kHz down to single daily samples, respectively. In addition, other data sources such as inspection reports and maintenance records can provide a wealth of relevant data; if the data can be captured, analyzed and presented.

From a commercial or military perspective the objective of employing a SHM system is to obtain the correct balance of how much investment should be made in any potential SHM system. The bottom line is a viable Return On Investment (ROI). When considering ROI it is not only the initial cost of investment that needs to be considered, but the ongoing maintenance cost of the SHM system which includes the software, hardware and,

importantly, the analysis. If this cost is comparable with the repair or failure cost, then it is only on mission critical components, systems or structures where it may be viable to consider a SHM system. When designing a SHM system the engineer should consider the potential clients' perspectives as all too often SHM equipment manufacturers provide specialized solutions that do not interact with other SHM systems. In this case, the client is left with a choice of solutions which are mutually exclusive and they have to work out which solution(s) if any is viable. What the client ideally wants is a system that is accessible on the Web, presents a complete 'snap shot' of the structure that accounts for all data streams and produces a maintenance schedule that is based on the structure's actual condition.

If multiple sensors and systems that can be wired and wireless are used that sense different phenomena, the optimal system to the end user must analyze all the data and present it in a User Interface (UI) that is intuitive to use and clear to understand. In such systems the structural health of a component can be extrapolated by indirect measurements. In addition, with most high value structures an inspection and maintenance regime is in place that can offer important information if the data can be extracted and digitized. Another feature of the ideal system would therefore be to analyze this data in conjunction with sensor data and present a 'full' picture of the structure's health in the UI. The capture, analysis, interpretation and presentation of multiple, independent, non-linear data streams has hitherto been a near impossible task. However, the development of cloud computing systems in conjunction with AI analysis has made such systems viable. In this paper the architecture of such a system is presented with detail of its operation and the results of a fully working system.

The Analatom SHM software architecture, as shown in Figure 1, is designed around the principles of strong cohesion and loose coupling using standard enterprise N-tier architecture. This results in a highly scalable and extensible solution. The architecture is built using Java core technologies due to the many industrially deployed and proven high quality open source libraries that can be leveraged.

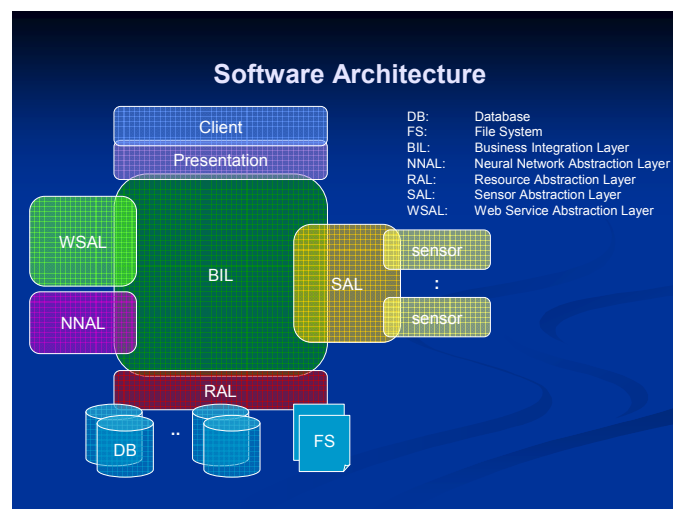


Figure 1: Software Architecture of the Analatom Inc. SHM Data Monitoring System.

The client tier is implemented using Asynchronous JavaScript and XML (AJAX) based technologies so that the user interface can be deployed and accessed easily across the web on a wide range of operating systems and devices. The presentation tier exposes a web service based application programmable interface (API) so that custom views and applications can be developed by the structure's user or third parties based around the core technology. The Business Integration Layer (BIL) brings together the services and marshals their transactions to ensure data integrity. The Sensor Abstraction Layer provides pluggable integration to sensors that third party vendors can develop against. This allows for any sensor to be integrated into the system through a standardized interface.

The core technology is the Standard Object Access Protocol (SOAP) that allows communication to remote sensors over open networks. The Resource Abstraction Layer (RAL) provides both federation and integration of data persistence solutions such as Databases (DB) and File Systems (FS). The Neural Network Abstraction Layer (NNAL) provides an interface to the data analysis systems. This again uses SOAP to allow analysis using

internet/cloud based resource allocation. The Web Services Abstraction Layer (WSAL) allows the system to integrate data from third party sources, e.g. weather or seismic data, to augment the analysis.

DEMONSTRATOR HARDWARE

The project is at the stage where all components in the system are being integrated to form the full SHM system with the data acquisition node and PMST. The detail of the Sensor Abstraction Layer (SAL) is now covered in more detail. Again, in Figure 1 the software architecture of the system is shown (acronyms are given in the figure). At the heart of the system is the Business Integration Layer (BIL), in its simplest form this is effectively the logic that interprets data from all sources and decides what to do with it. The main task for this project is to format the data into a standard form that the BIL can deal with. This is the task of the abstraction layers. Figure 1 could be represented differently where there is only a single abstraction layer and the sensors, web services resources and neural network are all connected to the abstraction layer. I.E. the data coming out of the abstraction layer(s) is standardized. To accomplish this, the system uses an XML format into the BIL. In this report the detail on the SAL will be given as this is the most relevant to the project. To examine the operation of the SAL a corrosion data file for the μLPR will be used as an example to show the procedure.

It should be noted that the abstraction layers are designed to be interfaced through a remote GUI and in full system implementation it is the BIL that interfaces with all abstraction layers. The user never directly sends commands to an abstraction layer. Rather, data requests can be made at the UI/client level and through the presentation layer the BIL sends requests to the SAL (abstraction layer). Alternatively, the BIL itself schedules the integration with the SAL or the NNAL can make a request to the BIL for data. In operation the SAL is given a directory by the BIL to search for data. The SAL reads in the sensor data files and converts them into the required XML file format outputting to the BIL. For the purpose of this demo the files are written back into the same directory as the original sensor data. In full operation the system would/may place the XML data into the local database depending on system architecture. The basic operation is shown in Figure 2.

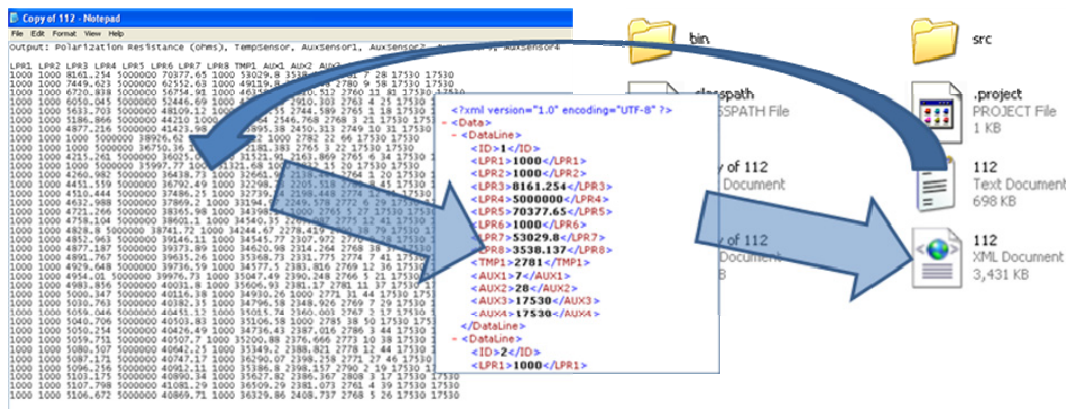


Figure 2: Schematic Representation of What the SAL Script Does.

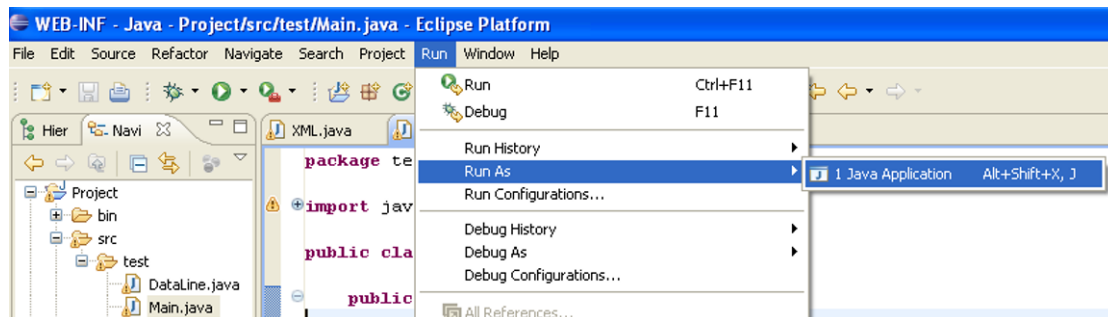


Figure 3: Running the SAL in Eclipse

For development and testing purposes, the SAL is run through Eclipse, a Java development toolset. The detail on the (Java) script is now given to emphasize the simplicity of the system, i.e. converting the script to operate on “Interface protocols and intelligence for accessing spare parts, and historical databases” requires the same script customized for each operation. The script is opened in the project folder and run (Go to Run > Run As >Java Application (Figure 3)).

At this point the script will prompt for user input that would ordinarily come from the BIL, i.e. in the Console window the script will prompt for the directory. Once the BIL supplies the directory and runs the script, the SAL will generate the XML files. The present script returns “Generated file successfully.” and the XML files will now be found in the specified directory. If not successful, there may be several reasons why 1.) There are no .txt files, in which case the program will print “There were no .txt files” or 2.) “There was a typo in the directory”, in which case the program will throw a NullPointerException. This is the same data that would be passed back to the BIL, and in this case the appropriate response needs to be programmed into the BIL. This can be either to send an error message out or to work on alternative logic that is dependent on the situation, e.g. a sensor system may not be available for a data dump.

The Main class prompts the user for a directory; it then stores all the names of the files with extension .txt. Then, for every .txt file in the directory, it will create an XML document. The XML class begins by declaring the private variables to be used later in the program and then uses a default constructor to prompt the BIL for the type of sensor data required. In this example it actually prompts the user for a file name (*.txt). The output XML file name is then constructed. In a fully implemented system this naming is dependent on other system information. In this case it is just dependent on the input file name. The sensor data in the file is now extracted according to the predetermined format.

DATA MINING AND PROCESSING OF SENSOR DATABASES

Analatom Inc. is employing a neural network to perform the data mining tasks to look at both prognostics and diagnostics of the data produced by the Analatom system. It should be noted that the PMST system is not yet fitted to any applications (be it military or commercial); hence no data collected by the system is available for

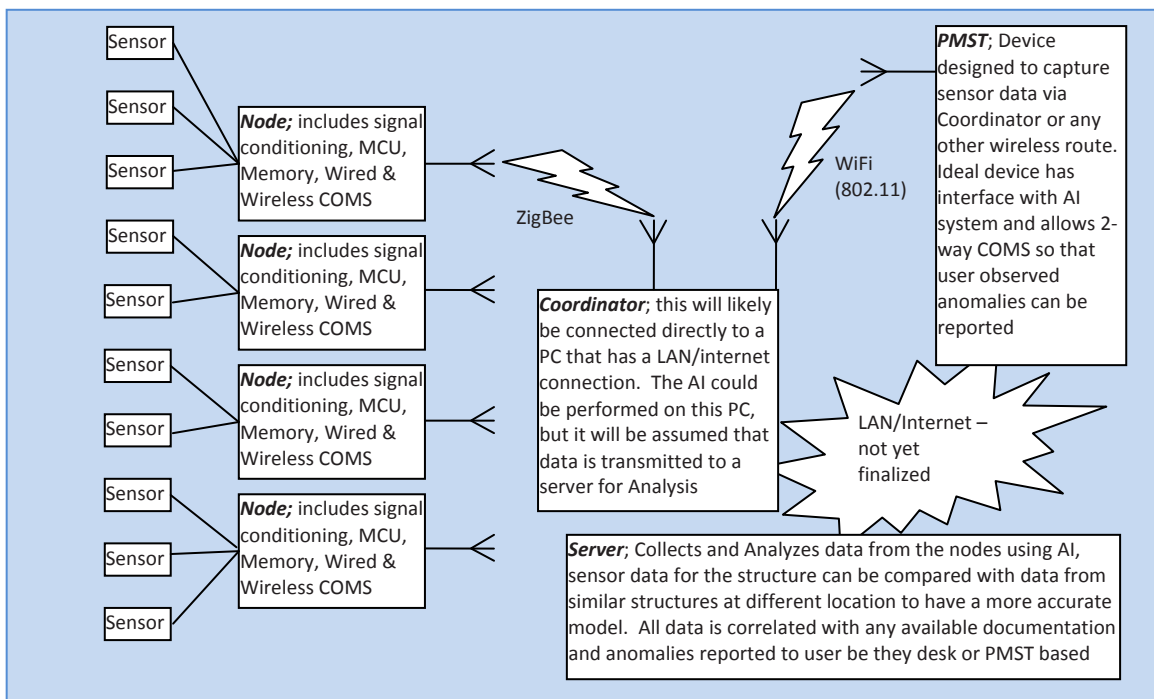


Figure 4: The complete PMST system. Note that the AI analysis is to reside on a central server. In this manner multiple data streams can be analyzed to give a more accurate diagnosis of the structure. At this stage in the project the form of communication between the PMST and AI server has not yet been finalized.

analysis. A primary question that should be asked is “why use AI software as opposed to writing a transfer function for the analysis”? The answer to the question is that once fitted the complete PMST system consists of a series of nodes to which arrays of different sensors are connected. The nodes transfer data to a central processing bank via a coordinator node. Hence, for each application, the practical situation on the ground is that large amounts of data are gathered. The data can be of differing types, formats and composition that can be of time or frequency domain. To write the algorithms to correctly analyze and present this data to an engineer can be a daunting task. The system that Analatom is building as part of this project is shown in [Figure 4](#).

Employing an AI system effectively reduces the data sets to ‘zero in’ on the determining sensor output(s) for each phenomenon that is of interest to the user. The AI system does initially need to be trained. However, this is a relatively simple task compared to determining a transfer function for each application and then having to code the function. Training the AI system requires a ‘skilled’ AI programmer in conjunction with support from a system engineer familiar with the structure that is being monitored. Once trained the AI system alerts users of anomalies. The great power of the system is that it tends not to call false positives during adverse conditions. For example, if a structure such as a bridge is being measured in a typhoon, strain reading limits that normally would set off alarms would be automatically increased by the AI system as all sensors in the system would be recording excessive behavior. An AI system can be trained to monitor the relative compliancy of a system—not absolute values but their ratios. By the same reasoning the system is very sensitive to low divergences from normal behavior. Hence, in the case of a slight decrease in strain when the system usually increases, the AI system sends out the alarm. This is a very good example of AI systems at their best, e.g. if a structural member is failing, the strain around it would decrease when loaded.

CONCLUSION

The PMST gathers data from a sensor node. To have an effective PMST system it is necessary to open up the number and types of sensors that the node supports. A fundamental parameter of SHM systems that the node needs to collect is strain. In this paper it has been described how the Analatom Inc. node has been adapted to read in critical physical data using *off the shelf* sensors and systems.

An interface for the PMST system has been presented that meets and exceeds all requirements of the initial system. The system is based on web applications and has been possible to develop due to the advances made in PDA technology which will form the basis of the PMST interface module. The PMST has been designed to collect node and sensor data from the nodes through a cellular modem. This has allowed for relatively advanced and ‘best in industry’ cellular PDA’s to be used as the PMST platform with an application on it that performs all the tasks required of the PMST. In operation, all the complex analysis and routing is completed by the server the application is connected to via the cell network. To the end user this is transparent. From the user’s perspective they are holding a complete, high asset structure health management tool in their hand.

All the software components for the system are now at an advanced stage of development. The example of the abstraction layer given in this report for the sensor data shows that the process of providing information to the Business Integration Layer (BIL) is a relatively simple process and can be applied to numerous records and data systems. All data handled by the BIL will be in XML format. The AI software will deliver the PMST the structure’s data, information, and documentation. The demonstrator system has been configured and supplied with data in the same manner to an actual PMST system. The AI system was tested on hold out data and predicted system failure. These system components are now ready to be integrated with a PMST system.

The system is now at the stage where initial testing on MDA systems would be appropriate. Analatom Inc. will now start sourcing real world applications for system implementation and testing.

ACKNOWLEDGEMENTS

The US Army Space and Missile Defense Command, Huntsville, Alabama 35807-3801 funded the work under contract number W9113M-07-C-0169. Approved for Public Release 09-MDA-4932 (2 OCT 09).

A Compact System for Measurement of Absorbance of Light

Adriano Jotadiemel Masi, Universidade Federal de Minas Gerais, Belo Horizonte, Brazil

amasi@ufmg.br

Meinhard Sesselmann, Universidade Federal de Minas Gerais, Belo Horizonte, Brazil

meinhard@ufmg.br

Denilson Laudares Rodrigues, Pontifícia Universidade Católica de Minas Gerais, Belo Horizonte, Brazil – denilsonlr@pucminas.br

ABSTRACT

In this work a compact device to measure absorbance based on light emitting diodes – LED - is proposed. Measurand is the concentration of specific chemical or biochemical components within the test fluid. The advantage of such a system lies in the use of low-cost standard optic-mechanical and electronic components that contribute to its compactness and robustness.

The proposed system measures absorbance (or transmittance) of monochromatic light inside a standardized cuvette of 10 mm light path within a temperature ranging from 25 to 40°C ($\pm 0,2^\circ\text{C}$). Some important features, such as stability, accuracy and precision of the measurement system are discussed. It is shown that the measurement stability is governed by the stability of the light source. An acceptable value is 0,002 units of absorbance per hour, which can be verified by measuring a dummy cuvette during a suitable long period. The accuracy and precision are estimated by means of traceable calibration standards throughout the desired spectrum of wavelengths. The wavelengths required for the target application of the proposed system are 340, 405, 505, 546, 600 and 700nm. Basic variables of influence are identified and a brief metrological analysis is presented in form of an uncertainty balance. First results obtained with the proposed system demonstrate uncertainties below 1,6 % relative to the measured value of absorbance.

1 Introduction

Due to its simplicity, versatility, velocity, accuracy and benefit-cost ratio, the molecular absorption spectrometry is a widely used technique to measure the concentration of specific chemicals or biochemical components within solutions. It consists of the measurement of absorption of monochromatic light passing through a sample.

Since the molecular absorption spectrometry has many different applications, a large number of equipments has been developed to attend these specific requirements. This implies in a large variety of configurations and performances and, consequently, costs. Normally, the process of sample collection also involves the storage and transport to a laboratory where it will be analyzed, which may compromise the integrity of the sample and increase costs. Therefore, the development of portable, robust and precise equipments allows the reduction of costs and time, once the samples are analyzed closer to where they are collected.

A light source that quickly substitutes traditional sources in many applications is the light emitting diodes (LED). Nowadays, there are available LEDs throughout the whole range of wavelengths most commonly applied in molecular absorption spectrometry. Commercially available LEDs emit radiation with wavelength ranging from ultraviolet to the infrared. Moreover, the luminous efficiency of these components has evolved significantly, competing with fluorescent lamps [1]. Thus, the use of LEDs as a source of radiation has several advantages which are: (1) low power consumption, (2) compactness and robustness, (3) emission of light in a narrow band of wavelengths, (4) simple power circuits, (5) low cost compared to other sources of radiation and (6) long lifetime. These features allow the design of more efficient, smaller, lighter and, therefore, more robust equipments.

Due to the characteristics listed above and the development of LEDs, several photometers have been proposed using them as a light source. As early as 1973, Flaschka et al. already proposed the construction of a photometer using a LED as light source and a phototransistor sensor. One important reason to apply LEDs in photometers is the need for field measurements and, hence, portable devices which have low power consumption and are compact. Palma et al. [2] present such a photometer for measuring potassium nitrate. To compensate the influence of temperature on the emission of the LED, a beam splitter and a reference sensor were used. The light intensity measured by the reference sensor controls the power to the LED. This configuration showed an average

consumption of 150mW and, hence, can be powered by a 9V battery or a small source of continuous power. Weiwei et al. [5] present the development of a portable device for measuring biochemical parameters. Their system uses optical fibers to divide the light from a LED and guide it to the sample and to the reference sensor. In order to develop a low cost photometer Yeh et al. [7] present a prototype that can be connected to a computer via serial port or run as a standalone instrument with seven wavelengths available to cover most part of the spectrum. Fairly small photometers can be developed when using LEDs as a light source. Yang et al. [6] present the design of a miniature portable photometer. Their project includes the resources of a microcontroller to implement the entire system-on-a-chip (called SoC). All the features of the photometer are carried out by a microcontroller that, beyond the digital input and output pins, has an A/D internal converter. To reduce the influence of ambient light, the dark signal (while the LED is switched off) is subtracted from the sample signal (while the LED is switched on). This cycle is repeated several times in order to obtain a good performance even under unstable ambient light conditions.

Several photometers have been developed containing multiple wavelengths. Gaião et al. [4] present a portable and low cost multi-LED photometer. The photometer consists of six LEDs and a phototransistor sensor and was applied for the measurement of ferrous ion in samples of syrup and total protein, albumin, urea, calcium, chloride and hemoglobin in blood samples. Fonseca et al. [8] present a photometer with seven wavelengths. The light from each LED is driven to a cuvette for measurement through optical fibers. After crossing the cuvette the light is conducted through optical fibers to the sensor. This arrangement enables continuous measurements at a chosen wavelength or the sequential activation of the LEDs for measuring multiple wavelengths. The configuration was applied to the simultaneous determination of zinc and copper in pharmaceutical samples and alloys. Another prototype using multiple LEDs and fiber optics was proposed by Hauser et al. [9]. The photometer contains seven wavelengths and the light of each LED is combined and guided to the measurement cuvette, as well as the reference sensor, using a 7 x 2 fiber optic coupler. Furthermore, measurements of absorbance and concentration obtained by this photometer were compared to those from a “standard” spectrophotometer. The results show a good linearity in the relationship between absorbance and concentration, as well as the influence of the difference between the wavelength of the emission peak of the LED and the peak absorbance of the samples.

2 Experimental

2.1 System configuration

The proposed system for measuring absorbance is composed of the following components: (1) light source, (2) set of lenses, (3) wavelength selector, (4) sample container (cuvette), (5) transducer, (6) signal conditioning and analog-digital converter (7) control system. Figure 1 presents a scheme of this type of system. Dashed lines indicate the flow of control signals. The control system consists of a microcontroller and electronic circuitry needed to drive and control electronics and optical-mechanical components of the measuring system.

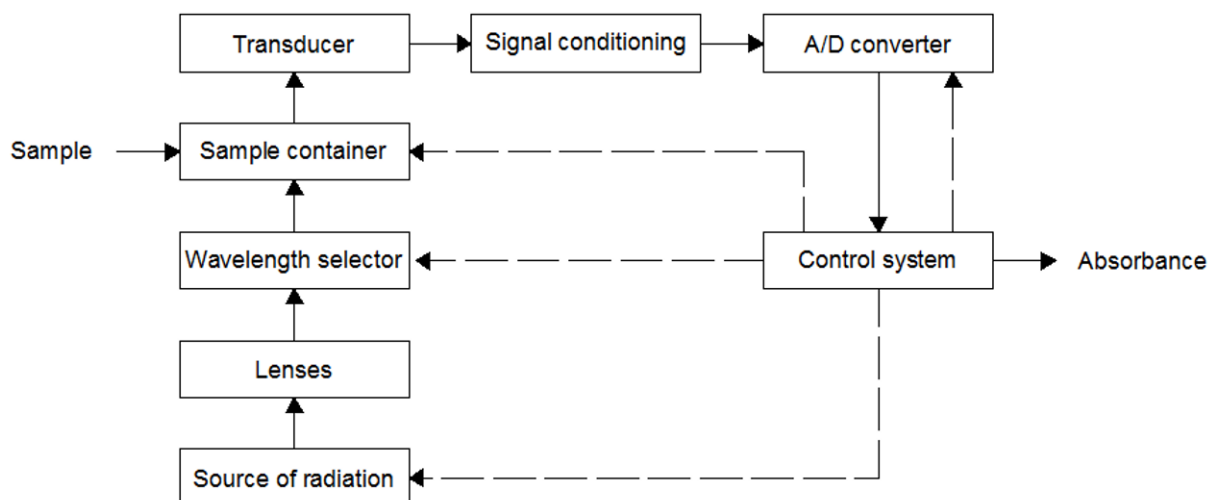


Figure 1. Schematic view of the measurement system proposed.

The use of LEDs significantly simplifies the design of the optical system, since they are small, have low power and emit radiation reasonably collimated and monochromatic. The low consumption results in low heat losses compared with tungsten lamps, and eliminate the need for heat sinks. The collimated light emission eliminates the need for extra lenses. The fairly monochromatic light emission may eliminate the need for filters.

The emission of radiation by LEDs is strongly influenced by temperature. As a consequence, a temperature drift may generate a drift of zero well above acceptable values for this particular target application. In order to reduce the influence of thermal instability, two light sensors are provided, one to directly measure the emission of the LED and another to measure the light transmitted through the sample. Drifts eventually observed in the transmitted light, but which are caused by thermal drifts of the LED, can thoroughly be compensated. For simplification, the first sensor is denominated reference sensor and the second sensor is denominated sample sensor throughout this work. Figure 2 illustrates this scheme.

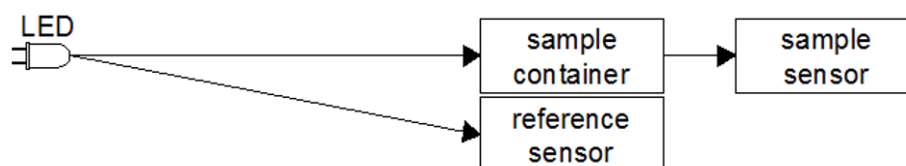


Figure 2. Scheme to detect and compensate thermal drifts of the LED.

The sensors used are photodiodes whose output signal is a current proportional to the power of light incident on its active area. The circuit of signal conditioning transforms the current signal in a voltage signal and applies a certain gain in order to adjust it to the dynamic range of the A/D converter. The circuit used was a transimpedance amplifier. Photodiodes with integrated amplifiers were applied whose schematic circuit is shown in figure 3.

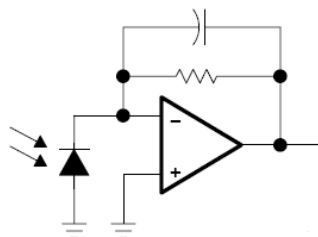


Figure 3. Schematic circuit of photodiodes with integrated amplifier.

Figure 4 shows a section view of the optic-mechanical set-up designed for the proposed measurement system which combines, among others, several items described previously.

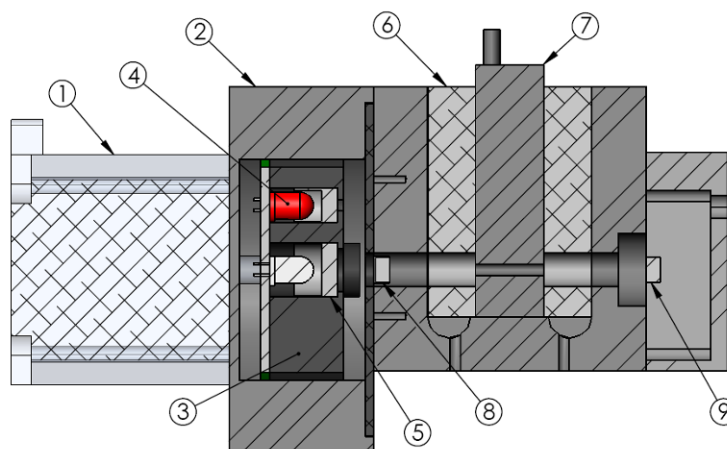


Figure 4. Section view of the optic-mechanical set-up.

(1) step-motor, (2) motor and wheel support, (3) filter and LEDs wheel, (4) LED, (5) interference filter, (6) support for the cuvette, (7) cuvette, (8) reference sensor, (9) sample sensor.

2.2 Measurement of thermal stability (stability of zero)

The verification of the stability of zero is made by measuring the output signal of the photodiodes during an appropriate period of time. The stability of zero is specified in terms of the variation of absorbance per hour.

It was evaluated by measuring the voltage of the two channels of the converter over a period of 90 minutes for each LED. The algorithm executed by the microcontroller for data acquisition has a flow diagram as illustrated in figure 5. Data acquisition is done through a serial port while the system is placed inside a black metal box in order to further reduce influences of ambient light. The optical-mechanical system, all necessary electronics and the power supply are mounted inside this box.

The stability of the system is determined by calculating the drift of absorbance values of each channel considering as the reference voltage the first reading of voltage and as the sample voltage all consecutive values. Then, the drift of absorbance is obtained using equation (1).

$$A = \log \frac{V_0 - V_d}{V - V_d} \quad (1),$$

where V_d is the dark voltage, V_0 is the reference voltage, V the sample voltage and A is the drift of absorbance. The absorbance is a dimensionless measure and, throughout this work, its unit is denominated Abs. Equation (1) is used to calculate the drift of absorbance at both, the reference and sample sensors. The corrected drift of absorbance is calculated according to equation (2).

$$A_{cor} = A_s - A_r \quad (2)$$

where A_s is the sample sensor absorbance, A_r is the reference sensor absorbance and A_{cor} is the corrected drift of absorbance.

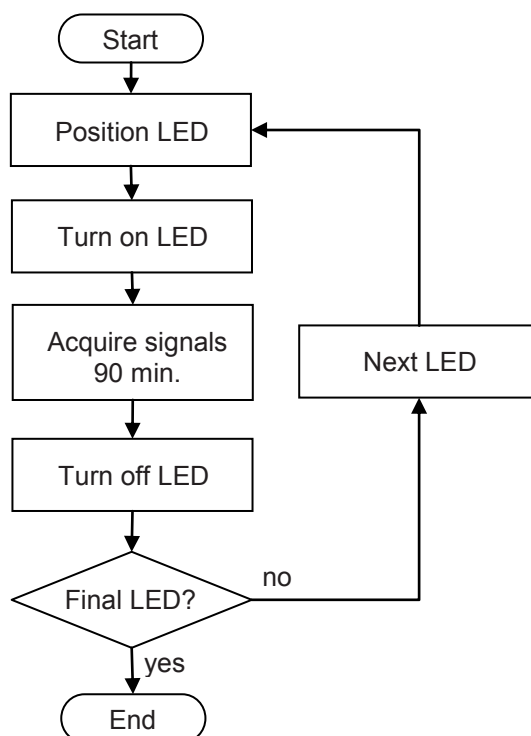


Figure 5. Flow diagram for the evaluation of thermal stability.

2.3 Calibration and measurement of absorbance

Several absorbance standards, identified by F2, F3 and F4, were utilized for the calibration of the proposed measurement system. Their “true” value of absorbance, together with its uncertainty, is well known for a wavelength of 546 nm, as documented by its calibration certificate. For all the other wavelengths that are not cited in the calibration certificate, but are applied within the measurement system proposed, their “true” absorbance value and their uncertainty were estimated by means of measurements with a “standard” spectrophotometer, model Spectronic GENESYS 2. The results of this procedure are summarized in [table 1](#).

Table 1. Conventional true value and uncertainty.

Standard	Wavelength [nm]				
	405	505	546	600	700
F2	0,251±0,003	0,236±0,003	0,229±0,002	0,245±0,003	0,224±0,003
F3	0,512±0,005	0,514±0,005	0,491±0,004	0,550±0,006	0,460±0,005
F4	1,041±0,010	0,984±0,010	0,958±0,007	1,000±0,010	0,769±0,008

The calibration of the proposed measurement system was performed using the following methodology

1. Position and turn on the desired LED;
2. Perform 20 consecutive measurements of the voltages of the dark;
3. Perform 20 consecutive measurements of the reference voltages;
4. Perform 20 consecutive measurements of the standard for low absorbance (F2);
5. Perform 20 consecutive measurements of the standard mean absorbance (F3);
6. Perform 20 consecutive measurements of the standard for high absorbance (F4);
7. Return to step 4 and repeat 4 times the measurement for the three standards;
8. Go to the next LED.

As a result, five absorbance values for each wavelength were obtained, while the value of each measurement represents the average of the 20 consecutive measurements. The measurements were performed with the proposed system mounted inside a black metal box.

2.4 Uncertainty balance for the measurement of absorbance

The main sources of uncertainty considered in the uncertainty balance for the measurement of absorbance are:

1. Nonlinearities of the system that contribute to a systematic portion of error (bias), due to the difference between the value indicated by the system and the conventional “true” value. Furthermore, these nonlinearities contribute to a random portion of error due to the limited repeatability of indications;
2. Uncertainty of calibration of absorbance standards that contributes with a random error due to the uncertainty of the conventional “true” value;
3. Stability of zero which contributes mainly to the random portion of error due to the time elapsed between the measurement of the reference voltage and the measurement of the standard.

Other sources of uncertainty that may further contribute to the total uncertainty of this measurement system were considered insignificant if compared to the previously cited ones.

3 Results and discussion

3.1 Thermal stability (stability of zero)

[Table 2](#) summarizes the performance obtained from the system. For each wavelength are listed the changes in absorbance due to drift at both sensors and the corrected drift of absorbance within a test period of 90 minutes. The stability of the zero obtained for all wavelengths remain within the desired limits of the system, specified to $\leq \pm 2$ mAbs/h for the particular target application. The LEDs 505 and 700nm present very small variations that are within the specified limit even without correction. For all the other wavelength, the desired stability was only achieved after correction according to equations 1 and 2.

Despite the variation with time of the intensity of the LEDs, this compensation method applying a reference sensor operated satisfactorily. The performance with the 546 nm LED showed a high variation for the first few seconds and after 50 seconds of operation, the corrected absorbance already presented an acceptable stability.

Table 2. Performance of system obtained from the stability

Wavelength [nm]	Observed variation of absorbance		
	Sample sensor [mAbs]	Reference sensor [mAbs]	Corrected absorbance [mAbs]
405	11,5	11,5	1,0
505	1,7	1,9	0,3
546	6,2 ⁽¹⁾	7,9 ⁽¹⁾	1,1 ⁽¹⁾
600	4,0	4,3	0,2
700	0,5	0,6	0,2

Note (1): after 50 seconds

3.2 Calibration of absorbance measurement

Table 3 presents an example for the uncertainty balance of the measurement of the standard F2 with LED 405nm. Analyzing the data shown in this table, it can be concluded that the most significant contribution to the combined standard uncertainty is the uncertainty of the proper standard. The relative small values observed for the other sources of uncertainty not only turn these standards inappropriate, but also demonstrate the high potential of the proposed system, capable of making stable and repeatable measurements enhancing the system precision. Comparable conclusion can be drawn from uncertainty balances obtained for all the other standards and wavelengths.

Table 3. Uncertainty balance for F2 – LED 405nm

Source of uncertainty		Sistematic effects	Random effects				
Symbol	Description	Bias [Abs]	gross value [Abs]	Type of distribution	divisor	u [Abs]	v
NL	Non-linearity	-0,0110	0,0006	normal	1	0,0006	4
Cal	Calibration of standard	0	0,0030	rectangular	$\sqrt{3}$	0,0017	∞
E ₀	Stability of zero	0	0,0005	rectangular	$\sqrt{3}$	0,0003	∞
T _c	Combined Bias	-0,0110					
u _c	Combined standard uncertainty			normal		0,0018	410
U	Expanded Uncertainty (95%)			normal		0,0037	

Table 4 presents the results of those uncertainty balances, namely mean value of absorbance, the bias and expanded uncertainty for each wavelength (absolute and relative value). Part of the systematic error of the measurement system may come from the difference of bandwidth between the interference filters and the measurement system used as standard. The interference filters have a bandwidth of 8nm while the measurement of absorbance of the calibration certificate used a bandwidth of 1nm and the reference spectrophotometer measured the absorbance with bandwidth of 2nm. The measurement of the standards by a reference system with a configuration of bandwidth closer to the filter specifications would provide a set of values more suitable for calibration of the measurement system. Since the most important source of uncertainty comes from the proper standard, the expanded uncertainties obtained are similar to those uncertainty values presented in table 1.

Table 4. Mean absorbance, bias and expanded uncertainty.

Wavelength [nm]		Standard		
		F2	F3	F4
405	Mean	0,2400	0,5017	1,0321
	Bias	-0,0110	-0,0103	-0,0089
	U ₉₅	0,0037	0,0059	0,0116
	U %	1,54	1,18	1,13
505	Mean	0,2216	0,4997	0,9714
	Bias	-0,0144	-0,0143	-0,0126
	U ₉₅	0,0035	0,0058	0,0116
	U %	1,57	1,16	1,19
546	Mean	0,2113	0,4734	0,9371
	Bias	-0,0177	-0,0176	-0,0209
	U ₉₅	0,0021	0,0041	0,0070
	U %	1,01	0,86	0,75
600	Mean	0,2316	0,5329	0,9749
	Bias	-0,0134	-0,0171	-0,0251
	U ₉₅	0,0035	0,0069	0,0115
	U %	1,50	1,30	1,18
700	Mean	0,2112	0,4481	0,7583
	Bias	-0,0128	-0,0119	-0,0107
	U ₉₅	0,0035	0,0058	0,0092
	U %	1,65	1,29	1,22

4 Conclusions

The use of LEDs as the light source has enabled the development of a compact, robust low cost system. With a source voltage of 12V the proposed system showed an average power consumption of only 370mW which makes it suitable for portable applications powered by battery. The system demonstrated sufficiently good performance for the target application, verified by stability tests and proved through calibration. The results obtained with the proposed system demonstrate, that uncertainties below 1% relative to the measured value of absorbance are feasible. However, in order to further investigate and exploit the potential of the proposed system, more appropriate standards with lower uncertainty need to be readily available.

5 Acknowledgements

The authors gratefully thank the support given by FAPEMIG, the Graduate Program in Mechanical Engineering at UFMG and CELER Biotecnologia S/A.

6 References

1. Bürmen, M.; Pernus, F.; Likar, B; LED light sources: a survey of quality-affecting factors and methods for their assessment – Measurement Science and Technology. **19** (2008) 122002
2. Palma, A. J.; Ortigosa, J. M.; Lapresta-Fernández, A.; Fernández-Ramos, M. D.; Carvajal, M. A.; Capitán-Vallvey, L. F.; Portable light-emitting diode-based photometer with one-shot optochemical sensors for measurement in the Field – Review of Scientific Instruments **79**, 103105 (2008)
3. Belz, M.; Klein, F. A.; Eckhardt, H. S.; Klein, K. F.; Dinges, D.; Grattan, K. T. V.; Optical Detection Techniques and Light Delivery with UV LEDs and Optical Fibres – Third International Conference on Optical and Laser Diagnostics – Journal of Physics: Conference Series **85** (2007) 012034

4. Gaião, E. N.; Medeiros, E. P.; Lyra, W. S.; Moreira, P. N. T.; Vasconcelos, P. C.; Silva, E. C.; Araújo, M. C. U.; Um fotômetro multi-LED microcontrolado, portátil e de baixo custo – *Química Nova*, vol. 28, No. 6, 1102-1105, 2005
5. Weiwei, Y.; Aiyu, Z.; Baoshan, H.; Xinxia, C.; A portable biochemical detection device based on fiber optic sensor – *Sensors and Actuators B* 130 (2008) 21-24
6. Yang, H.; Wei, X.; Liang, X.; Su, M.; Lu, X.; A SoC and LED based reconfigurable subminiature spectrometer for hand-held measurement applications – *Measurement* **41** (2008) 44-54
7. Yeh, T.; Tseng, S.; A Low Cost LED Based Spectrometer – *Journal of the Chinese Chemical Society*, 2006, 53, 1067-1072
8. Fonseca, A.; Junior, I. M. R.; A multichannel photometer based on an array of light emitting diodes for use in multivariate calibration – *Analytica Chimica Acta* 522 (2004) 223-229
9. Hauser, P. C.; Rupasinghe, T. W. T.; Cates, N. E.; A multi-wavelength photometer based on light-emitting diodes – *Talanta*, Vol. 42, No. 4, pp. 605-612, 1995

Fracture Mechanics Analysis in Frost Breakage of Reservoir Revetment on cold regions

Liu Xiaozhou^{1,2*} Liu Peng¹

(¹Key Laboratory for Prediction & Control on Complicated Structure System of the Education Department of Liaoning Province, Dalian University, Dalian, Liaoning 116622, China ². State Key Laboratory of Frozen Soil Engineering Cold and Arid Regions Environmental & Engineering Research Institute, Chinese Academy of Sciences, Lanzhou, Gansu 730000, China)

Abstract: Reservoir revetment on cold regions are often frost damaged resulting from the joint action of low-temperature and cryogenic environment in winter, and then reservoir revetments are often broken to decline the usage function, even to lose the function completely. In this paper, practical problems in engineering were analyzed for the drainage pumping station of Tuanjie Reservoir. Based on traditional method in analysis and calculation, fracture mechanics was brought to make quantitative analysis and calculation on the problems of anti-freeze damage from the viewpoint of fracture mechanics. So as to put forward a new idea to resolve anti-freezing of reservoir slope protection on cold regions, doing meaningful exploration.

Key words: slope protection; fracture mechanics; low temperature; ice stress

1 Introduction

In seasonal frozen soil area, the slope protection of reservoir and embankment of dam revetment in winter often easily have freezing damage resulting from the joint action of low-temperature and low-temperature environment, in the form of ice thrust damage, frost heaving failure, thawing break, the waves destruction etc. However, at present in the freezing damage calculation method of reservoir slope protection, there is no way to reflect the nature of frost breakage. In terms of its design, it is still using traditional methods and standards to consider ^[1], which is often easily leading to that ability of anti-frost damage of engineering is not high, even causing a direct frost damage of slope protection. In this paper, regarding the problems of frost breakage of Tuanjie Reservoir slope protection in Liaozhong County, Shenyang, an effective form of slope protection was proposed, and on the base of anti-frost breakage analysis of hydraulic structures in the past^[2,3], the frozen soils fracture mechanics was entered into, from the viewpoint of fracture mechanics, a quantitative analysis and calculation on the damage resulted from ice and freezing was carried out. A new approach has been put forward to address the anti-frost breakage of reservoir slope protection in cold region in winter.

2 Reservoir Project Overview

2.1 Project Location and function

The Tuanjie Reservoir is located in the north of Liaozhong County, in the territory of Liuerbao and Lengzibao County, on the main channel of Pu River. It is a medium-sized plain reservoir which is used for flood protection mainly, it also took account of irrigation and aquaculture. The main building of reservoir is 58m long, length of dam is 1100m, the dike of both sides is 19.02km in total, 9 ancillary buildings, left dike is 12.29km long, with 6 Buildings, right dike is 6.73km long, with 3 buildings.

2.2 Geological, hydrological and meteorological data of sites

- (1) Geological data: The reservoir basin is belong to the middle of Liao River Basin, where is no exposed bedrock on surface, which are covered up by the fourth quarter loose stratum sand. Most of soil filling gate dam embankment is sub-clay, part of which are mixed up with light sbu-clay of different thickness. The soil layer under base is divided into five levels from the top down, respectively, for silt loam layer, sub-clay layer, light sub-clay layer, sand layer and medium-fine sand layer. Soil layer above: bearing strength of silt loam layer is $9t/m^2$, bearing strength of sub-clay layer and light sub-clay layer is $16t/m^2$, bearing strength of fine sand layer is $15t/m^2$, other physical and mechanical properties as shown in Table 1.

**Tab.1 The physical and mechanical properties indicators of soil and sand
(Statistic of average temperature)**

Project name	Soil name	The basic physical indicators in natural state				Soil mechanical indicators						
		Water content	Unit weight		Void ratio	Relative density	Hydraulic conductivity	Compressibility	Angle of repose		Adhesive force	Angle of internal friction
			Wet	Dry					Dry	Under water		
%	g/cm^3	g/cm^3			cm/s	cm^2/kg	o	o	kg/cm^2	o		
Barrage	Sub-clay	23.4	1.91	1.57	0.71	1.06×10^{-6}	0.015			0.1	30	
	Light sub-clay	20.5	1.96	1.63	0.65	3.00×10^{-7}	0.018			0.1	30	
Dam base	Muddy loam	40.2	1.7	1.21	1.17	9.35×10^{-6}	0.047			0.1	21	
	Sub-clay	27.9	1.93	1.41	0.91	1.25×10^{-7}	0.021			0.2	23	
	Light sub-clay	26.3	1.96	1.55	0.73	4.42×10^{-6}	0.025			0.1	29	
	Yellow medium sand	21.0	1.90	1.57	0.69	0.6			35	32		
	Gray-black medium-fine sand	31.6	1.81	1.42	0.86	0.63			35	31.5		

- (2) Hydrological and meteorological data: Pu River belong to embranchment of right bank of Hun River, where Tuanjie Reservoir is located downstream Pu River. Upper reaches of the river

before sluice is 142 km long in the north of Liaozhong, river basin area is 1820 km². According to the local weather station data, over the years the average temperature is 8.7°C, accumulated temperature that is not less than 10°C is 3477.9 °C, frost-free period is generally 165 days long. The average depth of frozen soil is 1.2m. There is ice up in mid-November each year, and thawing in mid-March the following year. The average ice thickness of reservoir is 0.7m ~ 0.8m. The average temperature statistics many years are shown in [Table 2](#):

Tab.2 Statistic of average temperature

Month	1	2	3	4	5	6	Average
Average temperature °C	-11.9	-7.3	1.2	10.7	16.6	21.2	
<i>Month</i>	7	8	9	10	11	12	8.7
Average temperature °C	26.3	25.8	18.1	12.6	-0.6	-8.7	

2.3 Frost breakage situation

The reservoir is located in the typical seasonal frozen soil area and frozen area in northern China, belonging to plains-reservoir-type, geographical location and cold environmental conditions is those basic conditions for the damage of reservoir slope protection.

- (1) Although the form of buried stone slope protection is adopt in this reservoir, after many years of freezing and thawing cycle, there is up to 800m long slope protection occurred collapse, accounted for 2/5 of cross section of upstream batter. Meanwhile, the causeway slope height collapsed, average swell height of upstream batter slope is 1.1m.



Fig.1 the picture for frost damage of dyke



Fig.2 the picture for frost damage of slope protection

- (2) Many supporting constructions such as through-dam culvert have varying levels of frost heave fracture and water leakage, which is hard to work normally.
- (3) Although after several rebuilt in recent years, the capacity of reservoir slope protection has been strengthened, but still not fundamentally resolves the problems of frost heave and ice-push.

3 Analysis of frost breakage

Making the slope as the object of study, from the view of mechanics and physics to study its damage causes, There are three most basic aspects to consider: (a) External causes: It is external load mainly, including the load caused by environmental conditions, the load or external force on slope protection directly, such as ice load, and water blowed by wind to form "wave wash". (b) Interior causes: Slope protection structure should include the surface layer, filtration layer and anti-freeze layer, its underpart is base soil layer, which freeze into frozen soils in winter. It is well known that soil mass is frozen to produce frost heave deformation, when this distortion to be bound arises frost heave force. The frost heave of base soil layer is bound by the slope protection, so the frost heave force is produced on slope protection. The frost heave of base soil layer has also produced frost-heave force on the following soil, but this is not the force what we are interested in. Base soil layer generates frost heave deformation during the winter, when the weather warming, the temperature rise, the soil began to melt, the thawy soil drop from the position of frost heave deformation, and this is the thawing effect, which makes slope protection braces fall through. It can produced thawing effect similarly by their own fravity. The frost heave and thawing caused by base soil frost heave in slope protection is an interior cause that slope protection failure occurs. (c) Structural causes: The strength and stiffness of slope protection structure itself not reach design requirements, such as the bad entirety, discontinuity surface, not smooth, etc.

Through the above analysis we can see that there are three main factors for the frost breakage of this reservoir slope protection: ice thrust, frost heave and wave wash. Among them, ice thrust and frost heave play control roles, the wave wash plays a supporting role.

3.1 Ice thrust breakage

After reservoir has been icebound, in the weather that temperature becomes suddenly warming (such as after cold wave), the ice temperature increase rapidly, its volumetric expansion, so a great static ice pressure is produced, ice stress for short. The ice stress is acting on the slope, which makes slope upward displacement, sliding, rolling, etc. It is commonly known as ice-push effect, ice-push for short ^[5]. There are three basic conditions for the generation of ice-push: (a) There is a larger ice stress occurs in ice sheet. (b) There is a greater adfreezing force between ice sheet and slope protection. (c) The resistance force of cushion or base layer below the slope protection is smaller. In addition, the ice-push generally occurs in the plain reservoir, with shallow and long dam, where are little change in the water level in winter.

Early winter, seasonal cold wave often come, the temperature fluctuate. In the weather of temperature rising sharply after cold wave, there is a greater ice stress produced, if the overall strength of the slope is smaller, while the adfreezing force is larger, then the surface of cushion or base soil layer below the slope will sliding upward, squeeze out or misplace, resulting in extensive damage of the slope.

Early winter the ice is thin (20 ~ 30 cm) so that strength is small, but have a larger adfreezing force with the slope, when the ice stress produced in the ice sheet is also less than the adfreezing force, so that it is not enough to create ice-push, but it is easily to fracture in the weak part of ice sheet.

At the same time, it swells up from the ice breakage, showing a human-shaped arching, with

a loud sound, from a distance it looks like a long ice aris of dragon spine, which is commonly known as "unicorn", as shown in [Figure 3](#).

When the ice sheet took place "unicorn" phenomenon, the energy of the ice sheet has been released, if "unicorn" occurred in the vicinity of the slope, it may cause damage to the slope, but if away from the slope, it has a little effect on the slope.

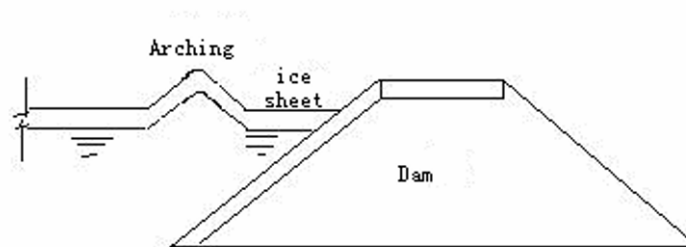


Fig.3 the picture for unicorn

Similarly, in the last winter with a sharp rising temperature, there is a greater ice stress occurs in ice sheet, with a total value of ice stress which is much greater than that in early winter. It is the risk period of damage on slope protection. Because the frequency of ice-push produced is higher in early winter, but the extent of damage is smaller, the damage degree is lower, while there are fewer ice-push in last winter, but the influence range is large, damage is heavy. Usually a whole line of many hundred meters even upto 1000 meters slope protection could collapse because of an ice push. Therefore, anti-ice-push damage control time should be the end of winter.

3.2 Frost heave and thawing

The slope protection frost heave issue refers to the destructive effect produced by frost heaving of base soil below slope protection, the base of the revetment structure of soil frost heaving damage arising from the role of plain earth dam slope below the base there are suitable conditions for frost heave. The base soil below plain reservoir slope exist conditions for frost heaving. First, it is soil quality, fine-grained soil is very sensitive to frost-heave; secondly, the moisture conditions are sufficient; again the slope have a light weight, so it is prone to frost heaving.

For the seasonal frozen soils, when the weather has turned warm after winter, ground temperature rising, frozen soils begin to melt, then the soils began to fall from the original position of frost heave, which produce thawing. Frost heave and thawing are interdependent. There is bound to frost heave with thawing, frost heave cause inevitably the local uplift, dislocation, tilt, crack, arching and other failure modes; when thawing can not reset, if there is wave wash effects exist, the melted soils under freezon soils layer has been undermined, there are large areas collapse while thawing. There are frost heave and thawing every year, the role accumulated year after year, then intensified.

Generally speaking, soil frost-heave must meet the following several conditions:

- (a) The soils is sensitive to frost heaving;
- (b) The initial moisture and external moisture (groundwater, atmospheric precipitation, water caused by human activities) supply;
- (c) Conditions and time are suitable for freezing.

These three conditions are indispensable, which are also anti-frost heaving and thawing conditions.

3.3 Wave wash

The revetment structure, thickness and filtration layer are all designed according to the requirements of anti-wave, which possess the capacity of anti-wave originally, it should not happen wave-wash damage. However, because of ice push and frost heave, the integrity and continuity of the slope protection surface are broken seriously, resulting in arching, dislocation, distortion, cracks and other damage forms. Cushion and base soil loose, causing filtration layer structure were damaged. The original design capacity of anti-wave are lost, causing severe damage of wave wash. Therefore, wave-wash roots from frost heave and thawing. The direct threat to the safety of reservoirs is serious wave wash on the base of ice-push and frost heave, therefore, anti-ice-push and anti-frost heave must in the first place.

4 Schematic design and calculation of frost breakage

4.1 Schematic design

According to analysis above, this slope project intends to use the form of reinforced concrete slab, as shown in Figure 4. Slope protection should be component of surface layer and cushion, thickness of surface layer is t_1 , thickness of cushion is t_2 , total thickness is

$t = t_1 + t_2$. The surface layer is reinforced concrete slab, of which thickness should be 10~25 cm, plane size should be $2\text{m} \times 2\text{m} \sim 4\text{m} \times 4\text{m}$, generally not too large, in order to prevent subsidence cracking. Cushions are laid with gravel, pebble and sand layers. The base soil layer is under cushion.

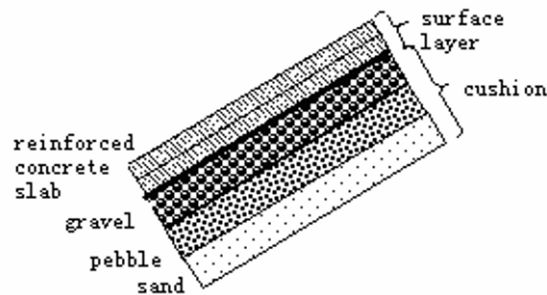


Fig.4 the slope protection structure of reinforced concrete flat slabs

In the design of slope protection it should be noted in the following: slope protection should be compositive of surface layer and cushion, surface layer thickness is t_1 , cushion thickness

is t_2 , total thickness is $t = t_1 + t_2$. Not only to make the thickness of the surface layer meet the requirements of anti-ice-push stability and strength, required to carry out checking computations of anti-waves, or the design of anti-waves, for anti-ice-push strength and rigidity checking, but also to make cushion thickness meet the requirements of anti-frost heaving, which is $t_2 = H_d - t_1$, frozen depth of project location is H_d .

4.2 Anti-ice-push Calculations

(1) Calculations of anti-ice-push stability of slope protection

The conditions of anti-ice-push stability of slope protection both are no-sliding in the whole, and local no-pull-off. From the views of fracture mechanics, push-slope force is P_H , resistance include: concrete slab and ice sheet self weight $W = G \sin \alpha$; frictional resistance $F = (P_V + G \cos \alpha)f + cL$, then safety factor of anti-ice-push stability K is as follows^[5,6]:

$$K = \frac{G \sin \alpha + (P_V + G \cos \alpha)f + cL}{P_H} \quad (1)$$

In which: G — the sum of weight of reinforced concrete slab and ice sheet above slab,

$$G = t_1 \sqrt{1 + m^2} [\gamma_k (H_1 + H_2)];$$

$$P_V \text{ — vertical force of ice thrust, } P_V = \frac{K' \tau \delta \sqrt{1 + m^2}}{m};$$

$$P_H \text{ — horizontal component of ice thrust, } P_H = K' \tau \delta \sqrt{1 + m^2};$$

$$L \text{ — the length of longitudinal slope above ice sheet, } L = H_1 \sqrt{1 + m^2};$$

In which: t_1 are reinforced concrete slab thickness (determined as $0.15m$ according to actual situation); γ_k are gravity density of reinforced concrete (determined as $25kN/m^3$); height of slope protection above and below ice are, respectively, $H_1 = 4m$, $H_2 = 1.57m$; slope ratio $m = 2.5$; The reduction factor of adfreezing force $K' = 0.55$; standard adfreezing force $\tau = 100kPa$; ice thickness $\delta = 1.0m$; slope angle $\alpha = 22^\circ$; friction factor $f = 0.25$; cohesion $c = 20kPa$.

Put each known condition into the formula, results are as follows:

$$\begin{aligned} G &= 0.15 \times \sqrt{1 + 2.5^2} [25 \times (4 + 1.57)] \\ &= 0.4 \times 139.25 = 55.7kN \\ K &= \frac{55.7 \times 0.37 + (59.24 + 55.7 \times 0.93) \times 0.25 + 20 \times 10.77}{148.09} \\ &= \frac{20.6 + 27.74 + 215.4}{148.09} = 1.78 \end{aligned}$$

Then get $K = 1.78 > 1$; which meet requirements of anti-ice-push stability.

(2) Structural strength calculation of slope protection

When calculating anti-ice-push strength, the slope can be simplified as a board on elastic foundation, to take $1m$ wide board for calculation. Base on the stress formula of plate on

elastic foundation, there are:

$$\sigma_r = 0.275(1 + \nu) \frac{P_V}{t^2} \lg \frac{Et^2}{kb^4} + P_H \quad (2)$$

Where:

P_V, P_H — Vertical, horizontal components of ice stress (kN);

E, ν — Elastic modulus and Poisson's ratio of the plate;

t — thickness of plating (m);

k — coefficient of soil reaction (kN/m^2);

b — Loaded area related parameters (m).

For reinforced concrete revetment plate, the corresponding parameters should be chosen as:

$$P_V = 59.24kN, P_H = 148.09kN, E = 2.6 \times 10^7 kPa, \nu = 0.18, t = 0.15m,$$

$$k = 10^5 kN/m^3, \text{ loaded area: } u \times u = 1m \times 1m, b = 0.57u = 0.57m.$$

The internal stress of reinforced concrete revetment plate is:

$$\begin{aligned} \sigma_r &= 0.275(1 + 0.18) \frac{59.24}{0.15^2} \lg \frac{2.6 \times 10^7 \times 0.15^3}{10^5 \times 0.57^4} + 148.09 \\ &= 854.37 \times 0.92 + 148.09 = 934.11kPa \end{aligned}$$

The total tension affecting the board of reinforced concrete revetment is:

$$F = \sigma_r \times 100 \times 0.15 = 934.11 \times 100 \times 0.15 = 140.11kN$$

If the reinforcement of reinforced concrete slope protection plane are adopt with 5 $\Phi 16$ rebar per meter, cross-sectional area of which are: $5 \times 2.0 = 10cm^2 = 10^{-3}m^2$, the tensile

strength of rebar $[R_p] = 240MPa = 240 \times 10^3 kPa$, assurance factor

$$K = \frac{240 \times 10^3 \times 10^{-3}}{140.11} = 1.71 > 1, \text{ so its anti-ice-push strength also meet the safety}$$

requirements.

4.3 Anti-frost-heaving calculation of reinforced concrete slope protection plate

Frost heaving damage of reinforced concrete slope protection is mainly produced from the cushion layer and the base soil layer, if the cushion layer is thick enough, then only the cushion layer frost, while the base soil layer becomes melted soil layer, which does not produce frost heave. In this case, only need to calculate the frost heave of cushion layer. The cushion layer is paved respectively with gravel, pebbles and sand, because frost heave produced by gravel and pebbles is extremely small, therefore, only need to calculate the frost

heave generated by sand of cushion layer. Otherwise, not only to calculate the frost heave generated by cushion layer, but also to calculate the frost heave produced by base soil layer. However, if the cushion material is not sensitive to frost heave, basically it doesn't produce frost heave, in this case, only the calculation of frost heave produced by the base soil layer is considered.

In addition, the anti-frost heaving designs are mainly for the slope above water surface, while the non-frozen zone below the water surface doesn't need to consider the issue of anti-frost heave.

According to the local measured data, frost depth is $H_d = 1.2m$, then the cushion thickness of structural slope protection of reinforced concrete slab should meet the following requirements: $t_2 = H_d - t_1 = 1.2 - 0.15 = 1.05m$, average depth of groundwater is calculated by $d = 0.95m$.

According to *Design specifications of hydraulic structures against ice and freezing action (DJ/T 5082—1998)*, the local sand surface frost-heaving capacity is $\Delta h = 35mm$, then the calculation formula for frost-heaving capacity of the sand layer under reinforced concrete slab is^[1]:

$$\Delta h' = \alpha_p \times \Delta h \times z_b / z_d \quad (3)$$

In which: α_p is load correction factor, which can be obtained by looking-up table:

$\alpha_p = e^{-0.034 \times 90} = 0.047$; design frost depth $z_d = 1.2m$; frost depth under base $z_b = z_f - d_s$, if it doesn't consider the ice layer, z_b can be calculated with $z_f = z_d + \varphi_a d_s - 1.67 \delta_i$, in which correction factor $\varphi_a = 0.35$, base thickness $d_s = 0.15m$, ice depth above base $\delta_i = 0$, then $z_f = 1.2 + 0.35 \times 0.15 - 1.67 \times 0 = 1.25m$, so $z_b = 1.25 - 0.15 = 1.1m$. To take the calculated parameters into the formula (3), frost-heaving capacity of sand layer under reinforced concrete slab can be obtained:

$$\Delta h' = 0.047 \times 0.35 \times 1.1 / 1.2 = 0.015m = 15mm$$

Then frost heave deformation of reinforced concrete slab slope protection can be calculated with formula (4) as following^[6, 7]:

$$W = 0.00406 \frac{qa^4}{D} \quad (4)$$

Where: according to *Design specifications of hydraulic structures against ice and freezing action (DJ/T 5082 — 1998)*^[1], normal frost heaving pressure $q = \sigma_n = 75kPa$, values for the remaining parameters are: slab length $a = 4m$;

E, ν are respectively taken as $E = 2.6 \times 10^7 \text{ kPa}$ and $\nu = 0.18$; $t_1 = 0.15 \text{ m}$; then the

known conditions are brought into formula to calculate for $D = \frac{Et_1^3}{12(1-\nu^2)}$. Finally when

calculated the thickness of sand is 0.9m, the frost heave deformation of reinforced concrete

slab is $W = 0.00406 \frac{75 \times 4^4}{7558} = 0.0103 \text{ m} \approx 10 \text{ mm}$.

Because the ability to resist deformation of reinforced concrete slab is strong, while the computed frost heave deformation of reinforced concrete slab is only 10mm, if it also considers the impact of gravel and pebble layer, then frost heave resulting from reinforced concrete slab will be even smaller, thus much less harm on the structure of slope protection.

5. Conclusion

(1) Through the analysis of frost breakage of Tuanjie Reservoir, it can be seen that there are three main factors leading to the frost breakage of reservoir slope protection: ice thrust, frost heave and wave wash. The role of the three is not single, but mutual influence and mutual coupling, thus increasing the destructive actions on structures of slope protection. Among the three ice thrust and frost heave control purposes, they are primary, while the wave wash stem from the ice thrust and frost heave, so to prevent wave wash must prevent ice thrust and frost heave firstly.

(2) The basic requirements for anti-ice thrust of slope protection structure are: (a) Integrity of slope protection is fine, stiffness and strength meet design requirements; (b) Slope protection surface is smooth, and the freezing power between ice sheet and slope is less than the intensity of ice; (c) Friction of cushion layer and base soil layer under slope protection is stronger than ice thrust, these three are indispensable. At the same time, the basic conditions caused frost heave are: (a) Cushion layer and base soil layer are sensitive to frost heave; (b) It is provided with initial moisture and the outside water supply; (c) Low-temperature environment and conditions, these three are also indispensable.

(3) In this paper, for the frost breakage of actual water conservancy project, based on the traditional analysis method the fracture mechanics approach was introduced, in the view of the stability and strength of fracture mechanics theory, taking into account the structures' own flaws and other factors, it comes in line with the actual ice breakage of hydraulic structure. Through the anti-freeze damage calculation of reinforced concrete slab slope, the results meet the requirements for anti-ice thrust and anti-frost heave. Meanwhile, the research methods also provide a new idea for the analysis to solve the problems of frost breakage of plain reservoir revetment.

Reference

- [1]. Electric Power Enterprise Standard of People's Republic of China. Design specifications of hydraulic structures against ice and freezing action (DJ/T 5082—1998) [S].Beijing:1998.
- [2].Li Hongsheng, Liu Xiaozhou, Shi Jun. eal. Analysis of Ice and Freezing failure and Design Schemes of Against Ice and Freezing action for Drainage Pumping Station[J].Journal of Glaciology and

Geocryology,2006,28(1):136-140.

[3].Liu Xiaozhou, Li Hongsheng, Shi Jun. eal. Fracture Mechanics Analysis in Frost Breakage of Hydraulic Structures[J],the 11th experimental mechanics science conference of china ,2005.

[5].Yang Guojin. Several Problems in Anti-Ice Structure Design of Bohai Ses[J].China Offshore oil & Gasengineering(Bimonthly).1994,6:5-16.

[6].Gu Pu,Zheng Fanghuai,Xie Zhiling. Mechanics of Materials[M].Beijing: Higher Education Press,1985.

[7].S.Timoshenko, S.Woinowsky. Theory of plates and Shells[M].Beijing:Science Press,1977.

Combined Experimental/Numerical Assessment of Compression After Impact of Sandwich Composite Structures

Michael W. Czabaj, Alan T. Zehnder,
Mechanical and Aerospace Engineering
Cornell University, Ithaca, NY 14853
atz2@cornell.edu

Barry D. Davidson, Abhendra K. Singh, and David P. Eisenberg
Mechanical and Aerospace Engineering
Syracuse University, Syracuse, NY 13244

ABSTRACT

An integrated experimental and computational study of residual compressive strength of composite laminate sandwich structures after low velocity impact (CAI strength) is performed using samples consisting of 8 ply graphite/epoxy face sheets bonded to aluminum honeycomb core. The study encompasses characterizing the indentation damage (dent depth and laminate fractures), measuring the CAI strength for a range of layups and core densities and computational modelling of indentation and CAI strength.

INTRODUCTION

Composite laminate sandwich panels are well known for their high specific strength and stiffness. A concern in the design of composite sandwich structures is low energy impacts that may cause damage that remains undetectable or "barely detectable" by visual inspection. The damage typically consists of matrix cracks, interlaminar delaminations and core crushing. Together these damage modes may significantly reduce the structure's residual compressive strength^{1,2}.

Damage tolerance for honeycomb sandwich composites is typically determined based on test data. However, to develop a deeper understanding of the mechanics of failure, to provide tools for performing trade studies of different material systems and for assessing critical regions of a structure for which more extensive testing should be undertaken, a synthesis of experimental and computational research is required.

In light of the above, the aim of this integrated experimental and numerical study is provide design guidelines and experimentally validated predictive models for assessing the damage resistance and tolerance of sandwich structures. Moreover, the goal of the experimental efforts is, through examination of parameters such as face sheet layup, core thickness and density, indenter geometry and state of indentation damage, to reveal the underlying mechanisms and competition between failure modes that drive failure.

MATERIALS AND SAMPLE PREPARATION

In this study all sandwich panel specimens were fabricated by co-curing eight-ply, HexPly® IM7/8552 unidirectional prepreg face sheets to HexWeb® CR-III, 3.2 mm cell size, 5052-H39 aluminum honeycomb core using an epoxy based 3M™ AF-555 film adhesive. Prior to cure the honeycomb core was primed using a 3M™ EW-5000 adhesive primer. The cure was performed in an autoclave based on the recommended cycle of the prepreg material. A total of thirteen,

38.1×38.1 cm panels were fabricated employing a combination of four distinct quasi-isotropic face sheet layups labeled Q1-Q4 and three honeycomb core types, labeled C1-C3. The face sheet and core types are defined in [Table 1](#).

Face sheet layups:	Core thickness and density:
Q1 - [45/0/-45/90] _s	C1 - 25.4 mm, 49.7 kg/m ³
Q2 - [45/-45/0/90] _s	C2 - 16.5 mm, 49.7 kg/m ³
Q3 - [-45/45/90/0] _s	C3 - 25.4 mm, 72.1 kg/m ³
Q4 - [45/90/-45/0] _s	

Table 1, Layups and core definitions.

Each panel was trimmed using a water cooled diamond wheel at 750 RPM with a feed rate of 5 cm/min into one of the following: 17.8×15.2 cm CAI (compression after impact) specimens, 17.8×5.1 cm EC (edgewise compression) specimens, 2.5×12.7 cm face sheet flexure specimens (debonded from the core), or a series of small square specimens for QSI evaluation tests. To facilitate a uniform load distribution during compression testing, the loading edges of all CAI and EC were potted using 3M™ EC-3524 B/A sealing compound and ground flat with a water cooled, 8000 RPM surface grinder.

Barely visible impact damage (BVID) was introduced into the CAI specimens using quasi-static indentation (QSI) of two steel spheres with diameters of 25.4 and 76.2 mm. For the 25.4 mm diameter indenter, the BVID load threshold was chosen to be 1300 N, which corresponded to a maximum permanent dent depth of 0.5 mm. For the 76.2 mm diameter indenter, the BVID load threshold was chosen to be 2800 N, corresponding to maximum permanent dent depth of approximately 1.0 mm. Full details of the indentation damage study are given in Singh et al.³

COMPRESSION AFTER IMPACT EXPERIMENTS

Test Setup and Procedures

The compression test setup, shown in [Figure 1](#) consists of an Instron 8502 load frame with a 250kN load cell, two compression platens, a spherical seat used for alignment, shadow Moiré, and the data acquisition equipment. The top platen, seen in [Figure 1](#), was bolted directly to the load cell. The lower platen was attached to a spherical seat, which was in turn bolted to 2.54 cm thick, steel load frame base adapter. The spherical seat allowed for precise tilting of the lower platen about the two axes perpendicular to the loading direction. The platen tilting was achieved by tightening or loosening the 4 adjustment bolts mounted in the front and back of the spherical seat and the two sides of the bottom compression platen. Based on a simple strength of materials approximation it was determined that global buckling of all panels considered should occur at approximately twice the compressive failure loads, thus it was deemed unnecessary to constrain the free edges of the specimen during testing.

To visualize the evolution of indentation damage during compression after impact, shadow Moiré was employed to map out-of-plane deformation⁴. The shadow Moiré setup consists of a linear reference grating, light source and a high definition video camera. Three distinct reference gratings were used in this study, all fabricated by Applied Image Inc. and printed on a 0.018 mm clear Mylar film. Responses of specimens indented with 25.4 mm diameter indenter were visualized using 4.7 lines per mm (lpmm) grating, and 2.4 and 3.5 lpmm grating for those indented using the 76.2 mm diameter indenter.

Each specimen was instrumented with four 3.2 mm gauge length strain gauges. Two strain gauges were mounted on each face sheet, midway between the loading sides, at a distance of 6.4 mm away from the free edge, and aligned with the loading direction. The data acquisition was

performed by collecting signals from six channels (4 strain gauges, cross-head position from LVDT, and load cell) at a rate of two data sets per second.

At the beginning of each test, the specimen was lightly loaded and the spherical seat adjusted with alignment bolts until the strains recorded on each of the 4 gauges were equal. This process was repeated several times at increasing loads up to about 25% of the failure load. Once aligned, the sample was unloaded and then the compression test initiated at a rate of 0.005 mm/sec. Once the compression load reached approximately 75 percent of the expected critical load, the load rate was reduced by a factor of four to 0.00125 mm/sec.

To provide a baseline, the undamaged compressive strength of each layup/core combination was obtained by testing 17.8 cm × 5.1 cm edgewise compression samples⁵.

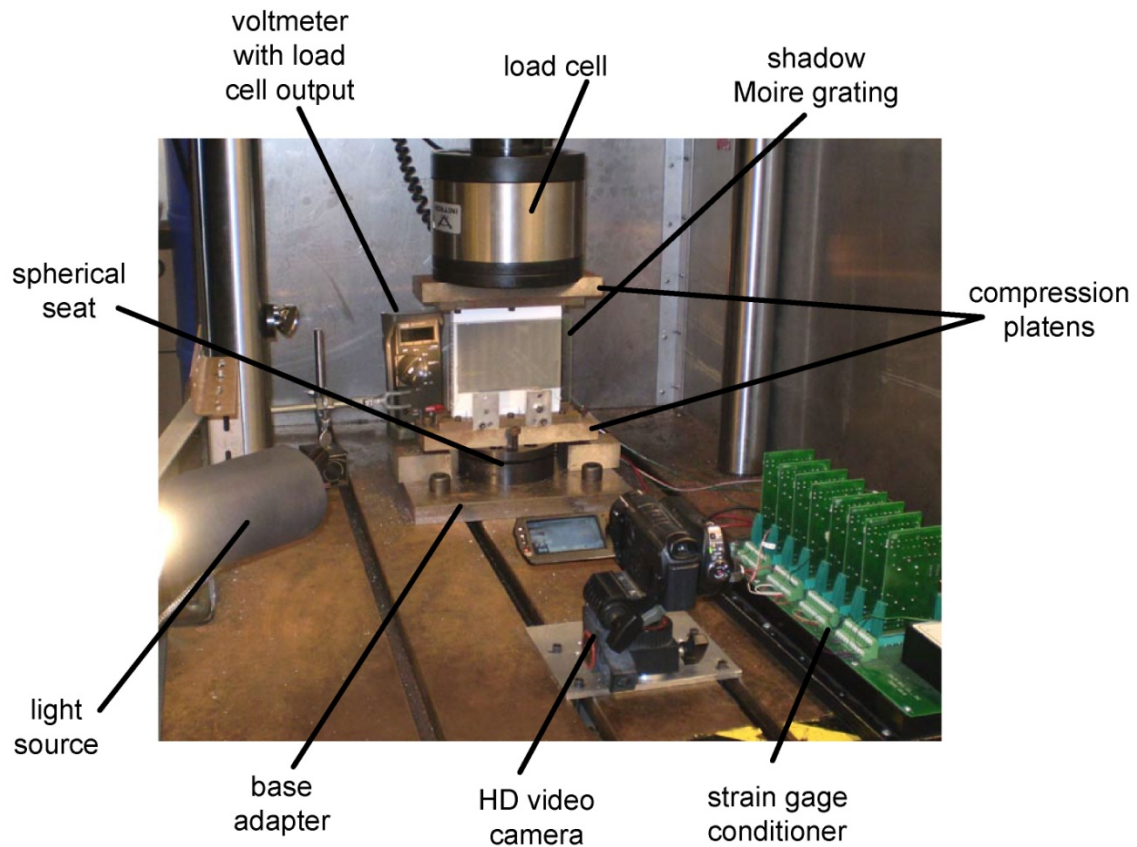


Figure 1, Compression after impact test setup.

Results

During the compression after impact testing of specimens indented with 25.4 and 76.2 mm diameter indentors, three distinct failure modes were observed, as seen in [Figure 2](#). In all tests, initiation of each mode of failure was always preceded by progressive increase of dent depth as evident by an increase in the shadow Moiré fringe count. This process is referred to as indentation growth (IG). In some specimens, this process continued until fiber failure (FF) initiated on both sides of the impact damage, causing rapid and catastrophic failure of the specimen ([Fig. 2a](#)). In number of specimens, during IG, a progressive out-of-plane buckling of interlaminar delaminations was observed ([Fig. 2b](#)). In all such cases the buckled regions originated above or below the indentation, becoming visible at reasonably high percentage of the failure stress. The catastrophic failure of specimens exhibiting delamination buckling (DB) generally occurred due to

the combined effects of IG, sudden increase in deflection of the delamination, unstable delamination growth as evident by audible noise, and fiber failure. Finally, in specimens with deep dents from the 76.2 mm diameter indenter, the steady IG become unstable causing rapid expansion of the indentation towards the free edges of the specimen, perpendicular to the load direction, resulting in global instability (GI) failure of the specimen (Fig. 2c).

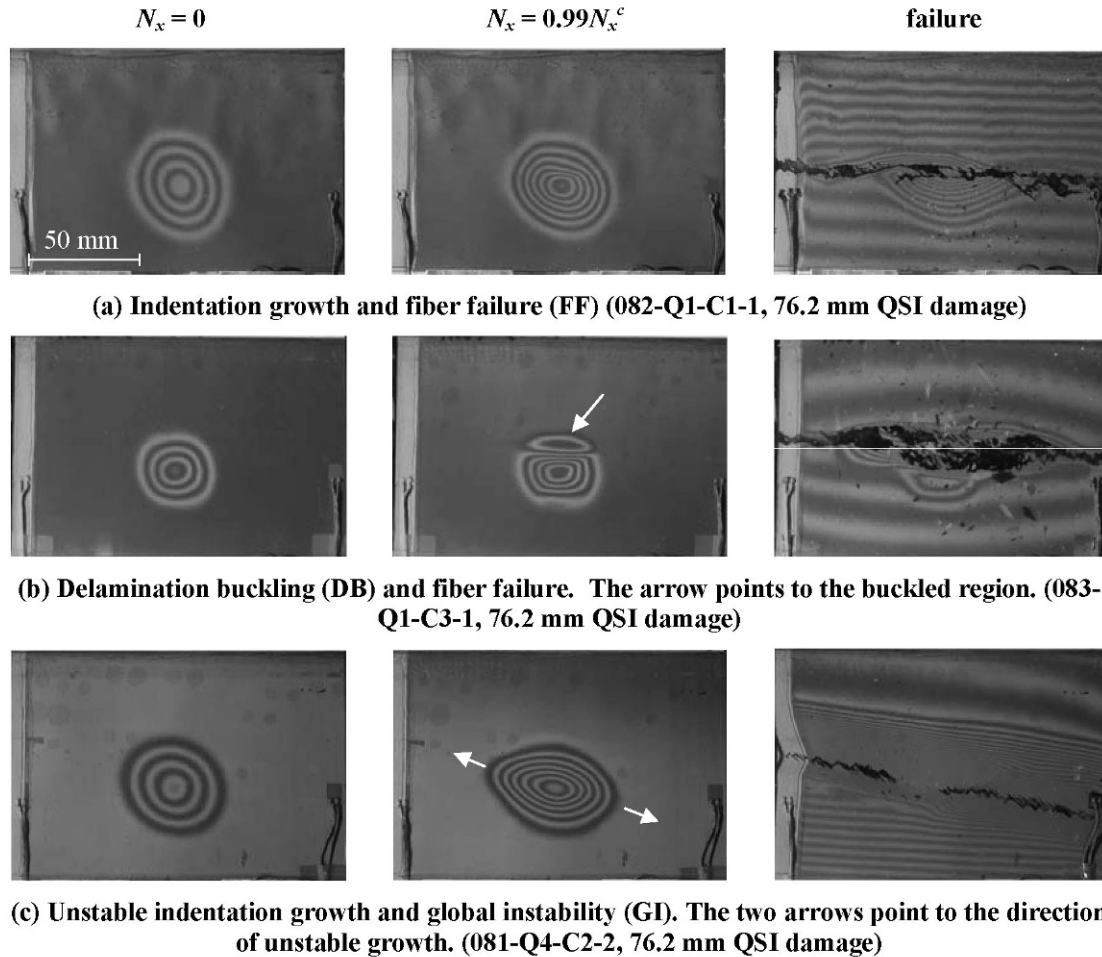


Figure 2. The three failure modes observed during compression after impact as captured by a 3.5 lpmm shadow Moiré. In all images, a single black or white fringe represents an out-of-plane displacement of approximately 0.14 mm. In the above, N_x is defined as the applied edge load, and N_x^c represents the critical edge load.

With these failure modes in mind, the CAI strengths and residual strengths (CAI strength normalized by undamaged strength.) data for all eight-ply specimens tested are presented in Figure 3 as a function of dent depth. In both figures the distinct symbol shapes represent each of the four face sheet layups; while the color scheme represents the three core types. Moreover, the solid symbols represent those specimens that failed by IG followed by FF, whereas the open symbols represent those that failed by combination IG, DB and FF. The 76.2 mm “high QSI load” specimens which failed due to unstable indentation growth and GI are marked individually using arrows.

Figure 3 shows that for a given specimen type and QSI indenter diameter, the CAI strength generally remains essentially constant (Q1-C1 and Q2-C1) or decreases with increasing dent depth. Accounting for data scatter, the primary exception to this trend appear to be the Q1-C2 samples which is likely due to different modes of failure observed for that configuration. The mode that controls final failure will be dictated by the damage (dent and delamination), the layout of the face sheets, and the type of core.

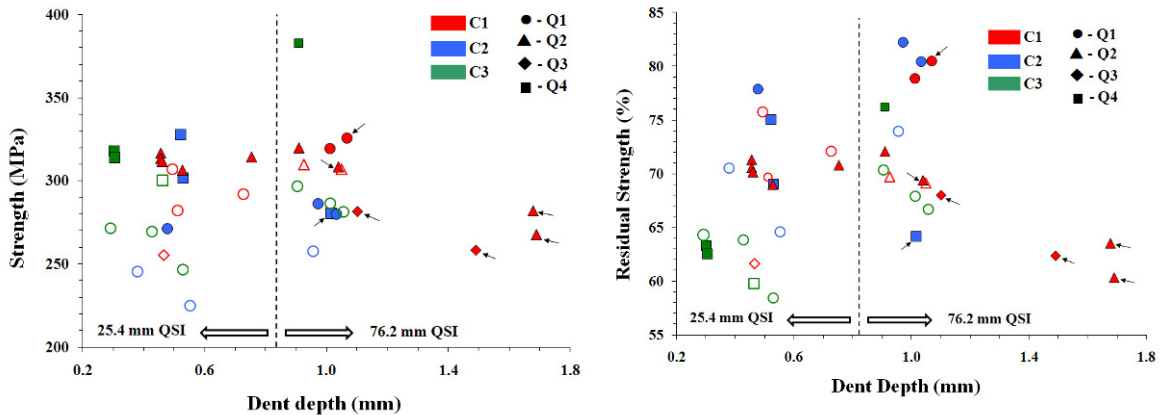


Figure 3, CAI test results for all eight-ply specimens tested. Solid symbols represent failure by IG & FF; open symbols represent failure by IG, DB & FF; specimens which failed by IG & GI are marked with arrows. The vertical dashed line divides the small and large diameter damage.

SIMULATION OF DAMAGE AND COMPRESSION AFTER IMPACT

FEM Model

An important aspect of this work is the development of experimentally validated, numerical model for the prediction of the initiation and state of indentation damage in honeycomb stiffened sandwich panels and for predicting damage evolution and resulting residual strength during compression after impact. In order to promote its applicability, the model is developed in a framework of finite element (FE) analysis using the commercially available ABAQUS®/Explicit 6.8 software. Given a wide range of failure mechanisms that need to be included, the model is extendable to allow their later incorporation. In the present work, the analysis focuses primarily on development of an appropriate honeycomb core model, the process of indentation, and compression after impact. The evolution of damage is restricted to the honeycomb; however, efforts are under way to include appropriate face sheet failure models.

The model uses continuum shell elements with orthotropic elastic properties to represent the face sheet. In regions where the core will be crushed, the core is explicitly represented using shell elements and an elastic-plastic material model with $E=70$ GPa, yield stress of 220 MPa, stress of 282 MPa at 1 percent, and constant flow stress thereafter. Regions of the core away from the indentation point are modeled with continuum elements with orthotropic elastic properties. To improve the performance of the explicit core model imperfections were introduced to the mesh geometry using random perturbation of the in-plane nodal coordinates of all elements by a magnitude ranging between ± 0.018 mm. The spherical indenter was approximated as a rigid, hemi-spherical shell. The material properties used for the models are summarized in Table 2.

The finite element model and the two steps of the simulation are shown in Figure 4. In the first step indentation is simulated by indenting the sample up to a fixed load which is then released. In the second step a compressive load is applied as shown in Figure 4b.

Property	E_1 (GPa)	E_2 (GPa)	E_3 (GPa)	G_{12} (GPa)	G_{13} (GPa)	G_{23} (GPa)	ν_{12}	ν_{13}	ν_{23}	Density (kg/m ³)	Thickness (mm)
Homogenized honeycomb	148E-6	147E-6	0.91 [*]	89E-6 ^{**}	0.170	0.127	1.0 ^{**}	1E-5 ^{**}	1E-5 ^{**}	49.7	-
IM7/8552 lamina	137.84 [*]	11.39 [*]	11.39 [*]	5.43 [*]	5.43 [*]	3.98	0.31 [*]	0.31 [*]	0.46	1770	0.127

^{*}Measured experimentally, ^{**}Estimated

Table 2, Material properties used for FE simulation.

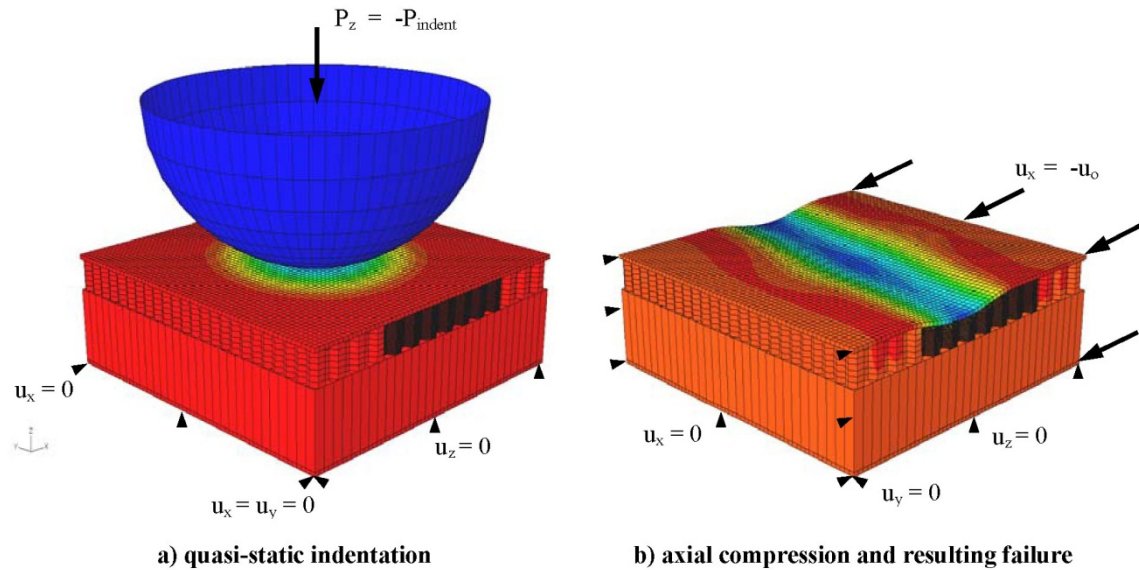


Figure 4, The finite element model of Q1-C1 panel indented with 76.2 mm dia. indenter.

Results

A small selection of the simulation results are given in [Figures 5 and 6](#). [Figure 5](#) shows the indentation profile obtained for the 25.4 and 76.2 mm diameter indentors in the first step of the simulation. The results show that the model captures the overall indentation depth well, but that the shape of the indentation differs somewhat from the experimental results. This is likely due to neglecting delaminations of the face sheets that occur during the indentation process. These delaminations will locally reduce the face sheet stiffness and cause a sharper indentation profile.

A sample numerical result from simulation of compression after impact a Q1-C1 panel with 76.2 mm QSI damage is presented in [Figure 6](#). The selection of this particular configuration was based on the experimentally determined failure mode of indentation growth followed by global instability, a process controlled largely by the core crushing response.

Comparing the slopes of both stress-strain curves in [Figure 6](#), there is a roughly 7% difference in axial stiffness, which is associated with a 6% difference between the theoretical and measured values of the laminate stiffness. The ultimate failure in the numerical model occurs at roughly 20 percent of the measured value. One explanation for this for this seemingly large discrepancy is the initially low dent depth. A slight increase in the indentation during simulation may translate into an increased core crushing around the perimeter of the indentation, making it susceptible to

unstable indentation growth at lower loads. A second possible explanation lies in the fact that the numerical model does not at present model initiation or evolution of face sheet damage which our preliminary analyses show to have a significant effect on ultimate failure. Presence of delaminations may not directly affect the axial stiffness of the panel; however, it may reduce the bending stiffness of the face sheet near the indentation effectively reducing its buckling resistance, lowering the onset of unstable indentation growth.

Complete results of the experiments and further details of the finite element simulation are given in Czabaj et al.⁶

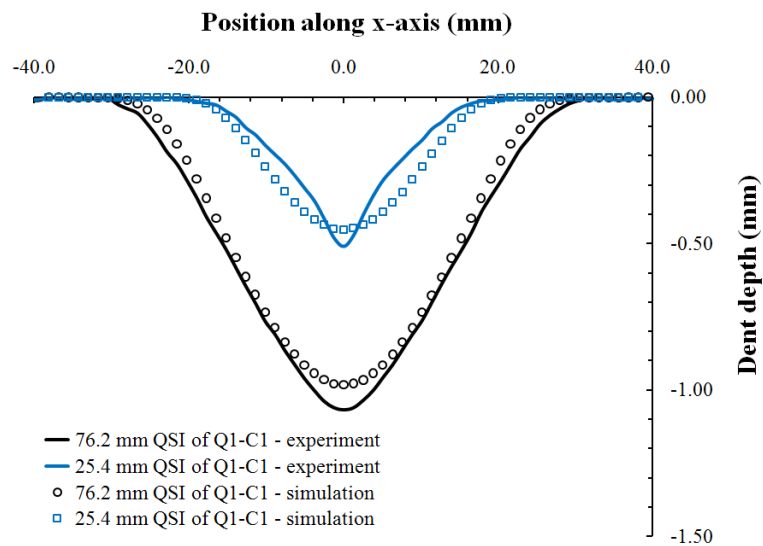


Figure 5, Indentation profiles resulting from quasi-static indentation – experiment versus simulation.

SUMMARY AND CONCLUSIONS

Damage, simulating low velocity impact at the barely visible threshold, was introduced into thin-skinned composite sandwich structures using quasi static indentation. The indentation damage, consisting of localized core crushing, face sheet delaminations and fiber fractures can significantly reduce the residual compressive strength of the structure. Experiments over a range of indenter diameters, face sheet layups and core densities and thicknesses show that the failure mode and failure stress are dependent on all of the above parameters. Samples indented with a blunt, 76.2 mm indenter generally failed by growth of the indentation followed by face sheet failure or by instability of the indentation as it crushes the core below it. Samples indented with the sharper, 25.4 mm diameter indenter failed by local buckling of delaminations in the face sheet or by failure of the face sheet in the damaged region. A finite element simulation of indentation damage followed by compressive loading is developed with the goal of providing a practical tool for the prediction of impact damage and residual strength. The model uses an explicit representation of the core in critical areas and a continuum model elsewhere. Results obtained to date are promising. The indentation is predicted well, the mode of failure for blunt indentors is predicted but the model over predicts the residual compressive strength.

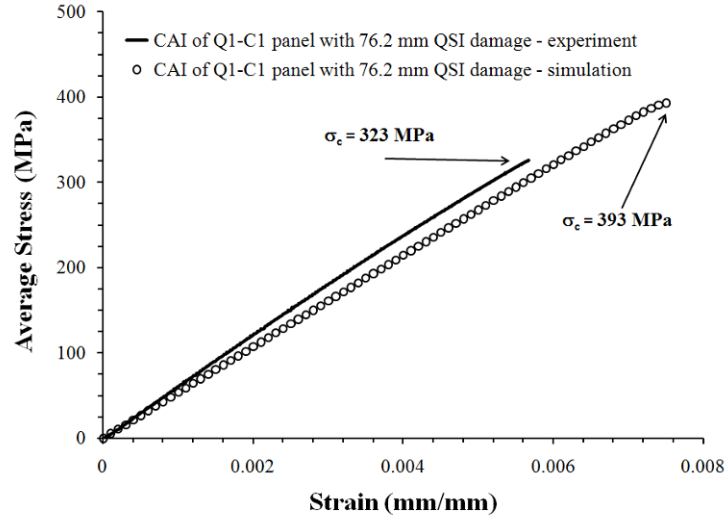


Figure 6, Simulation of the compression after impact test of a Q1-C1 specimen containing 76.2 mm diameter QSI damage.

ACKNOWLEDGEMENTS

This study was funded through the NASA Constellation University Institutes Project, under grant NCC3-989 with Claudia Meyer, project manager and by the NASA Exploration Technology Development Program / Advanced Composite Technologies Project, Mark Stuart, Project Manager. Experiments made use of the Shared Experimental Facilities of the Cornell Center for Materials Research, an NSF MRSEC (DMR-0520404).

REFERENCES

- ¹ Moody, C., Vizzini, A.J., "Damage Tolerance of Composite Sandwich Structures." *Final Report, Federal Aviation Administration Report*, DOT/FAA/AR-99/91, 2000.
- ² Nettles, A., Jackson, J., "Compression After Impact Testing of Sandwich Composites for Usage on Expandable Launch Vehicles." *Journal of Composite Materials*, Vol. 44(6), 2010, pp. 707-738.
- ³ Singh, A.K., Davidson, B.D., Eisenberg, D.P., Czabaj, M.W., Zehnder, A.T., "Barely Visible Impact Damage Evaluation of Sandwich Composite Structures." *51st AIAA/ASME/ASCE/AHS/ASC Structures, Structural Dynamics, and Materials Conference*, Orlando, FL, 2010.
- ⁴ Post, D., Han, B., Ifju, P., "Moiré Methods for Engineering and Science – Moiré Interferometry and Shadow Moiré." *Photomechanics, Topics in Applied Physics*, Vol. 77, 2000, pp. 151-196
- ⁵ ASTM C364, "Standard Test Method for Edgewise Compressive Strength of Sandwich Constructions." *Annual Book of ASTM Standards*, American Society for Testing and Materials, Vol. 15.03, 1996.
- ⁶ Czabaj, M.W., Zehnder, A.T., Davidson, B.D., Singh, A.K., and Eisenberg, D.P., "Compression After Impact of Sandwich Composite Structures: Experiments and Modeling." *51st AIAA/ASME/ASCE/AHS/ASC Structures, Structural Dynamics, and Materials Conference*, Orlando, FL, 2010.

Mechanical Behavior of Co-Continuous Polymer Composites

Dr. Lifeng Wang, Jacky Lau, Nicholas V Soane, Matthew J. Rosario, and Prof. Mary C. Boyce

*Department of Mechanical Engineering, Massachusetts Institute of Technology,
Cambridge, MA 02139*

ABSTRACT

Natural and synthetic composite materials consisting of two or more different materials are a major avenue for achieving materials with enhanced properties and combination of properties. The combination of hard and soft materials enables outstanding combination of mechanical performance properties including stiffness, strength, impact resistance, toughness, and energy dissipation. In this work, we demonstrate the potential to achieve materials with enhancements in stiffness, strength and energy dissipation. We consider co-continuous structures with simple cubic (SC), body-centered-cubic (BCC), and face-centered cubic (FCC) lattices, which are generated by 3D printing technology. The linear and nonlinear mechanical behavior of these composites including their elastic stiffness, yield, post-yield, and dissipative behaviors are investigated by compression tests. The experimental results are compared with finite element based micromechanical modeling of large elastic-viscoplastic deformation. We show that these 3D periodic cocontinuous composites can provide enhanced improvement in combinations of mechanical performance achieving a unique combination of stiffness, strength and energy absorption. These results provide guidelines for engineering and tailoring the nonlinear mechanical behavior and energy absorption of the composites for a wide range of applications.

Triply periodic minimal surfaces have been of great interest to physical scientists, material scientists and biologists; these co-continuous structures have been observed in block copolymers, micellar materials, nanocomposites, cell membranes, and biological exoskeletons. The co-continuous topological feature offers a desire avenue to provide multifunctional performance that segregated structures meet. Therefore, the relationship between macroscopic mechanical response and constituent material properties and the relative geometric arrangement holds great promise in the multifunctionality design of engineering structures and materials. Here we consider co-continuous structures with simple cubic (SC), body-centered-cubic (BCC), and face-centered cubic (FCC) Bravais lattices, which correspond to the triply periodic minimal surfaces known as the tubular P, I-WP, and F-RD respectively (see [Figure 1](#)). Prior works have found: 1) these level set structures to exhibit better elastic properties than their rod-connected model counterparts [1]; 2) these structures to provide multifunctional optimization, such as simultaneous optimization of transport of heat and electricity [2]; (3) these structures can be scaled down and fabricated at submicron length scales that enables the coupling of mechanical deformation with photonic or phononic properties [3,4]. Herein, we explore the linear and nonlinear mechanical behavior of these structures including their elastic stiffness, yield, post-yield, and dissipative behaviors.

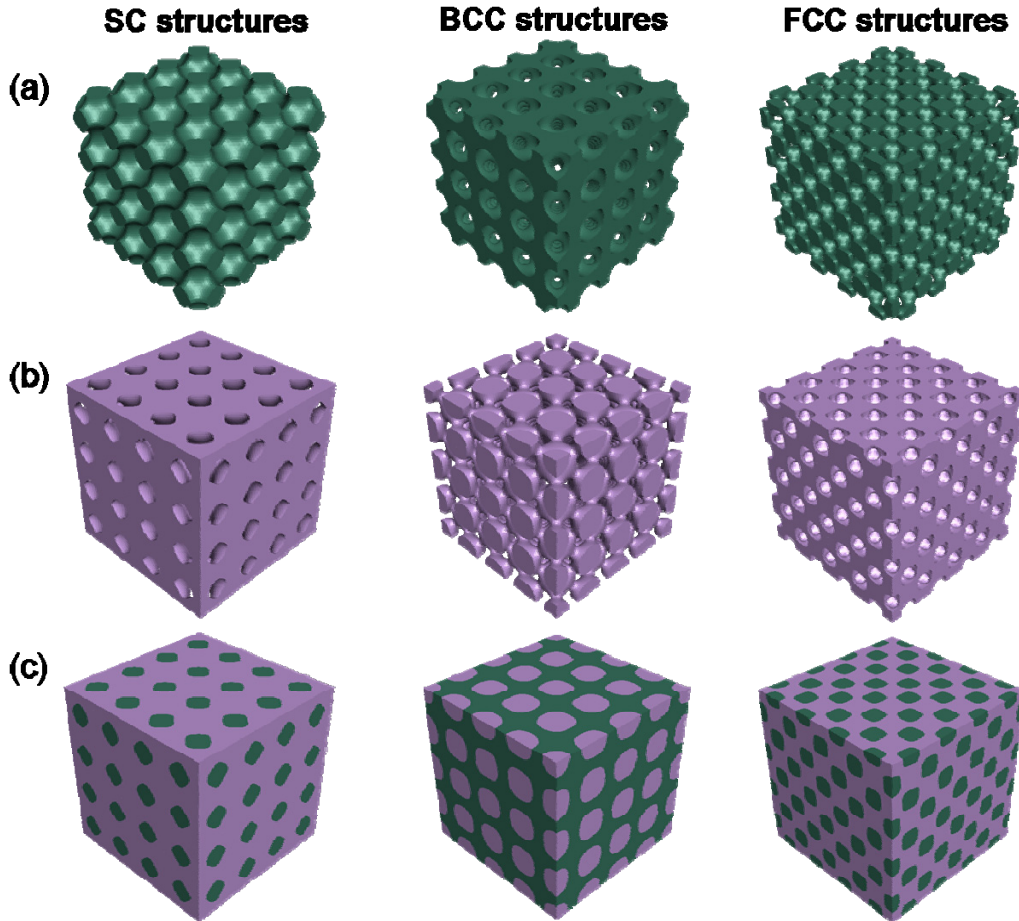


Figure 1. 3D periodic structures and cocontinuous composites consisting of $4 \times 4 \times 4$ unit cells. Left: simple cubic lattice; Center: body-centered-cubic lattice; Right: face-centered-cubic lattice. The volume fractions are fixed to 50%. (a) level set structures (Structure I); (b) the corresponding inverse structures (Structure II) to Structure I; (c) the corresponding cocontinuous composites consisting of two phases that have the same geometries with Structures I and II.

In order to establish the linear and nonlinear mechanical behaviors of these structures and cocontinuous composites, we consider constituent material properties of a glassy polymer and an elastomer. Finite element based micromechanical modeling of the co-continuous composites are constructed. The large deformation mechanical responses of these 3D periodic cocontinuous composites are investigated using a periodic representative volume element (RVE) of the microstructure together with the nonlinear constituent material stress-strain behaviors where the combinations of polymer/elastomer, and polymer/polymer are considered for these two-phase composites. [Figure 2](#) shows the mechanical responses of the polymer /polymer composites and the corresponding constituent porous structures separately under uniaxial compression. The mechanical interaction between two phases enhances the load transfer through the whole composites, which can be demonstrated in the simulated contours of stress and strain of the BCC co-continuous composites and the corresponding porous structures as shown in [Figure 2b](#) and [2c](#) respectively. The stress and strain are observed to concentrate locally to transfer load and deformation in the porous structures. But for the composites, the force is distributed more uniformly over the composite structure during compression due to mutual constraints of the two phase each other, rather than is focused at weak points in the structures. This is the reason that these co-continuous composites can exhibit optimal stress distribution and strain reduction.

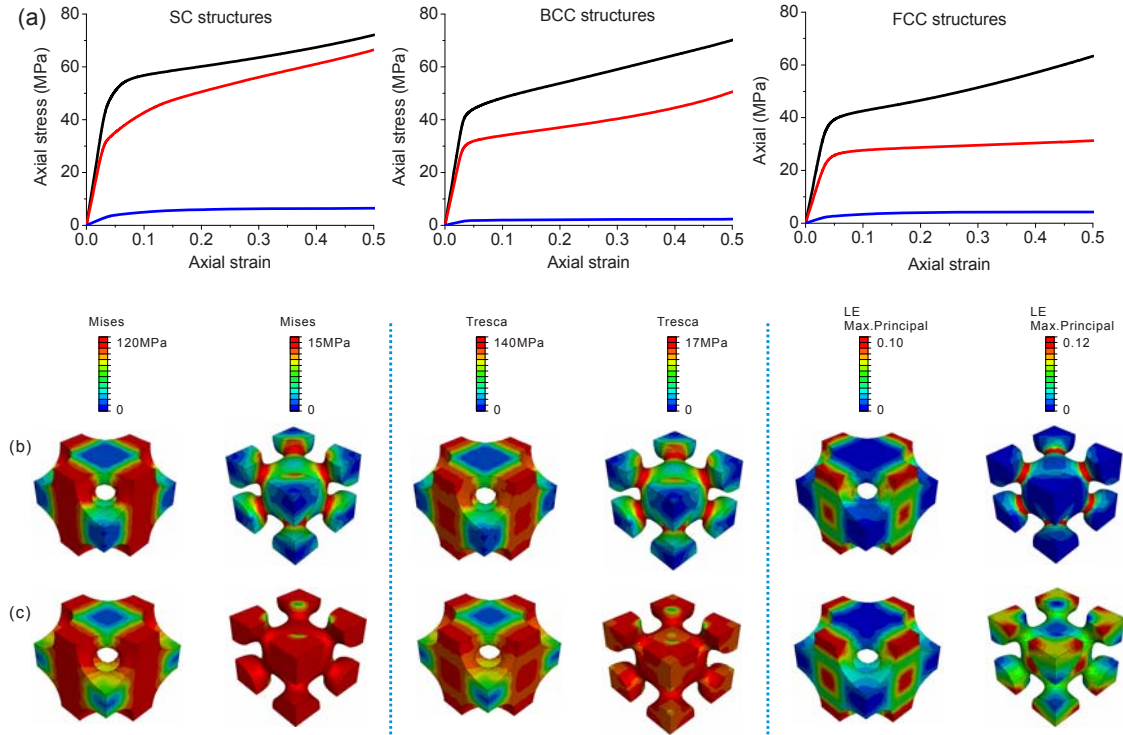


Figure 2. (a) Stress-strain behavior of the co-continuous polymer/polymer composites (black) and the constituent porous structures (red for structure I and blue for Structure II). (b) Simulated stress and strain contours of the porous structures. (c) the corresponding phases in composites.

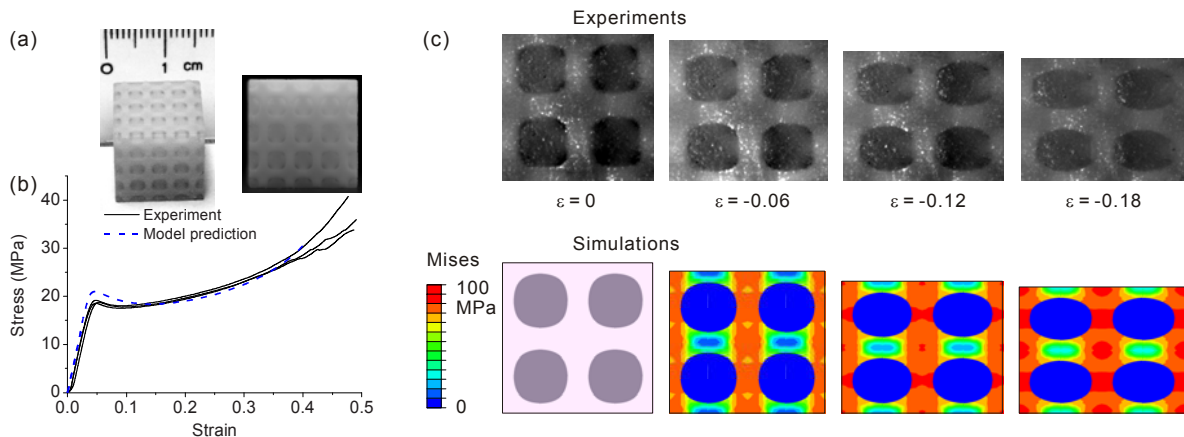


Figure 3. Comparison between experiments and simulations of BCC co-continuous composites. (a) BCC co-continuous composites fabricated through 3D printing. (b) true stress - strain curves showing simulation curve and 3 experimental curves. (c) experimental and numerical images of BCC composites at different levels of macroscopic strain: 0, -0.06, -0.12, and -0.18.

In order to realize our ideas in the experiments, we explore the mechanical behavior of these composites at sub-millimeter scale. The polymer/elastomer co-continuous composites were fabricated by a 3D printer which allows the simultaneous printing of two different materials. Uniaxial compression tests were conducted and the comparison is made between experimental results and FEA simulations (see Figure 3). There is an excellent agreement between the model predictions and

the experimental results. Simulation captures local deformation evolutions at different level of compression strain.

In summary, we have investigated the macroscopic mechanical responses of 3D periodic polymer/elastomer and polymer/polymer co-continuous composites with different geometric arrangements of the constituents numerically and experimentally. We have shown that 3D periodic co-continuous composites with interfaces that are the minimal surfaces can have greater mechanical performance achieving a unique combination of stiffness, strength and energy absorption. This design concept can be extended to other material combinations such as polymer/ceramic and polymer/metal in co-continuous composites, which potentially provides a much higher stiffness and strength. These results provide guidelines for engineering and tailoring the nonlinear mechanical behavior and energy absorption of the composites for a wide range of applications.

ACKNOWLEDGMENTS

This research was supported by the U.S. Army through the Institute for Soldier Nanotechnologies (ISN), under contract DAAD-19-02-D-0002.

REFERENCES

- [1] M. Maldovan, C. K. Ullal, J.-H. Jang, E. L. Thomas, Sub-Micrometer Scale Periodic Porous Cellular Structures: Microframes Prepared by Holographic Interference Lithography. *Adv. Mater.* 2007, 19, 3809.
- [2] S. Torquato, S. Hyun, and A. Donev, Multifunctional Composites: Optimizing Microstructures for Simultaneous Transport of Heat and Electricity. *Phys. Rev. Lett.* 2002, 89, 266601
- [3] Y.-H. Ha, R. A. Vaia, W. F. Lynn, J. P. Costantino, J. Shin, A. B. Smith, P. T. Matsudaira, E. L. Thomas, Three-Dimensional Network Photonic Crystals via Cyclic Size Reduction/Infiltration of Sea Urchin Exoskeleton. *Adv. Mater.* 2004, 16, 1091.
- [4] J.-H. Jang, C. K. Ullal, T. Gorishnyy, V. V. Tsukruk, E. L. Thomas, Mechanically Tunable Three-Dimensional Elastomeric Network/Air Structures via Interference Lithography. *Nano Lett.* 2006, 6, 740.

LABORATORY EVALUATION OF A SILICONE FOAM SEALANT FOR FIELD APPLICATION ON BRIDGE EXPANSION JOINTS

Ramesh B. Malla¹, Associate Professor, and Brian J. Swanson, Graduate Research Assistant
Department of Civil and Environmental Engineering, Unit - 2037

Montgomery T. Shaw, Research Professor,
Institute of Materials Science, Unit -3136

University of Connecticut, Storrs, CT 06269, U.S.A
(¹Corresponding author: MallaR@engr.uconn.edu)

ABSTRACT

A silicone foam sealant was developed to provide an alternative small-bridge joint sealant that was effective, easy-to-use, and economical. In the previous study various laboratory tests including tension, bonding, compression, shear, stress relaxation, and other were conducted to determine the engineering characteristics of the sealant. All these tests were limited to the concrete as the substrate to which the sealant was bonded to. In the present study, laboratory tests on the sealant were conducted using other substrates found in practice, including steel, asphalt and polymeric concrete. Some of the tests conducted included tension (pull to failure) test, oven-aged bonding test, salt water immersion test, and a performance-during-curing test that evaluated the strength and strain of the sealant.. Through the laboratory tests, it has been observed that the silicone foam can exhibits good bonding to various substrate materials and can easily accommodate small movement bridge expansion joints. In addition to these tests in small specimen, a procedure to produce larger quantity of sealant and apply it to an actual bridge expansion joint was developed using a simulated joint built in the laboratory. Through the development of this procedure and the eventual application of the sealant into various bridge expansion joints, it can be determined that the silicone foam presents an alternative sealant that is east-to-use and allows for quick installation.

INTRODUCTION

Expansion joints are a vital component to the design of a bridge. These joints accommodate movement of the road deck caused by temperature changes, seismic loading, and other factors. The bridge deck can be affected by many factors including temperature, humidity, shrinkage, and creep. It is these factors that keep bridge components in a constant state of expansion and contraction. Bridge expansion joints are designed to allow the bridge to continue this constant movement while maintaining its structural integrity [1]. If not sealed properly, however, the expansion joints permit leakage of water and deicing corrosive materials that can damage the components beneath the road deck, reducing the life of the bridge. In a worst case scenario this deterioration of the bridge deck and internal elements could result in structural failure of the bridge. Sealants for bridge expansion joints, thus, become a necessary element in the construction of new bridges and the maintaining of existing bridges.

A few commercial joint sealants specialized for bridges are available in market including Dow Corning 902 joint sealant [2] and the WABO two part silicone sealant distributed by the Watson Bowman Acme Corporation [3]. Joint sealants are, however, not impervious to damage or failure. There are many factors that can cause a joint seal to tear or pull off of a joint header. Accumulation of debris, damaged joint headers, water leakage, and an inability to move or expand with a joint are just a couple scenarios where a joint sealant could fail [4].

Previously, a study was conducted on the development of a silicone foam sealant with the ability to expand in volume as it cures [5]. The expansion of the foam means that only certain, carefully calculated, amounts of sealant need to be poured into the expansion joint. As the sealant expands it gradually fills the joint volume. In this previous investigation the sealant was subjected to various laboratory tests that evaluated its tensile strength, compressive strength, temperature effect, stress and creep behaviors, and bonding capabilities to concrete substrates.

Concrete is a common bridge joint header material; however other materials such as steel and polymeric concrete have been used as joint headers and also asphalt material can be present in or around the bridge expansion joint. While the previous studies [5] [6] [7] evaluated the silicone foam sealant's performance on concrete substrates, they did not investigate the performance of the sealant to bond with other substrates. This paper presents results from various laboratory tests on the silicone foam sealant with asphalt, steel, and polymeric concrete as substrates. The tests chosen were tension, oven-aged bonding, salt water immersion, and a performance-during-curing test.

In the present study a procedure to apply the silicone foam to an actual bridge expansion joint was developed using a simulated bridge joint setup. Various applicator tools and procedures were used until a quick and efficient option was developed.

SILICONE FOAM DEVELOPMENT

The silicone foam sealant prepared and studied here in is comprised of 5 parts: WABO two part silicone sealant, water, crosslinker, and platinum catalyst. When the two parts of the WABO sealant, one white and one gray, are mixed in equal volume this will create a rubber, solid sealant. The addition of water (1.53% of total sealant mass), hydrosilane crosslinker (2.3% of total sealant mass) [8] [9], and a platinum catalyst (0.38% of total sealant mass) [10] to the two part sealant creates the silicone foam. The tension, oven-aged bond and salt water immersion tests used the hydrosilane called Baysilone U 430 Crosslinker, which is produced by GE Bayer [8]. The strength vs. cure time test and the development of an application procedure used the hydrosilane from Momentive Performance Materials [9] called Silopren U Crosslinker 430. These tests are described below. The foaming of the sealant is the result of the reaction of water with hydrosilane. The reaction between these two materials produces silanol and hydrogen gas. Silanol helps with the polymerization while the hydrogen gas creates bubbles within the sealant, resulting in a foam material. In this experience the volume increase due to the foaming ranges between 50 and 70%.

LABORATORY METHODOLOGY

To evaluate the performance of the silicone foam sealant several laboratory tests were conducted, including tension, oven-aged bonding, salt water immersion, and another test that evaluates the sealant's strength as it cures. These tests were performed using difference bonding substrates including asphalt, steel, and polymeric concrete. The laboratory tests performed used test specimens of different materials. Each test specimen (see Figure 1) consisted of two blocks of the substrate material (that are separated by a 0.5-in. gap to be sealed). Each block has a length of 3-in., width of 2-in., and a depth of 0.5-in. For each test performed samples were made using asphalt and steel substrates. For comparison purposes the tests were also conducted using the WABO two part silicone sealant, which will now be called the solid sealant.

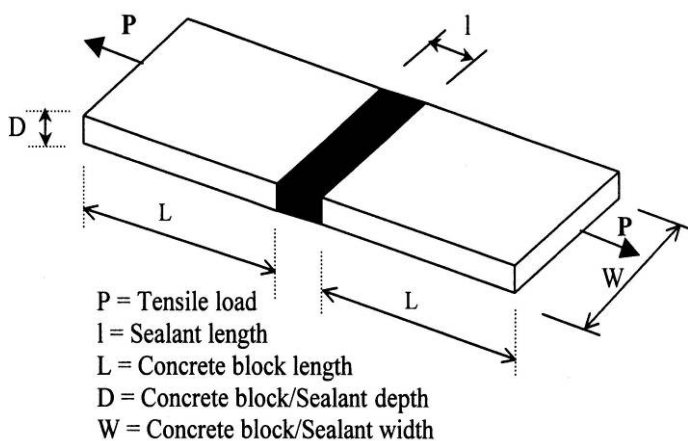


Figure 1. Schematic of Laboratory Test Samples



Figure 2. Laboratory Test Samples

Prior to pouring of the sealant to make the samples the substrates were cleaned with a lint free cloth and setup ensuring a 0.5-in. gap between the pieces. The sealants were hand mixed and immediately poured into the gap between the specimens. For the foam sealant enough was poured into the gap keeping in mind the sealant will

expand as it cures. For the solid sealant the entire 0.5-in. depth of the gap was sealed as the material does not expand.

The specimens, depending on which test was performed, were pulled at a specific crosshead velocity to a certain strain percentage or until the sealant failed. Failure means either a complete tearing within the sealant, a separation from the bonding substrate, or a mixture of both. Figure 3 shows a testing specimen using asphalt as a substrate being pulled until the sealant fails. Results from all tests are recorded in an attached computer in volts. Through calibration of the machine the voltage can be converted into Newtons (N), and subsequently converted into stress knowing the cross sectional bonding area between the sealant and substrate.

Various laboratory tests conducted are described below briefly:

Tension Test

Two types of tension tests were performed: pull to fail and load/unload. For each bonding substrate used (asphalt, steel, and polymeric concrete) eight samples, four for the foam sealant and four for the solid sealant, were made. All samples were cured for 21 days at room temperature (23°C). For the pull-to-fail tension tests specimens were placed in the Instron Tensile Tester and pulled apart at a crosshead velocity of 10 mm/min until failure. The load/unload testing was done by pulling the samples at a crosshead velocity of 10 mm/min up to 300% strain and unloading it until they reached zero strain. This loading/unloading process was repeated for another 4 cycles.



Figure 3. Testing Specimen Under Tensile Testing

Oven-Aged Bond Test

An oven-aged bond test was performed on the sealants to evaluate the effects of extreme changes in temperature on the bonding capabilities of the sealant as it cures. For each bonding substrate used (asphalt and steel) eight test specimens, four for the foam sealant and four for the solid sealant, were made. These samples were cured for 7 days at room temperature (23°C), and then they were placed in an oven for 7 days at 70 °C. After the oven aging the samples were placed in a box and held at -29 °C for 4 h using dry ice. After this cooling period the samples were tested by loading them at a crosshead velocity of 6 mm/min until they reached 100% strain. The samples were removed from the machine, left out on a table for 4 h and allowed to regain their original length. Once the samples self-recompressed to zero strain, they were once again placed back in the box, kept at -29 °C, then tested in the same fashion as before 4 more times. Thus, each sample was tested for 5 cycles of loading and self-recompression.

Salt Water Immersion Test

A salt water immersion test was performed on samples to evaluate the effects of prolonged exposure to salt on the bonding of the foam and solid sealants to different substrates. For each bonding substrate used (asphalt and steel) eight test specimens, four for the foam sealant and four for the solid sealant, were made. The samples were allowed to cure for 7 days at room temperature (23°C), and they were then placed in a bucket of saturated salt water for 2 weeks. During this time period the salt water was kept at a temperature of 45°C. After the 2 weeks of submersion the samples were removed from the water, allowed to dry for 4 h, and were tested in the Instron machine. A pull to fail tension test, as described above, was performed on the samples using a crosshead velocity of 10 mm/min.

Strength vs. Cure Time Test

The amount of time that the sealant has cured may have an effect on the strength of the sealant. To test this effect test specimens were made using the foam and solid sealant. In the previous study concrete this test was conducted using concrete as a substrate [5]. In the present study the test was conducted using asphalt and steel as the bonding substrates. For each bonding substrate used 4 test specimens were made with the foam, and

then 4 more were made with the solid sealant. All the samples were extended to 100% strain at 10 mm/min and unloaded first after curing 3 h. Subsequently, the loading/unloading test was repeated on the same samples at several other time intervals, including 6 hours, 18 hours, 24 hours, and then once everyday for the next 42 days [5].

RESULTS AND DISCUSSION

Results obtained from the laboratory tests and brief discussions on them are presented below.

Tension Test, Pull-to-Fail Results

The results from the tensile pull-to-fail test are shown in Figures 4(a-d). The ultimate stresses and strains for each test sample used are shown in Table 1. The average ultimate stresses of the foam sealant using steel, asphalt, and polymeric concrete as substrates are approximately 105.0 ± 15 , 83.2 ± 22 , and 69.6 ± 40 kPa, respectively. For the solid sealant the average ultimate stresses when bonded to steel, asphalt, and polymeric concrete are approximately 163.5 ± 223 , 94.6 ± 62 , and 148.7 ± 35 kPa, respectively. The data shows that the sold sealant exhibits a stronger ultimate stress than the foam sealant. The average ultimate strains using the

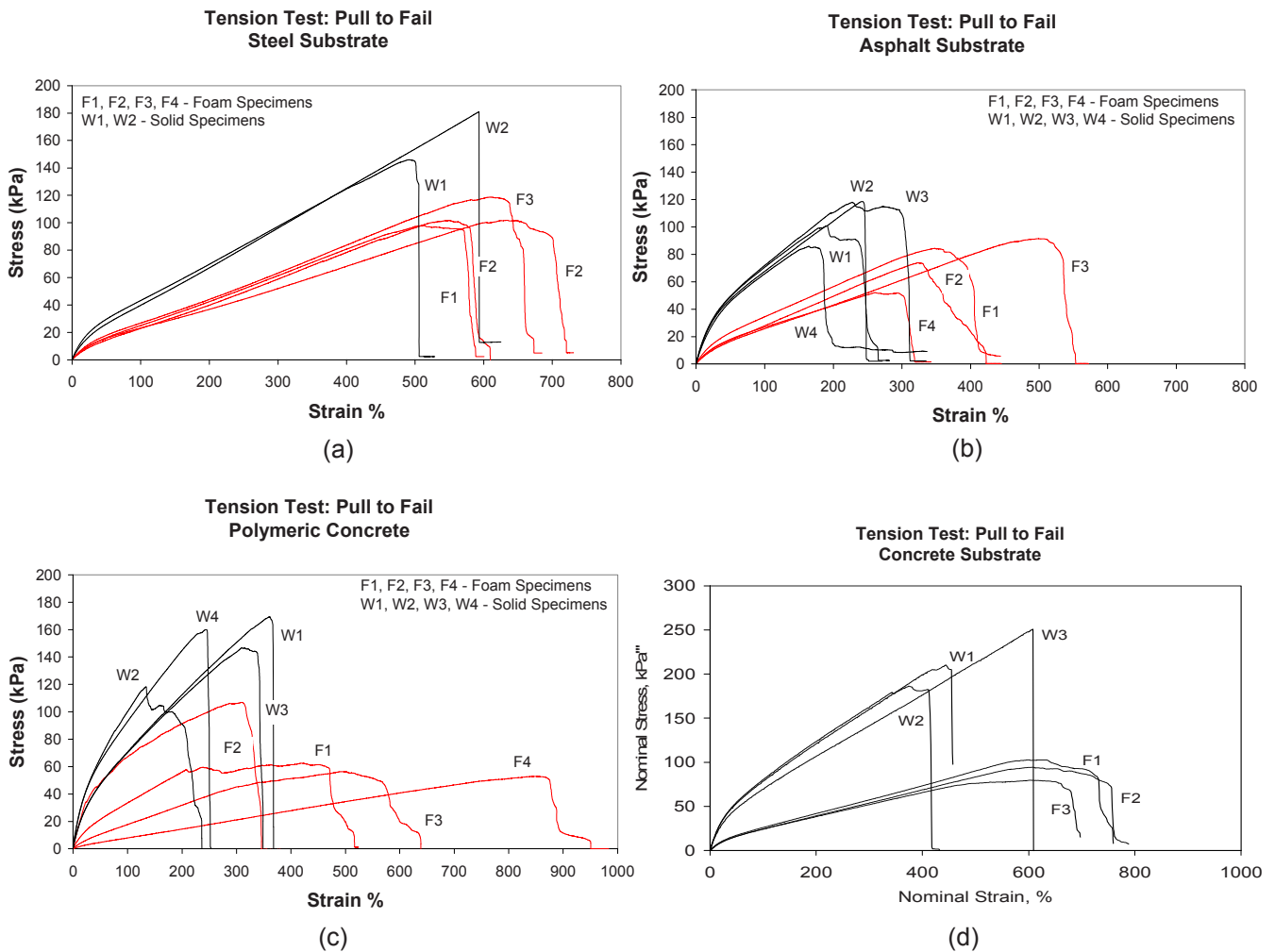


Figure 4. Tension Test, Pull to Failure using (a) Steel, (b) Asphalt, (c) Polymeric Concrete, and (d) Concrete Substrates

foam sealant on steel, asphalt, and polymeric concrete substrates are 577, 358, and 519% respectively. On the other hand the ultimate strains using the solid sealant when bonded to steel, asphalt, and polymeric concrete are 543, 206, and 262%, respectively. In the previous study the ultimate strain for the foam when bonded to concrete was 603% and for the solid when bonded to concrete was 475% [5]. The data shows that the solid sealant

exhibits larger ultimate stress at failure, compared to the foam sealant. However, the average ultimate strain of the foam, regardless of the type of substrate used, is higher than that of the solid. That means the foam elongated more than the solid before it fails.

The foam and solid sealants differ in average ultimate strength and strain, even when they are bonded to the same type of substrate material. Switching from the solid to foam sealant, the average ultimate strength decreases by 35.9% when the steel substrate is used. When the asphalt substrate is used the average ultimate strength decreases by 12.1%. When the polymeric concrete is used the average ultimate strength decreases by 53.2%. On the other hand, switching from the solid to foam sealant, the average ultimate strain increases by 6.2% when the steel substrate is used. When the asphalt substrate is used the average ultimate strain increases by 76.7%. When the polymeric concrete is used the average ultimate strength increases by 98.0%. While the solid sealant exhibits a higher ultimate strength, the foam sealant, on average, elongates farther than the solid before the sealant fails.

Table 1. Ultimate Stresses (kPa) and Strains (%), Tension Test, Pull to Failure

Sealant Type	Sample Number	Steel Specimen		Asphalt Specimen		Polymeric Concrete Specimen		Concrete ^c Specimen	
		Ultimate Stress (kPa)	Ultimate Strain (%)	Ultimate Stress (kPa)	Ultimate Strain (%)	Ultimate Stress (kPa)	Ultimate Strain (%)	Ultimate Stress (kPa)	Ultimate Strain (%)
Foam Sealant	F1	97.8	512.6	84.3	347.8	62.4	420.1	103	597
	F2	101.8	633.1	73.9	323.8	106.8	310.5	94	608
	F3	118.7	609.8	91.5	499.4	56.3	493.9	80	604
	F4	101.7	550.3	52.2	261.3	52.9	851.0		
	Average ^b	105.0 ± 15 ^a	576.5 ± 88	83.2 ± 22	358.0 ± 161	69.6 ± 40	518.9 ± 372	92 ± 30	603 ± 13
Solid Sealant	W1	145.9	491.0	100.7	190.4	169.4	360.2	210	444
	W2	181.0	593.3	118.5	242.3	118.4	133.9	186	374
	W3	-	-	118.1	227.6	146.8	309.8	251	607
	W4	-	-	85.9	164.2	160.2	244.5		
	Average	163.5 ± 223	542.6 ± 650	94.6 ± 62	206.1 ± 56	148.7 ± 35	262.1 ± 155	216 ± 81	475 ± 296

^a 95% Confidence Interval for the Averages

^b Average of the Samples

^c Results using the concrete specimens are from Malla et al., (2007)

Tension Test, Load and Unload Test Results

The loading/unloading tension tests further show the differing performances between the solid and foam sealants. Table 2 shows the stresses for the loading/unloading test using steel as a substrate. For the foam sealant the average loss in stress from the first to the fifth extension was approximately 14%. Of the total percent loss in stress, 6% occurred within the first and second cycle of loading and unloading. The solid sealant displayed an average loss in stress from the first to the fifth extension of 17%. The Tensile pull-to-failure tests have shown that the solid can have a high ultimate strain when bonded to steel. However any imperfection in the substrate surface or the material itself (i.e. a tear in the sealant) will result in a quick failure of the solid material. Imperfections in the sealant can be detrimental under cyclical loading, as shown in specimen W3 in Table 1. After the third extension the sealant failed and the test could no be completed with that specimen. After each cycle of loading and unloading the tears in the sealant get bigger, and eventually cause the sealant to fail.

Table 3 shows the stresses obtained for the asphalt substrate samples after each extension to 300% strain. On average, the sealant loses 37% of its stress from the first time it is extended to 300% strain the fifth time. This stress softening is a result of the Mullin's Effect where the stress continuously decreases after each cycle of loading and unloading when the maximum strain for each cycle is fixed [10]. When observing the effects of stress softening due to cyclical loading and unloading the changes in maximum stress between the first cycle and the second cycle are the most critical [11]. While the foam loses 37% of its maximum stress between the first and fifth cycle, the majority of the average loss falls between the first and second cycle (loss of approximately 20%). The Mullins Effect could not be observed on the solid sealant bonded to asphalt. As the pull to fail tension tests indicate the solid sealant fails before reaching 300% stain during the first cycle of loading. In this loading/

unloading tension test the solid sealants failed at 161, 127, 101, and 103% strain. Figure 5 is a representative graph showing the hysteresis of the foam and solid sealant. This figure displays the results using steel as a substrate due to failure of the solid sealant when bonded to the asphalt.

Table 2. Load/Unload Tension Test – Stress at 300% Strain – Steel Substrate

Sealant Type	Steel Specimen	1 st Extension Stress (kPa)	2 nd Extension Stress (kPa)	3 rd Extension Stress (kPa)	4 th Extension Stress (kPa)	5 th Extension Stress (kPa)
Foam Sealant	F1	53	50	48	44	43
	F2	41	39	38	37	36
	F3	64	61	59	58	57
	F4	56	52	50	48	47
	Average^a	53.5 ± 15^b	50.5 ± 14	48.8 ± 14	46.8 ± 14	45.8 ± 14
Solid Sealant	W1	69	67	66	65	64
	W2	118	112	110	107	106
	W3	120	113	108	-	-
	Average	102.3 ± 72	97.3 ± 65	94.6 ± 62	86.0 ± 267	85.0 ± 267

^a Average of the Samples
^b 95% Confidence Interval for the Averages

Table 3. Load/Unload Tension Test – Stress at 300% Strain – Asphalt Substrate

Sealant Type	Steel Specimen	1 st Extension Stress (kPa)	2 nd Extension Stress (kPa)	3 rd Extension Stress (kPa)	4 th Extension Stress (kPa)	5 th Extension Stress (kPa)
Foam Sealant	F1	56	54	52	50	48
	F2	49	40	37	33	26
	F3	39	19	12	10	6
	F4	57	53	51	48	47
	Average^a	50.3 ± 13^b	41.5 ± 26	38.0 ± 30	35.3 ± 29	31.8 ± 32
Solid Sealant	W1	94 (Failed at 161% Strain)	-	-	-	-
	W2	88 (Failed at 128% Strain)	-	-	-	-
	W3	71 (Failed at 101% Strain)	-	-	-	-
	W4	73 (Failed at 103% Strain)	-	-	-	-
Average	81.5 ± 18	- - -	-	-	-	

^a Average of the Samples
^b 95% Confidence Interval for the Averages

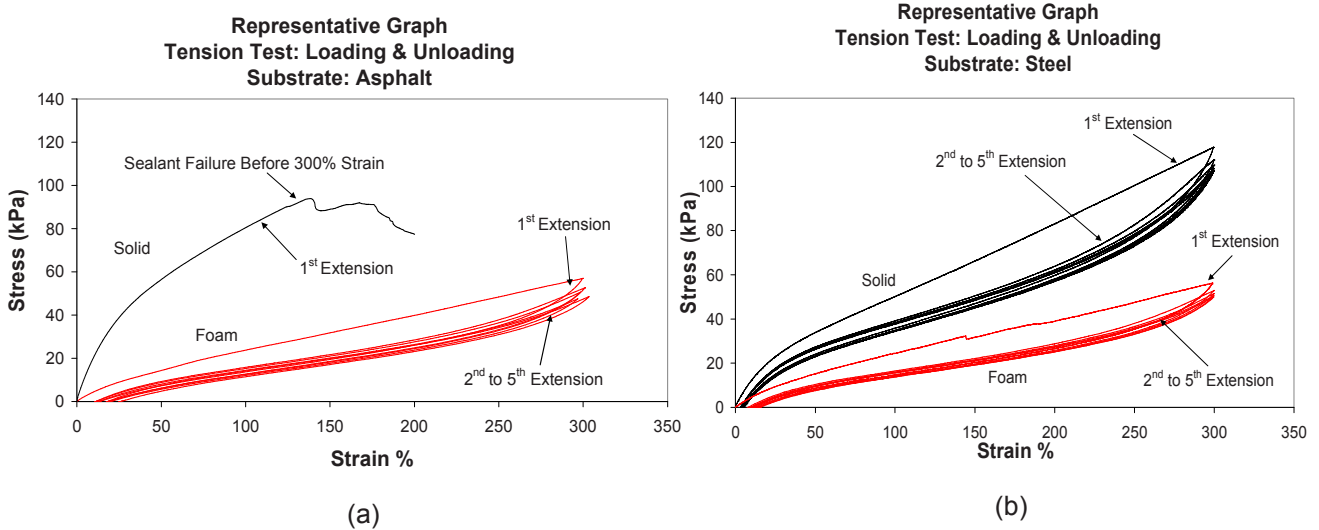


Figure 5. Representative Graph, Tension Test: Loading and Unloading using (a) Asphalt and (b) Steel Substrates .

Oven-Aged Bond Test Results

Figures 6(a) and 6(b) display the stress values for each specimen after the 5th extension to 100% strain for the oven-aged bond test. For the foam sealant the average 5th extension stress at 100% strain using the asphalt as a substrate is 26.7 ± 10 kPa, 54% lower than the solid sealant, which had an average stress of 58.2 ± 10 kPa. The foam sealant's average 5th extension stress at 100% strain using the steel as a substrate was 28.2 ± 4 kPa, 53% lower than that of the solid sealant, which was 59.9 ± 77 kPa.

Tables 4 and 5 display the stresses at each extension of 100% strain for the asphalt and steel specimens, respectively. An unpaired t test can be performed comparing the stresses at each extension to see if stretching the sealants repeatedly to 100% strain has an effect on the strength. For the foam sealant, when the average stress at the first extension is compared to the average stress at any of the other four extensions an unpaired t test results in a p value greater than 0.05. This means that the mean stress values of the 4 test samples for each of the 5 extensions to 100% strain are similar each other. This trend is seen for samples using asphalt and steel substrates. The solid sealant exhibits the same trend. These results from the t test show that despite the hot and freezing conditions that the samples are subjected to for the oven-aged bond test the sealants do not exhibit much change in strength for these few initial cycles of loading and unloading within 100% strain.

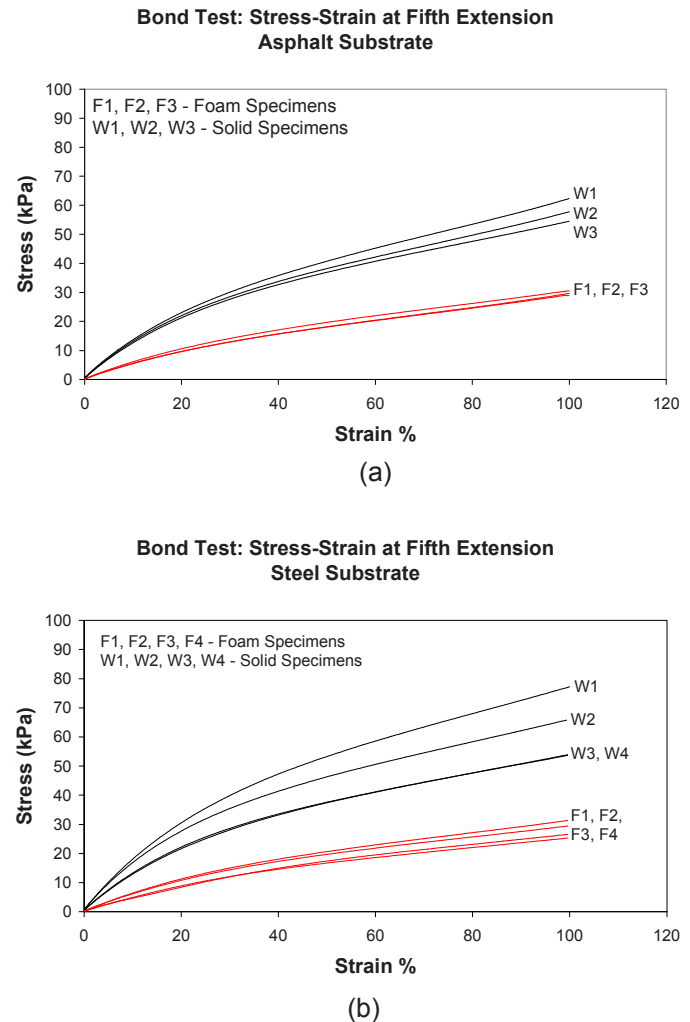


Figure 6. Oven Aged Bond Test, Stress – Strain at Fifth Extension using (a) Asphalt and (b) Steel Substrates

Table 4. Stresses at Each Extension of 100% Strain, Asphalt Substrate, Oven-Aged Bond Test

Sealant Type	Asphalt Specimen	1 st Extension Stress (kPa)	2 nd Extension Stress (kPa)	3 rd Extension Stress (kPa)	4 th Extension Stress (kPa)	5 th Extension Stress (kPa)
Foam Sealant	F1	30.4	29.9	29.6	28.9	28.9
	F2	32.0	21.6	18.1	18.3	17.8
	F3	32.2	30.9	30.3	30.1	29.7
	F4	33.7	31.5	31.08	30.3	30.5
	Average^a	32.1 ± 2^b	28.5 ± 7	27.3 ± 10	26.9 ± 9	26.7 ± 10
Solid Sealant	W1	59.2	58.6	58.2	58.0	57.8
	W2	49.7	49.0	51.1	49.8	54.5
	W3	60.4	61.7	65.0	62.3	62.3
	Average	56.4 ± 15	56.4 ± 16	58.1 ± 17	56.7 ± 16	58.2 ± 10

^a Average of the Samples
^b 95% Confidence Interval for the Averages

Table 5. Stresses at Each Extension of 100% Strain, Steel Substrate, Oven-Aged Bond Test

Sealant Type	Steel Specimen	1 st Extension Stress (kPa)	2 nd Extension Stress (kPa)	3 rd Extension Stress (kPa)	4 th Extension Stress (kPa)	5 th Extension Stress (kPa)
Foam Sealant	F1	24.3	26.8	27.3	26.5	26.5
	F2	25.4	26.7	29.4	29.9	29.5
	F3	27.1	31.5	31.7	32.7	31.5
	F4	25.4	25.4	25.3	23.3	25.3
	Average^a	25.6 ± 2^b	27.6 ± 4	28.4 ± 4	28.1 ± 6	28.2 ± 4
Solid Sealant	W1	63.3	66.6	67.0	65.9	65.9
	W2	77.3	77.8	78.6	77.2	53.8
	W3	54.0	54.4	54.1	53.2	-
	W4	52.1	53.4	53.7	-	-
	Average	61.8 ± 18	63.1 ± 18	63.4 ± 19	65.4 ± 30	59.9 ± 77

^a Average of the Samples
^b 95% Confidence Interval for the Averages

Salt Water Immersion Test Results

The results from the salt water immersion test are shown in Figures 7(a-b) and in Tables 6 and 7. There is a disparity between the average ultimate strain of both the foam and solid sealant using asphalt as a substrate and steel as a substrate. For the foam sealant the average ultimate strain using asphalt was 428.7% while for the steel it was 371.7%. The percent increase of the average ultimate strain of the foam using asphalt substrate to steel substrate is 15%. On the other hand, for the solid sealant using the asphalt substrate the average ultimate strain was 292.7% as opposed to 150.0% when the steel was used. The percent decrease of the solid from using asphalt substrate to steel substrate is 49%.

As presented in the Tension, Pull to Fail Test section, results from the tension tests on the regular specimens show that both the foam and the solid sealant have better bonding capabilities to the steel substrate than that to asphalt substrate. However, this is not the case with the salt water immersion test case. Switching from dry to immersed foam sealants the percent increase in the average ultimate strain for the foam using asphalt substrates was 20% while for the steel the percent decrease was 55%. On the other hand for the solid sealant switching from the dry to immersed test samples the average ultimate strain increases by 42% using the asphalt substrate and decreases by 72% using the steel substrate. The failure modes during the salt water immersion test for the foam sealant was internal. Internal failure of the sealant is a tearing of the material and not a separation from the bonding substrate. Failure of the solid sealant was seen at the bond for both asphalt and steel. For the both the

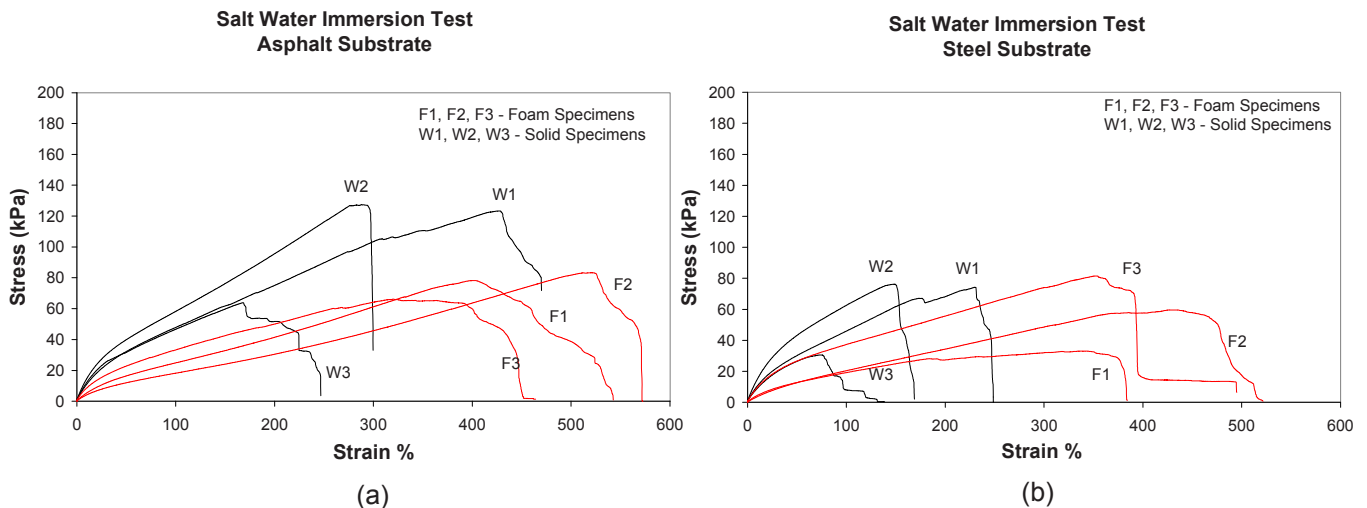


Figure 7. Salt Water Immersion Test, Pull to Failure using (a) Asphalt and (b) Steel Substrates

solid and foam sealants, the salt water has an effect on the sealant's ultimate strain. Upon close inspection the steel accumulated rust as it was contained in the salt water. While no rust was present on the bonding surface, which could be seen after the sealants were pulled to failure, the rust may have caused the solid sealant to separate at the corners of the steel pieces. It was observed that in any tensile pull-to-fail test with that the solid sealant, any slight imperfection on the bonding area of the substrate or the sealant resulted in a quick failure.

Table 6. Salt Water Immersion Test Data, Dry vs. Immersed Specimens, Asphalt Substrate

Sealant	Asphalt Specimen	Ultimate Strain (%)		Ultimate Stress (kPa)	
		Immersed	Dry	Immersed	Dry
Foam Sealant	F1	403	347.8	78	84.3
	F2	520	323.8	83	73.9
	F3	363	499.4	65	91.5
	F4	-	261.3	-	52.2
	Average^a	428.7 ± 202^b	358.0 ± 161	75.3 ± 23	83.2 ± 22
Solid Sealant	W1	428	190.4	123	100.7
	W2	282	242.3	127	118.5
	W3	168	227.6	64	118.1
	W4	-	164.2	-	85.9
	Average	292.7 ± 324	206.1 ± 56	104.7 ± 88	94.6 ± 62

^a Average of the Samples
^b 95% Confidence Interval for the Averages

Table 7. Salt Water Immersion Test Data, Dry vs. Immersed Specimens, Steel Substrate

Sealant	Steel Specimen	Ultimate Strain (%)		Ultimate Stress (kPa)	
		Immersed	Dry	Immersed	Dry
Foam Sealant	F1	334	512.6	33	97.8
	F2	427	633.1	60	101.8
	F3	354	609.8	82	118.7
	F4	-	550.3	-	101.7
	Average^a	371.7 ± 122^b	576.5 ± 88	58.3 ± 61	105.0 ± 15
Solid Sealant	W1	229	491.0	74	145.9
	W2	148	593.3	76	181.0
	W3	73	-	82	-
	W4	-	-	-	-
	Average	150.0 ± 194	542.6 ± 650	60.3 ± 63	163.5 ± 223

^a Average of the Samples
^b 95% Confidence Interval for the Averages

The data collected in Malla et al. (2007) regarding the concrete substrates showed that average ultimate strain for the foam and solid sealants decrease when submersed in salt water. Like the results for concrete substrate, the percent loss in strain for the steel substrate is greater in the solid sealant than the foam sealant. It can also be seen that while there was little change in the strength of the foam sealant, the strength of the solid in salt water is less than if it was dry.

Stress vs. Curing Time Test Results

The results for the performance during curing test using asphalt and steel as substrates are displayed in [Figures 8\(a-b\)](#) and in [Tables 8 and 9](#). The foam and solid sealants applied to asphalt substrates achieved 62 and 60% of their average 3 week strength, respectively, within their first 3 days of curing. The foam and solid sealants applied to steel substrates both achieved 63% of their average 3 week strength within their first 3 days of curing. Extension of the sealants to 100% strain does not show a large variation in data between the uses of concrete, asphalt, and steel substrates. The foam and solid sealants bonded to asphalt achieve 75 and 73% of their average 42-day strength, respectively, within the first week, 7 days, of curing. The foam and solid sealants bonded to steel achieve 73 and 83% of their average 42-day strength, respectively, within the first week, 7 days, of curing. The results ([Figs. 8a, b](#)) show, there is a quick gain in strength (nominal stress) tensile strength within the first week of curing which then slightly plateaus as time passes.

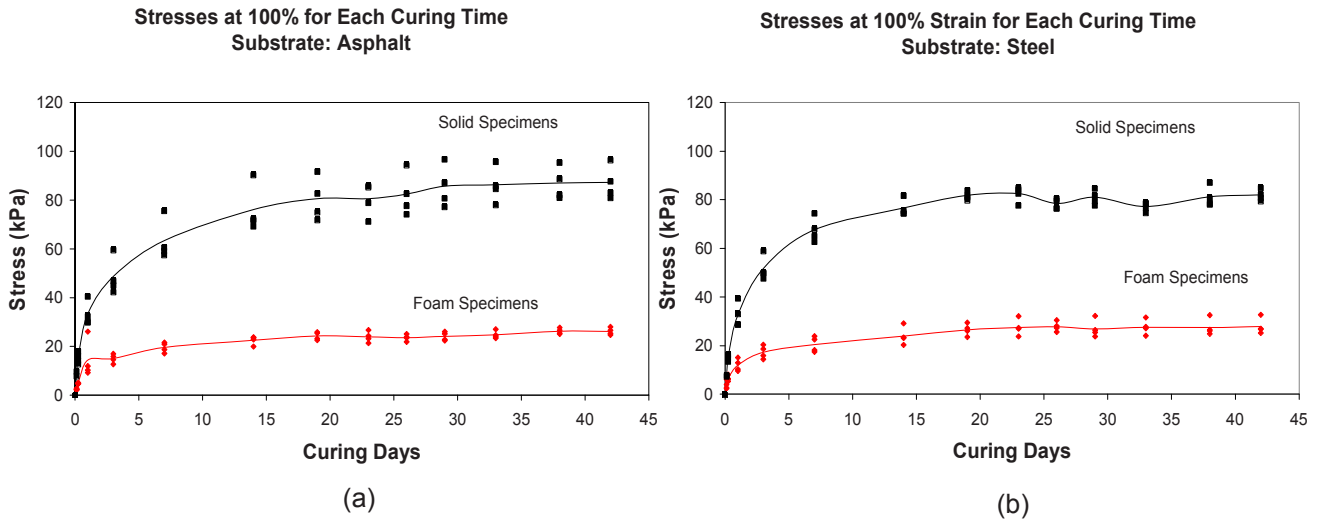


Figure 8 Stress during curing Substrates

Table 8. Average Stress^a (kPa) at 100% Strain for each Curing Time, Asphalt Substrate

Curing Hours	Foam Sealant Stress(kPa) At 100% Strain	Solid Sealant Stress(kPa) At 100% Strain	Curing Hours (Days)	Foam Sealant Stress(kPa) At 100% Strain	Solid Sealant Stress(kPa) At 100% Strain	Curing Hours (Days)	Foam Sealant Stress(kPa) At 100% Strain	Sealant Stress(kPa) At 100% Strain
3	2.37 ± 0.4 ^b	9.0 ± 13 ^b	72 (3)	15.0 ± 3	48.7 ± 12	624 (26)	23.6 ± 2	82.5 ± 14
6	4.33 ± 2	15.5 ± 4	168 (7)	19.6 ± 3	63.5 ± 13	696 (29)	24.1 ± 3	85.8 ± 14
18	8.6 ± 4	21.8 ± 7	336 (14)	22.5 ± 3	76.2 ± 15	792 (33)	27.3 ± 7	86.3 ± 12
24	14.4 ± 13	33.7 ± 8	456 (19)	24.3 ± 3	80.6 ± 14	912 (38)	26.2 ± 2	87.1 ± 11
			552 (23)	23.9 ± 4	80.6 ± 11	1008 (42)	26.2 ± 2	87.3 ± 11

^a Average stress of 4 Test Samples
^b 95% Confidence Interval for the Averages

Table 9. Average Stress^a (kPa) at 100% Strain for each Curing Time, Steel Substrate

Curing Hours	Foam Sealant Stress(kPa) At 100% Strain	Solid Sealant Stress(kPa) At 100% Strain	Curing Hours (Days)	Foam Sealant Stress(kPa) At 100% Strain	Solid Sealant Stress(kPa) At 100% Strain	Curing Hours (Days)	Foam Sealant Stress(kPa) At 100% Strain	Sealant Stress(kPa) At 100% Strain
3	3.8 ± 3 ^a	7.9 ± 3	72 (3)	17.4 ± 4	51.9 ± 8	624 (26)	27.9 ± 3	78.6 ± 4
6	6.5 ± 2	15.4 ± 2	168 (7)	20.5 ± 5	67.8 ± 8	696 (29)	27.0 ± 6	81.1 ± 5
18	9.3 ± 4	22.4 ± 9	336 (14)	24.0 ± 6	76.7 ± 6	792 (33)	27.6 ± 5	77.3 ± 3
24	12 ± 4	32.7 ± 8	456 (19)	26.6 ± 4	81.9 ± 3	912 (38)	27.5 ± 5	81.3 ± 7
			552 (23)	27.6 ± 5	82.6 ± 5	1008 (42)	28.0 ± 5	82.1 ± 4

^a Average stress of 4 Test Samples
^b 95% Confidence Interval for the Averages

DEVELOPMENT OF FIELD APPLICATION PROCEDURE

In order to come up with an adequate procedure/methodology for field application of the sealant in a real bridge expansion joints, the next step was to move beyond filling a small gap for laboratory test sample preparation and prepare larger quantity of sealant mix and fill larger and longer joint gap. For this purpose, in the laboratory setting two steel beams were set up to create a simulated expansion joint that was 7 feet in length and 1.5 inches in width. A backer rod was placed into the joint creating a joint depth of 1 inch. Figure 9 shows a schematic of the

prototype joint gap set-up and sealant filling. Using the simulated expansion joint a procedure for mixing and pouring the sealant into the joint was developed. Using the application procedure expansion joints on bridges in Connecticut, New Hampshire, Rhode Island, and New York were sealed using the silicone foam and the commercial solid sealant for comparison. Figure 10(a) shows an expansion joint in Connecticut being filled with the silicone foam, and Fig. 10(b) shows the same joint after the sealant application.

CONCLUSION

Based on the results obtained from the various laboratory tests on the silicone foam sealant developed in the first phase of this research and on a commercially available solid sealants, the following conclusions can be drawn:

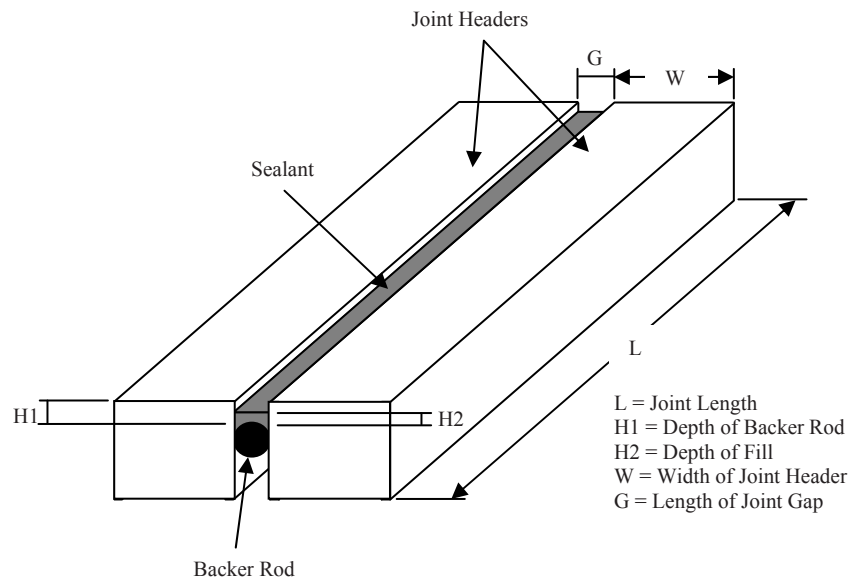


Figure 9 – Schematic Cross-Section of Sealed Bridge Expansion Joint

:

- The silicone foam has the capability of bonding to commonly used joint header materials (such as concrete, steel, and polymeric concrete) in the bridge expansion joint construction in practice. The foam also displays a better bonding to asphalt. Where as the solid sealant was observed to fail at the sealant-substrate interface at a much lesser strain (elongation) value.
- Regardless of which material is used as a bonding substrate the foam, while having a lower ultimate strength, will elongate longer than the solid sealant prior to failure. The large ultimate strain that the foam sealant exhibits indicates that it can easily accommodate movement of small movement expansion joints as these types of joints are designed to move between 1 and 2 inches.
- The foam and solid sealant did not exhibit a loss in strength after 5 cycles of loading and unloading, even though the sealants were subjected to hot and freezing temperatures prior to testing.
- The foam and solid sealants, bonded to asphalt and steel, display smaller ultimate strains after they were submersed in salt water. The effect is more severe when the solid sealant is bonded to steel.
- Both the foam and solid sealants gain strength as they cure overtime. The foam and solid sealants gain the majority of their strength within the first 2 weeks of curing, and then there is a slight, gradual strength gain over the next 4 weeks.



(a)



(b)

Figure 10. Sealant Installation in a Connecticut Bridge Joint

ACKNOWLEDGEMENT

The research reported was conducted under the “NETC 02-6 Phase 2 - Sealing of Small Movement Expansion Joints: Field Demonstration and Monitoring” project sponsored by the New England Transportation Consortium. The support is gratefully acknowledged. The authors extend sincere thanks to the state Departments of Transportation in Connecticut, New Hampshire, Rhode Island, and New York for providing the bridges in their states and the logistical help and facilities making it possible to install the sealants into the bridge expansion joints. The authors also acknowledge the Watson Bowman Acme Corporation in Amherst, New York, for their donating the WABO two part silicone sealant material. The contents of this paper reflect the views of the writers, who are responsible for the facts and accuracy of the data presented herein. The contents do not necessarily reflect the views of the NETC or the Federal Highway Administration.

REFERENCES

1. Dornsife, Ralph J., “Expansion Joints,” *Bridge Engineering Handbook*, CRC Press, 25-1, 1999.
2. Dow Corning Silicones. <http://www.dowcorning.com> (Oct. 2008).
3. Watson Bowman Acme Corp. “Wabo®SiliconeSeal.” <<http://www.watsonbowman.com/Products/ViewProductLine.aspx?ProductLineID=48>> (Sept. 2008).
4. Chang, L.M., and Lee, Y.J., “Evaluation of Performance of Bridge Deck Expansion Joints,” *Performance of Constructed Facilities*, 16(1), 3-9, 2002.
5. Malla, R., Shaw, M., Shrestha, M., and Brijmohan, S.B., “Development and Laboratory Analysis of Silicone Foam Sealant for Bridge Expansion Joints,” *J. of Bridge Engineering*, 12 (4), 438-448, 2007.
6. Malla, R., Shaw, M., Shrestha, M., and Boob, S., “Sealing Small Movement Bridge Expansion Joints,” *NETCR-58, Final NETC 02-6 Project Report*, New England Transportation Consortium, Fall River, MA; June 29, 2006, 112 pages.
7. Shrestha, M.R., Malla R.B., Boob, S., and Shaw M.T., “Laboratory Evaluation of Weathering and Freeze-Thaw Effects on Silicone.” *Proceedings of the 2006 SEM Annual Conference & Exposition*, St. Louis, Missouri, 8 pages, June 2006.
8. Gelest, Inc. <<http://www.gelest.com>> (Oct. 2008).
9. Momentive Performance Materials. “Silicones.” <http://www.momentive.com/Internet/Silicones/Brand/Silopren*/U_Crosslinker430?productid=16b927d09d67d110VgnVCM1000002a25340a____> (Oct. 2008).
10. Drozdov, A.D. “Mullins Effect in Thermoplastic Elastomers: Experiments and Modeling.” *Mechanics and Research Communications*, 36(4), 437-443, 2008.
11. Cantournet, S., Desmorat, R., and J. Besson, “Mullins Effect and Cyclic Stress Softening of Filled Elastomers by Internal Sliding and Friction Thermodynamics Model,” *International Journal of Solids and Structures*, 46(11-12), 2255-2264, 2008.

Effect of Prior Cold Work on the Mechanical Properties of Weldments

M. Acar*, S. Gungor, P. J. Bouchard and M. E. Fitzpatrick

Materials Engineering
The Open University, Walton Hall
Milton Keynes MK7 6AA, UK

*Corresponding author: m.o.acar@open.ac.uk

ABSTRACT

Heat exchanger units used in steam raising power plant are often manufactured using many metres of austenitic stainless steel tubes that have been plastically formed (bent and swaged) and welded into complex shapes. The amount of plastic deformation (pre-straining) before welding varies greatly. This has a significant effect on the mechanical properties of the welded tubes and on the final residual stress state after welding. The aim of the present work was to measure and understand the combined effects of pre-straining and welding on the properties and residual stress levels in stainless steel tubing weldments. Effects of plastic deformation were simulated by plastically straining three identical stainless steel tubes to different strain levels (0%, 10% and 20%). Then each tube was cut into two halves and welding back together. The variation in mechanical properties across weldments was measured using digital image correlation (DIC) and a series of strain gauges (SG). Residual stresses were measured on the 0% (undeformed) and 20% prestrained and welded tubes by neutron diffraction. It was found that the welding process had a marked effect on the tensile properties of parent material within 25mm of the weld centre-line. Evidence of cyclic strain hardening was observed in the tube that had not been pre-strained, and evidence of softening seen in the 10% and 20% pre-strained tubes. Macroscopic residual stresses were measured to be near zero at distances greater than 25 mm from the weld centre-line, but measurements in the 20% pre-strained tube revealed the presence of micro residual stresses having a magnitude of up to 50 MPa.

INTRODUCTION

The structural integrity, performance and life of weldments is determined by the mechanical properties of the weld metal, heat affected zone (HAZ) and parent materials. These properties depend on the full fabrication history including cold bending and swaging, welding, heat treatment and the effects of service ageing. For example, introduction of plastic strain can increase the susceptibility of materials to stress corrosion and creep damage [1,2]. It is important to quantify the initial material properties in weldments in order to understand and assess their influence on the life and integrity of components.

In this project, the separate and combined effects of manufacturing steps on austenitic stainless steel tube weldment properties at the room temperature were investigated. Effects of bending and swaging were simulated by plastically straining three identical stainless steel tubes to different levels (0%, 10% and 20%). Then each tube was cut into two halves and welding together. The aim of the work was to understand the combined effects of pre-straining and welding on the variation of mechanical properties and residual stress across the weldment. The variation in mechanical properties was measured using digital image correlation (DIC) and a series of strain gauges (SG). Residual stresses were measured on the 0% (undeformed) and 20% prestrained and welded tubes by using the neutron diffraction using the Stress-Spec instrument at the FRMII facility in Germany.

EXPERIMENTAL

Test specimens

A set of pre-strained and butt-welded tubes were supplied for the experimental programme by a power generation company (Table 1). The untreated tubes (before pre-straining and welding) were manufactured by extrusion and solution annealed at a temperature of 1100°C for 3 mins followed by water quenching. The tubing material is AISI Type 316H austenitic stainless steel with the composition given in Table 2. The initial tubing geometry was 38 mm in diameter and 4 mm in thickness. The test specimens were fabricated as follows. First two tubes were pulled uniaxially in tension up to 10 and 20% plastic strain (referred to as “pre-straining”). Secondly, these tubes plus a non-strained (0%) tube were each cut into two halves. Matching half-tubes were then welded together (after root tack welding) using a tungsten inert gas (TIG) welding process with Type 316L filler metal (see Tables 2 and 3).




Pre-strained and welded tubes	Degree of plastic deformation	Label of tubes	Label of the remote-end tensile specimens	Label of the cross-weld tensile specimens
	0%	A ₀	B ₀	C ₀
	10%	A ₁₀	B ₁₀	C ₁₀
	20%	A ₂₀	B ₂₀	C ₂₀

Table 1: Photographs and labeling of test specimens

	Cr	Ni	Mo	Mn	Si	Co	C
316H	16.89	11.25	2.04	1.55	0.53	0.089	0.05
316L	18.38	12.07	2.53	1.61	0.37	-	0.01

Table 2: The composition of the stainless steel tubing material (Type 316H) and the weld material (Type 316L)

Welding Type	TIG
Polarity	DCEN (Direct current electrode negative)
Shield & Purge Gas	Argon 99.995%
Current	65-140 A
Flow Rate	5 to 8 litres/min
Electrode	2.4 mm 2% Th or Ce Tungsten
Purge Rate	2 to 8 litres/min

Table 3: Weld procedure specification

The welded tubes A₀ and A₂₀ were used for neutron diffraction residual stress measurements. Thereafter, flat cross-weld (C₀, C₁₀, C₂₀) and remote-end (B₀, B₁₀, B₂₀) tensile test specimens were cut from A₀, A₁₀ and A₂₀ tubes by electro-discharge machining. The cut position and the dimensions of the tensile specimens are given in Figure 1.

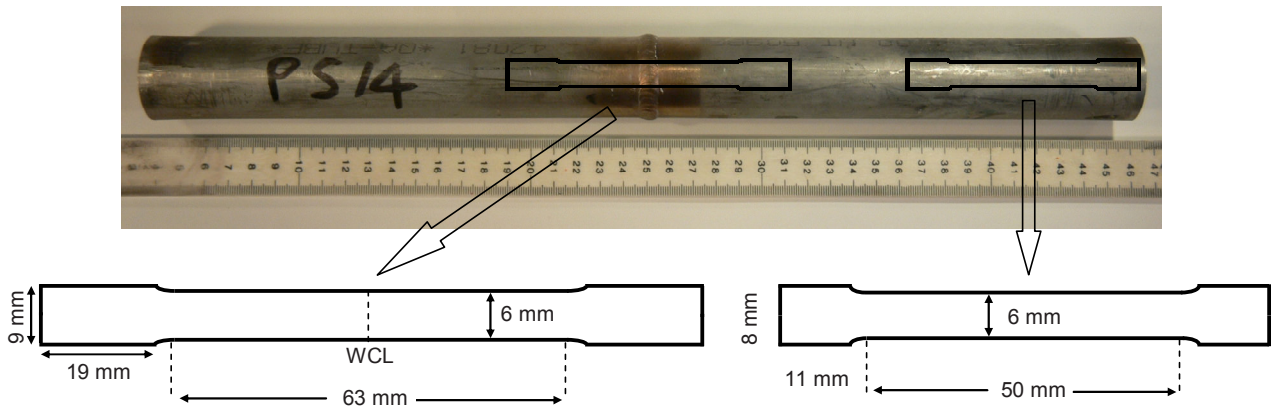


Figure 1: The cut position (top) and the dimensions of the cross-weld test specimens C_0 , C_{10} and C_{20} (bottom left) and tensile specimens B_0 , B_{10} and B_{20} (bottom right). Both types of specimen were 3mm thick.

Residual stress measurements using neutron diffraction

The Stress-Spec neutron diffraction instrument at the FRMII facility in Germany was used to determine the distribution of weld residual stresses in welded tubes A_0 and A_{20} . A wavelength of $\lambda = 1.5480 \text{ \AA}$ was obtained using a Si (400) monochromator. This wavelength allowed measurement of the austenitic steel (311) reflection at a scattering angle $2\theta_s \approx 91^\circ$. The gauge volume used in our measurements was $2 \times 2 \times 2 \text{ mm}^3$. For both tubes, the lattice strain response, ε_{lat} , in the axial, hoop and radial directions was measured at the mid-thickness along one half of the tubes with a position opposite to the start/stop point of the final weld pass, as shown in Figure 2. The measured data were analyzed with StressTexCalculator software using Gaussian fitting to obtain the peak positions in terms of 2θ angles which were then used to calculate the strain. Measurements at the remote end of welded tube A_0 in axial, hoop and radial directions were used as direction-dependent references (θ_0) to calculate the lattice strain for each measurement.

$$\varepsilon_{lat} = \frac{\Delta d}{d} = \frac{\sin \theta_0}{\sin \theta} - 1 \quad (1)$$

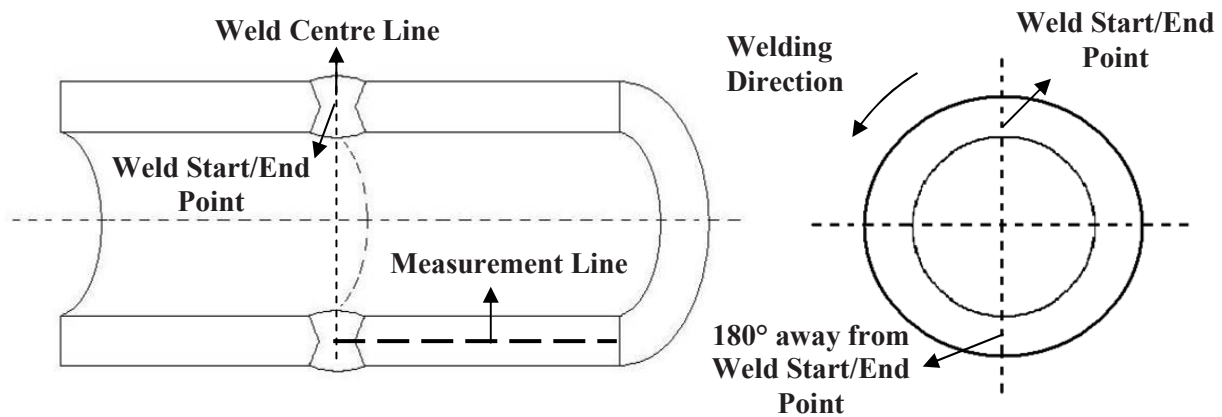


Figure 2: Sketch showing location of neutron diffraction measurement lines in specimens A_0 and A_{20}

The strain measured is in the direction of the scattering vector. To find out the stress state at any point in the sample, measurements are usually required in six orientations due to the fact that stress is a tensor. However, it was assumed that the principal stress axes coincide with the axial, hoop and radial directions of the tube [3]. Hence the stress in the principal directions can be calculated using the Hookes' law. For example, the stress in the axial direction was calculated using the following equation:

$$\sigma_{axial} = \frac{E}{(1+\nu)(1-2\nu)} \left[(1-\nu)\varepsilon_{axial} + \nu(\varepsilon_{hoop} + \varepsilon_{radial}) \right] \quad (2)$$

where crystallographic elastic constants for the (311) reflection were taken to be $E = 195$ GPa and $\nu = 0.29$.

Tensile tests and Digital Image Correlation

Tension tests on cross-weld specimens C_0 , C_{10} and C_{20} were carried out using a screw-driven tensile testing machine with a 30kN load cell. Mechanical wedge action grips were used to fix the specimens into the machine. Before each test commenced, the loading and specimen alignment was checked in order to avoid subjecting the specimen to any bending or torsion, i.e. to ensure the loading was pure uniaxial tension [4,5]. This was achieved by employing universal joints in the loading fixture, and checking the alignment with a pair of SGs attached on opposite faces of the specimen 20 mm away from the weld centre line (WCL), see Figure 3. Two more SGs were attached onto the back surface at the middle of the weld and in the HAZ (6.5 mm away from WCL). The data from these SGs were compared to the DIC results obtained from the area shown with dash rectangle in Figure 3.

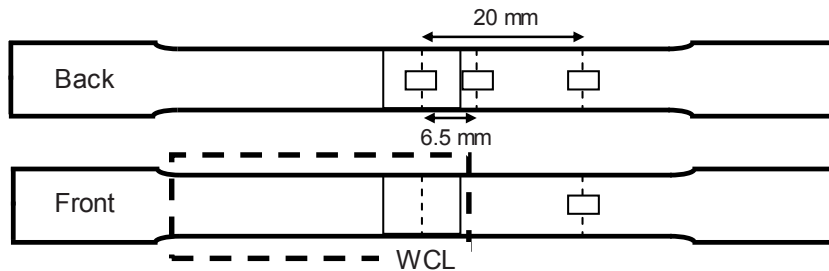


Figure 3: Positions of SGs on the back and front surfaces of specimens C_0 , C_{10} and C_{20}

The full field distribution of strain in the area shown in Figure 3 was obtained throughout each tensile test using DIC. The speckle pattern required for the DIC measurements was achieved by white light illumination of the rough surface produced by EDM [6]. After correcting the alignment of the specimen and grips, the tensile tests were performed with a constant extension rate of 0.1mm/min. During the tests, images of the front surface of the specimens were captured by a digital SLR camera (Nikon D300), with a sensor size of 4,288 x 2,848 pixels (12.3 Mega Pixels), and a 200 mm macro lens. A DC fibre optic light source was used to illuminate the surface. The images were taken every 10 seconds from the half-length of the specimen indicated in Figure 3 and the load and extension were recorded every second. Analysis of the images was performed using commercial DIC software [7].

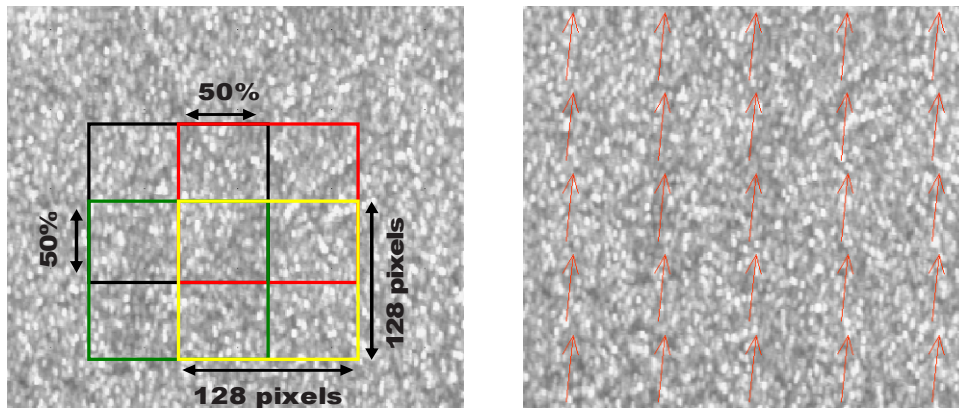


Figure 4: Reference image and the subsets used for the calculations (left) and the displacement vectors on the image of the deformed surface after 1190 sec (right)

All images from the three tension tests (of cross-weld specimens C_0 , C_{10} and C_{20}) were analyzed using the same optimized parameters as described in [6]. The pixel size on the real images for each test was about 11 μm . As a first step of analysis, all images were shift-corrected with respect to the reference image. Then, the displacement

vectors in the loading direction were calculated by multi-scanning the images using a '256x256 subset size with 50% overlap and 2 passes' and a '128x128 subset size with 50% overlap and 6 passes' respectively (Figure 4). After the displacement map in the loading direction was obtained using the DIC software, the strain was calculated by differentiating the displacement data using a Matlab script [6]. The error in the calculated strain is estimated to be about 50 microstrain; this is based on the precision of the DIC method which is given as 0.02 pixel displacement [7]. The strain on each image was averaged across the width of the specimen and a stress-strain curve was constructed for each subset. A linear line was fitted to the elastic region of each stress-strain curve and used to determine the 0.2% yield stress of the material.

RESULTS

Figure 5 illustrates tensile stress-strain curves for the parent material of tubes A_0 and A_{20} measured on specimens B_0 and B_{20} using an extensometer. These specimens were extracted from positions remote from the influence of the welds (see Figure 1). The 0.2% and 1% yield stress data derived from these curves are tabulated in Figure 5. The B_{20} curve superposes on the B_0 stress-strain curve if translated by 22.5% strain; this suggests that the A_0 tube must have been pre-strained slightly more than the 20% value reported by the supplier.

Stress-strain curves for cross-weld specimens C_0 , C_{10} and C_{20} at the weld centre obtained from SG and DIC measurements are given in Figure 6. Results from the two measurement techniques show a good correlation with each other for specimens C_{10} and C_{20} . Although the SG data for specimen C_0 suggest higher yield stress behaviour than measured by DIC it should be noted that these measurements were made on opposite sides of the test specimen. Overall the stress-strain properties of the weld metal in all three specimens are very similar to each other.

Stress-strain curves for cross-weld specimens C_0 , C_{10} and C_{20} at 6.5mm from the weld centre-line (WCL) obtained from SG and DIC measurements are given in Figure 7. Results from the two measurement techniques show a good correlation with each other for specimens C_0 and C_{10} . However, the DIC and SG stress-strain curves for specimen C_{20} deviate sharply from each other soon after first yield owing to necking of the weld metal (see discussion).

Stress-strain curves for cross-weld specimens C_0 , C_{10} and C_{20} at 10mm from the WCL obtained from DIC measurements are given in Figure 8. The sudden change in shape of the curves for specimens C_{10} and C_{20} at around 340 MPa is associated with necking of the weld metal (as indicated in Figure 8).

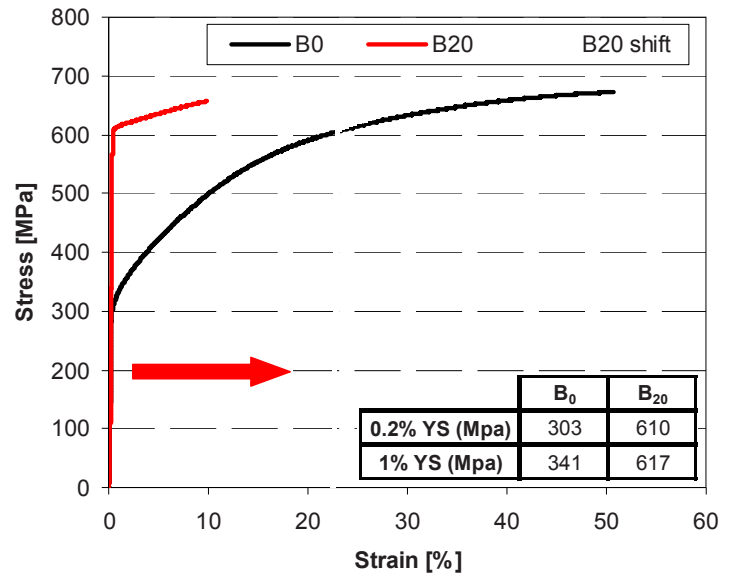


Figure 5: Stress-strain curves from specimens B_0 and B_{20} measured using a side extensometer

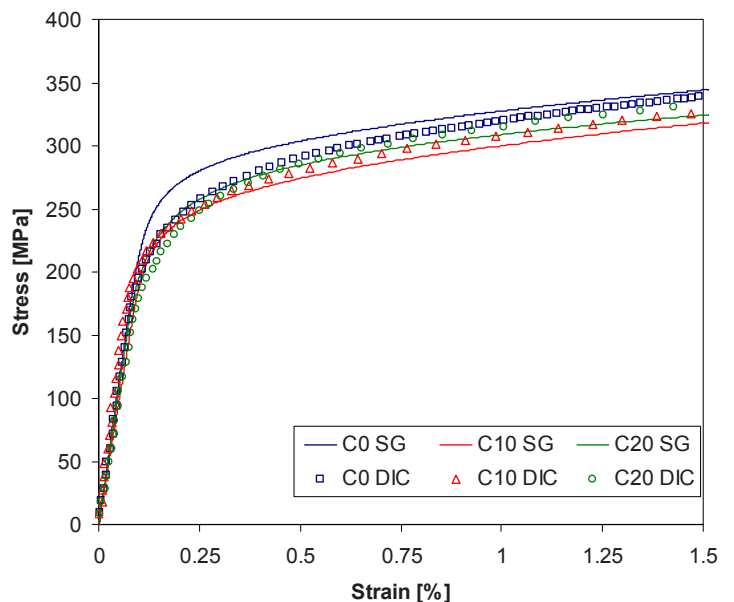


Figure 6: Stress-strain data measured using SG and DIC for the weld centre of test specimens C_0 , C_{10} , and C_{20}

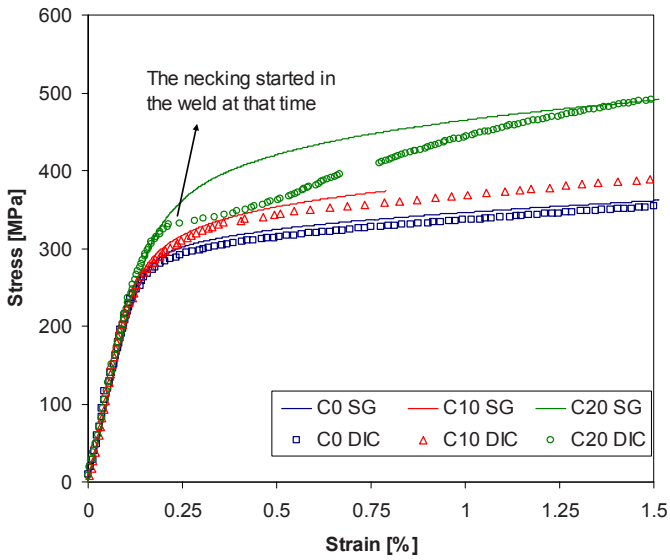


Figure 7: Stress-strain data measured using SG and DIC at 6.5mm from the WCL of test specimens C_0 , C_{10} , and C_{20} (the gap in C_{20} data at 0.7% strain is due to the connection problem between the camera and PC during the experiment and the SG on specimen C_{10} decohered after 0.8% strain)

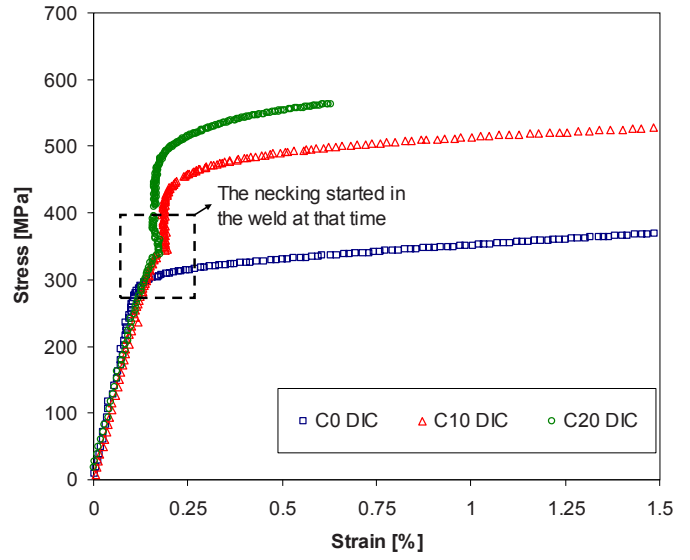


Figure 8: Stress-strain data measured using DIC at 10mm from the WCL of test specimens C_0 , C_{10} , and C_{20}

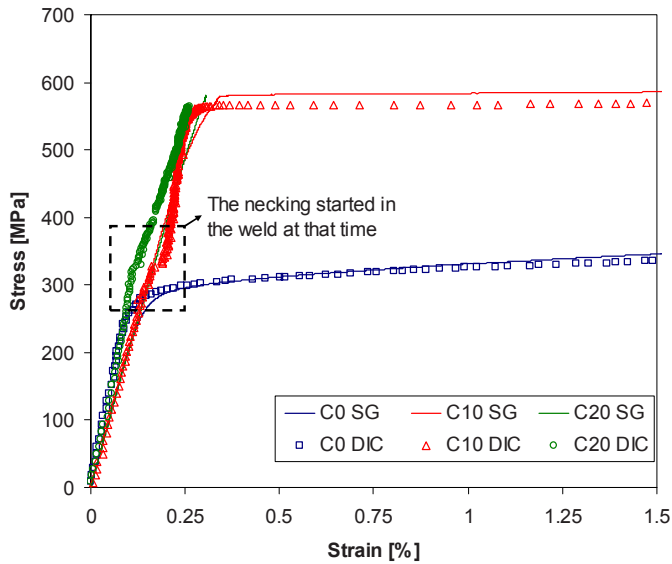


Figure 9: Stress-strain data measured using SGs and DIC at 20mm from the WCL of test specimens C_0 , C_{10} , and C_{20}

Stress-strain curves for cross-weld specimens C_0 , C_{10} and C_{20} at 10mm from the WCL obtained from SG and DIC measurements are given in Figure 9. The discontinuity in the shape of the curves for specimens C_{10} and C_{20} at around 340 MPa is again probably associated with necking of the weld metal (see Figures 7 and 8). But it is interesting that the SG data do not exhibit such a trend (see discussion).

Figure 10 plots the variation of 0.2% yield stress along the half-length of cross-weld specimens C_0 , C_{10} and C_{20} based on analysis of the DIC stress-strain curves. In specimen C_0 , the yield stress increases from a minimum of 268 MPa in the weld region to a maximum of 319 MPa at 10mm from the WCL and then drops gradually to a

steady value of 285 MPa at about 25mm from the WCL. In specimen C_{10} , the yield stress increases steadily from a minimum of 260 MPa in the weld region to a maximum of about 565 MPa at 16mm from the WCL. The trend in yield stress for specimen C_{20} is similar to C_{10} but in this case the yield stress is difficult to define because of necking behaviour of the weld metal.

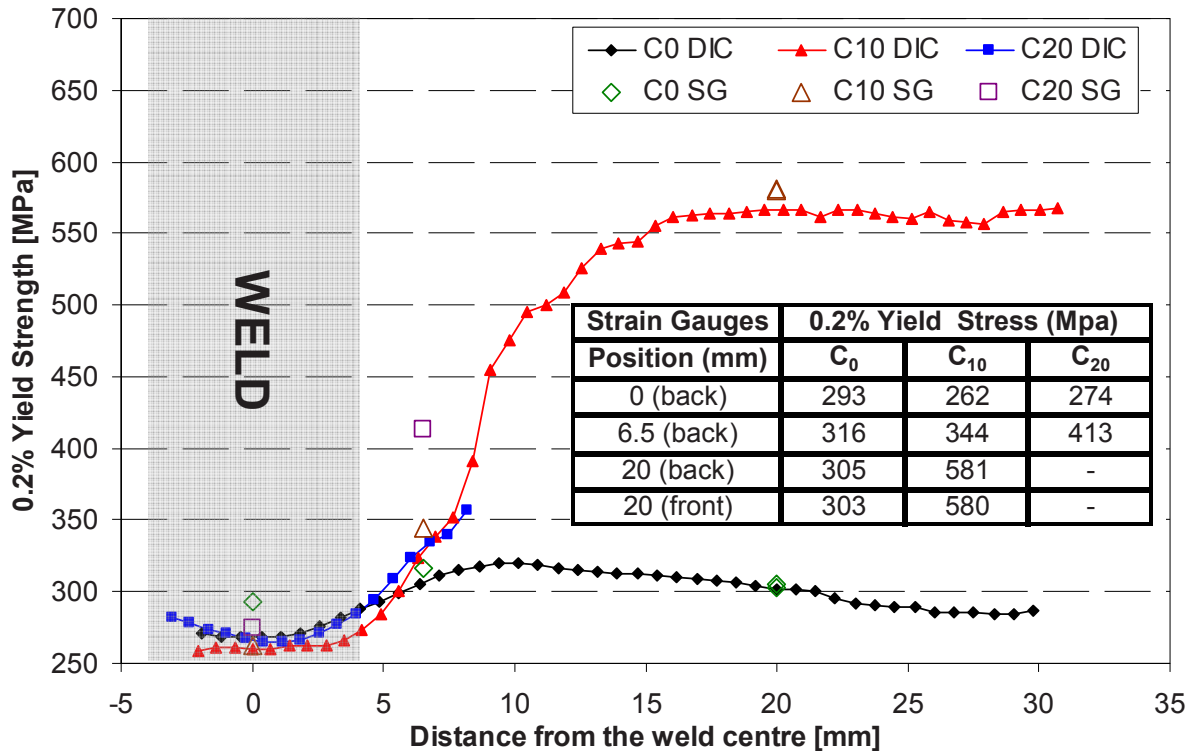


Figure 10: Variation in measured 0.2% yield stress moving away from the WCL test specimens C_0 , C_{10} , and C_{20} (derived from SG and DIC data).

The table in Figure 10 shows values of 0.2% yield stress obtained with the SGs at 0, 6.5 and 20mm away from the WCL for all cross-weld specimens (C_0 , C_{10} and C_{20}). The data are plotted with open symbols. It is seen that SG measurements show a reasonable correlation with the DIC results apart from the ones at the weld centre on specimen C_0 and at 6.5mm on C_{20} . The latter is 70 MPa higher than the DIC measurement at that point.

Figure 11 shows the distributions of axial, hoop and radial residual stresses measured at mid-radius of test specimens A_0 and A_{20} up to 60mm from the WCL. The results of particular relevance to this paper are in zone 2 (25 – 60mm from the WCL). In test specimen A_0 , the measured stresses in all three directions are almost zero. Whereas the average stresses in zone 2 of specimen A_{20} are 25 MPa, -15 MPa and -50 MPa in the axial, radial and hoop directions respectively. The differences in measured stress are indicative of micro-stresses caused by the 20% plastic prior deformation of material in specimen A_{20} remote from the influence of the weld.

DISCUSSION

The stress-strain curves measured using DIC and SGs are in reasonable overall agreement with each other (see figures 6, 7 and 9). The differences can be attributed to measurement position (Figure 3) and strain localization. Note that the DIC results were averaged over the respective gauge lengths of the SGs used.

At the WCL, strain was measured by a SG attached on the opposite face of the specimen to DIC observations. Small differences in the stress-strain curves (Figure 6) could be caused by slight misalignment during the tests or by real differences in weld metal properties. The small differences between the SG and DIC curves for the C_0 and C_{10} specimens at 6.5mm and 20mm (Figures 7 and 9 respectively) are unsurprising given that the SGs were located on the opposite face and at the opposite end of the specimens. The deviation in stress-strain behaviour for the specimen C_{20} (Figure 7) at about 0.2% strain was associated with necking of the weld metal. This

phenomenon also caused the discontinuities in the stress-strain curves of specimens C_{10} and C_{20} seen at 10mm and 20mm from the WCL (Figures 8 and 9). The weld metal was much weaker in these two specimens because the parent tubes were work hardened by pre-straining 10% and 20%.

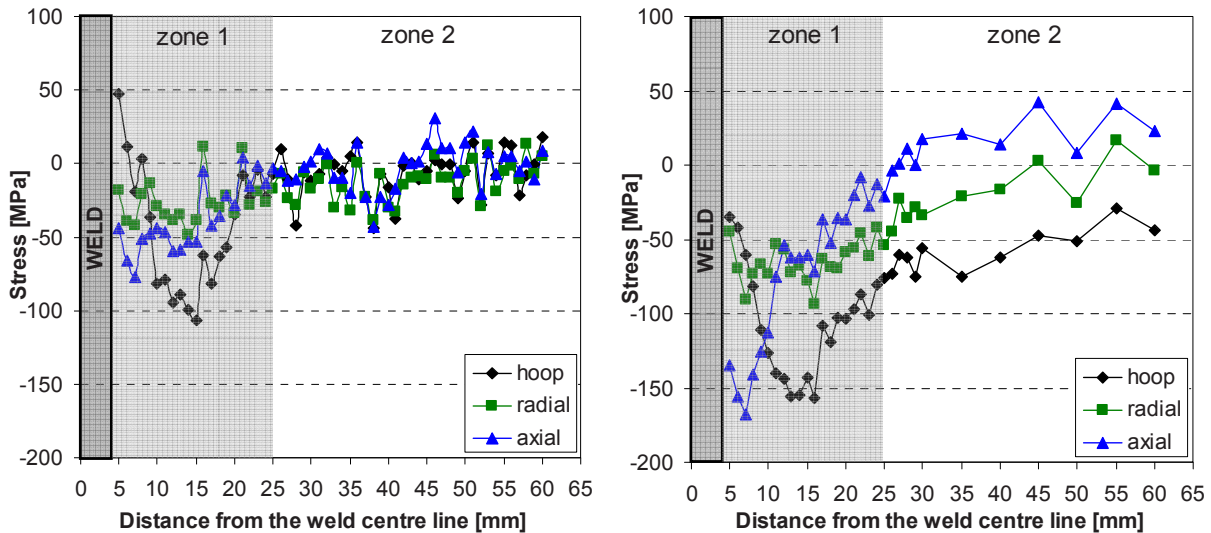


Figure 11: Variation in measured residual stress at mid-radius of test specimens A_0 (left) and A_{20} (right) up to 60mm from the WCL. The Stress-tech neutron diffractometer at the FRMII facility (Munich) was used for the measurements (using the 311 reflection).

Pre-straining had a marked effect on the fracture behaviour of the specimens. The tensile test limits for C_0 , C_{10} and C_{20} specimens were set to 15mm overall extension. Specimen C_0 didn't fail whereas C_{10} and C_{20} ruptured in the weld metal before they reached 10mm extension. In specimen C_0 the parent material yielded (0.2% yield stress of 285 – 303 MPa) and extended whereas the parent material of C_{20} specimen was in elastic region (0.2% yield stress was 610 MPa, see Figure 5) when the specimen fractured.

The variation in 0.2% yield stress measured along the half-length of specimens C_0 , C_{10} and C_{20} is given in figure 10. There is a very marked drop in yield stress in specimen C_{10} approaching the weld from about 16mm away from the WCL. This is caused by the welding process. Parent material near the weld was heated to temperatures where creep ($> 450^\circ\text{C}$) and dislocation annealing ($>700^\circ\text{C}$) mechanisms operated.

The slight increase in yield stress of specimen C_0 , in parent material between 5 and 25mm from the WCL is also associated with the welding process. But in this case the welding process has created strain hardening that has not entirely annealed out. The welding process introduces heat into adjacent parent material. This expands the material producing compressive residual stress of sufficient magnitude to initiate yielding. During cooling the region starts to contract and tensile strains develop. If the temperature gradient is high enough, this contraction can also yield the material in tension. Thus thermal cycles associated with welding can cause cyclic strain hardening in material adjacent to a weld. The extent of the yield zone in a thin welded plate can be estimated with the formula below [9]:

$$y_0 = \frac{1.033K}{\sigma_{yp}} \cdot \frac{\eta q}{vt} \quad (3)$$

where y_0 = radius of yield zone, mm q = arc power, J/sec t = thickness, mm
 K = a material constant, Nmm/J η = process efficiency
 σ_{yp} = 0.2% yield stress, MPa v = weld travel speed, mm/sec

This gives a yield length of 13.5 - 31 mm assuming a heat input of $q = 500 - 1100$ J/sec, $t = 4$ mm, $K\eta = 161$ Nmm/J, $\sigma_{yp} = 303$ MPa and $v = 5$ mm/sec. Adding this distance to the $\frac{1}{2}$ -width of the weld (4mm) gives a yield

distance of 15.5 - 33 mm from the WCL. This distance correlates with the yield stress distribution in specimen C₀ specimen shown in Figure 10.

The residual stresses measured by neutron diffraction (see Figure 11) show a complex variation approaching the weld (in zone 1); these results will be addressed in a future publication. The results of interest here are those in parent material unaffected by the welding process. Note the above results suggest that material further than 25mm away from the WCL is unaffected by hardening and softening mechanisms associated with welding. The residual stress measurements in zone 2 (25 – 60mm) of the non-pre-strained component, welded tube A₀, are close to zero in each direction. This confirms that material in this zone is unaffected by the weld. However, the average stresses in zone 2 of specimen A₂₀ are 25 MPa, -15 MPa and -50 MPa in the axial, radial and hoop directions respectively. The differences in measured stress are indicative of micro-stresses caused by 20% plastic prior deformation of material in specimen A₂₀ remote from the influence of the weld. In zone 1, the welding harshly alters the plastic strain which is already present in the material and that results in a very complicated strain distribution for different crystallographic planes [11].

CONCLUSIONS

1. The spatial variation in stress-strain behaviour across the weldment of plastically pre-strained welded tubes has been measured using DIC and conventional SGs and a reasonable agreement between the results obtained.
2. The DIC results were observed to be highly sensitive to deformation localization in the weld metal of the pre-strained sample.
3. The welding process had a marked effect on the tensile properties of parent material within 25mm of the weld centre-line. Evidence of cyclic strain hardening was observed in the tube that had not been pre-strained, and evidence of softening seen in the 10% and 20% pre-strained tubes.
4. Macroscopic residual stresses were measured to be near zero at distances greater than 25 mm from the weld centre-line, but measurements in the 20% pre-strained tube revealed the presence of micro residual stresses having a magnitude of up to 50 MPa.

ACKNOWLEDGEMENTS

The authors would like to thank British Energy Generation Limited for providing the welded tubes and funding the research. Professor Bouchard gratefully acknowledges Royal Society Industry Fellowship support. MEF is supported by a grant through The Open University from the Lloyd's Register Educational Trust, an independent charity working to achieve advances in transportation, science, engineering and technology education, training and research worldwide for the benefit of all.

REFERENCES

- [1] Willis M, McDonough-Smith A, Hales R, "Prestrain effects on creep ductility of a 316 stainless steel light forging" *International Journal of Pressure Vessels and Piping*, 76(6), 355-359 (1999)
- [2] Kamaya M, Wilkinson AJ, Titchmarsh JM "Quantification of plastic strain of stainless steel and nickel alloy by electron backscatter diffraction" *Acta Materialia*, 54(2), 539-548 (2006)
- [3] Hofmann M, Wimpory RC "NET TG1: Residual stress analysis on a single bead weld on a steel plate using neutron diffraction at the new engineering instrument STRESS-SPEC" *International Journal of Pressure Vessels and Piping*, 86(1), 122-125 (2009)
- [4] Christ BW, Swanson SR "Alignment Problems in the Tensile Test" *Journal of Testing and Evaluation (JTE)*, 4(6), 405-417 (1976)
- [5] Gray TGF, McCombe A "Influence of specimen dimension and grip in tensile testing steel to EN 10 002" *Ironmaking and Steelmaking*, 19(5), 402-408 (1992)
- [6] Acar M, Gungor S, Ganguly S, Bouchard PJ, Fitzpatrick ME, "Variation of Mechanical Properties in a Multi-pass Weld Measured Using Digital Image Correlation" *Proceedings of the SEM Annual Conference, Albuquerque New Mexico USA Society for Experimental Mechanics Inc.* (2009).
- [7] "StrainMaster 2D - Getting Started" *LaVision User Manual*.

- [8] Kotecki DJ, "Ferrite control in duplex stainless steel weld metal" *Weld. J.* 65 (10), 273-278 (1986).
- [9] Procedure R6 Revision 4. Assessment of the integrity of structures containing defects, Section IV.4, Gloucester, UK: British Energy Generation Ltd (2007).
- [10] Timoshenko SP, Woinowsky-Krieger "Theory of plates and shells" 2nd ed. New York, McGraw-Hill, 466-497 (1959).
- [11] Acar MO, Bouchard PJ, Fonseca JQ, Fitzpatrick ME, Gungor S "Intergranular Strains in Pre-Strained and Welded Pipes", *Material Science Forum*, 2009 (in press).

Use of Viscoplastic Models for Prediction of Deformation of Polymer Parts

Nils G. Ohlson
Department of Solid Mechanics
The Royal Institute of Technology
SE-100 44 Stockholm Sweden
moja.jernvag@telia.com

ABSTRACT

Polymers are extensively used in engineering applications, ranging from sealing rings to dampers and springs in centrifugal separators as well as in micro robots with piezoelectric excitation. The mechanical behaviour of these materials is highly non-linear and may be described by integral equations, taking into account the load history of the part considered. Paper shows that long-term deformation in creep and relaxation can be derived from tensile tests at several loading rates. The influence of cyclic loading is discussed. Tests show that material can fail in fatigue.

INTRODUCTION

Materials with memory of their loading history are frequently used in engineering. Metals at elevated temperatures and polymers at all temperatures may be characterized by an integral equation, in the uniaxial case of type

$$\varphi(\varepsilon) = \sigma(t) + \int_0^t K(t - \tau) \sigma(\tau) d\tau \quad (1)$$

where $\sigma(t)$ denotes the stress as a function of time, K is a kernel which may be fitted to results from material tests and $\varphi(\varepsilon)$ is the stress-strain relation for the hypothetical case when infinite strain rate is assumed. Function φ is built mathematically, once K has been determined. It is concluded that strain depends on instant time t as well as of stress at previous times.

It was shown in [1] that a useful approach to studying deformation of polymers like POM can be obtained by assuming

$$K(t - \tau) = \frac{k}{(t - \tau)^\alpha} \quad (2)$$

where k and α are material constants. This relation is valid for constant temperature but theory may be extended to variation of temperature and even moisture content, if desired, [2].

SCOPE

The purpose of the present study is to verify, by experiments, the validity of eq. (1) for creep and fatigue predictions.

TESTS AT VARIOUS LOADING RATES

As a minimum, tensile tests at three loading rates are needed for determining k , α and φ . Having obtained these, all kind of loading histories can be analyzed. [Figure 1](#) shows the stress-strain curves at three loading rates for POM at 25 deg C and the constructed curve φ above the experimental curves. Evaluation becomes particularly simple if stress rate is controlled in test,

$$\frac{d\sigma}{dt} = \text{const.} \quad (3)$$

which is fairly easy to perform using a modern servo-hydraulic testing machine. One finds that $k=0.025$, $\alpha=0.9$ and $\varphi=246 \text{ } \epsilon^{0.33}$ if time is measured in seconds and stress in MPa. For time in minutes, $k=0.037$ and for t in hours, $k=0.057$.

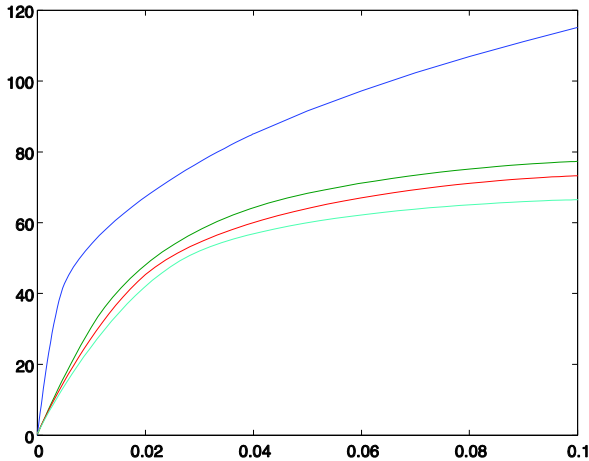


Figure 1. Stress (MPa) vs. strain (units) for strain rates 0.0004, 0.04, 1.1 per second and infinite.

CREEP TESTS IN TENSION

As our first verification, creep tests were carried out during 24 hours at constant stress, at 25 and 40 deg C, respectively, [Figure 2 & 3](#). Stress levels were 25, 32.5 and 48 MPa. Two specimens were run at the 32.5 level, shown in [Figure 2](#), in order to estimate the scatter of results. For high stress, creep rate will increase with time. It is unlikely that such behaviour can be modeled by eq. (1). Creep strain rate is decreasing slightly with time for lower stress. Obviously, no simple relation of power law type (Norton's law) is applicable to POM.

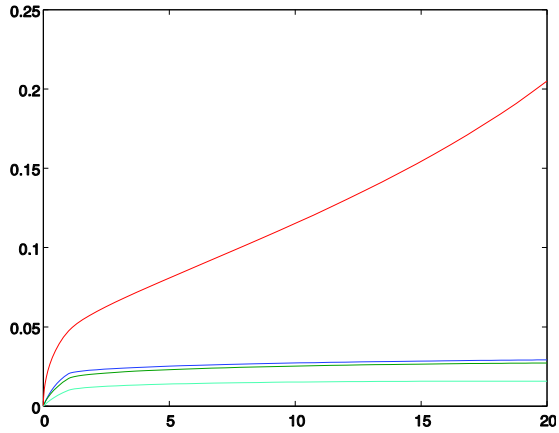


Figure 2. Creep strain (units) for 25, 32.5 (two curves) and 48 MPa at 25 deg C vs. time (hours)

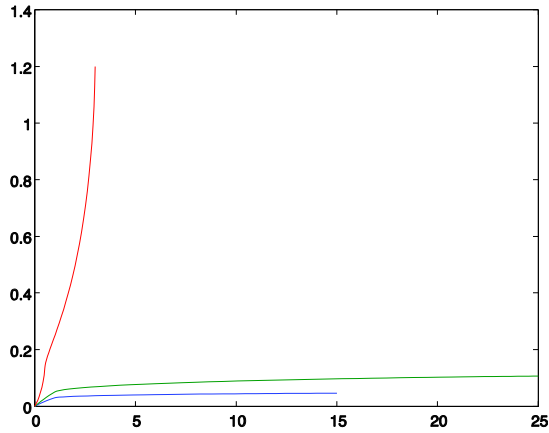
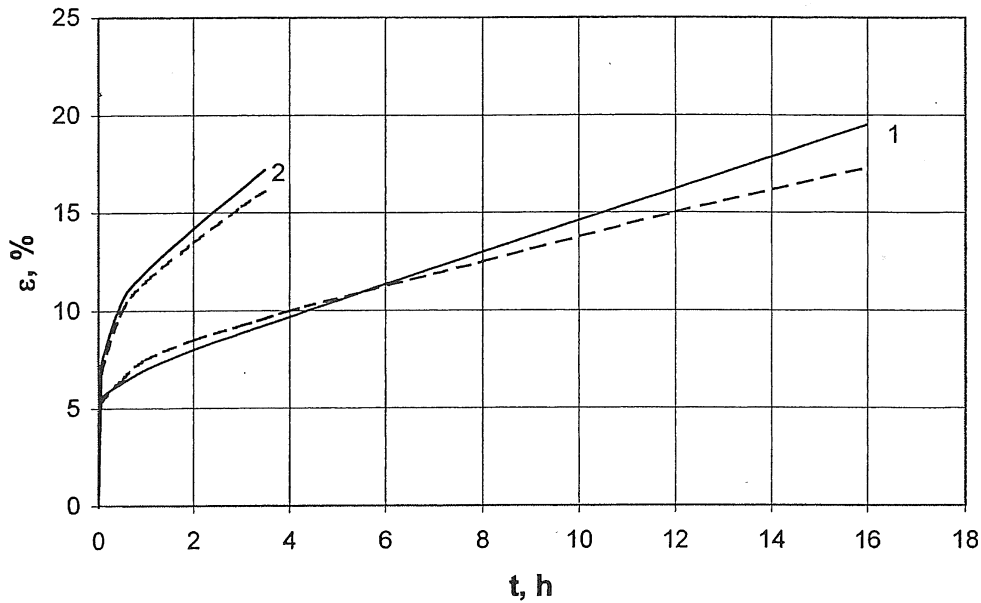


Figure 3. Same as in Fig 2 for 40 deg C.

For the 48 MPa test, creep rate increases with time and leads to instability in tension, a marked "waist" developing on specimens. Another two creep tests are displayed in [Figure 4](#) for extremely high stresses, beyond what should be used for this material, 66 and 70 MPa.



Creep curves at stresses σ : 1–66 MPa, 2–70 MPa. —experimental results, ---- calculated results.

Figure 4. Creep strain (%) for 66 and 70 MPa at 25 deg C vs. time (hours).

CREEP PREDICTION BY MEMORY INTEGRAL

For creep at constant stress when t is large, one has

$$\varphi(\varepsilon) = \sigma \left(1 + \frac{k}{1-\alpha} t^{1-\alpha} \right) \quad (4)$$

The parameters previously listed were used for verification in [Figure 4](#). The creep strain is somewhat underestimated by the prediction from eq. (4). However, the mapping of the short-term behaviour is satisfactory and the same holds for more modest stress levels at modest times, where the predicted creep strain is very close to test results.

It may be interesting to extend this prediction to longer times. In effect, it seems remarkable that long-term behaviour (hours) can be predicted from rapid tensile tests – the slowest of these took merely 45 seconds. It is not surprising, therefore, if predictions for hundreds of hours should become inaccurate.

A modification can be obtained while we still hold on to the original concept. The idea is to adjust or re-determine the material parameters, using creep tests, instead of utilizing rapid tensile tests only. One thus obtains $k=0.15$ (time in hours) and $\alpha=0.85$. This in turn also affects function φ , whose power of strain may be raised from 0.33 to 0.38 (but this was not changed in the present example). In doing so, a close fit to experiments may be reached even for long-term creep, [Figures 5 & 6](#). One obtains by eq. (4) that

$$\varepsilon = \left[\frac{\sigma}{246} \left(1 + \frac{0.15}{1-0.85} t_{hours}^{0.15} \right) \right]^{1/0.33} \quad (5)$$

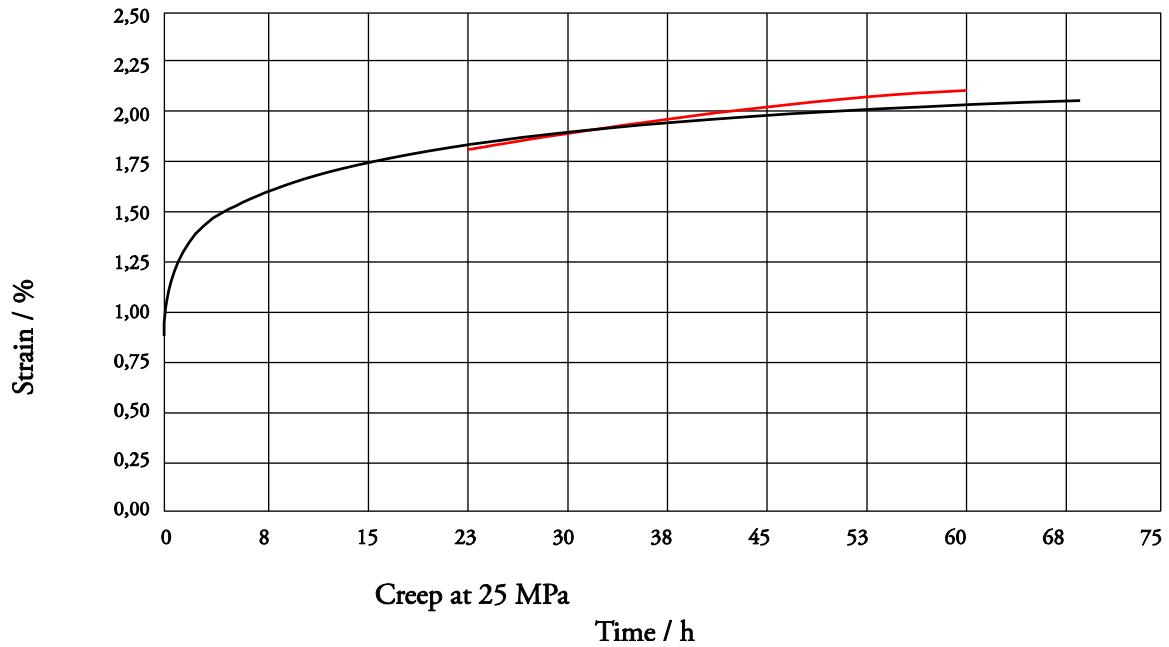


Figure 5. Experimental creep curve (black) and predicted curve (red) for 25 MPa.

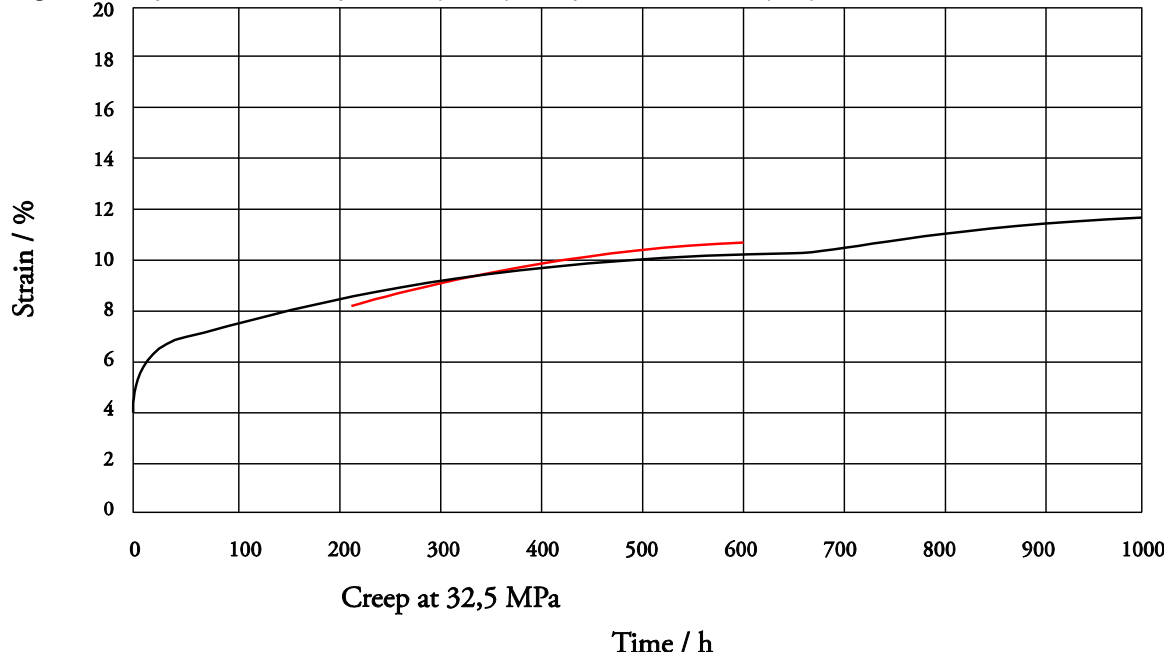


Figure 6. Same as in Fig 5 for 32.5 MPa.

CREEP IN BENDING

Many engineering applications concern beams subjected to bending moment. It is a well-known fact that an inhomogeneous stress state is obtained in bending. Moreover, the stress distribution in the cross-section of the beam should become non-linear in this case, owing to the form of the constitutive law for the material. It calls for a check-up with tests. Deflection was recorded at the outer end of a cantilever beam to which a bending moment was applied in such a way that it was approximately constant along the beam, [Figure 7](#).

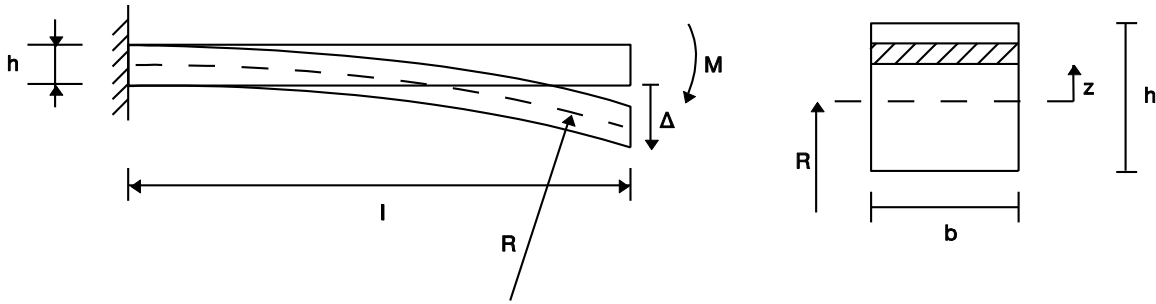


Figure 7. Beam with nomenclature used in test.

Elementary beam theory according to Bernoulli yields (cf [Figure 7](#)) that the strain becomes

$$\varepsilon = \frac{h}{2R} \xi \quad (6)$$

If we assume that stress can be written as

$$\sigma = \sigma_0 \xi^n \quad (7)$$

it is realized that $n=0.33$ is required. Thus, the deflection becomes

$$\delta = \frac{l^2}{2R} = C \frac{l^2}{b^3 h^7} M^3 \left(1 + \frac{k}{1-\alpha} t^{1-\alpha}\right)^3 \quad (8)$$

where

$C=(14/(3 \cdot 246))^3$. The function that relates t to deflection is of the same form as in tension where strain was the dependent variable. Good agreement for short times was obtained, see [Figure 8](#), for two values of M (blue curves). This figure also shows results from cyclic loading (in red) which will be discussed below.

Putting $M=2600$ Nmm yield deflection 14 mm at $t=+0$ which agrees well with test results. For long times, the same approach is recommended, as was suggested above in pure tension.

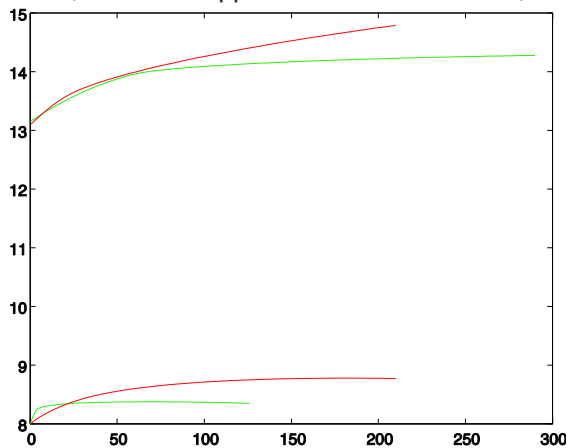


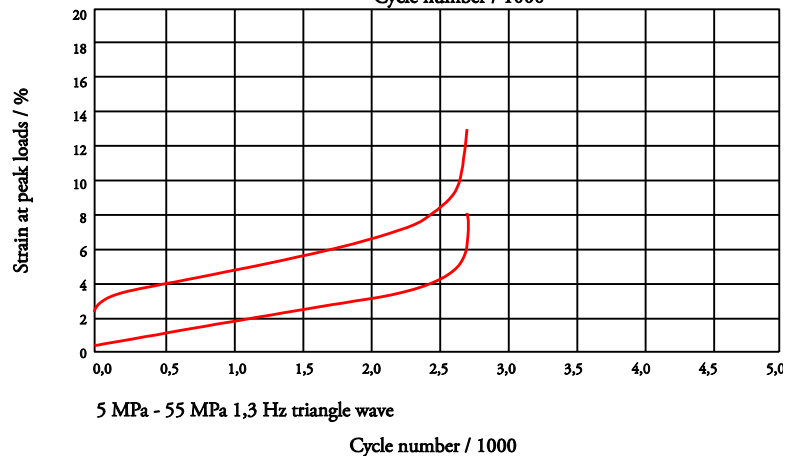
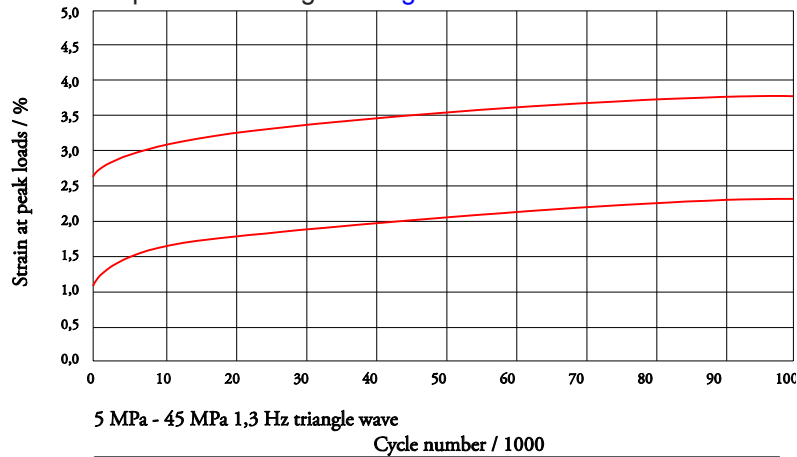
Figure 8. Deflection of beam (mm) vs. time (minutes). Green: static, two values of M . Red: cyclic at max and min load.

CYCLIC LOADING

Tension

Now assume that a pulsating load is applied to the specimen. Sinusoidal time dependence of frequency 1.3 Hz was used. Results are shown in [Figure 9 a, b and c](#) for three stress ranges, strain as a function of number of load cycles. Upper curves denote strain at maximum load during the cycle and lower curves minimum load. The mean stress values are well below those for which creep life was of the order of many hours and even without recorded fracture, see previous creep curves.

Certain tests recorded in [Fig 9](#) ended with increasing strain rate and failure. Some kind of material deterioration obviously takes place. In order to investigate further, temperature was recorded during the test with the highest peak stress and is also shown in [Fig 9](#). This typical plot shows temperature increasing almost linearly with time from 25 to 40 degrees. It is concluded, however, that the temperature increase alone cannot account for the enhanced creep rate, cf static creep test at 40 deg C of [Fig 3](#).



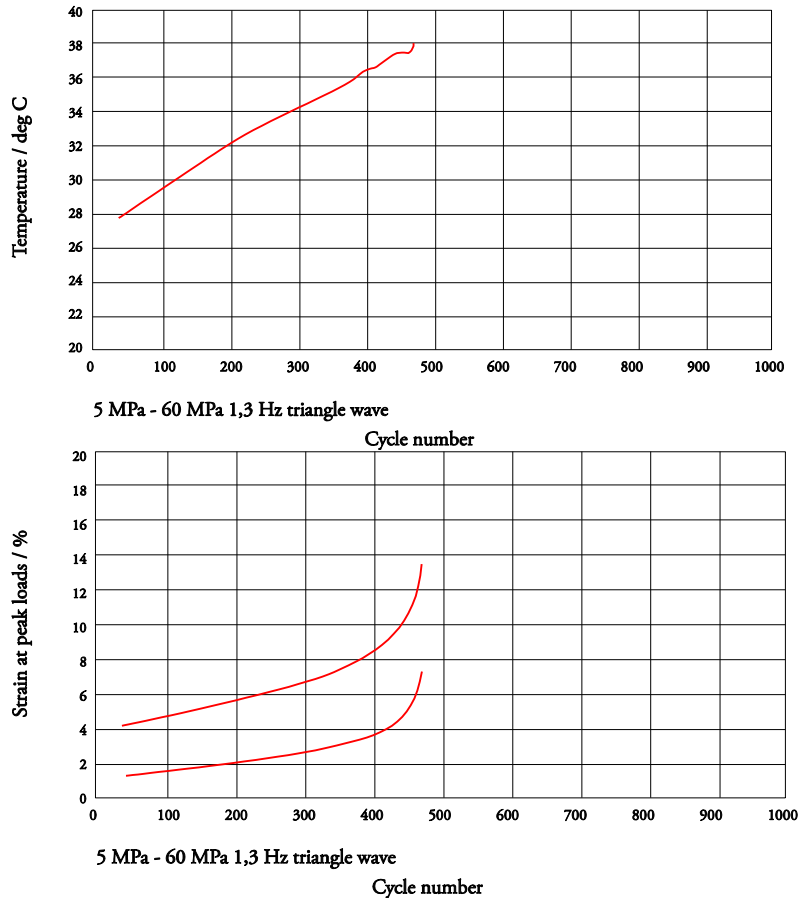


Figure 9. Strain vs. number of cycles for three stress ranges and temperature rise for one of the tests.

Fatigue damage model

Assume that the nominal stress is σ_0 and the nominal cross-section of the specimen is A_0 , whereas the real load-carrying cross-section is A and it carries real stress σ . Further assume that the deterioration is of the form of reduction of real area A , and this reduction is proportional to real stress and number of load cycle increase,

$$dA = -\sigma k dN = -\sigma_0 A_0 k dN / A \quad (9)$$

k being a factor of proportionality.

Integration, taking into account that $A=A_0$ at $N=0$ gives

$$\sigma = \sigma_0 / \sqrt{1 - 2\sigma_0 N k / A_0} \quad (10)$$

If failure is supposed to occur when the ultimate tensile stress σ_B is reached, the number of cycles to failure by fatigue damage can be found:

$$N_B = [1 - (\sigma_0 / \sigma_B)^2] / [2\sigma_0 k / A_0] \quad (11)$$

Bending

A similar investigation was undertaken in bending of the beam previously described, now with cyclic load applied. Results are shown in Fig 8, red curves. Maximum and minimum deflection during the cycle were plotted. Deflection increases somewhat faster with cyclic load than with static creep load in this bending case as well, but the increase is not so evident as it is in pure

tension. This bending test could not be continued for long, because of the experimental arrangement which caused a reduction of M when deflection became considerable.

DISCUSSION

Non-linear viscoplastic materials can be characterized by an integral equation which relates strain at a particular time to the instantaneous load as well as to the load history. It is an attractive thought that a few tensile tests at different stress or strain rates may be sufficient for deriving this equation which may be used for any type of loading.

Quantities like strain, deflection and elongation were shown to contain a shape function of type

$$\left[P \left(1 + \frac{k}{1-\alpha} t^{1-\alpha} \right) \right]^\gamma \quad (12)$$

where P is a generalized load and γ is a parameter which stems from the power law for the instantaneous stress-strain curve, $\phi = c \cdot \epsilon^{1/\gamma}$, $\gamma > 1$. Parameters k, α , γ and c may need to be adjusted by means of creep curves, if integral equation is to be used for prediction of long-term behaviour.

[Figure 10](#) illustrates the shape function of eq. (12) for a few sets of parameters. Stepwise changes of P can be handled in integrating eq. (1), but eq. (12) is not accurate for times immediately after a change in P.

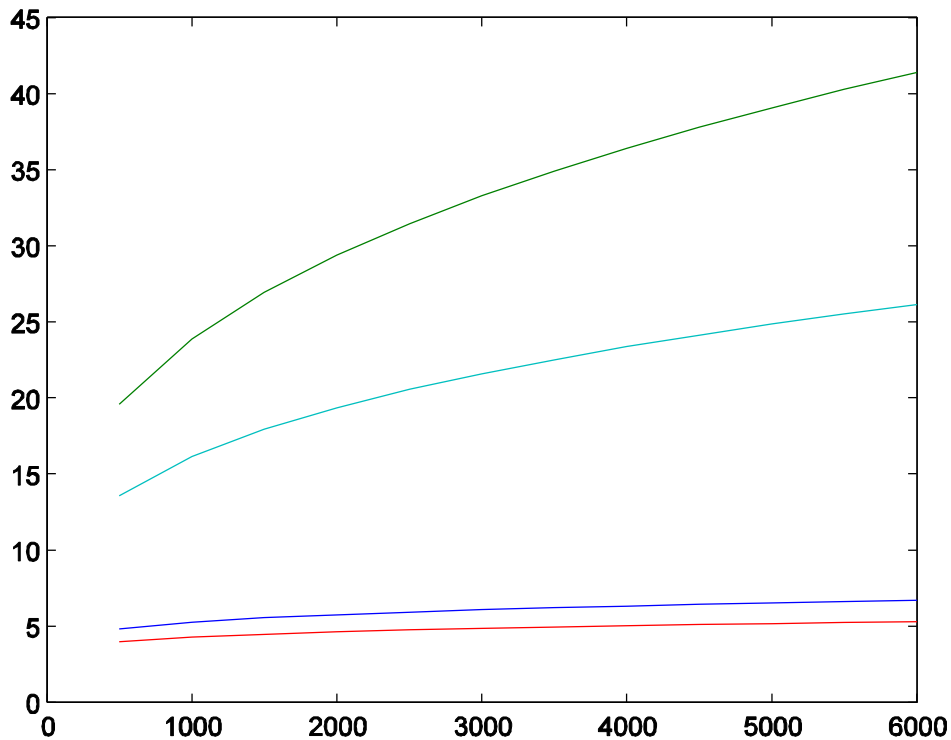


Figure 10. Principal behaviour of creep strain vs. time (minutes). $k=0.037$, $\alpha=0.9$, $\gamma=3$ and 2.63 (curves 2 & 1), further $k=0.15$, $\alpha=0.85$, $\gamma=3$ and 2.63 (curves 4 & 3), in order from bottom.

In [3], Vinogradov et al have applied the hereditary type equation for solving creep problems in PVDF which is a polymer with piezoelectric properties, whose mechanical behaviour is similar to that of POM.

CONCLUSIONS

Creep under static or stepwise changing load is rather accurately described by the hereditary equation. Cyclic load may cause material damage and eventually decrease, or even imply complete loss of, load-carrying capability, similar to fatigue in metals. The damage may start developing at first load cycle – indication of this is the heat dissipation in the specimen – or it may start after a certain number of cycles, for example, when the strain rate begins to increase. This requires further testing. However, the simple model for damage outlined above may serve as a first approximation of the lifetime under combined creep and fatigue conditions.

ACKNOWLEDGEMENT

The author is grateful to Hans Öberg and Martin Öberg, who carried out most of the tensile testing, and to Sven R Ohlson who assisted in improving the graphics of this paper.

REFERENCES

- [1] Suvorova, JV et al, An approach to the description of time-dependent materials, *Materials & Design* **24** 293-297 (2003)
- [2] Suvorova, JV et al, Temperature influence in the description of time-dependent materials, *Materials & Design* **24** 299-304 (2003)
- [3] Vinogradov, AM et al, Damping and electromechanical energy losses in the piezoelectric polymer PVDF, *Mechanics of Materials* **36** 1007-1016 (2004)

Mechanical Characterization of SLM Specimens with Speckle Interferometry and Numerical Optimization

C. Barile, C. Casavola, G. Pappalettera, C. Pappalettere
Politecnico di Bari, Dipartimento di Ingegneria Meccanica e Gestionale
Viale Japigia 182, Bari, 70126, ITALY
E-mail: casavola@poliba.it

ABSTRACT

This paper describes the process of mechanical characterization of specimens built via Selective Laser Melting (SLM). An hybrid approach based on the combination of phase-shifting electronic speckle pattern interferometry (PS-ESPI) and finite element analysis is utilized. Three-point-bending experimental tests are carried out. The difference between displacement values measured with ESPI and their counterpart predicted by FEM analysis is minimized in order to find the values of the unknown elastic constants.

1. INTRODUCTION

In Selective Laser Melting (SLM) parts are built by adding layers of metal powder. A focused laser beam selectively fuses powdered material by scanning cross-sections generated from a 3D CAD model of the part on the surface of a powder bed. After each cross-section is scanned, the powder bed is lowered by one layer thickness, a new layer of material is applied on top, and the process is repeated until the part is completed.

In order to obtain high density parts the powder mixture and SLM process parameters must be optimized. Since controlling all parameters involved in the manufacturing process may be very complicated, accurate mechanical characterization of SLM components is mandatory to properly assess mechanical response. The most general approach to mechanical characterization of materials is to search for an inverse solution of the elastic problem. In fact, the displacement field of a specimen generally loaded and constrained is univocally defined if material properties are known. This reverse engineering problem can be solved by minimizing the difference between displacements measured experimentally and their counterpart computed by FEM analysis.

Non-contact optical techniques such as *Electronic Speckle Pattern Interferometry* (ESPI) [1,2] fit very well in the identification process in view of their capability to accurately measure displacements in real time and to gather full field information without altering specimen conditions. ESPI can measure displacement components $u(x,y,z)$, $v(x,y,z)$ and $w(x,y,z)$ for each point (x,y,z) of the specimen surface. A system of fringes will appear on the specimen surface and each fringe represents the locus of an iso-displacement region. The frequency distribution of fringes can be used for recovering strain fields.

In this research, three-point-bending tests are carried out on SLM specimens. The experimental protocol was chosen in order to avoid rigid body motion and prevent speckle pattern decorrelation. The difference between the displacement field experimentally evaluated by ESPI and the displacement field computed with FE analysis is minimized. Elastic constants are in good agreement with results obtained of other experimental tests carried out independently.

2. EXPERIMENTAL TESTS

The three-point bending test was carried out on a prismatic sample made of AISI MARAGING 300. The specimen is long 127 mm, thick 7 mm and tall 7 mm. The specimen was placed on two supports placed at a distance of 90 mm. The SLM beam was preloaded in order to minimize rigid body motions which may cause speckle decorrelation. A thin coating layer was sprayed onto the specimen surface to improve contrast of speckle fringes. The loading apparatus is shown in [Figure 1](#) together with a detail of the ESPI setup. A 2 kg loading cell DS514QD was connected to the wedge in order to measure the applied load. Data were recorded by the System 5000

acquisition system. The load was transferred by a micrometric translational stage which pushes the loading wedge against the specimen.

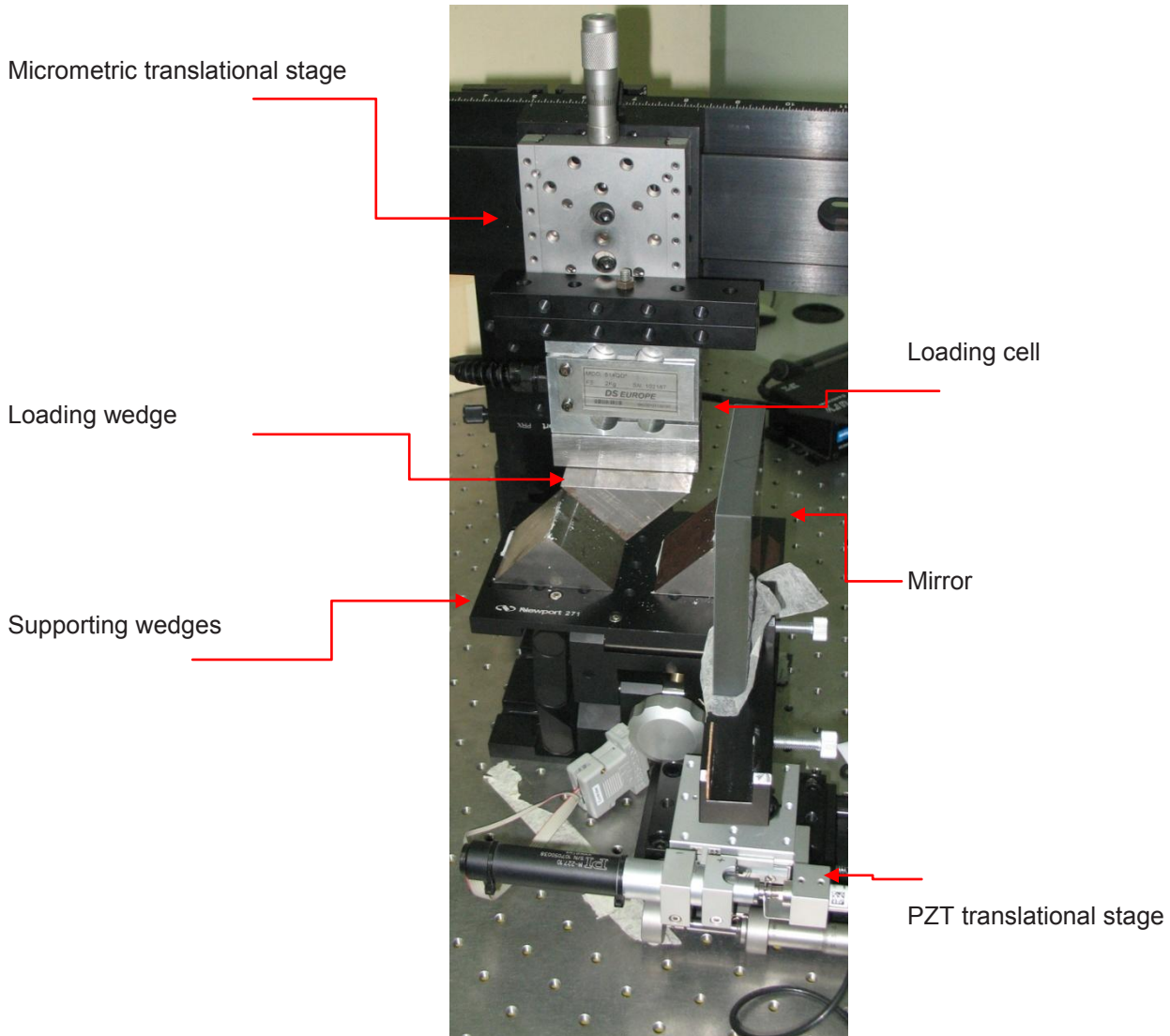
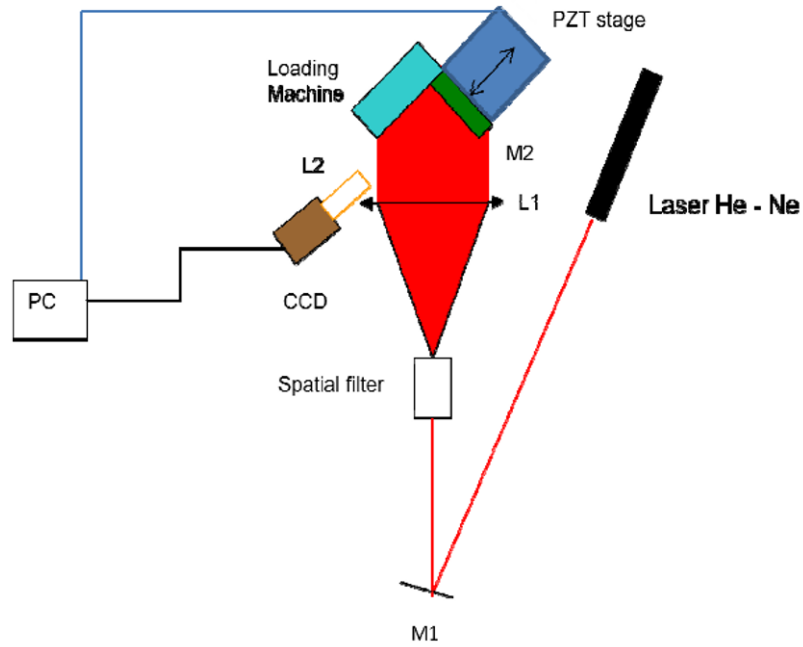


Figure 1. Loading apparatus and detail of the optical setup

The scheme of the optical set-up used for measuring u -displacements is shown in [Figure 2](#). It essentially consists of a double illumination Lendeertz interferometer [1,2]. The light emitted by a 17 mW He-Ne laser source ($\lambda=632.8$ nm) is expanded by a 20X microscope objective lens and spatially filtered by a 10 μm aperture pin-hole. The beam emerging from the pin-hole is successively collimated by the L1 plano-convex lens ($\phi=2''$, $f=40$ cm). One half of the beam is then sent towards the specimen under testing at the illumination angle $\theta_1=45^\circ$. The rest of the beam is intercepted by the planar mirror M2 that reflects the light towards the specimen thus realizing symmetric double illumination. The mirror is placed on a piezoelectric translational stage which allows the motion along the horizontal direction, parallel to the direction of sensitivity. The PZT is driven by a stabilized high-voltage power supply controlled by a PC. The minimum incremental displacement that can be generated is $d_m=10$ nm. Details of recording system are also presented in [Figure 2](#).



Number of pixel in the CCD sensor	1628 x 1236
Bit depth	8 bit
Field of View	21 mm
Working Distance	32 cm

Figure 2 Schematic of the double illumination ESPI setup and details of the recording system

Each beam generates a speckle pattern on the specimen surface. The superposition of those patterns leads to have the following distribution of intensity:

$$I(x, y) = I_{01}(x, y) + I_{02}(x, y) + 2\sqrt{I_{01}(x, y)I_{02}(x, y) \cos \gamma(x, y)} \quad (1)$$

where I_{01} and I_{02} are the background intensities while γ is the phase difference between the beams. If a point of the specimen surface displaces along the direction of sensitivity, Eq. (1) can be rewritten as:

$$I(x, y) = I_{01}(x, y) + I_{02}(x, y) + 2\sqrt{I_{01}(x, y)I_{02}(x, y) \cos(\gamma(x, y) + \Delta\varphi(x, y))} \quad (2)$$

The phase difference $\Delta\varphi$ is related to the u -displacement by the following equation:

$$\Delta\varphi = \frac{4\pi}{\lambda} u \sin \vartheta \quad (3)$$

Fringes are hence iso-displacement loci and the difference in displacement between points lying on two adjacent fringes is:

$$u = \frac{\lambda}{2 \sin \vartheta} \quad (4)$$

According to Eq. (4), the sensitivity of optical set-up is 447 nm.

Phase shifting was utilized in order to obtain the phase distribution of the speckle pattern. For that purpose, a shift in phase between the two beams was introduced by changing the optical path of one of the arms of the interferometer. Phase variations were produced by moving the PZT stage. Among the different phase shifting strategies available in literature [3], the five frame algorithm which consists in recording five interferograms with a relative phase shift $\delta = \pi/2$ was utilized. The intensity patterns corresponding to each phase shift can be described by the following equation:

$$I^{(n)}(x, y) = I_{01}(x, y) + I_{02}(x, y) + 2\sqrt{I_{01}(x, y)I_{02}(x, y)} \cos(\gamma(x, y) + \Delta\varphi(x, y) + n\frac{\pi}{2}) \quad (5)$$

Finally, the phase difference is computed as follows:

$$\Delta\varphi(x, y) = \tan^{-1} \left(\frac{2I^{(1)}(x, y) - I^{(4)}(x, y)}{2I^{(3)}(x, y) - I^{(5)}(x, y) - I^{(1)}(x, y)} \right) \quad (6)$$

The PZT was calibrated by recording an initial speckle pattern and moving the mirror at incremental steps of 10 nm. The speckle pattern corresponding to each shifted position was subtracted from the initial speckle pattern until a minimum of intensity was observed. The corresponding distance travelled by the PZT was related to the change of optical path yielding a 2π phase shift. Calibration of the camera pixel was done by recording the image of a calibration target and sampling the distance between two calibration marks with a certain number of pixels. The spatial calibration was 15 μm .

Specklegrams were processed using the procedure schematized in Fig.3. For each shift of phase the difference between the recorded image and the reference image was determined by digitally subtracting speckle patterns. A 9x9 pixel square median filter was then applied to the five images in order to reduce noise. A mask was applied in order to select the region of interest. Equation (5) was used in order to obtain the wrapped phase. Phase unwrapping operation was carried out by means of the minimum spanning tree algorithm [4]. Finally, displacement maps were recovered by using the scaling equation (3).

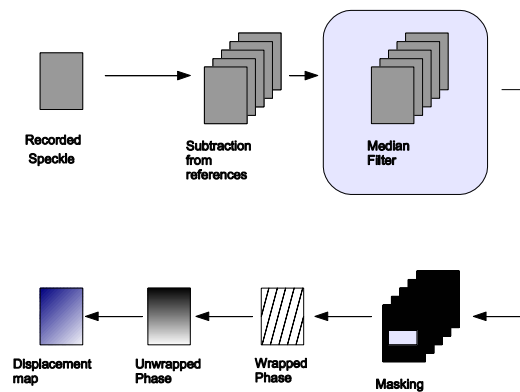


Figure 3. Flow chart of fringe processing

3. FEM ANALYSIS

A finite element model was developed in order to simulate the 3-point-bending test. The specimen is long 127 mm, tall 7 mm tall and thick 7 mm thick. Because of structural symmetry, only one half was modeled. The region

of interest considered along the x-direction was about 63 mm. Kinematic constraints were imposed in order to obtain a symmetric model and to reproduce correctly the mechanism with which the load is transferred to the specimen. FE analysis was carried out with the ANSYS 11.0 commercial software [5]. The specimen was modeled with three-dimensional elements SOLID45 including 8 nodes each of which has 3 degrees of freedom, the translations in the coordinate directions X, Y and Z. Although specimen thickness is small compared to length, the bar under 3-point-bending was however modeled as a 3D specimen in order to account for asymmetries eventually occurring in the loading process or related with constraint conditions. For example, it was seen that the specimen does not adhere perfectly to supports during the loading phase.

The specimen material was assumed as isotropic and linearly elastic. This modeling choice is justified by the fact that SLM specimens are realized layer by layer and each layer may be considered as isotropic. The experimental evidence seems to confirm this assumption: in fact, the u_x displacement measured through the thickness became null at the specimen midplane.

Convergence analysis was carried out in order to refine the model and to obtain a mesh independent solution. The mesh included 24500 elements and 28350 nodes (see Figure 4 with indications of loads and constraints). Mesh size was consistent with sampling of the speckle pattern. All finite element analyses were run on a standard PC equipped by an Intel® Pentium Dual-Core processor and 3GB RAM memory. The structural analysis was completed in about 5 minutes.

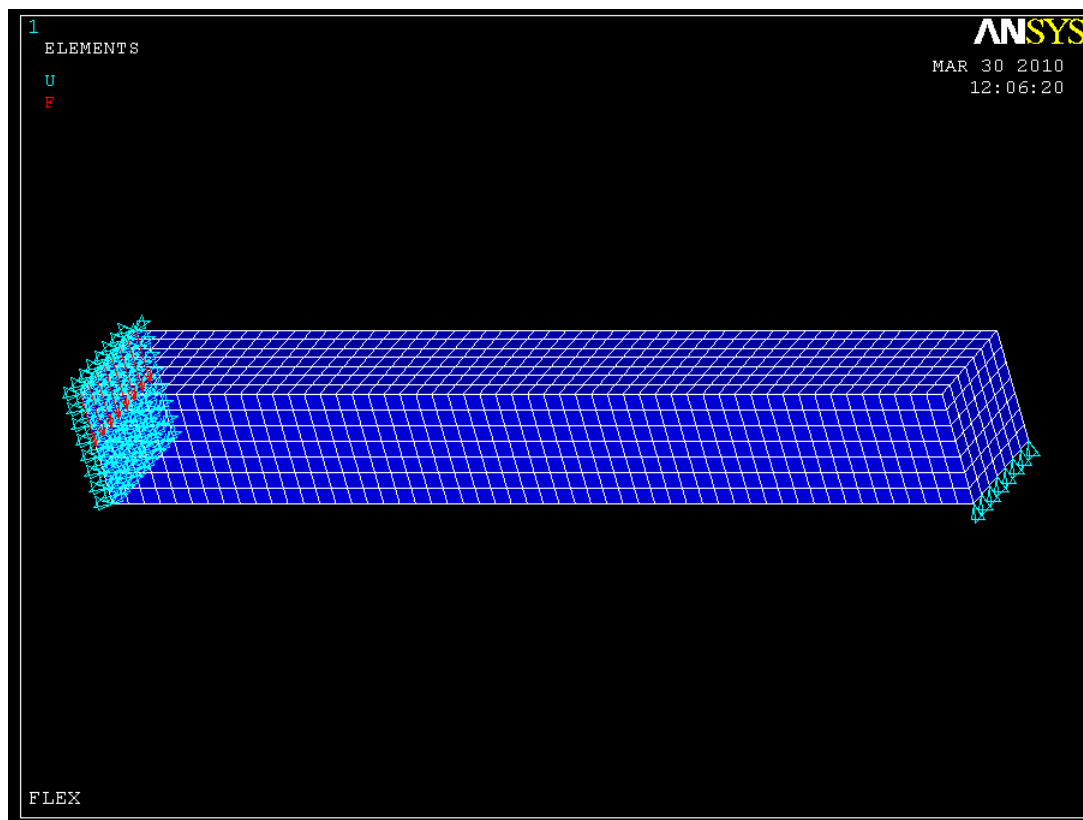


Figure 4. Finite element model of the 3-point-bending test simulated numerically

4. RESULTS AND DISCUSSION

The horizontal displacement measured by ESPI was taken as target value of FE analysis, Elastic constants were previously determined by standard mechanical tests: the Young's modulus was 152 ± 25 GPa while the Poisson's ratio was 0.3 ± 0.02 . In order to obtain redundant information two control locations were considered respectively at the distances of 2 and 4 mm from the constraint wedge. This region was far enough from the region where the load is applied to the specimen and therefore displacement values were practically the same.

Table 1 shows the results obtained by perturbing elastic constants. The data reported in the table are relative to different loads ranging from 183.5 to 398.5 g. It can be seen that the error on measured displacements is reduced as the loading level increased. This can be explained with the fact that rigid body motions should decrease at higher loads. It appears that at loads smaller than 300 g the system does not have enough sensitivity to record correctly the load-displacement path. This is confirmed by the sharp reduction in the displacement percent error observed until the load stays below 300 g. The residual error on displacements became less than 0.7% when the Young's modulus is equal to 140 GPa.

Table 1. Error on elastic constants for different load values

Applied Load [g]	Δu_x EXP [nm]	E=152 GPa		E=140 GPa	
		Δu_x FEM [nm]	Percent Error	Δu_x FEM [nm]	Percent Error
183.5	371	311	16.17%	337	9.16%
227.5	436	385	11.70%	419	3.90%
307.5	560	521	6.96%	565	0.89%
398.5	728	675	7.28%	733	0.68%

As expected iso u -displacement bands are almost parallel in the specimen region near the supporting wedges. The experimental pattern (Figure 5) is in excellent agreement with FE results (Figure 6). The difference in displacement between points located on vertical lines at different distances from the constrained edge of the specimen was found to be insensitive to the position. The same conclusion can be drawn for all load levels considered in the experiments.

Remarkably, the experimentally measured values of u -displacement were found to be symmetric with respect to the midplane of the specimen. This seems to confirm the assumption of isotropy made in the numerical analysis,

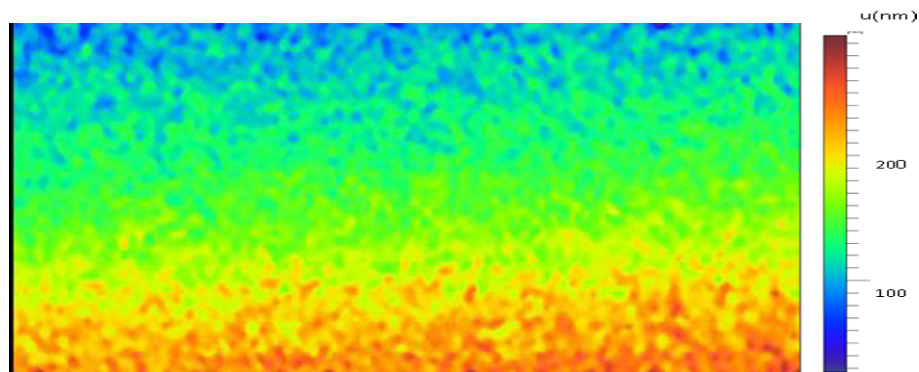


Figure 5. Horizontal displacement map near supporting wedge

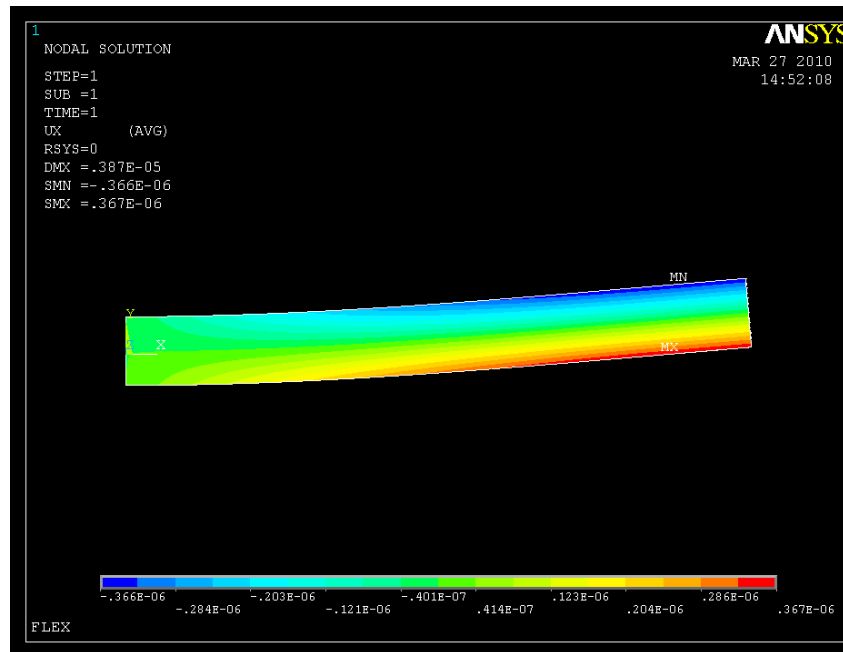


Figure 6. Horizontal displacement map evaluated via FEM

5. CONCLUSION

This paper presented a hybrid approach to characterize SLM specimen made of AISI MARAGING 300 steel. The displacement field under three point bending was measured by means of PS-ESPI and compared to FE predictions. Elastic constants were tuned until FE results matched experimental measurements. The procedure successfully converged to the value of flexural stiffness measured independently.

6. REFERENCES

- [1] Cloud G.L. *Optical Methods in Engineering Analysis*. Cambridge University Press, New York (USA), 1998.
- [2] Sciammarella C., " Overview of optical techniques that measure displacements: Murray Lecture", *Experimental Mechanics*, **43**, 1, 1-19, 2006
- [3] Creath, K. "Phase shifting speckle interferometry" *Applied Optics*, **24**, 18, 3053-3058, 1995
- [4] Ching N.H., Rosenfeld D. and Braun M., "Two-dimensional phase unwrapping using a minimum spanning tree algorithm", *IEEE Transactions on Image Processing*, **1**, 3, 355-365, 1992
- [5] The ANSYS 10.0 Users' Manual, Swanson Analysis System Inc., 2005

Torsion/compression Testing of Grey Cast Iron for a Plasticity Model

Timothy A. Doughty, Ph.D, Assistant Professor, University of Portland, 5000 N Willamette Blvd, Portland OR 97203, doughty@up.edu, Mary LeBlanc, Lee Glascoe, Ph.D. and Joel Benier, Ph.D. Lawrence Livermore National Laboratory (LLNL)

Abstract

To characterize the yield surface, combined torsion/compression experiments were conducted to help develop a plasticity model for grey cast iron. Loadings were sequential, allowing for better exploration of yield under different conditions. Hollow cylindrical specimens were machined and strain measurements were taken with multiple strain gages and verified with a digital image correlation system. With the use of effective and von Mises stresses and strains, test results produced intermediate data points for a plasticity model, such as the Johnson-Cook model. The data is shown to follow the predicted relationship qualitatively.

Introduction

Viscoplasticity models are used extensively in the simulation of large scale deformation. There are many models to choose from, with the appropriateness of the model form being dependent on the types of load conditions one wishes to simulate (Banerjee, December 2005). Furthermore, the model forms themselves are often under development. In essence, many modern materials (i.e. steel, aluminum, brass, etc), have working models that are well defined and largely accepted. Accurately modeling the behavior of cast iron is not as well defined. This paper describes a set of experiments providing combined torsion/compression data which, when employed with pure compression and pure tension data, characterize the yield surface for the cast iron material over a range of load conditions. In each case the loads were sequential, allowing for better exploration of the yield and failure models. Models for material behavior under combined loading have long been sought; see, for example, (Wilkins & Reaugh, 1980). The method of applying loads here produced intermediate data points for a plasticity model, such as the Johnson-Cook (Johnson & Cook, 1985) model.

Experimental Configuration

For the tests presented here, hollow cylindrical specimens were machined from a homogeneous set of cast iron samples. The specimens, shown in [Figure 1](#), were instrumented with two vertical axial gages and one rectangular rosette gage of vertical orientation, equispaced around the cylinder's perimeter. Additionally, a section of the surface was treated for strain measurement using an ARAMIS digital image correlation (DIC) system.

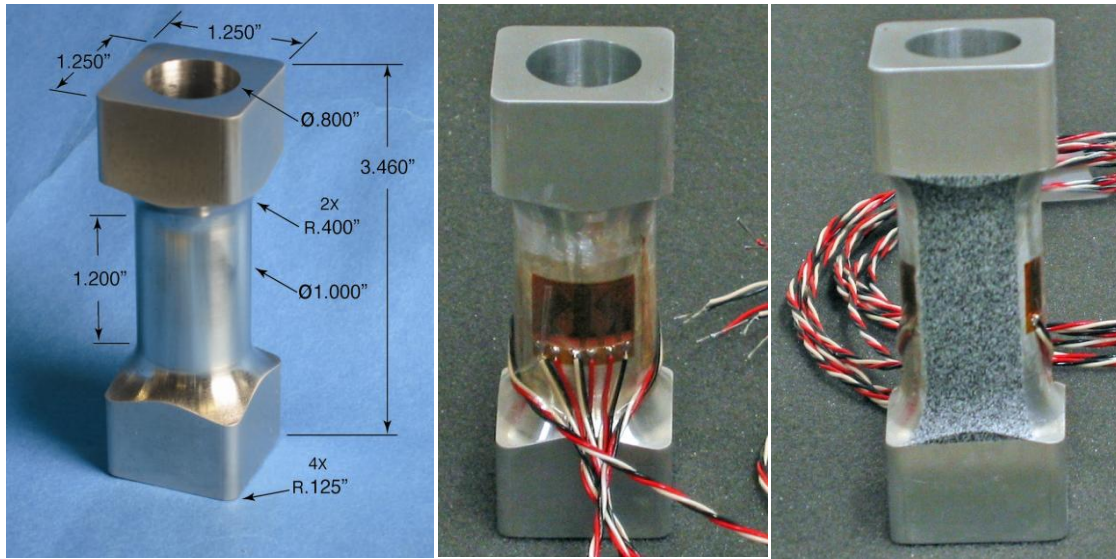


Figure 1 The compression/torsion sample instrumented with strain gages and with a speckle pattern for image correlation.

The tests were performed in a servo-hydraulic test machine having both axial and torsional capability. The sample was loaded in a subpress (Figure 2) which was accurately positioned along the rotational axis of the test machine actuator. Loading of the samples was performed in displacement (or rotation) control at a nominal strain rate of 10-4/s. The load, torque, and strain measurements were recorded on a Nicolet Vision System. Preliminary tests were run on aluminum alloy specimens to ensure correlation between the strain gage and DIC readings. It was determined that the strain gages produced better (less noisy) measurements at low strains. At larger strains (typically above 2%) the gages exceeded their usable range and were prone to break bonds with the specimen, and the DIC results were used. Several types of experiments were performed on the cast iron samples: pure torsion, elastic compression followed by torsion, and compression past yield followed by torsion.



Figure 2 Test configuration for combined compressive and torsional loading.

Results and Analysis

Representative data for average shear stress- shear strain results are shown in Figure 3a for the second of the four tests. The ARAMIS data provides results beyond the usable range of the strain gages. ARAMIS results at the indicated four instances during the experiment are shown in Figure 3b. The blue and green regions at the ends are on the radius section of the sample, which was outside the gage length. Data from the rectangular area in the middle was averaged to compare with the strain gage data. The light blue section line, which was vertical in the undeformed state, indicates the extent of shear rotation.

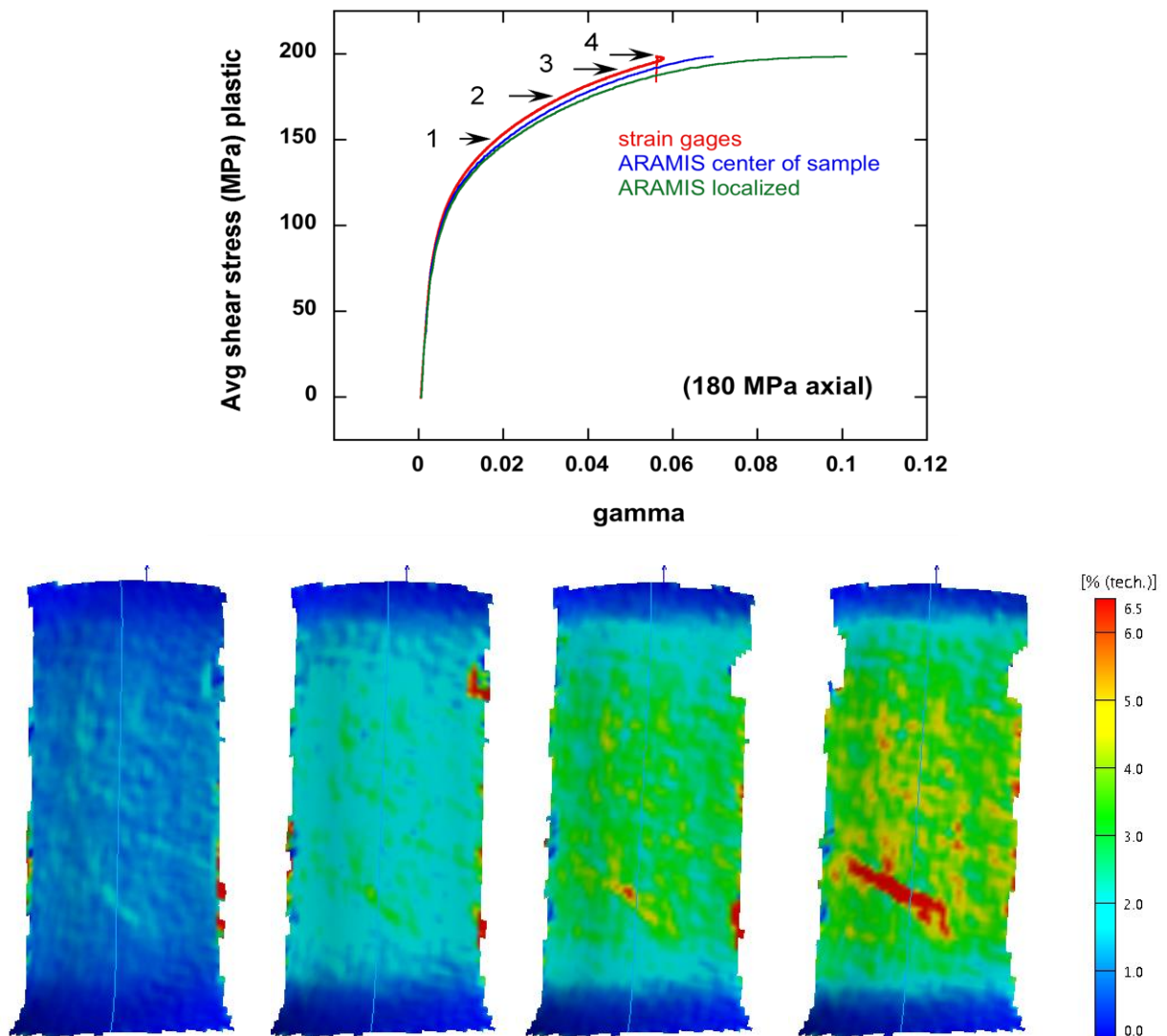


Figure 3 Representative shear stress-shear strain results (a) with a detail of the ARAMIS results at four stages during the loading (b).

The first test involved torsional loading only. Torque was increased through yielding and failure. A small axial load was sensed, resulting from the deformation associated with the applied torque. In this and each subsequent test with combined loading, the state of stress and state of strain were transformed to their principal values and then to their equivalent, or von Mises, values. In this way shear and axial components were resolved. The first test results, shown in Figure 4, demonstrate a smooth transition between the elastic and plastic region. An approximation of the linear relationship and the 0.2% convention were used to identify the yield point, and the strain at fracture is recognized as the rightmost data point.

The two curves represent bounds for the approximation of shear stress. Linear elastic theory proved an estimate of the maximum shear stress, $\hat{\tau}$, resulting from the measured applied torque, \hat{T} , with:

$$\hat{T} = \frac{\pi(r_o^4 - r_i^4)}{2r_o} \hat{\tau} \quad \text{EQ (1)}$$

where r_i and r_o are the inner and outer radii of the cylinder. In the model adjusted for plasticity, we assume the shear stress varies linearly over the wall thickness and apply equilibrium. The resulting average shear stress, $\bar{\tau}$, is given with:

$$\hat{T} = \frac{2\pi(r_o^3 - r_i^3)}{3} \bar{\tau} \quad \text{EQ (2)}$$

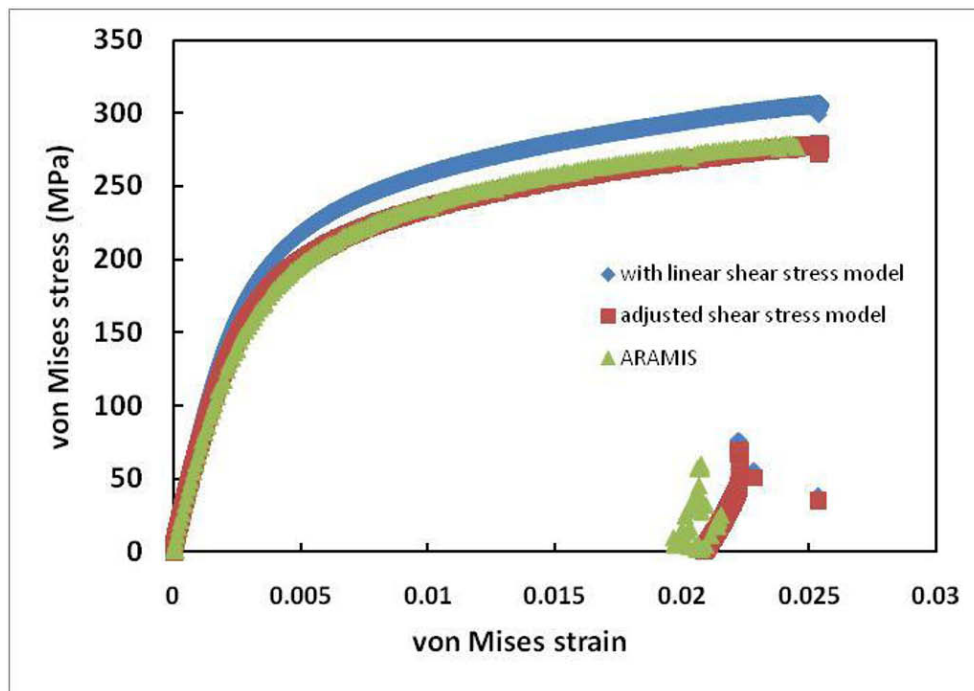


Figure 4 Von Mises stress strain results for purely torsional loading.

In the second experiment an initial compressive loading of approximately 90% of the yield strength (correspondingly 7380 lb.) was applied. This compressive load was then maintained, and the torsional

loading was increased until the specimen failed (Figure 5). In the effective stress/strain regime the different loadings produce different slopes, owing to the material's asymmetries. The material is less inclined to deform under compression than it is under torsion. Results during the compressive stage of the test produce estimates of Young's modulus that are consistent with those presented earlier for the ASTM standardized compression tests. Here, again, the slope of the linear region and the 0.2% convention were used to determine a yield point, and the point of fracture is clear.

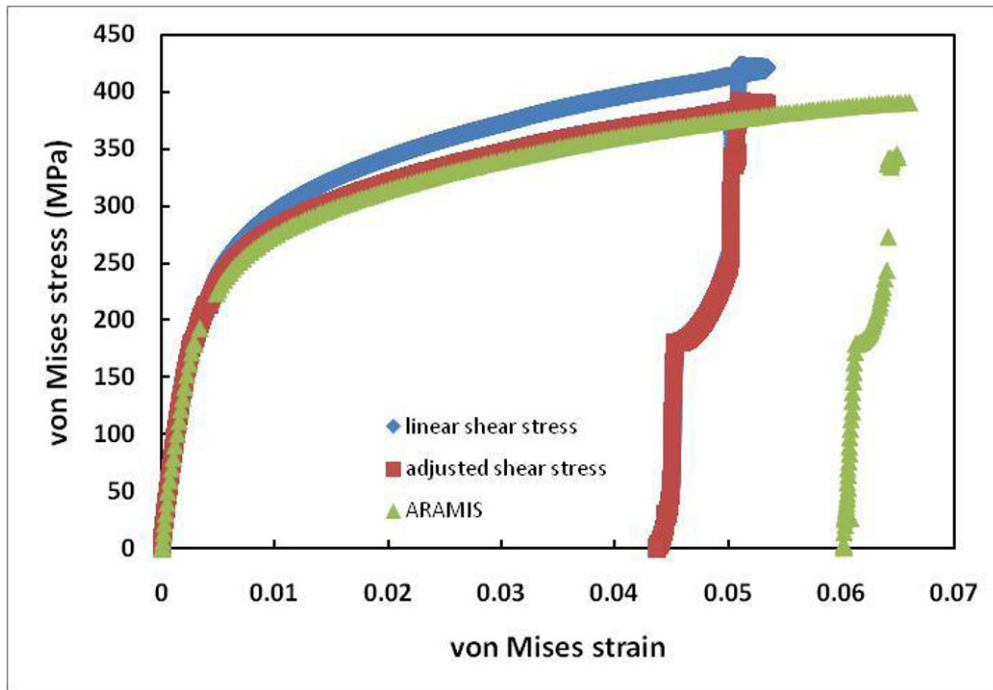


Figure 5 von Mises stress strain results for sequential compressive and torsional loading, with compressive loading to 90% of the yield strength.

In the third test the initial compression was held at 50% of yield (4095 lb) and the sample was again rotated until failure (Figure 6). Results show the transition from the linear region is more clearly defined and the estimate of yield point and fracture are obtained. The final test was given a compressive load of 15945 lb, which took the material beyond its yield point to 2% axial strain (Figure 7). With the compression held, torsion loading was increased to failure. The yield strength produced under compression here is consistent with those found for the prior in the study.

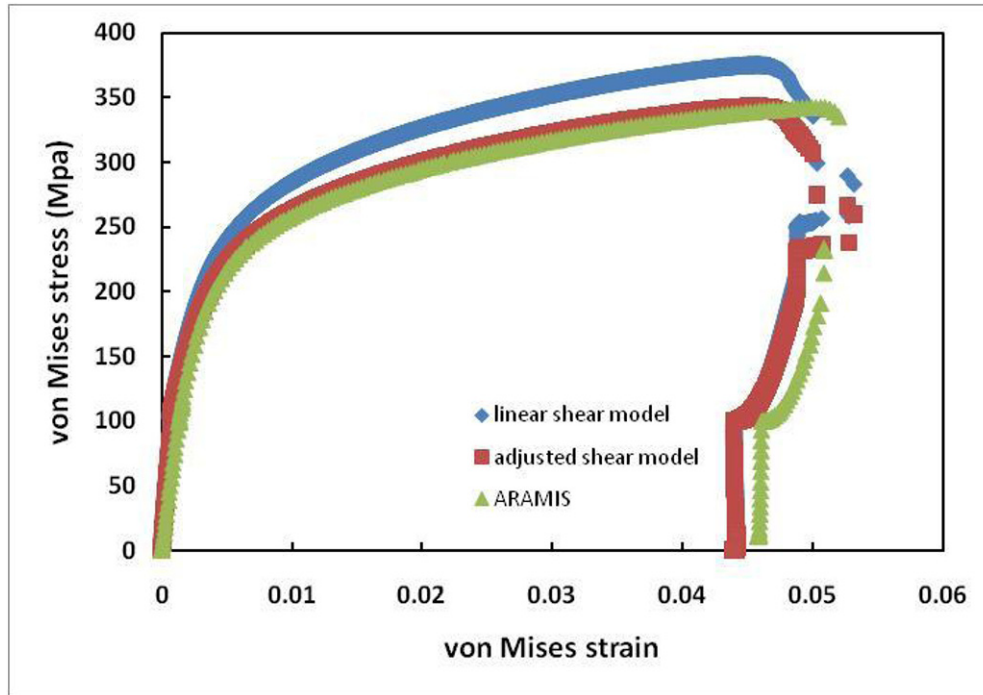


Figure 6 Von Mises stress strain results for sequential compressive and torsional loading, with compressive loading to 50% of the yield strength.

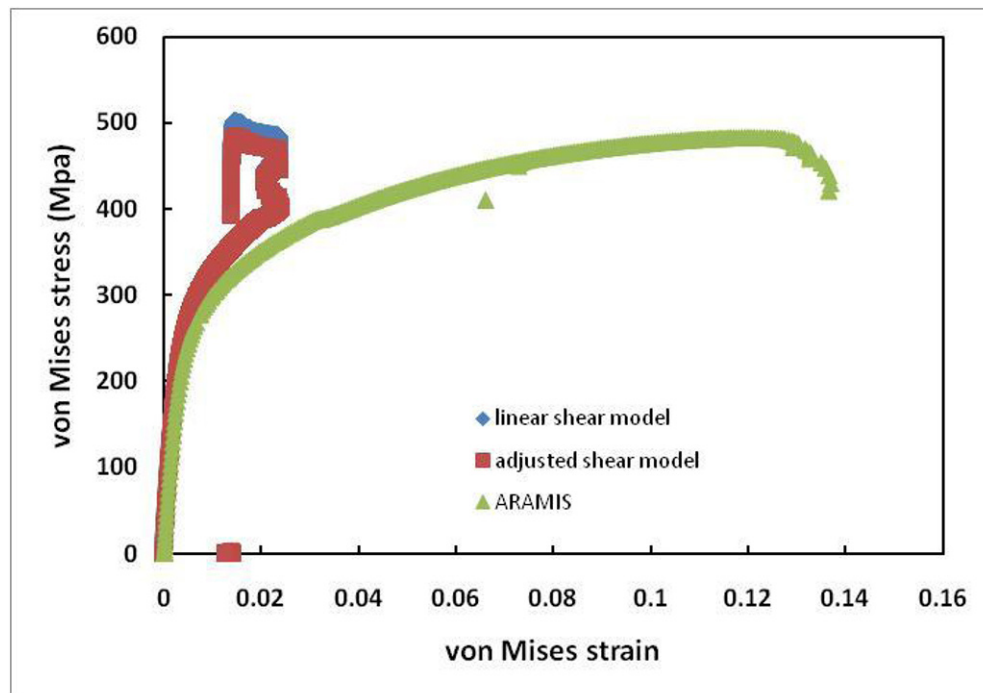


Figure 7 Von Mises stress strain results for sequential compressive and torsional loading, with compressive loading exceeding the yield strength.

The four tests illustrate the relationship between the effective yield stress and the pressure stress ratio, σ^* , where the pressure stress ratio is defined as the pressure (or average principal stress) over the von Mises stress (Figure 8). Here we see the cast iron yielding least readily to pure compressive loads at $\sigma^* = -1/3$ than under pure torsion $\sigma^* = 0$. This and the combined loading scenarios provide intermediate points along the curve. A plasticity model, such as the Johnson-Cook model, can be built assuming temperature and strain rate dependence; the resulting simplified form is a plot of effective strain at fracture vs. the pressure stress ratio following an expected exponential trend (Figure 9).

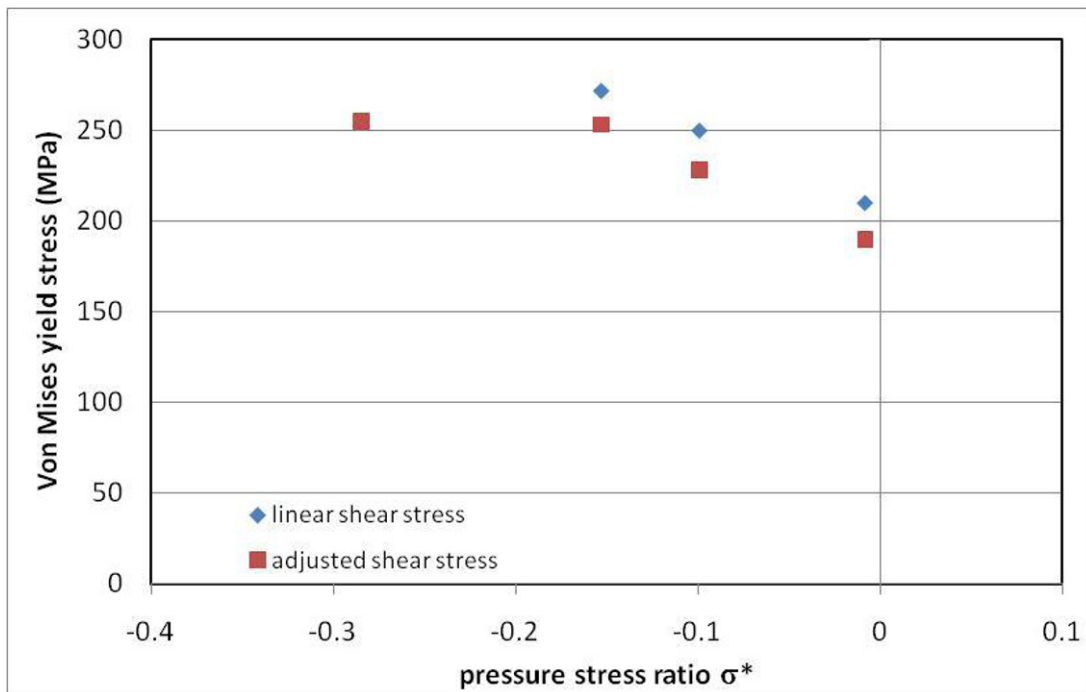


Figure 8 Von Mises yield strength (MPa) versus pressure stress ratio.

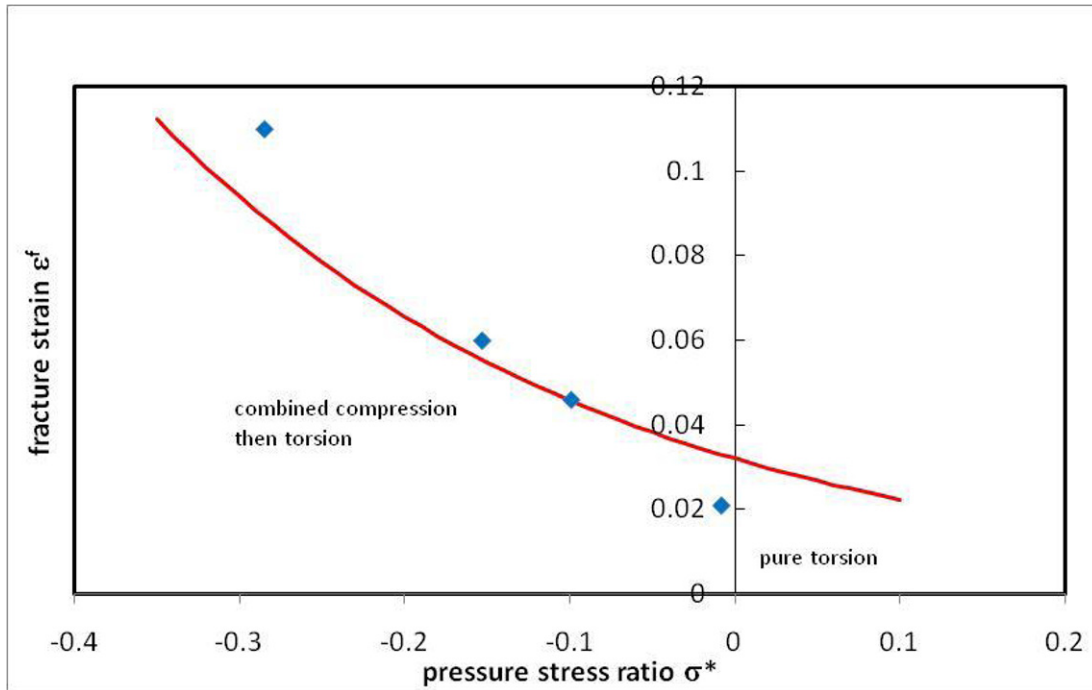


Figure 9 Fracture strain versus pressure stress ratio.

Conclusions

A set of sequentially-loaded experiments provided combined torsion/compression data to help characterize the yield surface for cast iron material over a range of load conditions. The method of applying loads here produced novel results which can be used in conjunction with data from traditional testing methods to populate and validate viscoplasticity models as suggested by, for instance, the Johnson-Cook (Johnson & Cook, 1985) model. These models can then be applied to the simulation of large scale deformation. While the appropriateness of the given model form can vary from application to application, the results here are accurate and unique for cast iron, albeit independent of temperature and strain rate effects.

Additionally, a method of approximating the shear stress associated with torsional loading is introduced. This method provides estimates for the stress strain relationship for materials undergoing plastic deformation. The linear elastic and adjusted calculations for von Mises stress are offered here as the upper and lower bound to the actual stresses occurring in the test specimen.

Acknowledgements and auspices

This work performed under the auspices of the U.S. Department of Energy by Lawrence Livermore National Laboratory under Contract DE-AC52-07NA27344. This is LLNL-CONF-425209. This work is sponsored by the Department of Homeland Security Science and Technology Directorate's Infrastructure and Geophysical Division.

Works Cited

Banerjee, B. (December 2005). An Evaluation of Plastic Flow Stress Models for the Simulation of High-Temperature and High-Strain-Rate Deformation of Metals. *imechanica.org* , 1-53.

Johnson, G. R., & Cook, W. H. (1985). Frature Characteristics of Three Metals Subjected to Various Strains, Strain Rates, Temperatures and Pressures. *Engineering Fracture Mechanics* , 21 (1), 31-48.

Wilkins, M. L., & Reaugh, J. E. (1980). Placticity Under Combined Stress Loading. *Century 2 Emerging Technology Conference, 80-C2 PVP-106*, p. 8. San Francisco.

Nucleation and Propagation of Portevin-Le Châtelier Bands in Austenitic Steel with Twinning Induced Plasticity

Louis G. Hector, Jr.
Chemical Sciences and Materials Systems Laboratory
General Motors R&D Center
30500 Mound Road
Warren, MI 48090
Louis.Hector@gm.com

Pablo D. Zavattieri
School of Civil Engineering
School of Mechanical Engineering (By Courtesy)
550 Stadium Mall Drive
Purdue University
West Lafayette, IN 47907-2051
zavattie@purdue.edu

ABSTRACT

Twinning induced plasticity (TWIP) steels have high manganese content and exhibit extreme strain hardening and elongation. Tensile flow curves show serrations due to dynamic strain aging associated with solute-dislocation interactions. Highly inhomogeneous plastic flow is manifested by Portevin-Le Châtelier (PLC) band nucleation and propagation. In this research, TWIP steel tensile specimens were quasi-statically deformed to fracture at room temperature. Images of one specimen surface were recorded with a variable framing rate high speed digital camera and custom image acquisition software. A digital image correlation technique was used to compute incremental strain rate maps that enabled study of PLC band nucleation and propagation. The impact of tensile specimen geometry on the location of band nucleation along the specimen gauge section was also explored. Fracture surfaces and material chemistry were examined with SEM and energy dispersive mapping.

KEY WORDS: Austenitic steel, twinning, manganese, Portevin-Le Châtelier (PLC) effect, dynamic strain aging (DSA), digital image correlation (DIC), uniaxial tensile tests

INTRODUCTION

Austenitic steels with twinning induced plasticity (TWIP) have attracted interest as potential structural materials for transportation industries [1] due to extreme ductility and hardening. The 150-400 MPa yield strengths of these materials are relatively low, similar to conventional high strength low alloy (HSLA) steels and the lower strength dual-phase (DP) and transformation-induced plasticity (TRIP) steels. Unique to TWIP steels is a high manganese (Mn) content. Manganese tends to stabilize austenite, although its role in the TWIP microstructure is still a subject of active research [2]. Twinning promotes retention of the austenitic microstructure, but competes with dislocation glide by impeding dislocation motion at twin boundaries and other dislocation-dislocation interactions (e.g. forest hardening). Twin formation is associated with a low room temperature stacking fault energy (SFE). A low SFE inhibits dislocation cross slip, a mechanism referred to as "dynamic Hall-Petch". A 25 mJ/m² critical stacking fault energy is thought to be necessary for twinning. However, twinning likely occurs over a much broader range of SFE, e.g. 18mJ/m² < SFE < 50-80mJ/m².

Austenitic steels often exhibit dynamic strain aging (DSA), a form of unstable plastic flow found in dilute metal alloys [3-8] and non-metals [9, 10]. Portevin-Le Châtelier bands (or the PLC effect) and serrated flow curves are common manifestations of DSA which occurs over a very wide temperature range [11]. The bands, which are regions of localized plasticity, are generically classified as: Type A (continuously propagates across the gage length of a tensile specimen); Type B (discontinuously propagate or “hop”); and Type C (no spatial correlation). A common explanation of DSA in metals centers on dislocation-solute interactions in which solute atoms diffuse to dislocations temporarily arrested at obstacles (or trapped by the local energy landscape in the lattice) thereby increasing the stress required to release the dislocations [12]. Following an aging time, the dislocations are suddenly released and the process repeats elsewhere. First reported in austenitic steel by Tamhankar et al. [13] in 1958, DSA has been the subject of numerous theoretical and experimental studies. Dynamic strain aging and the PLC effect in TWIP steels have been the focus of several recent investigations [14-17]. Differences in PLC band type have been noted due to testing temperatures and alloy chemistries, especially Mn content.

Accurate measurement of PLC band nucleation and propagation represents a significant challenge in experimental mechanics due to the localized nature of serrated flow. Great care must be exercised with the rate of data acquisition during testing due to rapid fluctuation of uniaxial load-time records beyond a critical strain required for the onset of DSA. In the present paper, a recently developed technique for variable framing rate digital image capture [18] is applied to investigate PLC band nucleation and propagation in austenitic TWIP steel in quasi-static, room temperature uniaxial deformation. Of main interest is the location of PLC band nucleation along the tensile specimen gage section and the type of bands per the generic classification above. Displacements and strain fields are computed with digital image correlation (DIC). Band propagation is tracked with contours of incremental axial strain rate. We demonstrate that contrary to common belief, PLC band nucleation does not always occur at the gripper ends of a tensile specimen which suggests an important influence of local fluctuations in TWIP steel texture.

MATERIAL

TWIP steel sheet, with a nominal thickness of 1.5mm, was acquired from POSCO in Korea. A chemical analysis, detailed in Ref. [14] indicated 17.2wt% Mn. Tensile properties are also found in Ref. [14]. [Figure 1a](#) is an SEM image of one fracture surface from a straight gage section tensile specimen. Ductile fracture resulted from microvoid coalescence. Horizontal channels, such as that near the top of [Fig. 1a](#), were noted in each of the fracture surfaces investigated. Common to most of the fracture surfaces analyzed were inclusions such as those denoted by “a” and “b” in the image. Fracture initiation may have in fact occurred at each inclusion. Surrounding each inclusion is a void. Energy dispersive spectroscopy (EDS) was used to probe the chemistry of TWIP fracture surfaces from the tensile tests, with particular attention to inclusion chemistry. [Figure 1b](#) is an EDS plot which shows a chemical breakdown of inclusion “a”. As expected, Mn and Ti are found along with alkaline earth metals such as Ca and Mg. High levels of Al as well as S in “a” are also noted. Similar observations apply to particle “b.”

EXPERIMENT

Tensile Specimen Geometry

The straight gage tensile specimen geometry is shown in [Fig. 2](#). The gray scale contrast pattern on the gage section consists of black and white spray paint droplets. Specimens were given a light polish immediately prior to testing so as to ensure paint adhesion up to fracture.

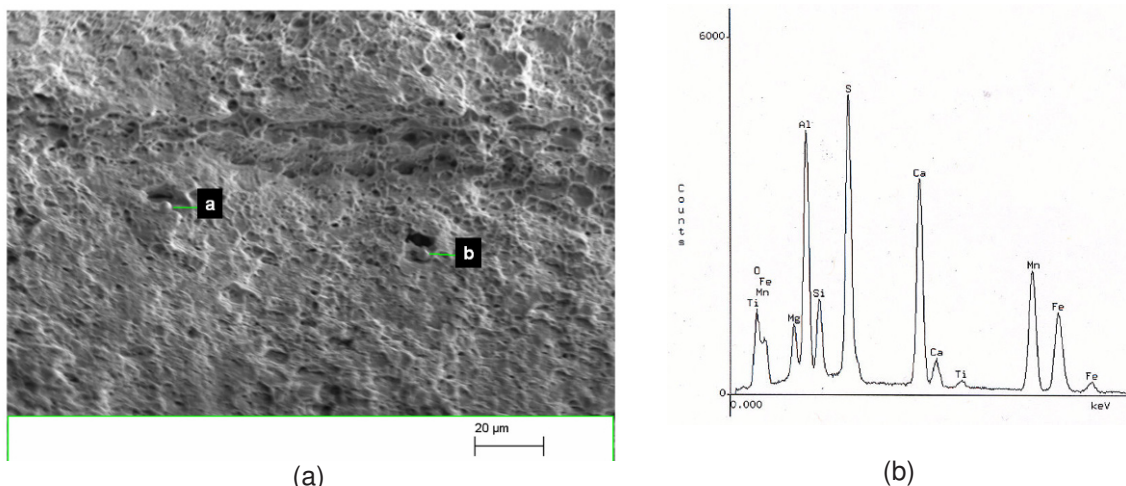


Fig. 1. (a) Scanning electron microscope image of TWIP tensile specimen fracture surface (b) Energy dispersive spectroscopy results of small particle “a” in (a).

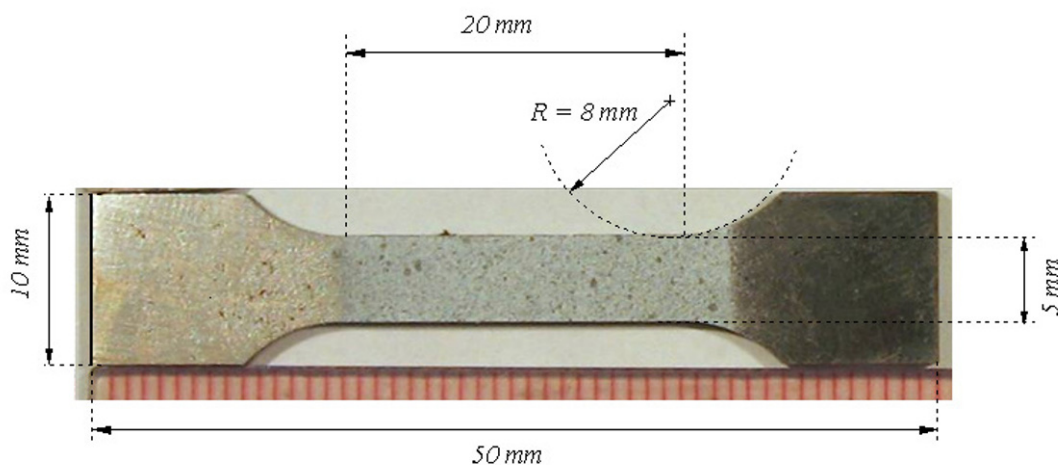


Fig. 2. Tensile specimen geometry.

Miniature Tensile Stage

The miniature screw-driven tensile stage used in this research was custom manufactured by Kammrath-Weiss in Dortmund, Germany. The tensile stage cross-head speed and direction are set with external controller hardware. Each test was conducted at an average constant cross-head speed of $13\mu\text{m/s}$ which corresponds to a nominal (logarithmic) strain rate in the $0.0005 - 0.001 \text{ sec}^{-1}$ range. Only the load reading from the load cell was necessary to compute true stress-true strain curves since displacement fields were computed during the post processing step with the DIC algorithm.

Camera

A Phantom 9.0 high speed digital camera from Vision Research was used to record 1632×1200 bitmap images (each 5.7Mbyte, $14\mu\text{m}/\text{pixel}$ resolution) of the entire gage section surface of each tensile specimen during testing. As many as 1400 images were captured in the 12GByte camera buffer during tensile tests in which the specimens were continuously elongated. A Nikon 105mm telecentric lens set at a 2.8 f-stop was used for all tests. Three lens extenders provided an adequate field of view of the tensile specimen gage section through adjustment of the image magnification (about 100X).

Variable Rate Image Acquisition Algorithm

A custom image acquisition algorithm written in the DASyLab code allowed for variable rate digital image acquisition. Acquisition rate was dictated by user-selected tensile load increment/decrement, displacement increment and time increment thresholds between successive images stored in the camera buffer. This required the DASyLab code to continuously monitor the analog signals from the load and displacement transducers during a test. Hence, more images could be captured and stored to the camera buffer during periods of a test when loads were increasing (or decreasing) rapidly over small displacements. Alternatively, during periods when loads changed very minimally with increasing displacement, fewer images were captured. Of particular importance was the capture of an adequate number of images during periods of PLC band activity as indicated by local fluctuations in the load-time record. Nominal framing rates over the duration of a test were approximately 0.3-6 f/sec, with the peak framing rate occurring during elastic loading and just prior to fracture. Additional details may be found in Ref. [18].

Digital Image Correlation

The SDMAP3D software detailed in Ref. [19] was used to post-process displacements, strains, and incremental strain rate fields from the images of a tensile specimen gage section surface as recorded during each test. The approach is similar to that of Sutton et al. [20], Bruck et al. [21], and Vendroux and Knauss [22]. An affine deformation mapping function with six parameters (constant displacement gradients) is employed for subset deformation. A bicubic spline interpolation is used for subpixel grayscale values. While various correlation algorithms are available, that of Sutton et al. [20] was used. This was found to be faster than that detailed in Ref. [22]. In addition, the strains are computed from a finite deformation formulation in terms of the displacement gradients. These are obtained through a post-DIC processing routine (a moving least squares smoothing or filtering routine) of the grid displacements. The errors in local in-plane displacements, rigid body rotation, and strain measurements are estimated to be 0.02 pixels, 0.03° and $30\mu\text{m/m}$, respectively.

RESULTS AND DISCUSSION

In this study, only Type A PLC bands were observed. Band nucleation occurred either at a gripper end (case 1) or at (or near) the center (case 2) of a tensile specimen gage section. In both cases, indication of PLC band activity in the load-time records first appeared just beyond a 0.3 true strain. Here, we examine a representative result from case 2 since this behavior is evidently less common than case 1. Band nucleation and propagation were examined via contours of incremental axial true strain rate, $\dot{\epsilon}_1$ (sec^{-1}). Contour values were computed by dividing the incremental true strains with the time step between the associated sequential images. Figure 3a is temporal sequence of strain contour maps that shows the nucleation and propagation of Type A bands at the center of specimen gage section. The red contours correspond to peak strain rates within each band and hence the greatest localized dislocation activity. The very first band appears around 850 sec into the test and propagates towards the left gripper end. After a period of nearly 30 sec, a second band nucleates and propagates towards the right gripper end. This process continues until 1600 sec into the test at which point band nucleation switches to the right gripper end as indicated by the very small red contour patch at the very bottom of Fig. 3a. Figure 3b shows the corresponding load-time record, while Fig. 3c is a zoom-in of the boxed portion in Fig. 3b. Here, the humps correspond to PLC band nucleation. Figure 3d shows substantial hardening is suggested in the computed true stress-true strain curve from DIC calculations. Figure 3e is a zoom-in of the boxed portion on Fig. 3f. Instead of the humps in Fig. 3c, PLC band nucleation is denoted by step-like serrations. Tapered specimens were also examined (see Ref. [14] for more detail) and band nucleation was neither limited to the region of the taper at the gage section center nor to either gripper end. Rather, there were some instances where band nucleation occurred at locations along the gage length that were intermediate to these regions.

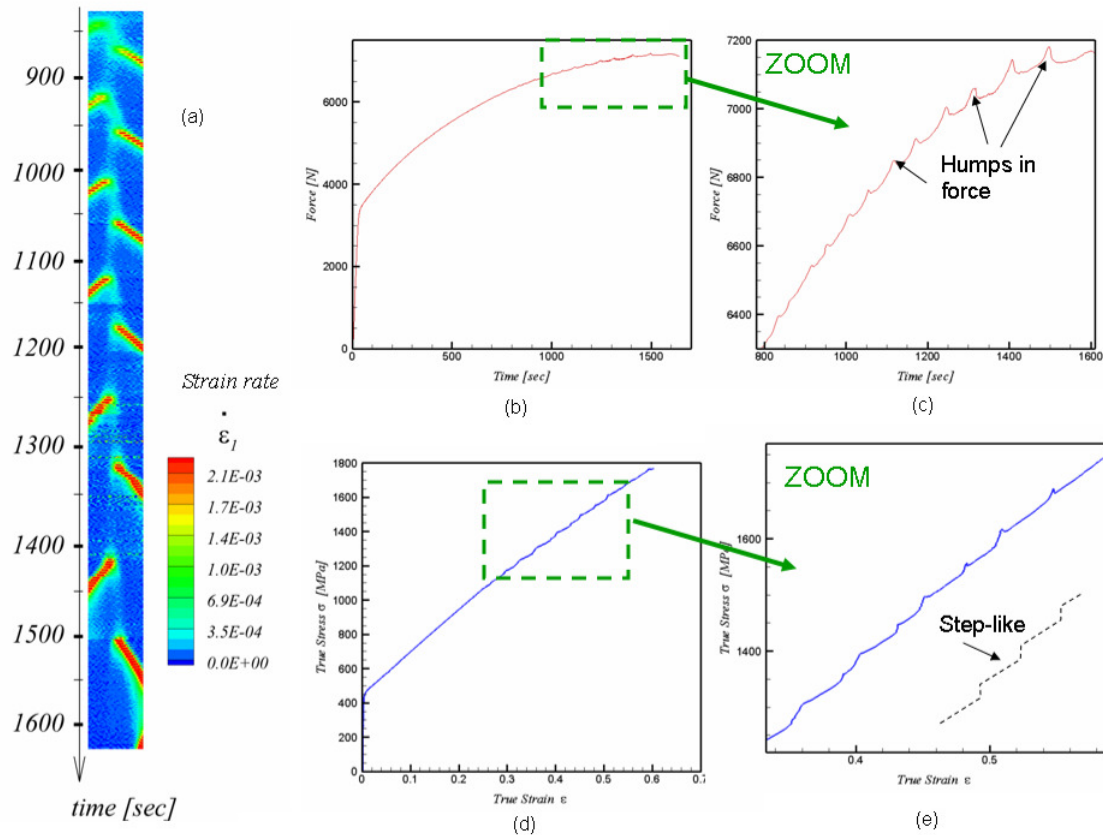


Fig. 3. Type A PLC Bands in TWIP tensile specimen. (a) Temporal sequence showing the nucleation and propagation of 12 bands near the center of a tensile specimen gage section (see Fig. 2). Note the time [sec] is total time elapsed since the start of the test. (b) Load-time record. (c) Zoom-in of load-time record within boxed region in (b) showing serrations or “humps” due to PLC bands. (d) True stress-true strain curve showing hardening. (e) Zoom-in of true stress-true strain curve within boxed region in (d) showing step-like serrations due to PLC band nucleation.

Figure 4 shows additional details at the later stage of the test from which the results in Fig. 3a were computed. Grid lines have been added to the two load-records to emphasize the superimposed open circles. Each circle corresponds to a captured image in the camera buffer during the test per user-selected tensile load increment/decrement, displacement increment and time increment thresholds. Note that a simple adjustment of these parameters could in fact have easily increased the number of captured images by an order-of-magnitude or more (for example). The blue lines with a single arrow head point from PLC band nucleation in the load-time records to corresponding strain rate contour maps in the time sequence at the right.

Figure 5 is a schematic of a typical true-stress curve. Here, band nucleation occurs at each serration or jump in the stress; this coincides with a peak in each hump in the load-time record in Fig. 3c. Propagation of an individual band occurs between each serration.

PLC band kinematics cannot be fully appreciated from the sequence of images showing the total strain or strain rate contour maps since many of the consecutive images were not taken at equal intervals of time. In order to investigate band kinematics, we kept track of the material point at which the strain rate field reached its maximum point. Figure 6 shows a schematic of this process. The maximum strain rate value (or strain rate peak) takes place at the material point

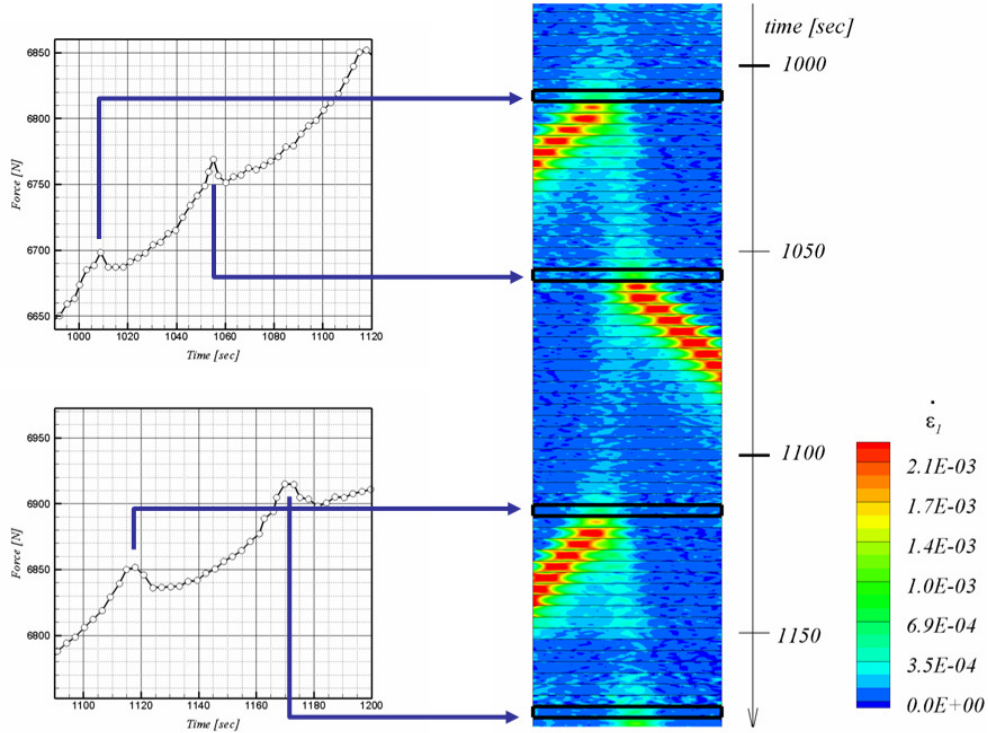


Fig. 4. Captured images denoted by open circles on portions of the load-time record from the time sequence in Fig. 3. Arrows link specific times associated with band nucleation to strain rate contours maps.

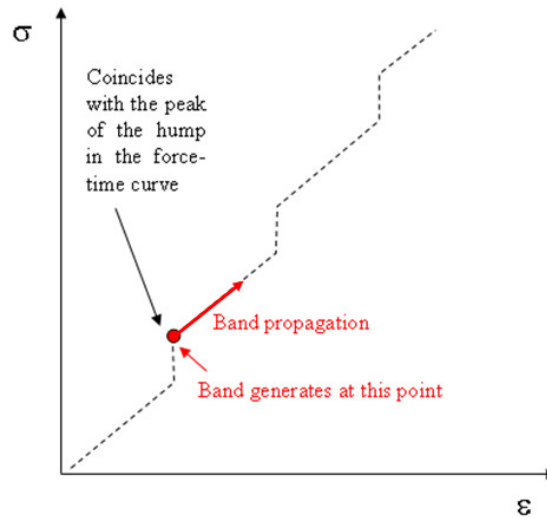


Fig. 5. Schematic of a true stress-true strain curve showing that band nucleation occurs at serrations or steps. Band propagation occurs between the steps, as indicated. The material locally hardens during band propagation.

with coordinate x . Since the strain rate peak always occurs along the middle line of the specimen, the y -coordinate is not needed for this analysis (in other words, we assume that the bands propagate along the axial direction of the specimen gage section).

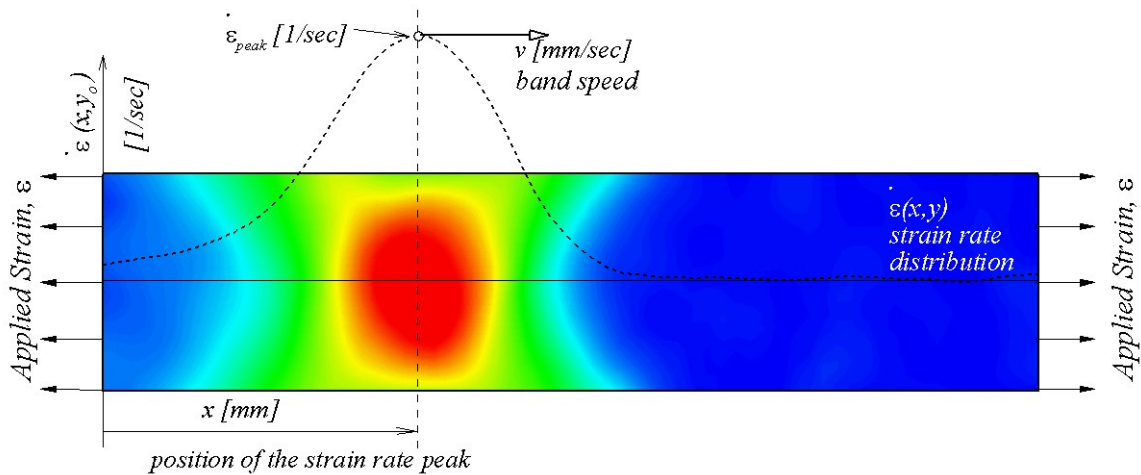


Figure 6: Position of the strain rate peak of a PLC band as it travels through a tensile specimen gage section (in mm) as a function of the applied strain

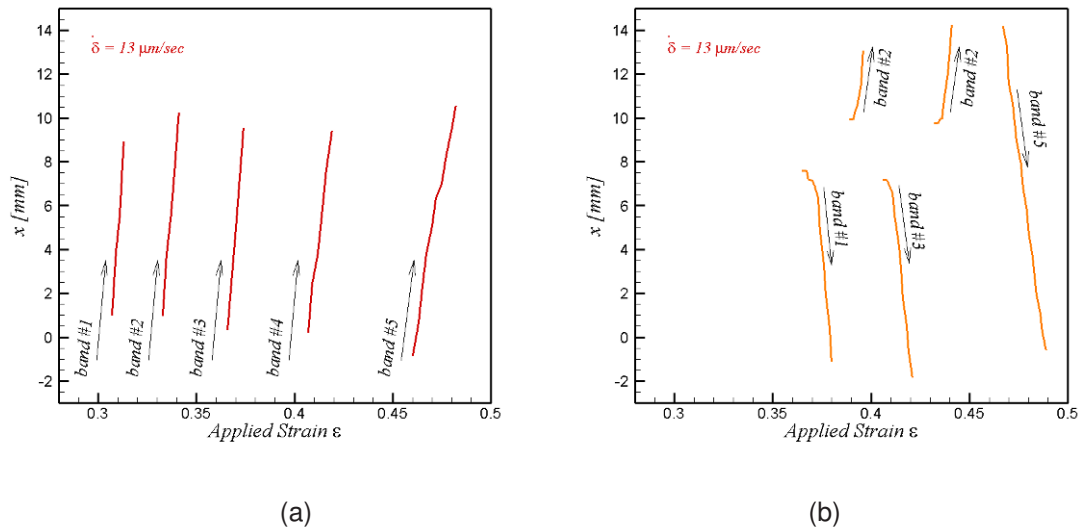


Figure 7: (a) Bands generated at the grips and propagating through the gage (b) Bands generated in the middle and propagate to the ends, including one last band generated at the end that propagates to the other end.

Two distinct cases are shown in Figs. 7a and 7b where the position of the strain rate peak is plotted against the applied strain. Note that the cross-head speed in both tests was $\delta=13 \mu\text{m}/\text{sec}$. Each line describes the “path” of the band, as the specimen is elongated in tension, with the applied strain, ϵ . The first case (Fig. 7a) involves band nucleation at the grippers, with subsequent propagation from left to right through the gage section. Figure 7b shows the case in which the first four bands nucleate in the middle of the specimen and travel to either gripper end (as described in Figs. 3 and 4). Interestingly, the paths associated with band nucleation at the center of the gage section show an initial non-linear variation with applied strain (unlike the behavior shown in Fig. 7a). The fifth band nucleated at a gripper end and, as is the case with all of the bands in fig. 7a, traveled the length of the gage section. More details on the band propagation analysis can be found in Ref. [14].

SUMMARY REMARKS

A technique based upon variable image capture rate has been used to investigate PLC band nucleation and propagation during quasi-state, room temperature tensile testing of austenitic TWIP steel. Band nucleation was found to occur either at one gripper end (case 1) or at (or near) the center (case 2) of the gage section of miniature TWIP tensile specimens. Detailed analysis of case 2, the less commonly observed case, revealed that band nucleation occurs at the crests of humps in the load-time record. These correspond to jumps or serrations in the true stress-true strain curve. It is expected that additional PLC band types will be observed at higher (or lower) testing temperatures than that considered herein, and with different Mn content.

REFERENCES

- [1] Horvath C.D. and Fekete, J.R. Opportunities and Challenges for Increased Usage of Advanced High Strength Steels in Automotive Applications, Proceedings of International Conference on Advanced High Strength Sheet Steels for Automotive Applications, 3-10, June 2004.
- [2] Chen, L. Kim, H.-S. Kim, S.-K. and De Cooman, B.C., Localized Deformation due to Portevin-Le Châtelier Effect in 18Mn-0.6C TWIP austenitic steel, *ISIJ International* 47, 1804-1812, 2007
- [3] Kumar S. and Pink, E., Dynamic Strain Aging in a Tungsten Heavy Metal, *Scripta Mat.* 35, 1047-1052, 1996.
- [4] Ziegenbein, A., Hähner P., and Neuhäuser, H., Correlation of Temporal Instabilities and Spatial Localization during Portevin-Le Châtelier deformation of Cu-10at.% Al and Cu-15at.% Al, *Computational Materials Science* 19, 27-34, 2000.
- [5] Robinson, J.M. and Shaw, M.P., Microstructural and Mechanical Influences on Dynamic Strain Aging Phenomena, *Int. Materials Reviews* 39, 113-121, 1994.
- [6] Trojanová, Z., Lukác, P., Kainer, K.U., and Gärtnerová, V., Dynamic Strain Ageing During Stress Relaxation in Selected Magnesium Alloys Containing Rare Earth Elements, *Advanced Eng. Materials* 7, 1027-1032, 2005.
- [7] Yakes, J.A., Li, C.-C., and Leslie, W.C., The Effects of Dynamic Strain Aging on the Mechanical Properties of Several HSLA Steels, *SAE Trans. (SAE 790009)*, 44-59, 1980.
- [8] Keh, A.S., Nakad, Y., and Leslie, W.C., Dynamic Strain Aging in Iron and Steel, in *Dislocation Dynamics*, McGraw-Hill, 381-408, 1968.
- [9] Dalla Torre, F.H., Dubach, A., Siegrist, M.E., and Löffler, J.F., Negative Strain Rate Sensitivity in Bulk Metallic Glass and its Similarities with Dynamic Strain Aging effect during Deformation, *Appl. Phys. Lett.* 89, 091918:1,3, 2006.
- [10] A. Gallardo-López, D. Gómez-García, A. Domínguez-Rodríguez and L. Kubin, Portevin-Le Châtelier Effect in Y₂O₃-ZrO₂ Single Crystals, *Scripta Mat.* 51, 203-207, 2004.
- [11] Skoczen, B., Bielski, J., Sgobba, S., Marcinek, D., Constitutive Model of Discontinuous Plastic Flow at Cryogenic Temperatures. *Int. J. Plasticity*, published on-line, doi:10.1016/j.ijplas.2010.02.003, 2010.
- [12] Curtin, W.A., Olmsted, D.A., and Hector, Jr., L.G., A Predictive Mechanism for Dynamic Strain Ageing in Aluminum-magnesium Alloys, *Nature Materials* 5, 875-880, 2005.
- [13] Tamhankar, R., Plateau, J., and Crussard, C., Etude de la Déformation Plastique à Chaud d'un fer Doux et d'une Austénite Stable au Nickel-chrome, *Rev. Métallurgie* 55, 383-400, 1958.
- [14] Zavattieri, P., Savic, V., Hector, Jr., L.G. Fekete, J.R., Tong, W., Xuan, Y. Spatio-temporal Characteristics of the Portevin-Le Châtelier Effect in Austenitic Steel with Twinning Induced Plasticity. *Int. J. Plasticity* 25, 2298-2330, 2009.

- [15] De Cooman, B.C., Chen, L., Soo Kim, H.-S. Estrin, Y., Kim, S.K., Voswinckel, H., State-of-the-Science of High Manganese TWIP Steels for Automotive Applications, in *Microstructure and Texture in Steels and Other Materials*, Springer, London, Chapter 10, 165-183, 2010.
- [16] Renard, K., Ryelandt, S., Jacques, P.J., Characterisation of the Portevin-Le Châtelier effect affecting an austenitic TWIP steel based on digital image correlation. *Mat. Sci. Eng. A* 527, 2969-2977, 2010.
- [17] Chen, L., Kim, H.-S., Kim, S.-K., and De Cooman, B.C., Localized Deformation due to Portevin-Le Châtelier Effect in 18Mn–0.6C TWIP Austenitic Steel, *ISIJ International* 47, 1804-1812, 2007.
- [18] Savic, V., Hector, Jr., L.G., Fekete, J.R., Digital Image Correlation Study of Plastic Deformation and Fracture in Fully Martensitic Steels, *Exp. Mech.* 50, 99-110, 2010.
- [19] Tong, W., 2005, An Evaluation of Digital Image Correlation Criteria for Strain Mapping Applications, *Strain* 41, 167-175, 2005.
- [20] Sutton, M. A., McNeill, S. R., Jang, J., and Babai, M., Effect of Sub-pixel Image Restoration on Digital Correlation Error Estimates. *Opt. Eng.* 27, 870–877, 1988.
- [21] Bruck, H. A., McNeill, S. R., Sutton, M. A. and Peters, W. H., Digital Image Correlation using Newton-Raphson Method of Partial Differential Corrections. *Exp. Mech.* 29, 261–267, 1989.
- [22] Vendroux, G. and Knauss, W. G., Submicron Deformation Field Measurements, Part 2. Improved Digital Image Correlation. *Exp. Mech.* 38, 86–91, 1988.

Identification and Enhancement of On-stage Acoustics in a Multipurpose Auditorium

C. Braden, B. Hayes, R. Averbach, V. Ranatunga, Miami University, Oxford, OH 45056

ABSTRACT

The objective of this research is to identify the measurable sound quality parameters of an existing multipurpose auditorium in which the acoustics are not adequate for orchestral purposes. The major problems have been identified as the lack of sufficient projection of sound from the stage area, the inability of the musicians to hear themselves and each other, and the poor reverberation time of the auditorium. The final goal of this study is to implement a solution which will produce a measurable and audible improvement of the on-stage acoustics for the musicians by implementing an acoustic shell which will surround the orchestra, thereby increasing the early reflections on-stage. During this study, one of the objective parameters used is 'Support', which depends on the amount of early and late reflections relative to the direct sound. The studied objective parameters have been used to assess the effectiveness of the acoustic shell by conducting acoustic measurements following the guidelines specified by ISO 3382-1:2009 for performance spaces. In the final paper, an objective analysis of these parameters will be presented with and without the shell in place, in order to verify the overall enhancement for the musicians provided by the acoustic shell.

INTRODUCTION

The acoustical analysis and enhancement of rooms is a subject which has been investigated by many researchers over the past few decades. The design of multipurpose auditoriums to cater to a wide variety of events is particularly demanding due to the varying acoustical needs of the venue. Motivation for this research originated from the accounts given by two area conductors on the orchestral acoustics of an existing auditorium on the Miami University Hamilton campus in Hamilton, OH. Parrish Auditorium is a 451 seat multipurpose auditorium, mostly used for theatre, lectures, and small amplified musical groups. The conductors' subjective impressions were identical, and highlighted three main acoustical deficiencies in Parrish for orchestral purposes: 1) Low reverberation, 2) Lack of sufficient projection of sound from the stage to the audience area, and 3) Musicians struggling to hear themselves and each other.

The main objective of this paper is to quantify the improvement of the *on-stage acoustics for musicians* provided by the addition of an acoustic shell. This was accomplished through the measurement and analysis of specific objective architectural acoustic parameters related to musician perception, with and without the shell in place. The following are the analyzed objective parameters:

Reverberation Time (RT_{60}) – The time required for the sound level in a room to drop 60 decibels after a source ceases to emit sound. A space is said to more “live” as RT_{60} increases. For multipurpose auditoriums, an optimal RT_{60} is within the range of 1.6 to 1.8 seconds. An RT_{60} of closer to 2 seconds is preferred for orchestral performances [1].

Clarity (C_{80}) – A parameter inversely related to reverberation time. It is the degree to which rapidly occurring individual sounds are distinguishable. For orchestral performances, a lower clarity provides sounds which flow more smoothly into one another. The desired range is usually between -4 and 0 dB [2].

Musician Support ($ST1$ or ST_{early}) – A measure relating to how well musicians can hear themselves and others around them. This parameter depends on the amount of early reflections available from surrounding stage surfaces. The optimal range for $ST1$ is between -13 and -11 dB [3].

Late Sound Level (G_{late} or $G_{80-\infty}$) – A parameter calculated from measured G (sound strength – closely related to “loudness”) and C_{80} values. It is a measure of the level of “reverberant sound”. G_{late} measured in the auditorium indicates the ability of the auditorium to provide an audible level of reverberant sound to the musicians on stage. Based on the recent research of J.J. Dammerud of the University of Bath, the optimal range for G_{late} in the auditorium is between 1 and 3 dB. G_{late} measured on-stage was found to be about 2 dB above G_{late} in the auditorium, for the most preferred halls in his study [4,5].

RESULTS

Measurements were performed in accordance with ISO 3382-1: “Measurement of room acoustic parameters”. The microphone used was an Earthworks M30 Omni-Directional. The source used was B&K – Type 4292 Dodecahedron with Power Amplifier B&K – Type 2734-A. The sound interface was Edirol UA-25EX. The signal output/input device was an HP Notebook computer using WinMLS V1.08 acoustic measurement and analysis software. The acoustic shell was a Wenger Legacy® Acoustical Shell. Fifteen towers and 11 ceiling panels were used - the ceiling covered about half of the area above the orchestra enclosure. The occupied/with orchestra conditions were estimated. G_{late} and ST1 showed the greatest improvements with the addition of the shell.

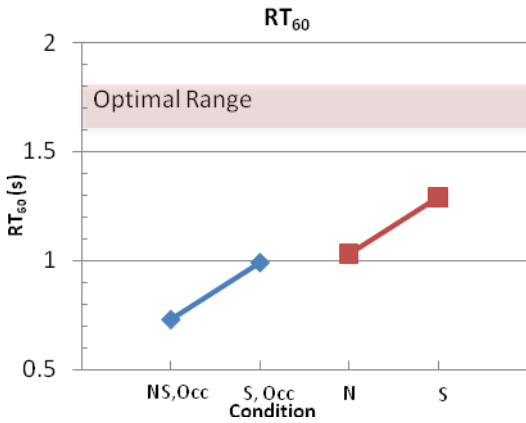


Figure 1. Reverberation Time (RT_{60})

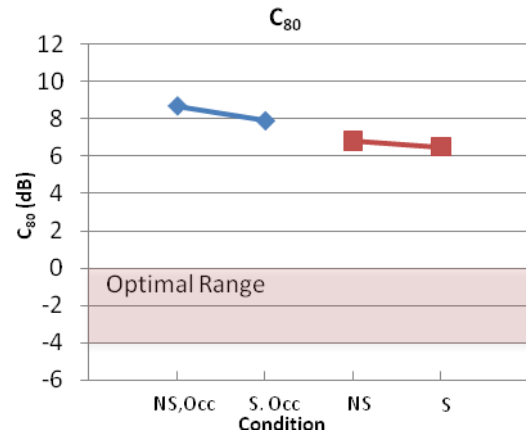


Figure 2. Clarity (C_{80})

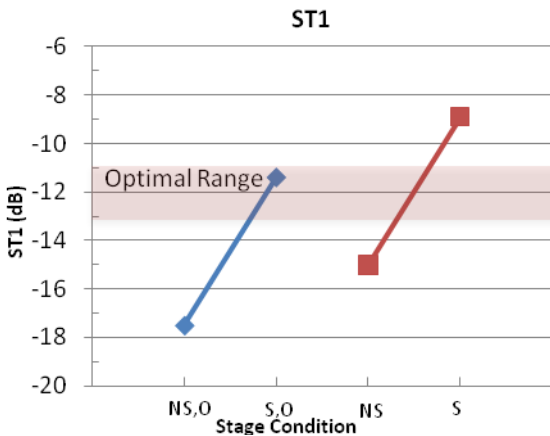


Figure 3. Musician Support (ST1)

	Without Shell (dB)	With Shell (dB)
$G_{late, stage}$	0.0	4.4
$G_{late, auditorium}$	-0.3	2.7
$(G_{late, stage}) - (G_{late, auditorium})$	0.3	1.7

Table 1. ($G_{late, stage}$) & ($G_{late, auditorium}$) Comparison

REFERENCES

[1]. Egan, M. David. *Architectural Acoustics*. Ft. Lauderdale, FL: J. Ross Publishing, 2007
 [2]. Long, Marshall. *Architectural Acoustics*. Burlington, MA: Elsevier, 2006.
 [3]. Barron, Michael. *Auditorium Acoustics and Architectural Design*. London: E & FN Spon, 1993
 [4]. Dammerud, J.J. "Re: Procedures." Message to the author. 9 Feb. 2010. E-mail.
 [5]. Jens Jorgen Dammerud. "Architectural Acoustics." *Facebook*. Web. 1 Oct. 2009.

Determination of Objective Architectural Acoustic Quality of a Multi-Purpose Auditorium

B. Hayes, C. Braden, R. Averbach, V. Ranatunga, Miami University, 501 East High St, Oxford, Ohio 45056

ABSTRACT

Significant differences in listening qualities have been reported by the audience attending wide variety of functions ranging from orchestral music to stage drama and public announcements at the multipurpose auditorium of the Miami University Hamilton campus. Preliminary investigations have been conducted to examine the difference in sound qualities utilizing impulse responses at various seating sections throughout the auditorium, based on the measurement procedures set forth by ISO 3382-1:2009 for performance spaces. Detailed comparisons of measured acoustic quality parameters have been made against the available data in literature for statistically determined optimal acoustic conditions. Each measured range of parameter values has been analyzed to determine the distribution characteristics over a pre-determined set of locations on the audience seating area. In the final paper, a detailed study of the acoustical parameters, including the enhancements proposed as a result of this investigation are presented.

INTRODUCTION

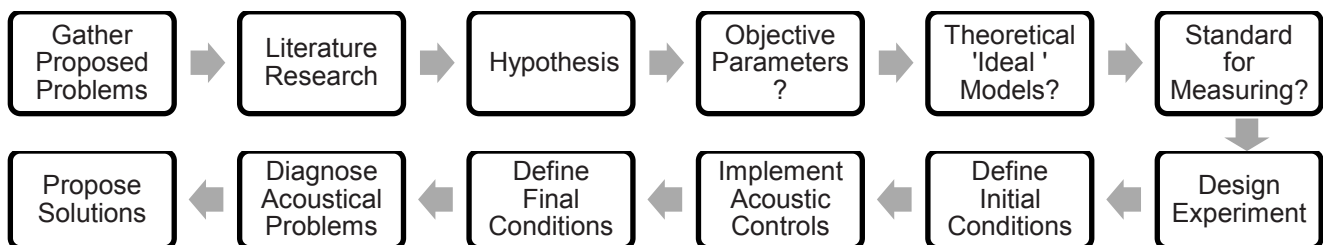


Figure 1: The Research Process

The subjectively proposed acoustic problems for unamplified music performances in this particular auditorium can be categorized as: 1) The space lacks reverberation; 2) There is a lack of sound projection from the stage to the audience; 3) The musicians have problems hearing each other and themselves. The main focus of this paper is to investigate the auditorium considering problems 1 and 2 relating to the audience perception.

Based on extensive literature research, interviewing several musical conductors, and communicating with expert acousticians, it was understood that the lack of sound projection and low reverberation time in the audience seating area is caused by a large surface area of 2 cm thick curtains and large fly space over the stage. These curtains make up 40% of the stage material composition and have the highest coefficient of absorption. Therefore, because the musicians are surrounded by these materials during a performance, the majority of sound waves are being absorbed and losing much of their acoustic energy before ever leaving the stage. Thus, our hypothesis is that the stage materials are greatly impeding upon the opportunity for quality auditorium acoustics.

The ISO 3382-1 standard [1] defines and sets forth measurement procedures for objective acoustic parameters which give indications to the quality of acoustics in a performance space. Although other parameters were studied (which will be presented in the final paper), two ISO 3382 parameters were selected which allow us to objectively quantify the proposed problems. They are: Sound Strength (G) and Reverberation Time (RT_{60}) which are defined below in equations 1 and 2:

$$G = 10 \log_{10} \left[\frac{\int_0^{\infty} p^2(t) dt}{\int_0^{\infty} p_{10}^2(t) dt} \right] dB \quad (Eqn.1)$$

$$RT_{60} = \frac{0.161 V}{\sum_{i=1}^n \alpha_i S_i} \text{ sec} \quad (Eqn.2)$$

Where p^2 = sound pressure measured in a space (Pa), p_{10}^2 = sound pressure in a free field 10m from the source (Pa), t = time (sec), V = Volume of the space (m^3), α = material coefficient of absorption, S = surface area of any material in the space (m^2), n = number materials in the space.

The *Sound Strength* G is the sound level in an auditorium normalized to the sound power level of the source. This parameter gives indications to the quality of sound projection in a space. The *Reverberation Time* RT_{60} is the time it takes for the sound level in a room to drop 60 decibels after a source ceases to emit sound. A space is said to more “live” as RT_{60} increases. Sound Clarity (C_{80}) will also be studied in the final paper.

RESULTS AND CONCLUSIONS

In order to direct the sound energy from the musicians to the audience more efficiently, the primary proposed solution is to surround the musicians with large reflective panels called an acoustic shell. As a variable acoustic control, the auditorium was tested with and without an acoustic shell in place. By comparing our measurements to proposed optimal values by Barron [2], it was observed that the overall acoustic qualities have been improved as a result of the added sound reflecting panels. Figure 2 and 3 below show results obtained by measuring parameters from 3 source locations on stage and 16 microphone locations throughout the auditorium.

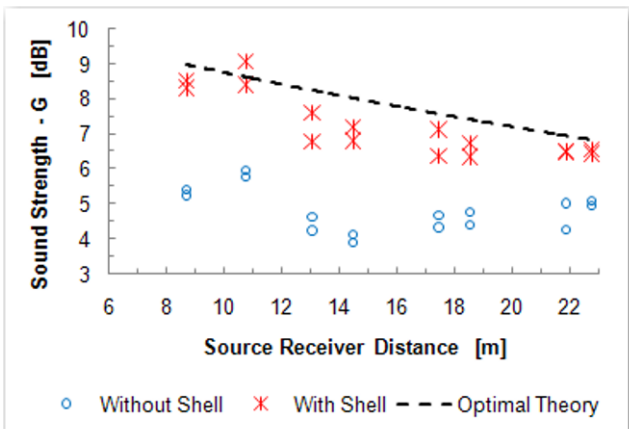


Figure 2: Sound Strength vs. Distance from Source

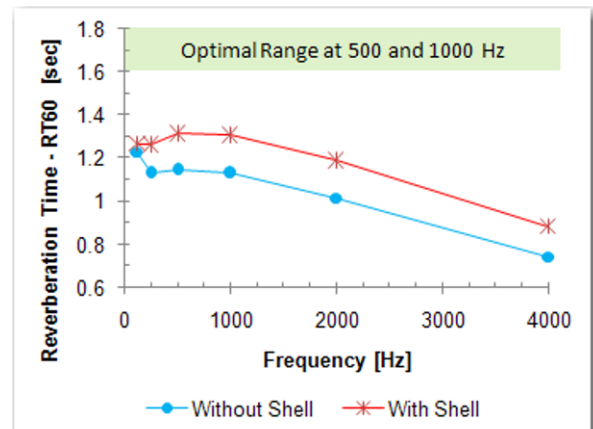


Figure 3: Reverberation Time vs. Frequency

Based on the measurements with and without the acoustic shell, it was concluded that sound projection is greatly enhanced by the shell while reverberation was only improved by a small amount. It was also discovered that the musicians’ ability to hear themselves was greatly improved with the addition of a shell. A thorough analysis of the measured parameters, proposed solutions, and suggestions for increasing RT_{60} will be presented in the final paper.

REFERENCES

[1] ISO 3382, “Acoustics-Measurement of room acoustic parameters”, Part One - Performance Spaces, (2009)
 [2] Barron. Micheal, “Energy relations in concert auditoria”, *Acous. Soc. Am*, **84**, 618-628, (1988)
 [3]. Long. Marshall. “*Architectural Acoustics*”. Burlington, MA: Elsevier, 666-682, 654-655, (2006).

Notch-interface experiments to determine the crack initiation loads

Arun Krishnan¹

Department of Civil and Environmental Engineering
 Station B 351831, Vanderbilt University, Nashville, TN 37235, USA

INTRODUCTION AND OBJECTIVES

The theory of fracture mechanics has been extensively developed for cracks (Williams, 1952; Hutchinson and Suo, 1992). However, notches are found a lot more than cracks in real life. Indeed, a crack is only a special case of a notch (notch angle being 0° for a crack). Recent experiments on composite laminates have indicated that impact-induced delamination will propagate under compressive loading (Krishnan and Xu, 2010, *Submitted to 2010 SEM Annual Conference*). This delamination front is a notch and not a mathematically sharp crack. Therefore, developing a generalized notch-interface failure criterion is very important for the field of fracture mechanics from a fundamental standpoint.

In the current investigation, a specimen as shown in Fig. 1 is designed and tested to determine the crack initiation load and to compare it with theoretical predictions. The angle of the notch (β), the loading point (S), the interfacial adhesive and the materials (same-material vs. bi-material) are used as variables to understand their effect on the crack initiation load. The specimen itself is made of two different parts which are bonded together. This is done to create a sharp notch angle as opposed to a rounded one.

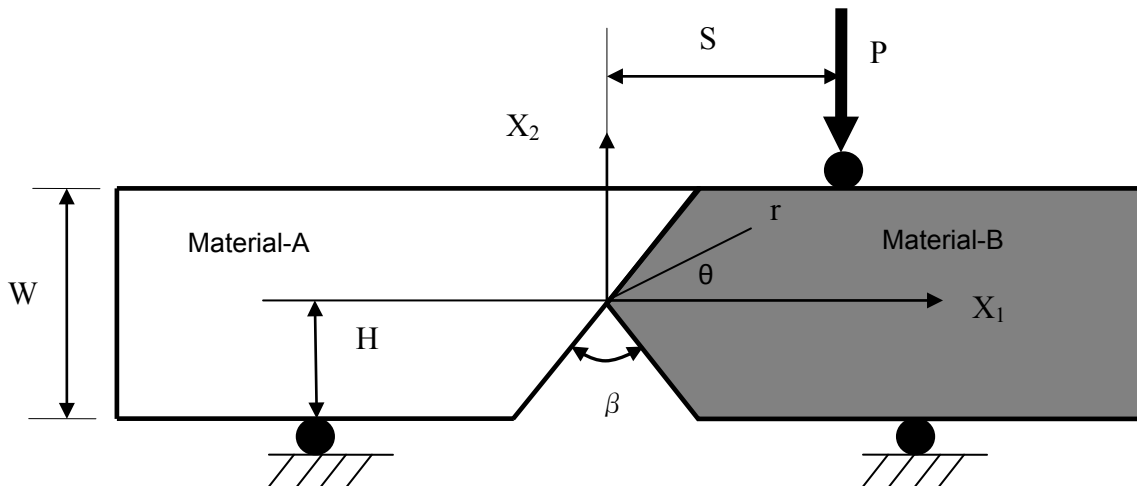


Fig.1 Schematic diagram representing notch-interface specimens

THEORETICAL BACKGROUND

For the same material with a notch but without any interface, crack will initiate from the notch tip and propagate along the specimen central line if the specimen is subjected to symmetrical loading. Theoretical results from Leguillon (2002) indicate that there should be an exponential increase in the value of crack initiation load with increase in the notch angle based on a new crack initiation criterion. The generalized stress intensity factor (GSIF) conception is used since the stress at the notch tip is singular. At the crack initiation, the critical stress intensity factor will exceed a critical material parameter including both the strength and the fracture toughness:

$$k \geq k_c^L = \left(\frac{G_{Ic}}{A} \right)^{1-\lambda} \sigma_c^{2\lambda-1} \quad (1)$$

¹ Corresponding Author, Tel: 615-818-5653, Fax: 615-322-3365. E-mail: arun.krishnan@vanderbilt.edu

where G_{IC} is the material mode-I fracture toughness; A is a function of the notch angle and the crack direction, σ_c is the material tensile strength, and $\lambda-1$ is the stress singularity order of the notch. For a crack (notch angle is zero): $\lambda=0.5$, this criterion becomes a typical fracture mechanics criterion proposed by Irwin (Anderson, 2005). If the notch angle is 180 degrees (a straight bar): $\lambda=1.0$, then this criterion becomes a typical tensile strength criterion in mechanics of materials. This criterion showed very good agreements with experimental results (Leguillon, 2002).

EXPERIMENTAL PROCEDURES

Specimens were made of polycarbonate and individual pieces were bonded using two types of adhesives: Weldon-10 (strong adhesive) and Loctite-384 (weak adhesive). These adhesives were specifically chosen such that their elastic modulus when cured was close to that of polycarbonate (2-4 GPa). This was done to simplify the mechanics of the polymer/adhesive/polymer interface. The experimental set-up consisted of three parts including a mechanical system to load the specimens, an optical system to capture fringe patterns and an imaging set-up to record the images (Krishnan and Xu, 2010). Two major fracture modes were observed: 1) if the notch angle is high, the initial crack kinks from the original crack path along the interface and 2) a crack propagates along the interfacial bonding if the notch angle is high. (Fig. 2)

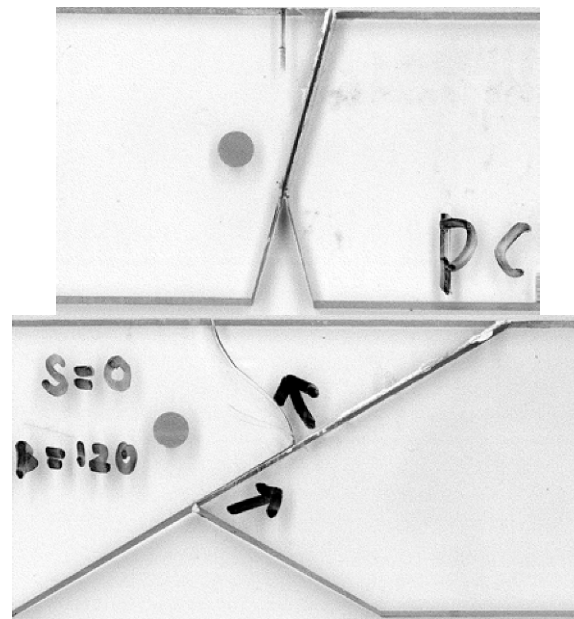


Fig. 2 Typical failure patterns in strong bonded polycarbonate specimens with notch angle of 30° and 120°.

DISCUSSIONS AND CONCLUSIONS

The crack initiation loads are calculated from the three-point bending experiments and will be used to verify the theoretical predictions. The mode-mixity and materials are varied to study their effect on the notch. Finite elements and cohesive elements will be used to model the specimen and understand their failure process.

REFERENCES:

1. Anderson T.L., Fracture mechanics 3rd ed.. CRC Press, Boca Raton.,2004
2. Krishnan A., Xu LR, Effect of the interfacial stress distribution on the material interfacial strength measurement, *Experimental Mechanics*, 50, 283-288, 2010.
3. Leguillon D., Strength or toughness? A criterion for crack onset at a notch, *European Journal of Mechanics-A/Solids*, 21, 61-72, 2002.
4. Hutchinson J.W., Suo Z., Mixed-mode cracking in layered materials, *Advances in Applied Mechanics*, 29, 63-191, 1992.
5. Williams M.L., On the stress distribution at the base of a stationary crack, *Journal of applied mechanics*, 24, 109-114, 1957.

Mechanical Characterization of Alternating Magnetic Field Responsive Hydrogels at Micro-scale

Shannon Meyer, Luke Nickelson, Rakim Shelby, Jon McGuirt, Jian Peng, Santaneel Ghosh
Department of Physics and Engineering Physics, Southeast Missouri State University, Cape Girardeau, MO, 63701

INTRODUCTION

Magnetically responsive hydrogels has become an interesting subject of study as they offer several potential advantages over other material systems for the controlled release of drugs, local heating of the tumors leaving all other regions unaffected and the temperature control within as well as outside the target region due to their response to the magnetic stimuli [1]. Magnetite provides the most attractive magnetic material of common use due to its strong magnetic property and low toxicity [2]. The integration of magnetic nano-particles in hydrogel therefore provide a new generation of material system for many potential applications, like magnetic pump, mimicking muscular movements, soft robotic actuators and magneto-optical sensors or to develop magnetic force based immunoassay [3]. Hydrogels based on poly(N-isopropylacrylamide) (PNIPAM) is a well known thermoresponsive polymer that undergoes a volume phase transition across the lower critical solution temperature (LCST, 32-33°C). Therefore, the inherent temperature-sensitive swelling/shrinkage properties of PNIPAM offer the potential to control gel performance with an alternating electromagnetic field.

The induced heat can be modulated inside the polymer monolith due to the hysteresis loss of Magnetite (Fe_3O_4) under exposure in an alternating magnetic field (3-12 kA/m, 100-500 kHz). Because of the hysteresis loss from the nano-magnets, temperature of the system goes up, and once the temperature crosses LCST, the thermoresponsive gel goes under large contraction. A cost effective, simple yet highly efficient magnetic hydrogel system can be designed as thermal and magnetic response can be tuned varying the size and concentration of the embedded nanoparticles and magnitude and frequency of the oscillating magnetic field, making them easy to operate with simple magnetic excitation. A lot of research has been done on the magnetic actuation of hydrogel for biomedical applications; however, no reports have been found on the studies specially designed to optimize the resulting material property at different (macro to micro) length scale for PNIPAM- Fe_3O_4 nano-composites (MPNIPAM). Thus, mechanical characterization of novel thermo-sensitive multifunctional material is necessary.

This study is designed to investigate mechanical properties extraction of soft polymeric materials at small (micron or sub-micron) length-scale. Thus, the success of this study will yield a very efficient magnetically controlled thermoresponsive material system for biomimetic motion, soft robotic applications and microfluidics, where, bending and/or shrinkage will take place inside an alternating magnetic field. The extracted mechanical properties will be helpful for microdevice design and smaller length-scale applications.

EXPERIMENTAL SETUP

The techniques used to extract the stress-strain relationship of large components cannot be applied to specimens with small length scales, as it is impossible to attach direct measurement devices such as strain gauges or extensometers. Indirect or non-contact measurement techniques have been employed to perform mechanical testing at smaller length scales. Among non-contact measurement methods, optical techniques (Moiré and microscopic Moiré) and image correlation have been used to extract mechanical properties. In image correlation (IC), no special surface preparation is necessary if the specimen surface is unique enough, thus this method becomes a lot simpler and cheaper, yet is highly effective. Moreover, although Moiré and microscopic Moiré are capable of providing the necessary spatial resolution, their sensitivity is limited. However, the sensitivity of the image correlation technique is independent of the method, i.e., it is possible to measure very small deformations by having very high magnification, which is achievable by observing the specimen surface with Scanning Electron

or Atomic Force Microscopy. For these reasons, the IC technique was deemed to be the best method for displacement measurement (Fig. 1).

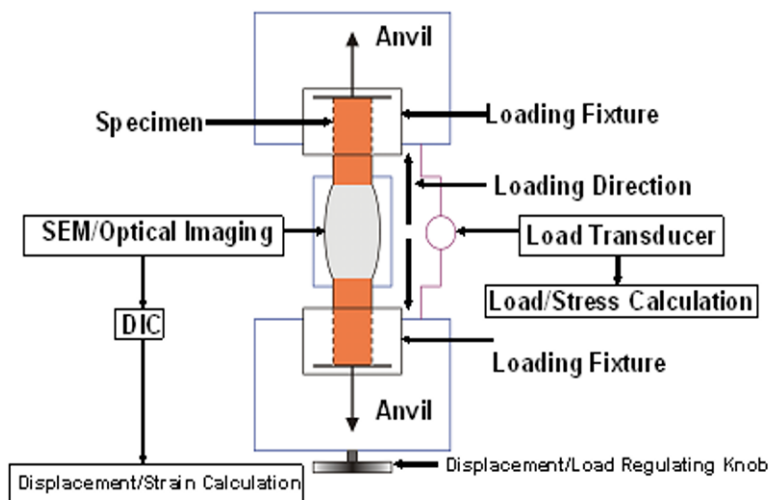


Fig.1: Micromechanical testing setup

The experiment is performed by the specially designed micro-mechanical testing stage [Gatan, Inc.]. The stage allows for movement in the horizontal plane of the entire tensile testing fixture. The loading was applied by the displacement of the anvils in the testing stage. A displacement controller increases or decreases the distance between the loading points, in turn, resulting in an increase or decrease in the applied load, respectively. The speed at which the loading is applied can also be controlled using this unit. The applied load is read from a transducer in the testing fixture and displayed on the displacement controller.

RESULTS

Before the actual material property is extracted, the methodology needs to be validated. Typical stress-strain response from a Copper wire (210 micron dia.) is observed (Fig. 2). The stress-strain curve is very reproducible for similar specimens and from the response, Young's modulus (65 GPa), yield stress (102 MPa), and fracture stress (312 MPa) is calculated. Thermo-sensitive MPNIPAM monolith is grown inside micro-fluidic channel (800 μm I.D) by the established procedure reported in our previous work [3]. Currently, we are performing stress-strain measurement of the MPNIPAM monolith below and above LCST behavior.

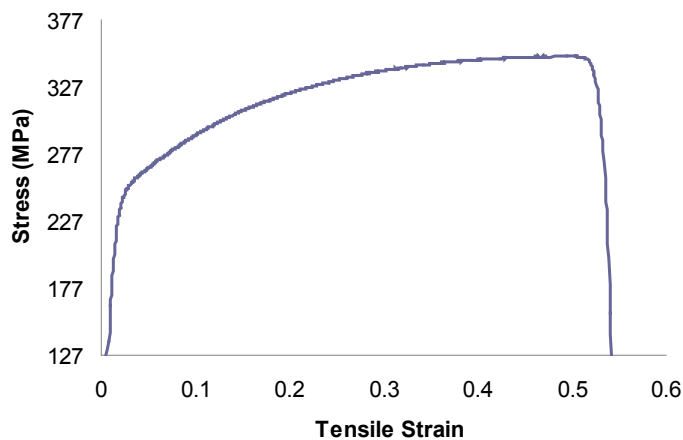


Fig.2: Stress-strain response of micro-scale Copper wire

CONCLUSION

A performance enhanced, alternating magnetic field responsive hydrogel nano-composite system is being investigated. The observed mechanical behavior will facilitate selection of nanoparticle content, particle size and polymer concentration for optimum material design. Fe_3O_4 concentration will be optimized to keep the influence optimum on polymer network properties, i.e. minimize the influence on deswelling property and LCST, yet producing enough hysteresis loss such that the actuation is possible in a low magnetic field, in the order of 3-8 kA/m.

ACKNOWLEDGEMENTS

This work was supported by the grant and research funding committee, Southeast Missouri State University. Research performed in part at NIST center of Nanoscale Science and Technology.

REFERENCES

- [1] Ghosh, S., GhoshMitra, S., Cai, T., Diercks, D., Mills, N., and Hynds, D., Alternating magnetic field controlled, multifunctional nano-reservoirs: Intracellular uptake and improved biocompatibility, *Nanoscale Research Letters*, Vol. 5, No. 1, pp. 195-204, **2010**, DOI 10.1007/s11671-009-9465-9.
- [2] Ma, M., Wu, Y., Zhou, J., Sun, Y., Zhang, Y., and Gu, N., Size dependence of specific power absorption of Fe_3O_4 particles in AC magnetic field, *J. Magn. Mater.* 268, 33-39, **2004**.
- [3] Ghosh, S., Yang, C., Cai, T., Hu, Z., and Mills, N., Oscillating magnetic field-actuated microvalves for micro- and nanofluidics. *Journal of Physics D: Applied Physics*, Vol. 42, No. 13, 135501(8 pp), **2009**.

Investigation of a force hardening spring system

E. Jones and D. Prisco, University of Illinois, 158 MEB, 1206 W Green St, Urbana, IL 61801

Abstract

This paper reports on the jump phenomenon as seen in a geometrically nonlinear mass spring system. Analysis and simplification of the governing differential equation results in two coupled equations, which were solved in MATLAB using various values for mass of the oscillator (M), effective spring stiffness (K), mass of the flywheel (m), radius of gyration of the flywheel (r), and damping (C) of the system. Depending on values of the parameters used, various theoretical system responses were seen for the cart amplitude as a function of driving frequency. Based on the output of the MATLAB program, components were chosen to implement into a mass spring system that would physically illustrate the jump phenomenon. The result is a nonlinear spring system that was able to show the jump down effect, but not the jump up.

Introduction

Nonlinearity of a system refers to a nonlinear relationship between force and displacement. In a force hardening system such as the one investigated in this paper, the apparent stiffness increases with increasing displacement; similarly, in a force softening system, the apparent stiffness decreases with increasing displacement.[1, 2]

Contrary to a linear system, the resonance frequency of a dynamically oscillating, nonlinear system is dependent on the amplitude of the system's motion. For a force hardening system, as the driving frequency is swept from low to high, the amplitude of the cart motion rises until it reaches a bifurcation point, at which point the cart amplitude suddenly jumps down and then remains fairly constant. As the driving frequency is swept from high to low, the cart amplitude increases slightly, jumps up at a second bifurcation point and then decreases. See Figure 2. These jumps are commonly called the jump phenomenon.

The purpose of this project was to investigate the characteristics and behavior of an oscillating, force-hardening system, and then to design and build a physical system, which displays the jump phenomenon, to be used as an educational tool in dynamics courses.[2]

Design

There are many ways to introduce nonlinearity to a system.[1, 2, 3] For this project, nonlinearity is inherent in the geometry of the system: The cart is attached to four linear bearings that move along to rods, constraining the cart to move in one direction.[2] Springs are attached to the cart so that they are perpendicular to the rods when the system is at rest (Figure 1). A DC motor (Bodine Electric Model 24A2BEPM) attached to the cart rotates

an off-balance flywheel, and the motor rotation speed is controlled by a Variac (Payne - 36TBP-1-5). This system was chosen because a quick jump response time of 2-3 seconds is expected (opposed to a longer jump time for a pendulum set-up)[1], system parameters (cart mass, spring constant, spring pretension, damping, et cetera) can be easily manipulated, and the system can be modified to show linear resonance as well, for educational demonstration purposes.

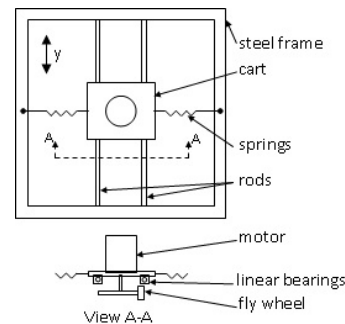


Figure 1: Schematic of nonlinear spring system

The amplitude of the force generated by the flywheel is found through Newton's second law to be Equation 1 where ω is driving frequency, and m and r are defined in the abstract. Note that the amplitude depends on the frequency of the motor, ω , contrary to the constant maximum amplitude found in the systems reviewed in the literature.[2]

$$F(\omega) = mr\omega^2 \quad (1)$$

The Euler-Lagrange method was used to find the governing differential equation for the system (Equation 2).

$$M\ddot{y} + C\dot{y} + 2Ky \frac{\sqrt{y^2 + d^2} - l_0}{\sqrt{y^2 + d^2}} = F(\omega) \cos(\omega t) \quad (2)$$

$$d = l_0 + \delta \quad (3)$$

where δ is the the initial extension of the spring, l_0 is the unstretched spring length, d is the length of the spring when the cart is at its equilibrium position, y is the distance the cart has traveled along the rods, and the other variables are defined in the abstract.[3] Keeping the first two terms of the Taylor series expansion of the stiffness term, and assuming the springs are initially almost unstretched (a necessary condition for strongly anharmonic motion) simplifies the equation. To solve the equation, a solution of the form $y = A \cos(\omega) + B \sin(\omega)$, where A and B are constants, is assumed and substituted into the governing differential equation. Ignoring higher harmonics, $\cos(3\omega)$ and $\sin(3\omega)$, two coupled equations are obtained (Equations 4 and 5), where variables were previously defined.

$$-AM\omega^2 + CB\omega + 2K\frac{\delta}{d}A + \frac{3}{4}K\frac{l_0}{d^3}(A^3 + AB^2) = mr\omega^2 \quad (4)$$

$$-BM\omega^2 - CA\omega + 2K\frac{\delta}{d}B + \frac{3}{4}K\frac{l_0}{d^3}(B^3 + A^2B) = 0 \quad (5)$$

A MATLAB function was written that took user-defined inputs for system parameters, iteratively solved the coupled equations, and plotted the expected system response (cart amplitude as a function of driving frequency). See Figure 2. Based on MATLAB simulations, final design parameters were chosen so that the physical system was expected to display the jump phenomenon.

Results and Discussion

During preliminary system operation, it was noticed that the frequency of the motor was dependent on the cart motion, i.e. that the motor was subject to feedback from the cart motion. For high cart amplitude, the maximum frequency attainable by the motor was greatly restricted. If the cart was constrained, however, high motor frequency could be attained. Therefore, two tests were run.

First, the system was initially at rest and unconstrained. The motor was then turned on and the motor frequency was gradually increased. With increasing motor frequency, the amplitude of the cart motion slowly rose (portion A to B on Figure 2); however, because of feedback, the motor was not able to spin fast enough (rotational energy lost to motion of the cart) to cause the cart frequency to reach the critical bifurcation point (point C), and the jump down in cart amplitude (C to E) was not observed.

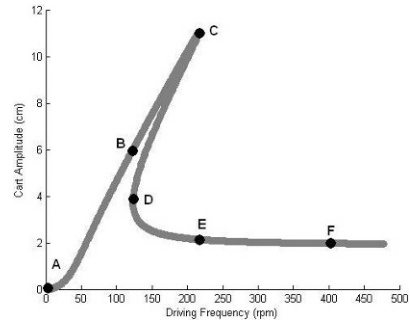


Figure 2: System response from MATLAB simulation with the following parameters: $M = 4.54$ kg, $C = 25.0$ Ns/m, $K = 3430$ Nm, $l_0 = 7.95$ cm, $\delta = 5$ mm, $m = 1.14$ kg, $r = 6.86$ cm

For the second test, the cart was constrained and the motor was turned on to maximum frequency. It was noticed that this maximum frequency was much higher than the maximum frequency attained in the first test. Then the cart was released, and it oscillated at a high frequency and small amplitude (point F on Figure 2). As the motor frequency was decreased, there was no noticeable change in cart amplitude until the second bifurcation point (D) was reached. At this critical cart frequency, the cart amplitude jumped up for approximately one cycle (D to B); subsequently, the cart amplitude and the motor frequency both decreased very quickly. It is hypothesized that feedback from the jump up in cart amplitude caused the jump down in motor frequency, and as a result of the sudden change in motor frequency, the amplitude of the cart jumped back down.

The authors recommend future work be focused on understanding the cause of feedback and on exploring different forcing options. A motor that is not sensitive to feedback (i.e. the motor frequency is independent of cart amplitude and frequency) would be ideal.

References

- [1] Tracy L. Johnson Donald P. Stockard and Francis W. Sears. Study of amplitude jumps. *American Journal of Physics*, 35:961–963, 1967.
- [2] J. N. Fox and J. J. Arlotto. Demonstration experiment using a dissectable aharmonic oscillator. *American Journal of Physics*, 36:326–330, 1968.
- [3] John Thomchick and J. P. McKelvey. Anharmonic vibrations of an "ideal" hooke's law oscillator. *American Journal of Physics*, 46:40–45, 1978.

Resonance Behavior of Magnetostrictive Sensor in Biological Agent Detection

Ramasamy, M. and Prorok, B.C, Department of Materials Engineering, 275 Wilmore Labs,
Auburn University, AL-36849

Abstract

The growing threat of biowarfare agents and bioterrorism has led to the development of specific field tools that perform rapid analysis and identification of encountered suspect materials. One such technology, recently developed is a micro scale acoustic sensor that uses experimental modal analysis. Ferromagnetic materials with the property to change their physical dimensions in response to changing its magnetization can be built into such sensors and actuators. One such sensor is fashioned from Metglas 2826MB, a Magnetostrictive strip actuated in their longitudinal vibration mode when subjected to external magnetic field. Due to mass addition, these magnetostrictive strips are driven to resonance with a modulated magnetic field resulting in frequency shifts. In Vibration Mechanics the frequency shift for a certain amount of mass will have a tolerance limit based on their distribution and discrete position over the sensor platform. In addition, lateral positioning of same amount of mass does not influence the resonant frequency shift of the sensor. This work concentrates on developing a model correlating theoretical, experimental and numerical simulations to determine the mass of *E. Coli O157:H7* cells attached to the sensor platform.

There has been a remarkable increase in the production and availability of chemical and biological weapons throughout the world in past decades. This has significantly increased the possibility of attack on human race using such weapons. Biological agents are often considered to be psychologically more threatening of the two and therefore provide more appeal to terrorists. The pathogenic limits of such biological agents have reduced in order of magnitudes from 10^{15} to 5 or 6 cells. This eventually leads us to focus our research on developing biological agents' detection techniques that are very rapid, sensitive and cost effective. Magnetostrictive materials developed into mass-based acoustic wave Sensors operated on longitudinal vibration mode is one such technique. Magnetostrictive materials are soft amorphous ferromagnetic materials that change in magnetic properties when stress is applied or vice versa. These Magnetostrictive materials are fashioned into acoustic wave sensors in the form of simple rectangular strips that are actuated in their longitudinal vibration mode when exposed to magnetic field. Due to the applied field, the strips resonate at a specific frequency which is dependent on their mass and physical dimensions.

In this research, the principle of detection of these sensors involves measuring a resonant frequency shift as the target biological species attaches to the sensor; effectively this addition of mass dampens the resonant behavior of the sensor platform. When biological agents attach to these magnetostrictive sensors in small amounts they represent discrete mass additions, whereas a large number may be more analogous to mass evenly distributed on the strip. It is therefore highly desirable to understand how spore/cell attachment location influences the resonant frequency of these magnetostrictive strips. When mass is evenly distributed over the sensor it effectively dampens the speed of the deformation waves propagating in the strip, which reduces its resonant frequency and is described by the following equation,

$$\Delta f = -\frac{f_o}{2} \left\{ \frac{\Delta m}{m_{sen}} \right\} \quad (1)$$

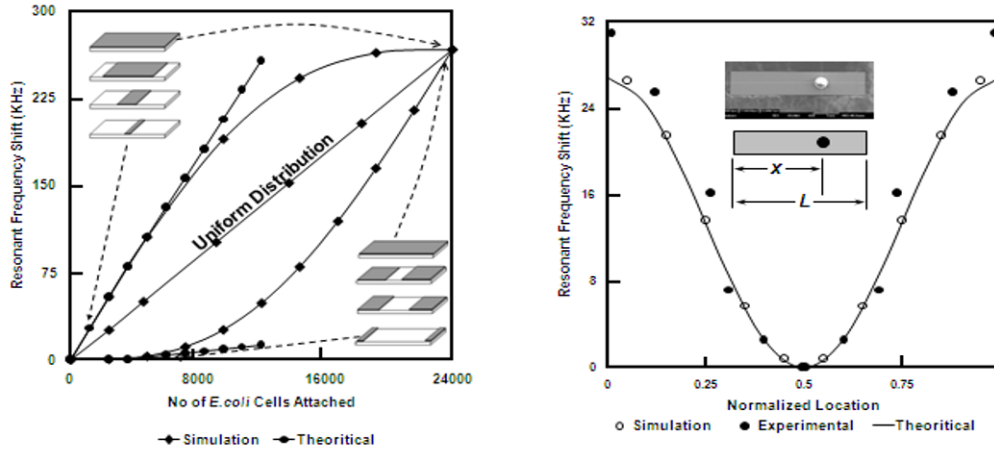
Δm is the mass bonded on a sensor, Δf is the resonant frequency change after mass attachment, m_{sen} and f_o is the sensor's initial mass and resonant frequency, respectively. However, when mass is not evenly distributed or is a discrete mass bonded in a particular location this equation is no longer valid. And hence, Frequency shift is not the same if the mass is concentrated at a particular location on the sensor platform compared to the uniform distribution of the mass. This is mainly due to reduction in wave speed of the sensor obstructed by the concentrated mass at discrete locations on the platform. In such cases the Maximum resonant frequency shift will be observed at the free ends of the sensor platform which can be determined using equation,

$$\Delta f = -f_o \left\{ \left(\frac{KL}{2\pi} \right) - 1 \right\} \quad (2)$$

Alternatively, minimum frequency shift for the same amount of mass would be observed when concentrated at the centre given by the equation,

$$\Delta f = -f_o \left\{ \frac{\Delta m}{m_{sen}} + \left(\frac{KL}{2\pi} \right) - 1 \right\} \quad (3)$$

The values were verified with the help of the simulation results obtained by distributing the mass uniformly and at various discrete positions on the sensor platform as shown in Fig. 1(a).



Irrespective of the amount of mass involved, the frequency shift is influenced by the position of the mass on the sensor platform as shown in Fig. 1(b). In this case, the wave speed on the side of the attached mass is less than the opposite side where no mass is attached. During resonance, the wave frequency must match on either side of the sensor. In order to account for the imbalance of wave speeds, the zero nodal point must shift such that the distance the waves travel on each side enables the waves to arrive at the nodal point at the same time to ensure they are in phase. In this case it must shift towards the side with the attached mass, resulting in larger frequency shifts. The simulation and experimental results using glass beads that were attached to the sensor proves this conception. Using these results an equation was developed, to represent the influence of position on the frequency shift of the sensor.

$$\Delta f = \frac{-f_o}{2} \left(\frac{\Delta m}{m_{sen}} \right) \left\{ 1 - \cos \left(\frac{\pi x}{L} \right) \right\} \quad (4)$$

The experimental and numerical simulation work presented the non-uniformity of mass attachment on longitudinally vibrated sensors. The resonance response of the sensor not only depends on the mass attached but also on the position and the physical dimensions of the sensor platform. A prediction model using microscale Magnetostrictive mass acoustic sensor has been developed and applied to detection of biological agents. Good agreement was found between the model and the experimental data.

References

1. C. Liang and B. C. Prorok, "Measuring the Thin Film Elastic Modulus with a Magnetostrictive Sensor," *J. Micromech. Microeng.*, vol. 17, pp. 709-716, 2007.
2. C. Liang, S. Morshed, and B. C. Prorok, "Correction for Longitudinal Mode Vibration in Thin Slender Beams," *Appl. Phys. Lett.*, vol. 90, pp. 221912, 2007.
3. M. L. Johnson, J. Wan and B. A. Chin et al., "A Wireless Biosensor using Microfabricated Phage-Interfaced Magnetoelastic Properties", *Sens. Act. A* 144, 38-47, 2008.
4. W. Shen, R.S. Lakshmanan and B.A. Chin et al., "Phage Coated Magnetoelastic Micro-Biosensors for real-time Detection of B.anthraxis spores", *Sens. Act. B* 137, pp.501-506, 2009.

Detection of Damage Initiation and Growth of Carbon Nanotube Reinforced Epoxy Composites

V.K.Vadlamani

University of Massachusetts Dartmouth, 285 Old Westport Road, North Dartmouth, MA, 02747

ABSTRACT

The effect of nano-deformation, damage and growth of carbon nanotubes (CNT's) reinforced polymer composites is investigated using electro-mechanical response at different loading conditions. Three different polymer systems namely epoxy, epoxy reinforced with gas bubbles (that induces porosity) and epoxy reinforced with Aluminum Silicate hollow microspheres (Cenospheres) are used in this study. CNT's of different weight percentages are loaded into above three polymer systems and a combination of shear mixing and ultrasonication processes are used to fabricate composites. A four-point probe method is used to measure high resolution electrical response when the above polymer systems are subjected to mechanical loads. The effect of various types of mechanical loading on different stages of deformation of test samples, onset of damage and growth as a function of either glass bubbles or cenospheres in epoxy are discussed using high-resolution electro-mechanical response of polymer systems.

INTRODUCTION

Due to their high electrical conductivity, carbon nanotubes are used as sensory network in polymers to understand their deformation and damage in the materials. Wang et al. [1] fabricated continuous carbon fiber reinforced polyphenylene sulfide (PPS) composites and interlaminar thermal damage was monitored using real-time measurement of electrical of interlaminar interface. Recently Thostenson and Chou [2] developed multi-wall CNT's reinforced glass fiber-epoxy laminated composites and they used the distributed sensory network of CNT's to evaluate the onset and the evolution of damage in their composites. In this study, thermoset epoxy was reinforced with two different particulates, the percolation network generated using multi-walled CNT's in epoxy. Extensive experimentation is conducted to understand the deformation, onset of damage and growth in these composites.

EXPERIMENTAL DETAILS

Fabrication Procedure

The thermoset epoxy resin and hardener, (used as matrix) consists of two parts: Part A (resin) and Part B (hardener). The specific gravity of part A is 1.1299 and part B is 0.97 and the mix ratio is 5:1.95. The viscosity of the epoxy is low and this makes it suitable for mixing particles up to 40% volume fraction without any air entrapment. Multi-walled CNT's are used to generate percolation network in the system. Typical diameter of MWCNT's is 30 ± 15 nm and length is 5-20 micron. Two different types of particulates cenospheres and glass bubbles are used in this study. The cenospheres are a by-product of the fly ash, obtained from coal-fired power plants and glass bubbles are the microscopic spheres of glass. The 0.5 wt% of MWCNT's is mixed in resin by shear mixing and ultrasonication. Then the particles are introduced and mixed using a shear mixer. The solution is degassed separately to remove the entrapped air. Both the parts are then mixed thoroughly and degassed again to remove any air entrapped during mixing. The mix is poured in suitable moulds to make the desired test specimens. Proper care is taken not to induce any air bubbles while pouring the mix into the moulds. The reason for degassing before mixing the parts is to reduce the degassing time after mixing, because the epoxy has a short gelation time of 20 min. The specimens are cured at room temperature for 24 hours in the mould.

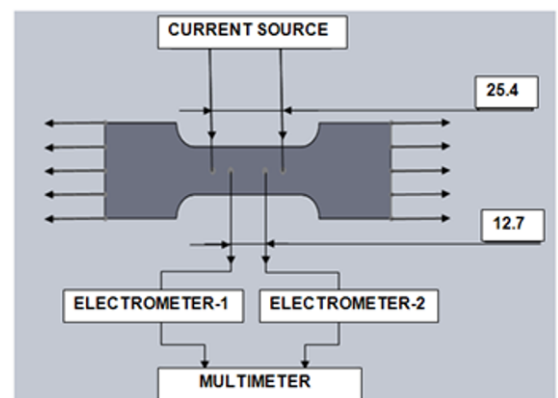


Fig. 1: Typical diagram under loading conditions.
(All dimensions are in mm)

Four-point probe system

The Four-point probe is a convenient tool for electrical measurements. This system consists of four probes which are attached to the sample, a DC current source (KEITHLEY6220) ranging from 2nA-100mA, electrometers (KEITHLEY6514) and a multimeter (KEITHLEY2000) ranging from 1μV-1000V. The probes are attached in linear fashion, where the current is passed through two outer probes; the voltage drop across inner probes is measured. Various currents are passed and resistance is measured. From the [Table -1](#) the resistance is constant in the range of 200nA-75nA. Hence the current is properly chosen within this range for measuring the resistance.

Experimental conditions

Tensile testing is performed for all the systems at a loading rate of 0.15in/mm using Instron machine. [Fig.1](#) represents the schematic of tensile testing of a typical sample.

Table 1. Different resistance values for varying currents

CURRENT(A)	RESISTANCE(Ω)
1.00E-04	3.64E+05
7.50E-05	3.84E+05
5.00E-05	4.16E+05
2.50E-05	4.82E+05
2.00E-07	1.21E+06
1.75E-07	1.21E+06
1.50E-07	1.21E+06
1.25E-07	1.18E+06
1.00E-07	1.22E+06
7.50E-08	1.19E+06
5.00E-08	1.32E+06
2.50E-08	1.13E+06
2.00E-09	1.90E+06

RESULTS AND DISCUSSION

[Fig. 2](#) shows the typical curve of % resistance change with load and displacement. As the load increases initially the change in resistance increases. This is due to the disconnection of CNT's. After that the decrease in resistance is due to the CNT's aligned in the direction of loading. The fluctuations observed in the curve are due to small micro cracks initiated in the system. Due to the presence of these micro cracks weaken and break the bond between CNT's but at the same time Vander Waal forces acts and are responsible for the CNT's attraction to each other. Due to this phenomenon there is a decrease in "percentage change in resistance". Later due to accumulation of cracks there is an increase in resistance change for a small displacement. This phenomenon leads to growth of crack. Due to this percentage change in resistance increases slowly until the fracture happens in the specimen.

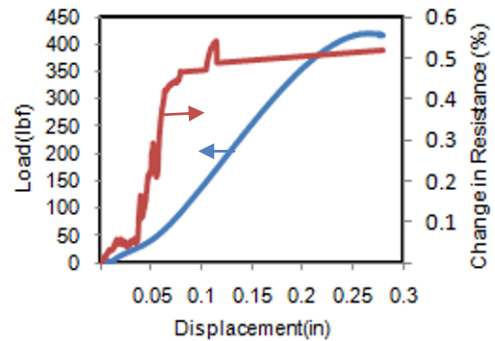


Fig.2. Change in resistance with load and displacement.

EXPERIMENTS IN PROGRESS

The effect of particles with volume fractions of 10%, 20%, 30% and 40% are tested to understand the crack growth. For each volume fraction of particles, different loading rates are applied to observe the deformations under the loading conditions. Loading and Unloading has to be done for all the volume fractions. Cyclic loading has to be applied to understand the effectiveness of self-healing methodology. Fracture experiments are performed on single edge notch tension (SENT) specimens using four-point probe method to understand the stresses around the crack tip [Fig. 3](#) shows typical loading set up for SENT specimens.

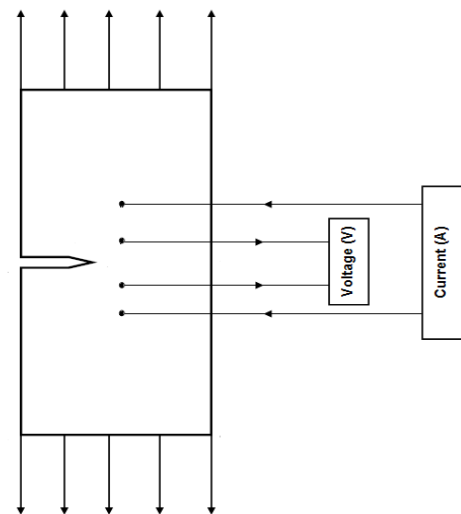


Fig. 3: Typical loading setup for SENT specimen.

REFERENCES

1. Wang S , Mei Z and Chung DDL, Interlaminar damage in carbon fiber polymer-matrix composites studied by electrical resistance measurement , Int. J. Adhes. Adhes, 21, 465-471, 2001
2. Thostenson and Chou, Carbon Nanotube Networks: Sensing of Distributed Strain and Damage for Life Prediction and Self Healing, Adv.Mater. 18, 2837-2841, 2006

Nano-mechanical Characterization of Polypropylene Fibers Exposed to Ultraviolet and Thermal Degradation

N.D. Wanasekara

University of Massachusetts Dartmouth, 285 Old Westport Road, North Dartmouth, MA, 02747

ABSTRACT

Nano-indentation studies using atomic force microscopy (AFM) was conducted to investigate the effect of accelerated ultra violet (UV) and thermal degradation on mechanical properties of Polypropylene textile fibers. The Polypropylene fibers with initial stabilizers were exposed to UV degradation using Q-UV Panel Weatherometer. The effect of degradation on gradation of Young's modulus values across fiber cross-section was investigated by doing progressive nano-indentation from the surface to the center of the fiber. It was identified that UV degradation initially increases the Young's modulus values from center to surface of the fibers until 120 hours of exposure and the values show decreasing trend at 144 hours of exposure. The Young' modulus values at 144 hours of exposure are less than those of unexposed fibers. To investigate thermal degradation effect on Polypropylene fibers, the fibers were exposed to 125°C as a function of number of weeks in increments of one week to four weeks. Results indicate that the thermal exposure did not have much impact on variation of Young's modulus values for the first three weeks and showed an increase in Young' modulus values at the surface when they are exposed to four weeks. Fourier Transform Infrared Spectroscopy (FTIR) and Wide Angle X-ray Spectroscopy (WAXS) were performed to identify the oxidation bonds and crystallinity. The increase in Young's modulus values of Polypropylene fibers exposed to UV and thermal degradation is attributed to increase in crystallinity.

INTRODUCTION

Photo-oxidative degradation of polypropylene (PP) has been a major concern for a long time. Blais et al. [1] explained that significant morphological and structural changes take place in crystalline or fibrillar regions showing much more resistance to scission than the amorphous regions. Billingham et al. [2] established that oxidation is confined to amorphous regions between crystallites since oxygen is insoluble in the crystal phase of polyolefins. In my work, I have investigated the gradation profile of change in mechanical properties from surface to center of the fibers using AFM for identifying effective treatments to mitigate the oxidation due to UV and thermal exposure.

EXPERIMENTAL DETAILS

The polypropylene fibers were subjected to Ultraviolet (UV) exposure using a Q panel UV (QUV) weatherometer (QUV, Q-Lab Corp. OH, USA). The exposed fibers were molded in an epoxy plug for nano-indentation characterization using AFM. An atomic force microscope (XE-100, Park Systems Inc, CA, USA) was used in the topographic imaging and nano-indentation of polypropylene fibers. FTIR microscopy (Varian FTIR Bench and Microscope, CA, USA) was used to identify the chemical groups present in the fiber samples. WAXS was done using a set-up from Molecular Metrology, Inc. using a 30w micro-source (Bede) with a 30x30 μm^2 spot size leading to a low divergence beam of monochromatic $\text{CuK}\alpha$ radiation (wavelength, $\lambda = 0.1542$)

RESULTS AND DISCUSSION

Fig.1 shows the contact mode image of a polypropylene fiber cross section and the indentation pattern. Force-deflection diagrams of the nano-indentation for UV exposed PP fibers is shown in Fig.2. These diagrams indicate that slope of the initial unloading curve decreases with increase of exposure. Fig. 3 shows the variation of Young's modulus values for PP from the center to surface as a function of UV exposure duration.

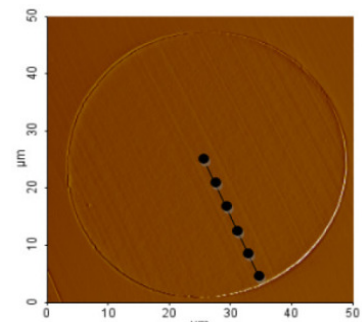


Fig. 1. Indentation pattern across the radius of the fiber.

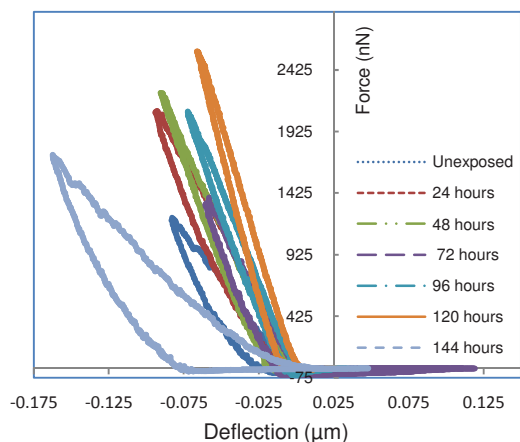


Fig.2. Typical force deflection diagrams of nano-indentation for polypropylene fibers of different UV exposure times

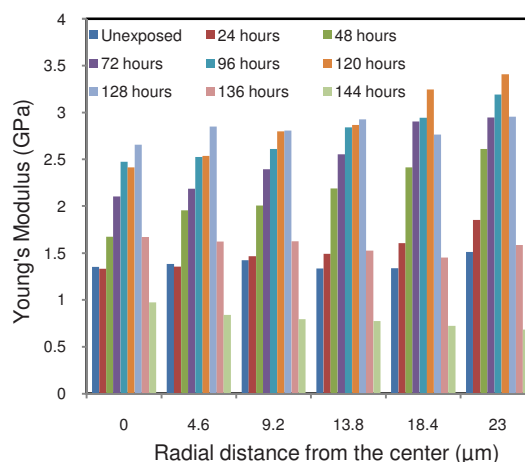


Fig.3. Variation of Young's modulus of UV exposed polypropylene fibers

Nano-indentation on UV exposed fibers proves that UV degradation initially increases the Young's modulus values from center to surface of the fibers until 120 hours of exposure and then becomes reduced when the exposure is further increased. The Young's modulus values at 128 and 136 hours show lower values than that of 120 hours, which implies that fiber micro-structural changes causing reduction of mechanical properties start at 120 hours. The Young's modulus values at 144 hours exposure are 50.9% of modulus values of unexposed fibers near the surface. Young's modulus values near to the surface of 120 hours UV exposed fibers showed an increase of 144.84% and at the center showed an increase of 73% compared to unexposed ones.

Wide Angle X-ray Spectroscopy (WAXS) was performed on the whole fiber to understand the changes of the fiber crystallinity. At an ultraviolet exposure of 120 hours, the diffraction arcs are turned into sharp spots and have been very prominent, implying that crystallinity and crystal orientation are highly developed. The 2D WAXS image of polypropylene exposed to 144 hours showed 'NO' crystallinity at all, only the amorphous halo was seen. These qualitative observations were verified by the calculation of percentage crystallinity. Table 1 shows the percentage crystallinity at each exposure. The unexposed fibers were 48.7% crystalline, while the 120 hours UV exposed fibers were 71.13% crystalline. When the UV exposure is further increased to 144 hours, the crystallinity is reduced to 32.16%.

Fourier transform infrared spectroscopy (FTIR) was performed on fibers to understand the new formations of chemical bonds upon UV exposure. The significant observation is the formation of carbonyl bond (C=O) corresponding to wavenumbers of $1681 - 1753\text{cm}^{-1}$ with increase of exposure. Young's modulus values were found to be almost unaltered up to three weeks of thermal exposure. A significant increase of Young's modulus values were observed closer to the surface in the fourth week. Variation of Young's modulus values of thermally exposed in the center of PP fiber remained the same. This implies that thermal degradation starts to have an effect on fiber microstructure closer to the surface on the fourth week at 125°C temperature and may propagate to fiber interior with an increase of time. The observed increase in Young's modulus values is attributed to the increase in crystallinity as confirmed by the WAXS analysis on thermally exposed PP fibers. The increase in crystallinity is caused by relaxation of chains, scissioned by thermal energy to folded structures within the amorphous regions.

Table 1: Percentage crystallinity for UV exposed PP fibers

UV Exposure Hours	Percentage Crystallinity (%)
Unexposed	48.70
24	69.68
48	67.71
72	66.58
96	66.70
120	71.13
128	39.62
136	38.13
144	32.16

REFERENCES

- Blais P, Carlsson DJ, Clark FRS, Sturgeon PZ, and Wiles DM., The Photo-oxidation of polypropylene mono-filaments, *Textile Research Journal*, 46: 641-648, 1976
- Billingham NC, Calvert PD. *Development of Polymer Stability*.3: 139. 1980

Detachment Dynamics of Cancer Cells

Chee Chung Wong,^{1,2} Julien Reboud,³ Jeffrey Soon,² Pavel Neuzil,⁴ and Kin Liao¹

¹ Division of Bioengineering, Nanyang Technological University, Singapore

² Institute of Microelectronics, A*Star, Singapore

³ Bioelectronics Research Centre, University of Glasgow, Glasgow

⁴ KIST Europe, Germany

Cell adhesion and detachment are crucial components in cancer spreading, often leading to recurrence and patient death [1]. Probing the mechanical behavior at the whole cell level while the cell is undergoing spreading and detachment during would enhance our understanding on cancer metastasis. However, these processes are not well understood in a quantitative sense, especially for the cancer cells [2]. In this article, we propose a bio-hybrid micro-device for the investigation of cellular attachment and detachment dynamics. This device comprises of silicon nanowires as electromechanical strain sensors, embedded in a suspended doubly-clamped silicon dioxide (SiO₂) microbridge (Fig. 1A & Fig. 2A) for breast cancer (MCF-7) cells seeding and attachment (Fig. 1B).

Polycrystalline silicon nanowires (NWs) 40 nm wide and 90 nm thick (Fig. 2A) were fabricated using conventional silicon process technologies as described in Reference [3]. The nanowires were strategically aligned along the length of a SiO₂ microbridge to maximize strain coverage and sandwiched between two layers of SiO₂ to eliminate surface effects of the NWs. Once released from the underneath substrate, the microbridge buckled upwards adopting a sinusoidal profile. The minute volume of NW as compared to that of the SiO₂ microbridge platform, all it to acts as “mechanically invisible” strain sensor for the measurement of topographical alterations in the buckled microbridge. MCF-7 cells with a concentration of 1×10^6 cells/ml were seeded on an arrays of 100 μm long, 20 μm wide and 0.5 μm thick suspended microbridges (see Fig. 2A). The cells were incubated at temperature 37 °C in 5% CO₂ for a period of 48 hours. Adhesion dynamic of MCF-7 cells were captured from the electrical response of the embedded NWs that were recorded at 6 hours intervals. After 2 days of incubation, MCF-7 cells form a conformal layer with a density of 3-5 cells over the length of the microbridges (see Fig. 1B). During the interrogation of MCF-7, their innate cell to cell communication was maintained with cells bridging from both anchors (see Fig. 1B). This approach allows precise cell quantification in terms of adhesion force, detachment dynamics as well as controlled sample interrogation, with high detection throughput.

The spreaded cells applied a traction force on the attached surface, analogous to an in-plane surface stress on the microbridge. This stress enhances the buckling amplitude of the microbridge which was measured as an increase in electrical resistance of the embedded NWs. The interface adhesion energy E_A between MCF-7 cells and the bridges is equivalent to the sum of flexural and elastic energy. While the elastic energy of the microbridge can be determined from the microbridge's elastic modules, its geometry and the extracted longitudinal axial strain in the NW, the flexural energy is a measure of the final microbridge topology. The longitudinal axial strain in NW is calculated from the ratio of normalized electrical change in the NW to piezoresistive gauge factor of the NW. Enhancement/reduction in buckling amplitude of microbridge was determined analytical with both the imposed strain and initial topographical parameters of the microbridge. The elastic energy was found to be two orders of magnitude larger than flexural energy for the same increase in buckling amplitude. Hence the normalized resistance change in NW can effectively evaluate the E_A of the cells on the microbridge.

Detachment dynamics of MCF-7 cells were conducted under reaction with digestive enzymes (trypsinization). Reductions in microbridge surface stress with the removal of cellular traction force on the bridge corresponds to an increase in electrical current (drop in resistance) in the embedded NWs (Fig. 3A). The cancerous cells exhibited exponential detachments profile at 37 °C (Fig. 3B) whereas control experiments conducted at 20 °C inhibited cell detachment. The E_A was $\sim 3 \text{ mJ/m}^2$ on each micro-beams with an average adhesion energy of 1~2 $\mu\text{J}/\text{cell}$. This bio-hybrid device has potential application in cancer therapeutics specifically for drugs targeted at adhesive receptors.

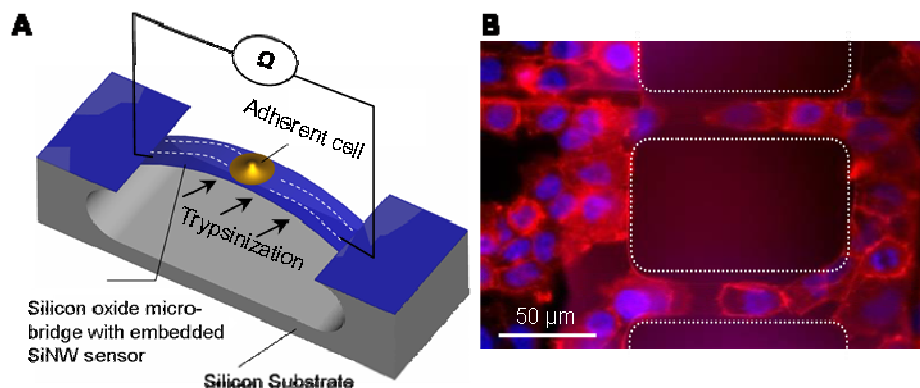


Figure 1. (A) Schematic of bio-hybrid micro-device with embedded silicon nanowires (NW) surface stress sensor for the investigation of cellular detachment dynamics (B) Fluorescence image of cancer cells aligned along the length of the microbridges (dotted in white) with nucleus stained in blue and actin cytoskeleton in red.

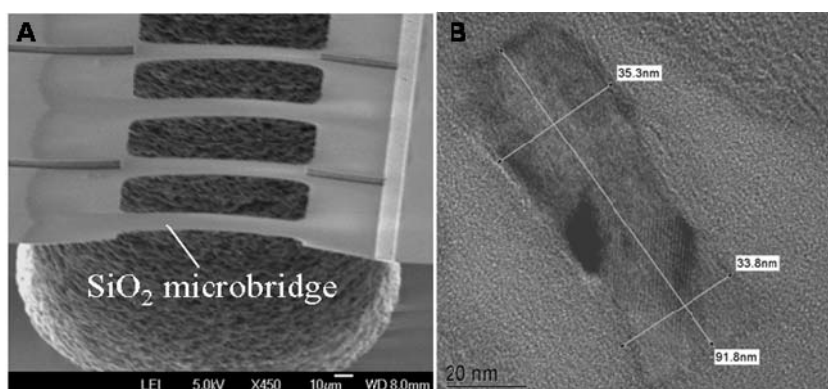


Figure 2. (A) Scanning electron micrograph of an array of suspended SiO_2 microbridges which buckled upwards due to the release of built-in stress gradient. (B) Cross-sectional TEM of an embedded polycrystalline silicon strain sensor.

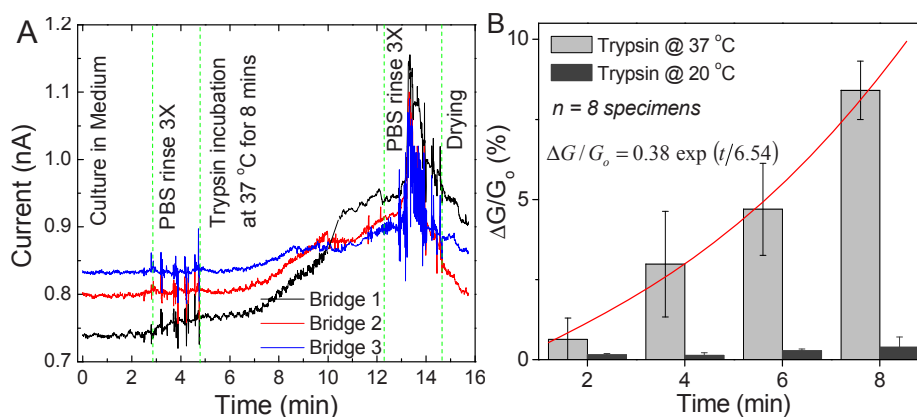


Figure 3. (A) Detachment dynamics of MCF-7 on 3 different microbridges. (B) Normalized conductance change in the NW as a function of trypsin incubation time.

[1] Friedl, P.; Wolf, K. Tumour-cell invasion and migration: Diversity and escape mechanism *Nature Reviews Cancer*, 3, (5), 362-374 **2003**.

[2] Schmidt, J.; Bosserhoff, A. K. Processing of MIA protein during melanoma cell migration *International Journal of Cancer*, 125, (7), 1587-1594 **2009**.

[3] Gao, Z. Q. et al. Silicon nanowire arrays for label-free detection of DNA *Analytical Chemistry*, 79, (9), 3291-3297 **2007**.

Compression Testing of Biomimetic Bones with 3D Deformation Measurements

Hang Yao, Wei Tong
Department of Mechanical Engineering
Southern Methodist University
Dallas, Texas 75275-0337 USA

ABSTRACT

Knowledge of mechanical properties of trabecular bones is important for the designing of bone replacements and implants as well as the research of bone diseases such as osteoporosis. However, due to difficulties on harvesting and preparing trabecular bone specimens, as well as uniqueness on microstructure and mechanical properties of each trabecular bone specimen, it is expensive to use real trabecular bone specimens to validate and to calibrate the experimental technique. In this research we use the open-cell aluminum foam as a replacement of the trabecular bone. Two 45° mirrors and two CCD cameras are used in our experimental setup to acquire images of four surfaces during the compression. Two-dimensional digital image correlation technique is used to measure surface deformations based on these images.

MATERIALS

Duocel open-cell aluminum foams (ERG Materials and Aerospace Corp., Oakland, US) with similar architecture as trabecular bones are used to as test materials in the compression testing. This aluminum foam has the range of nominal density 6-8% with various porosity, and is made of aluminum alloy 6101. Considering in compression testing of trabecular bones, soft tissues exist inside pores of trabecular bones, Sylgard 184 silicone elastomer (Dow Corning, Midland, US) is filled into pores of aluminum foam to mimic soft tissues. The specimens are cut in the size of 12mm by 12mm by 19mm (height).

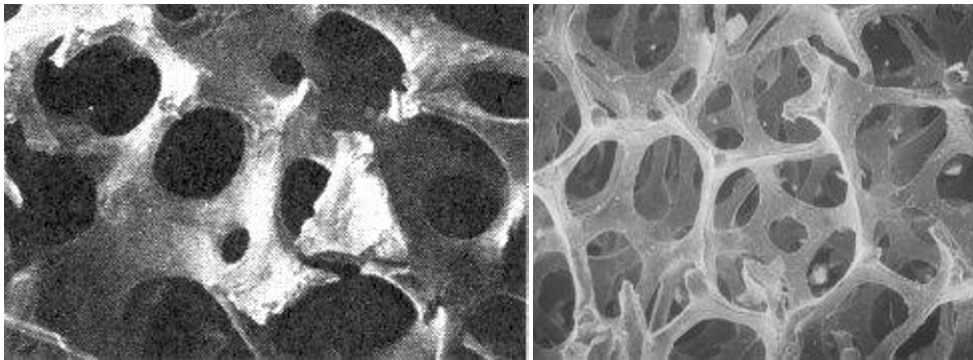


Figure 1. Left: human trabecular bone; right: Duocel aluminum foam (<http://www.ergaerospace.com/foamproperties/aluminumproperties.htm>).

EXPERIMENTAL METHOD

Instron E1000 testing machine is used to perform the compression testing. Two 45° mirrors and two CCD cameras are used to acquire images of all four surfaces during the compression testing. A camcorder is setup as a video extensometer on the side to measure the apparent strain.

Cyclic compression testing is performed. In order to observe failure behavior of the aluminum foam, the compression tests go beyond elastic deformation until the specimens fail. Apparent mechanical behaviors of aluminum foams, such as stiffness, strength, and failure, can be characterized.

Furthermore, using two-dimensional digital image correlation technique, the whole field, local surface deformations can be measured on all four surfaces. This feature is helpful to understand how microstructure contributes to the mechanical behaviors of the material.

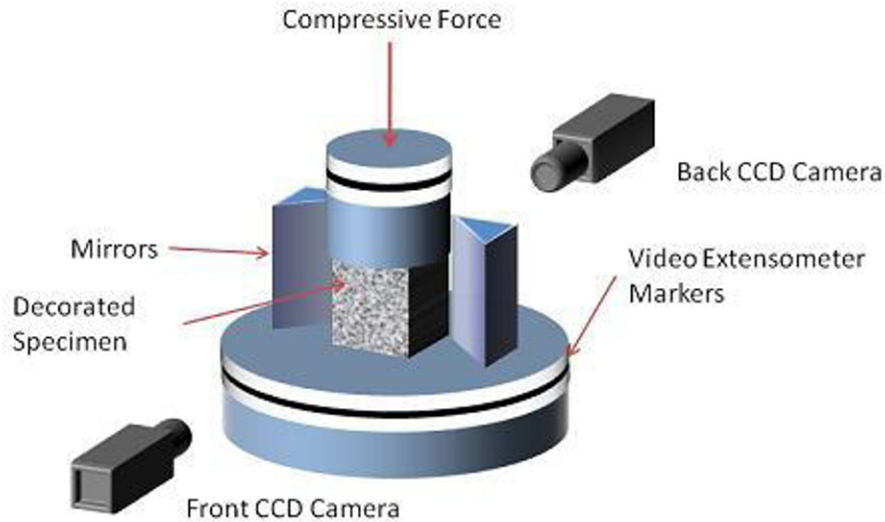


Figure 2. Experimental setup of the compression testing.

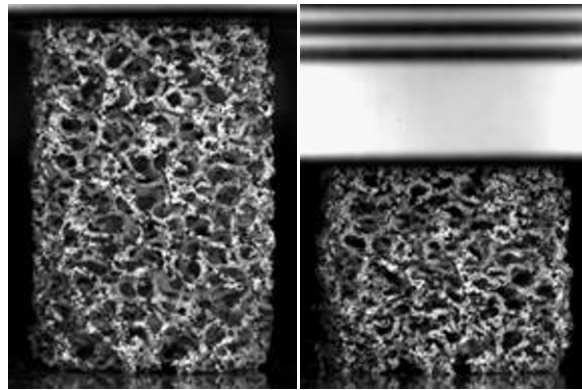


Figure 3. Images of the aluminum foam acquired from the CCD camera before and after the deformation.

CONCLUSION

The experimental techniques and measurement methods used on these biomimetic materials can be also applied to the future experiments on trabecular bones. Using biomimetic bones can avoid the problem caused by limitation of trabecular bone resources. Also this engineering material can be easily produced to achieve requirements on mechanical properties, such as density, porosity, and stiffness, to mimic specific trabecular bones if necessary.

Three-dimensional reconstructions can also be obtained by stacking sequential images created with a high resolution micro computed tomography scanner before and after the deformation. Using three-dimensional digital image correlation technique which has been developed, the 3D volume deformations can be measured and be correlated with the surface deformations, therefore validation of the 3D deformation measurement is established.